Springer Series in Materials Science 298

Horst Biermann
Christos G. Aneziris *Editors*

Austenitic TRIP/TWIP Steels and Steel-Zirconia Composites

Design of Tough, Transformation-Strengthened Composites and Structures

Springer Open

Springer Series in Materials Science

Volume 298

The Springer Series in Materials Science covers the complete spectrum of materials research and technology, including fundamental principles, physical properties, materials theory and design. Recognizing the increasing importance of materials science in future device technologies, the book titles in this series reflect the state-of-the-art in understanding and controlling the structure and properties of all important classes of materials.

More information about this series at http://www.springer.com/series/856

Horst Biermann · Christos G. Aneziris
Editors

Austenitic TRIP/TWIP Steels and Steel-Zirconia Composites

Design of Tough, Transformation-Strengthened Composites and Structures

Springer Open

Editors
Horst Biermann
Institut für Werkstofftechnik
TU Bergakademie Freiberg
Freiberg, Sachsen, Germany

Christos G. Aneziris
Institut für Keramik, Glas- und Baustofftechnik
TU Bergakademie Freiberg
Freiberg, Sachsen, Germany

ISSN 0933-033X ISSN 2196-2812 (electronic)
Springer Series in Materials Science
ISBN 978-3-030-42602-6 ISBN 978-3-030-42603-3 (eBook)
https://doi.org/10.1007/978-3-030-42603-3

This Springer imprint is published by the registered company Springer Nature Switzerland AG
The registered company address is: Gewerbestrasse 11, 6330 Cham, Switzerland

Preface

The fundamental development of new materials is an essential basis for scientific knowledge and economic success. This awareness motivates research into forward-looking technologies for the production of resource-saving materials. New material properties, such as those made possible by composite materials, are of central importance for new, durable products and safety components, particularly in the areas of mobility and mechanical engineering. This motivates the vision of the marriage of modern high-performance steels of the highest strength and formability with damage-tolerant ceramics as a prime example of innovative manufacturing technologies for a new class of high-performance composites.

In concrete terms, this book aims to combine new high-alloy TRIP steels (TRIP: TRansformation-Induced Plasticity) with zirconium dioxide ceramics on powder metallurgical routes and via melt infiltration to form new composite materials, the "TRIP-Matrix Composites". Groundbreaking new processes are used, such as the production and combination of metalloceramic paper, hollow and solid spheres and filigree honeycomb bodies, which enable excellent formability and a largely free geometric design of lightweight components for mobility applications.

This book is the final publication of the Collaborative Research Centre (SFB 799) "TRIP-Matrix Composite—Design of tough, transformation-reinforced composites based on Fe and ZrO_2". The Collaborative Research Centre funded by the German Research Foundation (DFG) ran from 2008 to 2020 at the Technische Universität Bergakademie Freiberg, Germany. The chapters contained in this book provide an overview of the most important results of the projects of the Collaborative Research Centre in the completed funding periods and at the same time present current, in some cases still unpublished results.

The book is thematically divided into three sections, (i) the synthesis of TRIP-Matrix Composites, (ii) the characterisation of the materials produced and (iii) simulation and modelling. In these three sections, new and innovative materials and their synthesis pathways were explored.

Powder metallurgical processes were an important focus of several projects, see Chaps. 1 and 5–9. An essential contribution to the production of the new composite materials is the development of new high-alloy austenitic stainless steels and steel

powders with excellent properties, which serve as matrix for the composite materials, as described in Chaps. 2 and 3, respectively. The melting metallurgical marriage of the steels with ZrO_2 presented in Chap. 4 also resulted in new effects and promising approaches. Finally, the joining of composite materials was also investigated, see Chap. 10.

The characterisation of the new composites and the steel alloys is described in Chap. 11 with respect to the microstructure and in Chaps. 12–14 for the uniaxial, quasi-static, dynamic, fracture mechanical, cyclic as well as multi-axial mechanical properties. A special insight into the kinetics of the occurring deformation and damage mechanisms is provided by the methods of in situ investigation of the new materials described in Chaps. 15 and 16. Corrosion research (Chap. 17) also plays an important role for later applications.

An integral part of the description of the material properties are the projects for modelling the processes (Chap. 18) and the thermodynamics of the phases involved (Chap. 19), the coupled thermodynamic-mechanical modelling (Chap. 20) and the continuum mechanical and multi-scale modelling of the behaviour of ZrO_2 (Chap. 21) and of TRIP steels (Chap. 22), as well as the micromechanical simulations (Chaps. 23 and 24). In these projects, new approaches for the description of materials and processes were developed and applied to the materials produced in the Collaborative Research Centre.

As speaker and deputy speaker, we would like to thank all current and former members of the Collaborative Research Centre for their constant support. The successful work would not have been possible without the dedicated cooperation of all scientists who worked on or supported the projects. We would also like to thank other contributors, all technical and administrative staff as well as the countless students for their outstanding cooperation.

Due to the excellent scientific work, the Collaborative Research Centre has been able to produce the basis for many scientific qualification theses, from habilitations and doctorates to student theses. In this way, numerous scientific careers have been established over 12 years and many graduates have been shaped scientifically. This young talent work was also promoted within the framework of a graduate school, which taught many soft skills in addition to professional qualifications.

We would also like to thank the public relations team, which made the scientific results available to a broad public and thus made an important contribution to the reputation of the Technische Universität Bergakademie Freiberg. This public relations work has also interested many students in the special research areas of the Collaborative Research Centre and thus drawn their attention to the university's courses of study.

We would also like to highlight the support of the industrial board.

Our special thanks go to the German Research Foundation for the trust it has placed in us and for funding (project number: 54473466), in particular to E. Effertz, S. Isernhagen and R. Nickel from the Collaborative Research Centres Department, F. Fischer, B. Jahnen and X. Molodova from the Materials Science and Engineering Department and Mrs. Hammel and Mrs. C. Niebus from the administration centre. We are also deeply indebted to all the experts who have

followed our work with interest as referees as well as to the members of the Senate Committee of the German Research Foundation.

Finally, we would like to thank Mrs. A. Beier and P. Michel, whose work in the office of the Collaborative Research Centre ensured the smooth running of all financial aspects and the organisation of all events.

Freiberg, Germany

Horst Biermann
Christos G. Aneziris

Contents

Contributors

Christos G. Aneziris Institute of Ceramic, Glass and Construction Materials, Technische Universität Bergakademie Freiberg, Freiberg, Germany

Christine Baumgart Institute of Materials Engineering, Technische Universität Bergakademie Freiberg, Freiberg, Germany

Harry Berek Institute of Ceramic, Glass and Construction Materials, Technische Universität Bergakademie Freiberg, Freiberg, Germany

Horst Biermann Institute of Materials Engineering, Technische Universität Bergakademie Freiberg, Freiberg, Germany

Sebastian Borrmann Institute of Mechanics and Fluid Dynamics, Technische Universität Bergakademie Freiberg, Freiberg, Germany

Anja Buchwalder Institute of Materials Engineering, Technische Universität Bergakademie Freiberg, Freiberg, Germany

Michael Budnitzki Institute of Mechanics and Fluid Dynamics, Technische Universität Bergakademie Freiberg, Freiberg, Germany

Andreas Burgold Institute of Mechanics and Fluid Dynamics, Freiberg, Germany

Humberto Chaves Institute of Mechanics and Fluid Dynamic, Technische Universität Bergakademie Freiberg, Freiberg, Germany

Sabine Decker Institute of Materials Engineering, Technische Universität Bergakademie Freiberg, Freiberg, Germany

Claudia Dommaschk Foundry Institute, Technische Universität Bergakademie Freiberg, Freiberg, Germany

Matthias Droste Institute of Materials Engineering, Technische Universität Bergakademie Freiberg, Freiberg, Germany

Ralf Eckner Institute of Materials Engineering, Technische Universität Bergakademie Freiberg, Freiberg, Germany

Olga Fabrichnaya Institute of Materials Science, Technische Universität Bergakademie Freiberg, Freiberg, Germany

Sergey Guk Institute for Metal Forming, Technische Universität Bergakademie Freiberg, Freiberg, Germany

Lars Halbauer Institute of Materials Engineering, Technische Universität Bergakademie Freiberg, Freiberg, Germany

Michael Hauser Institute of Iron and Steel Technology, Technische Universität Bergakademie Freiberg, Freiberg, Germany

Sebastian Henkel Institute of Materials Engineering, Technische Universität Bergakademie Freiberg, Freiberg, Germany

Claudia Heuer Institute of Ceramic, Glass and Construction Materials, Technische Universität Bergakademie Freiberg, Freiberg, Germany

Qiuliang Huang Institute of Iron and Steel Technology, Technische Universität Bergakademie Freiberg, Freiberg, Germany

Rudolf Kawalla Institute for Metal Forming, Technische Universität Bergakademie Freiberg, Freiberg, Germany

Björn Kiefer Institute of Mechanics and Fluid Dynamics, Technische Universität Bergakademie Freiberg, Freiberg, Germany

Volodymyr Kietov Institute of Materials Engineering, Technische Universität Bergakademie Freiberg, Freiberg, Germany

Markus Kirschner Institute for Metal Forming, Technische Universität Bergakademie Freiberg, Freiberg, Germany

Iurii Korobeinikov Institute of Iron and Steel Technology, Technische Universität Bergakademie Freiberg, Freiberg, Germany

Lutz Krüger Institute of Materials Engineering, Technische Universität Bergakademie Freiberg, Freiberg, Germany

Meinhard Kuna Institute of Mechanics and Fluid Dynamics, Technische Universität Bergakademie Freiberg, Freiberg, Germany

Robert Lehnert Institute of Materials Engineering, Technische Universität Bergakademie Freiberg, Freiberg, Germany

Marcel Mandel Institute of Materials Engineering, Technische Universität Bergakademie Freiberg, Freiberg, Germany

Stefan Martin Institute of Materials Science, Technische Universität Bergakademie Freiberg, Freiberg, Germany

Javad Mola Material Design and Structural Integrity Lab, Osnabrück University of Applied Sciences, Osnabrück, Germany

Mykhaylo Motylenko Institute of Materials Science, Technische Universität Bergakademie Freiberg, Freiberg, Germany

Sebastian Neumann Institute of Mechanics and Fluid Dynamics, Technische Universität Bergakademie Freiberg, Freiberg, Germany

Marie Oppelt Institute of Ceramic, Glass and Construction Materials, Technische Universität Bergakademie Freiberg, Freiberg, Germany

Ulrich Prahl Institute for Metal Forming, Technische Universität Bergakademie Freiberg, Freiberg, Germany

Stefan Prüger Institute of Mechanics and Fluid Dynamics, Technische Universität Bergakademie Freiberg, Freiberg, Germany

Markus Radajewski Institute of Materials Engineering, Technische Universität Bergakademie Freiberg, Freiberg, Germany

David Rafaja Institute of Materials Science, Technische Universität Bergakademie Freiberg, Freiberg, Germany

Paul Rähmer Albert Hoffmann GmbH, Eschweiler, Germany

Mohan Kumar Rajendran Institute of Mechanics and Fluid Dynamics, Technische Universität Bergakademie Freiberg, Freiberg, Germany

Ivan Saenko Institute of Materials Science, Technische Universität Bergakademie Freiberg, Freiberg, Germany

Stefan Sandfeld Institute of Mechanics and Fluid Dynamics, Technische Universität Bergakademie, Freiberg, Germany

Rüdiger Schwarze Institute of Mechanics and Fluid Dynamics, Technische Universität Bergakademie Freiberg, Freiberg, Germany

Andreas Seupel Institute of Mechanics and Fluid Dynamics, Freiberg, Germany

Rachel Strobl Institute of Mechanics and Fluid Dynamics, Freiberg, Germany

Christiane Ullrich Institute of Materials Science, Technische Universität Bergakademie Freiberg, Freiberg, Germany

Olena Volkova Institute of Iron and Steel Technology, Technische Universität Bergakademie Freiberg, Freiberg, Germany

Anja Weidner Institute of Materials Engineering, Technische Universität Bergakademie Freiberg, Freiberg, Germany

Christian Weigelt Institute of Ceramic, Glass and Construction Materials, Technische Universität Bergakademie Freiberg, Freiberg, Germany

Andreas Weiß Institute of Iron and Steel Technology, Technische Universität Bergakademie Freiberg, Freiberg, Germany

Marco Wendler Institute of Iron and Steel Technology, Technische Universität Bergakademie Freiberg, Freiberg, Germany

Carl H. Wolf Institute of Materials Engineering, Technische Universität Bergakademie Freiberg, Freiberg, Germany

Gotthard Wolf Foundry Institute, Technische Universität Bergakademie Freiberg, Freiberg, Germany

Chapter 1
Ceramic Casting Technologies for Fine and Coarse Grained TRIP-Matrix-Composites

Claudia Heuer, Marie Oppelt and Christos G. Aneziris

Abstract The present contribution focuses on the development of composite materials using innovative *ceramic casting technologies*. Within this work different processing routes, the relevance of their process parameters as well as the resulting mechanical and microstructural characteristics are discussed. The successfully developed TRIP-matrix foams as well as full beads reinforced with 5 and 10 vol.% zirconia achieve higher compressive strengths and energy absorption during deformation in comparison to the pure metal materials as references. The functionally graded beads allowed a compression of up to 20% with corresponding specific energy absorption of 10.7 kJ/kg. In a further approach, metal-matrix composites have been generated via *paper-manufacturing technology*. The partial replacement of cellulose fibers by commercially available zirconia fibers resulted in fiber reinforced TRIP-matrix composites with an increased tensile strength of approx. 33% as compared to the pure metal material as reference. Large-size ceramic matrix composites with high potential for applications requiring sufficient wear and thermal shock resistance have been successfully prepared via *pressure slip casting*. The last topic is concerned with the development of yttria-stabilized zirconia fibers with a tailored phase composition (monoclinic-tetragonal-cubic) via *electrospinning*.

1.1 Introduction

The increasing technological demand within the last decades led to the development of composites significantly enlarging the application field of conventional materials. The research efforts are not only concerned with innovative material systems but also with novel fabrication technologies, always with the aim to create composites with

C. Heuer (✉) · M. Oppelt · C. G. Aneziris
Institute of Ceramic, Glass and Construction Materials, Technische Universität Bergakademie Freiberg, Agricolastr. 17, 09599 Freiberg, Germany
e-mail: claudia.heuer@ikgb.tu-freiberg.de

H. Biermann and C. G. Aneziris (eds.), *Austenitic TRIP/TWIP Steels and Steel-Zirconia Composites*, Springer Series in Materials Science 298,
https://doi.org/10.1007/978-3-030-42603-3_1

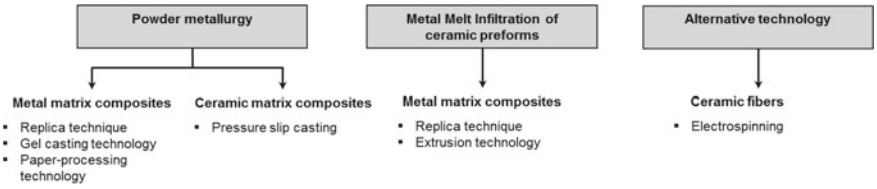

Fig. 1.1 Flowchart of the applied casting technologies

superior mechanical, thermal, thermo-mechanical, wear- and damping-related properties. Within the frame of the Collaborative Research Center 799—TRIP-matrix-composites based on metastable austenitic steel and magnesia partially stabilized zirconia are of interest. The combination of metastable austenitic steel with transformation induced plasticity with magnesia partially stabilized zirconia is advantageous in terms of high strength and specific energy absorption. [1, 2] Both materials exhibit a martensitic phase transformation triggered upon exposure to external stresses.

The present work focuses on the development of metal matrix and ceramic matrix composites using innovative casting technologies that are typically employed for the fabrication of ceramic components (Fig. 1.1). A main emphasis is the development *of metal matrix composites* (*MMC*) using the replica technique, the gel casting and the paper technology. Furthermore, the infiltration of ceramic preforms by TRIP-steel melts was studied. The preforms are prepared using the replica technique or extrusion technology. *Ceramic matrix composites* (*CMC*) are generated using the pressure slip casting technology. In addition to that electrospinning has been applied for the development of zirconia fibers with tailored phase compositions. Within the present work the different processing routes, the relevance of their process parameters and the resulting microstructural and mechanical characteristics will be illustrated and discussed.

1.2 Experimental Details

This work is divided into four main parts; the first one deals with the development of TRIP-matrix composites by replica technique, gel casting and paper-processing technology. The second part concerns the metal melt infiltration of ceramic preforms (obtained via replica technique and extrusion). The development of ceramic matrix composites by pressure slip casting was the third part of the study. Finally, an alternative technology for the fabrication of zirconia fibers is introduced. The following section will provide information on the raw materials as well as on the methods of characterization. The sample preparation for the mentioned technologies will be illustrated.

1.2.1 Raw Materials

1.2.1.1 Magnesia Partially Stabilized Zirconia

Within the present work three different types of fused cast magnesia partially stabilized zirconia (Saint Gobain, USA) have been used. The zirconia powders are hereinafter referred to as Mg-PSZ (fine) with $d_{50} = 1.3$ µm, Mg-PSZ (coarse) with $d_{50} = 3.0$ µm and Mg-PSZ (new) with $d_{50} = 4.3$ µm. The chemical compositions of the different Mg-PSZ powders are summarized in Table 1.1.

1.2.1.2 Austenitic Stainless TRIP-Steel

Three different types of austenitic stainless steel powder (TLS Technik Bitterfeld, Germany) have been utilized in the present work. The commercially available AISI 304 (X5CrMnNi18-1-10) with a mean particle size of 33 µm has been employed for the development of MMCs via replica technique. The other steel powders following referred to as X8CrMnNi16-7-3 ($d_{50} = 21.9$ µm) and X3CrMnNi16-7-6 ($d_{50} = 25$ µm) had a substantially higher manganese content, which partially replaced nickel. The true densities were determined to be 7.83 g/cm^3 (X5CrMnNi18-1-10), 7.78 g/cm^3 (X8CrMnNi16-7-3) and 7.83 g/cm^3 (X3CrMnNi16-7-6), respectively. During the investigations several steel batches have been used having minor differences in their chemical composition, see Table 1.2.

1.2.1.3 Alumina

Calcined and reactive alumina powders were used for the pressure slip casting of alumina based composites. The fine and coarse grained powders had mean particle

Table 1.1 Chemical compositions of the zirconia powders in wt.%

	ZrO_2	MgO	HfO_2	SiO_2	Al_2O_3	TiO_2
Mg-PSZ (fine)	Bal.	3.37	1.73	2.43	0.63	0.14
Mg-PSZ (coarse)	Bal.	2.82	1.74	0.41	0.38	0.13
Mg-PSZ (new)	Bal.	1.85	1.85	0.10	1.58	0.13

Table 1.2 Chemical compositions of the steel powders in wt.%

	Fe	Cr	Mn	Ni	C	Si	S
PMX5CrMnNi18-1-10	Bal.	17.50–18.10	1.13–1.30	7.8–8.74	0.03–0.05	0.40–0.55	0.01–0.02
PMX8CrMnNi16-7-3	Bal.	15.60–16.70	6.02–7.14	3.04–3.50	0.04–0.08	0.80–0.93	0.00–0.01
PMX3CrMnNi16-7-6	Bal.	15.90–16.30	7.10–7.20	6.60–6.90	0.02–0.03	1.00–1.16	0.01

sizes ranging from 0.2 μm to 3 mm and were provided by Almatis (Ludwigshafen, Germany) and Martinswerke (Bergheim, Germany), respectively.

1.2.1.4 Raw Materials for Electrospinning

For the development of nanofibers via electrospinning high purity zirconyl chloride octahydrate (Sigma Aldrich Steinheim, Germany), yttrium (III) nitrate hexahydrate (Sigma Aldrich Steinheim, Germany) and magnesium nitrate hexahydrate served as precursor materials for the synthesis of zirconia fibers stabilized with 3 mol.% yttria and 8 mol.% magnesia, respectively. Granular polyvinylpyrrolidone (PVP) with an average M_w of $1.3 \times 1\,0^6$ g/mol (Sigma Aldrich Steinheim, Germany) was employed as polymeric component. The starting materials were dissolved in deionized water and ethanol with a purity of ≥99.8% (Carl Roth Karlsruhe, Germany), respectively. Triton X (Sigma Aldrich Steinheim, Germany) was used as non-ionic surfactant.

1.2.2 Sample Preparation

1.2.2.1 Development of TRIP-Matrix Composites via Powder Metallurgy

Aneziris et al. [3] produced open cell foam structures via ***replica technique*** from 30 ppi (pores per inch) polyurethane foams with dimensions of 50 × 50 × 20 mm^3. Two different compositions based on 100 vol.% steel powder (0Z) and 90 vol.% steel powder and 10 vol.% Mg-PSZ powders (10Z) were evaluated. The composition of the impregnation slurries is shown in Table 1.3. The polyurethane foams were fully immersed in the slurry, afterwards the excess slurry was removed with the aid of a manual roller mill. After this first impregnation step the filters were dried at 90 °C for 1 h. In a second coating step the dried foams were sprayed with a spraying slurry based on the same composition as the impregnation slurry, see Table 1.3. The spraying slurry was prepared using a ViscoJet stirrer system. The spray coating was performed with the aid of a SATAjet B spraying gun 1.0 E nozzle type. In a further version, a dense coating (hereafter indicated by the letter "J" in the slurry compositions) of approx. 1.5 mm thickness was applied on the 50 × 20 mm^2 side surfaces for both slurry compositions. The corresponding samples were designated to as 0ZJ and 10ZJ. After drying the samples have been sintered at 1350 °C for 2 h in an electrical furnace Linn HT 1600 GT Vac with $MoSi_2$-heating elements in 99.9.% argon atmosphere.

Full and hollow TRIP-matrix composite beads were prepared with the aid of gel casting. The composition of the slurries with a powder to water ratio of 70:30 is given in Table 1.4. For the generation of full beads calcium chloride was chosen as hardener and the prepared aqueous hardener solution contained 0.8 wt.% calcium chloride [4]. For the fabrication of hollow beads calcium hydroxide had to be applied

Table 1.3 Composition of the slurries for replica technique in wt.% [3]

	Type	Supplier	0Z	10Z
Raw materials				
Austenitic TRIP- steel powder	PMX5CrMnNi18-1-10	TLS Technik, GER	94.99	87.67
ZrO_2	Mg-PSZ (coarse)	Saint Gobain, USA	–	7.32
Additives				
Antifoam	Axilat DF 581 B	C.H. Erbslöh, GER	0.11	0.11
Surfactant	PPG P400	Sigma-Aldrich, GER	0.55	0.55
Binder	Optapix PAF 35	Zschimmer and Schwarz, GER	1.66	1.66
Dispersant	Darvan C	R.T. Vanderbilt, USA	0.47	0.47
Binder	Ligninsulfonate T11B	Otto Dille, GER	1.66	1.66
Stabilizer	Axilat RH 50 MD	C.H. Erbslöh, GER	0.56	0.56
		Total	100	100
Dispersing fluid				
Water (coating)	Deionized		9.5	9.5
Water (spraying)	Deionized		19.2	19.2

Table 1.4 Composition of the slurries used for gel casting in wt.% [7]

	Type	Supplier	0Z	5Z	10Z	20Z	100Z
Raw materials							
Austenitic TRIP-steel powder	PMX8CrMnNi 16-7-3	TLS, GER	68.47	65.00	61.83	54.62	–
ZrO_2	Mg-PSZ (coarse)	Saint Gobain, USA	–	3.47	6.64	13.85	68.47
Additives							
Sodium alginate	FD 175	C.E. Roeper, GER	0.42	0.42	0.42	0.42	0.42
Plasticizer	Darvan C	R.T. Vanderbilt, USA	0.69	0.69	0.69	0.69	0.69
Stabilizer	KM2000	Zschimmer and Schwarz, GER	0.42	0.42	0.42	0.42	0.42
Dispersing fluid							
Water	Deionized		30	30	30	30	30

Table 1.5 Composition of the feedstocks excluding water in vol.%

	Type	Supplier	0Z	10Z	3ZF	6ZF
Raw materials						
Austenitic TRIP-steel powder	PMX3CrMnNi 16-7-6	TLS Technik, GER	78.5	71.2	78.5	78.5
ZrO_2	Mg-PSZ (new)	Saint Gobain, USA	–	7.9	–	–
ZrO_2-Fibers	Yttria-stabilized	Final GmbH, GER	–	–	2.5	5.0
Cellulose	–	Zellstoff Pöls AG, AT	14.5	14.1	12.0	9.5
Additives						
Starch	–	Südstärke Chemie, GER	7.0	7.0	7.0	7.0

as hardener in a 1.0 wt.% aqueous hardener solution [5]. The prepared slurries were added dropwise into the hardener solutions and thus solidification took place. Additionally, functionally graded beads were prepared as described by Oppelt et al. [6]. The wet green beads were removed from the hardener solution and dried for 24 h at 40 °C. After debinding, the beads were sintered in an inert atmosphere (Ar 5.0) in an XGraphit furnace (XERION Ofentechnik Freiberg, Germany) with a heating rate of 1 K/min up to 660 °C with a dwelling time of 60 min at 660 °C, followed by a heating rate of 5 K/min up to 1350 °C and a dwelling time of 120 min at 1350 °C. The cooling rate was 5 K/min.

The development of TRIP-matrix composites via ***paper-manufacturing technology*** comprised several steps. The pulp suspension contained 0.27 wt.% cellulose fibers and 0.01 wt.% cationic starch. In order to obtain the feedstock, a 90 wt.% aqueous suspension containing stainless steel, magnesia partially stabilized zirconia, and 0.17 wt.% anionic starch were added to the pulp suspension. In context of the development the cellulose pulp fibers have been partially replaced (2.5 and 5 vol.%) by commercially available yttria-stabilized zirconia fibers. Thus, fiber reinforced TRIP-matrix composites were prepared. The composition of the feedstock excluding water is given in Table 1.5. Square paper sheets with 200 mm in length were then formed on a laboratory sheet-forming device. The green sheets were stepwise dried starting from 40 °C up to 110 °C within 24 h. Subsequently, the dried paper sheets were calendered on a rolling mill applying a line load of 30 kN/mm at a roller speed of 0.1 m/s. The calendered sheets were thermally treated using an debinding and sintering process developed by Wenzel [8].

1.2.2.2 Development of TRIP-Matrix Composites via Metal Melt Infiltration of Ceramic Preforms

Open cell foam structures based on magnesia-partially stabilized zirconia for the infiltration with TRIP-steel melts were prepared using the ***replica technique***. The

fabrication of these foam structures comprises two coating steps as mentioned before. The impregnation of the polyurethane foams was done according to the description in Sect. 1.2.2.1. The spray coating procedure was modified and performed airstream assisted. The impregnated foam was therefore placed into a tubular sample holder connected to a vacuum unit. The distance between sample holder and spraying gun was set to 27 cm for all experiments; the pressure of the compressed air was maintained at 0.3 MPa. The mass flow of the slurry was set to 80 g/min and the foams were sprayed for 8 s. A detailed description of the experimental setup is given elsewhere [9]. The spraying slurries were prepared with different powder to water ratios. The spraying slurries contained 40 wt.% water, 45 wt.% and 55 wt.% water, respectively After coating, the foams were dried at 110 °C. Debinding and sintering was performed in an oxidizing atmosphere. Debinding took place at 500 °C with a heating rate of 1 K/min and a holding time of 60 min. Sintering was performed at 1600 °C with a heating rate of 5 K/min and a dwell time of 120 min.

The ***extrusion technology*** was applied as a further option for the fabrication of porous ceramic preforms, honeycombs and randomly arranged spaghetti-filters, which have been casted with TRIP-steel melt. The preparation and the extrusion of the different plastic feeds are described in detail by Wenzel and Aneziris [10] and Schärfl et al. [11]. Honeycomb specimens with 196 cpsi (channels per square inch) and a wall thickness of 250 μm as well as randomly arranged full strand-spaghetti-filters with a strand diameter of 1 mm have been prepared. Both extruded ceramic preform types were sintered in an electrical heating furnace with $MoSi_2$-heating elements in oxidizing atmosphere. The heating rate was 1 K/min to 350 °C with a holding time of 90 min and then 3 K/min to 1650 °C with a holding time of 120 min.

Subsequently, the ceramic preforms were infiltrated by a ***Cast*** X5CrMnNi16-7-7 steel melt in order to obtain bulk TRIP-matrix composites. Therefore, the preforms were preheated to 1000 °C with a holding time of 10 h and then placed in an unheated sodium silicate bonded SiO_2 sand mold. The samples were fixed to the bottom of the mold. The experimental setup is discussed in detail by Weider and Eigenfeld [12]. The steel casting took place with a temperature of 1600 °C in oxidizing atmosphere. A constant height of the feeder was guaranteed due to an inclined drainage for excess steel.

1.2.2.3 Development of Ceramic Matrix Composites via Pressure Slip Casting

Slip preparation comprised several steps, starting with the addition of the organic additives Welan Gum and Konjac flour in deionized water for 10 min using a Heidolph homogenizer DIAX 600 (Heidolph Instruments Schwabach, Germany). Subsequently, the solid fractions and the additive-water mixture have been homogenized for 15 min in an intensive laboratory mixer RV02 (Maschinenfabrik Gustav Eirich Hardheim, Germany) to obtain the slurries. Casting was performed in a modified industrial pressure slip casting device DGM80D (Dorst Technology Kochel am See, Germany). The suspension was pumped from a receiver tank into a polyurethane

mould (200 × 200 × 38 mm^3) at a pressure of 0.1–0.15 MPa. The pressure was then increased to 2 MPa and held constant for the whole casting time of 25 min. Afterwards, the pressure was released and the green specimens have been demoulded. The casted bodies were subsequently dried up to 110 °C. Debinding took place in an oxidizing atmosphere with a heating rate of 1 K/min up to 400 °C and a dwelling time of 90 min at 400 °C. Sintering was conducted in a XGraphit furnace (XERION Ofentechnik Freiberg, Germany) with a heating rate of 5 K/min to 1450 °C and a holding time of 120 min and an argon flow rate of 2.5 l/min at an excess pressure of 5 mbar.

1.2.2.4 Development of Ceramic Fibers Using Electrospinning

With the aid of the *electrospinning technology yttria-stabilized zirconia fibers* have been developed. First, a 18 wt.% precursor solution was prepared by dissolving $ZrOCl_2 \cdot 8\ H_2O$ and $Y(NO_3)_3 \cdot 6\ H_2O$ in deionized water in a ratio that corresponds to the final composition ZrO_2–3 mol.% Y_2O_3. In a second step, a 7 wt.% polymeric solution was obtained by dissolving the granular PVP in ethanol. The polymeric solution was stirred on a magnetic stirrer at 500 rpm for 30 min. The polymeric solution was then poured stepwise into the precursor solution with a 3:1 weight ratio. Finally, 0.5 wt.% Triton X was added and the stock solution was further stirred at 250 rpm for 240 min. The electrospinning was conducted using an electrospinning device NE 300 (Inovenso Istanbul, Turkey) with a bottom-up configuration and a 4-nozzles feeding unit, each nozzle having an inner diameter of 0.8 mm. The processing temperature and relative humidity were kept constant at 23 °C and 40%, respectively. The stock solution was fed at 3.5 ml/h with a high precision syringe pump (New Era Pump Systems Farmingdale, USA). The electrospinning was carried out at a voltage of 24 kV using a DC power supply at a distance between needle tip and collector of 75 mm. The fibers were collected on a drum that was covered with alumina foil and which was rotating at 300 rpm. The sintering of the nanofibers was performed at different temperature of 700, 1100, 1350 and 1650 °C.

1.2.3 Characterization of the Composite Materials

1.2.3.1 Rheological Characterization of the Slurries

The rheological properties of the slurries developed for the gel-casting of metal beads as well as for the impregnation and spraying of polyurethane foams were investigated using a rotational viscometer Haake RheoStress 150 (ThermoHaake Karlsruhe, Germany). The rheological experiments were carried out under shear control. For the gel-casting the slurries were investigated with a given shear rate of 1–500 s^{-1} in 150 s. After a holding time of 100 s at 500 s^{-1} the shear rate was decreased again. The slurries for the impregnation of the polyurethane foams were

investigated with given shear rates of 1–200 s^{-1} or 1000 s^{-1} in 300 s. After a holding time of 60 s at 200 s^{-1} and 1000 s^{-1} respectively it was stepwise decreased to 1 s^{-1}.

1.2.3.2 Thermal Analysis

Highly relevant aspects for the development of composite materials containing TRIP-steel are investigations on the thermal decomposition behavior of the temporary additives. Differential scanning calorimetry (DSC) combined with thermo-gravimetric measurements (TG) were performed using a STA 409 (NETZSCH Waldkraiburg, Germany). During decomposition experiments the DSC/TG device was flushed with synthetic air. For the fabrication of metal beads using gel-casting the decomposition behavior of sodium alginate was of fundamental importance. The chosen heating rate was 10 K/min to 1000 °C. For the paper-derived TRIP-matrix composites the decomposition behavior of the cellulose pulp fibers was investigated up to 800 °C with a heating rate of 1 K/min.

1.2.3.3 Physical Properties

The linear shrinkage after sintering was calculated according to DIN EN 993-10. For the full and hollow metal beads, the pressure slip-casted ceramic matrix composites as well as for the zirconia preforms obtained by extrusion the open porosity, the pore size distribution as well as the bulk density were investigated with the aid of a mercury porosimeter (PASCAL series, Porotec Hofheim am Taunus, Germany). The thickness of the paper-derived TRIP-matrix composites was determined after processing and calendering at five different positions for each sheet using a digital vernier caliper and an analogue dial gauge. The bulk density was determined from weight and volume measurements before and after sintering. The volume of the samples was determined by displacement in mercury volume meter. The theoretical density of the composite mixtures was calculated according to the rule of mixture using the density of the initial powders as measured by helium pycnometry.

1.2.3.4 Mechanical Properties

The mechanical properties of the different composites were determined. Compressive deformation tests have been performed on a 500 kN servohydraulic testing device type MTS 880 (MTS Systems Eden Prairie, USA) with a displacement rate of 0.016 mm/s for the TRIP-matrix composite foams prepared via ***replica technique***. For the hollow and full TRIP-matrix composite beads the compressive deformation strength was measured with a testing machine TT 2420 (TIRA Schalkau, Germany) arranged with a measuring equipment for single granules. 20 beads of each composition have been tested to failure with a displacement rate of 0.05 mm/s. In case of functionally graded beads the compressive strength was determined with a measuring

device for single granules and a displacement rate of 0.002 mm/s with a load cell of 10 kN. For these metal matrix composites the specific energy absorption (SEA) was calculated according to (1.1) and (1.2). SEA_V is defined as specific energy absorption per volume (V) unit, SEA_m refers to mass (m) unit, respectively.

$$SEA_V = \frac{W}{V} \quad SEA_m = \frac{W}{m} \tag{1.1}$$

$$W = \int_0^{S_b} P \mathrm{d}S \tag{1.2}$$

W is the total energy absorbed during sample deformation, P the load, S the displacement, and S_b is the strain at end of experiment according to Jacob et al. [13].

The tensile strength of the as-fabricated and calendered paper-derived materials was determined according to DIN EN ISO 1924-2 on a servohydraulic testing machine TT 28100 (TIRA Schalkau, Germany). The clamping length was 65 mm and the sample width was 10 mm. The crosshead speed for the as-fabricated samples was 5 mm/min, and for the calendered samples 3 mm/min. Different crosshead speeds had to be applied in order to ensure sample fracture within 5–30 s as given by the standard.

The tensile strength of the paper-derived TRIP-matrix composites after sintering was determined according to DIN EN ISO 6892-1. It was investigated on as-sintered samples with the following dimensions (before sintering): $l_0 = 150$ mm, $l_c = 115$ mm, $b = 20$ mm, $b_0 = 10$ mm, with a transition radius of 60 mm (DIN 50125 shape H). Tensile loading tests were also performed on the servohydraulic testing machine TT 28100 (TIRA Schalkau, Germany) at a clamping length of 98 mm. The test length was 70 mm at a crosshead speed of 2.35 mm/min.

Flexural strength (DIN EN 993-6, DIN EN 843-1) and Young's modulus by static flexure (DIN EN 843-2, Method A) were determined on a servohydraulic universal testing device type TT 28100 (TIRA Schalkau, Germany) with a support distance of 125 mm and a crosshead speed of 0.15 N/mm for the pressure slip casted ceramic matrix composites as well as for the zirconia preforms obtained by extrusion.

1.2.3.5 Microstructural Characterization

Microstructural characterization was conducted by digital microscopy VHX-2000 (Keyence, Germany) and scanning electron microscopy XL30 ESEM (Philips, Germany) equipped with energy dispersive X-ray spectroscopy technology (EDS). Phase identification was done using electron back scatter diffraction (EBSD) analysis (Philips XL30 with EBSD system TSL from Edax/Ametek). For EBSD analysis the samples were polished up to 1 μm grain. Final polishing for 20 h was realized using a VibroMet2 with a SiO_2-suspension MasterMet2 (0.02 μm grain size) (Buehler, USA). To avoid electric charging all samples were sputtered with Pt using

a sputter coater (Edwards, England). The crystallographic data used for phase determination were taken from ICDD-database. Detailed information are given in Berek et al. [14], Oppelt et al. [4, 5], Wenzel et al. [10, 15, 16] and Hasterok et al. [9]. Important features of the developed composites have been studied with the aid of a microfocus X-ray computed tomograph CT-ALPHA (Procon X-ray Sarstedt, Germany) equipped with a 160 kV X-ray source and a Hamamatsu detector with 2040 × 2040 pixels. For the open cell foam structure based on magnesia partially stabilized zirconia the homogeneity of the applied spray coatings was studied [9]. In case of the pressure slip casted ceramic matrix composites the homogenous distribution of the steel particles and the coarse alumina grains in the ceramic matrix was evaluated [8]. The deformation behavior of the open cell foam structures based on TRIP-steel and Mg-PSZ was evaluated using of X-ray tomography [3]. With the aid of a Zeiss Xradia 510 Versa X-ray microscope (XRM) the functionally graded beads were investigated with special regard to the formation of transition zones and the formation of cracks between the different layers [6].

1.3 Results and Discussion

1.3.1 Development of TRIP-Matrix Composites via Powder Metallurgy

1.3.1.1 Open Cell Foam Structures Based on TRIP-Steel/Mg-PSZ

TRIP-matrix composite foams have been prepared using the replica technique. In addition to the conventional coating procedure a dense coating (jacket) has been applied onto the side surfaces of the polyurethane foam template and the mass gain of the foams was registered (see Table 1.6). The linear shrinkage and the bulk density of the sintered foam structures are summarized in Table 1.7. The addition of zirconia particles in the steel matrix led to higher shrinkages. The MMCs without and with dense coating are displayed in Fig. 1.2a, b. The thickness of the dense coating has been determined to be 1.5 mm. SEM micrographs of the typical surface regions of the samples are shown in Fig. 1.3. During thermal treatment, the TRIP-steel matrix formed a nearly dense structure with only a few pores.

Table 1.6 Mass gain of the TRIP-matrix composite foams (mean values of 3 samples, with a standard deviation of less than 5%)

		0Z	10Z	0ZJ	10ZJ
Mass after impregnation	g	35.7	36.2	60.8	62.7
Mass after spraying	g	44.2	46.0	68.6	71.8
Mass after sintering	g	41.3	43.2	64.9	68.1

Table 1.7 Bulk density and linear shrinkage of the TRIP-matrix composite foams (mean values of 3 samples, with a standard deviation of less than 3%)

		0Z	10Z	0ZJ	10ZJ
Density	g/cm^3	1.1	1.2	1.7	1.8
Linear shrinkage in height	%	13.8	14.7	13.3	15.4
Linear shrinkage in width	%	10.9	11.2	9.5	10.6

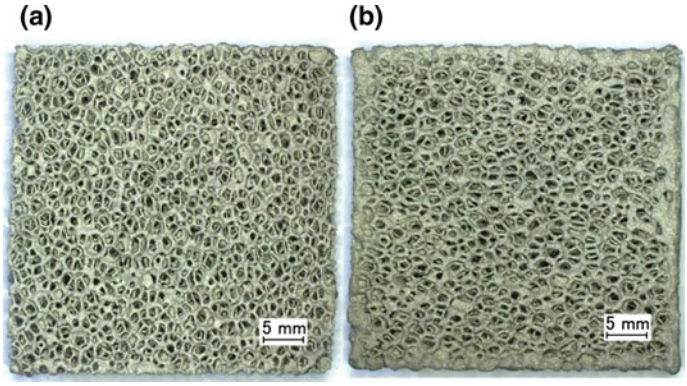

Fig. 1.2 Digital image of the TRIP-matrix composite foams **a** without dense coating (jacket) and **b** with dense coating (jacket) [3]

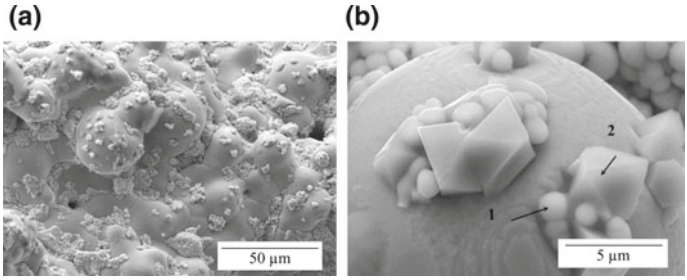

Fig. 1.3 SEM micrographs of the surface region of the composite with the composition 10ZJ [3]

With the aid of EDS measurements magnesia partially stabilized zirconia particles have been identified (see position 1 in Fig. 1.3b). The formation of spinel-type structures (see position 2 in Fig. 1.3b) has also been registered. These spinel-type structures have been analyzed by EDS. The results are summarized in Table 1.8.

Due to the significant differences in particle size between steel ($d_{50} = 30\ \mu m$) and zirconia ($d_{50} = 3.0\ \mu m$) clusters of zirconia particles were found between the steel particles. Berek et al. [17] investigated the phase composition of these reinforcing magnesia partially stabilized zirconia particles and found that approx. 80% of the

zirconia particles transform into the monoclinic state during thermal treatment up to 1350 °C in argon atmosphere. At the grain boundaries of the zirconia particles precipitates containing Mg are found.

The influence of compressive stress on the structure of TRIP-matrix composite foams was investigated by in situ CT, see Fig. 1.4. A compressive strain of 45% led to apparently broken cells. During deformation the cubic and tetragonal ZrO_2 (that is remaining after thermal treatment) is transformed into the monoclinic phase within the first 5% of compressive strain.

Figure 1.5 displays the compressive stress-strain curves of the developed TRIP-matrix composite foams; the corresponding values of the mass- and volume-specific energy absorption calculated according to (1.1) and (1.2) as a function of the compressive strain are presented in Table 1.9. It has to be mentioned that the calculated stress is the force divided by the nominal cross section after sintering (technical stress). The stress-strain curves of the TRIP-matrix composite foam structures with a dense coating (jacket) 0ZJ and 10ZJ show a large regime of strain hardening, followed by a plateau-like behavior with a flow stress of above 45 MPa at approximately 15% strain, followed by a long plateau stress in which deformation occurs at almost constant stress. The successive collapse of cell walls and struts of the cellular structure accounts for this long plateau which is typical for metallic foams. The reference material 0ZJ shows lower yield strength in comparison to the reinforced composite 10ZJ. In case of the samples without any dense coating similar behavior is registered, but with significantly lower yield strengths.

Table 1.8 Chemical composition (EDS) of spot 2 in Fig. 1.3b (oxides in wt.%, spinel-type structure)

MgO	Al_2O_3	ZrO_2	V_2O_5	Cr_2O_3	MnO	Fe_2O_3	NiO	TiO_2	SiO_2
2.78	26.45	5.43	1.33	34.20	25.51	2.59	0.47	0.80	0.42

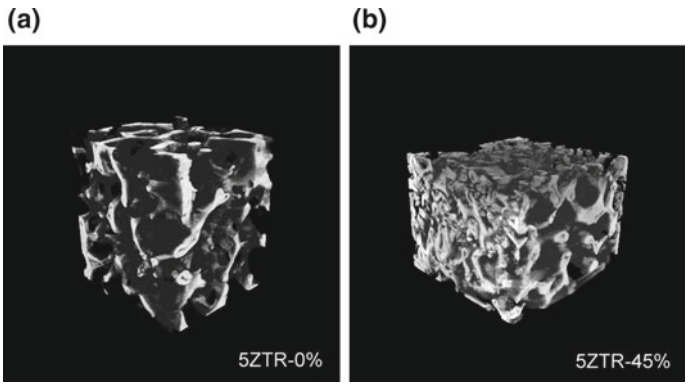

Fig. 1.4 3D CT images of a typical TRIP-matrix composite foam **a** before and **b** after 45% compressive strain [17]

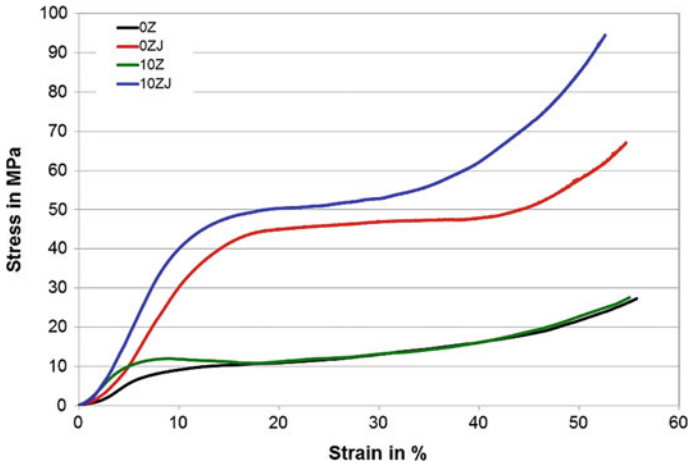

Fig. 1.5 Compressive stress-strain curves of the TRIP-matrix composite foams and the reference materials [3]

Table 1.9 Specific energy absorption (SEA) at 1, 2, 10, 20 and 50% compressive strain

	1% strain		2% strain		10% strain		20% strain		50% strain	
	kJ/kg	MJ/m^3	kJ/kg	MJ/m^3	kJ/kg	MJ/m^3	kJ/kg	MJ/m^3	kJ/kg	MJ/m^3
0Z	0.003	0.004	0.010	0.012	0.44	0.50	1.35	1.53	5.32	6.01
10Z	0.006	0.007	0.028	0.034	0.68	0.84	1.60	1.96	5.32	6.52
0ZJ	0.003	0.005	0.010	0.018	0.68	1.21	2.92	5.23	10.99	19.70
10ZJ	0.004	0.007	0.017	0.031	0.99	1.87	3.49	6.57	13.07	24.61

Strain hardening of the TRIP-matrix composite foams starts at smaller strains compared to the non-reinforced reference material and is independent if there is a dense side coating or not. This is of great importance and in accordance with the EBSD analysis. Thus, the reinforcement effect of magnesia partially stabilized zirconia in TRIP-matrix composites seems to be proven. This has also been observed for the mass and volume specific energy absorption, respectively. The specific energy absorption is higher in the composite foams as compared to the pure steel reference material especially up to a strain of 10% for all structures. The 10ZJ composite foam keeps its better performance in comparison to the reference material up to 50% compressive strain. The plotted results are average values of 5 samples with a deviation of approximately 5%.

1.3.1.2 Full or Hollow TRIP-Matrix Composite Beads and Functionally Graded Beads Using Gel-Casting

For the development of full and hollow beads an established additive system containing Darvan C and KM 2000 [8, 16] has been investigated in combination with sodium alginate. The sodium alginate was used for initial experiments since it is widely applied in food industry. Furthermore, sodium alginate has been successfully utilized for the fabrication of ceramic beads based on alumina [18]. Comprehensive rheological measurements have been carried out with a rotational viscometer (Haake RheoStress 150) with a given shear rate of 1–500 s^{-1} in 150 s with subsequent dwell of 100 s at maximum shear rate. The initial slurry had a powder to water ratio of 70:30. The addition of 0.3, 0.4, 0.7 and 1.0 wt.% sodium alginate based on the solid content was tested. Different powder to water ratios of 80:20 and 55:45 were tested at a fixed sodium alginate content of 0.4 wt.%. The different viscosity curves are displayed in Fig. 1.6a, b. All investigated slurries show a shear thinning behavior. For the slurries containing 0.3 and 0.4 wt.% sodium alginate a significant increase in viscosity can be recognized at shear rates below 50 s^{-1}. Slurries with 0.7 and 1.0 wt.% sodium alginate are not applicable in gel casting. Sodium alginate is a polysaccharide incorporating water in its structure; therefore highly viscous slurries are obtained that are not droppable through a cannula. Similar results are obtained if the water content is reduced to 20 wt.%. Taking the results of the rheological measurements into consideration, the optimum amount of sodium alginate is 0.4 wt.% for full beads and 0.7 wt.% for hollow beads. In addition to the rheological characterization of the slurries experiments relating to the possible size of the composite beads have been carried out. In this context, different syringe cannulas have been tested and beads with diameters ranging from 1.6 to 2.7 mm were fabricated. It has been verified that completely spherical composites are obtained with a cannula having a diameter of 1.1 mm. Subsequently, all further experiments were conducted with this cannula diameter. The sphericity of the composites does not only depend on the diameter of the cannula, but also on the distance between the injector and the

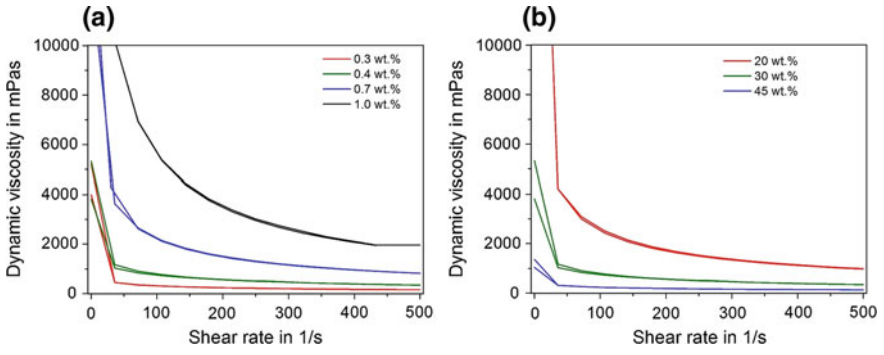

Fig. 1.6 Viscosity curves of the gel-casting slurries **a** with varying sodium alginate content at a powder to water ratio of 70:30; **b** with varying water content at a sodium alginate content of 0.4 wt.%

hardener solution. For the fabrication of spherical samples, the distance should be 13 mm (at a cannula diameter of 1.1 mm). At a greater distance the beads flattened and at a smaller distance "raindrop shaped" composites were produced as shown in Fig. 1.7. Hence, the level of the hardener solution should be continuously controlled during experiment. Depending on the chemical composition of the hardener solution hollow ($Ca(OH)_2$) or full beads ($CaCl_2$) can be produced as illustrated in Fig. 1.8 [5].

The wet green beads have been removed from the hardener solution after casting and subsequently dried. The full beads have been conventionally dried for 12 h at 40 °C. The development of a drying procedure for the hollow beads was more challenging. The shells of the hollow beads collapse due to their weight if conventional or vacuum drying procedures are used. The differences are illustrated in Fig. 1.9a, b.

Therefore, the hollow beads had to be freeze-dried. For the freeze-drying procedure the hollow beads were placed in a freeze-dryer. The hollow beads were frozen to −89 °C and the surrounding pressure reduced to under 6.11 mbar. According to the vapour pressure curve for ice and water, the frozen water sublimates directly from the solid to the gaseous phase without reaching the liquid state. With this drying method, the cavity within the hollow beads can be retained during the drying process and moisture is completely removed after 12 h.

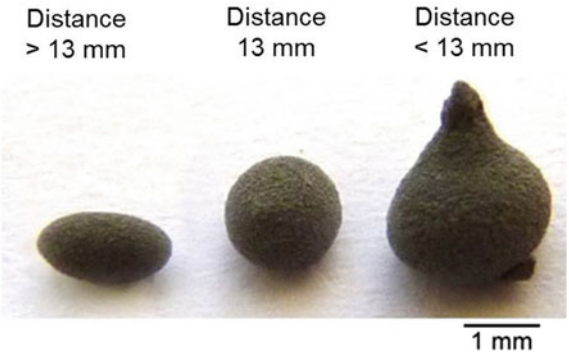

Fig. 1.7 Shape of composite beads as function of the distance between injector to hardener solution [4]

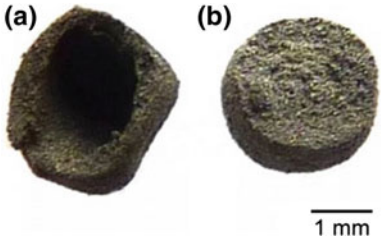

Fig. 1.8 Hollow (**a**) and full (**b**) composite beads [5]

The debinding of the green full and hollow beads is an essential processing step in the development of TRIP-matrix composite beads. Within the present work sodium alginate (gelation agent) as well as Darvan C and KM 2000 (binder system) were used as temporary additives. The thermal removal of the organic additives is not only a critical step in terms of defect-free debinding, but also in terms of the residual carbon content affecting the chemical and phase composition of the TRIP-steel powders [19]. The decomposition behavior of the sodium alginate in synthetic air at a heating rate of 10 K/min is displayed in Fig. 1.10a. Three exothermic peaks can be recognized at 250, 360 and 650 °C with the corresponding total mass loss of 41%, 45% and 59%, respectively. At 800 °C the decomposition is completed. For the evaluation of the debinding parameters the knowledge of the oxidation tendency of the ***PM***X8CrMnNi16-7-3 and ***PM***X3CrMnNi16-7-6 steel powders is essential. The results of the thermogravimetric measurements are shown in Fig. 1.10b. The increase in mass has been registered for both types of steel powder. The ***PM***X3CrMnNi16-7-6 steel powder possesses a lower oxidation resistance in comparison to the ***PM***X8CrMnNi16-7-3 steel powder.

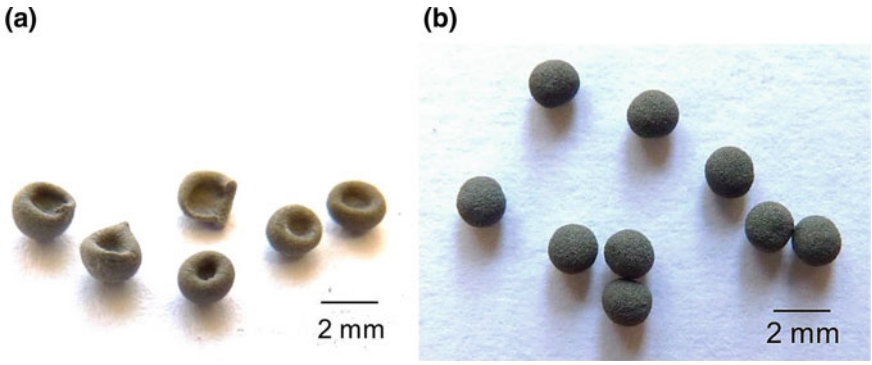

Fig. 1.9 Green hollow beads **a** conventionally dried **b** freeze-dried [7]

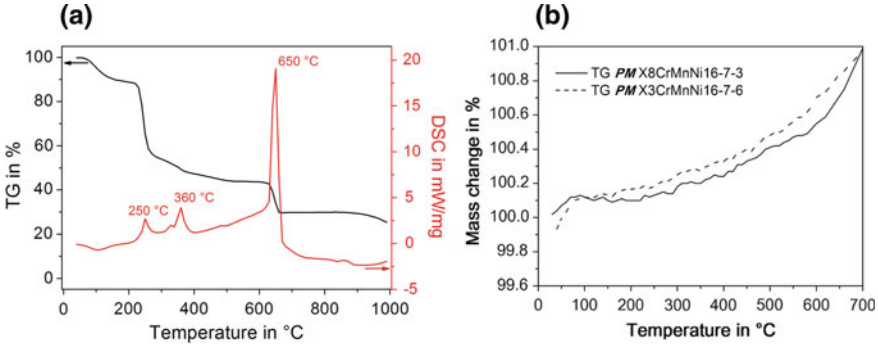

Fig. 1.10 Thermal analysis of **a** sodium alginate and **b** applied steel powders at a heating rate of 10 K/min in synthetic air [4, 8]

The oxidation rate significantly increases at temperatures above 400 °C. Within the present work the debinding temperature was set to 660 °C, which is a reasonable compromise between the binder removal and the oxidation of the steel powder. Based on the DSC/TG-analyses, the debinding experiments were conducted at 660 °C with varying dwell time at 250 °C and 660 °C, respectively. The heating rate was set to 1 K/min for a defect-free debinding of the composite beads. The residual carbon content as well as the oxygen content were determined in order to evaluate the debinding success (see Table 1.10). Using the above discussed debinding conditions, the carbon content can be reduced from 0.33 wt.% in the green beads to 0.048% in the binder-free beads. Within the present work the TRIP-matrix composite beads were sintered at 1350 °C as suggested by Weigelt [19]. The dwell time at maximum temperature was set to 120 min. The sintering was conducted with excess pressure of 5×10^{-4} MPa in order to reduce the evaporation of alloying elements. Argon 5.0 was chosen as flushing gas.

Figure 1.11a represents a SEM micrograph of a full bead containing 20 vol.% zirconia (20Z). These beads were characterized by a rough surface. The zirconia particles were evenly distributed within the steel matrix. Nevertheless poor densification of the composite during sintering led to a high porosity. A microstructural overview of the hollow beads is given in Fig. 1.11b. According to Oppelt and Aneziris [5] hollow beads are obtained if the hardener solution is highly alkaline.

Table 1.10 Results of the debinding experiments as a function of the thermal treatment (mean values of 3 measurements)

Dwell time in min at		Carbon content in wt.%	Oxygen content in wt.%
250 °C	660 °C		
15	0	0.049 ± 0.004	11.50 ± 3.61
15	15	0.048 ± 0.002	7.13 ± 3.17
15	30	0.048 ± 0.003	6.80 ± 1.91
30	0	0.053 ± 0.005	7.37 ± 1.55
30	15	0.053 ± 0.003	4.23 ± 1.06
30	30	0.051 ± 0.006	7.17 ± 1.80

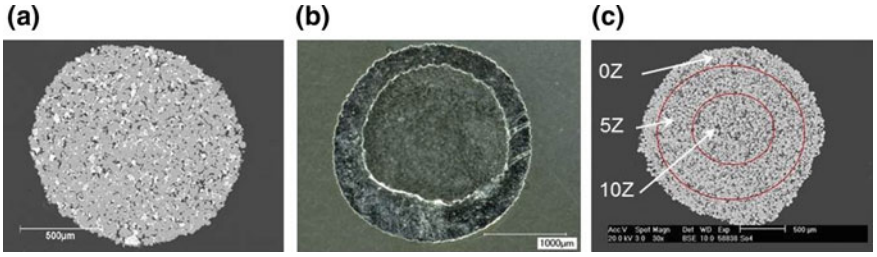

Fig. 1.11 Polished section micrographs of **a** single bead (SEM-micrograph) and **b** hollow bead (LOM-micrograph) and **c** functionally graded bead (SEM-micrograph)

In alkaline solutions the sodium alginate is readily soluble and forms an incoherent sodium alginate sol. If this sol gets in contact with bivalent Ca-ions the water insoluble calcium alginate gel is formed due to the ion exchange of Na^+ and Ca^{2+}. During fabrication the alginate containing slurries are added dropwise into the hardener solution. Upon contact with the calcium hydroxide containing hardener solution the drop surface solidifies and a solid shell is formed. This shell inhibits the further incorporation of Ca^{2+}-ions into the alginate structure. The transition from sodium alginate sol to calcium alginate gel proceeds exclusively within the shell and a cavity is formed. As a result of the fabrication process these cavities are irregularly shaped. Within the present study 94% of the examined hollow beads show pronounced cavities. Figure 1.11c shows an example for the prepared functionally graded beads. A full bead with the composition 10Z was coated with a slurry of the composition 5Z and finally a layer of the composition 0Z was applied. The initial bead had a diameter of 1.8 mm. The layer thicknesses were determined to be 76 ± 21 µm (1st layer) and 63 ± 5 µm (2nd layer). The microstructural differences are visible at higher magnifications (see Fig. 1.12). Since the sintering conditions are equal for all types of beads it can be assumed that the pH value of the hardener solution as well as the type of hardener agent influences the solidification process during casting. At neutral or low alkaline pH (using $CaCl_2$, pH = 7.2) the ion exchange from Na^+ to Ca^{2+} takes place at lower rates. Therefore the transition from sodium alginate sol to calcium alginate gel is decelerated and the resulting beads have a higher porosity in comparison to the hollow beads. In case of the hollow beads a better densification of the material is recognized. As stated above at higher alkaline pH (using $Ca(OH)_2$, pH = 13.4) the ion exchange as well as the transition from sol to gel takes place at higher rates. For the development of the functionally graded beads a different approach was chosen. The different layers were sprayed onto a full bead. The composition of the spraying slurries was adopted from the spray coating procedure for the development of TRIP-matrix composite foams. In Fig. 1.12c a functionally graded bead is shown. The 2nd coating had the composition 0Z and is characterized by a high residual porosity.

For all types of TRIP-matrix composite beads precipitation can be found at the steel/steel grain boundaries. The chemical and phase composition of these precipitations have been analyzed using EDS/EBSD. The results are displayed in Fig. 1.13. The lattice parameters of the considered phases for EBSD-analysis are given by

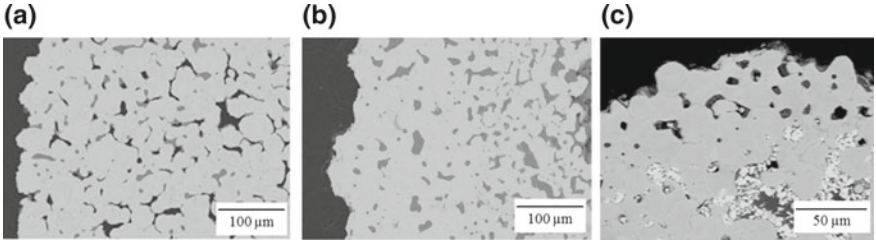

Fig. 1.12 SEM micrographs of **a** single bead, 0Z and **b** hollow bead, 0Z and **c** functionally graded bead, 10Z-5Z-0Z at higher magnifications [6]

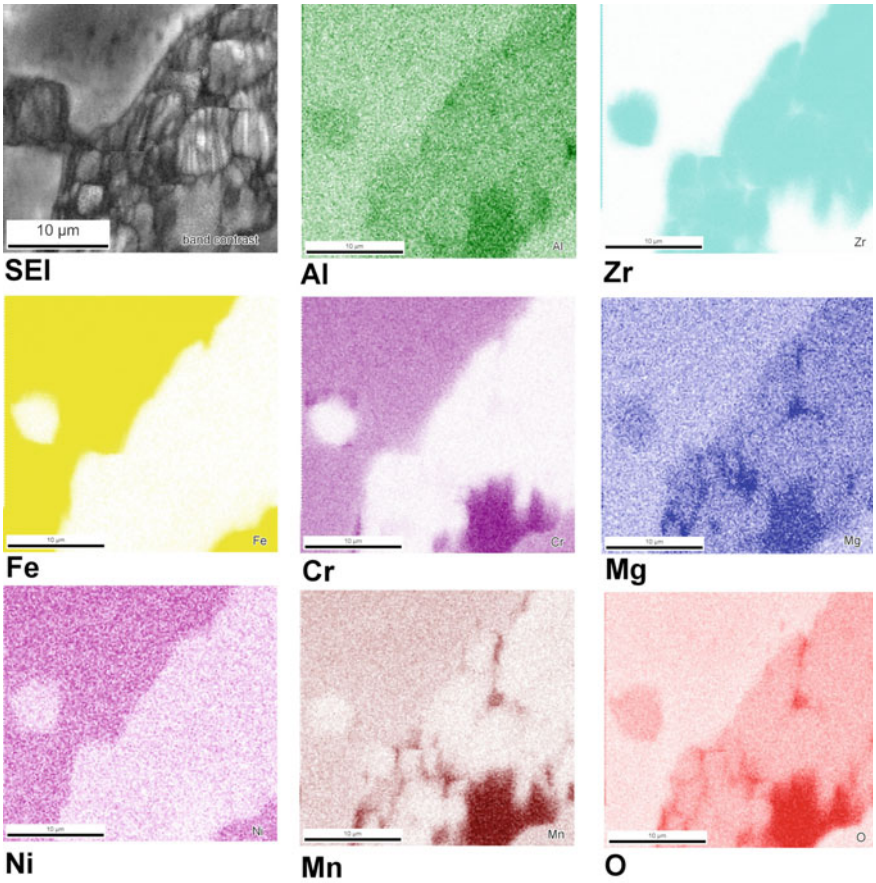

Fig. 1.13 EDS mapping of a full TRIP-matrix composite bead, composition 20Z (polished surface) [4]

Oppelt [7]. The steel matrix can be clearly distinguished due to the presence of Fe and Ni. The zirconia particles can be recognized due to the Zr-distribution pattern. Mixed spinel formation during sintering occurred due to diffusion processes [10] and is indicated by the distribution of Al, Mg, O, Mn and Mg, Cr. At the grain boundaries steel/steel three different types of precipitates Mn–Cr–O, Mn–Si–O and Cr–C have been found. By means of EBSD the precipitations could be identified as $MnCr_2O_4$, Mn_2SiO_4 and Cr_7C_3. The formation of carbides has been reduced due to optimization of the thermal processes.

The physical properties of the different TRIP-matrix composite beads are summarized in Table 1.11. For the full beads it can be recognized that the shrinkage increases if zirconia particles are incorporated in the steel matrix. Due to the chosen hardener agent ($CaCl_2$) the transition from sodium alginate sol to calcium alginate gel during casting is decelerated. The fabricated full beads therefore have high

Table 1.11 Properties of the TRIP-matrix composite beads, after sintering at 1350 °C

	Shrinkage %	Bulk density g/cm^3	Open porosity %	Compressive strength MPa	Strain at failure %	Total specific energy absorption kJ/kg
Full beads						
0Z	5.7 ± 0.1	4.1	11.3	398.3 ± 17.3	29.4 ± 0.8	11.5 ± 0.4
5Z	16.7 ± 0.0	–	5.9	344.4 ± 18.1	13.5 ± 0.7	6.3 ± 0.4
10Z	22.0 ± 0.1	4.7	3.7	359.1 ± 15.1	16.6 ± 0.2	7.9 ± 0.4
20Z	16.1 ± 0.1	6.1	15.0	240.3 ± 13.5	16.5 ± 0.2	3.9 ± 0.1
Hollow beads						
0Z	38.7 ± 5.9	5.6	10.2	61.4 ± 3.2	15.6 ± 3.1	2.4 ± 0.4
5Z	26.1 ± 2.6	4.9	9.0	98.8 ± 12.7	15.3 ± 2.2	3.7 ± 0.2
10Z	24.5 ± 5.4	4.8	12.7	104.0 ± 30.3	10.4 ± 4.5	1.5 ± 0.5
Functionally graded beads (10Z-95Z-0Z)						
dipped	24.4 ± 4.8	6.8	23.0	49.6 ± 4.9	4.6 ± 0.8	0.4 ± 0.1
sprayed	27.0 ± 1.8	7.7	10.1	551.3 ± 59.3	21.5 ± 3.0	13.7 ± 3.5

porosities in the green stage (35–47%). After sintering the composition 10Z has the lowest open porosity of 3.7% and the highest shrinkage of 22.0%. For the hollow beads shrinkages ranging from 24.5% (10Z) to 38.7% (0Z) have been determined. It has to be noted that the cavities of the hollow beads are reduced during thermal treatment. Therefore a higher overall shrinkage was measured. The hollow beads containing 5 and 10 vol.% zirconia show higher open porosities in comparison to the full beads. The functionally graded beads (FGS) were prepared by dip or spray coating of composites beads with the initial composition 10Z. Hence, the shrinkages of the FGS correspond to the shrinkage of the full beads with the composition 10Z. The difference in open porosity can be attributed to the choice of coating procedure. With the aid of spray coating a fine spray is generated and it presumably closed the open pores of the initial bead. This effect has not been recognized for the dip coated material. The mechanical properties of the different TRIP-matrix composite beads are also summarized in Table 1.11. The functionally graded beads (spray coating) exhibit the highest compressive strength with 551 MPa. The compressive strength of the reference material (full bead) with the composition 0Z was determined to be 399 MPa. This material also shows the highest strain at failure with 30%, whereas the functionally graded beads (spray coating) have a strain at failure of 21.5%. The functionally graded beads also show the highest total specific energy absorption with 13.7 kJ/kg, followed by the reference material with 11.5 kJ/kg. In Table 1.12 the specific energy absorption of the different TRIP-matrix composite beads is displayed as a function of compression strain. The full beads with the composition 0Z and the functionally graded beads (spray coated) allow a compression of up to 20%. At this compression the FGSs show the highest specific energy absorption with 10.7 kJ/kg.

At a compression of up to 15% all zirconia reinforced beads have a higher specific energy absorption compared to the reference material 0Z. Oppelt [7] has found that the reinforcing zirconia particles in the TRIP-matrix show a stress-assisted phase transformation. In Fig. 1.14, the results of the compressive testing are given for all developed TRIP-matrix composite beads. The full beads have a 4 times higher strength in comparison to the hollow beads. Up to a compression of 15% the full beads of the composition 5Z and 10Z show a significant higher strength than the reference material 0Z. The highest strength has been determined for the functionally graded beads even at compression above 15%.

1.3.1.3 TRIP-Matrix Composites via Paper-Manufacturing Technology

Square paper sheets with 200 mm in length have been formed on a laboratory sheet-forming device. Figure 1.15 shows the microstructure of as-fabricated and calendered green sheets. In contrast to the processing of pre-ceramic paper, where both filler particles and pulp fibers develop a negative surface charge in water, the steel particles used as fillers remained non-charged in water. Coagulation and flocculation therefore only took place for pulp fibers in the suspension due to the addition of organic additives. Figure 1.15a illustrates the domination of that fiber-to-fiber bonds. During wet paper processing via filtration, the steel particles were incorporated in between the fiber network, and steel clusters could be found. The solids retention was greater than 90 wt.%. The as-fabricated paper had a high porosity and surface roughness (Fig. 1.15c), which could be significantly reduced by calendering at 30 kN/mm (Fig. 1.15b, d). During calendering the steel particles deformed plastically due to the high surface load and may have undergone a martensitic phase transformation, which was reversible upon heat treatment.

Table 1.12 Specific energy absorption (SEA_m) in kJ/kg at 5, 10, 15 and 20% strain

	5% strain	10% strain	15% strain	20% strain
Full beads				
0Z	0.19 ± 0.02	1.11 ± 0.06	2.73 ± 0.18	5.22 ± 0.22
5Z	0.74 ± 0.01	3.34 ± 0.13	–	–
10Z	0.75 ± 0.01	3.39 ± 0.22	7.27 ± 0.18	–
20Z	0.29 ± 0.01	1.27 ± 0.03	3.08 ± 0.3	–
Hollow beads				
0Z	0.26 ± 0.05	1.14 ± 0.06	2.08 ± 0.40	–
5Z	0.39 ± 0.02	1.45 ± 0.14	3.14 ± 0.30	–
10Z	0.57 ± 0.05	1.51 ± 0.53	–	–
Functionally graded beads (10Z-95Z-0Z)				
dipped	0.34 ± 0.04	–	–	–
sprayed	0.64 ± 0.19	2.95 ± 0.54	6.89 ± 0.90	10.7 ± 0.23

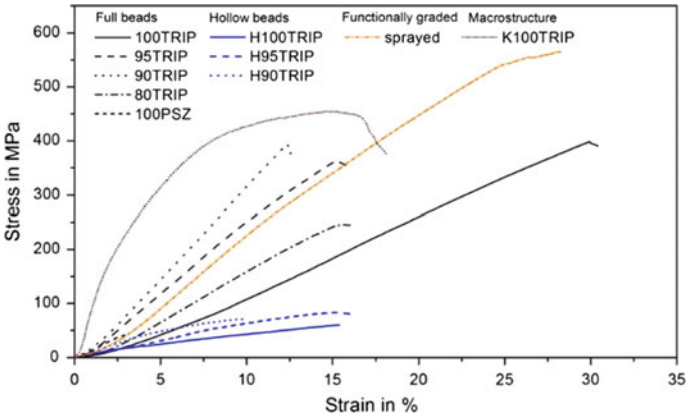

Fig. 1.14 Stress-strain curves for the different TRIP-matrix composite beads [7]

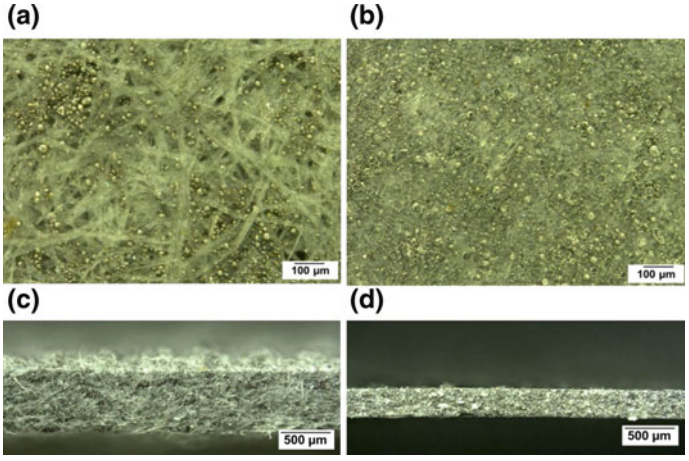

Fig. 1.15 LOM micrographs of a green paper sheet, composition 0Z, **PM**X8CrMnNi16-7-3. Top surface view: **a** uncalendered, **b** calendered at 30 kN/mm. Cross-sectional view: **c** uncalendered, **d** calendered at 30 kN/mm [15]

The properties of the green composites are summarized in Table 1.13. In the as-fabricated state, the fibers were loosely arranged with many interspaces, whereas calendering led to the firm embedding of the fibers between the filler particles. In consequence, the total porosity and the surface roughness are decreased due to calendering, which also increases the tensile strength of the calendered samples. The calendered sheets therefore offer enough stability to be further processed (e.g. punching of samples for determination of tensile strength after sintering, preparation of corrugated cardboard structures).

Table 1.13 Properties of the TRIP-matrix paper composites in green state

Recipe		0Z	5Z	10Z
Thickness as-fabricated	mm	1.00 ± 0.05	0.97 ± 0.05	0.97 ± 0.06
Thickness after calendering	mm	0.31 ± 0.03	0.31 ± 0.01	0.31 ± 0.1
Tensile strength as-fabricated	N/mm^2	6.1 ± 0.9	5.3 ± 0.6	5.2 ± 0.5
Tensile strength after calendering	N/mm^2	13.2 ± 1.7	14.0 ± 2.9	15.6 ± 3.2

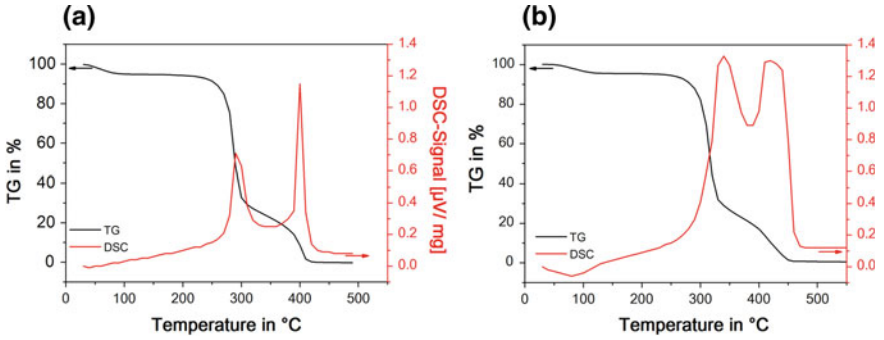

Fig. 1.16 DSC/TG analysis of the cellulose fibers in oxidizing atmosphere applying different heating rates: **a** 1 K/min, **b** 5 K/min [15]

The debinding of the calendered paper sheets is an essential processing step in the development of TRIP-matrix composites by paper-manufacturing technology. The total organic quantity of the as-fabricated paper sheets was 40–45 vol.%. The thermal removal of the organic additives is therefore not only a critical step in terms of defect-free debinding, but also in terms of residual carbon (resulting from an insufficient debinding) affecting the chemical and the phase composition of the TRIP-steel matrix. The thermal decomposition behavior of the cellulose pulp fibers at heating rates of 1 and 5 K/min are summarized in Fig. 1.16. For both heating rates, two exothermic peaks can be distinguished. At a heating rate of 5 K/min, the peaks are shifted to higher temperatures and appear less pronounced. At a heating rate of 1 K/min, the maxima of both exothermic reactions are given at 290 and 400 °C. The decomposition was completed at 420 °C. At a heating rate of 5 K/min, the exothermic reactions shifted to 340 and 430 °C, respectively, and the reaction was completed at 460 °C.

As a result of the DSC/TG analyses the debinding rate was set to 0.5 K/min. The maximum debinding temperature was set to 460 °C, with a dwell time of 90 min. The carbon content for the composition 0Z after debinding was determined to be 0.044%, which corresponds to the carbon content of the initial steel powder. The microstructure of the sintered sample 5Z is displayed in Fig. 1.17. The paper manufacturing technology requires the use of cellulose pulp fibers, which are thermally removed by a debinding process, leaving pores within the material. The sintering at

1350 °C with a dwell time of 60 min did not result in a sufficient densification of the steel matrix. The incorporated zirconia particles form agglomerates, which are embedded in the interstices of the steel particles and the process derived pores. It can be furthermore recognized that no interfacial reaction occurred between the zirconia particles and the surrounding steel matrix. Nevertheless, precipitates are formed at the grain boundaries steel/steel.

The chemical as well as the phase composition of the precipitates has been analyzed using EDS/EBSD. According to the EDS mappings two different types of precipitates have formed during sintering as shown in Fig. 1.18a, b. In the center of the investigated sample the precipitates are composed of chromium, manganese, and carbon and were identified as trigonal $(Cr, Mn, Fe)_7C_3$. The second type of precipitation was occasionally found at the sample edges. These precipitates are composed of manganese, silicon, and oxygen and have been identified as orthorhombic Mn_2SiO_4. The manganese silicate is surrounded by an iron, chromium, carbon rich area that was identified as trigonal $(Cr, Mn, Fe)_7C_3$. The potential of the paper-derived TRIP-matrix composites regarding the desired deformation-assisted austenite to martensite phase transformation is significantly lowered due to the presence of carbides. The influence of the sintering atmosphere on the formation of carbides is discussed in [8]. In a further investigation the calendered paper sheets have been sintered in a purified argon atmosphere with the aim to prohibit the formation of carbide precipitations. The resulting microstructure is shown in Fig. 1.19. Obviously, the incorporated zirconia particles form agglomerates and they are embedded within the pores. The formation of carbide precipitates has not been registered. According to EDS/EBSD the steel matrix shows segregations with higher concentrations of chromium and lower concentrations of nickel than the surrounding matrix. Furthermore, the material contains randomly dispersed oxide precipitations that were most likely formed during heat treatment. These oxide precipitations have been identified as orthorhombic $(Mg, Mn)_2SiO_4$.

If the thermal treatment was conducted in a non-purified atmosphere, the mechanical properties of the paper-derived metal-matrix composites were deteriorated due

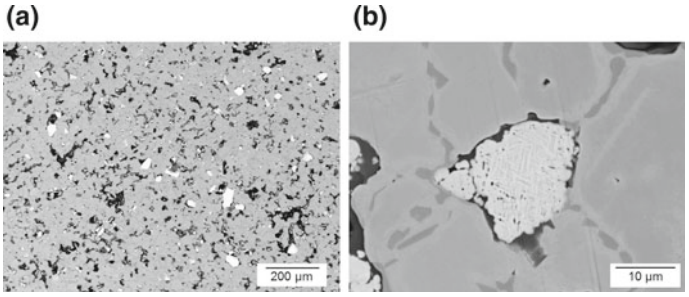

Fig. 1.17 SEM micrographs (BSE-mode) of the sintered composites prepared by paper-manufacturing technology (light grey: zirconia, dark grey: steel matrix with precipitations) [8]

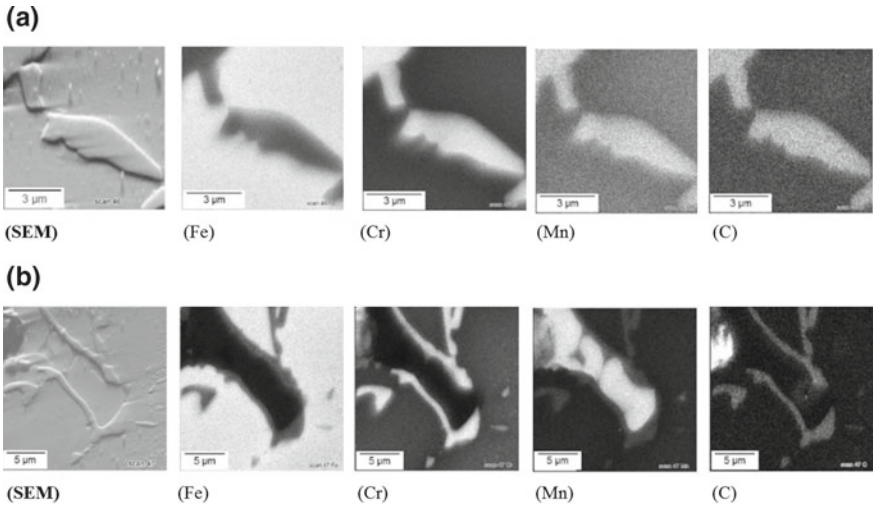

Fig. 1.18 EDS mapping of the reference material 0Z at the grain boundaries, sintered at 1350 °C, **a** in the center of the sample, **b** at the edge of the sample [8]

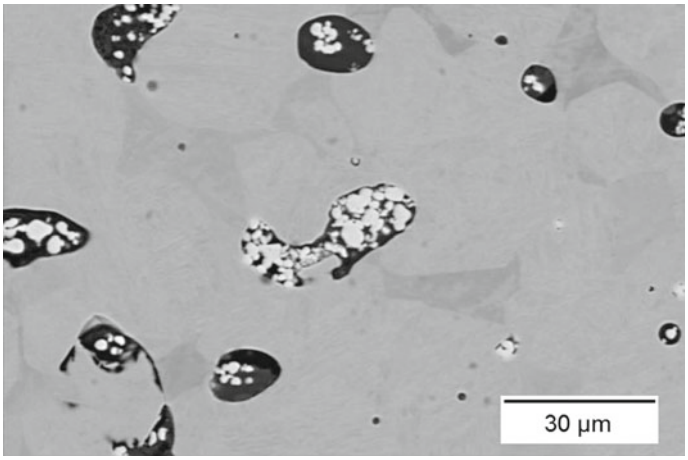

Fig. 1.19 SEM micrograph (BSE-mode) of the paper-derived TRIP-matrix composite 10Z sintered in a purified argon atmosphere [8]

to the presence of carbides. The highest tensile strength was determined for the reference material 0Z with 176.6 ± 12.1 MPa at a total porosity of 66%. The composition 5Z (5 vol.% zirconia) showed a lower tensile strength of 123.3 ± 3.1 MPa. For the composite 10Z (10 vol.% zirconia) a tensile strength of 103.3 ± 14.4 MPa was determined. The materials failed at a maximum strain of 0.6% and showed brittle fracture behavior.

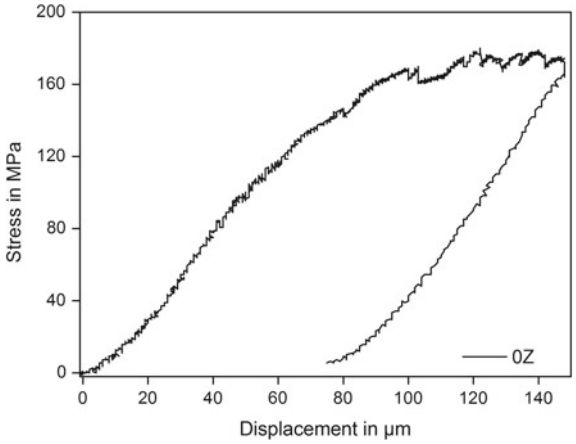

Fig. 1.20 Stress-displacement curve of the reference material 0Z during tensile load testing [8]

An in situ tensile test was carried out for the reference material 0Z in a scanning electron microscope MIRA 3 XMI (Tescan, Czech Republic) in order to characterize the deformation and damage behavior of the material under quasi-static load at a crosshead speed of 1 µm/s. The evolution of the microstructure was registered as a function of the crosshead displacement. The corresponding stress-displacement curve is shown in Fig. 1.20.

Figure 1.21a shows the microstructure of the reference material 0Z in its initial state. The carbide precipitates are clearly visible at the grain boundaries. Pores are filled with Mn_2SiO_4. At a crosshead displacement of 110 µm the carbide precipitates start to break, and cracks are initiated on macroscopic scale (see Fig. 1.21b, c). The single cracks joined to a large main crack when the crosshead displacement is further increased, see Fig. 1.21d. The crack tip passes along the carbide grain boundaries toward bigger pores. The precipitates debond from the steel matrix and fracture in a transgranular manner.

In case of the paper-derived TRIP-matrix composites sintered in a purified argon atmosphere significant higher tensile strength has been determined. A purified atmosphere and the optimized composition of the paper-sheets led to tensile strength of 170.6 ± 18.7 for the composition 0Z and 142.4 ± 10.5 MPa for the composition 10Z at total porosities of 26%. The incorporation of commercially available zirconia fibers led to further improvements of the mechanical performance. At a fiber incorporation of 3 vol.% the tensile strength was determined to be 207.0 ± 17.4 MPa at a total porosity of 25%. However, these optimized TRIP-matrix composites showed also a brittle fracture behavior.

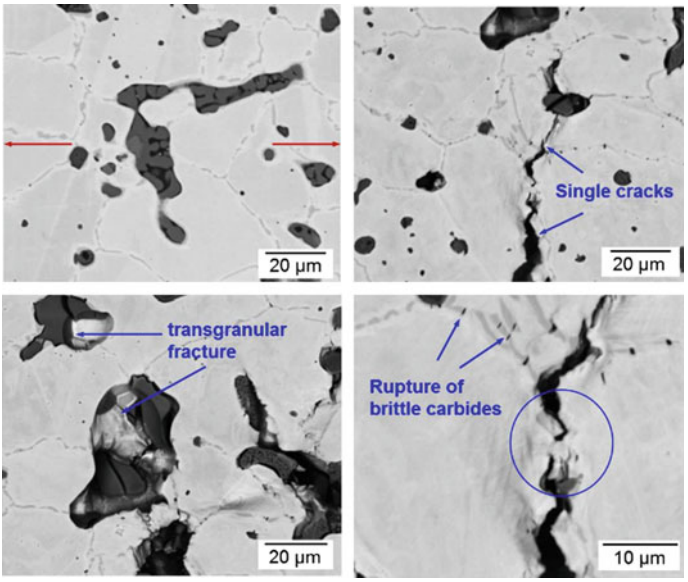

Fig. 1.21 SEM micro-graphs of the reference material (0Z) during tensile loading at different displacements (red arrows: load direction) [8]

1.3.2 Development of TRIP-Matrix Composites via Metal Melt Infiltration of Ceramic Preforms

1.3.2.1 Open Cell Foam Structures Based on Magnesia-Partially Stabilized Zirconia

Open cell foam structures based on magnesia partially stabilized zirconia have been prepared using the replica technique. In a preliminary study an adequate additive system has been developed. Comprehensive rheological measurements have been carried out. In Fig. 1.22 the viscosity curves for the different spraying slurries are displayed. According to literature [20] typical shear rates for spray processes are 10^3–10^5 s^{-1}. At a shear rate of 1000 s^{-1} the viscosities of the slurries have been determined to be 126 mPas (40 wt.% water), 100 mPas (45 wt.% water) and 63 mPas (55 wt.% water). These low viscosities favor the formation of a fine spray during the spray coating procedure. The appropriate additive system additionally assists to keep the slurries stable in idle state. It was recognized that the conventional spray coating procedure led to a poor coating of the foam struts especially in the foam center. If the spray coating procedure was done air stream assisted, a better deposition of the spray droplets on the polyurethane foams has been established. In addition to that less pore blocking has been registered. With the aid of computer tomography the homogeneity of the coatings has been analyzed [9]. In Fig. 1.23, a comparison between conventional and airstream assisted coating procedure is given.

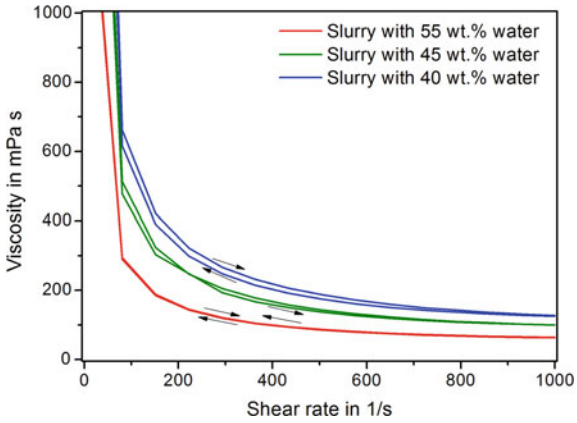

Fig. 1.22 Viscosity curves of the zirconia slurries at different powder to water ratios [9]

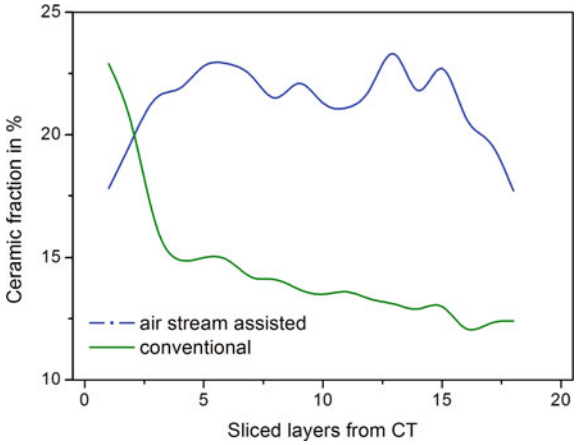

Fig. 1.23 Homogeneity of coated open foam cell structures using the different spray coating procedures [9]

For the conventional spray coating, the ceramic portions are mainly deposited on the surface of the open cell foam structures. In the first layer of the foam it was determined to be 22% and decreases to 15%. In the center of the open cell foam structure the ceramic portion is negligible. Quite different results have been found if the spraying procedure was done air stream assisted. It can be seen that the ceramic fraction was always greater than 20% throughout the considered volume of the open cell foam structure.

The influence of the solid content of the spraying slurry on the homogeneity of the spray coating has also been investigated. The slurry with 55 wt.% water had a

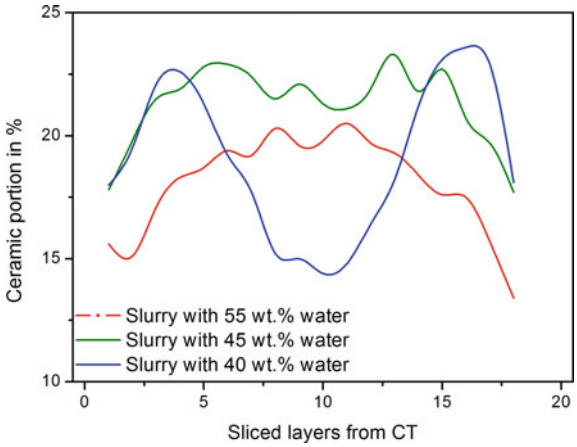

Fig. 1.24 Influence of the solid content of the spraying slurry on the homogeneity of the spray coating [9]

viscosity of 63 mPas and a yield stress of 13 Pa. Due to the low viscosity the slurry easily penetrates the foam structures.

As it can be seen in Fig. 1.24 the ceramic portion in the middle of the foam was determined to be greater than 20%. However, the ceramic portion is rather small on the upper surface of the sprayed foam. Presumably the yield stress of the slurry is exceeded due to the air pressure of the spray. For the slurry with 40 wt.% water a different effect can be seen. On the upper surface of the open cell foam structure the ceramic fraction was determined to be greater than 22%. Due to the higher yield stress the slurry strongly adheres onto the struts of the top surface and is not transported deeper into the structure. The best distribution of the ceramic fraction throughout the entire foam structure has been achieved if the slurry with 45 wt.% water was used for the spray coating procedure. Due to the yield stress of 20 Pa, the slurry remains on the struts. The viscosity of this slurry was determined to be 100 mPas and is therefore able to deeply infiltrate the foam structure.

The sintered open cell foam structures were infiltrated by a ***Cast*** X5CrMnNi16–7–7 steel melt in order to obtain TRIP-matrix composites. The phase composition of the infiltrated foam structures has been analyzed with the aid of EBSD. In Fig. 1.25, a SEM micrograph of the polished sample surface is presented. According to the EBSD-phase analysis the infiltrated foam structure contained 4.5% monoclinic zirconia, 49.8% tetragonal zirconia and 45.7% cubic zirconia. Thus, approximately 50% of the ceramic material is able to transform stress-assisted. No martensite has been detected by EBSD-analysis; the analyzed part consisted of 100% austenite.

1.3.2.2 Extrusion Technology for Honeycombs and Randomly Arranged Spaghetti-Filters

Ceramic preforms of honeycomb or spaghetti filter type have been prepared via extrusion technology. After sintering at 1650 °C in oxidizing atmosphere the preforms have been infiltrated by a ***Cast*** X5CrMnNi16-7-7 steel melt in order to obtain TRIP-matrix composites. For a sufficient infiltration the preforms had to be preheated to 1000 °C. The honeycombs were joined by a cold joining technique. Schärfl et al. [11] prepared spaghetti filters with a diameter of 70 mm and a height of 120 mm in one piece. Wenzel et al. [10] extruded spaghetti filter discs of with a diameter of 50 and 25 mm height. Before infiltration, these filters were stack to give a preform of 120 mm height. For the honeycomb structures as well as for the spaghetti filters an incomplete infiltration was registered. The metal melt froze during casting, presumably due to the high ceramic portion as well as due to the dense arrangement of the strands/honeycombs. A sufficient infiltration has been obtained if the hollow spaghetti filters have been used, see Fig. 1.26. It can be seen that the hollow strands are infiltrated. Presumably the thermal shock at the beginning of the steel casting caused the cracking of the hollow zirconia strands; moreover there is a significant density gradient between zirconia and steel. At the interface between zirconia and steel a crack network has been formed.

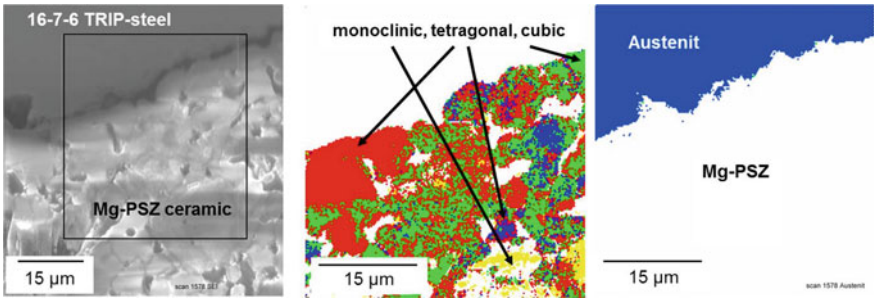

Fig. 1.25 SEM micrograph of the infiltrated open cell foam structure and the corresponding results of the EBSD-analysis [9]

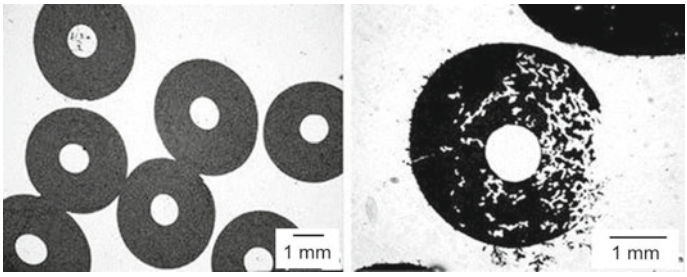

Fig. 1.26 LOM micrograph showing infiltrated hollow rods [11]

1.3.3 Development of Ceramic Matrix Composites via Powder Metallurgy

Another focus of the present work was the fabrication of ceramic matrix composites using pressure slip casting. The developed materials were based on zirconia and alumina with additions of up to 20 vol.% TRIP-steel powder (**PM** X8CrMnNi16-7-3). The zirconia matrix composites were cast as fine and coarse grained components, whereas the alumina matrix composites were only cast as coarse grained components. In a previous studies [16] an organic binder system containing KM 1001, KM 2000 and Optapix PAF 35 has been successfully established for the rheological stabilization of zirconia-steel slurries. For the casting of large components ($200 \times 200 \times 38$ mm^3) two additional binders, Welan gum and Konjac flour, had to be applied in order to guarantee the dimensional stability of the cast green bodies after demoulding. Due to the adjustment of the solid content as well as the optimization of the particle packing the casting times for these large components could be set to 90 min (fine grained slurries) and to 25 min (coarse grained slurries). The maximum casting pressure was 2 MPa. After drying the cast components were sintered at 1550 °C in argon atmosphere. The microstructure of the CMCs for the components containing 80 vol.% alumina (coarse) or 80 vol.% zirconia (fine) is exemplarily shown in Fig. 1.27. The homogenous distribution of the steel particles within the matrix materials has been verified with the aid of the microfocus X-ray computed tomograph. As a result of the casting technology and the sintering temperatures the pressure slip casted ceramic matrix composites features open porosities of $\geq$27%.

The wear behavior of the pressure slip casted composites has been investigated. Therefore the surfaces of the materials have been polished using different grinding media down to 1 μm grain size. Wear tests have been performed using a pin-on-disc tribometer with a WC-Co pin at room temperature under a normal force of 50 N and at a sliding speed of 0.05 m/s and a maximum sliding distance of 200 m. The wear tracks are at least 4 mm in width and can be clearly distinguished from the untreated surface as shown in Fig. 1.28. The wear resistance of the test specimens is characterized by their mass loss and the wear rates of the materials as given in

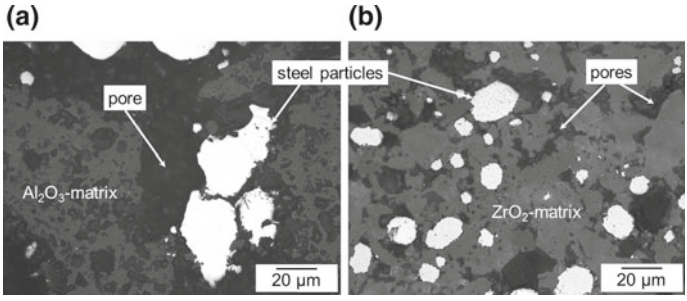

Fig. 1.27 LOM micrograph of pressure slip casted CMCs of the compositions **a** 80 vol.% alumina coarse and **b** 80 vol.% zirconia fine

Table 1.14. All investigated materials present severe wear with wear rates in the order of 10^{-1} to 10^{-4} mm^3/Nm. The wear tracks are characterized by abrasion, adhesion as well as fracture processes. Especially the coarse grained zirconia matrix composites are characterized by severe abrasive wear. The finer zirconia matrix material was significantly worn off; as a result also the coarser grains broke out of the matrix. For the coarse alumina composites identical wear mechanisms have been identified. With the aid of EDS the deposition of the counter body material tungsten carbide-cobalt in the wear track was registered. The fine grained zirconia matrix composites are

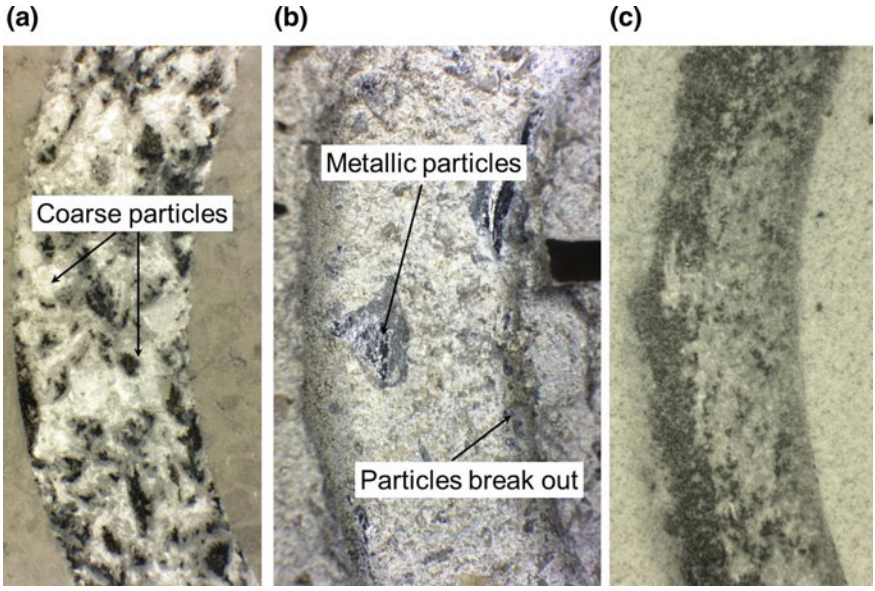

Fig. 1.28 Wear tracks of **a** 100 vol.% alumina (coarse), **b** 90 vol.% zirconia (coarse), **c** 100 vol.% zirconia (fine)

Table 1.14 Mass loss and wear rate of the investigated ceramic matrix composites

Matrix material	Metal fraction	Mass loss g	Wear rate 10^{-2} mm^3/Nm
Alumina (coarse)	0	0.015 ± 0.009	0.050 ± 0.024
	10	0.033 ± 0.032	0.103 ± 0.117
	20	0.014 ± 0.009	0.037 ± 0.027
Zirconia (coarse)	0	1.949 ± 1.322	49.099 ± 33.318
	10	1.233 ± 0.405	11.828 ± 38.863
	20	0.853 ± 0.421	7.789 ± 3.847
Zirconia (fine)	0	0.008 ± 0.011	0.024 ± 0.025
	10	0.027 ± 0.034	0.081 ± 0.028
	20	0.034 ± 0.001	0.076 ± 0.022

characterized by less material abrasion. The continuous stresses may cause surface fatigue in such a way that occasionally larger fragments of the material break out. In these areas the material abrasion is enhanced due to the rough surfaces. The wear behavior of the pressure slip casted composites is similar to existing results in literature. It may be significantly improved if the sintering parameters will be optimized, e.g. performing of the sintering at higher temperatures (1650–1700 °C). However, a compromise between sintering temperatures of the ceramic material and the reinforcing metal particles has to be found.

1.3.4 Development of Ceramic Components Using Alternative Technologies

Intensive research work has been conducted in terms of the development of partially stabilized zirconia fibers using the electrospinning technology. The fibers were prepared from polyvinylpyrrolidone (PVP), $ZrOCl_2 \cdot 8\ H_2O$ and $Y(NO_3)_3 \cdot 6\ H_2O$. The appearance of the as-spun fibers with a mean fiber diameter of 225 nm is displayed in Fig. 1.29. The thermal decomposition behavior has been studied with the aid of DSC/TG-analysis. Three different peaks have been identified and the corresponding total weight loss was determined to be 80%. The first weight loss of 15% from room temperature to 200 °C is caused by the removal of water and ethanol. The second weight loss (47%) is related to exothermic reactions as shown by the DSC curve, see Fig. 1.30. The exothermic peaks at 358, and 400 °C are associated with the decomposition of the PVP. From 400 to 504 °C there was a weight loss of approx.

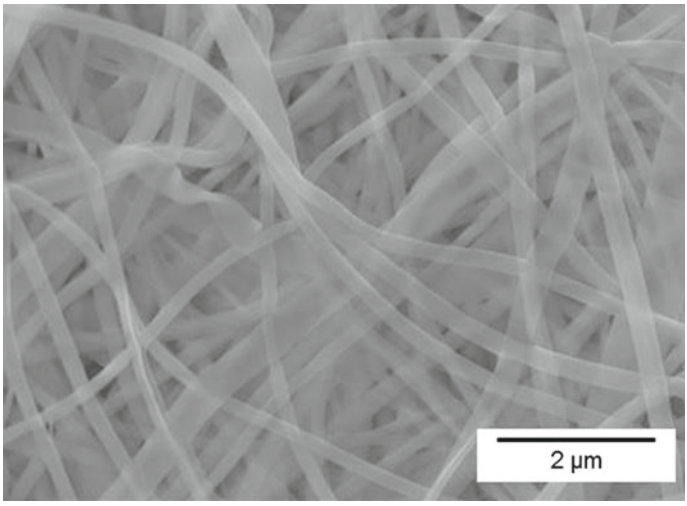

Fig. 1.29 SEM micrograph of the as-spun fibers with a mean fiber diameter of 225 nm

19%, which can be assigned to the transition from $ZrOCl_2$ to ZrO_2 and the further decomposition of PVP.

The as-spun fibers have been sintered at 700, 1100, 1350 and 1650 °C with heating rates of 1 K/min and 10 K/min. The evolution of the crystalline structure has been analyzed using X-ray diffraction. If the sintering was conducted at 700 °C only tetragonal zirconia has been identified, see Fig. 1.31. With increasing sintering temperature the peaks become tapered. Sintering at 1100 °C with a heating rate of 1 K/min led to a decrease of the tetragonal phase in intensity and a monoclinic pattern appears, see

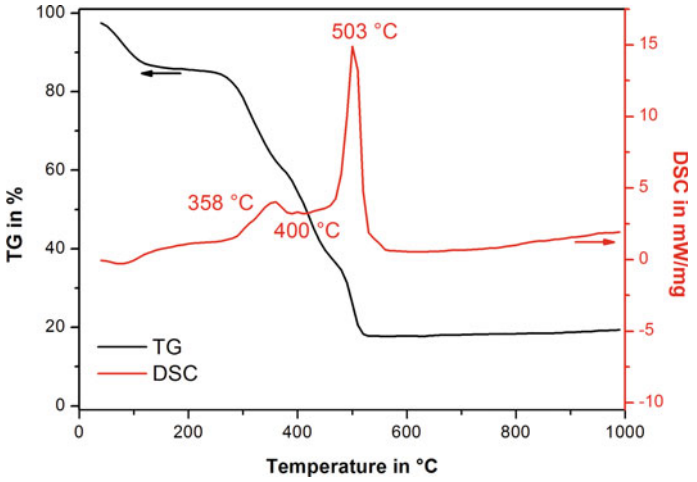

Fig. 1.30 DSC/TG-analysis of the as-spun fibers

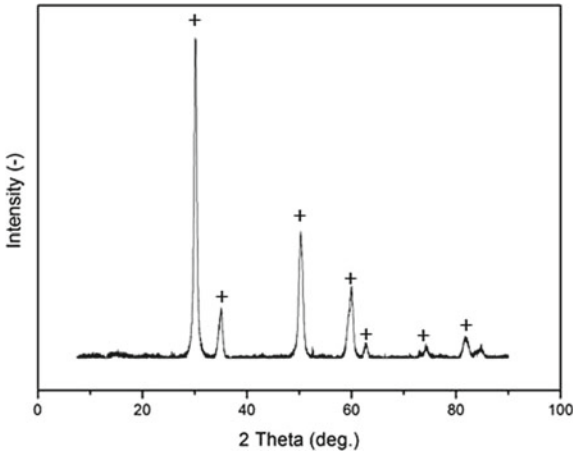

Fig. 1.31 X-ray diffraction pattern of the yttria stabilized zirconia fibers after sintering at 700 °C, tetragonal phase indicated by +

Fig. 1.32. These results are consistent with the observations made by Davies et al. [21] and may be attributed to the coarsening of the zirconia grains/fibers. If the heating rate has been increased to 10 K/min (at the same sintering temperature) the formation of a monoclinic phase and coarsening of the zirconia fibers/grains could not be registered, see Figs. 1.32b and 1.33. At sintering temperatures of 1350 and 1650 °C the tetragonal phase dominates, since the thermal treatment has been conducted in the tetragonal solid solution field. At sintering temperatures of 1350 °C, the fiber structure disappears as shown in Fig. 1.34. The final microstructure is characterized by a high open porosity.

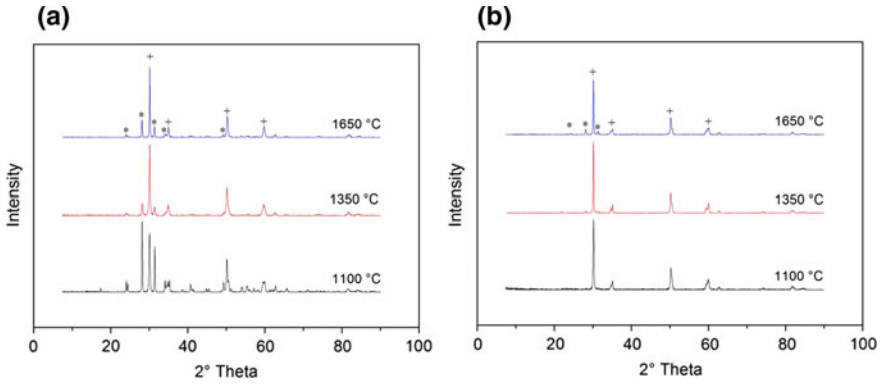

Fig. 1.32 X-ray diffraction patterns of the yttria-stabilized zirconia fibers as a function of the sintering conditions, **a** heating rate of 1 K/min **b** heating rate 10 K/min, (monoclinic phase indicated by *, tetragonal phase indicated by +)

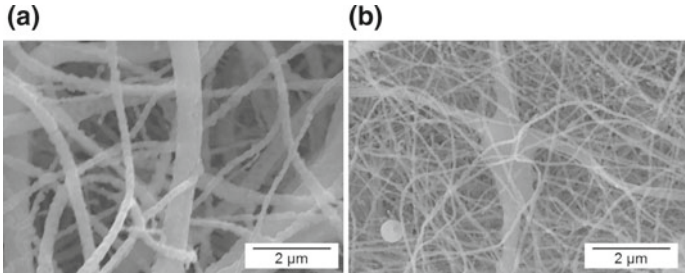

Fig. 1.33 SEM micrographs of the yttria-stabilized zirconia fibers, sintered at 1100 °C with a heating rate of **a** 1 K/min and **b** 10 K/min

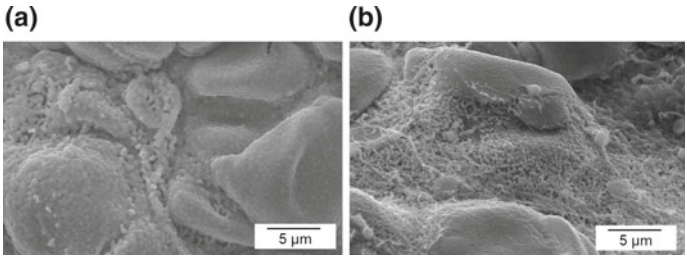

Fig. 1.34 SEM micrographs of the yttria-stabilized zirconia fibers, sintered at 1350 °C with a heating rate of **a** 1 K/min and **b** 10 K/min

1.4 Summary

The present work focused on the development of metal matrix composites and ceramic matrix composites using ***innovative casting technologies*** that are typically employed ***for the fabrication of ceramic components***.

The ceramic processing route of polyurethane foams at room temperature has been applied for the development of open cell foam structures based on austenitic stainless TRIP-steel and TRIP-steel/zirconia composite materials. Advantages have been achieved in terms of higher compressive stresses as well as energy absorption during deformation. Particularly, the supplement of the TRIP-matrix composite with a dense coating (jacket) at the foam macrostructures led to a light structure design with excellent energy absorption values. Due to EBSD-analysis the stress-induced martensitic phase transformation of metastable tetragonal zirconia has been identified at compressive strains below 2%.

Full and hollow beads based on austenitic stainless TRIP-steel have been developed using the gel casting technology. A major success was the development of functionally graded beads prepared via ***gel casting*** in combination with a specific heat treatment. The developed full beads (composition 10Z) as well as the functionally graded beads have compressive strengths of approx. 380 MPa at a compression of 15%. The pure metal reference material (0Z) shows a significantly lower strength of 150 MPa at the same compression. At about 15% compression the full TRIP-matrix beads collapse. The functionally graded beads have a good integrity up to 30% compression and have a significantly higher strength. At small deformation, the stress level of macroscopic bead structures is well above single beads, but then fails due to the poor joining strength. Therefore, the joining between the beads should be optimized to combine the properties of the particle-reinforced beads and functionally graded beads with the good properties of the spherical macrostructures. The functionally graded beads as well as the particle-reinforced beads with 5 and 10 vol.% zirconia show greatest potential within the group of metal beads obtained by gel casting in terms of energy absorption.

Paper-derived metal matrix composites have been developed using the ***paper-manufacturing technology***. Initially sintered TRIP-matrix composites were characterized by a strong carbide formation, resulting in a brittle fracture behavior of these materials. The crack initiation always started from the precipitates and the cracks propagated along the grain boundaries. The highest tensile strength was determined for the zirconia-free reference material with 177 MPa at a total porosity of 66%. A further sintering approach concerned the purification of the flushing gas Argon 5.0 and the improvement of the sealing performance of the furnace. As a result the formation of carbide precipitations was prevented. In a further development, cellulose pulp fibers have been successfully replaced by commercially available zirconia fibers. The resulting fiber reinforced TRIP-matrix composites showed improved tensile strength of 207 MPa, which was approx. 33% higher than for the zirconia-free reference material at a significantly lower porosity. The easy casting technology of the paper-derived metal matrix composites, the possibility to tune the functional properties as well as the raw material selection allows a wide range of applications e.g. as filter material, heat exchanger or catalyst material.

Open cell foam structures based on magnesia partially stabilized zirconia were prepared using the ***replica technique***. If the spray coating procedure was done airstream assisted the homogeneity of the ceramic struts was significantly improved. The optimized slurry based on magnesia partially stabilized zirconia contained 45 wt.% water. After the infiltration of the sintered foam structures the TRIP-matrix composite contained 4.5 vol.% monoclinic zirconia, 49.8 vol.% tetragonal zirconia and 45.7 vol.% cubic zirconia. Thus, approximately 50 vol.% of the ceramic material is able to transform stress-assisted. The steel matrix consisted of 100% austenite.

Another emphasis of the present work was the fabrication of ceramic matrix composites using ***pressure slip casting***. After successful casting the composites were sintered at 1550 °C in argon atmosphere and the homogenous distribution of the steel particles within the matrix materials has been verified. As a result of the casting technology and the sintering temperatures the pressure slip casted ceramic matrix composites had open porosities of $\geq$27%. Within this work package the wear behavior of the composites has been investigated using a pin-on-disc test. The wear behavior of the pressure slip casted composites was similar to existing results in literature and will be improved if the sintering parameters are optimized. Moreover, the pressure slip casted ceramic matrix composites have a high potential for applications at elevated temperatures, since they show a good resistance to thermal shock [16].

A further challenge was the development of zirconia fibers with a tailored phase composition via ***electrospinning***. Fibers were successfully prepared from polyvinylpyrrolidone (PVP), $ZrOCl_2 \cdot 8\,H_2O$ and $Y(NO_3)_3 \cdot 6\,H_2O$. Up to a sintering temperature of 1100 °C single zirconia fibers can be obtained. Due to the addition of varying amounts of yttrium (III) nitrate hexahydrate the phase composition was successfully tailored.

Acknowledgements The authors gratefully acknowledge the financial support of the Deutsche Forschungsgemeinschaft (DFG, German Research Foundation) for funding this research project A1

within the frame of the Collaborative Research Center (CRC) 799—TRIP-Matrix-Composites—project number 54473466.

We would like to thank our former colleagues Dr.-Ing. Wolfgang Schärfl and Dipl.-Ing. Manuel Hasterok for their contribution to the subproject A1. For the experimental support we would like to acknowledge the support of Dipl.-Ing. Anna Schneider and M.Sc. Christian Krumbiegel. Moreover, we like to thank our colleagues of the CRC 799, particularly Dr.-Ing. Anja Weidner, Dr.-Ing. Anke Dalke, Dr.-Ing. Katja Pranke and Dipl.-Ing. Christine Baumgart. We greatly appreciate the support of our colleagues at the Chair of Ceramics, in particular Dr.-Ing. Christian Weigelt, Dr.-Ing. habil. Harry Berek, Dr.-Ing Christiane Biermann and M.Eng. Ashish Pokhrel.

References

1. C. Aneziris, W. Schärfl, H. Biermann, U. Martin, Int. J. Appl. Ceram. **6**, 727 (2009)
2. C.G. Aneziris, H. Biermann, P. Scheller, TU Bergakademie Freiberg, German Patent, DE10 2007 044 160, 19 June 2008
3. C.G. Aneziris, H. Berek, M. Hasterok, H. Biermann, S. Wolf, L. Krüger, Adv. Eng. Mater. **12**, 197 (2010)
4. M. Oppelt, C. Wenzel, C.G. Aneziris, H. Berek, Metall. Mater. Trans. B. **45**, 2000 (2014)
5. M. Oppelt, C.G. Aneziris, J. Alloys. Compd. **634**, 43 (2015)
6. M. Oppelt, T. Leißner, H. Berek, C. Baumgart, L. Krüger, U. Peuker, C.G. Aneziris, Adv. Eng. Mater. **21**, 1 (2018)
7. M. Oppelt, Dissertation, Technische Universität Bergakademie Freiberg (2018)
8. C. Wenzel, Dissertation, Technische Universität Bergakademie Freiberg (2016)
9. M. Hasterok, C. Wenzel, C.G. Aneziris, U. Ballaschk, H. Berek, Steel Res. Int. **82**, 1032 (2011)
10. C. Wenzel, C.G. Aneziris, Steel Res. Int. **82**, 1057 (2011)
11. W. Schärfl, H. Berek, C.G. Aneziris, M. Weider, A. Yanina, Adv. Eng. Mater. **13**, 480 (2011)
12. M. Weider, K. Eigenfeld, Steel Res. Int. **82**, 1064 (2011)
13. G.C. Jacob, J.F. Fellers, S. Simunovic, J.M. Starbuck, J. Compos. Mater. **36**, 813 (2002)
14. H. Berek, C.G. Aneziris, M. Hasterok, H. Biermann, S. Wolf, L. Krüger, Solid State Phenom. **172–174**, 709 (2011)
15. C. Wenzel, C.G. Aneziris, K. Pranke, Metall. Mater. Trans. A. **47**, 160 (2016)
16. C. Wenzel, C. G. Aneziris, Mater. Sci. Eng., B **176**, 32 (2011)
17. H. Berek, C.G. Aneziris, M. Hasterok, H. Biermann, S. Wolf, L. Krüger, Adv. Eng. Mater. **13**, 1037 (2011)
18. C.G. Aneziris, W. Schärfl, TU Bergakademie Freiberg, German Patent, DE10 2007 001 724 A1, 11 July 2008
19. C. Weigelt, Dissertation, Technische Universität Bergakademie Freiberg (2013)
20. J.S. Reed, *Principles of Ceramic Processing*, 2nd edn. (Wiley, New York, 1995)
21. E. Davies, A. Lowe, J. Am. Ceram. Soc. **91**, 1115 (2008)

Chapter 2
Design of High Alloy Austenitic CrMnNi Steels Exhibiting TRIP/TWIP Properties

Qiuliang Huang, Marco Wendler, Javad Mola, Andreas Weiß, Lutz Krüger and Olena Volkova

Abstract This chapter is centered on the development of austenitic high strength cast CrMnNi steels with excellent strength-ductility combination by triggering TWIP and TRIP effects. Special attention is given to obtain a high yield strength and a good formability. For this purpose, three generations of steels were developed. The 1st generation is comprised of cast X3CrMnNi16-7-x steels. Their Ni concentration was varied in order to manipulate the stacking fault energy of austenite and change the operative deformation mechanisms. Based on the mechanical properties of the 1st generation steels, the 2nd generation steels were developed with a composition similar to the X3CrMnNi16-7-6 steel. Interstitial alloying elements were added to take advantage of solid solution strengthening and precipitation hardening effects. The substitutional alloy contents were carefully adjusted to ensure the occurrence of TRIP/TWIP effects during plastic deformation. For the 3rd generation, two steels from the 2nd generation, X16CrNiMnN15-3-3 and X16CrNiMnN19-4-3, were treated with tailored quenching and partitioning (Q&P) processing routines to further increase

Q. Huang (✉) · M. Wendler · A. Weiß · O. Volkova
Institute of Iron and Steel Technology, TU Bergakademie Freiberg, Freiberg, Germany
e-mail: qhuang@iest.tu-freiberg.de

M. Wendler
e-mail: marco.wendler@iest.tu-freiberg.de

A. Weiß
e-mail: weiss@iest.tu-freiberg.de

O. Volkova
e-mail: volkova@iest.tu-freiberg.de

J. Mola
Material Design and Structural Integrity Lab, Osnabrück University of Applied Sciences, Osnabrück, Germany
e-mail: j.mola@hs-osnabrueck.de

L. Krüger
Institute of Materials Engineering, TU Bergakademie Freiberg, Freiberg, Germany
e-mail: krueger@ww.tu-freiberg.de

H. Biermann and C. G. Aneziris (eds.), *Austenitic TRIP/TWIP Steels and Steel-Zirconia Composites*, Springer Series in Materials Science 298,
https://doi.org/10.1007/978-3-030-42603-3_2

the strength, especially the yield strength. The developed Q&P cast steels exhibited an outstanding strength-ductility combination, e.g. a yield strength over 1000 MPa and a total elongation exceeding 20% for the steel X16CrNiMnN15-3-3 containing 0.12 wt% N.

2.1 Introduction

Conventional austenitic stainless steels such as AISI 304 have been widely accepted in industry due to their outstanding properties such as superior toughness and extraordinary formability [1]. They are usually used in the annealed state and exhibit relatively low strength. Therefore, efforts have been made to develop metastable austenitic steels with low stacking fault energy (SFE) to enhance the strength-ductility combination by introducing transformation-induced and twinning-induced plasticity (TRIP and TWIP) effects during deformation of the steels [2–4].

To enable martensitic transformation at a certain temperature, the Gibbs free energy of martensite must be lower than that of austenite. The temperature, where the Gibbs free energies of the two phases are equal, is usually denoted as T_0 [5]. In practice, a sufficient undercooling below T_0 is often required to supply the interfacial energy between the austenite and the martensite nuclei as well as the elastic strain energy associated with the transformation [6]. Under external loading, deformation can proceed via martensitic transformation, twinning and other plasticity mechanisms. The occurrence of these mechanisms depends on the chemical composition and temperature, as they both influence the SFE [7–10]. It is commonly accepted that a SFE below 20 mJm^{-2} favors the transformation of austenite into martensite by either the sequence $\gamma \rightarrow \varepsilon \rightarrow \alpha'$ or direct $\gamma \rightarrow \alpha'$ transformation [11, 12]. The deformation-induced transformation to martensite is regarded to be responsible for the so-called TRIP effect [13].

When SFE increases to a value between 20 and 40 mJm^{-2}, the formation of mechanical twins is often observed [14]. The twins have different crystal orientations with respect to the matrix and hence, they reduce the effective glide distance of dislocations. The latter leads to an enhanced strain hardening, especially in the presence of a high twin density. This mechanism in TWIP steels is described as the dynamic Hall-Petch effect [15]. With an even higher SFE, where dissociation of perfect dislocations is energetically unfavorable, deformation proceeds mainly by the wavy glide of perfect dislocations [16]. It results in dislocation cell structures with almost dislocation-free interiors [17].

Decreasing SFE enhances the planar slip of dislocations, which promotes the formation of deformation bands with numerous stacking faults (SF) localized on parallel {111} planes of austenite. At a given strain rate, the associated ductility increases significantly compared to steels with high SFE, where wavy glide serves as the dominant deformation mechanism [18]. Table 2.1 summarizes the temperature dependence of austenite SFE [19]. SFE can also be modified by careful adjustment of the alloy content. The Cr, Si, and Mn addition in Fe–Cr–Ni austenitic stainless steels

Table 2.1 Variation of austenite SFE with temperature ($d\gamma_{SF}/dT$) [19]

Alloys (wt%)	$d\gamma_{SF}/dT$ (mJm^{-2} K^{-1})	Temperature range (°C)	References
Fe–18Cr–14Ni–4Si	0.04	$-123 \leq T \leq 127$	[7]
Fe–18.3Cr–10.7Ni	0.05	$25 \leq T \leq 325$	[7, 23]
Fe–7.8Cr–12Ni	0.05	$-150 \leq T \leq 100$	[24]
Fe–17.8Cr–14.1Ni	0.06	$-180 \leq T \leq 27$	[7, 8]
Fe–15.9Cr–12.5Ni	0.08	$-115 \leq T \leq 100$	[7, 8]
Fe–18.7Cr–16.9Ni	0.10	$25 \leq T \leq 325$	[7, 23]
Fe–18Cr–7Ni–0.18C	0.10	$20 \leq T \leq 330$	[7, 25]
Fe–19.9Mn–4Cr–0.48C	0.08	$27 \leq T \leq 127$	[26]

was found to lower SFE and promote the planar dislocation arrays, while the Ni and C alloying raises SFE and encourages a cellular dislocation arrangement [20]. There is no consensus regarding the effect of N on SFE. In an Fe–21Cr–6Ni–9Mn steel, SFE reduces from 53 mJm^{-2} at 0.21 wt% N to 33 mJm^{-2} at 0.24 wt% N [21]. Further increase in N content up to 0.52 wt% does not vary the SFE. In the Fe–18Cr–10Mn steel, on the contrary, SFE increases from 10 mJm^{-2} at 0.39 wt% N to 23 mJm^{-2} at 0.69 wt% N [22].

The present work focuses on developing CrMnNi cast stainless steels as the matrix for novel composite materials, TRIP-Matrix-Composites, for the Collaborative Research Center 799. Efforts, including varying the Ni content, addition of different interstitial contents, and application of tailored quenching and partitioning (Q&P) processing routines, were made to achieve a high strength combined with a high ductility in the cast CrMnNi stainless steels.

2.2 Experimental Methods

The steels were all melted in a VIM12 vacuum induction melting and casting facility (ALD Vacuum Technologies GmbH) and cast in water-cooled copper molds as illustrated in Fig. 2.1. Details about the production of the steels can be referred to [27–29].

Hollow specimens with a length of 10 mm, an outer diameter of 4 mm and an inner diameter of 2 mm were used for dilatometry experiments on Bähr 805 A/D dilatometer with a cryogenic unit, which enabled subzero quenching to −130 °C. The as-quenched α'-martensite fraction ($f^{Q}_{\alpha'}$) was determined by subtracting the δ-ferrite fraction estimated by optical microscopy from the ferromagnetic phase fraction quantified by magnetic measurements. The latter was obtained based on the measured magnetization after corrections for the effect of alloying elements on the magnetization of pure iron. The accuracy is therefore dependent on the accuracy of the corrections for the effect of chemical composition and is usually within ±1 vol%.

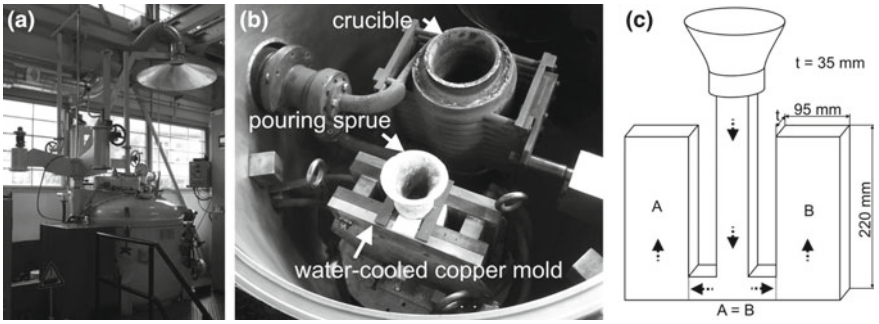

Fig. 2.1 **a** VIM 12 vacuum induction melting and casting facility used for the fabrication of the cast steels; **b** Components inside the furnace chamber; **c** Schematic view of the cast mold with arrows indicating the flow direction of the melt during casting [29]

The mechanical properties of the steels were evaluated by tensile testing on a Zwick 1476 universal testing machine at various temperatures. Tensile specimens with a gauge diameter of 6 mm and a gauge length of 30 mm were machined according to ISO 6892-1. The tensile direction was parallel to the height of ingots A and B in Fig. 2.1c. To minimize the adiabatic heating of tensile specimens, the crosshead displacement speed was set to 1 mm min^{-1}. This corresponds to an initial strain rate of 4×10^{-4} s^{-1}. For each alloy, three specimens were tested at each temperature. Strain-induced α'-martensite fraction ($f_{\alpha'}^{\text{ind.}}$) was determined by subtracting the α'-martensite fraction ($f_{\alpha'}$) in the undeformed grip section from the α'-martensite fraction in the uniformly-deformed gauge section. After $f_{\alpha'}^{\text{ind.}}$ values at various testing temperatures are obtained, the first temperature where $f_{\alpha'}^{\text{ind.}}$ becomes 1 vol% is determined as M_d.

Besides optical microscope, microstructures were examined using a Zeiss ULTRA 55 GEMINI-type field emission scanning electron microscope (FESEM) equipped with an AMETEK-EDAX analysis system for chemical composition and elemental distribution analysis. The deformed microstructures were characterized by electron backscatter diffraction (EBSD) measurements and electron contrast channeling imaging (ECCI). The step size for EBSD examinations was 0.1–0.2 μm and the camera (DIGIVIEW) output rate was 70 frames per second. ECCI was performed using an angle-selective backscatter electron detector (ASB) and a large aperture in the high current mode. The precipitation of carbides was verified by selected area electron diffraction (SAED) and Fast-Fourier Transformation (FFT) of high-resolution images in a Jeol JEM-2200FS transmission electron microscope (TEM). Efforts were made to avoid martensitic transformation during sample preparation by grinding and polishing at 80 °C and final electropolishing. The fracture surfaces of tested tensile specimens were examined using the secondary electron (SE) detector at an acceleration voltage of 10 kV.

2.3 Austenitic CrMnNi Cast Steels

For the 1st generation steels, the SFE was modified by varying the Ni content in cast X3CrMnNi16-7 steels from 3 to 9 wt%. Tensile testing at various temperatures reveals pronounced TRIP effect at RT in the cast steels with 3 and 6 wt% Ni.

2.3.1 Constitution and Special Methods

The chemical compositions of the 1st generation CrMnNi steels are shown in Table 2.2. To determine martensite start (M_s) temperatures, dilatometry cycles involving heating under vacuum to 1050 °C at 10 K/s and cooling to −130 °C at 10 K/s after a holding time of 30 min were performed [30]. Prior to tensile tests, tensile specimens were solution annealed at 1050 °C for 30 min under vacuum to reduce the compositional inhomogeneity of substitutional elements generated during solidification. Tensile tests were done at temperatures ranging from −196 to 250 °C.

2.3.2 Initial Microstructures of 16-7-3/6/9 Steels

The microstructures of the cast steels were predicted based on Schaeffler diagram (Fig. 2.2) with Cr− and Ni-equivalents (Cr_{eq} and Ni_{eq}) calculated according to the following equations proposed for cast austenitic stainless steels [32]:

$$\begin{aligned} Cr_{eq} = {} & \%Cr + \%Mo + 4\%Ti + 4\%Al + 1.5\%Si \\ & + 1.5\%\,V + 0.9\%Nb + 0.9\%Ta + 0.5\%W \end{aligned} \tag{2.1}$$

$$\begin{aligned} Ni_{eq} = {} & \%Ni + 30\%C + 18\%N + 0.5\%Mn \\ & + 0.3\%\,Co + 0.2\%Cu - 0.2\%Al \end{aligned} \tag{2.2}$$

The microstructures and phase fractions of the cast steels are demonstrated in Fig. 2.3. With increasing Ni content, the fractions of α'-martensite and δ-ferrite decrease until a fully austenitic microstructure is obtained for the 9% Ni alloy. The SFE of the steels at RT is calculated according to the empirical relationship in (2.3)

Table 2.2 Chemical compositions of the 1st generation CrMnNi steels in wt% [31]

Steels	Steel ID	Cr	Mn	Ni	Si	C	N
Cast X3CrMnNi16-7-3	16-7-3	16.40	7.00	3.10	1.00	0.03	0.01
Cast X3CrMnNi16-7-6	16-7-6	16.20	7.10	5.90	1.10	0.03	0.01
Cast X3CrMnNi16-7-9	16-7-9	16.40	6.90	9.00	1.09	0.03	0.01

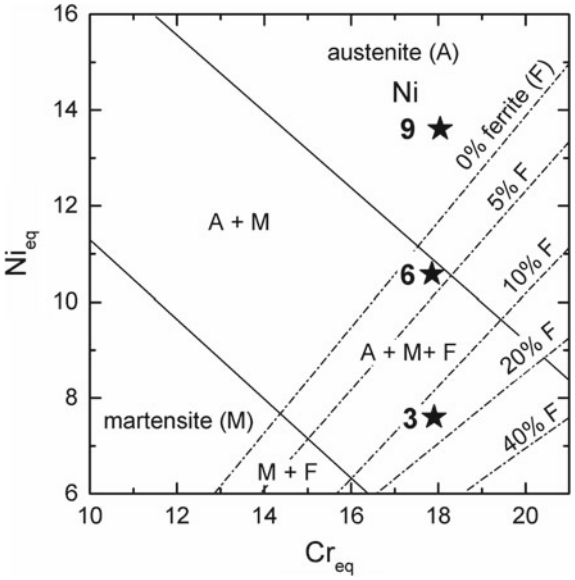

Fig. 2.2 Position of 16-7-3/6/9 steels in Schaeffler diagram based on (2.1)–(2.2)

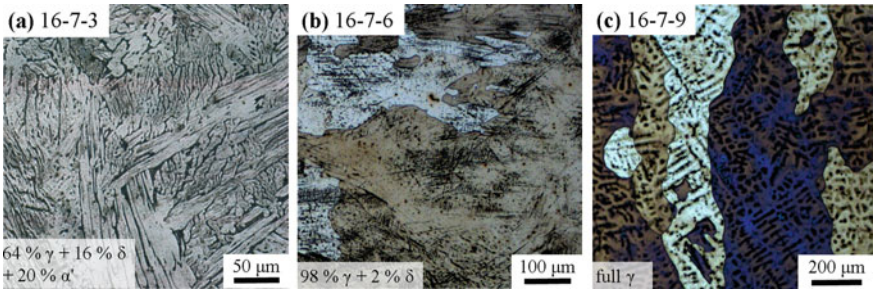

Fig. 2.3 Optical micrographs and phase fractions of the steels **(a)** 16-7-3, **(b)** 16-7-6 and **(c)** 16-7-9 solution annealed at 1050 °C for 30 min. Note that the straight lines (black) in some austenitic regions of (**b**) represent deformation bands induced in the first solidified regions (dendrite cores) during the metallographic preparation. The depletion of alloying elements and the low stability of austenite in such regions may lead to the formation of preparation-induced martensite. The samples were etched with Beraha I solution [34]

[33]. The calculated SFEs and the M_s temperatures determined using dilatometry are shown in Table 2.3.

$$\begin{aligned}\mathrm{SFE} = {} & 39 + 1.59\%\mathrm{Ni} - 1.34\%\mathrm{Mn} + 0.06\%\mathrm{Mn}^2 - 1.75\%\mathrm{Cr} + 0.01\%\mathrm{Cr}^2 \\ & + 15.21\%\mathrm{Mo} - 5.59\%\mathrm{Si} + 26.27(\%\mathrm{C} + 1.2\%\mathrm{N})(\%\mathrm{Cr} + \%\mathrm{Mn} + \%\mathrm{Mo})^{1/2} \\ & + 0.61[\%\mathrm{Ni}(\%\mathrm{Cr} + \%\mathrm{Mn})]^{1/2} - 60.69(\%\mathrm{C} + 1.2\%\mathrm{N})^{1/2} \end{aligned} \quad (2.3)$$

2.3.3 Mechanical Properties of 16-7-3/6/9 Steels

The stress-strain curves of the cast steels are indicated in Fig. 2.4. The associated mechanical properties and the $f_{\alpha'}$ values are summarized in Fig. 2.5. Analogous to M_s temperatures, M_d temperatures calculated based on $f_{\alpha'}^{\text{ind.}}$ in Fig. 2.5d reduce with raised Ni contents (120 → 60 → 30 °C). With decreasing tensile test temperature from 250 °C to M_d temperature the elongation increases (Fig. 2.5b) due to the reduced SFE, which promotes the propagation of SFs and restricts climb and cross slip of dislocations [35]. Below M_d temperature, where strain-induced α'-martensite formation can be triggered, elongation decreases as a result of the early occurrence of α'-martensite during tensile tests and the accompanied obstruction of planar dislocation motion in the austenite. Intersection points of slip bands, SFs, ε-martensite and twins may act as nucleation sites for the strain-induced α'-martensite formation.

The elongation of the 16-7-9 steel decreases first below 20 °C and then increases again when the temperature drops from −70 to −196 °C. The latter increase is related to an attenuated α'-martensitic transformation below Néel temperature (T_N), which enhances the plasticity. The influence of T_N on α'-martensite formation is discussed in detail in Sect. 2.4.3.

Owing to the presence of a high $f_{\alpha'}^{Q}$ in the undeformed condition, the 16-7-3 steel (Fig. 2.5d) exhibited almost always the smallest $f_{\alpha'}^{\text{ind.}}$ (Fig. 2.5c) but the highest total $f_{\alpha'}$ after tensile tests (Fig. 2.5d). This explains the higher ultimate tensile strength (UTS) of the 16-7-3 steel compared to 16-7-6 and 16-7-9 steels (Fig. 2.5a). The presence of 16 vol% δ-ferrite in the initial microstructure of the 16-7-3 steel might have also contributed to its higher strength as ferrite often offers a higher strength than austenite. In contrast, the fully austenitic 16-7-9 steel provides the lowest tensile strength.

At RT, the UTS and total elongation (TE) are 1013 MPa and 23% for the 16-7-3 steel, 765 MPa and 53% for the 16-7-6 steel, and 550 MPa and 72% for the 16-7-9 steel, respectively. Due to the higher Ni content and SFE of the 16-7-9 steel compared to the other two steels, the α'-martensitic transformation was almost fully suppressed during testing at RT. In contrast, a pronounced TRIP effect was observed in both 16-7-3 and 16-7-6 steels. The products of UTS and TE are 23.3, 40.5 and 39.6 GPa% for the 16-7-3, 16-7-6, and 16-7-9 steels, respectively.

To examine the formability of steels at RT, an austenitic cast steel with a chemical composition similar to the 16-7-6 steel, namely X4CrMnNi16-7-7, was cold rolled in 22 passes to reduce the thickness from 14.3 mm to 0.7 mm. The total reduction

Table 2.3 M_s temperatures and SFE based on (2.3) for 16-7-3/6/9 steels [31]

Steel ID	M_s (°C)	SFE at RT (mJm^{-2})
16-7-3	61	10
16-7-6	1	16
16-7-9	−47	22

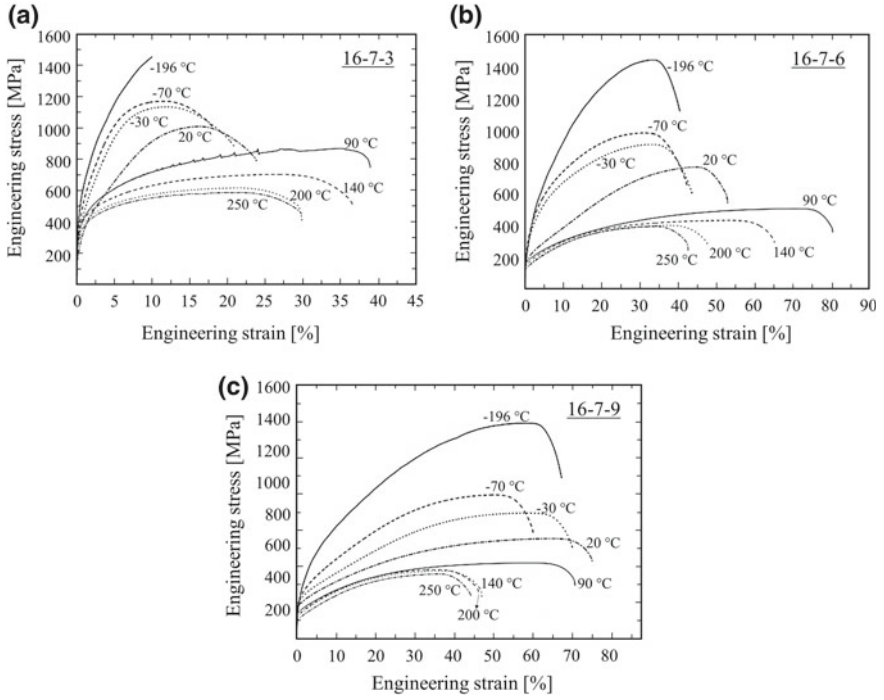

Fig. 2.4 Stress-strain curves of **a** 16-7-3, **b** 16-7-6, and **c** 16-7-9 steels tested at various temperatures [31]

ratio was 95%. Between consecutive passes, the steel was allowed to cool down to RT. As shown in Fig. 2.6a, the TRIP effect occurred already in the second pass. After the final pass, 21 vol% strain-induced α'-martensite was formed, which increased the hardness from 143 to 515 HV. In spite of its coarse cast dendritic microstructure, the ingot could be successfully rolled without any intermediate annealing.

The outstanding mechanical properties of the cast steels of the present study, regardless of their cast microstructure which is usually characterized by a coarse grain size and poor ductility [36], can be attributed to the low SFE of the steels ranging between 10 and 22 mJm^{-2}. At these SFE values, plastic deformation proceeds by planar glide of partial dislocations and may be aided by TRIP/TWIP effects. The formation of deformation bands, strain-induced α'-martensite and mechanical twins fragments the coarse cast structure and decreases the grain size of the initial austenite. They serve as obstacles to dislocation motion and hence, reduce the dislocation mean free path. The associated enhanced strain hardening postpones the necking of the material according to the Considère criterion. In this way, the drawback of a coarse cast structure is partly compensated.

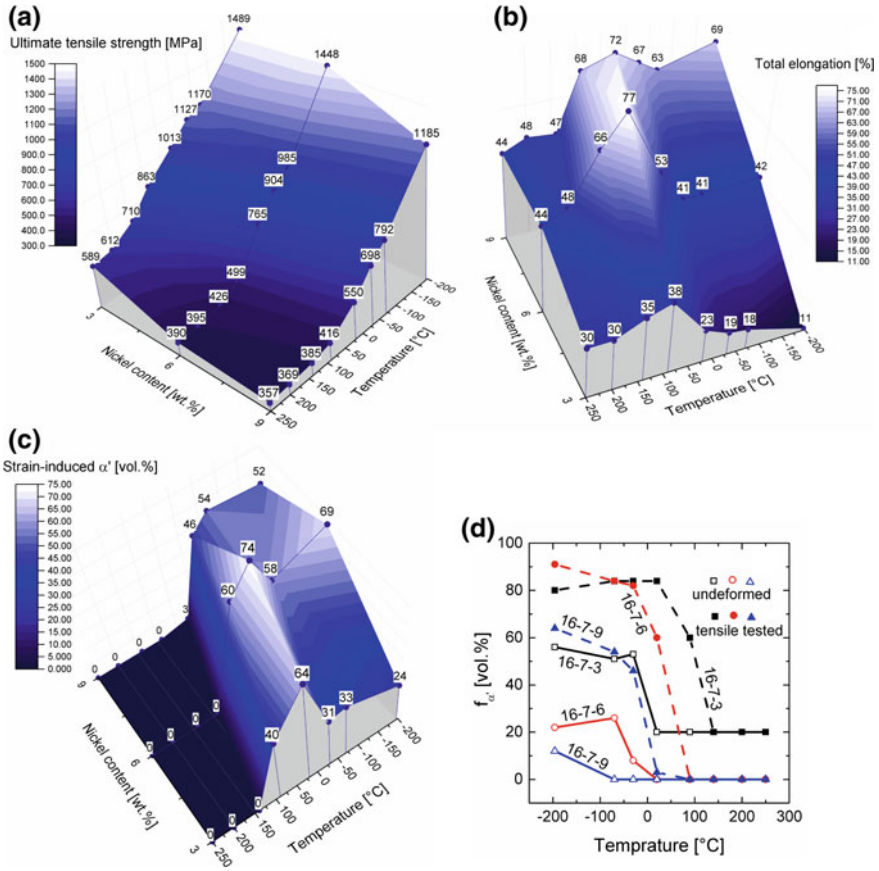

Fig. 2.5 **a** UTS, **b** TE, **c** $f_{\alpha'}^{\text{ind.}}$, and **d** $f_{\alpha'}^{Q}$ (open symbols) and total $f_{\alpha'}$ after tensile tests (solid symbols) at various Ni contents and temperatures

2.3.4 *Conclusions for the 1st Generation Steels*

The mechanical properties of the 1st generation cast stainless steels consisting of X3CrMnNi16-7-3/6/9 were investigated in the temperature range of −196 to 250 °C. In general, all steels exhibited a tensile behavior typical for austenitic steels with deformation-induced plasticity mechanisms. At decreasing tensile temperatures, the tensile elongation increases to a peak value before it reduces at temperatures below $M_d^{\gamma \rightarrow \alpha'}$. The temperature corresponding to the peak elongation decreases at higher Ni content. In addition, the grain fragmentation resulting from the formation of deformation bands, strain-induced α'-martensite and mechanical twins compensates the disadvantages of the coarse cast structures in the studied steels and results in their excellent mechanical properties at RT.

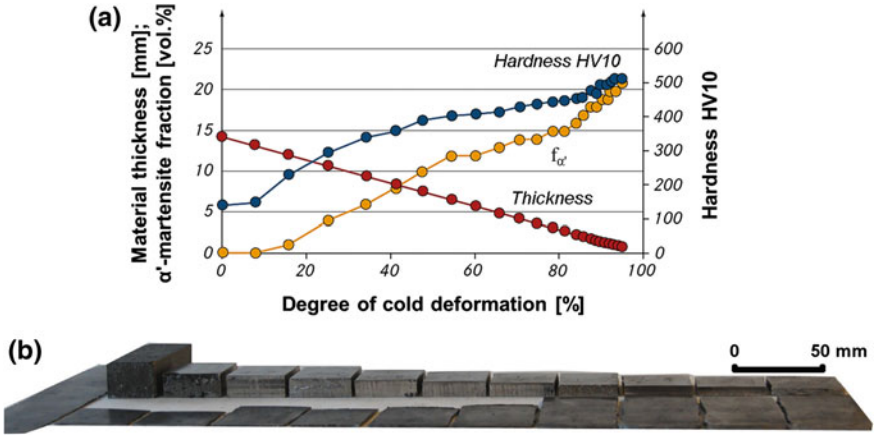

Fig. 2.6 **a** The variation in thickness, $f_{\alpha}{}'$ and hardness of an X4CrMnNi16-7-7 cast ingot during 22 passes of cold rolling; **b** Pictures showing thickness reduction during rolling [37]

2.4 Austenitic CrMnNi–C–N Cast Steels

Although the steels studied in the first period, especially 16-7-6, provide excellent strength-ductility combination, their strength level at RT remains low (below 1000 MPa). Therefore, the target for the 2nd generation was to achieve a high strength, especially yield strength (YS), by the addition of interstitial alloying elements to make use of their solid solution strengthening effect as well as precipitation hardening by the formation of carbides, nitrides and carbo-nitrides. To counterbalance the austenite stabilizing effect of interstitial alloying, the substitutional contents were modified to facilitate the occurrence of TRIP effect during plastic deformation.

2.4.1 Constitution and Special Methods

Two series of steels with compositions shown in Tables 2.4 and 2.5 were produced. In both series, the N content is maintained nearly constant (target N contents of either 0.10 wt% in Series I and 0.15 wt% in Series II) while C contents are varied between 0.05 and 0.25 wt% in steps of 0.05 wt%. To achieve high N contents of nearly 0.15 wt% in Series II, their Cr contents were raised to 19 wt% to increase the N solubility in the liquid steel [38]. In short, Series I steels with the designation X(0.05-0.25)CrNiMnN15-3-3 are denoted as Cr15NC10.X and Series II steels with the designation X(0.05-0.25)CrNiMnN19-4-3 are referred to as Cr19NC15.X, where X indicates the C concentration in wt% times hundred. The molten steels were cast in a copper mold with a cross section dimension of 95 × 35 mm^2.

Table 2.4 Chemical compositions of interstitially-alloyed X(0.05–0.25) CrNiMnN15-3-3 steels in wt% and the respective SFEs based on (2.1) [39]

Steel	Steel ID	Cr	Ni	Mn	Si	N	C	SFE (mJm^{-2})
Cast X5CrNiMnN15-3-3	Cr15NC10.05	14.90	2.86	3.11	0.51	0.103	0.052	12
Cast X10CrNiMnN15-3-3	Cr15NC11.10	15.20	2.89	3.20	0.48	0.107	0.100	14
Cast X16CrNiMnN15-3-3	Cr15NC12.16	14.90	2.91	2.97	0.53	0.122	0.155	18
Cast X20CrNiMnN15-3-3	Cr15NC11.20	15.10	3.23	2.99	0.49	0.106	0.200	20
Cast X25CrNiMnN15-3-3	Cr15NC13.25	14.90	3.03	3.02	0.57	0.132	0.250	24

Table 2.5 Chemical compositions of interstitially-alloyed X(0.05–0.25) CrNiMnN19-4-3 steels in wt% and the respective SFEs based on (2.1) [19]

Steel	Steel ID	Cr	Ni	Mn	Si	N	C	SFE (mJm^{-2})
Cast X5CrNiMnN19-4-3	Cr19NC14.05	18.90	4.02	2.90	0.53	0.140	0.051	14
Cast X10CrNiMnN19-4-3	Cr19NC15.10	19.20	3.97	3.09	0.53	0.149	0.097	17
Cast X16CrNiMnN19-4-3	Cr19NC14.16	19.20	4.11	3.20	0.50	0.140	0.156	21
Cast X20CrNiMnN19-4-3	Cr19NC16.21	19.30	4.09	3.15	0.54	0.162	0.208	26
Cast X25CrNiMnN19-4-3	Cr19NC15.26	19.10	4.17	3.06	0.49	0.146	0.264	30

The addition of interstitial elements inevitably introduces precipitates such as $M_{23}C_6$ carbides and M_2N nitrides (M denotes Fe and Cr) during cooling of the ingots. These precipitates would reduce the solute interstitial contents of steels. Hence, the steels were solution annealed at temperatures above their full dissolution points prior to the tensile tests. The full dissolution temperatures increase at higher interstitial contents as predicted by phase diagrams in Fig. 2.7. The applied solution annealing temperatures as marked in Fig. 2.7 were chosen based on the results obtained by dilatometry and Thermo-Calc. Annealing was performed for 30 min followed by water quenching to RT to suppress the re-formation of precipitates.

The influence of T_N temperature on the α'-martensite formation was investigated using Cr15NC10.X steels. T_N of the alloys were calculated by extrapolating the available thermodynamic database of Thermo-Calc version S [40] to temperatures below RT. The sensitivity of T_N to the C concentration was quite low. The calculated T_N temperatures were −132 °C and −128 °C for the steels Cr15NC13.25 and Cr15NC10.05, respectively. To determine the effect of the antiferromagnetic to paramagnetic transition of austenite at T_N on the formation of α'-martensite, solution annealed cylindrical specimens with a dimension of Ø6 mm × 3.5 mm were

quenched to temperatures between −196 °C and RT and held for 10 min. The spontaneous α'-martensite fractions were subsequently quantified by magnetic saturation measurements.

2.4.2 Initial Cast Microstructures of the Steel Series

The used ingot mold had a cross section of 95 × 35 mm^2 different from the 50 × 50 mm^2 employed for the 1st generation steels. The increased contact area of the liquid steel with the mold, arising from the rectangular shape of the cross section, boosted the heat dissipation into the mold and resulted in the refinement of dendrites during solidification. As indicated in Fig. 2.8, the primary dendrite spacing of the cast ingots was significantly finer than those of the 1st generation steels, leading to a less pronounced microsegregation of main alloying elements.

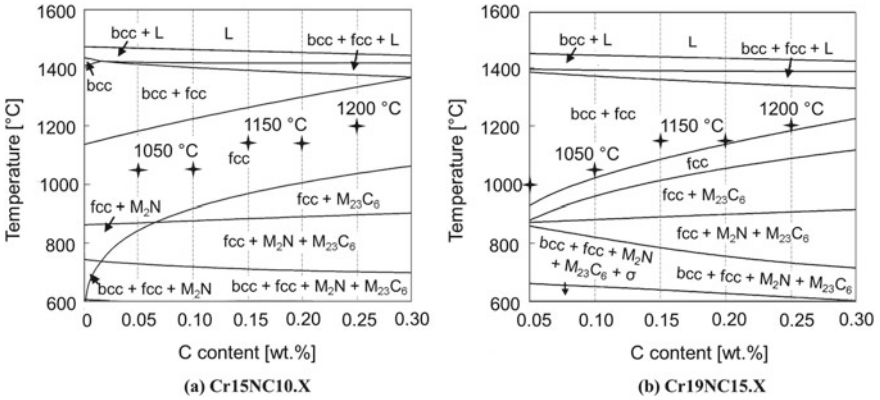

Fig. 2.7 Phase diagrams of **a** Cr15NC10.X [39] and **b** Cr19NC15.X [19] steels. Symbols indicate solution annealing temperatures prior to tensile tests

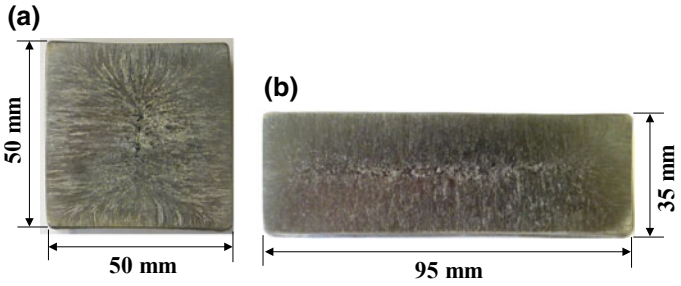

Fig. 2.8 Cross sections of **a** 16-7-6 and **b** Cr15NC11.20 cast ingots

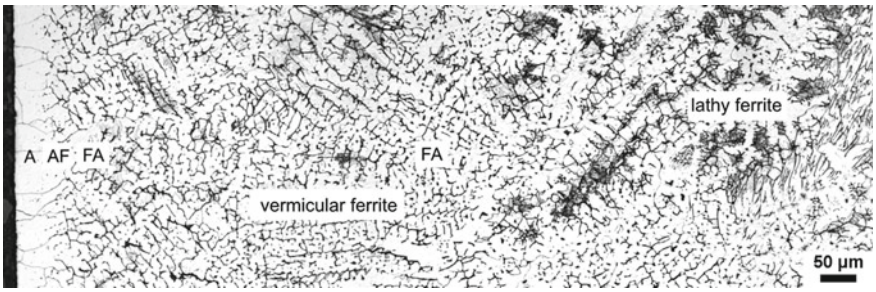

Fig. 2.9 Varied solidification mode from the outer surface (left) towards the core (right) of the Cr19NC14.16 ingot: A → AF → FA. V_2A reagent was used as etchant [19]

All the cast ingots exhibit pronounced dendritic microstructures and heterogeneous phase distribution as exemplified by Cr19NC14.16 in Fig. 2.9. At the outer layer of the ingot, due to the enormous undercooling of the melt generated by its direct contact with the cold mold, austenite forms at first with segregation of ferrite stabilizer Cr in the melt. The solidification heat release in the front reduces the undercooling of the melt. Along with the enriched Cr content in the melt, the solidification mode changes from primary Austenite (A) to Austenite-Ferrite (AF). Therefore, from the outer layer towards the center, the solidification mode varies in sequence: primary Austenite (A) → Austenite-Ferrite (AF) → Ferrite-Austenite (FA). The solidification modes were estimated according to substitutional distributions obtained from energy-dispersive X-ray spectroscopy (EDS) analysis.

The microstructures and corresponding phase fractions of the cast steels are revealed in Figs. 2.10 and 2.11. With increasing C contents, the microstructure of Cr15NC10.X steels at RT varies in sequence: $\gamma + \alpha' + \delta \rightarrow \gamma + \alpha' \rightarrow \gamma$. For the Cr19NC15.X steel, on the other hand, the sequence changes with increasing C contents from $\gamma + \delta$ to γ.

2.4.3 *Austenite ↔ α′-Martensite Transformation Behavior*

As illustrated in Fig. 2.12, the M_s, A_s, and A_f temperatures of Cr15NC10.X steels decrease all linearly at higher interstitial contents [39]. Figure 2.13 shows the $f^Q_{\alpha'}$ of Cr15NC10.X steels at various temperatures. With decreasing temperature, $f^Q_{\alpha'}$ in all steels initially increases and then decreases below a certain temperature. The transition temperatures, ranging from −81 to −141 °C as marked by crosses, are in the vicinity of T_N (between −132 and −128 °C). This phenomenon has been reported in [41]. At T_N, the magnetic state of austenite changes from paramagnetic to antiferromagnetic. This is accompanied by changes in the physical properties, such as a reduction in the elastic modulus, thermal conductivity and thermal expansion coefficient [42]. The associated magnetic ordering also reduces the entropy of austenite [43], so that the free energy of austenite increases at a smaller rate with decreasing

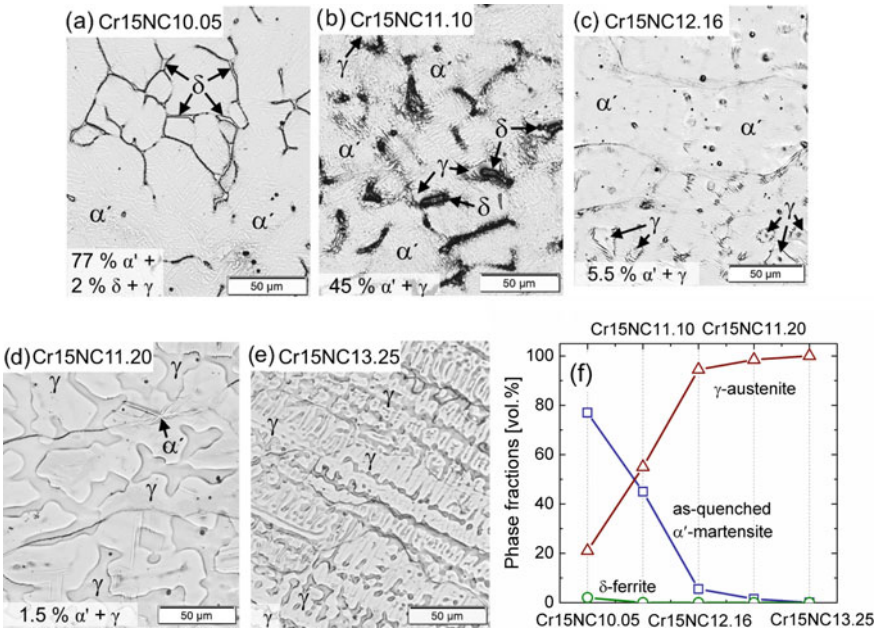

Fig. 2.10 **a**–**e** Microstructures and **f** phase fractions of cast Cr15NC10.X steels. Etchant: HNO_3 Adapted from [19]

temperature. As a consequence, the absolute difference between the free energy of austenite and α'-martensite is reduced. In other words, the chemical driving force for α'-martensitic transformation is lowered. Hence, $f^{Q}_{\alpha'}$ stops increasing even in the presence of a high austenite fraction (e.g. Cr15NC11.20). In addition, the decayed kinetics of isothermal α'-martensitic transformation [44] leads to a decrease in $f^{Q}_{\alpha'}$ below T_N. Therefore, the reduction in $f_{\alpha'}$ after passing through a peak at cryogenic temperatures can be attributed to the reduction in both the chemical driving force and the kinetics of transformation at temperatures below T_N.

For the Cr19NC15.X series, even after a cryogenic treatment in liquid nitrogen, it was not possible to introduce as-quenched α'-martensite in the solution annealed cast steels.

2.4.4 *Mechanical Properties of Cr15NC10.X Steel Series*

The stress-strain curves and associated mechanical properties are exemplified by those tested at RT and 200 °C as shown in Fig. 2.14. In Fig. 2.15, the mechanical properties and $f^{\text{ind.}}_{\alpha'}$ are presented as functions of the tensile test temperature. The M_s temperatures of steels are also marked by vertical dash-dotted lines. In most steels, YS improves from RT to 100 °C due to the precipitation of fine transition carbides

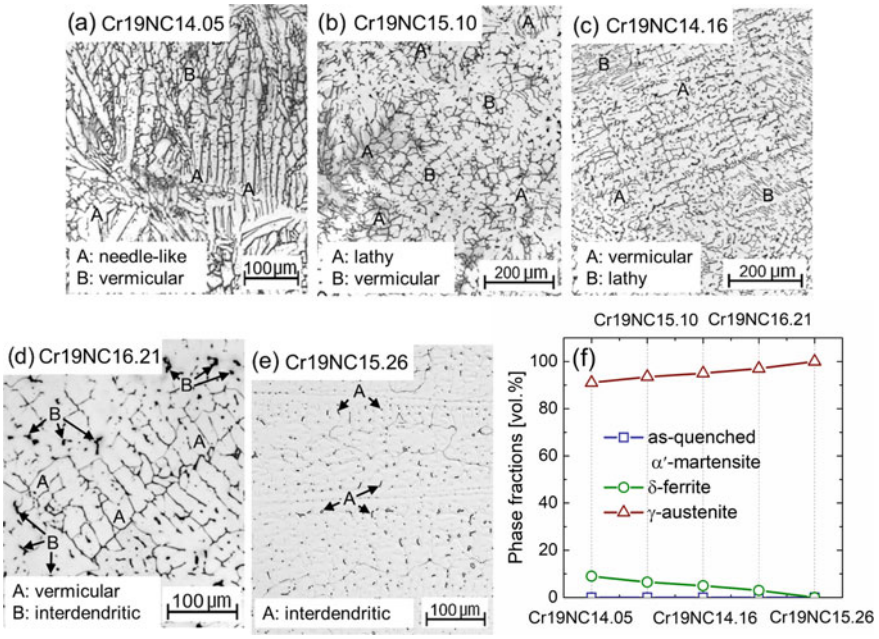

Fig. 2.11 **a**–**e** Microstructures and **f** phase fractions of cast Cr19NC15.X steels. Etchant: HNO_3. Adapted from [19]

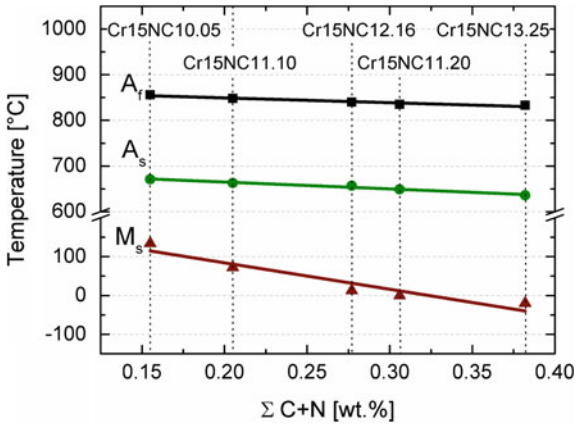

Fig. 2.12 M_s, A_s, A_f temperatures of Cr15NC10.X steels [39]

and nitrides in the α'-martensitic constituent, while TE and UE increase as a result of improved austenite stability against α'-martensitic transformation. Accordingly, $f_{\alpha'}^{\text{ind.}}$ decreases, except for the steels with 0.05–0.16 wt% C when temperature increases from −40 °C to RT. The latter variation is due to the raised $f_{\alpha'}^{Q}$ at −40 °C compared

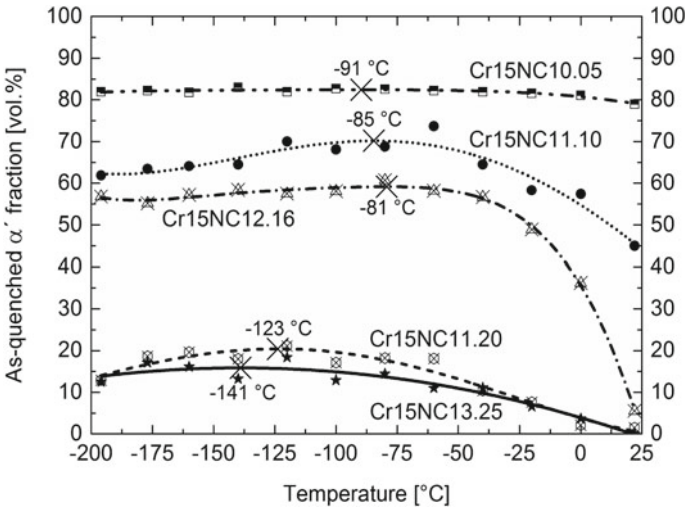

Fig. 2.13 $f_{\alpha'}^{Q}$ of Cr15NC10.X steels after holding for 10 min at various temperatures [39]. The crosses mark the temperatures associated with maximum $f_{\alpha'}^{Q}$

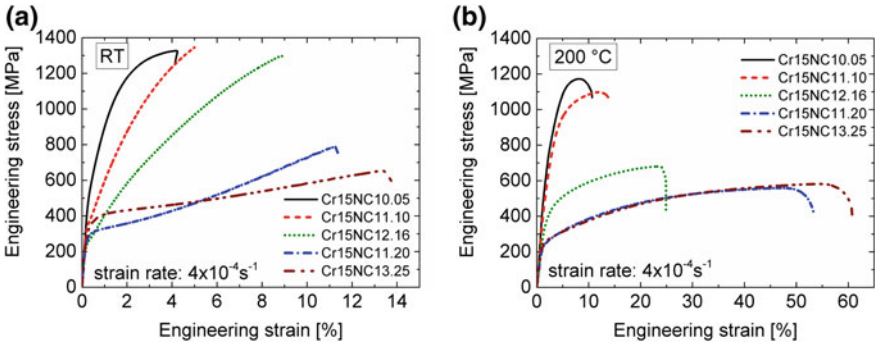

Fig. 2.14 The stress-strain curves of Cr15NC10.X steels at RT (**a**) and at 200 °C (**b**) [39]

to RT. Namely, the lower initial fractions of retained austenite at −40 °C resulted in a smaller $f_{\alpha'}^{\text{ind.}}$ than that tensile tested at RT.

The high stability of austenite at 200 °C is primarily a result of a raised SFE. Nevertheless, in alloys containing as-quenched α'-martensite such as Cr15NC10.05 and Cr15NC11.10, the thermal stabilization of austenite might have also contributed to its enhanced stability [45]. Although the temperature is too low for the long-range diffusion of C and N in the austenite, it is sufficiently high for them to diffuse from the supersaturated α'-martensite to the $\gamma - \alpha'$ phase boundaries. For instance, the diffusion distance of C in the α'-martensite is 4–20 nm at 200 °C within the timeframe of 20 min necessary for the temperature equalization of the tensile test specimens

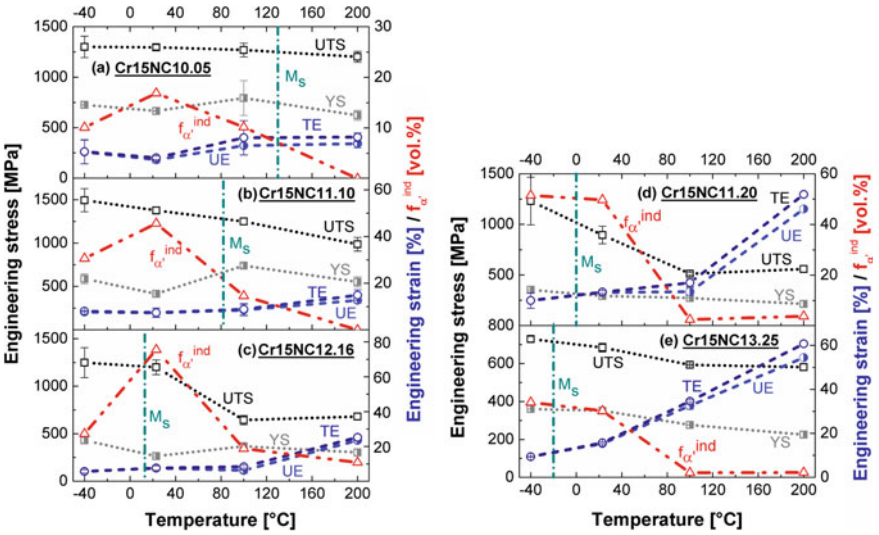

Fig. 2.15 Mechanical properties, $f_{\alpha'}^{\text{ind.}}$ and $M_s^{\gamma \rightarrow \alpha'}$ temperatures of Cr15NC10.X [19]

before tensile loading [39]. The enrichment of C atoms at phase boundaries reduces the potential nucleation sites for α'-martensite and hence, improves the resistance of austenite against α'-martensitic transformation. This effect was confirmed by quenching two solution annealed Cr15NC11.10 samples in liquid nitrogen. One of them was thermally treated at 200 °C for 20 min before quenching in liquid nitrogen. After quenching, the sample held at 200 °C showed a $f_{\alpha'}$ of only 46 vol% compared to 63 vol% α'-martensite formation in the sample without treatment at 200 °C. Due to the local interstitial content change leading to thermal stabilization of austenite, the M_d temperatures could not be determined.

2.4.5 Mechanical Properties of Cr19NC15.X Steel Series

Figure 2.16 shows the stress-strain curves of the Cr19NC15.X steels deformed at −40 and 200 °C. The S-shape curves at −40 °C imply the deformation-induced α'-martensite formation. In contrast, no noticeable increase in work hardening can be detected at 200 °C. At −40 °C, YS increases from 372 MPa at 0.05 wt% C to 413 MPa at 0.26 wt% C. This is due to the solid solution strengthening effect of C. The highest UTS of 1326 MPa combined with a TE of 44% is achieved in the case of the Cr19NC14.16 steel. In stable austenitic steels, an increase in the SFE is expected to decrease the elongation. This behavior can be justified by the dominance of wavy glide mode and the reduced planarity of dislocation glide. Nevertheless, at 200 °C, where $f_{\alpha'}^{\text{ind.}}$ equals zero in all alloys, the tensile elongation enhances as the C concentration and thereby the SFE of austenite increases [46]. Consistent with the

enhanced elongation, the ECC images of the deformed steels in Figs. 2.17a, c and e reveal a higher density of deformation bands at higher C contents.

The improved ductility at higher C contents can be attributed to the increasing segregation of substitutional elements including Cr, Mn and Ni. The higher Ni_{eq} alters the solidification mode from FA to AF [47]. For Fe–Cr–Ni alloys, the distribution coefficients between the primary δ-ferrite and the melt are 0.95–1.05 for Cr and 0.7–0.8 for Ni [48]. The distribution coefficients between the primary austenite and the melt, on the other hand, are 0.7–0.8 for Cr and 0.95 for Ni [48]. Due to the much higher Cr content of the studied steels compared to their Ni content, the change of solidification mode from FA to AF promotes the substitutional segregation, primarily Cr segregation, to the interdendritic regions. This was also confirmed by EDS analysis. The associated inhomogeneity of the chemical composition in turn leads

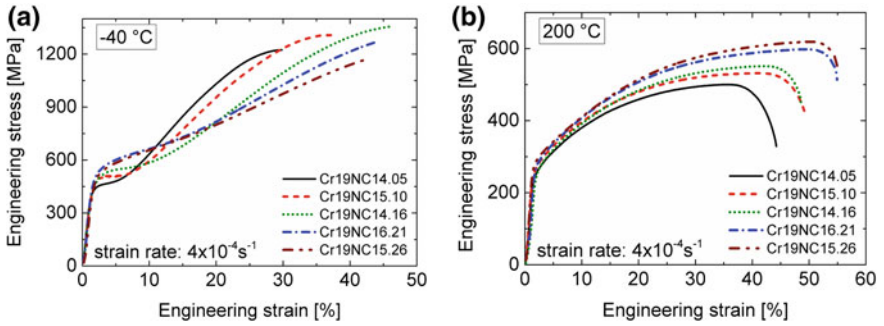

Fig. 2.16 Stress-strain curves of Cr19NC15.X steels at −40 °C (**a**) and at 200 °C (**b**) [19]

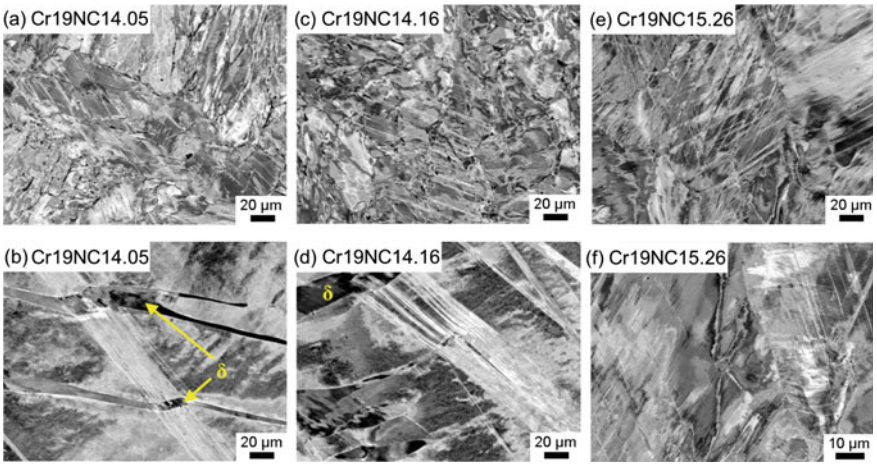

Fig. 2.17 ECC images of indicated steels strained to **a**, **b** 42%, **c**, **d** 48%, and **e**, **f** 55% at 200 °C. The samples were taken from the uniformly deformed regions in gauge section [19]

to regions with varying SFE and local variations in the plastic deformation accommodation mechanism. As shown in Fig. 2.17e for the Cr19NC15.26 steel, multiple deformation mechanisms were activated in one austenite grain. The diversification of deformation mode results in the enhanced tensile elongation.

Different interaction behavior was observed between slip bands and δ-ferrite depending on the thickness of δ-ferrite. According to Fig. 2.17b, it appears that at small thickness, although deformation bands stop at the phase boundaries, the deformation propagate to the adjacent austenite region and activate further slip bands. At high thickness (Fig. 2.17d), the strain is accommodated by the thick δ-ferrite and no further slip bands are generated in the next austenite region.

The temperature dependences of mechanical properties in Cr19NC15.X series as well as $f_{\alpha'}^{\text{ind.}}$ and M_d temperatures are summarized in Fig. 2.18. At higher temperatures, YS decreases nearly linearly, while UTS decreases with a stronger dependence on $f_{\alpha'}^{\text{ind.}}$. M_d decreases from 106 °C at 0.05 wt% C to 46 °C at 0.26 wt% C.

The maximum TE is achieved at temperatures where pronounced twinning occurs. This is exemplified in Fig. 2.19 by the Cr19NC14.16 steel tested at 60 °C and the Cr19NC15.26 steel tested at 80 °C. The elongation peaks of Cr19NC16.21 and Cr19NC15.26 steels are clearly broadened, especially Cr19NC15.26 with the maximum TE of approximately 65% at 40–80 °C. This is related to the coexistence of regions with various austenite stabilities as a result of pronounced substitutional segregation under AF solidification mode. Local variations in the stability/SFE is in turn associated with local variations in the temperature dependence of ductility. Accordingly, the overall temperature dependence of ductility is the weighted average of the different regions. This can in turn result in a broadened elongation peak. In

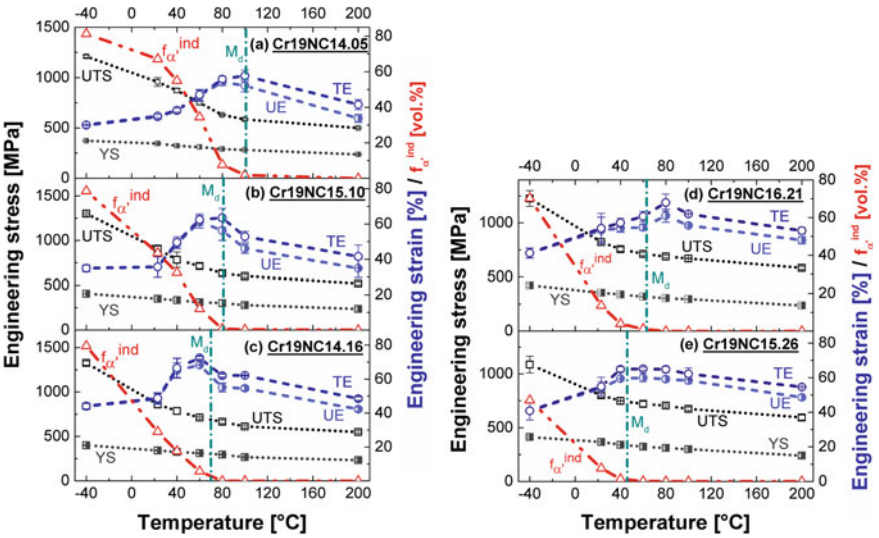

Fig. 2.18 Mechanical properties, $f_{\alpha'}^{\text{ind.}}$ and $M_d^{\gamma \rightarrow (\text{SF}, \varepsilon) \rightarrow \alpha'}$ temperatures in Cr19NC15.X [19]

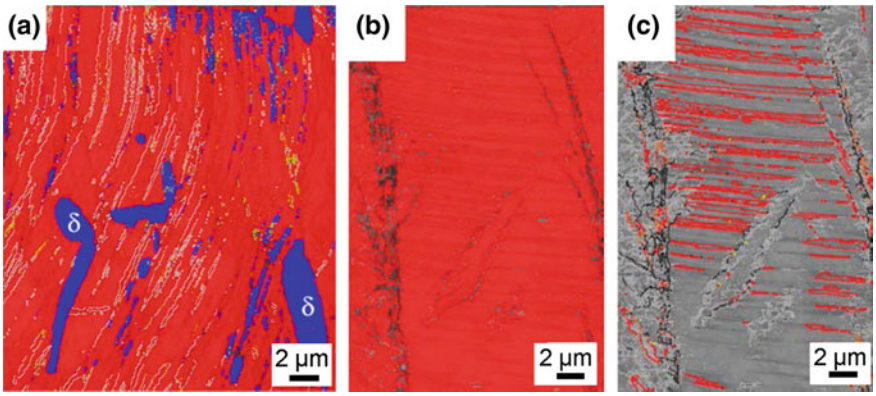

Fig. 2.19 Phase maps of **a** Cr19NC14.16 steel tested at 60 °C [28] and **b** Cr19NC15.26 tested at 80 °C [19]; **c** Map of Σ3 twin boundaries (red lines) superimposed with image quality map corresponding to the phase map in (**b**) [19]. In (**a**) and (**b**): red: austenite, blue: δ-ferrite or α'-martensite, yellow: ε-martensite, white: twin boundaries, grey: not indexed

addition, pronounced substitutional segregation in a cast Fe–14.3Cr–5.5Mn–5.5Ni–0.5Si–0.37N–0.02C steel was found to result in an enhanced ductility at cryogenic temperatures despite the occurrence of a high $f_{\alpha'}^{\text{ind.}}$ [49]. α'-martensitic transformation mostly started in the dendritic regions depleted from substitutional alloying elements. Nevertheless, the formation of fresh α'-martensite at temperatures below M_d was compensated by the enhanced glide planarity and ductility of the surrounding interdendritic regions, leading to an enhancement of TE.

2.4.6 *Conclusions for the 2nd Generation Steels*

The 2nd generation steels consist of interstitially-alloyed cast stainless steels Cr15NC10.X and Cr19NC15.X with C concentrations ranging from 0.05 to 0.25 wt%. The following conclusions were drawn:

1. Upon quenching, $f_{\alpha'}^{Q}$ stops increasing in the vicinity of T_N before the exhaustion of austenite. This is due to the decreased chemical driving force for transformation and the reduced kinetics of transformation at temperatures below T_N.
2. The phase constituents, SFE, M_s and M_d temperatures, as well as mechanical properties at RT of Cr15NC10.X and Cr19NC15.X steels are summarized in Tables 2.6 and 2.7.
3. At 200 °C, strain-induced α'-martensitic transformation was fully suppressed in Cr19NC15.X steels. Both strength and ductility enhance at increasing C concentrations. The improved ductility was attributed to more pronounced substitutional segregation generated during primary austenitic solidification.

Table 2.6 Summarized properties of Cr15NC10.X steels

X	0.05	0.10	0.15	0.2	0.25
Cast microstructure	$\gamma + \alpha' + \delta$	$\gamma + \alpha'$	$\gamma + \alpha'$	$\gamma + \alpha'$	γ
$f_{\alpha'}$ of cast (vol%)	77	45	5.5	1.5	0
SFE (mJm^{-2})	12	14	18	20	24
M_s (°C)	135	82	13	0	−20
YS at RT (MPa)	665	415	263	293	352
UTS at RT (MPa)	1296	1377	1199	895	684
TE at RT (%)	4	7	8	13	15
UTS × TE (GPa%)	5.2	9.6	9.6	11.6	10.3

Table 2.7 Summarized properties of Cr19NC15.X steels

X	0.05	0.10	0.15	0.2	0.25
Cast microstructure	$\gamma + \delta$	$\gamma + \delta$	$\gamma + \delta$	$\gamma + \delta$	γ
δ fraction of cast (vol%)	9	6.5	5	3	0
SFE (mJm^{-2})	14	17	21	26	30
M_d (°C)	100	81	70	63	46
YS at RT (MPa)	345	351	342	355	368
UTS at RT (MPa)	956	903	861	822	801
TE at RT (%)	35	36	48	54	55
UTS × TE (GPa%)	33.5	32.5	41.3	44.4	44.1

4. The prominent substitutional segregation at 0.20 and 0.26 wt% C in Cr19NC15.X also leads to the broadening of the elongation peak in the diagrams exhibiting the temperature dependent average mechanical properties.

2.5 Q&P Processing of Austenitic CrMnNi-C-N Cast Steels

The 2nd generation steels exhibit either a high YS with a low TE due to a large $f_{\alpha'}^{Q}$ (e.g. an average YS of 650 MPa and an average TE of 9% for the Cr15NC11.10 steel) or a low YS with an excellent TE (e.g. an average YS of 325 MPa and an average TE of 60% for the Cr19NC14.16 steel). Clearly, a high YS demands the presence of tempered α'-martensite. Therefore, Q&P processing was applied for the 3rd generation steels to obtain austenitic-martensitic microstructures to ensure an adequate combination of strength and ductility. Ever since its proposal in 2003 [50], Q&P processing has been widely applied to low-alloy and stainless steels [51–53]. It involves partial transformation of austenite into α'-martensite, followed by heating to a higher temperature, where the diffusion of the supersaturated C and N

from fresh α'-martensite into austenite is enabled [54]. The final microstructure consists of C-enriched austenite and C-depleted α'-martensite. Two steels with medium C contents, Cr15NC12.16 and Cr19NC14.16, were selected for the application of Q&P processing. The 3rd generation steels are denoted as AMC based on their final microstructures containing Austenite and tempered α'-Martensite with embedded Carbides.

2.5.1 Constitution and Special Methods

The Q&P processing routine for the Cr15NC12.16 steel with a composition given in Table 2.4 is illustrated in Fig. 2.20a. It involves solution annealing at 1150 °C followed by quenching to RT and subsequently to a subzero temperature above T_N to create a sufficiently high $f_{\alpha'}^{Q}$. Based on the $f_{\alpha'}^{Q}$ values presented in Fig. 2.13, −130 °C was selected for subzero quenching. The resulting microstructure consisted of 58 vol% α'-martensite and 42 vol% austenite. It was then partitioned at 450 °C for 3 min. In contrast, no α'-martensite could be obtained in Cr19NC14.16 steel (composition shown in Table 2.5) even when quenched in liquid nitrogen. Hence, α'-martensite was introduced by deformation below M_d subsequent to quenching from 1150 °C (Fig. 2.20b). The pre-strained specimens were then partitioned at 450 °C for 3 min. This process is referred to as Quenching-Deformation-Partitioning (QDP) processing. As shown in Fig. 2.18c, the steel Cr19NC14.16 possesses an M_d temperature of 70 °C. At lower testing temperatures, a smaller strain is required to generate strain-induced α'-martensite. Hence, pre-straining was performed at −40 °C. The degree of pre-straining required to induce a desirable $f_{\alpha'}^{\text{ind.}}$ was determined by a tensile test at −40 °C with in situ magnetic measurement to estimate the $f_{\alpha'}^{\text{ind.}}$ evolution according to the procedure described in [55]. In addition, interrupted tensile testes at engineering strains of 5, 15 and 25% were performed to quantify $f_{\alpha'}^{\text{ind.}}$ with ex situ magnetic measurements. The C and N enrichment in the austenite during

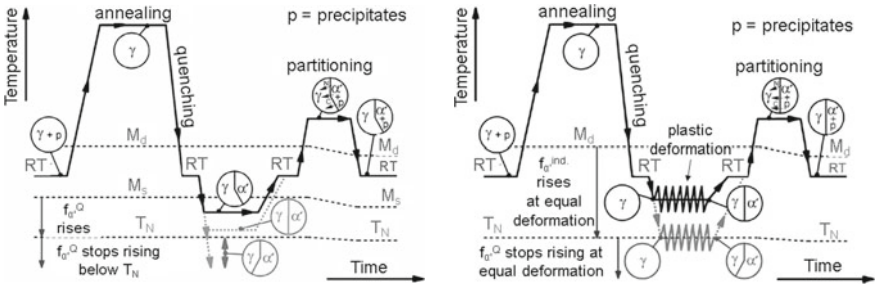

(a) Cr15NC12.16 (b) Cr19NC14.16

Fig. 2.20 Schematic illustrations of **a** Q&P processing for Cr15NC12.16 steel [27] and **b** QDP processing for Cr19NC14.16 steel [28]

partitioning was studied based on the variations in the austenite lattice parameter. This was done by X-ray diffraction (XRD) measurements using Cu Kα radiation in a Seifert-FPM RD7 diffractometer.

2.5.2 Q&P Processing of Cr15NC12.16 Steel

The microstructure of Cr15NC12.16 steel quenched to −130 °C is demonstrated in Fig. 2.21a. Due to the low austenite stability prior to partitioning, α'-martensitic transformation occurs during specimen preparation for metallography (preparation-induced α'-martensite), leading to a $f^{Q}_{\alpha'}$ of over 58 vol% based on an optical microscopy estimation. The remaining untransformed austenite in the micrograph represents the chemically-stabilized interdendritic regions. Based on the EDS analysis of the region marked in Fig. 2.21a as shown in Figs. 2.21b–d, elements including Cr, Mn and Ni are enriched in the austenitic regions. The segregation is most pronounced for Cr and least for Ni.

Based on the diffusion equation proposed by Ågren [56], the diffusion distance of C in austenite upon holding at 450 °C for 3 min is 693 nm. As N atoms have a higher diffusion coefficient at 450 °C than C atoms, i.e. 5.21×10^{-11} cm^2 s^{-1} versus 1.46×10^{-11} cm^2 s^{-1} [57], it is assumed, that the stabilization of austenite could be more significant by N. Substitutional elements are assumed to be immobile in both phases during the applied partitioning conditions [58]. During partitioning, M_3C carbides formed in α'-martensite, indicating a reduction in the interstitial content available for the partitioning process. Figure 2.22a shows the SAED pattern of an M_3C-type carbide in a martensitic matrix. Figure 2.22b shows a high resolution TEM micrograph of another M_3C-type carbide with a size of approximately 20 nm.

As a result of the enriched interstitial content, austenite peak profiles determined by XRD shift towards lower angles after partitioning. This is exemplified by the $(311)_\gamma$ peak in Fig. 2.23. The asymmetric peak profiles could be related to the non-uniform interstitial enrichment of austenite arising from differences in the size and distribution of austenitic regions. An increase in the solute C content by 1 at.% was

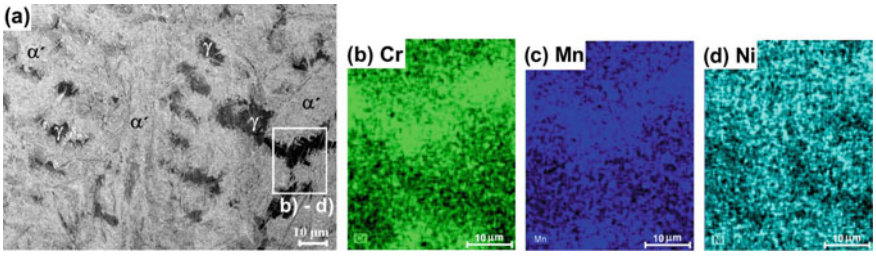

Fig. 2.21 **a** Optical micrograph of Cr15NC12.16 steel quenched to −130 °C; **b–d** Distribution of substitutional alloying elements Cr, Mn and Ni in the region demarcated in (**a**) [27]

reported to expand the austenite lattice parameter by 0.00045 nm [59]. Accordingly, assuming a similar austenite lattice dilatation effect for N, the peak shift in Fig. 2.23 implies an increase in the interstitials content of austenite by 0.1 wt%. In other words, the average interstitial content of austenite increased from 0.28 to 0.38 wt% after partitioning.

The stress-strain curves of the solution annealed steel are demonstrated in Fig. 2.24a. After Q&P processing, both UTS and TE were greatly improved (Fig. 2.24b). Because of the high tempered $f_{\alpha'}$ and the dispersed fine M_3C carbides, a YS of 1050 MPa and a UTS of 1550 MPa were achieved at RT. Furthermore, the coexistence of tempered α'-martensite with C-stabilized austenite resulted in a TE of 22% (Fig. 2.24c). The phase fractions of the tested Q&P specimens are shown in

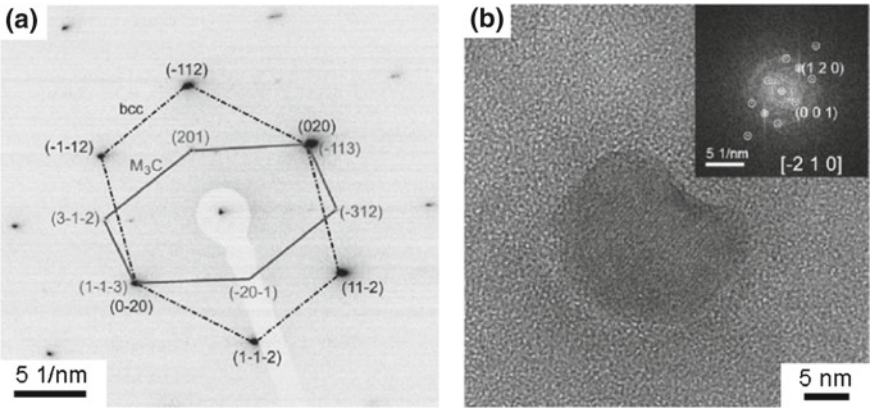

Fig. 2.22 **a** A SAED pattern of an M_3C-type carbide embedded in tempered α'-martensite. The zone axes are $[201]_{\alpha'}$ and $[17\text{-}2]_{M3C}$, respectively; **b** High resolution TEM image of an M_3C-type carbide and the corresponding FFT image with a $[-210]_{M3C}$ zone axis for the carbide [27]

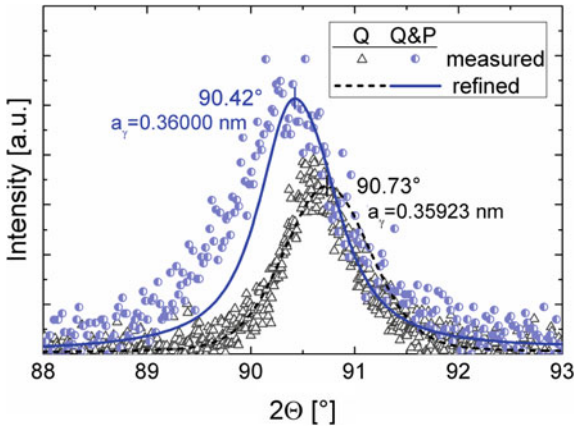

Fig. 2.23 XRD $(311)_\gamma$ peak profiles of Cr15NC12.16 in the as-quenched condition (Q) and after partitioning (Q&P) [27]

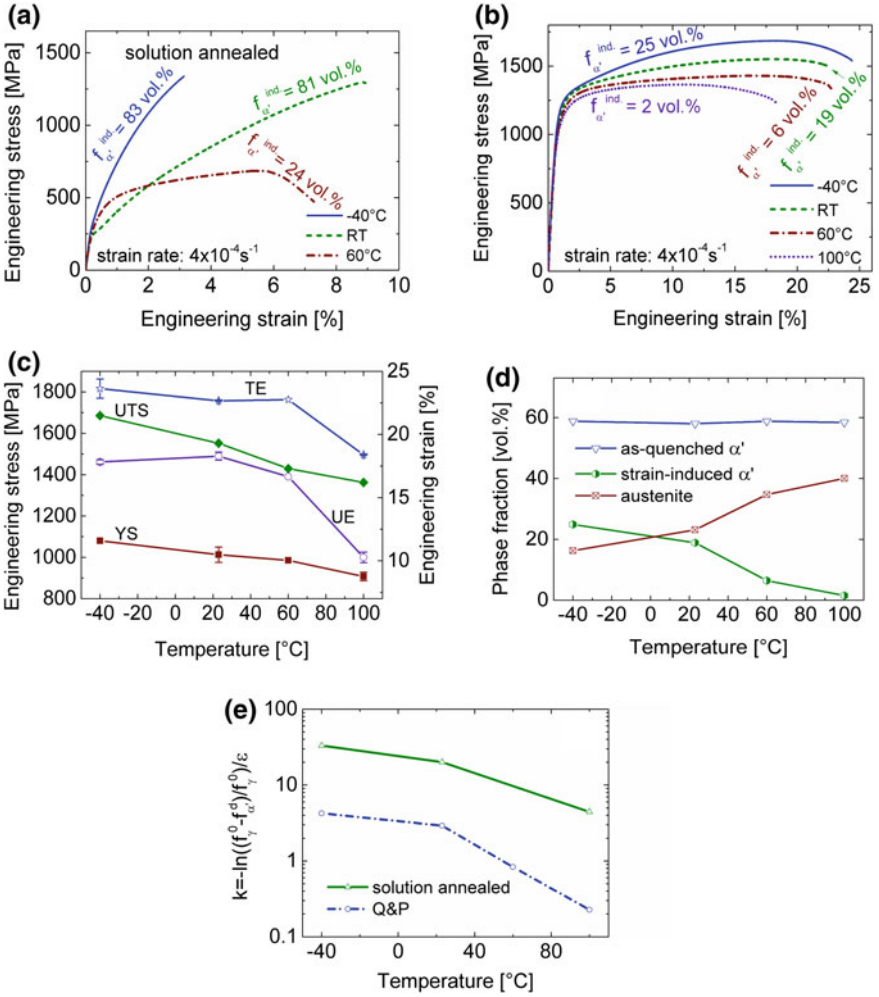

Fig. 2.24 The stress-strain curves of the Cr15NC12.16 steel in the solution annealed condition (**a**), and after quenching to −130 °C and partitioning at 450 °C (**b**); **c** average mechanical properties and **d** phase fraction evolution of AMC Cr15NC12.16; **e** mechanical stability of austenite in the solution annealed and Q&P conditions [27]

Fig. 2.24d. The formation of strain-induced α'-martensite inside the austenite deformation bands and at their intersections reduces the mean free path of dislocations (Fig. 2.25a) and hence, improves the strength as well. This justifies the increase in the strain hardening rate at lower temperatures. Within the slip bands in the austenite deformed at 60 °C (Fig. 2.25b), less α'-martensite was formed compared to that tested at RT. At 100 °C with $f_{\alpha'}^{ind.}$ equal to zero, the strain hardening rate is relatively low.

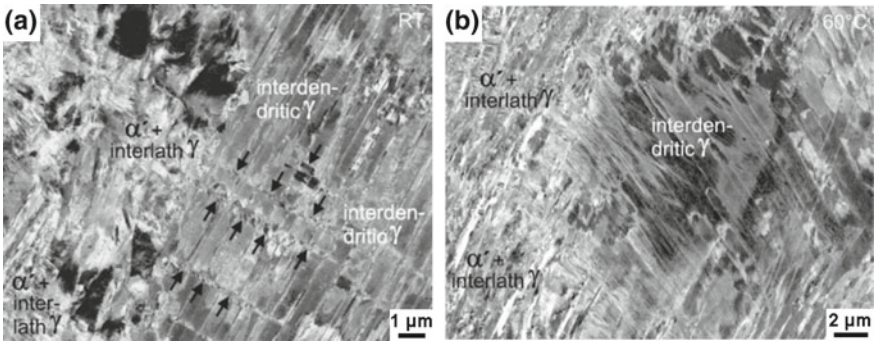

Fig. 2.25 ECC images of AMC Cr15NC12.16 steel tensile tested at RT (**a**) and 60 °C (**b**) [27]. The arrows mark strain-induced α'-martensite platelets in the deformation bands

The average mechanical stability of austenite was quantified using the following equation proposed by Sugimoto et al. [60]:

$$k = -\ln\left(\left(f_{\gamma}^{\circ} - f_{\alpha'}^{\text{ind.}}\right)/f_{\gamma}^{\circ}\right)/\varepsilon \tag{2.4}$$

where, f_{γ}° is the initial austenite fraction, ε is the applied true strain, and k is a parameter that is inversely proportional to the mechanical stability of austenite. k calculated using global strain is shown in Fig. 2.24e. The enriched interstitial contents after partitioning indeed improved the austenite stability as confirmed by a much smaller k in the Q&P condition. The mechanical stability at −40 °C in partitioned condition nearly equals that of the solution annealed steel at 100 °C.

Similar to [49], TE of the AMC Cr15NC12.16 steel increases even at temperatures below M_d, where the $f_{\alpha'}^{\text{ind.}}$ increases. This can be attributed to various austenite stabilities in the dendritic and interdendritic regions. Apart from the elemental redistribution between liquid and solid phases during solidification, Q&P Processing increases the chemical inhomogeneity and the inequality of the austenite stability in different regions. As the α'-martensitic transformation upon quenching leads to the fragmentation of austenite, the quenched microstructure consists of martensitic laths and austenitic regions with various sizes. Fine interlath austenite exhibits the highest stability against strain-induced martensitic transformation [61, 62]. Furthermore, the adjacent α'-martensite prevents them from noticeable straining during tensile test. Apart from the morphology, small austenitic regions, especially interlath austenite with a large interfacial area with the surrounding α'-martensite, experiences a more significant interstitial enrichment during partitioning.

Figure 2.26 shows the inverse pole figures (IPF) of austenite and α'-martensite phases in the AMC Cr19NC14.16 steel tested at RT. Figure 2.26a reveals the presence of two interdendritic austenitic regions marked by ellipses, which were only partially transformed into α'-martensite, indicating their superior austenite stability compared to the surrounding dendritic regions. The strong variant selection for the strain-induced α'-martensite within the marked areas in Fig. 2.26b distinguishes this type

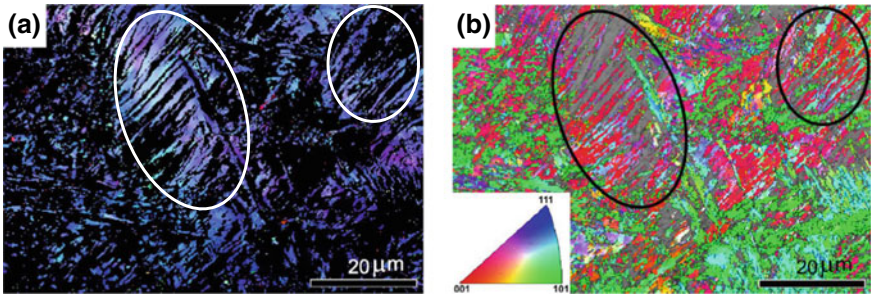

Fig. 2.26 IPF maps of (**a**) austenite and (**b**) α'-martensite in AMC Cr15NC12.16 tested at RT with tensile direction vertical in the plane of view [27]. Colors indicate crystal directions horizontal in the plane of view

of α'-martensite from as-quenched α'-martensite, which often consists of a larger number of α'-martensite variants.

2.5.3 QDP Processing of Cr19NC14.16 Steel

$f_{\alpha'}$ evolutions during tensile testing at −40 °C of the solution annealed Cr19NC14.16 steel were quantified by in situ and ex situ magnetic measurements. As shown in Fig. 2.27a, both types of results are in reasonable agreement. Using these data, the coefficients α and β in the equation proposed by Olson and Cohen for the evolution of $f_{\alpha'}^{\text{ind.}}$ were determined [63]. With the exponent n equal to 4.5 [64], α and β were fitted to be 7.49 and 2.09, respectively. Engineering strains of 0.15 and 0.25, associated with 25 and 56 vol% strain-induced α'-martensite, respectively, were selected for the pre-straining of the solution annealed Cr19NC14.16 steel at −40 °C. The two QDP steels are accordingly denoted as QDP_15% PS and QDP_25% PS. The pre-strained

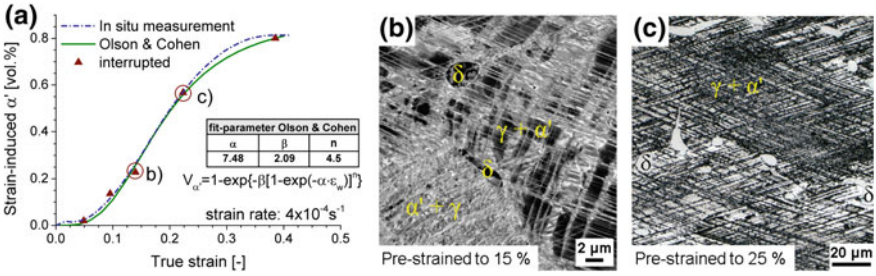

Fig. 2.27 **a** $f_{\alpha'}^{\text{ind.}}$ evolution during the tensile testing of the solution annealed Cr19NC14.16 steel as quantified by in situ and ex situ magnetic measurements and an Olson-Cohen fit to the data using the listed fitting parameters; **b**, **c** ECC images corresponding to engineering strains of 0.15 and 0.25 [28]

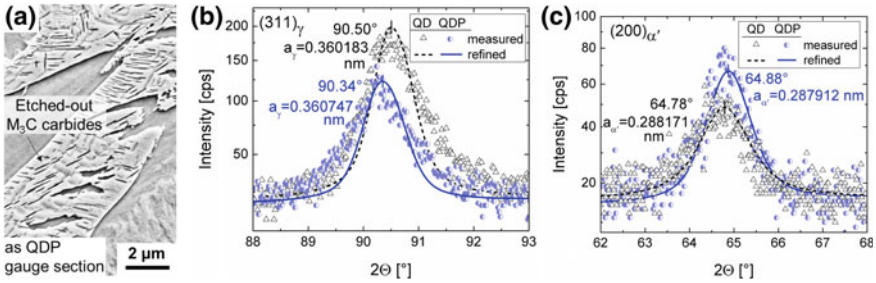

Fig. 2.28 **a** SEM image of electrolytically-etched α'-martensite in the final microstructure of the QDP_25% PS Cr19NC14.16 steel; **b** $(311)_{\gamma}$ and **c** $(200)_{\alpha'}$ peak profiles before and after partitioning [28]

microstructures are shown in Fig. 2.27b, c. In both conditions, a high density of slip bands are visible on multiple sets of {111} glide planes with α'martensite present within the bands and at their intersections.

Subsequent to partitioning, M_3C carbides also formed in the α'-martensite phase of the QDP AMC Cr19NC14.16 steel (Fig. 2.28a). According to $(311)_{\gamma}$ peak profiles, the interstitial content partitioned into the austenite is estimated to be 0.28 wt% for the QDP_25% PS (Fig. 2.28b). Concurrently, the depletion of interstitial contents in α'-martensite results in the shift of its $(200)_{\alpha'}$ peak to a higher angle (Fig. 2.28c).

In Fig. 2.29, the stress-strain curves of the AMC Cr19NC14.16 steel are compared with those in the solution annealed condition (quenched to RT). Due to the absence of α'-martensite formation during tensile tests, the solution annealed steel provides a generally low tensile strength, except at −40 °C. TE of the solution annealed steel ranges from 44 to 73%. With the introduction of α'-martensite and a subsequent partitioning, tensile strength of the AMC Cr19NC14.16 steel is clearly enhanced at the expense of tensile elongation. The premature failure of QDP_15% PS at 60 and 100 °C is associated with severe localized deformation in the transition zone from gauge section to the grip section of tensile specimens as shown in Fig. 2.30a. Based on magnetic measurements, with an applied pre-strain of 15%, strain-induced α'-martensite only formed in the gauge section, while the transition and the grip sections retained a γ-δ microstructure. The absence of α'-martensitic constituent provided no opportunity to enhance austenite stability by interstitial partitioning. Furthermore, as shown in Fig. 2.19a for the solution annealed condition, it is expected that the QDP steel exhibits a pronounced TWIP effect in the transition area at 60 °C, leading to a facilitated localized deformation and an early fracture. In contrast, the heavier pre-straining in QDP_25% PS caused strain-induced α'-martensite formation even in the gauge to grip transition zone (Fig. 2.30b). This enabled interstitial enrichment of austenite in such regions during partitioning. The associated strengthening and the enhancement of austenite stability in such regions inhibited localized deformation and premature failure of the QDP_25% PS steel at 60 and 100 °C. Compared to Q&P Cr15NC12.16, the work hardening rate of QDP_25% PS is smaller as shown in Fig. 2.29c. Its negligible work hardening can be explained on one hand by the absence

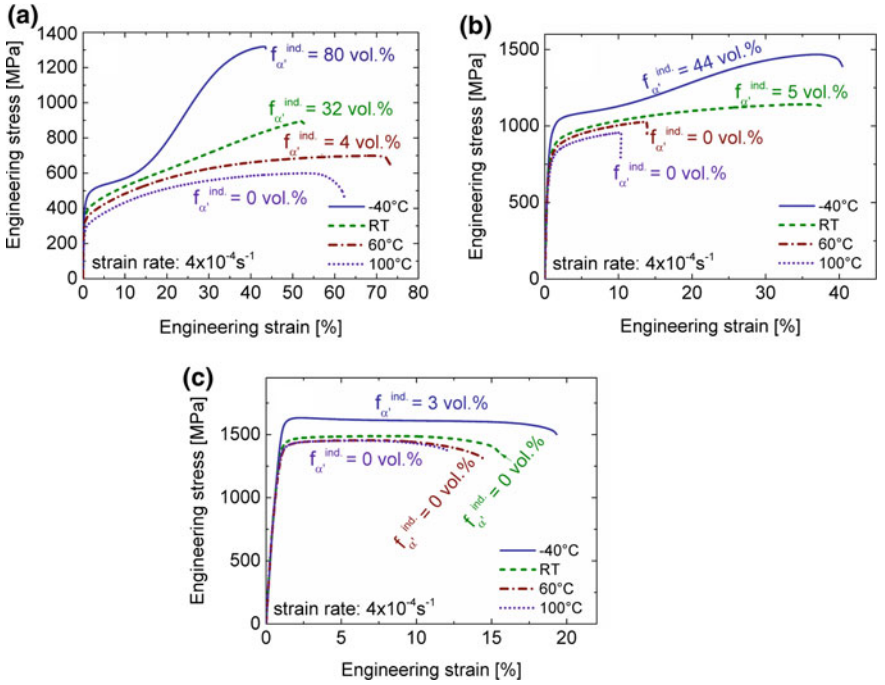

Fig. 2.29 Stress-strain curves of Cr19NC14.16 steel in various conditions [19, 28]: **a** Solution annealed and quenched to RT; **b** QDP_15% PS; **c** QDP_25% PS

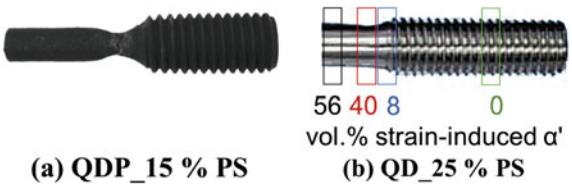

Fig. 2.30 Tensile specimens of **a** QDP_15% PS tested at 60 °C [19] and **b** QD_25% PS tested at 60 °C with $f_{\alpha'}^{ind.}$ at different areas

of $f_{\alpha'}^{ind.}$ and on the other hand by the recovery of SFs during partitioning. They were generated at −40 °C in the course of pre-straining and then narrowed/annihilated at 450 °C due to raised SFE [65]. Such constricted SFs in the pre-existing deformation bands can widen upon further deformation at lower temperatures without necessity of activating new glide systems.

The phase fraction evolution and the mechanical properties of AMC Cr19NC14.16 steel are summarized in Fig. 2.31. M_d temperature decreases from 70 °C in the solution annealed condition to nearly RT and −40 °C after QDP_15% PS and QDP_25% PS processing, respectively. The lower M_d of the latter can be attributed to the higher interstitial enrichment in the austenite due to a larger $f_{\alpha'}^{ind.}$.

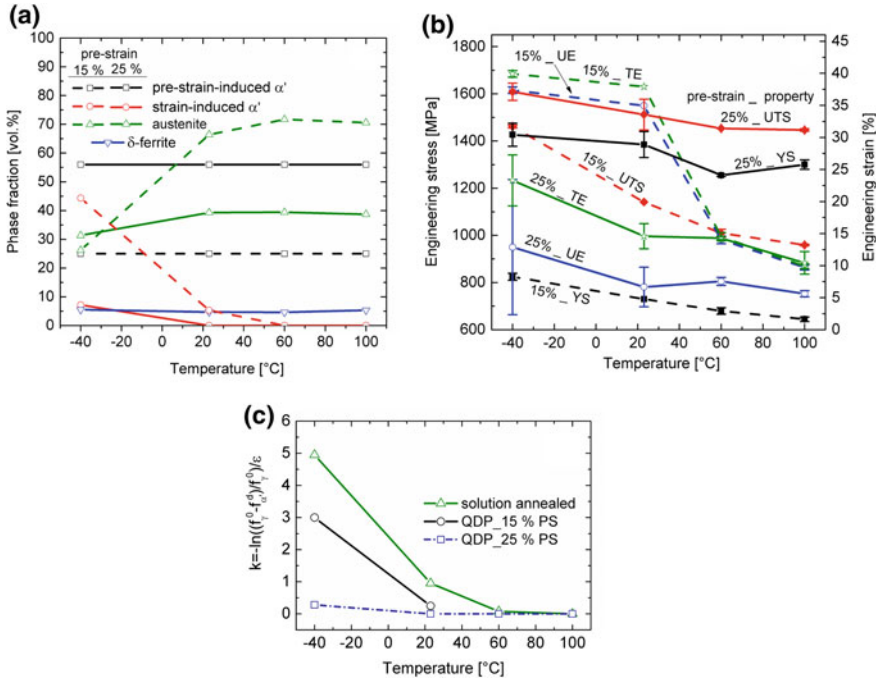

Fig. 2.31 **a** Evolution of phase fractions, **b** mechanical properties and **c** calculated k parameter of AMC Cr19NC14.16 tested at various temperatures [19]. Due to the localized deformation in the gauge to grip transition zone, k values for QDP_15% PS at 60 and 100 °C are not given. k values for the solution annealed condition are shown for comparison

Both steels exhibit excellent tensile strength, which increases at lower temperature. QDP_15% PS steel provides a YS of 644–824 MPa and a UTS of 960–1461 MPa, while QDP_25% PS steel exhibits a YS of 1300–1426 MPa and a UTS of 1446–1608 MPa. Similar to the Q&P-processed AMC Cr15NC12.16 steel, a concurrent enhancement of tensile strength and elongation at temperatures below M_d was observed. This can be explained by the occurrence of elemental segregation during solidification and the inhomogeneous interstitial enrichment of austenite in the partitioning step. The mechanical stability of austenite, expressed in terms of the k-parameter is shown in Fig. 2.31c. Due to the occurrence of localized deformation in the transition zone, this parameter was not determined for the QDP_15% PS steel tested at 60 and 100 °C. As a result of the interstitial enrichment, the mechanical stability of austenite was significantly improved after QDP Processing.

The fracture surfaces of QDP_25% PS tested at RT and −40 °C are illustrated in Fig. 2.32. Both specimens exhibit a ductile cup-and-cone fracture surface (Figs. 2.32a, d). At RT, intensive dimples formed often around inclusions (Fig. 2.32b), especially around Al_2O_3 inclusions based on the EDS analysis. Parallel aligned dendrites were observed, such as those hundreds μm long marked by ellipses in Fig. 2.32b. Their longitudinal direction denotes their growth direction during solidification and reveals the thickness direction of the cast ingot, namely the heat

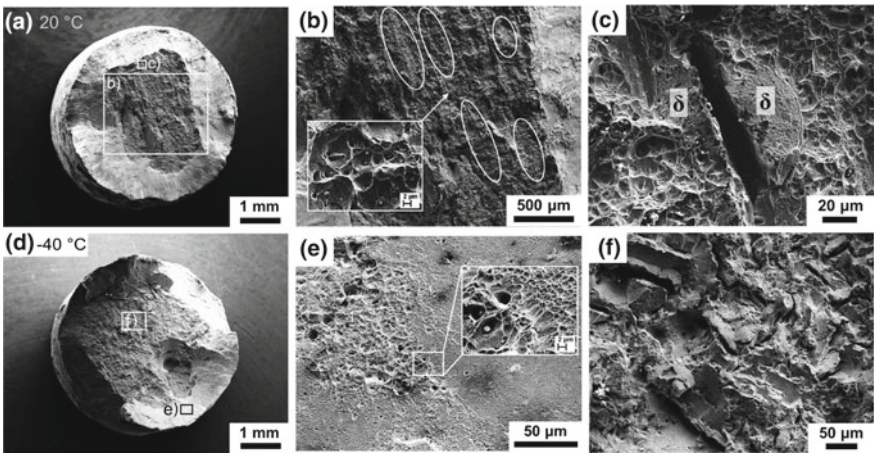

Fig. 2.32 Fracture surfaces of QDP_25% PS tested at RT (**a**–**c**) and at −40 °C (**d**–**f**) [28]: **a**, **d** overview of the entire fracture surface; **b**–**c**, **e**–**f** magnified view of the regions marked by rectangles in **a**, **b**. **b**, **e** dimples formation; **c**, **f** decohesion

dissipation direction (Fig. 2.8). Material decohesion was only observed occasionally in the central fracture region. As shown in Fig. 2.32c, the separation initiates very likely within δ-ferrite or at prior austenite/ferrite boundaries. At −40 °C, pronounced formation of dimples with various sizes was observed as well (Fig. 2.32e). Compared to the test at RT, cracks due to the decohesion at grain boundaries were more obvious as exemplified in Fig. 2.32f. This is to some extent due to the higher tensile elongation at −40 °C. In other words, the damage tolerance evaluated by the ductility was even higher than at RT, which can be ascribed to the enhanced glide planarity of austenite.

2.5.4 Conclusions for the 3rd Generation Steels

The 3rd generation steels were developed by treating Cr15NC12.16 and Cr19NC14.16 steels with tailored Q&P processing. The aim was to improve the tensile strength, especially YS, without significant loss of ductility. Following conclusions can be drawn:

1. The processing parameters and mechanical properties at RT of AMC Cr15NC12.16 and Cr19NC14.16 steels are presented in Table 2.8.
2. After partitioning at 450 °C for 3 min, M_3C carbides formed in α'-martensite, leading to an interstitial loss that competed with the interstitial enrichment in the austenite.
3. The high fractions of α'-martensite strengthened by M_3C carbides enhanced YS significantly. The YS exceeded 900 MPa for the Q&P Cr15NC12.16 and

Table 2.8 Summarized processing parameters and mechanical properties at RT of AMC Cr15NC12.16 and Cr19NC14.16 steels

Steels	Cr15NC12.16	Cr19NC14.16	
Method to create α'-martensite	Quench to −130 °C	15% pre-strain at −40 °C	25% pre-strain at −40 °C
$f_{\alpha'}$ prior to partitioning (vol%)	58	25	56
YS at RT (MPa)	1013	730	1385
UTS at RT (MPa)	1550	1141	1510
TE at RT (%)	22	38	15
UTS × TE (GPa%)	34.1	43.4	22.7

QDP_25% PS steels. The latter reaches even 1426 MPa due to the additional work hardening in the course of pre-straining.

4. After partitioning, both strength and ductility increase at lower temperatures. The enhanced ductility in spite of the formation of strain-induced α'-martensite is attributed to the chemical composition inhomogeneities, which originated from the solidification and was reinforced during the Q&P processing.
5. Deformation was mostly accommodated by the planar glide of dislocations in the austenite phase of partitioned steels. In QDP steels, the constriction of the pre-straining-induced SFs in the subsequent partitioning step and their easy separation during further deformation at lower temperatures excludes the need for activating new glide system. This leads to a negligible work hardening rate.

2.6 Conclusions

This chapter focuses on the development of cast CrMnNi stainless steels exhibiting excellent strength-ductility combination with the aid of TRIP/TWIP effect. Figure 2.33 summarizes the mechanical properties of the three generation steels presented in this chapter. The 1st generation steels include interstitial-free 16-7-3/6/9 steels with SFEs ranging from 10–22 mJm^{-2}. Regardless of their coarse cast microstructures, both 16-7-6/9 steels provided an excellent product of UTS and TE of approximately 40 GPa% due to the dynamic Hall-Petch effect by the formation of deformation bands, twins and strain-induced α'-martensite. Nevertheless, their YS was mostly below 400 MPa due to the almost fully austenitic microstructures. Therefore, interstitially-alloyed steels Cr15NC10.X and Cr19NC15.X were produced for the 2nd generation steels, aiming at solid solution strengthening, second phase strengthening by introducing as-quenched α'-martensite, and precipitation hardening. Within the studied C content range of 0.05–0.25 wt%, YS decreased and TE increased at higher C contents in the Cr15NC10.X steel series. Accordingly, YS in excess of 600 MPa was mostly accompanied by a TE of less than 10%. The

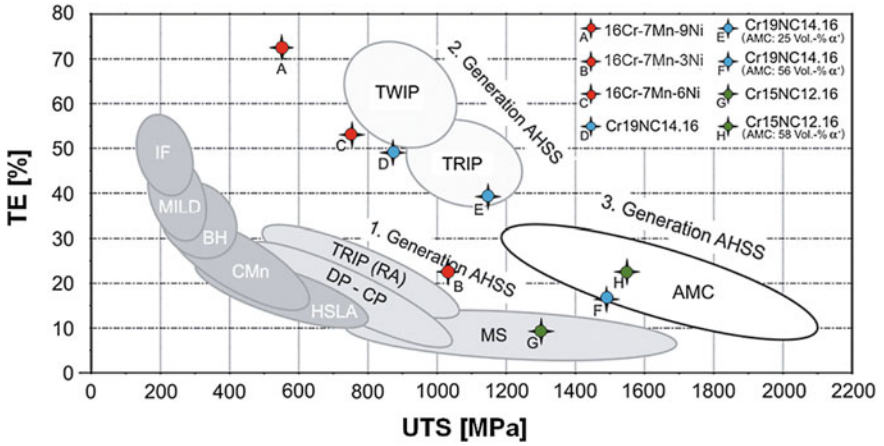

Fig. 2.33 Mechanical properties of steels presented in this chapter compared to those of advanced high strength steels (AHSS) [19]

enhanced ductility and reduced strength at higher C contents was due to the increase in the fraction and stability of austenite. Cr19NC15.X steel series with almost fully austenitic microstructures exhibited excellent ductility but YS below 450 MPa. To further enhance the YS, Q&P and QDP processing were applied to the Cr15NC12.16 and Cr19NC14.16 steels, respectively, to develop the 3rd generation steels. For the former, 58 vol% α'-martensite was created by quenching from 1150 °C to RT and then to −130 °C, while for the latter with an M_s temperature below −196 °C, 25 and 56 vol% α'-martensite were introduced by tensile straining at −40 °C to strains of 15% and 25%. Partitioning was then performed at 450 °C for 3 min. Due to the high fractions of α'-martensite with embedded fine M_3C carbides, AMC Cr15NC12.16 steel and QDP_25% PS exhibited excellent YS above 900 MPa in the temperature range of −40 to 200 °C. The QDP_25% PS steel exhibited an especially high YS of 1426 MPa at −40 °C owing to the additional work hardening in the course of pre-straining. The chemical segregation generated during solidification is intensified during Q&P processing, which results in an enhanced ductility even at tensile temperatures below M_d temperature where deformation-induced α'-martensitic transformation takes place. As indicated in Table 2.8, the product of UTS and TE at RT reaches 34, 43 and 23 GPa% for Q&P Cr15NC12.16, QDP Cr19NC14.16 with 15% and 25% pre-straining, respectively.

Acknowledgements The authors would like to thank Dr. A. Jahn for the research on the 1st generation steels. Sincere thanks are due to the colleagues at the Institute of Iron and Steel Technology (IEST) and the Institute of Materials Science (IWW) for their support and assistance on the experiments: Dr. R. Rahimi, Ms. C. Ullrich and Dr. C. Schimpf for the SEM, ECCI and XRD measurements; Dr. M. Motylenko for the TEM examinations; Mr. M. Hauser for the tensile tests with in situ magnetic measurements; Dr. T. Kreschel und Mr. G. Franke for the heat treatments; Mrs. G. Schubert for the dilatometry experiments and hardness tests; Mr. P. Neuhold for producing the steels; Mr. G. Schade for the tensile tests; Mrs. I. Grahl and Mrs. J. Kreschel for the metallographic

sample preparation and light optical microscope observations; Mr. M Block for the machining of specimens; and all the student assistants for the magnetic measurements.

This work was funded by the Deutsche Forschungsgemeinschaft (DFG, German Research Foundation)—Projektnummer 54473466—SFB 799 under the subproject A2. The financial support is gratefully acknowledged. The authors would also like to thank Prof. P. R. Scheller, the previous director of IEST, for his support on preparing the A2 subproject proposal. Special thanks are extended to all the colleagues from SFB 799 for the valuable and fruitful scientific discussions.

References

1. M. Naghizadeh, H. Mirzadeh, Metall. Mat. Trans. A **47**, 4210 (2016)
2. S.H. Bak, M.A. Abro, D.B. Lee, Metals **6**, 169 (2016)
3. E. Polatidis, W.-N. Hsu, M. Šmíd, T. Panzner, S. Chakrabarty, P. Pant, H. Van Swygenhoven, Scr. Mater. **147**, 27 (2018)
4. I. Karaman, H. Sehitoglu, Y.I. Chumlyakov, H.J. Maier, JOM **54**, 31 (2002)
5. L. Kaufman, M. Cohen, Prog. Met. Phys. **7**, 165 (1958)
6. G.B. Olson, M. Cohen, Metall. Trans. A **7**, 1897 (1976)
7. L. Rémy, A. Pineau, B. Thomas, Mater. Sci. Eng. **36**, 47 (1978)
8. F. Lecroisey, B. Thomas, Phys. Stat. Sol. (a) **2**, K217 (1970)
9. T. Yonezawa, K. Suzuki, S. Ooki, A. Hashimoto, Metall. Mat. Trans. A **44**, 5884 (2013)
10. M. Wendler, A. Weiß, L. Krüger, J. Mola, A. Franke, A. Kovalev, S. Wolf, Adv. Eng. Mater. **15**, 558 (2013)
11. A. Dumay, J.-P. Chateau, S. Allain, S. Migot, O. Bouaziz, Mater. Sci. Eng. A **483**, 184 (2008)
12. A. Saeed-Akbari, L. Mosecker, A. Schwedt, W. Bleck, Metall. Mat. Trans. A **43**, 1688 (2012)
13. D. Fahr, Dissertation, University of California, 1969
14. S. Martin, S. Wolf, U. Martin, L. Krüger, Solid State Phenom. **172–174**, 172 (2011)
15. B.C. De Cooman, O. Kwon, K.-G. Chin, Mater. Sci. Technol. **28**, 513 (2012)
16. H.-J. Kestenbach, Philos. Mag. **36**, 1509 (1977)
17. M. Pozuelo, J.E. Wittig, J.A. Jiménez, G. Frommeyer, Metall. Mat. Trans. A **40**, 1826 (2009)
18. J. Mola, in *Austenitic Stainless Steels—New Aspects*, eds. by W. Borek, T. Tanski, Z. Brytan (InTech, 2017), pp. 7–28
19. M. Wendler, Dissertation, Technische Universität Bergakademie Freiberg, 2017
20. R.E. Schramm, R.P. Reed, Metall. Trans. A **6**, 1345 (1975)
21. R. E. Stoltz, J. B. Vander Sande, Metall. Trans. A **11**, 1033 (1980)
22. T.-H. Lee, E. Shin, C.-S. Oh, H.-Y. Ha, S.-J. Kim, Acta Mater. **58**, 3173 (2010)
23. R.M. Latanision, A.W. Ruff, Metall. Trans. **2**, 505 (1971)
24. F. Lecroisey, A. Pineau, Metall. Mat. Trans. B **3**, 391 (1972)
25. F. Abrassart, Metall. Trans. **4**, 2205 (1973)
26. L. Rémy, A. Pineau, Mater. Sci. Eng. **26**, 123 (1976)
27. M. Wendler, C. Ullrich, M. Hauser, L. Krüger, O. Volkova, A. Weiß, J. Mola, Acta Mater. **133**, 346 (2017)
28. M. Wendler, M. Hauser, M. Motylenko, J. Mola, L. Krüger, O. Volkova, Adv. Eng. Mater. **21**, 1800571 (2019)
29. M. Wendler, M. Hauser, E.F. Sandig, O. Volkova, Metall. Mat. Trans. B **49**, 581 (2018)
30. A. Jahn, A. Kovalev, A. Weiß, P.R. Scheller, Steel Res. Int. **82**, 1108 (2011)
31. A. Jahn, A. Kovalev, A. Weiß, S. Wolf, L. Krüger, P.R. Scheller, Steel Res. Int. **82**, 39 (2011)
32. A. Weiss, H. Gutte, M. Radtke, P. Scheller, WO/2008/009722 (25 January 2008)
33. Q.-X. Dai, A.-D. Wang, X.-N. Cheng, X.-M. Luo, Chin. Phys. (Overseas Edition) **11**, 596 (2002)
34. A. Jahn, Dissertation, Technische Universität Bergakademie Freiberg, 2012

35. R. Rahimi, C. Ullrich, V. Klemm, D. Rafaja, B.C. De Cooman, H. Biermann, J. Mola, Mater. Sci. Eng., A **649**, 301 (2016)
36. Y. Maehara, Y.S.U. Tani, K. Gunti, Trans. ISIJ **25**, 8 (1985)
37. A. Weiss, M. Wendler, H. Gutte, H. Biermann, Int. J. Foundry Res. **65**, 2 (2013)
38. Y. Kobayashi, H. Todoroki, N. Shiga, T. Ishii, ISIJ Int. **52**, 1601 (2012)
39. M. Wendler, M. Hauser, O. Fabrichnaya, L. Krüger, A. Weiß, J. Mola, Mater. Sci. Eng. A **645**, 28 (2015)
40. J.-O. Andersson, T. Helander, L. Höglund, P. Shi, B. Sundman, Calphad **26**, 273 (2002)
41. M. Hauser, M. Wendler, O. Fabrichnaya, O. Volkova, J. Mola, Mater. Sci. Eng. A **675**, 415 (2016)
42. Y.S. Zhang, X. Lu, X. Tian, Z. Qin, Mater. Sci. Eng. A **334**, 19 (2002)
43. A. Sato, E. Chishima, Y. Yamaji, T. Mori, Acta Metall. **32**, 539 (1984)
44. G. Ghosh, V. Raghavan, Mater. Sci. Eng. **80**, 65 (1986)
45. O.N. Mohanty, Mater. Sci. Eng. B **32**, 267 (1995)
46. P.J. Brofman, G.S. Ansell, Metall. Trans. A **9**, 879 (1978)
47. J.W. Fu, Y.S. Yang, J.J. Guo, W.H. Tong, Mater. Sci. Technol. **24**, 941 (2008)
48. T. Koseki, M.C. Flemings, Metall. Mat. Trans. A **27**, 3226 (1996)
49. J. Mola, M. Wendler, A. Weiß, B. Reichel, G. Wolf, B.C.D. Cooman, Metall. Mat. Trans. A **46**, 1450 (2015)
50. J. Speer, D.K. Matlock, B.C. De Cooman, J.G. Schroth, Acta Mater. **51**, 2611 (2003)
51. R. Eckner, L. Krüger, C. Ullrich, M. Wendler, O. Volkova, Int. J. Fract. **215**, 139 (2019)
52. J. Mola, B.C.D. Cooman, Metall. Mat. Trans. A **44**, 946 (2013)
53. Q. Huang, C. Schröder, H. Biermann, O. Volkova, J. Mola, Steel Res. Int. **87**, 1082 (2016)
54. J.G. Speer, F.C. Rizzo Assunção, D.K. Matlock, D.V. Edmonds, Mater. Res. **8**, 417 (2005)
55. M. Hauser, M. Wendler, S.G. Chowdhury, A. Weiß, J. Mola, Mater. Sci. Technol. **31**, 1473 (2015)
56. J. Ågren, Scr. Mater. **20**, 1507 (1986)
57. H. Oettel, H. Schumann, *Metallografie: mit einer Einführung in die Keramografie* (Wiley, 2011)
58. L. Yuan, D. Ponge, J. Wittig, P. Choi, J.A. Jiménez, D. Raabe, Acta Mater. **60**, 2790 (2012)
59. T. Minemura, A. Inoue, T. masumoto, Trans. ISIJ **21**, 649 (1981)
60. K.-I. Sugimoto, M. Kobayashi, S.I. Hashimoto, Metall. Mater. Trans. A **23**, 3085 (1992)
61. A. Rosen, R. Jago, T. Kjer, J. Mater. Sci. **7**, 870 (1972)
62. K. Nohara, Y. Ono, N. Ohashi, Tetsu-to-Hagane **63**, 772 (1977)
63. G.B. Olson, M. Cohen, MTA **6**, 791 (1975)
64. J. Talonen, H. Hänninen, P. Nenonen, G. Pape, Metall. Mat. Trans. A **36**, 421 (2005)
65. Q. Huang, B.C.D. Cooman, H. Biermann, J. Mola, Metall. Mat. Trans. A **47**, 1947 (2016)

Chapter 3
Tailoring of Thermophysical Properties of New TRIP/TWIP Steel Alloys to Optimize Gas Atomization

Iurii Korobeinikov, Humberto Chaves and Olena Volkova

Abstract This work is dedicated to the optimization of the inert gas atomization process applied for production of steel powders. One aim is the optimization of melt parameters with the target to reduce the particle size of atomized powder. A second aim is focused on the atomization equipment optimization. In order to study thermophysical properties of steel melts the development of a new research units was accomplished: Maximum Bubble Pressure device for measurement of the surface tension and density of liquid steels and alloys, patented vibrating finger viscometer, dedicated to the investigation of low-viscosity fluids under the conditions of high temperatures and high reactivity of the studied media; density measurement cell based on the Archimedean principle for the precise estimation of steel alloys density. Then, the effect of thermophysical properties on the inert gas atomization of high-alloy steels was studied. The effects of alloying with Mn and Ni were studied as well as microalloying with S, P, Se on the surface tension and viscosity of liquid steels. Surface tension and viscosity modification of the alloys led to considerable reduction of the size of inert gas atomized powders. Alloying with N allowed finding effect on the powder phase structure.

I. Korobeinikov (✉) · O. Volkova
Institute of Iron and Steel Technology, Technische Universität Bergakademie Freiberg, Freiberg, Germany
e-mail: Iurii.Korobeinikov@iest.tu-freiberg.de

O. Volkova
e-mail: volkova@iest.tu-freiberg.de

H. Chaves
Institute of Mechanics and Fluid Dynamic, Technische Universität Bergakademie Freiberg, Freiberg, Germany
e-mail: Humberto.Chaves@imfd.tu-freiberg.de

H. Biermann and C. G. Aneziris (eds.), *Austenitic TRIP/TWIP Steels and Steel-Zirconia Composites*, Springer Series in Materials Science 298,
https://doi.org/10.1007/978-3-030-42603-3_3

3.1 Surface Tension and Density of the TRIP/TWIP Steels

The main target of the research from the very beginning was a development of new steel grades which may be used as a steel matrix of the steel-ceramic composites. The solid state subproject has developed 3 Cr–Mn-Ni steels with varying Ni content: 16%Cr7%Mn3%Ni (in Table 3.1 and further it refers to **16-7-3**), 16%Cr7%Mn6%Ni (**16-7-6**) and 16%Cr7%Mn9%Ni (**16-7-3**). As long as these 3 new TRIP/TWIP-effect steel grades were developed, the thermophysical properties of them in a liquid state had to be investigated (Table 3.1). The primary objective of such investigation is to deliver insights on the surface tension and density of the new alloys, as well as their infiltration into ceramics capabilities.

Institute of Iron and Steel Technologies (IEST) was already equipped with a high-temperature microscope capable for the measurement of wetting angle and surface tension with the classical sessile drop method. It is well known from the literature that Mn-containing steels in a liquid state intensively lose manganese due to evaporation. At the same time, classical sessile drop method features high surface to volume ratio of the investigated liquid sample. Therefore, it was decided to widen the range of applied methods for estimation of thermophysical properties of Mn-containing steels in order to have better validity of obtained results. One of the best alternative methodologies for the estimation of surface tension is a classical maximum bubble pressure technique (MBP). Among its' features are low surface to volume ratio and low sensitivity to the atmosphere around the sample.

Maximum bubble pressure technique is a well-established method for measuring of a surface tension applicable for a variety of liquids ranging from alcohols at room temperatures to liquid metals and oxides at temperatures well above their melting points. A detailed description of the technique can be found in dedicated literature [1, 2]. The main idea of the method is to measure maximum pressure in the bubble blown in the liquid. The bubble is typically blown through the capillary of a precisely defined inner diameter and with a sharpened tip. Maximum pressure of the gas inside the bubble of a defined diameter indicates the surface tension of the studied liquid. Pressure in the bubble is measured by the sensor attached to the other side of the capillary (to gas supply system). Pressure in the bubble is defined as:

$$P_{\max} = \frac{2\sigma}{r_{\text{capillary}}} + \rho * g * h \tag{3.1}$$

where σ is a surface tension, r is a radius of the bubble (inner radius of the capillary), ρ is a density of the liquid, g is an acceleration of free fall, h is an immersion depth.

The surface tension is then calculated as:

$$\sigma = 0.5 * p_{\max}(h = 0) * r_{\text{capillary}} \tag{3.2}$$

The density of the studied liquid (ρ) is calculated as a slope of the linear regression ($\Delta p_{\max}/\Delta h$) and acceleration of free fall:

Table 3.1 Chemical composition of the samples, modified after [3]

	C	Si	Cr	Mn	Ni	Al	Mo	N	O_{tot}	S	P
	%							Mass ppm			
16-7-3	0.027	0.89	15.4	7.25	3.03	0.0010	0.095	147	61	57	151
16-7-6	0.036	0.92	15.6	7.34	5.73	0.0020	0.101	167	69	80	146
16-7-9	0.035	0.95	15.9	7.37	9.20	0.0033	0.105	135	57	70	133

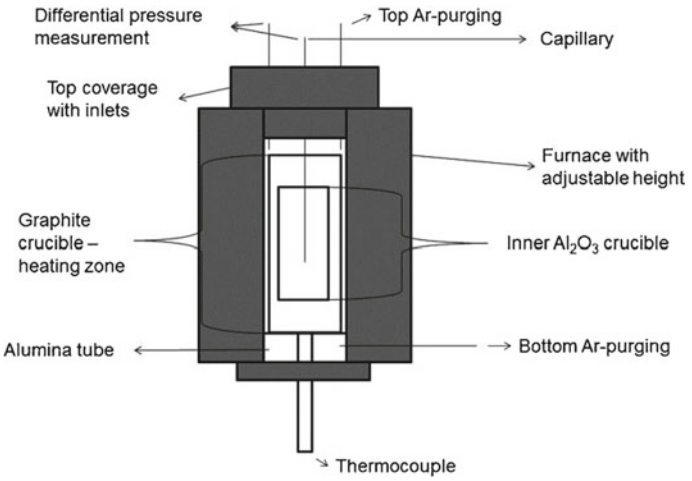

Fig. 3.1 Scheme of the maximum bubble pressure measurement cell [3, 4]

$$\rho = \frac{\Delta p_{\max}}{\Delta h * g} \tag{3.3}$$

The maximum bubble pressure unit had a scheme as shown in the Fig. 3.1. The sample is molten inside the alumina crucible placed in a graphite heating element. Graphite heating element is inductively heated by the copper coil imbedded in ceramic walls of the furnace. The inner volume of the furnace is continuously flushed with argon 5.0 (99.999% purity) from the liquid storage tank. Presence of carbon in the heating zone of the furnace ensures the elimination of the oxygen around the sample. Temperature control of the sample is executed via a thermocouple attached to the bottom of the ceramic crucible. Alumina capillary of 1.0 mm inner diameter is sealed with the zero press rings to the argon supply tube. Immersion of the capillary inside the sample is done by moving of the furnace in a vertical direction. The precision of the capillary position is controlled with 0.005 mm error with the use of WayCon system. For one temperature point a total of approximately 200 bubbles were measured—ca. 10 bubbles with a step of 1 mm between 10 and 20 mm depth along the immersion and subtraction of the capillary.

As a reference, the samples were also investigated with the use of a drop weight method. This method allows deriving the surface tension of the liquid from the weight of the droplet passing through the orifice of known diameter. Principal scheme of the measurement cell is shown on Fig. 3.2. Steel melt is pressed out of the alumina crucible through the ZrO_2 capillary by a stamp (piston) and forms a droplet on the orifice of the capillary surrounded by Ar gas (99.999% purity). As soon as gravity force exceeds the surface tension force, the droplet detaches from the capillary tip. The weight of the droplets is measured with the use of high precision balance. Thus, the (3.4) is used for the estimation of the surface tension of the sample.

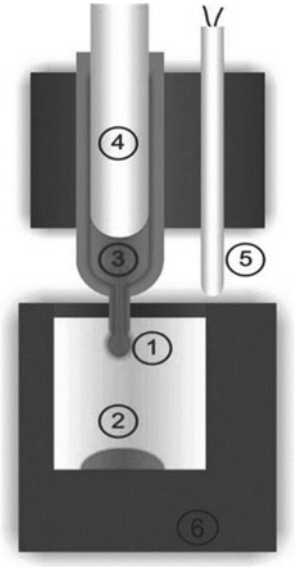

Fig. 3.2 Scheme of the drop weight method for the investigation of surface tension of liquid metals. (1) capillary, (2) crucible, (3) liquid metal bath, (4) stamp, (5) thermocouple, (6) precision balance, modified after [3]

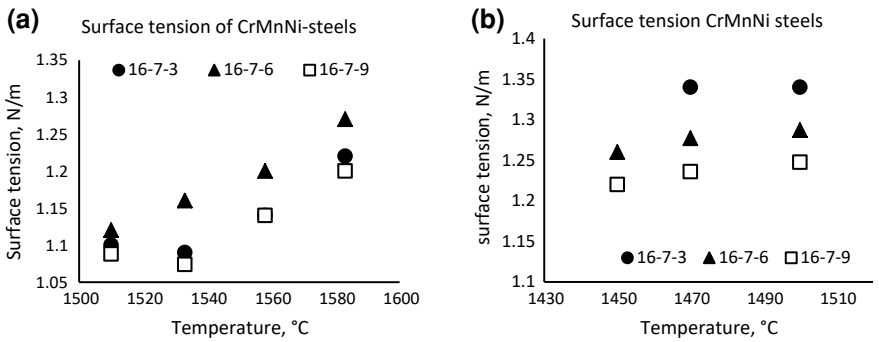

Fig. 3.3 The surface tension of Cr–Mn–Ni-steels determined by **a** the maximum bubble pressure method (MBP) and **b** drop weight method (DWM), based on [3]

$$\sigma = \frac{m * g}{2 * \pi * r * \psi} \tag{3.4}$$

where m is mass of drop, g is an acceleration of free fall, r is a radius of the drop (radius of the capillary), and ψ is a correction factor.

Experiments showed that the surface tension of the investigated alloys is relatively low—in the range of 1.1–1.3 N/m (Fig. 3.3). Drop weight method gave higher values of surface tension than MBP technique. Another significant fact revealed by this

Table 3.2 Temperature coefficient of surface tension $d\sigma/dT$ for investigated steel types, based on [3]

	MBP (Nm^{-1} K^{-1})	DWM (Nm^{-1} K^{-1})
16-7-3	$+1.7 \times 10^{-3}$	$+7.0 \times 10^{-5}$
16-7-6	$+2.0 \times 10^{-3}$	$+5.1 \times 10^{-4}$
16-7-9	$+1.7 \times 10^{-3}$	$+4.2 \times 10^{-4}$

study was that the surface tension of these alloys rose with the temperature increase (Table 3.2). Measurement with the MBP technique also delivered the first data on the density of the new TRIP/TWIP alloys (Fig. 3.4). Besides that, the wettability of samples on the ZrO_2 ceramics was investigated (Fig. 3.5).

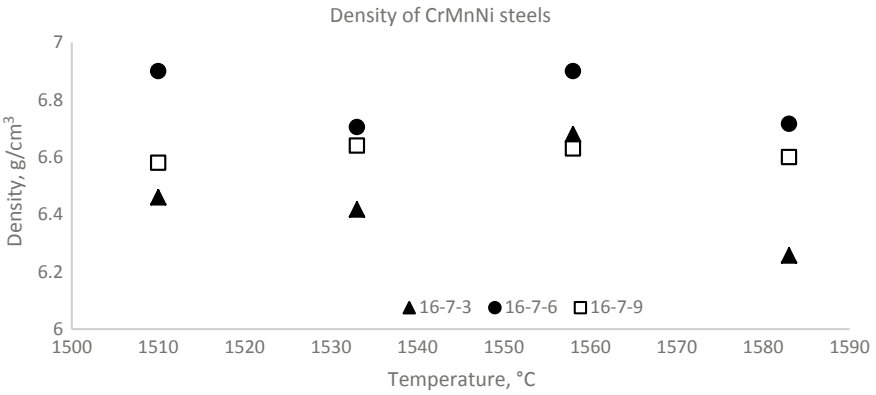

Fig. 3.4 Density of selected Cr–Mn–Ni-steels determined by the maximum bubble pressure method (MBP), based on [3]

Fig. 3.5 Wettability of investigated steel grades on ZrO_2 under Ar 5.0 atmosphere (<2 mass ppm O_2), 1550 °C; based on [3]

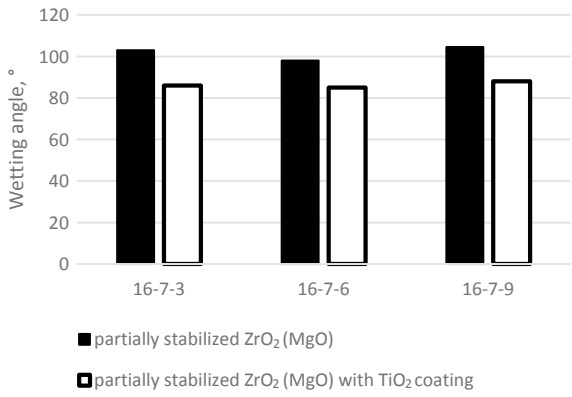

Also, maximum bubble pressure unit was tested on metallurgical slags with the excellent results what showed a capability to their measure surface tension and density [5]. In order to withstand interaction with the slag, the measurement cell was modified—the capillary and crucible were made of molybdenum.

3.2 Control of Atomization by the Thermophysical Properties of the Atomized Media

The next research focus was targeted towards investigations of various alloying options of the TRIP/TWIP steels 16-7-3, 16-7-6, and 16-7-9. Besides that, the MBP measurement cell was updated with new capillaries. Preliminary tests showed that ZrO_2 ceramic is more corrosion-resistant at high temperatures. Particular interest to this issue was paid due to substantial contents of Mn in these steel alloys.

New yttria-partially stabilized ZrO_2 capillaries were applied for the measurement of surface tension and density of the TRIP/TWIP alloys together with the reference steel grade AISI 304 and electrolytic copper. A surface tension and a density of copper and 304 steel was rather correctly estimated with the applied measurement cell. Remarkably, that a surface tension results of 16-7-3, 16-7-6 and 16-7-9 are in a good agreement with the results obtained in previous work [3] (Fig. 3.6).

This study showed the effect of nickel on the surface tension of liquid steel. Increase of nickel content from 6 to 9% led to a small decrease of a surface tension

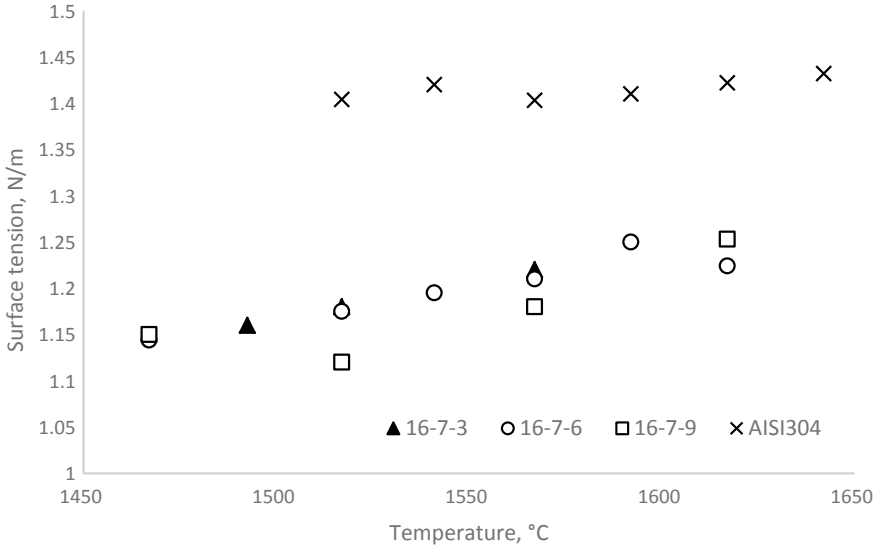

Fig. 3.6 Surface tension of and of TRIP/TWIP alloys compared to AISI 304 (Cr–Ni on the plot) steel, based on [6]

(Fig. 3.7a). Moreover, the experiments allowed to gain more accurate data on the density of the new alloys (Fig. 3.7b).

Later measurements of the surface tension of TRIP/TWIP steels have shown similar results [7]. It is a notable fact that surface tension values measured with maximum bubble pressure technique are higher than those measured with the sessile drop technique (Fig. 3.8). Simultaneously, a benchmark study was accomplished with the electromagnetic levitation technique (EML) in the DLR facility (Cologne, Germany). It allowed confirming the surface tension of TRIP (16-7-3) steel at temperatures around their liquidus line. However, the features of the EML technique

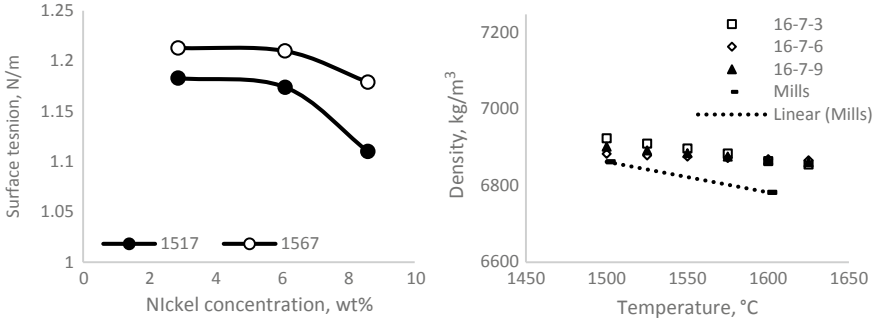

Fig. 3.7 **a** Effect of nickel on the surface tension of steel. **b** Density of 16-7-3, 16-7-6 and 16-7-9 steels measured with MBP technique, based on [6]

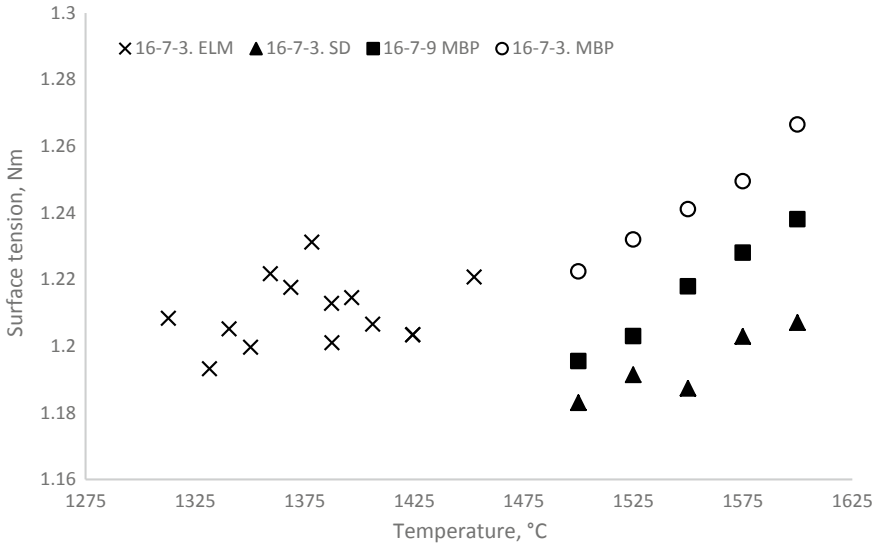

Fig. 3.8 Surface tension of 16-7-3 and 16-7-9 steels measured with maximum bubble pressure (MBP), sessile drop (SD) and electromagnetic levitation (EML) techniques, Modified after [7]

have led to severe evaporation of manganese. 16-7-3 sample has lost nearly 4 out of 7 wt% of manganese.

Chemical analysis of the samples before and after the experiments showed the remarkable loses of sulphur. This phenomenon could explain the positive surface tension coefficient.

Besides Ni, the effects of Mn, S, Se, P on the surface tension of CrNiMn alloys were investigated (Table 3.3) [8]. As can be seen in Fig. 3.9, manganese at low concentrations (until 5%) significantly reduces the surface tension of the CrMnNi alloy. Further growth of Mn concentration led to a minor surface tension reduction. Furthermore, the effect of Mn concentration on surface tension diminished with temperature increase.

Alloying with up to 0.22% phosphorus (Table 3.4) did not reveal a clear trend of the effect on surface tension. The surface tension of alloy 16-7-6 slightly rose when phosphor content increased from 0.02 to 0.05% and further remained stable (Fig. 3.10). At higher temperature (1600 °C) the surface tension of an investigated alloy deviated on ± 0.03 N/m around 1.21 N/m.

Among other surface-active elements, selenium is known for its strong effect on the surface tension of liquid iron [9, 10]. Therefore, a series of Se-microalloyed steels on base of 16-7-6 composition was prepared on VIM-12 unit (Table 3.5). Same as in case of P, Mn, and Ni, the surface tension of the alloys was measured with the MBP technique. The results of experiments, presented in Fig. 3.12, showed that even a minimum amount of Se (0.009%) led to significantly lower ST values than steel alloyed with a comparable amount of sulphur (Fig. 3.11).

3.2.1 Investigation of the Effect of Surface Tension on Inert Gas Atomization

Inert gas atomization is one of the variants of a metal powder production. Its main advantages are the sphericity, surface cleanness and controlled chemical composition of the final powder. Among disadvantages are relative complexity of the equipment and high cost of the obtained metal powders. Currently, inert gas atomization technology is the primary source of high-quality powders for the emerging metal 3d-printing industry. The principle of the gas atomization is based on the disintegration of the liquid metal stream by the gas jet/jets which is well described in the literature [11, 12]. In the present project the inert gas atomization unit VIGA-1B (ALD-Vacuum Technologies) was used. Principal scheme of the atomizer is given in Fig. 3.13. Sample of metal is inductively heated and melted in a 1 litre tundish located in the upper chamber of the atomizer. Upper chamber can provide vacuum, argon or nitrogen atmosphere. When the liquid is heated to a target temperature, the stopper rod is lifted and metal can flow thru a zirconia nozzle out of the tundish. A stream of metal meets super-sonic close-coupled confined gas jet, streaming out of the steel ring nozzle. Sprayed liquid droplets rapidly solidify while falling into the bottom of the

Table 3.3 Chemical composition of Mn-alloyed samples, modified after [8]

Alloy	C	Si	Cr	Mn	Ni	Al	Mo	N	O_{tot}	S	P
	%							ppm			
V_Mn_1	0.041	1.06	15.9	0.15	6.12	0.0202	0.060	250	36	11	170
V_Mn_2	0.046	1.04	16.0	2.95	6.02	0.0249	0.077	229	42	25	191
V_Mn_3	0.042	1.1	16.1	4.81	5.96	0.0262	0.086	231	37	102	221
V_Mn_4	0.039	0.99	16.0	9.86	5.86	0.0265	0.112	300	16	87	145
V_Mn_5	0.040	0.98	16.1	15.3	5.78	0.0160	0.192	255	25	105	190
V_Mn_6	0.072	0.81	16.3	24.8	5.73	0.0054	0.352	398	20	117	–

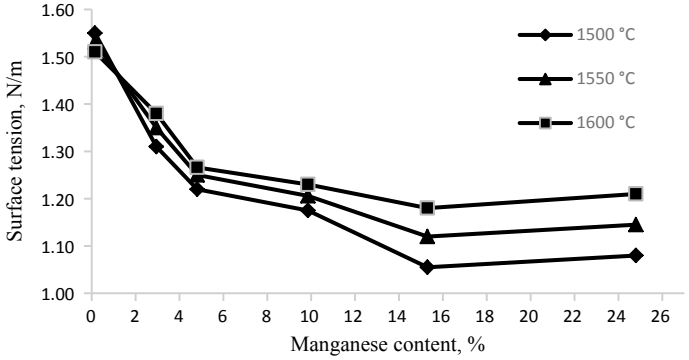

Fig. 3.9 Surface tension of CrMnNi alloy as a function of Mn content and temperature measured with MBP technique, modified after [8]

atomization vessel. After cooling of the unit, a fine powder is collected from the powder can (trap).

For the atomization of metals argon gas was used in VIGA-1B. Gas was supplied from the liquid storage tank and was re-gasified before injection into the ring nozzle. Gas pressure was 26 bar. In all the experiments the gas flow rate was kept constant and was equal to the technical maximum for the atomization unit.

The main target was to investigate the effect of thermophysical properties of the liquid alloys on the inert gas atomization. One of the easiest characteristics for modification of the molten steel is surface tension. To date, a vast amount of literature data is available on the surface-active elements, which can be applied for steel. Sulphur is known for its strong reducing effect on a surface tension of iron and iron-based alloys [10, 15]. Therefore, a series of alloys based on 16-7-9 steel was prepared with variable sulphur content in the range of 114–984 mass ppm S (Table 3.6). The surface tension of the alloyed steels was measured with the application of MBP-technique. Figure 3.11 shows that surface tension temperature curves lay substantially lower with the growth of sulphur content in the alloy. As a result, the surface tension of the 16-7-9 alloy at the target atomization temperature of 1600 °C dropped from 1250 to 1050 mN m^{-1} what was a 16% reduction.

Further these sulphur-alloyed steels together with 304 steel (which has much higher surface tension due to lower Mn-content) were atomized at a constant gas pressure and mass flow rate. Analysis of the median particle size (d_{50}) of the obtained powders (Fig. 3.14) showed a clear and strong dependence of d_{50} on the surface tension of the atomized metal.

Thus, sulphur alloying has shown a remarkable effect on the atomization. Sulphur itself is known as one of the least desirable trump element for most of the steel applications. With this regard, it was decided to check the possibility of d_{50} reduction with other surface active elements. As was given above, selenium showed further tremendous reduction of the surface tension of steel alloy with already low surface tension (Figs. 3.14 and 3.15a).

Table 3.4 Chemical composition of the samples alloyed with phosphorus, modified after [8]

	C	Si	Cr	Mn	Ni	Al	Mo	N	O_{tot}	S	P
	%							ppm			
P200	0.032	1.02	15.9	6.87	5.95	0.0234	0.078	227	17	136	182
P400	0.031	1.09	16.0	6.91	5.99	0.0152	0.077	249	27	114	423
P500	0.034	1.02	15.9	6.98	5.94	0.0096	0.081	260	16	111	505
P1000	0.031	1.09	16.0	6.90	5.90	0.0105	0.083	255	14	118	1210
P1500	0.036	0.93	15.8	7.06	6.01	0.0099	0.077	268	32	116	1600
P2000	0.033	1.00	16.1	6.92	5.80	0.0061	0.084	290	19	112	2160

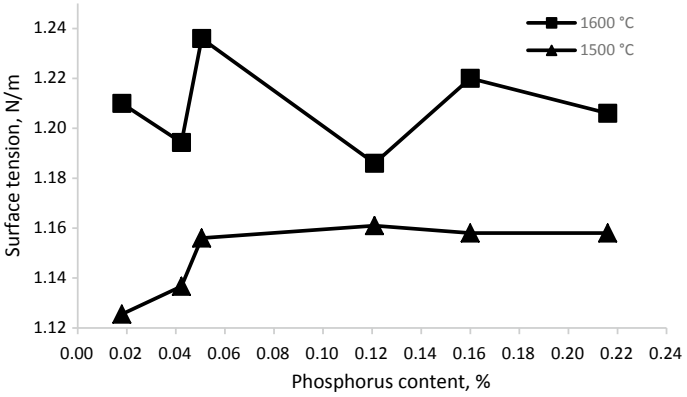

Fig. 3.10 Surface tension of CrMnNi alloy (16-7-6) as a function of phosphorus content measured with MBP technique, modified after [8]

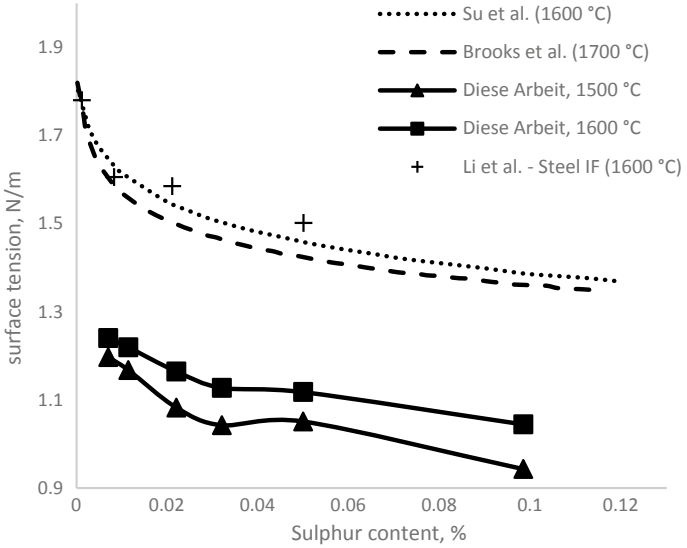

Fig. 3.11 Surface tension of 16-7-9 alloy as a function of sulphur content, modified after [8]

Results of atomizations of Se-alloyed steels showed the same trend on the reduction of median particle size due to a surface tension reduction (Fig. 3.15b). However, data points had higher scatter compared to S-alloyed powders.

Table 3.5 Chemical composition of samples alloyed with selenium, modified after [8]

	C	Si	Cr	Mn	Ni	Al	Mo	N	O_{tot}	S	P	Se
	%							ppm				
V_Se_1	0.030	0.99	16.1	6.94	5.96	0.0081	0.095	219	34	70	187	190
V_Se_2	0.028	0.98	15.8	7.06	5.94	0.0051	0.097	326	24	40	163	934
V_Se_3	0.029	1.01	16.1	7.14	5.98	0.0237	0.079	292	33	97	73	90
V_Se_4	0.023	1.00	16.1	7.02	5.96	0.0130	0.090	301	20	90	109	304
V_Se_5	0.026	1.05	16.0	6.97	6.10	0.0297	0.097	275	17	76	81	637

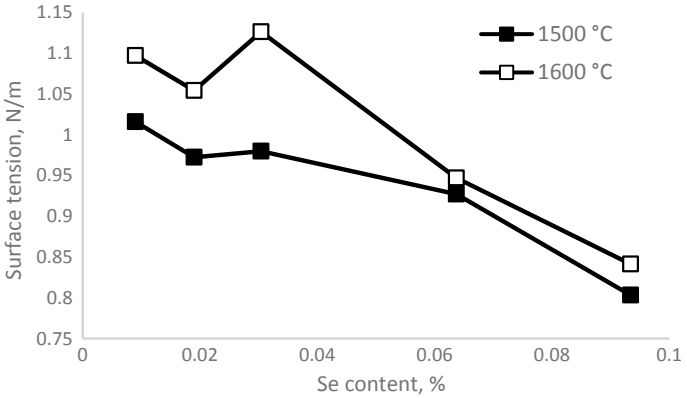

Fig. 3.12 Surface tension of 16-7-6 alloy as a function of selenium content measured with MBP technique, based on [8]

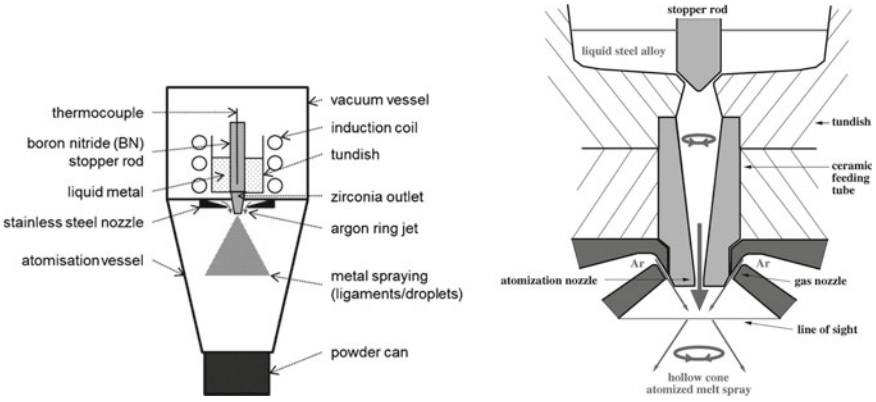

Fig. 3.13 Scheme of the inert gas atomization unit VIGA-1B [13, 14]

3.2.2 Effect of the Viscosity of Liquid Metal on the Inert Gas Atomization

It is known from literature, that atomization process is affected by the viscosity of the atomized liquid. In order to investigate this phenomenon, it was necessary to alloy the atomized steels with viscosity modifier. One of the studies accomplished in the framework of CRC 799 has indicated improvement of flowability of the phosphorus-alloyed steel [16]. Moreover, addition of phosphorus did not affect the surface tension—another parameter influencing atomization. Therefore, phosphorus was an ideal alloying element to study the modification of viscosity while other melt parameters being fixed.

Table 3.6 Chemical composition of the samples alloyed with sulphur, modified after [8]

	C	Si	Cr	Mn	Ni	Al	Mo	N	O_{tot}	S	P
	%							ppm			
16-7-9 S1	0.037	1.09	16.1	6.98	9.17	0.0063	0.082	215	21	114	111
16-7-9 S2	0.020	0.87	16.0	6.93	8.80	0.0040	0.078	222	11	220	173
16-7-9 S3	0.036	1.00	15.9	7.14	8.98	0.0063	0.084	240	9	320	71
16-7-9 S5	0.037	1.01	15.8	6.90	9.12	0.0056	0.090	214	10	499	61
16-7-9 S10	0.035	1.02	16.0	6.88	9.04	0.0049	0.080	241	14	984	36

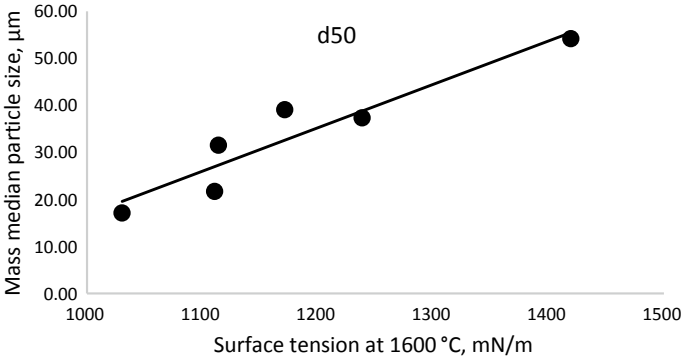

Fig. 3.14 Surface tension of sulphur-alloyed steel (**a**) and the effect of surface tension on the median particle size of the atomized powder (**b**), based on [13]

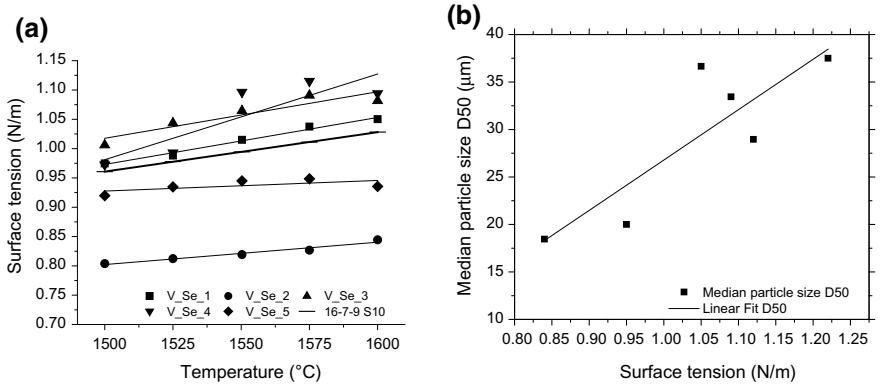

Fig. 3.15 Surface tension reduction by Se-alloying (**a**), modified after [8], the effect of surface tension on the median particle size d_{50} (**b**)

However, viscosity research required a high-precision viscosity measurement device. High precision was required in order to address even minor changes of such low-viscous liquids as molten Fe-alloys. It is known that steels have a viscosity only slightly higher than water. Beside that, it should be measured at temperatures well above 1450 °C. Additionally, alloys of interest contained 7% of Mn, what posed additional challenge to selection of materials for measurement instrument. All the above mentioned topics illustrates that the development of the viscosity measurement device was not a trivial task.

An entirely new device capable of low viscosity measurements was developed and patented [17]. Figure 3.16 shows the scheme of the unit and its' measurement head. Vibrating finger viscometer has a unique resonance oscillating head with the amplitude controlled by a laser micrometer. The amplitude is provided by the neodymium magnet excited by a field coil. As soon as a vibrating finger, attached to the oscillating

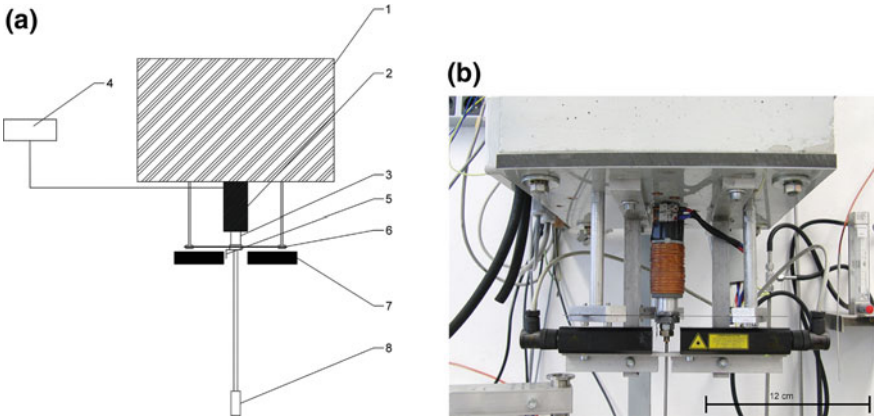

Fig. 3.16 Vibrating finger viscometer: **a** scheme of the unit, where (1) absorber, (2) field coil, (3) neodymium magnet, (4) microcontroller 12-bit ADC, (5) diaphragm, (6) spring and spring holder, (7) laser micrometer, (8) BN–ZrO_2 finger [18]; **b** appearance of the oscillating system [19]

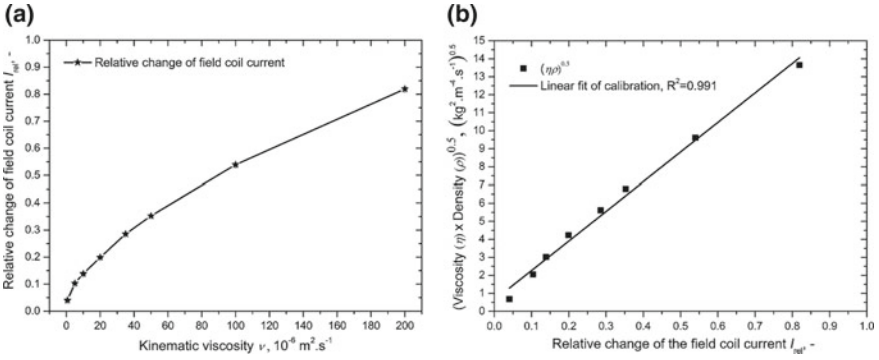

Fig. 3.17 Relative change of the field current as a function of the kinematic viscosity (**a**) and linear fit of the calibration as a function of the field coil current (**b**) [19]

head, touches the liquid the current in the field coil rumps-up in order to keep stable amplitude. For the measurement of viscosity, the vibrating finger is immersed into the liquid on 20 mm depth. The square root of the product of density and viscosity is a function of relative current change in this case:

$$\sqrt{\eta\rho} = I_{\text{rel}} \cdot b + a \tag{3.5}$$

In order to define the viscosity of the measurement a cell is calibrated at room temperature. Calibration is accomplished with the reference liquids of known viscosity (silicon oils) in the range of 0.7–200 mPa s. As a result, the calibration line is obtained (Fig. 3.17). As can be seen from (3.5), for the estimation of viscosity, the density of the liquid is required.

An essential aspect of a new cell development was the selection of the material for vibrating finger. The requirements to this material were as follows: easy machinability in order to create complex geometry (screw-thread), high-temperature corrosion resistance to withstand contact with liquid metals and alloying elements, relatively low cost. All these requirements were met in a boron nitride ceramic which was further used as a material for vibrating finger.

The new measurement cell was tested on the metals with vast reference data on their viscosity. The vibrating finger was immersed into liquid gold, silver and tin. Density data on these metals were taken from the previous study [20]. Viscosity values obtained by the newly developed unit are in a very good agreement with the literature values. A viscosity of the liquid gold measured with a vibrating finger viscometer was ~ 0% higher than previously reported in literature and decreased from 5.6 mPa s at 1100 °C (1373 K) to 4.0 mPa s at 1400 °C (1673 K). A viscosity of liquid silver was 10–20% lower than in available literature and decreased from 3.4 mPa s at 1000 °C (1273 K) to 2.3 mPa s 1400 °C (1673 K). Liquid tin showed viscosity ~20% lower than reported in literature and reducing from 1.3 mPa s at 600 °C (873 K) to 1.1 mPa s at 800 °C (1073 K). This research has proven the ability of new viscometer to measure the viscosity of low reactive metals at elevated temperatures.

After a successful measurement of noble metals' viscosity, the next step was to apply the vibrating finger viscometer for the study of the viscosity of the liquid steel alloys. Research cell was used to investigate the effect of nickel content on the viscosity of the Cr–Mn–Ni steel alloys in the temperatures range of 1500–1600 °C [18]. The measurements were accomplished without severe erosion of vibrating finger surface and geometry changes. As can be seen from Figs. 3.18 and 3.19, the viscosities of CrMnNi steels decrease with temperature and significantly reduce at 20% of Ni.

In order to investigate the effect of melts' viscosity on the atomization process, a series of phosphorus alloyed steels were prepared (Table 3.5). It is known from literature that phosphorus significantly reduces the viscosity of liquid iron and iron-based alloys [21]. Application of a vibrating finger viscometer has confirmed a decrease of viscosity due to additions of phosphorus. Increase of phosphorus content from 0.022 to 0.2% led to a reduction of viscosity from 5.0 mPa s to 3.2 mPa s measured at 1600 °C [8].

Atomization of the phosphorus alloyed steels showed a tremendous effect of viscosity on the size of the powder particles [22]. As it can be seen in Fig. 3.20, there is a linear dependence of the median particle size on the dynamic viscosity at 1600 °C. Decrease of viscosity of 36% (from 5.0 to 3.2 mPa s) led to reduction of d_{50} of 34% (from 39.5 to 26 μm).

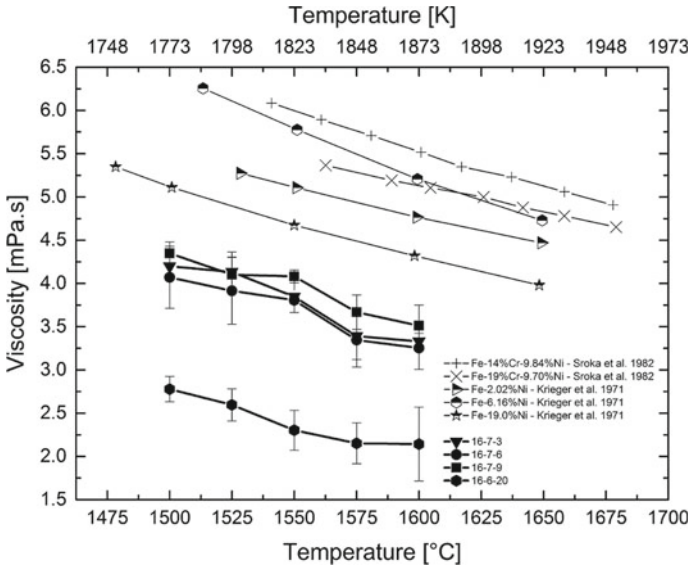

Fig. 3.18 Viscosity of the 16-7-3, 16-7-6, 16-7-9 and 16-7-20 alloys measured with the vibrating finger viscometer compared to previously reported values in the literature [18]

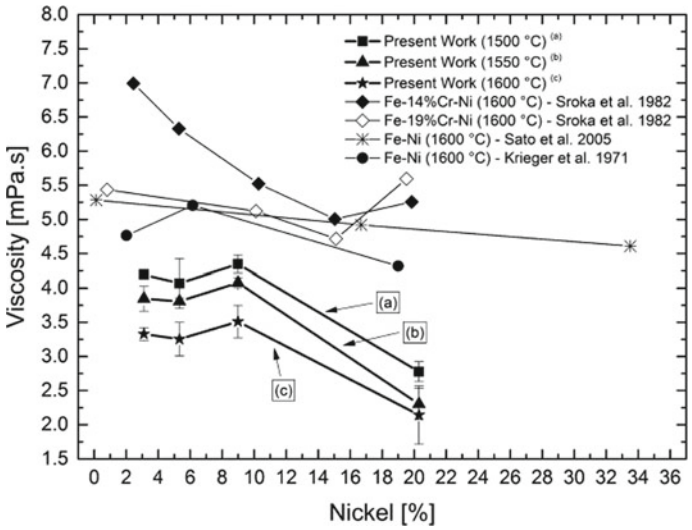

Fig. 3.19 Isothermal viscosity of Cr–Mn–Ni steel with varying nickel content and literature values [18]

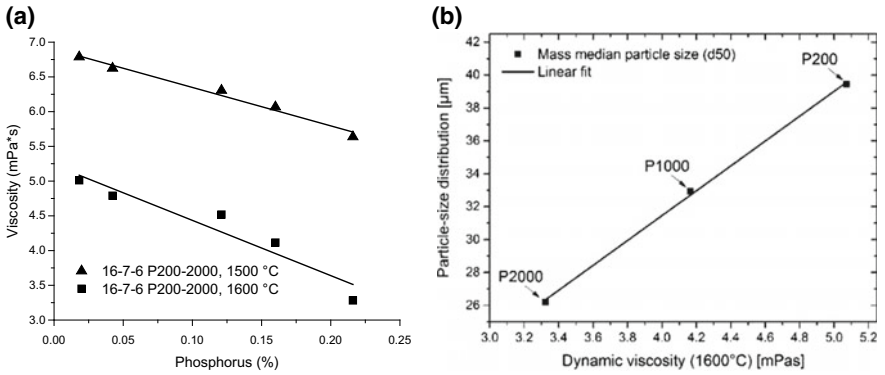

Fig. 3.20 Viscosity of 16-7-6 alloy as a function of phosphorus content measured at 1500 and 1600 °C based on [8] (**a**), and effect of viscosity on the median particle size d_{50} of atomized powder based on data from [8, 22] (**b**)

3.3 Density of Nitrogen Alloyed Steels

3.3.1 Development of Density Measurement Cell

One of the further targets was to develop a more precise density measurement cell based on the Archimedean principle. Why was the Archimedean principle selected to measure density? There are two features of the density measurement with the Archimedean principle to be selected:

1. High precision. The error of the density values reported in literature for liquid iron is less than 0.5% [23]
2. Low evaporation of sample and its alloying elements. The sample is usually measured in a ceramic crucible what means low surface to volume ratio.

There are several versions of the direct Archimedean principle methods to measure the density of liquids. In a classical single-sinker method one utilizes one body of a known volume which is immersed in the liquid. The body is suspended on a wire or attached to a thin rod. Presence of the rod has an almost negligible effect on the error of the measurement when single sinker method is applied for measurement of low surface tension liquid, e.g. water or oils. However, when the metals are measured, the effect of a surface tension on the rod has to be accounted for. Surface tension effect depends on the wetting angle between the liquid and the rod material and also on the capillary meniscus direction. These two factors are the primary source of errors for the estimation of liquid metals density with the use of the single-sinker method.

In order to overcome this effect of surface tension, a variety of modifications are proposed in literature [24]. They are based on the idea to use two bodies with different volume but the same rod diameter. When bodies are immersed, the effect of surface tension on their rods is supposed to be the same. However, the weight change

difference between the two different volumes indicates the density of the measured liquids (3.6). Therefore, the two-sinker method was selected for the measurement of the liquid iron alloys density:

$$\rho = \frac{(W_1 - W_0) - (w_1 - w_0)}{V_1 - V_2} \tag{3.6}$$

where W_1 is the weight of the big sinker immersed in liquid, W_0 is the weight of big sinker before immersion; w_1 is the weight of small sinker after immersion in liquid; w_0 is the weight of small sinker before immersion; V_1 is a volume of a big sinker, V_2 is a volume of a small sinker.

An additional measurement cell was added to existing MBP and vibrating finger viscometer facility in such a way that all three measurement units are utilizing the same induction furnace, positioning system and computer hardware. Scheme of the new unit is shown in the Fig. 3.21a. As it can be seen on the scheme, measurement of a density is accomplished via a high-precision balance (1) with the sinker assembly attached to its bottom hook. The assembly consists of molybdenum rod (2) connected to the ceramic rod with the sinker at the end (5). Additional weight (3) can be loaded on the assembly to keep it in vertical direction. The furnace has an extra thermocouple which measures temperature near the melt surface (10). The thermal field in the crucible was checked by immersion of a shielded thermocouple in the molten Ni and also in solid Mo. It was estimated that temperature in the melt was 8–10 K lower than the one measured by the side thermocouple. Therefore, side thermocouple is used as a sensor of melt temperature during experiments.

The procedure of measurement consists of:

(1) Heating of the sample to a target temperature with the rate of 20–30 K per minute
(2) 30 min holding time in order to get thermal equilibrium
(3) Measurement of sinker weight on 2–3 mm above the melt
(4) Immersion of sinker into the melt on 1 mm below the target level
(5) Subtraction of the sinker on the target level and measuring the weight change for 5 min
(6) Repetition of steps 4–5 two more times
(7) Measuring of sinker weight above the melt
(8) Withdrawing of sinker and repetition of steps 3–7 with the second sinker.

Step 4 was added after the preliminary test in liquid lead that showed significant improvement of accuracy due to reducing of a surface tension effect on the ceramic rod (Fig. 3.21b). All the sinkers used in this measurement cell before experiments were immersed into deoxidized water in order to estimate their volume (volume difference of pairs) at room temperature.

Copper, silver, and tin metals were selected for the first application of the measurement cell. The materials were melted in ZrO_2 crucibles (yttria-stabilized) and measured with ZrO_2 (MgO-stabilised) sinkers. As can be seen in the Fig. 3.26a, density of copper measured by Archimedean principle decreased from 8.06 g/cm^3 at

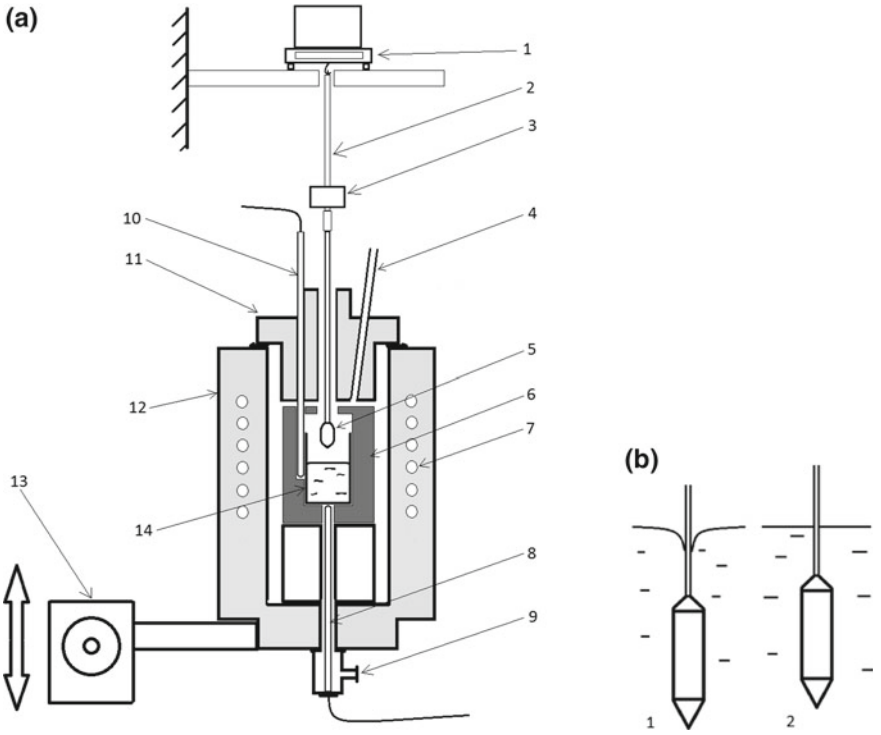

Fig. 3.21 **a** Density measurement cell. 1 Mettler-Toledo XS105 balance placed on a fixed platform; 2 molybdenum rod; 3 extra load (Cu); 4 top input of gas (argon); 5 ceramic sinker; 6 graphite heating crucible; 7 inductor coil; 8 bottom thermocouple (type B); 9 bottom gas input (argon); 10 side thermocouple (tape B); 11 ceramic cover of the reaction chamber; 12 ceramic furnace; 13 electric drive for vertical positioning; 14 graphite crucible [25]. **b** Shape of the capillary meniscus when sinker is immersed on 1 mm below the target level (1) and capillary meniscus when sinker is returned to target level (2)

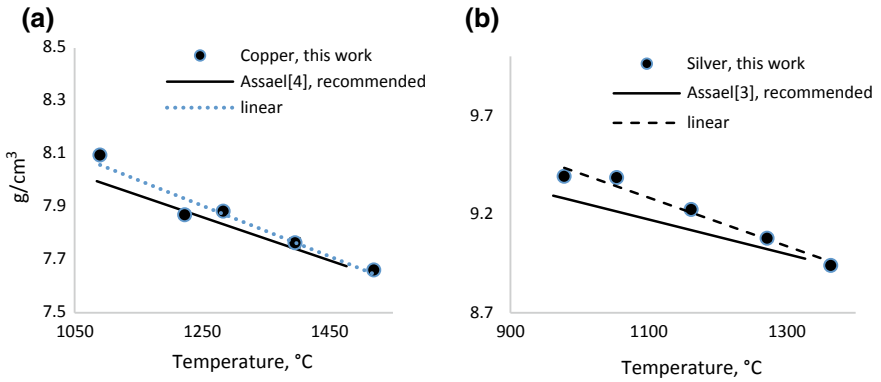

Fig. 3.22 Density of the copper (**a**) and silver (**b**) measured with the Archimedean principle with two sinkers method, based on [25]

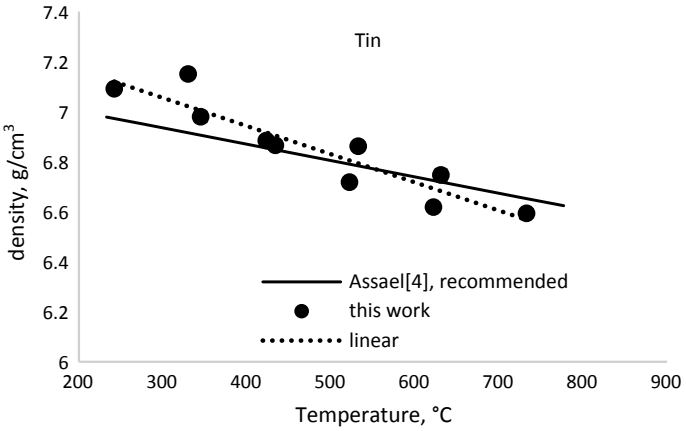

Fig. 3.23 Density of tin measured with the Archimedean principle with two sinkers method, based on [25]

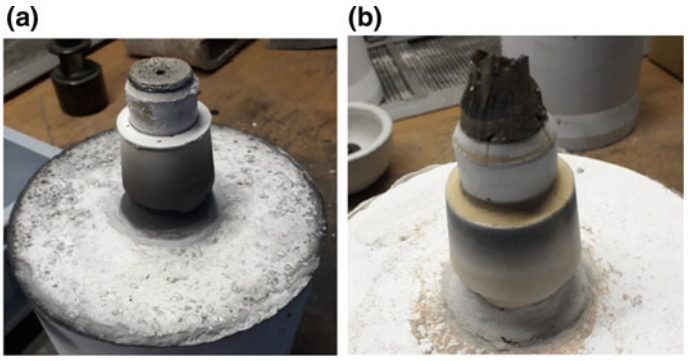

Fig. 3.24 Frozen metal formed on the face of tundish nozzle (crown) after atomization. **a** Crown is almost absent. **b** Severe crown formation [28]

1090 °C to 7.65 g/cm^3 at 1520 °C. Measured density deviates not more than 1% from values recommended in literature [26]. Density of silver had slightly higher deviation from recommended values [27] (Fig. 3.22b). Measured density decreased from 9.44 g/cm^3 at 978 °C to 8.94 g/cm^3 at 1364 °C. As for liquid tin, obtained density (Fig. 3.23) deviated up to 3% from recommended values [26]. Possible source of the error in the measurement of tin was oxidation of the surface level at temperatures below 700 °C.

In general, the measurement cell showed a relatively good accuracy and is considered for further study of iron-based alloys. It was decided to test a two-sinker method on the investigation of the density of steel alloys 15NC10.15 and 19NC15.15.

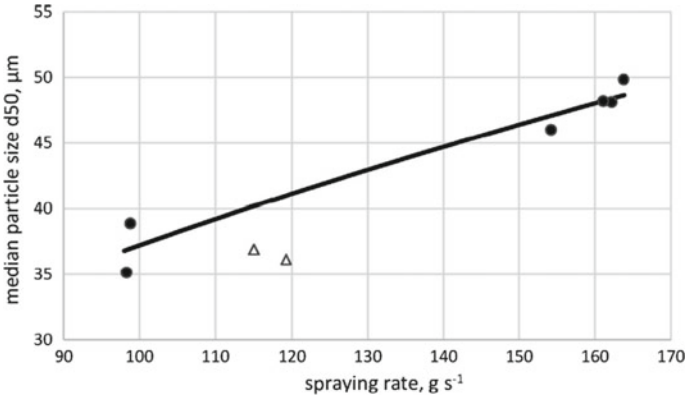

Fig. 3.25 Effect of spraying rate and temperature on the median particle size. Bullet atomized at 1600 °C, Triangle atomized at 1650 °C, square root trend line is built for all experiments at 1600 °C [28]

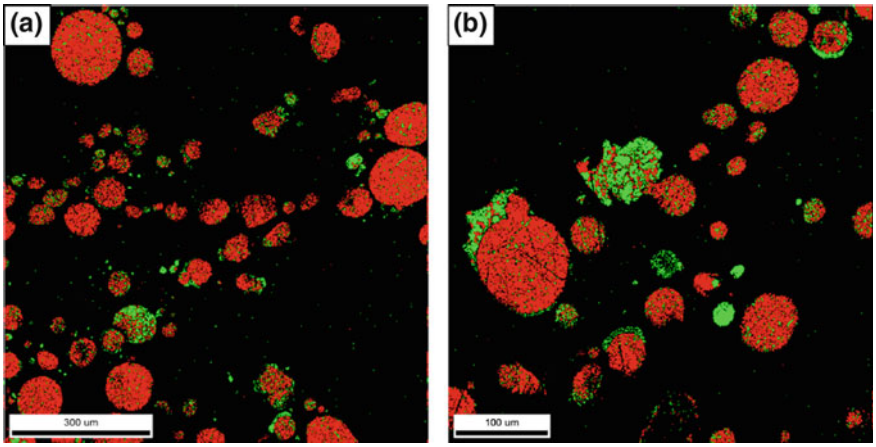

Fig. 3.26 EBSD analysis results for 19NC15.15+V with 2384 ppm N; **a** overviewand **b** higher magnification. Red colour represents the austenite phase and green color ferrite phase [28]

3.3.2 Atomization of Nitrogen Alloyed Steels

Along the duration of the CRC 799 inew steels 15NC10.15 and 19NC15.15 (Table 3.7) were developed. Exceptional tensile strength features of these steels are provided by high nitrogen content. At the same no extensive information on the effect of nitrogen alloying of the melt on the atomization process was found in the literature. Therefore, it was decided to conduct a series of atomization of the new nitrogen-alloyed steels [28]. In this study two parameters were selected as variables—nitrogen content and the temperature of the atomized melt. In order to

Table 3.7 Chemical composition of the nitrogen alloyed steels, modified after [28]

	C	Si	Cr	Mn	Ni	Al	Mo	V	N	O_{tot}	S	P
	%								ppm			
15NC10.15	0.151	0.427	15.5	2.97	2.91	0.0043	0.048	0.082	1089	45	67	203
19NC15.15	0.156	0.434	19.0	3.09	4.14	0.0089	0.059	0.085	1554	68	78	194
19NC15.15V	0.159	0.504	18.9	2.82	4.24	0.0132	0.046	0.620	3187	24	90	89

broaden the range of soluble nitrogen content in the steel 19NC15.15 it was alloyed with 0.65% of vanadium and was named as 19NC15.15+V. Atomizations were also accomplished at 1600 and 1650 °C for steels 15NC10.15 and 19NC15.15.

The amount of dissolved nitrogen in the liquid alloy was provided by adjusting argon/nitrogen ratio in the atmosphere in the upper vessel of VIGA-1B. A sampling at 1550 °C was done before atomization was launched. Unfortunately, not all samplings were successful. However, with the exception of 19NC30.15+V results showed relatively low nitrogen loss directly during atomization—in a range of 80–130 ppm. As for 19NC15.15+V, the significant difference between the sample and the powder nitrogen composition could be explained with the sampling procedure described in reference [28].

Series of atomization with variable nitrogen content did not reveal an apparent effect on the median particle size d_{50}. At the same time, another factor showed a strong influence on particles size. During the atomizations a frozen crown was formed on the face of the tundish nozzle (Fig. 3.24). The size of this crown was a defining factor for the metal flow rate. During big crown formation, the metal flow rate was reduced what led to lower spraying rate (higher gas/metal ratio). It is known that in industrial practice the gas/metal ratio is the main parameter to control powder size [11]. The results of these experiments were in very good agreement with the typical square root dependence of d_{50} from gas/metal ratio (see Fig. 3.25).

Series of atomization conducted at 1650 °C showed a significant shift of the value d_{50} below the square root trendline of 1600 °C, thus, illustrating the effect of temperature on refining the size of the particles. These results are in a good agreement with the existing literature on this topic [29].

The samples of two powders with maximum and minimum nitrogen content were analyzed with the use of magnetic saturation method. The results showed that powder with 765 ppm on *N* had 54% of ferrite, while sample with 2384 ppm *N* had only 17% of ferrite phase. Further analysis with electron backscatter diffraction of SEM confirmed a prevailing of austenite phase in high *N*-containing alloy (Figs. 3.26 and 3.27). Furthermore, particles smaller than 20 μm had more ferrite phase than bigger ones ($20 < d < 200$ μm). This indicated control of both cooling rate and nitrogen upon the austenite stabilization.

3.4 Analysis of Gas Atomization Process

This research was dedicated to the production of the inert gas atomized powders with the defined properties for further application in the TRIP-Matrix-Composites. Therefore, a commercial inert gas atomization facility supplied by ALD Vacuum Technologies was applied.

The main targets were:

- To measure and analyse the atomization process
- To study of new nozzles' geometries and systems

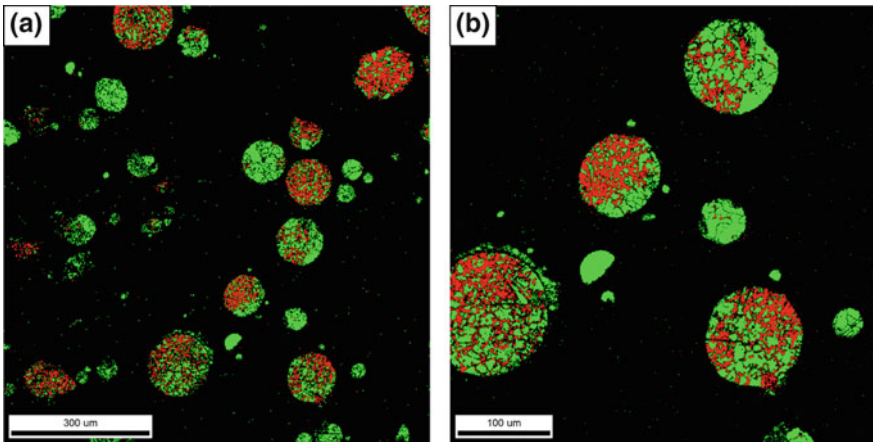

Fig. 3.27 EBSD analysis results for 19NC15.15+V with 765 ppm N_2; **a** overview and **b** higher magnification. Red color represents the austenite phase and green color ferrite phase [28]

- Targeted influence on the atomization process to produce steel powders of predefined size.

In order to affect the process of atomization it is necessary to accurately study the process of metal spraying. With this regard two special measurement units were developed for the 2-dimensional in situ measurement of temperature and velocity of the fluid particles within the gas atomization process.

3.4.1 Temperatures of the Particles

For measurement of the particle surface temperature a 2-color thermographic camera unit was developed [30]. The setup consists of two commercial CCD-cameras with installed dielectric optical filters, optical beam splitter and two lenses as object lenses. The components were selected with the requirements for being operational in the selected filter wavelengths. The maximal spectral emissive power of the studied liquid metal droplets at 1873 K is expected to be close to a wavelength of 1.5 µm. CCD camera sensors have their peak sensitivity typically at 0.5 µm. Their sensitivity at 0.9 µm is only a tenth of the maximum value. Therefore, the combined effect is that the recorded signal, i.e. intensity times sensitivity is low. In order to handle this shortcoming longer exposure times are used. This means that not the surface temperature of individual droplets is recorded, but a temporal average of the droplets that cross the area imaged onto each pixel. The cameras have a resolution of 1600 × 1200 pixels of 4.4 µm pixel size. Maximum frame rate is 16 fps. Images were obtained in an 8-bit greyscale. The optical dielectric bandpass filters have central transmission wavelengths at $\Lambda_1 = (850 \pm 8)$ nm and $\Lambda_2 = (900 \pm 8)$ nm. The set-up

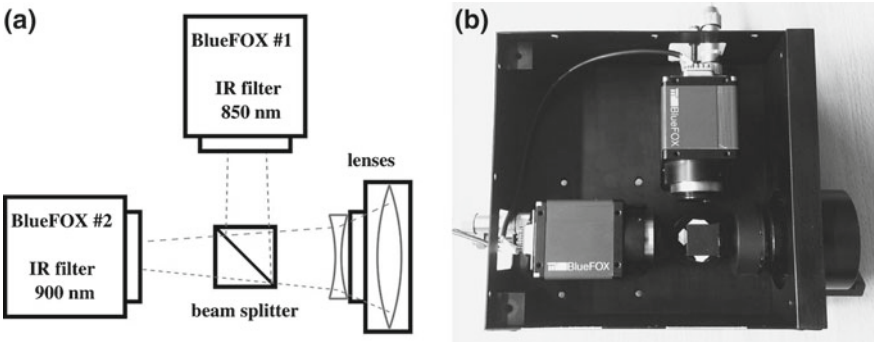

Fig. 3.28 Scheme (**a**) and picture (**b**) of the two-color pyrometer [14]

of the two-color pyrometer is shown in Fig. 3.28. The image was focused with the objective "Rollei-HTF Distagon 2.8/35". The images were focused onto the CCD sensors through the beam splitter cube. It splitted the optical path for the two camera sensors.

3.4.2 Image Processing

Two-color pyrometer was calibrated using a high-temperature furnace and a sample of silicon carbide in a temperature range of 1273–1873 K. The temperature of the sample was measured with a type B thermocouple assuring ± 1.5 K absolute measurement error. After calibration a particular correction term was obtained.

The newly developed two-color pyrometer was applied for the measurement of the metal stream temperature distribution at atomization in the VIGA-1B unit described previously in Fig. 3.13. The liquid steel (16-7-6 alloy) was heated ca. 200 K over its liquidus line to 1873 K. When the target temperature was reached, the atomization was launched. Figure 3.29 shows the results of measurements of the time-averaged temperature of the surface of the droplets. Due to the small depth of the field features of the camera, the pictures represent cross-sections of the spraying cone in the first half-second after the metal spraying initiation. The 0 mm point in the figure refers to the line of sight, which was 40 mm below the ceramic nozzle face. At 0.0 s the gas jet was not launched and only the metal stream is visible. At 0.1 s the disintegration of the metal flow began due to the gas stream. After 0.3 s the cone of sprayed metal was formed and later remained relatively stable. The primary breakup point was situated about 20 mm below the line of sight. Below that level a hollow cone of atomized melt with the length of approximately 50 mm was formed. At lower levels the hollow cone disintegrated on ligaments and droplets. Temperature iso-lines indicate that between 60 and 80 mm below the line of sight (nozzle metal) material was cooled down to its liquidus line. It corresponds to 100–120 mm distance from the nozzle face. This

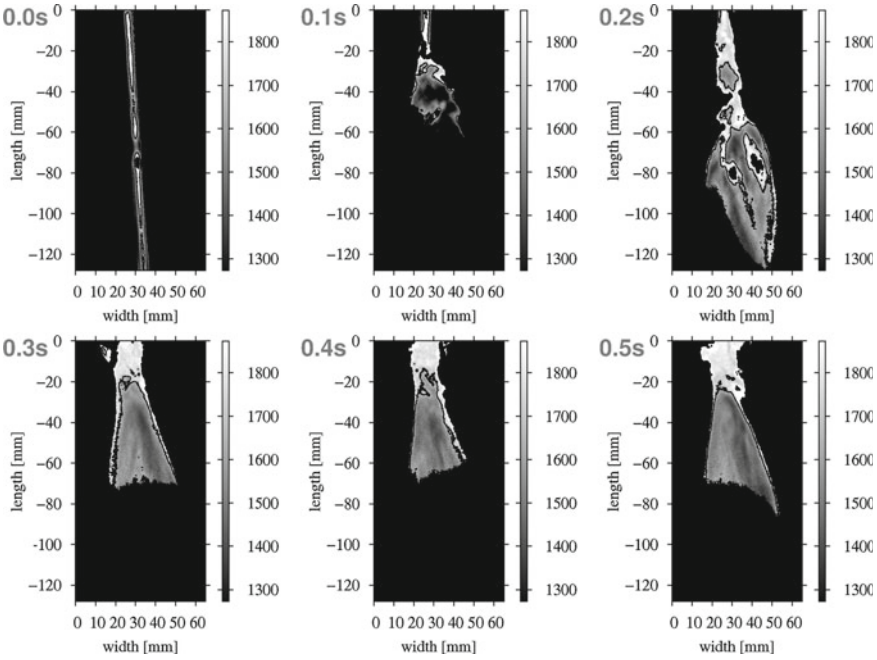

Fig. 3.29 Contour maps of the two-dimensional temperature measurement (in K) of the melt atomization. The quantity in the upper right corner of each temperature distribution is the image acquisition time t_{imag}. The black line within the region of the spray denotes the isoline of the liquidus temperature of 1673 K. The purple background means all temperatures are smaller than 1273 K which are out of the measurement range of the pyrometer, [14]

distance is about 30 times the diameter of the nozzle and is in a good agreement with literature data [31].

3.4.3 Velocity of the Particles

For the measurement of the velocity of the particles during metal atomization a special Particle Image Velocimetry (PIV) was applied (Fig. 3.30) [30]. The PIV measurement method is a non-contact optical method for measuring particle velocities in a 2D observation area within a particle flow. This area is defined by a thin light sheet generated by the passage of a laser pulse through a cylindrical lens. Two pulse laser cavities emit two laser pulses with an adjustable temporal separation. The pulse duration is on the order of 5 ns. The scattered light of the illuminated particles is picked up by a double-frame PIV camera arranged perpendicular to the light cross-section. Due to the time interval, the local positions of the particles differ in the double images. Special PIV evaluation software detects these positional differences

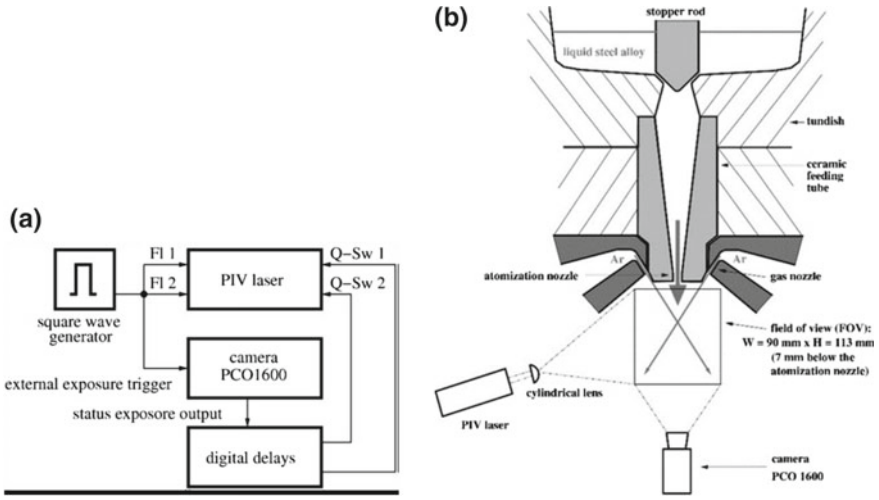

Fig. 3.30 **a** Block-diagram of the applied measurement apparatus. Square wave generator triggers the measurement with the frequency of 10 Hz. First, the flash-lamps Fl1 and Fl2 are triggered which pump the laser medium with energy. Simultaneously starts the double-images capturing with the PIV camera PCO 1600. In this case, digital delay units send control signals to the Q-Sw 1 and Q-Sw 2 Q-switches, whereby the laser pulses are triggered. The time of the 2nd double image is set in-camera. **b** Scheme of the atomization area of the VIGA 1B together with the position and size of the observed area (FOV) [30]

using correlation algorithms within the small windows in the image area, which defines a uniform grid structure. From the position difference at the correlation maximum and the time interval, a particle velocity vector is then calculated and assigned to the respective window center point. The result is a 2D velocity distribution in the observation area. PIV measurements in steel atomizers differ from those in continuous flows due to other boundary conditions.

Usually tracer particles are supplied to the fluids to be examined, which emit scattered radiation when passing the laser light section detected by the camera. Through this controlled particle addition (seeding), the number density of the determined velocity vectors can be significantly increased that aim to measure the flow velocity of the gas. In the present case of steel atomization, the aim is to truly measure the velocity of ligaments and droplets that constitute the particles. The use of a narrow band filter, whose wavelength coincides with that of the PIV laser, effectively blocks the thermal radiation of the melt.

Due to its large particle sizes, the melt in the vicinity of the ceramic nozzle scatters light strongly which leads to over-exposure of adjacent pixels on the camera sensor (blooming effect) and images with overexposed areas. Therefore, the correlation evaluation of the double images gives the wrong velocity data in this region.

Based on numerical simulations [32], it is known that gas velocities in the range of 400–500 m/s occur near the atomizer nozzle. The particle velocities in the axial range were calculated to be up to 250 m/s. The measurement of such high speeds

requires a correspondingly small time interval between the double pulses of the laser in the order of 2–3 μs. The entire measuring system must be triggered exactly in time in order to minimize the measuring error component of the time interval.

Measurements of the particle velocities were conducted for atomization of two steels: X5CrNi18-10 and X3CrNiMo13-4 in VIGA 1B unit. Both steel samples were atomized at the same conditions. Atomization was initiated at ca. 200 K superheating above the liquidus line at 1600 °C. Evolution in time of the measured particles velocities in the first 0.5 s after atomization launch is seen in the Figs. 3.31 and 3.32. The plots show a section through atomization cone. It can be seen that after 60 mm below the ceramic nozzle the metal stream breaks up and forms a hollow cone confirming the results published in [14]. The high speeds in the upper third of the observation window are due to the blooming effect. In the area of the interaction of the melt and atomizing gas, the measured particle velocities range between 120 and 210 m/s. The white dashed line indicates the area where the solidification temperatures are reached. The particle velocities of both melts in the solidification area are approximately 120 m/s. Obtained velocities are in a good quantitative agreement with numerically determined data, e.g. as [33]. Comparison of the averaged particles' velocities of two steels revealed that in case of X3CrNiMo13-4 the velocities were smaller than for X5CrNi18-10.

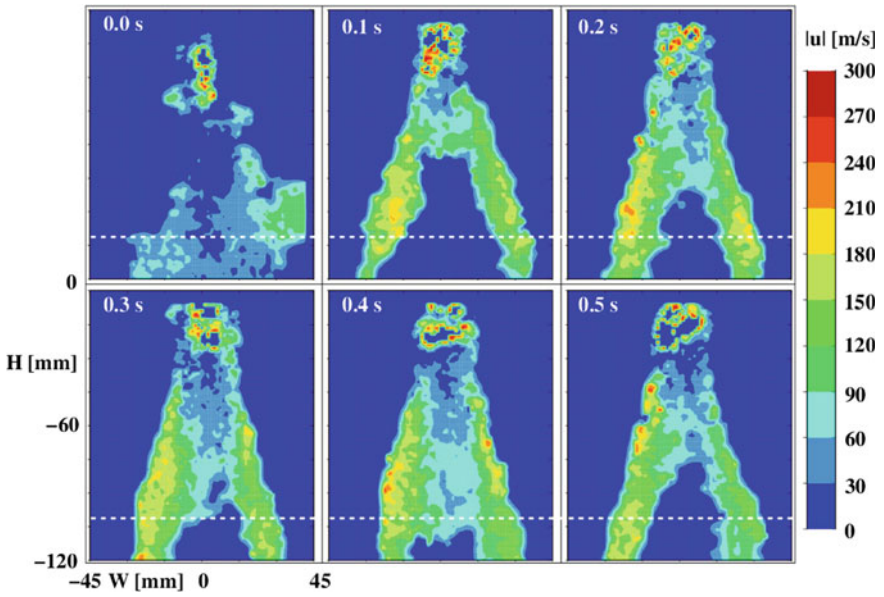

Fig. 3.31 Particle velocities for atomization of X5CrNi18-10 steel [30]

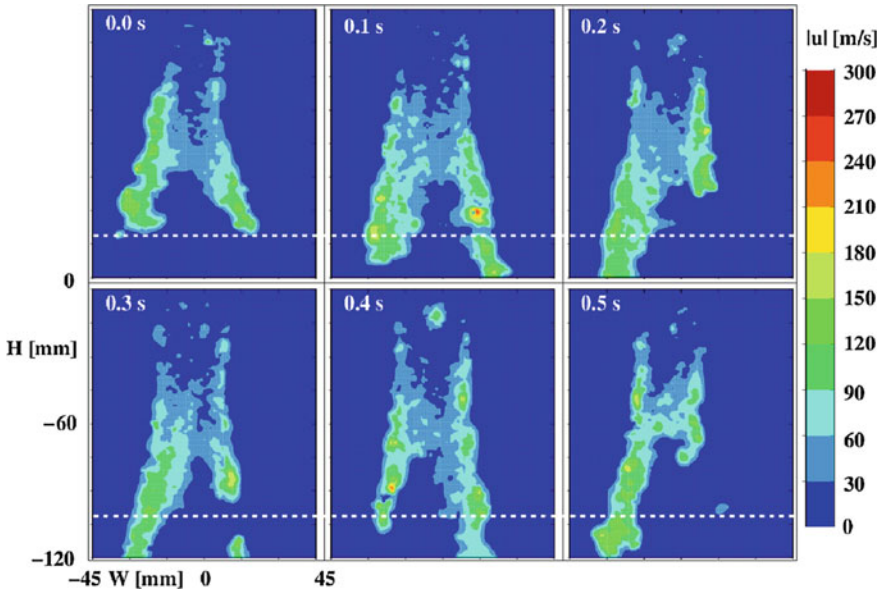

Fig. 3.32 Particle velocities for atomization of X3CrNiMo13-4 steel [30]

3.4.4 New Geometry and a Set-Up for an Inert Gas Atomization

Based on the results obtained in the previous chapters it became clear that there are three fundamental problems in the existing inert gas atomization techniques. The first problem is the very thick melt stream coming out of the nozzle. This is necessary to avoid freezing of the nozzle [34]. The result shows that the atomizing inert gas first breaks the stream into larger ligaments and sheets that have to be broken up in further steps downstream of the nozzle. The second problem is extremely low temperature of the gas when it contacts with the melt. The argon has expanded from an initial temperature around or slightly above room temperature to a velocity higher than Mach 1 up to 3 depending on the particular geometry. The result shows that the gas has a temperature around −50 °C for Mach 1 and down to −150 °C for higher Mach numbers. In principle, the high velocity of the gas is necessary for atomization but when it is that cold, it is counterproductive. This is the reason for the very high superheat of the melt needed for the VIGA set-up (200 K). Finally, the break-up of a thick stream in the centre of the flow with a surrounding gas can be changed. A thin layer of melt on the inner wall of a high-velocity nozzle for the gas is the closest the melt can be exposed to the gas. This is only possible if the gas is hot enough otherwise the nozzle would freeze. This rationale led to the development of a new set-up which has been patented [35]. The idea has been implemented first for the atomization of tin as a proof of principle. Figure 3.33a shows schematically

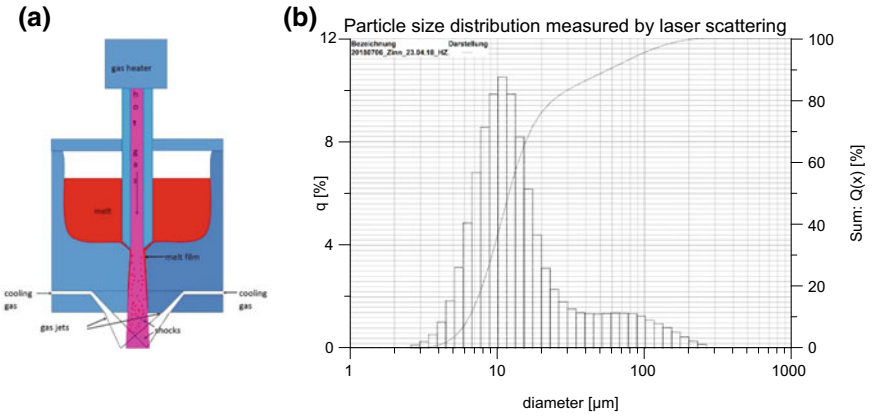

Fig. 3.33 Schematic set-up of the new atomization technique (**a**) and particle size distribution resulting for the atomization of tin using the new technique (**b**)

the tin atomization set-up. Figure 3.33b shows the resulting particle size distribution measured by laser scattering. The peak of the distribution centers at 10 μm for the first experiments. This factor is 2–3 lower than the VIGA results. Of course, the one result is for tin, and the other is for steel. However, when comparing with literature results for tin using similar set-ups as the VIGA the factor 3 is still valid [35].

3.5 Conclusions

The present work is focused on the investigations of inert gas atomization and the effects of thermophysical properties of liquid steel alloys' atomization process. Several new research units capable of measuring thermophysical properties of TRIP/TWIP steel melts as well as gas atomization were successfully developed, such as: maximum bubble pressure unit, patented vibrating finger viscometer, density measurement cell based on Archimedean principle, two-colour pyrometer, particle-image-velocimetry unit. The project allowed to gain new data on the surface tension, viscosity and density of the newly developed TRIP/TWIP alloys. Moreover, results regarding the effects of microalloying on the surface tension and viscosity of the steel were obtained. The primary research and practical results of the project development were:

- The surface tension of the TRIP/TWIP steel can be considerably reduced by microalloying with sulphur and selenium;
- reduction of a surface tension reduces the median particle size of the gas-atomized powders;
- The viscosity of the investigated TRIP/TWIP steel can be reduced with phosphorus;

- The viscosity directly affects the median particle size of the atomized powder;
- Nitrogen alloying does not significantly affect the inert gas atomization process in terms of particle sizes, however, powders phase composition is affected;
- Nitrogen leads to an increase of austenite phase fraction in ready powder particles;
- Temperature of atomization can be an effective measure to affect powder size;
- Measurements delivered data on particles temperature and velocity upon inert-gas atomization.

In general, besides delivering new thermophysical data on liquid alloys and metals, the primary outcome of the research is the confirmation of the successful control of the atomization process by modifying thermophysical properties of the atomized liquid.

Acknowledgements Authors would like to express sincere thanks to the former and current colleagues of the TP A2 and A3 who contributed to development of the CRC 799: Prof. Piotr-Roman Scheller, Dr. Andreas Jahn, Dr. Tobias Dubberstein, Clemens Cirmse, Peter Neuhold, and others. This work was funded by the Deutsche Forschungsgemeinschaft (DFG, German Research Foundation)—Projektnummer: 54473466-SFB 799.

References

1. K.J. Mysels, Colloids Surf. **43**, 241 (1990)
2. K.J. Mysels, Langmuir **2**, 428 (1986)
3. T. Dubberstein, M. Hötzel, R. Hagemann, P. Heller, P.R. Scheller, Steel Res. Int. **82**, 1122 (2011)
4. T. Dubberstein, P.R. Scheller, in *Scientific Reports on Resource Issues* (TU Bergakademie Freiberg, Freiberg, 2011), p. 7
5. T. Dubberstein, H.-P. Heller, P.R. Scheller, in *Ninth International Conference on "Molten Slags, Fluxes and Salts (Molten12)"* (Beijing, China, 2012), p. 10
6. T. Dubberstein, H.-P. Heller, Adv. Eng. Mater. **15**, 583 (2013)
7. T. Dubberstein, H.-P. Heller, J. Klostermann, R. Schwarze, J. Brillo, J. Mater. Sci. **50**, 7227 (2015)
8. T. Dubberstein, Beiträge zu den thermophysikalischen Eigenschaften flüssiger Metallschmelzen, Ph.D. Thesis, TU Bergakademie Freiberg, 2015
9. K. Ogino, K. Nogi, O. Yamase, ISIJ Int. **23**, 234 (1983)
10. B.J. Keene, Int. Mater. Rev. **33**, 1 (1988)
11. J. J. Dunkley, in *Powder Metal Technologies and Applications* (ASM International, 1998), p. 2762
12. J. J. Dunkley, in *Advances in Powder Metallurgy* (Elsevier, 2013), pp. 3–18
13. T. Dubberstein, H.-P. Heller, Steel Res. Int. **84**, 845 (2013)
14. C. Kirmse, H. Chaves, J. Therm. Spray Technol. **24**, 690 (2015)
15. Y. Su, Z. Li, K.C. Mills, J. Mater. Sci. **40**, 2201 (2005)
16. A. Jahn, K.-P. Steinhoff, T. Dubberstein, P. Franke, M. Weider, S. Wolf, A. Kovalev, A. Glage, A. Weiß, W. Schärfl, K. Eigenfeld, L. Krüger, P.R. Scheller, Steel Res. Int. **85**, 477 (2014)
17. T. Dubberstein, M. Schürmann, H.-P. Heller, H. Chaves, DE102014015301 (25 February 2016)
18. T. Dubberstein, H.-P. Heller, O. Fabrichnaya, C.G. Aneziris, O. Volkova, Steel Res. Int. **87**, 1024 (2016)
19. T. Dubberstein, M. Schürmann, H. Chaves, H.-P. Heller, C. G. Aneziris, Int. J. Thermophys. **37** (2016)

20. T. Dubberstein, H.-P. Heller, High Temp.-High Press. **44**, 393 (2015)
21. A.A. Romanov, V.V. Kochegarov, Phys. Metalle Und Metallkunde (Физика Металлов И Металловедение) **18**, 876 (1964)
22. T. Dubberstein, H.P. Heller, Adv. Mater. Res. **875–877**, 1265 (2014)
23. M.J. Assael, K. Kakosimos, R.M. Banish, J. Brillo, I. Egry, R. Brooks, P.N. Quested, K.C. Mills, A. Nagashima, Y. Sato, W.A. Wakeham, J. Phys. Chem. Ref. Data **35**, 285 (2006)
24. K.-C. Chou, J.-H. Hu, MTB **22**, 27 (1991)
25. I. Korobeinikov, D. Chebykin, X. Yu, S. Seetharaman, O. Volkova, Arch. Mater. Sci. Eng. **92**, 28 (2018)
26. M. J. Assael, A. E. Kalyva, K. D. Antoniadis, R. Michael Banish, I. Egry, J. Wu, E. Kaschnitz, W. A. Wakeham, J. Phys. Chem. Ref. Data **39**, 033105 (2010)
27. M.J. Assael, A.E. Kalyva, K.D. Antoniadis, R.M. Banish, I. Egry, J. Wu, E. Kaschnitz, W.A. Wakeham, High Temp. High Press. **41**, 161 (2012)
28. I. Korobeinikov, A. Perminov, H.-P. Heller, and O. Volkova, Adv. Eng. Mater. (2018)
29. D. M. Goudar, V. C. Srivastava, and G. B. Rudrakshi, EJ **21**, 155 (2017)
30. C. Kirmse, H. Chaves, Steel Res. Int. **87**, 1295 (2016)
31. R. Gjesing, J. Hattel, U. Fritsching, Eng. Appl. Comput. Fluid Mech. **3**, 471 (2009)
32. R. Kaiser, C. Li, S. Yang, D. Lee, Adv. Powder Technol. **29**, 623 (2018)
33. N. Zeoli, H. Tabbara, S. Gu, Appl. Phys. A **108**, 783 (2012)
34. K. Bauckhage, D. Bergmann, U. Fritsching, H. Lohner, P. Schreckenberg, Chem. Ing. Tech. 10 (2001)
35. H. Chaves, C. Kirmse, H. P. Heller, T. Dubberstein, DE 10 2015107 876A1 (2016)

Chapter 4
Production of Ceramic Steel Composite Castings Through Infiltration

Paul Rähmer, Claudia Dommaschk and Gotthard Wolf

Abstract TRIP-matrix composites unite the outstanding properties of austenitic-martensitic cast steels with those of ceramics. To manufacture them via infiltration by steel melt, basic investigations are needed. Therefore, the following aspects were studied: the influence of sodium silicate bonded sand molds on solidification of high alloyed TRIP-steels, chemical reactions between steel and molding sand and the positive impact of sulfur and phosphorus on the infiltration quality. Composite materials made of steel and ceramics, in particular, melt-broken zircon corundum, have comparatively high wear resistance. The wear behavior of the composites is characterized by a ring-block test rig. In order to generate a stable bond between the steel and the ceramic phase, the ceramics were coated with titanium oxide prior to infiltration. During infiltration of the coated ceramics, spinel compounds are formed which reduce expansion-related cracks in the boundary layer.

4.1 Introduction

A combination of different materials enables a targeted combination of material advantages while reducing lagging. Composite materials made of metals and oxides show high innovative potential .

The materials produced primarily by powder metallurgical (PM) processes offer a wide range of applications. Due to the high manufacturing costs of PM processes however, the production of composite materials using suitable casting processes is an important alternative. A combination of the properties of newly developed TRIP/TWIP alloys, which have a high deformation potential and also a high energy

P. Rähmer
Albert Hoffmann GmbH, Bergrather Straße 66–70, 52249, Eschweiler, Germany
e-mail: p.raehmer@albert-hoffmann.de

C. Dommaschk (✉) · G. Wolf
Foundry Institute, Technische Universität Bergakademie Freiberg, Bernhard-von-Cotta-Str. 4, 09599, Freiberg, Germany
e-mail: Claudia.Dommaschk@gi.tu-freiberg.de

H. Biermann and C. G. Aneziris (eds.), *Austenitic TRIP/TWIP Steels and Steel-Zirconia Composites*, Springer Series in Materials Science 298,
https://doi.org/10.1007/978-3-030-42603-3_4

absorption capacity, with a wear-resistant ceramic enables the production of fracture-resistant, wear-resistant components [1].

For the production of the MMCs basic investigations are necessary and different ways for the production of these are pointed out.

4.2 Thermal and Chemical Interactions Between Casted High Alloyed TRIP-Steel and Molding Systems

For the infiltration of macro porous ZrO_2 ceramic filter by liquid TRIP-steel melt a special mold, shown in Fig. 4.1, was developed [2, 3]. The depicted mold consists of an infiltration area in the middle of the mold with a height of 100 mm and a diameter of 50 mm. Floating of the ceramics foams into the feeder is prevented by quartz rods and a filter located underneath. The feeder is equipped with an outlet to ensure uniform metallostatic pressure and the bottom outlet allows more melt to flow through the infiltration area. The solidification time has a high impact on the infiltration quality of the TRIP-matrix materials and is influenced particularly by the molding material. Therefore, the solidification times of three different types of molding sands were investigated. In addition, the modification of the steel composition near the molding material was discussed. As molding sand for the ester hardened sodium silicate bounded mold, H32 (silica sand), chromite sand and Cerabeads 650 (synthetic mullite) were used. Because of the high density, the chromite sand has a binder content of only 2 mass%, while the other molding sands are bound with 3.5 mass% binder. The temperature was measured in the middle of the infiltration area by Pt-Rh/Pt-thermocouples [2, 3].

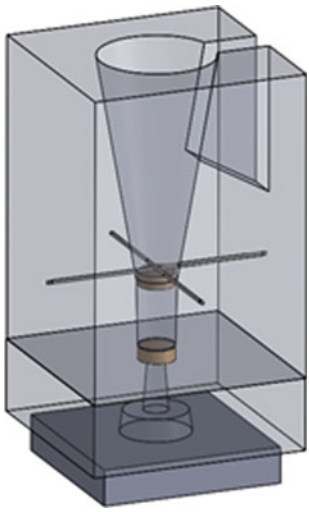

Fig. 4.1 Top pouring infiltration mold with floating preventing ceramic foams and quartz rods

4.2.1 Solidification Time Depending on the Molding Sand

The different molding sands have a strong effect on the cooling of the casting, and thus also on the solidification time of the steel. As shown in Fig. 4.2 the castings solidify faster in molds containing chromite sand than silica sand or Cerabeads. These results can be used to achieve a maximum solidification time, and thus to give the infiltration of the ceramics as much time as possible. Furthermore, the solidification can be specifically controlled by the use of the various molding sands, so that feeders or chills could be saved.

The different cooling times can mainly be explained by the different thermal conductivities and specific heat capacity. The thermal conductivity of Cerabeads is the lowest. Up to a temperature of 625 °C, chromite sand has a higher thermal conductivity and higher specific heat than silica sand, hence the amount of heat dissipated in this range is significantly greater and the castings tend to solidify faster [2, 4].

With the choice of molding sands the solidification time of the TRIP steel can be controlled and modified. Chromite sand has a cooling effect, while Cerabeads are insulating and therefore, they are best suited for the infiltration process [2, 3].

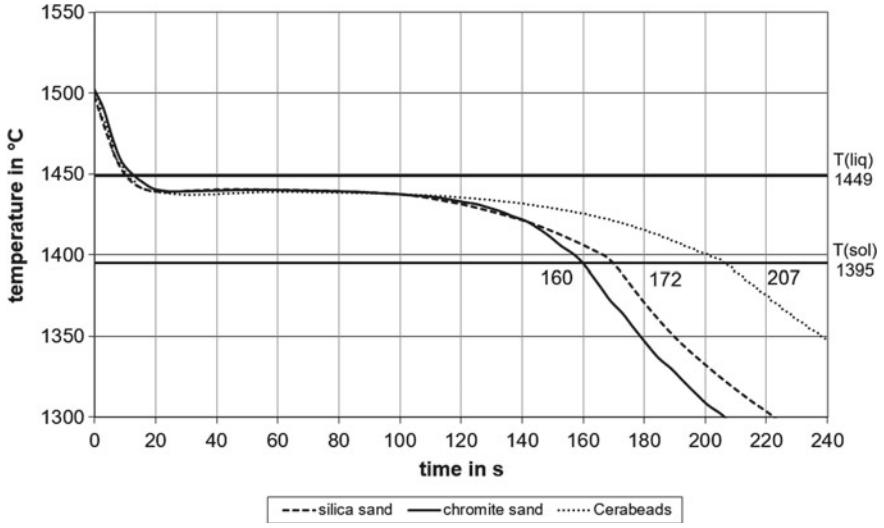

Fig. 4.2 Cooling curves of cast X3CrMnNi 16-7-6 TRIP-steel cylinders containing liquidus and solidus temperature depending on molding systems. Adapted from Weider [3]

4.2.2 Chemical Interactions Between Steel and Mold

The composition of the used steel is given in Table 4.1. To investigate the chemical interactions, samples were taken from the different thermally loaded layers of the molding material and were wet-chemically analyzed. The results are shown in Table 4.2. In addition, the bound and unbound molding materials were also examined without thermal loading. Locally, the exchange of elements is mainly restricted to the sintering zone, which is in direct contact with the melt. The organic components contained in the binder, e.g. the ester, are responsible for an increase of the carbon content in the melt. The chemical interactions can be measured in the molding sand and the casted steel. The exchange of the elements depends on the composition of the molding sand and their thermal behavior. Particularly noteworthy is the reactive element manganese through the combination of high vapor pressure and oxygen affinity [5]. This results in a strong degradation of acid refractory materials, so that especially the silica sand reacts with the manganese of the melt.

It can be concluded that all basic mold materials tend to accumulate alloying elements in the sintered layer. Cerabeads appear to form a very dense sintered layer, as there were found low levels of chromium and iron. Silica sand is relatively strongly enriched with MnO in the sintered layer, which only influences the casting composition locally at the surface [2].

4.3 Influence of the Ceramic Preheating Temperature and Phosphorus as Alloying Element on the Infiltration Quality

To determine the influence of the preheating temperature and the porosity of the ceramics, the top pouring infiltration was arranged according to the test described above. The casting temperature of the inductive melted steel, according to Table 4.1, was constant at 1600 °C. The ceramic preforms consisting of piled filters were preheated in an electric furnace to temperatures around 200, 600, 1000 and 1400 °C. To study the basic effects with molten steel and the general mechanism of the infiltration process commercial pouring filters where used, manufactured by Drache GmbH, Germany, with a porosity of 10 ppi. The quantification of the infiltration quality was done by measuring the infiltratable cavity thickness inside of the ceramics and by relating the infiltrated fraction of these cavities to the investigated area of the casting.

Table 4.1 Chemical composition of the used high-alloyed steel in mass% [3]

	C	Si	Mn	Cr	Ni	Fe
X3CrMnNi 16-7-3	0.035	0.89	7.21	16.36	3.09	Bal.
X3CrMnNi 16-7-6	0.05	1.06	7.10	16.20	5.94	Bal.

Table 4.2 Chemical composition of the molding sand before (without binder) and after thermal loading (sodium silicate bonded) in mass% [3]

Type and location of the samples		C	SiO_2	MnO	Cr_2O_3	Fe_2O_3	Na_2O	Al_2O_3	Others
Silica sand	Basic material	0.038	>99.0	<0.1	<0.1	<0.1	0.01	<0.1	
	Sintered layer	0.046	88.2	14.0	2.1	0.2	0.41	<0.1	
	Thermal affected	0.047	>99.0	<0.1	<0.1	<0.1	0.41	<0.1	
	Thermal unaffected	0.190	>99.0	<0.1	<0.1	<0.1	0.42	<0.1	
Chromite sand	Basic material	0.021	<0.1	0.1	30.6	26.2	0.014	15.5	<27.6
	Sintered layer	0.024	2.2	3.6	30.8	25.4	0.19	15.4	<22.4
	Thermal affected	0.035	0.1	0.15	30.6	26.0	0.22	15.6	<27.3
	Thermal unaffected	0.115	0.1	0.1	30.5	26.0	0.23	15.3	<27.6
Cerabeads	Basic material	0.038	35.8	<0.1	<0.1	1.1	0.49	61.7	
	Sintered layer	0.044	34.4	<0.1	1.9	2.0	0.78	60.8	
	Thermal affected	0.060	36.7	<0.1	<0.1	1.2	0.90	61.1	
	Thermal unaffected	0.158	36.3	<0.1	<0.1	1.2	0.92	61.5	

According to Dubberstein and Heller [6], the dynamic viscosity can be reduced by increasing the phosphorus content in the melt [6]. Therefore, the phosphorus contents in the steel melt were increased up to 0.2 mass% [7].

The effect of the preheating temperature on the infiltration of 10 ppi ceramic filter with a cast steel X3CrMnNi 16-7-6 is shown in Fig. 4.3. Due to the fact, that the melt cools down while flowing through the ceramic, the infiltration quality generally decreases with increasing depth of infiltration. The infiltratable cavity thickness is primarily dependent on the sample position, and thus on the flow length within the filter. A significant influence can only be detected in the middle section of the sample at a preheating temperature of 1400 °C. In the case of the proportion of infiltrated cavities, in addition to the dependence on the sample position, a dependence on the preheating temperature can also be determined, which is best visible in the lower areas. When these lower areas are underheated due to the low temperature of the melt or not efficient preheating of the ceramic filter, the melt solidifies faster, and the infiltration of the small cavities was impossible. As a result, the tests were performed with an additional cavity in the lower part of the mold, yielding a more uniform infiltration quality [3, 7].

The effect of the phosphorus content in the melt on the infiltration quality is shown in Fig. 4.4. By adding phosphorus, it is possible to infiltrate the 10 ppi filters preheated to 1000 °C nearly independent of the sample area. The best results concerning to the cavity thickness as well as the fraction of the infiltrated cavities were achieved by a phosphorus content of 0.2 mass% [3, 7].

To conclude, the infiltration quality depends primarily on the phosphorus content of the melt and thus on the viscosity and the melt flow through the filter package.

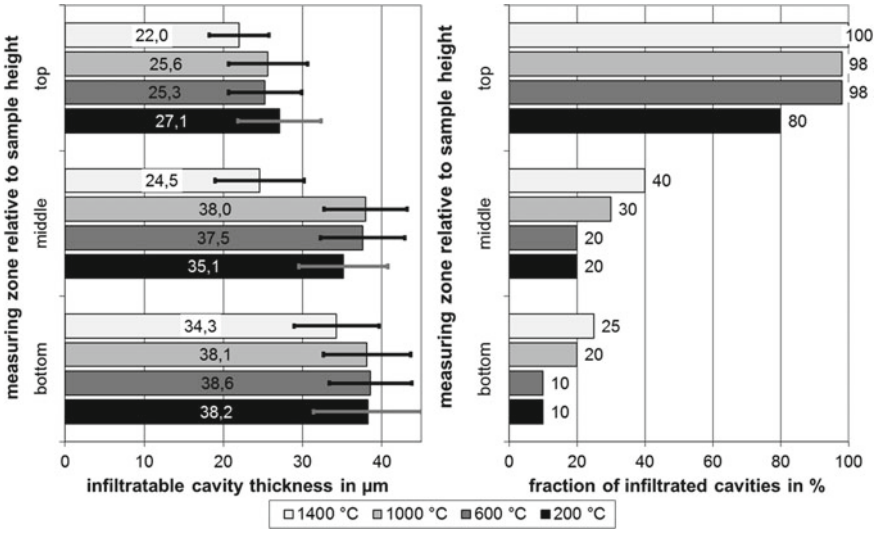

Fig. 4.3 Effect of the preheating temperature on the infiltration quality (cast steel X3CrMnNi 16-7-6 and 10 ppi filter). Adapted from Weider [3]

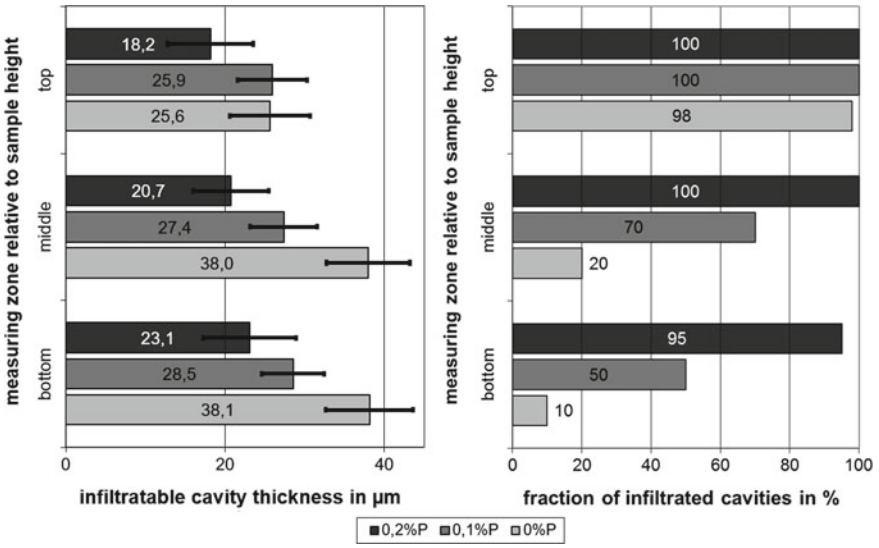

Fig. 4.4 Effect of phosphorus on the infiltration quality (cast steel X3CrMnNi 16-7-6 and 10 ppi filter). Adapted from Weider [3]

The influence of the preheating temperature of the ceramic filter before casting is less important in comparison to the location of the filter. In order to ensure a better infiltration quality, it is advisable to have an additional cavity under the filter package to preheat the ceramics by the additional melt flowing through the filters [3, 7].

4.4 Wear Properties of ZrO_2-Based Metal-Matrix-Composites

Metals can be reinforced with hard particles to increase the wear resistance of casings. For example, wear resistant parts are often made of white cast iron with a high content of carbide building elements, hard particles precipitating during solidification and heat treatment. If the hardness and wear resistance of the composites increases, the toughness often decreases. Therefore metastable austenitic-martensitic steels were chosen as matrix material, which demonstrates a TRIP-effect and transforms into α´-martensite by applying a load. As a consequence, the core of the castings is comparatively tough compared to the transformed wear area [8, 9].

To ensure good bonding of the steel to the ceramic, it is advisable to influence the thermophysical properties of the liquid melt. In addition to the contact angle and viscosity, the surface tension of the liquid melt can be reduced and the ability to infiltrate small pores in the porous ceramic structures can be increased. The flowability of CrMnNi steels can be increased by up to 0.18% of phosphorus content, so that

porous structures are infiltrated without any negative influence on the mechanical properties of the steel [7]. Furthermore, the contact angle between ceramic and melt can be reduced by adding titanium on the ceramic surface [10]. Dubberstein et al. reported in [11] about the influence of sulfur on the contact angle. Accordingly, the contact angle decreases from 102° at a sulfur content of 137 ppm to 92° at a sulfur content of 696 ppm.

4.4.1 Three-Body Abrasive Test

The characterization of the abrasive wear properties was carried out at a block/ring-testing station. The block/ring-testing station allows a variety of sample sizes, abrasive materials and metal pairings at different speeds and contact pressures. The results of the tribological test are a system parameter [12]. The most important advantage to other wear testing techniques is the variable sample size, so that the tests are also possible with MMCs with infiltrated hard particles in the range from 5 mm to 10 mm. The castings, needed for producing the wear samples, were manufactured as described in chapter 4.2. A 3.4 mass% magnesia partially stabilized zirconia foam structure with a porosity of 30 ppi was infiltrated. As matrix material metastable austenitic-martensitic X3CrMnNi 16-7-3 and 16-7-6 steels were chosen. The steel is poured into the infiltration mold at a casting temperature of 1600 °C. After solidification and cooling, the casting is machined and samples are taken out from the center of the infiltration area to investigate the wear properties. The samples had the dimensions 65 × 25 × 20 mm^3 with a 5 mm 45° bevel. A schematic illustration of the block/ring-testing station can be seen in Fig. 4.5 [9].

Abrasive particles can be dispersed in front of the sample for three-body abrasion. In these tests silica sand with a grain size of 0.1–0.5 mm flow out constantly in front of the chamfered edge to ensure new sand grains for each rotation. The sample was pressed onto the NiHard 4 ring with a load of 0.5 MPa, whereby the ring with a

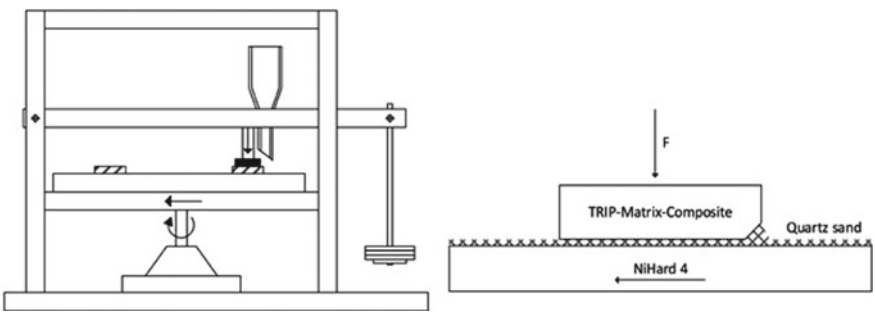

Fig. 4.5 Schematic illustration of the block/ring wear test [8]

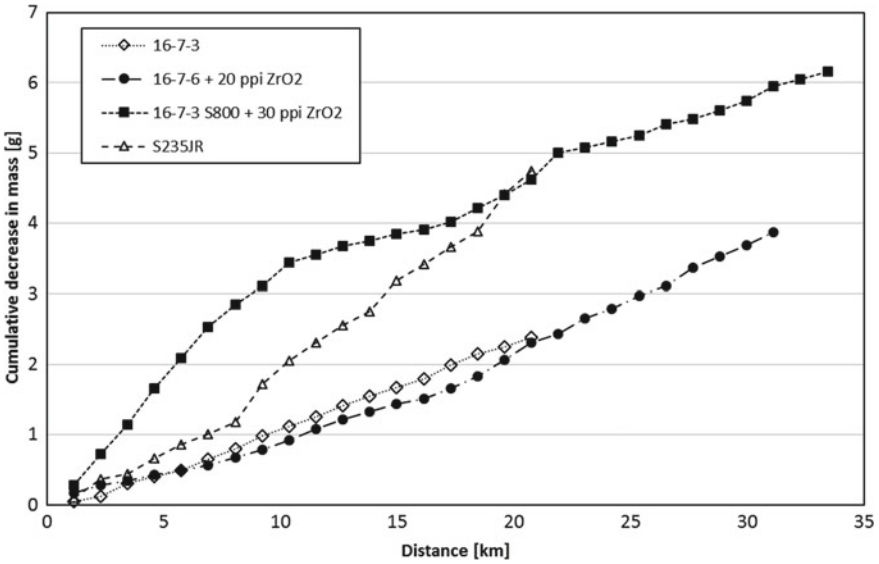

Fig. 4.6 Cumulative decrease in mass versus distance

circumference of 1.153 m was rotated with 26 min^{-1}. After 1000 rounds, the mass of the sample was measured and the wear test continued for at least 15 km [8, 9].

Figure 4.6 shows the decrease in mass of the wear samples over the distance on the block/ring-testing station. After an uneven loss of mass during the begin of the measurement, it stabilizes with increasing mileage. At the first 10 km, the 16-7-3-ZrO_2 sample demonstrates higher wear in comparison to the other samples. After that, it has decreased strongly and stabilized at 22 km. The pure TRIP steel has a significantly lower wear rate compared to construction steel. In order to evaluate the results better, the increase in wear is related to the distance. However, only the areas after the wear has evened out are considered. The results are shown in Table 4.3. The designations S800, S1000, P1800 and P2000 given therein describe the respective sulfur and phosphorus content in ppm.

Due to the lower M_s-temperature of the steel 16-7-3 compared to the steel 16-7-6, even smaller local stresses lead to martensitic transformation and thus to better wear behavior. The wear also increases with a fineness of the foam ceramics and with the sulfur as well as with the phosphorus content of the samples. The better infiltration tendency of sulfur-alloyed steels cannot compensate for the tendency of increasing wear known from the literature [9]. The finer foam ceramics have thin struts as well as a high microporosity due to the manufacturing process. This means that the ceramics have little resistance to abrasive wear, which is associated with breaking out of the metal matrix.

Table 4.3 Average wear in mass loss per distance and its standard deviation. Adapted from Acker [9]

Material	Mass loss per distance (mg/km)	Standard deviation (mg/km)
16-7-3	116	31
16-7-6	134	55
S235JR	241	64
16-7-3 S800 + 30 ppi ZrO_2	103	35
16-7-3 P1800 + 60 ppi ZrO_2	207	72
16-7-3 P2000 + 60 ppi ZrO_2	263	114
16-7-6 S1000	318	99
16-7-6 + 20 ppi ZrO_2	139	42
16-7-6 + 30 ppi ZrO_2	223	78

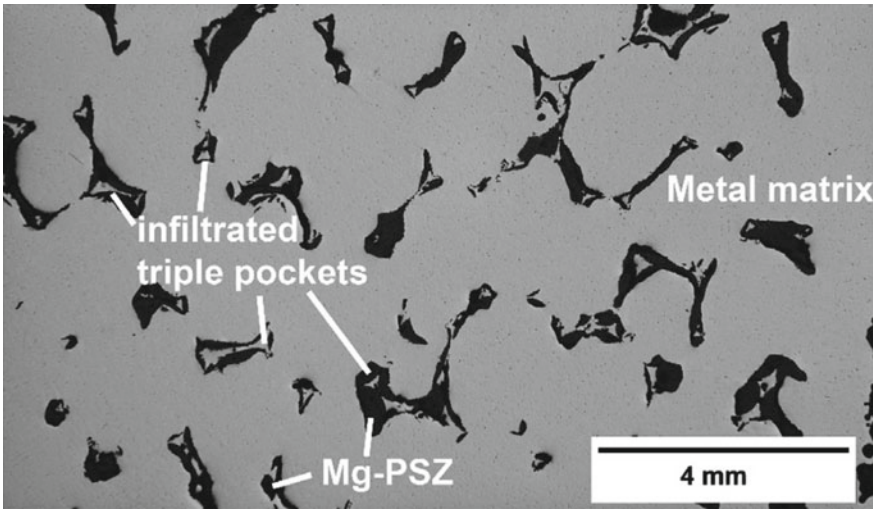

Fig. 4.7 Optical micrograph of a MMC containing cast steel X3CrMnNi 16-7-3 steel, alloyed with 800 ppm sulfur, and 30 ppi Mg-PSZ-foam ceramic [8]

4.4.2 Microscopy of the MMC

After casting, the samples were cut out of the middle part of the infiltration area at a distance of approx. 20 mm from the wall. Besides an optical microscope evaluation (Olympus BX51M), a scanning electron microscope investigation was carried out (ZEISS LEO 1530) with 20 kV in the backscattered contrast mode.

Figure 4.7 shows a micrograph of a 30 ppi Mg-PSZ foam and X3CrMnNi 16-7-3 alloyed with 800 ppi sulfur. Macroscopically no shrinkage cavities are visible. From a sulfur content of 500 ppm, the surface of the melt is covered with sulfur and thus

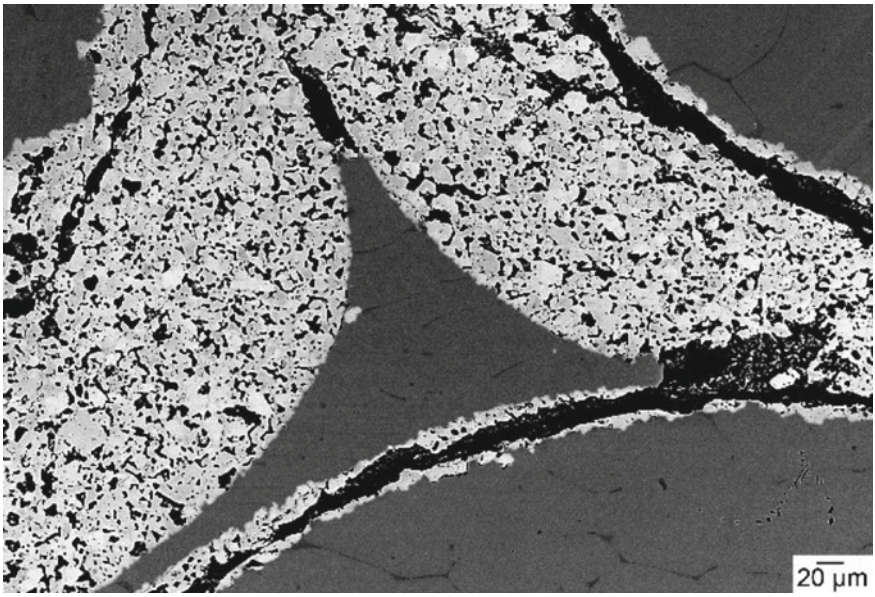

Fig. 4.8 SEM image of a 30 ppi Mg-PSZ foam infiltrated by cast X3CrMnNi 16-7-3 steel with cracks in the ceramic structure [9]

the surface tension of the melt is determined, so that the triple pockets could be filled [13].

In a closer SEM investigation, as displayed in Fig. 4.8, the good quality of the interface bonding is visible on a microscopic level. Due to the porosity-related low strength of the ceramic, the cracks do not run along with the interface, but within the ceramic. The different coefficients of expansion of steel and ceramic and the good interface bonding are leading to a stress gradient in the ceramic and the interface, which ultimately leads to cracks in the porous ceramic foams [14]. The tendency to crack formation is promoted by the infiltration of foam structures, since ceramic struts of different widths allow the melt to cool locally at different rates, which is associated with an increase in stress differences.

4.5 Infiltration of Loose Ceramic Particles with Steel and Their Wear Behavior

The MMC containing TRIP-steel and foam ceramics described in the previous chapter have no significant influence on the wear resistance. The expected phase transformation in the Mg-PSZ ceramic foam cannot be observed, because the force transmission of the deforming steel matrix is not sufficient. As a consequence the effect of closing micro cracks due to the transformation of the ceramic does not

occur in the present case [3]. In addition to the infiltration of the ceramic foams, the infiltration of loose ceramic particles has proven to be a practical way of producing wear-loaded cast parts with local ceramic reinforcement. Basic tests were carried out with the mold shown in Fig. 4.1. Special attention was paid to the wear resistance of the MMC and the interface between steel and ceramic. In order to transfer the knowledge gained to practice, a new possibility was developed to produce locally reinforced MMC in gravity casting. For this purpose, the lower density of the ceramics was exploited by rinsing the hard particles in a targeted manner.

4.5.1 Static Infiltration of Loose Ceramic Particles

Similar to the infiltration of ceramic foams, loose ceramic bulks were infiltrated. As matrix material, a high alloyed metastable austenitic-martensitic X3CrMnNi 16-7-3 was chosen. The composition is shown in Table 4.4. Due to its low M_s-Temperature of 61 °C, the chosen steel needs only low triggering stresses to transform from austenite to martensite [15]. As reference material, NiHard 4 in its cast and heat treated state was investigated. The composition is also displayed in Table 4.4.

As reinforcing material three hard particles, displayed in Table 4.5, were infiltrated. The aluminum oxide spheres have a particle size of 6.4 mm (Mühlmeier Mahltechnik, Germany). The white fused mullite (WFM) and the fused zirconia mullite (ZrM) (Imerys Fused Minerals, Germany) have a particle size between 4 and 12 mm. The WFM shows a uniform Al_2O_3-rich mullite structure with approx. 80% Al_2O_3 and 20% SiO_2 containing only minor SiO_2-rich areas. The ZrM consists of a mullite structure with incorporated ZrO_2-grains. All three ceramics exhibit lower thermal expansion coefficients between 5.0 and 6.4 10^{-6} K^{-1} compared to high alloyed stainless steels with a range of 16–18 $\times$ 10^{-6} K^{-1} [16].

According to their higher insulation capacity according to silica sand, CeraBeads 650 (Hüttenes-Albertus, Germany) were used as molding sand [4]. Sodium silicate binder is well known to minimalize the chemical reactions between the steel and the

Table 4.4 Chemical composition of the used TRIP-steels and the reference material. Adapted from Acker [9]

Alloy	C	Si	Cr	Mn	Ni	Mo	P	S	Fe
	(mass%)								
X3CrMnNi 16-7-3 ZrM	0.045	0.84	15.9	6.8	3.4	0.042	<0.003	0.009	Bal.
X3CrMnNi 16-7-3 WFM	0.045	0.85	15.7	6.7	3.4	0.034	<0.003	0.006	Bal.
X3CrMnNi 16-7-3 Al_2O_3	0.054	0.88	15.7	6.7	3.3	0.037	<0.003	0.007	Bal.
NiHard 4 heat treated	3.26	1.37	10.2	0.6	5.7	0.180	0.015	0.07	Bal.

Table 4.5 Composition of the infiltrated hard particles. Adapted from Acker [9]

Ceramic	Size	Al_2O_3	SiO_2	Fe_2O_3	CaO	MgO	Na_2O	K_2O	TiO_2	$ZrO_2 + HfO_2$
	(mm)	(mass%)								
Al_2O_3-spheres	6.4	99.5	0.1	<0.1	<0.1	0.2	<0.1	0.01		
WFM	4–7	76.0	23.5	0.05	0.02		0.2		0.02	
ZrM	5–12	45.7	17.8	0.1	0.1		0.1		0.1	36.0

molding sand and is therefore used. The steel was melt in a 30 kg open induction furnace. Directly before casting the preheated ceramics up to 1400 °C were filled into the mold. In order to prevent floating of the ceramics a 10 ppi casting filter (Drache, Germany) was placed on the ceramic heap and secured against floating with glass rods (Fig. 4.1). To ensure a minimum of heat loss, the melt was poured with a temperature of 1600 °C directly from the induction furnace into the mold.

After casting and cooling microscope investigation and three-body-abrasive tests were carried out.

4.5.1.1 Microscopy

All samples were completely infiltrated, depicted in Fig. 4.9. There was no macroscopic porosity and because of the directional solidification from the lower area to the upper one, there were no local cold runs visible.

At higher magnification, shown in Fig. 4.10, gaps of 10–20 μm can be seen for the Al_2O_3-steel composite. In the shown section no bonding between the steel and the aluminum oxide spheres is visible. The gaps result in breaking out of the spheres during machining. With the help of the SEM examination, it was possible to prove that oxides from the corundum side are on the steel surface and chromium, iron and manganese are located on the ceramic side. It can be therefore assumed that wetting has taken place and that the bond has broken as a result of solidification and cooling. The two materials move away from each other as a result of shrinkage. The cracks are caused by the stresses generated by the different thermal expansion coefficients.

Both mullites show a better interface connection. Slag phases were formed in the mullites. The white fused mullite formed a spessartite phase with a composition of 34% MnO, 40% SiO_2 and 22% Al_2O_3 and a resulting melting phase of 1195 °C. In zirconium mullite, the spessartite-like phase formed had a composition of 26% Al_2O_3, 37% SiO_2, 30% MnO and 2% NaO with a melting point below 1300 °C [17, 18]. The comparatively low melting point of the slags buffers the stresses arising during cooling down to their solidification temperature.

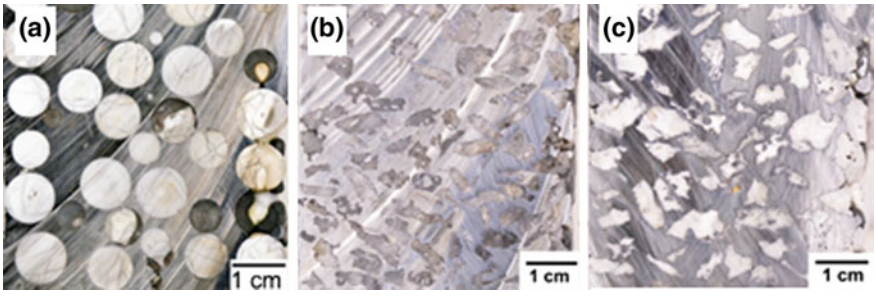

Fig. 4.9 Sectional views of the MMC, **a** Al_2O_3-spheres, **b** WFM, **c** ZrM

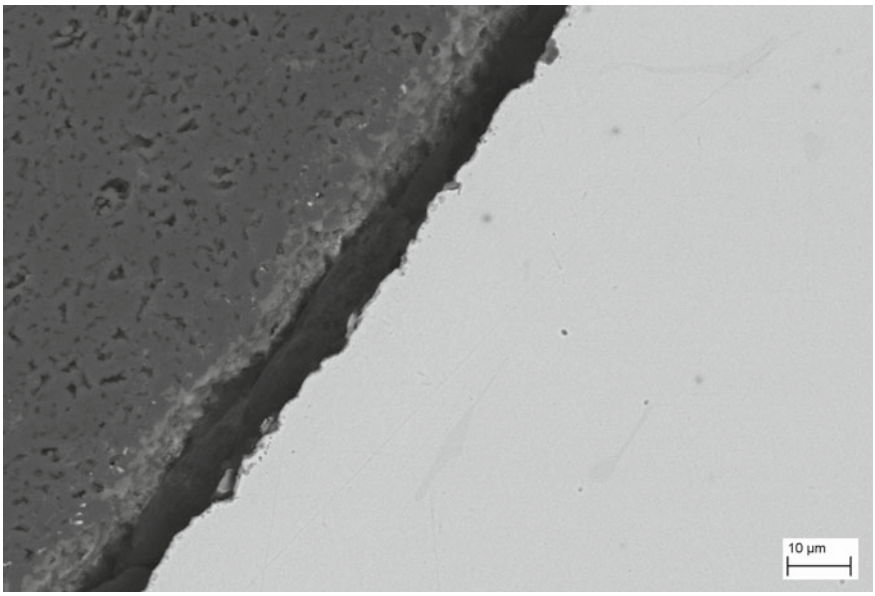

Fig. 4.10 SEM image of a MMC consisting of 9.6 mm Al_2O_3 spheres and X3CrMnNi 16-7-3 with the cooling crack between both materials

The irregular grain shapes creates a frictional connection between the matrix and the reinforcing phases. In addition, there was a different shrinkage in different directions of the ceramics because of the irregular particle shapes. The molten steel could image even small gussets on the ceramic side. Therefore, cracks in the boundary layer caused by cooling were unavoidable.

4.5.1.2 Wear Behavior

The wear behavior of the samples was investigated at a block/ring-station, as described above. The results are shown in Fig. 4.11. When comparing the wear rate as a decrease in mass per distance, the zirconia mullite based MMC demonstrates a wear reduction down to 93 mg km^{-1} and white fused mullite based MMC of 64 mg km^{-1}. Due to the breaking out of the corundum spheres, the wear value of the Al_2O_3-steel composite was not evaluated.

Generally, the mullite-based composites show better wear rates compared to NiHard4 and the cast X3CrMnNi 16-7-3 steel. The amount of α'-martensite in the investigated TRIP-steel is increasing up to 97% at the loaded surface [8]. The effect of the near-surface martensitic transformation and the associated increase in hardness is intensified by the addition of ceramics, which are form-fittingly embedded in the matrix.

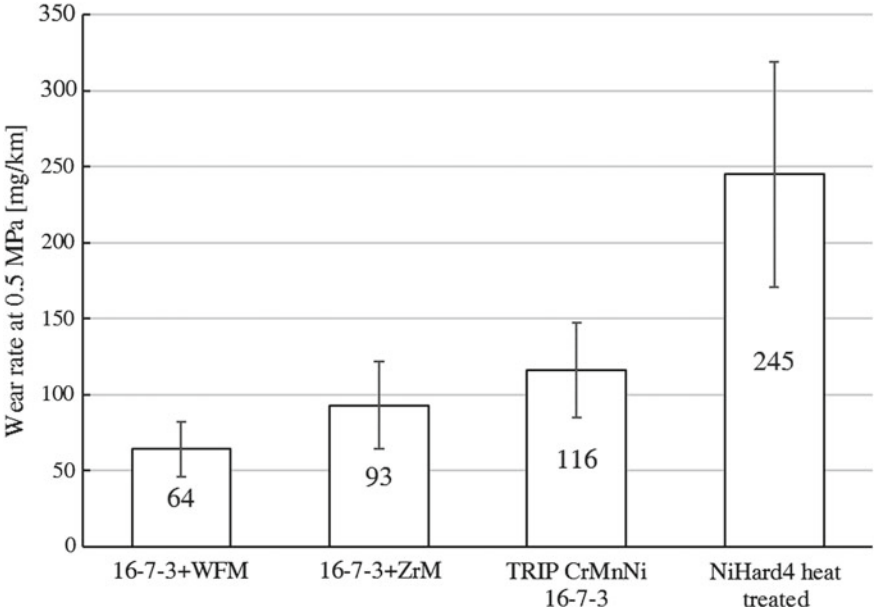

Fig. 4.11 Wear rate as a decrease in mass per distance

4.5.1.3 Interfacial Optimization by Coating with Titanium Oxide

Titanium is known as an alloying element because it is soluble in steels and also as an oxide in Al_2O_3. The absorption of titanium into the ceramic surface creates a layer that can serve as a bonding layer between metal and ceramic [17]. Especially on aluminum oxide, titanium melts can lead to an improvement of the interfacial bonding through the formation of titanium oxides and (Ti, $Al)_2O_3$ phases as well as intermetallic phases [18]. With this background, the interest was to improve the interface between steel and ceramics by the formation of aluminum titanate with the aim of crack reduction. Aluminum titanate is a high temperature phase which decomposes without the presence of stabilizers such as Fe_2O_3 or Si_2O_3 into rutile and α-Al_2O_3 at a temperature below 1280 °C [19].

First, the corundum spheres and mullite particles were produced by pelletizing in aqueous suspension, consisting of 30% TiO_2 powder and water, by dipping, drying and subsequent sintering. After mixing the spheres for 180 s, they were separated from the slurry using a sieve and then dried in a drying furnace for 24 h at 60 °C. The subsequent firing process was carried out at 1050 °C, to prevent the formation of aluminum titanate, as it can form at temperatures of 1100 °C and above [20].

After steel infiltration, the titanium oxide coated materials had a peripheral zone, which can be seen in Fig. 4.12. During the infiltration process, a reaction took place between the titanium oxide and the aluminum oxide. The interface layer between steel and ceramic had a thickness of about 10 μm and yielded a better connection. The

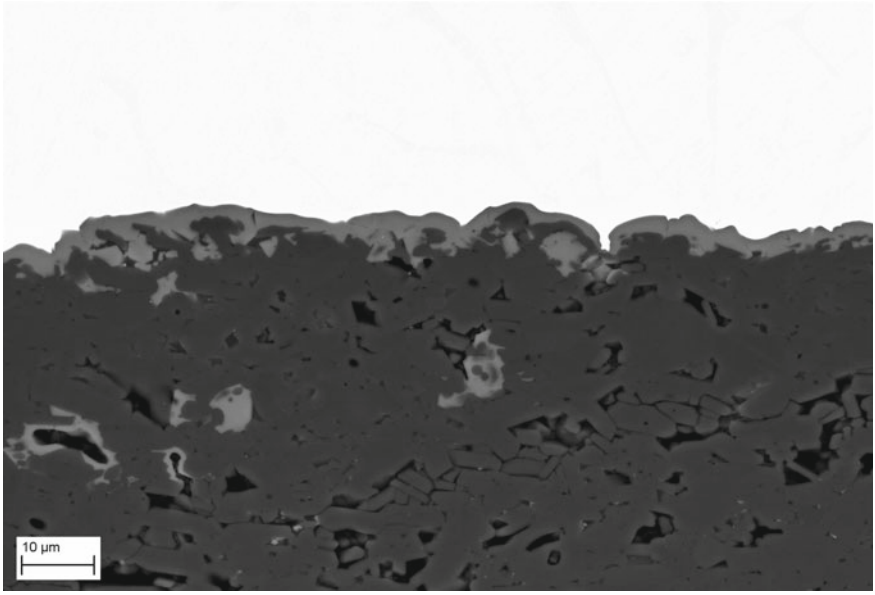

Fig. 4.12 SEM image of the interface between coated corundum spheres and X3CrMnNi 16-7-3

Table 4.6 Composition of the interface

	Al_2O_3	MnO	TiO_2	Cr_2O_3
	(mass%)			
Boundary layer	50	41	2	7
Incorporated spinel	52	38	6	4

EDX analysis of the interface, shown in Table 4.6, demonstrates, that a manganese-rich compound was formed with titanium oxides and aluminum oxide, which had a liquid phase fraction of up to 1100 °C and can therefore reduce stresses arising during cooling. The macroscopically visible discolorations consist of Al_2O_3 grains with incorporated spinel compound, which had a composition similar to the boundary layer. It can be assumed that the temporarily formed aluminum titanate has been transformed into manganese aluminate and manganese titanate by the presence of manganese.

4.5.2 Dynamic Infiltration of Loose Ceramic Particles

With the static infiltration method, it is difficult to produce industrial castings with a local ceramic reinforcement. In addition to static infiltration, where the ceramics

are infiltrated as bulk, the ceramics can also be infiltrated dynamically. This means that the ceramics are transported flow-induced through the melt to their destination. The large difference in density between steel and ceramics can consciously be used to rinse ceramics in the upper part of the casting.

Initially, a casting mold was developed, which makes only infiltration of ceramic particles possible, as it turned out that ceramic foams have no positive effect on the wear resistance. The gating system was deliberately designed generously, as the ceramics remove a large amount of heat from the melt despite preheating and this deficit has to be compensated by a larger melt mass.

The aim of the developed infiltration mold is to produce samples for the block/ring-testing station with a local ceramic reinforcement in the wear area, according to Fig. 4.13, with minimal resource expenditure. Between the wear sample and the spherical feeder is the flow zone in which various possibilities can be tested to stop the further buoyancy of the ceramics and to ensure a glistening distribution of these. A 5 mm thick ceramic filter has proven its worth as insert for the flow zone. A cell filter with a mesh width of 2 mm is used, as foam filters of this thickness possess not sufficient strength. The falling casting system was chosen, so that the preheated ceramics, which were filled in the sprue directly before casting, were carried along by the turbulences arising during the casting process. As can be seen in Fig. 4.14,

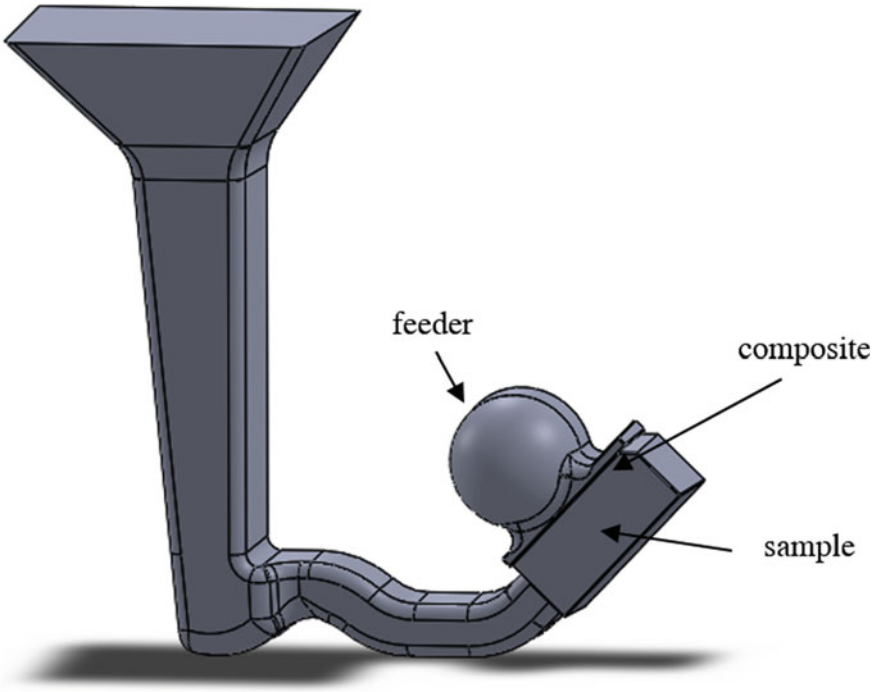

Fig. 4.13 CAD model of the infiltration casting with the wear sample below the spherical feeder

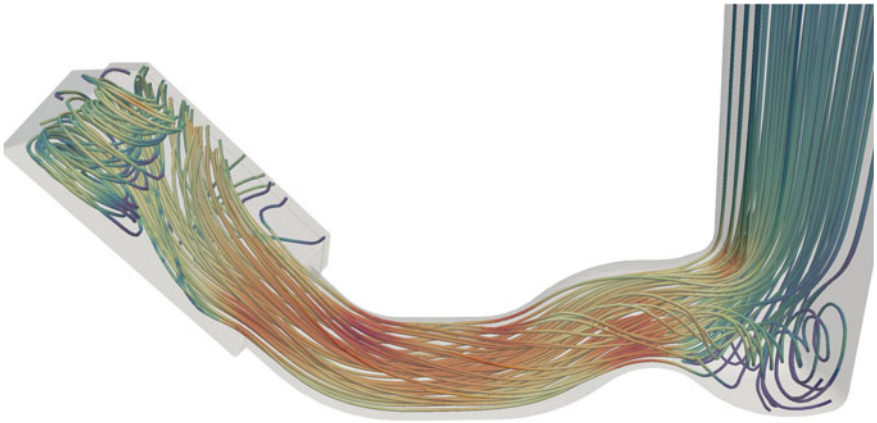

Fig. 4.14 Simulated static flow conditions in the lower area of the mold at the end of the casting process

Table 4.7 Chemical composition of the casted steels

Alloy	C	Si	Cr	Mn	Ni	Mo	Fe
	(mass%)						
X3CrMnNi 16-7-3	0.04	1.08	16.91	6.4	2.93	0.02	Bal.
Mn-Hard	1.47	0.643	0.34	13.58	0.11	0.004	Bal.

the pressurized casting system leads to high flow velocity in the gate, so that as few ceramic particles as possible accumulate on the molding material wall. Due to the 45° inclination of the test specimen, the ceramics were rinsed specifically against the filter. After cooling down and solidification, the casting was machined by removing the gating and the feeder system with the flow zone, so that the resulting wear sample can be used directly at the block/ring-testing station.

A TRIP steel X3CrMnNi 16-7-3 and a Hadfield steel (called Mn-Hard) were selected for the tests. The compositions are shown in Table 4.7. Melting took place in a 50 kg induction furnace. After deoxidizing with 0.05 mass% aluminum, the melt was poured into the mold at a pouring temperature of 1600 °C. Before casting, the zircon corundum particles were heated up to 1400 °C in a laboratory furnace. Above 1400 °C, a sintering process begins so that the particles cannot be preheated at higher temperatures. An infiltration of not preheated ceramics could not be carried out successfully, because a solidified steel shell immediately formed around the ceramics, which prevented the ceramics from flowing away as well as an infiltration of the particles. The composition of the particles (Imerys Fused Minerals, Germany) with a size between 1230 and 1765 µm is shown in Table 4.8.

Table 4.8 Composition of the infiltrated zircon corundum particles

Al_2O_3	ZrO_2 + HfO_2	TiO_2	Fe_2O_3	Si-, Mg-, Ca-, Na-, K-Oxide
(mass%)				
55.0	41.0	3.0	0.1	0.9

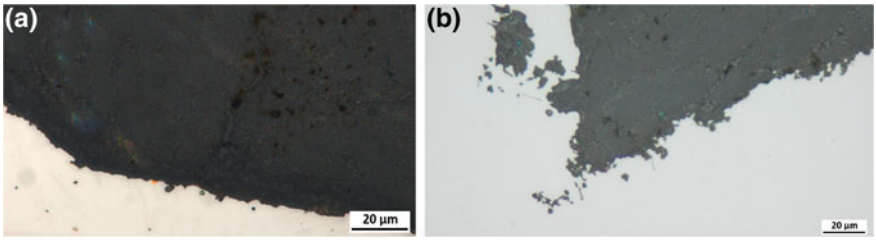

Fig. 4.15 Optical microscope images of infiltrated zirconia corundum with X3CrMnNi 16-7-3 (**a**) and Mn-Hard (**b**)

4.5.2.1 Microscopy

In order to assess the interface connection, microscopic examinations were carried out analogously to the previous chapters. On the one hand, images were taken with an optical microscope and on the other hand, pictures including line scan were performed with SEM. Figure 4.15 shows the bonds between the TiO_2 coated zirconia corundum and the two different types of steel. The ceramic has only a low porosity, which is important for good wear behavior. Both steels show a very good bond. By this kind of infiltration, whereby the ceramics are whirled by the melt, the liquid steel has sufficient time to heat the ceramics, so that a very good clinging takes place between steel and ceramics. The dynamical process is leading to an infiltration of small recesses in the ceramics. Due to the non-compact accumulations of the ceramics, local solidification between the ceramics and thus also the tensions in the boundary layer are reduced. It can be assumed that the steel can shrink onto the ceramic and thus the movement of the materials away from each other is prevented.

In order to analyze the composition of the boundary layer, examinations at a SEM with the aid of EDX are suitable. The line scan is useful to make statements about the change in concentration. The right area of Fig. 4.16 shows the steel, which is characterized by the high iron content. In the left area the ceramic is present, which consists of aluminum, zirconium and oxygen. The visible connecting layer has a thickness of approx. 7 µm. In comparison to the ceramics, the elements Mn, Ti and Zr are enriched in this area. The content of Al is below that in the ceramic. These facts coincide with the findings in Sect. 4.5.1.3. Complex manganese-rich mixing phases with a fluctuating Zr and Al content arise, which lead finally to a chemical bond between steel and ceramics.

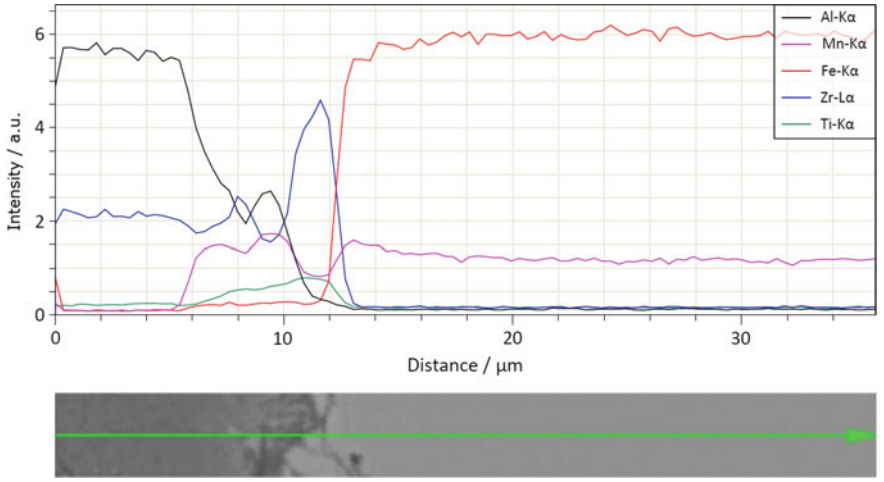

Fig. 4.16 EDX line scan of the boundary layer of TiO_2 coated zirconium corundum infiltrated by Mn-Hard steel

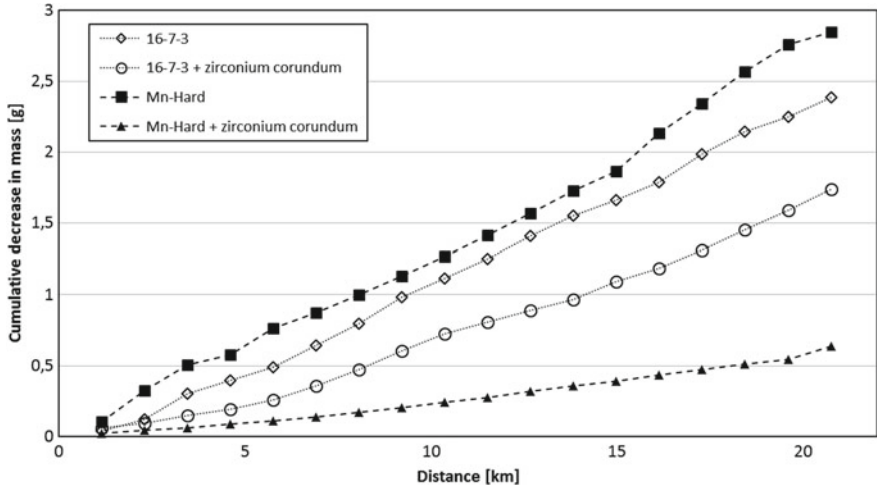

Fig. 4.17 Cumulative decrease in mass versus distance

4.5.2.2 Wear Behavior

The wear behavior of the samples was investigated at the block/ring-station. By optimizing the block/ring-testing station with a steadier supply of quartz sand, a more uniform wear behavior could be observed, which is reflected in straighter curves in Fig. 4.17. The investigations on the block/ring-testing station showed that the X3CrMnNi 16-7-3 steel behaves similarly in the point of abrasive wear behavior

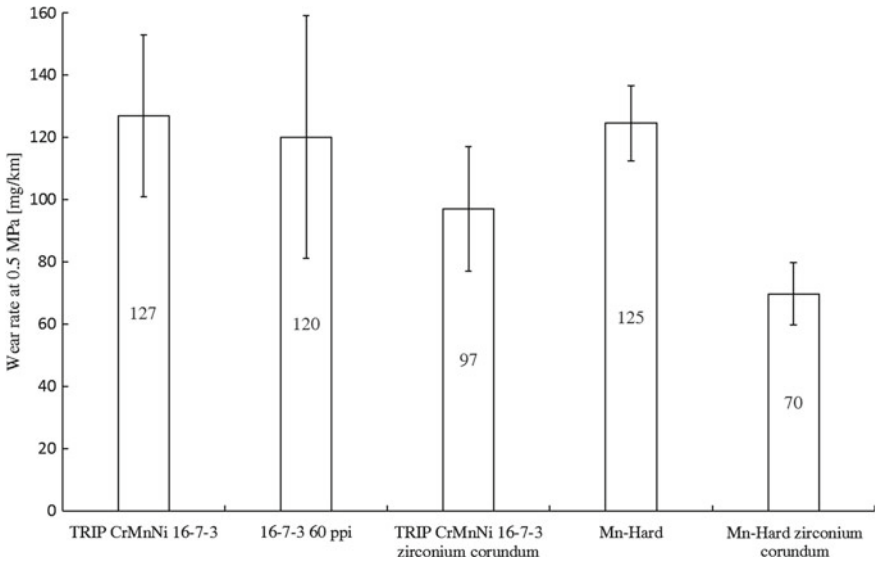

Fig. 4.18 Wear rate as a decrease in mass per distance

compared to the high manganese alloyed steel Mn-Hard. As can be seen in Fig. 4.18, the combination of Mn-Hard and zircon corundum shows the lowest abrasive wear. With a wear value of 70 mg/km, the MMC is significantly more wear resistant than the non-reinforced material. The low standard deviation of the wear value is reflected in the very good bonding and toughness of the zirconium corundum ceramic. These ceramics protrude from the metal matrix and do not break out in brittle layers. Investigations on a 3D microscope showed that the ceramics protrude up to 300 µm from the ablated metal matrix. The manufacturer's data show that the fine crystalline structure combined with the high proportion of tetragonal stabilized zirconium oxide produces a very pronounced self-sharpening effect during grinding. In addition to the self-sharpening effect of the ceramic, the good bonding between the steel and the ceramic has proven to be effective.

4.6 Conclusions

The manufacturing process of novel metal ceramic composite materials is described. First, basic investigations were carried out on the TRIP steel infiltration of ZrO_2 ceramic foams. Different mold materials were investigated and it turned out that Cerabeads have an insulating effect as mold material and that the chemical interactions were lowest. By adding 0.2% phosphorus, the infiltration quality of X3CrMnNi 16-7-6 melt can be significantly increased, while the melt temperature in this test arrangement has a lower effect. Furthermore, fine gussets in the ceramic foams can

be filled by the addition of sulfur. In order to characterize the wear behavior of the new composite materials, tests were carried out on the block/ring-testing station. The investigations revealed that MMCs with infiltrated ceramic foams show no advantage with regard to wear resistance. Rather, the MMCs with ceramic particles have the best wear properties. Particularly noteworthy is the composite of Mn-Hard steel with melt-broken zircon corundum. In addition to the positive effect on the boundary layer by coating the ceramics with TiO_2, the interlocking of the irregular particles leads to a reliable connection between ceramics and the steel. Based on these findings, a process was developed to produce a locally reinforced casting. The preheated ceramic particles were filled into the casting mold and then rinsed directly with the molten steel to the desired areas within the mold. The lower density of the ceramics is thus exploited in a targeted manner. This process significantly reduces the tendency to form cracks in the boundary layer between ceramic and steel. Since the ceramics are loose, the steel can shrink onto them. In the future, this process could be used to manufacture wear-resistant components, such as excavator teeth, etc. Figure 4.19 shows a section through the tip of a bucket tooth locally reinforced with ceramic particles, whereby the core of the tooth is free of ceramics and can therefore withstand the impacting stresses. The service life of such components can be extended because of the higher wear resistance, so that costs may be reduced.

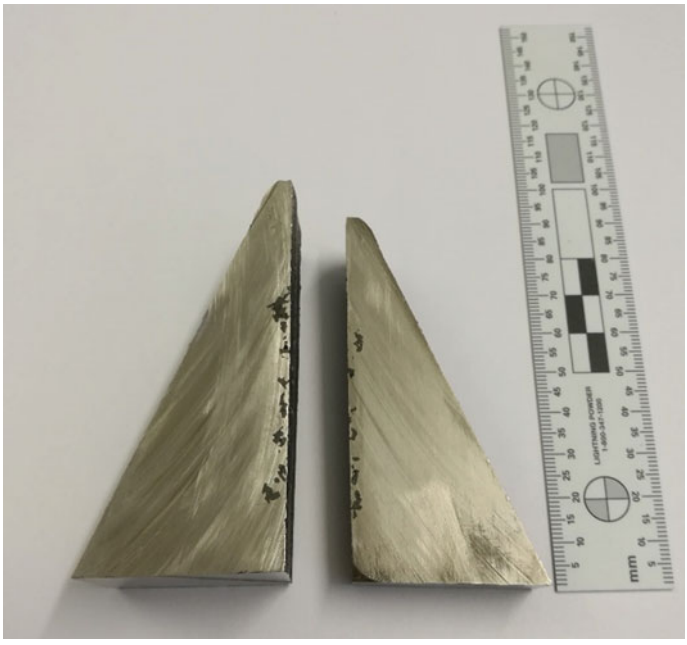

Fig. 4.19 Section through the tip of a bucket tooth locally reinforced with ceramics

Acknowledgements The authors gratefully acknowledge the financial support for this research by the Deutsche Forschungsgemeinschaft (DFG, German Research Foundation, Project number 54473466—CRC 799) and Prof. Dr.-Ing. Klaus Eigenfeld, Dr.-Ing. Marco Weider as well as Dr.-Ing. Richard Acker for the fundamental research in the field of steel casting infiltration by liquid melt in the subprojects A4, S1 and T4 of the collaborative research center (CRC799) "TRIP-Matrix-Composite".

References

1. A. Jahn, A. Kovalev, A. Weiβ, P.R. Scheller, S. Wolf, L. Krüger, S. Martin, U. Martin, Mechanical properties of high alloyed cast and rolled CrMnNi TRIP steels with varying Ni contents. ESOMAT **2009**, 05013 (2009). https://doi.org/10.1051/esomat/200905013
2. M. Weider, H. Polzin, K. Eigenfeld, W. Schärfl, Thermal interactions between casted high-alloyed TRIP steel and sodium silicate bonded moulding systems. Refract. World Forum **3**, 136 (2011)
3. M. Weider, Doctorate Thesis, TU Bergakademie Freiberg, 2015
4. W. Tilch, M. Martin, Properties and application of alternative moulding sands for the manufacture of light-weight-castings. Gießereiforschung **58**, 18 (2006)
5. F.D. Richardson, J.H.E. Jeffes, The thermodynamics of substances of interest in iron and steel making from 0 °C to 2400 °C: I-oxides. Iron Steel Inst. **160**, 160–261 (1948)
6. T. Dubberstein, H.-P. Heller, Effect of steel viscosity on metallurgical processing, in *6th International Congress on the Science and Technology of Steelmaking*, China Machine Press 2015
7. M. Weider, K. Eigenfeld, Steel Res. Int. **82**(9), 1064–1069 (2011). https://doi.org/10.1002/srin.201100071
8. R. Acker, S. Martin, K. Meltke, G. Wolf, Steel Res. Int. **87**(8), 1111–1117 (2016). https://doi.org/10.1002/srin.201500471
9. R. Acker, Doctorate Thesis, TU Bergakademie Freiberg, 2018
10. K. Lemster, T. Graule, J. Kuebler, Mater. Sci. Eng. A **1–2**, 385 (2005)
11. T. Dubberstein, H.-P. Heller, C. Wenzel, C.G. Aneziris, in *Proceedings of the 10th International Conference of Molten Slags, Fluxes and Salts* (Springer International Publishing, Basel, 2016), pp. 1371
12. A. Rosin, Doctorate Thesis, TU Bergakademie Freiberg, 2014
13. S. Seetharaman (ed.), *Fundamentals of Metallurgy* (Woodhead Publishing Limited, Cambridge, 2005)
14. V. Grethe, Doctorate Thesis, TU Clausthal, 1994
15. A. Kovalev, A. Jahn, A. Weiß, S. Wolf, P.R. Scheller, Steel Res. Int. **82**(9), 1101–1107 (2011). https://doi.org/10.1002/srin.201100065
16. W. Martienssen, H. Warlimont, *Handbook of condensed matter and materials data* (Springer, Heidelberg New York, 2005)
17. D. Wittig, A. Glauche, C.G. Aneziris, T. Minghetti, C. Schelle, T. Graule, J. Kuebler, Mater. Sci. Eng., A **488**, 580–585 (2008). https://doi.org/10.1016/j.msea.2007.11.065
18. L. Espié, B. Drevet, N. Eustathopoulous, Metall. Mater. Trans. A **25**, 599–605 (1994). https://doi.org/10.1007/BF02651601
19. C. Weigelt, C.G. Aneziris, D. Ehinger, R. Eckner, L. Krüger, C. Ullrich, D. Rafaja, J. Compos. Mater. **49**(28), 3567–3579 (2015)
20. J. Bossert, C. Ludwig, Materialwiss. Werkstofftech. **28**(5), 241–245 (1997)

Chapter 5
Ceramic Extrusion Technologies for Fine Grained TRIP Matrix Composite Materials

Christian Weigelt, Marie Oppelt and Christos G. Aneziris

Abstract Metal-Matrix-Composites (MMCs) based on steel with certain ceramic additions offer a wide range of applications in automotive, construction, and mechanical engineering. These MMCs combine the specific properties of steels such as their room temperature deformation behavior with the advantageous hard but brittle ceramic reinforcements which makes them favorable in crash-absorbing or strengthening components. However, common technologies such as casting or infiltration of ceramic preforms by metal melts suffer from the differences between metal and ceramic material characteristics involved during material processing and from geometrical restrictions. The adaption of the ceramics-derived extrusion technology at ambient temperature on materials established in the powder metallurgy (PM) enables an efficient manufacturing process of advanced fine-grained materials with particularly cellular (lightweight) structures as well as bulk specimens. Using powder raw materials enables a wide range of material combinations between TRIP/TWIP steels and various ceramic components considering the pronounced material characteristics of the composite. Knowing the influence of the raw materials, the processing parameters for shaping and the indispensable thermal processing transforming the formed powders into a solid material is crucial for proper manufacturing of MMCs with tailored characteristics. The joining process for these components extends the applicability of the investigated PM-MMCs.

5.1 Introduction

Composite materials based on metal and ceramic have been investigated for several years. The principle of combining different materials in order to achieve a new type of material that associates the specific properties of each component, proposes not only improvements of existing products, but also the creation of new materials

C. Weigelt (✉) · M. Oppelt · C. G. Aneziris
Institute of Ceramic, Glass and Construction Materials, Technische Universität Bergakademie Freiberg, Agricolastr. 17, 09599 Freiberg, Germany
e-mail: christian.weigelt@ikgb.tu-freiberg.de

H. Biermann and C. G. Aneziris (eds.), *Austenitic TRIP/TWIP Steels and Steel-Zirconia Composites*, Springer Series in Materials Science 298,
https://doi.org/10.1007/978-3-030-42603-3_5

and fields of application. Metal-matrix composites gained in popularity, since they provide a large variety of tailored characteristics, especially due their deformation behavior. Such materials enable various applications in the mobility or engineering sector due to their mechanical properties under static and dynamic loading at ambient temperatures. Further benefits as compared with conventional materials may be achieved by their thermal-, corrosion-, and wear-related properties. MMCs composed of a steel showing a transformation induced plasticity (TRIP) effect offer a matrix material with outstanding ductility, high strength, and reasonably high capacity for absorption of mechanical energy. These properties originate from the strain-induced martensitic phase transformation from austenite to α'-martensite under mechanical loading. Additionally, the phase transformation can be overlapped by a twinning induced plasticity (TWIP) effect, which further improves the deformability and strain hardening of such steels. The deformation mechanisms are governed by the austenite stability and by the stacking fault energy γ_{SF} (SFE) that depend on the chemical composition of the alloy and on the temperature applied during deformation [1–3]. The material concept covered by the CRC799 is focused on high-alloyed stainless CrMnNi-steels. The SFE determining the dominant deformation mechanism can be estimated by various empirical equations. The presence of austenite and martensite can be predicted from the chemical composition by using the proportions and individual weighting factors for each element of the alloy [4]. The nickel equivalent [Ni_{eq}, (5.1)] is calculated from the austenite promoting elements (e.g. Ni, C, Mn), while the chrome equivalent [Cr_{eq}, (5.2)] considers the ferrite stabilizing character of elements such as Cr, Ti, and Si. Apparently, the alloy composition is of great importance for the phase composition and their ability to undergo the desired deformation mechanisms.

$$\begin{aligned} Ni_{eq} = {} & \text{wt\%Ni} + 30 \times \text{wt\%C} + 18 \times \text{wt\%N} + 0.5 \times \text{wt\%Mn} \\ & + 0.3 \times \text{wt\%Co} + 0.2 \times \text{wt\%Cu} - 0.2 \times \text{wt\%Al} \end{aligned} \tag{5.1}$$

$$\begin{aligned} Cr_{eq} = {} & \text{wt\%Cr} + \text{wt\%Mo} + 4 \times \text{wt\%Ti} + 4 \times \text{wt\%Al} + 1.5 \times \text{wt\%Si} \\ & + 0.9 \times \text{wt\%Nb} + 0.5 \times \text{wt\%W} + 0.9 \times \text{wt\%Ta} + 1.5 \times \text{wt\%V} \end{aligned} \tag{5.2}$$

Zirconia (ZrO_2) ceramics offer enhanced mechanical properties at ambient temperature due to its polymorphism. The polymorphism is associated with the appearance of room temperature stable monoclinic (m-ZrO_2, space group $P2_1/c$) and high temperature stable tetragonal/cubic (t-ZrO_2, space group $P4_2/nmc$, and c-ZrO_2, space group Fm-3 m, respectively) crystal structures at ambient pressure. The martensitic phase transformation from the tetragonal to the highly distorted monoclinic modification during cooling below 1170 °C occurs simultaneously with a volume expansion of roughly 3% and which generates stress in the surrounding material resulting in cracking and failure of pure zirconia components. By the addition of stabilizing agents, such as MgO (forming magnesia partially stabilized zirconia—Mg-PSZ), the high temperature ZrO_2-modifications can be metastably retained at ambient temperature. These polymorphs are capable to undergo a delayed tetragonal to monoclinic phase

transformation, providing the well-known stress-assisted transformation-toughening mechanism and which results in the specific characteristics of commercial zirconia applications. The distinctive phase transformation triggered by external loading cannot only improve the mechanical properties of ceramics but also reinforce metal-matrix materials.

MMCs based on a TRIP/TWIP steel-matrix with certain ceramic additions have been in focus of several investigations. However, common technologies suffer from the different material characteristics involved during processing. Numerous MMCs have been investigated in the past using a variety of manufacturing processes such as stir casting [5], squeeze casting [6], spray forming [7], infiltration of ceramic preforms [8, 9] or powder manufacturing [10–14]. However, these conventional techniques cannot produce cellular structures with a wall thickness on the micron scale, since they are restricted to bulk structures or components. Therefore, powder metallurgy is of great interest in the development of new materials and their processing technologies. The adaption of the ceramics-derived extrusion (also referred to as plastic processing) technology at ambient temperatures on mixtures of steel and ceramic powder raw materials enables an efficient manufacturing of advanced fine-grained materials with particularly cellular (lightweight) structures as well as bulk fabrics. Thus, these materials are applicable in certain applications, such as crash-absorber, engineering or structural components, and damping elements. Figure 5.1 illustrates the latitude of the plastic enabling honeycomb structures with various cell geometries and cell densities (indicated as channels per square inch—cpsi) at cell widths of 250–450 μm and relative densities of 0.3–0.4.

The extrusion process is widely known in the production of ceramic materials covering, among others: tiles, rods, and thermocouple protection tubes. This process was initially applied to natural plastic raw materials (clay) and later adapted to non-plastic raw materials. In the latter case, solid powders are transferred into a room-temperature plastic paste by admixing organic additives and solvents (usually

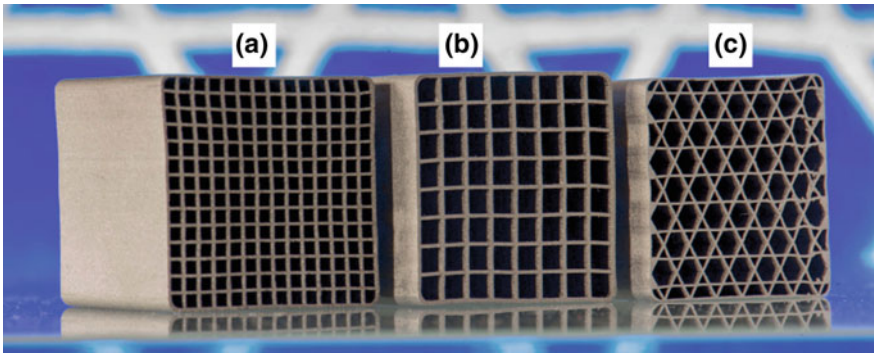

Fig. 5.1 Variants of cellular structures manufactured with the ceramics-derived extrusion process at room temperature: honeycombs with 196 cpsi (**a**), 64 cpsi (**b**) and with the 172 cpsi Kagome lattice structure (**c**), all variants with outer dimension 25 × 25 mm^2

water). Then, the paste can be easily shaped by forcing it through a rigid die with the geometry of the component to be produced. The thermal treatment comprising drying, removal of organic additives (debinding) at moderate temperatures and the sintering transfers the materials into their final state (see Fig. 5.2). Previous investigations on alumina [15] materials successfully demonstrated the efficient processing of honeycomb structures, and therefore, the processing has been selected as the most suitable method for forming metal-ceramic composite structures in the frame of the present study. Beyond, the ceramics-derived processing involves the cost- and material-efficient near-net shaping at ambient temperatures and the processing of any steel/ceramic ratio. However, the pressureless sintering implies higher remaining porosities and pronounced interactions between the metal and ceramic components as compared to MMCs prepared by pressure-assisted consolidation methods such as hot-pressing (HP) [11] or spark plasma sintering (SPS) [10].

Composite materials based on austenitic stainless steel with particulate reinforcement prepared via cold extrusion are in focus of the present work. The correlation of the initial materials, the processing and the resulting properties of the materials are presented. A very important part of this work deals with chemical and microstructural interactions between the components steel and the reinforcing ceramic particles during sintering. Hereto, no studies on magnesia partially stabilized zirconia in conjunction with high manganese steels have been reported.

The addition of ceramic particles to a ductile matrix increases the strength, but lowers the material's deformability by inducing typical damage events like debonding, particle fracture or crack coalescence even at moderate fractions of ceramic particles. Thus, improving the interface bonding between the metal matrix and the zirconia particles is of major importance. Wittig et al. [8] reported the pressureless infiltration of zirconia preforms with a CastX38CrMoV5-1 (AISI H11) steel by adding 20 wt% elemental titanium. Previous investigations revealed similar results with alumina preforms [16]. The high diffusibility of Ti, the formation of TiO_x interlayers, and the improved wetting behavior promote sufficient infiltration and the formation of reliable interface boundaries. Titanium is also used as an active component in the brazing of zirconia/zirconia or zirconia/alloy joints [17, 18]. Beyond

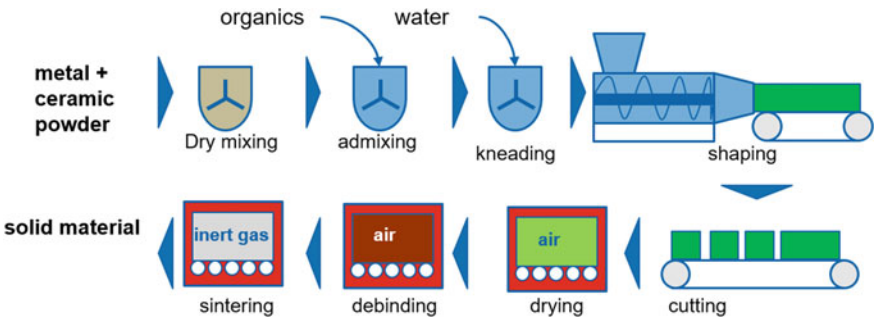

Fig. 5.2 Scheme of the plastic processing route

this, titanium is known for its partial stabilization efficiency in zirconia ceramics by sintering in inert gas atmosphere [19, 20]. Variants of steel and magnesia partially stabilized zirconia were admixed with minor fractions of titanium in order to improve the interface formation during sintering in the frame of this work. The influence of the active interface agent on the mechanical properties has been tested by quasistatic compression tests. The microstructure and the phase compositions were investigated in order to correlate the mechanical response with the desired phase transformations of TRIP steel and zirconia.

Nevertheless the aspiration of improving the mechanical behavior, especially the increase of the specific energy absorption (SEA) capacity, leads to intensive investigations of the raw materials, the selection of materials, the adaption of process parameters and finally to the knowledge of the processing-characteristic-knowledge of a branch of composite materials. Not only the well-known zirconia reinforcing particles but also the introduction of alternative ceramics led to significant improvements of the material properties. In general, the steel/zirconia interface shows destabilization due to the diffusion of Mg out of the particles and the formation of precipitations at the metal/ceramic interface as a result of indispensable thermal treatment at temperatures inappropriate for zirconia sintering. These ZrO_2 particles with high amounts of non-transformable monoclinic zirconia are loosely embedded in the metal matrix. Thus, the ability of the reinforcing phase transformation is restricted to the low remaining amount of tetragonal/cubic zirconia. The alloying elements of TRIP/TWIP steels are also prone to diffusional interchange which boosts the interface formation but also the shift of the steel composition. But the interfacial reactions can also improve the material characteristics when exploiting alternative reinforcing ceramics. By replacing zirconia with aluminium titanate (Al_2TiO_5) a new family of MMCs with advanced mechanical properties under compressive and under tensile deformation is generated.

Furthermore an important issue in this work was the joining of MMCs using a ceramic-derived technology. Bulk specimens from the pure CrMnNi steel, and MMC variants reinforced with 5 or 10 vol% magnesia partially stabilized zirconia were used as joint partners. The samples were prepared via the ceramics-derived extrusion technology and different material combinations were joined in their dry green state using an aqueous paste to form the bonding. The mechanical testing comprised quasistatic tensile deformation tests of the base materials and of the sinter-joint variants at room temperature. The microstructural analyses revealed considerable differences between the ceramic joining process and the conventional welding of steel materials which is beneficial in future practical applications [21, 22].

5.2 Experimental Details

5.2.1 *Plastic Processing of Steel/Zirconia Composite Materials*

Numerous experiments have been performed in order to evaluate proper material compositions, processing parameter and thermal treatment conditions. The initial plastic pastes based on the extrusion of alumina honeycombs [15] as listed in Table 5.1 are prepared with a standardized grade steel powder of type AISI 304 (German grade 1.4301) [23–25]. Various powder types were used in the frame of the present study due to the intense research on the alloying concept and the related mechanical characteristics (cf. Table 5.1). The steel variants and their chemical compositions are summarized in Table 5.2. All steel powder variants (TLS, Germany) were manufactured via the gas atomization process which resulted in the formation of mainly spherical shape particles with some satellite particles and a few imperfections (see exemplary Fig. 5.3). Three variants of magnesia partially stabilized zirconia were used in the frame of the present study. Their compositions are given in Table 5.3.

Table 5.1 Composition of the initial mixtures, in wt% [23]

Material	Raw materials		Recipes		
	Type	Supplier	0Z	5Z	10Z
Austenitic steel	AISI 304 d_{50} = 45 µm	TLS, Germany	95.50	91.84	88.17
ZrO_2 with 3.5 wt% MgO	PMG3.5 d_{50} = 2 µm	Unitech, UK	–	3.66	7.32
Plasticizer flour	HW FGB	Kampffmeyer, Germany	2.60	2.60	2.58
Tenside	Denk mit	Henkel, Germany	0.40	0.40	0.43
Dispersant	Castament FS 60	Degussa, Germany	0.15	0.15	0.15
Plasticizer methyl cellulose	HPMC 874	Aqualon, Germany	1.35	1.35	1.35
Water	Deionized	–	4.5	4.8	5.0

Table 5.2 Chemical composition of steel powder variants, in wt%

Type	Fe + Others	Cr	Mn	Ni	C	Si
PMX2CrMnNi18-1-8A	Bal.	18.1	1.4	8.3	0.02	0.4
PMX2CrMnNi18-1-8B	Bal.	18.3	1.4	8.1	0.02	0.3
PMX1CrMnNi18-1-9	Bal.	18.4	1.1	9.3	0.01	0.7
PMX5CrMnNi18-1-8	Bal.	17.5	1.3	8.4	0.05	0.4
PMX5CrMnNi17-7-3	Bal.	16.7	7.1	3.4	0.05	0.9

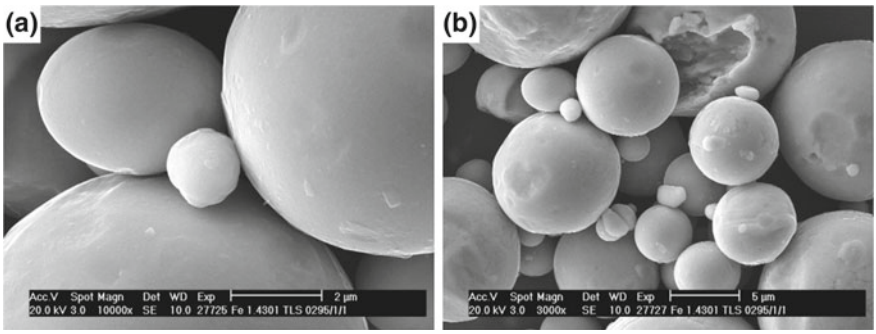

Fig. 5.3 SEM image of the as-delivered spherical steel powder at different magnification (PMX2CrMnNi18-1-8B)

Table 5.3 Composition of the zirconia powder variants, in wt%

Type	Supplier	ZrO_2 + Others	MgO	SiO_2	Al_2O_3	TiO_2	HfO_2
PSZ1	Unitech, UK	Bal.	3.4	n.m.	0.7	0.2	0.8
PSZ2	Saint-Gobain, USA	Bal.	2.8	0.4	0.4	0.1	1.7
PSZ3	Saint-Gobain, USA	Bal.	3.4	2.4	0.6	0.1	1.7

Recipe 0Z consists of 100 vol% TRIP steel and recipes 5Z and 10Z are based on 95 or 90 vol% TRIP steel with 5 or 10 vol% zirconia, respectively. In a further step, the plasticizers and water have been added to the batch during mixing. Because of a piston extruder (ECT, Germany), honeycombs 25.5 mm × 25.5 mm with 164 channels (200 cpsi) and a wall thickness of 250 µm have been extruded. The applied pressure was between 10 and 11 MPa. After extrusion, cube-shaped samples (25.5 mm × 25.5 mm × 25.5 mm) have been cut before stepwise water-removal in an air-circulated dryer. After drying, the debinding process has been carried out at 350 °C for 90 min in air in the same aggregate. The binder-free samples have been placed in an alumina crucible and protected against O_2 contamination by a Ti casketing. The samples have then been sintered at 1350 °C for 2 h in an electrical furnace with high purity flushing Argon atmosphere.

Microstructure characterization was performed using scanning electron microscopy (SEM), energy dispersive X-ray analysis (EDS) and electron backscatter diffraction (EBSD). In addition, phase labeling was performed on sintered surfaces by X-ray diffraction (XRD) with Cu–Kα radiation. The relative phase content of zirconia was determined by the method described by Evans et al. [26]. The open porosity, the average pore radius and the pore size distribution of the sintered samples were measured by mercury porosimetry. The macroscopic structure of the honeycomb samples after deformation was examined by optical microscopy of metallographic sections. The mechanical in-plane testing of the sintered specimens was carried out under compressive loading in a 500 kN servohydraulic universal testing machine type MTS 880 with a displacement rate of 0.016 mm/s at ambient temperature.

Table 5.4 Composition of mixtures for Ti-activated interface formation, in vol% [27]

Recipe	0Z	10Z	10Z-1T	10Z-2T	10Z-3T
Stainless steel	100	90	89	88	87
Zirconia	0	10	10	10	10
Titanium	0	0	1	2	3

A gas-atomized high-purity >99.7% Titanium powder (TLS, Germany) with a mean diameter of 13 μm and a spherical particle shape was used in some tests as interface activation agent. The basic composition for MMC production was a mixture of 90 vol% steel (PMX5CrMnNi18-1-8) and 10 vol% zirconia (see Table 5.4). In MMC compositions with minor titanium fractions (1, 2, or 3 vol%) of the matrix material were replaced by Ti powder. Additionally, the pure steel specimens provide a reference material without any additions. Taking the interest of interface reactions and the mechanical properties into consideration, a bulk sample geometry was used, but prepared from a modified processing route.

5.2.2 Composite Variants with Additions of Zirconia and/or Aluminium Titanate

Further work was conducted on the development of alternative reinforcing mechanisms since the zirconia particles are prone to undergo the tetragonal to monoclinic phase transformation during thermal processing of the composite materials. Alumina and yttria are well established as reinforcing additions for steel-matrix composites [28, 29]. However, the alumina particles show no phase transformation and insignificantly interface formation. A new approach is the introduction of aluminium titanate as a reinforcing material which is a promising refractory material due to its excellent thermal properties but not prestigious for its mechanical properties.

Bulk specimens were prepared by the well-established ceramic-extrusion technology with an austenitic stainless steel of type PMX5CrMnNi17-7-3 (see Table 5.2) with a median diameter of 18.1 μm. The reference materials with the standard zirconia reinforcing powder were prepared from the commercially available Mg-PSZ of type PSZ2 (cf. Table 5.3). Aluminium titanate was synthesized from a stoichiometric mixture of high-purity 99.8 wt% alumina Martoxid MR70 (Martinswerk, Germany) and 98 wt% titania Hombikat N100 (Sachtleben, Germany) since proper batches are not commercially available. The addition of 6 mol% of a of high-purity grade (98%) MgO powder (neoLab, Germany) improved the thermal stability and protected the aluminium titanate from decomposition on cooling after reactive sintering. The mixture was pre-fired at 1400 °C in an oxidizing atmosphere in order to ensure high Al_2TiO_5 formation, and crushed after cooling to obtain powder fineness similar with the zirconia powder. The Al_2TiO_5 mean particle diameter was 4.2 μm and consisted of 95% aluminium titanate with minor residues of unreacted alumina and titania

Table 5.5 Composition of mixtures, in vol%

Recipe	0Z	5Z	10Z	5AT	10AT	2.5ZAT	5ZAT
Steel	100	95	90	95	90	95	90
Zirconia	0	5	10	0	0	2.5	5
Tialite	0	0	0	5	10	2.5	5

according to X-ray analysis. The basic composition 0Z refers to the pure steel material without any ceramic additions. The composite variants were prepared with solely zirconia (Z) or aluminium titanate (AT) or with balanced fractions of both (ZAT) at a total fraction of 5 or 10 vol% (see Table 5.5).

The plastic processing was similar to previous materials with certain modifications of the binder system and the water fraction necessary for shaping. The specimens were heated up to 450 °C in an oxidizing atmosphere, applying a heating gradient of 1 K/min and a dwell time of 30 min at maximum temperature to eliminate organics from the extrusion process. After cooling to room temperature (at a rate of 1 K/min), the specimens were reloaded into a second furnace with a graphite lining and graphite heating elements (Xerion, Germany). The sintering step was conducted in a flushing argon atmosphere using a heating rate of 5 K/min and a maximum temperature of 1350 °C and a dwell time of 2 h at the maximum temperature before cooling with a maximum cooling gradient of 5 K/min.

The fired specimens were processed to a cylindrical geometry (6 mm in diameter and height) for compressive loading tests, as well as to round tensile specimens with a gauge diameter of 5 mm and a gauge length of 30 mm according to DIN EN ISO 6892-1 for tensile loading tests. The tensile test series were performed with a 100 kN universal testing machine of type Zwick 1476. Compression tests utilised a 200 kN servo-hydraulic testing machine of type MTS 810. All tests were carried out at a quasistatic nominal strain rate of 0.001 s^{-1} at room temperature.

5.2.3 Innovative Joining of Powder Metallurgically Processed TRIP/TWIP Steel Materials

The manufacturing of a composite structure by extrusion is limited to a uniform cross section throughout its entire length, which limits later use. Thus, the availability of a reliable (mechanical) joining technique is a major task in the development of MMCs for commercial applications. Fundamental research was performed on the adaption of a ceramics-derived joining process by adding a slurry on the joining partners at room temperature with the subsequent thermal processing.

Pure steel specimens, the composite variants, and the joining paste were composed of the steel powder batch PMX5CrMnNi17-7-3 (see Table 5.2). The ceramic component was the commercially available magnesia partially stabilized zirconia of type PSZ2 (cf. Table 5.3) [22, 30]. The basic composition (0Z) corresponds to 100%

steel without any ceramic additions. Composite mixtures were prepared with fractions of 5 vol% (5Z) or 10 vol% (10Z) zirconia in their total solids composition. The powders were mixed for 90 min in their dry state before adding the organic binder system and water. Rods of 11 mm in diameter were extruded using a single-screw extruder of type LK III 2A (Linden, Germany) at ambient temperature. The water was removed stepwise in an air circulated dryer applying a maximum temperature of 110 °C. Dried samples of each composition were cut to a length of 50 mm and the surfaces to be joined were then polished with a rotary grinding machine to obtain a smooth surface.

The aqueous joining paste was prepared from pure metal powder and water with a ratio of 9:1 by weight. In addition, an organic binder system composed of 1.0 wt% KM2000 (Zschimmer & Schwarz, Germany), 0.6 wt% KM1001 (Zschimmer & Schwarz, Germany) and 2 wt% Optapix G1457 (Zschimmer & Schwarz, Germany) was necessary in order to ensure a sticky paste with well dispersed steel particles.

The joining paste was brushed on the polished end faces of the partners to be joined immediately before these specimens were manually assembled which led to some leaking of the paste and, thus, complete filling of the gap between both parts. The joined specimens were placed on the firing auxiliaries and handled without any rigid clamping during further processing. Then the samples were again dried stepwise in an air circulated dryer starting at 40 °C and increasing to a maximum temperature of 110 °C. Debinding and sintering was performed as shown before. The fired specimens were machined to round tensile loading test geometry with a gauge diameter of 4 mm and a gauge length of 25 mm according to DIN EN ISO 6892-1. The test series with 5–9 samples of each variant were performed at room temperature with a 50 kN universal tensile testing machine of type Tiratest 2850 (Germany) at a quasistatic nominal strain rate of 0.001 s^{-1}. Microstructural characterization was conducted using light optical microscopy and scanning electron microscopy (SEM, Philips XL30). Energy dispersive X-ray analysis (EDS, EDAX Inc., USA) complemented the microstructural study.

Hardness profiles were recorded using a LECO M400 micro hardness tester. Measurement of the profiles was carried out after Vickers procedure with HV0.3 (2.94 N, 10 s load duration) in a triple row with a total length of 6 mm and 100 μm increment. Furthermore, macro hardness was likewise measured on a conventional hardness testing device after Vickers with HV10 (98.04 N, 10 s load duration).

5.3 Results and Discussion

5.3.1 Characteristics of Materials Prepared via Plastic Processing

The many opportunities of geometries processed via the ceramics-derived extrusion technology are illustrated in Fig. 5.4. Lightweight honeycomb structures as well as

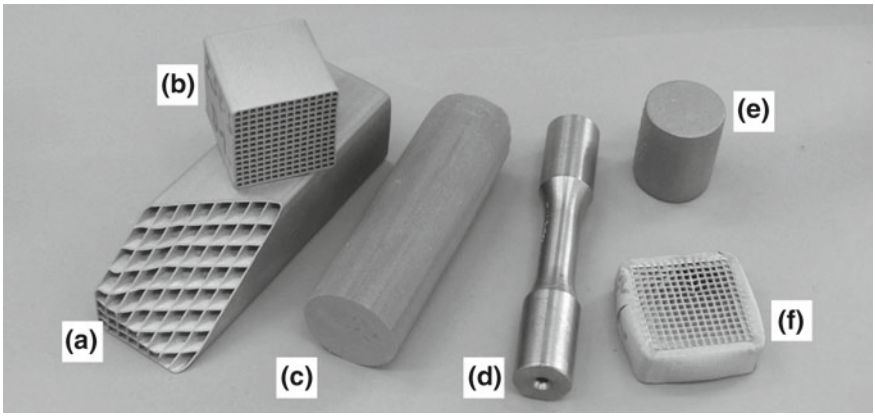

Fig. 5.4 Variations of sample geometries produced by the powder metallurgical route via extrusion: honeycomb structures with 64 cpsi (**a**) and 200 cpsi (**b**), green body rod (**c**) for fatigue specimens (**d**) and compressive test (**e**), 200 cpsi honeycomb at 50% compressive strain (**f**) [24]

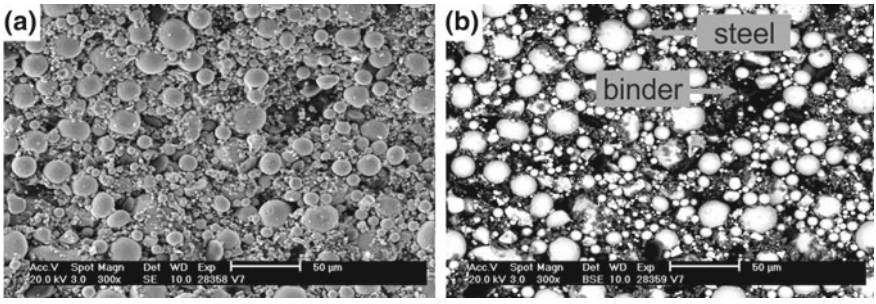

Fig. 5.5 SEM-image of a honeycomb structure (exemplary material variant without any ceramic additions) after drying with steel particles (bright) and polymer binder (dark) in secondary electron mode (**a**) and backscatter electron mode (**b**) [24]

bulk specimens can be processed with almost similar plastics pastes enabling a large variety of sample geometries. Thus, the mechanical testing, e.g. under compressive or under tensile loading tests, fatigue tests and ductility tests can be performed with respect to mutual applications.

Figure 5.5 illustrates the microstructure of the 100% steel sample without any ceramic additions after the extrusion process and their dry state. The spherical steel particles are surrounded uniformly by the organic additives. A certain porosity is derived from the particle size distribution of the metal powder and the removed water portion necessary for sound extrusion. The microstructure undergoes fundamental changes during thermal processing. The organic components, as being removed during debindering, cause not only porosity but also impurities (ash) and carbon residue from inappropriate settings. The pressureless sintering at temperatures slightly below the melting temperature of the metal initiates the final consolidation.

The carbon content is crucial for the mechanical characteristics of TRIP/TWIP steel-matrix materials since carbon crucially affects the deformation mechanism of the steel matrix. Furthermore, the presence of enhanced carbon fractions promotes the formation of carbides during sintering which are likely to decrease the strength and ductility of the material. Thus, the complete removal of the organic processing aids during thermal treatment is essential for the mechanical properties of powder metallurgically processed materials. The carbon fraction decreases by increasing the maximum temperature during debindering. However, the thermal binder removal at higher temperatures is limited due to the oxidation of the steel particles. These oxides are thermodynamically stable during sintering causing undesired inclusions even in the material without any further addition of ceramic particles. The binder removal for honeycomb structures is possible with heating rates up to 2 K/min. Faster heating results in cracks and incomplete binder removal in the center of test specimens. Figure 5.6 presents the microstructure of a typical sample fracture surface of the composite variant 5Z after sintering at 1350 °C. Here, a continuous steel matrix with well dispersed zirconia particles can be seen. The fine grained ceramic particles usually appear as agglomerates in the interstices of the coarser grained metal. According to EDS-analysis three different regions can be identified. First, the composition of the steel matrix which largely correlates with the chemical composition of the as-delivered material, and second, the ceramic regions with dominating zirconia content can be observed. Further on, particles that were not present in the starting materials and that were most likely formed during sintering are randomly spread throughout the whole material. They are characteristically composed of varying compositions of chromium, manganese, magnesium, aluminium and silicon and they are detectable among all materials processed via the plastic processing. They are particularly not exclusively present in the composite variants but also in pure steel samples.

Another aspect of the pressureless sintering is the thermally induced tetragonal to monoclinic phase transformation of the zirconia particles. Figure 5.7 presents the EBSD-phase analysis of zirconia agglomerates (dispersed in PMX1CrMnNi18-1-9) in the material variant 5Z after sintering, and after 20% compressive deformation [3].

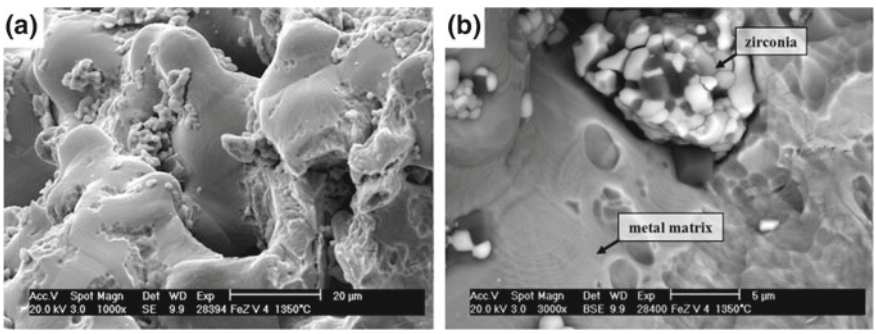

Fig. 5.6 SEM image of a typical fracture surface region of the composite material 5Z in the as-fired state at different magnifications [3]

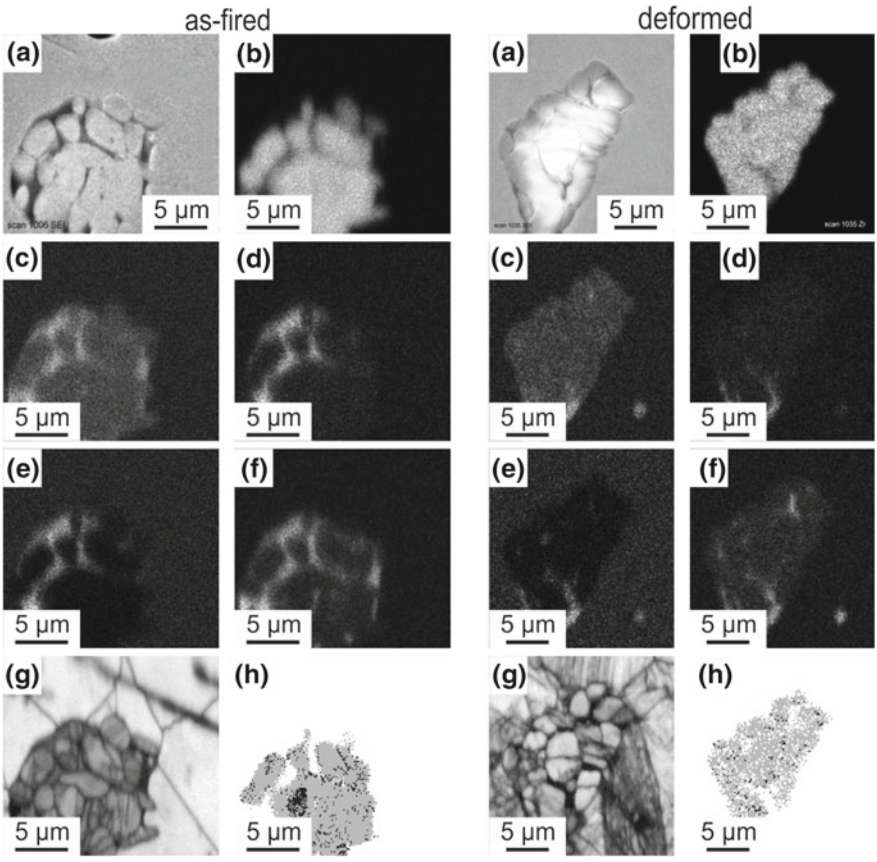

Fig. 5.7 Cross-section of zirconia agglomerates in the as sintered state A) and after 20% compressive strain B) with the composition 5Z: **a** SEI, **b** EDS Zr map, **c** EDS O map, **d** EDS Mg map, **e** EDS Mn map, **f** EDS Si map, **g** EBSD quality map, **h** EBSD phase map showing t/c-ZrO_2 (black), and m-ZrO_2 (gray) [3]

Both spots show zirconia agglomerates embedded in the steel matrix. The EDS maps clarify the edge between metal and ceramic phase enabling separated phase analysis. The EBSD image quality for zirconia particles is lower in comparison to steel in case of the as-fired specimen. After plastic deformation, both components appear with nearly the same validity due to distorting the crystal lattices during deformation. The dominating amount of non-metastable monoclinic phase after sintering is obvious. Nevertheless, the m-ZrO_2 quantity is increased after compressive deformation.

The interactions between the steel matrix and the zirconia particles were investigated in detail from model mixtures of the zirconia variants PSZ2 and PSZ3 with solely additions of the main alloying elements (Cr, Ni, Mn and Fe) [21]. The addition of Cr leads to several chemical reactions associated with a change of phase composition in zirconia matrix. Up to 18% of the steel mass are delivered as chromium, which

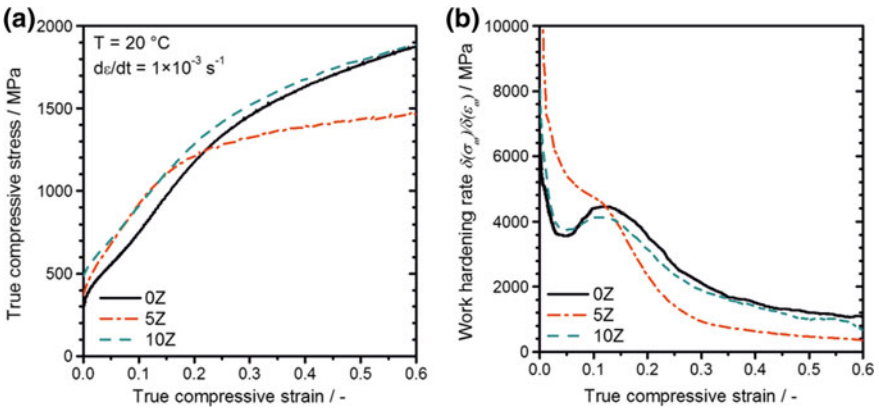

Fig. 5.8 Mechanical behavior of the compressed specimens indicating the reinforcing effect of Mg-PSZ on the compressive yield strength and on the work hardening: **a** flow stress curves, **b** work hardening rates [31]

reflects the importance of PSZ-Cr interactions in the present composite materials. Sintering magnesia partially stabilized zirconia at 1300–1400 °C causes pronounced changes in the phase composition with a minor fraction of tetragonal and/or cubic ZrO_2 after firing. Additions of Mn and Fe already start reacting with zirconia matrix when sintering at 1300 °C leading to either destabilization (Fe) or stabilization (Mn). Further heating to 1400 °C indicates the reaction of chromium with stabilizer magnesia to form magnesia chromite. Variations of the dwell time at maximum temperature have negligible effects on ZrO_2 phase composition. In contrast Ni has no significant influence on the sintering progress and phase composition of the fired zirconia.

Figure 5.8 depicts the stress-strain behavior of the materials under quasistatic compressive deformation. The composite materials showed higher stresses over a wide range of strain than the unreinforced material 0Z. The yield strength at 0.2% plastic compressive strain was ≈70 MPa higher for both MMC variants as compared with the pure steel specimens. The composites 10Z revealed a pronounced strengthening effect under quasistatic compressive loading up to a deformation degree of approximately 45%. In contrast, the strengthening effect of material 5Z was exhausted when exceeding 18% compressive strain. Comparing these results with values from SPS material prepared from similar materials indicates the dominating effect of the consolidation process [28]. The lower strengthening effect of the present specimens is due to higher porosity in the matrices, the larger austenite grain size, and the distinctive reactions at the steel/zirconia interfaces. Because of damage initiation and propagation, the compression stress of composite materials dropped below the values measured for the pure steel specimen at higher strain levels. The characteristics of the matrix material mainly controlled the stress-strain level and the deformation behavior of all specimens tested. The matrix strain hardening was driven by the dislocation movement, by the accumulation of dislocations and by the strain-induced α'-martensite formation (TRIP effect) [28]. The work hardening rates, as shown in

Fig. 5.8, illustrate the strengthening effect of the ceramic particles in a certain range of strain followed by a decreasing work hardening rate at further deformation [31].

A similar material behavior was observed under quasistatic tensile loading (see Fig. 5.9). As expected, the pure steel specimens exhibited the highest tensile strength and fracture strain among all materials tested. The composite materials suffer from poor interfacial connections between the metal matrix and zirconia reinforcing particles. Therefore, the presence of ceramic dispersed within the ductile steel matrix lowers the material's deformability, inducing typical damage events like debonding, particle fracture or crack coalescence, which initiates MMC's failure at lower strain [10, 32, 33]. This effect is more pronounced under tension than under compression. The influence of the ceramic fractions on the MMCs' tensile yield strengths is negligibly small. Nevertheless, the composite variant 5Z shows a higher stress level than the pure steel at the expense of their ductility. As similar to compressive deformation the material 5Z fails at lower strain than specimens with 10 vol% zirconia which is most likely caused by larger pores and voids in the matrix material. The in situ tests revealed the kinetics of strain-induced α'-martensite during deformation. The 0Z specimens exhibited the highest overall percentage of strain-induced α'-martensite. The lower formation of strain-induced α'-martensite in the composite variants was in accordance with the less pronounced sigmoidal shape of their strain hardening response.

The strength of the steel/zirconia-interface is of great importance for the global mechanical behavior of the composite material. Adding small fractions of Ti is one opportunity for the initiation of reliably bonded ZrO_2 particles within the steel matrix. The particle size distribution of the initial solid powder mixtures demanded a large number of organic agents to allow adequate paste processing [24, 34]. Nevertheless, the debinding settings provide samples with carbon contents of (0.05 ± 0.01)% and which corresponded to the concentration of the as-delivered steel powder (cf. Table 5.2). Hence, the formation of carbides during high-temperature processing was

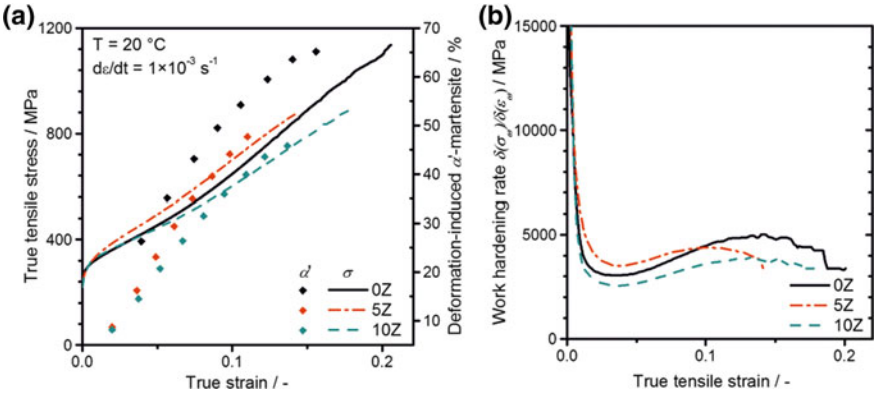

Fig. 5.9 Tensile properties of the TRIP steel and the composite variants showing the strengthening and embrittling effect of certain ceramic fractions: **a** flow stress curves, **b** work hardening rates [31]

unlikely to occur. The sintered specimens appeared with a glossy metallic surface indicating the absence of considerable metal oxidation during thermal processing. Shrinkage, bulk density and porosity of all material variants considered in the frame of interface modification experiments are summarized in Table 5.6. Only small differences between the pure steel and MMC material can be recognized. The shrinkage of specimens with additions of titanium is lower than in recipes 0Z/10Z but rises as a function of the Ti fraction. The calculated porosities declined from 10.7 to 4.6% by rising the titanium fraction from 1 to 3 vol% [27].

Figure 5.10 shows representative flow curves of the quasistatic compressive loading tests at room temperature. The presence of 10 vol% magnesia partially stabilized zirconia particles lead to a significant increase of the compressive stress level in a wide range of deformation. At 0.2% plastic strain the pure TRIP steel specimens show an engineering stress of 206 ± 8 MPa and a sigmoidal stress-strain curve on further deformation that could be related to the martensitic phase transformation. In comparison, the 10Z composite material is characterized by a similar behavior with higher yield strength of 249 ± 4 MPa and advanced mechanical response at moderate strain (up to 100 MPa higher stress level than 0Z). However, the strengthening effect of material 10Z was exhausted when exceeding $\varepsilon_{\text{true}} = 0.5$ and the stress level of the composite material dropped below the specimens without any ceramic additions (0Z). The essential material characteristics of 0Z and 10Z specimens were similar to

Table 5.6 Properties of the as-fired specimens [27]

Recipe	SS	10Z	10Z-1T	10Z-2T	10Z-3T
Shrinkage (%)	11.2 ± 0.5	11.4 ± 0.2	10.3 ± 0.3	10.6 ± 0.3	10.8 ± 0.4
Bulk density (g/cm^3)	7.01 ± 0.02	6.79 ± 0.03	6.77 ± 0.04	7.06 ± 0.04	7.16 ± 0.01

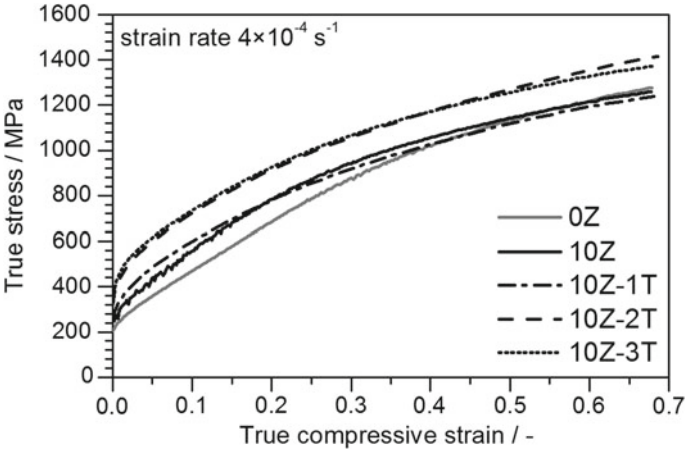

Fig. 5.10 Compression stress versus strain of the steel and the composite variants illustrating the effect of titanium [27]

composite materials reported by Martin et al. [28]. The higher level of mechanical response could be assumed to origin from less than 2% porosity as the samples were prepared by spark plasma sintering. The influence of titanium on the mechanical properties differs in a wide range. In general the presence of Ti results in an increase of the yield strength: 260 ± 21 MPa (1 vol% Ti), 327 ± 3 MPa (2 vol% Ti) and 345 ± 4 MPa (3 vol% Ti). Specimens with 1% Ti exhibited higher true stresses in a certain range of strain in comparison to pure TRIP steel specimens and 10Z composite material. However, the points of intersection can be observed at a true strain of approx. 0.2 and 0.4, respectively. The mechanical properties of composite materials with 2 and 3 vol% titanium are almost equal.

5.3.2 *Effect of Zirconia and Aluminium Titanate on the Mechanical Properties of Composite Materials*

As already mentioned, the conventional pressureless sintering process facilitates chemical reactions, segregations, and the formation of δ-ferrite in the unreinforced TRIP steel specimens and in the composite variants during firing [35] (Table 5.7). Thus, the ferromagnetic volume fraction in the as-fired state strongly depends on the material's composition and particularly on the presence of primary aluminium titanate in the material variants. The highly dense metal matrix exhibited several pores and precipitations that were characterized by high concentrations of Mn, Mg, and Si as measured by EDS. It was assumed that these precipitations originated from the refractory material used in the gas atomization process. In general, the steel grains exhibited segregations at grain boundaries with enhanced concentrations of Cr and lower concentrations of Ni, forming δ-ferrite. The pronounced transformation of the highly metastable steel from austenite to martensite on the specimens' surfaces is a result of mechanical polishing. The ferromagnetic phases δ-ferrite and α'-martensite were confirmed by magnetic balance measurements. The presence of carbides was negligible. The characteristic microstructure of composite specimens with zirconia is shown in Fig. 5.11. The ceramic particles are randomly dispersed and widely embedded in the surrounding steel matrix. Delamination and broken-out particles indicate the loose bonding at the metal/ceramic and ceramic/ceramic interfaces. This is most likely a consequence of the firing temperature of the composite material, which was considerably below the normal sintering temperature of such zirconia ceramics (>1600 °C).

Table 5.7 Physical characteristics of the material variants

Recipe	0Z	5Z	10Z	5AT	10AT
Shrinkage (%)	15.9 ± 0.1	16.4 ± 0.1	15.9 ± 0.1	15.2 ± 0.2	12.5 ± 0.1
Bulk density (g/cm^3)	0.1 ± 0.1	0.1 ± 0.0	0.4 ± 0.3	0.4 ± 0.4	14.1 ± 0.7
Porosity (%)	7.54 ± 0.05	7.34 ± 0.04	7.25 ± 0.05	7.26 ± 0.05	6.39 ± 0.12

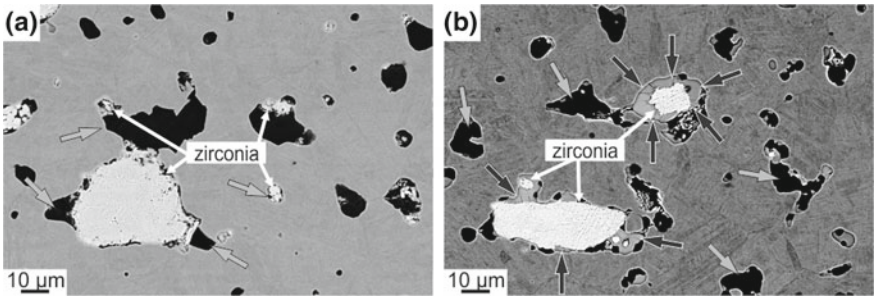

Fig. 5.11 Microstructure of MMC specimens with combinations of zirconia and aluminium titanate in their as-fired state showing the particular inclusion of zirconia particles by aluminium titanate/spinel (light grey arrows) and a solid solution of Zr–Ti–O also containing Mn (dark grey arrows): **a** 2.5ZAT, **b** 5ZAT [36]

The in situ tests revealed the kinetics of strain-induced α'-martensite during deformation. The S100 specimens exhibited the highest overall percentage of strain-induced α'-martensite at rupture (see Fig. 5.12). The lower formation of strain-induced α'-martensite in the composite variants 5Z/2.5ZAT was in accordance with the less pronounced sigmoidal shape of their strain hardening response. The reduction of the austenite stabilizing alloying element Mn was caused by its evaporation, diffusion and the formation of phases containing Mn at the metal/ceramic interfaces like $(Mg, Mn)Si_2O_4$ and/or $(Mn, Mg)(Al, Ti, Cr)_2O_4$, and led to a distinct shift of the initial metallic phase composition. This mechanism is more pronounced in MMCs

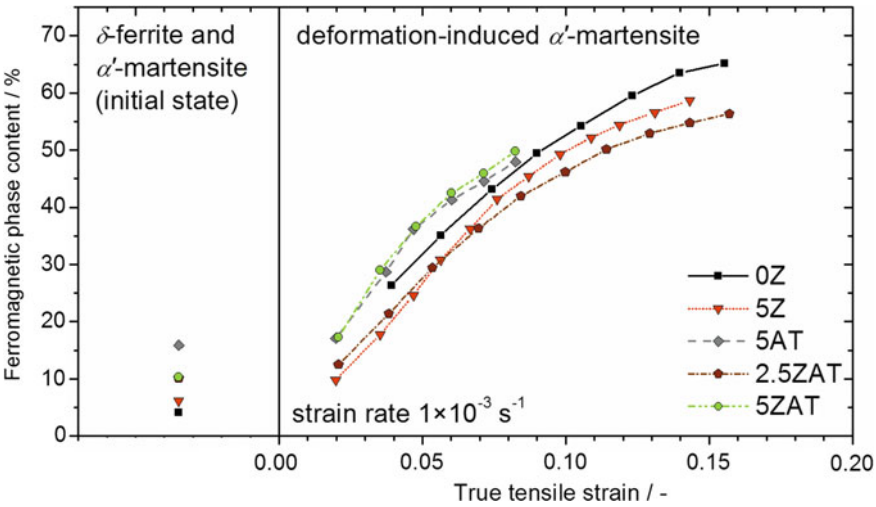

Fig. 5.12 Evolution of the ferromagnetic phase fraction under tensile deformation at room temperature, normalized by the metal fraction in the material [36]

with aluminium titanate as compared with steel/zirconia mixtures. Hence, the composites of types 5AT and 5ZAT reveal a higher α'-martensite content and formation rate at the beginning of plastic deformation. Then, the constrained matrix of the work hardened austenitic/martensitic steel suffers from the lack of strain relaxation, which promotes crack initiation and propagation [36].

The microstructure of the specimens after tensile deformation tests was analyzed in order to explain the mechanical behavior as well as the characteristic failure mode of the material and is shown in Fig. 5.13. The small strengthening effect of zirconia in the MMCs is a result of the loose embedding of the Mg-PSZ particles, of the irregular formation of silicates as an intermediate layer between steel/zirconia and zirconia/zirconia particles and of the lack of pronounced metastable ZrO_2 phase regions. The zirconia agglomerates are broadly crushed and fissured after tensile deformation; considerable delamination occurred at the steel/ceramic interface, which indicates loose interface boundaries [37, 38]. Thus, sufficient load transfer from the steel matrix can be assumed. Still, the sintering temperature of the composite material was well below the regular sintering temperature of Mg-PSZ, thus the clustered particles are expected to fail at lower stresses as compared with the commercially available bulk material. Since the majority of the zirconia particles exhibited the non-transformable monoclinic crystal structure already after sintering, the probability of the desirable tetragonal to monoclinic phase transformation is low. However, a large amount of voids in the ceramic sections, caused by broken-out particles, hampered a detailed and representative phase analysis of the material.

It is obvious that the zirconia particles with a silicate intermediate layer and these silicate structures remained reliably bonded in the matrix material, whereas a large amount of zirconia particles was broken out after specimen preparation. The tensile deformed microstructure of MMCs with 5 vol% initial aluminium titanate powder is characterized by the spinel particles that maintained their pronounced interface bonding to the steel matrix despite the extended multiple-crack formation in the interior of the ceramic particles. In contrast, debonding was the dominant damage initiation mechanism in previous TRIP steel/Mg-PSZ composites [11, 38, 39]. The intact particle/matrix interfaces indicate a higher shear strength at the interface than

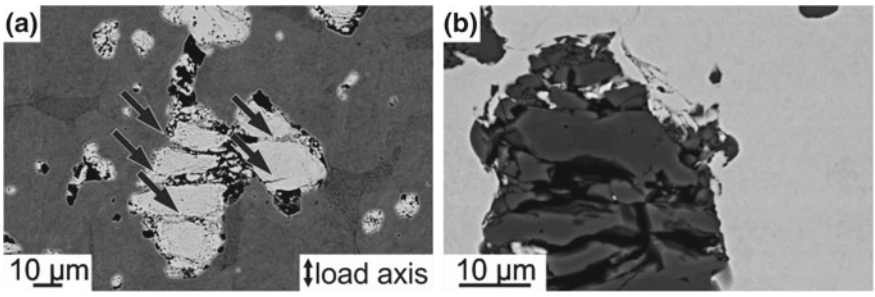

Fig. 5.13 SEM image of the composite materials at fracture strain showing broadly crushed ceramic particles and isolated cracks in the surrounding steel matrix: **a** 5Z, **b** 5AT [36]

the particle fracture strength which is a further indication for the improved interface-related performance of the MMCs with initial Al_2TiO_5 [37, 40]. Still, some of the small-grained spinel particles were nearly intact and exhibited neither cracking nor debonding. Although these composites underwent internal damage by crack initiation and the ceramic particles show no phase transformation or decomposition as compared with composite materials comprising metastable zirconia particles [3, 28], the addition of aluminium titanate results in a higher strain-induced α'-martensite formation and these MMCs sustain a higher stress level than the pure matrix material. The microstructure of the composite materials with concurrent additions of Mg-PSZ and aluminium titanate largely complied with the observations on 5Z and 5AT and the specific features for each type of ceramic particles. Here, the zirconia particles were subject to intense cracking but less to debonding due to the formation of the Ti-enriched spinel interlayer between the ZrO_2 particles and the steel matrix. The mutual interference of the zirconia particles and the initial aluminium titanate particles was apparently more pronounced in the MMCs with the higher ceramic volume fraction due to the coincidental distribution of these particles within the steel matrix [36].

The stress-strain curves of the TRIP steel alloy and the MMCs determined under compressive and tensile loading at a quasistatic strain rate of 0.001 s^{-1} at ambient temperature are displayed in Figs. 5.14 and 5.15. The stress level of the TRIP-matrix composites under compressive loading is significantly higher than the pure steel material considering a certain range of plastic deformation. As a consequence of damage initiation and propagation, the compression stress of material 10AT firstly dropped at approximately 11% engineering strain below the values measured for the pure steel specimen. Finally, catastrophic failure with sample fragmentation was induced achieving 45% strain. The strengthening effect of 5 vol% Mg-PSZ was

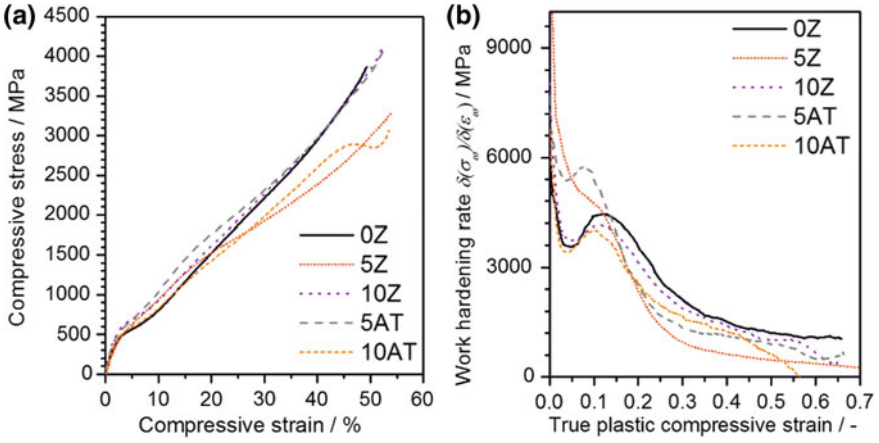

Fig. 5.14 Mechanical behavior of the specimens tested under quasistatic compression: **a** engineering stress-strain curves and **b** work hardening rates versus plastic compressive strain [35]

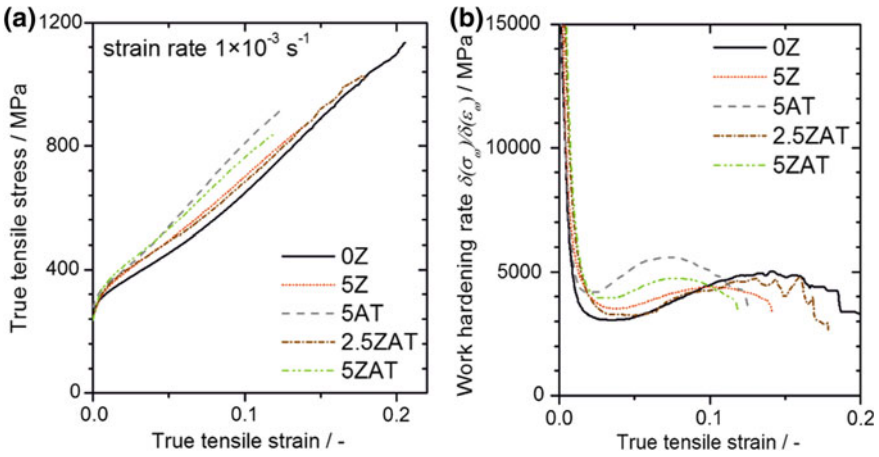

Fig. 5.15 Tensile deformation behavior of the material variants showing the strengthening and strain-depressing effect of certain ceramic fractions: **a** flow stress curves, **b** work hardening rates [36]

Table 5.8 Properties of the fired base materials without joining [30]

	0Z	5Z	10Z
Shrinkage (%)	16.0 ± 0.2	16.5 ± 0.1	15.9 ± 0.2
Total porosity (%)	4.1 ± 1.4	4.4 ± 0.6	4.5 ± 0.5
Bulk density (g/cm^3)	7.46 ± 0.11	7.34 ± 0.04	7.24 ± 0.04

exhausted when exceeding 18% compressive strain. However, the strain range with enhanced compressive stress compared with the pure TRIP steel was extended for the MMCs comprising 5 vol% Al_2TiO_5 and 10 vol% Mg-PSZ up to approximately 45% deformation. All composite materials exhibited higher yield strengths than the variant without any ceramic additions. The work hardening rates also illustrate the strengthening effect of the ceramic particles in a certain range of strain followed by a decreasing work hardening rate on further deformation [35].

5.3.3 Joining of Zirconia Reinforced MMCs

The base materials for joining experiments show similar macrostructure and microstructure as compared with the standard bulk materials previously reported. The determination of the physical characteristics (shrinkage, porosity and density) of the fired specimens revealed similar properties among all base materials (see Table 5.8) regardless the ratio of zirconia particles dispersed within the steel matrix. The residual porosity of approximately 4–5% is caused by the particle size of the

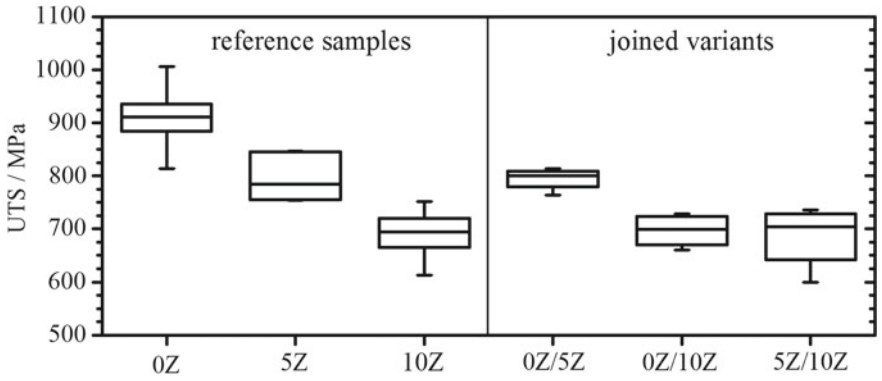

Fig. 5.16 Ultimate tensile strength of the materials tested under a quasistatic tensile loading at a rate of 0.001 s^{-1} at room temperature, featuring the minima, maxima and the 25%-, 50%-, and 75%-percentiles [22]

raw materials, the presence of the binder system during extrusion, and the applied pressureless sintering. The fired specimens appeared with a glossy metallic surface indicating the absence of considerable metal oxidation during thermal processing.

The results of tensile tests are given in Fig. 5.16. As expected, the composite materials had a lower ultimate tensile strength (UTS) and fracture strain as compared with the pure steel specimens. The decline of UTS by increasing the zirconia volume fraction results from the partial replacement of the ductile matrix material by brittle ceramic particles and which facilitates crack initiation and propagation.

Since the surface preparation is of major interest in joining processes, the sample preparation and material derived variations have to be taken into consideration. Nevertheless all surfaces to be joined appeared smooth with some transverse stress marks from the rotating grinding wheel indicating the definitive inclusion of the steel particles in the binder matrix in their dry green state. Break-off of particles and spalling on the edges of the samples was not observed. The addition of 5 or 10 vol% Mg-PSZ did not significantly affect the properties of the surface to be joined, since the ceramic particles were well dispersed and reliably fixed in the composite variants with their metal/binder matrix. The average roughness value R_a of the machined joining surface of the material variants (21.7 µm—0Z; 20.2 µm—5Z; 18.1 µm—10Z) marginally deviates among all materials tested and, thus, a preparation-driven impact on the material characteristics is not to be expected [22, 30].

The location of the joints could easily be assigned in the as-fired state due to some leaked paste from the joining process. The microstructure of the material combinations 0Z/10Z and 5Z/10Z is shown in Fig. 5.17. The base materials show a homogeneous microstructure with some pores and inclusions (all), and a good dispersion of the ceramic particles at a certain degree of agglomeration (5Z and 10Z). The smaller sized zirconia particles tended to form coarse-grained agglomerates in the interstices of the steel particles during manufacturing, which is more pronounced in the specimen with 10 vol% zirconia.

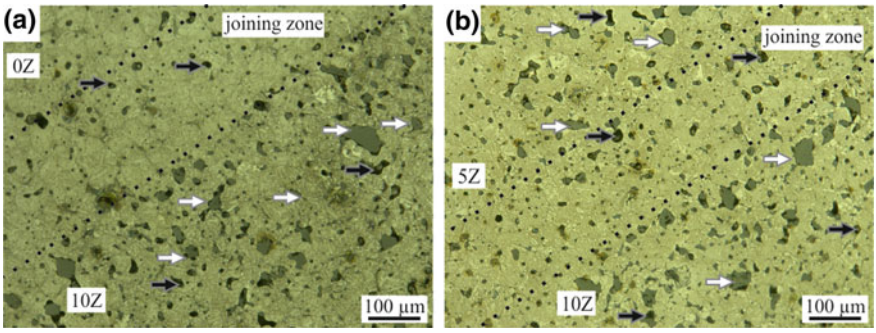

Fig. 5.17 Micrograph of sinter-joint variants: **a** 0Z/10Z, **b** 5Z/10Z; black arrows: pores and nonmetallic inclusions, white arrows: zirconia particles [22]

The formation of distinctive sections, e.g. heat-affected zone and welding seam as known from fusion welding, was neither detected by light optical microscopy nor scanning electron microscopy in the present sinter-joint samples. The joining interface is characterized by a smooth transitional area at a thickness of roughly 100–400 µm. The measurement of the width is only feasible in the material combination 5Z/10Z due to an enlarged zirconia-free intersection between the base materials (see Fig. 5.17b). Contaminations and nonmetallic inclusion are present in all material variants since the pressureless sintering promotes the formation of silicates and spinels at the steel/zirconia interface and even in the pure steel material [3, 41]. Firing the pure joining paste under equivalent thermal conditions results in the formation of a microstructure (e.g. grain size, porosity, and precipitations) similar to the fired 0Z base material [22].

The micro hardness profiles of the joint variants transverse to the joining zone were examined. The microstructure and the elemental distribution of the material combination 0Z/10Z is shown in Fig. 5.18. Both components (0Z and 10Z) are characterized by a similar microstructure with randomly dispersed pores and nonmetallic inclusions. The location of the joining zone could clearly be allocated by taking the presence of the zirconia particles and the concentration of Fe and Zr (using EDS) into consideration. The presence and concentration of Si is not a function of the zirconia volume fraction, since Si was incorporated as a contamination of the initial steel as well as of the zirconia powder (cf. Tables 5.2 and 5.3). The investigation of samples with material combinations 0Z/5Z and 5Z/10Z revealed similar results, however the smaller the difference in zirconia volume fractions between both joining partners, the more difficult was the localization and identification of the joining zone [22].

All joined material combinations failed at lower UTS and strain than the stronger component. The failure of all sinter-joint material combinations was initiated within the base material containing the higher volume fraction of Mg-PSZ particles. As pressureless sintering of the powder metallurgical processed composites involves thermal treatment for several hours at high temperature interactions between all components affect the microstructure and the material properties. Both the alloying elements of

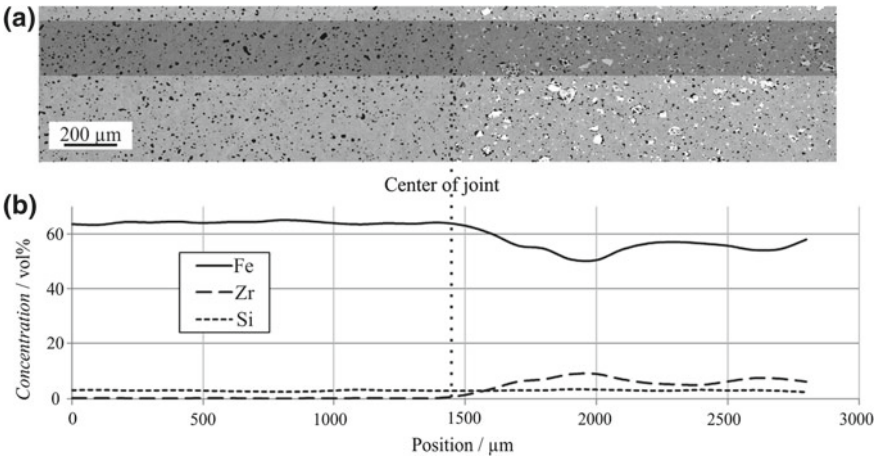

Fig. 5.18 Microstructure of combination 0Z/10Z after firing: **a** SEM image: dark grey: steel, light grey: zirconia; black: pores and nonmetallic inclusions, **b** transversal EDS line scan of the joint section showing the concentrations of Fe, Zr, and Si including the highlighted area (measuring field size 200 µm × 200 µm, step size 100 µm) [22]

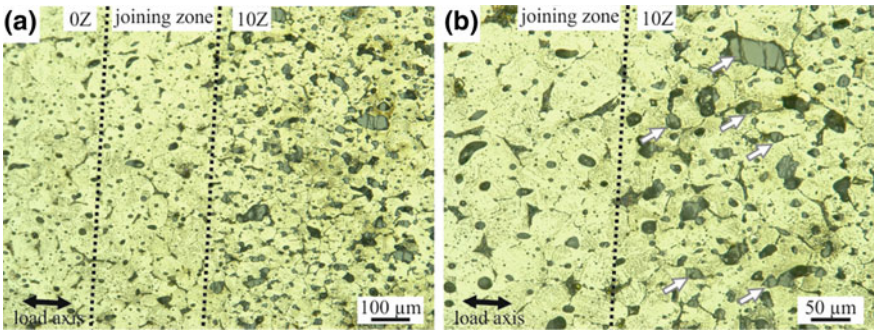

Fig. 5.19 Micrograph of the material combination 0Z/10Z after 20% tensile deformation showing particle fracture in large zirconia particles (indicated by white arrows), rare debonding at the metal/ceramic interface, and the well-preserved joining zone [22]

TRIP steel and the stabilizing agent of the zirconia reinforcing particles (Mg) are prone to diffusional interchange [21]. However, the composite material suffers from poor interfacial bonding, which is apparently more pronounced under tensile than under compressive loading. Thus, the reinforcing particles or agglomerates debond in an early state of deformation and micro crack formation initiates MMC's failure at lower strain than the pure steel material. Also the pronounced multiple crack formation within the coarse zirconia agglomerates could be observed as shown in Fig. 5.19 [35]. In contrast, the sinter-joint appeared almost intact and the boundary surface between the joining zone and the base materials indicated no detachment [22].

5.4 Conclusions

The ceramics-derived extrusion technology has been successfully applied on the manufacturing of metallic matrix composites. The combination of austenitic stainless TRIP/TWIP steel matrix variants with certain ceramic additions at metal volume fractions $\geq$90% is feasible. Mixing solid powders with an aqueous organic binder system enables the shaping of bulk and cellular lightweight structures at room temperature. The particle size and shape of the starting powders, the metal/ceramic-ratio, and the binder system crucially affect the shaping process and the microstructure of the shaped specimens. Generally, the ceramic particles were homogeneously dispersed within the metal matrix with a certain degree of agglomeration. To improve the particle dispersion, the size distribution of the metal and the ceramic component should be narrow and compliant to avoid clustering of fine reinforcing particles in the interstices of the metal matrix. Set proper drying parameters (temperature, heating rate) prevents the material from detrimental crack formation and damage of the materials. The subsequent thermal processing comprising the binder removal (debindering) and the consolidation (sintering) transfers the material into its final state. Pressureless sintering of the powder metallurgically processed materials requires temperatures slightly below the metal melting temperature with maximum temperatures of 1300–1400 °C and distinct dwell time of 1–2 h. The thermally induced diffusional interchange of the alloying elements of the steel and the ceramic fractions led to mutual alterations of the components. The crystal structure of zirconia in the MMCs was predominantly monoclinic due to diffusion of Mg out of the particles and the formation of spinel and/or silicate precipitations at the steel/zirconia interface during firing. Thus, the desired tetragonal to monoclinic transformation of the zirconia particles during mechanical testing is hampered.

The reinforcing mechanism of ceramic particles dispersed in TRIP/TWIP steel matrices enables composite materials with superior mechanical properties in a certain range of deformation. The stress-strain and deformation behavior of the materials were mainly controlled by dislocation hardening and α'-martensite phase formation in the steel matrix further affected by the reinforcing mechanisms of the ceramic particles. Finally, all composite materials failed at a lower strain than the unreinforced matrix material by internal damage after cracks have initiated in the steel matrix surrounding the ceramic particles and which is more pronounced under compressive deformation than under tensile loading. Advanced properties of the composite variants have been observed in terms of higher compressive stresses as well as an improved energy absorption capability. The desired martensitic phase transformation was proven in both, the matrix material and the zirconia particles with pronounced phase evolution in an early stage of deformation. Upon exceeding a critical strain the materials without ceramic additions benefit from the lack of non-plastic particles leading to higher strength at equivalent deformation. The addition of 1–2 vol% titanium improves the densification of the matrix material and the firm incorporation of zirconia particles into steel matrix. The formation of a Ti–Zr–O solid solution was observed at the metal/ceramic interface that promotes reliable interface boundary.

Aluminium titanate was identified as a proper reinforcing material for TRIP/TWIP composite materials in the frame of the present study. The diffusional interchange of the alloying elements of the steel and the aluminium titanate particles led to the decomposition of the aluminium titanate and the formation of a dense (Mn, Mg)(Al, Ti, Cr)$_2$O$_4$ spinel structure during firing. The intergranular bonding strength and the toughness of the metal/ceramic interfaces seem to be higher than in composites with loosely embedded zirconia particles. The composite materials with aluminium titanate offered a significant strengthening effect and a distinctive strain hardening under quasistatic compressive and tensile loading as compared with the matrix material. The void-free interface between the steel and the spinel structures of the initial microstructure offered optimal conditions for the load transfer; the intergranular bonding strength and the toughness of the metal/ceramic interfaces are assumed to be higher than in composites with zirconia particles. The combination of Mg-PSZ and Al_2TiO_5 further improved the stress level of the MMCs during deformation.

An innovative technique for joining metal-matrix composite materials with minor fractions of zirconia reinforcing particles was studied. The bulk specimens were prepared with the powder metallurgical processing route via extrusion of plastic pastes at room temperature. Various combinations of the base materials with 0, 5 or 10 vol% zirconia were joined by applying an aqueous high-solids paste on the surfaces to be joined in their dry green state at room temperature. The preparation of the surfaces before joining comprised cutting and rotary grinding with low mechanical and thermal impact on the base materials. During consecutive thermal processing the material's consolidation and the generation of the joint took place simultaneously. Thus, the formation of a consistent metal-matrix composite material and the formation of high bonding strength were initiated. Microstructural analysis revealed a homogeneous structure without inhomogeneities within the metal matrix nor segregation of the ceramic particles. Since the sintering and joining proceeded simultaneously the formation of a heat-affected influence zone as known from metal joints prepared by brazing or welding did not occur. The hardness of the pure steel specimens, the composite materials and the joining zone was measured in terms of Vickers's indention method. Since the fired specimens showed certain porosity and precipitations, the addition of zirconia particles showed no excessive hardening in the composite materials. Also, the formation of the joining zone had a negligible effect on the micro hardness. Mechanical tests under quasistatic tension at room temperature revealed similar strength of the joint variants as compared with the base materials. Strength and plasticity decreased as soon as ceramic particles were present in the base materials. Therefore, the deformation behavior of the joint variants is closely related to the mechanical properties of the base materials. In general the failure is initiated within the joining partner with the higher zirconia volume fraction without fracture at the bonding interface. The sinter joining technology is applicable for a wide range of material combinations and geometries. Efforts to improve the mechanical properties of joint materials demand improved base materials, since the materials are prone to fail beyond the joint.

Acknowledgements The authors gratefully acknowledge the financial support of the Deutsche Forschungsgemeinschaft (DFG, German Research Foundation) for funding the research project A5 and transfer project T1 within the frame of the Collaborative Research Center 799—TRIP-Matrix-Composites—project number 54473466. Additionally, the authors thank all technical employees and students who were involved in processing, machining, and analyzing the materials.

References

1. S. Martin, S. Wolf, U. Martin, L. Krüger, Solid St. Phenom. **172–174**, 172 (2011)
2. H. Biermann, J. Solarek, A. Weidner, Steel Res. Int. **83**, 512 (2012)
3. C. Weigelt, C.G. Aneziris, H. Berek, D. Ehinger, U. Martin, Adv. Eng. Mater. **14**, 53 (2012)
4. A. Weiß, H. Gutte, M. Radke, P.R. Scheller, Patent No. WO 002008009722A1 (24.08.2008)
5. M. Hajizamani, H. Baharvandi, Adv. Mater. Ph. Chem. **1**, 5 (2011)
6. E.G. Okafor, V.S. Aigbodion, Tribol. Ind. **32**, 31 (2010)
7. K. Kaur, O.P. Pandey, J. Alloys Compd. **503**, 410 (2010)
8. D. Wittig, A. Glauche, C.G. Aneziris, T. Minghetti, C. Schelle, T. Graule, J. Kuebler, Mater. Sci. Eng., A **488**, 6 (2008)
9. L.M. Peng, J.W. Cao, K. Noda, K.S. Han, Mater. Sci. Eng., A **374**, 9 (2004)
10. Y. Guo, Y. Zhou, X. Duan, D. Li, T. Lei, J. Mat, Sci. Technol. **19**, 137 (2003)
11. A. Glage, C. Weigelt, J. Räthel, H. Biermann, Int. J. Fatigue **65**, 9 (2014)
12. S. Decker, L. Krüger, S. Richter, S. Martin, U. Martin, Steel Res. Int. **83**, 521 (2012)
13. Y. Guo, Y. Zhou, X. Duan, D. Li, T. Lei, Ceram. Int. **30**, 6 (2004)
14. S.S. Panda, A. Upadhyaya, D. Agrawal, J. Mater. Sci. **42**, 966 (2007)
15. C.G. Aneziris, W. Schärfl, B. Ullrich, J. Europ. Ceram. Soc. **27**, 3191 (2007)
16. K. Lemster, T. Graule, J. Kuebler, Mater. Sci. Eng., A **393**, 229 (2005)
17. D. Sciti, A. Bellosi, L. Esposito, J. Europ. Ceram. Soc. **21**, 8 (2001)
18. W.B. Hanson, K.I. Ironside, J.A. Fernie, Acta Mater. **48**, 4 (2000)
19. C. Lin, D. Gan, P. Shen, J. Am. Cer. Soc. **71**, 6 (1988)
20. R.F. Domagala, S.R. Lyon, R. Ruh, J. Am. Cer. Soc. **56**, 584 (1973)
21. C. Weigelt, S. Giersberg, C. Wenzel, C.G. Aneziris, Adv. Eng. Mater. **12**, 486 (2010)
22. C. Weigelt, H. Berek, C.G. Aneziris, R. Eckner, L. Krüger, Mater. Sci. Forum **825–826**, 498 (2015)
23. C.G. Aneziris, W. Schärfl, H. Biermann, U. Martin, Int. J. Appl. Ceram. Technol. **6**, 727 (2009)
24. C. Weigelt, C.G. Aneziris, A. Yanina, S. Guk, Steel Res. Int. **82**, 1080 (2011)
25. H. Biermann, U. Martin, C.G. Aneziris, A. Kolbe, A. Müller, W. Schärfl, M. Herrmann, Adv. Eng. Mater. **11**, 1000 (2009)
26. P.A. Evans, R. Stevens, J. Binner, Br. Ceram. Trans. **83**, 39 (1984)
27. C. Weigelt, H. Berek, C.G. Aneziris, S. Wolf, R. Eckner, L. Krüger, Ceram. Int. **41**, 2328 (2015)
28. S. Martin, S. Richter, S. Decker, U. Martin, L. Krüger, D. Rafaja, Steel Res. Int. **82**, 1133 (2011)
29. M.P. Phaniraj, D.K. Kim, J.H. Shim, Y.W. Cho, Acta Mater. **57**, 9 (2009)
30. C. Weigelt, E. Jahn, H. Berek, C.G. Aneziris, R. Eckner, L. Krüger, Adv. Eng. Mater. **17**, 1357 (2015)
31. C. Weigelt, C.G. Aneziris, R. Eckner, L. Krüger, in *Proceeding of the World PM2016 Congress and Exhibition*, The European Powder Metallurgy Association, Hamburg, Germany, 9–13 Oct 2016
32. W. Zhang, J. Xie, C. Wang, Mater. Sci. Eng., A **382**, 387 (2004)
33. S. Noh, A. Kimura, T.K. Kim, Fusion Eng. Des. **89**, 1746 (2014)
34. Z. Chen, K. Ikeda, T. Murakami, T. Takeda, J. Am. Cer. Soc. **83**, 1081 (2000)
35. C. Weigelt, C.G. Aneziris, D. Ehinger, R. Eckner, L. Krüger, C. Ullrich, D. Rafaja, J. Compos. Mater. **49**, 3567 (2015)

36. C. Weigelt, G. Schmidt, C.G. Aneziris, R. Eckner, D. Ehinger, L. Krüger, C. Ullrich, D. Rafaja, J. Alloys Compd. **695**, 9 (2017)
37. N. Chawla, Y.-L. Shen, Adv. Eng. Mater. **3**, 357 (2001)
38. R. Eckner, M. Krampf, C. Segel, L. Krüger, Mech. Compos. Mater. **51**, 707 (2016)
39. M. Droste, H. Biermann, Mater. Sci. Forum **825–826**, 176 (2015)
40. S. Prüger, L. Mehlhorn, U. Mühlich, M. Kuna, Adv. Eng. Mater. **15**, 542 (2013)
41. H. Berek, A. Yanina, C. Weigelt, C.G. Aneziris, Steel Res. Int. **82**, 1094 (2011)

Chapter 6
Understanding of Processing, Microstructure and Property Correlations During Different Sintering Treatments of TRIP-Matrix-Composites

Sergey Guk, Rudolf Kawalla and Ulrich Prahl

Abstract This chapter presents scientifically robust results on the sintering behavior of transformation-induced plasticity (TRIP)-matrix composites based on different consolidation processes, such as conventional sintering, resistance sintering and hot pressing. The correlation of the processing parameters to the adjusted properties, such as the density, porosity, grain size, phase composition and mechanical properties is discussed. The theoretical modeling, including validation with experiments, enabled us to describe, understand and quantitatively optimize the sintering process.

6.1 Introduction

Powder metallurgy (PM) is an attractive production route for conventional metal matrix composites (MMCs) because it offers a wide range of reinforcing particle size amounts and distributions in the matrix material. The additional advantages of PM processes are that the grain growth is lower than that from the ingot metallurgy route, and the reaction between the matrix and reinforcing particles can be minimized by using solid-phase sintering processes. This route is most commonly used in the case of composite materials with steel or other high-performance materials as a matrix that cannot be produced by means of the conventional ingot metallurgy route due to the high processing temperatures, different melting points or different densities of the composite components. Conventional PM production normally consists of three steps: blending the metal and ceramic powders, compacting and sintering. In some cases, a sizing step follows the sintering step. During the processing, such when the blending and compacting of the powder particles and pores inside the green compact are adjusted, consolidation processes, such as conventional or conductive sintering, hot pressing (HP) or hot isostatic pressing (HIP), complete the final compaction of the composite material. They differ in the type of heating that occurs (radiative or

S. Guk (✉) · R. Kawalla · U. Prahl
Institute for Metal Forming, Technische Universität Bergakademie Freiberg,
Bernhard-von-Cotta-Str., 09599 Freiberg, Germany
e-mail: sergey.guk@imf.tu-freiberg.de

H. Biermann and C. G. Aneziris (eds.), *Austenitic TRIP/TWIP Steels and Steel-Zirconia Composites*, Springer Series in Materials Science 298,
https://doi.org/10.1007/978-3-030-42603-3_6

conductive heating) and whether additional consolidation acceleration occurs due to the presence an external compressive load (conductive sintering, HP and HIP).

In the past, the described advantages of PM instigated many investigations into MMCs that dealt with the optimization of the sintering processes. In several studies, conventionally sintered composite materials, such as functionally gradient materials (FGMs), that were based on stainless steel with a ceramic component, namely, ZrO_2, were investigated [1–4]. The results showed significant residual stresses in the consolidated composite material that resulted in a high concentration of microcracks after the completion of all manufacturing steps. These stresses can be attributed to a difference in the thermal expansion coefficients between the ceramic and steel and the volume expansion during phase transformation. However, an optimal selection of sintering conditions that considers the layer structure leads to good interface quality. For example, a 4-layer FGM extruded in the form of a tube, consisting of a 316L steel matrix and yttrium partially stabilized ZrO_2 (PSZ), was produced after sintering at 1350 °C for 1.5 h with a good layer interface quality [5]. The good interface formation in composite materials is based on a chemical reaction at the phase interface, which can cause destabilization of the tetragonal(t) phase of ZrO_2 [6]. A variation of the sintering atmosphere showed that while nitrogen positively influenced the mechanical properties of the sintered composite materials, good corrosion properties were achieved by sintering in a vacuum or hydrogen [7].

The consolidation of powders by conductive sintering can be based on different technologies, such as spark plasma sintering (SPS), pulsed electric current sintering (PECS), pulse discharge sintering (PDS), plasma activated sintering (PAS), and field activated sintering technique (FAST). The resistance sintering used in this research is characterized by a direct conversion of electrical energy into heat in the sintered material by applying an electrical voltage to the sample. In [8], a sintering progress was investigated on chromium powder ПХ1М in the temperature range from 1300 to 1500 °C and for sintering times that reached 5 min. The results showed that at the beginning of the isothermal holding time, the effect of the electric current dominated, after which small pores were distributed in the microstructure. The increasing holding time at constant temperature caused low coagulation and enlargement of the pores as well as an increase in the microscopic stresses, which was explained by the action of Laplace forces. Similar investigations of iron powder showed that the densification of a sample to 95% of its relative density when it had dimensions of ∅12.8 mm × 3.6 mm was possible by heating at 600 K/s to a sintering temperature of 800 °C and with a sintering time of 6 min [9]. The tests were carried out with a relatively low voltage of 3–10 V and with high current values above 10 kA. The authors indicated that fast densification of the material occurred during the heating phase since at this time, the elevated resistance caused a high Joule heating effect. Furthermore, a theoretical prediction of the influence of the composition of the conductive and nonconductive phases on the physical-mechanical properties of the composite materials was carried out [10]. Theoretical modeling that included experimental validation showed that the limit of percolation (the limiting value of the conductor content at which the conductivity becomes zero) depends on the ratio of the particle sizes of the conducting and the insulating phases. As long as the particle size of the

conducting phase decreases compared to that of the insulating phase, the percolation limit decreases (conductivity can also be achieved with a small content of the conducting phase). In other cases, the percolation limit increases (a small content of the insulating phase leads to the composite material becoming insulating).

Many investigations and broad experience from industrial practice have proven that an externally applied pressure accelerates the sintering process of a porous body. The influence of the pressure on the sintering kinetics at different pressures and temperatures results from the different deformation mechanisms in the porous sintered material, which have been described in detail in Geguzin [11]. The advantages of processes that apply pressure include the manufacturing of dense materials with lower sintering temperatures and shorter sintering times than those of conventional sintering processes; this results in sintered parts with an increased strength that quite often do not require sintering aids. While a substantial amount of knowledge has already been gained regarding the HP of ceramics, metals and cermets, there are only a few papers regarding HP of steel-ZrO_2 composites. For example, the properties of a ZrO_2(2Y)/transformation-induced plasticity (TRIP)-steel composite produced by HP were investigated depending on the value of applied stress [12]. The powder mixtures were subjected to HP at 1250 °C at 20 MPa for 30 min. The results indicated that the tensile strength and the modulus of elasticity of the composite material decreased under static loading with increasing ZrO_2 content up to 35 vol% due to weak bonding at the ZrO_2–ZrO_2 and ZrO_2-TRIP steel phase interfaces. The dynamic yield strength of the composite was greater than that of the static composite due to the induced martensite transformation, which provided improved plasticity and overall formability. The effect of the ZrO_2 content on the tensile strength of the composite material at the beginning of dynamic deformation was not evident. The rheological stresses increased with increasing ZrO_2 content and deformation in the ZrO_2(2Y)/TRIP-steel composites. Nevertheless, the formability and dynamic strength of the composites decreased with decreasing ZrO_2 content. Furthermore, manufacturing of FGMs based on tetragonal zirconia polycrystal (TZP) and stainless steel or Ni in the form of SUS304-TZP or Ni-TZP, respectively, could be achieved by HP at 1250 °C for 1 h in a nitrogen atmosphere with 5 K/min heating and cooling rates [13–15]. Finite element modeling of the process indicated that the coefficient of thermal expansion of the composite components was a decisive factor in the production of FGMs free of residual stresses and cracks caused by cooling. Thus, Ni-TZP composites were demonstrated to have better thermal insulating properties than SUS304-TZP.

The postdensification of sintered parts can be achieved by HIP. Unfortunately, there are no data available in the literature about the postdensification of TRIP steel-ZrO_2 composites, while sufficient information is available on the HIP behavior of stainless steel powders. The HIP investigations showed that the relative density of AISI 316L samples was more influenced by the HIP temperature than they were by the HIP pressure. The maximum density of 97% was achieved by HIP at 1250 °C and 120 MPa [16]. Furthermore, the compression behavior of AISI 304 steel-based components at various manufacturing parameters was investigated in [17], whereby the manufacturing route consisted of compacting by selective laser sintering (SLS) with

simultaneous cold isostatic pressing (CIP) in the range between 300 and 600 MPa and then sintering in the temperature range between 1250 and 1350 °C for 1 h under a vacuum of 10^{-3} Pa. Finally, the components were hot isostatically pressed at 1200 °C at 120 MPa for 1 h. The component manufactured at the maximum CIP pressure and sintering temperature achieved a maximum density of 97% after HIP.

The aim of the present work is the investigation of the densification behavior and final mechanical properties of TRIP-matrix composites depending on the different fabrication processes.

6.2 Materials and Methods

Both stainless steel and PSZ powders were used for the investigations. The gas-atomized steel powder was purchased commercially as grade AISI 304 stainless steel (grade 1.4301 stainless steel). Three batches were available, and each was used for one of the three consolidation routes. The batches differed slightly in chemical composition and the resulting delta ferrite fraction (Table 6.1). The particle size varied minimally from batch to batch and was in the range of approximately $d_{10} = 10\ \mu m$, $d_{50} = 25\ \mu m$ and $d_{90} = 45\ \mu m$.

The solidus temperatures of the stainless steel powder batches calculated with the help of the FactSage® program based on the present chemical analysis were 1426 °C (conventional sintering), 1361 °C (resistance sintering) and 1405 °C (HP).

ZrO_2 powder was used for the investigations in the partially stabilized ZrO_2 (PSZ) form. MgO was applied as a stabilizer. The chemical composition of the powder is shown in Table 6.2. The ceramic particles had an angular shape with a approximate particle size in the range of $d_{10} = 0.2\ \mu m$, $d_{50} = 3\ \mu m$ and $d_{90} = 22\ \mu m$. The phases were distributed among the monoclinic (m), t and cubic (c) phases at nearly equal amounts of 35:32:33%.

The fabrication of MMCs was carried out by conventional and resistant sintering as well as by HP with partial application of the HIP process. The preparation of the powder mixture for all consolidation routes was carried out either by blending for conventional sintering and HP with partial application of the HIP process or by mechanical alloying of the powder mixtures for resistance sintering. Before blending, the volume fraction of ZrO_2 was adjusted from 0 to 30 vol%. The inorganic powder mixture was then blended by means of ZrO_2 balls stabilized with yttrium for approximately 30 min in a ball mill. Especially for the conventional sintering process, approximately 2.5 mass% of organic binder was added.

The powder mixture was prepared for resistance sintering using a mechanical alloying technique in a vibrating mill with high energy output (attritor) [18]. The grinding duration was approximately 90 s for each 250 g of the initial powder mixture. At the end of the process, the powder mixture was fabricated with an activated surface.

Compacting the green bodies for conventional sintering was carried out by extrusion of the prepared powder mixture. Extruded rods 20 mm in diameter were fabricated using a single-screw extruder with a vacuum chamber in combination with

Table 6.1 Chemical composition of the AISI 304 stainless steel powder for the respective consolidation route, wt%

Consolidation route	C	Mn	Si	S	Cr	Ni	Mo	Ti	Nb	N	δ-ferrite
Conventional sintering	0.01	0.9	0.2	0.007	17.5	10	0.03	0.004	0.007	0.04	7
Resistance sintering	0.08	0.8	0.8	0.014	21.3	11.9	–	–	–	0.25	9
Hot pressing	0.03	1.4	0.3	0.006	16.7	8.5	0.3	0.007	0.035	0.126	18

Table 6.2 Chemical composition of ZrO_2 powder, wt%

ZrO_2	Y_2O_3	SiO_2	Al_2O_3	HfO_2	CaO	MgO	TiO_2	K_2O	Na_2O	BaO	Fe_2O_3
96.3	–	0.4	–	–	0.6	2.8	0.13	–	0.1	–	0.13

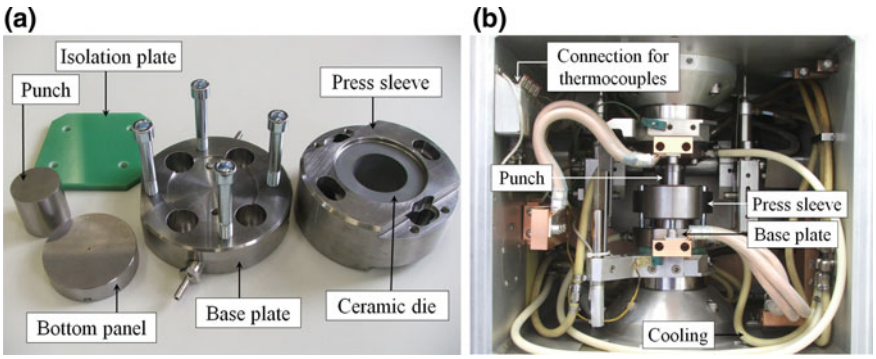

Fig. 6.1 Parts of the tool for resistance sintering (**a**) and their locations in the test chamber of the GLEEBLE HDS-V40 (**b**)

a kneading machine. After the extrusion process, the green compacts were cut into segments of the required length. Afterwards, the water added to the powder mixture before kneading was removed by an air dryer. The relative density of the extruded green bodies was approximately 60%. The subsequent removal of the organic binder occurred in the air at 350 °C for a duration of 5 h. The heating took place up to 100 °C at a rate of 2 K/min and at a rate of 0.2 K/min above 100 °C. The cooling took place at the same rates.

Conventional sintering was performed on extruded and debindered green compacts in an Astro 1100-60100-M1 model refractory metal hot-zone laboratory furnace (Thermal Technology LLC_{TM}). The accuracy of the temperature measurement was ±4 K over the applied temperature range. According to the furnace manufacturer, the typical temperature homogeneity of the furnace at 1700 °C is ±3 K for 35% and ±6 K for 50% of the furnace chamber volume. The sintering process took place in argon and nitrogen atmospheres (class 5.0) as well as in a vacuum of 10^{-6} mbar. The heating rate was approximately 5 K/min, while the cooling rate was approximately 10 K/min.

A multifunctional GLEEBLE HDS-V40 simulation system (Dynamic Systems Inc.) was used for the resistance sintering. The parts of the specially designed tool for resistance sintering in the GLEEBLE are shown in Fig. 6.1 and consisted of water-cooled base plates, a bottom panel, a ceramic die (Si_3N_4) with conical inward and outward design features, and a steel press sleeve to reinforce the ceramic die and a punch. To reduce the heat dissipation from the face of the sample in the front through the bottom panel, additional plates of carbon-fiber-reinforced carbon (with a thermal conductivity of 3 Wm^{-1} K^{-1} and specific electrical resistance of 26 μΩ)

were interposed for thermal insulation. Furthermore, a higher electrical conductivity than that of steel was achieved by using punches fabricated from a material based on a molybdenum alloy with the addition of Ti and Zr. The base plates had current connections but were electrically insulated from the other parts of the GLEEBLE by isolation plates. The powder mixture to be sintered filled the ceramic die before resistance sintering, where the mass of the powder mixture to be sintered was always 250 g. The dimensions of the sintered samples were ∅50 mm × 18 mm. The ceramic die and tool surfaces were lubricated by hexagonal boron nitride spray before each test to improve the removal of the sintered sample from the tool after the process. To avoid welding the powder mixture to the bottom panel and the punch as well as carburization of the sample by the carbon-fiber-reinforced carbon plates, a tantalum foil was placed in those areas. After closing the ceramic die with the punch and applying a critical presintering pressure of approximately 50 MPa, the resistance sintering was carried out according to a specified temperature-time cycle with an almost constant sintering pressure of approximately 20 MPa. The temperature of the sample during the sintering process was continuously controlled and adjusted with the help of a thermocouple that was located in the bottom panel and carbon-fiber-reinforced carbon plate so that the heating rate was approximately 50 K/min. Another thermocouple was used for the temperature measurement of the punch and was placed near its working surface. The sample resistance controlled the sintering temperature depending on the ZrO_2 content, the presintering pressure and the sintering pressure as well as the temperature profile. In the course of the resistance sintering tests, the voltage and current values were measured and recorded with an accuracy of ±0.01 V and ±1 A using an ALMEMO 2690-8 measuring instrument. The peak values of the voltage and current were approximately 4 V and 6 kA, respectively. Based on the determined values, the electrical resistance of the samples R was calculated according to the following equation:

$$R = I/U, \tag{6.1}$$

where I is an electrical current and U is an electrical voltage.

After the tests, the samples were cooled in the sintering tool before they were removed.

Preliminary tests that directly hot pressed the powder mixtures in the molds (at 1250 °C for 2 h at 30 MPa) resulted in destruction of the graphite molds as a result of the penetration of the mixture into the mold gaps and its interaction with the mold material. For this reason, two methods of mixture precompaction into billets were tested: die cold pressing (CP) of the powder mixture and CIP followed by short-term presintering in a hydrogen atmosphere (Table 6.3). Significant advantages of the first method include the simplicity of the process, high productivity and possibility of mechanization. However, a significant heterogeneity of the billets in terms of the density and inability to produce parts with a complex shape did not allow us to consider this as a universal method. The second method overcomes the disadvantages of the die CP step, but the size inaccuracy of fabricated green compacts and their high surface roughness require the application of additional labor-intensive machining. To

Table 6.3 HP consolidation routes

Method	Steps and their processing parameters			
1st	**CP** $P = 60$ MPa		**HP** $T = 1100$, 1200, 1250, 1275 °C $t = 1$ h $P = 30$ MPa	–
2nd	**CIP** $P = 350$ MPa	**Presintering** $T = 1100$ °C $t = 1$ h H_2 atmosphere		**Post-HIP** $T = 1225$ °C $t = 1$ h $P = 100$ MPa

avoid the appearance of cracks and stratifications in the billets after CIP, the addition of short-term sintering in a hydrogen atmosphere was carried out, and a relative density of approximately 85% was achieved.

The dimensions of the HP samples were ∅80 mm × 20 mm. To remove the residual porosity in the specimens after HP, HIP in an ABRA press apparatus (ABRA Fluid AG) was added and its impact on the microstructure and property evolution was investigated.

The density of the sintered samples was determined in accordance with DIN EN 623-2. The samples for metallographic analysis and mechanical testing were cut from the machined sintered workpieces. Tensile tests were carried out on an AG-100kNG universal testing machine at room temperature according to DIN EN ISO 6892-1 on cylindrical specimens with dimensions of ∅4 mm × 20 mm. The impact toughness of the 55 mm × 10 mm × 10 mm samples with a V-shaped stress concentration was tested on a RKP450 impact testing machine at room temperature according to DIN EN ISO 148-1. In all cases, samples were obtained in the axial direction for conventionally sintered samples and in the transverse direction for the resistance sintered or hot-pressed samples. The hardness HV10 was determined according to DIN EN ISO 6507-1 on a ZHU250 instrument. The microstructure and fracture surface analysis of the tested samples were carried out by light and scanning electron microscopy. A quantitative evaluation of the micrographs was conducted to determine the pore shape factor f according to Equation:

$$f = 4\pi A / C^2, \tag{6.2}$$

where A is a grain surface area and C is a circumference of a grain.

The size of the pores and grains was determined with the help of the image processing program Archive4Images. The phase analysis of the ceramics after different consolidation routes was conducted with X-ray diffraction (URD 6 X-ray diffractometer) with an accelerating voltage of 40 kV and current of 30 mA; energy-dispersive X-ray spectroscopy was also conducted.

Based on the experimental results, it was possible to model the sintering behavior with kinetics calculations equations [19] as follows:

$$\rho_{\mathrm{rel}}(t, \vartheta, Z) = \left(1 + z_1 \cdot Z + z_2 \cdot Z^2\right) \cdot (\rho_{\min} + (\rho_{\max} - \rho_{\min})) \cdot \left(1 - \mathrm{e}^{-\left(\frac{t}{T(\vartheta)}\right)^q}\right) \tag{6.3}$$

where ρ_{rel} is a relative density, t is a time, ϑ is a temperature, Z is a ZrO_2 content, z_1 and z_1 are constants to be determined from the available data. Furthermore,

$$T(\vartheta) = \frac{q}{k} \cdot \mathrm{e}^{\frac{Q}{R \cdot (\vartheta - \vartheta_B)}} \tag{6.4}$$

Here, parameters occurring in the equation, such as the Avrami exponent and activation energy, were determined using experimental results and the mathematical-numerical method of nonlinear least square approximation. It was assumed that heating did not have a significant influence on the sintering process, i.e. the assumption of isothermal conditions was used. The modeling approach was sufficient to allow interpolation of the measured values after their successful validation for the purpose of design of optimum technological parameters and thus find an understanding of the changes taking place in the material.

6.3 Results

6.3.1 Conventional Sintering

The results from the investigations showed that the development of the microstructure and pore morphology in the undoped steel matrix (ceramic free) was significantly influenced by the sintering temperature [20, 21]. Particle rearrangement processes took place at a temperature of 1300 °C, which was reflected in the local growth of the pore area (Fig. 6.2). The temperature increase led to the growth of sinter bridges between particles and the associated increase in relative density. This effect is based on the small pores combining with large pores to reduce the surface energy (Ostwald ripening). The final stage of the sintering process was characterized by morphological changes. This involved pore rearrangement due to the ongoing Ostwald ripening phenomenon, including the effect of enclosed gases, as well as the nearly doubled the austenite grain growth. Finally, only closed pores that were isolated from each other were present. The sintering carried out at 1430 °C indicated that the shape of the sample began to change, and this limit was noted.

To achieve advantageous mechanical properties, the favorable sintered microstructure should have, on the one hand, the highest possible value of the shape factor in combination with the lowest possible value of the pore area. On the other hand, minimal grain coarsening should occur. This combination of favorable microstructure properties was achieved at a sintering temperature of 1390 °C.

For the case of a steel matrix doped with ceramic constituents, the sintering behavior was analyzed based on measurements of the electrical resistance of the

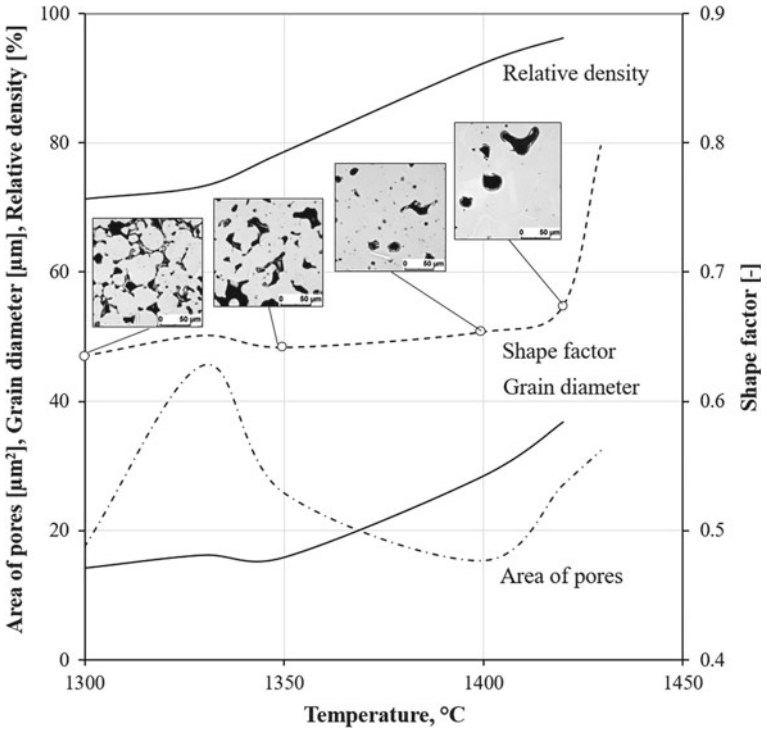

Fig. 6.2 Development of the microstructure and pore morphology in the undoped steel matrix with increasing sintering temperature for a sintering time of 2 h

specimen. Figure 6.3 presents exemplary results for the composite with 5% ZrO_2. The results show that the electrical resistance trend can be divided into three zones for this specimen [22]. In the first zone, the contact between the powder particles was substantially responsible for the electrical resistance of the specimen. The contact area of the powder particles increased during the sintering process, which was reflected in the significant decrease in the electrical resistance. Furthermore, in the first zone, a local region that experienced a resistance increase can be clearly seen in the continuously decreasing electrical resistance near the temperature of 730 °C, where the δ-ferrite phase was dissolved in the austenitic steel matrix according to the phase transformation diagram. Austenitic steel has a specific resistance up to 7 times greater than that of ferritic steel, which caused an increase in the electrical resistance of the composite material. In the second zone, the rate at which the electrical resistance decreased was noticeably reduced. Finally, in the third zone, the resistance passed into the range of pure material resistance. After the sintering process completed and while the specimen cooled, the resistance was slightly reduced due to its temperature dependence.

The scanning electron microscopy (SEM) images, including the chemical element distribution across the interface of the steel matrix doped with ZrO_2, showed that there

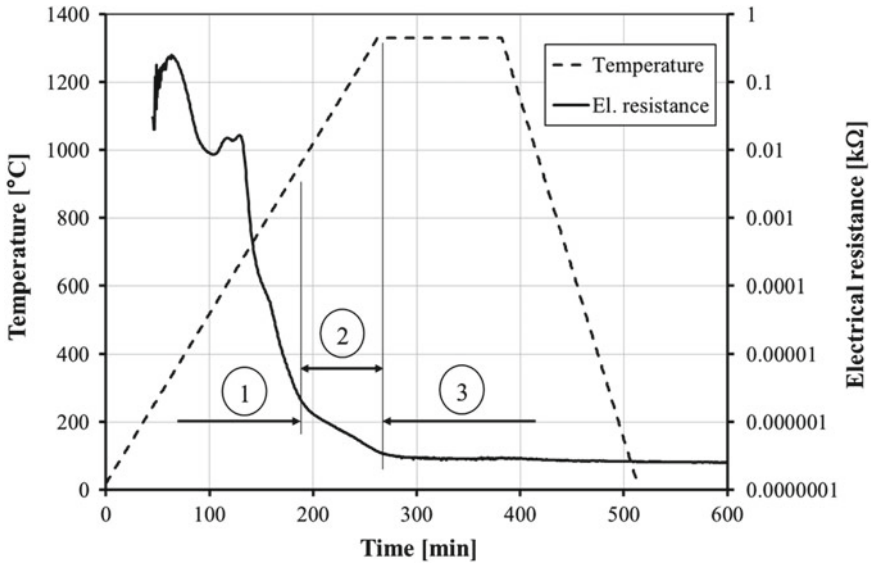

Fig. 6.3 Electrical resistance of the composite material with 5% ZrO_2 during conventional sintering

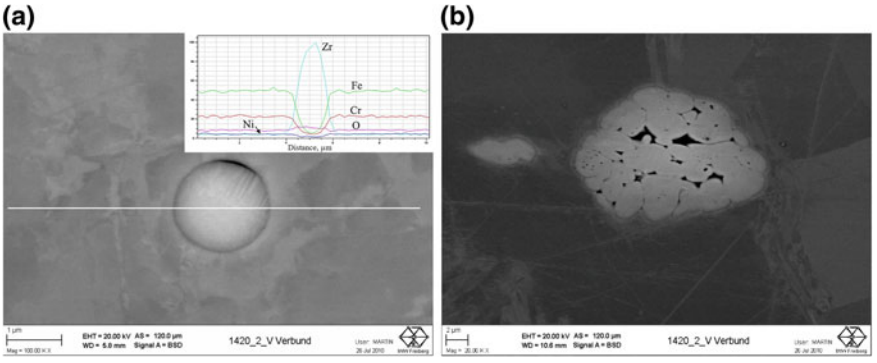

Fig. 6.4 Bonding between the ceramic and steel matrix for a composite with 2.5% ZrO_2 sintered at 1420 °C for 2 h for a single ceramic particle (**a**) and a ceramic agglomerate (**b**)

was a good bond between the ceramic particles and the matrix after sintering, while individual particles in the ceramic agglomerates were poorly sintered together due to the sintering temperature being too low for ceramic constituents (Fig. 6.4). The agglomerate formation of the ceramic particles in the cavities of the steel matrix was caused by a significant size difference between the steel and ZrO_2 powder particles. Furthermore, an increase in the sintering temperature of up to 1430 °C led to the formation of undesired Al–Mn–Mg-rich areas within the ceramic phase due to diffusion processes through the steel-ceramic interface [23].

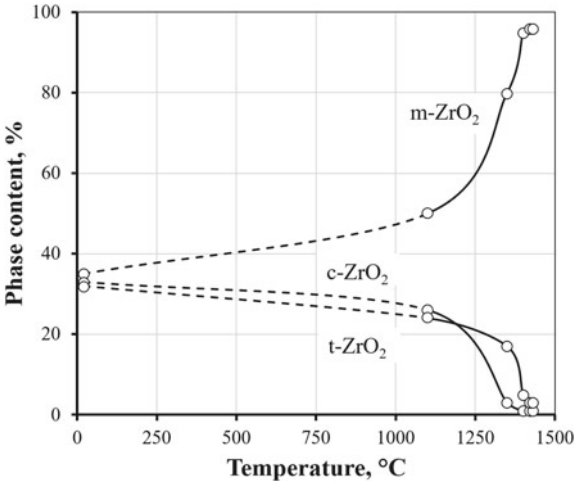

Fig. 6.5 Influence of the sintering temperature on the phase composition of ZrO_2 for the composite material with 5% ZrO_2 sintered in vacuum

The variation of the sintering atmosphere indicated that sintering under vacuum achieved a higher material density than that upon sintering in argon or nitrogen atmospheres. This resulted from practically no gas molecules being present in the pores, which facilitated the rapid shrinkage of the pores. After vacuum sintering, the material had fine pores with a high pore shape factor. However, the disadvantage of vacuum sintering lies in the evaporation of alloying elements from the steel matrix, such as C and Mn, which influenced the austenite stability, the characteristic temperatures of the martensite transformation (M_s, M_f) and finally the associated mechanical properties.

Furthermore, the negative influence of a high sintering temperature on the phase composition of the ceramic constituent was determined [24]. The exemplary results for the composite material with 5% ZrO_2 are shown in Fig. 6.5. It can be seen that increasing the sintering temperature led to an increased content of the undesired m ZrO_2 phase (m-ZrO_2) at the expense of the c (c-ZrO_2) and t (t-ZrO_2) phases, which were reduced.

The sintering of composite materials with varied ZrO_2 content showed that the density of the steel matrix doped with 2.5% ZrO_2 was similar to that of the undoped steel but with a slight deviation of up to 2% depending on temperature and time, while the material with 5% ZrO_2 had a density value similar to that for the composite with 10% ZrO_2. The increase in ZrO_2 content of up to 10% caused a density increase and associated microstructural developments in the composite materials. The ceramic particles became settled in cavities between the steel particles, which caused, among other things, a decrease in the porosity. An additional increase in the ZrO_2 content of up to 30% led to the formation of large ceramic particle agglomerates outside the cavities, which had an unfavorable effect on the densification process and thus on the density of the specimen (Fig. 6.4). Therefore, Fig. 6.6 shows the density of the undoped steel and composite materials with 10 and 30% ZrO_2 as a function of the sintering temperature and time. The steel matrix doped with 30% ZrO_2 had the lowest

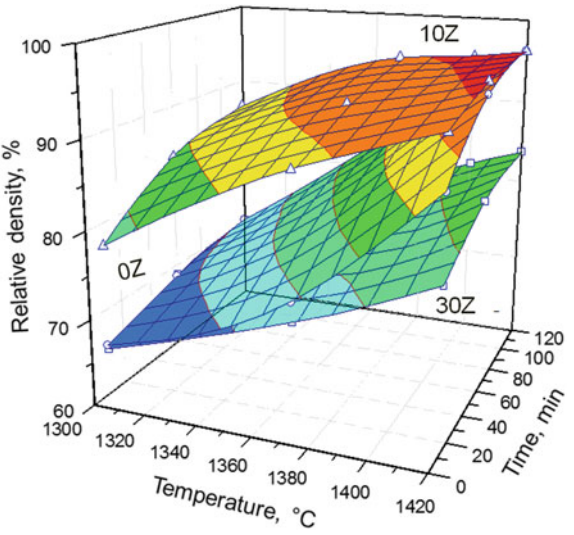

Fig. 6.6 The relative density of the vacuum-sintered steel (0Z) and composite materials with 10% (10Z) and 30% ZrO_2 (30Z) as a function of the sintering time and temperature

density values herein over the entire investigated time and temperature ranges. After sintering at 1300 °C, its density values were almost as high as those of the undoped steel, regardless of the sintering time. However, a further increase in temperature increased the density difference by up to approximately 13%. The maximum density was 85%. The relative density increase in the steel in the investigated temperature and time ranges was approximately 30%, while that of composite materials was a maximum of 20%. Among the materials investigated over the entire temperature and time ranges herein, the 5 and 10% ZrO_2 composites had the highest relative densities. Thus, the optimal sintering conditions from the point of view of the relative density were determined for the composite materials with a ceramic content of up to 10% ZrO_2. These optimal results were obtained at the temperature of 1420 °C and sintering times of 1–2 h. Under these circumstances, the composite materials with 5 and 10% ZrO_2 after sintering showed a maximum radial shrinkage of approximately 24% compared to that of approximately 18% for the undoped steel.

The results of subsequent modeling were able to show that the applied physical-empirical approach with regard to the ZrO_2 content (6.3) reflected the obtained experimental results sufficiently well (Fig. 6.7). Among the samples herein, the maximum density was observed for a composite with approximately 10–15% ZrO_2. As expected, the density increased with increasing sintering temperature. Figure 6.7b provides an example of how the relative density was influenced by the sintering time for a sintering temperature of 1420 °C and for ZrO_2 contents up to 30%. It is obvious that the ZrO_2 content caused a relative density decrease that reached approximately 13%.

The good validation agreement between the experimental results and the modeling values made it possible to quantify the densification rate of composite materials by a derivation of (6.3) over time. Figure 6.8 shows an exemplary of the densification

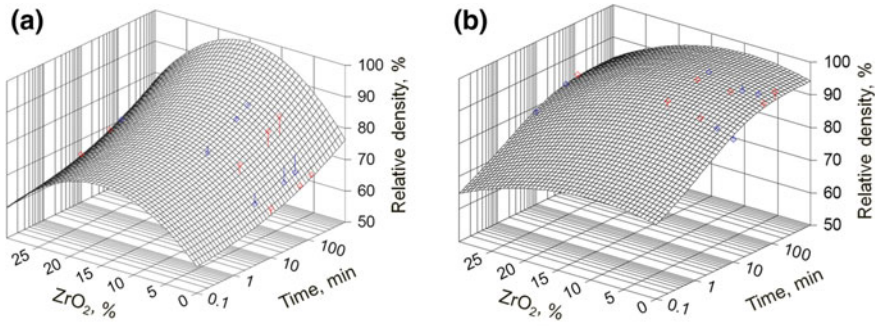

Fig. 6.7 Modeling results for the relative density development in relation to the ZrO_2 content and the sintering time at sintering temperatures of 1300 °C (**a**) and 1420 °C (**b**). The experimental results are marked with dots

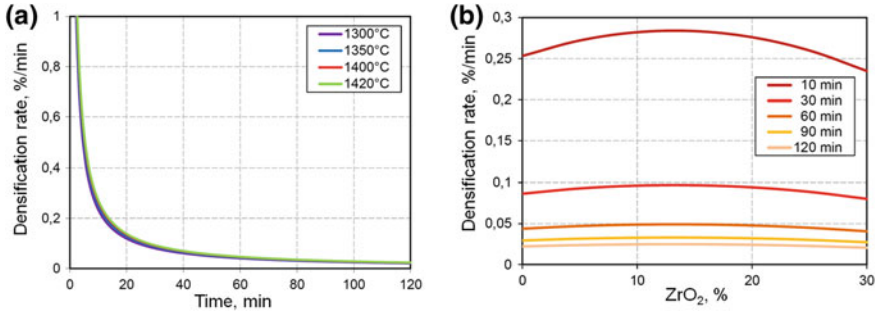

Fig. 6.8 Densification rate of the composite material with 5% ZrO_2 as a function of the sintering temperature and time (**a**) and the ZrO_2 content at the sintering temperature of 1420 °C (**b**)

rate for a composite material with 5% ZrO_2 as a function of the sintering temperature and time. Figure 6.8a shows, for example, that the densification rate at the beginning of sintering rapidly decreased from very high values to rates below 0.1%/min within a few minutes, while the dependence on temperature was comparatively very low. The sintering process was thus almost completed after a sintering time of 2 h, and it was confirmed that an optimum was achieved with regard to both the advantageous material properties and fabrication effort.

It can also be seen that the densification rate in the investigated temperature range showed a low dependency on the ZrO_2 content (Fig. 6.8b). The composite material with approximately 15% ZrO_2 content had the maximum densification rate among the samples herein at the experimentally realized shortest sintering time of 10 min, while the material with 30% ZrO_2 showed the lowest densification rate at the same time. Furthermore, the results indicate that the densification rate at sintering times of approximately 1 h and above is practically independent of the ZrO_2 content.

Figure 6.9 shows the mechanical properties of the sintered composites as a function of the relative density and ceramic phase content. It is obvious that while the

tensile strength was linearly dependent on the relative density (Fig. 6.9a), the dependence of the total elongation had an exponential relationship (Fig. 6.9b). The increasing in the ceramic content tended to contribute to an increase in the tensile strength, while its large values presented a decrease in the tensile strength due to the increasing tendency of the ceramic to form agglomerates.

The investigation of the fracture surfaces of the undoped tensile specimens revealed that two fracture phenomena occurred depending on the sintering temperature: a prevalent intergranular failure at 1330 and 1350 °C (Fig. 6.10a) and a ductile fracture with a characteristic void structure at 1400 °C (Fig. 6.10b). The microscopic relief of the fracture surfaces in the investigated temperature range essentially depended on the porosity, which was adjusted by the sintering temperature and sintering time. Residual pores and nonmetallic inclusions in the SiO_2 and MnO are also visible on the fracture surface since crack propagation through these areas was facilitated.

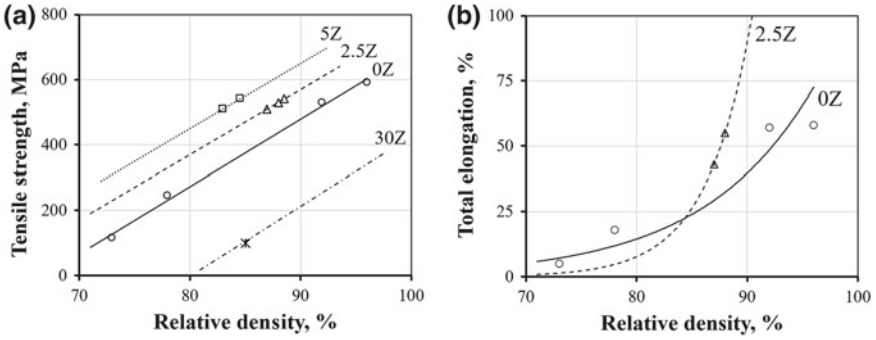

Fig. 6.9 Tensile strength (**a**) and total elongation development (**b**) for steel (0Z) and composite materials (from 2.5 to 30Z) after conventional sintering under vacuum

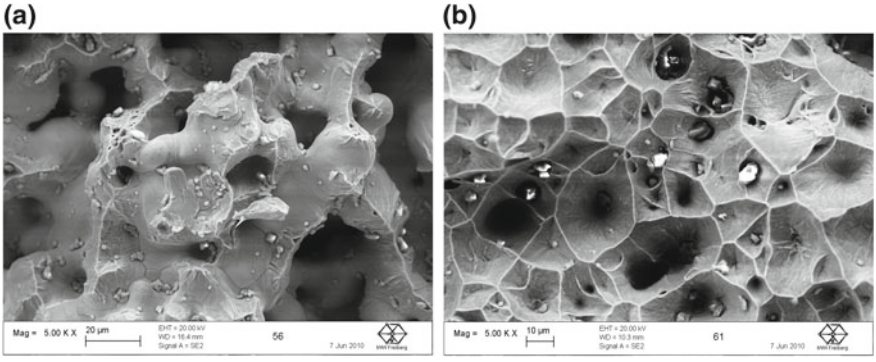

Fig. 6.10 The fracture surfaces for steel samples sintered under vacuum for 2 h at sintering temperatures of 1350 °C (**a**) and 1400 °C (**b**)

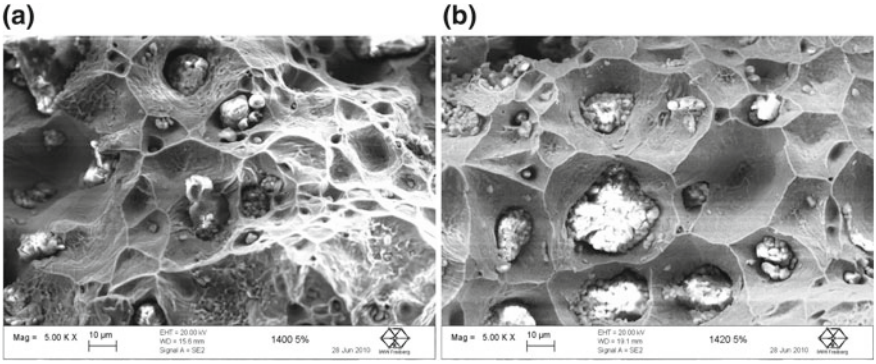

Fig. 6.11 The fracture surfaces for a composite material with 5% ZrO_2 sintered under vacuum for 2 h at sintering temperatures of 1400 °C (**a**) and 1420 °C (**b**)

The SEM images of the fracture surfaces of the composite material with 5% ZrO_2 show a similar failure behavior to that the an undoped steel matrix (Fig. 6.11). Here, single embedded ceramic particles and agglomerates are visible in the austenitic matrix. Pores can be seen in the area between the two phases. In addition, there are visible ZrO_2 particles on the fracture surface, like nonmetallic inclusions and pores, that represent the most favorable places for crack initiation and propagation.

The fracture behavior of MMCs with up to 5% ZrO_2 after tensile loading was influenced by the relative density and associated strength and ductility. Thus, the MMCs with up to 7% residual porosity showed ductile fracture behavior, which was caused by the void formation mechanism and the coalescence of the micropores. The fracture occurred along the grain boundaries near the residual pores in the steel matrix or near the ZrO_2 particles in the MMCs. This effect can be explained by the inhomogeneous distribution of the stress and strain fields due to the mechanical loading of the porous material. The stresses were more likely to be located in the interface region between the grain boundary and the pore than elsewhere since the radius there was minimal. As the sintering temperature increased and the sintering time increased, the material densified to a certain extent while the porosity was eliminated. In the final stage of the sintering process, when only closed pores were present in the microstructure, the intracrystalline pores were formed. The disadvantage of intracrystalline pores is that they can be reduced neither in number nor in size due to the low activation energy for volume diffusion. The advantage is that the intracrystalline pores can be spherical, and spherical pores have a lower stress concentration than that of other shapes, and thus they had a decreased tendency to form notches.

6.3.2 Resistance Sintering

Figure 6.12 shows the temperature and force trends during a stroke-controlled sintering process of the TRIP-matrix composite with 5% ZrO_2. The process consisted of three stages [25]. In the first stage, there was a temporary increase in the force for a time up to approximately 400 s, where in the middle of the sample, the temperature increased to 950 °C. This force increase was due to the thermal expansion of the sample and tools. The immediately following second stage is characterized by a reduction in the force with a corresponding large specimen shrinkage and decrease in the porosity. Finally, in the third and final stage, the shrinkage slowed dramatically, which was reflected in the force stabilizing at a constant level. During the entire sintering process, the electrical resistance decreased almost continuously to a few mΩ.

Metallographic analysis for the center of a densely sintered composite material showed an average grain diameter of $d_{50} = 9.6\ \mu m$ (Fig. 6.13a). Such a fine-grained microstructure resulted from both the mechanical alloying technique and the short residence time at the sintering temperature, where the resistance sintering was dominant. In the high-magnification SEM images, good bonding of the ZrO_2 particles to the steel matrix can be seen in addition to individual residual pores on the phase interface (Fig. 6.13b). In contrast, the ceramic particles in the agglomerates demonstrated a poor local bonding quality.

However, the microstructure of sintered samples sectioned across their median showed sufficient inhomogeneities (Fig. 6.14). The highest obtained relative density of approximately 99% was reached in the middle of the sample at the side of the

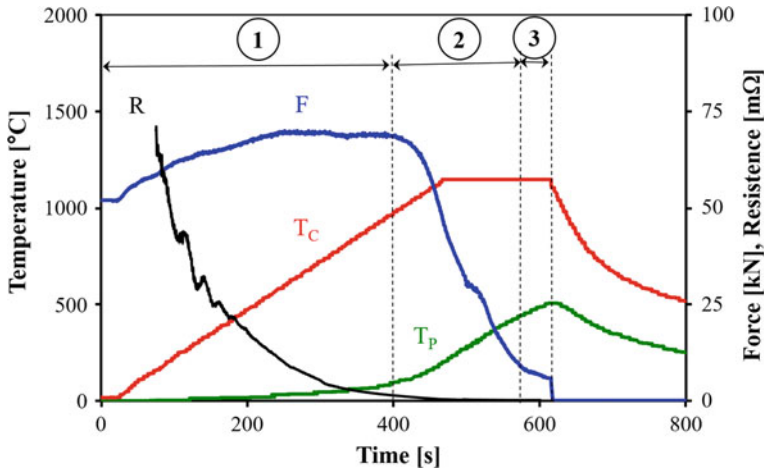

Fig. 6.12 Development of the electrical resistance R and the force F during a stroke-controlled resistance sintering process of the TRIP-matrix-composite with 5% ZrO_2 (T_C and T_P are the temperatures in the center of the sample and on the punch working surface, respectively)

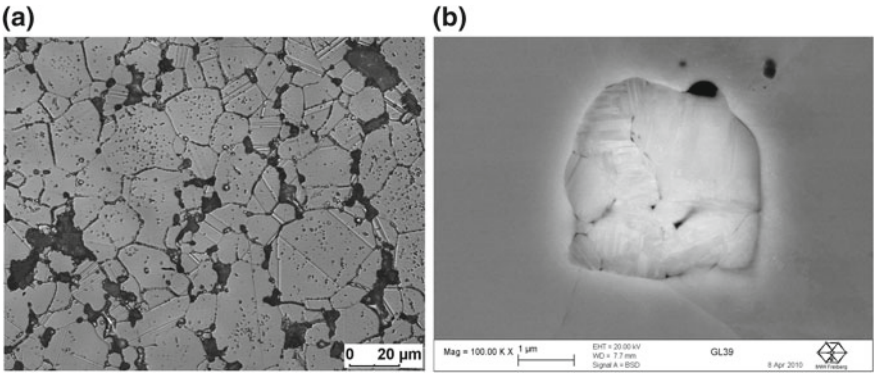

Fig. 6.13 Light microscopy image for a composite sample with 5% ZrO_2 sintered at 1100 °C for 11 min (**a**) and SEM image of the resulting bonding between ZrO_2 particles agglomerate and the steel matrix (**b**)

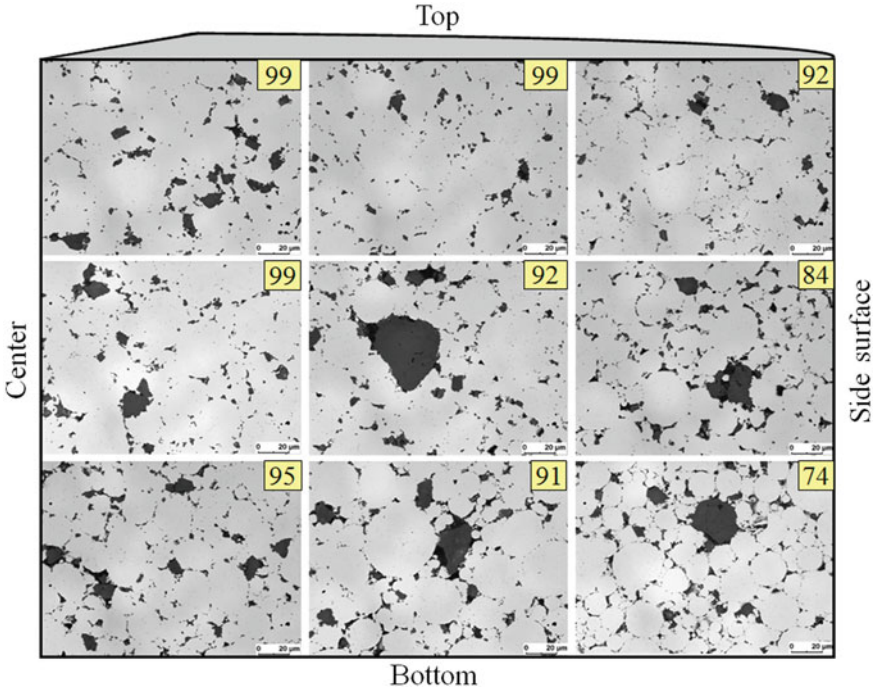

Fig. 6.14 Inhomogeneity of the sintered microstructure shown by a quarter cut of a 5% ZrO_2 composite sample. The numbers in the square represent the local relative density measured in %

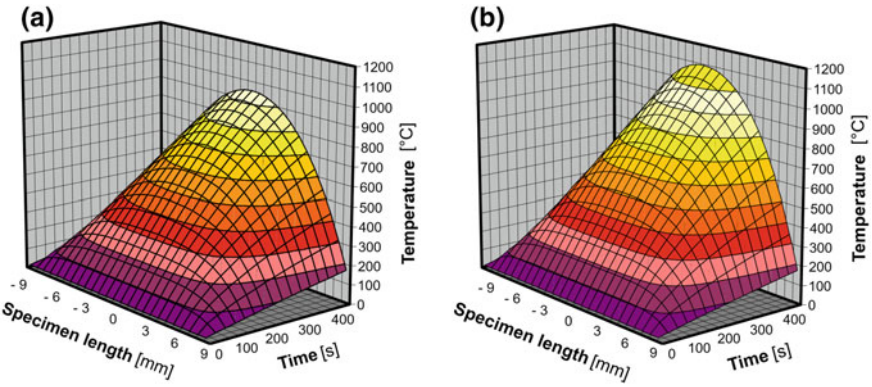

Fig. 6.15 Temperature evolution in a sintered sample with 5% (**a**) and 20% ZrO_2 (**b**) as a function of the sintering time for an electrical current value of 290 A

punch (top). These values then decreased in the direction of the side surface of the sample and the water-cooled bottom panel as a result of heat dissipation.

Since the microstructure evolution depended essentially on the temperature distribution in the sample, an analytically closed solution in the form of a Fourier series was searched for by mathematical means and solved numerically for the implemented sintering conditions with regard to the temperature profile [26]. The plot in Fig. 6.15a shows the distribution of the temperature field that arose in a sintered sample with increasing sintering time for an electrical current value of 290 A. The sintered material used here was a mixture of the steel powder with 5% ZrO_2 powder. This clearly shows that a temperature gradient of approximately 800 K between the side surface and the center of the sample accumulates after 400 s. When the ZrO_2 content increased to 20% and the same electrical current value was maintained, the heating process correspondingly increased due to the increased electrical resistance. This led to a temperature increase of 150 K in the center of the sample (Fig. 6.15b). At the same time, however, the temperature gradient increased, and the microstructure became even more inhomogeneous.

The evolution of the mechanical properties of the resistance sintered samples was similar to that of the conventionally sintered samples. Figure 6.16a shows the local macrohardness measured over the sample cross section as a function of the relevant relative density. The dependence represents a linear relationship. The increase in the nonconductive ZrO_2 phase content from 5 to 20% drastically influenced the conductive sintering process since the electrical current only flowed through the steel matrix. Thus, the individual ZrO_2 particles in the ceramic agglomerates were not attached to each other. This led to a decrease in the macrohardness. The tensile strengths calculated from the macrohardness values using the correction factor of 3.3 are shown in the plot in Fig. 6.16b. The small differences in the development of the mechanical properties for conventional and resistance sintered specimens were due, on the one hand, to the chemical composition of the initial powders and; on the

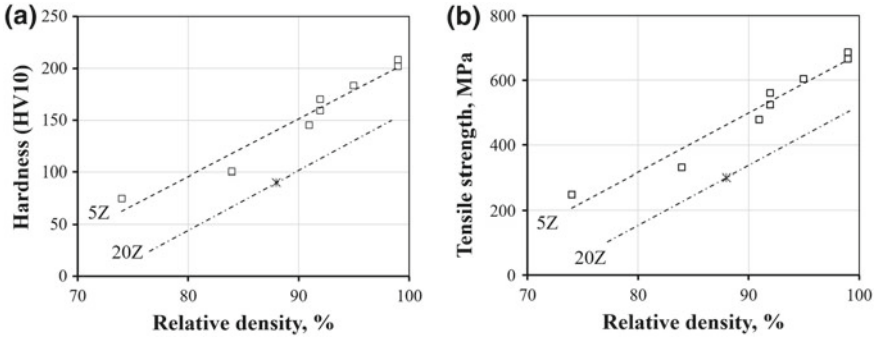

Fig. 6.16 Measured macrohardness (**a**) and calculated tensile strength (**b**) for composite materials with different ZrO_2 contents after resistance sintering under vacuum

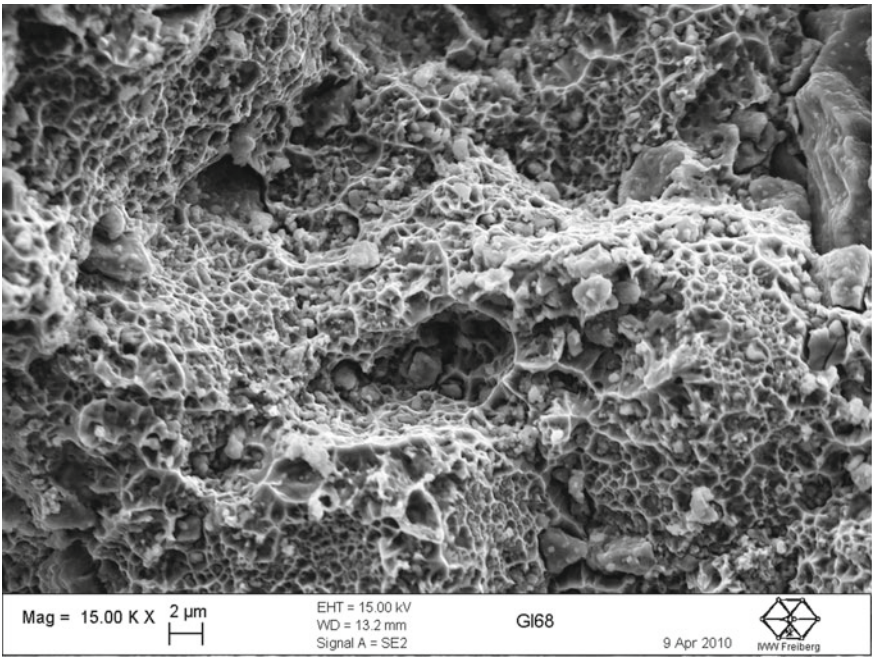

Fig. 6.17 Fracture surface of a composite sample with 5% ZrO_2 sintered at 1100 °C for 11 min

other hand, they were due to the different thickness of the surface oxide layer on the particles, which was influenced by the mechanical alloying technique since the particle size distribution of the powders was the same.

The fracture surface of a sintered sample with 5% ZrO_2 is shown in Fig. 6.17. The fine-grained void structure of the austenite with embedded ZrO_2 particles can be observed.

6.3.3 Hot Pressing

Figure 6.18 shows the microstructure of the composites with 5% and 10% ZrO_2 as a function of the HP temperature. According to the figure, the microstructure consists of austenite grains (light gray) with pronounced twins, PSZ (dark gray) and residual pores (black). A quantitative evaluation of the microstructure indicated that

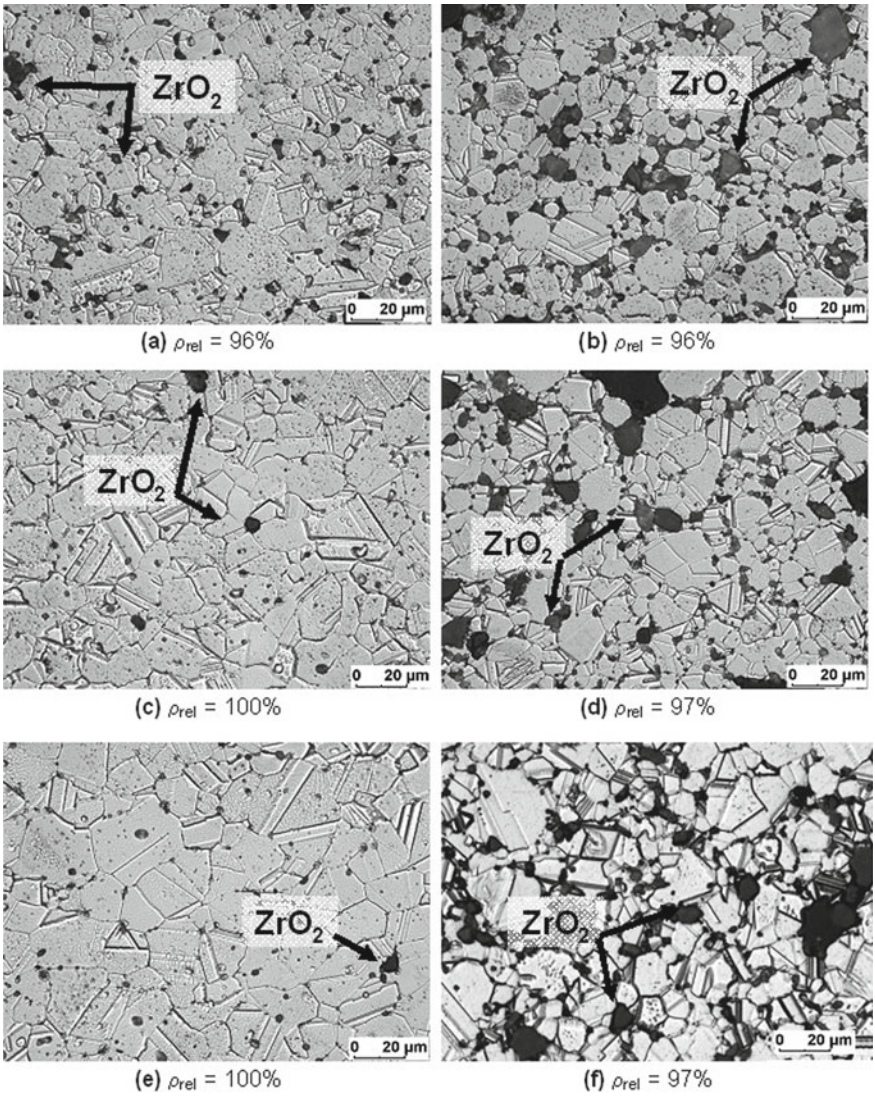

Fig. 6.18 **a**, **c**, **e** microstructure evolution of composites with 5% and **b**, **d**, **f** 10% ZrO_2 after HP by the 2nd method at (**a**, **b**) 1100 °C, (**c**, **d**) 1200 °C and (**e**, **f**) 1250 °C

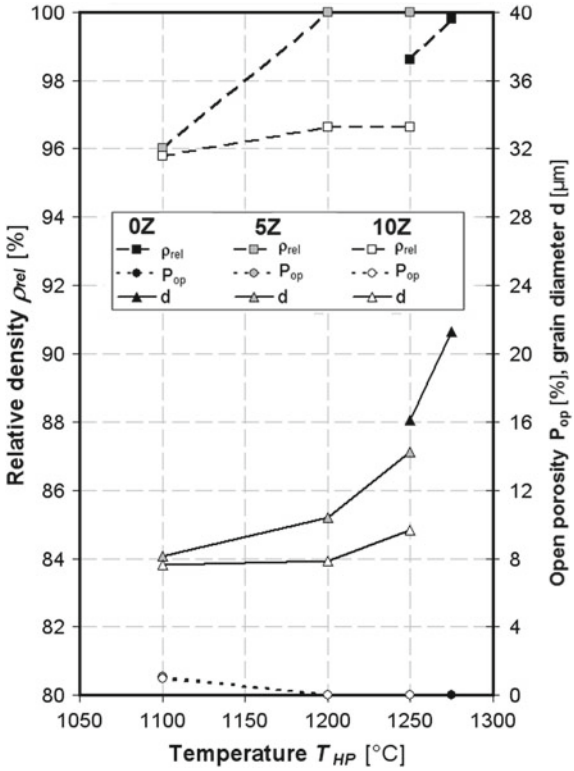

Fig. 6.19 Relative density, open porosity and average grain size produced by the 2nd precompaction method for fabricating composites as a function of the HP temperature

an increase in the HP temperature led to a decrease in the residual porosity and growth of austenitic grains (Fig. 6.19). For all investigated ceramic contents in the steel matrix, the absence of open pores in the samples was observed beginning at the HP temperature of 1200 °C. While the theoretical density of the undoped steel matrix was only achieved at 1275 °C, the addition of 5% ZrO_2 into the powder mixture had a positive effect on the reduction of the required HP temperature by 25 K. The presence of ceramic components in the mixture also had a significant effect on the reduction of the austenitic grain growth. For example, when 10% ZrO_2 was added, the size of the austenite grains at a HP temperature of 1250 °C was reduced by approximately half compared to that of the undoped steel matrix.

The investigations showed that the same HP conditions for composites with 5% ZrO_2 according to the 1st and 2nd precompaction methods to compress the powder mixture into billets without HIP had a different effect on the size of austenitic grains and final relative density of the finished part (Table 6.4). The presintering operation led to an increase in the relative density of the finished part at the expense of the austenite grain growth, which increased by approximately 25%.

To increase the relative density of the undoped steel samples pressed by the 2nd precompaction method at 1250 and 1275 °C to their theoretical value, they were subjected to a final HIP at 1225 °C at a pressure of 100 MPa. The results of the

Table 6.4 Relative density and average grain size of the composite with 5% ZrO_2, hot pressed at 1250 °C according to the 1st and 2nd precompaction methods that compact the powders without HIP

Method	ρ_{rel} (%)	d (μm)
1st	98.6	11.5
2nd	100	14.3

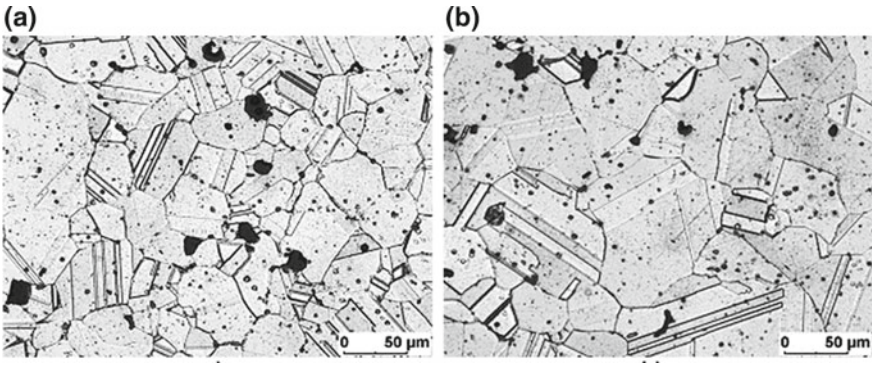

Fig. 6.20 Microstructure development after HP by the 2nd precompaction method at 1250 °C without (**a**) and with a final HIP operation at 1225 °C (**b**)

Table 6.5 Influence of the post-HIP operation on the relative density and the average grain diameter of the undoped steel powder mixture after HP by the 2nd HP precompaction method

HP temperature, °C	After HP		After post-HIP	
	ρ_{rel} (%)	d (μm)	ρ_{rel} (%)	d (μm)
1250	98.6	16.1	100	44.1
1275	99.8	21.3	100	48.3

microstructural analysis showed that as a result of an additional thermomechanical treatment, there was significant growth of the austenitic grains (Fig. 6.20). Despite the complete densification of the samples, the grain size more than doubled (Table 6.5). A similar effect was also observed in [27] on the same material.

The analysis of the mechanical properties of hot-pressed composites was based on the already observed linear dependence of the tensile strength and exponential dependence of the total elongation on the relative porosity of the material. As shown in Fig. 6.21, the extrapolation of the results into the area of low relative porosity correlated well with the previous results obtained by conventional and resistance sintering of the composites. The insignificant deviations are due to differences in the initial chemical composition of the powder mixture. A comparison of the mechanical properties of the composites with 5 and 10% ZrO_2 shows that a material with 10% ZrO_2 shows increased strength values and decreased total elongation.

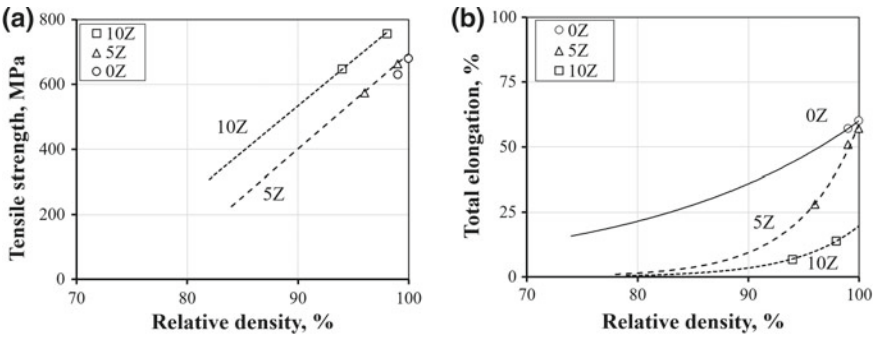

Fig. 6.21 Influence of the relative density of composites with 0% (0Z), 5% (5Z) and 10% ZrO_2 (10Z) on the tensile strength (**a**) and total elongation (**b**) after fabrication by HP according to the 2nd method of precompaction

The results of the tensile tests for samples with 5% ZrO_2 by the 1st method of precompaction of the powder mixture into billets indicated a total elongation that decreased by 3 times and an insignificant reduction in the strength; the tensile strength, in particular, was reduced by 1.4 times. The mechanical properties of the undoped steel specimens subjected to the final HIP operation showed that the additional technological step led to a reduction in the yield strength by more than 20% and tensile strength by 1.5 and 3% while increasing the total elongation by 6 and 18% in accordance with the HP temperature [28].

The results of the impact toughness measurements of the composites with 5% ZrO_2 showed an increase from 9 to 37 J in the investigated range of HP temperatures [29]. At the same time, the composite with 10% ZrO_2 remained brittle because its impact toughness values did not exceed 5 J. The results of the impact toughness measurement on the samples fabricated by the 1st precompaction method also showed lower values than that of the 2nd precompaction method over the whole investigated temperature range. For example, the impact toughness values of the composite with 5% ZrO_2 showed a decrease of nearly 4 times to 10 J in the case of the 1st method of precompaction.

Figure 6.22 shows the fracture surfaces of the hot-pressed samples after tensile testing. The precompaction of the powder mixture was carried out by the 2nd method at the HP temperatures of 1100 and 1250 °C. A common feature of the fracture surfaces for the composite with 5% ZrO_2 was the ductile nature of the failure with individual brittle ceramic particles. The higher HP temperature of 1250 °C enabled a high elongation of the sample and the production of inhomogeneous and deep dimples on the ductile fracture surface (Fig. 6.22c). The increase in ZrO_2 content led to a decrease in the fraction of ductile fracture over the entire investigated HP temperature range. In the fractures of the composite with 10% ZrO_2, finely dimpled and mixed failure areas along the phase boundaries corresponding to low ductility are observed (Fig. 6.22b, d).

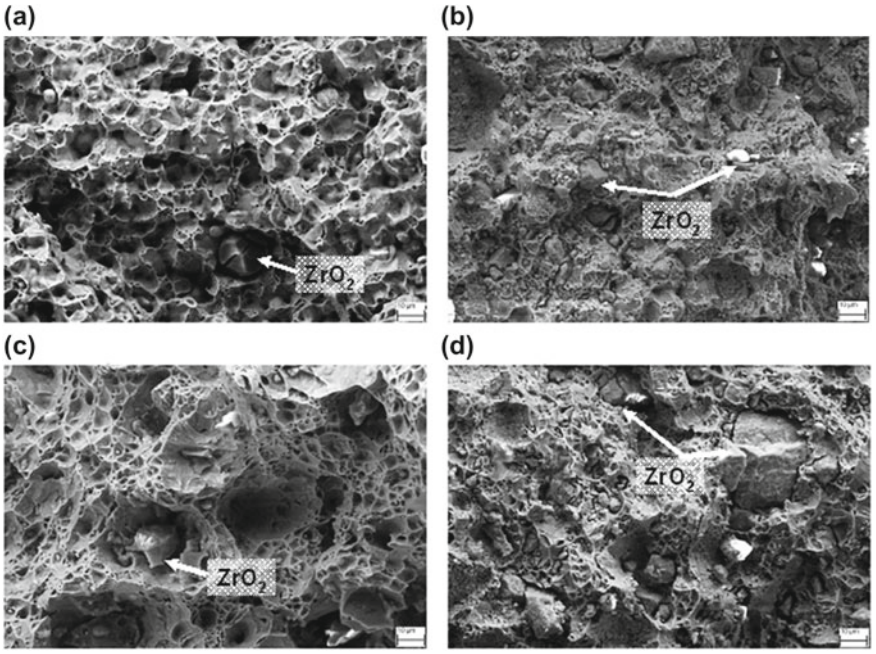

Fig. 6.22 Fracture surfaces of the hot-pressed composites with 5% ZrO_2 at (**a**) 1100 °C and (**c**) 1250 °C. Fracture surfaces of the composites with (**b** and **d**) 10% ZrO_2 hot pressed by the 2nd precompaction method

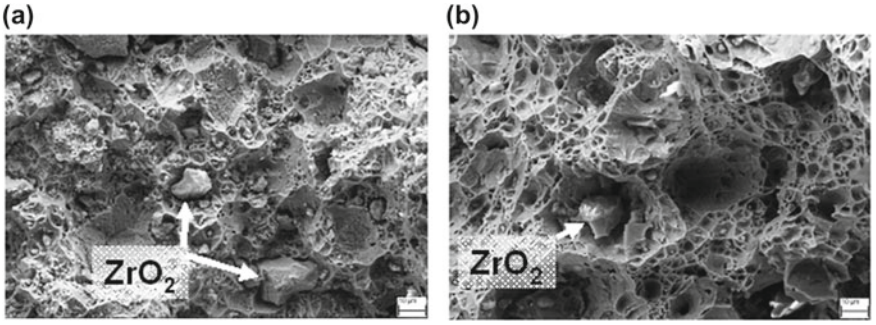

Fig. 6.23 Fracture surfaces of hot-pressed composite with 5% ZrO_2 by 1st (**a**) and 2nd precompaction methods (**b**)

A comparison of the fracture surfaces for the composite with 5% ZrO_2 after HP at 1250 °C showed that the samples precompacted by the 1st method (Fig. 6.23a) are characterized by a mixed failure mode and differ significantly from the ductile dimpled structure of the samples precompacted by the 2nd method (Fig. 6.23b).

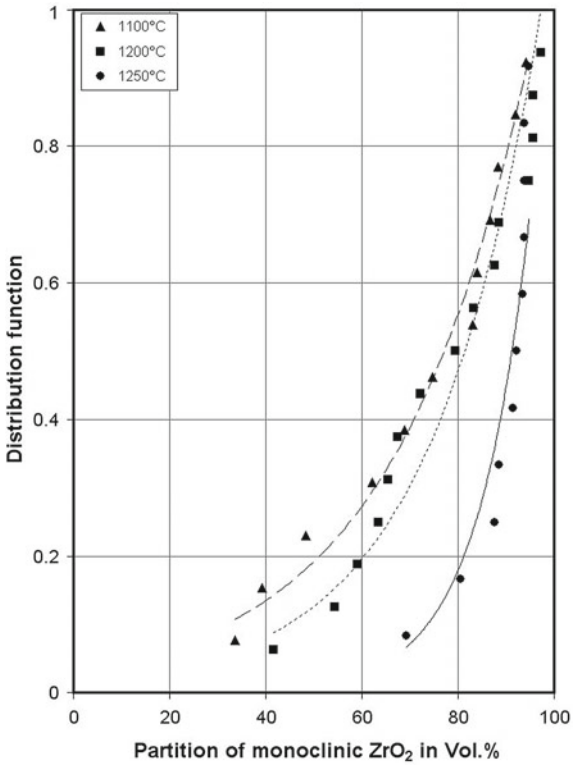

Fig. 6.24 Influence of the HP temperature (2nd precompaction method) on the amount of m-ZrO_2 in the composite with 10% ZrO_2

Figure 6.24 shows that the distribution of the m-ZrO_2 crystallographic phase in a composite with 10% ZrO_2 depended on the HP temperature. The results indicate that the distribution function of the ceramic particles that underwent transformation into the monoclinic phase had an exponential dependence [30]. The increase in the HP temperature led to the displacement of the 20% quantile toward an increase in the m-ZrO_2 content. A similar tendency in the slightly smoothed form is also observed for the 50% quantile, whose values increased from 79 to 92% with increasing HP temperature.

6.4 Conclusions

In this work, the densification behavior and final mechanical properties of TRIP-matrix composites were investigated. The composites were based on 1.4301 stainless steel powder, which was available in the form of three batches with slight differences in their chemical composition and contained up to 30% MgO-PSZ. The materials were fabricated using three different PM consolidation processes: conventional sintering, resistance sintering and HP. In the case of resistance sintering, a special tool

was designed and optimized to achieve low heat dissipation from the specimen. The microstructure evolution and material properties along each consolidation route were compared to each other. The experimental analysis of the densification kinetics was based on electrical resistance measurements and microstructure evaluation. It was shown that the chemical composition of the steel matrix had a significant influence on the optimum sintering temperature among the investigated sintering technologies.

Experimental investigations of resistance sintering have shown that increasing the presintering and sintering pressures and decreasing the heating rate result in an elevated density of the material. The sintering residence time for composites with a high ZrO_2 content should be extended compared to those with a low ZrO_2 content since the ZrO_2 content delays the consolidation process.

The investigations on HP showed an almost optimal production route, namely, by CIP, subsequent presintering at 1100 °C for 1 h and then HP. The HIP treatment has proven to be ineffective for the postcompaction of hot-pressed samples.

During conventional sintering, the dependence of the composite density on the sintering temperature and sintering time as well as on the ZrO_2 content was quantified by means of a physical-mathematical approach and experimentally supported modeling. It was shown that the densification rate in the investigated temperature range had a low dependency on the ZrO_2 content. The temperature distribution and evolution in the sintered material during resistance sintering was determined based on the physical-mathematical equations as a function of the electrical current value, the sample geometry and the ZrO_2 content. The modeling provided the basis for the densification kinetics and the local character in the composite specimen volume.

A fine austenite microstructure and higher density and tensile strength was achieved with the optimized HP route (2nd precompaction method) and presented a better combination of properties than those of conventional and resistance sintering. Furthermore, low sintering temperatures and short sintering times made the optimized process favorable. The optimally determined HP parameters are 1250 °C with a holding time of 30 min to 1 h and pressure of 30 MPa.

Furthermore, it was shown that the mechanical properties of the consolidated composites primarily depended on the relative density of the material and the ceramic content in the composite. Here, a linear correlation of the tensile strength and an exponential correlation of the total elongation with the relative density of the material was observed. There was no significant influence of the consolidation technique on these mechanical properties. The insignificant deviations could be explained by differences in the initial chemical composition of the powder mixture. With a particle content of approximately 10–30% ZrO_2, strength increases of up to approximately 40% were found. An increase in the tensile strength was accompanied by a decrease in the total elongation. The obtained dependences partially exceeded the mechanical properties of the particle-reinforced composites with a light metal matrix [31]. However, an increasing ZrO_2 content up to 20% caused early failure of the composite under tensile loading due to the formation of ceramic agglomerates with poor bonding to the ZrO_2 particles. Therefore, the best mechanical properties require sufficient

fineness of the ceramic particles (<10 μm) and a uniform distribution as well as good bonding into the steel matrix and low destabilization of the t-ZrO_2 crystallographic modification.

Finally, it was shown that the content of m-ZrO_2 increased with increasing sintering temperature. The increase in the impurities in the ceramic powder caused a greater initial destabilization of the metastable t-ZrO_2 crystallographic phase. In contrast, the influence of the PM consolidation processes investigated in this research on the m-ZrO_2 content had a secondary effect.

Acknowledgements The authors are grateful to the employees of the Institute for Metal Forming (*) and of the Fraunhofer Institute for Ceramic Technologies and Systems (**), who participated in the powder compaction processes: Dr.-Ing. Anna Yanina (*), Dr.-Ing. Werner Jungnickel (*), Dr.-Ing. Wolfhart Müller (*), Dr. rer. nat. habil. Mathias Herrmann (**) and Dipl.-Ing. Jan Räthel (**). Special thanks are addressed to Dr. rer. nat. Dr.-Ing. habil. Harry Berek for the SEM investigations. The authors gratefully acknowledge the German Research Foundation (DFG) for supporting the Collaborative Research Center TRIP-Matrix-Composites (Project number 54473466—CRC799 subproject A6).

References

1. E.C. Bain, The nature of martensite. Trans. Am. Inst. Min. Metall. Eng. **70**, 25–46 (1924)
2. S.P. Buyakova et al., Механическое поведение пористого диоксида циркония при активной деформации сжатием. Pisma v JETF **25**, 44–48 (1999)
3. A.G. Bratuhin et al., Высокопрочные коррозионно-стойкие стали современной авиации (MAI, Moscow, 2006)
4. Y.G. Jung, U. Paik, S.C. Choi, Influence of the particle size and phase type of zirconia on the fabrication an residual stress of zirconia/stainless steel 304 functionally gradient material. J. Mater. Sci. **34**, 5407–5416 (1999)
5. W. Zhang, J. Xie, C. Wang, Fabrication of multilayer 316L/PSZ gradient composite pipes by means of multi-billet extrusion. Mater. Sci. Eng. A **383**, 371–377 (2004)
6. M. Wildan, H.J. Edrees, A. Hendry, Ceramic matrix composites of zirconia reinforced with metal particles. Mater. Chem. Phys. **75**, 276–283 (2002)
7. J. Abenojar et al., Atmosphere influence in sintering process of stainless steels matrix composites reinforced with hard particles. Compos. Sci. technol. **63**, 69–79 (2003)
8. L.O. Andryschik et al., Влияние параметров спекания на структуру спеченного электроконтактным нагревом порошкового хрома. In: Порошковая металлургия (1989)
9. K. Feng et al., Rapid sintering of iron powders under action of electric field. Powder Metall. **48**, 203–204 (2005)
10. O.V. Konstantinova et al., Численное моделирование влияния соотношения размеров частиц проводящей и изолирующей фаз на проводимость композитов типа проводник-изолятор порошкового происхождения. Порошковая металлургия **1/2**, 31–40 (2005)
11. J.E. Geguzin, Physik des Sinterns Deutscher Verlag für Grundstoffindustrie, 1973
12. Y. Zhou et al., Effects of load mode on mechanical properties of ZrO_2(2Y)/TRIP steel composites. Trans. Nonferr. Met. Soc. China **13**, 1086–1091 (2003)
13. H.L. Yakel, Atom distributions in sigma phases. Acta Cryst. **39**, 20–28 (1983)

14. Y. Yamada et al., Effect of debonding at the phase interface on Young's modulus in sintered PSZ/stainless steels composites. Mater. Trans. JIM **35**, 814–820 (1994)
15. Y.-G. Jung, U.-G. Paik, Residual stress and thermal properties of zirconia/metal (nickel, stainless steel 304) functionally graded materials fabricated by hot pressing. J. Mater. Sci. **32**, 3841–3850 (1997)
16. L.Z. Liang et al., Characteristics of complicated AISI 316L automobile components manufactured by powder metallurgy. J. Mech. Sci. Technol. **23**, 1924–1931 (2009)
17. Z.L. Lu et al., Investigation into the densification of AISI 304 parts fabricated by hybrid powder metallurgy techniques. Indian J. Eng. Mater. Sci. **17**, 49–55 (2010)
18. C. Suryanarayana, E. Ivanov, V.V. Boldyrev, The science and technology of mechanical alloying. Mater. Sci. Eng. **304–306**, 151–158 (2001)
19. W. Müller, Temperaturverhältnisse und Reaktionskinetik beim Ziehen und Wärmebehandeln von Draht. Bd. B292 (TU Bergakademie Freiberg, 1998)
20. S. Guk, A. Yanina, R. Kawalla, Ch. Aneziris, W. Schärfl, Ch. Weigelt, Bewertung und Vorhersage von mechanischen Eigenschaften und Porosität von Metall-Keramik-Compositen mit Zirkoniumdioxid, in *Proceedings of the 2nd International Conference* "*Pavlovs lectures*" in Baikov Institute of Metallurgy and Materials Science (IMET) Moskau der russischen Akademie der Wissenschaft (RAN) 2–627. Oktober 2010, pp. 504–511
21. A. Yanina, S. Guk, R. Kawalla, Ch. Aneziris, W. Schärfl, Ch. Weigelt, Einfluss der Sinterparameter auf die Sinterkinetik und mechanische Eigenschaften von MMC, in *Proceedings of the 2nd International Conference "Pavlovs lectures"* in Baikov Institute of Metallurgy and Materials Science (IMET) Moskau der russischen Akademie der Wissenschaft (RAN) 26.–27. Oktober 2010, pp. 493–499
22. A. Yanina, S. Guk, W. Müller, R. Kawalla, Influence of sintering parameters on the mechanical properties of TRIP-matrix composite materials, in Book series *Materials and Material Engineering Applications*, Band 37, ed. by B. Wielage (Chemnitz, 2011), pp. 236–243, ISBN 978-3-00-032471-0
23. A. Yanina, S. Guk, W. Müller, R. Kawalla, Einfluss der Sinterparameter auf die mechanischen Eigenschaften von TRIP-Matrix-Composit-Werkstoffen, in Tagungsband zum 13. Werkstofftechnischen Kolloquium. ISBN 978-3-00-032471-0, Chemnitz 30.09.–1.10.2010, pp. 236–243
24. A. Yanina, S. Guk, Special features of sintering TRIP-matrix-composites based on steel and ceramic by conductive heating, Tagungsband der internationalen Konferenz Fortschrittliche Technologien zur Plastischen Deformation 21–26. September 2009, MISIS, Moskau, ISBN 9785-87623-278-6, pp. 151–152
25. A. Yanina, S. Guk, W. Müller, R. Kawalla, C. Weigelt, Herstellung und Weiterverarbeitung von TRIP-fähigen Partikelverbundwerkstoffen. Tagungsband der internationalen Konferenz MEFORM 2012 "Material technology and forging processes". ISBN 978-3-86012-434-5, Freiberg 28.03.–30.03.2012, pp. 216–231
26. S. Guk, A. Yanina, W. Müller, R. Kawalla, Mathematical-physical model of resistance sintering with current conducting electrode punches of steel ceramic composites. Mater. Sci. Eng. Technol. **41**(1), 33–38 (2010)
27. S. Irukuvarghula, H. Hassanin, C. Cayron, M.M. Attallah, D. Stewart, M. Preuss, Evolution of grain boundary network topology in 316L austenitic stainless steel during powder hot isostatic pressing. Acta Meterialia **133**, 269–281 (2017)
28. S. Guk, K. Pranke, W. Müller, A. Yanina, Development of high-strength TRIP-matrix-composite materials, in *Proceedings of the International Conference of production and processing of cladded materials and metal matrix composites MEFORM 2014*, ISBN 978-3-86012-481-9, Altenberg 26.03.–27.03.2014, Herausg.: ACATRAIN e.V., Verein für Weiterbildung an der TU Bergakademie Freiberg, Institut für Metallformung, pp. 149–159
29. A. Yanina, S. Guk, R. Kawalla, New TRIP-matrix-composite production, properties and softening behaviour during warm forming. Tagungsband der internationalen Konferenz "Neuere Entwicklungen in der Massivumformung". ISBN 978-3-88355-386-3, Fellbach/Stuttgart 17.05.–18.05.2011, pp. 271–281

30. S. Guk, A. Yanina, R. Kawalla, H. Berek, J. Räthel, Densification and properties of an Mg-PSZ reinforced TRIP-Matrix-Composite produced by hot pressing: Comparison with other powder metallurgy techniques, in *International Science and Technology Congress OMD-2014, Hrsg.*: MISIS, Moskau, ISBN: 978-5-905714-27-6, pp. 364–369
31. Manufacturer specifications: DWA Composite Specialties Inc., Chatsworth, Ca., USA and DACC Dural Aluminium Composites Corp., San Diego, Ca., USA

Chapter 7
Understanding of Processing, Microstructure and Property Correlations for Flat Rolling of Presintered TRIP-Matrix Composites

Sergey Guk, Rudolf Kawalla and Ulrich Prahl

Abstract Descriptions of material behavior during forming operations have become increasingly important in recent years due to the increasing use of simulation systems for understanding processing-microstructure-property correlations and regulating forming facilities. This information has become particularly important for composite materials, including metal matrix composites. This necessity poses new challenges in particular for testing technology, which significantly contributes to the analysis of material characteristics. The characteristic values of materials are prerequisites for the numerical design of manufacturing processes. This chapter presents an overview of the strategies currently available for describing material behavior during flat rolling; the materials investigated herein are presintered TRIP-matrix composites. In addition, the test procedures and methods necessary for determining material parameters are briefly listed and explained. Furthermore, this chapter presents both the classical test methods and equipment and their areas of application, which have been further developed in recent years.

7.1 Introduction

For the development, industrial production, and processing of materials, it is becoming increasingly necessary to describe and optimize the associated technologies as completely as possible with the help of models. Depending on the manufacturing conditions, the corresponding models can then be used to estimate important characteristics of the surface (scale), geometry, microstructure, texture, internal stresses, mechanical properties, and physical properties of materials. For the customer, the mechanical properties of construction materials, which—depending on the field of application—may be combined with the chemical or special physical properties of the semifinished product or component, are often in the foreground [1].

S. Guk (✉) · R. Kawalla · U. Prahl
Institute for Metal Forming, Technische Universität Bergakademie Freiberg,
Bernhard-von-Cotta-Str. 4, 09599 Freiberg, Germany
e-mail: sergey.guk@imf.tu-freiberg.de

H. Biermann and C. G. Aneziris (eds.), *Austenitic TRIP/TWIP Steels and Steel-Zirconia Composites*, Springer Series in Materials Science 298,
https://doi.org/10.1007/978-3-030-42603-3_7

The entirety of the material description often represents an almost insoluble task in its complexity. Rather, individual models are linked together on different bases and used depending on a particular specification as well as scientific and technical requirements [2].

From the process description perspective, material models for flow curves, formability and physical properties, such as thermal conductivity and heat capacity as a function of temperature, are required for the forming process, among other things [3, 4]. Such models enable the material flow in the forming zone to be described and the characteristic values for the load and design of forming facilities to be calculated in advance. For multistage forming processes, some models must include time as an influencing factor, especially for all diffusion-controlled processes during deformation pauses. The resulting structural changes must be incorporated into the description via metallurgical models, which contributes to better calculation results.

The product properties of components are ultimately determined by the microstructure conditions, which can be specifically influenced during fabrication and further processing using various forming operations. The interaction of forming and microstructural development is illustrated in Table 7.1. A continuous description of the material behavior according to the column "Technologically related parameters" is possible with several methods if the necessary forming parameters and the physical properties are known. Microstructural development can be determined through the simplest methods of regression, semiempirical or semiphysical equations or complex computational methods on a physical basis.

The relationships between the forming conditions and the microstructural development during the production of cold and hot strips from transformation-induced plasticity (TRIP)-matrix composites, which are highlighted in *italics* in Table 7.1, are described below. The remaining microstructural developments, such as grain growth or precipitation of the δ-ferrite phase, have either already been discussed in

Table 7.1 Interlocking interaction of forming and microstructural development in cold and hot forming processes

Process	Technological step	Technologically related parameters	Microstructural development
Cold forming	Forming	Distribution of forming parameters	*Strain hardening* *Formability* Material flow/texture
Hot forming	Heating	Heating curve Temperature profile	Grain growth *Dissolution of precipitates*
	Forming	Distribution of forming parameters Cooling curve Temperature profile	*Strain hardening* *Strain softening* *Formability* *Material flow*/texture Precipitation
	Cooling	Cooling curve Temperature profile	Phase transformation Precipitation

the Chap. 6 of this volume or are of minor relevance compared to the others in this context. The material used was a TRIP-matrix composite produced by the powder metallurgical route with different fractions of ceramic particles. In this chapter, the details of material data, sample preparation, and testing to characterize the material behavior during deformation under conditions similar to flat rolling at different temperatures are provided in Sect. 7.2. Section 7.3 presents the results of the experimental observations and corresponding discussions involving comparisons with the state of the art. Finally, the investigation is concluded in Sect. 7.4.

7.2 Materials and Methods

The investigated material is based on two components: a Mn-containing gas-atomized metastable high-alloyed TRIP-steel powder ($d_{10} = 8$ µm, $d_{50} = 23$ µm, $d_{90} = 45$ µm, and $\rho = 7.81$ g/cm^3). On the other hand, there is a powder of MgO partly stabilized ZrO_2, which was separated by means of wind sifting into four fractions with corresponding particle size distributions:

1. <10 µm ($d_{10} = 0.7$ µm, $d_{50} = 2.5$ µm and $d_{90} = 9.0$ µm);
2. 10–30 µm ($d_{10} = 12.5$ µm, $d_{50} = 20.7$ µm and $d_{90} = 29.1$ µm);
3. 30–50 µm ($d_{10} = 32.2$ µm, $d_{50} = 39.0$ µm and $d_{90} = 48.6$ µm) and
4. >50 µm ($d_{10} = 52.4$ µm, $d_{50} = 56.8$ µm and $d_{90} = 81.9$ µm).

The chemical composition of the steel and the ceramic powders are shown in Table 7.2. The proportions of the phases in ZrO_2 were distributed between monoclinic (m), tetragonal (t) and cubic (c) crystallographic modifications at approximately equal amounts of 35:32:33%. By varying the ceramic particle content between 0 and 30% during blending as well as varying the ceramic particle size distribution, different powder mixtures were obtained. These mixtures were cold precompressed into disc form with a diameter of 155 mm and a height of 36 mm at a uniaxial pressure of 90 MPa and finally hot-press sintered. The sintering was carried out under a Varigon (5% H_2 and 95% Ar) atmosphere at 1250 °C and 30 MPa for 30 min. Metallographic examinations clearly showed that the particle distribution in the steel matrix was nearly homogenous. Only small agglomerates of ceramic particles were found for the composites with 20 and 30% ZrO_2 (Fig. 7.1). The porosity measurements using

Table 7.2 Chemical compositions of the investigated powders (wt%)

Steel powder											
C	Cr	Mn	Ni	Si	N	S	Mo	Ti	Nb	Al	δ-Ferrite
0.03	16.4	6.3	6.3	0.9	0.06	0.008	0.02	0.003	0.021	0.10	16
ZrO_2 powder											
ZrO_2		SiO_2		HfO_2		CaO		MgO	TiO_2		Fe_2O_3
Bal.		0.41		1.74		0.15		2.82	0.13		0.13

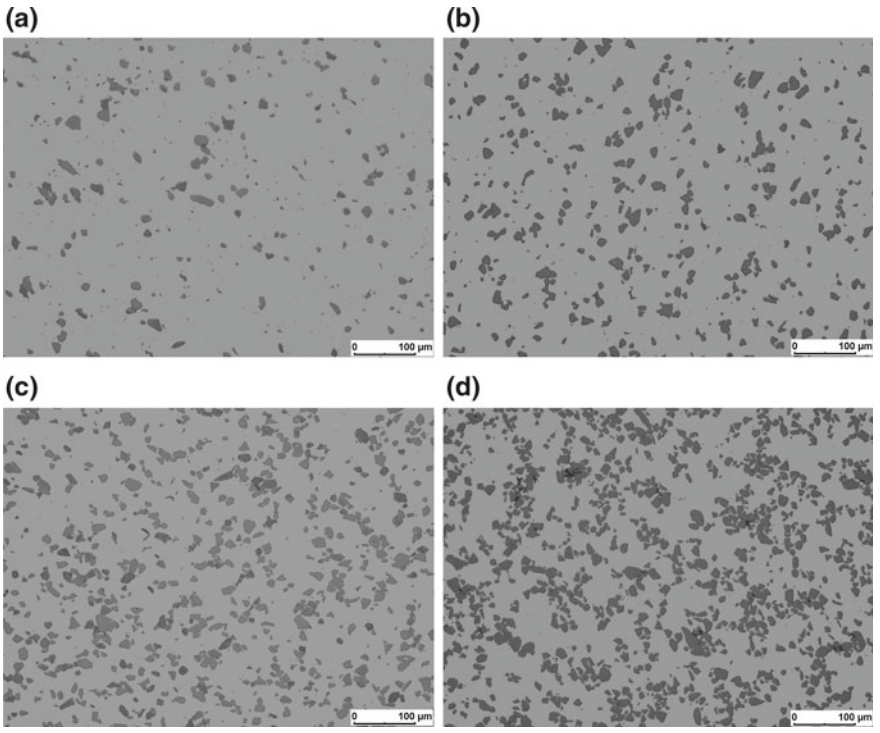

Fig. 7.1 Distribution of second-phase particles of ZrO_2 with particle sizes between 10 and 30 µm in the steel matrix: **a** 5%, **b** 10%, **c** 20%, **d** 30% ZrO_2 [5, 6]

the Archimedes method, conducted in accordance with DIN EN 623-2:1993, showed that nearly full density was achieved: the values of total porosity were at most 0.1%. The measured proportions of m-, t- and c-ZrO_2 after hot pressing were 60:7:33%.

The solution state of the steel matrix defined by the selected heating rates and temperatures was calculated for the investigated chemical composition using ChemSage, a computer program for calculating complex chemical equilibria, and SteelMap, a program specializing in calculations with steels. The calculation took place in a temperature interval between 200 and 1200 °C in 10 K steps. The calculated solution states are valid for the thermodynamic equilibrium and reflect the possible maximum values related to the experimental test conditions.

A completely new approach was chosen to determine the nonrecrystallization temperature. Usually, an attempt is made to determine the region of nonrecrystallization using a torsion machine [7, 8]. The machined samples are subjected to torsional stress and then evaluated. However, a decisive disadvantage lies in the sample geometry because the stress is not distributed homogeneously over the cross-section of the sample. Therefore, a MAXStrain® device in the multifunctional simulation system GLEEBLE HDS-V40 (Dynamic Systems Inc.) was applied to determine the nonrecrystallization temperature (Fig. 7.2). Due to the cube-shaped geometry of the

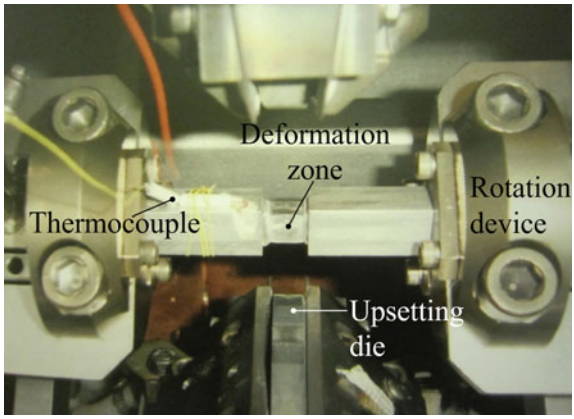

Fig. 7.2 Determination of the nonrecrystallization temperature using the MAXStrain® device

deformation zone in the MAXStrain® specimens, this influence is eliminated. An alternating deformation of the cube-shaped zone of the specimen with a strain value of 0.5 per deformation step is carried out by means of upsetting dies and a 90° rotation of the specimen after each deformation step. Twenty deformation steps were performed with a strain rate of 10 s^{-1} and a pause time of 8 s. Then, by recording the stress development during the reduction in deformation temperature from 1100 to 700 °C at 20 K decrements per deformation step, the region of nonrecrystallization due to strongly increasing stress levels can be determined.

To determine the strain hardening behavior of consolidated samples, compression tests were carried out at room temperature and in the range between 700 and 1200 °C with a 100 K step using the servo-hydraulic test system with a maximum force of 400 kN. The upsetting samples to be tested were taken from the hot-pressed discs in the axial direction. The specimen dimensions for the cylindrical compression tests were ∅10 mm × 18 mm. The test was carried out in accordance with DIN 50106:2016. The strain rates were 0.1, 1 and 10 s^{-1}. To reduce friction, the end faces of the cylindrical specimens were lubricated with oil (for tests under room temperature) or graphite solution (for tests under high temperatures). Flow curves were calculated based on the data obtained with friction and temperature adjustments [9]. These adjustments were based on the physical and tribological properties, such as density, heat capacity and friction coefficient, which were determined experimentally for all investigated composite material states.

To evaluate the kinetics of the α'-martensite evolution for the steel matrix under room temperature testing conditions, the ferromagnetic phase fraction of the samples with different contents of ZrO_2 particles were measured using magnetic balance testing (Metis Instruments and Equipment NV) and a previous calibration. The measuring principle is based on a magnetic induction method. In the investigated steel matrix, ferromagnetic phases, such as δ-ferrite and α'-martensite, can be found. At the beginning of each experiment (i.e., in the α'-martensite-free state), the amount of δ-ferrite was determined to extract these contents from the measurement values of the experiment, thereby determining the exact amount of α'-martensite.

The determination of the softening kinetics was carried out on the multifunctional simulation system GLEEBLE HDS-V40 by means of a cylinder compression test (dynamic softening) and a double compression test (static softening). In the double compression test, a specimen was deformed at a constant strain rate of 1 s^{-1} up to a strain of 0.4, unloaded and, after a variable isothermal holding time, was loaded again at the original strain rate up to the strain value above. Here, cylindrical samples with dimensions of ∅10 × 18 mm, which were taken from the hot-pressed disc axis direction, were heated to the deformation temperature at a heating rate of 3 K/s and held at this temperature for 1 min. The double compression tests were carried out at temperatures between 900 and 1100 °C. To minimize the influence of friction and heat of deformation on the flow stress and subsequently on the hardening and softening characteristics, all measured flow curves were subjected to a temperature and friction adjustment [9]. The flow curves were evaluated according to the offset method [10]. The modeling of the dynamic softening behavior was carried out with the help of reaction kinetic calculation equations [10–13] based on data from the experimentally generated flow curves. For strains over the critical value, dynamic recrystallization can take place. Otherwise, only dynamic recovery occurs. The part of the dynamic recovery is described by

$$\sigma_{\mathrm{DRV}}(\varepsilon) = u \cdot \sqrt[n_2]{1 - \exp(-r \cdot \varepsilon^{n_1})}. \tag{7.1}$$

The dynamic recrystallization degree is described by

$$\sigma_{\mathrm{DRX}}(\varepsilon) = a \cdot \dot{\varepsilon}^{c} \cdot \exp\left(\frac{\Theta_2}{R \cdot \Theta}\right). \tag{7.2}$$

The static recrystallization degree is described by

$$X_{\mathrm{stat}} = 1 - \exp\left(h_1 \cdot \left[\frac{t}{t_{0.5}}\right]^{h_2}\right). \tag{7.3}$$

To determine the cold formability of the composite materials under deformation conditions similar to flat rolling, transverse extrusion tests were carried out on the servo-hydraulic press with a maximum force of 400 kN at room temperature (Fig. 7.3a); these tests were repeated six times for each sample type. A simplified illustration of the transverse extrusion tool used is shown in Fig. 7.3b. Cylindrical specimens with dimensions of ∅10.65 mm × 19 mm were machined from the hot-pressed discs. Before inserting a specimen into the test tool, it was lubricated on all sides with hydraulic oil. The strain rate in all tests was 0.1 s^{-1}. The evaluation of the tests was carried out according to the methodology described in [14, 15].

The hot formability was characterized according to the methodology of [16] based on the hot flow curves measured under different temperatures and strain rates. The energy dissipation and an instability map were generated based on these experimental

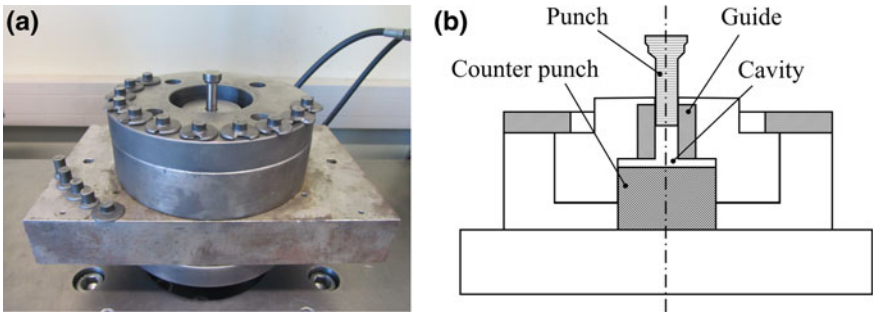

Fig. 7.3 Transverse extrusion tool: **a** photograph and **b** schematic drawing

results, and a process map was derived. The numerical analysis was carried out by means of a MATLAB® subroutine.

The hot rolling tests were carried out on a reversible stand with a dual roll mill, which has a maximum rolling force of 2.4 MN and a maximum rolling torque of 60 kN m. The rolls used had a diameter of 360 mm. The rolls were preheated to approximately 150 °C. The roll speed was chosen to be constant at 0.5 m/s. The samples were preheated in a furnace and purged with inert argon gas to prevent scale formation on the metallic surface. After rolling, the samples were cooled to room temperature in air.

Sheets, stuck rolling specimens and wedge rolling specimens were flat rolled. Stuck rolling specimens were only partially rolled products that—after removing the specimen from the roll gap—produce a largely realistic image of the deformation conditions directly in the roll gap. This technique made it possible to carry out extensive and complex investigations on the influence of the roll gap geometry on the extension and overall spread of material, the rolling force and torque, and the mean deformation resistance during hot rolling. Moreover, this technique helped clarify the material flow along the length of the contact arc as a function of the roll gap geometry. In contrast, the wedge rolling specimens represented initial semifinished products with a wedge-shaped longitudinal cross-section of 135 × 20 mm^2, which consequently undergo different strains over the specimen length during rolling with a constant roll gap. Thus, the evaluation of the rolling parameters, such as pass reduction, deformation temperature and strain rate, could be carried out with fewer initial samples. For mesoscopic characterization of the material flow, the initial specimens were marked with grid patterns (line spacing of 5.0 mm and a depth of approximately 0.3 mm) for forming strain analysis by means of the laser marking system Lasebox XS (Östling Marking Systems GmbH) on the surface and cross-sectional area [17, 18]. On the microscopic scale, densification processes and material flow were analyzed using light microscopy and scanning electron microscopy (SEM) on transverse and longitudinal sections from the different areas of the deformation zone. For this aim, the samples were cut, ground and polished. The degree of orientation of partially oriented linear structure elements AI and Ω_{12}, which characterize the

banding of the material, was measured in accordance with ASTM E 1268:94. These degrees of orientation were calculated with the following equations:

$$AI = \frac{\overline{N_{L\perp}}}{\overline{N_{L\parallel}}} \tag{7.4}$$

$$\Omega_{12} = \frac{\overline{N_{L\perp}} - \overline{N_{L\parallel}}}{\overline{N_{L\perp}} + 0.571 \cdot \overline{N_{L\parallel}}}, \tag{7.5}$$

where $\overline{N_{L\perp}}$ and $\overline{N_{L\parallel}}$ are the numbers of feature interceptions with test lines perpendicular to the deformation direction and in parallel direction, respectively. The degree of orientation Ω_{12} can vary from zero for a completely random distribution to one for a fully oriented material (banding microstructure).

7.3 Results

7.3.1 Heating and Dissolution of Precipitates

The investigations on the dissolution behavior of precipitates during heating of the steel matrix aimed to determine in advance the possible causes for influencing recrystallization and determine an optimum heating temperature for the composite material before forming from the perspective of the completely dissolved alloying elements. After heating to 900 °C and holding for 3 min, undissolved precipitates were determined in the steel matrix using the energy-dispersive X-ray spectroscopy (EDX) method; these precipitates essentially consisted of chromium (Fig. 7.4a). The precipitates have a size range from 70 to 300 nm [19].

Figure 7.4b shows the precipitation fraction as a function of the heating temperature. According to this figure, chromium carbonitrides are precipitated at 900 °C after

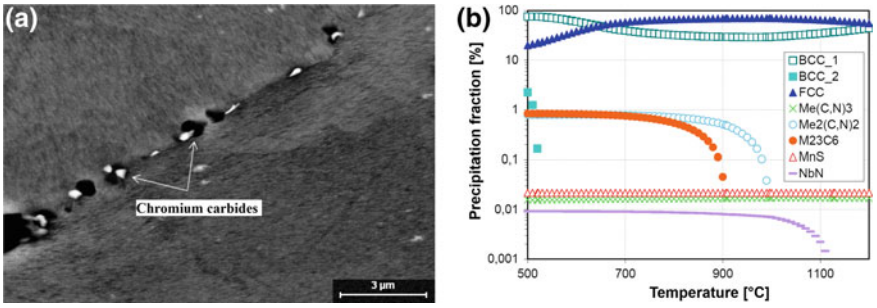

Fig. 7.4 **a** SEM image of the steel matrix with Cr carbides precipitated at the grain boundaries and **b** the calculated dissolution behavior of the precipitates of the investigated steel matrix

heating close to equilibrium; this finding has also been validated. The identification of the precipitates was carried out by means of EDX analysis. This analysis showed a high chromium content of 28%. The figure also shows that NbN precipitates in steel are resistant up to a temperature of 1120 °C and only then dissolve. For this reason, it was decided to set the heating temperature to 1100 °C to obtain a homogeneous matrix with dissolved chromium carbonitrides, inhibit normal grain growth, and prevent abnormal grain growth at the cost of retaining NbN precipitates, which were not dissolved at this temperature.

7.3.2 *Strain Hardening and Its Partitioning Between the Present Phases of the Composite*

To characterize the hardening behavior of the composite material during cold forming, interrupted compression tests were performed. The documentation of geometric changes of the specimen shape enabled the calculation of axial, tangential and hydrostatic stress components for the different material states [20]. The hydrostatic stress located close to the circumferential surface of the compression test sample is represented in Fig. 7.5a, which is exemplary of the composite material with a ZrO_2 particle distribution between 10 and 30 μm. The hydrostatic stress is illustrated, which is in fact negative. It is obvious that a significant change in the curve progression starts from 20% ZrO_2 content upwards. The further development of the model according to Pyshmintsev [21] allowed an exact prediction of the strain-induced $\gamma \rightarrow \alpha'$ phase transformation from the measured values of the axial strain and the calculated hydrostatic stress. The results showed very good agreement with the experimental values determined with the help of the magnetic balance [5]. Due to the small fraction of the t-ZrO_2 phase in the initial state of the composite after hot pressing, the $t \rightarrow m$ phase transformation was not taken into account. According to the general mixture

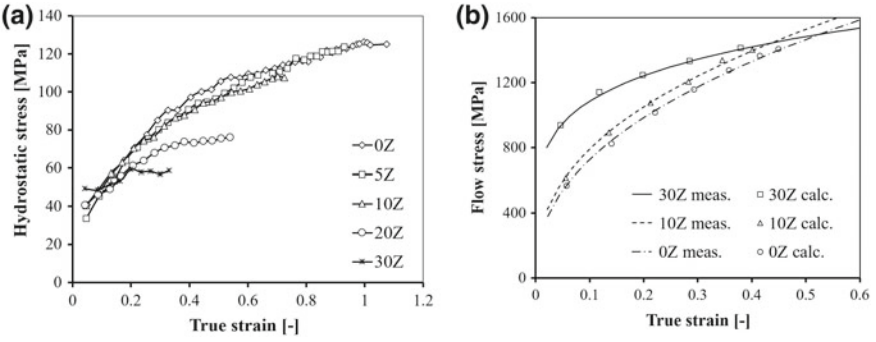

Fig. 7.5 **a** Variation in hydrostatic stress (negative) for different ZrO_2 contents and **b** a comparison between the predicted and the measured cold flow curves [5, 6]

rule by Tamura et al. [22], the flow stress of the composite was defined from the flow stresses of the single microstructural phases, such austenite γ, α'-martensite and ZrO_2, as well each phase volume fraction as

$$\sigma_{\text{mix.}}(\varepsilon_{\text{mix.}}) = f_{\gamma}(\varepsilon_{\text{mix.}}) \cdot \sigma_{\gamma}\left(\varepsilon_{\gamma}\right) + f_{\alpha'}(\varepsilon_{\text{mix.}}) \cdot \sigma_{\alpha'}(\varepsilon_{\alpha'}) + f_{ZrO_2} \cdot \sigma_{ZrO_2}\left(\varepsilon_{ZrO_2}\right) \tag{7.6}$$

under the condition that the sum of all phase volume fractions remains constant at any moment of the deformation

$$f_{\gamma}(\varepsilon_{\text{mix.}}) + f_{\alpha'}(\varepsilon_{\text{mix.}}) + f_{ZrO_2} = 1. \tag{7.7}$$

Assuming that the energy density has the same value for each single microstructural constituent and for the whole sample at every moment of the deformation (the so-called ISO-E hypothesis), the flow curves of the composites with different ceramic contents were calculated (Fig. 7.5b). The results showed very good accuracy between the calculated and measured datasets. The specific prediction accuracy of the correlation is 2%, 2% and 1% for the chosen ZrO_2 contents of 0%, 10% and 30%, respectively. Thus, a fast and accurate method was developed for predicting the strain hardening behavior of TRIP-matrix composites under cold deformation conditions [5].

To improve the convergence of calculation based on the mixture rule, the accuracy of the total strain estimates for the composite has to be increased. The mixture strain of the composite is determined by

$$\varepsilon_{\text{mix.}} = f_{\gamma} \cdot \varepsilon_{\gamma} + f_{\alpha'} \cdot \varepsilon_{\alpha'} + f_{ZrO_2} \cdot \varepsilon_{ZrO_2} \tag{7.8}$$

using the local strains and volume fractions of each phase.

Because the experimental determination of local phase strains is fraught with difficulties [23], the ISO-E method in inverse mode was used. Based on this approach, the relationship between the mixture strain of the composite and the local strain values of each phase was determined (Fig. 7.6). The figure shows that the curves for each phase component are nonlinear. The deformation of austenite in the low mixture strain range of the composite corresponds substantially to the composite strain. With a further increase in the mixture strain of the composite, the local deformation of austenite tends to have higher strain values than the composite. The local strains of martensite and ZrO_2 are significantly lower than the mixture strain of the composite.

Based on the calculations performed, a graphical working map was developed to predict the mixture strain of the composite according to the known ZrO_2 volume fractions and mixture stress. In Fig. 7.7, an example is illustrated and marked with arrows. For a composite with 10% ZrO_2 and a mixture stress of 900 MPa, a mixture strain of the composite $\varepsilon_{\text{mix.}} = 0.16$ is determined. On the lower left side, the known ZrO_2 content of 10% (0.1) is used, and the mixture stress gives the value of $\varepsilon_{ZrO2} = 0.03$. On the upper right side, the known mixture stress and the isoline for $\varepsilon_{ZrO2} = 0.03$ are used to find the strain $\varepsilon_{\text{mix.}} = 0.16$.

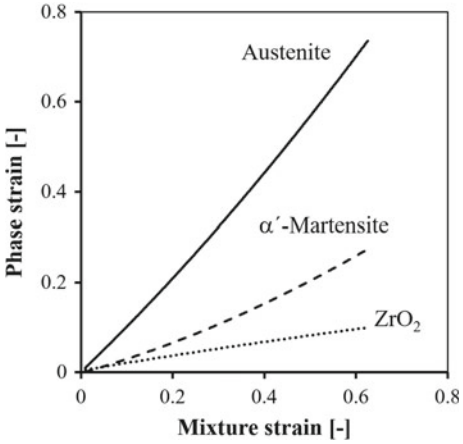

Fig. 7.6 Relationship between the mixture strain of the composite and the local strain values of each phase within the composite under cold forming conditions calculated with the ISO-E method [6]

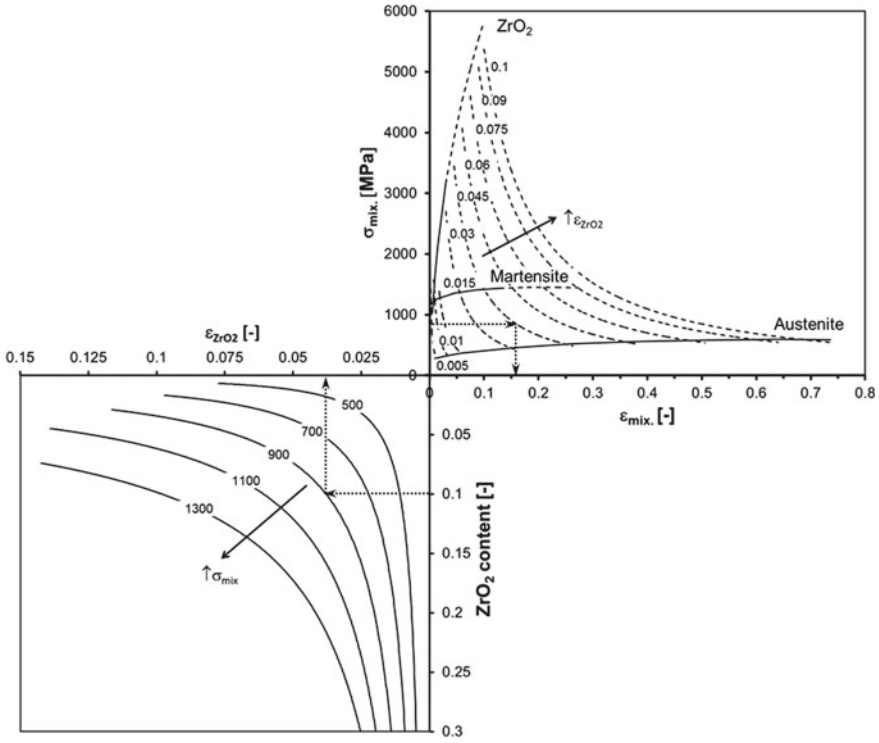

Fig. 7.7 Working map for strain dependence of the composite under cold forming conditions [6]

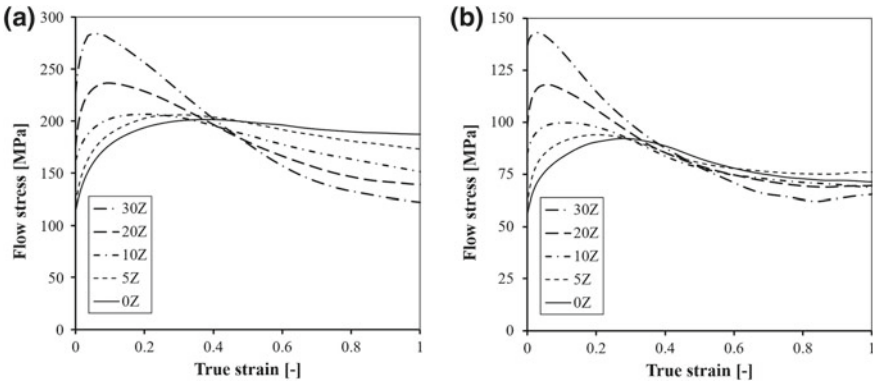

Fig. 7.8 Influence of the ZrO_2 content with a particle size less than 10 μm on the flow curve at a strain rate of 0.1 s^{-1} for **a** 900 °C and **b** 1100 °C

To separate the hot forming temperature region from the cold forming temperature region, investigations were carried out to determine the nonrecrystallization temperature. The results showed that the addition of ZrO_2 with the investigated contents and particle distributions had no significant effect on the nonrecrystallization temperature and that this temperature remained at approximately 900 °C. The result is not surprising given the large size of the ceramic particles (>1 μm) compared to the hardening phases (<0.01 μm) in precipitation hardening alloys of delayed recrystallization kinetics.

Under hot forming conditions, the flow stress was determined as a function of the ceramic content and the technological influencing variables, such as deformation temperature and strain rate. There is no strain-induced $\gamma \rightarrow \alpha'$ phase transformation in this temperature region. The ZrO_2 content had a considerable influence on the flow curves. Figure 7.8 shows the courses of two flow curves for composite materials with a ZrO_2-particle size less than 10 μm. This figure clearly shows that the hardening at the beginning of the hot deformation is much more pronounced in samples with a high ZrO_2 content than in samples with a lower ZrO_2 content. Specimens with a ZrO_2 content of 30% reach their maximum flow stress of 280 MPa at a strain of approximately 0.1. On the other hand, the undoped steel matrix exhibits a flow stress of 177 MPa at this strain value. Thus, the composite exhibits up to 58% higher flow stress at low strain values. However, this effect is not valid over the entire range of the flow curve. Therefore, from a strain over 0.25–0.4, the flow stress level of the undoped steel matrix is higher than that of the composite material. At a strain of 1.0, the undoped steel matrix has a flow stress of 185 MPa and the composite material has a flow stress of 120 MPa, which corresponds to a decrease of 35%. Thus, the ZrO_2 content has a clear influence on the hardening and softening behavior of the composites. The hypothesized reason for the different hardening behavior is that the ZrO_2 particles under hot deformation conditions only participate insubstantially in the deformation process (cf. Sect. 7.3.4). Therefore, the applied force must be distributed over a smaller volume. Consequently, the strain in the steel matrix is

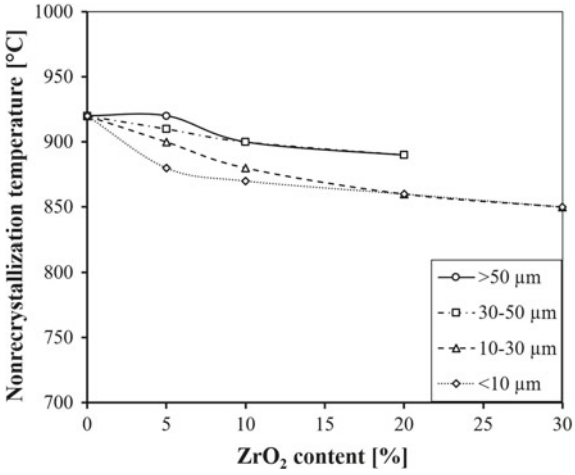

Fig. 7.9 Influence of the ZrO_2 content in the composite on its nonrecrystallization temperature

significantly higher than initially assumed. As a result, the strain rate ultimately increases, which leads to faster hardening of the composite material. The higher level of strengthening can also be explained by the deformation-induced $t \rightarrow m$ phase transformation of the ZrO_2. Due to this phase transformation, a hydrostatic stress condition occurs that enables higher strains in the matrix, which also leads to higher hardening. By enabling higher strains in the matrix, all samples from 0 to 30% ZrO_2 also achieve similar macroscopic strain values of approximately 1.

These findings show that the critical strain required for recrystallization beginning is achieved sooner than the macroscopic deformations suggest. This phenomenon is also confirmed by measurements to determine the nonrecrystallization temperature. As the compilation of determined values in Fig. 7.9 shows, the addition of ZrO_2 in the investigated contents and particle distributions slightly decreases the nonrecrystallization temperature. The results confirm the hypothesis. Therefore, the flow curves with increased ZrO_2 contents exhibit monotonic changes at lower strains. Furthermore, from this point of view, the load-bearing cross-section of the samples changes. The applied force is distributed only over the steel matrix, which ultimately results in a lower flow stress. Figure 7.8a can be used as an example of this behavior. According to this consideration, the load-bearing cross-section of the sample is reduced by the proportion of the ZrO_2 content. The undoped steel matrix achieves a flow stress in the steady-state range of approximately 185 MPa, and with the addition of 30% ZrO_2, the achievable flow stress also decreases by a similar percentage (35%) to 120 MPa. The same tendency can also be seen in Fig. 7.8b.

On the basis of the determined influence of the ZrO_2 content on the characteristics of the hot flow curves of the composite, a modification of the well-known Freiberg flow curve approach for homogeneous conventional materials was carried out so that the ZrO_2 content was taken into account. Since the influence of the strain rate is not important for the consideration of the dependence of the ZrO_2 content, this factor was not implemented in the calculation of the flow curves. The basic prerequisite

for the approximation of the hot flow curves was the Freiberg approach number 4 according to the form [9]

$$\sigma_{\text{mix.}} = A \cdot e^{m_1 \cdot T} \cdot \varepsilon^{m_2} \cdot e^{\frac{m_4}{\varepsilon}} \cdot (1+\varepsilon)^{m_5 \cdot T} \cdot e^{m_7} \tag{7.9}$$

To adapt the Freiberg approach to the deformation conditions of the composite materials, this approach was modified by adding four factors. At first, this is the ZrO_2 content Z. With increasing Z, the hardening of the composite material also increases; thus, the factor ε^{m_2} changes to $\varepsilon^{m_2 \cdot Z}$, and the factor $(1+\varepsilon)^{m_5 \cdot T}$ changes to $(1+\varepsilon)^{m_5 \cdot T \cdot Z}$. After reaching the critical strain for the beginning of recrystallization, the softening factor is also influenced and results in $e^{\frac{m_4}{\varepsilon} \cdot Z}$. Moreover, the Freiberg approach was extended by an e-function for a better approximation in the range of increased strains and by two exponential functions dependent on ε and Z, which take into account the increased strain hardening. This resulted in a modified Freiberg approach for hot deformation of composite materials, which is expressed as

$$\sigma_{\text{mix.}} = A \cdot e^{m_1 \cdot T} \cdot \varepsilon^{m_2} \cdot e^{\frac{m_4}{\varepsilon}} \cdot (1+\varepsilon)^{m_5 \cdot T} \cdot e^{m_7 \cdot \varepsilon} \cdot \varepsilon^{m_{11} \cdot Z} \cdot e^{m_{12} \cdot Z} \cdot (1+\varepsilon)^{m_{13} \cdot Z \cdot T} \tag{7.10}$$

Table 7.3 shows, for example, the coefficient and exponents determined for ZrO_2 particle sizes below 10 µm. Moreover, the modified Freiberg flow curve approach also provides a very high coefficient of determination and a small standard deviation for a ZrO_2 content of 0%.

Based on the modified Freiberg flow curve approach, the flow curves were then calculated using a combination of the ISO-E method and the mixture rule. Assuming that the energy density in the steel matrix and in the ZrO_2 particles is the same during the deformation of the composite material, the area integrals of the hot flow

Table 7.3 Parameters for the modified Freiberg flow curve approach for hot deformation of composites with particle sizes <10 µm (valid for temperatures between 900 and 1200 °C)

Parameter	Value	ZrO_2 content, %	Coefficient of determination	Standard deviation, MPa
A	4559.889	0	0.977	16.90
m_1	−0.002793			
m_2	0.285427	5	0.987	11.50
m_4	0.000837			
m_5	−0.001802	10	0.997	4.10
m_7	0.424686			
m_{11}	−0.187844	20	0.989	12.40
m_{12}	1.330402			
m_{13}	0.00485	30	0.987	15.10
		100	0.983	51.50

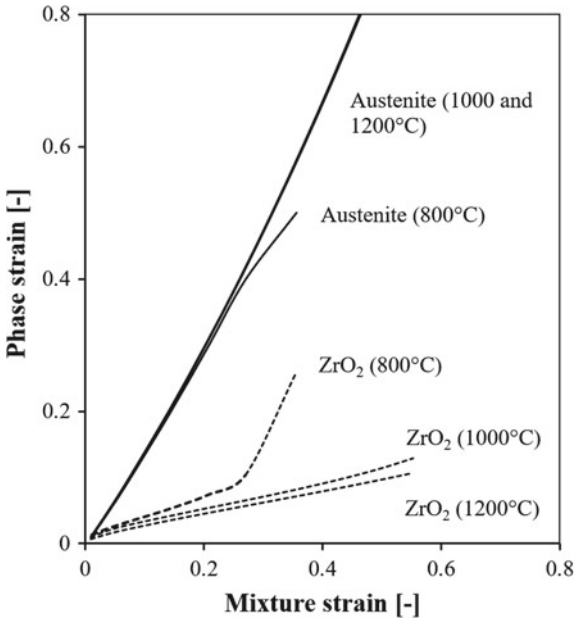

Fig. 7.10 Relationship between the mixture strain of the composite and the local strain values of each phase within the composite under hot deformation conditions calculated with the ISO-E method

curves of the steel and the ceramic can also be equated. The integration limits ε_1 and ε_2 are the strains here. By means of a previous determination of the equations for flow stress using the modified Freiberg approach, it was now possible to calculate the corresponding strain of ZrO_2 by specifying a strain for the steel matrix. The strain dependencies for the three selected temperatures are shown in Fig. 7.10. This figure clearly shows that the specification of the ISO-E method at low temperatures imposes very high strains on the ZrO_2. Even at higher temperatures and high steel matrix strains, the ZrO_2 achieves strains that are significantly higher than the strains from the compression tests. The flow stresses calculated using the mixture rule were compared with the measured values. This comparison shows that the calculated flow stresses exceed the actual flow stresses by up to 600%.

The reasons for the large deviations are diverse and can be justified by the mixture rule. For example, by equating the area below the flow curve (energy density), the ZrO_2 is forced to deform to an excessively high strain, or the steel matrix is not loaded to failure. This results from the fact that if a high strain is specified for the steel matrix, the integral also assumes very high values. However, these can only be equalized by means of high ZrO_2 strains.

This finding shows that the deformation in the high temperature range is not divided among the present phase components but nearly exclusively among the steel matrix. Thus, the assumption of an evenly distributed energy density regarding the deformation of steel and ceramics at high temperatures can be rejected.

Another approach would be to consider the composite as a viscous fluid with hard inclusions. The maximum stress the composite can withstand is the flow stress of

the steel matrix. As a result, the ZrO_2 particles cannot be subjected to higher stresses than the matrix. This aspect is completely ignored by the ISO-E method. For this consideration, only the volume fraction of the ZrO_2 is decisive for the development of the flow curve. Thus, a high ZrO_2 content corresponds to a low matrix content, which leads to a lower flow stress because the deformation is only localized in the matrix.

This approach is of course not suitable for very high ZrO_2 contents. As soon as the particles "touch" each other and form a kind of "skeleton" in the matrix, they can also absorb a portion of the applied stress, thereby contributing significantly to the hardening of the composite. On the other hand, a small fraction of ZrO_2 means a higher flow stress because more material is available to cope with the stress.

In conclusion, the presented modified Freiberg approach is the most advantageous variant with regard to the modeling of hot flow curves of composite materials. The ISO-E method does not provide any useful results due to errors caused by a principle calculation assumption.

7.3.3 Strain Softening

The dynamic softening behavior was analyzed on the basis of warm flow curves (cf. Fig. 7.8). All measured hot flow curves have a maximum value and then decrease continuously with increasing strain due to dynamic recovery and recrystallization processes. As the shape of the flow curves shows, dynamic recrystallization and dislocation hardening are the determining processes during hot deformation. One of the main reasons for this phenomenon is the low stacking fault energy of the face-centered cubic (FCC) crystal structure of the steel matrix [24].

The ZrO_2 particles represent barriers to dislocation movement in the hardening processes due to faster and higher hardening values. After exceeding the critical flow stress, the new grains form near the ZrO_2 particles due to the increased dislocation density in these locations. Compared to the undoped steel matrix, the addition of ZrO_2 to the composite material creates an additional grain boundary surface, which favors the formation of new grains. Therefore, the softening processes run faster in composite materials (cf. Fig. 7.8) [25].

Figure 7.11a shows exemplary results from modeling dynamic softening on the basis of reaction kinetic calculation equations. The model calculation shows that a largely complete dynamic recrystallization can only be achieved at higher strains of approximately 1.5. In contrast, the influence of temperature is less pronounced in the investigated area and causes faster dynamic softening only in the medium strain range with increasing temperature. This effect can be explained by thermal activation.

The static softening behavior was measured by means of double compression tests. In the entire investigated temperature and strain rate range, the composite material showed a sigmoidal softening process. As expected, static softening occurred faster with increasing strain rate and rising deformation temperature. The results indicated

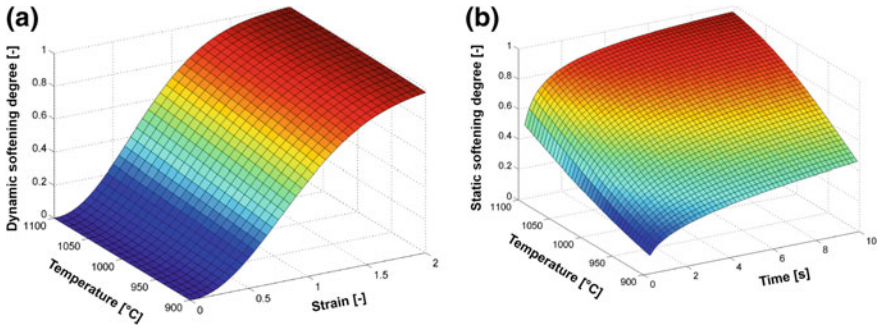

Fig. 7.11 **a** Dynamic and **b** static softening kinetics of composite material with 10% ZrO_2 as a function of deformation temperature, strain and pause time at a strain rate of 1 s^{-1}

that the ZrO_2 particles present in the composite material significantly accelerate the processes of static softening compared to the undoped steel matrix.

The investigations have contributed to the development of a model for static softening based on kinetic reaction equations. Figure 7.11 shows exemplary results from modeling the composite material with 10% ZrO_2 at a strain rate of 1 s^{-1}. An increase in temperature from 900 to 1100 °C at a constant pause time of 10 s led to a doubling of the static softening degree, resulting in a completely recrystallized microstructure.

7.3.4 Formability

Transverse extrusion tests were used to characterize the cold formability of the composite materials with different ZrO_2 contents. Figure 7.12a shows an example of the change in cold formability for the ceramic particle distribution of 10–30 µm, wherein the values are normalized to the formability of the undoped steel matrix. The results indicate that the normalized cold formability decreases nearly hyperbolically with increasing ZrO_2 content in the composite material. For ceramic phase contents below 20%, the normalized cold formability decreases by approximately 2.5% per 1% increase in ceramic content. This trend correlates well with the decreasing content of transformed α'-martensite and subsequently with the decreasing value of macroscopic residual compressive stresses generated in front of the crack tip, which increase the crack propagation velocity. The decreasing cold formability is visible in the changing appearance of the cracked flange area of the specimen after failure. Figure 7.12a shows that the increase in the ceramic content leads to an increasing number of small radial macrocracks, which developed under the effect of tangential tensile stresses starting from the specimen flange edge. Considering the fact that microcracks always occur at the largest microstructural inhomogeneities [26], which in this case is at the ZrO_2 particles, at high ceramic contents, there is always

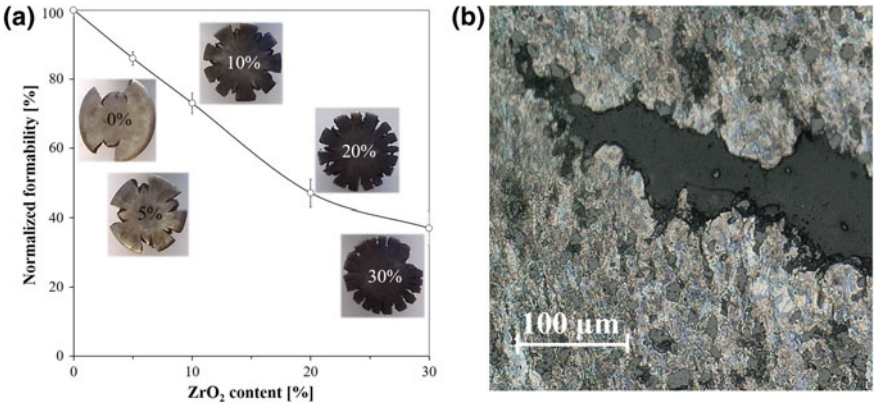

Fig. 7.12 **a** Development of the normalized cold formability with increasing ZrO_2 content determined by means of transverse extrusion tests with appearances of the cracked flange area of the specimen after failure. **b** Image of a macrocrack on the flange area of the specimen with 20% ZrO_2, in which the ZrO_2 particles are shown in light gray and the pores are shown in black

at least one large particle at the edge of the sample where the maximum tangential tensile stresses are acting during deformation. Due to the strain obstruction, stress concentrations occur at these points in the steel matrix in the vicinity of the ceramic particles. These stress concentrations lead to cracking in the steel matrix near the phase interfaces. Once local damage occurs, crack propagation initiates under the acting tangential tensile stress. Here, the free path length between ceramic particles determines the size of the damage zone in front of the growing crack, in which mainly the steel matrix fails at the phase interface (Fig. 7.12b). The positive phenomenon of the failure by means of delamination at the phase boundary is reflected in the decreasing crack propagation velocity in the steel matrix because the pores formed by the delamination locally increase the multiaxiality and slow the crack propagation, which occurs through local plastic deformation. The microcracks formed in this way quickly combine to form a larger macrocrack, the growth rate of which is ultimately determined by the hardness and toughness of the steel matrix. Figure 7.12b shows that the microcracks also grow outside the main crack path. There, energy is converted, which does not serve the propagation of the main crack. The results show that when the ZrO_2 content is 30%, more ceramic particles are located in the damage zone, thereby inhibiting the crack propagation velocity through the formation of secondary cracks and crack branching. With a constant ceramic content in the microstructure, the crack propagation velocity decreases with increasing particle size because the free path length between two ZrO_2 particles increases. Based on the investigations, it was possible to limit the maximum ZrO_2 content for cold rolling processes to 10% due to an increased risk of edge cracking.

The hot formability was characterized according to the methodology in [16] based on the measured hot flow curves. The resulting calculation of process maps made it

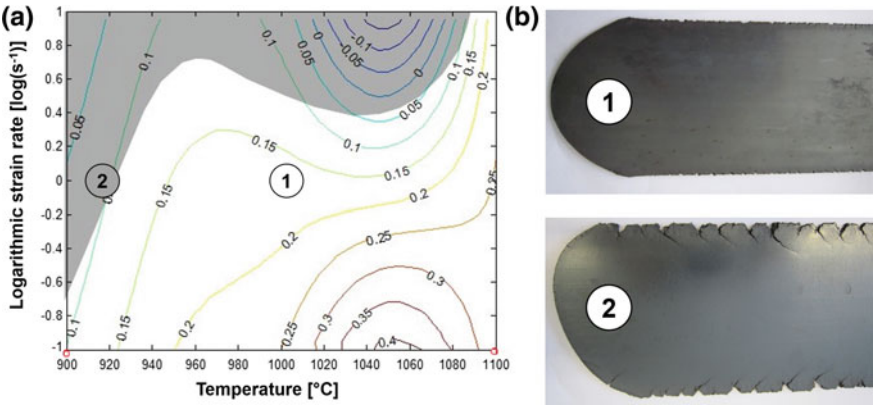

Fig. 7.13 **a** Process map for hot deformation conditions of composite with 10% ZrO_2 and strain of 0.3 and **b** the validation results after hot rolling

possible to determine the optimum process window from the point of view of failure-free deformation. Figure 7.13a shows an exemplary process map for the composite material with 10% ZrO_2 content for a strain of $\varepsilon = 0.3$ in the temperature interval of 900–1100 °C and the strain rate interval of 0.1–10 s^{-1}. The bright and gray areas of the map correspond to stable (fracture free) and unstable deformation, respectively. The values at the isolines reflect the efficiency of the dissipation process. One part of the energy used for deformation gets lost (for example, due to heating) and is not available for the dynamic recovery, the dynamic recrystallization, the closing of pores and so on. A comparison of the process maps and the experimental data of all investigated composites showed their dependence on the different deformation conditions. It was obvious that some combinations of strain rate, temperature and composite microstructure led to failure (gray areas of the maps; for example, position 2 in Fig. 7.13a). The technological combinations reflected the main role of ZrO_2 content and coarse particle fraction during the deformation process. However, it was deduced that at the lowest investigated deformation temperatures of 700 and 800 °C, failure is only slightly influenced by the increased ZrO_2 content. Here, an increased risk of failure already occurred in the course of strain hardening. The best hot deformation conditions for the investigated temperatures of 900 and 1100 °C are at a maximum strain rate of approximately 0.2 and 10 s^{-1}, respectively (cf. position 1 in Fig. 7.13a). It is obvious that the agglomerates lead to failure, and the increase in deformation temperature extends the interval of failure strains. Regarding the initial material condition, it was shown—analogous to cold deformation—that composite materials with finer ceramic particles are significantly more sensitive to material failure due to the reduced free path length between ceramic particles for the same ceramic content. Further investigations using light microscopy and SEM confirmed interfacial delamination as the cause of failure. The results showed that, from the point of view of thermomechanical treatment, only conventional rolling in the high

temperature range is suitable for achieving sufficient formability of the composite material [27].

7.3.5 Material Flow During Rolling

Investigations on the deformation behavior and the quantitative microstructure analysis showed that after a rolling reduction of approximately 30%, the porosity was eliminated in all composites. Furthermore, the results show that the number of pores is accompanied by an agglomeration affinity of the composite. It is important to mention that the composites with high rates of agglomerates have twice the number of pores than found in the initial state in the case of maximal deformation. This behavior can be explained with the help of a model, which is qualitatively shown in Fig. 7.14. There are large pores around single ZrO_2 agglomerates in the initial state, which are still present on the phase borders because of insufficient sintering results (Fig. 7.14a). As elaborated in [28], the larger particles of irregular shape produce a greater effect on the local curvature, especially at lower deformation. The angular component of the deformation tensor can be evaluated at the turning of phase and grain boundaries and has a higher influence on inhomogeneous deformation. The primarily common plasticization of the steel matrix is promoted, and the realignment of ZrO_2 particles is observed. This process is the initial phase of local plastic deformation, which can create local bonding between composite phases according to their form and structure. The local inhomogeneity of deformation promotes local flow stress. The initial large pores can split into many small pores (Fig. 7.14a) and move or align in the direction of local stress together with the grain boundaries, phase boundaries, and agglomerates. The changeable influence of the composite microstructure on the evolution of the number of pores confirms the reality of a qualitative model [27].

Furthermore, the results show that reorientation of single ZrO_2 particles with partial line formation depends on the agglomeration grade of the composite. This behavior applies to the less agglomerated composites and is related to single enclosed ZrO_2 particles or to the small line groups (clusters) consisting of 4–8 particles. Their arranged length is correlated to the austenite grain size during plasticization of the steel matrix (Fig. 7.14b). In contrast, a destruction of large agglomerates could not be revealed.

Regarding the material flow and the particle rearrangement resulting from deformation, metallographic investigations were carried out on sheets and on the compression, wedge rolling and stuck rolling specimens. The light microscopy images were examined based on quantitative metallographic parameters. Thus, the determined anisotropy index AI provides information on the homogeneous distribution of the particles. For the same strain value, no influence of particle size, deformation temperature or deformation zone geometry on AI was determined for the hot-compressed specimens. In contrast, investigations on the wedge rolling specimens showed that the particle distribution in the composite material becomes anisotropic with increasing

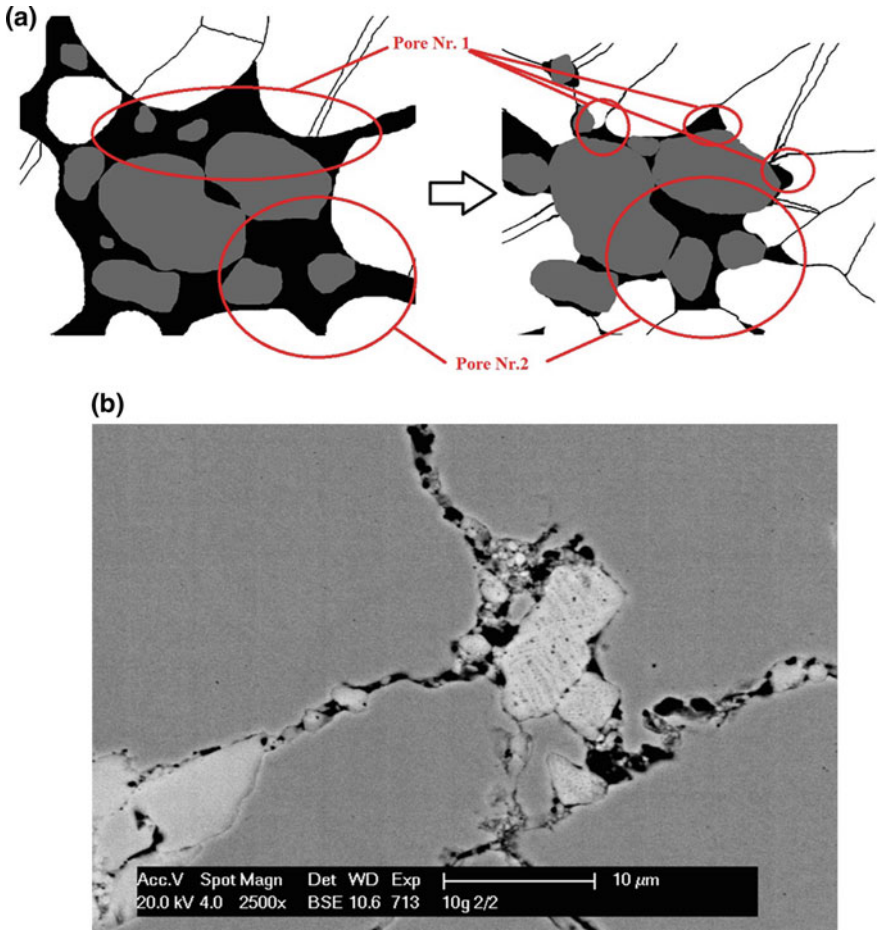

Fig. 7.14 **a** Qualitative model of the deformation behavior around a ZrO_2 agglomerate and **b** realignment of ZrO_2 particles [27]

strain. The corresponding increase in anisotropy depended primarily on the deformation temperature. A further characterization of the material flow during deformation with regard to a preferred direction of the particles is given by the degree of orientation Ω_{12}. This value also increased with increasing strain (Fig. 7.15a). This finding supported the conclusion that the ceramic particles move with the flowing steel matrix as a result of the deformation and align in the flow direction (cf. Sect. 7.3.2 and Fig. 7.15b) [29].

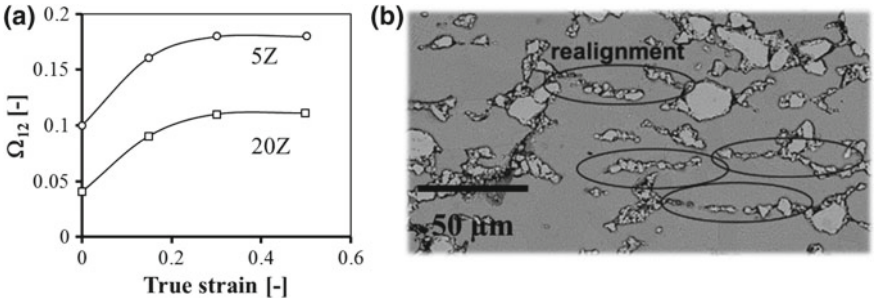

Fig. 7.15 **a** Development of the degree of orientation Ω_{12} of ZrO_2 particles with respect to the true strain for composites with 5 and 20% ZrO_2 and **b** the realignment (line) formation in the microstructure after hot rolling with a thickness reduction of 45% [27, 29]

7.4 Conclusions

Currently, models are increasingly being used to perform computer simulations of material manufacturing and further processing from semifinished products to finished parts and to predict the mechanical properties of the finished components. In this chapter, the deformation behavior of the TRIP-matrix composite under conditions similar to flat rolling in a wide temperature range was tested and analyzed using current test methods. The initial material was available in the presintered form with different ceramic contents between 0 and 30% and with closely spaced particle sizes between approximately 2 and 60 µm (classified by wind sifting) in the high-alloy austenitic steel matrix.

In the field of cold deformation, interrupted compression tests were carried out. The registration of geometrical changes in the specimen shape enabled the calculation of axial, tangential and hydrostatic stress components for different material states. These were implemented in the flow curve modeling. A comparison with the experimental results showed that the prediction accuracy is very good. In further calculations, it was possible to create a flow stress work map for materials with different compositions, where a prediction of local phase strain is possible from the measured macroscopic strain in the composite material.

In the field of hot deformation, technological parameters such as the deformation temperature and the strain rate showed effects on the flow stress level already known from conventional materials. The influence of the varying material condition at constant deformation conditions was expressed as follows. The increase in the ZrO_2 content at constant particle size generally leads to an increase in flow stress. The finer the ZrO_2 particles are, the greater the increase in flow stress. The deformation temperature has the primary influence and the strain rate has a secondary influence. Based on the determined influence of the ZrO_2 content on the characteristics of the hot flow curves of the composite material, the well-known Freiberg flow curve approach for homogeneous materials was modified so that the ZrO_2 content was taken into account. For a ZrO_2 content of 0–100%, this modified approach provided a very high

coefficient of determination and a small standard deviation. Based on the Freiberg flow curve approach, the flow curves were then modeled using a combination of the ISO-E method and the mixture rule. This method did not provide any useful results due to errors caused by a principle assumption that is applicable in the determination of cold flow curves but cannot be applied in the area of hot forming.

The analysis of the measured flow curves enabled the following interpretation of the dynamic hardening and softening processes. At temperatures up to 800 °C, softening occurs exclusively through recovery, whereby the flow curve does not pass through a maximum. Above this deformation temperature, dynamic recrystallization appears to be the dominant softening mechanism. The ZrO_2 content has the primary influence and the particle size has a secondary influence on the critical strain. The latter decreases with increasing ceramic content and finer particle size.

Transverse extrusion tests were used to characterize the cold formability of the composite materials with different ZrO_2 contents. The results indicated that the normalized cold formability decreased hyperbolically with increasing ZrO_2 content in the composite material. This trend correlated well with the decreasing fraction of transformed α'-martensite and subsequently with the decreasing value of the resulting macroscopic residual compressive stresses in front of the crack tip, which increased the crack propagation velocity. The results showed that if the ZrO_2 content was 30%, more ceramic particles were in the damage zone, thereby inhibiting the crack propagation velocity through secondary crack formation and crack splitting. With a constant ceramic content in the microstructure, the crack propagation velocity decreased with increasing particle size because the free path length between two ZrO_2 particles increased.

Based on the measured flow curves, the optimum process window was determined from the point of view of failure-free deformation by creating process maps in accordance with the methodology reported in [30]. It could be deduced that at the lowest investigated deformation temperatures of 700 and 800 °C, failure was only slightly influenced by the ZrO_2 content. Here, an increased risk of failure already occurred in the course of strengthening. With regard to the condition of the material, it can be seen that composite materials with finer ceramic particles at the same ceramic content were significantly more sensitive to material failure. Further investigations using light microscopy and SEM confirmed that interfacial delamination between phases was the cause of failure. Furthermore, the results showed that, from the point of view of thermomechanical treatment, only conventional rolling was suitable for achieving sufficient formability of the composite material in a wide temperature-strain rate window.

With regard to the material flow and the particle rearrangement caused by deformation, metallographic examinations of sheets and the upsetting, wedge rolling and stuck rolling specimens were carried out. These examination quantitatively verified that the ceramic particles move with the flowing matrix material as a result of the deformation and align in the direction of flow. An influence of the deformation temperature within a constant strain value could not be verified.

Acknowledgements The authors are grateful to the employees of the Fraunhofer Institute for Ceramic Technologies and Systems (*) and of the Institute for Metal Forming (**), who participated in the powder separation, presintering and rolling processes: Dr. rer. nat. habil. Mathias Herrmann (*), Dipl.-Ing. Jan Räthel (*), Dr.-Ing. Katja Pranke (**) and Dr.-Ing. Wolfhart Müller (**). Special thanks are addressed to Dr. Gizo Bokuchava from the Joint Institute for Nuclear Research, Dubna, Russia, for the execution of the neutron diffraction studies. The authors gratefully acknowledge the German Research Foundation (DFG) for supporting the Collaborative Research Center TRIP-Matrix-Composites (Project number 54473466—CRC799 subproject A6).

References

1. R. Kawalla, A. Nam, S. Guk, Technological methods to control the final properties of the rolled product. J. Chem. Tech. Metall. **50**(6), 606–612 (2015)
2. S. Guk, K. Pranke, R. Kawalla, Modeling of properties of sheet metal products from the TRIP-matrix-composite along the process chain. Postersession im Rahmen der 5. ICAFT/22. SFU Tagung vom 10. bis 11. November 2015 am Fraunhofer-Institut für Werkzeugmaschinen und Umformtechnik IWU in Chemnitz
3. F. Qayyum, S. Guk, M. Schmidtchen, R. Kawalla, U. Prahl, Modelling and understanding the deformation behaviour of TRIP steel at microstructural level using DAMASK. Konferenz MEFORM2019 "Simulationsbasierte Technologieentwicklung", Freiberg, den 20.–21.03.2019
4. A. Yanina, S. Guk, W. Müller, R. Kawalla, C. Weigelt, Herstellung und Weiterverarbeitung von TRIP-fähigen Partikelverbundwerkstoffen. Tagungsband der internationalen Konferenz MEFORM 2012 "Material technology and forging processes". ISBN 978-3-86012-434-5, Freiberg 28.03.–30.03.2012, pp. 216–231
5. S. Guk, K. Pranke, W. Müller, Flow curve modelling of an Mg-PSZ reinforced TRIP-matrix-composite. ISIJ Int. **54**(10), 2416–2420 (2014)
6. S. Guk, W. Müller, K. Pranke, R. Kawalla, Mechanical behaviour modelling of an Mg-stabilized zirconia reinforced TRIP-matrix-composite under cold working conditions. Mater. Sci. Appl. **5**, 812–822 (2014)
7. S. Solhjoo, R. Ebrahimi, Prediction of no-recrystallization temperature by simulation of multi-pass flow stress curves from single-pass curves. J. Mater. Sci. **45**, 5960–5966 (2010)
8. S. Vervynckt, K. Verbeken, P. Thibaux, Y. Houbaert, Evaluation of the austenite recrystallization by multideformation and double deformation tests. Steel Res. Int. **82**(4), 369–378 (2011)
9. T. Spittel, M. Spittel, Ferrous alloys (2009)
10. C. Biegus, Anwendung von Werkstoffmodellen auf das Entfestigungsverhalten und die Ferritkorngröße mikrolegierter Baustähle. Diss (1996)
11. F. Bubeck, *Charakterisierung und Modellierung der Gefügeentwicklung bei der Warmumformung von Kupferwerkstoffen* (Diss, TU Bergakademie Freiberg, 2007)
12. W. Müller, Temperaturverhältnisse und Reaktionskinetik beim Ziehen und Wärmebehandeln von Draht. Bd. B292. TU Bergakademie Freiberg (1998)
13. H.-P. Schmitz, Entfestigungsverhalten kohlenstoffarmer Stähle bei der Warmumformung im Ferritgebiet. Diss. Freiberger Forschungshefte B307, TU Bergakademie Freiberg (2000)
14. S. Guk, R. Kawalla, Prozessnahe Beurteilung der Umformbarkeit beim Kaltfließpressen. MassivUmformung (März 2017) pp. 64–68. ISSN 2366-5106
15. F. Qayyum, S. Guk, R. Kawalla, U. Prahl, Experimental investigations and multiscale modeling to study the effect of Sulphur content on formability of 16MnCr5 alloy steel. Steel Res. Int. (2018). https://doi.org/10.1002/srin.201800369
16. Y.V.R.K. Prasad, T. Seshacharyulu, Modelling of hot deformation for microstructural control. Int. Mater. Rev. **43**(6), 243–258 (2013)

17. S. Guk, D. Plotnikova, R. Kawalla, The effect of microstructural and geometric inhomogeneities induced by laser for forming strain analysis on sheet metal formability. Mater. Sci. Appl. **7**, 247–256 (2016)
18. S. Guk, M. Preiß, R. Kawalla, Metal formability interactions in laser marking for creating of grid patterns for forming strain analysis of high strength steels. Key Eng. Mater. **746**, 92–98 (2017)
19. S. Guk, K. Pranke, W. Müller, A. Yanina, Development of high-strength TRIP-matrix-composite materials, in *Proceedings of the International Conference of Production and Processing of Cladded Materials and Metal Matrix Composites MEFORM 2014*, ISBN 978–3-86012-481-9, Altenberg 26.03.–27.03.2014, Herausg.: ACATRAIN e.V., Verein für Weiterbildung an der TU Bergakademie Freiberg, Institut für Metallformung, pp. 149–159
20. M. Abdel-Rahman, M.N. El-Sheikh, Workability in forging of powder metallurgy compacts. J. Mater. Process. Technol. **54**, 97–102 (1995)
21. I. Pyshmintsev, M. Meyer, B. Cooman, R. Savray, V. Shveykin, M. Vermeulen, The influence of the stress state on the plasticity of transformation induced plasticity-aided steel. Metall. Mater. Trans. A **33**, 1659–1667 (2002)
22. I. Tamura, Y. Tomota, H. Ozawa, in *Proceedings of 3rd International Conference on Strength of Metals and Alloys* (Cambridge, England, 1973), p. 611
23. G.D. Bokuchava, Y.E. Gorshkova, V. Papushkin, S. Guk, R. Kawalla, Investigation of plastically deformed TRIP-composites by neutron diffraction and small-angle neutron scattering methods. Surf. Invest. X-ray, Synchr. Neutr. Tech. **12**(2), 227–232 (1995)
24. A. Yanina, S. Guk, W. Müller, R. Kawalla, C. Weigelt, Dynamic and static softening of sintered MgO-PSZ/TRIP-matrix composites with up to 10 vol-% ZrO_2. Steel Res. Int. **82**(9), 1158–1165 (2011)
25. A. Yanina, S. Guk, R. Kawalla, New TRIP-matrix-composite production, properties and softening behaviour during warm forming. Tagungsband der internationalen Konferenz "Neuere Entwicklungen in der Massivumformung". ISBN 978-3-88355-386-3, Fellbach/Stuttgart 17.05.–18.05.2011, pp. 271–281
26. M. Petrov, S. Guk, P. Petrov, J. Bast, Kraft- und Deformationscharakteristika beim Umformen eines Stahlblech-Verbundwerkstoffs. Lightweight Des. **5**(5), 50–57 (2012)
27. S. Guk, D. Milisova, K. Pranke, Influence of deformation conditions on the microstructure and formability of sintered Mg-PSZ reinforced TRIP-matrix-composites. Key Eng. Mater. **684**, 86–96 (2016). Advanced materials and processes of metalworking. ISBN-13: 978-3-03835-522-9
28. S.S. Gorelik, *Recrystallization in metals and alloys* (MIR Publishers, Moscow, 1981)
29. K. Pranke, S. Guk, Material flow in Mg-PSZ particle reinforced TRIP-matrix-composites due to hot-rolling. Key Eng. Mater. **684**, 97–103 (2016). Advanced materials and processes of metalworking. ISBN-13: 978-3-03835-522-9
30. Y. Prasad, S. Sasidhara, *Hot working guide: a compendium of processing maps* (ASM International, Materials Park, 1997)

Chapter 8
Powder Forging of Presintered TRIP-Matrix Composites

Markus Kirschner, Sergey Guk, Rudolf Kawalla and Ulrich Prahl

Abstract This chapter addresses bulk forming processes-especially powder forging-used to produce complex shaped components from presintered TRIP-matrix composites. Based on experimentally determined material and process parameters (e.g., shrinkage, Poisson's ratio, elastic modulus, oxidation behavior), extended process maps for compressible materials were presented. Subsequently, a characterization of the material flow as a function of the material conditions was reproduced via the visioplastic method and metallographic analysis, and then connections were drawn between the results and the extended process maps. The knowledge gained was used to develop a powder forging tool for a Gleeble HDS-V40, which was used to conduct model tests aiming to improve the component properties. The tool was equipped with compensating gaps to provide better compaction to the components. To find the optimal compaction for the solid material, different variants of compensating gaps were investigated. The components obtained through this approach were examined on the basis of their mechanical properties and microstructures. Furthermore, the deformation of graded components was analyzed in this study. In addition to the formation of a damage-tolerant interface and the shear strength of the different layers, special attention was paid to process-relevant parameters, such as the maximum deformation degree, the tool and specimen temperature and the pressure holding time.

M. Kirschner (✉) · S. Guk · R. Kawalla · U. Prahl
Institute for Metal Forming, Technische Universität Bergakademie Freiberg, Freiberg, Germany
e-mail: markus.kirschner@imf.tu-freiberg.de

S. Guk
e-mail: sergey.guk@imf.tu-freiberg.de

R. Kawalla
e-mail: rudolf.kawalla@imf.tu-freiberg.de

U. Prahl
e-mail: ulrich.prahl@imf.tu-freiberg.de

H. Biermann and C. G. Aneziris (eds.), *Austenitic TRIP/TWIP Steels and Steel-Zirconia Composites*, Springer Series in Materials Science 298,
https://doi.org/10.1007/978-3-030-42603-3_8

8.1 Introduction

The integration of various properties and functions in a component or in an assembly is constantly increasing to shorten product manufacturing times and enhance resource conservation. The required high functionality of materials often leads to chemical-physical requirements that cannot be met by a single material. In some cases, the use of high-performance materials can lead to compromises. Moreover, the range of properties of these innovative high-performance materials is often insufficient to cover all requirements, which is why composite materials are used to provide a combination of the desired properties.

Powder forging is a combination of sintering and precision forging technology that blends the advantages of sintering technology in terms of component design possibilities, good material utilization and narrow tolerances with the high strength of forged components [1–3]. Powder forging is used to turn pressed and sintered semifinished products into solid components with outstanding material properties for use in all types of applications [4, 5].

Therefore, the main task of powder forging is to achieve full density [6]. Based on the material flow that occurs, two process variants of powder forging exist [3, 7, 8, 9].

– "Hot repressing": Hot compression without significant material flow, which corresponds to uniaxial compression.
– "Upsetting" (also referred to as "flow forging" or "powder forging"): Hot forming process with significant material flow, wherein a preform with a simple shape is formed into a finished part with a more complicated shape.

The special advantage of powder forging over other compacting processes, such as hot isostatic pressing, lies in the combination of forging technology with the advantages of powder metallurgy. Here, the recrystallization to a finer grain structure and the texture, which is introduced into the component during the forging process, are decisive advantages over other processes. In addition, specimens with complex geometries that exhibit excellent mechanical properties can be produced in large quantities without or with very little further mechanical treatment.

Therefore, powder-forged components are used especially for high dynamic and vibration loads [10–12]. This approach can also produce graded components, which means that components can be manufactured with an inexpensive base material by using a second wear-resistant material for the highly stressed regions [1, 2, 13].

However, this capability is of little use in industry, as the final density of reinforced components and the distribution of the reinforcement phase after powder forging are difficult to control [14, 15]. Due to material flow and the forming process, reordering processes occur in the component that cannot yet be precisely defined. In addition, an additional phase, especially if it is a composite material of two different material classes, represents a barrier to compaction in a component during powder forging; thus, achieving a compact material becomes more difficult [16–18].

This work focuses on the development of basic principles for the production of compact components with different property profiles from a transformation-induced

plasticity (TRIP)-matrix composite. The main process used is powder forging in temperature ranges from 700 to 1100 °C, which follows the sintering process. The test specimens have a residual porosity and the forming process in the final stage is characterized as uniaxial deformation with and without lateral material flow. For this purpose, model compression tests are carried out on the forged specimens in a closed die in order to make a detailed statement on the rearrangement processes of ZrO_2 particles due to friction with contact surfaces, in which the local material flow during compaction is analyzed as a function of the geometry of the forming zone. The challenge here is to investigate the compaction process and the material flow during powder forging of homogeneously reinforced and graded materials. A further challenge is investigating the ability to generate a force-transmitting flat phase boundary via powder forging in the previously designed tool. The technological goal is to produce axially graded components during forming while retaining the graded structure when the material flow begins.

8.2 Materials and Methods

The investigated material is a composition of gas-atomized steel powder, which was austenitic in structure ($d_{10} = 12.4$ µm, $d_{50} = 25.9$ µm and $d_{90} = 46.6$ µm), and Mg-PSZ ceramic powder ($d_{10} = 0.2$ µm, $d_{50} = 4.3$ µm and $d_{90} = 30$ µm). The chemical compositions of both the metastable high alloyed TRIP steel (indicated as X3CrMnNi16-7-6) and the ZrO_2 ceramic are given in Table 8.1. The ceramic particle content was set to 0 vol% (0Z), 5 vol% (5Z), 10 vol% (10Z), 15 vol% (15Z), 20 vol% (20Z) and a graded layer structure. The structures of these five contents are shown in Fig. 8.1.

A binder (1.0 wt% Optapix PAF 35, Zschimmer & Schwarz, Burgstädt, Germany) is used to achieve a more homogeneous density distribution in powder pressing. This binder is added to the powder mixture of ZrO_2 and TRIP steel before powder pressing.

The powder pressing took place at room temperature in a one-sided coaxial press with a pressing force of 200–600 kN depending on the desired residual porosity; the specimens used in this process had a diameter of 10 mm and a height of 10 mm. The individual layers of the graded particle distribution have a height of 2 mm and are stacked individually, precompressed with a low force, and then pressed as a complete component. The subsequent debinding and sintering of the specimens after pressing took place in a furnace (Carbo-Lite/Gero HTK 8 MO/16-1). The debinding was completed before the actual sintering process started. This process took place at a heating rate of 300 K/h and a holding time of 1 h at 1100 °C, followed by a cooling rate of 600 K/h under vacuum (10^{-6} mbar) until reaching room temperature.

For the tests, cylindrical specimens with a height of 10 mm and a diameter of 10 mm were produced. Forming was carried out in a Gleeble HDS-V40 rolling simulator from DSI Europe GmbH (path-controlled) at appropriate temperatures, press forces and deformation degrees. For the desired compression of the specimens, the following three silicon nitride dies, shown in Fig. 8.2, with corresponding tungsten

Table 8.1 Nominal chemical compositions of the TRIP steel powder and Mg-PSZ powder

TRIP steel	Fe	C	Cr	Ni	Mn	Si	N	Al	S	Mo	Ti
[wt%]	bal.	0.03	16.3	6.6	7.2	1.0	0.09	0.04	<0.01	<0.01	<0.01

MgO-PSZ	ZrO_2	HfO_2	MgO	SiO_2	Al_2O_3	CaO	TiO_2	Y_2O_3
[wt%]	bal.	1.85	3.25	0.1	1.58	0.06	0.13	0.13

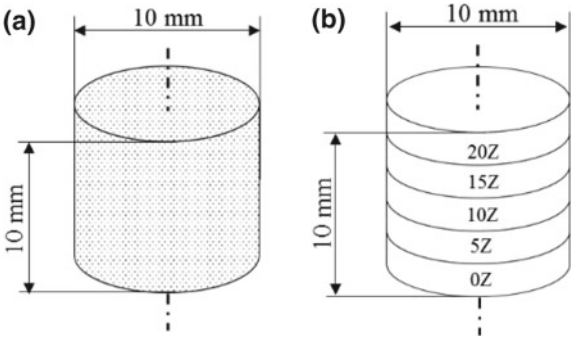

Fig. 8.1 Investigated specimens with **a** homogeneous particle distribution and **b** graded particle distribution

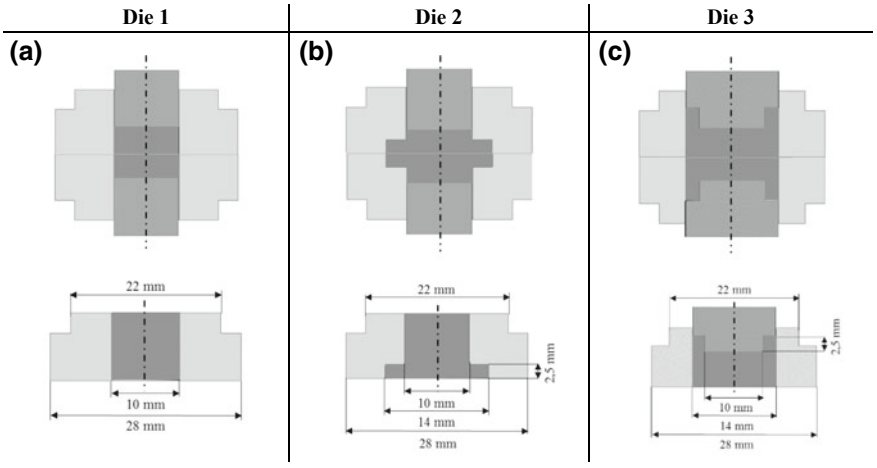

Fig. 8.2 Different die shapes for the investigation of the material flow: **a** Die 1: without a compensating gap; **b** Die 2: with lateral compensating gaps; and **c** Die 3: with upward compensating gaps

carbide punches were available for forming, in which the specimen was conductively heated prior to forming.

Boron nitride was used as a lubricant to reduce friction between the die and the material because carburization may occur during powder forging due to the high temperatures. To avoid this phenomenon, graphite was not used as a lubricant.

The density was determined by means of a hydrostatic balance at room temperature. For this purpose, the specimens were placed in distilled water in a water bath under vacuum for four hours. A magnetic stirrer at the bottom of the water tank prevented the formation of bubbles and kept the water moving. The mass was then determined in distilled water and in air by hydrostatic weighing.

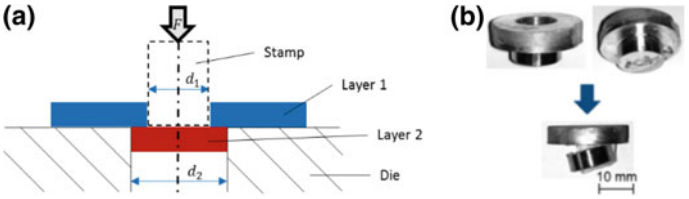

Fig. 8.3 Illustration of the **a** adhesion test and **b** the specimens before and after each test

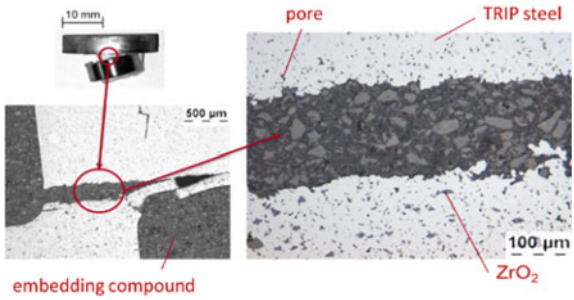

Fig. 8.4 Cross-section through the failure point in an adhesion test specimen

During the adhesion test, the two layers of the graded layer structure of the specimens were generated and the adhesion of the two layers was measured, as shown in Fig. 8.3. The pull-off forces of the individual composite layers were tested in accordance with DIN EN ISO 4624 in an AG-100 testing machine (Hegewald & Peschke, Siebenlehen, Germany). To check whether the phase boundary of the individual layers was also tested, a cross-section was made through the failure point. The results show that the crack did run exactly as desired through the phase boundary of the two structures, as shown in Fig. 8.4.

8.3 Results

To realize this production path, the process-dependent parameters were first examined to limit the process window for the model tests. The focus was on the shrinkage, the density-dependent Poisson's ratio, the density-dependent elastic modulus and the oxidation behavior of the material and on the creation of process maps. Subsequently, model tests were carried out with particular attention to the maximum possible compaction as a function of shear strain, elongation and temperature and to the phase boundary connection between ceramic and steel, which will enable the production of a compact material with complete particle bonding in the matrix. The mechanical properties were then determined from these specimens. Finally, the graded layer structures were investigated following the same approach, and the material properties of the graded layer structures were compared to those of the homogeneous material.

In the following sections, the results of the individual investigations are presented. Note that the analysis takes place in the Cartesian coordinate system and with the different ZrO_2 contents being represented as percentages.

8.3.1 Determination of Material- and Process-Dependent Parameters

Various process parameters were analyzed and evaluated to determine the optimum forging conditions. These parameters include the shrinkage, the density-dependent Poisson's ratio, the elastic modulus/density relationship, and the oxidation behavior of the specimens and process maps. The shrinkage of the components was investigated to calculate the dimensions of the components after sintering and forging, which was necessary for the calculation of the dimensions of the final part and the die dimensions. To consider the density-dependent Poisson's ratio, it is necessary to know the ratio of the horizontal to vertical material load direction when the pore density falls below 10%. The relationship between the density and the elastic modulus was used to determine the start of deformation or plastic flow under external loads. The oxidation behavior was analyzed to investigate the time of transfer between the furnace and the die. Process maps were used to calculate the process window of the different composite states.

8.3.2 Determination of Shrinkage

For the investigation of the specimens after sintering, the shrinkage behavior of the individual ZrO_2 contents was measured with a caliper; the results are shown in Fig. 8.5. The density of the specimens after sintering was 7.1 $\frac{g}{cm^3}$.

The results show that the shrinkage percentage of the sintered specimens reduces considerably with increasing ZrO_2 content. The smallest value of 0.4% can be seen with 20Z, whereas the highest value is 2.2% with 0Z. The specimens with an increasing ZrO_2 content show a decrease in shrinkage. The graded specimen with the value

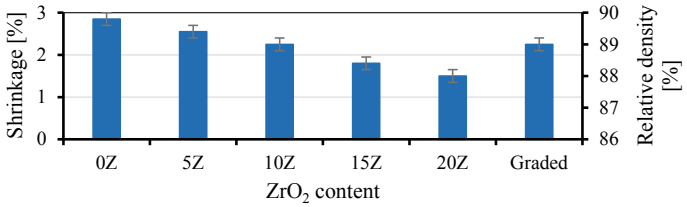

Fig. 8.5 Determination of shrinkage after sintering and powder forging

of 0.7% lies between the specimen with 20Z and the specimen with 15Z. The results also show that there is a considerable difference in shrinkage between the specimen with 0Z and the specimen with 20Z. This difference is important because the shrinkage of the TRIP steel is 2.2%, whereas the shrinkage of ZrO_2 is approximately 0% because the material does not sinter together and is only present as particles in the matrix. Therefore, the shrinkage values of the specimens with a ZrO_2 content are between the shrinkage values of the pure materials. This finding also shows that with increasing ZrO_2 content, the shrinkage of the specimens moves from that of the TRIP steel to that of the ZrO_2 in this particular case.

If these data are compared with shrinkage data from other metal matrix composites (MMCs), it is noticeable that the shrinkage of the TRIP-matrix composite is greater the shrinkage data of other MMCs. For copper matrix composites with a SiC reinforcement phase, the shrinkage is 0.3% [19, 20]. However, note that these specimens had a reinforcement phase content of 70%. A shrinkage of 0.75% was observed in aluminum MMCs, wherein the reinforcement phase was only 0.5% [21, 22]. Thus, the TRIP-matrix composites exhibit greater shrinkage than other particle-reinforced MMCs. However, compared to pure iron steel specimens without particle reinforcement, the specimens in this study exhibit significantly less shrinkage. The high shrinkage in this previous study occurred because a shrinkage of 2.5–3% can be observed in iron powder [23].

Observations show that, similar to the homogenous specimens, the graded specimens exhibit isotropic shrinkage.

The reduction in shrinkage with increasing particle content in the specimens can be explained by the particles themselves. Due to the number of particles in the sintered specimens, there is no specimen shrinkage during sintering because only the matrix material is sintered. The ceramic particles are simply present in the matrix without interacting with the matrix or with each other. The more matrix there is in a specimen, the more the specimen can shrink during sintering. Conversely, this phenomenon means that the more reinforcing particles there are in the matrix (i.e., more of the matrix is replaced), the less the specimen can shrink, as the ceramic particles prevent this shrinkage. This phenomenon can be seen in Fig. 8.5, as the shrinkage of the specimens decreases with increasing ZrO_2 content. The linear expansion coefficient of the matrix is $18.3 \times 10^{-6}\ K^{-1}$, whereas that of ZrO_2 particle is $10.5 \times 10^{-6}\ K^{-1}$.

With regard to shrinkage behavior, there are different approaches that describe the so-called shrinkage parameter. In Fig. 8.6, different shrinkage models are compared to the measured shrinkage of the TRIP-matrix composites. This figure clearly shows that the model according to Coble [24] comes closest to the shrinkage of the TRIP-matrix composite. The value from the Skorokhod model [25] after 60 min of sintering time comes close to the value of the composite, even if the value is an overestimation, whereas the Tikkanen Mäkipirtti model [26] does not show any similarity with the measured value. Note that in the Coble model, the porosity at a certain time works in conjunction with various other material constants, whereas the Skorokhod model and the Tikkanen Mäkipirtti model try to solve the problem via density differences and sample volume differences, respectively.

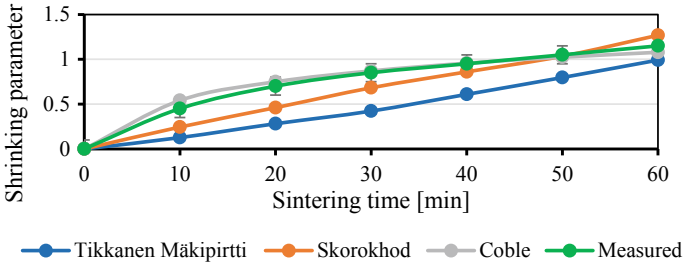

Fig. 8.6 A comparison of different shrinkage models with the measured parameters under the following conditions: 5% ZrO_2 and a residual porosity of 10%

However, in all equations there is no approach for a second material in the equation, which strongly influences the shrinkage parameter due to a different shrinkage. Therefore, the following equation was established on this basis for composite materials:

$$v_s = (-0.13Z + 0.15) \cdot \sqrt{t} \tag{8.1}$$

where Z is the volume content of the second material and t is the sintering time. The equation used here is similar to the equation according to Coble because both equations are based on the specimen porosity and the sintering time. However, this equation further discusses the properties of composites, since the amount of the second phase in the matrix is also taken into account. Thus, a coefficient of determination of 0.98 can be achieved.

8.3.3 Poisson's Ratio as a Function of Density

The Poisson's ratio was determined by compression tests, which were carried out on a Bähr MDS 830 testing system. The Poisson's ratio was determined in accordance with the literature [27]. The specimen was lubricated with boron nitride, and the strain was 0.5 at room temperature.

Figure 8.7 shows that the Poisson's ratio decreases with increasing residual porosity. This finding can also be found in the literature [27]. The reason for this phenomenon is the compression of the material during the compression test with increased residual porosity. The results also show that apart from some fluctuations in the results within the fault tolerance, there are no deviations from the theoretically determined Poisson's ratio. The minor deviations are due to measurement uncertainties.

When considering the dependence of the Poisson's ratio on the density, it is noticeable that the Poisson's ratio increases with increasing density, as shown in Fig. 8.8. This trend corresponds to the general state of the art [27–29]. Furthermore,

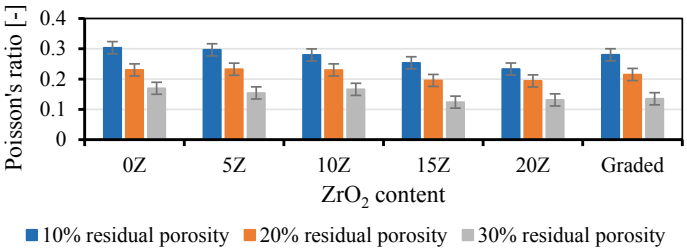

Fig. 8.7 Change in Poisson's ratio under different residual porosities

Fig. 8.8 Dependence of Poisson's ratio on density

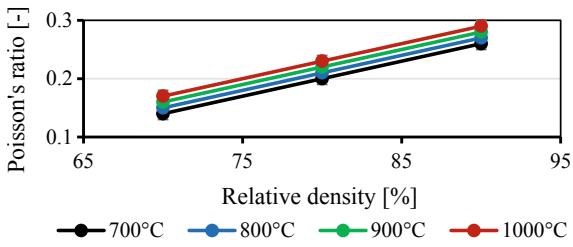

the results show that with increasing density, the Poisson's ratio changes slightly. This trend can be described using the following equation:

$$\vartheta_\rho = (0.6 \cdot \rho_0) + T \cdot 10^{-4} - a \tag{8.2}$$

where ρ_0 is the relative density, T is the working temperature in [°C] and a is a material constant. In this case, a is approximated to a value of 0.35. The equation is an extension equation according to Kuhn and Downey [30]. The equation was extended by the temperature term and a material constant. Nevertheless, the relative density plays a more decisive role in the equation than the temperature. This equation has a determination coefficient of 0.99 with the empirically determined data.

This phenomenon mainly occurs due to the relationship between the elastic modulus, shear modulus and the Poisson's ratio. Due to the heating of the material, the elastic modulus and shear modulus are reduced. As the shear modulus is doubled in the Poisson's ratio formula, the Poisson's ratio increases at higher temperatures.

For upsetting, the ratio of the material flow perpendicular to the pressing direction to that in the pressing direction can be described with a density-dependent Poisson's ratio [8, 30, 31, 32], as shown in Fig. 8.9 for the material here. The figure clearly shows that with increasing ZrO_2 content the density-dependent Poisson's ratio decreases. This phenomenon means that with increasing ZrO_2 content, the ratio of material flow perpendicular to the pressing direction to that in the pressing direction decreases. Moreover, this behavior can be explained by the ZrO_2 particles, which oppose the material flow. For this reason, the ratio of material flow in the pressing direction to that in the pressing direction also decreases.

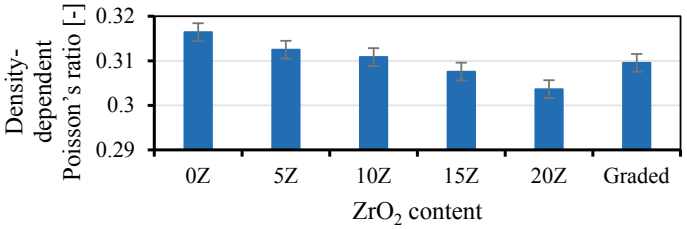

Fig. 8.9 Density-dependent Poisson's ratio with different ZrO_2 contents at a residual porosity of 10%

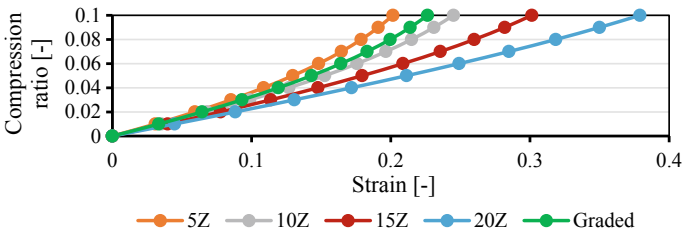

Fig. 8.10 Compression ratio as a function of strain over the Poisson's ratio determined at different ZrO_2 contents

Figure 8.10 shows the dependence of the compression ratio as a function of strain over the Poisson's ratio determined at different ZrO_2 contents, which was previous described for iron powder in the literature [33, 34].

In a composite, this relationship can be described using the following equation:

$$\phi_\rho = \left(25Z^2 - 13.95Z + b\right) \cdot \varphi^2 + 0.2\varphi \tag{8.3}$$

where φ is the strain and b is a material constant of the reinforcement content. In this case, b is approximated to a value of 1.9. This equation was derived from the empirical data to calculate the compression ratio of a composite with a corresponding strain. For this reason, the volume content of the reinforcement phase and the strain are also included in the equation. This equation has a determination coefficient of 0.98 with the empirically determined data.

A comparison of the data with those found in the literature shows that the values for iron powder are slightly higher than those for the TRIP-matrix composite, whereas the values for aluminum MMCs are clearly higher than those for the TRIP-matrix composite. However, note that the reinforcement phase in aluminum MMC is significantly higher at 70% [21]. The same trend (i.e., the values are higher than those for the TRIP-matrix composite) applies to magnesium MMCs that have a reinforcement phase of SiC, wherein the proportion of the reinforcement phase is approximately 30% [35]. Thus, it can be stated that the iron powder comes closest to the values of the TRIP-matrix composite.

8.3.4 Relationship Between Young's Modulus and Density

To determine the axial component of the Young's modulus, the formula of Pavlov et al. [27] was used, which makes it possible to determine the modulus of elasticity through compression tests, which were carried out on a Bähr MDS 830 testing system.

Figure 8.11 clearly shows that the modulus of elasticity increases with increasing ZrO_2 content. Moreover, the modulus of elasticity decreases with increasing residual porosity. This finding is particularly evident at ZrO_2 contents of 15 and 20%. Although the values are almost identical for ZrO_2 contents of 0 and 5%, an increase in the modulus of elasticity can already be seen in the specimen with 10%. The results also clearly show that the specimens with a graded layer structure have a modulus of elasticity between the elastic moduli of the specimens with 10 and 15% ZrO_2. In addition, it can be clearly seen that the measured values of the modulus of elasticity are the same as the values calculated according to the Tsai–Halpin mixing rule [36].

In this composite, the modulus of elasticity can be described using the following equation:

$$E = 90Z + 170\rho_0 \tag{8.4}$$

For simplification, an equation has been derived from the empirical data that agrees with the mixing rule according to Tsai–Halpin. The reinforcing phase and the relative density are included. Here, the relative density plays a larger role than the second phase. This equation has a determination coefficient of 0.95.

Figure 8.12 shows the relationship between the elastic modulus and density. This figure clearly shows that the modulus of elasticity decreases with increasing temperature. Furthermore, the modulus of elasticity increases with increasing density, as described in the literature [37, 38].

The decrease in the modulus of elasticity at elevated temperatures can be described by the temperature dependence of the bonding conditions. Due to the decreasing bonding forces in the matrix, the material flows more quickly. This explains the drop in the modulus of elasticity at elevated temperatures [38]. This change can be described by the following equation:

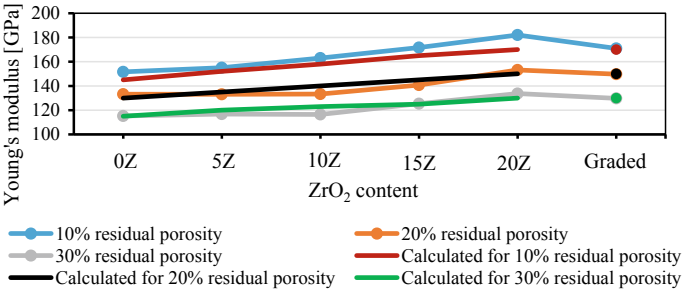

Fig. 8.11 Change in the modulus of elasticity with different residual porosities

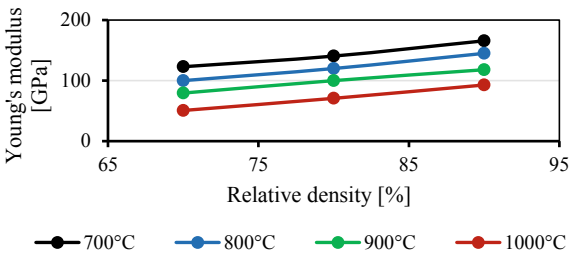

Fig. 8.12 Dependence of the modulus of elasticity on the density of the material with 5Z

$$E = 214\rho_0 - 0.0002T^2 - 0.1T \tag{8.5}$$

This equation was derived from the empirical data for calculating the Young's modulus of a composite at a certain temperature and relative density. For this reason, the density of the specimen and the temperature are also included in the equation. Moreover, the relative density plays a more decisive role in the equation than the temperature. This equation has a determination coefficient of 0.99 with the experimentally determined data.

8.3.5 Oxidation Behavior

For the experimental determination of the scale layer and the associated oxidized specimens were annealed at 1000 °C for 1 h in an inert gas atmosphere and subsequently oxidized in air at intervals of 0, 10, 30 and 60 s. These time periods reflect the transfer times from the furnace to the die in the industry. The oxidation states were then frozen and microsections were made. In addition, calculations of the scale thickness were carried out. This approach was done to simulate the process in industry, where powder forging is usually carried out directly from the sintering furnace. The tests were carried out on compact specimens and porous specimens with a relative density of 80%.

The compact material in Fig. 8.13 shows an average oxide layer of approximately 22 µm. In addition, the scale thickness calculations clearly show that there is a slight difference in the scale thickness of the specimens with 0 and 5% ZrO_2 and that of the specimens with 10 and 20% ZrO_2. In addition, the results show that there is no difference between the sampling times of 0 and 10 s. The first difference observed in the scale thickness of the specimens occurred at a sampling time of 30 s. Here, it can be seen that the specimens with a high ZrO_2 content have a thicker scale than the specimens with a smaller ZrO_2 content. This phenomenon becomes clearer with a sampling time of 60 s.

The porous material in Fig. 8.14 shows an average oxide layer of approximately 66 µm. In addition, the calculations of scale thickness show that there are clear differences between the specimens with 0% ZrO_2, the specimens with ZrO_2 contents of 5, 10, 20% and the graded structure because the latter are already higher than the

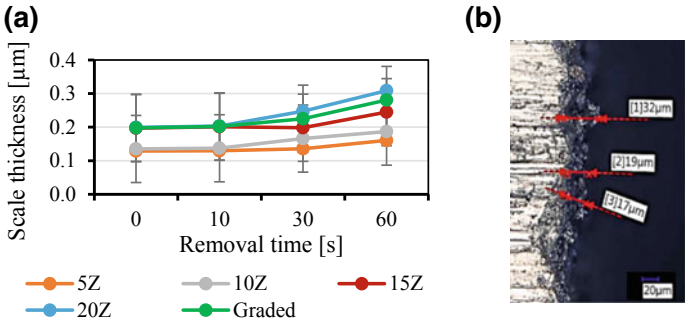

Fig. 8.13 Oxidation behavior of compact material: **a** scale thickness and **b** micrograph

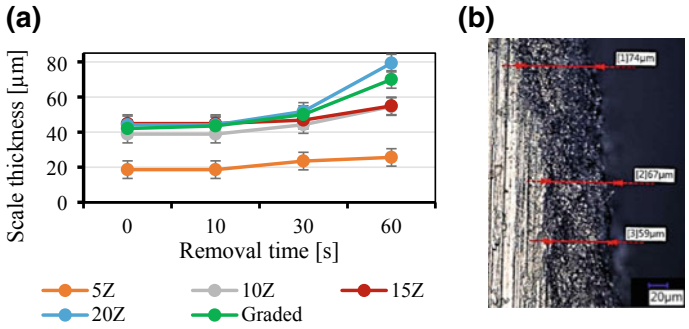

Fig. 8.14 Oxidation behavior of porous material: **a** scale thickness and **b** micrograph

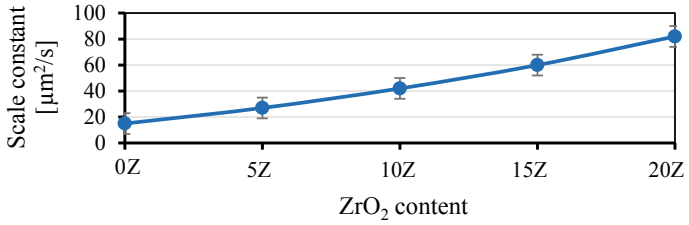

Fig. 8.15 Scale constant as a function of ZrO_2 content at 1000 °C

pure steel at the beginning of oxidation. In addition, there is no difference in specimen oxidation between the removal times of 0 and 10 s; the first notable difference occurred at a sampling time of 30 s. This phenomenon becomes clearer at a sampling time of 60 s. Here, it can be clearly seen that the specimens with ZrO_2 have a larger scale thickness than the specimens without ZrO_2.

This finding means that the different ZrO_2 contents have different scale constants (K_m), as shown in Fig. 8.15; these constants were calculated with the Wagnerian

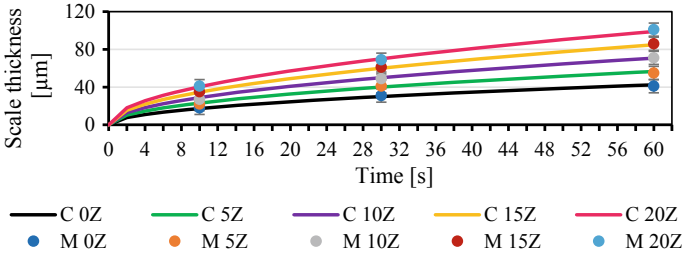

Fig. 8.16 Measured scale thickness at 1000 °C with different ZrO_2 contents (C—calculated and M—measured data)

Fig. 8.17 Temperature dependence of the scale constants

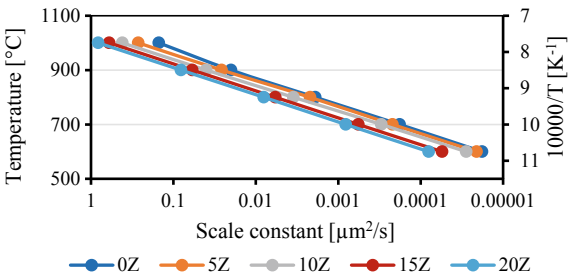

scale theory (parabolic scale growth). The scale constant shown here corresponds to that in the literature [39, 40]. This figure clearly shows that the scale constant increases with increasing ZrO_2 content.

With this scale constant, it is possible to calculate the scale thickness of the individual ZrO_2 contents, as shown in Fig. 8.16. This figure clearly show that with increasing time, the scale layer increases significantly, as reported in the literature [40]. Moreover, with increasing ZrO_2 content, the scale thickness increases. In addition, the simulated values correspond to the measured scale thicknesses.

The results also show that the scale constant is temperature dependent, as previously described in the literature [39, 40]. Figure 8.17 shows that the scale constant behaves linearly at all ZrO_2 contents. In addition, as the ZrO_2 content increases, the curve of the scale constant moves farther away from that of the TRIP steel without ZrO_2.

The oxidation behavior of the specimens generally shows that the scale thickness increases with increasing ZrO_2 content; this phenomenon occurs because the closed surface structure is broken up by the ZrO_2 particles on the surface. This broken structure has more points of attack for oxidation than a closed body. However, note that the porosity of each specimen on the surface is the same as that in the core. The same applies to the values of the porous specimens. Compared to a closed surface, this irregular, porous surface provides a larger area of attack for oxidation. In addition, there is a time factor. Because the porosity increases the area of attack, the more

time there is to oxidize the porous surface, the higher the scale thickness, as shown in Fig. 8.15.

For the same reason, each ZrO_2 content has its own scale constant, which increases with increasing ZrO_2 content in the specimen. The different scale thicknesses can easily be explained by the different scale constants and the different temperature dependencies.

It should therefore be noted that the optimum time for introducing the semifinished products from the sintering furnace into the forging tool is up to 10 s. As previously mentioned, there are no significant deviations in oxidation from a removal time of 0 s in either the nonporous or porous material. Due to the rapid and large formation of oxide layers, it is not advisable to allow for insertion times longer than 10 s.

8.3.6 Process Map Extension for Compressible and Graded Materials

Prasad et al. [41] developed a process map that is helpful in characterizing formability, optimizing the hot forming process and controlling the microstructure of the materials. The only disadvantage is that this process can only be used for incompressible materials. For this reason, this procedure is not applicable to compressible materials such as those used in powder metallurgy. However, in order to create process maps for powder metallurgical production processes that assume a porous initial state, important adjustments must be made. However, powder metallurgical materials can be produced as both homogeneous materials and graded materials. Hence, some adjustments must be made to the compressible material model for the creation of process maps. These modifications include adjustments of the friction due to the different material compositions between the specimen foot and the specimen head and adjustments to the specimen diameter due to the different bulges in the individual layers, which result from differences in composition, stresses, and residual porosity in the individual layers.

Powder forging was simulated on specimens with different ZrO_2 contents and different residual porosities. Therefore, the temperature range 700–1050 °C was investigated. The following conclusions can be drawn from Fig. 8.18.

For TRIP steel, it can be observed that the energy dissipation, starting from a residual porosity of 30% up to a residual porosity of 10%, creates new isolines and strongly shifts the existing isolines. Moreover, the solid material contains considerably fewer isolines than the specimens with residual porosity. In addition, the power dissipation of the compact material is significantly higher (between 15 and 40%) than the power dissipation in the specimens with residual porosity (between 5 and 20%). Furthermore, the only range that does not permit forming is between the forming speeds of 10 and 1 s^{-1} at all temperatures. In addition, component failure occurs at forming speeds of 10^{-1} s^{-1} and 0.1–0.01 s^{-1} in a temperature range of 750–800 and

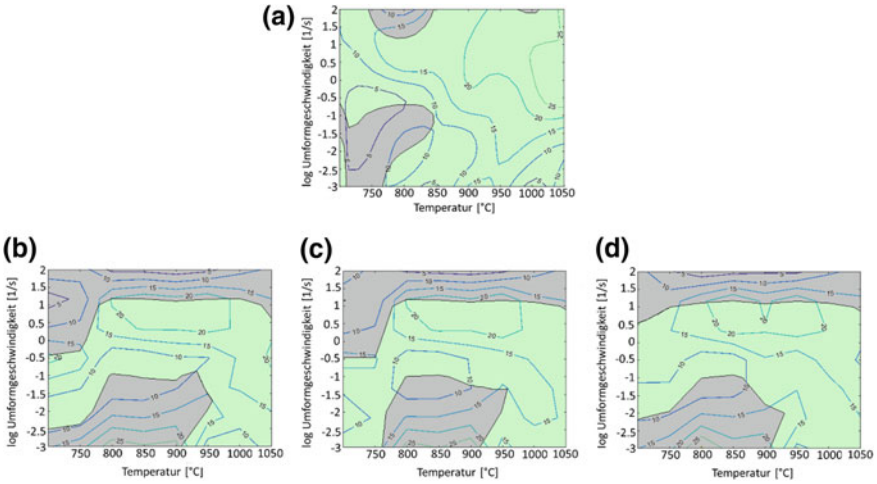

Fig. 8.18 Process maps with 10 vol% ZrO_2: **a** a solid specimen and specimens with residual porosities of **b** 10%, **c** 20% and **d** 30%

900–950 °C. In addition, as the residual porosity increases, the proportion of area where deformation can occur without failure increases.

The unstable area in the upper left corner of all process maps is due to the forming speed. At high forming speeds, the material has no time to absorb the resulting high stresses and subsequently flow. This phenomenon leads to cracking under further external loads. At higher temperatures, the yield strength of the material decreases to such an extent that, despite the rapid deformation, there is greater material flow.

The differences in power dissipation can be explained by the compaction process. Instead of converting energy of the forming process into another form, such as heat, the energy is used to compact the specimen. Therefore, the power dissipation also increases with decreasing residual porosity until reaching a maximum value in the solid material. Detailed and further information can be found in the literature [42].

8.4 Model Experiments on Powder Forging

For the simulation of powder forging and for the verification of the previously obtained data, model experiments of powder forging are presented. Powder forging using the visioplastic method was carried out to investigate the dependence of the shear strain percentage on the compression ratio and the associated mechanical properties. To check the theoretical pore closing behavior during powder forging, metallographic images were examined in various forming stages. In addition, this method was used to investigate the phase angle and boundary between ceramic and steel in order to determine whether the reinforcing particles are firmly embedded

in the matrix and contribute to the mechanical strength. In addition, the relationship between strain and temperature was analyzed to determine the minimum strain required for complete compaction and the temperatures at which optimum and rapid compaction occurs. At the end of powder forging, relative densities of 99.9% were achieved.

8.4.1 Visioplastic Method

The visioplastic method was used to determine the material flow and the associated compaction. For this purpose, cylindrical specimens with a diameter of 10 mm were separated along the sagittal plane and a grid was applied to the inside with a laser (Lasonall XS25, Östling, Solingen, Germany), as shown in Fig. 8.19. The grid mesh was 1 mm, and the depth of the grid was 0.1 mm.

The specimens were recombined. The specimens were compacted in a Gleeble HDS-V40 (Dynamic Systems Inc., Weissenhorn, Germany) (path-controlled) rolling simulator at appropriate temperatures and pressure and in dies 1–3. The temperature was set to 1000 °C, and the strain rate was set to 1 s^{-1}. After forming, the specimen halves were separated from each other again and the grid distortion was measured. Subsequently, with the help of the AutoGrid system (Vialux, Chemnitz, Germany), the major and minor strains were determined.

When considering the residual porosity as a variable parameter, the results show that the strain decreases with increasing residual porosity, as shown in Fig. 8.20. However, the deformed area increases with increasing residual porosity.

This finding can be explained by the increasing compression of the compressible material with increasing residual porosity: with higher residual porosity, there is more volume in the specimen that must first be compacted. This phenomenon leads to very early deformation and to distortion of the applied grid. In contrast, with a low residual porosity (i.e., a small pore volume), the deformation of the component only occurs later because the component exerts a counterforce against the deformation; thus, lower degrees of deformation occur in the samples with low residual porosity. This assertion is confirmed by considering the effective strain. Here, the results show that with increasing residual porosity, the degree of effective strain decreases slightly, whereas the deformed area exhibits a relatively strong increase. This behavior is also

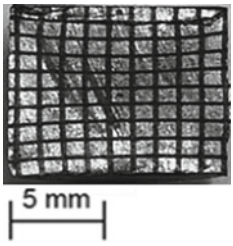

Fig. 8.19 Half of a specimen used for visioplastic analysis after grid preparation

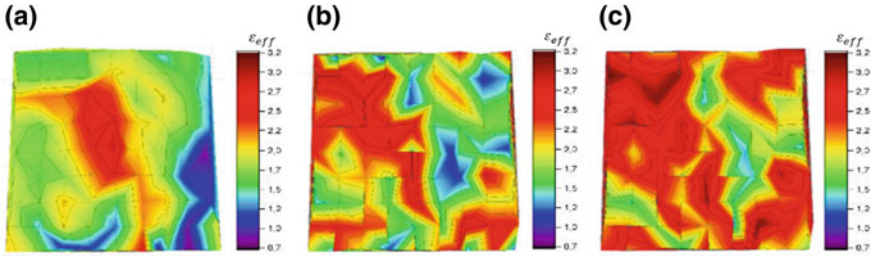

Fig. 8.20 Comparison of effective strain with different residual porosities: **a** 10% residual porosity, **b** 20% residual porosity, and **c** 30% residual porosity

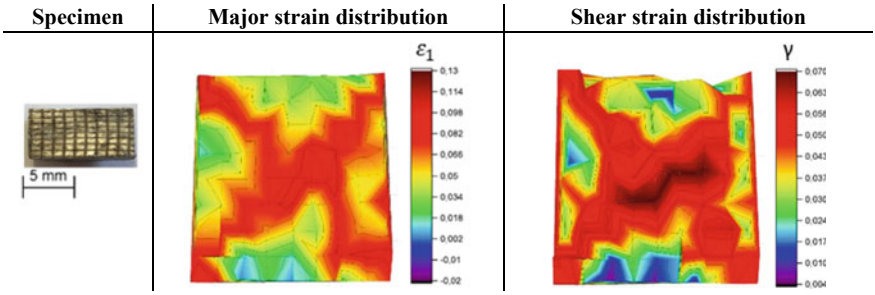

Fig. 8.21 Major strain and shear strain for the specimens in die 1

attributed to the compression of the residual pore volumes in the specimens with increasing residual porosity.

If the different dies (dies 1–3) with their different arrangements of compensating gaps are regarded as variable parameters, then the following information can be determined:

The results show that the major strain is found mainly at the outer corners and in the center of the specimen, as shown in Fig. 8.21. In addition, the specimen shear strain in die 1 is lower than that in the dies, and this shear strain only occurs at the outer corners and in the center of the specimen.

This result reflects the general representation of a forging cross. The creation of the forging cross can be explained simply by Schmid's shear stress law. This phenomenon occurs because the greatest shear stress in a body is at a 45° angle to the main stress axis. For this reason, the largest plastic deformation in the matrix occurs at a 45° angle from the corners of the specimen, which results in a forging cross in a real specimen. Because there are no compensating gaps in die 1 and the material is only compressed and compacted, a significant shearing of the component occurs. The typical bulging of the specimen during the formation of the forging cross is prevented by the die. The very slight shear strain is due to compression and the associated material flow during compression.

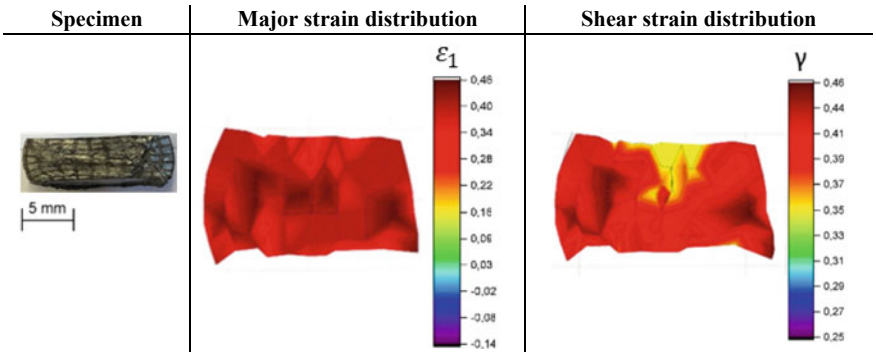

Fig. 8.22 Major strain and shear strain for the specimens in die 2

With die 2, the major strain is highest and can be found nearly exclusively at the level of the compensating gap. The material that has not flowed into the compensating gap shows nearly no deformation compared to the rest of the specimen, as shown in Fig. 8.22. A shear strain analysis shows that the specimen shear strain in die 2 is higher than that in the other two dies. Moreover, the highest shear strain is found in the area of a compensating gap, whereas there is approximately no shear strain in the area without a compensating gap.

This finding must be explained in terms of the material flow into the compensating gap during forming. When the material flows into the compensating gap, the specimen is subjected to a large shear, which results in a large deformation of the specimen and a very high major strain distribution. This phenomenon is verified by the proportion of shear strain in the specimen, which can also only be found in the area of the compensating gap. Due to this shear and the material flow, a forging cross is not formed. However, a high shear strain rate results in a strong compression of the specimen, as is the case in theory.

The specimen strain in die 3 is between that in dies 1 and 2. In addition, the largest major strain can also be seen at the outer edges and in the center of the specimen. With this die, the proportion of shear strain is concentrated primarily on the center and on the tips of the outer edges, whereas in other areas, there is approximately no shear strain, as shown in Fig. 8.23. Detailed and further information can be found in the literature [43].

On the one hand, this behavior can be traced back to the forging cross, which forms in the center of a body during compression. The high shear rates at the outer corners of the specimens are due to the shear of the specimen material with the punch, as the material flowed into the compensating gap at the desired points. However, note that the shear strain experienced by the material in this way is substantially lower than the shear strain produced by the structure of die 2. Thus, the density of the test specimens from die 3 is also lower than that of the test specimens from die 2.

If the relative density is now compared with respect to the selected die and the ZrO_2 content, it can be seen that the highest relative density was achieved with the dies

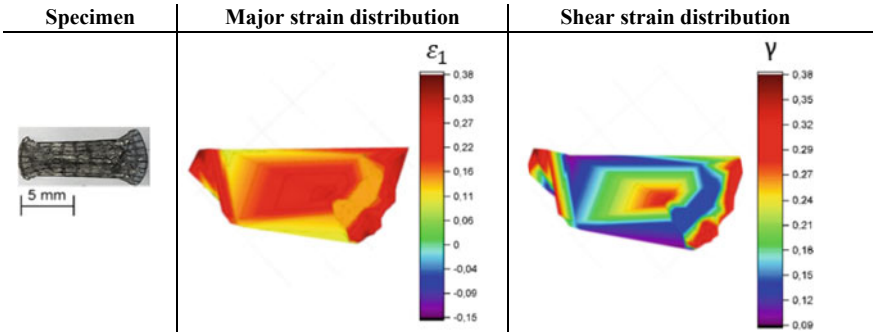

Fig. 8.23 Major strain and shear strain for the specimens in die 3

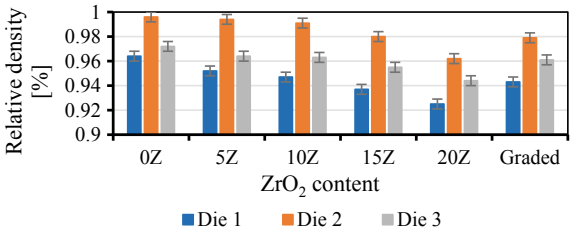

Fig. 8.24 Comparison of relative densities with different dies and ZrO_2 contents

with compensating gaps. In addition, as the ZrO_2 content increases in the specimens, the relative density of the final components decreases, as shown in Fig. 8.24. The change in theoretical density with increased ZrO_2 content was taken into account.

The large difference in the maximum relative densities achieved can be explained by the dies and the associated forming conditions. With pure compression without transverse flow, die 1 represents pure repressing. The state of the art is in agreement that with pure repressing only, relative densities up to a maximum of 95–96% are possible [1, 12, 44, 45, 46, 47, 48]. Therefore, the values measured here are in a very high range with respect to the achieved densities. Dies 2 and 3 have compensating gaps and should achieve a relative density of 100% due to the transverse flow of the material. This relative density was nearly achieved in some of the specimens in die 2. However, for die 3, the relative density of 100% was not reached due to the high stress on the matrix in the shear zone. Due to this stress, new pores and cracks occur within the specimen, as shown in Fig. 8.25. For this reason, complete compaction of the material is not possible in die 3.

The decreasing final density of the specimens with increasing ZrO_2 content is due to the increasing hydrostatic stresses in the matrix of the material, which increase due to the increasing number of reinforcing particles. These hydrostatic stresses oppose the yield stress, thereby inhibiting the material flow. However, shear strain and the associated material flow are the main mechanisms for the compression of compressible bodies. Thus, a compression of the specimens with a high ZrO_2 content is not exactly given, as with specimens with a low ZrO_2 content.

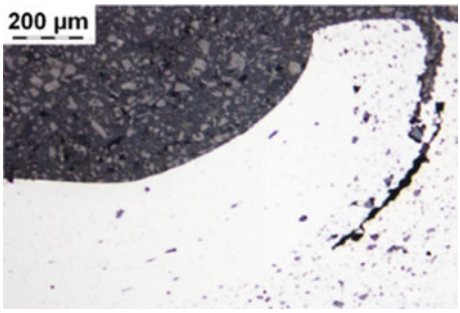

Fig. 8.25 New pores and cracks that appear during forming in die 3

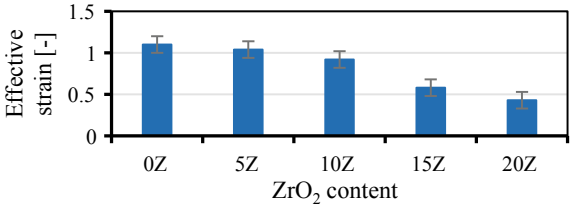

Fig. 8.26 Effective strain at different ZrO_2 contents in die 2

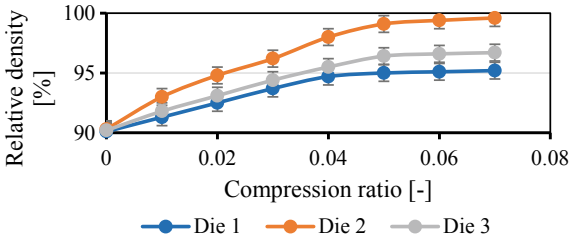

Fig. 8.27 Relationship between compression ratio and relative density for a specimen with a residual porosity of 10% and 5Z

An examination of the effective strain with variable ZrO_2 contents from die 2 shows that with increasing ZrO_2 content, the effective strain decreases strongly, as shown in Fig. 8.26. In addition, the deformed surface remains nearly constant.

These findings lead to the conclusion that as the ZrO_2 content increases in the samples, the hydrostatic stresses in the sample volumes increase due to the particle reinforcement and thus a material flow is inhibited. Thus, the force required for the same degree of deformation is increased accordingly. Hence, the particle amplification represents an obstacle for the material flow and generates a hydrostatic stress field that counteracts the stress field of the flowing material and brings a portion of the material to a standstill, which makes a postcompaction of the compressible material into the compact state more difficult or impossible.

Note that the presence of compensating gaps and a high effective strain lead to a high relative density and that the arrangement of the compensating gaps plays an essential role in the compaction, as shown in Fig. 8.27. The results clearly show

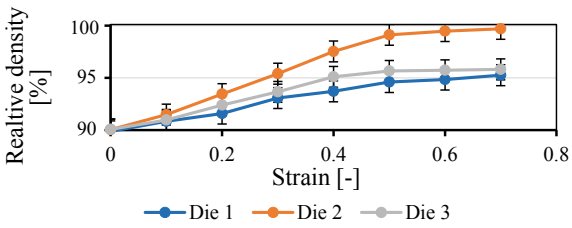

Fig. 8.28 Influence of the strain on the density during powder forging with the different dies at a working temperature of 1000 °C and 5Z

that dies 2 and 3 achieve a higher relative density than die 1 at the same degree of compression.

Thus, the arrangement of the compensating gaps plays a decisive role. The arrangement of the compensating gap must ensure that the greatest possible shear strain is generated in the component and that the greatest possible material flow is achieved. This influence of the compensating gap arrangement is demonstrated by the fact that the compaction in die 2 is greater than that in die 3, although both have compensating gaps.

The relationship between strain and temperature is investigated to find the minimum strain required for complete compaction and at which temperatures optimum and rapid compaction occurs.

To find the die with the best compression properties, the individual relative densities of the specimens were compared with the matrices depending on the strain. Figure 8.28 shows the influence of the strain on the relative density in labor tests with the different dies.

In addition, the results show that from a strain of 0.5, no significant compaction of the specimen occurs. Overall, the maximum achievable density is highest for die 2 at 99.8%, followed by die 3 at 96.3%, and finally by die 1 at 94.6%; note that die 1 was designed without a compensating gap and represents a pure postcompaction. The case of die 1 represents the worst compaction to solid material. From this finding, it can be deduced that the matrices with compensating gaps have a higher density than the matrices without compensating gaps. Thus, a higher density is achieved if transverse flow or shear strain occurs in the material.

The increase in density in die 3 is weaker than that in die 2, which is due to the arrangement of the compensating gap and the associated different shear deformation. In die 2, the material shears the specimen by a transverse extrusion process, whereas in die 3, there is a pure upsetting first and then shearing at the punch edges. According to the state of the art, the decisive factor for compaction is the hydrostatic stress component; however, for optimum full compaction, a certain mixture of hydrostatic stress component and shear strain is more suitable. Based on the available data, it can be assumed that the shear strain must correspond to the hydrostatic stress to achieve full compaction and that the shear strain should not begin subsequently as with die 2. Therefore, the arrangement of the compensating gaps in the die plays a decisive role in compaction.

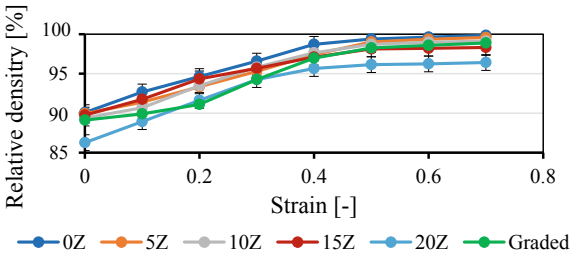

Fig. 8.29 Influence of the strain on the density in die 2

Figure 8.29 shows the influence of the different ZrO_2 contents and the strain on the density during powder forging with die 2. Note that the possible compaction decreases with increasing ZrO_2 contents. However, a higher density can be achieved overall with die 2 (i.e., with compensating gaps) than with die 1. In addition, from a strain of 0.5, no significant compaction of the specimen takes place. The increase in density from a strain of 0.5 is greater in die 2 than in die 1. In the case of specimens with a ZrO_2 content of 15 and 20%, the compaction is even less. Additionally, this phenomenon can be traced back to some measuring tolerances in the determination of the density. A maximum density of 99.8% can be achieved with a ZrO_2 content of 5%.

The differences in compaction between the individual ZrO_2 contents are due to particle reinforcement. With increasing ZrO_2 content in the specimens, the initial density of the specimens decreases. As previously stated, the stress field emanating from the reinforcing particles works against the hydrostatic stress component required for compaction. Since the ZrO_2 cluster formation additionally reinforces the stress fields, the material flow and the subsequent compaction nearly comes to a standstill. The reason that a higher compaction is still possible with these high ZrO_2 contents in die 2 lies in the previously described compensating gaps and the breakage of particle clusters due to shear strain. These phenomena allow material flow and compaction. However, from a ZrO_2 content of 20%, the stress field of the particles seems to be so large that even the shear strain is not sufficient to overcome it.

Furthermore, the specimens do not undergo significant compaction after a strain of 0.5. This finding could be explained by the fact that the material has already undergone full shear deformation in the compensating gaps; thus, a sharp increase in density has already occurred. Therefore, the specimen is now compressed and compacted only by postcompaction and no longer by shear strain. This compression only has a slow increase in relative density, which explains the slow increase in density from a strain of 0.5. Detailed an further information can be found in the literature [49].

8.4.2 Metallographic Examination

To examine the microstructure, metallographic microsections were carried out at each strain and the microstructure was analyzed. The images were taken at the forging cross of the specimens from die 2, as shown in Fig. 8.30. In this case, the specimen contains only 5Z. The residues on the specimens originate from V2A etching.

The metallographic examination (Fig. 8.31) shows the microstructure and some artifacts of the V2A etching, which are marked here as gray areas. Moreover, it is clearly visible that at a strain of 0, the individual grains of the TRIP matrix and the reinforcing particles are still visible. With increasing strain, the holes are compressed and stretched, as described in the literature [27, 50], until a large pore becomes many finely distributed pores. These pores are compressed and distributed by the beginning material flow, as observed in the microstructure of the specimen with a strain of 0.3. Moreover, the microstructure of the specimen with a strain of 0.3 is finer than the individual powder particles in the microstructure with a strain of 0. This phenomenon becomes very clear at a strain of 0.5. The results show that the material recrystallizes during powder forging. However, this recrystallization process is not accelerated or excited by the reinforcing particles since these particles are above a particle volume fraction-to-particle size ratio of 0.2 μm^{-1}; therefore, according to some authors, the particles do not support recrystallization [35, 51]. The grain size at the beginning of powder forging, measured via laser granulometry, was 37 μm, whereas the grain size after powder forging was only 19 μm, which confirms recrystallization.

For the analysis of the surfaces of the individual layers of the graded layer structure after forming, metallographic images of the surfaces of the individual phases were made according to different strains. These images were taken because these areas

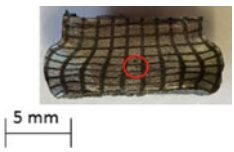

Fig. 8.30 Illustration where the microstructure of the specimens from die 2 were recorded

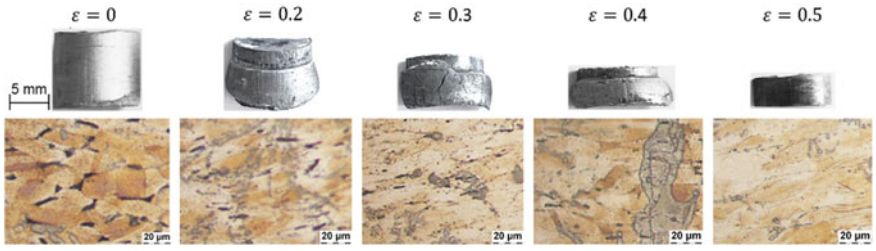

Fig. 8.31 Microstructure at the corresponding strain at the center of the specimen

that are most susceptible to interference (i.e., weak spots) in graded layer structures. These locations are particularly susceptible to interference due to the different stress fields in the individual layers. To fully utilize the mechanical properties of these components, a good connection of the individual phases is very important.

At the interface of the individual layers of the graded layer structure, no special features in the sense of defects can be recognized; however, the different ZrO_2 content is clearly recognizable, which distinguishes the layers from each other. Figure 8.32 also shows the bulging structure in the graded specimen at a strain of 0.4. This bulging structure deviates from the symmetric barrel-shaped bulge of homogeneous specimens. This deviation was taken into account when calculating the process maps of compressible graded materials; this phenomenon was mathematically described in that section.

8.4.3 Formation of the Interfaces of Phases

For the analysis of the ceramic/steel interfaces, metallographic images were taken both in the shear zone (Fig. 8.33) and in the forging cross (Fig. 8.34) of a specimen from die 2 after powder forging at 1000 °C.

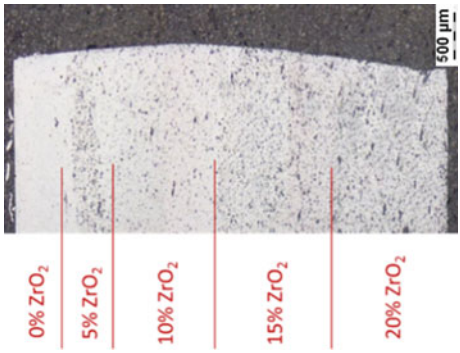

Fig. 8.32 Micrograph through the different layers of a graded specimen

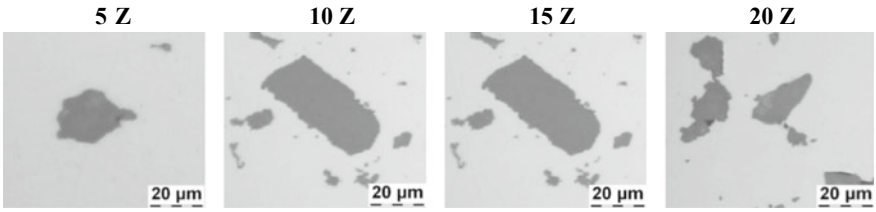

Fig. 8.33 Ceramic/steel interface in the shear zone with corresponding ZrO_2 contents

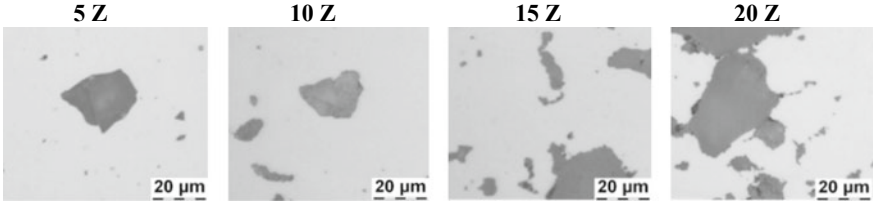

Fig. 8.34 Ceramic/steel interface in the forging cross with corresponding ZrO_2 contents

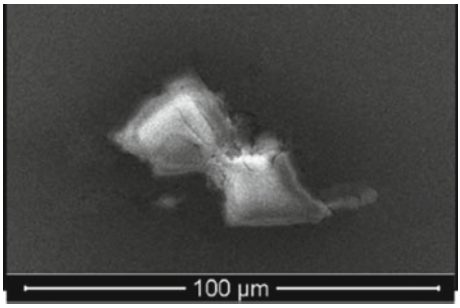

Fig. 8.35 SEM image of the interphase ceramic/steel at a ZrO_2 content of 10% (HV: 20 kV; WD: 10; and Mag.: 2000)

The microstructures in the shear zone of the specimens show a fixed bond between the reinforcing particle and the matrix for the specimens with 5, 10 and 15% ZrO_2. In addition, no pores or cracks are visible. In the specimen with 20% ZrO_2, pores or holes in the steel matrix are visible at the poles of the particles. Thus, there is no 100% binding of the reinforcing particles to the matrix. Smaller and isolated particles are fully bound to the matrix, whereas large particles or whole particle clusters show corresponding pores in the matrix.

The images in the forging cross of the specimens show that the specimens with ZrO_2 contents of 5, 10 and 15% also exhibit a firm bond between the reinforcing particle and the matrix. The specimen with 20% ZrO_2 also shows pores in the matrix and in the shear zone. However, the pores are more frequently found in the matrix than in the shear zone.

Images from a light microscope indicate that the specimens with a low particle content show a good phase bonding between matrix and reinforcing particles. This good phase bond is also visible during scanning electron microscopy (SEM) observations, as shown in Fig. 8.35. This finding confirms the assumptions from the light microscope images.

However, fewer pores are present in the specimens in the shear zone than in the specimens in the forging cross. This discrepancy can be explained by the hydrostatic stress field and the yield stress. As the ZrO_2 content increases, stresses form in the matrix that counteract the hydrostatic stress, thereby preventing the specimen from compacting. These yield stresses become particularly large in clusters of reinforcing particles. These stresses can become so great that they completely stop the flow of material. The difference in the residual porosity between the shear zone and

the forging cross is mainly to be found in the forming or the material flow. Since the specimens in the shear zone undergo a large deformation due to the shear and the associated shear strain, there is a greater yield stress in this section, as shown in Sect. 8.4.1; thus, a greater material flow occurs due to the compression of the specimen. In the case of the specimens in the forging cross, no correspondingly high shear strain occurs due to the lack of a strong material flow, which can also be seen from the only slightly distorted grid on the specimen in Fig. 8.21. As a result, the yield stress is sufficiently large to counteract the hydrostatic stress field and to subsequently counteract full compaction. This assertion is supported by the increased occurrence of pores in places where many particles meet. Detailed and further information can be found in the literature [52].

8.4.4 Mechanical Properties

When considering the hardness distribution within the different dies, as shown in Fig. 8.36, the highest density is achieved in die 2, whereas die 1 produces the lowest hardness.

These results can be explained by the density of the specimens. The higher the density of the specimen is, the better the mechanical properties and the higher the hardness of a powder-forged specimen. The highest compaction was achieved in die 2. The hardness measurements showed that the hardness of the specimens increased with increasing ZrO_2 content. This increase in hardness can be explained by the fact that the reinforcing particles counteract the deformation caused by the hardness tester.

It is possible to calculate the tensile strength of a material from the hardness of the material [53]. According to this model, the data from Fig. 8.37 were collected.

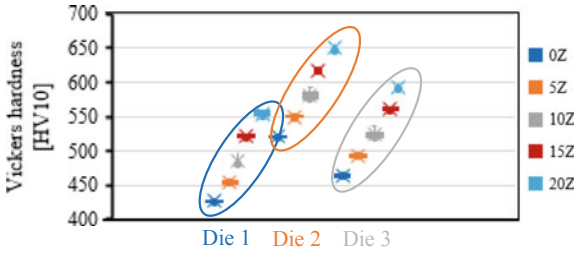

Fig. 8.36 Hardness distribution at different ZrO_2 contents in the different dies

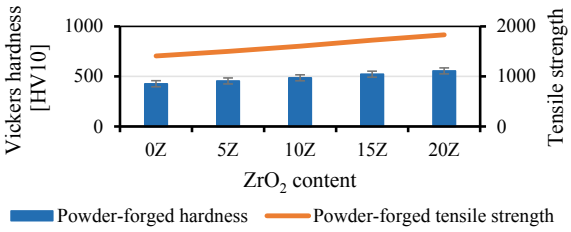

Fig. 8.37 Hardness and tensile strength after powder forging in die 2

8.4.5 *Shear Strength of the Layers with a Graded Layer Structure*

The adhesion of the layers of the graded layer structure was measured in the graded material systems to determine the shear strength of the individual layers and to be able to make possible predictions for the failure location. When measuring the shear strength of the individual layers, it was found that with increasing ZrO_2 content in the individual layers, the shear strength generally decreases, as shown in Fig. 8.38.

With increasing ZrO_2 content, the shear strength decreases on average by 17% with increasing ZrO_2 content, both in forged and sintered specimens. In addition, the shear strength of forged specimens is significantly higher than that of sintered specimens. On average, the shear strength of forged specimens is 72% higher than that of sintered specimens.

This phenomenon can be explained by the increase in reinforcing particle fractions and the fact that as the number of particles contained in the matrix increases, the amount of matrix present at the interface of two layers decreases. Similarly, the poles represent flaws where crack initiation begins. These flaws also increased with increasing ZrO_2 content.

When comparing the shear strength of the individual layers with data from similar cladding processes used to coat materials onto a steel sheet, the values of the layers of the graded layer structure appear to be on the same level or higher than the values in the literature, as shown in Fig. 8.39. Only the stainless steel cladded on a steel sheet achieved an adhesive strength of 200 MPa [54–56].

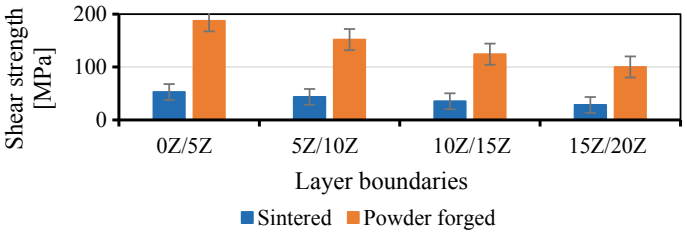

Fig. 8.38 Adhesion of individual layers before and after powder forging

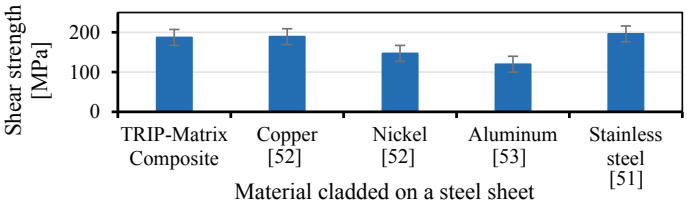

Fig. 8.39 Shear strength of materials cladded on a steel sheet

The shear strength in relation to the compaction ratio, as shown in Fig. 8.40, indicates that the shear strength of the layers increases with increasing compaction ratio. In addition, increasing the compaction ratio increases the shear strength of the forged specimens more than that of the sintered specimens. This phenomenon can be described by the following equation:

$$S = \Phi_{\rho}(c \cdot \rho_0) \tag{8.6}$$

where c is a material constant with a value of 2013 and ρ_0 is the relative density. Due to the differences in density between powder-forged and sintered specimens, the relative density of the specimen plays a decisive role in the equation, as does the compression ratio. This equation has a determination coefficient of 0.98 with the experimentally determined data.

These results can be explained by the compression itself. In the case of the specimens prior to powder forging, only sintered necks hold the specimen together, whereas the powder-forged specimens have a microstructure. The force required to break a sintered neck is much less than the force required to introduce sufficient energy into the matrix to maintain crack initiation and propagation.

Fig. 8.40 Comparison of adhesive strength and compaction degree

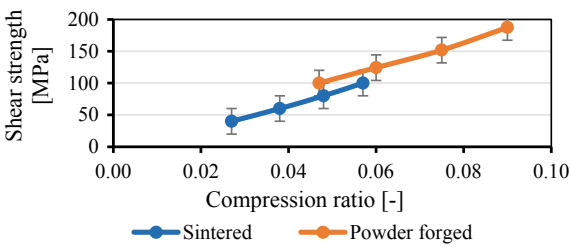

8.5 Conclusions

In general, this study showed that ZrO_2 particle-reinforced TRIP steels can be produced via the powder metallurgical route and that the produced samples achieved solid material densities and exhibited enhanced mechanical properties.

In addition, this same production approach can produce components with graded particle reinforcements and compact the components to a density of solid material without losing the graded structure. The following process parameters were the most successful for the process route. The highest obtained density was achieved in dies with compensating gaps, in which shearg occurred immediately during forming. If the compensating gaps are arranged in such a way that only a pure compression followed by shear occurred, a compact material was not produced; the same phenomenon occurred when no compensating gaps were used. In addition, the highest densities were achieved at a temperature of 1000 °C and a strain of 0.5 in the same die. In addition, up to a reinforcement particle content of 10%, excellent bonding was observed between the reinforcement particles and the matrix.

Acknowledgements This work was funded by the Deutsche Forschungsgemeinschaft (DFG, German Research Foundation), project number 54473466—SFB 799, subproject A6.

References

1. W. König, R.S.G. Röber, Umformtechnikmagazin **426** (1992)
2. G. Röber, Powder forging of gearwheels in layered composite technology—stress-compliant production and component behaviour, Doctorate thesis, RWTH Aachen, 1991
3. K. Vossen, Powder forging of spur and helical cylindrical gears, Doctorate thesis, RWTH Aachen, 1987
4. M. Abdel-Rahman, M.N. El-Sheikh, J. Mater. Process. Technol. **97** (1995)
5. T. Nakagawa, T. Amano, K. Obara, Y. Nishino, Y. Maeda, in *13th International Machine Tool Design and Research Conference* (1972), p. 455
6. A. Salak, Hutnicke Listy 418 (1990)
7. G. Zapf, *Engineering Handbook. Primeval Forming* (Carl Hanser Verlag, München, 1981)
8. H.A. Kuhn, B. Lynn, Metal Powder Industries (1990)
9. H.E. Exner, H. Danninger, *Gmelin Handbook of Inorganic Chemistry, Metallurgy of Iron. Powder Metallurgy of Steel*, 10th edn. (Springer, Berlin, Heidelberg, 1992)
10. F.J. Esper, *Powder Metallurgy. The Flexible and Advanced Method for Economical and Reliable Components; with 15 Tables* (Expert-Verlag, 1996)
11. G. Durrant, V.D. Scott, Compos. Sci. Technol. **49**, 153 (1993)
12. G. Eberhardt, *Powder Forging. Manufacturing Technology* (Hochschule, Pforzheim, 2013)
13. W. Schaub, M. Stilz, R. Geiger, *Forming technology—Handbook for Industry and Science. Volume 4: Special Processes, Process Simulation, Tool Technology, Production*, 2nd edn. (Springer, Berlin, 1993)
14. P.B. Prangnell, S.J. Barnes, S.M. Roberts, P.J. Withers, Mater. Sci. Eng., A **220**, 41 (1996)
15. B.-A. Behrens, N. Vahed, H. Brand (eds.), *Powder Metallurgical Production of Graded Tool Materials* (Verlag Meisenbach, Bamberg, 2013)
16. F. Klocke, W. König (eds.), *Fertigungsverfahren 5, Gießen, Pulvermetallurgie, Additive Manufacturing*, 4. Auflage (Springer Vieweg, Berlin, Heidelberg, 2015)

17. F. Klocke in *Fertigungsverfahren 5. Gießen, Pulvermetallurgie, Additive Manufacturing*, ed. by F. Klocke, W. König (Springer Vieweg, Berlin, Heidelberg, 2015), p. 39
18. M. Krehl, *Einführung in die Pulvermetallurgie* (FPM, 2019)
19. G. Arth, A. Samoilov, Berg Huettenmaenn Monatsh **157**, 306 (2012)
20. D. Rogowski, Process for the preparation of preforms for metal matrix composites, Patentschrift: DE 10 2008 054 561 A1 (2009)
21. H. Engel, *Sintered Materials from Non-ferrous Metals* (Springer, Berlin, Heidelberg, 1993)
22. I. Lenke, *Metall Matrix Composits* (Thinking Ceramics, CeramTec, Plochingen, 2002)
23. G. Zapf, Mater. Sci. Technol. **171** (1979)
24. R.L. Coble, *Reactive Sintering* (MIT, Cambridge, MA, 1984)
25. V.V. Skorokhod, *Mechanism for Improving the Mechanical Properties of Sintered Iron–Copper Composites Alloyed with Molybdenum*
26. S. Mäkipirtti, On the sintering of W-Ni-Cu heavy metal. Zugl.: Helsinki, Inst. of Technology, Diss., 1959 (The Finnish Acad. of Technical Sciences, Helsinki, 1959)
27. V. Pavlov, M. Nosenko, B. Popov, S. Jakunin, Poroshkovaja metallurgija **20** (1987)
28. TU Graz (ed.), *The Physical Properties of Steels „The 100 Steels Programme"*, Part I: Tables and Figures (Graz) (1994)
29. U. Frank, The Piosson's ratio of plastics, illustrated by the example of amorphous thermoplastics, Dissertation, Universität Stuttgart, 1984
30. H.A. Kuhn, C.L. Downey, Int. J. Powder Metall., **15** (1971)
31. W. Schatt, K.-P. Wieters, B. Kieback, *Powder Metallurgy. Technologies and materials*, 2., bearbeitete und erweiterte Auflage (Springer, Berlin, Heidelberg, 2007)
32. H.A. Kuhn, M.M. Hagerty, H.L. Gaigher, A. Lawley, (New York, Plenum Press, 1971), p. 463
33. N. Nguyen, Influence of process parameters in powder forging on the properties of the finished workpieces, Doctorate thesis, TU Bergakademie, Freiberg, 1995
34. B. Lorenz, A contribution to the theory of forming powder metallurgical initial forms, Habilitation thesis, TU Freiberg, 1995
35. L. Ceschini, G. Minak, A. Morri, F. Tarterini, Mater. Sci. Eng., A **513–514**, 176 (2009)
36. J.C. Halpin, S.W. Tsai, Air Force Materials Laboratory (1967)
37. W. Bleck, S. Münstermann, *Einflußgrößen auf den Elastizitätsmodul von Stählen für den Fahrzeugbau,* Forschungsvereinigung Automobiltechnik, 182 (2004)
38. H. Foell, *Elastische Module*, Material Science 1, Universität Kiel, (2015)
39. D. Hünert, *Corrosion processes and carburization of ferritic-martensitic steels in H2O-CO2 atmospheres*. Doctorate thesis TU Bergakademie Freiberg, 2010 (Bundesanstalt für Materialforschung und -prüfung (BAM), Berlin, 2010)
40. R. Viscorová, Investigation of the heat transfer during splash water cooling under consideration of the influence of scaling, Doctoral thesis, TU Clausthal (2007)
41. Y.V.R.K. Prasad, K.P. Rao, S. Sasidhara, *Hot Working Guide. A Compendium of Processing Maps*, 2nd edn. (ASM International, Materials Park, OH, 2015)
42. M. Kirschner, Mater. Sci. Forum **2019**, 15 (2019)
43. M. Kirschner, R. Eckner, S. Guk, L. Krüger, R. Kawalla, U. Prahl, Deformation behavior of particle reinforced TRIP steel / Mg PSZ composite at hot working temperatures. Steel Res. Int. (2018). https://www.doi.org/10.1002/srin.201800334
44. B.-A. Behrens, T. Yilkiran, N. Vahed, C. Frischkorn (eds.), *Influence of Material Flow on Compaction During Sinter Forging* (2014)
45. F. Li, J. Yi, J. Eckert, Metall. Mat. Trans. A **48**, 6027 (2017)
46. H. ElRakayby, H. Kim, S. Hong, K. Kim, Adv. Powder Technol. **26**, 1314 (2015)
47. G.-S. Shim, M.S. Kim, W.Y. Kim, H. Yamagata, MSF **439**, 40 (2003)
48. A. Salak, M. Selecká, Powder Metall. Prog. **3** (2005)
49. M. Kirschner, S. Guk, Beitrag zur Bewertung des Verdichtungsgrades mittels Visioplatsizität. Kongress & Fachmesse Werkstoffwoche 2019, Dresden, den 18–20.09.2019, Dokumenten-Bibliothek der Deutsche Gesellschaft für Materialkunde e.V. (2019)
50. A. Flodin, M. Andersson, A. Miedzinski, Met. Powder Rep. **72**, 107 (2017)

51. K.K. Deng, X.J. Wang, W.M. Gan, Y.W. Wu, K.B. Nie, K. Wu, M.Y. Zheng, H.G. Brokmeier, Mater. Sci. Eng., A **528**, 1707 (2011)
52. M. Kirschner, S. Guk, R. Kawalla, U. Prahl, Forming complex graded and homogeneous components by joining simple presintered parts of TRIP-matrix composite through powder forging. Metals (2020)
53. R.J. Meyer, E. Pietsch (eds.), *Eisen - Härteprüfverfahren*, Beziehung zwischen Härte und Zugfestigkeit, Achte Völlig neu Bearbeitete Auflage (Springer, Berlin, Heidelberg, s.l., 1974)
54. W. Rädeker, Steel and Iron (1938)
55. H. Schaumburg, *Materials* (Vieweg + Teubner Verlag, Wiesbaden, 1990)
56. M. Schmidtchen, R. Kawalla, in *Rolling of Flat Products*, ed. by H.G. Bauer, W. Schadt (Springer, Berlin, 2017), p. 87

Chapter 9
Synthesis of TRIP Matrix Composites by Field Assisted Sintering Technology—Challenges and Results

Sabine Decker, Markus Radajewski and Lutz Krüger

Abstract This chapter analyses options to synthesis TRIP matrix composites (reinforced with Mg-PSZ), which stand out due to a high strength and the possibility to undergo a stress- and strain-induced phase transformation. These composites are processed using Field Assisted Sintering Technology (FAST). Both, the influence of the powder treatment before sintering and the impact of parameter setting during sintering by FAST are discussed. Due to a careful alignment of these factors, a TRIP matrix composite (reinforced with 5 vol% Mg-PSZ) with an 1% compressive yield strength of 700 MPa was generated. Furthermore, both composite components exhibited a phase transformation during compressive deformation. The fundamental investigations are the basis for the development of Functionally Graded Materials (FGM) with a varying Mg-PSZ content along the sample height. To synthesize these FGMs by FAST, a temperature gradient has to be generated during sintering, which allows to sinter the pure ceramic layer without melting the steel phase. Several possibilities to generate a temperature gradient are discussed.

9.1 Introduction

With the aim to develop a composite material with a high strength while keeping a sufficient ductility and toughness, a Transformation Induced Plasticity (TRIP) steel was combined with MgO Partially Stabilized Zirconia (Mg-PSZ). Both materials have the ability to undergo a phase transformation, if a certain stress or deformation is applied, which improves strength and toughness. TRIP steels have the possibility to transform from austenite into α'-martensite, if a certain trigger stress is reached.

S. Decker (Emeritus)
Institute of Materials Engineering, Technische Universität Bergakademie Freiberg, Gustav-Zeuner-Straße 5, 09599 Freiberg, Germany

M. Radajewski · L. Krüger (✉)
Institute of Materials Engineering, Technische Universität Bergakademie Freiberg, Gustav-Zeuner-Straße 5, 09599 Freiberg, Germany
e-mail: krueger@ww.tu-freiberg.de

H. Biermann and C. G. Aneziris (eds.), *Austenitic TRIP/TWIP Steels and Steel-Zirconia Composites*, Springer Series in Materials Science 298,
https://doi.org/10.1007/978-3-030-42603-3_9

Under this requirement, the α′-martensite content increases with ongoing deformation. The α′-martensite nuclei form mainly in deformation bands and restrict the dislocation movement. This leads to an increase in material strength similar to grain refinement [1–3].

Due to the partial stabilization with MgO, the high temperature phases (cubic and tetragonal) of zirconia are stable at room temperature in Mg-PSZ [4]. If a certain stress is applied, the tetragonal phase transforms into the monoclinic phase. This phase transformation comes along with a volume expansion, which is able to close cracks and introduces compressive stresses to the surrounding area [5]. This effect is used to improve the toughness of ceramic materials. The combination of both materials, the TRIP steel and the Mg-PSZ, holds the possibility to get a composite with a high strength and still a high ductility and toughness. Furthermore, it is assumed, that both phase transformations trigger each other [6].

A promising technique to process high-strength materials on a powder metallurgical route is the Field Assisted Sintering Technology (FAST), known as Spark Plasma Sintering, as well. This sintering technique is similar to hot pressing. That means, the powder is uniaxially compressed inside a die during sintering. However, heat is generated directly in the powder and/or in the sintering tool by an electric current, running through the electrically conductive powder and/or the electrically conductive die. Depending on the producer of the FAST device, the electric current is an alternating current or a direct current, which can be pulsed or continuous. The current passes merely through the electrically conductive die, if the powder is electrically nonconductive [7]. If the current runs through the powder, especially powder particle contacts are areas with a high electrical resistivity, which cause an extreme rise in temperature. Hence, the heat is generated at locations where it is most needed. Due to the heat generation directly within the powder or close to the powder, very fast heating rates can be attained and dwell times can be kept short [7, 8]. Caused by the short sintering process, diffusion driven mechanisms like grain growth and formation of precipitations or solid solutions occur in a reduced manner [7, 8]. Hence, extraordinary microstructures can be achieved and the sintered material exhibits a high strength due to its small grains.

Composites consisting of stainless steel and yttria stabilized zirconia were already sintered by FAST [9–11]. However, none of these studies addressed the effect of FAST parameters on microstructure and in none of these studies phase transformations under mechanical loading in both, in metastable stainless steel and in PSZ, were tried to achieve. However, to develop a high strength material it is important to understand how steel and ceramic influence each other and how the process parameters control the microstructural evolution and the achieved mechanical properties. Since 2008, researchers at TU Bergakademie Freiberg/Germany comprehensively investigate Mg-PSZ reinforced TRIP matrix composites in a collaborative research center (CRC 799). Among other topics, the influence of sintering parameters during FAST, chemical composition of the steel matrix and homogeneity of the composite powder on microstructural evolution and mechanical properties were studied. Based on the results, it was possible to develop a composite material with a high strength and sufficient ductility, where both composite constituents experienced a phase transformation under mechanical loading. Furthermore, the results are the basic principles for

the processing of functionally graded materials (FGMs). To sinter FGMs by FAST, several possibilities to adjust temperature gradients during FAST were investigated. The achieved results are presented in the next paragraphs.

9.2 Experimental Methods

For FAST experiments, different steel (Table 9.1) and Mg-PSZ powders (Table 9.2) were used. The distribution of powder particle size of different powders is shown in Table 9.3. Due to the complexity of nomenclature, the steel and the Mg-PSZ powders are abbreviated with S1–6 and Z1–3, respectively (see Tables 9.1 and 9.2).

The powders Z1, Z2 and Z3 are commercial powders from Saint-Gobian. While the steel powders S1, S5 and S6 were gas atomized by TLS Technik GmbH & Co. Spezialpulver KG (Bitterfeld/Germany), the powders S2, S3 and S4 were gas atomized at the Institute of Iron and Steel Technology at TU Bergakademie Freiberg (Germany). The steel powders consisted of austenite and α′-martensite. As the α′-martensite completely transforms to austenite during sintering, an exact indication of α′-martensite within the steel powder is not required.

Table 9.1 Chemical composition of the steel powders

[wt%]	Cr	Mn	Ni	Si	N	C	S	Fe
PM X3CrMnNi16-6-6								
S1	16.40	6.30	6.30	1.00	0.06	0.03	0.01	Bal.
PM X5CrMnNi14-6-5								
S2	14.37	5.98	5.46	0.97	0.05	0.05	0.02	Bal.
PM X3CrMnNi14-7-8								
S3	14.20	7.98	8.40	0.94	0.03	0.03	0.02	Bal.
S4	14.08	6.68	8.99	0.94	0.04	0.04	0.10	Bal.
PM X4CrMnNi16-6-6								
S5	16.10	5.96	5.97	0.89	0.04	0.04	0.01	Bal.
PM X4CrMnNi16-7-3								
S6	15.60	7.10	3.03	0.01	0.05	0.04	0.01	Bal.
PM X2CrMnNi16-7-6								
S7	16.40	7.10	6.30	0.11	0.06	0.02	0.00	Bal.

Table 9.2 Chemical analysis of the Mg-PSZ powders

[wt%]	SiO_2	MgO	Al_2O_3	CaO	TiO_2	Na_2O	Fe_2O_3	ZrO_2
Z1	4.23	3.37	0.63	0.21	0.14	0.09	0.1	Bal.
Z2	0.41	2.82	0.38	0.15	0.13	0.10	0.13	Bal.
Z3	0.10	3.25	1.58	0.06	0.13	–	0.02	Bal.

Table 9.3 Powder particle size distribution

Powder	d_{10} [μm]	d_{50} [μm]	d_{90} [μm]
TRIP steel			
S1	7.4	20.7	41.3
S2 < 25 μm	6.1	12.3	21.4
S2 25–45 μm	11.7	24.1	36.9
S2 45–63 μm	13.1	38.4	56.2
S3	10.8	37.3	124.2
S4	5.5	17.1	103.6
S5	10.3	28.1	44.4
S6	7.8	19.9	33.0
S7	12.4	25.9	46.6
Mg-PSZ			
Z1	0.1	1.3	10.8
Z2	0.2	3.1	22.4
Z3	13.4	21.1	32.9

The powder Z1 exhibited 10 vol% monoclinic, 37 vol% tetragonal and 53 vol% cubic phase, while the powder Z2 contained 35 vol% monoclinic, 32 vol% tetragonal and 33 vol% cubic phase. Only 1 vol% monoclinic phase was present in powder Z3 while 38 vol% were in the tetragonal and 68 vol% were in the cubic phase.

Composite powders with varying Mg-PSZ contents were mixed in a planetary ball mill PULVERISETTE 6 classic line (FRITSCH GmbH, Germany). For mixing, steel balls with a diameter of 10 mm were used and a ball mass to powder mass ratio of 5:1 was applied. Mixing was carried out for four hours. To achieve a sufficient swirling of the powder, the rotation speed was calculated by using (9.1) [12] depending on used milling vessel size to be 100 or 110 rpm for simply homogenization. A rotation speed of 250 rpm was utilized for high energy milling. Merely, the composite powders that are based upon S6 and Z2 were mixed in a PET vessel for one hour, using yttria stabilized zirconia balls.

$$N_0 = \frac{32}{\sqrt{d}} \tag{9.1}$$

N_0 rotation speed in rpm
d diameter of milling vessel in meter.

Afterwards, pure steel samples, pure Mg-PSZ samples, composites with constant Mg-PSZ volume content (5%, 10% or 40%) and FGMs with varying Mg-PSZ content were sintered. FGMs were prepared by layering composite powders with decreasing Mg-PSZ content on top of each other inside a graphite die. Unless specified otherwise, all sintering experiments were carried out using a FAST device HP D 25 (FCT Systeme GmbH, Germany). To start the sintering process, it is necessary to apply at

least a uniaxial load of 5 kN. Thus, a complete pressureless sintering is not possible in this device. All performed sintering cycles were carried out under fine vacuum and the cooling process after sintering was unregulated by simply switching off the power supply. The used dies and punches consisted of graphite (type 2333 from Mersen, Germany). After sintering, the relative density of the sintered samples was determined by Archimedes density measurements. Considering thermal expansion and elastic deformation of powder and punches during sintering, the evolution of the relative density during sintering was calculated in accordance to [13] by using (9.2).

$$\rho_i = \rho_0 \cdot e^{\varepsilon_{zi}} \tag{9.2}$$

ρ_i density at time i
ε_{zi} shrinkage in z-direction at time i
ρ_0 initial density before sintering.

To investigate the mechanical properties under compressive loading conditions, cylindrical samples with a diameter to height ratio of 1:1 were machined and quasi-static compression tests (10^{-3} s^{-1}, MTS 810) were carried out to a maximum of 60% compressive deformation. Furthermore, hardness measurements were conducted in the layers of FGMs, using Vickers hardness at a load of 9.807 N (HV1). The microstructure of the as sintered samples and of the compressed samples was characterised by XRD measurements, light optical microscopy and scanning electron microscopy in combination with electron backscatter diffraction (EBSD).

9.3 Results and Discussion

9.3.1 Influence of the Composite Powder on the Microstructural Evolution and Mechanical Properties of the Sintered Composite

If the results of a sintering experiment are evaluated, they are not only a consequence of sintering parameters, set on the sintering device. They are a product of chemical composition and the earlier treatment of the material (e.g. mixing). Some aspects of such treatments and chemical variations, which could be used to set the powder into a good initial position to achieve a high-strength material, are discussed in this chapter.

First of all and very important, the **chemical composition** of the steel powder influences the phase composition of the composite. During sintering, the Mg-ions diffuse from the Mg-PSZ into the steel matrix [14]. Thus, the Mg-PSZ destabilizes and the monoclinic phase content increases. However, the alloying elements of the

steel influence the Mg-PSZ as well. For example, Mn from the steel stabilizes Mg-PSZ [14, 15]. Accordingly, it is possible that the Mg-PSZ is destabilized during sintering by FAST depending on the steel matrix. If an PM X5CrNi18-10 was used as matrix material, which contains 0.96 wt% Mn, approximately 45 vol% of the Mg-PSZ were destabilized during sintering [16]. However, if the steel matrix was similar to an PM X3CrMnNi16-6-6, only a few percent of the Mg-PSZ transformed to the monoclinic phase during sintering by FAST [17], as a consequence of the increased Mn content.

Less percentage of Mg-PSZ destabilized, if the **Mg-PSZ content** within the composite increased. Hence, no destabilization was measured, if pure Mg-PSZ was sintered [18]. Furthermore, the Mg-PSZ content influences the material properties, which the composite exhibits after sintering by FAST in general. Not only hardness and strength increase with increasing Mg-PSZ content (Fig. 9.1). Mg-PSZ particles have a pinning effect on the grain boundaries of the steel matrix. Thus, the grain growth within the steel phase is impeded with increasing Mg-PSZ fraction [16, 18]. Accordingly, the strength of the composite is not only a function of the Mg-PSZ content, but also of the grain size of the steel matrix as well. With decreasing steel grain size, the strength of the steel increases, which was already shown by the Hall-Petch relation [19].

In addition, the remaining porosity after sintering by FAST influences the material strength and the ductility [18]. However, the effect of porosity depends on the Mg-PSZ content, as well. Due to more steel-to-steel contacts, composites with a lower Mg-PSZ content exhibit a sufficient ductility, for example 80% true compressive strain for a composite reinforced with 5 vol% Mg-PSZ and only 8% true compressive strain for a composite reinforced with 40 vol% Mg-PSZ (composites containing powders Z1 and S1, see Fig. 9.1) [18].

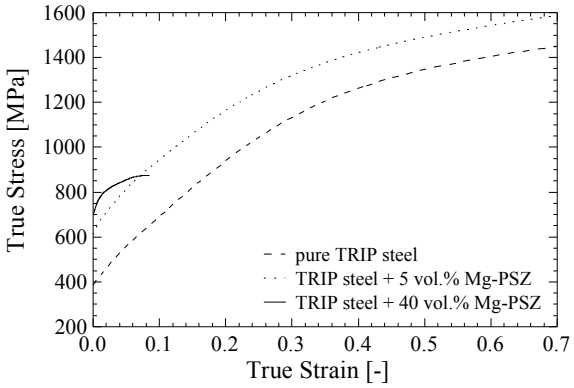

Fig. 9.1 Increase in compression strength with Mg-PSZ content (10^{-3} s^{-1})

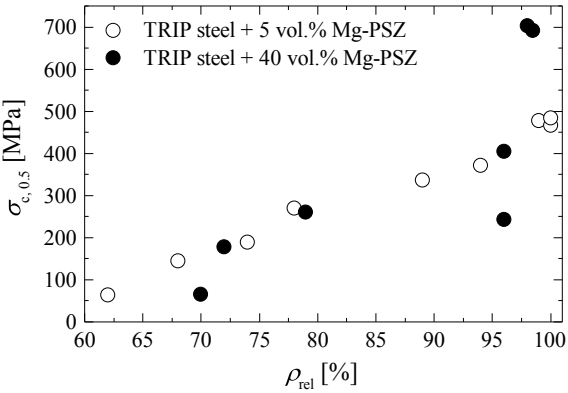

Fig. 9.2 Influence of relative density ρ_{rel} on 0.5% compressive yield strength $\sigma_{c,0.5}$ of composites consisting of Mg-PSZ (Z1) and a TRIP steel (S1), sintered using various parameters

The same effect applies for porosity. Composites with a low Mg-PSZ content can be deformed up to 80% true compressive strain even with a porosity of 22 vol% [18]. However, strength drastically decreases with increasing porosity (Fig. 9.2) [18]. While the 0.5% compressive yield strength increases linearly with relative density for a composite with 5 vol% Mg-PSZ, composites with 40 vol% Mg-PSZ (composites containing powders Z1 and S1) exhibit a strong increase in 0.5% compressive yield strength for a relative density >96%. Besides, for the composites with 40 vol% Mg-PSZ, values for 0.5% compressive yield strength deviate more (Fig. 9.2).

This deviation is caused by weakly sintered Mg-PSZ clusters. For a large relative density the strong increase in 0.5% compressive yield strength is a result of an increase in interfacial strength of Mg-PSZ/steel interfaces. However, the present weakly sintered Mg-PSZ clusters are the initiation areas for failure and they appear more frequently in composites with a higher Mg-PSZ content [18].

Since the α′-martensite formation is strain-induced, α′-martensite content increased with ductility of the composite. Hence, maximum 10 vol% α′-martensite was formed in composite material containing 40 vol% Mg-PSZ (containing S1 and Z1), due to its brittle material performance [18]. With decreasing Mg-PSZ content, ductility increases and more α′-martensite is formed [20]. Besides, the content of strain-induced α′-martensite depends on the chemical composition of the steel matrix, as well [16, 17]. However, a decrease in Mg-PSZ content does not lead necessarily to an increase in strain-induced α′-martensite [16]. As Martin et al. [6] proved, α′-martensite is formed preferential at poles of hard reinforcing particles under compressive deformation. Hence, a certain content of reinforcing phase triggers the α′-martensite formation.

In contrast, pores diminish the α′-martensite formation. If a porous material is compressed, a large content of deformation is engaged with closing pores, which does not involve extensive formation of deformation bands. Deformation bands are the sites for α′-martensite nucleation [2, 21]. For a composite containing 5 vol% Mg-PSZ (consisting of S1 and Z1), a porosity < 10 vol% is necessary to form the maximum possible strain-induced α′-martensite content [18]. With increasing Mg-PSZ content, more Mg-PSZ clusters are formed, which are the origin of damage. Cracks run preferentially through Mg-PSZ clusters and along steel/Mg-PSZ interfaces [16–18]. Hence, the failure behavior becomes more brittle and less α′-martensite is generated.

Thus, to optimize ductility and strength, it is important to achieve a **homogeneous distribution** of the reinforcing phase within the matrix and to avoid clustering of the ceramic particles. This is possible by adjusting the **particle sizes** of matrix powder and reinforcing powder. That means, coarse Mg-PSZ powder is needed and the steel powder has to be refined. To get fine steel powder, it could be sieved to receive the fine fraction of gas atomized powder, or it could chemically be changed in a way to reduce the surface tension. This would lead to smaller particles during gas atomization [22].

However, the used powder particle size distribution influences the densification rate and grain size distribution of the compacted samples [1]. As demonstrated, using steel powder S2, which was sieved to fractions < 25 μm, 25 μm–45 μm and 45 μm–63 μm, the densification rate slightly increased with decreasing particle size. Hence, it is possible to reduce dwell time during sintering by FAST with decreasing particle size [1]. While the steel powder (S2) with a particle size of 45–63 μm needed a dwell time of 4.3 min, dwell time could be reduced to 3 min for the steel powder (S2) with a particle size <25 μm [1]. Furthermore, the maximum in shrinkage is shifted to slightly lower temperatures with decreasing particle size. Thus, the maximum sintering temperature can be reduced, as well [1]. With increasing particle size, it is most likely to get large grains, which can exceed the initial particle size, due to the strong overheating at the few particle contacts of the coarse powder particles [1]. Therefore, the powder mixture should contain a variety of particle sizes to facilitate a large number of powder particle contacts. Furthermore, small particles have small grains, which lead to an increased compressive yield strength due to the Hall-Petch-effect. However, the work hardening rate is higher in large grains due to a higher α′-martensite formation rate. In small grains, α′-martensite formation sets in at larger strain values compared to coarse grains. More energy is needed in small grains in comparison to larger grains to expand deformation bands, which are the locations for α′-martensite formation [1]. But after 60% compression, steel samples sintered from powder particles <25 μm exhibited a similar compressive strength like samples sintered from powder particles in the range of 45–63 μm [1].

Another possibility to reduce the steel particle size as a result of gas atomization is the reduction of the surface tension of liquid steel melt. Thus, smaller steel drops and thereby smaller steel particles are generated during gas atomization [22]. A possibility to reduce this surface tension is the addition of sulfur to the steel melt. Using the steels S3 (0.02 wt% sulfur) and S4 (0.1 wt% sulfur), the influence of sulfur content on microstructure and mechanical properties was investigated. The sulfur content

did not influence the grain size of the steel matrix after sintering of unreinforced steel, due to the high driving force for grain growth in fine grained material [22]. In contrast, the grain size of the steel matrix varied with sulfur content in the composite material due to pinning of the grain boundaries by Mg-PSZ (reinforced with 10 vol% Mg-PSZ of Z1). A smaller grain size was measured, if the sulfur content within the composite material was high. The reinforcing Mg-PSZ particles impeded the grain growth and almost kept the grain size of the initial steel particles [23]. The sulfur formed precipitations during sintering by FAST. According to EBSD measurements, these precipitations were CrS, Cr_2S_3 and MnS [22]. The amount of precipitations increased with sulfur content and resulted in an increase of 40 MPa in compressive yield strength and a rise in work hardening [22]. If the TRIP steel (S4) was reinforced with 10 vol% Mg-PSZ (Z1), more than 50% of the precipitations consisted of MnS and they were formed mainly at the steel/Mg-PSZ interfaces [23]. Due to the binding of Mn in precipitations, less Mn was on hand to stabilize the Mg-PSZ. Thus, more Mg-PSZ destabilized in steel matrix S4 during sintering [23]. Independent of the presence of reinforcement by Mg-PSZ, the compressive yield strength increased 40 MPa due to the increase of the sulfur content from 0.02 to 0.1 wt% and the combined forming of precipitations. Furthermore, the compressive yield strength of the steel increased by 140 MPa due to the addition of 10 vol% Mg-PSZ [23].

In addition to the adjustment of particle sizes of matrix and reinforcing powder, a possibility to avoid clustering of the ceramic is high energy ball milling. By this intensive milling, the Mg-PSZ is knead into the steel matrix and distributed more homogeneously (Fig. 9.3). Furthermore, the steel matrix is strongly deformed. Thus, the steel recrystallizes during sintering and becomes very fine grained [24]. The steel matrix exhibits an average grain diameter of approximately 1.4 µm (determined by EBSD) after ball milling at 250 rpm and sintering at 1100 °C and 5 min dwell time (composite contains 5 vol% Mg-PSZ Z1 and TRIP steel S1) [18]. If the composite powder was mixed at 100 rpm and sintered under the same conditions, the average grain diameter was 2.4 µm [18]. Furthermore, shrinkage rate is drastically increased due to the higher number of dislocations and vacancies within the steel matrix as

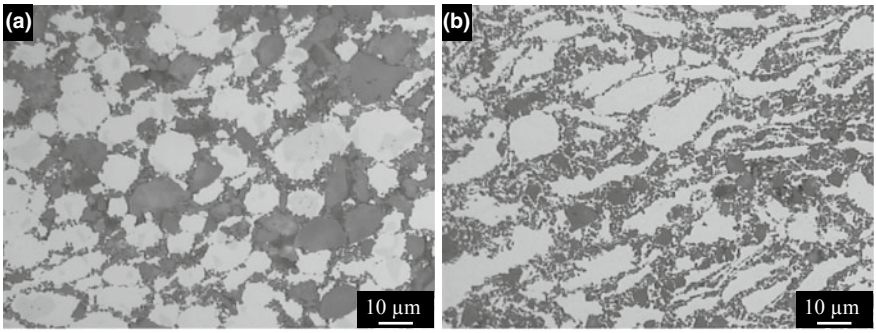

Fig. 9.3 Microstructure of a TRIP matrix composite, reinforced with 40 vol% Mg-PSZ (S1, Z1) after sintering by FAST, powder milled with **a** 100 rpm and **b** 250 rpm

a result of the milling process. Therefore, the necessary temperature for sintering decreases about 75 K, if the powder was milled at 250 rpm [18, 24]. However, due to the homogeneous distribution of the Mg-PSZ within the steel matrix, more Mg-PSZ/steel interfaces exist. Hence, the area where the Mg-ions have the possibility to diffuse into the steel matrix is larger and more Mg-PSZ destabilizes during sintering. Depending on the used powder batch and sintering parameters, approximately 35–45 vol% of the Mg-PSZ are in the monoclinic phase after sintering [18, 24]. Due to the better clamping of the Mg-PSZ with the steel matrix, the interfacial strength is increased and results in an improved transmission of loading from the steel matrix to the Mg-PSZ. Thus, the content of stress-induced phase transformation increases and 40–55 vol% of the Mg-PSZ transform stress-induced into the monoclinic phase under compressive loading [18, 24]. All in all, the compressive strength was drastically affected by the used TRIP steel and the Mg-PSZ content. For a composite (consisting of S1 and Z2) reinforced with 40 vol% Mg-PSZ, the 1% compressive yield strength increased from 776 to 1328 MPa, if the rotation speed was increased from 100 to 250 rpm. The effect of powder processing was further illustrated by the shift of 1% compressive yield strength of a composite with 5 vol% Mg-PSZ (S1 and Z1) from 540 MPa (100 rpm) to 625 MPa (250 rpm) [18]. Even further improvement to 700 MPa was possible by adjusting sintering parameters [18].

9.3.2 Influence of Sintering Parameters on the Microstructure and the Mechanical Properties of the Sintered Composite

Besides the requirements of the initial powders to achieve a high-strength material, which has the ability to undergo phase transformations under mechanical loading, the coordination of the sintering process is decisive for the microstructural evolution and the mechanical properties of the sintered material. In the case of FAST, sintering temperature, heating rate, cooling rate, dwell time, pressure and setting of die and punches influence the result of the sintering process.

If the **pulsing** of the current exhibits an explicit effect on densification behavior and the material properties, is discussed controversially in literature. Chakraborty et al. for example found a decreased relative density for ZrB_2 after sintering by FAST, if the off time of the pulse profile exceeded the on time [25]. Shen et al. reported a slight increase of the temperature which is needed for densification of alumina with increasing on:off pulse ratio [26]. Belmonte et al. found an increase in peak voltage and a shift of the maximum shrinkage rate to lower temperature with decreasing number of pulses and increasing off time during sintering of silicon nitride [27]. Moreover, an influence of the on:off ratio on the presence of an alumina layer on the surface of aluminum powder particles, and on the reactivity of aluminum with carbon was determined by Lalet et al. [28]. As well, they found melting of aluminum already at 500 °C, which is 150 K below the actual melting point of

aluminum, if the dc on:off ratio was < 1 [28]. Furthermore, Jiang et al. reported an improved interfacial reaction between aluminum and Si_3N_4 in an aluminum matrix composite with decreasing pulse ratio. However, the mechanical properties of this composite were best at a short pulse time and an dc on:off ratio > 1 [29]. In contrast, Xie et al. investigated the influence of the frequency of pulsed electric current during sintering on the mechanical and electrical properties of aluminum and found no effect [30]. Furthermore, Chen et al. proved, that the pulse pattern of the current does not influence the formation and growth of an reaction layer between Mo and Si [31].

Using a composite powder (mixed at 100 rpm), consisting of 40 vol% Mg-PSZ (Z1) and 60% of TRIP steel (S1), for sintering by FAST, several pulse pattern were tested (3:1 ms; 12:2 ms; 27:9 ms, 30:2 ms) during heating up to 1020 °C and a dwell time of 5 min (51 MPa uniaxial compression, 20 mm sample diameter) using a FAST device Dr. Sinter 2050 (Sumitomo Coal Mining Co., Ltd., Japan). However, no obvious effect of pulse pattern on densification, grain size and phase fraction was detected. Only temperature measurements during heating to 950 °C in a drill hole to the center of a densified steel sample (S1) and at the surface of the surrounding graphite die indicated a slight increase in temperature deviation with increasing off time. In this case, the sample center was hotter than the die, whereas the die temperature was the control variable. Hence, a temperature deviation of 33 ± 7 K was indicated for a pulse pattern of 27 ms: 9 ms while all remaining pulse pattern lead to a deviation of approximately 21 ± 5 K.

To create a composite material by FAST, it is advisable to understand the sintering behavior of the composite constituents first. Especially for such different composite partners like steel and ceramic, it is necessary to find a parameter range, where both constituents sinter.

Independent of the **heating rate**, the TRIP steel (S1) begins to shrink between 550 and 600 °C (Fig. 9.4) [1, 18]. Above 1100 °C, the TRIP steel starts to melt

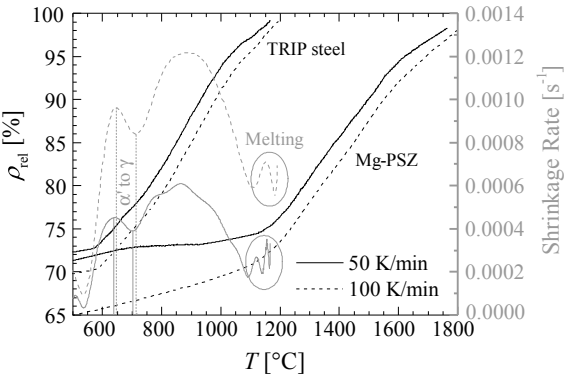

Fig. 9.4 Increase of relative density ρ_{rel} and evolution of shrinkage rate with temperature T of TRIP steel (S1) and Mg-PSZ (Z1) at a constant pressure of 51 MPa

[18] while the actual melting point of this steel is at 1416 °C [32]. The melting of the steel at lower temperatures during FAST is a result of graphite diffusion from the die into the sample during sintering. Due to the increase of carbon content, the melting point is drastically reduced. Furthermore, the temperature is measured by a pyrometer inside a hole in the graphite punch, 5 mm away from the sample surface. Thus, the actual temperature inside the sample is going to be higher than the measured temperature. Hence, the maximum temperature to sinter TRIP steel in this sintering setup is 1100 °C. Mg-PSZ, however, begins to shrink at a temperature slightly above 1100 °C (Fig. 9.4) and its optimum sintering temperature is between 1400 and 1600 °C [18]. With increasing heating rate, shrinkage rate increased [18]. Thus, a higher heating rate of 100 K/min is beneficial. However, caused by the melting of the TRIP steel, the maximum sintering temperature to densify the composite has to be 1100 °C. Higher temperatures are possible for the sintering of composites. However, the graphite die and the graphite punches are destroyed by the occurring steel melt. Besides, the steel melt partly flows out of the die. Furthermore, clustering of Mg-PSZ has to be avoided due to the poor sintering of Mg-PSZ at 1100 °C.

With increasing **temperature**, not only shrinkage occurs, but phase transformation as well. For example, α′-martensite was generated during milling due to deformation by the milling balls. During sintering, the α′-martensite transforms into austenite while heating. For the steel S1, the temperature range for transformation is between 650 and 730 °C (Fig. 9.4) [1, 18]. This effect is marked by a flattened region in the relative density-temperature-curve and a decrease in shrinkage rate (Fig. 9.4). To prove this fact, bulk samples, where first 70 vol% α′-martensite were formed by compressive deformation at −196 °C, were afterwards heated to 700 and 850 °C in a FAST device. While only 10 vol% α′-martensite remained within the sample heated to 700 °C, 99% austenite were measured after heating to 850 °C [1, 18].

The Mg-PSZ undergoes a phase transformation during sintering, as well. While the composite powder with 40 vol% Mg-PSZ (consisting of S1 and Z1) exhibited 18 vol% monoclinic phase, no monoclinic phase was indicated by XRD after heating to 1100 °C without applying a dwell time. Even after sintering at 1100 °C of pure Mg-PSZ (Z1) powder with initially 10 vol% monoclinic phase, no monoclinic phase remained [18]. This is in accordance with Berek et al., who found a phase transformation from monoclinic to tetragonal phase of Mg-PSZ within the temperature range of 700–1200 °C [33]. However, as already mentioned, if Mg-PSZ is in contact with steel, the Mg-ions diffuse into the steel matrix and Mg-PSZ destabilizes. This effect is intensified with increasing temperature due to the rise in diffusion rate. Thus, 28 vol% monoclinic Mg-PSZ were determined within the Mg-PSZ of the composite reinforced with 5 vol% Mg-PSZ (consisting of S1 and Z1) after sintering by FAST at 1200 °C and only 11 vol% monoclinic phase after sintering at 1100 °C. In both cases, no dwell time was used and a pressure of 16 MPa was applied [18]. An equal trend was indicated for a composite reinforced with 40 vol% Mg-PSZ (consisting of S1 and Z1) using the same FAST conditions. While no monoclinic phase was detected after sintering at 1100 °C, 7 vol% of the Mg-PSZ exhibited the monoclinic phase after densification at 1200 °C [18].

An increase of **dwell time** from 5 to 10 min had no influence on grain size distribution within the steel matrix of a composite with 5 vol% Mg-PSZ (consisting of S1 and Z1) [24]. However, during the first five minutes, the grains of the steel matrix grew approximately 2 µm and 4 µm inside composites with 5 and 40 vol% Mg-PSZ (consisting of S1 and Z1), respectively [18]. An exponential reduction of grain growth during dwell time was already reported by Shen et al. [26]. Even though steel grains grow during dwell time and a decrease in composite strength is expected, the compressive yield strength of the composite slightly increased with dwell time. While it was only a slight increase in compressive yield strength and it was within standard deviation, statements concerning correlations between increase in compressive yield strength and dwell time have to be handled with care. However, due to the absence of a decline in compressive yield strength, it is to assume that an increase in dwell time causes an improved interfacial strength by diffusion processes, which counteracts a decline in compressive strength caused by grain growth [18]. This assumption can be confirmed by micrographs (Fig. 9.5) of compressed composites, which exhibit a large number of cracks at steel/Mg-PSZ interfaces, if they were sintered without a dwell time, and, which show particle cracking and only a few locations of delamination, if a dwell time of five minutes was applied.

As already mentioned, the monoclinic phase of the Mg-PSZ transforms during sintering into the tetragonal phase. However, due to the loss of Mg-ions to the steel matrix, the Mg-PSZ destabilizes and more monoclinic phase is formed. These two processes are in the opposite direction. Thus, after sintering at 1100 °C without dwell time no monoclinic phase was indicated in the composite with TRIP steel matrix type S1 [18]. However, destabilization dominates during dwell time. Depending on the used steel matrix and the pre-treatment of the powder, 15–40 vol% of the Mg-PSZ are in the monoclinic phase after sintering at 1100 °C and five minutes dwell time [16–18, 24].

The applied **pressure** during sintering by FAST has an extreme influence on densification. If a composite with 5 vol% Mg-PSZ (consisting of S1 and Z1) is

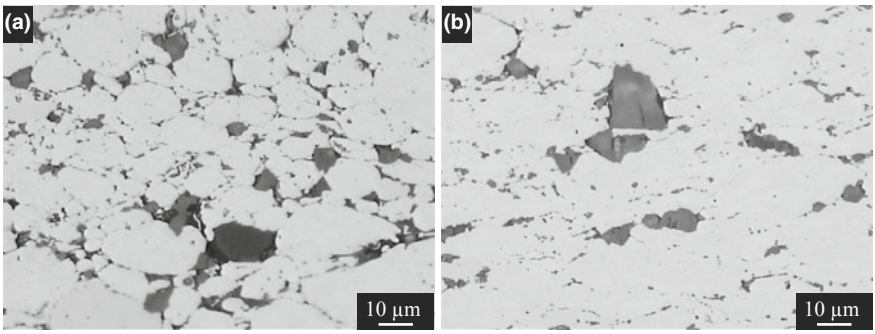

Fig. 9.5 Delamination and cracks after compressive deformation to 60% in a composite reinforced with 5 vol% Mg-PSZ (consisting of S1 and Z1), sintered using FAST at 1100 °C under an uniaxial pressure of 16 MPa and **a** no dwell time, **b** 5 min dwell time

sintered at 1100 °C without dwell time and 16 MPa applied pressure, the composite exhibits a relative density of 78%. A relative density of 99% is realized, if a pressure of 51 MPa is used. The relative density of a composite with 40 vol% Mg-PSZ (consisting of S1 and Z1) rises from 72 to 96% under the same FAST conditions, if the pressure is increased from 16 to 51 MPa [18]. Due to an increased pressure, the particle contacts deform at elevated temperatures. Thus, porosity is reduced by creep of the material [18]. By increasing the pressure, it is possible to reduce the necessary maximum temperature for sintering and shrinkage starts at lower temperatures. This temperature difference increases with increasing Mg-PSZ content. If the pressure is increased from 16 to 51 MPa, onset temperature of shrinkage is reduced 45 K for a composite with 5 vol% Mg-PSZ (consisting of S1 and Z1) and 250 K for a composite with 40 vol% Mg-PSZ (consisting of S1 and Z1) [18]. The grain size of the steel matrix varies only for small Mg-PSZ contents with pressure. If a low pressure is applied during heating up and dwell time, the grain size becomes more heterogeneous. In this case, the porosity is quite high at the beginning of dwell time and only a few steel to steel contacts exist where the current passes through. Inside these preferred paths of the current, very large and elongated grains form, while the grains within electrically isolated areas remain small [18]. For higher Mg-PSZ contents, the influence of the pressure on grain growth decreases.

Due to the overheating at current paths during sintering at low pressure, Mg-PSZ particles, which are close to these current paths, destabilize. Thus, the monoclinic content within the Mg-PSZ of composites with a low Mg-PSZ content increases, if a low pressure is applied during sintering [18].

The interfacial strength between Mg-PSZ and steel of the composite is improved by applying a high pressure during sintering. Hence, composites (reinforced with 40 vol% Mg-PSZ, consisting of S1 and Z1, 4% porosity), which were sintered using a pressure of 16 and 51 MPa exhibited a 0.5% compressive yield strength of 242 and 404 MPa, respectively. Furthermore, a maximum compressive deformation of 3% was reached, if a pressure of 51 MPa was applied. In contrast, the composite sintered using a pressure of 16 MPa fractured after 1% compressive deformation [18]. Certainly, both composites were indeed sintered at the same temperature of 1100 °C but with different dwell times to achieve the same porosity. While no dwell time was needed, if a pressure of 51 MPa was applied, 5 min dwell time were necessary to achieve the same density at a pressure of 16 MPa. An increase in interfacial strength with prolongation of dwell time would be expected. However, the effect is not as strong as an increase in uniaxial pressure. Due to the improvement of interfacial strength by increasing the uniaxial pressure during sintering, slightly more strain-induced α'-martensite is formed during compressive deformation. However, this effect is characteristic for composites with a large Mg-PSZ content [18].

The stress-induced phase transformation of the Mg-PSZ is independent of Mg-PSZ content of the composite, dwell time and applied pressure. After compressive deformation, a constant monoclinic content within the Mg-PSZ (Z1) of approximately 40 vol% was measured within composites with a steel phase type S1 [18]. The initial monoclinic content after sintering depends on the used FAST parameters and the Mg-PSZ content. Thus, different amounts of stress-induced monoclinic phase

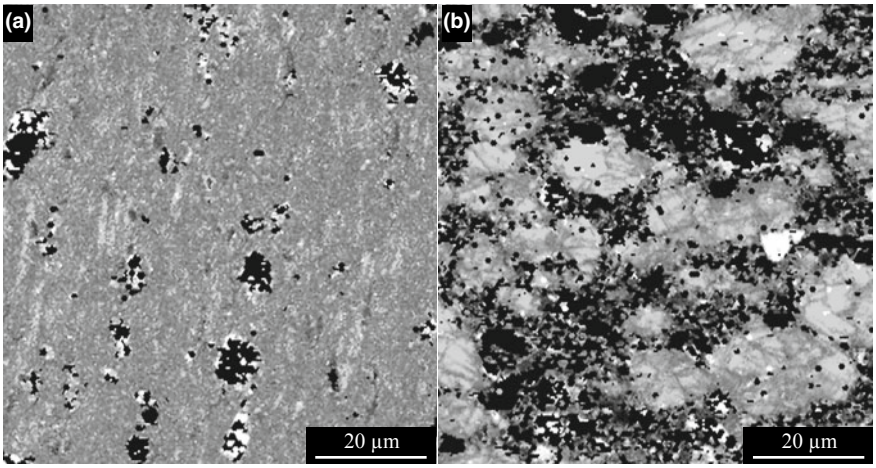

Fig. 9.6 EBSD analysis of the composite with **a** 5 vol% Mg-PSZ after 60% compression and **b** 40 vol% Mg-PSZ after compression to fracture (10^{-3} s^{-1}, grey: steel, white: monoclinic phase, black: tetragonal and cubic phase of the Mg-PSZ)

were formed during compressive deformation due to the chosen sintering parameters. However, it seems, that in this composites only 40 vol% of the Mg-PSZ were able to transform into the monoclinic phase (Fig. 9.6) [18].

If the stress-induced phase transformation of the Mg-PSZ influences positively the compressive flow behavior of the composite is questionable. Martin et al. [6] compared the compressive flow behavior of a composite reinforced with 5 vol% Mg-PSZ to a composite reinforced with 5 vol% alumina. They explained the higher compressive strength of the composite, reinforced with Mg-PSZ, with the stress-induced phase transformation of Mg-PSZ. However, the interfacial strength between matrix and reinforcing phase is not the same in these composites. Furthermore, the median particle size of alumina was 1 µm larger than that of the Mg-PSZ. Thus, the benefit by the stress-induced phase transformation is not entirely proven.

A simplified semiempirical model [see (9.3)] was developed on the basis of the rule of mixture [34], which considers the Mg-PSZ content, the Hall-Petch equation [19] for the influence of steel grain size, the equation of Haynes [35] taking into account the influence of the porosity, the equation of Olson and Cohen [36], which describes the α′-martensite evolution and the equation of Ludwik [37] for the reproduction of the flow behavior of the austenite. With this model, the compressive flow curve under quasi-static loading is well described for TRIP steel (S1) and composites (consisting of S1 and Z1) [18].

$$\sigma_d(\varepsilon_w) = (1 - V_{\mathrm{PSZ}})\left(\left(\sigma_{0\,0.5\%,\mathrm{St}} + \frac{k}{\sqrt{d}} + A \cdot \varepsilon_w^n\right) \cdot (1 - V_\alpha) + V_\alpha \cdot \sigma_\alpha\right) + V_{\mathrm{PSZ}} \cdot \sigma_{0\,\mathrm{PSZ}} \tag{9.3}$$

$\sigma_d(\varepsilon_w)$	true compressive flow stress
V_{PSZ}	volume content of Mg-PSZ
$\sigma_{0\,0.5\%,St}$	0.5% compressive yield strength of the steel phase
V_α	volume content of α′-martensite
σ_α	compressive flow stress of α′-martensite
d	grain size of steel phase
$\sigma_{0\,PSZ}$	critical compressive strength of Mg-PSZ
k, A, n	constants
ε_w	true compressive deformation.

However, the stress-induced phase transformation was not taken into account in this model. Thus, the stress-induced phase transformation obviously does not increase the compressive flow strength, if the compressive flow curve is well described without a considered contribution by the stress-induced phase transformation.

Next to FAST parameters like temperature, dwell time and uniaxial pressure, the used **die geometry** influences the sintering result, as well. The influence of a varying die wall thickness on temperature distribution is well known [38]. But, if for example, the die wall thickness is constant and the sample diameter is increased, the relation between cross-sectional area of the die and cross-sectional area of the sample decreases. Hence, more electrical current is going to run through the electrical conductive sample instead through the die. Thus, the sample is more intensively heated up and onset of densification is shifted to lower temperature.

For example, intensive shrinkage of a composite, reinforced with 5 vol% Mg-PSZ (consisting of S1 and Z1) and sintered in a die with 10 mm wall thickness, begins at 650 °C, if the sample had a diameter of 20 mm, and at 530 °C, if the sample had a diameter of 40 mm [18]. Furthermore, using the same FAST parameters results in different relative densities. Due to the high energy input in larger samples, grain boundaries break away from pores and the pores get inside the grains, which makes it very difficult to close these [12]. However, the porosity increased only 2%. The grain size of the steel phase was not influenced by the sample diameter [18]. Though, the destabilization of the Mg-PSZ was intensified by using a larger sample diameter and the combined increase in energy input inside the sample. The monoclinic content of the Mg-PSZ was doubled in composite samples with 5 vol% Mg-PSZ (consisting of S1 and Z1) sintered with a diameter of 40 mm in comparison to those samples sintered with a diameter of 20 mm [18]. Due to no changes in steel grain size and only a slight difference in porosity, the compressive flow behavior was independent form the sample diameter [18]. However, it is advised to keep the relation between cross-sectional area of the die and cross-sectional area of the sample constant for upscaling, to receive a similar microstructure after sintering by FAST.

It is of great interest in research to determine the acting processes, which lead to densification during sintering by FAST. Kieback and Trapp evaluated several processes suggested in literature critically [39]. They summarized the acting processes to be local heating and melting of powder particle contacts, breaking of oxide layers by electrical breakdown, prevention of grain growth, plastic deformation, diffusion

creep, grain boundary sliding, electron wind and thermodiffusion due to temperature gradients [39]. These processes are supported by a high heating rate and a high pressure [39].

Li et al. developed a way to determine shrinkage mechanisms during FAST. They adapted the load increasing test, which is used to calculate the strain rate exponent m for creep tests [40]. Using this approach for pure steel and composites with 5 and 40 vol% Mg-PSZ (consisting of S1 and Z1) at a test temperature of 1000 °C, strain rate exponents of 0.48 ± 0.22 and 0.47 ± 0.05 were identified for pure steel and composite with 5 vol% Mg-PSZ, respectively. The composite with 40 vol% Mg-PSZ had a strain rate exponent of 0.32 ± 0.10. In this temperature range, mainly the steel is shrinking and the strain rate exponent describes the behavior of the steel phase. According to the calculated strain rate exponents, grain boundary sliding ($m = 0.5$) and potentially dislocation creep ($m = 0.3, \ldots, 0.5$) are the main occurring mechanisms [40].

The load increase test using pure Mg-PSZ was carried out at 1400 °C and a strain rate exponent of 0.37 ± 0.25 was calculated. In this range of the strain rate exponent, sliding and climbing of dislocation dominates [41]. Taking into account the standard deviation, grain boundary sliding is possible as well [40]. At first, deformability of a ceramic seems unlikely, but for example Chen et al. proved that a deformation to 30% of zirconia at 1300 °C is possible [42].

9.3.3 *Sintering of Functionally Graded Materials (FGM) by FAST*

Based on the presented results, FGMs with varying Mg-PSZ contents were developed. Therefore, several layer arrangements were tested using TRIP steel powder S5. For this purpose, composite powders with different amounts of Mg-PSZ (Z1) and TRIP steel were mixed and layered on top of each other to receive a gradation of Mg-PSZ along the height of the sample (diameter: 40 mm). This gradation reached from 0 vol% Mg-PSZ to 40 vol% Mg-PSZ, while every layer should have a thickness of 1 mm after complete densification. Samples with layer arrangements of 0 vol%–20 vol%–40 vol% Mg-PSZ, of 0 vol%–10 vol%–20 vol%–40 vol% Mg-PSZ and of 0 vol%–10 vol%–20 vol%–30 vol%–40 vol% Mg-PSZ were generated (Fig. 9.7). To densify these layer systems, they were heated up with a heating rate of 100 K/min

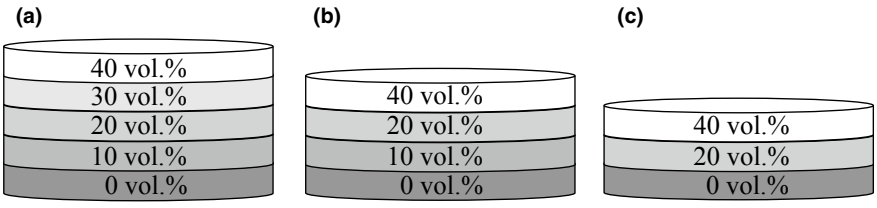

Fig. 9.7 Tested layering systems for the FGM with an Mg-PSZ content from 0 to 40 vol%

to 1100 °C within a FAST device. During heating, the powder was uniaxially compressed while the pressure increased up to 100 MPa and was kept constant during the dwell time of 10 min.

Radwan et al. found a significant influence of layering system of FGMs consisting of stainless steel and alumina on densification behavior and residual stresses [43]. However, no distinct influence on mechanical properties and microstructure was indicated for the FGMs consisting of TRIP steel and Mg-PSZ. Independent of the layer system, the FGMs had a similar hardness, bending strength and grain size of the steel matrix. Except, the four layer system (0 vol%–10 vol%–20 vol%–40 vol% Mg-PSZ) was crack free after sintering, while cracks were found within the FGM with three and five layers. Thus, much higher thermal stresses were present in the three and five layer systems compared to the four layer system. These high thermal stresses caused these cracks. The reduction of thermal stresses is a function of Mg-PSZ layer system. While the tested three layer and five layer systems exhibit a linear increase in Mg-PSZ content, the Mg-PSZ content of the four layer system follows an exponential function. These results confirm the assumption of Radwan et al., that an exponential increase in ceramic content leads to a reduction of thermal stresses [43].

As to be expected, the grain size of the steel matrix decreased with increasing ceramic content of the layer due to the pinning effect of the Mg-PSZ particles. Likewise hardness increased with Mg-PSZ content.

The FGMs exhibited a bending strength of 511 MPa (steel layer on tensile stress). This is 100 MPa larger than the bending strength of a steel matrix composite reinforced with 40 vol% Y_2O_3-PSZ [44]. However, the FGMs were not completely dense. The porosity increased with Mg-PSZ content. Furthermore, the graphite dies do not withstand the high mechanical pressure of 100 MPa during sintering by FAST at all times. Therefore, the pressure had to be decreased.

To completely densify the whole FGM especially applying a pressure < 100 MPa, the temperature distribution within the sintering setup has to be understood and systematically adapted. A vertical temperature gradient has to be expected by sintering of steel/ceramic FGMs using FAST due to the changing electrical conductivity along the sample height with changing ceramic content (Fig. 9.8). However,

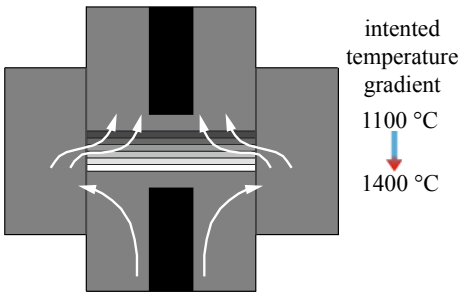

Fig. 9.8 Current path (marked by white arrows) through the sintering tool and the FGM and necessary sintering temperatures

zirconia-rich regions need a temperature of 1200–1300 °C [45] for nano sized powder and 1400–1600 °C for coarser powder [18] to be compacted. Furthermore, steel melts at those temperatures. To densify steel using FAST, temperatures of 1000–1100 °C are required [1]. Thus, a temperature gradient is needed, where the ceramic-rich regions are hotter than the steel-rich regions.

To investigate the vertical temperature gradient caused by the changing ceramic content, an FGM with the layer arrangement 0 vol%–5 vol%–10 vol%–30 vol%–60 vol%–100 vol% Mg-PSZ (from top to bottom, powders S6 and Z2) was sintered (maximum temperature 1100 °C measured in top punch, maximum pressure 51 MPa, dwell time 13 min, heating rate 100 K/min). During densification, the temperature was measured by pyrometer and thermocouples (TCs) within drill holes inside the die 3 mm away from the inner die surface, on the level of the middle of the sample in vertical direction and 2 mm above and below the centric hole. These temperature measurements indicated a much higher temperature at the top, which was close to the steel-rich regions compared to the Mg-PSZ-rich regions at the bottom of the sample [46]. During dwell time, the top and bottom temperatures slightly converged and differed ≈20 K at the end of dwell time. Hence, the steel-rich regions are ≈20 K warmer than the ceramic-rich regions, while it has to be the other way around to densify the FGM properly.

Some researchers introduced vertical temperature gradients by using tapered dies [9, 47] and found a vertical temperature gradient of 220 K. To obtain the required die geometry, extensive simulations and tests are necessary. Other researchers did not change the die geometry. They moved the sample from the die center to the bottom and placed the die directly on the lower larger punch to create a vertical temperature gradient within the sample [48, 49]. However, the temperature gradient varies strongly with the sintering material and the die geometry [50]. Vanmeensel et al. reported a strong increase in electrical resistivity with increasing number of surfaces [51] and therefore, with increasing number of graphite foils at the front surface of the sample. Hence, graphite foil can be used as heating element. To generate heat close to the ceramic-rich regions of the FGM in this study [46], two additional graphite foils were placed between graphite punch and 100% Mg-PSZ layer. Thus, the temperature within the ceramic-rich region converged to the temperature of the steel-rich regions, as indicated by temperature measurements inside the die [46]. During dwell time, the temperature of the ceramic-rich region even exceeded the temperature of the steel-rich region to 10 K [46]. Already, these slight temperature changes led to a lower porosity, improved bending strength and hardness (Fig. 9.9) [46]. However, a higher temperature is needed in the ceramic-rich region.

Since the ceramic-rich regions sinter during dwell time, the temperature gradient has to be existent during dwell time, as well. Furthermore, temperature measurements directly inside the sample are necessary to understand the temperature evolution inside the sample. Only a few studies dealt with direct temperature measurement using homogeneous materials, especially at process temperatures at or above 1000 °C. Temperature measurements utilizing TCs (at least one TC directly within the sample) were performed in the studies of Matsugi et al. [52] or Wang et al. [53].

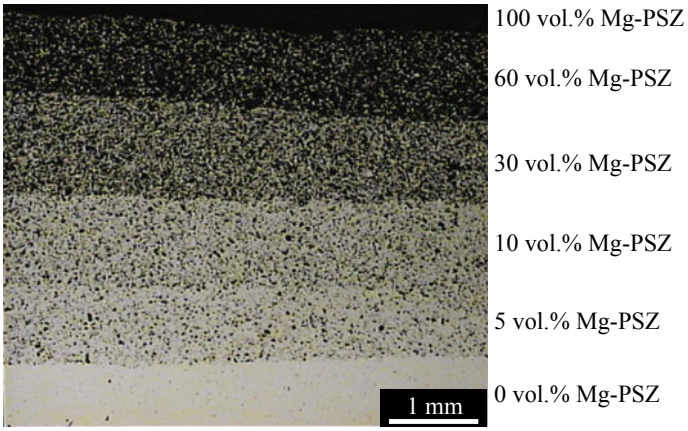

Fig. 9.9 FGM, sintered with additional graphite foils

Furthermore, the thermal insulation around the sintering tool influences the temperature distribution inside the sample. The application of thermal insulation by graphite felt as well as heating elements manufactured by CFRC and its influence on the temperature homogeneity within a conductive (austenitic steel) or non-conductive (8 mol% Y_2O_3 fully stabilized zirconia) sample was studied by Laptev et al. [54]. Particularly for large sample diameter ($\leq$50 mm), the fully thermal insulation of the die was not sufficient to achieve an acceptable horizontal temperature gradient (< 20 K) from the center to the edge of the (conductive) sample. Thus, further thermal insulation by the utilization of CFRC heating elements is required. In the case of non-conductive materials, an optimization (e.g. modification of the die thickness) of the sintering tool, in addition to the application of graphite felt and carbon fiber reinforced carbon (CFRC) heating elements, is often required to obtain an almost homogenous temperature distribution within the sample.

Thus, a further study concerning the temperature distribution within an FGM (consisting of S7 and Z3) during the FAST process dealt with the direct temperature measurement of the vertical temperature gradient of pre-sintered FGMs (at 1050 °C for 15 min) during the dwell time at 1000 °C (duration: 8 min). In reference [43] an equation for the calculation of the steel volume content of each layer within a steel/ceramic FGM is given. A total number of six layers, including the pure Mg-PSZ and steel layer, was selected for the FMG sample (layer thickness: 1.5 mm). For $P = 2$ (material concentration exponent), a steel-rich concentration profile was received, leading to an ceramic volume content of the interlayers of 4, 16, 36 and 64 vol% between the layers of pure steel and Mg-PSZ.

The direct temperature measurement using type S TCs took place within cylindrical bore holes (diameter: 3.5 mm), which had an offset to each other of 90°. The TC-measured temperature T_{TC} was determined in the center of the sintering tool, above (M1), centered (M2) and below (M3) the FGM sample, which is shown in Fig. 9.10. Alumina tubes were used to protect the TCs from high electrical currents,

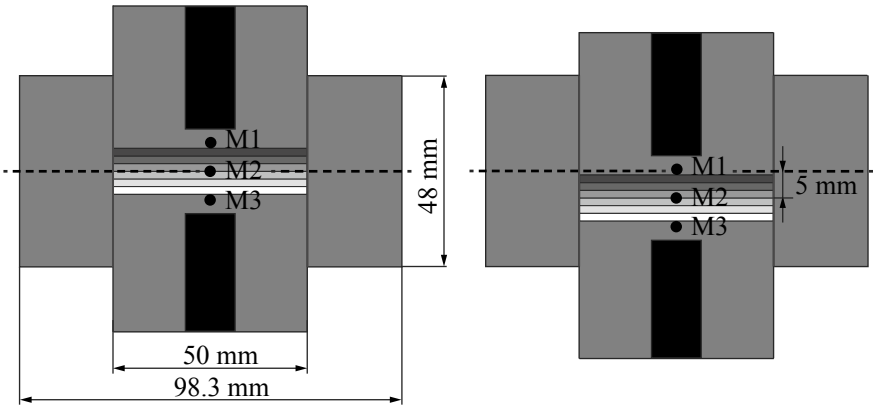

Fig. 9.10 Sintering tool setup, **a** symmetrical tool setup, **b** asymmetrical tool setup—FGM sample shifted by 5 mm downwards

carbonization or sintering to the sample surface. In addition to the experiments with a symmetrical sintering tool setup, asymmetrical sintering tool setups were investigated. For this purpose, the FGM sample was shifted by 5 mm upwards or downwards for both options—with the pure ceramic or steel layer on top.

For all temperature measurement experiments, the outside surface and the top and bottom side of the die were covered with graphite felt (SGL Group: Sigratherm GFA10) to reduce thermal radiation losses. Furthermore, the influence of CFRC discs on the temperature distribution during the SPS/FAST process was investigated.

In general, an 80–90 K higher T_{TC} in comparison to the pyrometer-measured process temperature T_{Pyro} was determined for the symmetrical sintering tool setup at M1 independent of the sample arrangement (pure ceramic layer at the top or at the bottom) and the application of CFRC discs. Furthermore, the highest vertical temperature gradient of approximately 80 K existed for the symmetrical sintering tool setup using an FGM sample with the fully ceramic layer at the top without utilizing CFRC discs for this FAST process. For the same sintering tool, the vertical temperature gradient decreased to approximately 15 K by the application of CFRC discs for the sintering process. Generally, in consequence of the utilization of CFRC discs for the FAST process, the heat was retained in the sintering tool and the electrical power required for the FAST process decreased. Both, the symmetrical or asymmetrical sintering tool setups exhibited vertical temperature gradients < 40 K while using CFRC discs for the sintering process. Despite the application of an asymmetrical sintering tool setup without using CFRC discs for the SPS/FAST process, the vertical temperature gradient never exceeded 80 K. Although, this temperature gradient is still not sufficient to sinter void free FGM, it is an improvement.

9.4 Conclusions

The combination of TRIP steel with Mg-PSZ in a composite and additionally processing this composite by applying FAST resulted in a material with a high strength and a sufficient ductility. By carefully adapting sintering parameters, the material had the ability to undergo strain-induced (TRIP steel) and stress-induced (Mg-PSZ) phase transformations under compressive loading. How the condition of the composite powder and the setting of FAST parameters influence the microstructure and the mechanical properties of the composite is schematically shown in Figs. 9.11 and 9.12. Due to the very short sintering time, only a small amount of the Mg-PSZ transformed into the monoclinic phase during sintering and the steel matrix exhibited very fine grains. Thus, the composites had a high strength. The amount of strength, however, depends on many factors concerning the used parameters, powder characteristics and powder treatment in preparation of FAST. Thus, parameters have to be carefully aligned for every powder condition. However, porosity can remain in the material even after tuning of the sintering parameters, as recently shown on a PM X15CrNiMnN19-4-3 [55]. This steel has a high nitrogen content of 0.17 wt%, which evaporates during sintering and remains partly as porosity (≈5 vol% pores).

Even though the Mg-PSZ has the ability to transform stress-induced after processing by FAST, this stress-induced phase transformation seems to have no influence on flow behavior under compressive deformation. On the one hand, the transforming amount of the Mg-PSZ is very low. On the other hand, the very ductile steel matrix does not transfer all loading to the Mg-PSZ. Thus, composites with a steel matrix, which has a higher strength (e.g. PM X16CrNiMnSiN 15-3-3), are investigated currently in order to increase the strength due to the stress-induced phase transformation of the Mg-PSZ. However, even without an effect of the stress-induced phase transformation, already an addition of 5 vol% Mg-PSZ to a TRIP steel matrix (S1, Z1) increases the specific energy absorption at dynamic deformation at room temperature by 5% [56].

So far, the introduced composites were carefully mechanically characterized by cyclic deformation [57] and by compression tests in a wide range of strain rates and temperatures [16, 17, 56]. Their corrosion behavior was investigated as well [58–60]. A detailed analysis of these results would go beyond the scope of the presented work. So far, weakly sintered ceramic clusters and a low interfacial strength between steel and Mg-PSZ are obstacles for a further improvement of the materials. Especially, the improved sintering of Mg-PSZ-rich layers for the development of FGM requires further research effort.

Acknowledgements The Authors would like to thank Prof. Zhijian James Shen from Stockholm University for his helpful advice and the possibility to carry out experiments using the FAST device (Dr. Sinter 2050, Sumitomo Coal Mining Co., Ltd., Japan) from his group. Furthermore, the authors would like to thank Dr. Tobias Dubberstein (subproject A2) for providing the steel powders with varying sulfur content and Michael Hötzel (subproject A3) for making steel powder, sieved to different particle fractions, available. The authors would like to thank the German Research Foundation (DFG) for supporting the investigations, which were part of the Collaborative Research Center TRIP-Matrix Composites (project number 54473466—SFB 799, subproject A6).

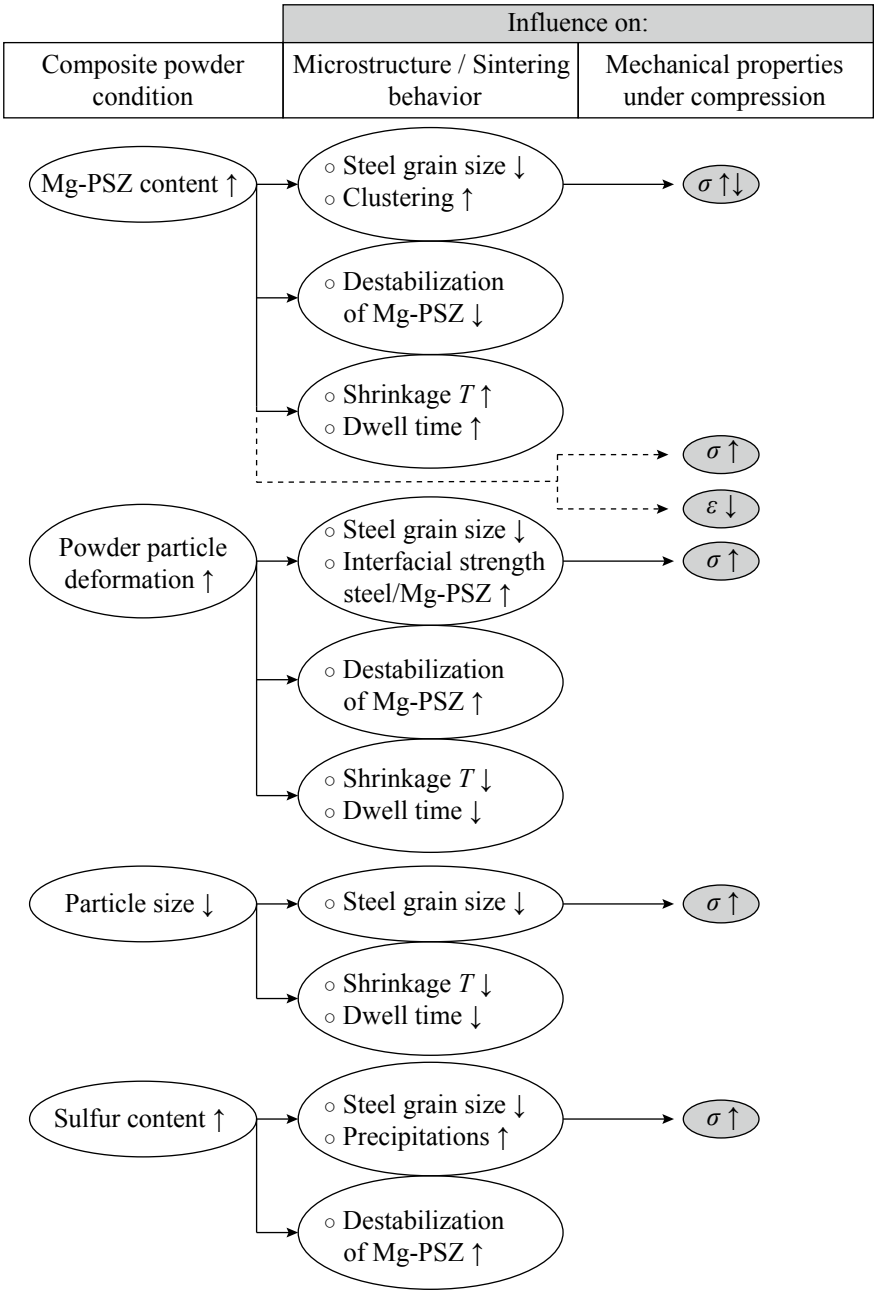

Fig. 9.11 Influence of composite powder condition on sintering behavior, microstructure and mechanical properties (T: temperature, ε: ductility, σ: compressive yield strength)

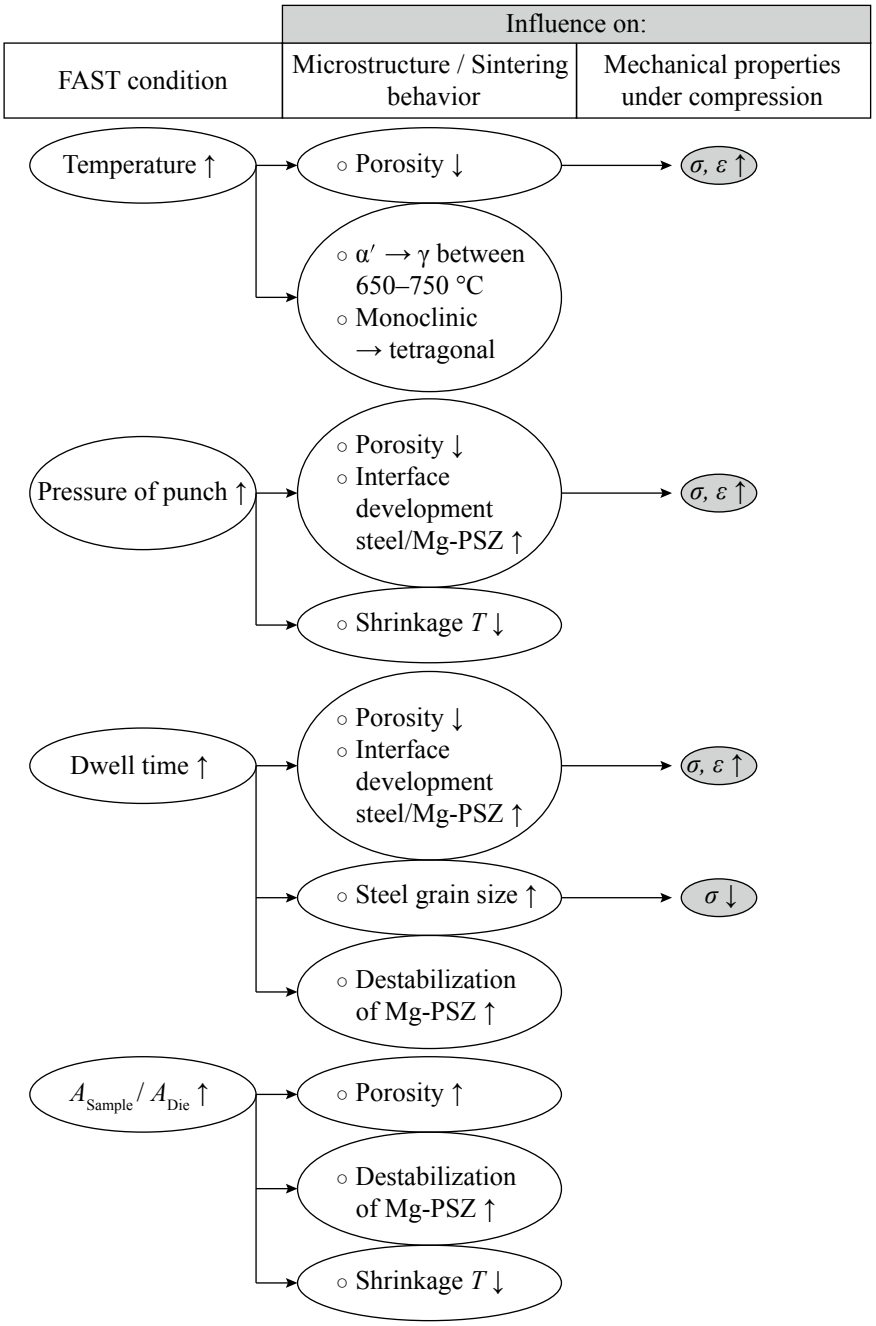

Fig. 9.12 Influence of FAST condition on sintering behavior, microstructure and mechanical properties (A_{Sample}: cross section of sample, A_{Die}: cross section of die, α′: α′-martensite content, γ: austenite content, T: temperature, ε: ductility, σ: compressive yield strength)

References

1. S. Decker, S. Martin, L. Krüger, Metall. Mater. Trans. A **47**, 1 (2016)
2. J.A. Venables, Philos. Mag.: J. Theor. Exp. Appl. Phys. **7**, 73 (2006)
3. O. Grässel, L. Krüger, G. Frommeyer, L. Meyer, Int. J. Plast **16**, 10–11 (2000)
4. H. Salmang, H. Scholze, *Keramik* (Springer, Berlin, 2007)
5. J.R. Kelly, I. Denry, Dent. Mater. **24**, 3 (2008)
6. S. Martin, S. Richter, S. Decker, U. Martin, L. Krüger, D. Rafaja, Steel Res. Int. **82**, 9 (2011)
7. O. Guillon, J. Gonzalez-Julian, B. Dargatz, T. Kessel, G. Schierning, J. Räthel, M. Herrmann, Adv. Eng. Mater. **16**, 7 (2014)
8. Z.A. Munir, U. Anselmi-Tamburini, M. Ohyanagi, J. Mater. Sci. **41**, 3 (2006)
9. M. Tokita, Mater. Sci. Forum 308–311 (1999)
10. L. Hälldahl, M. Nygren, Mater. Sci. Forum 492–493 (2005)
11. K. Ichikawa, S. Murakami, S. Miyamoto, Y. Nakayama, M. Tokita, Mater. Sci. Forum 423–425 (2003)
12. R.M. German, *Powder Metallurgy and Particulate Materials Processing* (Metal Powder Industries Fed, Princeton, NJ, 2005)
13. M.N. Rahaman, *Ceramic Processing and Sintering*, 2nd edn. (CRC Press (Taylor & Francis), Boca Raton, 2003)
14. H. Berek, A. Yanina, C. Weigelt, C.G. Aneziris, Steel Res. Int. **82**, 9 (2011)
15. C. Weigelt, S. Giersberg, C. Wenzel, C.G. Aneziris, Adv. Eng. Mater. **12**, 6 (2010)
16. L. Krüger, S. Decker, R. Ohser-Wiedemann, D. Ehinger, S. Martin, U. Martin, H.J. Seifert, Steel Res. Int. **82**, 9 (2011)
17. S. Decker, L. Krüger, S. Richter, S. Martin, U. Martin, Steel Res. Int. **83**, 6 (2012)
18. S. Decker, Entwicklung der Mikrostruktur und der mechanischen Eigenschaften eines Mg-PSZ-partikelverstärkten TRIP-Matrix-Composits während Spark Plasma Sintering, Dissertation, TU Bergakademie Freiberg (Logos Berlin, Berlin, 2015)
19. E.O. Hall, Proc. Phys. Society. Sect. B **64**, 9 (1951)
20. S. Decker, L. Krüger, Mater. Sci. Eng. A **761** (2019)
21. S. Martin, Deformationsmechanismen bei verschiedenen Verformungstemperaturen in austenitischem TRIP/TWIP-Stahl, Dissertation, TU Bergakademie Freiberg (Freiberger Forschungshefte TU Bergakademie Freiberg, Freiberg, 2014)
22. S. Decker, K. Lange, L. Krüger, T. Dubberstein, Steel Res. Int. **86**, 5 (2015)
23. S. Decker, K. Lange, T. Dubberstein, L. Krüger, Adv. Eng. Mater. **17**, 9 (2015)
24. S. Decker, L. Krüger, J. Compos. Mater. **50**, 13 (2015)
25. S. Chakraborty, A.R. Mallick, D. Debnath, P.K. Das, Int. J. Refract. Metals Hard Mater. **48** (2015)
26. Z. Shen, M. Johnsson, Z. Zhao, M. Nygren, J. Am. Ceram. Soc. **85**, 8 (2002)
27. M. Belmonte, M.I. Osendi, P. Miranzo, Scripta Mater. **65**, 3 (2011)
28. G. Lalet, H. Kurita, T. Miyazaki, A. Kawasaki, J.-F. Silvain, J. Mater. Sci. **49**, 8 (2014)
29. H. Jiang, Z. Xu, Z. Xiu, L. Jiang, H. Gou, C. Zhou, G. Wu, J. Alloy. Compd. **763** (2018)
30. G. Xie, O. Ohashi, K. Chiba, N. Yamaguchi, M. Song, K. Furuya, T. Noda, Mater. Sci. Eng., A **359**, 1–2 (2003)
31. W. Chen, U. Anselmi-Tamburini, J.E. Garay, J.R. Groza, Z.A. Munir, Mater. Sci. Eng., A **394**, 1–2 (2005)
32. T. Dubberstein, M. Hötzel, R. Hagemann, P. Heller, P.R. Scheller, Steel Res. Int. **82**, 9 (2011)
33. H. Berek, C.G. Aneziris, C. Wenzel, T. Westphal, W. Schärfl, Refractories Worldforum **3**, 3 (2011)
34. N. Chawla, K.K. Chawla, *Metal Matrix Composites*, 2nd edn. (Springer, New York, 2013)
35. R. Haynes, Met. Powder Rep. **46**, 2 (1991)
36. G.B. Olson, M. Cohen, Metall. Trans. A **6**, 4 (1975)
37. P. Ludwik, *Elemente der technologischen Mechanik* (Springer, Berlin, 1909)
38. J. Räthel, M. Herrmann, W. Beckert, J. Eur. Ceram. Soc. **29**, 8 (2009)

39. B. Kieback, J. Trapp, in *Sintern - der zentrale Prozess der Pulvermetallurgie*, ed. by H. Kolaska (Heimdall, Hagen, 2011), p. 47
40. W. Li, E.A. Olevsky, J. McKittrick, A.L. Maximenko, R.M. German, J. Mater. Sci. **47**, 20 (2012)
41. J. Weertman, Trans. ASM **61** (1968)
42. I.-W. Chen, L.A. Xue, J. Am. Ceram. Soc. **73**, 9 (1990)
43. M. Radwan, M. Nygren, K. Flodström, S. Esmaelzadeh, J. Mater. Sci. **46** (2011)
44. K. Tohgo, T. Kawaguchi, Key Eng. Mater. 297–300 (2005)
45. J. Langer, M.J. Hoffmann, O. Guillon, J. Am. Ceram. Soc. **94**, 1 (2011)
46. S. Decker, L. Krüger, Mater. Des. **115** (2017)
47. Z. Zhang, X. Shen, C. Zhang, S. Wei, S. Lee, F. Wang, Mater. Sci. Eng. A **565** (2013)
48. Y. Zhang, Z. Li, C. Li, Z. Yu, Ceram. Int. **41**, 10 (2015)
49. M. Belmonte, J. Gonzalez-Julian, P. Miranzo, M.I. Osendi, Acta Mater. **57**, 9 (2009)
50. C. Morin, S. Le Gallet, M. Ariane, F. Bernard, Ceram. Int. **42**, 2 (2016)
51. K. Vanmeensel, A. Laptev, J. Hennicke, J. Vleugels, O. Van der Biest, Acta Mater. **53**, 16 (2005)
52. K. Matsugi, H. Kuramoto, T. Hatayama, O. Yanagisawa, J. Mater. Process. Technol. **134**, 2 (2003)
53. Y.C. Wang, Z.Y. Fu, Q.J. Zhang, Key Eng. Mater. 224–226 (2002)
54. A.M. Laptev, M. Bram, K. Vanmeensel, J. Gonzalez-Julian, O. Guillon, J. Mater. Process. Technol. **262** (2018)
55. M. Radajewski, R. Eckner, S. Decker, M. Wendler, L. Krüger, Adv. Eng. Mater. **21**, 5 (2019)
56. S. Decker, L. Krüger, Mater. Des. **114** (2017)
57. A. Glage, S. Martin, S. Decker, C. Weigelt, M. Junghanns, C.G. Aneziris, U. Martin, L. Krüger, H. Biermann, Steel Res. Int. **83**, 6 (2012)
58. M. Mandel, L. Krüger, S. Decker, Corros. Sci. **90** (2015)
59. M. Mandel, L. Krüger, S. Decker, Mater. Corros. **66**, 12 (2015)
60. M. Mandel, L. Krüger, S. Decker, Mater. Werkst. **46**, 10 (2015)

Chapter 10
Electron Beam Technologies for the Joining of High Alloy TRIP/TWIP Steels and Steel-Matrix Composites

Lars Halbauer, Anja Buchwalder and Horst Biermann

Abstract The use of new, high-alloy TRIP/TWIP steels and the corresponding composite materials requires innovative joining processes. Due to the high power density, the inert working atmosphere and the software-based control, the electron beam is predestined to study different joining strategies. This paper shows how the electron beam can be used as a tool to join high-alloy TRIP/TWIP materials with and without particle reinforcement. Microstructure-property relationships based on the microstructure and tensile tests are established and correlated to the material used. From this, a corresponding joining strategy is derived for each material, which is presented on the basis of various evaluation criteria.

10.1 Introduction

Modern lightweight constructions are subjected to the conflicting demands for lower weight and higher load-bearing capacity. To overcome these challenges, a composite material was developed which combines good ductility, high strength and high specific energy absorption potential [3, 4, 6, 54]. This is achieved by reinforcing a metastable austenitic steel matrix (γ) with MgO partially stabilized zirconia (Mg-PSZ) particles. During deformation between the martensite start M_s- and the M_d-temperature (temperature where 1% strain induced martensite is formed), the matrix of the composites is able to transform into α'-martensite. The associated TRIP effect (TRansformation Induced Plasticity) involves an exceptional strain-hardening capac-

L. Halbauer (✉) · A. Buchwalder · H. Biermann
Institute of Materials Engineering, Technische Universität Bergakademie Freiberg,
Gustav-Zeuner-Str. 5,
09599 Freiberg, Germany
e-mail: lars.halbauer@iwt.tu-freiberg.de

A. Buchwalder
e-mail: anja.buchwalder@ww.tu-freiberg.de

H. Biermann
e-mail: biermann@ww.tu-freiberg.de

H. Biermann and C. G. Aneziris (eds.), *Austenitic TRIP/TWIP Steels and Steel-Zirconia Composites*, Springer Series in Materials Science 298,
https://doi.org/10.1007/978-3-030-42603-3_10

ity with still high ductility under tensile loading [36, 37]. However, the deformation behavior of the matrix material depends strongly on the stacking fault energy (SFE) [29, 41, 50]. At relatively high stacking fault energies ($> 40\,mJ/m^2$), the preferred deformation mechanism is movement of dislocations (wavy glide). Stacking fault energies in the range of 20–40 mJ/m^2 favor the formation of deformation twins (TWinning Induced Plasticity, TWIP effect) [29] which is accompanied by a significant increase in ductility. In steels with a stacking fault energy lower than 15–20 mJ/m^2, the TRIP effect occurs [29, 43, 45, 55]. With applied stress, the Mg-PSZ particles can undergo a phase transformation as well, where the tetragonal phase transforms into monoclinic particles [12]. Consequently, a stress field within the matrix is counteracted by the resulting volume expansion of the particle and thus the fracture resistance of the component is further increased [28].

For the evaluation of a potential application, the weldability of the material has to be investigated. According to DIN ISO/TR 581:2007 [11], the term weldability is referred to as the interdependence of three component properties (cf. Fig. 10.1):

Material	The weldability depends on the material properties such as their chemical composition (e.g. hardening) and their microstructure (e.g. elimination of precipitation hardening, coarsening of grains). The material properties have a strong dependence on the necessary constructional properties and only a weak dependence on the welding process.
Construction	As a generic term, the constructional properties describe the possibility to weld. They are defined by the joint geometry and the type of stress that is applied during or after welding. Constructional properties are strongly dependent on the welding process (which process for which joint geometry) and slightly dependent on the material properties (e.g. metallurgical notches).
Process	Finally, the weldability is defined by the process parameters, which are determined by the type of welding process and the inherent welding parameters. The choice of parameters strongly depends on the material properties and weakly depend on the constructional properties.

Comparable to the laser beam (LB), the electron beam (EB) can be applied for a high energy fusion process. The difference to conventional joining approaches is the use of highly accelerated electrons as energy source which allows the application of very high energy densities. The EB as a joining tool allows essential process parameters such as beam power, feed rate or focal point to be set freely and reproducibly. This also makes comprehensive monitoring of the process possible. At the same time, due to the adjustable power density, both deep welding and heat conduction welding can be established to investigate the influence of the welding process. Due to the high positioning accuracy, the dilution can also be precisely controlled in dissimilar weld joints to set the materials properties. In addition, solid state joining processes, such as soldering, can be carried out via the freely programmable, almost inertia-free

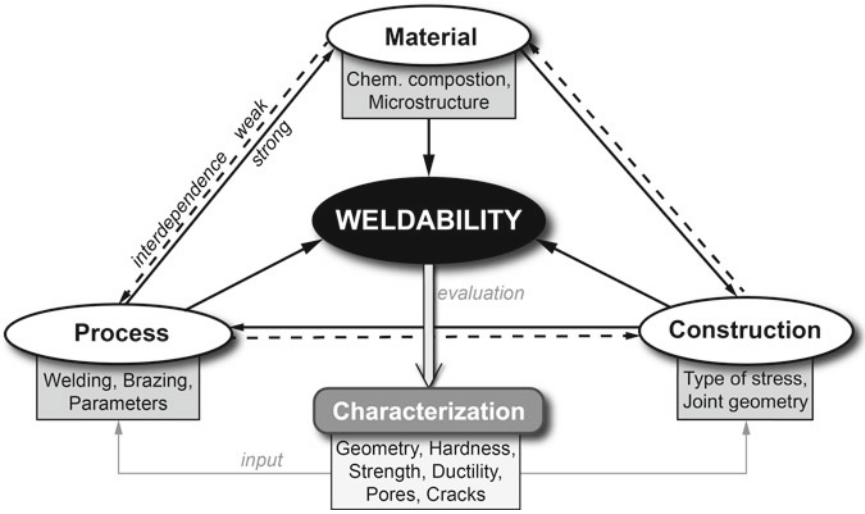

Fig. 10.1 Weldability of TRIP-matrix composites dependent on the the material, the construction and the process (according to DIN ISO/TR 581:2007 [11])

deflection of the EB. Oxide and pore formation is significantly inhibited due to the process inherent vacuum atmosphere. However, it should be noted that elements with a high vapor pressure (such as Mn) may be able to degas.

For high-alloy (HA) TRIP/TWIP-matrix composites the weldability has not been studied yet. First experiments from Buchwalder et al. show a good weldability of the HA base material but no experiments were carried out on the composite [8]. Thus, only partial information on the weldability of similar steels or composites can be obtained from the literature. Reference materials for the base material are low-alloy (LA) TRIP steels and HA TWIP steels. LA TRIP steels, which mainly consist of ferrite, bainite, martensite and retained austenite, show a significant TRIP effect during deformation and are therefore comparable in terms of mechanical behavior to the HA TRIP steels with low SFE. The welding of LA TRIP steels was carried out with a broad variety of welding processes, such as gas metal arc (GMA) [21, 26], resistance spot [22, 34], friction stir [30], and LB welding [7, 25, 42]. Failure takes place within the heat affected zone of the material [22, 26]. The welding seam shows a significant increase in hardness (up to 510 HV) which decreases with decreasing cooling rate [42].

HA TWIP steels can also be welded with various welding processes [33]. During welding, however, the main alloying element manganese has an increasing tendency to evaporate with higher temperatures and lower atmospheric pressure [46]. Mujica et al. showed that the evaporation rate for continuous processes decreases with increasing power density [32]. Typically, up to 2 wt% Mn is evaporating during LB welding [27]. Pulsed welding leads to an above-average evaporation rate of manganese. Due to their fully austenitic microstructure and the strong tendency for

segregation of manganese, HA TWIP steels have a high susceptibility for hot-crack formation [56]. For the hot-rolled alloy Fe–25Mn–3Al–3Si an hardness increase from the base material to the fusion zone from ≈1700 to 2400 HM is reported and explained by the grain refinement after welding [27, 31]. High cooling rates, such as those generated by laser beam welding, can also lead to a significantly increased hardness within the fusion zone (up to 300 HV) [32]. Due to the evaporation and the lower grain size, the stacking fault energy of the welded seam is locally lower than in the base material. Therefore, the welding seam of HA TWIP steels is not capable to deform as much as the TWIP base material. Accordingly, rupture occurs within the base material where the deformation is concentrated [31, 39, 40, 44].

To the current state of the art, there is no suitable process for joining steel-ceramic composites though. Weigelt et al. proposed a method for the joining of Mg-PSZ reinforced steel matrix composites in the green-body state [53]. While the mechanical properties are outstanding, the process is not applicable for components which are not produced by powder metallurgical processing and rely on welding or brazing. Experiments carried out by Tseng et al. [52] showed a strong negative influence of zirconia during fusion welding. The addition of ZrO_2 particles with a diameter ≥0.3 µm leads to the deterioration of weld seam quality due to crack formation and concave root surface.

With respect to the weldability Al-SiC systems can be regarded as alternative composite materials and have already been successfully joined by fusion welding processes, using tungsten inert gas (TIG), LB or EB welding [18, 38]. The melting temperature (T_M) of the ceramic particles of Al-SiC and TWIP-matrix composites are very close to each other ($T_{M,\,SiC} = 2730\,°C$, $T_{M,\,ZrO_2} = 2715\,°C$). The melting point difference ΔT_M between matrix and reinforcement phase of Al-SiC composites ($\Delta T_M = 2070\,°C$) is about 775 K higher than in the case of TRIP-matrix composites with Mg-PSZ ($\Delta T_M = 1295\,°C$). However, this is negligible as the temperatures within the keyhole during deep penetration welding can reach temperatures greater than 10^4 K [51] during electron beam welding (EBW) and 8×10^3 K during laser beam welding (LBW). It was found, that during laser beam welding, the SiC particles are partially melted, move within the melt pool and form clusters [9]. In contrast, welding with electron beam leads to the ejection of molten material due to the evaporation of SiC [18]. For amounts higher than 1% SiC, the ejected volume strongly increased. If the Al matrix is precipitation hardened, softening occurs in the joining zone. In contrast, the formation of Al_3C_4-carbides leads to an increase of hardness. The particle clusters in the weld seam act as locations for stress concentration under external load and cause brittle material failure. This drastically reduces both the strength of the welded joints and the ductility. Rupture occurs within the fusion zone [18, 35]. It can be derived from past investigations that the joining result for metal-matrix composites strongly depends on the material and the joining process selected.

Consequently, the weldability of TRIP/TWIP-matrix composites with the use of the electron beam is examined in this work. First, the influence of the chemical composition is investigated with similar joints of non-reinforced as-cast steels. Second, the effect of added Mg-PSZ is studied in dissimilar joints with TWIP-matrix compos-

ites, which was already published in [13–15]. Furthermore, it is investigated how the electron beam can be used to establish a brazing process to join similar TWIP-matrix composites (see [16]). Finally, the loadability is studied under different loading conditions for similar joints.

10.2 Materials and Methodology

This section gives an overview about the key parameters used for the experiments. To maintain readability, the parameters that were altered for specific experiments are repeatedly given in the particular sections.

10.2.1 Electron Beam Facility and Temperature Measurements

All joining experiments were carried out within an K26-80/15 universal electron beam chamber facility (PRO-BEAM, Neukirchen, Germany) at an ambient pressure of 2×10^{-2} mbar. In general, three different processes were applied, i.e. similar electron beam welding (S-EBW), dissimiliar electron beam welding (DS-EBW) and electron beam brazing (EBB). The corresponding parameters are given in Table 10.1 and the sample geometry in Fig. 10.2a.

During S-EBW and DS-EBW the samples were fixed within an clamping device to prevent unwanted movement. It should be noted, that all similar joining experiments were carried out without welding gap (zero gap) to neglect the influence of the joint faces on the welding results. The dissimilar welding experiments were carried out on butt joints. If a beam offset Δx was applied, the offset in x-direction was referred to as the distance between the EB and the dissimilar weld joint face. To increase the accuracy of the electron beam position, a notch ($0.3\,\text{mm} \times 45°$) was applied to the joint edge.

For the brazing experiments, a temperature-controlled power regulation system was used to control the temperature within the energy transfer field (ETF). This

Table 10.1 EB parameters used: acceleration voltage U_A, beam current I_B, offset to beam current ΔI_B, welding speed v_s, holding time t_H, beam shift relative to the joint gap Δx, offset to lens current ΔI_L, oscillation figure OF, diameter of oscillation figure d_{OF}

Process	U_A (kV)	I_B (mA)	ΔI_B (mA)	v_s (mm/s)	t_H (s)	Δx (mm)	ΔI_L (mA)	OF	d_{OF} (mm)
S-EBW	80	5 …180	0	1 …80	–	0	−5 …+75	Circle	0.5
DS-EBW		30 …110	0	5 …45	–	0 …0.8	−5 …+30		
EBB	60	0	70	–	43 …600	0	+10	Field	–

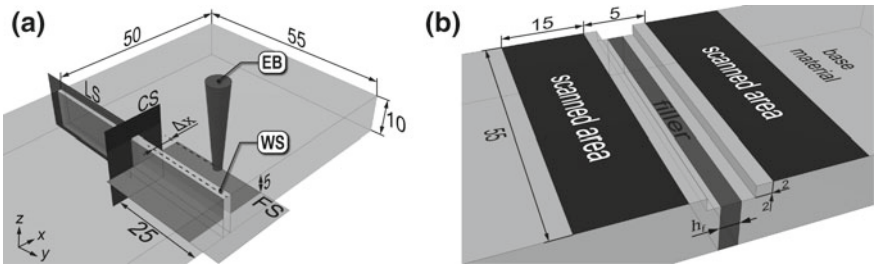

Fig. 10.2 Sample geometry and positioning of EB for **a** all joining methods with beam offset (if applied) and information about cross-sections (CS), longitudinal-sections (LS) and flat-sections (FS) with respect to the welding seam (WS); **b** electron beam brazing with material setup and dimensions of the beam interaction field used. All dimensions in (mm)

system consisted of a temperature sensor (two-color pyrometer, regulation time = 3 ms) and a software that calculated the power output. It was necessary to assign an initial beam current (I_B) and a beam current offset (ΔI_B) for the brazing process. The temperature sensor was placed at the edge between the joint gap and the ETF. Figure 10.2b shows the dimensions of the field. During the experiments, the filler gap (h_f) was increased in the range of 200–1500 µm. To ensure constant temperatures alongside the filler gap, an polynomial energy distribution P_y according to (10.1) was used with $-27.5 < y < 27.5$. It was found, that the energy in the center of the scanning area had to be lowered to a minimum of $P_{min} = 0.8$.

$$P(y) = (1 - P_{min}) \left(\frac{y}{27.5}\right)^2 + P_{min} \tag{10.1}$$

An infrared camera was used to evaluate the temperature distribution across the sample width and depth. For a detailed explanation regarding the temperature measurements, please refer to [16].

10.2.2 Base Materials

Different types of base materials with the chemical compositions given in Table 10.2 were used for the three joining approaches (S-EBW, DS-EBW, EBB). It should be mentioned, that the amount of alloying elements for the composite material (TWIP+Mg-PSZ) refers to the steel matrix. Accordingly, the chemical composition of the zirconia particles is given in Table 10.3. The base materials were available in three different states:

AC cast-material which was produced by AC-TECH GMBH (Freiberg, Germany) by means of sand casting with a grain size of ≈2 mm

HR commercial grade AISI 304 in hot-rolled condition (grain size ≈130 µm)

Table 10.2 Chemical composition (in wt%) of the basic materials used sorted according to the joining process used. The materials were available in as-cast (AC), hot-rolled (HR) and powder metallurgically produced (PM) (containing 10 vol% ZrO_2) conditions

Process	Steel name	Short	State	Fe	C	Cr	Mn	Ni	Si
S-EBW	16Cr-7Mn-3Ni	16-7-3	Cast	*Bal.*	0.055	15.9	6.7	3.1	0.75
	16Cr-7Mn-6Ni	16-7-6		*Bal.*	0.048	16.3	6.6	6.3	0.85
	16Cr-6Mn-9Ni	16-6-9		*Bal.*	0.074	15.9	6.2	9.1	0.82
DS-EBW	AISI 304	A304	HR	*Bal.*	0.022	16.8	1.93	7.8	0.23
	TWIP+Mg-PSZ	MMC	PM	*Bal.*	0.03	13.4	7.4	8.7	0.64
EBB	AISI 304	A304-B	HR	*Bal.*	0.01	19.19	1.84	8.23	0.28
	TWIP+Mg-PSZ	MMC	PM	*Bal.*	0.031	14.77	6.97	10.03	1.01

Table 10.3 Chemical composition of the Mg-PSZ powder used for producing the MMC

(wt%)							
ZrO_2	HfO_2	MgO	SiO_2	Al_2O_3	CaO	TiO_2	Fe_2O_3
Bal.	1.73	3.37	2.43	0.63	0.21	0.14	0.01

Table 10.4 Chemical composition and nomenclature of the filler material used

		(wt%)					(°C)
Filler	DIN EN 1044	Ni	Cu	Si	Cr	B	T_f
HTL 5	NI 105	*Bal.*	–	10.1	19	<0.03	1190

PM composite which was produced by mixing steel and Mg-PSZ powders (SAINT-GOBAIN, USA, see Table 10.3) by ball milling (100 rpm, 30 min) and subsequent hot pressing (1050 °C, 30 min) at FRAUNHOFER IKTS (Dresden, Germany).

Table 10.4 shows both the chemical composition and working temperature T_f of the filler paste (BOEHLER WELDING, Hamm, Germany) used. The composite was produced with a d_{50} of 55 µm for the matrix material. Due to local agglomeration of the Mg-PSZ powder, clusters of particles with sizes of up to 20 µm were formed during hot pressing.

Before joining, the samples were demagnetized and cleaned with ethanol without additional grinding of the joint faces. For the brazing experiments, the joint faces were ground in direction of gravity.

10.2.3 Microstructural Characterization

After joining, the samples were cut, ground and polished with diamond paste up to 1 µm. For light optical investigations, the materials were etched either with V2A reagent at a temperature of 60 °C or with LICHTENEGGER solution. The Electron Backscattered Diffraction (EBSD) investigations were carried out with a LEO 1530 (TESCAN, Czech Republic), an acceleration voltage of 20 kV, 120 µm aperture, 70° tilting and 17 mm working distance. Channel 5 (Oxford, HKL) was used as analysis software. Detailed investigations of the connection quality for dissimilar welded materials were carried out on focussed ion beam (FIB) prepared samples at the transmission electron microscope (TEM) JEM 200 FS from JEOL (Japan) at U_A = 200 kV with varying apertures. The investigations were carried out using the analysis software DIGITAL MICROGRAPH from GATAN and ANALYSIS STATION from JEOL.

10.2.4 Mechanical Characterization

The microhardness (HV0.3) of the welding seams was determined with an semi-automatic tester (LECO, Mönchengladbach, Germany). Therefore, hardness indentations with an indentation distance of 0.08 mm were linearly distributed across the welding seam (WS). After brazing the hardness of the different microstructural constituents within the filler was evaluated using a nanohardness tester Fischerscope (HELMUT FISCHER, Sindelfingen, Germany) with increasing load conditions and a maximum indentation force of 50 mN. For all joining processes, the mechanical properties of the material were evaluated in quasistatic tensile tests under displacement control on standard testing machines from HEGEWALD & PESCHKE (Nossen, Germany) and ZWICK ROELL (Ulm, Germany). Figure 10.5 gives a summary of the geometries of the tensile specimens used.

Table 10.5 Specimen dimensions and the location of the joining zone (JZ) for the quasistatic tensile tests for different joining processes. All dimensions in (mm)

Process	a	b	c	d	e	f	R
S-EBW	30	97	27	5	-	M8	10
DS-EBW	16	71	18	4	2	8	12
EBB	30	97	27	5	2	9	12

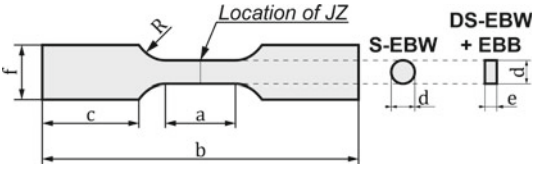

10.2.5 Non-destructive Testing

In order to determine the volume defects within the WS, such as pores or shrinkage, X-ray examinations were carried out with an acceleration voltage of 120 kV at a working distance of 90 cm on parts of the longitudinal sections (see LS, Fig. 10.2a). The samples were placed on an X-ray storage foil and irradiated for an exposure time of 4–8 min (depending on the thickness) with an ERESCO (UK) 200/8 X-ray inspection system.

For the non-destructive ultrasonic immersion tests, a high-frequency USPC 3060 UHF ultrasonic imaging system (INGENIEURBÜRO DR. HILLGER, Braunschweig, Germany) was used (Fig. 10.3). During the test procedure, the test specimen and the immersion probe were located within a liquid coupling medium (deionized water with 1.25% Echokor LF anti-corrosion reagent), which ensured uniform coupling. The specimens (height: approx. 10 mm, cf. Fig. 10.2a) were scanned parallel to the yz plane, while the shortest increment size in the y and z directions was 13 µm. A focused broadband transducer (6–12MHz) STS 6 PB 6 12 P 15 (KARL DEUTSCH, Wuppertal, Germany) with an active diameter of 6 mm and a focal length of 15 mm in water was applied.

The focal depth inside the TWIP matrix composite was ≈3.1 mm and the one-way water path between the transducer and the front surface of the specimen was set to 3 mm, respectively. For the acoustic parameters, densities of 7.883 g/cm^3 (AISI 304) and 7.594 g/cm^3 (MMC) and impedances of 45.4 kg/m^{2}s (AISI 304) and 44.3 kg/m^{2}s (MMC) were used. The wave velocity was measured using a Panametrics V109 transducer (5 MHz). The Archimedes method was applied for the density measurements of both welded materials.

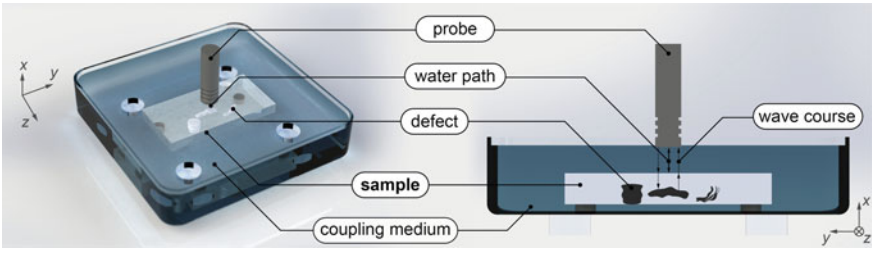

Fig. 10.3 Schematic illustration of the ultrasonic immersion testing method [15]

10.2.6 *Electron Beam Welding of Similar Joints Without Reinforcement*

10.2.6.1 Influence of the Welding Parameters on the Seam Geometry

In order to investigate the welding behavior of the base material without the influence of the ceramic particles, welding was carried out on cast steels with different nickel contents (cf. Table 10.2). Figure 10.4a shows the evolution of the geometric parameters weld seam depth (t_{WS}), weld seam width (b_{WS}), nail head width (b_{NH}) and face reinforcement (h) as a function of the beam current for a constant welding speed of 10 mm/s.

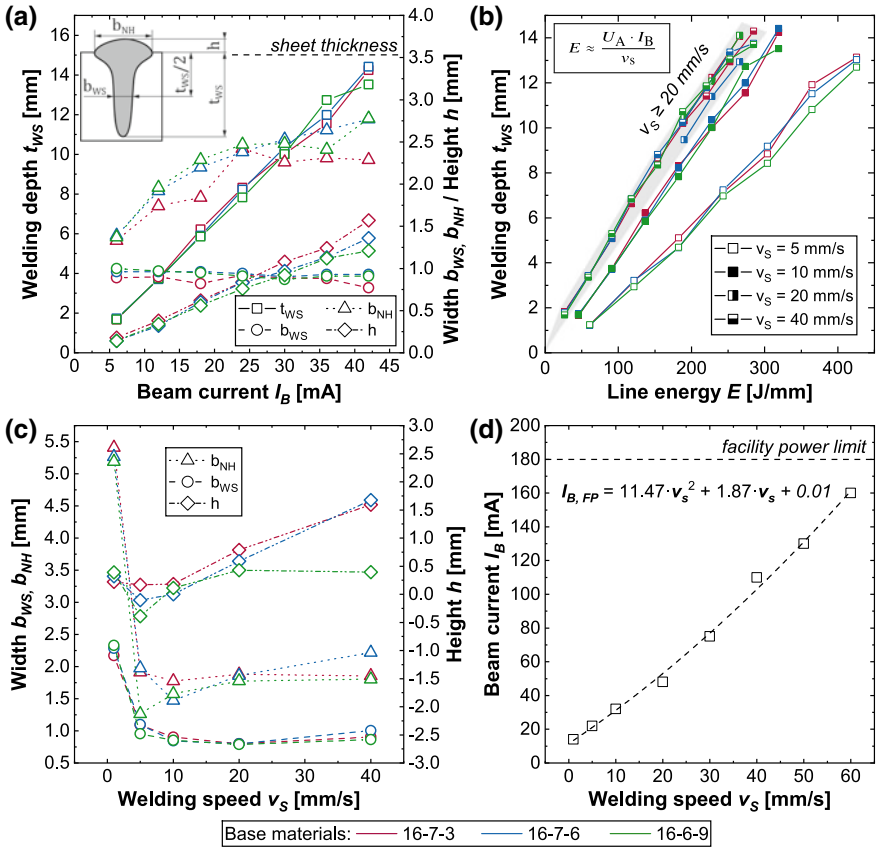

Fig. 10.4 Influence of the welding power on the weld seam geometry depending on **a** the beam current I_B for $v_s = 10$ mm/s; **b** the line energy E and the welding speed v_s; **c** the welding speed during full penetration welding; **d** the beam current required for full penetration ($I_{B,FP}$; $t_{WS} = 10$ mm) at different welding speeds

In the examined beam current range the welding depth is directly proportional to the beam current. Since the welds were placed in 15 mm thick sheets, the selected test parameters did not result in full penetration welding. As a result, the welding depth exhibits fluctuations which depend on the welding speed. At 5 mm/s the standard deviation of the welding depth and the maximum depth difference were determined to 0.49 mm and 1.59 mm, respectively. For higher welding speeds, the fluctuation of the welding depth decreases to an average of 0.11 mm and a maximum of 0.44 mm. According to Huang et al. [17], this is caused by protuberances formed by the recoil pressure within the keyhole, leading to irregular temperature distributions within the capillary. Based on these results, no clear tendency could be derived with regard to the differences in welding depth between the individual test materials. With regard to the welding depth, all three investigated materials showed the same tendency and almost identical welding depths could be achieved. The width of the weld seam of all materials exhibited only a slight decrease with increasing beam current. This was attributed to the formation of the keyhole even at low power inputs.

To evaluate the influence of the welding speed and the beam current on the welding depth, the line energy (cf. Fig. 10.4b) was calculated after (10.2) with an efficiency $k \approx 1$.

$$E = k \cdot \frac{U_A \cdot I_B}{v_s} \tag{10.2}$$

For welding speeds lower than 20 mm/s, the welding depth depends on both the welding speed and the line energy. With increasing welding speed, the welding depth becomes independent on the welding speed used. Again, this behavior can be attributed to the deep penetration effect. Lower welding speeds require lower beam currents to achieve the same line energy as with higher welding speeds. Thus, the lower the welding speed, the lower the power density for equal line energies. Since the deep penetration effect depends primarily on the power density, it is only incompletely formed at low welding speeds. In order to produce deep penetration welds at a given energy input per line length, the welding speed has to be increased to compensate the higher required power density. Accordingly, a stable formation of the keyhole occurred above a certain welding speed threshold of 20 mm/s. At higher welding speeds only the welding depth is increased proportional to the beam power, while the other geometrical parameters remain nearly constant.

In most application-relevant processes, it is necessary to produce a weld seam over the entire sheet thickness with a single pass (full penetration welding). For this purpose, tests were carried out in which the beam current was increased for various welding speeds until the root was completely formed. The beam current needed for full penetration ($I_{B,FP}$) is shown in Fig. 10.4d as a function of the welding speed. The fitting function was a parabola and proved to be valid for all three investigated materials. Experimental practice has also shown that the fit was suitable for both interpolation and extrapolation of beam currents.

In full penetration welds the welding depth is constant for all welding speeds (cf. Fig. 10.4c). With increasing welding speed from 1 to 10 mm/s, both the seam and

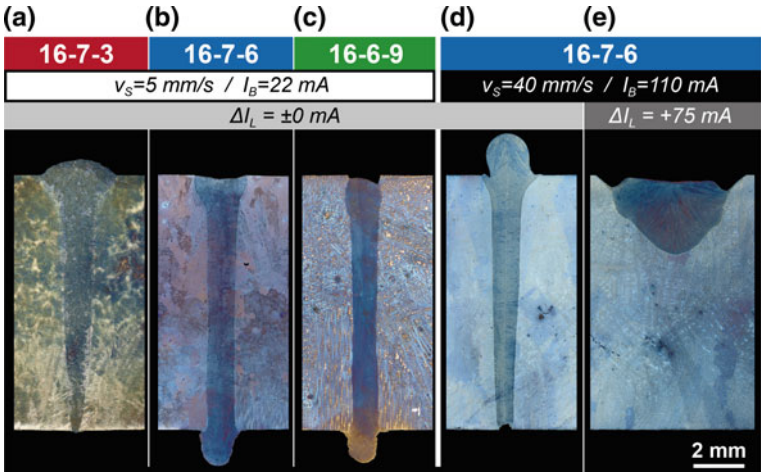

Fig. 10.5 Macroscopic appearance of the welding seam dependent on the welding speed, the base material and the focal plane

the nail head width decreased independent of the base material used. A reason for this was the limited sample volume used in the experiments. At low welding speeds a significant heat build-up occurred which contributed to the widening of the weld seam in the keyhole area. Although an influence on the welding seam width could have been expected due to differences in the thermal conductivity of the samples (due to the varying nickel content), no clear correlation could be found between the weld width and the material used. This was attributed to the fact that the seam width varies over the seam length due to the keyhole oscillation. Consequently, the seam widths fall within a scatter band. At a welding speed of 10 mm/s, a beam current of 32 mA was necessary to achieve full penetration. This was very similar to the threshold of the beam current ($I_{\mathrm{Th}} = 25$ mA), that was found for a stable keyhole welding in the experiments with increasing beam current (cf. Fig. 10.4a). Due to the limitation of t_{WS}, welding speeds >10 mm/s led to a slight increase of b_{WS}, while b_{NH} remained nearly constant.

10.2.6.2 Macroscopic Appearance of the Welding Joints

Figure 10.5 shows representative cross sections of the three materials welded with different welding speeds and focal offsets. It is shown that the steel 16-7-3 was barely fully penetrated at a beam current of 22 mA (Fig. 10.5a). An increasing nickel content leads to a stronger formation of the root face and an increasing root convexity (Fig. 10.5a–c). Steel 16-6-9 already shows undercuts (cf. Fig. 10.5c). At the same time, the V-shape of the seams decreases with increasing nickel content. While steel 16-7-3 still has a pronounced nail head due to its higher thermal conductivity, steel

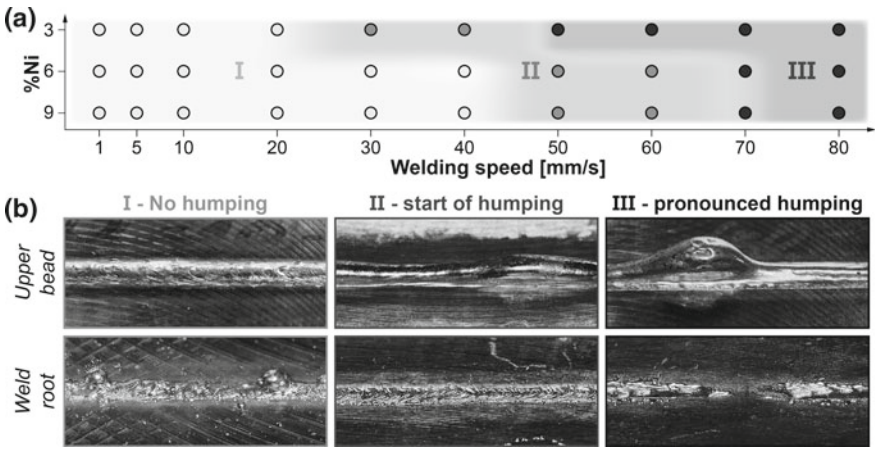

Fig. 10.6 **a** Representative appearance of upper bead and weld root for different humping tendencies; **b** humping tendency dependent on the welding speed for the three high alloy steels

16-6-9 shows almost completely parallel fusion faces. This is attributed to the fact that $I_{B,FP}$ for the formation of the keyhole has been reached and slightly exceeded for steels 16-7-6 and 16-6-9 respectively. On the other hand, higher beam currents would have been necessary for 16-7-3 steel to increase the deep penetration effect.

This effect disappears at higher welding speeds, so that all welds look as in Fig. 10.5d at 40 mm/s. They exhibit nearly parallel fusion faces and a pronounced nail head formation. The reason for this is the increasing power density, which produces a keyhole at higher welding speeds independent of the material selected. To prove the assumption of the correlation between power density and the deep penetration effect, welds were carried out with a strong defocus (cf. Fig. 10.5e, $\Delta I_L = +75$ mA). It was observed that a reduction of the power density resulted in a significant decrease of the welding depth and an increase of the seam width (cf. Fig. 10.5d, e). The typical seam shape is present, as it is created by heat conduction during GMA or TIG welding. Due to the circular beam oscillation, undercuts are formed on the weld face. Apart from undercuts at individual welding speeds, which were caused by too high beam currents or beam oscillation, no macroscopic defects such as cracks, pores or non-metallic inclusions were detected within the welds.

During the experiments, it was noticed that depending on the welding speed, the formation of humping occurred. Thereby the appearance of the weld face and root could in principle be divided into three stages (I–III), which are illustrated in Fig. 10.6b. In stage I the weld face showed no differences in height except for the typical scaling. Only in the lower bead single material elevations were detected which were caused by the oscillation of the keyhole described above. This represented the humping-free state and the predominant portion of the samples. Stage II was characterized by height differences in the upper caterpillar. The seam scaling was not visible at the weld face and could only be found in the root layer, which in addition

showed no significant height differences. In stage III typical humping features were observed. For example, the weld seam showed periodic protuberances, an incomplete root face and a considerable proportion of ejected weld metal.

The stages described occurred as a function of welding speed and material (Fig. 10.6a). As expected, the humping started at high welding speed ($v_s \geq 50$ mm/s). In addition, steel 16-7-3 had a much stronger tendency to hump and already showed signs of humping at a welding speed of 30 mm/s. Above a welding speed of 50 mm/s the material could not be considered weldable due to strong humping effects. The steels 16-7-6 and 16-6-9 showed signs of humping only at 50 mm/s. The weldability limit for the selected parameter set was found at 60 mm/s. Above this speed the weldability could no longer be guaranteed.

It is known from the literature [5] that humping starts at a certain welding speed and strongly depends on the welding depth and the alloying elements of the base materials. Therefore, it is pointed out that these results are only valid for the investigated sheet thickness of 10 mm and have to be re-evaluated for other chemical compositions and/or thicknesses of the base material used.

10.2.6.3 Influence of the Welding Parameters on Evaporation

During DPW, the material is locally molten and vaporized to form a keyhole of plasma surrounded by a molten pool. Elements with low vapor pressure, such as manganese, tend to evaporate during welding which is intensified by the low ambient pressure within the vacuum chamber. It was investigated how the process parameters effect the chemical composition of the welding seam with respect to the base material. Independent of the welding speed, no change of the main alloying elements chromium and nickel was detected. In contrast, manganese exhibited a strong evaporation tendency which was dependent on the welding speed (cf. Fig. 10.7a).

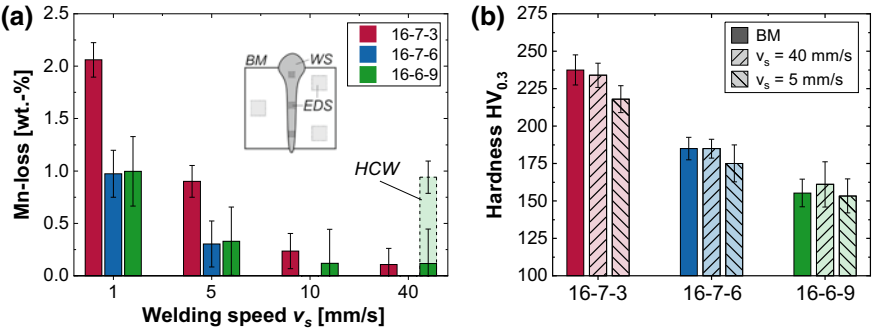

Fig. 10.7 **a** Manganese loss within the welding seam produced by DPW compared to the base material dependent on the welding speed. HCW: welds produced by HCW; **b** mean hardness within the base material and the welding seam for two different welding speeds

At a welding speed of 1 mm/s, DPW led to a loss of 1–2 wt% manganese. This corresponded to a reduction of the Mn content within the base material by about 17–33%. However, it should be noted that such welding speeds are rather unusual in practice and have been investigated as extreme values. As the welding speed increased, the manganese loss decreased sharply. For welding speeds of 5 mm/s the weld seam exhibited about 0.3–0.9 wt% manganese loss. At 10 mm/s a slight manganese loss of 0.24 wt% could be detected for the 16-7-3 steel. The manganese loss of the other two steels was in the range of scatter. For welding speeds >10 mm/s no measurable manganese loss could be detected during DPW. Regardless of the welding speed, the 16-7-3 steel always showed the maximum loss of manganese. This was attributed to the increased thermal conductivity and the associated enlargement of the nail head. A proof for this assumption were welding seams, which were produced without keyhole welding (Fig. 10.7a, HCW). With HCW welding, a loss of almost 1 wt% manganese was measured, which increased with a lower welding speed following the described tendency (up to 2.5 wt% Mn-loss). It was therefore assumed that the deep welding effect at reasonable welding speeds had no measurable effect on Mn evaporation. Rather, the Mn evaporation was mainly determined by the liquid fraction of the weld seam. There are two effects to be considered:

1. the reduction of the welding speed increases the interaction time of the melt with the environment and more manganese can evaporate.
2. lower welding speeds increase the seam width and, thus, also increasing the area of interaction with the environment.

In order to minimize evaporation, therefore, the lowest possible proportion of HCW like increasing the welding speed or the power density as given in Fig. 10.4 should be set during welding.

To characterize the influence of manganese loss, hardness measurements were performed in both the weld seam and the base material (see Fig. 10.7b). With increasing nickel content the hardness of the base materials was reduced from 240 HV0.3 (3% Ni) to 155 HV0.3 (9% Ni). At a welding speed $v_s = 40$ mm/s no significant influence on the hardness was found, which correlates to the low manganese loss. In contrast, welds with a lower feed rate (5 mm/s) showed a slight loss of hardness in the weld seam. The decrease in hardness decreased with increasing nickel content. For steel 16-7-3 there was a decrease in hardness of about 20 HV0.3. Steel 16-7-6 showed only a slight decrease in hardness of about 10 HV0.3. The difference in hardness between the weld and the base material was in the range of scatter for steel 16-6-9. These results are in good agreement with the manganese losses which also implies, that low welding speeds should be avoided to minimize the loss of hardness.

10.2.6.4 Microstructure of the Welding Joints

For the investigation of the microstructure, the coloring of the Lichtenegger etching allowed conclusions to be drawn about the primary solidification behaviour of the samples. Typically ferrite (δ) remains **white**, austenite solidified primarily from

the melt (γ_P) becomes **blue** and austenite, formed by solid phase transformation (secondary austenite, γ_S) is colored **brown** [48].

According to FACTSAGE calculations, a primary ferritic solidification should be present for all three materials studied [20]. For steel **16-7-3**, the primary solidification mode was not clearly recognizable for both the base material and the weld seam (cf. Fig. 10.8a, d). Typical segregation zones around the ferrite were missing. Both the austenite and ferrite were etched by the reagent. Weld seam and base material showed a comparable plate-shaped morphology of the ferrite. In the weld seam, whose appearance was almost independent of the welding speed, dark etched areas were also visible (Fig. 10.8d). These consisted of stress induced martensite which had been formed unavoidably during the preparation routine. It was assumed that the etching process favored the martensitic areas and therefore falsified the typical Lichtenegger etching reaction. However, measurements of the element distribution over the ferrite regions (Fig. 10.9a) showed an opposed distribution of Cr and Ni, which typically occurs during primary ferritic solidification [49].

For steel **16-7-6** this primary ferritic solidification was very well recognizable in both the base material and the weld seam (cf. Fig. 10.8b, e). Although the ferrite had a dark coloration, it was expectedly located within the dendrite core (DC) surrounded by typical bright segregation zones of the austenitic interdendritic region (IDR). The ferrite possessed a skeletal morphology (or 'vermicular' in American terminology), which was randomly distributed within the former dendrites (Fig. 10.8e). Measurements of the element distribution over single dendrites showed atypical element distributions. As can be seen in Fig. 10.9b, both the DC and the IDR were enriched with Cr. However, areas were found in which there was both an equal and an opposite elemental distribution. According to the authors, this could result from the peritectic

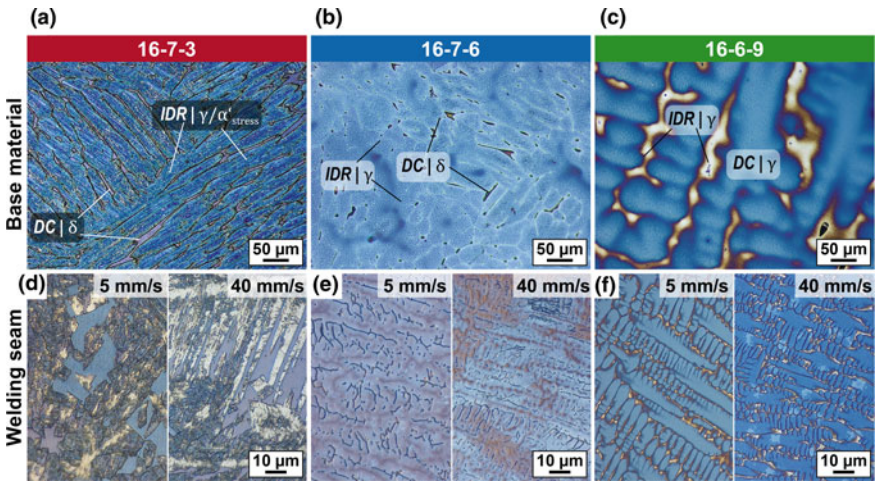

Fig. 10.8 Light optical appearance of the base material and the welding seam ($v_s = 5$–40 mm/s) for different steels after etching

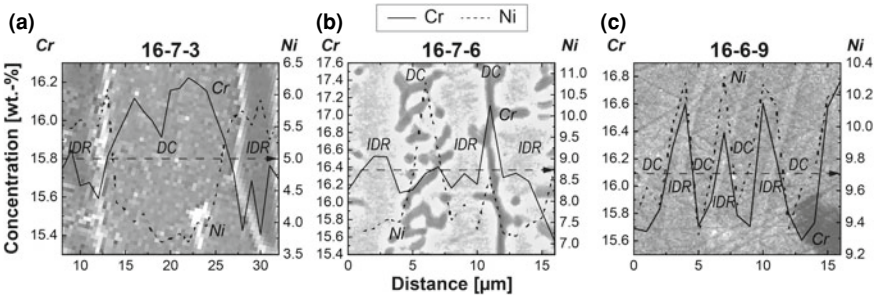

Fig. 10.9 Influence of the base material on the element distribution of Cr and Ni regarding the dendrite core (DC) and interdendritic regions (IDR) measured by EDS line scans

reaction calculated for both steel 16-7-6 and 16-6-9. It is known from literature [19] that simultaneous crystallization of the δ and γ phases does not occur during technical solidification. Accordingly it is assumed for the 16-7-6 steel that first a ferritic solidification took place which subsequently was followed by a peritectic reaction. In this reaction, the austenite phase was preferred and segregation of Cr and Ni took place in opposite as well as in the same direction.

The steel 16-6-9 showed a fully austenitic structure in the base material as well as in the weld seam with clearly recognizable primary austenitic components (cf. Fig. 10.8c, f). The solidification structures were completely dendritic and the IDR had a light coloration without a clearly recognizable phase boundary. During welding the dendritic arm spaceing (DAS) became smaller, otherwise the behavior did not change. In addition, an equidistant distribution of Cr and Ni could be detected (Fig. 10.9c), which supported the assumption of the primary austenitic solidification mode (cf. [23]).

In conclusion, the solidification of the steels 16-7-3 and 16-7-6 was classified as ferritic-austenitic (FA) mode, whereas the steel 16-6-9 solidified according to the austenitic-ferritic (AF) mode.

10.2.6.5 Mechanical Behavior of the Welding Joints

The quasi-static behavior of the investigated materials is summarized in Fig. 10.10. A δ ferrite content of 7.4% was detected in the base material of the **16-7-3** steel. In the milled samples, about 20–24% grinding martensite was determined. With increasing strain (up to 12% engineering strain), the martensite content increased to about 50–65%. This indicated that a TRIP effect was occurring with corresponding martensite formation. For all samples of the steel 16-7-3 less martensite was detected in the base material than in the weld seam. At a welding speed of 5 mm/s, about 5–10% less martensite was detected compared to the weld seams welded with 40 mm/s.

This behavior was attributed to the reduction of the grain size in the weld seam. With increasing welding speed a reduction of the sub-grain size and thus an intrinsic

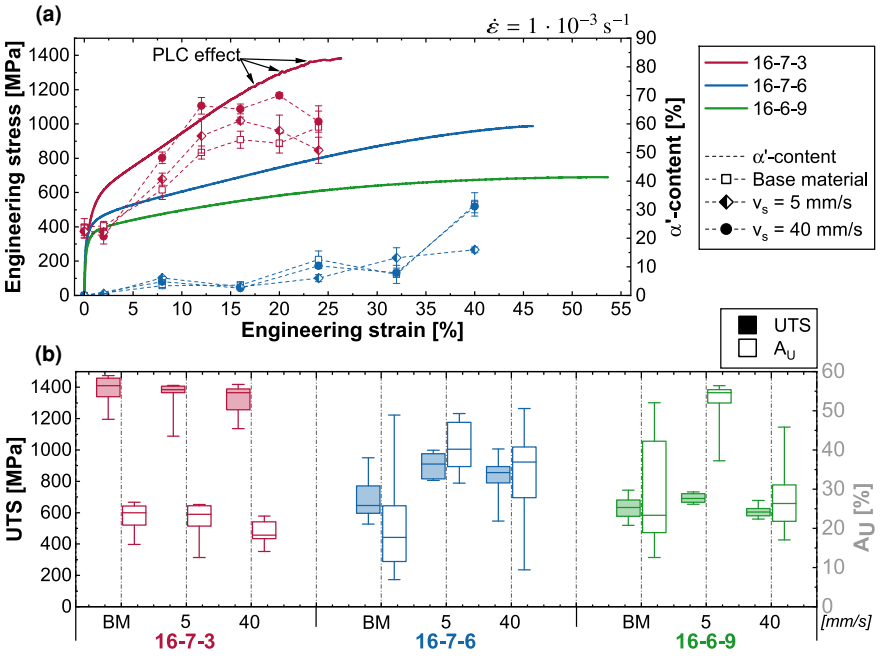

Fig. 10.10 **a** Representative stress/strain-curves with martensite evolution for the tested materials; **b** mechanical properties with ultimate tensile strength (UTS) and elongation at UTS (A_U) dependent on the welding parameters and the base material (BM) used

increase of the SFE could be proven. This shifts martensite formation to higher temperatures, leading to increased martensite formation at room temperature. The typical inflection points of the stress-strain curve were not visible and the Portevin-Le Châtelier effect (visible as serrations in the stress-strain curve, Fig. 10.10a) occurred at higher stress levels.

A slight increase in martensite content was also observed in the **16-7-6** steel (Fig. 10.10a), which contained approximately 1.2% δ ferrite in the initial state. However, this was significantly lower than for steel 16-7-3 and no clear influence of the welding parameters on the martensite evolution was observed. Between 32 and 40% technical strain, samples welded with 40 mm/s showed a sharp increase in martensite content to about 30%. Since the base material exhibited the same values, it is assumed that this was an influence of the chemical composition (due to segregation within the as-cast material).

Steel **16-6-9** showed the lowest strain hardening behavior and the highest elongation of all investigated materials (Fig. 10.10a). Neither δ ferrite nor α' martensite could be detected in the base material or in the weld seam.

Independent on the base material and the welding parameters used, all specimens broke outside the welding seam. The steel **16-7-3** exhibited a UTS of about 1400 MPa regardless of the welding condition (cf. Fig. 10.10b). The ductility of the specimens

decreased slightly at higher welding speed, which could be attributed to the higher amount of martensite. Nevertheless, the data were equivalent within scatter. Steels **16-7-6** and **16-6-9** showed a slight increase in strength after welding of the samples which, however, was also within scatter (cf. Fig. 10.10b). In addition, a strong scatter of elongation values was observed (Fig. 10.10b). After further examination of the broken specimens, it was found that a large number of pores was present in the cross-section of the specimens. They were responsible for the sharp decrease in elongation values and reduced strength in both materials. Accordingly, the maximum strength was achieved in the welded condition. At a lower welding speed ($v_s = 5\,\text{mm/s}$), the strength and elongation of the welding joint was higher than for high welding speed ($v_s = 40\,\text{mm/s}$). This was attributed to the slightly increased seam width and the higher degassing at low welding speeds. Thus, steel **16-7-6** achieved strengths of about 950 MPa at a maximum elongation of 36–47%. The steel **16-6-9** exhibited tensile strengths of about 720 MPa at an elongation at rupture of 52–56%.

10.2.7 Electron Beam Welding of Similar Joints with Reinforcement

The preliminary investigations showed that the welding process has no negative influence on the mechanical behavior of the AC material. Therefore, the welding result of the composite material with added Mg-PSZ particles was investigated. A hot-pressed composite based on steel 16-6-9 with 10% Mg-PSZ was used. Figure 10.11 shows the cross section of a typical weld.

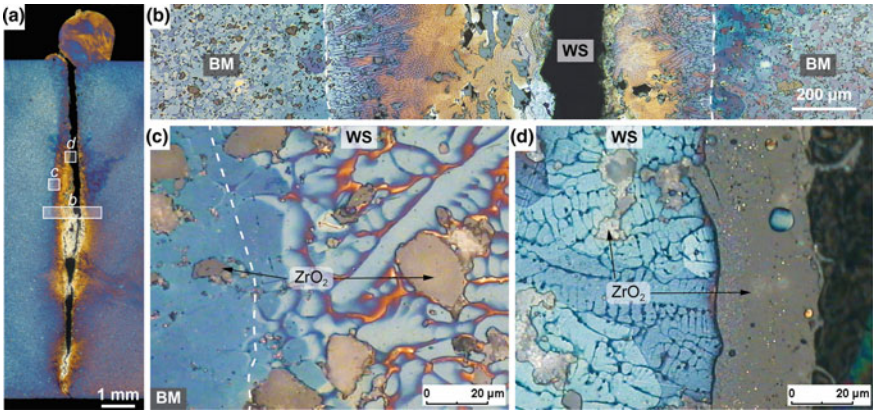

Fig. 10.11 Light optical micrographs of a respresentative welding seam ($I_B = 15\,\text{mA}$, $v_s = 5\,\text{mm/s}$). **a** Macroscopic view; **b** enlarged section of the joint; **c** transition zone between BM and WS; **d** transition zone between WS and the cavity. Dashed lines mark the melting line

Irrespective of the parameter set selected, the formation of a cavity occurred in the centerline of the weld which extended across the entire weld depth. During the welding process, strong spatter formation occurred, resulting from the explosive evaporation of the ceramic particles. As can be seen in Fig. 10.11c, individual Mg-PSZ particles appeared to remain unchanged in the weld. Other ceramic particles were partially melted and deposited at the edge of the cavity (cf. Fig. 10.11d).

Parameter studies showed that the cavity could not be avoided. Its size could be minimized by the following measures:

1. reduction of welding speed (down to 5 mm/s)
2. increase of oscillation width up to 1.5 mm
3. shift of the beam focus below the sheet surface.

Investigations on welds without keyhole showed that the ceramic particles only tend to evaporate when the deep welding effect occurs. With wide melting baths and low penetration depths, it was possible to produce defect-free remelting paths. The ceramic particles floated on top of the melt and formed a firmly adhering, cracked top layer during cooling. The residual melt was almost free of Mg-PSZ. Other process specific optimizations, such as a pulsed beam current and the use of several concurrent welding spots (Multi-Spot-technique) had no significant influence on the formation of cavities.

Concludingly, deep penetration welding of the similar joints with particle-reinforced composite materials was not feasible. In the following, two alternative joining processes are presented: On the one hand, a welding partner of the joint was replaced by a conventional steel (Sect. 10.3). On the other hand, a soldering process with the electron beam was implemented in order to dispense with the deep welding effect (Sect. 10.4).

10.3 Electron Beam Welding of Dissimilar Joints with TWIP-Matrix Composites

10.3.1 Typical Microstructure of the Welded Zone

To investigate the influence of the ceramic particles on the welding behavior of the MMC, dissimilar joints between a TWIP matrix composite and a particle-free stainless steel (AISI 304) were produced. In order to minimize the influence of the chemical composition, a stainless steel was selected which is chemically very similar to the matrix of the composite material due to its C, Cr, Mn and Ni content. In order to describe the quality of the welding seams, a catalog of criteria was used based on DIN EN ISO 13919-1. The main defects observed were porosity, underfill and lack of fusion. Based on the criteria shown in Table 10.6, the welds were classified into evaluation groups (EG) ranging from ‘B’ (best weld quality) to ‘D’ (worst weld quality).

Table 10.6 Criteria for categorization of welding seams into evaluation groups (EG) according to DIN EN ISO 13919-1. f_P: area of cavities, h^*: underfill, LoF: dimension of lack of fusion, t: sheet thickness

EG	f_P	h*	LoF
B	≤0.7	≤0.1 t	n.p.
C	≤2	≤0.2 t	n.p.
D	≤6	≤0.3 t	≤0.25 t

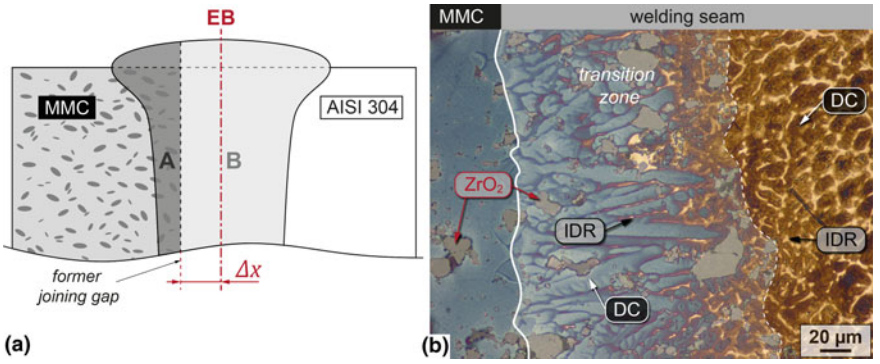

Fig. 10.12 **a** Schematic illustration for measuring the beam displacement and calculating the level of dilution (D). **b** Representative section of the transition zone (TZ) between the TWIP MMC base material and the welding seam [15]. $I_B = 45$ mA, $v_s = 15$ mm/s, $\Delta x = 0.4$ mm

To obtain a defect-free weld, the beam offset Δx had to be shifted relative to the particle-reinforced material (Fig. 10.12a). The level of dilution (D) was used as a measure of the amount of Mg-PSZ introduced into the weld pool (Fig. 10.12a).

Figure 10.12b shows the typical microstructure of the welded samples with a beam offset $\Delta x = 0.4$ mm. The fusion zone consisted of the two base materials (TWIP Mg-PSZ and steel AISI 304) and the welding seam, which could further be divided into two separate regions. Firstly, on the right of Fig. 10.12b, typical dendritic structures were present with brown-colored dendrite cores (DC) (cf. Suutala et al. [48]). This was the area where the steel AISI 304 was molten. Due to the primary ferritic solidification of the steel AISI 304, the ferrite was transformed into secondary austenite during cooling. Secondly, a TZ was present between the MMC material and the welding seam. In this TZ, Mg-PSZ particles were embedded within dendritic structures with a blue etching color. This coloring was due to the primary austenitic solidification of the TWIP matrix material [14]. Previous investigations have shown that the Mg-PSZ is introduced into the welding seam by the electron beam welding process, where it is agglomerated, melted and partially evaporated. This evaporation process leads to the formation of a mixture of oxides of zirconium and magnesium, which can accumulate during welding in cavities or during braze-welding in the joining gap [14]. As Fig. 10.12b shows, the particles in the welding seam and in the base

metal possessed approximately the same dimensions. It was therefore assumed that some Mg-PSZ particles could have been introduced into the melt pool. A current field of interest is the manner in which the Mg-PSZ particles interact with the melt, the electron beam and the keyhole.

10.3.2 Influence of Beam Parameters on the Weld Quality

During the welding experiments without beam displacement ($\Delta x = 0$ mm), the molten metal was periodically ejected (similar to the humping effect). This led to material loss and the formation of cavities (Fig. 10.13a) in the welding seam, which is known from the similar welding joints (Sect. 10.2.7).

With increasing beam displacement (up to 0.3 mm), material separations along the entire weld length, even reaching the weld face were observed. Moreover, pronounced cavity formation was visible (Fig. 10.13b). From a beam offset of 0.4 mm (Fig. 10.13c), the typical smoothly scaled upper bead and a microscopically flawless welding seam were obtained. Occasionally, the welding seam was widened, though material separation did not occur. In summary, the welding quality improved with decreasing amounts of Mg-PSZ within the weld pool.

An underfill was evident at a beam offset of 0.4 mm. Despite having the same bevel geometries, higher beam offsets (0.5–0.6 mm) did not result in underfill, but produced joints with the same scaling of upper beads (Fig. 10.13d). In order to counteract the underfill, tests were carried out without machining a bevel on the samples, with these samples exhibiting a general reduction and, partly, a complete prevention of seam

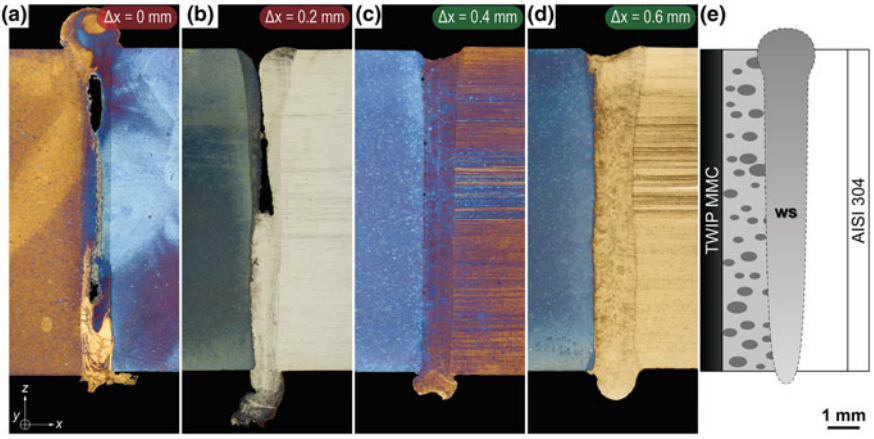

Fig. 10.13 Influence of the beam offset Δx on the weld quality (red: EG < 'D', green: EG better than 'D'); **a**–**d** light optical cross sections, **e** schematic position of the welded materials. Beam parameters: $I_B = 45$ mA, $v_s = 15$ mm/s [15]

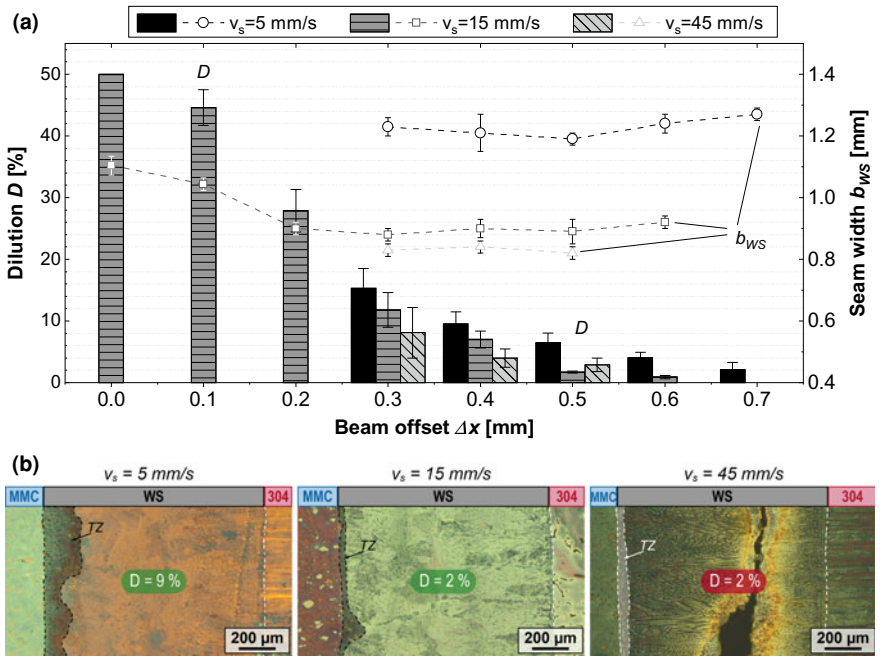

Fig. 10.14 **a** Resulting level of dilution (shown in bars, left axis) for different welding speeds as a function of the beam offset used. Datapoints mark the corresponding seam width (right axis). **b** Influence of the welding speed v_s and the level of dilution D on the weld quality with respect to the area of the transition zone (TZ) for $\Delta x = 0.5$ mm. $v_s = 5$ mm/s: $I_B = 30$ mA, EG = 'C', $v_s = 15$ mm/s: $I_B = 45$ mA, EG = 'D', $v_s = 45$ mm/s: $I_B = 110$ mA, EG < 'D' [15]

concavity. Further examinations were then carried out with a beam offset of 0.4 mm, and did not exhibit any underfill. For all tests without bevels, an upper bead was produced that was free of macroscopic faults. Even without a bevel, the welding gap could be located easily with the monitoring system of the EB facility.

The experiments had shown that the beam displacement was associated with characteristic defects in the welding seam. With the level of dilution (D), there was an additional characteristic value which acted as a measure for the ingress of the Mg-PSZ particles and the corresponding width of the mixing zone. In Fig. 10.14a, the degrees of mixing for different welding speeds (5–45 mm/s) are plotted with the corresponding welding seam widths as a function of the beam offset used. As expected, the level of dilution decreased with increasing beam offset regardless of the welding speed. The defect-free welds with a beam offset of 0.4–0.6 mm corresponded to an ingress of <10% (Fig. 10.14a). All samples with higher dilution exhibited pores, underfills or other significant defects. The standard deviations determined were also the smallest in the offset range for samples without defects (0.4–0.6 mm) and increased with decreasing beam offset. Consequently, the process stability increased with increasing beam displacement.

Based on the results of welding experiments at 15 mm/s, it could be deduced that starting from $\Delta x = 0$ mm, the welding seam width decreased with increasing beam offset up to a beam offset of 0.2 mm. This was due to the significantly lower thermal conductivity of the TWIP MMC compared to the austenitic AISI304 steel, which led to heat accumulation and, thus, to seam broadening. Above a beam offset of 0.3 mm and with less than 28% dilution, the welding seam width remained approximately constant, which was due to the decreasing influence of TWIP MMC material. In addition, it was shown that there was no significant change in welding seam width for welding speeds of 15–45 mm/s. On the other hand, welds with 5 mm/s exhibited an increase in welding seam width of ≈35% compared to welds produced at 15 mm/s. The reason for this was the limited sample volume, which was discussed in Sect. 10.2.6.1. Regardless of the set level of dilution, all welds carried out with a welding speed of 45 mm/s had significant defects. The micrographs in Fig. 10.14b show that despite similar levels of dilution, there were significant differences in welding quality. The ingress of the Mg-PSZ particles was therefore not the only factor that impaired the weldability of TWIP Mg-PSZ. It became clear that despite similar energy inputs per unit length, pore-containing seams were produced at welding speeds of 45 mm/s, while pore-free joints could be welded at 15 mm/s. At the same time, a higher energy input per unit length also led to an improvement in the quality of the welding seam. Therefore, it was not possible to identify any clear tendencies for the evaluation of the welding seam quality from the selected value of E. However, the influence of the welding speed on the quality of the welding seam was proven in this work. In contrast to the work of Chen et al. [10], improvement of the weld quality with increasing welding speed could not be found for the TWIP MMC used.

Thus, in the case of a very large beam offset ($\Delta x = 0.6$ mm), it was possible to change the seam geometry by lowering the welding speed to $v_s = 5$ mm/s in such a way that almost parallel edges of the seam were created. This prevented connection faults in the root position area. Tests were carried out to select the optimum welding beam current at small beam offsets ($\Delta x = 0.4$ mm) and correspondingly high entries of Mg-PSZ ($D \approx 12\%$) into the weld pool. It was observed that the minimal beam currents necessary for full-penetration welding often led to pore formation and connection errors in the root position. Raising the beam current by ≈20% led to better melt degassing, on the one hand, and to more parallel weld edges on the other hand, which positively influenced both the connection quality and the melt degassing. However, the welding seam could only be classified as EG = 'D' due to the presence of underfill.

Further tests on the influence of the focal plane position on the seam quality showed that a sharp surface focus–(ΔI_F) = 0 mA–led to strong shrinkage, underfill, and a scaled seam surface (cf. Fig. 10.15b). It should be noted that all experiments were carried out with a beam offset of 0.4 mm, i.e. the TWIP MMC was molten and cavity formation occured, which is associated with the ingress of Mg-PSZ to the weld pool. The formation of cavities could be prevented with a shift of the focal plane over the top of the sheet metal ($\Delta I_F = 5$ mA), but the underfill increased drastically (Fig. 10.15a). A defocus of $\Delta I_F = -5$ mA below the sheet surface, on the other hand,

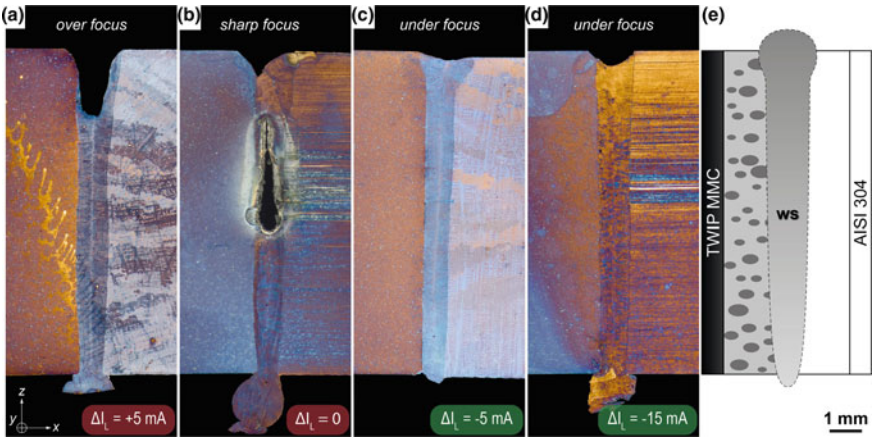

Fig. 10.15 Influence of the focal position of the EB on the weld quality (red: EG < 'D', green: EG better than 'D'), according to the lens current used; **a**–**d** light optical cross sections; **e** schematic position of the welded materials. Beam parameters: $I_B = 45\,\text{mA}$, $v_s = 15\,\text{mm/s}$, $\Delta x = 0.4\,\text{mm}$ [15]

produced a pore-free welding seam with a finely scaled bead surface and without underfill (Fig. 10.15c). With further defocusing of the beam, however, the porosity was unaffected (pore size <80 µm), but the underfill was increased (see Fig. 10.15d). This was attributed to the dependence of process stability on the stability of the keyhole. With a sharp focus on the surface, the capillary was not opened wide enough, and was quite susceptible to the ingress of ceramic particles. A larger opening of the steam channel resulted in better degassing and, therefore, better welding results. Tests on welded aluminum joints by Ahn et al. showed similar tendencies [2].

10.3.3 Verification of Welding Defects

For the ultrasonic immersion tests, the entire welding seam was scanned in the longitudinal direction (see Fig. 10.3). The aim of the non-destructive testing was to detect welding defects, such as a lack of fusion or cavities. In addition to the determination of the defect position in the y-z direction, the flaw depth was determined while taking into consideration the longitudinal wave velocity of the AISI 304 steel. The size of the Mg-PSZ particles was below the resolution limit, which meant that no negative influence could be detected using either the ultrasonic immersion test or X-ray inspection.

Figure 10.16a1 shows the D-scan of a welding seam with pores and lack of fusion for a sample with EG < 'D'. With respect to the D-scan, it was assumed that a connection was only present at the edge of the sample. This was confirmed by the light optical micrographs in Fig. 10.16a3, a4. The flaw depth information indicated a planar defect (lack of fusion) at a depth of ≈5.5–6.5 mm (indicated by the light

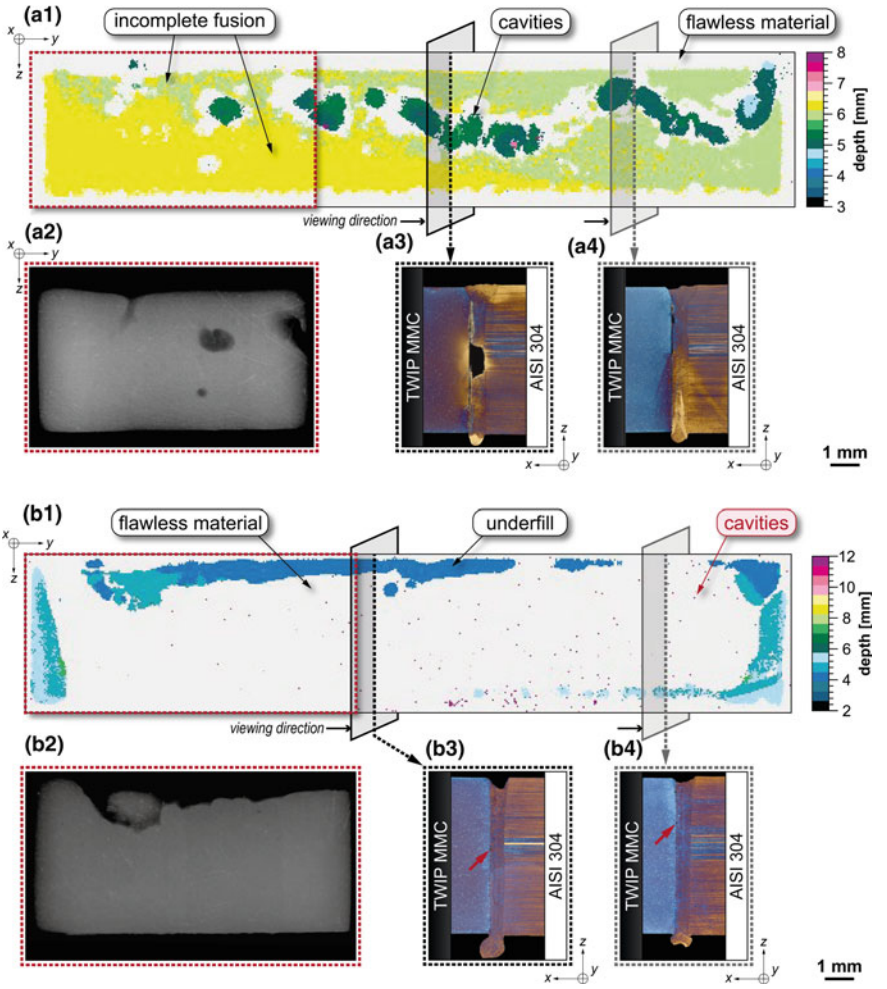

Fig. 10.16 **a** Testing results of sample with EG = 'C', beam parameters: $I_B = 46\,mA$, $v_s = 15\,mm/s$, $\Delta x = 0.6\,mm$; **b** testing results of sample with EG < 'D', beam parameters: $I_B = 45\,mA$, $v_s = 15\,mm/s$, $\Delta x = 0.4\,mm$. 1 Ultrasonic immersion results with the depth information of the signal (testing axis: x). 2 X-ray image of the marked section (red dashes, testing axis: x). 3, 4 Cross sections at positions marked in 1 (dashed arrows) [15]

green to yellow color), which was assigned to the TWIP MMC. Small deviations in the measured depths of planar defects resulted from deviations in plane-parallelism in the processing of samples for the ultrasonic immersion testing. The areas with the dark green color in Fig. 10.16a1 indicated weld defects—where ultrasonic waves are reflected earlier than from planar defects. Taking into account the shape of the defect, which extended into the welding seam, the occurrence of pores in the sample was assumed. The light optical micrograph in Fig. 10.16a3 supports this assumption.

Indeed, the formation of worm-holes was assumed due to the irregular arrangement of the pores in the longitudinal direction of the welding seam. Worm-holes are formed by rising gases that remain in the welding seam. In addition to the verification of the investigation via ultrasonic immersion testing, X-ray inspection was applied for a selected area of the sample (see Fig. 10.16a2). Volume defects such as pores were located within the X-ray image, which concurred with the D-scan carried out by means of ultrasonic immersion testing and the light optical micrographs. However, no information was available about the flaw depth. Furthermore, a lack of fusion was not detected via X-ray inspection.

Figure 10.16b1 shows the D-scan of a welding seam for a sample with EG = 'C'. The welding seam exhibited an almost flawless connection between the joining partners. However, an underfill and pores at the micrometer scale were derived from the D-scan. Furthermore, due to slope-in and slope-out effects, a defective connection was observed at the edge of the sample. The existence of pores at the micrometer scale was verified by light optical micrographs (see red arrows in Fig. 10.16b3 and Fig. 10.16b4). Thus, the detection limit for the pore diameter was 90–100 µm. According to DIN EN ISO 13919-1, individual pores with this dimension can be tolerated within welding seams if no special type of load is defined. Hence, an adequate resolution limit existed to detect all significant defects via ultrasonic immersion testing. By X-ray inspection, both the underfill and the microporosity were determined to a resolution limit of 25 µm (see Fig. 10.16b2).

10.3.4 Mechanical Characterization

Investigations were carried out to determine whether the welding process was associated with a change in hardness from the base material (TWIP) to the welding seam and, in particular, to the transition zone (cf. Fig. 10.17). In the transition zone, a drop in Martens hardness of about 300 MPa was detected compared to the remaining welding seam (Fig. 10.17). These differences were due to the different solidification modes from the transition zone (AF mode) as well as the welding seam (FA mode) and the associated δ-ferrite contents.

Furthermore, the presence of Mg-PSZ particles within the base material led to higher measured hardness values. On the other hand, the absence of those particles within the transition zone again led to lower measured hardness values. Due to the very similar chemical composition of both joining partners, however, no significant change in hardness was found within the measured profile. Individual areas that had a very high degree of hardness ($\approx$2600 MPa) in the TWIP base material were interpreted as Mg-PSZ particles.

Figure 10.18 shows the mechanical properties of the tensile test for a comparative characterization of the welded joints with different levels of dilution. With respect to the experiments at $v_s = 15$ mm/s, it became clear that the highest ultimate tensile strengths were present at D of 12% ($\Delta x = 0.3$ mm). The median tensile strengths achieved were at 545 MPa with an uniform strain of 8.2%. However, these welding

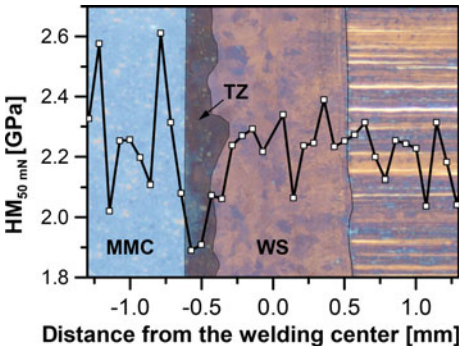

Fig. 10.17 Microhardness profile across the welded materials and the fusion zone. Beam parameters: $I_B = 30\,\text{mA}$, $v_s = 5\,\text{mm/s}$, $\Delta x = 0.5\,\text{mm}$, $D \approx 9\%$ [15]

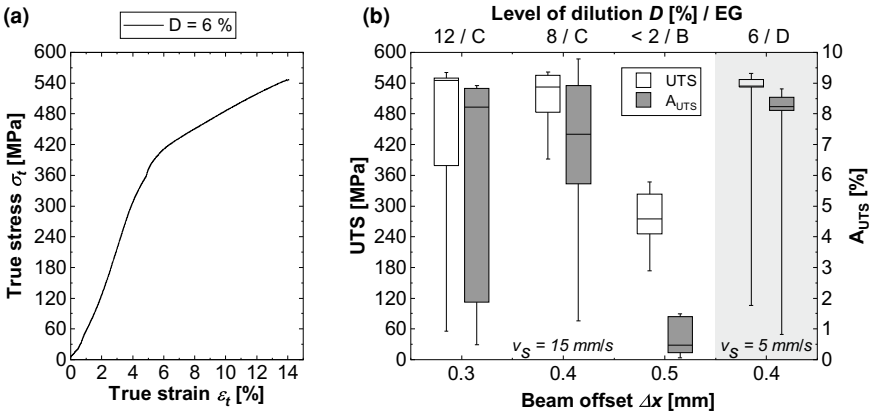

Fig. 10.18 Influence of the level of dilution and the beam offset on the mechanical properties. **a** Representative stress-strain curve for $D = 6\%$; **b** boxplot of the ultimate tensile strength and the uniform strain (A_U) as a function of Δx and D [15]

seams were categorized as EG = 'C' due to the very high porosity. Therefore, failure took place within the welding seam with a very high amount of scatter. At lower degrees of mixing ($D = 8\%$, $\Delta x = 0.4\,\text{mm}$), the joints could also be evaluated as EG = 'C', but exhibited slightly lower strength and strain values (UTS = 532 MPa, $A_{UTS} = 7.3\%$, both medians). Individual large pores within the welding seam led to failure of the samples. Joints that exhibited hardly any melting of the base metal ($D < 2\%$, $\Delta x = 0.5\,\text{mm}$) exhibited the worst mechanical properties. Failure took place alongside the fusion line even at low stress levels ($UTS_{med.} = 275\,\text{MPa}$). The samples broke in an almost brittle manner with hardly any measurable elongation ($A_{UTS,\,med.} = 0.5\%$).

Contrary to these findings, the joints were free of pores, exhibited neither underfill nor lack of fusion and were evaluated as EG = 'B' according to DIN EN ISO 13919-1.

Halbauer et al. [13] attribute the low mechanical properties at very high beam offsets to the formation of an oxide-containing layer at the fusion line, which prevents complete joining of the two welding materials. Since the occurrence of planar defects and, in particular, non-wettable oxide layers are not covered by DIN EN ISO 13919-1, the mechanical properties of the welding joints could not be derived solely from the evaluation group. Instead, further investigations were required to determine, in particular, the quality of connectivity. The investigation of this bonding strength on the microscopic scale will be discussed in detail in a future publication. Improvement of the mechanical properties was achieved by using a lower welding speed ($v_s = 5\,\mathrm{mm/s}$) and setting a low dilution level of the TWIP MMC ($D = 6\%$, $\Delta x = 0.4\,\mathrm{mm}$). In this way, tensile strengths of 535 MPa (med.) were achieved with a uniform elongation of 8.2% and with minimum scatter of the tensile strength. Since no significant porosity was found, rupture of the samples took place within the base material of the TWIP MMC. This was made possible by the significantly longer interaction time between the EB and the melt, which led to better degassing and calming of the melt. According to DIN EN ISO 13919-1, these welds had to be categorized as EG = 'D' due to the presence of underfill. However, these defects were not relevant for the mechanical properties due to the high ductility of the steel AISI 304 within the welding seam.

10.4 Electron Beam Brazing of TWIP-Matrix Composites

10.4.1 Macroscopic Phenomena

It was investigated, how the energy distribution $P(y)$ of the electron beam as a function of the position can influence the temperature distribution at the sample surface (Fig. 10.19) during the brazing process. First, heating experiments without filler material were carried out with a constant energy across the EB field width (Fig. 10.19a). As expected, the temperature exhibited a maximum at the center of the separate energy transfer fields and a sharp temperature gradient towards the edges was present (Fig. 10.19c). Accordingly, this temperature distribution led to partial melting in the middle of the EB interaction field and high distortion in x-direction.

Second, $P(y)$ was adjusted according to (10.1) with $P_{\min} = 0.8$ (Fig. 10.19b). Due to the variation of energy input, the resulting temperature distribution was homogeneous in y-direction, which allowed the filler to melt more homogeneous, prevented partial surface melting and reduced the distortion of the samples significantly (Fig. 10.19d). If $P_{\min}$ was further decreased, more energy was introduced to the edges of the samples, which again led to inhomogeneous temperature distributions and partial melting of the sample surface. All samples discussed in the following were brazed with this adjustment of the energy distribution.

Figure 10.20a illustrates the evolution of the filler gap (h_f) after brazing and is representative for the investigated samples in the longitudinal section (y-direction). The gap width after brazing was much smaller than the initial gap width ($h_{f,init}$) (i.e.

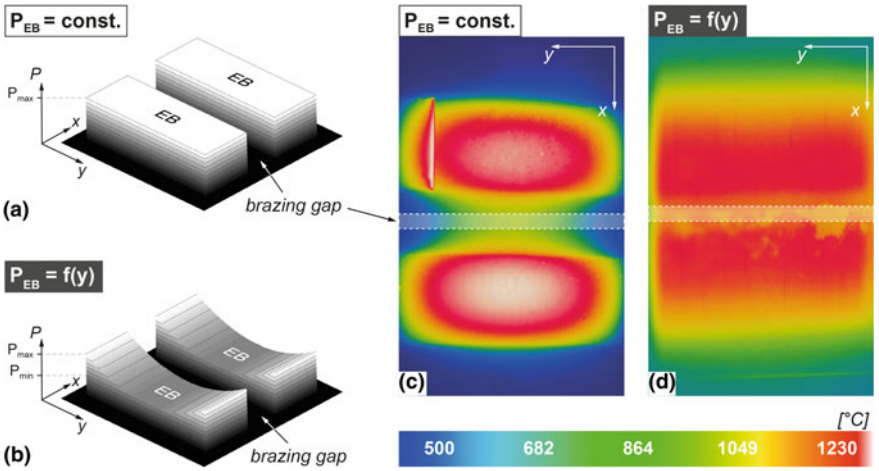

Fig. 10.19 Influence of the energy distribution on the temperature distribution at the sample surface during brazing. **a**, **b** Schematic illustrations of the set beam interaction field; **c**, **d** resulting temperature distribution measured with a thermographic camera (adapted from [16])

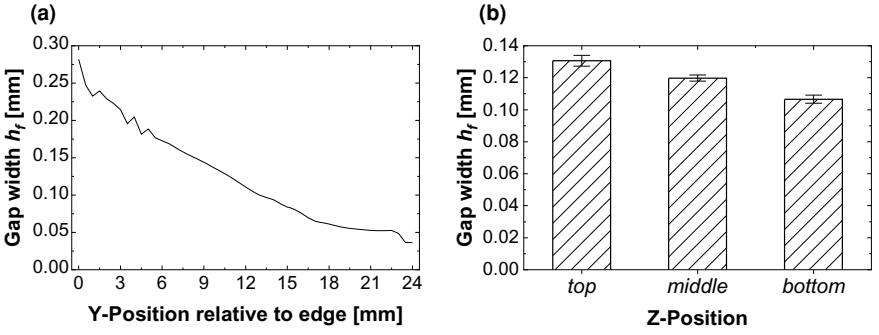

Fig. 10.20 Evolution of the filler gap width (h_f) after brazing **a** depending on the distance from the sample edge (longitudinal section); **b** depending on the z-position of the measurement (cross-section). Initial gap = 800 µm, t_H = 67 s (adapted from [16])

$h_{f,init} = 1200\,\mu m$, $h_{f,max} = 300\,\mu m$). During heating, the width of the gap decreases according to thermal expansion, since the samples are fixed within the clamping device. If the gap is too small, the clamping device is able to compensate the contact stress with an internal suspension. However, during cooling, the solidified filler material prevented the base material from retaining its original shape which clearly led to internal stresses. After brazing the resulting gap width decreased sightly from the top ($130 \pm 3\,\mu m$) to the bottom ($106 \pm 2\,\mu m$) of the samples (cf. Fig. 10.20b). Due to the high sheet thickness, the unilateral heating of the samples and the short holding time a temperature gradient of $\approx 100\ K$ from the top to the bottom of the samples (z-direction) developed. However, in the authors' opinion the resulting gra-

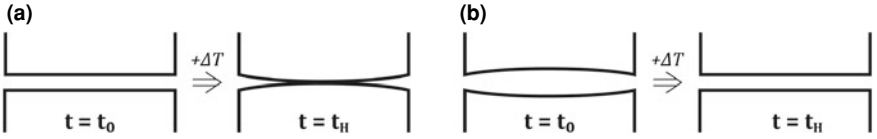

Fig. 10.21 Evolution of the filler gap geometry before ($t = t_0$) and during brazing ($t = t_H$) due to distortion **a** without uniform gap, **b** with crowned gap geometry. $t_0 = 0$ s (after [16])

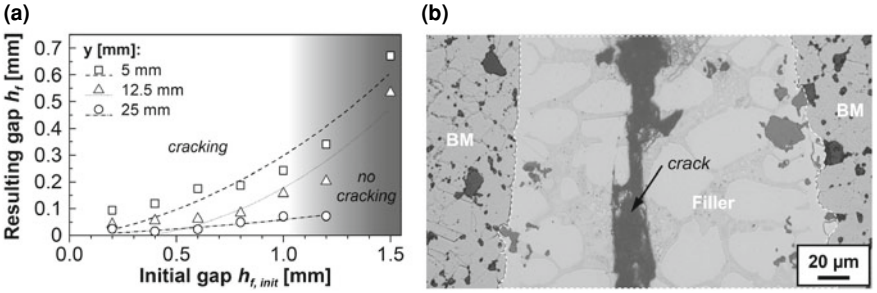

Fig. 10.22 **a** Gap width after brazing (resulting gap) 2 mm below the sheet surface as a function of the initial gap at different distances from the sample edge ($t_H = 52$ s); **b** Typical crack within the center of the brazing gap (modified from [16])

dient in thermal expansion from the top to the bottom was negligible and was not the reason for the gradient of the gap width. It was more likely, that diffusion controlled mechanisms such as erosion, caused the gap to widen at the top, which is explained in detail in Sect. 10.4.2.

Though the energy field was optimized to ensure uniform temperatures across the sample, the thermal expansion exhibited a gradient from the center (high) to the edge (low) (Fig. 10.21a). This gradient could be compensated by the addition of a crowned gap geometry (Fig. 10.21b).

The gap width h_f was also influenced by the initial gap width before brazing, cf. Fig. 10.22a. As expected, the resulting gap width decreased with the decreasing initial gap. For $h_{f,init}$ <1 mm the two joining partners had direct contact in the center of the gap and therefore h_f was mainly influenced by the solidification of the surrounding filler material and exhibited cracks due to insufficient feeding (cf. Fig. 10.22b). With increasing $h_{f,init}$ (>1.2 mm) the gap width was mainly influenced by the thermal expansion across the sample and no cracks were observed. Concludingly, a gap width ≥1.2 mm should be used for potential application.

10.4.2 Microscopic Characterization

Figure 10.23 shows an exemplary cross section of the joint between the particle reinforced TWIP steel (TWIP matrix composite (TMC)) with Ni-filler and $h_{f,init}$ = 1.2 mm. From the edge to a distance of $y \approx 10$ mm neither pores nor cracks were found. Due to the strong distortion during heating, the center of the gap exhibited solidification cracks across the whole sample height. A dendritic microstructure consisting of dendrite cores (DC) (Fig. 10.23b, light grey) and an interdendritic region (IDR) (Fig. 10.23b, dark grey) were present. Following the temperature gradient in z-direction, a transition zone was detected (Fig. 10.23c, d), which decreased in width from the top (≈ 85 µm) to the bottom (≈18 µm) of the samples. In this transition zone, particles from the base material were visible. The chemical composition of the matrix between the particles was similar to that of the filler material. Based on the investigations made, the transition zone formed as a result of a diffusion induced erosion and the formation of phases between the filler and the base material. The IDR consisted of low melting phases, exhibited a fine, lathy internal structure (Fig. 10.23b) and is believed to be an eutectic phase.

The distribution of the low melting phases was investigated by the binarization of the light optical micrographs. Independent on the base material used, the joined area consisted of ≈ 50% eutectic phases and the phases were distributed heterogeneously across the sheet thickness. If a very long holding time was applied (t_H = 600 s), the

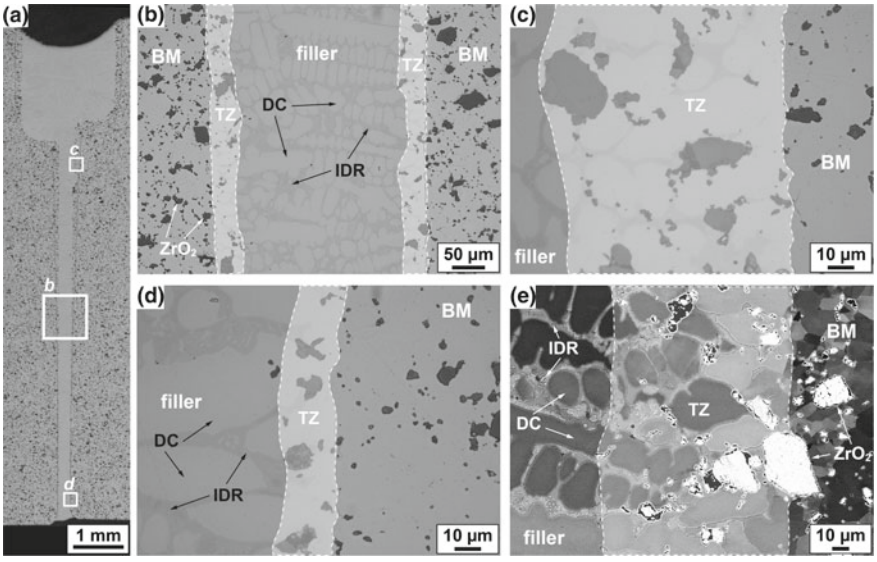

Fig. 10.23 Microstructure of the brazed samples (cross sections at 5 mm from the sample edge), **a**–**d** light optical investigations at different positions, **e** SEM image of the gap center (detail). BM: base material, TZ: transition zone, IDR: interdendritic region [16]

content of eutectic phases could be reduced to at least 35% with a minimum of 20% at the middle of the sample height. However, due to the high amount of energy input, such long holding times have to be considered critically in terms of efficiency and economics. To minimize the content of brittle phases, either the dendritic solidification has to be enhanced drastically by applying significantly higher solidification rates or a change of the alloying system has to be considered.

The evolution of the transition zone was further analyzed by a combination of EBSD investigation with parallel energy-dispersive X-ray spectroscopy (EDS) (Fig. 10.24). The transition zone between the base material and the filler consisted of FCC dendrite cores (Fig. 10.24b) and Cr-Ni-Si intermetallic compounds with varying stoichiometry within the IDR. According to literature, these compounds are likely to occur as eutectic phases within the Cr-Ni-Si system. They are characterized by a good oxidation resistance but are also very brittle [1, 24, 47]. Also the tetragonal phase of zirconia was present, which implies, that zirconia particles would still be able to undergo a phase transformation during deformation. At the fusion line, a strong orientation relationship between the filler and the base material was present (Fig. 10.24c). Furthermore, a preferred orientation in [001]-direction was found within the dendrites, which is common for materials with a cubic microstructure.

Though the filler material was initially free of iron, significant iron contents were found within the filler after brazing. Concludingly, a diffusion of Fe from the BM into the filler had happened. As expected, the dendrite cores were also enriched with Cr and Ni, since these were the main constituents of the filler material. The IDRs were enriched with Si due to the formation of the intermetallic phases. Zr was primarily found within the Mg-PSZ particles of the base material and the transition zone within the filler (Fig. 10.24e–h). It should be noted, that a strict separation between Zr and Si is not possible due to the EDS analysis method. The Kα peak of silicon and the Lα peak of zirconium have a very similar energy level. As a result the analysis software tends to detect Si in regions enriched with zirconium and vice versa. Accordingly, the very high amounts of silicon within the ceramic particles (Fig. 10.24g) should not be considered as realistic. The Mg-PSZ particles were only found at a distance of 18–85 µm from the fusion line and were distributed as homogeneously as in the base material. It was concluded, that the particles penetrated into the filler with a significant melt flow. This rather suggested, that an erosion process had taken place during the brazing process, which was incorporated with a chemical dissolution of the matrix and without movement of the particles. Since the erosion ensures the wettability of the base material it is a desired phenomenon and should not be avoided. Altogether, the formation of the brazing zone can be described as followed:

1. erosion of the BM by the filler and formation of a Fe–Cr–Ni–Si system
2. epitactic growth of the filler onto the BM with primary FCC-solidification
3. formation of a preferred orientation in growth direction
4. enrichment of the remaining melt with Si and Ni
5. formation of low melting phases/eutectics within the IDR
6. contraction of the dendrite cores during further cooling.

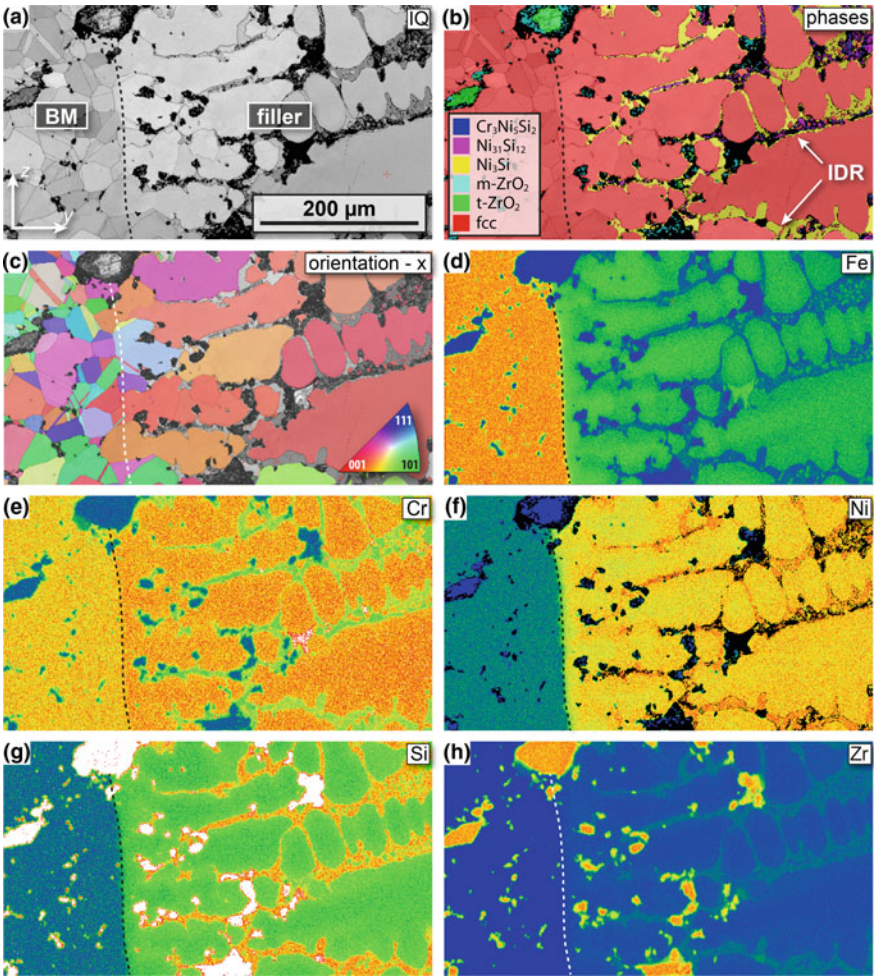

Fig. 10.24 EBSD investigation of the transition zone between BM and filler. **a** Image quality (IQ) map, **b** phase distribution map + IQ, **c** grain orientation in x-direction. **d**–**h** EDS mapping of different alloying elements as heat maps (the warmer the color, the higher the local content; black/white areas indicate data below/above the scale). Dashed lines represent the fusion line [16]

10.4.3 Tensile Tests

Figure 10.25 shows the results of the tensile tests with the mechanical properties UTS and elongation at rupture (A_R). Brazing joints with TMC reached up to 358 MPa and 3.3% elongation (Fig. 10.25a). The mechanical properties can be compared to the base material only to a limited degree since the production process and chemical composition have a huge impact. When compared to braze welded flat tensile specimen (TWIP + as-cast TRIP), the UTS dropped to ≈ 62% of the base material (BM:

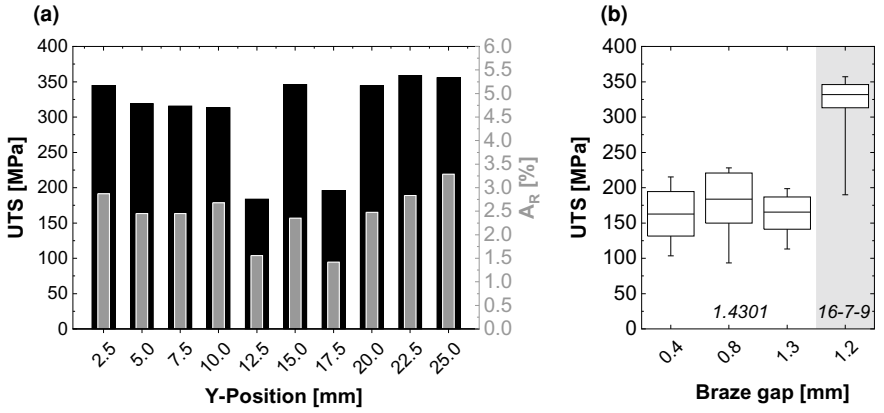

Fig. 10.25 Results of tensile tests with Ni-based filler. **a** UTS and A_R depending on the position of preparation (TMC, t_H = 67 s, h_f = 1200 µm), **b** UTS dependent on the brazed material and the width of the initial braze gap [16]

UTS = 558 MPa) and only 12% of the elongation was left (BM: A_R = 26%). These values are in good agreement with the investigations on round tensile specimen [14] (UTS = 573 MPa, A_R = 29%). Eckner et al. investigated a TRIP/TWIP steel with 6.6% Ni and found a true tensile strength of 686 MPa and 21% true strain for a SPS sintered base material. Though the samples exhibited high differences in the gap width, the mechanical properties remained nearly constant within all tested samples (Fig. 10.25a). At some positions, a sudden drop in strength and ductility was detected, which correlated with an incomplete filling of the gap due to pores or material separation.

Moreover, the gap width had an influence on the UTS of joints with steel 1.4301 and Ni-filler (Fig. 10.25b). Though the scatter decreased slightly with increasing $h_{f,init}$, the strength of the braze joint was independent of the initial gap width. As a result of the higher amount of eutectic phases, joints with steel 1.4301 exhibited a significantly lower tensile strength compared to the TWIP matrix composite. The samples exhibited mostly elastic deformation and always broke within the filler material. Investigations with nano hardness measurements confirmed the existence of brittle phases within the IDR (cf. Fig. 10.26). These phases could not be avoided by the variation of the holding time and had a Martens hardness of HM 50 mN = 6.8–7.4 GPa. Due to the limitation of the minimum force and the positioning system, the separate phases within the IDR could not be investigated separately. Accordingly, the hardness is averaged across all phases of the IDR. Neither the hardness values of the IDR nor of the dendrite core were dependent on the holding time applied. With higher holding time the content of eutectica as well as the scatter of hardness decreased, due to the more homogeneous distribution of the formed phases. Since the formation of brittle phases is intensified by the formation of large dendrites within the Ni-filler, they could be minimized by decreasing the DAS value either with even shorter holding times or smaller gaps. Since shorter holding times would lead to higher heating rates, the temperature differences between the sheet surface

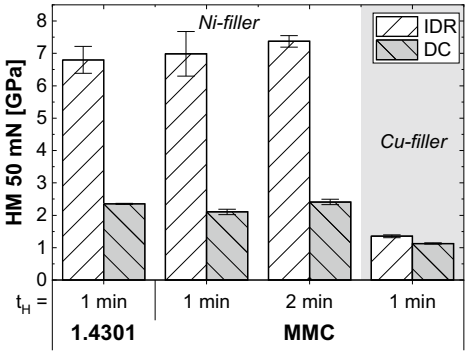

Fig. 10.26 Nano hardness investigation of the filler components depending on both the holding time and filler material. DC: dendrite core, IDR: interdendritic region (adapted from [16])

and bottom would also increase, which is not desirable for thick sheets. Smaller gaps would imply, that the joint geometry had to be changed. Two possible ways are the overlap joint, which would be beneficial for thin sheets, or the production of crowned geometries for butt joints for thick sheets. For future work, a Cu-based filler material was pre-investigated, which has the advantage of a single phased solidification and a very low overall hardness (1.13 ± 0.02 GPa). Individual phases formed within the IDR were on a comparable hardness level (1.35 ± 0.04 GPa) which could result in significantly higher deformation of the brazing joints.

10.5 Summary

The contribution deals with the investigation regarding the weldability of high-alloy TRIP/TWIP materials (sheet thickness 10 mm) with and without particle reinforcement. A very good weldability was found for the as-cast material without particle reinforcement. The influence of the nickel content on the welding seam geometry was only marginal. Independent of the nickel content the welding seams were free of pores and cracks and had almost parallel seam flanks.

During the welding process manganese evaporated from the base material. For welding speeds $\leq$5 mm/s, Mn loss up to 0.9 wt% was detected by EDS measurements. The evaporation correlated with the expansion of the molten zone at the upper bead. With both decreasing welding speed and power density the manganese evaporation increased. No significant change in the chemical composition was observed with a fully pronounced deep penetration welding effect.

The weldability of the base materials was essentially limited by humping. Similar to conventional stainless steels, increasing welding speed is accompanied by an increased tendency to hump, as shown in the literature. Steel 16-7-3 showed the highest tendency of humping. This steel was fully weldable up to a welding speed of 20 mm/s and showed first signs of humping up to 40 mm/s. The beginning of humping for the 16-7-6 and 16-6-9 steels was at 50–60 mm/s. For welding speeds $\geq$80 mm/s, all materials were not weldable due to pronounced humping.

The mechanical characteristics of the joints were not negatively affected by the welding process. As the nickel content increased, a decrease in strength and an increase in elongation were observed. It could be proven that the deformation mechanisms of the base material also remain effective in the weld seam. Accordingly, the weld seam also showed a very good ductility.

The particle-reinforced composite material could not be welded with keyhole. A strong melt ejection occurred and a cavity was formed in the middle of the welding zone. This cavity could be minimized, but could not be avoided by any welding parameter.

If the amount of Mg-PSZ introduced into the weld pool of dissimilar welding joints was lower than a threshold of ≈10% the welding seam was free of pores and cracks. The tolerable proportion of Mg-PSZ increased with decreasing welding speed. At welding speeds of 5 and 15 mm/s, 9 and 2% Mg-PSZ were tolerable, respectively. The resulting welds were free of pores and cracks and showed mechanical properties at the level of the base material. Higher levels of dilution and velocities caused the formation of the center cavity. Furthermore, it could be shown that an underfocus of about −5 mA had to be set to produce a flawless weld seam. It was assumed that this had a positive influence on the degassing behavior of the samples and was therefore necessary. Basically, it was observed that all parameters which favor degassing of the melt led to an improvement of the welding result. However, the decisive parameter for weldability was always the level of dilution. Therefore, when changing individual parameters, it may be necessary to check to what extent the weld width and thus the degree of dilution will change.

It was found that the Mg-PSZ that enters the welding zone is partially melted and tends to form clusters. Particles detected in the dendritically solidified weld metal showed no morphological changes. Therefore it was concluded that only a part of the particles interacted with the keyhole and only this part contributed to the deterioration of the material behavior. Thus, current investigations focus on the interaction of the Mg-PSZ with the electron beam.

A soldering process was carried out on butt joints consisting of a TWIP matrix composite (MMC) and a nickel-base filler material with a sheet thickness of 10 mm. In order to keep the temperature within the soldering field as constant as possible, a polynomial energy distribution of the electron beam was used. The control of this process was realized by a temperature controlled power regulation system. Due to the geometry-related strain obstruction at the edge of the specimen, the center of the joints exhibited a lack of fusion. A complete filler connection was therefore only possible at the edge of the specimen.

Chemical erosion created a transition zone from the filler to the MMC with metallic bonding character. Thus, the nickel-base filler formed an excellent connection with the base material and a high mechanical loadability of joints was expected. Due to the high silicon content of the filler material, silicon-rich intermetallic phases were formed in the solidified solder. Due to their brittleness, the samples broke within the IDR of the filler outside of the transition zone. This lowered both the strength and the ductility of the samples.

Acknowledgements This work was supported financially by the German Research Foundation (DFG) within the framework of the Collaborative Research Center "TRIP matrix composites" (CRC 799, project number 54473466, subproject A7). Special thanks of the authors go to Prof. Rolf Zenker for his commitment to project management in the second funding period. Our thanks also go to his helpful suggestions and professional input. The authors gratefully acknowledge Dr. Karsten Rüthrich for his helpful discussions, his initial work and commitment regarding the electron beam facility. Furthermore, the authors like to thank Prof. P. Hübner for the realization of the X-ray analysis, Dipl.-Ing. G. Schade for the many tensile tests as well as G. Bittner for the hardness measurements.

References

1. R. Ahmad, R.F. Cochrane, A.M. Mullis, The formation of regular αNi-γ(Ni31Si12) eutectic structures from undercooled Ni–25 at.% Si melts. Intermetallics **22**, 55–61 (2012). https://doi.org/10.1016/j.intermet.2011.10.021
2. J. Ahn, E. He, L. Chen, J. Dear, C. Davies, The effect of Ar and He shielding gas on fibre laser weld shape and microstructure in AA 2024–T3. J. Manuf. Process. **29**, 62–73 (2017). https://doi.org/10.1016/j.jmapro.2017.07.011
3. C.G. Aneziris, W. Schärfl, H. Biermann, U. Martin, Energy-absorbing TRIP-steel/Mg-PSZ composite honeycomb structures based on ceramic extrusion at room temperature. Int. J. Appl. Ceram. Technol. **6**(6), 727–735 (2009). https://doi.org/10.1111/j.1744-7402.2008.02321.x
4. C. Baumgart, D. Ehinger, C. Weigelt, L. Krüger, C.G. Aneziris, Comparative study of TRIP/TWIP assisted high density composite honeycomb structures under compressive load. Compos. Struct. **136**, 297–304 (2016). https://doi.org/10.1016/j.compstruct.2015.09.053
5. P. Berger, H. Hügel, A. Hess, R. Weber, T. Graf, Understanding of humping based on conservation of volume flow. Phys. Proc. **12**, 232–240 (2011). https://doi.org/10.1016/j.phpro.2011.03.030
6. H. Biermann, U. Martin, C.G. Aneziris, A. Kolbe, A. Müller, W. Schärfl, M. Herrmann, Microstructure and compression strength of novel TRIP-steel/Mg-PSZ composites. Adv. Eng. Mater. **11**(12), 1000–1006 (2009). https://doi.org/10.1002/adem.200900210
7. V. Braga, R.A.d.F. Mansur, R.H.M.d. Siqueira, M.S.F.d. Lima, Formability of in-situ Austempered transformation-induced plasticity steels after laser beam welding. Soldagem & Inspeção **23**(3), 402–412 (2018). https://doi.org/10.1590/0104-9224/si2303.09
8. A. Buchwalder, K. Rüthrich, R. Zenker, H. Biermann, Electron Beam welding of high alloy CrMnNi cast steels with TRIP/TWIP effect. Adv. Eng. Mater. **15**(7), 566–570 (2013). https://doi.org/10.1002/adem.201200355
9. I. Calliari, M. Dabalà, M. Penasa, Pulsed Nd-YAG laser welding of MMCs. Adv. Eng. Mater. **2**(10), 653–656 (2000). https://doi.org/10.1002/1527-2648(200010)2:10<653::AID-ADEM653>3.0.CO;2-Q
10. H.C. Chen, A.J. Pinkerton, L. Li, Fibre laser welding of dissimilar alloys of Ti-6Al-4V and Inconel 718 for aerospace applications. Int. J. Adv. Manuf. Technol. **52**(9–12), 977–987 (2011). https://doi.org/10.1007/s00170-010-2791-3
11. Deutsches Institut für Normung e.V.: Schweißbarkeit—Metallische Werkstoffe—Allgemeine Grundlagen (2007-04-01)
12. T.K. Gupta, F.F. Lange, J.H. Bechtold, Effect of stress-induced phase transformation on the properties of polycrystalline zirconia containing metastable tetragonal phase. J. Mater. Sci. **13**(7), 1464–1470 (1978). https://doi.org/10.1007/BF00553200
13. L. Halbauer, A. Buchwalder, R. Zenker, H. Biermann, Influence of EB parameters on the microstructure and mechanical properties of dissimilar welded joints in high alloy TRIP/TWIP steels, in *JOM18 Conference Proceedings* (JOM Institute for the Joining of Materials, 2015)

14. L. Halbauer, A. Buchwalder, R. Zenker, H. Biermann, The influence of dilution on dissimilar weld joints with high-alloy TRIP/TWIP steels. Weld. World **60**(4), 645–652 (2016). https://doi.org/10.1007/s40194-016-0324-x
15. L. Halbauer, R. Laubstein, M. Radajewski, A. Buchwalder, L. Krüger, H. Biermann, Electron beam welding and characterization of dissimilar joints with TWIP matrix composites. Adv. Eng. Mater. **114**, 1800586 (2018). https://doi.org/10.1002/adem.201800586
16. L. Halbauer, P. Proksch, A. Buchwalder, R. Zenker, H. Biermann, Joining of TWIP-matrix composites by electron beam brazing. Weld. World **62**(1), 19–27 (2018). https://doi.org/10.1007/s40194-017-0519-9
17. B. Huang, X. Chen, S. Pang, R. Hu, A three-dimensional model of coupling dynamics of keyhole and weld pool during electron beam welding. Int. J. Heat Mass Transf. **115**, 159–173 (2017). https://doi.org/10.1016/j.ijheatmasstransfer.2017.08.010
18. R. Hunag, S. Chen, J.C. Huang, Electron and laser beam welding of high strain rate superplastic Al-6061/SiC composites. Metall. Mater. Trans. A **32A**, 2575–2584 (2001)
19. H. Inoue, T. Koseki, Clarification of solidification behaviors in austenitic stainless steels based on welding process. Nippon Steel Tech. Rep. **95**, 62–70 (2007)
20. A. Jahn, Einfluss der Martensitbildung auf die mechanischen Eigenschaften von ein- und mehrphasigen gegossenen und warm gewalzten Cr-Mn-Ni Stählen. Doctoral thesis, Technische Universität Bergakdemie Freierg, Freiberg, Germany, 2012
21. N. Kapustka, C. Conrardy, S. Babu, C. Albright, Effect of GMAW process and material conditions on DP 780 and TRIP 780 welds. Weld. Res. Suppl. **87**(6), 135–148 (2008)
22. M.I. Khan, M.L. Kuntz, Y. Zhou, Effects of weld microstructure on static and impact performance of resistance spot welded joints in advanced high strength steels. Sci. Technol. Weld. Join. **13**(3), 294–304 (2008). https://doi.org/10.1179/174329308X271733
23. C.J. Lippold, W.F. Savage, Solidification of austenitic stainless steel weldments: part 2—the effect of alloy composition on ferrite morphology. Weld. Res. Suppl. **2**, 48–58 (1980)
24. X. Liu, M. Lin, S. Yang, J. Ruan, C. Wang, Experimental investigation of phase equilibria in the Ni-Cr-Si ternary system. J. Phase Equilib. Diffus. **35**(3), 334–342 (2014). https://doi.org/10.1007/s11669-014-0279-9
25. V. Lopez, A. Reyes, P. Zambrano, Effect of the Heat input in the transformation of retained austenite in advanced steels of transformation induced plasticity (TRIP) welded with gas metal arc welding. Appl. Mech. Mater. **339**, 700–705 (2013). https://doi.org/10.4028/www.scientific.net/AMM.339.700
26. V.H. López Cortéz, G.Y. Pérez Medina, F.A. Reyes Valdéz, H.F. López, Effects of the heat input in the mechanical integrity of the welding joints welded by GMAW and LBW process in transformation induced plasticity steel (TRIP) used in the automotive industry. Soldagem & Inspeção **15**(3), 234–241 (2010). https://doi.org/10.1590/S0104-92242010000300010
27. L.l. Ma, Y.H. Wei, L.F. Hou, C.l. Guo, Evaluation on fatigue performance and fracture mechanism of laser welded TWIP steel joint based on evolution of microstructure and micromechanical properties. J. Iron Steel Res. Int. **23**(7), 677–684 (2016). https://doi.org/10.1016/S1006-706X(16)30105-4
28. S. Martin, S. Richter, S. Decker, U. Martin, L. Krüger, D. Rafaja, Reinforcing mechanism of Mg-PSZ particles in highly-alloyed TRIP steel. Steel Res. Int. **82**(9), 1133–1140 (2011). https://doi.org/10.1002/srin.201100099
29. S. Martin, S. Wolf, U. Martin, L. Krüger, D. Rafaja, Deformation mechanisms in austenitic TRIP/TWIP steel as a function of temperature. Metall. Mater. Trans. A **47**(1), 49–58 (2016). https://doi.org/10.1007/s11661-014-2684-4
30. G.P. Medina, H.L. Ferreira, P.Z. Robledo, A.M. Pérez, F.A.R. Valdés, Microstructural development in a TRIP-780 Steel joined by friction stir welding (FSW): quantitative evaluations and comparisons with EBSD predictions. Soldagem & Inspeção **21**(2), 146–155 (2016). https://doi.org/10.1590/0104-9224/SI2102.04
31. L. Mujica, S. Weber, C. Thomy, F. Vollertsen, Microstructure and mechanical properties of laser welded austenitic high manganese steels. Sci. Technol. Weld. Join. **14**(6), 517–522 (2009). https://doi.org/10.1179/136217109X434243

32. L. Mújica Roncery, Development of high-strength corrosion-resistant austenitic TWIP steels with C+N. Doctoral thesis, Ruhr–Universität Bochum, Bochum, Germany, 2010
33. L. Mújica Roncery, S. Weber, W. Theisen, Welding of twinning-induced plasticity steels. Scripta Mater. **66**(12), 997–1001 (2012). https://doi.org/10.1016/j.scriptamat.2011.11.041
34. S. Nayak, V. Baltazar Hernandez, Y. Okita, Y. Zhou, Microstructure-hardness relationship in the fusion zone of TRIP steel welds. Mater. Sci. Eng. A **551**, 73–81 (2012). https://doi.org/10.1016/j.msea.2012.04.096
35. J. Niu, L. Pan, M. Wang, C. Fu, X. Meng, Research on laser welding of aluminum matrix composite SiCw/6061. Vacuum **80**(11–12), 1396–1399 (2006). https://doi.org/10.1016/j.vacuum.2006.01.023
36. G.B. Olson, M. Cohen, A mechanism for the strain-induced nucleation of martensitic transformations. J. Less Common Metals **28**, 107–118 (1972)
37. M. Onyuna, H. Oettel, U. Martin, A. Weiß, On the deformation behavior and martensitic transformations of metastable austenitic steels. Adv. Eng. Mater. **6**, 529–535 (2004)
38. S. Pichumani, R. Srinivasan, V. Ramamoorthi, Mechanical properties, thermal profiles, and microstructural characteristics of Al-8 %SiC composite welded using pulsed current TIG welding. J. Mech. Sci. Technol. **32**(4), 1713–1723 (2018). https://doi.org/10.1007/s12206-018-0130-4
39. P. Podany, M. Koukolikova, T. Kubina, R. Prochazka, A. Franc, Fe-Mn(Al, Si) TWIP steel—strengthening characteristics and weldability. IOP Conf. Ser. Mater. Sci. Eng. **179**, 012057 (2017). https://doi.org/10.1088/1757-899X/179/1/012057
40. P. Podany, C. Reardon, M. Koukolikova, R. Prochazka, A. Franc, Microstructure, mechanical properties and welding of low carbon. Medium manganese TWIP/TRIP steel. Metals **8**(4), 263 (2018). https://doi.org/10.3390/met8040263
41. D. Rafaja, C. Krbetschek, C. Ullrich, S. Martin, Stacking fault energy in austenitic steels determined by using in situ X-ray diffraction during bending. J. Appl. Crystallogr. **47**(3), 936–947 (2014). https://doi.org/10.1107/S1600576714007109
42. U. Reisgen, M. Schleser, O. Mokrov, E. Ahmed, Numerical and experimental investigation of tensile behavior of laser beam welded TRIP700 steel. ISIJ Int. **51**(3), 429–434 (2011). https://doi.org/10.2355/isijinternational.51.429
43. L. Remy, A. Pineau, Twinning and strain-induced F.C.C. → H.C.P. transformation in the Fe-Mn-Cr-C system. Mater. Sci. Eng. **28**(1), 99–107 (1977)
44. D.C. Saha, Y. Cho, Y.D. Park, Metallographic and fracture characteristics of resistance spot welded TWIP steels. Sci. Technol. Weld. Join. **18**(8), 711–720 (2013). https://doi.org/10.1179/1362171813Y.0000000151
45. K. Sato, M. Ichinose, Y. Hirotsu, Y. Inoue, Effects of deformation induced phase transformation and twinning on the mechanical properties of austenitic Fe-Mn-Al alloys. ISIJ Int. **29**(10), 868–877 (1989)
46. P.J. Spencer, J.N. Pratt, A study of the vapour pressure of manganese using a new high-temperature torsion—effusion apparatus. Brit. J. Appl. Phys. **18**(10), 1473–1478 (1967). https://doi.org/10.1088/0508-3443/18/10/314
47. S. Subramanian, D.A. Muller, J. Silcox, S.L. Sass, Chemistry, bonding and fracture of grain boundaries in Ni3Si. Acta Metall. **45**(9), 3565–3571 (1997)
48. N. Suutala, T. Takalo, T. Moisio, Ferritic-austenitic solidification mode in austenitic stainless steel welds. Metall. Mater. Trans. A **11A**, 717–725 (1980)
49. N. Suutala, T. Takalo, T. Moisio, Ferritic-austenitic solidification mode in austenitic stainless steel welds. Metall. Trans. A **11**(5), 717–725 (1980). https://doi.org/10.1007/BF02661201
50. J. Talonen, Effect of strain-induced α'-martensite transformation on mechanical properties of metastable austenitic stainless steels. Ph.D. thesis, Helsinki University of Technology, Helsinki, Finland, 2007
51. D.N. Trushnikov, G.M. Mladenov, V.Y. Belenkiy, E.G. Koleva, S.V. Varushkin, Current-driven ion-acoustic and potential-relaxation instabilities excited in plasma plume during electron beam welding. AIP Adv. **4**(4), 047105 (2014). https://doi.org/10.1063/1.4870944

52. K.H. Tseng, Study on surface appearance, geometry size, and delta-ferrite content of ZrO2-aided TIG welding of AISI 316LN stainless steel. Int. J. Adv. Manuf. Technol. **89**(5–8), 2355–2362 (2017). https://doi.org/10.1007/s00170-016-9280-2
53. C. Weigelt, H. Berek, C.G. Aneziris, R. Eckner, L. Krüger, Joining of Zirconia reinforced metal-matrix composites. Mater. Sci. Forum **825–826**, 498–505 (2015). https://doi.org/10.4028/www.scientific.net/MSF.825-826.498
54. C. Weigelt, G. Schmidt, C.G. Aneziris, R. Eckner, D. Ehinger, L. Krüger, C. Ullrich, D. Rafaja, Compressive and tensile deformation behaviour of TRIP steel-matrix composite materials with reinforcing additions of zirconia and/or aluminium titanate. J. Alloys Compd. **695**, 9–20 (2017). https://doi.org/10.1016/j.jallcom.2016.10.176
55. M. Wendler, A. Weiß, L. Krüger, J. Mola, A. Franke, A. Kovalev, S. Wolf, Effect of manganese on microstructure and mechanical properties of cast high alloyed CrMnNi-N steels. Adv. Eng. Mater. **15**(7), 558–565 (2013). https://doi.org/10.1002/adem.201200318
56. J. Yoo, K. Han, Y. Park, J. Choi, C. Lee, Evaluation of solidification cracking susceptibility of Fe-18Mn-0.6C steel welds. Sci. Technol. Weld. Join. **19**(6), 514–520 (2014). https://doi.org/10.1179/1362171814Y.0000000216

Chapter 11
Microstructure Aspects of the Deformation Mechanisms in Metastable Austenitic Steels

David Rafaja, Christiane Ullrich, Mykhaylo Motylenko and Stefan Martin

Abstract This chapter presents microstructure features, which are responsible for transformation-induced and twinning-induced plasticity in austenitic steels, gives an overview of relevant microstructure defects and shows how the microstructure defects and their interactions affect the deformation behaviour of these steels. Numerous examples illustrate the capability of scanning and transmission electron microscopy and X-ray and electron diffraction to detect, to identify and to quantify dislocations, stacking faults, twins and their clusters. In this context, the benefits of the in situ techniques of microstructure analysis are emphasized. As the presence and arrangement of stacking faults in austenite play a central role in the plasticity of the austenitic steels, a large part of this chapter is devoted to the characterization and description of their formation, widening and ordering. A novel method for determination of the stacking fault energy is presented that utilizes in situ X-ray or synchrotron diffraction under deformation. Finally, the dependence of the stacking fault energy on the chemical composition of the steel and on the deformation temperature is addressed, and considered as an effective tool for design of steels with desirable mechanical properties.

11.1 Introduction

The highly tunable properties of metastable austenitic steels are typically based on polymorphic phase transformations that allow a desired phase composition and microstructure of the steels to be adjusted. Moreover, the phase transformations and the twinning in metastable austenite are the most important mechanisms behind the transformation-induced plasticity (TRIP) and for the twinning-induced plasticity (TWIP) of these steels.

D. Rafaja (✉) · C. Ullrich · M. Motylenko · S. Martin
Institute of Materials Science, Technische Universität Bergakademie Freiberg,
Gustav-Zeuner-Straße 5, 09599 Freiberg, Germany
e-mail: rafaja@ww.tu-freiberg.de

H. Biermann and C. G. Aneziris (eds.), *Austenitic TRIP/TWIP Steels and Steel-Zirconia Composites*, Springer Series in Materials Science 298,
https://doi.org/10.1007/978-3-030-42603-3_11

At room temperature and ambient pressure, pure iron possesses *bcc* lattice that is stabilized by the ferromagnetic ordering of magnetic moments [1]. When the ferromagnetism is deactivated, e.g., through a high hydrostatic pressure (> 13 GPa), a hexagonal close packed modification of iron with a smaller specific volume becomes stable [2, 3]. Above 911 °C the *fcc* modification and above 1392 °C up to the melting point at 1536 °C the *bcc* structure are thermodynamically stable. By alloying iron with substitutional elements like chromium, nickel and manganese or with interstitial elements like carbon or nitrogen, the high temperature *fcc* phase can be stabilized down to room temperature. Such steels are known as *austenitic stainless steels*, as a high chromium content (> 12 wt%) impedes corrosion.

The *fcc* metals and alloys are usually ductile and show an excellent formability. Their stress-strain curves are characterized by the occurrence of high elongation and modest strain hardening that typically depend on the deformation temperature. In Fig. 11.1a, b, the temperature dependence of the mechanical behavior is illustrated on the true stress-strain curves measured under tensile load and on the strain hardening calculated from these stress-strain curves, respectively. The different characteristics of oxygen-free high conductive (OFHC) copper and a metastable austenitic stainless steel of the type X3CrMnNi16-6-6[1] illustrate the effect of the alloying elements. The yield stress and the applied stress needed to maintain plastic deformation are much higher for the alloyed steel than for the OFHC copper. Consequently, the alloyed steel shows a higher strain hardening than the OFHC copper.

Further differences are visible in the temperature dependence of the mechanical properties. Whereas the strain hardening of the OFHC copper increases only slightly

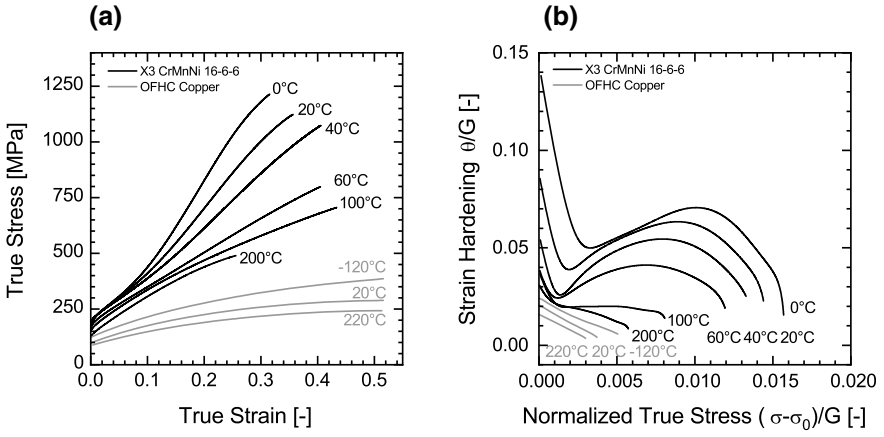

Fig. 11.1 Mechanical properties of X3 CrMnNi16-6-6 TRIP/TWIP steel [4] and pure (OFHC) copper [5] obtained from tensile testing at different temperatures: **a** stress-strain behavior and **b** corresponding strain hardening depicted in form of the Kocks-Mecking plot

[1]Chemical composition 16 wt% Cr, 6 wt% Mn, 6 wt% Ni, 1 wt% Si, 0.03 wt% C of the reference stainless steel in this Chapter, deviating chemical compositions from this one are given.

with decreasing deformation temperature, the increase of the strain hardening in the metastable austenitic steel plastically deformed at low temperatures is much more pronounced. Below 100 °C, the steel shows a tremendous increase of the strength and an additional hardening in the strain range between approx. 0.05 and 0.25. This difference in the temperature dependence of the mechanical properties can be explained by different deformation mechanisms in the OFHC copper and in the TRIP/TWIP steels, and by different activities of underlying microstructure defects and microstructure phenomena like dislocations, stacking faults and deformation-induced martensitic phase transformations.

In this Chapter, the role of dislocation slip, dissociation of dislocations, formation of partial dislocations, expansion of stacking faults and martensitic transformations in the plastic deformation of the TRIP/TWIP steels is discussed in order to explain the specific stress-strain behavior of these materials. Particular attention is paid to the effect of the stacking fault energy on the dislocation glide, nucleation of the martensites and to the interaction of microstructure defects and features among each other.

11.2 Fundamental Microstructure Defects, Their Activity and Configurations in Austenitic Steels

11.2.1 Dislocations and Stacking Faults in fcc *Materials*

Plastic deformation of metals is typically based on dislocation slip. Perfect dislocations in *fcc* austenite have the Burgers vectors ⟨110⟩ and glide on the close-packed planes {111}. In austenitic steels, the perfect dislocations tend to split into Shockley partial dislocations, which can be described by the following reaction:

$$\frac{a}{2}\left[10\bar{1}\right] \rightarrow \frac{a}{6}\left[11\bar{2}\right] + \frac{a}{6}\left[2\bar{1}\bar{1}\right] \tag{11.1}$$

In (11.1), a is the lattice parameter of the *fcc* structure and $\frac{a}{2}\left[10\bar{1}\right]$ the Burgers vector of the original perfect dislocation. The Burgers vectors of the Shockley partials are $\frac{a}{6}\left[11\bar{2}\right]$ and $\frac{a}{6}\left[2\bar{1}\bar{1}\right]$. This dissociation reaction is a consequence of the line energy reduction upon dissociation. As the line energies of dislocations are proportional to the square of their Burgers vectors [6], the sum of the line energies of the partials is lower than the line energy of the perfect dislocation. The equilibrium dissociation width x_0 is reciprocally proportional to the stacking fault energy (SFE) γ_{SF}. For screw dislocations, the following relationship holds [6]:

$$x_0 = \frac{Gb_p^2}{8\pi\gamma_{\mathrm{SF}}}\frac{2-3\nu}{1-\nu} \tag{11.2}$$

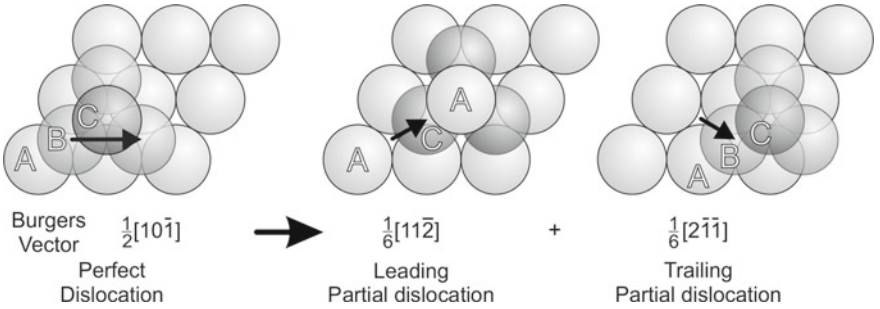

Fig. 11.2 Schematic arrangement of the atoms in the close-packed layers in an unfaulted *fcc* crystal (left), after the passage of the leading partial dislocation (middle) and beyond the stacking fault terminated by the trailing partial (right). Adopted from [8]

In (11.2), G is the shear modulus, b_p the magnitude of the Burgers vector of the partial dislocations and ν the Poisson ratio. The reciprocity of the equilibrium dissociation width and SFE means that the dissociation width is small for metals with a high SFE like Al (~200 mJ/m^2 [7]), where it is comparable with the length of the Burgers vector, and large for *fcc* materials with a low SFE, e.g. Ag (~25 mJ/m^2 [7]).

The occurrence of partial dislocations modifies the stacking order of the adjacent atomic planes {111}. In unfaulted *fcc* crystals, the stacking sequence of the close-packed planes {111} along the respective perpendicular direction ⟨111⟩ is *ABCABC* (Fig. 11.2, left). After the passage of the leading partial having the Burgers vector $\frac{a}{6}[11\bar{2}]$, it is modified to *ABCACA* (Fig. 11.2, middle). The passing of the trailing partial with the Burgers vector $\frac{a}{6}[2\bar{1}\bar{1}]$ reconstitutes the original stacking sequence (Fig. 11.2, right). The stacking fault is spanned between the partial dislocations.

Upon loading, the Burgers vectors of the partials interact with the external load, which modifies the movement of the partial dislocations and the widening of the stacking faults. This interaction was described by Copley [9] and Byun [10] as

$$\left[\hat{l}\times\left(\overleftrightarrow{\tau}\cdot\overrightarrow{b_1}\right)\right]\cdot\hat{x}=\gamma_{SF}-\frac{G}{2\pi x_0}\left[\left(\overrightarrow{b_1}\cdot\hat{l}\right)\left(\overrightarrow{b_2}\cdot\hat{l}\right)+\frac{\left(\overrightarrow{b_1}\times\hat{l}\right)\left(\overrightarrow{b_2}\times\hat{l}\right)}{1+\nu}\right]+f_0 \tag{11.3}$$

$$\left[\hat{l}\times\left(\overleftrightarrow{\tau}\cdot\overrightarrow{b_2}\right)\right]\cdot\hat{x}=-\gamma_{SF}+\frac{G}{2\pi x_0}\left[\left(\overrightarrow{b_1}\cdot\hat{l}\right)\left(\overrightarrow{b_2}\cdot\hat{l}\right)+\frac{\left(\overrightarrow{b_1}\times\hat{l}\right)\left(\overrightarrow{b_2}\times\hat{l}\right)}{1+\nu}\right]+f_0 \tag{11.4}$$

In (11.3) and (11.4), $\overrightarrow{b_1}$ and $\overrightarrow{b_2}$ are the Burgers vectors of the partial dislocations, $\overleftrightarrow{\tau}$ is the stress tensor, $\hat{l}$ corresponds to the line vector of the dislocation,

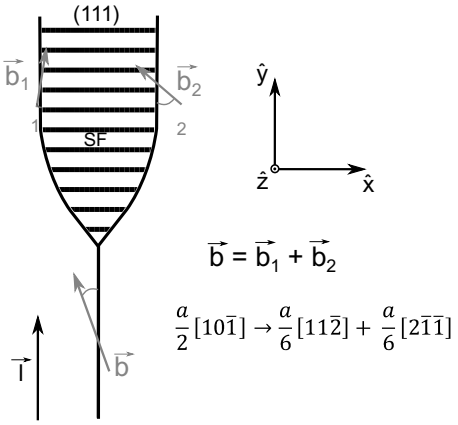

Fig. 11.3 Dissociation of a perfect dislocation with the Burgers vector $\vec{b}$ to partial dislocations with the Burgers vectors $\vec{b}_1$ and $\vec{b}_2$ spanning a stacking fault [10]

$\hat{x}$ is the unit direction according to the setup in Fig. 11.3, x_0 the separation distance of the partials and f_0 the lattice friction force. The different forces acting on the leading and trailing partial that are induced by the external stress are represented by the left-hand sides of (11.3) and (11.4) [11]. The SFE (γ_{SF}) pulls the partials together, whereas the repulsive interaction force due to their stress fields, i.e., $\pm\frac{G}{2\pi x_0}\left[\left(\vec{b_1}\cdot\hat{l}\right)\left(\vec{b_2}\cdot\hat{l}\right)+\frac{\left(\vec{b_1}\times\hat{l}\right)\left(\vec{b_2}\times\hat{l}\right)}{1+\nu}\right]$, pushes the partials apart. The lattice friction against the dislocation movement (f_0) is equal for leading and trailing partial dislocation. Using these equations, the equilibrium of the dynamic force under an applied stress can be calculated. The maximum stress effect on the dissociation width is found for screw dislocations. For such dislocations, the separation distance x_0 can be calculated as [10]:

$$x_0 = \frac{(2-3\nu)Gb_p^2}{8\pi(1-\nu)\left[\gamma_{SF}-\tau_{zx}b_p/2\right]} \tag{11.5}$$

Consequently, the dissociation distance between the partial dislocations is strongly affected by the SFE (γ_{SF}) and external stress (τ_{zx}). Both effects are illustrated in Fig. 11.4, where the dependence of x_0 on τ_{zx} is plotted for several SFE values. The separation distance increases drastically above a critical stress level [10],

$$\tau_{zx}^{crit} = 2\gamma_{SF}/b_p, \tag{11.6}$$

at which the separation distance in (11.5) approaches infinity. In reality, the stacking fault extends through the entire grain. In materials with lower SFE, wide stacking faults are formed and the critical stress for quasi-infinite dissociation is lower than in materials with higher SFEs. Wide stacking faults are found in the microstructure of deformed austenitic CrMnNi steels and are the reason for their special mechanical behavior. As the SFEs of the austenitic CrMnNi steels with TWIP and TRIP

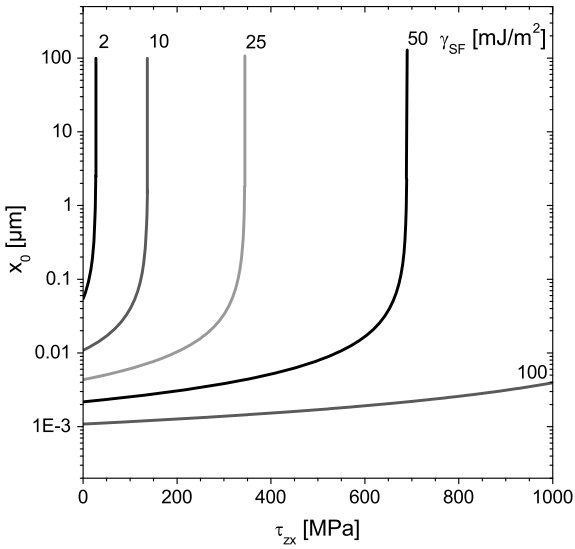

Fig. 11.4 The dissociation width as a function of the applied stress, plotted for several SFE values according to [10]

effect range between 2 and 40 mJ/m^2 [12, 13], wide stacking faults form in their microstructure already at low deformations and affect the deformation behavior seriously.

11.2.2 Dislocations and Stacking Faults in Austenitic Steels, Their Configurations and Interactions

The most important microstructure defects in metastable austenite are dislocations with the Burgers vectors $\frac{a}{2}\langle 110\rangle$ and the stacking faults on the lattice planes {111}. Their configurations and interactions are depicted in the transmission electron microscopy (TEM) micrographs in Fig. 11.5, which were taken in an austenitic steel containing 16 wt% Cr, 7 wt% Mn, 9 wt% Ni, 1 wt% Si, 0.02 wt% C and 0.02 wt% N that was subjected to 2% deformation.

Nearly perfect dislocations (SFs with a very short dissociation width) are visible in area I of Fig. 11.5a, b. They stem from the Frank-Read-like dislocation sources [14]. One example of the Frank-Read source can be seen in the area II of Fig. 11.5a. Larger dissociation is observed for dislocations that are suitably oriented with respect to the applied force. The largely dissociated Shockley partial dislocations form stacking faults that are highlighted by red arrows in Fig. 11.5a. As the partial dislocations can only move on their slip planes, their cross slip to other planes is impeded and only possible, if the partials constrict and recombine. Furthermore, both perfect and partial dislocations are piling up at obstacles during plastic deformation (see, e.g., area I in Fig. 11.5b). These obstacles might be the stress fields produced by immobile dislocations or dislocation clusters as well as the grain boundaries. The pile-ups

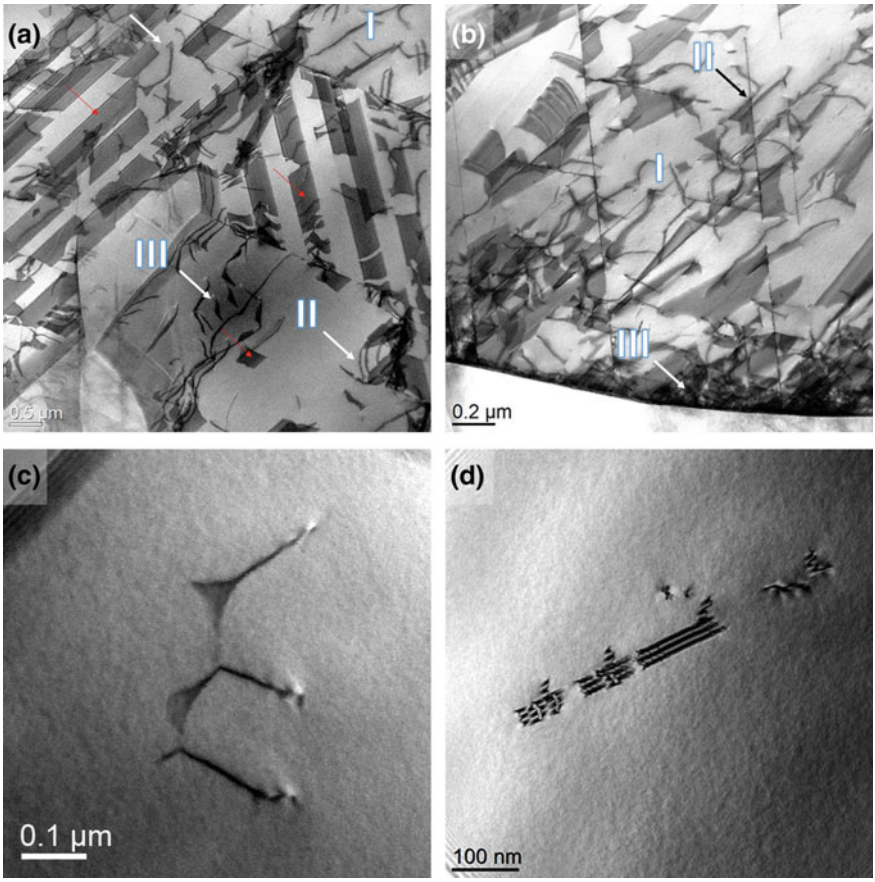

Fig. 11.5 Characteristic dislocation configurations in X2CrMnNi16-7-9 stainless steel having a low stacking fault energy after 2% straining. **a** Depending on the resolved shear stress on individual glide planes, dissociated dislocations form short or wide stacking faults (area III). **b** Beginning of the SF interaction, the deformation band formation, dislocation pile up and Lomer-Cottrell lock formation. **c** Dislocation nodes spanning stacking faults in between. **d** Overlapping stacking faults indicating the SF band formation. Micrographs (**a**) and (**b**) were taken in the scanning TEM mode, micrographs (**c**) and (**d**) in the TEM mode

generate long-range stress fields, which enable further dislocation reactions like the cross-slip of screw dislocations [15].

If multiple slip systems are activated, which is generally the case for plastic deformation of polycrystalline metals, the dislocations can interact with SFs and specific dislocation reactions occur. Dissociated dislocations on intersecting slip planes form Lomer-Cottrell locks [16, 17] as seen in Fig. 11.5b, area II. These locks are generated, when stacking faults on different slip planes encounter. This can be illustrated by the edge-on stacking faults, which seem to stop the SFs on the other slip planes. The normal directions of the edge-on stacking faults lie in

the plane of the TEM sample, thus they are visible just as thin lines in the TEM micrograph. Such locks immobilize SFs on both slip planes, which are now in a sessile configuration, and can cause further dislocation reactions or pile-ups, as the locks are obstacles for following dislocation slip. In Fig. 11.5b, area III, an intense interaction between dislocations and SFs near the grain boundary is obvious. The generation and slip of perfect dislocations, their dissociation, the formation of stacking faults and their widening are the microstructure phenomena that dominate the behavior of the metastable austenitic steels upon plastic deformation [18].

If three dislocations with different Burgers vectors meet on the same slip plane, then they form dislocation nodes [19], as shown in Fig. 11.5c. In the center of such a node, a small stacking fault is produced. This dislocation node behaves like a Lomer-Cottrell lock and persists, therefore, in a stable configuration, which can affect the slip or the formation of following dislocations and SFs [18, 19].

In contrast, the overlap of multiple SFs located on the same slip plane initiates the formation of deformation bands that are depicted in Fig. 11.5d. In this micrograph, the overlap of the parallel stacking faults and the presence of the bordering partial dislocations cause a change in the fringe contrast. The stacking faults accumulated within a deformation band are highly correlated. The deformation bands form first on a primary slip system that possesses the maximum Schmid factor and that experiences the highest shear stress. With increasing applied stress, the deformation bands widen, until they extend over the entire grain size. Concurrently, the increasing applied stress triggers the formation of deformation bands on secondary slip systems. In low-SFE austenitic steels, the formation of deformation bands is the most important deformation mechanism [20].

11.2.3 Arrangement of the Stacking Faults in Austenite: Formation of ε-Martensite and Twinned Austenite

11.2.3.1 Crystallographic and Thermodynamic Aspects of the Stacking Fault Arrangement in *Fcc* Materials

In *fcc* materials, the stacking faults form on the {111} lattice planes via dissociation of perfect dislocations and repulsion of the Shockley partials. As explained in Sect. 11.2.1, the separation distance of partial dislocations and the width of the stacking faults are controlled by the stacking fault energy and by the magnitude of the local shear stress on the glide plane. These two parameters influence, furthermore, the number and/or the density and the arrangement of the stacking faults. At low SF densities, the stacking faults are typically randomly distributed. At (locally) high SF densities, the distances between next stacking faults become much smaller. Consequently, the stacking faults start to arrange.

Two stacking fault configurations deserve a special attention—the arrangement of the stacking faults on ***every second*** {111} plane and the arrangement of the stacking

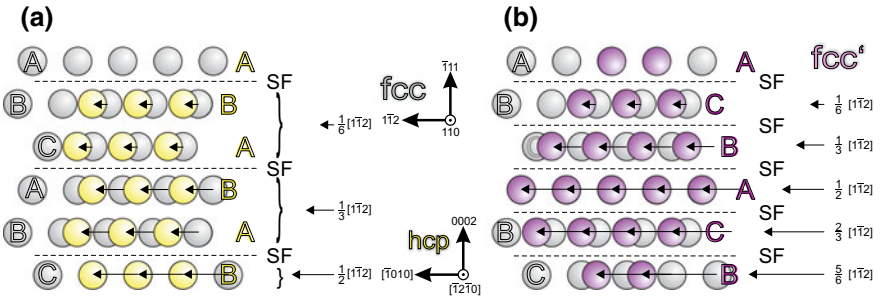

Fig. 11.6 Schemes of special local arrangements of stacking faults (SF) in austenite. **a** The stacking faults are located on every second {111} lattice plane, which leads to the *hcp* stacking. **b** The stacking faults are located on every {111} lattice plane, which leads to the formation of twins (fcc') according to [4]

faults on ***every*** {111} plane. The arrangement of stacking faults in an *fcc* structure on every second {111} glide plane (Fig. 11.6a) introduces regular *hcp ABABAB* stacking sequence, which is called ε-martensite for the originally austenitic steels. The arrangement of stacking faults on every {111} lattice plane (Fig. 11.6b) reverses the original stacking order *ABCABC* to *CBACBA*, which is denoted as twinning.

From the thermodynamic point of view, the tendency of the stacking faults in austenite to arrange on each second lattice plane {111} is quantified by the Gibbs free energy of the phase transformation of *fcc* γ-austenite to *hcp* ε-martensite ($\Delta G^{\gamma\to\varepsilon}$) [21, 22]. The relationship between $\Delta G^{\gamma\to\varepsilon}$ and the stacking fault energy (γ_{SF}) was described by Olson [21] and Ferreira [23] as

$$\gamma_{\mathrm{SF}} = n\rho_A\left(\Delta G^{\gamma\to\varepsilon} + E^{\mathrm{str}}\right) + 2\sigma(n) + \sigma_p \tag{11.7}$$

In (11.7), n is the number of the lattice planes {111} that form ε-martensite, ρ_A the molar area density within the close packed lattice planes (mol per area), E^{str} the strain energy resulting from the faulting and $2\sigma(n)$ the interface energy between the faulted structure and the undistorted austenitic matrix (along the $\{111\}_{fcc}$ planes), and σ_p the strain energy of the partial dislocations. The meaning of this formula was discussed in detail by Geissler et al. [22] and De Cooman et al. [12]. The strain energy term (E^{str}) originates from the formation of ε-martensite that is embedded in the austenite matrix. E^{str} is widely accepted to be negligible, because the relative change in the molar volume during the $\gamma \to \varepsilon$ transformation is very small (1.2% in the present case). The dependence of $\sigma(n)$ on n is hardly assessable by experiment, but it can be estimated from the results of ab initio calculations [24]. The contribution of the strain fields of partials (σ_p) can be neglected, in particular if the stacking faults are wide [21].

For isolated stacking faults affecting just two neighboring lattice planes ($n = 2$), (11.7) can be rewritten into the following form that is used for estimation of the SFE from the Gibbs energy of the $\gamma \to \varepsilon$ phase transformation

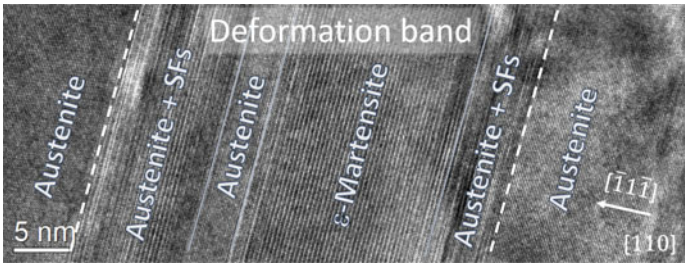

Fig. 11.7 HRTEM image of a 5% strained tensile sample of an X2CrMnNi16-7-6 steel showing various clusters of stacking faults within a deformation band

$$\gamma_{\mathrm{SF}}\left[\mathrm{mJ/m^2}\right] = 2(\rho_A \Delta G^{\gamma\to\varepsilon} + \sigma) \tag{11.8}$$

Both parameters $\Delta G^{\gamma\to\varepsilon}$ and σ are strongly dependent on the chemical composition of the steel and on temperature. Still, according to Geissler [22] the term $\rho_A \Delta G^{\gamma\to\varepsilon}$ is approximately one order of magnitude larger than the contribution of the interface energy, $\rho_A \Delta G^{\gamma\to\varepsilon} \cong 5-50\ \mathrm{mJ/m^2}$ versus $\sigma \cong 0.1-27\ \mathrm{mJ/m^2}$, despite the huge span of values available in literature for austenitic steels [22, 25, 26]. It is worth noting that the highest interface energies reported in literature for austenitic steels are not necessarily physically reasonable, because the interfaces between ε-martensite and austenite are almost perfectly heteroepitaxial. Thus, the term $\rho_A \Delta G^{\gamma\to\varepsilon}$ is the most important parameter influencing the stacking fault energy.

It is known from experiments that the distribution of SFs is not homogeneous, as the SFs are typically arranged in deformation bands in plastically deformed samples (Fig. 11.7). This local clustering of SFs has manifold reasons, but most of them are related to a localized nucleation of SFs at stress concentrations, which occurs through the dislocation interactions, local chemical inhomogeneities, or at crystallite boundaries [12].

The stress relaxation through the formation of SFs in austenite is connected with a lattice shear deformation (γ), which is proportional to the magnitude of the Burgers vector of the partial dislocations, $\left|\vec{b}_p\right| = a\left|\left[1\bar{1}2\right]\right|/6$, and which scales with the distance between the next SFs as $\gamma = \left|\vec{b}_p\right|/(n_d d_{111})$. a is the lattice parameter of austenite, $d_{111} = a/\sqrt{3}$ the distance of the close packed lattice planes (neglecting a change of d_{111} near the partials) and n_d the SF distance expressed in the units of d_{111}. The largest shear deformations are achieved in ε-martensite and in twinned austenite. For ε-martensite, where the SFs appear after each second lattice plane {111}, the lattice shear deformation is about $\gamma_{hcp} = \frac{a}{6}\left|\left[1\bar{1}2\right]\right|/(2d_{111}) = \sqrt{2}/4$. For twins, the lattice shear is twice as large, $\gamma_{\mathrm{twin}} = \frac{a}{6}\left|\left[1\bar{1}2\right]\right|/d_{111} = \sqrt{2}/2$, because the SFs are present on each close packed lattice plane. Consequently, the formation of domains, which contain either hexagonally ordered close packed planes of austenite (basal planes of ε-martensite) or twinned austenite, is the most effective way to reduce the local stress concentrations. These domains, which are typically located within

the deformation bands, are fully crystallographically coherent with the austenitic matrix along the respective $\langle 111 \rangle_{fcc}$ or $\langle 0001 \rangle_{hcp}$ direction but incoherent in the perpendicular directions, where the SFs are confined by partial dislocations.

The occurrence of the local stress concentrations in austenitic steels is expected to rise with increasing SFE. According to the stacking fault model from Sect. 11.2.1, the shear stress needed to separate the partials in SFs increases with increasing SFE [10]. Assuming that the amplitude of the local stress concentrations increases if the overall stress level increases, more intense stress concentrations and strongly clustered SFs will appear in austenite with a higher SFE. Very low SFE, in contrast, will facilitate the widening of SFs already at a low overall stress level. This mechanism will prevent strong stress concentrations and local arrangement of the SFs.

11.2.3.2 Detection of the Stacking Faults and Their Arrangements by Diffraction Methods

The impact of stacking faults (SFs) on the diffraction patterns of *fcc* metals was described by Wilson [27], Paterson [28], Warren and Warekois [29] and Warren [30]. This description comprises an anisotropic (i.e., *hkl*-dependent) shift of the diffraction lines, their anisotropic broadening and asymmetry. In the approaches above, the faulting of an *fcc* structure is described as a change in the regular sequence of the lattice planes {111} along the respective normal direction ⟨111⟩. The translation vectors of the regular and faulted *fcc* stacking, $\vec{t} = \left(\frac{1}{3}a_h, \frac{2}{3}a_h, \frac{1}{3}c_h\right)$ and $\vec{t}_| = \left(\frac{2}{3}a_h, \frac{1}{3}a_h, \frac{1}{3}c_h\right)$, respectively, are typically defined in the hexagonal coordinate system obeying the orientation relationship $\left[11\bar{2}0\right]_{hcp} \parallel \left[1\bar{1}0\right]_{fcc}$ and $(0001)_{hcp} \parallel (111)_{fcc}$ with respect to the cubic system (Fig. 11.8). The hexagonal lattice parameters a_{hcp} and c_{hcp} are related to the cubic one (a_{fcc}) as

$$a_{hcp} = a_{fcc}/\sqrt{2} \text{ and } c_{hcp} = 2a_{fcc}/\sqrt{3} \tag{11.9}$$

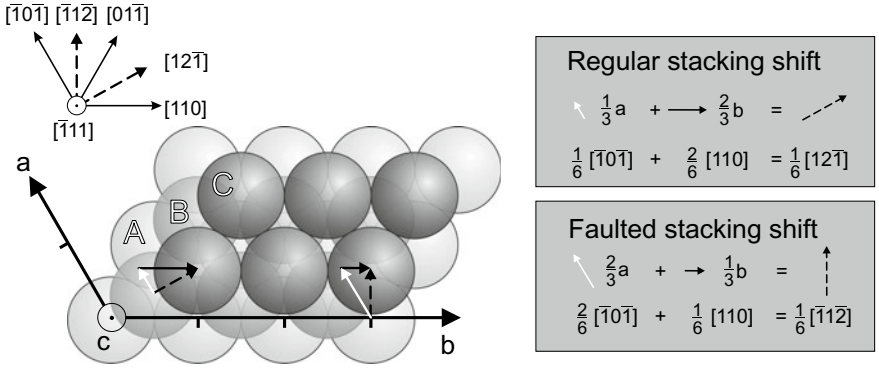

Fig. 11.8 Description of the in-plane shift in the *fcc* lattice in a hexagonal coordinate system as stacking sequence of {111} austenite lattice planes. Adopted from [31]

Martin et al. [31] simulated the effect of the layer stacking on the powder X-ray diffraction (PXRD) patterns using the DIFFaX routine [32] for different stacking fault configurations. The relevant stacking faults configurations are summarized in Table 11.1, the corresponding diffraction patterns are plotted in Fig. 11.9.

As long as the regular *fcc* stacking is maintained ($P_{\text{regular}} = 1$), only the diffraction lines corresponding to the *fcc* structure appear (black curve in Fig. 11.9a). The

Table 11.1 Overview of the SF sequences that were used for the DIFFaX simulation (Fig. 11.9) of the PXRD patterns

Sequence of the lattice planes	Probability	Microstructural interpretation
…ABC…	P_{regular}	Relative amount of undistorted *fcc* phase
…CAB$_{\perp}$ABC…	P_{intr}	Relative amount of isolated intrinsic (single) SFs
…CAB$_{\perp}$A$_{\perp}$CAB…	P_{extr}	Relative amount of isolated extrinsic (double) SFs
…CAB$_{\perp}$AB$_{\perp}$ABC…	P_{hcp}	Relative amount of narrowly spaced SFs appearing repetitively after two lattice planes $\{111\}_{fcc}$
…CAB$_{\perp}$A$_{\perp}$C$_{\perp}$B$_{\perp}$…	P_{twin}	Relative amount of twins (SFs appearing repetitively after each lattice plane $\{111\}_{fcc}$)
…CAB$_{\perp}$A$_{\perp}$C$_{\perp}$B$_{\perp}$…	P_{tl}	Extent of the twins (tl—twin length)

The sequence of lattice planes is related to the *fcc* lattice planes {111}. The appearance of a SF is depicted by the symbol ⊥. The DIFFaX probability is denoted by the respective symbol *P*

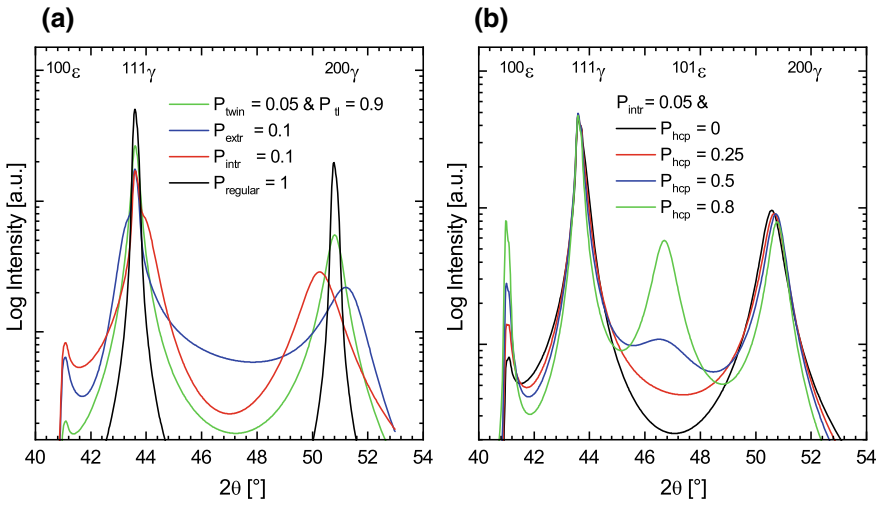

Fig. 11.9 Influence of the stacking fault arrangements on the diffraction pattern: **a** Effect of the isolated SFs and specific SF arrangements on the diffraction pattern, **b** influence of increasing probability (P_{hcp}) for SF arrangements on every second {111} glide plane forming hexagonal intensities

presence of isolated intrinsic and extrinsic SFs leads to the line shift and to the line broadening (Fig. 11.9a). Extrinsic SFs and twins make the diffraction profiles strongly asymmetric. According to the Warren theory [30], the line shift caused by the isolated intrinsic stacking faults depends on the diffraction indices (*hkl*) like

$$\Delta 2\theta(^\circ) = 2 \cdot \frac{180^\circ}{\pi} \cdot \frac{\sqrt{3}\alpha}{4\pi} \cdot \frac{\sum_{(\text{affected})} \pm(h+k+l)}{\left(h^2+k^2+l^2\right)m_{hkl}}, \tag{11.10}$$

where α is the probability of the occurrence of the isolated intrinsic SFs and m_{hkl} the multiplicity of the lattice planes $\{hkl\}$. Concurrently, the occurrence of isolated (intrinsic and extrinsic) SFs breaks the coherence of the parts of the crystal structure, which are mutually separated by the stacking faults. This loss of the coherence leads to a line broadening, which can be written in the reciprocal space units as

$$\Delta d^*_{hkl} = \frac{1}{D} + \frac{1.5\alpha+\beta}{a} \sum_{(\text{affected})} \frac{|h+k+l|}{m_{hkl}\sqrt{h^2+k^2+l^2}} \tag{11.11}$$

In (11.11), D is the average crystallite size, β the density of extrinsic SFs and a the cubic lattice parameter. The meaning of other symbols is the same like in (11.10). In both equations, the summations are performed over the indices of the diffraction lines, which are affected by the stacking faults, i.e., for $(h+k+l) \bmod 3 \neq 0$. In (11.10), the positive sign applies for $(h+k+l) \bmod 3 = 1$, the negative one for $(h+k+l) \bmod 3 = 2$.

In contrast to the isolated SFs and twins, SFs appearing repetitively after two lattice planes cause a marginal shift and broadening of the diffraction lines (Fig. 11.9b), but they imitate a hexagonal crystal structure, which is known as ε-martensite in the transformed austenite. Thus, these correlated SFs are not recognized by the diffraction methods as SFs in austenite but as a new phase. The DIFFaX model was tested on the diffraction pattern of a fine-grained sample of an X2CrMnNi16-6-6 TRIP steel that was compressed to 15%. The best agreement between the measured and simulated diffraction patterns was achieved with the probabilities $P_{\text{intr}} = 0.018$, $P_{hcp} = 0.9$, $P_{\text{twin}} = 0.04$ and $P_{\text{tl}} = 0.96$. The successful modelling of the measured XRD pattern using the SF model shows that faulted austenite and ε-martensite present in the microstructure of plastically deformed TRIP steels can be described using specific SF configurations.

Alternatively, the microstructure of deformed steel samples can be described in terms of microstructure components (austenite, ε-martensite and α'-martensite) and microstructure features (dislocation densities and SF probabilities in relevant phases) that are available in most microstructure models used for the whole pattern refinement, i.e., for the Rietveld-like refinement of the XRD patterns. The individual phases (*fcc* austenite, *hcp* ε-martensite and *bcc* α'-martensite) are described using their intrinsic (non-disturbed) crystal structures. The effect of SFs in austenite on the line positions is quantified using (11.10), the effect of SFs in austenite on the line broadening using (11.11) and the effect of SFs in ε-martensite on the line broadening using

(11.14), see Sect. 11.4. The effect of perfect dislocations on the line broadening is described for all phases using (11.15).

The Rietveld refinement of the diffraction pattern of the fine-grained sample X2CrMnNi16-6-6 compressed to 15%, cf. previous simulation using the DIFFaX model, revealed an intrinsic stacking fault probability in ε-martensite of about 10%, which agrees well with the value of $1 - P_{hcp}$ obtained from the DIFFaX model. The volume faction of ε-martensite correlates directly with P_{hcp}. In the austenite, the intrinsic and extrinsic SF probabilities calculated using the DIFFaX model and the Warren model can be compared directly as well. The parameter P_{twin} can hardly be compared with the microstructure parameters obtained from the Warren model, because the twinning does not cause any shift of the diffraction lines but only a line broadening, see (11.11). However, as it can be seen from (11.11), the densities of intrinsic (isolated) SFs (α) and extrinsic SFs (β) terminating the twins cannot be determined simultaneously solely from the line broadening, but only in conjunction with the analysis of the line shift, or from the line asymmetry [30]. However, as the density of the twin boundaries in the steels under study is much lower than the density of intrinsic SFs, it cannot be determined reliably using the combined analysis of the line shift and line broadening. The analysis of the line asymmetry fails as well, as the asymmetry of the diffraction lines is not very pronounced [33].

Another result of the Rietveld refinement was that the distance between the adjacent $\{111\}_{fcc}$ lattice planes within the faulted stacking sequences was smaller than the interplanar spacing within the regular stacking sequences. Consequently, the ε-martensite had the c/a ratio of 1.62, which is slightly below the value of $c/a = 2\sqrt{2/3} = 1.633$ that corresponds to a pseudo-cubic *hcp* crystal structure with $a = a^{fcc}/\sqrt{2}$ and $c = 2d_{111}^{fcc} = 2a^{fcc}/\sqrt{3}$.

11.2.3.3 Coexistence of Different Stacking Fault Arrangements: Continuous Transition Between ε-Martensite and Twinning

The coexistence of different stacking fault arrangements in highly alloyed metastable austenitic steels with a SFE of approx. 20 mJ/m^2 was confirmed by X-ray diffraction (see previous Section) that found isolated stacking faults together with hexagonal faulted sequences and twins in the samples under study. The local nature of the stacking fault clusters was revealed by electron backscatter diffraction in a scanning electron microscope (EBSD/SEM) and by transmission electron microscopy with high resolution (HRTEM). On a mesoscopic scale, EBSD disclosed that the crystal structure defects are concentrated in the deformation bands, which contain typically ε-martensite slabs and deformation twins (Fig. 11.10). The character of the deformation bands (predominantly ε-martensite or mainly deformation twins) depends generally on the SFE and deformation state. The occurrence of these deformation bands varies with the crystallographic orientation of the originally austenitic grains with respect to the deformation direction.

On the atomic scale, the coexistence of the different stacking fault arrangements was proven by HRTEM that was complemented by the fast Fourier transform (FFT) of

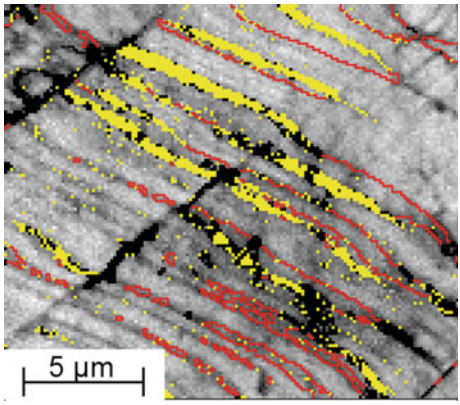

Fig. 11.10 EBSD mapping of deformation bands in compressed X5CrMnNi16-6-9 steel, austenite in grey, ε-martensite in yellow, twin boundaries in red, unindexed pixels in black. Adopted from [34]

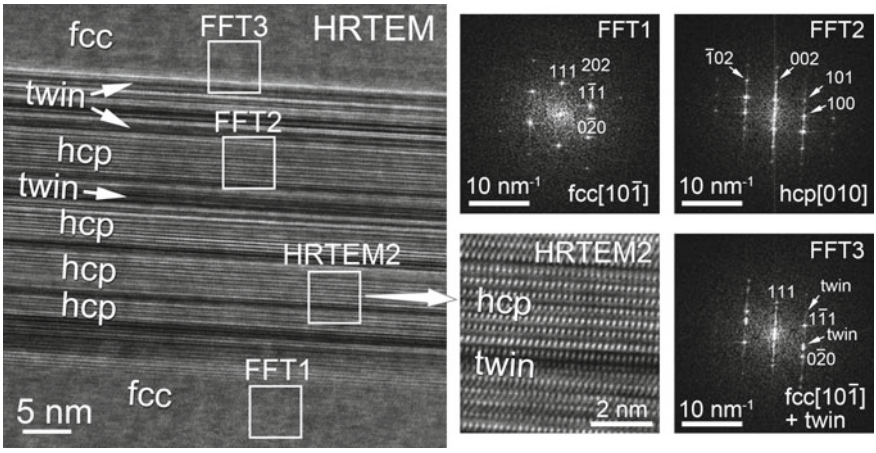

Fig. 11.11 HRTEM image of a deformation band, where atomic arrangements of both twins and ε-martensite are found coexisting in close vicinity

the HRTEM micrographs. Figure 11.11 illustrates the different stacking sequences of the former $\{111\}_{fcc}$ lattice planes, which can be described as an irregular ordering of stacking faults. Extended sequences $AB_{\perp}AB_{\perp}AB_{\perp}AB$ of the lattice planes $\{111\}_{fcc}$ are interpreted as *hcp* ε-martensite, extended sequences $ABCAB_{\perp}A_{\perp}C_{\perp}B_{\perp}\ A_{\perp}C_{\perp}$ as twins. The irregular sequences of SFs produce streaks in the reciprocal lattice of austenite along the faulted $\langle 111\rangle_{fcc}$ direction, which include the reciprocal lattice points of ε-martensite (see FFT2 in Figs. 11.11 and 11.12b). The streaks stem from superimposed truncation rods produced by thin slabs of faulted austenite [28, 35, 36]. The presence of extended slabs of ε-martensite or extended twins leads to the

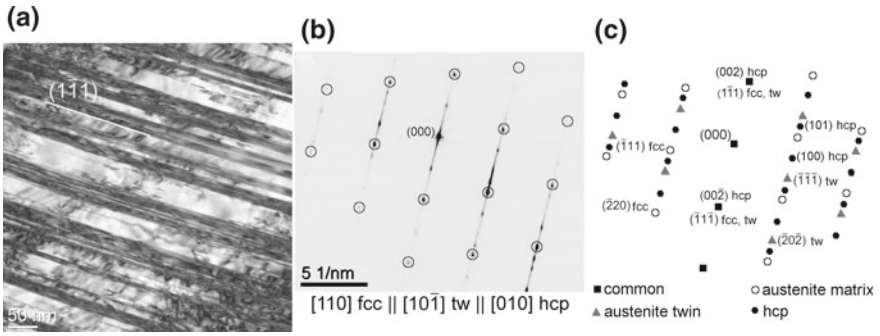

Fig. 11.12 TEM characterization of deformation bands in PM X5CrMnNi16-6-9 steel. **a** Bright-field image of parallel deformation bands, **b** corresponding SAED, recorded with a 200 nm aperture, **c** indexing of spots assigned to austenite matrix, twin and ε-martensite. Adopted from [34]

fragmentation of the streaks and to the formation of separated diffraction spots that correspond to ε-martensite or to twins in austenite (see FFT2 and FFT3 in Fig. 11.11). These microstructure features are interpreted in a very similar way by all diffraction methods, i.e., EBSD (Fig. 11.10), selected area electron diffraction (SAED) in TEM (Fig. 11.12) and XRD (Fig. 11.9).

The crystallographic explanation of these diffraction phenomena is based on the stacking fault models from Figs. 11.6 and 11.7, and on the orientation relationships between austenite, ε-martensite and twinned austenite that can be described as $(0001)_{hcp} \parallel \left(1\bar{1}1\right)_{fcc} \parallel \left(1\bar{1}1\right)_{\text{twin}}$ and $\left[01\bar{1}0\right]_{hcp} \parallel [110]_{fcc} \parallel \left[10\bar{1}\right]_{\text{twin}}$, cf. Fig. 11.12b, c. The deformation bands visible in the TEM micrograph (Fig. 11.12a) contain remainders of the austenite matrix, uncorrelated SFs and areas, which are interpreted as ε-martensite or as twins in austenite. In the SAED pattern (Fig. 11.12b), the remainders of the austenite matrix, the ε-martensite areas and the twinned austenite produce intense diffraction spots, the uncorrelated SFs streaks along the $\left(1\bar{1}1\right)_{fcc}$ reciprocal space direction.

From the thermodynamic point of view, the simultaneous occurrence of twinned austenite and ε-martensite can be discussed in terms of SFE and interface energy [22]. In the case of a low thermodynamic driving force ($\Delta G^{\gamma\to\varepsilon} \cong 0$, cf. Sect. 11.2.3.1), all arrangements of stacking faults corresponding to isolated intrinsic and extrinsic SFs, ε-martensite and twins result in the same overall energy. Therefore, the transition between the transformation-induced plasticity (TRIP) and the twinning-induced plasticity (TWIP) is continuous. Assuming that there are no other obstacles for the phase transition, the TRIP effect and the generation of a local hexagonal stacking sequence are preferred for $\Delta G^{\gamma\to\varepsilon} < 0$, while for $\Delta G^{\gamma\to\varepsilon} > 0$, the twinning dominates.

An important consequence of this microstructure model is an improved atomistic description of the ε-martensite formation. Although SFs were always regarded as nucleation precursor [21] of the ε-martensite formation, the ε-martensite has been treated as a metastable martensitic phase occurring along the $\gamma \to \varepsilon \to \alpha'$ transformation path [37, 38] and as a product of bulk martensitic transformation of austenite

[39]. The current understanding of ε-martensite, which evolves during plastic deformation of austenite, is that it is rather a heavily faulted austenite than a distinct phase.

Using electron microscopy, the ε-martensite was found to appear within deformation bands [31, 40], where a high density of stacking faults is present. Consequently, the deformations bands and hence the ε-martensite form during the plastic deformation of austenite, when a low SFE facilitates the SF formation as a competing mechanism to the dislocation mobility. On the other hand, the deformation bands and the ε-martensite act as repositories of dissociated dislocations, which are bound to their slip planes. Hence, the dynamic recovery is inhibited, as the annihilation would be possible only for perfect dislocations, which are not stable, as their dissociation is facilitated by the low SFE.

11.2.3.4 Thermal Stability of the Deformation-Induced ε-Martensite

The defective character of ε-martensite was confirmed by the thermal behavior of the X2CrMnNi16-7-6 TRIP steel, which was deformed to 25% true compressive deformation at room temperature. In this deformation state, the originally austenitic steel contained 51 vol% *fcc* austenite, 30 vol% *bcc* α'-martensite and 19 vol% *hcp* ε-martensite. The in situ high-temperature XRD measurement carried out upon heating revealed that the ε-martensite disappears between 250 and 350 °C, while the α'-martensite vanishes at approximately 600 °C (Fig. 11.13a). The transformation of α'-martensite to γ-austenite was confirmed by differential scanning calorimetry (DSC), which showed a distinct maximum of the heat flux between 500 and 600 °C (Fig. 11.13b), that is in agreement with the existence range of the *bcc* phase from Fig. 11.13c. The σ-phase from the phase diagram was not observed, because its formation was kinetically inhibited through the rapid quenching.

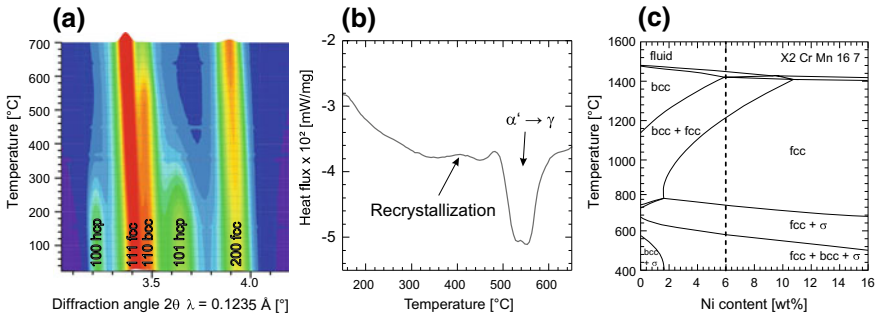

Fig. 11.13 Thermal behavior of an X2CrMnNi16-7-6 TRIP steel deformed to 25%. **a** X-ray synchrotron diffraction patterns recorded during continuous heating. The intensities are plotted in logarithmic scale. **b** The DSC heat flux signal during continuous heating at 10 K/min. **c** Isopleth section of the X2CrMnNi16-7-x steel for Ni concentrations between 0 and 15%

The ε-martensite is no thermodynamically stable phase, thus its existence cannot be proven by the phase diagram. Also in the DSC measurement, no pronounced signal related to the back transformation of ε-martensite was detected. The small differences in the heat flux measured between 250 and 350 °C are comparable with the DSC signal that originates from recrystallization, i.e., from the annihilation of the crystal structure defects in austenite [41, 42]. The absence of a pronounced DSC signal stemming from the dissolution of ε-martensite confirms that the reverse transformation of ε-martensite to austenite happens via 'unfaulting' [43], for which no pronounced diffusion activity of the lattice atoms is needed.

The recovery of austenite and the disappearance of SFs upon heating are supported by the increase of the SFE with increasing temperature (δSFE/δT), which is between 0.05 and 0.1 mJ/(m^{2}K) [7, 44]. Thus, the energy stored in the existing stacking faults increases with increasing temperature. The increase of SFE produces a significant constriction force that acts on partial dislocations and reduces the width of the stacking faults. Large stacking faults collapse and the SFs arrangement in deformation bands disappears in favor of the recovery of original austenite.

11.2.3.5 Phase Transformations in Austenitic Steels Under High Pressure

Pure iron is known to undergo a *bcc* → *hcp* transformation during hydrostatic compression between 8 and 13 GPa and room temperature [45–48]. This transition was explained theoretically by a change of the magnetic state of iron from a ferromagnetic one to a non-magnetic or antiferromagnetic one, when hydrostatic pressure is applied [49–51]. In order to find out possible analogies between the formation of ε-martensite in austenitic steels and the *hcp* high-pressure phase in ferrite under hydrostatic pressure, in situ high-pressure synchrotron diffraction experiments up to 18 GPa were carried out on a *fcc* TRIP steel using a multi-anvil apparatus [52].

For this purpose, small cylinders of the austenitic X2 CrMnNi16-7-6 TRIP steel were encapsulated in an MgO container together with indium that served as a pressure standard, and compressed by WC anvils. The XRD patterns were collected in the energy-dispersive mode at the diffraction angle $2\theta = 3.1557°$ (calibrated by a LaB_6 standard). An excerpt of the analyzed raw data is displayed in Fig. 11.14a. The effective applied pressure was calculated from the change of the specific volume of the reference material.

In contrast to ferrite (pure iron), where the phase transition occurs between 8 and 13 GPa, the *hcp* phase in the TRIP steel appeared already at approx. 0.5 GPa [52]. Its amount was about 20 vol%. This earlier phase transformation may be facilitated by shear stress components, which result from the strong crystallographic anisotropy of the elastic constants of austenite and from the polycrystalline nature of the investigated sample. The local shear stress components and the stress concentrations at the grain boundaries are released by local plastic deformation involving dislocation slip and formation of stacking faults and deformation bands, which support the martensitic transformation of *fcc* austenite to *hcp* ε-martensite. For these reasons, the

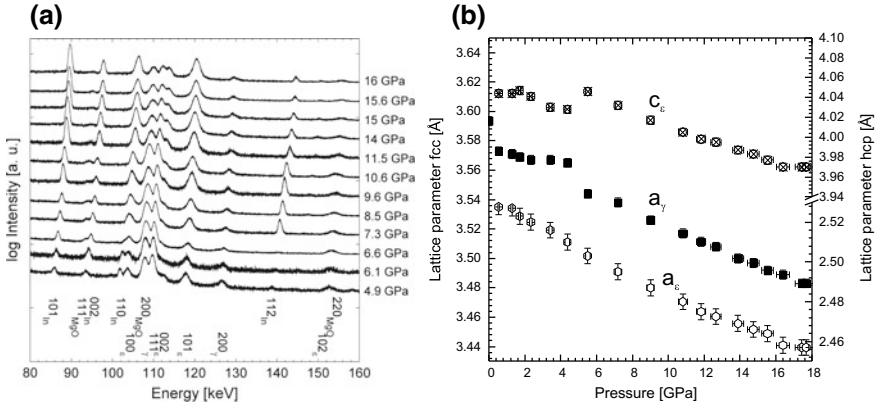

Fig. 11.14 Evolution of the ε-martensite formation at increasing hydrostatic compression. **a** Raw data of the compression experiments show a clear increase of the *hcp* phase fraction with increasing hydrostatic pressure. **b** Evolution of the lattice parameters. Adopted from [52]

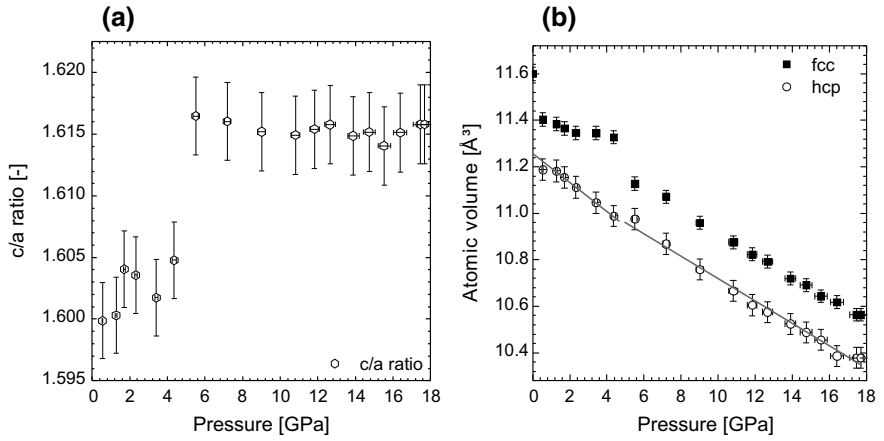

Fig. 11.15 Structural changes in *fcc* austenite and *hcp* ε-martensite during hydrostatic compression. **a** Evolution of the *c*/*a* ratio in *hcp* ε-martensite during compression. **b** Change of the atomic volume (volume per Fe atom in the unit cell) in both phases. According to [52]

hcp phase found in austenite subjected to high hydrostatic pressures above 5 GPa is inherently of the same nature as the deformation-induced ε-martensite, which is produced by uniaxial loading. Still, up to the hydrostatic pressure of 5 GPa the *c*/*a* ratio calculated from the lattice parameters of the *hcp* phase (Fig. 11.14b) was between 1.600 and 1.605 (Fig. 11.15a) [52], which agrees well with the $c/a = 1.602 - 1.603$ reported for the high-pressure phase of iron by Mao et al. [46], Takahashi et al. [47] and Giles et al. [48].

Above the hydrostatic pressure of ~6 GPa, more than 50 vol% of the sample transformed to ε-martensite. This phase transformation was accompanied by an apparently higher compressibility of the austenite and by an abrupt increase of the *c*/*a* ratio from ~1.605 to 1.617, which was caused mainly by the expansion of the hexagonal lattice parameter *c* (Fig. 11.14b). A generally smaller specific volume of the *hcp* phase hexagonal structure in comparison with the *fcc* phase together with the higher compressibility of austenite and a faster reduction of its volume at the pressures above 6 GPa (Fig. 11.15b) can be, according to Le Chatelier's principle [53, 54], a significant driving force for the phase transformation. The value of $c/a = 1.617$ approaches the *c*/*a* ratio in ε-martensite produced by plastic deformation. The change of the *c*/*a* ratio from 1.605 to 1.617 is possibly related to the change in the ordering of magnetic moments. As the change of the *c*/*a* ratio is accompanied by a slight expansion of the elementary cell of the *hcp* ε-martensite at ~6 GPa, a transition from the paramagnetic to the antiferromagnetic state is expected.

11.3 Formation of α'-Martensite

The formation of *bcc* α'-martensite is a characteristic feature of metastable austenitic steels with a low SFE that has a prominent effect on their mechanical properties. The α'-martensite formation is triggered by cooling the metastable austenite below a critical temperature and enhanced by mechanical load [55]. The driving force of the $\gamma \rightarrow \alpha'$ transformation is proportional to the difference in the Gibbs energies of the *fcc* and the *bcc* phase, $\Delta G^{\gamma \rightarrow \alpha'}$, which, in turn, depends on temperature and on the chemical composition of the steel [56]. In metastable austenite, $\Delta G^{\gamma \rightarrow \alpha'}$ is negative below the thermodynamic equilibrium temperature T_0, which is about 600 °C (see Fig. 11.13c) for the austenitic TRIP steel X3CrMnNi16-7-6.

However, as the transformation temperature, which is observed experimentally, e.g., by dilatometry, is affected by several factors, the martensite start temperature (M_S) is introduced that describes the real onset of the phase transformation in terms of a characteristic amount of undercooling. The difference between T_0 and M_S is caused by the obstruction of the $\gamma \rightarrow \alpha'$ transformation—mainly through the formation of the γ/α' interfaces and through the lattice strain resulting from the approx. 2% volume expansion during the $\gamma \rightarrow \alpha'$ transformation. The formation energy of the γ/α' interface and the lattice strain produced by the phase transformation must be compensated by a sufficiently negative value of $\Delta G^{\gamma \rightarrow \alpha'}$. The plastic deformation of austenite caused by external force may aid the martensitic transformation by imposing shear stress that acts as mechanical driving force [55] and by providing favorable nucleation sites for α'-martensite. Thus, a threshold temperature (M_D), below which the deformation-induced martensitic transformation occurs, is located between M_S and T_0.

In high alloy metastable austenitic steels, which possess a low SFE (< 20 mJ/m^2 [12]) and which show the TRIP effect [57], the transformation path follows mostly the $\gamma \rightarrow \varepsilon \rightarrow \alpha'$ sequence [21, 58, 59]. This sequence implies that α'-martensite is

formed predominantly by shearing the previously formed ε-martensite. This particular conclusion is confirmed by the SEM/EBSD micrographs of plastically deformed TRIP steels, which show that α'-martensite arises mainly at the intersections of deformation bands containing ε-martensite (see left-hand side of Fig. 11.16). The stages of the phase transformation are schematically depicted in the middle column and on the left-hand side of Fig. 11.16. The phase transformation starts with a simple arrangement of stacking faults on parallel {111} lattice planes and the formation of deformation bands (panel (1) in Fig. 11.16). When at a higher strain such deformation bands form on crystallographically equivalent {111} planes and intersect, then the intersections provide, according to the Olson-Cohen model [21, 60], favorable nucleation conditions for α'-martensite (panel (2) in Fig. 11.16). The phase transformation within a deformation band can even be triggered by a single stacking fault appearing on a secondary slip plane that crosses the deformation band (Fig. 11.16 panel (2)) [61–63].

According to the Bogers-Burgers mechanism [64], the *fcc* → *bcc* transformation can be realized by two shears on different slip planes, which are equal to $a/18[211]$ on

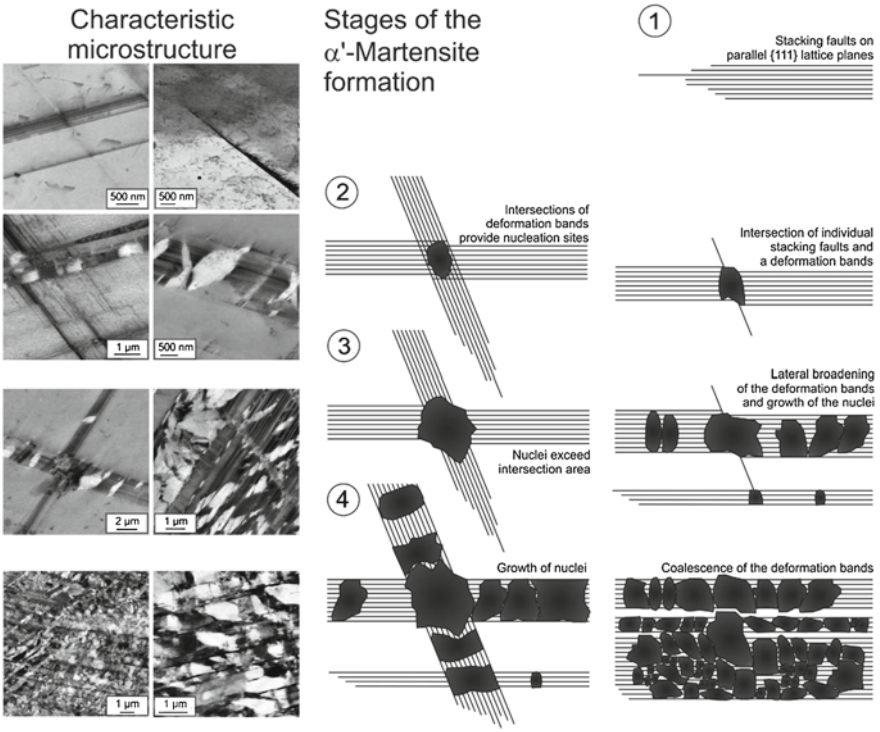

Fig. 11.16 Stages of the deformation-induced α'-martensite transformation in an X2 CrMnNi16-7-6 steel as seen by ECCI (left-hand side), and depicted schematically for nucleation at deformation band intersections (centre) and inside deformation bands (right), respectively

the $(\bar{1}11)$ plane and to $a/12[21\bar{1}]$ on the $(1\bar{1}1)$ plane [60]. The first shear corresponds to one third of the twinning shear; the second shear is equivalent to the shear of partial dislocations passing on every second {111} plane, or within the ε-martensite slab [65]. The resulting local atomic arrangement resembles the *bcc* structure of α'-martensite, and can be described by a hypothetic intersection of a perfect and a faulted ε-martensite bands. The formation of ε-martensite comprises already a shearing (leading to the development of the *hcp* stacking sequences), which reduces significantly the energetic barrier for the α'-martensite nucleation.

Upon further straining, the α'-martensite nuclei grow and eventually outrun the original deformation band at the intersection points (panel (3) in Fig. 11.16). Finally, the α'-martensite nuclei grow together, thus the former deformation bands containing the ε-martensite slabs gradually transform into α'-martensite (panel (4) in Fig. 11.16). Due to the thickening of the α'-martensite regions, the distances between individual deformation bands become smaller and the originally separated α'-martensite regions merge partially, so that entire grains of original austenite transform to α'-martensite.

The mechanism of the α'-martensite formation was confirmed by TEM and FFT/HRTEM (Fig. 11.17). Inside of a deformation band (labelled as (2)), which intersects with few individual SFs but not with a pronounced deformation band, several α'-martensite nuclei (labelled as (3)) were identified. This case was discussed in Fig. 11.16, panel (2), above. In addition to the local phase identification, the FFT/HRTEM patterns from the adjacent regions A, B and C in Fig. 11.17, were used for the analysis of the orientation relationships (ORs) between original austenite (phase 1), faulted ε-martensite (phase 2) and α'-martensite (phase 3). The faulting of austenite and ε-martensite produces diffraction contrasts in the TEM micrograph and perpendicular streaks in the FFT pattern. From the coincidence of the distinct reciprocal lattice points in the FFT/HRTEM patterns, the following parallelisms of

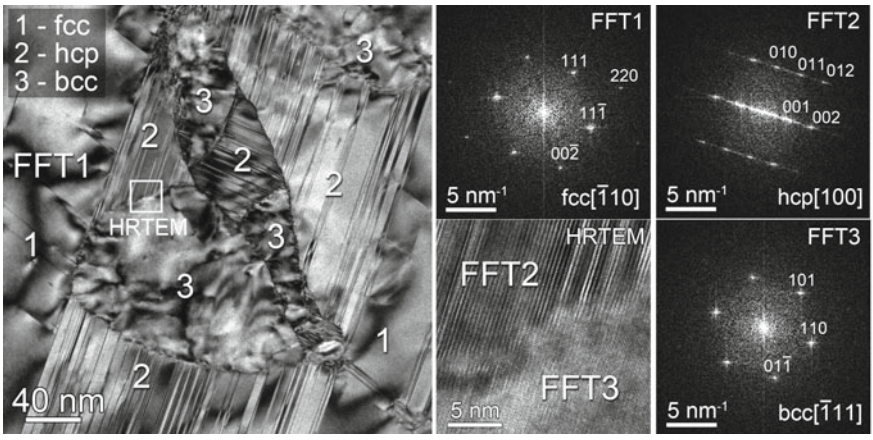

Fig. 11.17 TEM micrograph of the martensitic transformation in a deformation band, FFTs of high-resolution TEM images revealing the local crystal structure and orientation in the marked areas. The crystal structure identified in different regions is indicated by numbers

the close-packed planes and directions were concluded:

$$\{11\bar{1}\}_{fcc} \| \{001\}_{hcp} \| \{110\}_{bcc} \tag{11.12}$$

$$\langle \bar{1}10 \rangle_{fcc} \| \langle 100 \rangle_{hcp} \| \langle \bar{1}11 \rangle_{bcc} \tag{11.13}$$

In literature, these relations are known as Kurdjumow-Sachs OR [66] (for the *fcc*/*bcc* interface) and as Shoji-Nishiyama OR (for the *fcc*/*hcp* interface) [67]. In particular, the OR between *fcc* austenite and *hcp* ε-martensite corroborates the concept of the formation of ε-martensite by stacking faults.

11.4 Quantification of Microstructure Features and Microstructure Defects in TRIP/TWIP Steels, Determination of the Stacking Fault Energy in Austenite

11.4.1 Experimental Methods for Quantitative Microstructure Analysis

The characteristic microstructure features of the TRIP/TWIP steels are the amounts of original metastable γ-austenite and twinned austenite, ε-martensite and α'-martensite, the size of the grains or crystallites of the respective phase, the densities of microstructure defects (mainly dislocations and stacking faults), the preferred orientations of crystallites and the macroscopic or mesoscopic lattice deformations. The mechanisms of the microstructure defect formation and phase transformations were described in Sects. 11.2 and 11.3. Preferred orientation of crystallites is a result of local lattice rotations occurring during the plastic deformation. Macroscopic (elastic) lattice deformations stem from the external load, which is not relieved by the crystal plasticity. Mesoscopic elastic lattice deformations are induced by the interaction of neighboring grains or phases at their interfaces.

From the historical point of view, the first microstructure feature of interest in the TRIP steels was the amount of α'-martensite, as the progress of the martensitic phase transformation was related to the strength and the strain hardening of these steels [68]. For the quantification of the α'-martensite phase fraction, several methods were established. One of them utilizes the measurement of the magnetic permeability by a magnetic balance (ferritescope). The physical background of this method is that α'-martensite is a ferromagnetic phase, while austenite and ε-martensite are not ferromagnetic. The main drawbacks of the permeability measurement are that it cannot distinguish between α'-martensite and δ-ferrite,[2] and that the magnetization of

[2]The δ-ferrite is another ferromagnetic phase that can be retained in austenitic steels as a high-temperature *bcc* phase during the dendritic solidification.

α'-martensite depends on the strain. Hence, the ferritescope must be calibrated using a fully martensitic standard [69]. The advantage of the magnetic measurement is that it covers a large sample volume and provides a good statistics even for coarse-grained cast steels.

As ε-martensite and residual austenite are non-ferromagnetic phases, their amounts are typically quantified using diffraction methods like XRD and EBSD. For the phase identification, γ-austenite is described as an *fcc* phase (structure type Cu) with the lattice parameter about 3.59 Å, ε-martensite as a *hcp* phase (structure type Mg) with the lattice parameters $a \approx 2.54$ Å and $c \approx 4.11$ Å, and α'-martensite as a *bcc* phase (structure type W) with the lattice parameter about 2.87 Å. For the phase quantification, XRD uses the intensity ratios [70]. Nowadays, the phase quantification using XRD is usually carried out by employing the Rietveld analysis of the diffraction pattern [71, 72]. Phase quantification using EBSD is based on the comparison of the respective phase areas.

In comparison to the magnetic measurement, XRD and EBSD probe a significantly smaller sample volume. The penetration depth of X-rays (Cu Kα radiation) in TRIP/TWIP steels is about 8 μm, the irradiated area usually several mm^2. Typical information depth of the backscattered electrons in steels is about 70 nm (at the acceleration voltage of 20 kV), the analyzed area below 1 mm^2. Still, in most cases the amount of α'-martensite determined using XRD agrees very well with the values obtained from the magnetic measurement, as it is illustrated in Fig. 11.18 for several compression steps.

The quantification of the phase fractions using EBSD is generally biased by a low quality of the Kikuchi patterns in the regions that experienced a high local deformation, e.g., within the deformation bands. In such regions, the indexing of the Kikuchi patterns is frequently not possible, thus heavily deformed austenite and ε-martensite are not be considered for the quantitative phase analysis. For this reason, EBSD

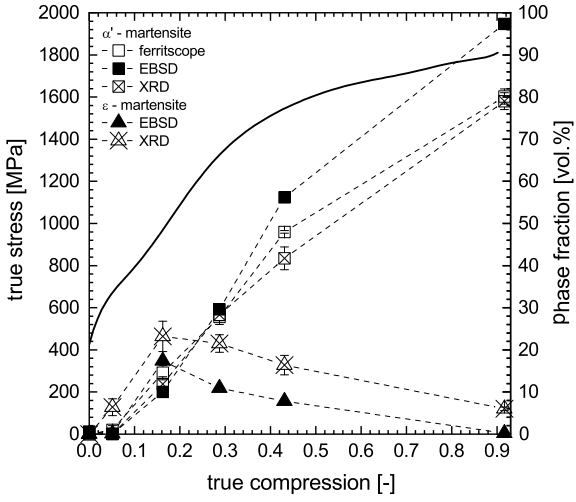

Fig. 11.18 Comparison of the results of the ε- and α'-martensite quantification using magnetic measurement, EBSD and XRD. The stress-strain curve (solid line) shows the deformation state of the PM X3CrMnNi16-7-6 steel

systematically underestimates the amount of ε-martensite, which contains a considerable amount of SFs. Furthermore, thin ε-martensite lamellae having a thickness below 100 nm cannot be resolved by EBSD, because the Kikuchi patterns from the ε-martensite lamellae are superimposed by the Kikuchi pattern from the surrounding (faulted) austenite. Finally, the α'-martensite fraction determined using EBSD in highly strained samples is overestimated at the expense of the deformed austenite, which is not recognized (because not indexed) due to a high defect density. Consequently, XRD provides a better accuracy in determining the ε-martensite fraction than EBSD. The influence of this effect is perceptible in Fig. 11.18, where the results of the quantitative phase analysis using EBSD and XRD are compared.

Another microstructure component, which is important for explanation and modelling of the mechanical behavior of the TWIP steels, is the twinned austenite [12, 73–76]. However, as the strength of the steels is governed rather by the density of the twin boundaries restraining the dislocation slip [75] than by the volume fraction of the twins, the density of the twin boundaries is the relevant quantity, which has to be determined experimentally. However, due to the usually very fine morphology of the twins (thickness ~50 nm), neither SEM nor XRD can quantify the density of the twin boundaries accurately. The typically practiced EBSD orientation mapping [73, 77, 78] cannot account for the very fine twin structure, as its lateral resolution is limited. The twins can be more easily identified by electron channeling contrast (ECC). However, the ECC images are not commonly used as additional information for automated EBSD phase analysis.

The effect of the limited lateral resolution of EBSD on the result of the quantitative microstructure analysis is illustrated in Fig. 11.19. The ECC image reveals twin bundles, which are only partly recognized as twins in the corresponding EBSD mapping. In case of the not recognized twins, the measured Kikuchi pattern is a superposition of the Kikuchi patterns from the matrix and from twins that is indexed according to the dominant diffraction volume, which is the matrix. The only technique, which is capable of resolving the nanoscopic twin structures, is HRTEM (see, e.g., Figure 11.11). However, it is limited to small sampling sizes and therefore it suffers from the statistical unreliability.

The quantification of the twin density in austenite by XRD is difficult, as the twinning causes mainly an *hkl*-dependent asymmetry of the diffraction lines [30]. For low twin densities, the line asymmetry is relatively weak, because the shape of the diffraction lines from the *fcc* phase is dominated by the undisturbed austenite regions, while the contribution of the twins is negligible. Furthermore, the influence of the twinning on the line broadening and shift is small as compared to isolated stacking faults [33].

Still, XRD is capable of quantifying the density of isolated stacking faults in austenite and ε-martensite. In austenite, the isolated stacking faults affect both the positions and the broadening of diffraction lines as described in Sect. 11.2.3.2. In ε-martensite, the presence of isolated stacking faults leads to the broadening of diffraction lines $\beta_{hkl}^{\mathrm{SF}}$ with $h - k = 3n \pm 1$ that is equal to [30, 79]

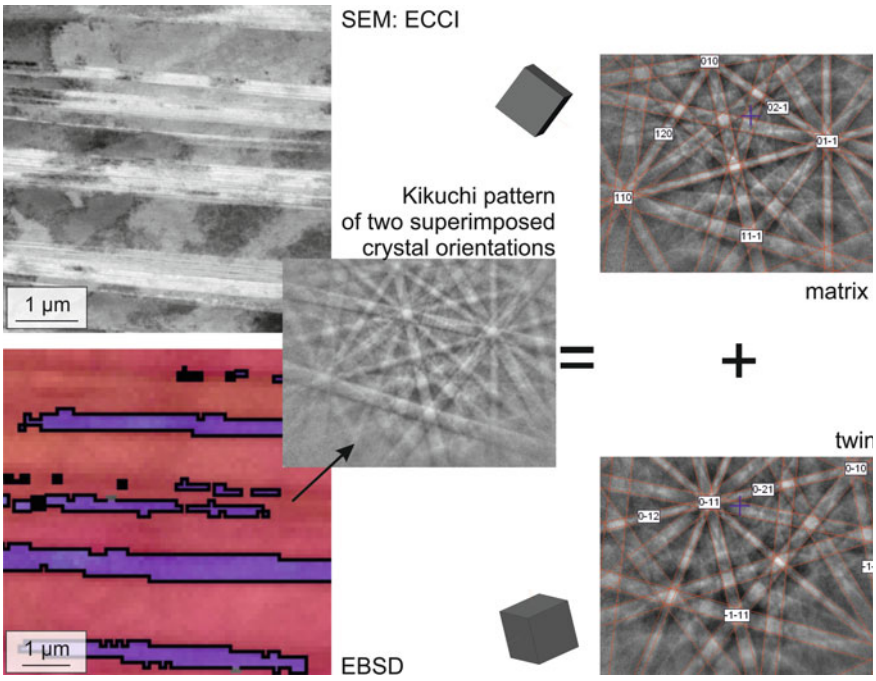

Fig. 11.19 Difficulty of indexing twin bundles by EBSD due to the limited resolution and the superposition of Kikuchi patterns in the fine-scale microstructure

$$\beta_{hkl}^{\mathrm{SF}} = \frac{3l\alpha}{c^2 d_{hkl}^*}, \tag{11.14}$$

where l is the diffraction index, c the hexagonal lattice parameter and d_{hkl}^* the interplanar spacing in the reciprocal space. The densities of dislocations are determined from the *hkl*-dependent line broadening as well. The line broadening caused by dislocations is proportional to the square root of the dislocation density (ρ) and to the square root of the contrast factor of dislocations ($\bar{C}_{hkl}$) [80–85]:

$$\beta_{hkl}^{disl} = \sqrt{\frac{\pi}{2}} M \sqrt{\rho} b \sqrt{\bar{C}_{hkl}} d_{hkl}^* \tag{11.15}$$

Further parameters affecting the magnitude of the line broadening in (11.15) are the Wilkens factor M, the Burgers vector b and the length of the reciprocal space vector (d_{hkl}^*). As the contrast factors describe the elastic response of the material on the presence of dislocations, they are basically calculated from the elastic constants of the material under study [82, 83, 86]. Nevertheless, Ungár et al. showed that for cubic and hexagonal materials, the *hkl*-dependence of the contrast factors must comply with the crystallographic anisotropy of the elastic constants [84, 87]. Therefore, it can be described by the respective crystallographic invariant:

$$\bar{C}_{hkl}^{\text{cub}} = \bar{C}_{100}\left[1 - A\frac{h^2k^2 + k^2l^2 + l^2k^2}{\left(h^2 + k^2 + l^2\right)^2}\right] \tag{11.16}$$

$$\bar{C}_{hkl}^{\text{hex}} = \bar{C}_{hk0} + \frac{\left[2A\left(h^2 + hk + k^2\right) + Bl^2\right]l^2}{\frac{9}{4}\left(ad_{hkl}^*\right)^4} \tag{11.17}$$

The factors A and B characterize the degree of the crystallographic anisotropy. In the computer routines employed for the Rietveld refinement of the XRD patterns, the dependence of the dislocation-induced line broadening on the diffraction indices is calculated using the Popa model [88].

11.4.2 Methods for Determination of the Stacking Fault Energy (SFE) in fcc *Crystals*

As discussed above, the knowledge of the SFE is crucial for the prediction of the deformation behavior of *fcc* metals and alloys, because it determines the occurring deformation mechanisms and consequently the strain hardening. In literature, various attempts to measure the SFE are reported that are mostly based on TEM or XRD methods. The most common TEM technique is the measurement of the separation distance of the partial dislocations [89–92]. Usually, weak beam imaging is utilized to identify the dissociation distance between the partials, which amounts several nanometers and depends on the dislocation character (edge or screw). Indeed, detectable dissociation widths are found in materials with a relatively low SFE only. Another TEM approach examines extended dislocation nodes, in particular the curvature radius, from which the SFE is concluded [93–96]. Some problems might arise from the delicate preparation of thin TEM foils, which can produce undefined strains in the area close to the investigated triangle dislocation node. Another source of systematic errors is a high sensitivity of the width of the dislocation nodes to the local concentration of the alloying atoms [90]. A general drawback of TEM is its limited statistical relevance.

The first technique for the SFE determination using XRD was developed by Dillamore [97, 98], who proposed obtaining SFE from the degree of the preferred orientation of crystallites, and directly from the ratio of two different texture components extracted from the pole figures. The idea behind this approach is that the formation of a crystallographic texture requires cross slip of perfect dislocations, which is a competing mechanism to the dislocation dissociation driven by a low SFE. This method can be applied for a wide range of SFEs, but is purely empirical and offers only a rough estimation of the SFE.

A more reliable XRD technique for the SFE determination is based on the analysis of the broadening and shift of the diffraction lines in XRD patterns of plastically deformed samples [99, 100]. Within this approach, the SFE (γ_{SF}) is proportional to the ratio of the squared dislocation-induced microstrain measured in the ⟨111⟩

direction $\left(\left\langle\varepsilon_{111}^2\right\rangle\right)$ and the SF probability (α):

$$\gamma_{\mathrm{SF}} = \frac{K_{111}\omega_0 G_{111} a_0}{\pi\sqrt{3}} \cdot \frac{\left\langle\varepsilon_{111}^2\right\rangle}{\alpha} \tag{11.18}$$

The microstrain and the SF probability are determined from the line broadening and from the line shift, respectively, using the Warren model [30]. Further quantities in (11.18) are the shear modulus of austenite in the fault plane (G_{111}) and the lattice parameter (a_0). $K_{111}\omega_0$ is a proportionality factor describing the relationship between the microstrain and the dislocation density, the dislocation character and the dislocation interaction [99]. This approach is commonly employed [101–103] despite the problems with the determination of the proportionality factor $K_{111}\omega_0$.

An alternative method for the SFE determination using XRD [104] is based on the proportionality between the SFE and the critical shear stress component (τ_{zx}),

$$\gamma_{\mathrm{SF}} = \frac{\tau_{zx} b_p}{2}, \tag{11.19}$$

that is valid for the formation of very wide stacking faults, [cf. (11.6)]. $b_p = a_0|\langle 211\rangle|/6$ is the magnitude of the Burgers vector of the partial dislocations. According to Copley and Byun [9, 10], the separation distance between partial dislocations follows from the balance of the forces that act on the partial dislocations terminating a stacking fault, and is given by:

$$d_s = \frac{1}{8\pi} \cdot \frac{2-3\nu}{1-\nu} \cdot \frac{G b_p^2}{\gamma_{\mathrm{SF}} - \frac{\tau_{zx} b_p}{2}}, \tag{11.20}$$

see also (11.5). In (11.20), ν is the Poisson ratio and G the shear modulus. If the distance between the partials becomes 'infinite', the work resulting from the impact of the shear stress component τ_{zx} on the partials must be in equilibrium with the stacking fault energy as described by (11.19). In the XRD approach from [104], the shear stress τ_{zx} is calculated from a (uniaxial) internal stress σ_x, which is needed to produce 'infinitely' wide SFs, and from the mean Schmid factor (M) that corresponds to the respective deformation state

$$\tau_{zx} = M\sigma_x. \tag{11.21}$$

The stress σ_x is proportional to the 'residual' elastic lattice deformation, which remains in the austenite after the plastic deformation. If the applied load is uniaxial and if the lattice deformation is measured in a direction perpendicular to this load [105], then the proportionality between stress and deformation is described by

$$\varepsilon_z^{hkl} \equiv \frac{d_z^{hkl} - d_0}{d_0} = s_1^{hkl}\sigma_x, \tag{11.22}$$

where $s_1^{hkl} = -\nu^{hkl}/E^{hkl}$ is the X-ray elastic constant (XEC) of austenite. The indices *hkl* emphasize the crystallographic anisotropy of the elastic constants. As for cubic materials, the interplanar distances can be converted directly to the lattice parameters,

$$\varepsilon^{hkl} \equiv \left\langle \frac{d^{hkl} - d_0}{d_0} \right\rangle = \left\langle \frac{a^{hkl} - a_0}{a_0} \right\rangle, \tag{11.23}$$

the internal stress in *fcc* austenite can be determined from the measured lattice parameters a^{hkl}. However, as the presence of the stacking faults leads to additional shift of the diffraction lines, [cf. (11.10)], the lattice parameter affected by the internal stress and stacking faults has the form of [104, 105]

$$\begin{aligned} a^{hkl} &= a_0\left(1 + \sigma_x s_1^{100}\right) + 3a_0\left(s_1^{111} - s_1^{100}\right)\sigma_x \Gamma_{hkl} \\ &+ \frac{\sqrt{3}}{4\pi} a_0 \alpha G_{hkl}^{\mathrm{SF}} - a_0 \cot\theta \, \Delta\theta \end{aligned} \tag{11.24}$$

a_0 is the intrinsic lattice parameter of austenite (unaffected by internal stress and SFs), α the SF probability and $G_{hkl}^{\mathrm{SF}} = \sum_{af} \pm(h + k + l)/\left[\left(h^2 + k^2 + l^2\right)m_{hkl}\right]$ the contrast factor of SFs from (11.10). In (11.24), the XEC s_1^{hkl} was replaced by

$$s_1^{hkl} = s_1^{100} + 3\Gamma_{hkl}\left(s_1^{111} - s_1^{100}\right), \tag{11.25}$$

where

$$\Gamma_{hkl} = \frac{h^2k^2 + k^2l^2 + l^2h^2}{\left(h^2 + k^2 + l^2\right)^2} \tag{11.26}$$

is the cubic invariant describing the crystallographic anisotropy of XECs. The last term in (11.24) describes the correction of the measured lattice parameters for instrumental aberrations, which cause a line shift $\Delta\theta$. The fitting of measured lattice parameters with the function from (11.24) yields the intrinsic lattice parameter of austenite (a_0), the internal stress (σ_x) and the SF probability (α). Finally, the internal stress is used for calculation of the SFE:

$$\gamma_{\mathrm{SF}} = \frac{\tau_{zx} b_p}{2} = \frac{1}{2} M \sigma_x \frac{a_0}{6} |\langle 211 \rangle| = \frac{\sqrt{6}}{12} M \sigma_x a_0 \tag{11.27}$$

Another important method is the SFE calculation. Within the thermodynamic approach [23, 25, 106, 107], the SFE is calculated from the difference in the Gibbs energies of austenite and ε-martensite and from the strain and interface energies resulting from the faulting, see Sect. 11.2.3.1. The thermodynamic calculations are applied mainly to estimate the influence of certain alloying elements on the SFE. Nowadays, they are increasingly complemented by first-principles studies [24, 108].

However, if not based on experimental data, the modelled predictions often fail in giving reasonable trends, and show a systematic offset [107]. Therefore, the SFE calculations must be combined with experimental studies [92] or supported by other approaches like multivariate linear regression [109] or data driven machine-learning [110] in order to be verified.

11.4.3 In Situ Diffraction Studies on TRIP/TWIP Steels During Plastic Deformation

The capability of XRD methods to track the microstructure changes in TRIP/TWIP steels during their plastic deformation was tested on samples containing 3, 6 and 9 wt% Ni (PM X4CrMnNi16-7-3, X3CrMnNi16-7-6, PM X2CrMnNi16-7-9) that possess different SFEs and consequently different stabilities of metastable austenite. One part of the in situ XRD experiments was performed with a laboratory source under bending the samples in a four-point bending apparatus (Fig. 11.20). Advanced synchrotron XRD experiments were carried out at the PETRA III/DESY beamline P07 in Hamburg (Germany) in a deformation dilatometer.

During the XRD measurement in the four-point bending apparatus from Fig. 11.20, the total deformation force and the amount of the bending are measured in addition to the XRD patterns. These quantities are converted into the mechanical tensile stress σ_x^{mech} and into the strain in the outer fiber $\varepsilon_x^{\text{mech}}$ [105], respectively. The lattice parameters obtained from the line positions are plotted for selected deformation states as function of $3\Gamma_{hkl}$, cf. Fig. 11.21 and (11.24). In Fig. 11.21, the slope of the diagram is proportional to the internal stress σ_x, the departure of the lattice parameters from the linear dependence scales with the SF probability. As the measured line positions were corrected using an internal standard, the line shift in (11.24) was set to zero for fitting ($\Delta\theta = 0$).

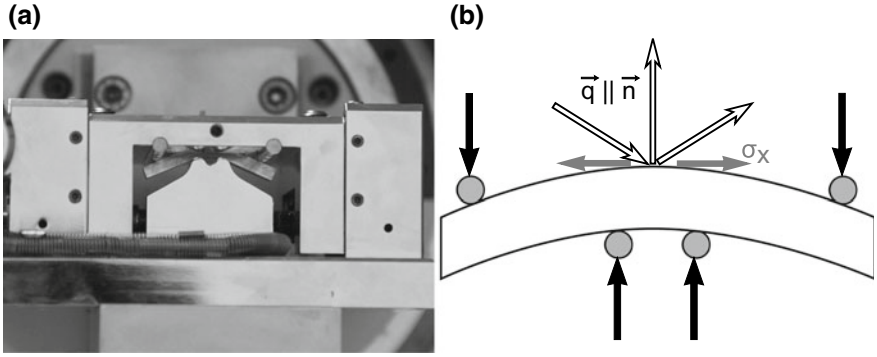

Fig. 11.20 Bending table used for the in situ XRD experiments (**a**). The beam path is shown schematically by the hollow arrows in (**b**)

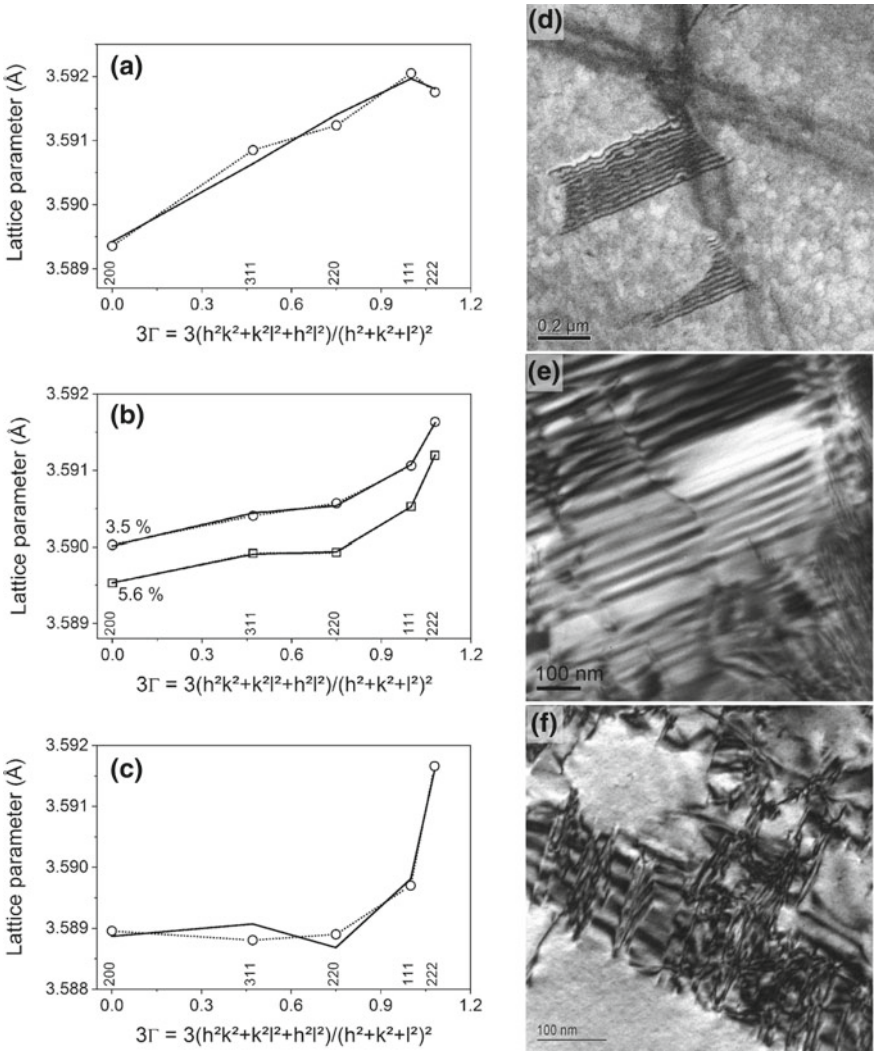

Fig. 11.21 Left-hand side: Lattice parameters of austenite deformed at the strains in the outer fiber of 1% (**a**), 3.5% and 5.6% (**b**), and 8.3% (**c**). Measured lattice parameters are plotted by interconnected open symbols, the lattice parameters fitted using (11.24) by solid lines. Corresponding TEM micrographs (d–f) at the right-hand side of the figure were taken in samples deformed to 0.5, 5 and 9%. Adopted from [104, 105]

The comparison of the measured lattice parameters with the lattice parameters fitted using (11.24) shows that the applied microstructure model is not valid for all deformation states (Fig. 11.21). While an excellent agreement between the measured and the calculated (fitted) lattice parameters was achieved for medium deformation states (Fig. 11.21b), the microstructure model cannot explain the anisotropy of the

lattice parameters observed at the lowest and highest deformations (Fig. 11.21a, c). The reason for the observed discrepancies is the invalidity of the Warren model for short (Fig. 11.21d) and crossing (Fig. 11.21f) stacking faults. Consequently, the application of this microstructure model to the measured lattice parameters can be used for verification of the presence of wide but non-intersecting SFs.

In Fig. 11.22, the lattice parameters a_0, the SF probabilities and the in-plane stresses (σ_x) are plotted against the strain in the outer fiber, and compared with the changes in the phase composition of the steel. As the intrinsic lattice parameter a_0 is supposed to stay constant during the deformation, its increase observed for $\varepsilon_x^{\text{mech}} < 2\%$ and $\varepsilon_x^{\text{mech}} > 6\%$ is another indicator of the invalidity of the Warren SF model. Analogously, the apparently negative SF probability observed for $\varepsilon_x^{\text{mech}} < 2\%$ is related to the early stage of the SF formation (cf. Fig. 11.21d). From the difference of the stress values σ_x, $\sigma_{\parallel}(311)$ and $\sigma_{\parallel}(222)$ in Fig. 11.22d, it can be supposed that the interaction of the local strain fields produced by partial dislocations in narrow SFs changes the crystallographic anisotropy of the SFs contrast factors. The SF crossing at larger deformations ($\varepsilon_x^{\text{mech}} > 6\%$, cf. Fig. 11.21f) leads to an apparent change of the crystallographic anisotropy of XECs, which can be seen on the difference

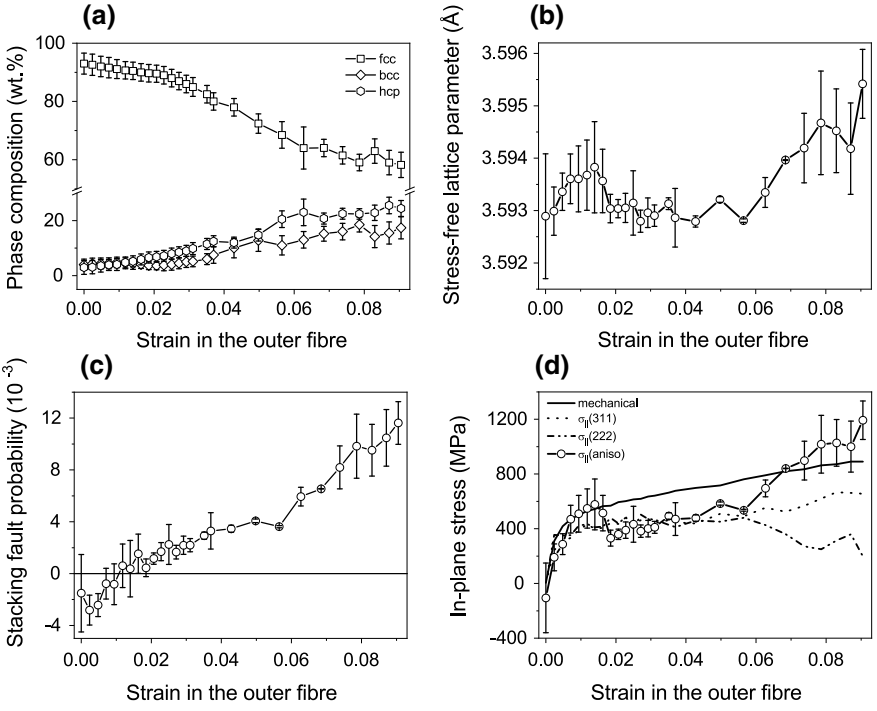

Fig. 11.22 Changes in the phase composition (**a**) and microstructure characteristics of the TRIP steel during plastic deformation. The lattice parameter a_0 (**b**), SF probability (**c**) and the internal stress in austenite σ_x (**d**) were obtained by fitting the measured lattice parameters according to (11.24)

between $\sigma_{\parallel}(311)$ and $\sigma_{\parallel}(222)$. These stresses were calculated directly from the lattice deformations measured in the respective crystallographic direction:

$$\sigma_{\parallel}(hkl) = \left(s_1^{hkl}\right)^{-1} \frac{d^{hkl} - d_0}{d_0} = \left(s_1^{hkl}\right)^{-1} \frac{a^{hkl} - a_0}{a_0} \tag{11.28}$$

The XECs, $s_1^{311} = -1.60 \times 10^{-12}\,\mathrm{Pa}^{-1}$, $s_1^{222} = s_1^{111} = -9.52 \times 10^{-13}\,\mathrm{Pa}^{-1}$ and $s_1^{100} = s_1^{200} = -2.17 \times 10^{-12}\ \mathrm{Pa}^{-1}$, were calculated using the Kröner approach [111] from the single-crystalline elastic constants of austenite, i.e., $C_{11} = 1.975 \times 10^{11}$, $C_{12} = 1.245 \times 10^{11}$ and $C_{44} = 1.220 \times 10^{11}$ Pa that were taken from the Landolt-Börnstein database [112].

The comparison of the SF densities (Fig. 11.22c) with the phase compositions (Fig. 11.22a) and the corresponding TEM micrographs (Fig. 11.21d–f) confirmed that up to $\varepsilon_x^{\mathrm{mech}} \cong 2\%$, the deformation behavior of austenite is dominated by the formation and widening of SFs. For $\varepsilon_x^{\mathrm{mech}}$ above 2%, the SF density increases, which leads to the local ordering of SFs that is recognized by XRD as the ε-martensite formation. At the deformations above 6%, the SFs form also on crystallographically equivalent lattice planes {111} and interact, which facilitates the formation of α'-martensite as explained in Sect. 11.3.

The validity range of the Warren model that was identified by the above routine was used for calculation of the SFE from the internal stress (σ_x, $\sigma_{\parallel}(311)$ or $\sigma_{\parallel}(222)$) and from the lattice parameter a_0 measured by XRD. For the SFE calculation, (11.27) was employed. As the change in the preferential orientation of crystallites was negligible in this deformation range, the Schmid factors were assumed constant (independent of the deformation state) and obtained from the EBSD measurements that were carried out on non-deformed samples. The SFEs determined using this method were 17.5 $\pm$ 1.4 mJ m^{-2} for the TRIP steel X3CrMnNi16-7-6 and 8.1 $\pm$ 0.9 mJ m^{-2} for the TRIP steel X4CrMnNi16-7-3 [104], and 24.1 $\pm$ 2.5 mJ m^{-2} for the TRIP steel X2CrMnNi16-7-9.

For a comprehensive description of the microstructure development during plastic deformation, the TRIP/TWIP steels PM X4CrMnNi16-7-3, X3CrMnNi16-7-6 and PM X2CrMnNi16-7-9 containing 3, 6 and 9 wt% Ni, respectively, were investigated using in situ synchrotron diffraction during compression [113]. In the non-deformed state, the samples had cylindrical shape ($\varnothing$ 4 mm $\times$ 8 mm), and were fully austenitic and fine-grained. The synchrotron diffraction experiments were carried out at beamline P07 of PETRA III at DESY (Hamburg, Germany). The high energy and the short wavelength of the synchrotron radiation (100 keV, $\lambda = 0.1235$ Å) enabled measurements in transmission diffraction geometry, which is more appropriate for explanation of the bulk materials properties than the surface-sensitive laboratory XRD studies [114]. Furthermore, the short wavelength of the synchrotron radiation provided a broad coverage of the reciprocal space up to

$$q = \frac{2\pi}{d} = \frac{4\pi \sin\theta}{\lambda} = 8.87\,\text{Å}^{-1}, \tag{11.29}$$

which is beneficial for measurements in a broad range of the diffraction indices *hkl*, especially in materials with relatively small elementary cell. For austenite, nine diffraction peaks were recorded (up to 422). In (11.29), q is the maximum magnitude of the diffraction vector and d the minimum interplanar spacing that are accessible at the maximum diffraction angle $2\theta = 10°$ and at the wavelength of 0.1235 Å. High flux of the synchrotron beam enables real in situ measurements. Relaxation effects in the sample during the acquisition of the individual diffraction patterns (measuring time about 1 s) are almost eliminated.

The samples were deformed in a deformation dilatometer (BÄHR DIL 850) until the maximum force, corresponding to a technical stress of 1590 MPa. The in situ compression was carried out in 35 quasi-static discrete load steps. The holding time between the deformation steps (approx. 1 s) resulted from the time that was needed for recording the diffraction patterns. The load direction was perpendicular to the direction of the primary synchrotron beam (Fig. 11.23). In this diffraction geometry, the angle Ψ between the load direction and the diffraction vector varies between $2\theta/2$ and 90° along the Debye rings. The continuous change of the angle Ψ allows the determination of internal stresses and preferred orientations of crystallites in all present phases from a single 2D diffraction pattern.

For the analysis of the 2D diffraction patterns, the recorded images were integrated in 5° wide sections along the Debye rings in order to conserve the Ψ-dependent information. The 72 diffraction patterns (diffracted intensities versus diffraction angles for individual Ψ sections, see Fig. 11.24) were subjected to a coupled Rietveld refinement using MAUD [115, 116]. The microstructure models employed for the Rietveld refinement of individual diffraction patterns included: (i) anisotropic line broadening from perfect dislocations according to the Popa model [88], (ii) anisotropic line

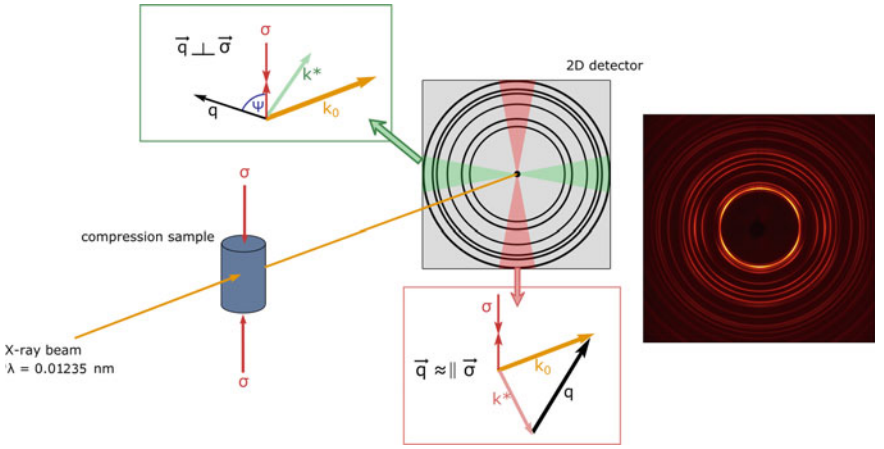

Fig. 11.23 Setup of the in situ compression tests in transmission geometry. The sketches in the green and red boxes show the alignment of the diffraction vector that is perpendicular and nearly parallel to the load direction in the correspondingly colored segments of the 2D diffraction pattern. On the right-hand side of the panel, a single 2D diffraction pattern is shown

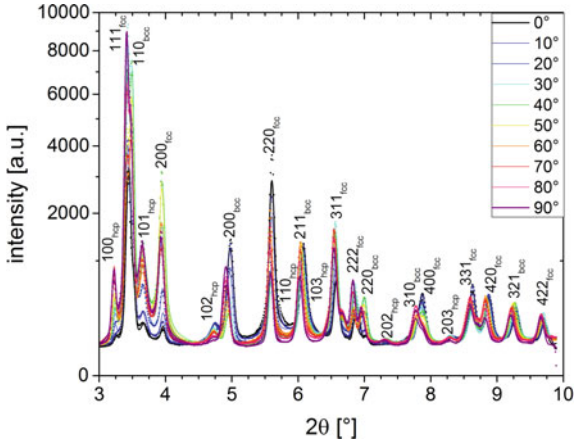

Fig. 11.24 The 1D diffraction patterns integrated over 5° wide segments of the 2D diffraction pattern from Fig. 11.23

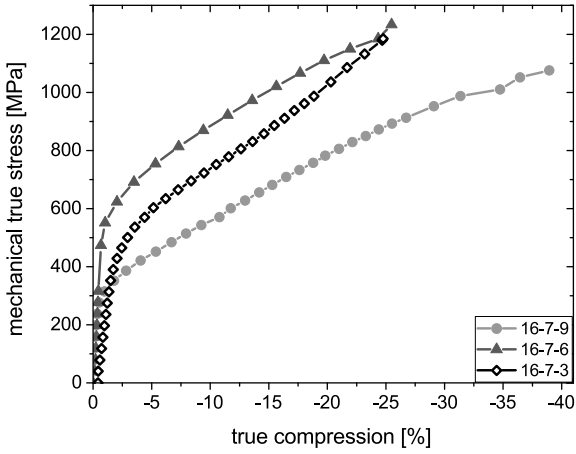

Fig. 11.25 True stress—true strain curves measured during the compressive deformation of the 16Cr-7Mn-xNi steels. Adopted from [113]

broadening and anisotropic line shift caused by SFs according to the Warren model [30] and (iii) anisotropic line shift caused by anisotropic elastic lattice deformation according to the Moment Pole Stress model [117]. In the Moment Pole Stress model, only the stress component σ_{33} was considered. The same elastic constants of the austenite were used like for the in situ XRD experiments during bending. Fractions of individual phases were determined after the diffracted intensities have been corrected for preferred orientations of crystallites using the Ψ dependence of the diffracted intensities [115, 118], because the texture correction improves significantly the reliability of the quantitative phase analysis [119].

Mechanical behavior of the Cr–Mn–Ni 16-7-x TRIP/TWIP steel samples during the compressive load is depicted in Fig. 11.25. The deformation and the applied force were measured by the dilatometer and converted to true stress and true strain. The material with the highest SFE (24.1 mJ/m^2) and with the highest Ni content

(9%) exhibits the lowest stress level and a nearly constant strain hardening. This kind of strain hardening is commonly associated with the TWIP effect [120]. The sample with the lowest SFE (8.5 mJ/m^2) and lowest Ni content (3%) possesses the most pronounced strain hardening, which results in a sigmoidal flow curve that is characteristic for intense martensitic transformation [121]. In the sample containing 3 wt% Ni, the formation of ε-martensite begins at ca. 1% compression.

The maximum amount of ε-martensite (about 19 vol%) is reached at 20% deformation (Fig. 11.26). The α'-martensite forms at relatively low deformations. At the deformation of 15%, it becomes the dominant martensitic phase, which grows at the expense of austenite and ε-martensite at deformations exceeding 20%. In sample X2CrMnNi16-7-9, the formation of ε-martensite is delayed and the α'-martensite does not form up to a 40% compression. This dependence of the martensites formation on the Ni content is a result of a lower driving force for the martensitic transformation in materials with higher SFE that was discussed in Sects. 11.2.3 and 11.3. The sample containing 6% Ni (SFE = 17.5 mJ/m^2) shows almost constant strain hardening like the steel X2CrMnNi16-7-9, while the development of the phase composition resembles the TRIP steel with 3 wt% Ni. However, the stress level in sample X3CrMnNi16-7-6 measured beyond the onset of the plastic deformation is clearly too high. The results of the diffraction analysis (see below) support the assumption that the high stress level is related to an incompletely recrystallized initial microstructure.

The σ_{33} component of the internal stress in austenite, which is parallel to the applied compression, increases during the sample compression (Fig. 11.27a), but is constantly lower than applied mechanical stress (cf. Fig. 11.25). The increase of σ_{33} indicates the strain hardening that is caused by the increase of dislocation density and thus by the increase of dislocation-induced microstrain (Fig. 11.28), and by the interaction of dislocations in austenite with the newly formed martensites [113].

The interplay of these effects can be illustrated on the lowest internal stress (Figs. 11.24 and 11.27a), lowest microstrain (Fig. 11.28) and delayed martensite

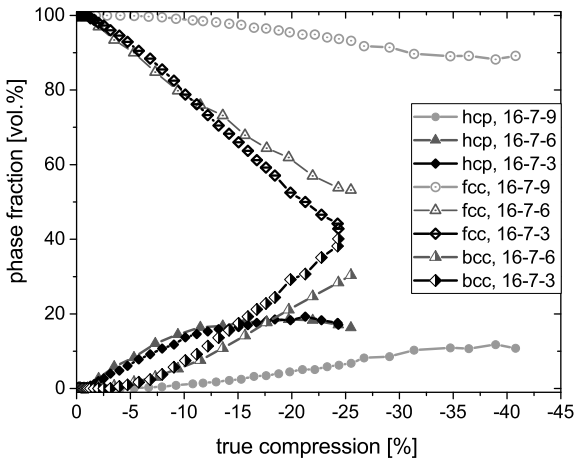

Fig. 11.26 Phase fractions of *fcc* austenite, *hcp* ε-martensite and *bcc* α'-martensite during the deformation of the samples. Adopted from [113]

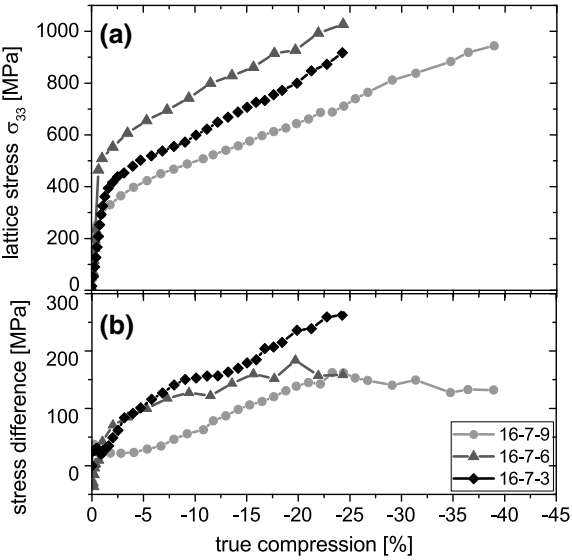

Fig. 11.27 **a** Internal elastic lattice stress in austenite in the compression direction, obtained from the in situ synchrotron diffraction. **b** Difference between the (total) mechanical true stress from Fig. 11.25 and the lattice stress, adopted from [113]

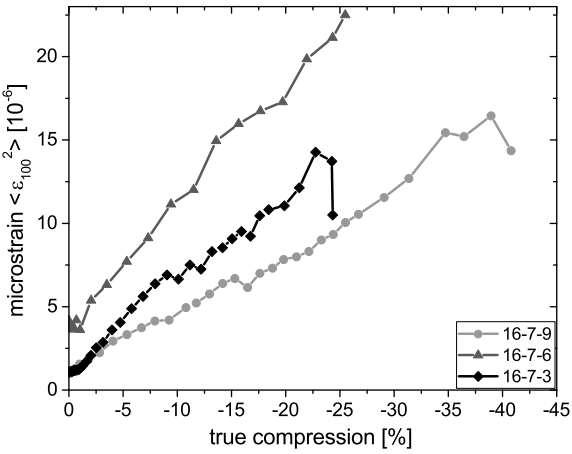

Fig. 11.28 Squared microstrain—a quantity proportional to the dislocation density

formation (Fig. 11.26) in sample X2CrMnNi16-7-9. Weaker defect formation and retarded martensitic phase transformation are also the reasons for the smallest difference between the applied mechanical stress and internal (elastic) lattice stress in sample X2CrMnNi16-7-9 (Fig. 11.27b).

The largest difference between the mechanical stress and σ_{33} observed in sample X4CrMnNi16-7-3 for deformations beyond 7.5% suggests that newly formed martensites carry a significant part of the external load. In this deformation range, the amount of α'-martensite increases most quickly in the steel with lowest Ni content (sample X4CrMnNi16-7-3 in Fig. 11.26).

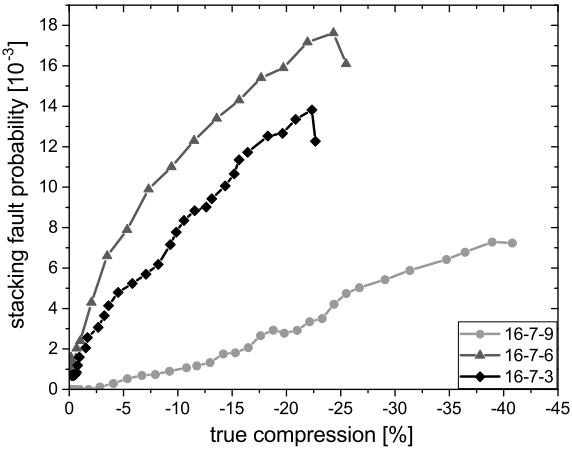

Fig. 11.29 Evolution of the probability of isolated intrinsic stacking faults in austenite under compression

The stacking fault probabilities (SFPs, Fig. 11.29) correlate generally with the amount of ε-martensite (Fig. 11.26), because the ε-martensite is formed by the ordering of dense stacking faults, see Sect. 11.2. For this reason, both quantities are expected to increase with decreasing SFE. Still, at the lowest deformations, the SFs must be created before ε-martensite can form, thus the initial increase of SFP occurs always earlier, i.e., at lower strains than the onset of the ε-martensite formation. The steep increase of the SFP in samples X4CrMnNi16-7-3 and X3CrMnNi16-7-6 and the early onset of the ε-martensite formation indicate the dominant role of stacking faults as deformation mechanism. The unexpectedly high SFP in the deformed steel X3CrMnNi16-7-6 as compared with the SFP in the steel X3CrMnNi16-7-3 (Fig. 11.29) is caused by a higher density of dislocations in incompletely recrystallized initial sample X3CrMnNi16-7-6 (Fig. 11.28). The lowest SFPs were measured for the 9% Ni steel, because this steel possesses the highest SFE. Especially in this steel, the onset of the SF formation is slightly delayed (shifted to higher strains), because the initial deformation is realized by dislocation slip. Because of its higher SFE, the formation of twins is expected in this steel, but the presence of the twins cannot be evidenced easily from the diffraction data.

Although the formation of SFs and the martensitic transformations are the dominant deformation mechanisms in the TRIP steels, the role of perfect dislocations is not neglectable, because the perfect dislocations are the precursors of partial dislocations, SFs and ε-martensite (or twins in TWIP steels). In order to visualize the development of the dislocation density in the TRIP/TWIP steels during their plastic deformation, the squared microstrain $\langle \varepsilon_{100}^2 \rangle$ was plotted as a function of the true compression in Fig. 11.28. According to Wilkens [122], the squared microstrain is proportional to the dislocation density [cf. (11.15)]

$$\left\langle \varepsilon_{hkl}^2 \right\rangle = \frac{\pi}{8} M^2 \rho b^2 \bar{C}_{hkl}, \tag{11.30}$$

and can be determined directly from the dependence of the diffraction line broadening on the magnitude of the diffraction vector ($|\vec{q}| = 2\pi d^*_{hkl}$):

$$\beta_{hkl} = \frac{K}{D} + \beta^{\mathrm{SF}}_{hkl} + 2\sqrt{\langle \varepsilon^2_{hkl} \rangle} \cdot d^*_{hkl}. \tag{11.31}$$

Additional contributions to the measured line broadening stem from the (small) crystallite size (K/D) and from stacking faults ($\beta^{\mathrm{SF}}_{hkl}$), [cf. (11.14)].

In the steels containing 3 and 6% Ni, the dislocation-induced microstrain increases steeply during initial straining (Fig. 11.28). The offset of both curves is caused by the incompletely recrystallized initial microstructure of sample X3CrMnNi16-7-6 that contained a higher dislocation density. The higher dislocation density persists throughout the whole deformation process, and accounts for the higher SFP, higher lattice stress level and more intense ε-martensite formation in this sample. While the squared microstrain in steel X3CrMnNi16-7-6 increases almost linearly with increasing deformation, in the steel with a lower Ni concentration (X4CrMnNi16-7-3) the increase of the squared microstrain is reduced after ca. 9% compression, due to an intense stacking fault formation and martensitic transformation. The squared microstrain in the steel X2CrMnNi16-7-9 increases also almost linearly, but its increase is slower than in the steel X3CrMnNi16-7-6.

The comparison of the evolution of the dislocation-induced microstrain in the three steels under study suggests that the dislocation density and consequently the expected contribution of the dislocation slip to the plastic deformation decreases with decreasing SFE. Other deformation mechanisms such as the formation of stacking faults and phase transformations become dominant [113]. This change in the dominant deformation mechanism goes along with the transition from the TWIP to the TRIP behavior, and can be substantiated by microscopic studies using, e.g., ECCI and EBSD.

The ECCI and EBSD micrographs of the TRIP/TWIP steels deformed up to the maximum compression depicted in Fig. 11.30 show dislocation arrangements, stacking faults, deformation bands and α'-martensite nuclei. The characteristic microstructure features of the 3% Ni steel are pronounced deformation bands existing on several slip planes, single stacking faults and regions transformed to α'-martensite (Fig. 11.30a). The 6% Ni steel (Fig. 11.30b) exhibits similar features, which are finer scaled because of the incompletely recrystallized initial microstructure. Distinct dislocation structures and their mutual interactions can be seen in deformed steel X2CrMnNi16-7-9 (Fig. 11.30c), where some deformation bands become curved due to their intense interaction with the dislocation arrangements. As twins in austenite are hardly to be distinguished from ε-martensite using ECCI (see Sect. 11.4.1), the nature of the deformation bands and the relative density of the stacking faults within the bands were investigated by EBSD in the 9% Ni steel (Fig. 11.30d).

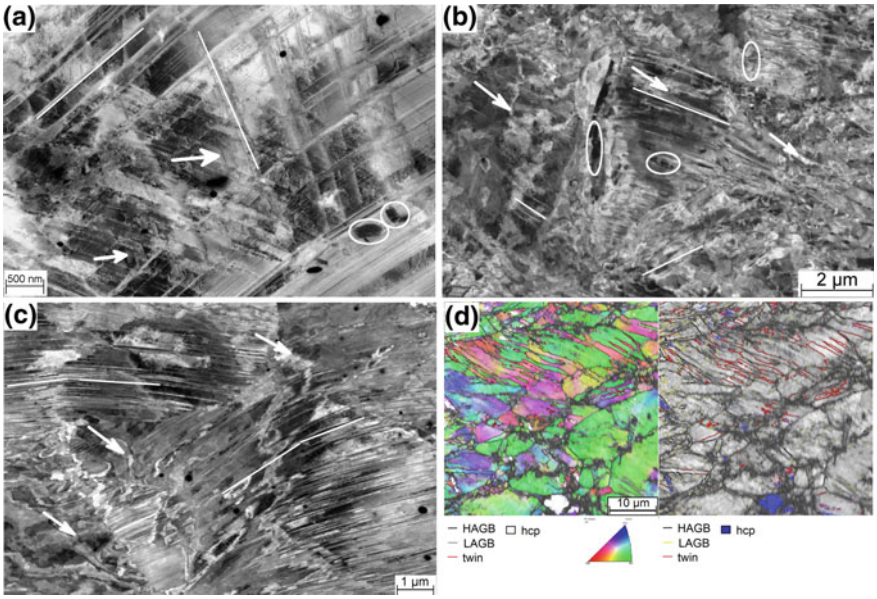

Fig. 11.30 SEM microstructure characterization of deformed samples after the respective maximum compression. **a** ECC image of the 3% Ni steel showing deformation bands (lines), single stacking faults (arrows) and α'-martensite nuclei (circles). **b** ECC image of the highly defective microstructure in the 6% Ni steel showing deformation bands (lines), dislocation arrangements (arrows) and α'-martensite nuclei (circles). **c** Curved deformation bands (lines) and dislocation structures (arrows) in the 9% Ni sample. **d** EBSD maps of this sample, at the left: grain orientation and grain boundaries, especially twins (red lines), as well as local occurrence of *hcp* ε-martensite (white); at the right: mapping of the same area, grain and twin boundaries are plotted together with the band contrast (gray)

11.5 Interplay of Deformation Mechanisms, Development of Deformation Microstructure

11.5.1 Interaction of Microstructure Defects in Deformation Bands

The formation of deformation bands plays a central role in the strain hardening of austenitic steels. As discussed above, the deformation bands accommodate dense SFs that serve as precursors of martensitic phase transformations and twinning in austenite. From the micromechanical point of view, the deformation bands produce strain fields, which interact with the microstructure defects existing outside of the deformation bands. This interaction is illustrated by the TEM image shown in Fig. 11.31, where a deformation band formed on the primary slip system acts as an obstacle for the motion of SFs and for the dislocation slip on the secondary slip systems. The interaction between the primary deformation band and the dislocations gliding on the

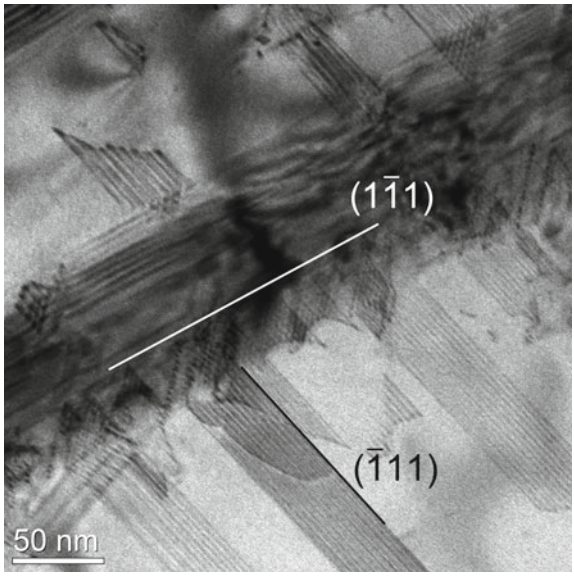

Fig. 11.31 TEM micrograph evidencing the obstacle effect of a deformation band for the dislocation motion on secondary slip systems. Adopted from [34]

secondary slip systems reduces the mean free path length of the dislocations [120, 123, 124], which is a phenomenon that is known as dynamic Hall-Petch effect.

A secondary stacking fault impinging a twin or deformation band must constrict, which means that the partial dislocations of the SF must recombine in order to be able to react with the stacking fault arrangement. Such a dislocation reaction is energetically unfavorable, and can only occur under a local stress concentration [125]. The interactions between deformation bands and other microstructure defects are illustrated exemplarily in Fig. 11.31, where the secondary stacking faults ($\bar{1}$11) that are stopped at the deformation band on the (1$\bar{1}$1) plane seem to constrict partially, but a straight intersection of SFs located on the primary slip system by the SFs located on the secondary slip system is not observed.

Furthermore, the presence of the deformation bands inhibits the annihilation of nearly perfect dislocations having opposite Burgers vectors, as these dislocations are simply separated from each other. The annihilation of dislocations is additionally obstructed by their reduced cross-slip. The deformation bands also impede an arrangement of the dislocations in lower-energetic cell structures. Hence, the presence of deformation bands suppresses the dynamic recovery and enhances the dislocation storage capacity of the material. Dislocations accumulate in the interspace between the deformation bands much more than in materials without planar defects. This finding is confirmed by the continuous increase of the dislocation-induced microstrain measured by XRD in compressed steel PM X5CrMnNi16-6-9 (Fig. 11.32). The simultaneously increasing SF probability indicates that the stacking faults form during the whole deformation process, also on secondary slip systems, contribute continuously to a refinement of the microstructure, and thus maintain a high strain-hardening rate by reducing the mean free paths of gliding dislocations.

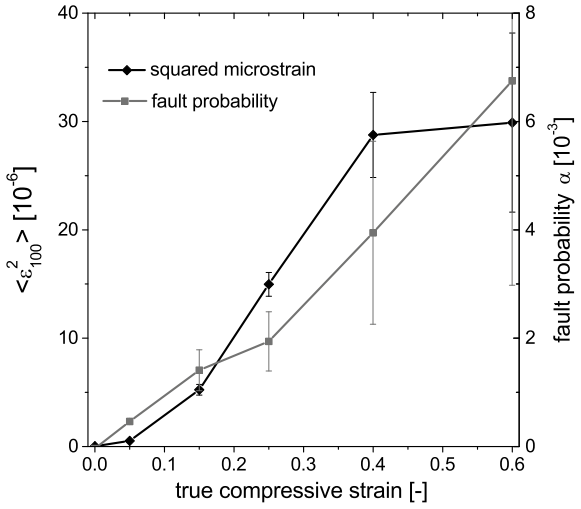

Fig. 11.32 Trends of squared microstrain and SF probability for a deformed PM X5CrMnNi16-6-9 steel evidencing the reduced recovery and resulting high dislocation density [34]

The interactions of microstructure defects discussed above can be found in deformation bands containing isolated SFs and concentrated SFs in form of ε-martensite and twins in austenite. Nevertheless, the extent of the interaction increases with the SF density, thus it is superior for imperfect twins. Correspondingly, enhanced strain hardening was reported for the TWIP steels showing no martensitic transformation [12, 120, 126].

If α'-martensite forms within the deformation bands, even enhanced strengthening is observed. The dislocation glide within the deformation bands is additionally obstructed by the newly formed phase boundaries. The mechanisms of the deformation band formation and the strengthening by the α'-martensite nucleation are summarized in Fig. 11.33.

During plastic deformation, the equilibrium dissociation width of beneficially oriented partial dislocations in austenite (1) is increased by external applied shear stress (2). New dislocations are generated and the deformation band forms (3), which is accompanied by conventional cold work strengthening. Formation of SFs and deformation bands on the secondary slip systems produces local strain fields that facilitate the nucleation of α'-martensite (4) having a specific volume of about 2.5% larger than austenite. The α'-martensite boundaries and the lattice strains resulting from the volume expansion are hard obstacles for the dislocation motion. They pin existing SFs, thus the further plastic deformation produces new (perfect) dislocations alongside the existing deformation band and leads to their dissociation (5). This explains the observed lateral growth of the deformation bands [40] and the high volume fraction of the ε-martensite of ≤ 25 vol% (Figs. 11.18 and 11.26) at moderate stages of straining.

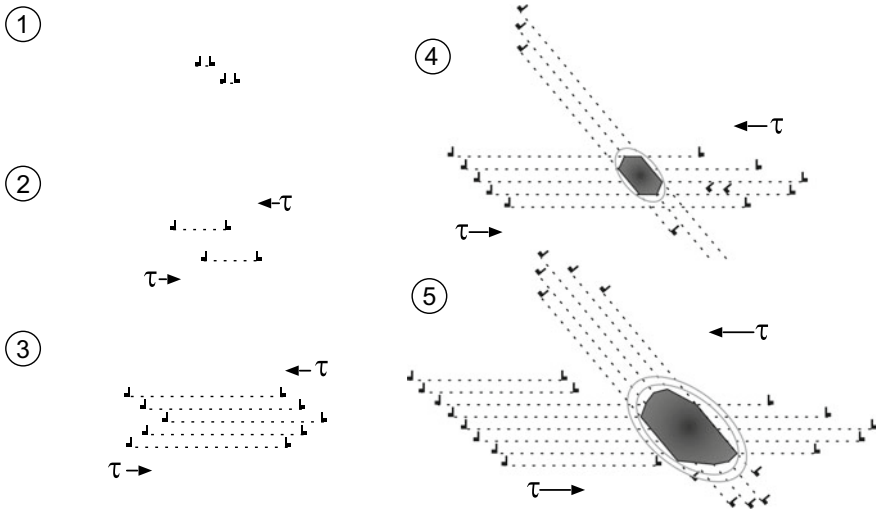

Fig. 11.33 The interplay of the deformation band formation and the α'-martensite nucleation contributes additionally to the strain hardening in austenite. Adopted from [61]

11.5.2 Orientation Dependence of the Stacking Fault and Deformation Band Formation

A complex, heterogeneous microstructure is observed in deformed austenitic steels, even if they consist of equiaxed grains with unimodal grain-size distribution. As shown in the ECCI micrograph in Fig. 11.34, in some grains the stacking faults and deformation bands dominate, whereas other grains are free of planar defects and exhibit dislocation structures instead.

These differences in the deformation behavior can be explained by the orientation dependence of the stacking fault and deformation band formation, which follows from the dependence of the difference between the Schmid factors of the leading and trailing partials on the individual grain orientation (Fig. 11.35a). These partial dislocations experience different shear stresses, which depends on the orientation of their Burgers vector with respect to the direction of the external load [9]. From Fig. 11.35a, it can be concluded that the grains oriented with their ⟨001⟩ direction nearly parallel to the applied compression should have the highest tendency to the stacking fault formation. In these grains, the leading partial dislocation has a clearly higher Schmid factor than the trailing one, thus the SFs are widened upon compression. For the grain orientations with a negative Schmid factor difference (Fig. 11.35a), the trailing partial dislocations move faster than the leading ones, thus the stacking fault is closed.

For the grains with negative difference of the Schmid factors of leading and trailing partial dislocation, this trend was confirmed by EBSD measurements, which revealed

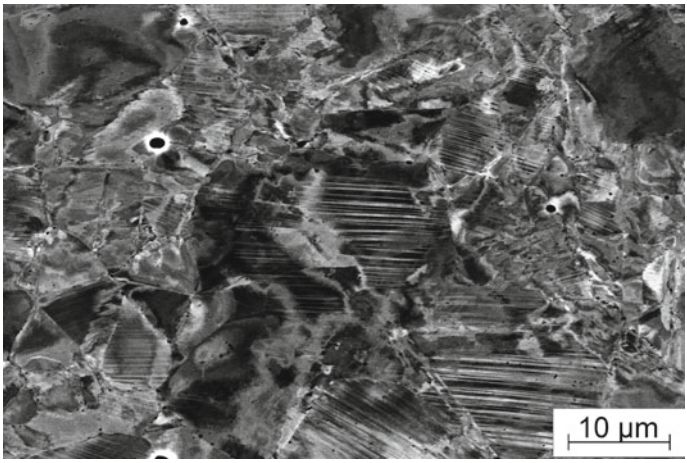

Fig. 11.34 Electron channeling contrast (ECC) image of the heterogeneous microstructure in a 15% strained PM X5CrMnNi16-6-9 steel. Adopted from [34]

that grains with the orientations between ⟨101⟩ and ⟨111⟩ along the deformation direction were almost free of deformation bands (Fig. 11.35c, e). In Fig. 11.35c, these grains are highlighted. Figure 11.35e shows their orientation density distribution. The highest density of SFs and deformation bands should be observed for grain orientations with positive Schmid factor difference (Fig. 11.35a). However, this expectation was not confirmed experimentally, as the ECCI/EBSD measurement (Fig. 11.35d, f) revealed that the grains with the highest density of SFs and deformation bands have orientations between ⟨102⟩ and ⟨113⟩ with respect to the compression direction. The reason for this apparent discrepancy is that the dissociation of perfect dislocations must be preceded by their formation that is activated according to the Schmid factor from Fig. 11.35b. After the initiation of faulting, the grain orientation can still be rotated by dislocation slip (on secondary slip systems), producing the typical formation of a ⟨101⟩ compression texture in *fcc* materials. This results in the observation of Fig. 11.35f that faulted grains are not sharply clustered around ⟨001⟩, but rather found between ⟨102⟩ and ⟨113⟩ orientations. The grains without stacking faults are oriented according to the ⟨101⟩ fiber texture in compressive load direction.

Consequently, the orientation dependence of the stacking fault and deformation band formation in austenite is controlled by the Schmid factors of perfect dislocations and SFs, because the plastic deformation of austenite is activated by the formation of perfect dislocation and their dissociation. For compression, the interplay of these mechanisms favors the SF formation on the primary slip system for orientations between ⟨102⟩, ⟨113⟩ and ⟨001⟩, while the formation of the deformation bands is delayed in grains having the orientations between ⟨101⟩, ⟨111⟩, ⟨113⟩ and ⟨102⟩. For tensile deformation, the favorable and unfavorable grain orientations are exchanged, because the sign of the Schmid factors of the partials switches with the inversion of the load direction.

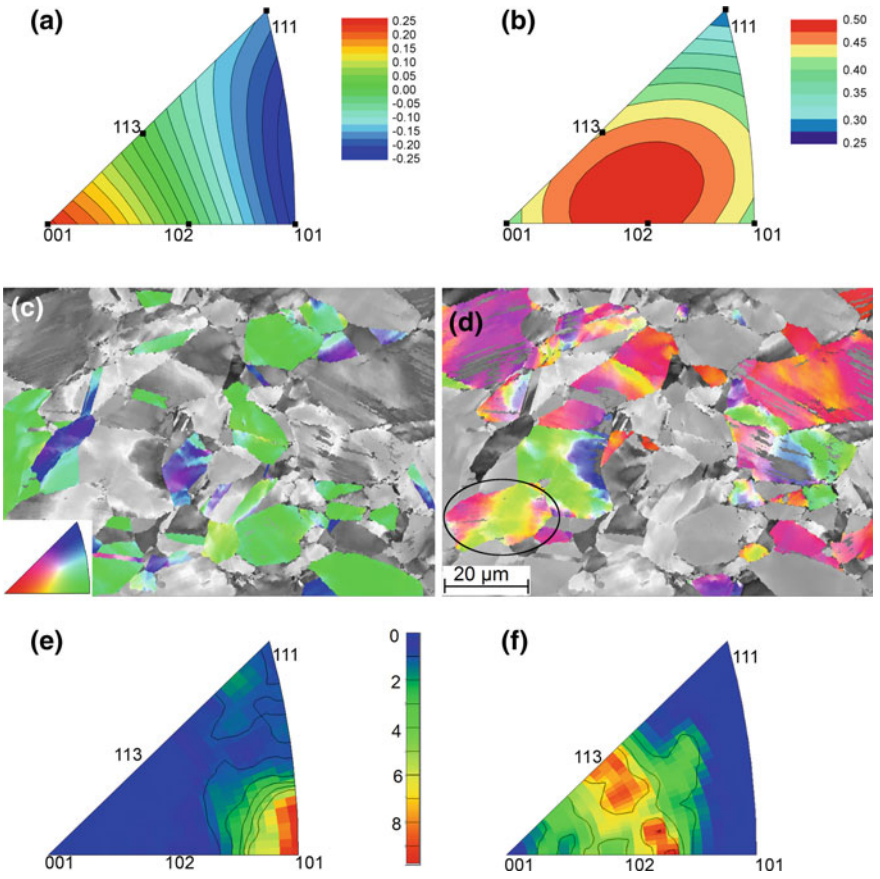

Fig. 11.35 Orientation dependence of the stacking fault and deformation band formation after 15% compression. In panel (**a**), the difference between the Schmid factors of leading and trailing partial for compression is presented. In panel (**b**), the orientation dependence of the Schmid factor for perfect dislocations on the primary slip system is plotted. EBSD maps show the orientation of grains that are almost free of deformation bands (**c**) and that accommodate pronounced deformation bands (**d**). The grey scale values in panels (**c**) and (**d**) are related to the EBSD band contrast. The corresponding inverse pole figures shown in panels (**e**) and (**f**) depict the orientation density distribution of the respective grains. Adopted from [34]

11.5.3 Dependence of the Deformation Mechanisms on Local Chemical Composition and Temperature

The dependence of the stacking fault and deformation band formation on the local orientation of the austenite grains is no exclusive reason for the existence of complex heterogeneous microstructures that are typically observed in deformed austenitic steels. In general, the prevailing deformation mechanism in these steels depends on the SFE of austenite, which is, from the thermodynamic point of view, a function

of the difference between the Gibbs energy of austenite and the Gibbs energy of ε-martensite (Sect. 11.2.3.1). As the difference of the Gibbs energies depends on the chemical composition of the steel, the deformation mechanisms are strongly influenced by the concentrations of the alloying elements. This is not only true on the macroscopic scale, where the SFE is generally affected by the overall chemical composition of the TRIP/TWIP steels (Sect. 11.4.3), but also on the microscopic scale, where local concentration fluctuations lead to a coexistence of deformation mechanisms even within individual grains [127].

Another result of the thermodynamic consideration of SFE is that the stacking fault energy increases with increasing temperature (through the temperature dependence of the Gibbs energies). The corresponding dependence of the deformation mechanisms on the temperature is illustrated in Fig. 11.36 for the steel composition X3CrMnNi16-6-6. From the XRD patterns, it can be seen that at the end of the uniform elongation the amount of the martensitic transformation decreases with increasing deformation temperature. As discussed in Sects. 11.2 and 11.3, both martensites (ε and α') occur in deformation bands, which accommodate a high density of (ordered) SFs. With decreasing deformation temperature, the SFE decreases, which facilitates the formation of extended SFs and the transformation of austenite to ε- and α'-martensites. The sample deformed at −60 °C contains mainly α'-martensite. At higher temperatures (above room temperature), the increase of SFE with increasing deformation temperature hinders the SF formation. Above approx. 60 °C, the deformed steel X3CrMnNi16-6-6 consists predominantly of austenite. The diffraction peaks corresponding to the *bcc* phase that were observed above 100 °C stem from initial δ-ferrite,

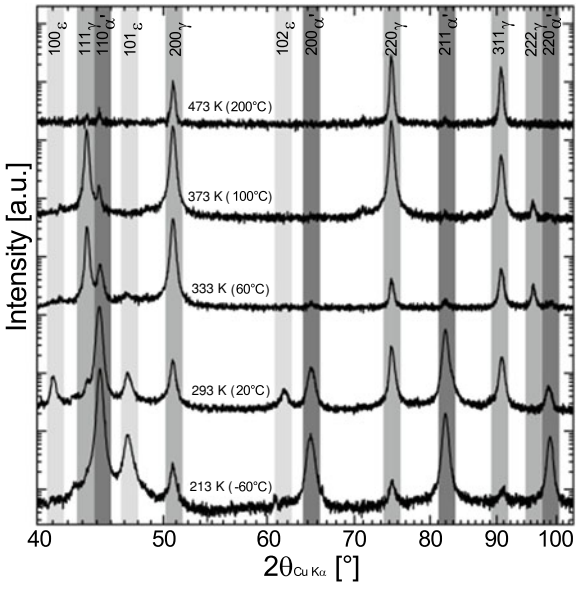

Fig. 11.36 XRD patterns after mechanical straining of cast TRIP steel samples at different testing temperatures until the end of uniform elongation (see right column of Fig. 11.37), indicating different amounts of martensitic transformation and remaining austenite [4]

which is also present in small fractions from the primary ferritic solidification of the cast material.

The results of XRD phase analysis were complemented by the SEM/EBSD experiments (Fig. 11.37), which helped in visualization of the microstructure defects and their arrangement that are related to the change in the phase composition of the deformed samples.

It was confirmed that the martensites, which form at the deformation temperatures below 60 °C, grow first inside and later out of the (former) deformation bands (Fig. 11.37a, b, f and g). At deformation temperatures above 60 °C, the martensite formation is reduced, while the twinning of austenite and the formation and slip of perfect dislocations become the most important mechanisms of the plastic deformation (Fig. 11.37c, d, e, h, i and j). At the deformation temperature of 60 °C, all microstructure features, i.e., α'-martensite, SFs, ε-martensite and twins in austenite are present (Fig. 11.37c, h), which means that the deformation mechanisms facilitated by the formation of the respective microstructure feature coexist. At the deformation temperatures above 60 °C, the density of twins in austenite increases rapidly (Fig. 11.37d, i). As the twins act as obstacles for dislocation glide, the perfect dislocations are concentrated in the areas between the deformation bands consisting of twins (Fig. 11.37d, e). At 200 °C, twins are only scarcely observed and dislocation configurations indicate that the deformation was essentially carried by perfect dislocation slip (Fig. 11.37e, j).

The temperature dependence of the deformation mechanisms discussed above is depicted schematically in Fig. 11.38. The link between the deformation temperature and SFE (γ_{SF}) emphasizes that the deformation mechanisms are essentially controlled by the stacking fault energy. The SFE at room temperature was determined experimentally (Sect. 11.4.3). The increase of SFE with increasing temperature was calculated from the change of $\Delta G^{\gamma\rightarrow\varepsilon}$ with temperature (Sect. 11.2.3.1).

The dislocation-induced plasticity is the fundamental deformation mechanism, thus its occurrence is highlighted by a grey hachure in the entire temperature range. At room temperature, the perfect dislocations dissociate quickly upon deformation, and form stacking faults. The stacking faults concentrate in deformation bands and form ε-martensite, below the critical temperature (M_D) also α'-martensite. Below the martensite start temperature (M_s), the formation of α'-martensite is further accelerated even without deformation. A high volume of α'-martensite at low (deformation) temperatures is one of the reasons for a high ultimate tensile stress (UTS in Fig. 11.38). Another reason for the increase of UTS with decreasing deformation temperature is the reduction of the mean free path of dislocations in the deformation bands by the successive nucleation of α'-martensite crystallites (cf. Sect. 11.5.1).

In contrast to UTS, which decreases monotonously with increasing deformation temperature, the uniform elongation (UE) shows pronounced maximum between room temperature and 150 °C, which corresponds to the SFE range between 15 and 34 mJ/m^2. In this temperature/SFE range, an intensified formation of ε-martensite and twins was observed that was already reported for various austenitic stainless steels in literature [59, 128]. The high amount of local shear approaching $0.35\left(\cong \sqrt{2}/4\right)$ and

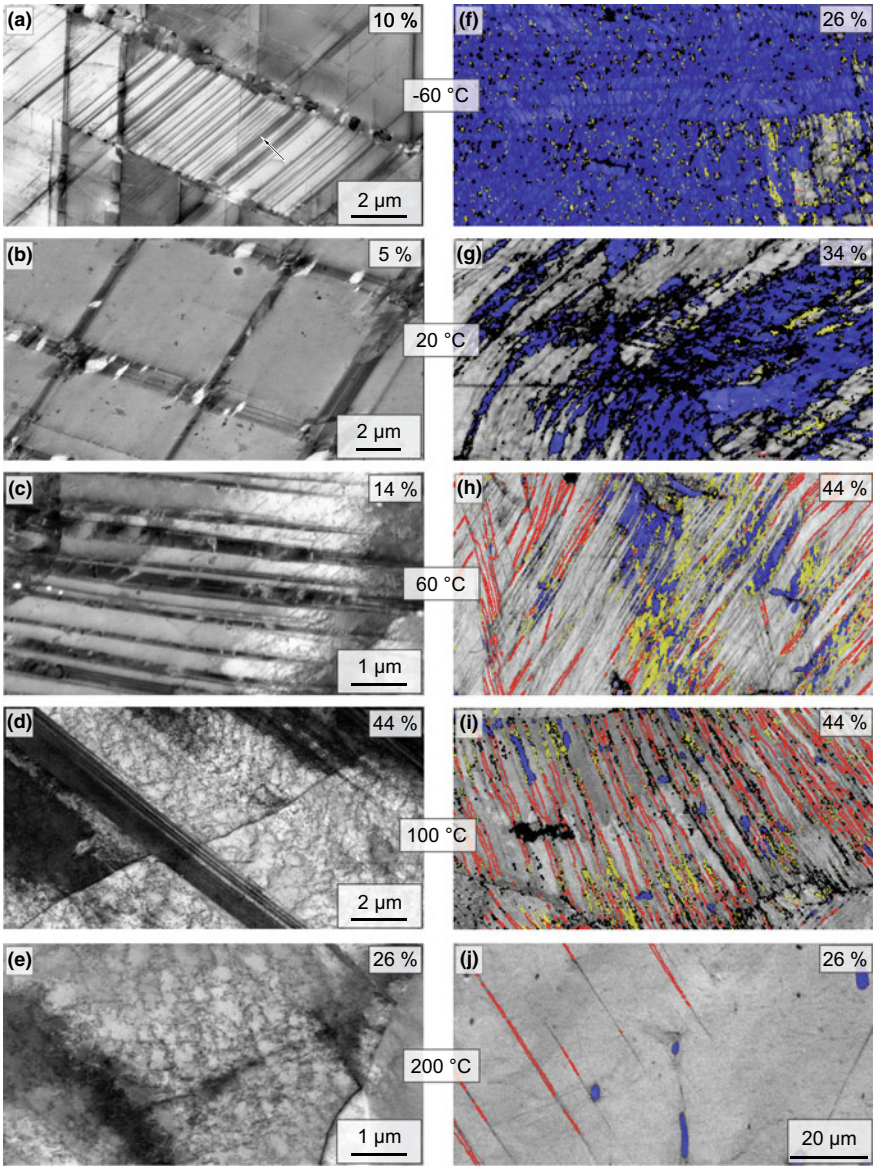

Fig. 11.37 Micrographs of coarse-grained TRIP/TWIP steel samples deformed at different strains at various testing temperatures. Left column: inverted ECCI images showing the deformation microstructures. Right column: EBSD phase maps highlighting austenite (the grey scale corresponds to the band contrast), ε-martensite (in yellow), α'-martensite (in blue) and not indexed regions (in black). The red lines mark the $\Sigma 3$ boundaries between deformation twins. All EBSD maps share the same scale bar. According to [4]

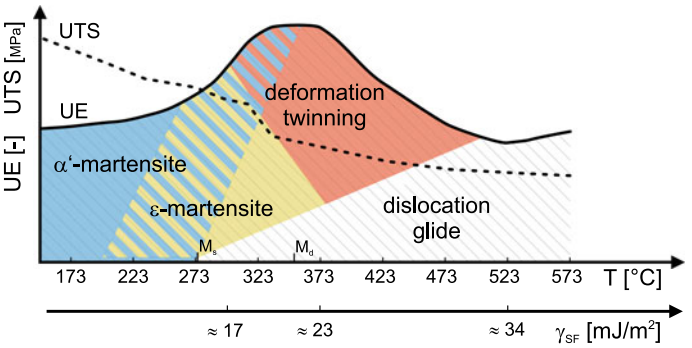

Fig. 11.38 Schematic representation of temperature dependence of the active deformation mechanisms in the X3 CrMnNi16-6-6 steel and their influence on ultimate elongation (UE) and ultimate tensile strength (UTS) [4]. The relationship between temperature and SFE (γ_{SF}) is shown in order to make clear that the dominant deformation mechanisms in austenitic steels are controlled by the stacking fault energy

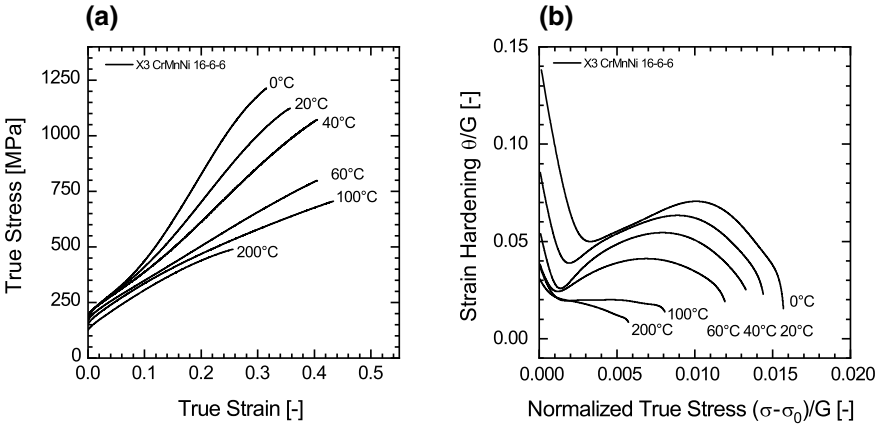

Fig. 11.39 Stress-strain curve (**a**) and strain hardening (**b**) of the X3CrMnNi16-6-6 TRIP/TWIP steel deformed at temperatures between 0 and 200 °C [4]

$0.71(\cong \sqrt{2}/2)$ for ε-martensite and twins, respectively, which is stored within the deformation bands because of the high SF density (see Sect. 11.2.3.1), contributes significantly to the overall dislocation based plasticity.

The alteration of deformation mechanisms with the temperature is also responsible for the change of the shape of the stress-strain curve and for the magnitude of the strain hardening (Fig. 11.39). The correlation between Figs. 11.38 and 11.39 confirms that the α'-martensite formation is a very effective hardening mechanism.

11.6 Conclusions

In this Chapter, the microstructure aspects of the deformation mechanisms in metastable austenitic steels were discussed. It was shown that the presence and form of the deformation bands play a crucial role in understanding the mechanical properties of the steels. It was demonstrated, that the deformation bands are composed of wide and tightly arranged stacking faults and, in some cases, of crossing deformation bands. The formation and widening of the stacking faults are the consequences of a low stacking fault energy of austenite, which facilitates the dissociation of perfect dislocations and the separation of partial dislocation under applied mechanical load. A high density of stacking faults within the deformation bands is recognized by diffraction methods (XRD, EBSD, SAED, FFT/HRTEM) either as an *hcp* stacking sequence, i.e., as ε-martensite, or as twinned austenite—depending on the SF density. A continuous transition between ε-martensite and twinned austenite is possible.

As the stacking fault energy of austenite depends strongly on its chemical composition and on temperature, already small variations in the kind and concentrations of the alloying elements and/or in the deformation temperature of the steel lead to serious changes in the dominant deformation mechanism. In many cases, perfect dislocations, isolated SFs, SF clusters, ε-martensite, twins and/or α'-martensite occur concurrently, but their fractions depend always on the stacking fault energy, and therefore on the steel composition, on the deformation temperature and on the deformation degree. Based on these results, the mechanical behavior of the TRIP/TWIP steels (mainly the ultimate tensile stress and the ultimate elongation) were related to the present microstructure defects and to their complex interplay. Formation of α'-martensite was found to contribute considerably to the strain hardening.

Finally, the potential of the in situ diffraction methods was illustrated. It was shown, how the stacking fault energy can be determined from the internal stresses measured during the deformation process and how the development of the deformation microstructure can be followed during an in situ deformation experiment.

Acknowledgements Former SFB799 project collaborators are highly acknowledged for their contributions: Daria Borisova, Anna Poklad, Benedikt Reichel and Volker Klemm. Further we thank Sabine Decker, Markus Radajewski, Steffen Wolf, Ralf Eckner, Christine Baumgart, Marco Wendler and Andreas Jahn for sample production and deformation experiments. The German Research Foundation (DFG) is acknowledged for funding the Collaborative Research Center SFB 799 (Project number 54473466).

References

1. H. Hasegawa, D.G. Pettifor, Phys. Rev. Lett. **50**, 130 (1983)
2. D. Bancroft, E.L. Peterson, S. Minshall, J. Appl. Phys. **27**, 291 (1956)
3. T. Takahashi, W. Bassett, Science **145**, 483 (1964)

4. S. Martin, S. Wolf, U. Martin, L. Krüger, D. Rafaja, Metall. Mater. Trans. **47**, 49 (2016)
5. W. Bleck, Werkstoffprüfung in Studium und Praxis, 15th edn. (Verlagsgruppe Mainz, 2011)
6. J.P. Hirth, J. Lothe, *Theory of Dislocations*, 2nd edn. (Krieger Publishing, Malabar, 1982)
7. P.C.J. Gallagher, Metall. Trans. **1**, 2429 (1970)
8. E.H. Lee, M.H. Yoo, T.S. Byun, J.D. Hunn, K. Farrell, L.K. Mansur, Acta Mater. **49**, 3277 (2001)
9. S.M. Copley, B.H. Kear, Acta Metall. **16**, 227 (1968)
10. T.S. Byun, Acta Mater. **51**, 3063 (2003)
11. M. Peach, J.S. Koehler, Phys. Rev. **80**, 436 (1950)
12. B.C. De Cooman, Y. Estrin, S.K. Kim, Acta Mater. **142**, 283 (2018)
13. A. Das, Metall. Mater. Trans. A **47**, 748 (2016)
14. F.C. Frank, W.R. Read, Phys. Rev. **79**, 722 (1950)
15. D. Hull, D.J. Bacon, *Introduction to Dislocations*, 5th edn. (Butterworth Heinemann, Oxford, 2011)
16. W.M. Lomer, Phil. Mag. **42**, 1327 (1951)
17. A.H. Cottrell, Phil. Mag. **43**, 645 (1952)
18. D. Borisova, V. Klemm, S. Martin, S. Wolf, D. Rafaja, Adv. Eng. Mater. **15**, 571 (2013)
19. N. Thompson, Proc. Phys. Soc. B **66**, 481 (1953)
20. S. Martin, C. Ullrich, D. Rafaja, Mater. Today: Proc. **2**, 643 (2015)
21. G.B. Olson, M. Cohen, Metall. Trans. A **7**, 1897 (1976)
22. D. Geissler, J. Freudenberger, A. Kauffmann, S. Martin, D. Rafaja, Phil. Mag. **94**, 2967 (2014)
23. P.J. Ferreira, P. Müllner, Acta Mater. **46**, 4479 (1998)
24. L. Vitos, J.-O. Nilsson, B. Johansson, Acta Mater. **54**, 3821 (2006)
25. A. Saeed-Akbari, J. Imlau, U. Prahl, W. Bleck, Metall. Mater. Trans. A **40**, 3076 (2009)
26. J. Nakano, P.J. Jacques, Calphad **34**, 167 (2010)
27. A.J.C. Wilson, Proc. R. Soc. London Ser. A **180**, 277 (1942)
28. M.S. Paterson, J. Appl. Phys. **23**, 805 (1952)
29. B.E. Warren, E.P. Warekois, Acta Metal. **3**, 473 (1955)
30. B.E. Warren, *X-Ray Diffraction*, 2nd edn. (Dover Inc., New York, 1990)
31. S. Martin, C. Ullrich, D. Šimek, U. Martin, D. Rafaja, J. Appl. Cryst. **44**, 779 (2011)
32. M.M.J. Treacy, J.M. Newsam, M.W. Deem, Proc. Roy. Soc. A **433**, 499 (1991)
33. L. Balogh, G. Ribárik, T. Ungár, J. Appl. Phys. **100**, 23512 (2006)
34. C. Ullrich, R. Eckner, L. Krüger, S. Martin, V. Klemm, D. Rafaja, Mater. Sci. Eng. A **649**, 390 (2016)
35. M.J. Whelan, P.B. Hirsch, Phil. Mag. **2**, 1303 (1957)
36. G. Thomas, W.L. Bell, H.M. Otte, Phys. Status Solidi A **12**, 353 (1965)
37. B. Cina, Acta Metall. **6**, 748 (1958)
38. C.W. Sinclair, R.G. Hoagland, Acta Mater. **70**, 4160 (2008)
39. H. Schumann, Krist. Tech. **9**, 1141 (1974)
40. A. Weidner, S. Martin, V. Klemm, U. Martin, H. Biermann, Scr. Mater. **64**, 513 (2011)
41. M. El-Tahawy, Y. Huang, T. Um, H. Choe, J.L. Lábár, T.G. Langdon, J. Gubicza, J. Mater. Res. Technol. **6**, 339 (2017)
42. C. E. Rodriguez Torres, F. H. Sánchez, A. González, F. Actis, R. Herreara, Metall. Mater. Trans. A **33**, 25 (2002)
43. K. Guy, E. Butler, D. Wes, J. de Phys. Colloques. **43**, 575 (1982)
44. L. Rémy, Acta Metall. **25**, 173 (1977)
45. R. Clendenen, H. Drickamer, J. Phys. Chem. Solids **25**, 865 (1964)
46. H.-K. Mao, W.A. Bassett, T. Takahashi, J. Appl. Phys. **38**, 272 (1967)
47. T. Takahashi, W.A. Bassett, M. Hokwang, J. Geophys. Res. B **73**, 4717 (1968)
48. P.M. Giles, M.H. Longenbach, A.R. Marder, J. Appl. Phys. **42**, 4290 (1971)
49. M. Friák, M. Šob, Phys. Rev. B **77**, 174117 (2008)
50. M. Friák, Steel Res. Int. **82**, 86 (2011)
51. N.A. Zarkevich, D.D. Johnson, Phys. Rev. B **91**, 174104 (2015)

52. S. Ackermann, S. Martin, M.R. Schwarz, C. Schimpf, D. Kulawinski, C. Lathe, S. Henkel, D. Rafaja, H. Biermann, A. Weidner, Metall. Mater. Trans. A **47**, 95 (2016)
53. H. Le Chatelier, Comptes Rendus **99**, 786 (1884)
54. M. Hillert, *Phase Equilibria, Phase Diagrams and Phase Transformations*, Chapter 6.9, 2nd edn. (Cambridge University Press, 2008)
55. J.R. Patel, M. Cohen, Acta Metall. **1**, 531 (1953)
56. L. Kaufman, M. Cohen, Prog. in Met. Phys. **7**, 165 (1958)
57. I. Tamura, Met. Sci. **16**, 245 (1982)
58. J.A. Venables, Phil. Mag. **7**, 35 (1962)
59. F. Lecroisey, A. Pineau, Metall. Trans. **3**, 387 (1972)
60. G.B. Olson, M. Cohen, J. Less Comm. Met. **28**, 107 (1972)
61. S. Martin, S. Wolf, S. Decker, L. Krüger, U. Martin, Steel Res. Int. **86**, 1187 (2015)
62. X.-S. Yang, S. Sun, T.-Y. Zhang, Acta Mater. **95**, 264 (2015)
63. Y. Tian, O.I. Gorbatov, A. Borgenstam, A.V. Ruban, P. Hedström, Metall. Mater. Trans. A **48**, 1 (2017)
64. A.J. Bogers, W.G. Burgers, Acta Metall. **12**, 255 (1964)
65. L. Bracke, L. Kestens, J. Penning, Scripta Mater. **57**, 385 (2007)
66. G. Kurdjumow, G. Sachs, Z. Phys. **64**, 325 (1930)
67. Z. Nishiyama, *Martensitic Transformation*, 1st edn. (Academic Press, New York, 1978)
68. G. Olson, M. Azrin, Metall. Mater. Trans. A **9**, 713 (1978)
69. J. Talonen, P. Aspegren, H. Hänninen, Mater. Sci. Technol. **20**, 1506 (2004)
70. L.S. Zevin, G. Kimmel, I. Mureinik, *Quantitative X-Ray Diffractometry* (Springer, New York, 1995)
71. H.M. Rietveld, J. Appl. Cryst. **2**, 65 (1969)
72. R.A. Young, *The Rietveld Method* (Oxford University Press, IUCr, 1993)
73. S. Allain, J.-P. Chateau, D. Dahmoun, O. Bouaziz, Mater. Sci. Eng. A **397–389**, 272 (2004)
74. O. Bouaziz, Scripta Mater. **66**, 982 (2012)
75. D.R. Steinmetz, T. Jäpel, B. Wietbrock, P. Eisenlohr, I. Gutierrez-Urrutia, A. Saeed-Akbari, T. Hickel, F. Roters, D. Raabe, Acta Mater. **61**, 494 (2013)
76. S. Allain, J.-P. Chateau, O. Bouaziz, Steel Res. Int. **79**, 299 (2002)
77. K. Renard, P.J. Jacques, Mater. Sci. Eng. A **542**, 8 (2012)
78. D. Barbier, N. Gey, S. Allain, N. Bozzolo, M. Humbert, Mater. Sci. Eng. A **540**, 212 (2012)
79. C. Schimpf, M. Motylenko, D. Rafaja, Mater. Char. **86**, 190 (2013)
80. M.A. Krivoglaz, *Theory of X-ray and Thermal Neutron Scattering by Real Crystals* (Plenum Press, New York, 1969)
81. M. Wilkens, Phys. Status Solidi A **2**, 359 (1970)
82. P. Klimanek, R. Kužel, J. Appl. Cryst. **21**, 59 (1988)
83. R. Kužel, P. Klimanek, J. Appl. Cryst. **21**, 363 (1988)
84. T. Ungár, G. Tichy, Phys. Status Solidi A **171**, 425 (1999)
85. T. Ungár, I. Dragomir, Á. Révész, A. Borbély, J. Appl. Cryst. **32**, 992 (1999)
86. A. Borbély, J. Dragomir-Cernatescu, G. Ribárik, T. Ungár, J. Appl. Cryst. **36**, 160 (2003)
87. I. Dragomir, T. Ungár, J. Appl. Cryst. **35**, 556 (2002)
88. N.C. Popa, J. Appl. Cryst. **31**, 176 (1998)
89. D.J.H. Cockayne, Phil. Mag. **20**, 1265 (1969)
90. C.C. Bampton, I.P. Jones, M.H. Loretto, Acta Metall. **26**, 39 (1978)
91. M.J. Mills, P. Stadelmann, Phil. Mag. A **60**, 355 (1989)
92. J. Lu, L. Hultman, E. Holmström, K.H. Antonsson, M. Grehk, W. Li, L. Vitos, A. Golpayegani, Acta Mater. **111**, 39 (2016)
93. M.J. Whelan, Proc. Roy. Soc. A **249**, 114 (1959)
94. A. Howie, P.R. Swann, Phil. Mag. **6**, 1215 (1961)
95. A. Ruff, L. Ives, Acta Metall. **15**, 189 (1967)
96. R.M. Latinision, A.W. Ruff, Metall. Trans. **2**, 505 (1971)
97. I.L. Dillamore, Phil. Mag. **9**, 517 (1964)
98. I.L. Dillamore, Metall. Trans. **1**, 2463 (1970)

99. R.P. Reed, R.E. Schramm, J. Appl. Phys. **45**, 4705 (1974)
100. R.E. Schramm, R.P. Reed, Metall. Trans. A **6**, 1345 (1975)
101. J. Talonen, H. Hänninen, Acta Mater. **55**, 6108 (2007)
102. T.-H. Lee, E. Shin, C.-S. Oh, H.-Y. Ha, S.-J. Kim, Acta Mater. **58**, 3173 (2010)
103. J.S. Jeong, W. Woo, K.H. Oh, S.K. Kwon, Y.M. Koo, Acta Mater. **60**, 2290 (2012)
104. D. Rafaja, C. Krbetschek, C. Ullrich, S. Martin, J. Appl. Cryst. **47**, 936 (2014)
105. D. Rafaja, C. Krbetschek, D. Borisova, G. Schreiber, V. Klemm, Thin Solid Films **530**, 103 (2013)
106. S. Allain, J.-P. Chateau, O. Bouaziz, S. Migot, N. Guelton, Mater. Sci. Eng. A **387–389**, 158 (2004)
107. S. Curtze, V.-T. Kuokkala, A. Oikari, J. Talonen, H. Hänninen, Acta Mater. **59**, 1068 (2011)
108. A. Abbasi, A. Dick, T. Hickel, J. Neugebauer, Acta Mater. **59**, 3041 (2011)
109. G.M. de Bellefon, J.C. van Duysen, K. Sridharan, J. Nucl. Mater. **492**, 227 (2017)
110. N. Chaudhary, A. Abu-Odeh, I. Karaman, R. Arróyave, J. Mater. Sci. **52**, 11048 (2017)
111. E. Kröner, Z. Phys. **151**, 504 (1958)
112. A. G. Every, A. K. McCurdy, Fe-Al-Nb-O, in *Springer Materials—The Landolt–Börnstein Database*ed. by D.F. Nelson (2011)
113. C. Ullrich, S. Martin, C. Schimpf, A. Stark, N. Schell, D. Rafaja, Adv. Eng. Mater. **21**, 1801101 (2019)
114. H. Van Swygenhoven, S. Van Petegem, Mater. Charact. **78**, 47 (2013)
115. L. Lutterotti, S. Matthies, H.-R. Wenk, A.S. Schultz, J.W. Richardson, J. Appl. Phys. **81**, 594 (1997)
116. L. Lutterotti, S. Matthies, H.-R. Wenk, IUCr Commission on Powder Diffraction Newsletter **21**, 14 (1999)
117. S. Matthies, G.W. Vinel, Phys. Status Solidi A **112**, K111 (1982)
118. M. Ferrari, L. Lutterotti, J. Appl. Phys. **76**, 7246 (1994)
119. A. Creuziger, C.A. Calhoun, W.A. Poling, T. Gnäupel-Herold, J. Appl. Cryst. **51**, 720 (2018)
120. S. Allain, J.-P. Chateau, O. Bouaziz, Mater. Sci. Eng. A **387–389**, 143 (2004)
121. T. Narutani, Mater. Trans. JIM **30**, 33 (1989)
122. M. Wilkens, Phys. Status Solidi A **104**, K1 (1987)
123. L. Rémy, Acta Metall. **26**, 443 (1978)
124. I. Gutierrez-Urrutia, D. Raabe, Acta Mater. **60**, 5791 (2012)
125. L. Rémy, Metall. Trans. A **12**, 387 (1981)
126. O. Bouaziz, S. Allain, C.P. Scott, P. Cugy, D. Barbier, Curr. Opin. Solid State Mater. Sci. **15**, 141 (2011)
127. S. Martin, O. Fabrichnaya, D. Rafaja, Mater. Lett. **159**, 484 (2015)
128. L. Rémy, A. Pineau, Mater. Sci. Eng. **28**, 99 (1977)

Chapter 12
Investigations on the Influence of Strain Rate, Temperature and Reinforcement on Strength and Deformation Behavior of CrMnNi-Steels

Ralf Eckner, Christine Baumgart, and Lutz Krüger

Abstract This section presents the results of comprehensive investigations into the strength and deformation behavior of CrMnNi-TRIP/TWIP steels and particle-reinforced TRIP-Matrix-Composites. These investigations combined quasi-static and dynamic tensile, compressive, and plate impact tests with ex situ microstructure analysis using electron microscopy and diffraction techniques on representative samples. The aim was the investigation and microstructurally-based description and modeling of the temperature and strain rate dependent strength, deformation and failure behavior of these advanced materials. It could be shown that the behavior of austenitic CrMnNi steels is controlled by different deformation mechanisms. These include mechanical twinning and martensitic phase transformations, whose occurrences or interactions are influenced by the chemical composition or the austenite stability, the stacking fault energy, the deformation temperature and rate as well as by the loading direction. Furthermore, the mechanical properties of honeycomb structures made of CrMnNi steel or TRIP-Matrix-Composites have been investigated. These are intended as lightweight and high strength components to improve the crash performance of constructions in the field of mobility. Since their mechanical properties are influenced by several parameters such as the chemical composition of the material, the structure type or the reinforcement content, detailed analyses are necessary before their application in vehicle components.

R. Eckner (Emeritus)
Institute of Materials Engineering, Technische Universität Bergakademie Freiberg, Gustav-Zeuner-Str. 5, 09599 Freiberg, Germany

C. Baumgart · L. Krüger (✉)
Institute of Materials Engineering, Technische Universität Bergakademie Freiberg, Gustav-Zeuner-Str. 5, 09599 Freiberg, Germany
e-mail: krueger@ww.tu-freiberg.de

H. Biermann and C. G. Aneziris (eds.), *Austenitic TRIP/TWIP Steels and Steel-Zirconia Composites*, Springer Series in Materials Science 298,
https://doi.org/10.1007/978-3-030-42603-3_12

12.1 Introduction

The automotive industry is always looking for ways to increase safety and performance while reducing fuel consumption. These requirements led to the development of so-called *High Strength Steels* (HSS) and *Advanced High Strength Steels* (AHSS). Among these, high-alloy austenitic stainless steels are characterized by extraordinary properties such as excellent formability, high corrosion resistance, and good weldability, and are used for applications ranging from cryogenic up to elevated temperatures. Such steels take advantage of the TRIP- and/or TWIP-effects (TRansformation Induced Plasticity or TWinning Induced Plasticity), which are both triggered by plastic deformation and depend strongly on the stacking fault energy of the steel. At relatively high stacking fault energies (>40 mJ/m^2), the material deforms and hardens substantially due to the motion of dislocations. Stacking fault energies between 20 and 40 mJ/m^2 favor the emergence of stacking faults and deformation twins (TWIP-effect) [1–3]. Such planar defects act as obstacles for further dislocation movement and consequently increase the strain hardening rate of the material, which is known as the "dynamic Hall-Petch effect" [4]. In steel with lower stacking fault energy, the TRIP-effect is evident which is associated with the formation of ε- and α'-martensite and involves the enhancement of strength and ductility below the M_d-temperature [5–7]. The stacking fault energy mainly depends on the chemical composition of the steel and the deformation temperature [8]. The necessary mechanical driving force for the transformation $\gamma \rightarrow \alpha'$ is provided by the mechanical stress applied on the material [7]. Both mechanisms are already being used in the development of modern advanced high strength steels, e.g. for automotive applications [9]. These materials offer great potential for improving occupant safety in the event of a crash as well as for lightweight construction to reduce weight and energy consumption.

Within the Collaborative Research Center 799, two development routes are utilized in order to generate weight efficient energy absorbing materials. On the one hand, the combination of two different material groups. This exploits the beneficial properties of each component, like in the case of mother-of-pearl, and is implemented by reinforcing ductile TRIP-steel with high strength MgO partially stabilized zirconia (Mg-PSZ) [10]. On the other hand, the use of these metal matrix composites (MMC) in cellular networks follows the example of wood or cork which could have a favorable strength to weight ratio [11]. Those cellular materials belong to the honeycomb-like structures. Unlike established materials for cellular structures such as aluminum, titanium or magnesium, TRIP-steel and TRIP-Matrix-Composites do not belong to light metals. However, it has been proven that the deformation induced phase transformation of TRIP-steels is an energy consuming process which helps to balance the influence of a higher density when comparing the specific energy absorption capability of different structures [12].

The intention of the present survey is to highlight the deformation mechanisms which are active under dynamic loading and under shock wave loading by flyer-plate impact in bulk cast high-alloy CrMnNi TRIP/TWIP-steel. Detailed investigations of the developed microstructure were performed in order to explain the experimental results, with special focus on the martensitic transformation. Furthermore, static

compression tests were conducted at room temperature in order to compare the fundamental performance of the different cellular materials made of TRIP-steel and TRIP-Matrix-Composites with focus on the compressive strength, deformation and damage behavior.

12.2 High Strain Rate Deformation of Austenitic High-Alloy TRIP/TWIP Steel

12.2.1 Processing and Experimental Methods

Table 12.1 represents the chemical compositions of the investigated high-alloy austenitic TRIP/TWIP steel. The examined material is based on a patent-protected development [13] and is described as 16-6-6, according to the concentrations of Cr, Mn, and Ni in wt%. The material was cast in plates (dimensions 200 × 200 × 16 mm^3) by ACTech GmbH (Freiberg, Germany) using sand casting technology. The manufactured samples were subsequently solution-heat-treated at 1323 K (1050 °C) for 30 min to retransform any martensite induced by previous machining. A dendritic austenite microstructure with coarse grains in the range of 100–1000 μm was received. Due to the chemical composition of the steel, a certain amount of δ-ferrite (~2 vol%) was formed during solidification. This steel belongs to AHSS of the 1st generation and is characterized by a high strain hardening capacity in combination with high formability, though the yield strength is rather low (YS ~200 MPa, UTS ~800 MPa, total elongation ~50%) [14].

Quasistatic compression tests at 0.0004 1/s were performed in a servohydraulic universal testing machine. For the dynamic impact and high-rate experiments up to 2300 1/s a drop weight tower and a Split-Hopkinson pressure bar system (SHPB) were used [15]. All mechanical tests were carried out on cylindrical samples with 6 mm in diameter and 6 mm in height. The samples were instrumented with strain gauges in order to allow a local deformation measurement even at high deformation speeds. In order to obtain consistent high rate compressive stress/strain data, the SHPB apparatus was modified by a pulse shaping technique using OFHC-copper platelets [16] and numerical dispersion correction [17].

In order to determine the strength properties of the test material, a flyer-plate impact assembly of the Russian Academy of Sciences, Institute of Problems of Chemical Physics, Chernogolovka near Moscow was used, which is shown schematically in Fig. 12.1. The test specimens had a thickness of 5 mm with a square area of 45 ×

Table 12.1 Chemical composition of the investigated high-alloy CrMnNi TRIP/TWIP steel

(wt%)	C	N	Cr	Mn	Ni	Si	Fe + others
Cast X3CrMnNi16-6-6 (abbr.: 16-6-6)	0.03	0.03	15.5	6.1	6.1	0.9	Bal.

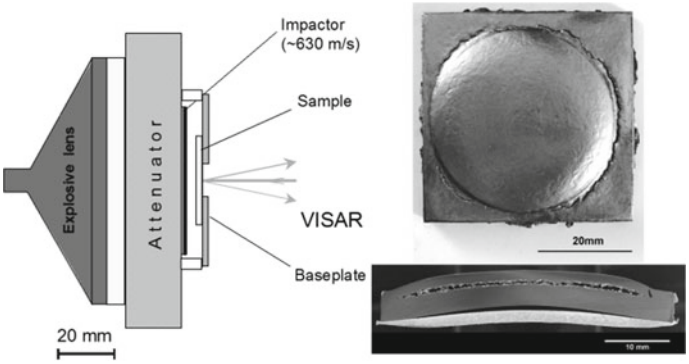

Fig. 12.1 Schematic setup of the plate impact experiments to determine the strength properties under planar shock loading at room temperature [20]

45 mm^2 and were shocked by plates (thickness 2 mm) of technically pure aluminum. The acceleration of the flyer-plates was carried out by means of a blasting lens to speeds of 650 ± 30 m/s. The shock pressure yielded 7–8 GPa and the strain rate behind the wave front and before spallation was 5–6 × 10^4 1/s. The planar impact of the aluminum plate produced a shock wave within the target sample and resulted in a uniaxial state of deformation over a pulse length of less than one microsecond. Therefore, the free surface velocity profiles were recorded using VISAR Laser Doppler Velocimetry [18] with a time resolution of ~1 ns and a space resolution of ~0.1 mm^2, giving a measurement accuracy of ~5 m/s. Evaluation of such plate-impact experiments is described in detail for instance in [19].

For shock wave experiments on large-volume samples at higher pressures, a plate-impact setup of the Freiberg High Pressure Research Center (FHP) was also used, which is shown schematically in Fig. 12.2. This experimental setup was originally developed for the high-pressure synthesis of ultra-hard materials (Diamond, c-BN, γ-Si_3N_4) and builds up on the findings and specifications of the EMI (Ernst Mach-Institute) in Freiburg [21]. The difference to the above-described plate impact structure of the Russian Academy of Sciences consists in the ability to produce reproducible pressures up to 120 GPa or more within the sample and thereby have a much larger sample volume available.

In the experiments, the amount of explosive used was varied, whereby pressures of 30, 60, 90 and 120 GPa (or 0.3–1.2 Mbar) could be set. After ignition, the flyer-plate was accelerated over a distance of 20 mm and then hit flat on the sample surface. Depending on the amount of explosive, the final velocity varied between 1.5 and 4 km/s. The target, the cylindrical material sample, was located in a form-fitting round container with a diameter of 220 mm, which was made of structural steel S355 (St-52). Below the sample a hardened steel plate was positioned, which was supported on a sand bed and acted as a damping plate or impulse trap. This design pursued two goals; on the one hand, the sample container prevented the free adiabatic expansion of the sample. On the other hand, the impedance difference between the

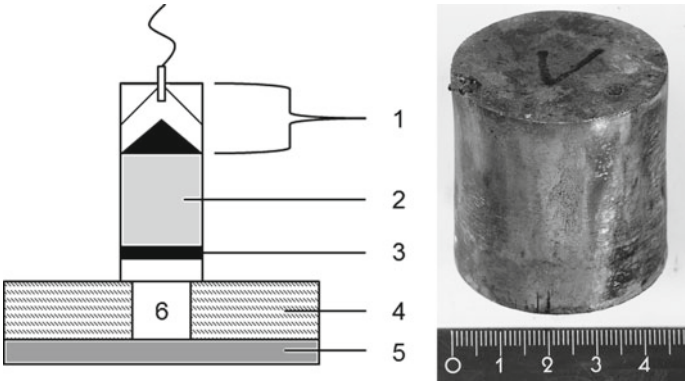

Fig. 12.2 Setup for shock experiments on large-volume samples: (1) plane wave generator with electric detonator (PETN explosive) (2) C-4 explosive (3) CrMnNi steel flyer-plate, (4) structural steel container (S355), (5) QT steel plate, (6) CrMnNi steel sample [22]

sample and the overlay was small, so that the shockwave was not reflected at the interface and the spallation could be prevented. Thus, the sample remained intact during the experiment and could then be mechanically removed from the sample container.

After mechanical testing, the α'-martensite volume fraction was quantified using a Metis MSAT type magnetic saturation device for both, the deformed compression specimens and shock-loaded conditions. For light-optical characterization, the samples were ground, polished, and etched with Beraha II etchant or V2A etchant, in order to contrast the deformation features such as deformation bands or martensite. Subsequently, microstructural investigations were carried out by scanning electron microscopy (SEM), transmission electron microscopy (TEM) in combination with electron backscatter diffraction (EBSD), selected area electron diffraction (SAED) or convergent beam electron diffraction (CBED) techniques.

12.2.2 Approaches to Rate-Dependent Constitutive Modeling

The influence of strain rate on the flow curves and the hardening behavior of metastable austenitic CrMnNi steels is of great importance considering technical application fields. Their plastic deformation is based essentially on the separation of Shockley partial dislocations and the subsequent stacking fault and deformation band formation [23, 24]. The increasing stacking fault density as well as the development of ε- and α'-martensite nuclei leads in consequence to strain hardening or to the dynamic Hall-Petch effect. However, the adiabatic sample heating effect increases with increasing strain rate, whereby much of the plastic deformation work remains in the sample as thermal energy. A nonlinear development of strain and strength characteristics with increasing strain rate is usually caused by this phenomenon. It

was as well shown that the α'-martensite formation rate decreases with increasing strain rate and tends towards zero at high strain values ($\varepsilon \geq 0.3$) [25], caused by an increasing stacking fault energy and a reduction in chemical driving force for the $\gamma \rightarrow \alpha'$ transformation [26, 27]. Previous studies highlighted the influence of a temperature change on the SFE and the separation distance of dislocations in detail [28]. The splitting into partial dislocations and the corresponding stacking fault formation require a critical stress level, which increases with increasing SFE. The SFE in turn increases with increasing temperature. In addition, both an increase in temperature and an increased strain rate increase the threshold stress for martensite formation [28, 29]. However, this effect is partly compensated, since the threshold stress for stacking fault or twin formation can be achieved at even lower strain values due to the rise in yield strength with increasing strain rate [30].

The reduced rate of martensite formation and the consequent decreasing strain hardening with increasing strain rate cause a decrease in flow stress with increasing deformation [25, 31]. On this occasion, the so-called curve crossing phenomenon can occur, whereby the strain softening leads to the intersection of the dynamic flow curves with the quasi-static flow curves [32]. In general, flattening of the flow curves can be observed at high strain rates, which is associated with a reduced maximum strength. The characteristic strain hardening curve is shifted to lower values and lower deformations, and the sigmoidal character changes into a plateau or disappears [33–35]. Furthermore, sample heating in high-speed tests leads to a decrease in the volume fraction of austenite converted into α'-martensite [25, 27, 36, 37]. Depending on the alloy composition and the degree of sample heating, a change in the dominant deformation mechanism is also possible, from stacking fault/ε-martensite formation to twinning or dislocation glide [8]. This transition is associated with decreasing strain hardening capability during deformation. Figure 12.3 shows results of strain-rate-dependent compression tests on the 16-6-6 steel alloy as an example for the effects mentioned. As expected, increasing strain rate led to crossing of the flow curves (Fig. 12.3a) owing to reduced strain hardening due to a lower fraction of α'-martensite formed (Fig. 12.3b).

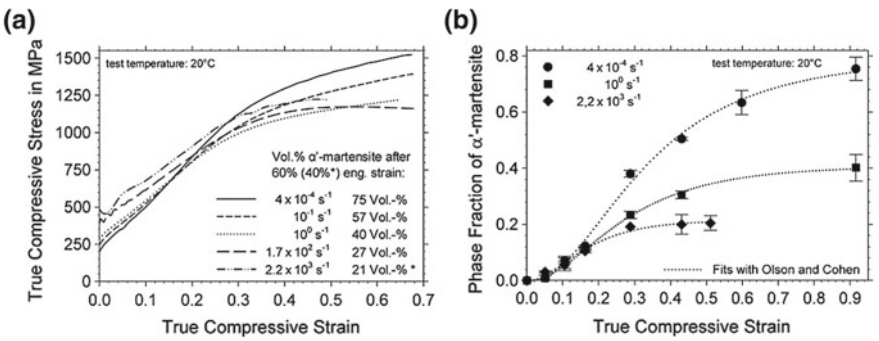

Fig. 12.3 CrMnNi16-6-6 steel: **a** Strain rate dependent mechanical behavior under compressive loading and **b** martensite kinetics at various strain rates (fitted according to [6]) [38]

Within the scope of the investigations, an empirical model of the flow stress on the basis of the rule of mixture (RM) was developed, which includes all important microstructural deformation mechanisms of CrMnNi TRIP steels as a function of temperature and strain rate. Several earlier research works dealt with the problem of modelling a deformation-induced martensitic transformation in austenitic steels. At this point, the publications of Ludwigson and Berger [39] and of Narutani et al. [40] are considered more in detail, representing two of the most significant works.

Ludwigson and Berger pointed out that the flow behavior of austenitic steel differs significantly from that of carbon steel due to the strain-induced martensitic transformation. For this reason, the flow curve cannot be described only by the relationship in (12.1),[1] which is valid for a variety of steels.

$$\sigma = K \cdot [\ln(1+\varepsilon)]^n \tag{12.1}$$

They assumed an autocatalytic formation reaction of the martensite and were therefore able to extend the existing model by a strength contribution of the martensitic phase depending on the actual strain value. Ludwigson and Berger introduced a factor A, which describes the ease with which an austenitic structure can undergo a strain-induced transformation to martensite, and the factors C and Q which characterize the martensite strength contribution. Equation (12.2)[2] shows the corresponding flow-curve equation relating true stress to strain.

$$\sigma = K[\ln(1+\varepsilon)]^n \cdot \left[1 - \left(1 + \frac{\varepsilon^{-B}}{A}\right)^{-1}\right] + C\left(1 + \frac{\varepsilon^{-B}}{A}\right)^{-Q} \tag{12.2}$$

Narutani et al. later recognized that for a more accurate description of the flow curves, it is also necessary to incorporate a softening term into the model. This necessity arises from the operation of the martensitic transformation as an additional deformation mechanism. For this reason, they developed a strain-corrected rule of mixture model (SCRM), based on the data of a metastable austenite, a stable austenite and a martensitic steel variant. Their complete constitutive relation for the plastic flow of metastable austenitic steel shows the following (12.3).[3]

---

[1] K = strength factor
n = strain-hardening index.

[2] A = factor describing the driving force for strain-induced $\gamma \rightarrow \alpha'$ transformation
B = factor describing the autocatalytic effect of transformed martensite
C = factor representing the flow stress of a fully martensitic structure
Q = factor describing stress contribution of the transformed martensite.

[3] $f_{\alpha'}$ = volume fraction of α'-martensite
α, β = material coefficients from the analysis of experimental data
σ_γ = flow stress of stable austenite
$\sigma_{\alpha'}$ = flow stress of martensite.

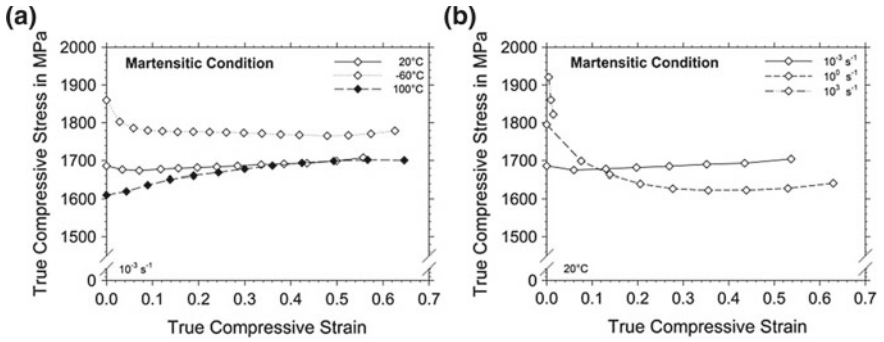

Fig. 12.4 CrMnNi16-6-6 steel: True stress-true strain curves of the α'-martensite phase: **a** influence of temperature and **b** strain rate effects [41]

$$\sigma = \left\{[1 - f_{\alpha'}] \cdot \sigma_{\gamma}(\varepsilon - \alpha \cdot f_{\alpha'}) + f_{\alpha'} \cdot \sigma_{\alpha'}(\varepsilon - \alpha \cdot f_{\alpha'})\right\} \cdot \left[1 - \beta \cdot \frac{df_{\alpha'}}{d\varepsilon}\right] \quad (12.3)$$

Recently, the existing approaches have been extended by Wolf et al. [38, 41, 42] in order to be able to model the behavior of highly metastable CrMnNi steels with low SFE by incorporating their temperature and strain rate dependence. They used the flow stress data of 16-6-6 steel in the strain rate regime 10^{-3} to 10^{3} 1/s and included the effect of thermal softening as a function of strain and strain rate. Of particular note is that the flow behavior of the martensitic phase was characterized at different temperatures and strain rates (see Fig. 12.4). Due to the low carbon content of the 16-6-6 alloy, the martensite phase received excellent ductility under compression loading up to 10^{0} 1/s. This was most likely also promoted by a few volume percent of unavoidable residual austenite. With increasing strain rate the flow stress of the martensite increased, but the influence of thermal softening also increased in significance up to adiabatic shear banding at 10^{3} 1/s.

For the formulation of the model, it was first necessary to represent the strain rate dependence of yield strength and strain hardening of the two phases austenite and martensite. To describe the yield stress, the technical proof stress values at 0.2% compression strain were used whose strain rate dependence for both phases can be described by the following logarithmic relationships[4] [38]:

$$\sigma_{d0.2}(\gamma) = \sigma_{d0.2}(\dot{\varepsilon}_{\text{ref}}) + (0.954 \cdot \ln(\dot{\varepsilon}) + 10.564) \cdot \ln\left(\frac{\dot{\varepsilon}}{\dot{\varepsilon}_{\text{ref}}}\right) \quad (12.4)$$

$$\sigma_{d0.2}(\alpha') = 16.094 \cdot \ln(\dot{\varepsilon}) + 1796.8 \quad (12.5)$$

[4] $\sigma_{d0.2}$ = proof stress value at 0.2% compression strain
$\dot{\varepsilon}_{\text{ref}}$ = reference strain rate (0.0004 1/s).

The strain hardening of a stable austenite phase could be described by (12.4), while no strain hardening was assumed for the martensitic phase based on the quasi-static results. In agreement with Narutani [40], the amount of strain caused by the martensitic phase transformation was also considered by the following correlation $\varepsilon_T = \alpha \cdot f_{\alpha'}$ with $\alpha = 0.12$. The introduction of a correction term was of particular importance in order to account for the dynamic softening caused by adiabatic sample heating.

For this purpose, a term was inserted, which originates from the well-known model of Johnson and Cook [43] [(12.6)[5]]. The amount of temperature increase originates from [44] with the extension by Meyer et al. [45].

$$\sigma_{\text{Mod}} = \sigma_{\text{Cal}} \cdot \left[1 - \left(\frac{\Delta T}{T_S - T_{\text{ref}}}\right)^m\right] \tag{12.6}$$

All the above considerations are included in the constitutive flow curve model of Wolf et al. [38] which is presented in (12.7). An estimation of the transformed volume fraction of α'-martensite $f_{\alpha'}$ can be done by using experimental data from magnetic measurements or on the basis of the model by Olson and Cohen [6], which is given in (12.8).[6]

$$\sigma_{\text{Mod}} = \left[\sigma_{d0.2}(\gamma) \cdot (\varepsilon + \varepsilon_T) \cdot f_\gamma + \sigma_{d0.2}(\alpha') \cdot f_{\alpha'}\right] \cdot \left[1 - \left(\frac{\Delta T}{T_S - T_{\text{ref}}}\right)^m\right] \tag{12.7}$$

$$f_{\alpha'} = 1 - \exp\left\{-\beta \cdot \left[1 - \exp(-\alpha \cdot \varepsilon)\right]^n\right\} \tag{12.8}$$

Figure 12.5 shows the modeled flow curves of 16-6-6 steel for three different strain rates in comparison with experimental data points. The accordance is very good and especially the curve crossing phenomenon at higher strain rates due to thermal softening effect is reproduced in the model. Thus, the goal could be achieved, to include the essential physical mechanisms of deformation in high-alloy CrMnNi TRIP/TWIP steels into a constitutive flow curve model. The underlying microstructural deformation mechanisms during high-speed loading are also of great importance and will be discussed more in detail below.

[5] σ_{Mod} = predicted flow stress with temperature correction
σ_{Cal} = calculated flow stress without temperature correction
T_S = melting temperature
T_{ref} = reference temperature at which the material is tested.

[6] α = parameter which defines the shear band formation with strain
β = parameter which defines the intersection of shear bands with strain
n = fixed exponent, which is fitted to the experimental data.

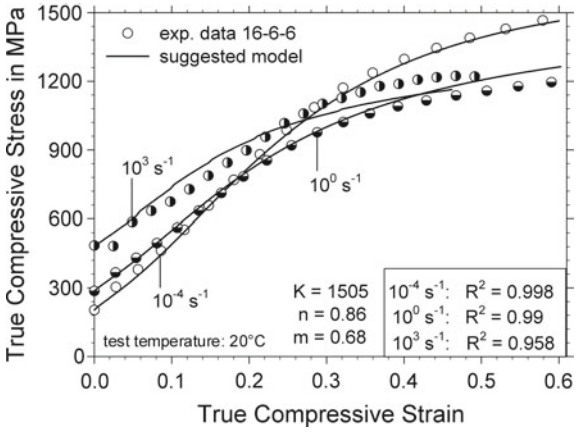

Fig. 12.5 Flow stress prediction of the developed constitutive model and experimentally determined flow stress data of 16-6-6 TRIP steel for three different strain rates [38]

12.2.3 Microstructural Deformation Mechanisms at High Strain Rates

As mentioned above, the primary deformation mechanism of TRIP/TWIP steels is the formation of planar defects such as separated Shockley partial dislocations, stacking faults or twins [8, 23, 24]. These mechanisms cause greater strength and strain hardening in comparison with wavy dislocation glide, which is active in common steel variants. The great particularity is the strong temperature dependence of these special deformation mechanisms, which means that the occurrence of glide planarity and martensite formation depends strongly on the respective environmental conditions during deformation. The investigations of Wolf et al. have shown that the same deformation mechanisms are active also in the high strain rate regime up to 10^3 1/s [25, 41, 42].

Figure 12.6 shows an example of the comparison of the microstructure of steel 16-6-6 after quasi-static compressive loading and dynamic compressive loading. In both cases, the microstructure of the deformed state up to 60% compression loading consisted of fine deformation bands and α'-martensite (cf. Fig. 12.6). Thin deformation bands evolved in the austenitic phase already at low strain values. With further straining, these deformation bands grew larger, crossed each other and α'-martensite nuclei were formed at their intersections. After quasi-static deformation the microstructure contained more and thicker bands, whereas after dynamic loading the bands appeared to be very thin and they were often oriented in one direction only. These findings were confirmed also by magnetic balance measurements, the results of which are already shown in Fig. 12.3b and indicated that an increasing strain rate caused a decreasing martensite formation due to adiabatic sample heating.

Generally, it is of great interest to use the additional deformation mechanisms, such as the TRIP- or the TWIP effect, since these lead to an increase in the energy

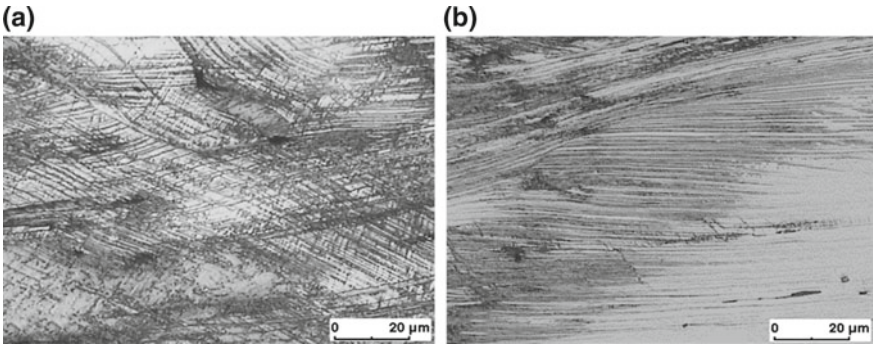

Fig. 12.6 Microstructure of steel 16-6-6 after deformation up to 60% compressive strain at strain rate of **a** 10^{-4} 1/s and **b** 10^{2} 1/s [25]

absorption capability of a material [25, 46] and thus, for example, to improved occupant protection in the event of impact in the automotive sector. Borisova et al. have shown that the high energy absorption results from interactions between individual microstructure defects with complex defect structures in which the formation of stacking faults can absorb approximately 1/30 of the whole deformation energy only [47]. Other essential absorption mechanisms include: (1) transition regions between ε-martensite and twinned austenite, (2) the formation of α'-martensite in deformation bands and (3) the formation of Lomer-Cottrell locks, stacking fault tetrahedra, and dislocation clusters. Nevertheless, the absorption of mechanical energy corresponds to the product of achievable strength level and the maximum ductility. Martin et al. showed that the strain hardening in TRIP/TWIP steels results from a continuous fragmentation of the dislocation mean free path due to deformation bands, stacking faults or the nucleation of α'-martensite [23]. A comparative consideration demonstrated that α'-martensite (G/25)[7] has a higher work hardening capacity than twins (G/50) in the austenite. However, the tensile elongation contribution is much more pronounced when twinning occurs. Huang et al. measured the greatest increase in ductility as soon as a high degree of glide planarity occurred, that means the occurrence of separated dislocations, stacking faults or austenite twins [48]. By contrast, the increase in tensile elongation due to α'-martensite formation was at best only 1/4 of that due to twinning.

As shown above, both the temperature dependence and the strain-rate dependence of the mechanical properties are important factors if the use of TRIP/TWIP steels for dynamically loaded components is considered. When the strain rate is further increased up to 10^{4} 1/s or above, the deformation and stresses are characterized by the propagation of elastic and plastic waves through the material. The deformation over the entire specimen cannot longer be considered as equilibrium, because stresses are transferred between several atomic layers, similar to a pulse with a length of only a few nanoseconds. Iron and steels have been subject to numerous shock wave studies

[7] G = shear modulus.

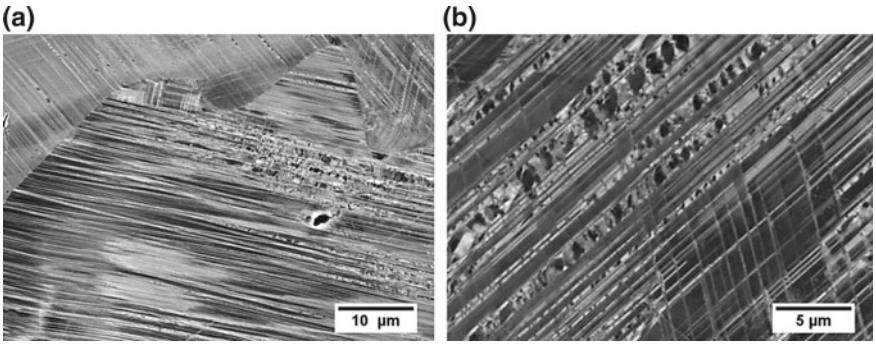

Fig. 12.7 SEM micrographs of the post-shock microstructure: **a** deformation band contrasts from backscattered electrons; **b** lenses within the bands indicate α'-martensite. The loading direction was vertical [20]

in the past. Especially the polymorphic phase transformation in iron from α-Fe to ε-Fe has been investigated extensively [49, 50]. However, in alloys with low stacking fault energy, e.g., in austenitic stainless steels, shock waves can cause additional martensitic transformations. Several studies have been carried out on steels corresponding to the composition of AISI 304 (~18% Cr, 8% Ni) under strain rates up to 10^5 1/s [51, 52]. On this occasion, the results confirmed the presence of the $\gamma \rightarrow \alpha'$ phase transformation up to such high loading rates. The microstructural changes comprised the formation of shear bands with a high concentration of deformation, whose intersections could act as nucleation sites for ε- and α'-martensite. Generally, shock prestraining led to increased microhardness and refined grains, due to high dislocation density and deformation twinning, which are both responsible for a strengthening effect [53].

Using the flyer-plate method, it was possible to identify the deformation mechanisms of CrMnNi TRIP/TWIP steels which are active under shock loading. Eckner et al. showed that an elastic-plastic shock wave produces a microstructure characterized by a high density of deformation bands, stacking faults and deformation-induced α'-martensite [20]. Figure 12.7 shows micrographs of this microstructural features, whereby the bands are clearly visible in BSE contrast. The grains had different deformation band densities and orientations, depending on the orientation to the load axis. Preferentially, their sites of origin were on active {111} slip planes of the face-centered cubic crystal lattice, due to the highest shear stresses under plastic deformation. Within the bands and at their intersections, α'-martensite was recognizable as small lenses. In accordance with results of quasi-static measurements, it could also be demonstrated that the driving force for the martensite formation increased at low temperature shock loading [20].

In order to demonstrate the deformation mechanisms, detailed TEM analyses were subsequently performed on the test samples [54]. It became clear that the austenite retained a high defect density through the plate impact and exhibited fine band structures. Intersection points of the deformation bands preferably showed

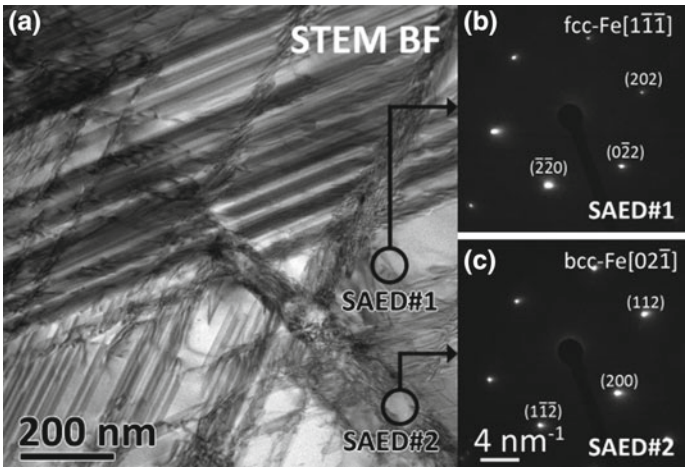

Fig. 12.8 Scanning TEM-micrograph of closely spaced deformation bands (**a**) in three different orientations (slip systems) within the γ-phase (**b**). The band intersections acted as nucleation sites for the formation of bcc α′-martensite (**c**) [54]

α′-martensite islands. At high magnification of the bands, their structure became clear as an arrangement of numerous parallel stacking faults or planar defects. In areas with high stacking fault density, it could be shown that α′-martensite was formed as assumed at the crossing points of the stacking fault bands. Figure 12.8 shows the STEM image of such a region. The enlargement of a nodal point of broader deformation bands shows that areas of the body-centered cubic phase have formed there. Using selected area electron diffraction (SAED), the lattice structure could be detected. In the area of the intersection point, the image contrasts indicated a very high defect density in the material. As reported by Martin et al. [23], the formation of α′-martensite nuclei led to the obstruction of the dislocation movement within the deformation bands and the accumulation of dislocations at the phase boundaries. In addition, the volume increase associated with the phase transformation caused a certain stress field around this area. However, the austenite outside of the bands was less deformed and parallel stacking faults could be detected here occasionally.

In the present case, the signal of the VISAR system was used to determine the characteristic strength values in the plate impact tests. A typical free surface velocity history, acquired during flyer-plate impact testing, is shown in Fig. 12.9a for the metastable austenitic CrMnNi16-6-6 cast steel. The wave form obtained was rather typical for elastic-plastic material behavior, and contained information about the yield point and the fracture strength. Initially, the elastic precursor arrived at the free end, which determined the Hugoniot elastic limit (HEL). Thereafter, the surface velocity increased again, which was associated with plastic deformation and ended in the steady Hugoniot state. The subsequent drop in surface velocity was due to the release wave or rarefaction, which reduced the pressure on the material and led to

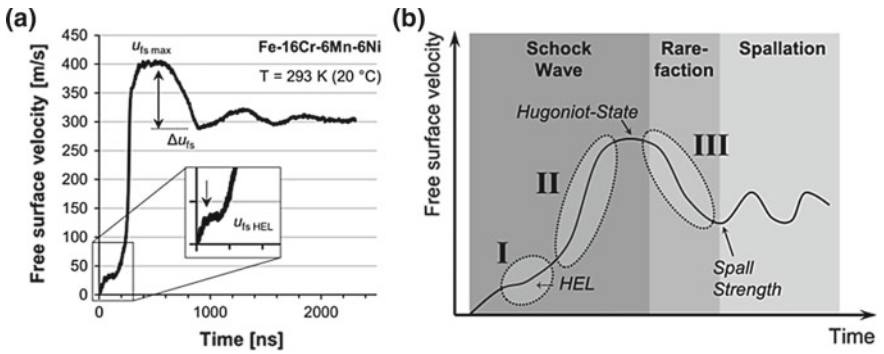

Fig. 12.9 **a** Free surface velocity profile of 16-6-6 cast steel impacted by an aluminum flyer plate at room temperature; **b** Schematic representation of the deformation mechanisms of metastable austenitic TRIP/TWIP steel during different loading states under flyer-plate impact [54]

spall fracture. The velocity pullback (Δu_{fs}) was used to determine the spall fracture strength.

Figure 12.9b presents a scheme of the deformation mechanisms of metastable austenitic TRIP/TWIP steel during shock wave loading, which was developed on the basis of the above shown experimental results of the microstructure analysis [54]. In stage I, at the very beginning of the shock deformation, elastic deformation and localized microplasticity occurred, based on the nucleation of stacking faults and thin deformation bands (planar dislocation glide). Slip occurred on several intersecting and closely-spaced planes, due to the very thin shock front and the uniaxial strain during the compression wave. In the following stage II, progressive strain hardening developed, due to a static and dynamic Hall-Petch effect caused by partial dislocation separation, slip band formation, increasing deformation band density and the formation of ε-martensite and α'-martensite nucleation sites. After the steady state (Hugoniot state), in stage III an expanding wave followed the shock wave, which reduced the materials density. The occurring tensile stresses promoted the $\gamma \rightarrow \varepsilon \rightarrow \alpha'$–transformation through an increase in formation and intersection probability of deformation bands with subsequent martensite nucleation and growth. Internal cavitation occurred, due to stresses generated by the interaction of stress waves which exceeded the local dynamic tensile strength of the steel. The coalescence of the cavities created a fragment (spall) which was finally separated from the free end of the plate.

Generally, this scheme of deformation mechanisms is also applicable to low or high temperature; however, there are various peculiarities that need to be considered here. Under shock conditions below room temperature, the thermodynamic driving force for the $\gamma \rightarrow \alpha'$–transformation increased strongly. This generally led to an increase in the strength characteristics of metastable austenitic steels, while at the same time the deformability was reduced. In addition, when the temperature fell below the M_S temperature (at about 1 °C for the CrMnNi 16-7-6 cast steel [14]), the α'-martensite also formed athermically, i.e. without the contribution of a mechanical

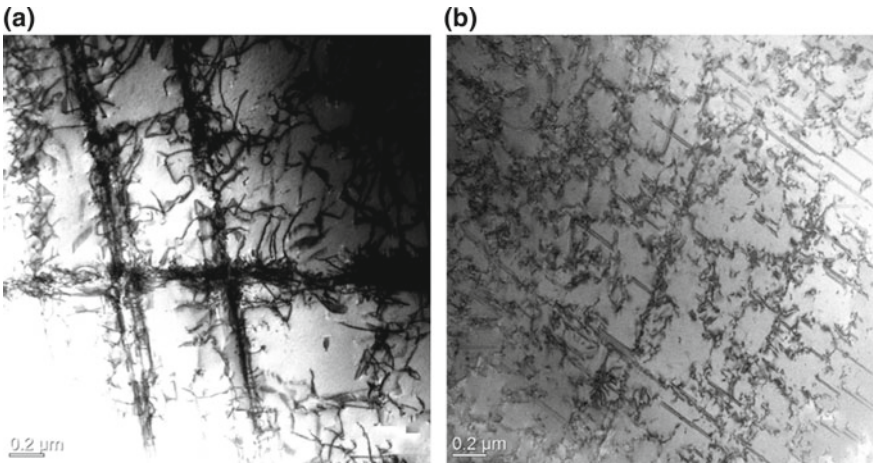

Fig. 12.10 Scanning TEM-micrographs of defect structures in CrMnNi16-6-6 steel after flyer-plate impact at **a** 100 °C and **b** 200 °C

deformation. Here, in addition to the deformation band structures already present at room temperature, coarse laths appeared within the microstructure, which also had a needle-like internal structuring. This was the cooling martensite or lath martensite, which is predominant in steels with <0.4% carbon. Similar martensite blocks can also be easily formed without further deformation in a simple cooling test. In general, the structure of the samples deformed at low temperatures was characterized by a very high density of deformation bands, which were evenly distributed over the entire inner sample area.

Furthermore, the more detailed analysis of samples tested at 100 °C and higher test temperatures showed partly fine deformation bands without significant α'-martensite nuclei at their intersection points. Also signs for wavy glide could be found, which is typical for face-centered cubic steels at high temperatures or materials with high stacking fault energies. Figure 12.10 shows exemplifying TEM images from the generated microstructures after plate impact at high temperatures. From previous investigations it is known that the deformation mechanisms change with increasing test temperature for the TRIP/TWIP steel investigated here [8]. Consequently, at 100 °C, the mechanical twinning or TWIP effect was a primary deformation mechanism also under shock loading. Moreover, there was a simultaneous occurrence of stacking fault bands (see Fig. 12.10a) and twins, which was not uncommon, since the movement of partial dislocations is a prerequisite for the occurrence of the TWIP effect [55]. Still, ε-martensite was identifiable at a low level after 100 °C shock loading, whereas nuclei of α'-martensite were only very rarely recognizable. The shock loading at 200 °C caused only a small degree of the occurrence of planar defects in the microstructure (see Fig. 12.10b). At such a high deformation temperature, it was to be expected that the deformation proceeds primarily due to dislocation glide. The

separation width of partial dislocations can only be small, due to the increased stacking fault energy. As a result, only isolated stacking fault contrasts could be found and twins were also extremely rare in this temperature range.

12.3 Honeycomb-Like Structures Made from TRIP-Steel and TRIP-Matrix-Composites

The introduction of novel cellular materials in crashworthiness-related fields of application requires a characterization of structure response and microstructure evolution in the cell wall material as a function of different parameters. In the following sections, the influence of the loading direction and the cell wall composition on the strength, deformation and damage behavior of honeycomb-like structures will be discussed in detail. Closer information about the effects of an altered test temperature and strain rate can be found in [12, 56–58].

12.3.1 Deformation Behavior of Honeycomb-Like Structures

The periodic 2D arrangement of unit cells in the investigated honeycomb-like structures results in an anisotropic material behavior which makes a distinction into two load modes necessary. The Out-Of-Plane (OOP) mode indicates the application of load parallel to the channel axis, defined as the $X3$-direction in Fig. 12.11, whereas in In-Plane (IP) mode the load is applied parallel to the $X1$–$X2$ plane.

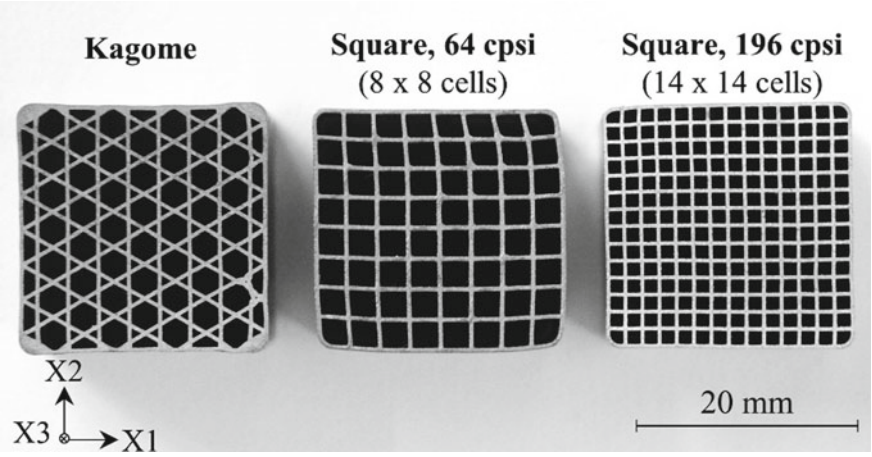

Fig. 12.11 Cross-section of investigated honeycomb-like structures in sintered state

In order to investigate the differences of OOP and IP deformation behavior, compression tests on samples with an approximate aspect ratio of 1:1 were conducted. Mechanical machining on the front sides ($X1$–$X2$ plane) ensured the desired sample dimensions and the orthogonal alignment of the cell walls, especially in OOP mode. The use of servohydraulic universal testing machines with load cells of 250 and 500 kN served for testing at quasi-static strain rates. Subsequent microstructural investigations on the deformed samples, using light optical microscopy and scanning electron microscopy in connection with EDX- and EBSD-measurements, supported the identification of the effective deformation mechanisms in the TRIP-steel matrix and the Mg-PSZ particles. The quantification of ferromagnetic α'-martensite evolution was realized by magnetic balance measurements at the beginning of the project and later continued with a MSAT magnetic saturation device.

Table 12.2 gives an overview on the TRIP-steel batches which were used for comparing the OOP and IP deformation characteristics and analyzing the effect of an altered cell wall composition. In addition, the table contains the calculated chromium and nickel equivalents, the stacking fault energies according to [59] and the additional constituents of the MgO partially stabilized zirconia.

12.3.1.1 Out-of-Plane Direction

The compressive deformation in OOP direction causes a stretch-dominated deformation mechanism in the honeycomb-like structures. Initially, the cell walls are elastically compressed until the yield strength is exceeded. With increasing compression a distinct strain hardening takes place characterized by a continuous rise in stress. In agreement with the observations of Côté et al. [60], the flow curve incline of a cell wall of the honeycomb-like structures and the respective bulk material are similar up to certain strains in this deformation stage called pre-buckling region. However, the offset in the absolute stress value derives from the varying microporosity amounting up to 15% in the struts of the cellular materials [57]. A higher microporosity results in reduced strength and deformation values, as discussed by Bocchini et al. [61].

The point of deviation in flow curve incline of cellular material from bulk material identifies the onset of structure bifurcation and hence the transition from stable to instable plastic deformation. With the onset of this post-buckling stage, progressive damage processes in the cell walls lead to a reduced strain-hardening potential. As a result, a stress maximum is formed. Within the ensuing deformation range, the buckled and fractured cell walls are compressed by an almost constant force until contacts between neighboring cell walls are formed. The densification of the entire structure involves a steep stress increase. Principally, all the investigated honeycomb-like structures display these characteristic deformation stages. However, the relative density $\bar{\rho}$ of the structures has a great influence on the achievable strength level and the strains at which a transition in deformation behavior occurs [12, 62].

Table 12.2 Overview of steel alloying elements and additional constituents of MgO partially stabilized zirconia in wt%

Batch	Abbr.	Cr	Mn	Ni	C	N	Si	Mo	Cr_{eq} [13]	Ni_{eq} [13]	γSFE[a]
X1CrNi 18-9	18-1-9	18.4	1.1	9.3	0.009	0.127	0.67	0.028	19.4	12.4	23
X3CrMnNi 17-8-10	17-8-10	16.6	7.7	10.1	0.025	0.065	1.17	0.002	18.4	15.9	19
X3CrMnNi 16-7-7	16-7-7	16.3	7.2	6.6	0.030	0.088	1.00	0.007	17.8	12.7	14
X3CrMnNi 17-7-6	17-7-6	17.0	6.5	6.1	0.030	0.082	0.30	<0.01	17.5	11.7	16
X5CrMnNi 17-7-3	17-7-3	16.7	7.1	3.4	0.050	0.097	0.91	0.024	18.1	10.2	9

[a] according to Dai et al. [59] $\gamma = 39 + 1.59\%Ni - 1.34\%Mn + 0.06\%Mn^2 - 1.75\%Cr + 0.01\%Cr^2 + 15.21\%Mo - 5.59\%Si + 26.27(\%C + 1.2\%N)(\%Cr + \%Mn + \%Mo)^{0.5} + 0.61(\%Ni(\%Cr + \%Mn))^{0.5} - 60.69(\%C + 1.2\%N)^{0.5}$

	MgO	SiO_2	HfO_2	Al_2O_3	CaO	TiO_2	ZrO_2
Mg-PSZ	3.4	2.4	1.7	0.6	0.2	0.1	Bal.

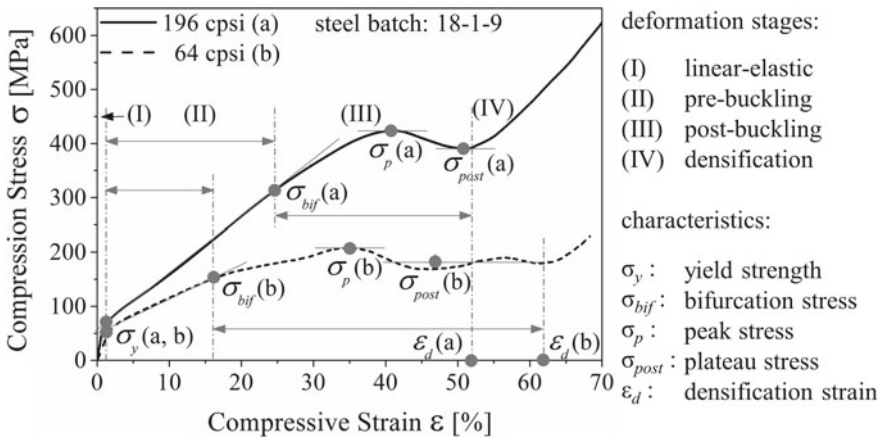

Fig. 12.12 Stress-strain curves of square-celled structures with 64 cpsi and 196 cpsi made from steel batch 18-1-9, compressed at quasi-static strain rates and room temperature [62]

An estimation of $\bar{\rho}$ for the square-celled structures can be made according to (12.9).[8] In addition, the ratio of global structure density ρ^* and density of the cell wall material ρ_s is also suitable to calculate this structure parameter [62, 63].

$$\bar{\rho} = \frac{\rho^*}{\rho_s} \cong (1 - p_m)\left[2\left(\frac{t}{l}\right) - \left(\frac{t}{l}\right)^2\right] \approx 2(1 - p_m)\frac{t}{l} \tag{12.9}$$

Both investigated square-celled structures have a comparable average cell wall thickness of approx. 300 µm (64 cpsi) and 320 µm (196 cpsi) and a residual amount of porosity in the cell walls due to the manufacturing process. However, the cell edge length differs considerably from approx. 2400–1500 µm resulting in relative densities of 0.24 and 0.36 [57]. Differences of these parameters in varying batches of honeycomb-like structures can be traced to an altered amount of microporosity and shrinkage. Figure 12.12 visualizes that minor strength is provided by the low-density structure over the whole deformation range. Besides, structural damages and the ultimate collapse identified by the peak stress are initiated at lower strains. In comparison to the 196 cpsi structure, a distinct stress plateau is developed in the cellular material with 64 cpsi prior to densification which takes place at higher strains. These tendencies conform with findings of other research groups [60, 63] reporting an increase of peak stress and a reduced densification strain with increasing

8 $\bar{\rho}$ = relative density
ρ^* = global structure density
ρ_s = density of the cell wall material
t = cell wall thickness
l = cell edge length
p_m = cell wall microporosity.

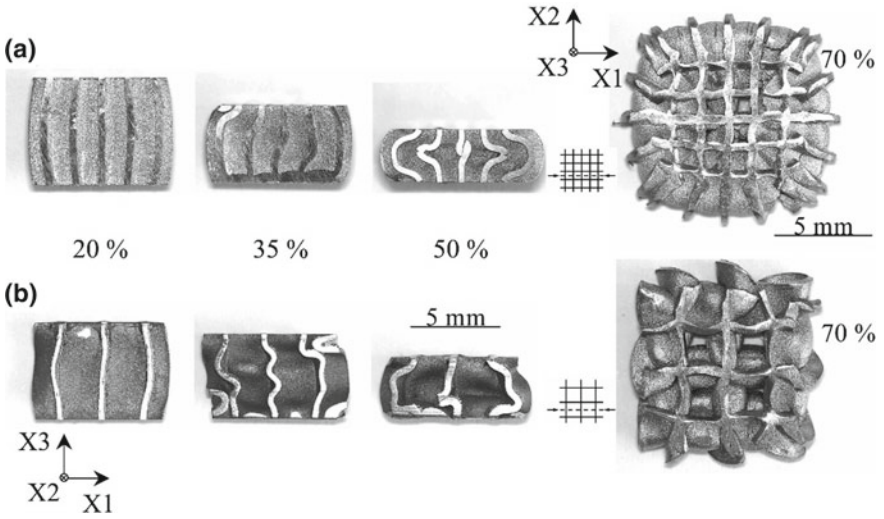

Fig. 12.13 Side view of buckling and failure patterns within the core of down-scaled samples made from steel batch 18-1-9 at different deformation stages and top view of 70% strained state: **a** 196 cpsi and **b** 64 cpsi structure [57]

relative density. However, the formation of a pre-buckling stage seems to be more common for steel matrix structures than for structures composed of aluminum [64]. Object of investigation is further the number of cells required to describe the stress-strain behavior properly. In order to assess this aspect, segments with 4 × 4 and 2 × 2 cells and an equal aspect ratio are cut out of the 196 cpsi and 64 cpsi structure, respectively. Quasi-static compression tests on the down-scaled samples demonstrate that no significant difference is recorded in the linear-elastic and pre-buckling stage. The absence of the stiffened outer skin causes only a slight shift of peak stress to lower strains, cf. [12, 57].

Interrupted compression tests serve to record the different macroscopic deformation mechanisms of the two structures. In the 196 cpsi sample, stable plastic deformation is accompanied by axial crushing and global buckling of cell walls within the $X1$–$X3$ and $X2$–$X3$ plane (cf. Fig. 12.13a). The radius of curvature increases with increasing compressive strain, until plastic kinks are built involving the onset of instable deformation. However, centered cell walls are restricted to deform freely due to the constraining effect of the outer elements. Hence, shear failure and fracture is promoted. In contrast to this global plastic "Euler-type" buckling, the low-density structures deform by local and torsional buckling which leads to folding collapse (cf. Fig. 12.13b) [57].

Sometimes the structures exhibit manufacturing related defects like cracks and inhomogeneities in the undeformed state which can be visualized by computer-tomographic investigations [65]. In order to generate a better comparability of batches

with a varying amount of imperfections the recorded stress is normalized to the relative density of the particular structure in the following sections.

12.3.1.2 In-Plane Direction

At the beginning of deformation, the stress-strain behavior in IP direction is determined by the elastic compression of cell walls similar to OOP mode. However, in case of the square-celled structures, the passing of compressive yield strength is closely linked to the compressive peak strength indicating that no stable plastic deformation within a pre-buckling stage takes place (Fig. 12.14). The subsequent steep stress decrease initiates the plateau stage which is characterized by an almost constant stress signal with only small oscillations and limited by structure densification [62]. By comparing the stress-strain response with the one in OOP mode, it is obvious that less mechanical work is required for IP deformation. An explanation is given by the macroscopic failure mechanism.

Ideally, the sintered honeycomb-like structures with square cells possess exactly aligned cell walls as predetermined by the employed die of the extrusion process. Therefore, the struts oriented parallel to the applied force, will be loaded with primarily axial stresses. As a result of the sintering process, cavities in the green bodies are more and more eliminated leading to a shrinkage of 10–15% [67]. Despite the occurrence of an almost homogenous shrinkage, small deflections of the cell walls cannot be excluded. These structural imperfections in addition to residual pores and cracks have a wider impact on IP deformation, because they are initiation points of instable plastic deformation. The onset is concentrated in the cell row with the highest deviation of structural integrity. Therefore, bending moments are initiated leading to cell wall rotation processes around adjacent cell nodes. In addition, the lattice design of the square-celled structure provides no sufficient transverse rigidity so that asymmetric shearing takes place with increasing strain, cf. Fig. 12.15. In contrast to

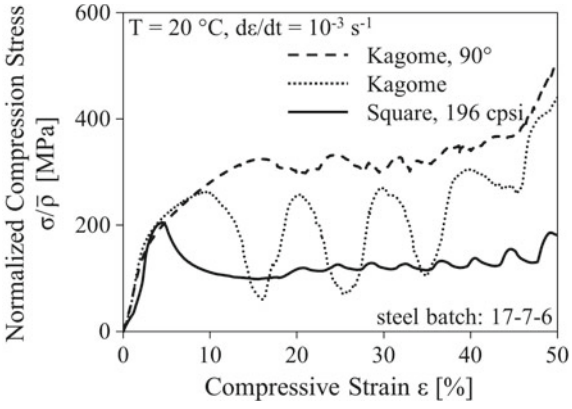

Fig. 12.14 Quasi-static stress-strain curves of Kagome (deformation in $X1$-direction), Kagome 90° (deformation in $X2$-direction) and square-celled structures recorded in IP mode according to [66]

Fig. 12.15 Deformation patterns of Kagome (deformation in $X1$-direction), Kagome 90° (deformation in $X2$-direction) and square-celled structures at engineering strains of 25% for IP mode and quasi-static strain rates according to [66]

OOP mode, where all three spatial directions are affected, IP plastic deformation is limited in the $X1$–$X2$ plane due to the 2D assembling of cells [62, 66].

In order to improve the IP properties of the honeycomb-like structures, altered cell designs are investigated by simulation on the basis of Finite Element Method (FEM) analysis [68]. Computation is conducted by the use of an isotropic, strain rate dependent and isothermal material model, based on true stress-strain curves of steel 18-1-9 and an explicit solver in ABAQUS. Nine main profiles serve as input files. For five of these profiles, a 90°-rotation is necessary to describe the whole mechanical behavior in IP mode due to the axial anisotropy of the lattice. The mass-specific (m) energy absorption capability as a characteristic value and integral information of the force (F)-displacement (s) curve is chosen to compare the performance of the investigated structures. It can be calculated as follows:

$$\mathrm{SEA}_m = \frac{\int_0^{s_i} F(s)\mathrm{d}s}{m} \tag{12.10}$$

As a result of the FEM analysis, the Kagome lattice, which consists of an ordered sequence of hexagons and triangles, provides superior properties compared to the square-celled structure. In OOP direction the relative increase of specific energy absorption capability is moderate whereas in IP mode the increment for both Kagome orientations is immense. The comparative experimental investigations of the Kagome and the square-celled lattice, both manufactured out of steel batch 17-7-6, serve to verify the results of the FEM analysis [66, 68]. In OOP mode the increase of static energy absorption capability of the Kagome configuration is no more than 2 kJ/kg at 40% engineering strain and hence less than 5% of the absolute value. However, in IP direction the static absorption capability of the Kagome structure loaded in $X2$-direction (denoted as Kagome 90°) is more than twice as much as that of the square-celled structure and in $X1$-loading (denoted as Kagome) a raise of approx. 70% is measureable. By considering the progression of the stress-strain curve in Fig. 12.14, a continuous raise of stress takes place after passing the transition point from elastic to plastic deformation for both Kagome alignments in contrast to the square-celled structure. Furthermore, the average stress level in the plateau stage is

higher than compared to the square-celled structure. Fundamental reason for the IP improvement is the change of deformation mechanism. As discussed in literature [69, 70], stretching-dominated cellular materials provide a higher stiffness and a greater strength as compared to bending-dominated structures. The latter mechanism is predominant in the square-celled structure due to the mentioned manufacturing-caused imperfections.

The deformation patterns are also in good agreement with the simulation. For both Kagome orientations, plastic deformation is symmetric with respect to the direction of loading, cf. Fig. 12.15. For $X1$–loading, the deformation pattern is characterized by buckling of angled lattice struts and cell wall rotation processes around adjacent cell nodes with increasing strain. A mainly triangle-shaped deformation pattern, which is formed by buckling of the vertical cell walls, defines the deformation in $X2$-orientation. At high strain levels a combination with upper deformation bands takes place.

12.3.2 Selection of Cell Wall Materials

Apart from the loading direction and the lattice design, the mechanical properties of honeycomb-like structures are significantly influenced by the characteristics of the cell wall material. In the following, the effect of nickel content in the steel matrix and the volume fraction of Mg-PSZ particles have been analyzed to demonstrate how the OOP deformation behavior of the 196 cpsi honeycomb-like structure can change.

12.3.2.1 Influence of Nickel Content

Metastable austenitic steels can respond to plastic deformation with different deformation mechanisms. The transformation from γ austenite into ε- or α'-martensite, called TRIP-effect, represents one possibility in addition to dislocation glide. Another alternative is the occurrence of mechanical twinning, called TWIP-effect. Decisive for the occurring mechanism are several parameters like chemical composition, stacking fault energy (SFE), temperature, stress state and strain rate, which can interact with each other [8, 25, 71–74].

Principally, a spontaneous transformation of austenite into martensite is possible if the difference in Gibbs free energy of both phases exceeds a certain threshold value below the martensite start temperature M_s. However, in plastically deformed TRIP-steels an amount of mechanical work can be added to the chemical driving force causing the start of martensite nucleation to shift to temperatures above M_s. The upper limit for deformation induced martensite formation is determined by the M_d temperature. At this temperature, the applied load is still sufficient to generate the critical shear stress in order to form 1 vol% of α'-martensite [7, 75].

Whether the selected steel is able to show the TRIP-effect and how great the extent will be, strongly depends on the austenite stability which is affected by the

chemical composition. Alloying elements like carbon, nitrogen, nickel and manganese promote the stability. The weighting of their influence is contained in the equation of the nickel-equivalent, cf. (12.11) in wt% [13]. In connection with the chromium equivalent, a classification within the Schaeffler-diagram is possible and hence the estimation of microstructure constitution for a given chemical composition at room temperature in the undeformed state. The closer the alloys are situated at the separation line of the single phase austenite and the two-phase austenite/martensite region in this diagram, the greater the tendency for a deformation induced phase transformation. The nickel-equivalent can also be employed for the estimation of M_s as Jahn et al. [76] demonstrated on the basis of dilatometer measurements on CrMnNi steels with varying chemical composition. According to this, M_s shows a parabolic increase with decreasing Ni_{eq}, which is closely associated with a reduction of austenite stability.

$$Ni_{eq} = \%\ Ni + 30\%\ C + 18\%\ N + 0.5\%\ Mn + 0.3\%\ Co + 0.2\%\ Cu\ - 0.2\%\ Al \quad (12.11)$$

Another parameter with great impact on the occurring deformation mechanism is the SFE which is a function of chemical composition and temperature [8, 59]. Austenitic steels with a low SFE possess Shockley partial dislocations with a great split-up implying that recombination of partial dislocations is not favored. For this reason, plastic deformation is dominated by planar glide and localized in deformation bands. With increasing strain, the amount of stacking faults on every second {111} plane increases and hcp ε-martensite therefore can be measured [77]. Furthermore, more and more nucleation sites for the α'-martensite transformation are built by the intersection of these deformation bands in addition to an increasing stress level which finally exceeds the triggering stress [75]. Austenitic steels with high SFE require a high stress to separate partial dislocations and form large stacking faults. Besides, the energy barrier for the ε-martensite formation increases and thus the formation of an hcp structure becomes unfavorable from the thermodynamic point of view [78]. As a consequence, stacking faults are generated on every successive {111} plane leading to the formation of mechanical twins (TWIP-effect) [79]. Regarding the nature of glide in steels with high SFE, lower stresses have to be applied to cause a recombination of partial dislocations. Therefore, cross-slip is possible resulting in a lower strain hardening potential. At a certain amount of SFE, plastic deformation proceeds by pure dislocation glide since the stress level required for the separation of partial dislocation exceeds the fracture strength of the steel.

Martin et al. [8, 73] conducted microstructural investigations on CrMnNi samples deformed at different temperatures. Since the variation in temperature is accompanied with a change in SFE energy, they extrapolated the SFE under the assumption that the SFE increases by 0.075 $mJK^{-1}\ m^{-2}$. Therefore, SFE ranges with characteristic deformation mechanisms could be proposed. Above 40 $mJ\ m^{-2}$ pure dislocation glide is prevalent whereas between 20 and 40 $mJ\ m^{-2}$ pronounced deformation twinning occurs. For energies below 20 $mJ\ m^{-2}$, a continuous transition to ε- and α'-martensite formation takes place which is always supported by dislocation glide.

In Fig. 12.16 the effect of varying deformation mechanisms within the steel matrix is displayed for the square-celled 196 cpsi honeycomb-like structures. Mayor difference of the investigated samples is the nickel content which influences the nickel equivalent and the stacking fault energy, as Table 12.2 reveals.

The graph shows that the compressive yield strength increases by decreasing the nickel content. Furthermore, plastic deformation in the pre-buckling stage generates the highest flow stress and the greatest strain-hardening in the honeycomb-like structure containing 3 wt% nickel, followed by the 7 wt% nickel sample. However, considering the onset of structure bifurcation and the start of softening due to immense structural damages at the peak stress, a decreasing triggering strain with decreasing nickel content becomes obvious. Nevertheless, the stress level of 3 and 7 wt% nickel containing samples is still higher in comparison to the sample with 10 wt% nickel. Consequently, the area enclosed by the stress-strain curve, which correlates with the energy absorption potential of the structures, decreases with increasing nickel content. Interrupted compression tests in combination with MSAT-measurements served to monitor the evolution of α'-martensite in

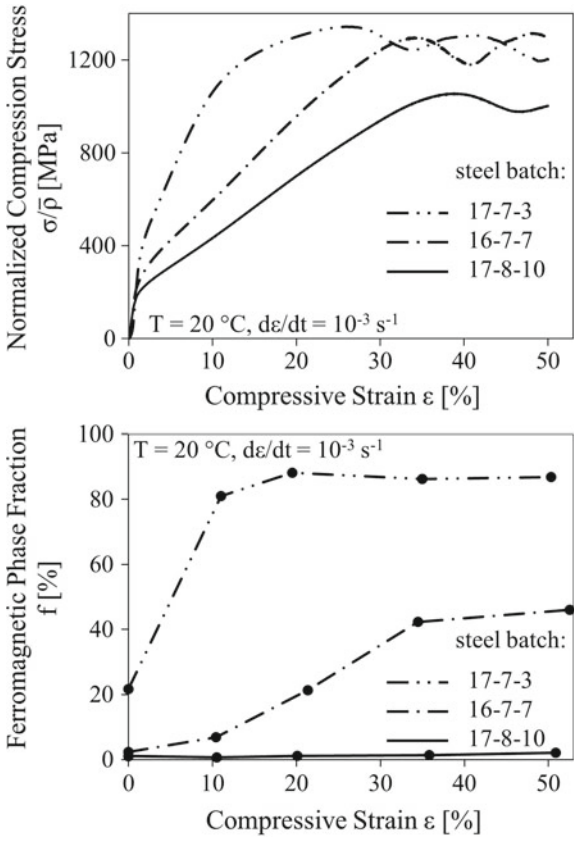

Fig. 12.16 Stress-strain behavior and α'-martensite evolution of CrMnNi square-celled honeycomb-like structures with varying nickel contents deformed in OOP mode, data used from [46]

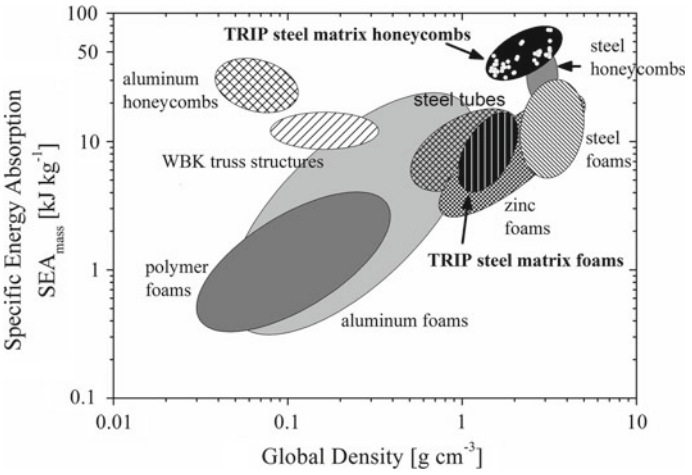

Fig. 12.17 Comparative overview of mass specific energy absorption of TRIP-steel matrix honeycombs and other structures according to [12], additional results of samples made from 17-7-3, 16-7-7 and 17-8-10 steel batches have been added (each single white dot refers to one single measurement result)

the structures, cf. Fig. 12.16. As expected, the highest amount of deformation induced α'-martensite is found in the 3 wt% nickel sample possessing the lowest Ni_{eq} and the lowest SFE. At 20% engineering strain the saturation content of α'-martensite is already reached. Due to the small amount of interstitial alloying elements, the lattice distortion and hence the strength of the α'-martensite islands is comparatively low. Nevertheless, α'-martensite is an effective obstacle regarding dislocation movement which contributes to a distinct strengthening effect [24]. The high driving force for the TRIP-effect in the 3 wt% nickel structure results, however, in the restriction of deformation capacity. Similar observations are made in the related bulk material, cf. uniform/fracture elongation [72].

In the 7 wt% nickel containing sample, the TRIP-effect is less dominant as indicated by the lower absolute ferromagnetic phase fraction. Besides, it becomes obvious that a higher amount of plastic strain is necessary to achieve the saturation content of α'-martensite in these samples. Microstructural investigations visualize that α'-martensite has an oval lense-shaped appearance and forms within deformation bands. Increasing the nickel content up to 10 wt% shifts the deformation mechanism to ε-martensite formation and mechanical twinning (TWIP-effect). Therefore, no significant ferromagnetic content is measureable even at 50% engineering strain. The microstructure images prove that an increased amount of stacking fault arrangements is contained in the samples but no α'-martensite is recognizable [46].

In order to classify the obtained results, the energy absorption performance of the honeycomb-like samples (196/64 cpsi) at 50% engineering strain is compared to several other structures, cf. Figure 12.17. All considered data refer to quasi-static compressive loading and to OOP mode in case of honeycomb(-like) structures and

tubes. The TRIP-steel matrix honeycombs belong to the cellular materials with high global density, but they still provide a great mass specific energy absorption capability. The TRIP-steel matrix honeycombs based on the initial 18-1-9 steel batch already exhibit a maximum absorption capability of 54 kJ/kg, as presented in [12]. With introduction of the 16-7-7 and 17-7-3 steel generation, the energy consumption can be further increased up to 74 kJ/kg, due to the higher driving force for the deformation induced martensitic phase transformation leading to an enhanced strength level. However, the honeycombs made from steels with a lower austenite stability are more prone to structural softening as a result of quasi-adiabatic sample heating even at strain rates of 10^2 1/s. Curve crossing phenomena of statically and dynamically deformed samples are shifted to lower strains which is also valid for the bulk material [33, 46]. Therefore, it has to be considered that the dynamic energy absorption capability can adapt or can fall even below the quasi-static one at elevated strains [25].

12.3.2.2 Effect of Particle Reinforcement

The addition of MgO partially stabilized zirconia particles in the TRIP-/TWIP-steels is intended to increase the strength of the composite which bases on several mechanisms. On the one hand, external applied loads are supposed to be transmitted from the matrix through the interface to the stronger ceramic. Additionally, the different ductility of the components and the misfit due to the varying crystal structures contribute to an increase in strength. On the other hand, an indirect strengthening mechanism results from the different coefficients of thermal expansion. During cooling from processing temperature, the steel contracts stronger in comparison to the ceramic so that dislocations are generated at the interfaces and the material is subjected to strain hardening. In principle, the effectiveness of the mechanisms depends on the volume content, the shape and the orientation with respect to the load direction of the reinforcing phase [80].

Apart from the described mechanisms, which are the basis for all metal matrix composites (MMC) with superior strength properties, the Mg-PSZ particles are supposed to contribute to further strengthening by a martensitic phase transformation. At initial state the particles exhibit a cubic/tetragonal microstructure which transforms into monoclinic state by mechanical loading in connection with exceedance of the triggering stress. The transformation is accompanied by a volume expansion generating an additional amount of compressive strain in the surrounding matrix. Hence, more mechanical work is available for the TRIP-effect in grains with a favorable orientation. Martin et al. [81] proved the occurrence of this interaction and its positive effect on the mechanical properties by comparing MMCs reinforced with 5 vol% Al_2O_3 and Mg-PSZ, respectively. The greatest flow stress in the whole deformation range was provided by the Mg-PSZ sample although the content of α'-martensite was lower as compared to the non-reinforced sample. This fact was explained by the limited deformability in the ceramic which restricts plastic flow in the TRIP-matrix. However, an increase in monoclinic phase fraction with increasing strain

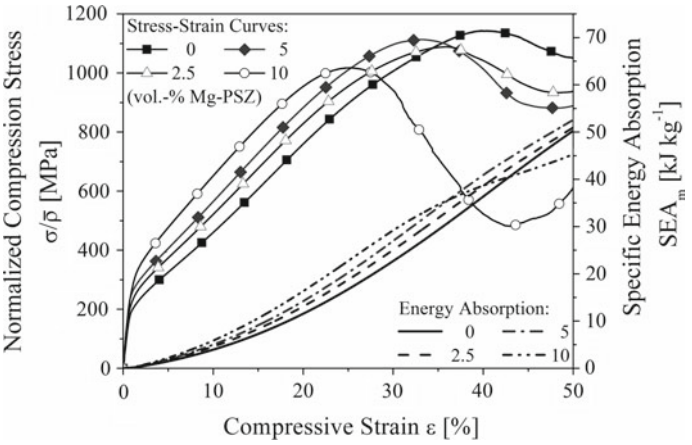

Fig. 12.18 Quasi-static stress-strain response of 196 cpsi honeycomb-like structures composed of 18-1-9 steel batch with 0 to 10 vol% Mg-PSZ particles, data used from [67]

was detected and more α'-martensite was measured in the Mg-PSZ sample than in the one containing Al_2O_3.

In order to exploit the whole potential of these mechanisms, the amount of monoclinic phase has to be reduced at initial state. For bulk material, synthesized by Spark Plasma Sintering, this precondition can be ensured as the results of Krüger et al. [10] demonstrated. However, the honeycomb-like structures are manufactured by conventional sintering which requires high temperatures and long dwell times to receive dense products. The manufacturing parameters permit diffusion processes both in direction of the steel and the other way around, as Berek et al. [82] reported. As a consequence, magnesium reacts to silicates and spinels with alloying elements of the steel and is no longer stabilizing the ceramic in the cubic/tetragonal phase. However, Weigelt et al. [83] observed that exposing pure Mg-PSZ to temperatures of 1300 °C, which is close to the tetragonal → monoclinic phase transformation temperature, resulted also in a significant decrease of stabilized cubic/tetragonal phase even without a steel interaction. At initial state 90% of the Mg-PSZ microstructure was of cubic/tetragonal phase whereas only 30% remained after firing at 1300 °C for 3 h. Elevating the sintering temperatures to 1400 °C was favorable for a greater cubic/tetragonal phase content, but is close to the melting temperature of the steel. Consequently, the strengthening effect of the martensitic phase transformation within the Mg-PSZ is comparatively low in conventionally sintered honeycomb-like structures [84].

The effect of different Mg-PSZ volume contents, varying between 2.5 and 10 vol%, on the OOP deformation behavior of square-celled 196 cpsi honeycomb-like structures is depicted in Fig. 12.18. In accordance with the mechanical response of the related bulk material, the compressive yield strength of the honeycomb-like structures increases with increasing amounts of Mg-PSZ [57]. The enhancement of

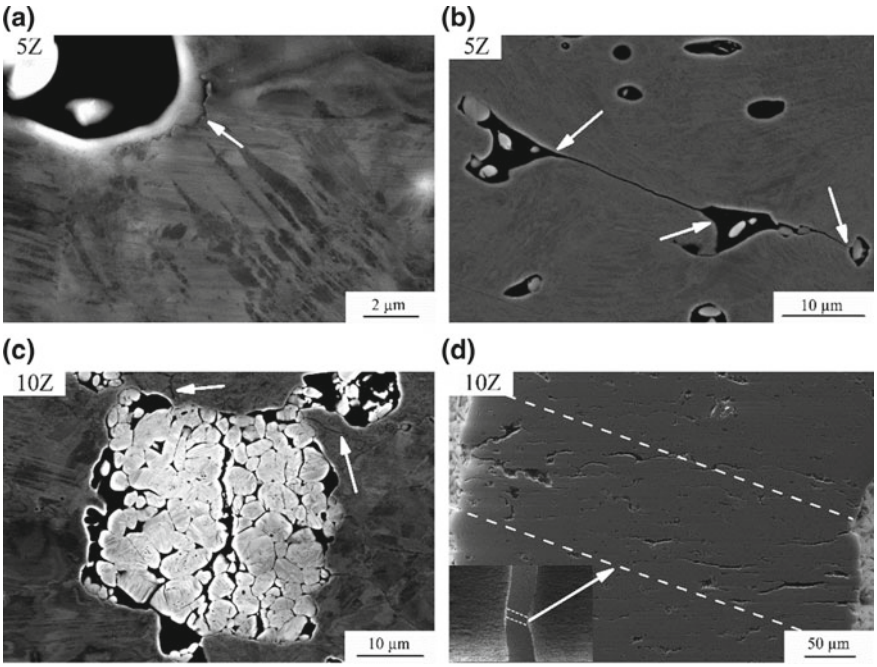

Fig. 12.19 Damage processes of TRIP-Matrix-Composites according to [62] at $\varepsilon = 20\%$ **a** interface debonding, **b** crack bifurcation at particles and pores, **c** failure of Mg-PSZ agglomerate as well as matrix cracks and **d** weakened cell wall cross-section at $\varepsilon = 35\%$; Z denotes vol% Mg-PSZ

plastic compression stress and work hardening rate continue up to certain deformation stages in the pre-buckling stage due to a constrained plastic flow in the matrix arising by the presence of the rigid ceramic particles. In addition, the polygonal shape of the Mg-PSZ leads to stress concentrations at the interfaces between matrix and particle, possessing a perpendicular orientation to the loading direction. Depending on the crystal orientation of the surrounding austenitic grains, more dislocations can form, further glide systems can be activated and an increased ε- and α'-martensite formation is possible [81]. It is obvious that the more particles are contained the greater the impact of these mechanisms on the resulting strength.

However, the increasing inhomogeneous stress distributions can finally exceed the steel/ceramic interfacial strength and the fracture strength of the steel matrix, respectively. Debonding processes and crack initiation are the result, visualized by Fig. 12.19a. Additionally, the fracture of brittle ceramic particles, cracking of Mg-PSZ agglomerates and crack bifurcation contribute to material softening processes, cf. Figure 12.19b, c. Hence, with increasing Mg-PSZ content a lower crush resistance (maximum strength) is provided and failure shifts to lower strains, cf. Figure 12.18. The steeper stress decrease of the composite structures within the post-buckling stage arises by the formation of micro crack networks which can combine to macro cracks. Especially areas with high particle density and great strain localizations are prone to

cracking which is accompanied with particle rearrangement processes. As a result, Mg-PSZ particles are lined up in unattached cluster chains leading to a weakening of the cell wall cross section, cf. Figure 12.19d.

The sum of damage processes is adverse for the α'-martensite evolution as the measurements of ferromagnetic phase content reveal. At low engineering strains (up to approx. 10%), partially higher α'-martensite contents can be identified in the central deformation areas of the composite honeycomb-like structures whereas at 50% engineering strain the highest α'-martensite content within the same area is found in the non-reinforced sample [62, 67]. Nevertheless, the reinforcement of TRIP-steel with Mg-PSZ particles can contribute to an increased energy absorption capability up to 50% engineering strain as the comparison of the non-reinforced and the 5 vol% Mg-PSZ containing sample in Fig. 12.18 shows.

Thus, the main finding—likewise on basis of other employed steel batches—is the increase of energy absorption capability by reinforcing the steel with Mg-PSZ particles being most effective for low strains where material damages are not pronounced [46].

12.4 Conclusions

The material behavior of metastable TRIP-steels was investigated in the form of bulk material and honeycomb-like structures. Strain-rate and temperature dependent compression tests with subsequent microstructural investigations on the bulk samples led to the following findings:

- In dependence of the deformation temperature different deformation mechanisms are dominating: below 100 °C the deformation-induced formation of ε- and α'-martensite, between 100 and 250 °C mechanical twinning and above 250 °C dislocation glide.
- An own model was presented to describe the material behavior under consideration of the strain rate sensitivity of austenite and martensite, adiabatic heating and strain hardening of the austenite. The model, which is based in a modified rule of mixture, provides excellent results.
- The dominant deformation mechanisms of the 16-6-6 CrMnNi steel in the strain rate range of 10^{-3} up to ~5×10^4 1/s were the accumulation of stacking faults in lamellar deformation bands and the strain-induced formation of ε- and α'-martensite. Low temperatures raised the driving force for α'-martensite formation also in shock loading. The particularly high strain rates during flyer-plate impact induced α'-martensite formation even at very low strains. However, the $\gamma \rightarrow \varepsilon$ transformation still occurred as an intermediate step.

Compression tests on honeycomb-like structures in dependence of loading direction, nickel content in the steel and volume content of Mg-PSZ can be summarized as follows:

- In OOP mode the cell walls were exposed to a stretch-dominated deformation mechanism and the occurrence of a plastic pre-buckling stage was identified. The strength level and strain hardening potential, respectively, in this stage were controlled by the relative density of the structure, the deformation mechanisms in the steel and the steel/Mg-PSZ particle interactions.
- IP compression resulted in a lower strength and thus in a reduced energy absorption capability in comparison to OOP loading. However, altering the cell shape from square-celled to Kagome configuration contributed considerably to an enhanced IP performance.
- Decreasing the austenite stability and the stacking fault energy led to an increase of flow stress and strain hardening rate. Even though the failure strain at the peak stress decreased with decreasing nickel content, the low nickel containing samples exhibited the highest TRIP-effect, and thereby possessed the greatest energy absorption capability.
- The reinforcement with Mg-PSZ particles contributed to an increase of flow stress and energy absorption capability. Damage processes like interfacial debonding, particle cracking and crack bifurcation caused a shift of structural collapse to lower stresses and strains.

Acknowledgements This work was funded by the German Research Foundation or Deutsche Forschungsgemeinschaft (DFG), and was created as part of the Collaborative Research Center TRIP-Matrix-Composites (Project number 54473466—CRC 799). The build-up of the Freiberg Shock Wave Laboratory was fully financed by the Dr. Erich Krüger foundation. Special thanks are addressed to Dr. D. Ehinger and Dr. S. Wolf for their outstanding work in this sub-project generating numerous publications and hence significant foundation for this book chapter. Prof. T. Halle of OVGU Magdeburg supported the project with FEM-calculations. Moreover, part of the experimental work was done by Ms. C. Ullrich, Dr. M. Motylenko, Dr. A. S. Savinykh and Prof. S. V. Razorenov (RAS, Chernogolovka, Russia), for which we would like to express our sincere thanks. Additionally, the authors thank all technical employees who were tasked with mechanical processing of samples for mechanical testing and microstructure analysis as well as all students supporting the research project.

References

1. L. Remy, A. Pineau, Mater. Sci. Eng. **28**, 99 (1977)
2. O. Grässel, L. Krüger, G. Frommeyer, L.W. Meyer, Int. J. Plast **16**, 1391 (2000)
3. G. Frommeyer, U. Brüx, P. Neumann, ISIJ Int. **43**, 438 (2003)
4. O. Bouaziz, S. Allain, C. Scott, Scr. Mater. **58**, 484 (2008)
5. V.F. Zackay, E.R. Parker, D. Fahr, R. Busch, Trans. ASM **60**, 252 (1967)
6. G.B. Olson, M. Cohen, Metall. Trans. A **6**, 791 (1975)
7. I. Tamura, Met. Sci. **16**, 245 (1982)
8. S. Martin, S. Wolf, U. Martin, L. Krüger, D. Rafaja, Metall. Mater. Trans. A **47**, 49 (2016)
9. O. Bouaziz, H. Zurob, M. Huang, Steel Res. Int. **12**, 937 (2013)
10. L. Krüger, S. Decker, R. Ohser-Wiedemann, D. Ehinger, S. Martin, U. Martin, H.J. Seifert, Steel Res. Int. **82**, 1017 (2011)
11. C.G. Aneziris, W. Schärfl, H. Biermann, U. Martin, Int. J. Appl. Ceram. Technol. **6**, 727 (2009)

12. D. Ehinger, L. Krüger, S. Krause, U. Martin, C. Weigelt, C.G. Aneziris, EPJ Web Conf. **26**, 1056 (2012). https://doi.org/10.1051/epjconf/20122601056
13. A. Weiß, P.R. Scheller, A. Jahn, Patent WO 2008/009722, 24 Jan 2008
14. A. Jahn, A. Kovalev, A. Weiß, S. Wolf, L. Krüger, P.R. Scheller, Steel Res. Int. **82**, 39 (2011)
15. G.T. Gray III, Mechanical testing and evaluation, in *ASM Handbook,* vol. 8 ed. by H. Kuhn, D. Medlin (ASM International, Materials Park, OhioText, 2000), p. 462
16. D.J. Frew, Exp. Mech. **45**, 186 (2005)
17. J.C. Gong, L.E. Malvern, D.A. Jenkins, J. Eng. Mater. Technol. **112**, 309 (1990)
18. L.M. Barker, R.E. Hollenbach, J. Appl. Phys. **43**, 4669 (1972)
19. G.I. Kanel, S.V. Razorenov, V.E. Fortov (eds.), *Shock-Wave Phenomena and the Properties of Condensed Matter* (Springer, New York, 2004)
20. R. Eckner, B. Reichel, A.S. Savinykh, L. Krüger, S.V. Razorenov, G.V. Garkushin, Metall. Mater. Trans. A **47**, 75 (2016)
21. K. Thoma, U. Hornemann, M. Sauer, E. Schneider, Meteorit. Planet. Sci. **40**, 1283 (2005)
22. R. Eckner, L. Krüger, C. Ullrich, D. Rafaja, T. Schlothauer, G. Heide, Metall. Mater. Trans. A **47**, 4922 (2016)
23. S. Martin, S. Wolf, S. Decker, L. Krüger, U. Martin, Steel Res. Int. **86**, 1187 (2015)
24. A. Weidner, H. Biermann, JOM **67**, 1729 (2015)
25. L. Krüger, S. Wolf, S. Martin, U. Martin, A. Jahn, A. Weiß, P.R. Scheller, Steel Res. Int. **82**, 1087 (2011)
26. L. Krüger, S. Wolf, U. Martin, S. Martin, P.R. Scheller, A. Jahn, A. Weiß, J. Phys: Conf. Ser. **240**, 12098 (2010)
27. J. Talonen, H. Hänninen, P. Nenonen, G. Pape, Metall. Mater. Trans. A **36**, 421 (2005)
28. J. Talonen, H. Hänninen, Acta Mater. **55**, 6108 (2007)
29. M. Isakov, S. Hiermaier, V.-T. Kuokkala, Metall. Mater. Trans. A **46**, 2352 (2015)
30. T.S. Byun, Acta Mater. **51**, 3063 (2003)
31. L. Krüger, S. Wolf, M. Rüssel, U. Martin, A. Jahn, A. Weiß, P.R. Scheller, MP Materials Testing **52**, 588 (2010)
32. A. Andrade-Campos, F. Teixeira-Dias, U. Krupp, F. Barlat, E.F. Rauch, J.J. Grácio, Strain **46**, 283 (2010)
33. R. Eckner, L. Krüger, KEM **742**, 113 (2017)
34. G.L. Huang, D. Matlock, G. Krauss, Metall. Trans. A **20**, 1239 (1989)
35. A. Bäumer, J.A. Jiménez, W. Bleck, Int. J. Mater. Res. **101**, 705 (2010)
36. L. Krüger, S. Wolf, U. Martin, P. Scheller, A. Jahn, A. Weiß, in *Proceedings of the 9th International Conferences on the Mechanical and Physical Behaviour of Materials under Dynamic Loading (DYMAT 2009),* Brussels, Belgium, 7–11 September 2009
37. A.Y. Chen, H.H. Ruan, J. Wang, H.L. Chan, Q. Wang, Q. Li, J. Lu, Acta Mater. **59**, 3697 (2011)
38. S. Wolf, S. Martin, L. Krüger, U. Martin, Mater. Sci. Eng., A **594**, 72 (2014)
39. D.C. Ludwigson, J.A. Berger, J. Iron Steel Inst. **207**, 63 (1969)
40. T. Narutani, G.B. Olson, M. Cohen, J. Phys. **43**, 429 (1982)
41. S. Wolf, S. Martin, L. Krüger, U. Martin, U. Lorenz, Steel Res. Int. **83**, 529 (2012)
42. S. Wolf, Dissertation, TU Bergakademie Freiberg, 2012
43. G.R. Johnson, W.H. Cook, in *Proceedings of the 7th International Symposium on Ballistics,* The Hague, The Netherlands, 19–21 April 1983
44. S. Nemat-Nasser, Mechanical testing and evaluation, in *ASM Handbook,* vol. 8, ed. by H. Kuhn, D. Medlin (ASM International, Materials Park, OhioText, 2000), p. 429
45. L.W. Meyer, N. Herzig, T. Halle, F. Hahn, L. Krüger, K.P. Staudhammer, J. Mater. Process. Technol. **182**, 319 (2007)
46. C. Baumgart, D. Ehinger, C. Weigelt, L. Krüger, C.G. Aneziris, Compos. Struct. **136**, 297 (2016)
47. D. Borisova, V. Klemm, S. Martin, S. Wolf, D. Rafaja, Adv. Eng. Mater. **15**, 571 (2013)
48. Q. Huang, O. Volkova, H. Biermann, J. Mola, Mater. Sci. Technol. **33**, 1224 (2017)
49. D. Bancroft, E.L. Peterson, S. Minshall, J. Appl. Phys. **27**, 291 (1956)
50. L.M. Barker, R.E. Hollenbach, J. Appl. Phys. **45**, 4872 (1974)

51. S.A. Maloy, G.T. Gray, C.M. Cady, R.W. Rutherford, R.S. Hixson, Metall. Mater. Trans. A **35**, 2617 (2004)
52. L.E. Murr, J.A. Korbonski, Metall. Trans. **1**, 3333 (1970)
53. K. Chen, C. Zheng, Z. Yuan, J. Lu, X. Ren, X. Luo, Mater. Sci. Eng., A **587**, 244 (2013)
54. R. Eckner, L. Krüger, M. Motylenko, A.S. Savinykh, S.V. Razorenov, G.V. Garkushin, EPJ Web Conf. **183**, 3007 (2018). https://doi.org/10.1051/epjconf/201818303007
55. C. Ullrich, R. Eckner, L. Krüger, S. Martin, V. Klemm, D. Rafaja, Mater. Sci. Eng., A **649**, 390 (2016)
56. D. Ehinger, L. Krüger, U. Martin, C. Weigelt, C.G. Aneziris, Steel Res. Int. **82**, 1048 (2011)
57. D. Ehinger, L. Krüger, U. Martin, C. Weigelt, C.G. Aneziris, Int. J. Solids Struct. **66**, 207 (2015). https://doi.org/10.1016/j.ijsolstr.2015.02.052
58. D. Ehinger, L. Krüger, U. Martin, C. Weigelt, C.G. Aneziris, Adv. Eng. Mater. **15**, 646 (2013)
59. Q.-X. Dai, A.-D. Wang, X.-N. Cheng, X.-M. Luo, Chin. Phys. **11**, 596 (2002)
60. F. Côté, V.S. Deshpande, N.A. Fleck, A.G. Evans, Mater. Sci. Eng., A **380**, 272 (2004)
61. G.F. Bocchini, Int. J. Powder Metall **22**, 185 (1986)
62. D. Ehinger, Dissertation, TU Bergakademie Freiberg, 2013
63. L.J. Gibson, M.F. Ashby, *Cellular Solids* (Cambridge University Press, Cambridge, 1997)
64. W.E. Baker, T.C. Togami, J.C. Weydert, Int. J. Impact Eng **21**, 149 (1998)
65. U. Ballaschk, H. Berek, D. Ehinger, C.G. Aneziris, L. Krüger, Adv. Eng. Mater. **15**, 590 (2013)
66. C. Baumgart, C. Weigelt, C.G. Aneziris, L. Krüger, EPJ Web Conf. **183**, 3014 (2018). https://doi.org/10.1051/epjconf/201818303014
67. D. Ehinger, L. Krüger, U. Martin, C. Weigelt, C.G. Aneziris, Steel Res. Int. **83**, 565 (2012)
68. C. Baumgart, T. Halle, C. Weigelt, L. Krüger, C.G. Aneziris, Sci. Technol. Mater. **30**, 35 (2018)
69. V.S. Deshpande, M.F. Ashby, N.A. Fleck, Acta Mater. **49**, 1035 (2001)
70. A.-J. Wang, D.L. McDowell, J. Eng. Mater. Technol. **126**, 137 (2004)
71. M. Wendler, A. Weiß, L. Krüger, J. Mola, A. Franke, A. Kovalev, S. Wolf, Adv. Eng. Mater. **15**, 558 (2013)
72. A. Jahn, A. Kovalev, A. Weiβ, P.R. Scheller, S. Wolf, L. Krüger, S. Martin, U. Martin, in *Proceedings of the 8th European Symposium on Martensitic Transformations (ESOMAT 2009),* Prague, Czech Republic, 7–11 September 2009
73. S. Martin, S. Wolf, U. Martin, L. Krüger, Solid State Phenom. **172–174**, 172 (2011)
74. T. Iwamoto, T. Tsuta, Y. Tomita, Int. J. Mech. Sci. **40**, 173 (1998)
75. H. Schumann, Krist. Tech. **10**, 401 (1975)
76. A. Jahn, A. Kovalev, A. Weiß, P.R. Scheller, Steel Res. Int. **82**, 1108 (2011)
77. S. Martin, C. Ullrich, D. Šimek, U. Martin, D. Rafaja, J. Appl. Crystallogr. **44**, 779 (2011)
78. G.B. Olson, M. Cohen, Metall. Trans. A **7**, 1897 (1976)
79. F. Lecroisey, A. Pineau, Metall. Mater. Trans. B **3**, 391 (1972)
80. N. Chawla, Y.-L. Shen, Adv. Eng. Mater. **3**, 357 (2001)
81. S. Martin, S. Richter, S. Decker, U. Martin, L. Krüger, D. Rafaja, Steel Res. Int. **82**, 1133 (2011)
82. H. Berek, A. Yanina, C. Weigelt, C.G. Aneziris, Steel Res. Int. **82**, 1094 (2011)
83. C. Weigelt, S. Giersberg, C. Wenzel, C.G. Aneziris, Adv. Eng. Mater. **12**, 486 (2010)
84. C. Weigelt, C.G. Aneziris, H. Berek, D. Ehinger, U. Martin, Adv. Eng. Mater. **14**, 53 (2012)

Chapter 13
Cyclic Deformation and Fatigue Behavior of Metastable Austenitic Steels and Steel-Matrix-Composites

Horst Biermann and Matthias Droste

Abstract The present contribution highlights the cyclic deformation behavior of metastable austenitic steels focusing on the effects of different (i) chemical compositions, (ii) manufacturing methods and (iii) strengthening methods in terms of a particle reinforcement and a quenching and partitioning treatment. The investigations are based on total strain controlled fatigue tests and the observed mechanical properties are discussed in context with the microstructural processes in the material, in particular the fatigue-induced α'-martensite formation. Overall, a major relevance is ascribed to the stacking fault energy and the grain size of the material. The fatigue behavior of the steels with different chemical compositions and the steels processed via casting, additive manufacturing, reversion annealing and hot pressing, respectively, is dominated by these two factors. In contrast, the most important factor in case of the reinforced steel-matrix-composites are the Mg-PSZ particles. The advantage of increasing stress amplitudes with increasing particle fraction is purchased with particle-related damage mechanisms like debonding and particle rupture causing a shorter fatigue life. The quenching and partitioning steel on the other hand benefits from higher α'-martensite fractions after partitioning increasing both, the strength and the fatigue life of the material.

13.1 Introduction

Metastability of austenitic steels means the tendency of the material for a martensitic phase transformation to reach a state of lower energy. More precisely, the face centered cubic (fcc) austenite exhibits the ability to transform to the body centered cubic (bcc) α'-martensite under mechanical loading [1–3] or due to a temperature decrease below the material-specific martensite start temperature M_s. Under loading the diffusionless phase transformation is the reason for the so-called TRIP (TRansformation

H. Biermann (✉) · M. Droste
Institute of Materials Engineering, Technische Universität Bergakademie Freiberg, Gustav-Zeuner-Straße 5, 09599 Freiberg, Germany
e-mail: biermann@ww.tu-freiberg.de

H. Biermann and C. G. Aneziris (eds.), *Austenitic TRIP/TWIP Steels and Steel-Zirconia Composites*, Springer Series in Materials Science 298,
https://doi.org/10.1007/978-3-030-42603-3_13

Induced Plasticity) effect, i.e. an increase in strength and ductility in comparison to a stable austenitic steel without a phase transformation, e.g. [4, 5]. Thus, these steels are also known as TRIP steels. However, in contrast to the stress-assisted phase transformation occurring during pure elastic loading, the deformation-induced α'-martensite formation requires plasticity to generate potential nucleation sites in terms of intersecting deformation bands and stacking faults, respectively [1].

Besides the austenite stability, an essential factor for activation of particular deformation mechanisms is the stacking fault energy (SFE). Of course, dislocation movement is always present in case of plastic deformation, but the dislocation glide characteristic, i.e. wavy or planar glide, strongly depends on the SFE and the presence of short range order [6]. At low SFE dislocations split up in Shockley partial dislocations forming a stacking fault promoting planar glide and the formation of α'-martensite. With increasing SFE the dominance of α'-martensite formation decreases and a transition to ε-martensite formation (cf. Sect. 13.3.2, [7]) and later on twinning sets in [5, 8, 9]. The latter leads to the TWIP (TWinning Induced Plasticity) effect which in comparison to the TRIP effect is characterized by a reduced increase in strength but an even higher increase in ductility [5]. Finally, at high SFE neither deformation-induced twinning nor a phase transformation occur but wavy dislocation glide is favored. Overall, the SFE has a quite strong influence on the mechanical properties and is itself determined by the temperature and the chemical composition of the material [5, 8–11].

Like in case of other materials, many structural components out of metastable austenitic steels are subjected to cyclic loads during their application. As fatigue cracks initiate and propagate far below characteristic quasi-static values like the yield strength or ultimate tensile strength, the knowledge of the respective fatigue properties is of utmost importance. Accordingly, the present chapter aims to describe the fundamental principles of the cyclic deformation and fatigue behavior of metastable austenitic steels and steel-matrix composites and to highlight the correlation to the observed deformation mechanisms.

At first, the influence of the chemical composition and, thus, of the SFE on the cyclic deformation behavior and in particular on the fatigue life is presented in Sect. 13.3 [12, 13]. Subsequently in Sect. 13.4, the influence of the manufacturing method of austenitic steels is discussed including additively manufactured [14, 15], cast [12] and ultrafine-grained material states [16].

However, like for other materials there are efforts to further improve the mechanical properties of austenitic steels of course. Two approaches, namely particle reinforcement and quenching and partitioning (Q&P) processing are presented in context with their individual benefits and drawbacks.

For aluminum for instance, particle reinforcement is a common and well known way for increasing the strength. In case of the present high alloy austenitic steels (cf. Sect. 13.3) particles of MgO partially-stabilized zirconia (Mg-PSZ) are used for reinforcement [17]. The MgO addition stabilizes the tetragonal phase of ZrO_2 to room temperature and, thereby, enables a stress-assisted phase transformation to the monoclinic phase during loading. This phase transformation is accompanied by a volume expansion of the Mg-PSZ producing compressive stresses in the vicinity.

The influence of the particle reinforcement on the fatigue behavior is presented in Sect. 13.5 [13, 18, 19].

Quenching and partitioning (Q&P) processing [20, 21] has been another intensely investigated topic for many researchers over the last years. Their mutual aim is to design steels which meet the criteria for the 3rd generation of Advanced High Strength Steels (AHSS), i.e. a significant enhancement of the strength compared to common metastable austenitic steels (2nd generation of AHSS) but still at a reasonable ductility better than martensitic steels. So far, most publications focus on developing and investigating the process and the achieved monotonic properties, however, the fatigue behavior is hardly considered. Hence, Sect. 13.6 presents one of the first investigations on the cyclic deformation behavior of an ultra-high strength steel processed via a modified Q&P route including the fatigue life and the microstructure after cyclic deformation [22].

13.2 Methodology

This chapter introduces the experimental details and methodical issues necessary for understanding and interpretation of the results discussed afterwards. Therefore, the chemical composition and manufacturing methods of the different test materials are presented. In addition, the details of fatigue testing as well as the analytical methods used for characterization of the cyclic deformation behavior are pointed out.

13.2.1 Materials

The investigated materials are high alloy austenitic TRIP and TWIP steels and their particle-reinforced counterparts. An overview of the chemical compositions and particle size distributions is given in Table 13.1 for the steels and in Table 13.2 for the Mg-PSZ reinforcement particles. It should be noted, that the last steel of Table 13.1 (Cr14NC11.15) is austenitic at room temperature (RT) after solution annealing, but exhibited a relatively high α'-martensite fraction before cyclic deformation due to a novel quenching and partitioning (Q&P) treatment, cf. Sect. 13.2.2.

The steel powders were gas atomized by TLS (Bitterfeld, Germany) and the Mg-PSZ powder (Table 13.2) was mechanically milled and delivered by Saint-Gobain (USA). However, the steel powders used for hot pressing (HP) and electron beam melting (EBM) differed significantly regarding the particle size distribution. Whereas the HP powders exhibited d_{50} values in the range 26–28 µm and a d_{90} of 44 µm, the equivalent values were 73 µm and 119 µm, respectively, for the EBM powder.

Table 13.1 Chemical compositions of the investigated steel alloys in wt.% and their designations in this chapter. In addition, the last column indicates the average grain sizes in µm

Steel Alloy	Designation in this book	Cr	Mn	Ni	C	N	Si	Fe	$\bar{d}$
X8CrMnNi16-6-4	HP 16-6-4	16.2	6.0	3.5	0.08	0.08	0.9	Bal.	11
X4CrMnNi16-6-6	HP 16-6-6	16.1	6.0	6.0	0.04	0.04	0.9	Bal.	10
X5CrMnNi16-6-9	HP 16-6-9	15.8	5.6	8.9	0.05	0.06	1.0	Bal.	15
X6CrMnNi15-6-6	Cast 15-6-6	15.2	5.5	5.7	0.06	0.06	1.0	Bal.	774
X5CrMnNi16-6-6	EBM 16-6-6	15.8	6.4	5.9	0.05	0.04	0.9	Bal.	38
X4CrMnNi17-7-6	UFG 17-7-6	16.6	7.1	6.4	0.04	0.02	1.0	Bal.	0.7
X15CrNiMnN14-3-3	Cast Cr14NC11.15	14.2	3.0	3.3	0.15	0.11	0.4	Bal.	/

Table 13.2 Chemical composition of the delivered Mg-PSZ powder in wt.% and its designation in this book (5 and 10, respectively, indicate the volume fraction). In addition, the d_{10}, d_{50} and d_{90} values of the particle size distribution in μm and the phase fractions in vol.% are given

	Designation in this book	MgO	HfO_2	ZrO_2	d_{10}	d_{50}	d_{90}	mon.	tetr.	cub.
Mg-PSZ	5Z/10Z	2.82	1.74	Bal.	0.2	3.1	22.4	≈35	≈32	≈33

13.2.2 Manufacturing Methods

Hot pressing (HP) is a powder metallurgical processing route under vacuum atmosphere. The powder was hot pressed by Fraunhofer IKTS (Dresden, Germany) at 1250 °C for 30 min at a pressure of approximately 30 MPa applied via a piston. The heating and cooling rates were set to 10 and 5 K/min, respectively. The HP discs exhibited a diameter of 150 mm at a height of 15–20 mm.

Casting was carried out either by ACTech (Freiberg, Germany) using the sand-casting technique in case of the Cast 15-6-6 steel or by the Institute of Iron and Steel Technology (TU Bergakademie Freiberg, Germany) using die-casting for the Cast Cr14NC11.15 material. The latter was melted in a vacuum induction furnace and cast into a water-cooled copper mold placed in the furnace chamber. After casting, all steels were solution annealed for 30 min at 1050 °C (Cast 15-6-6) and at 1150 °C (Cast Cr14NC11.15), respectively.

Electron beam melting (EBM) is a powder-bed based additive manufacturing technology. The component is built in layers under a controlled atmosphere, i.e. a low helium pressure, enabling the electron beam to melt the powder. For the fatigue tests, cylindrical rods with a diameter of 14 mm and a height of 130 mm were built upright, i.e. parallel to the building direction. An Arcam A2X (Mölndal, Sweden) EBM machine was operated at a helium pressure of 2×10^{-3} mbar with beam parameters set to: acceleration voltage 60 kV, beam current 7.5 mA, scan speed 4.500 mm/s and hatch distance 50 μm. A meander-shape scan strategy in combination with a rotation of the scan direction of 90° after each layer was used. The layer thickness was 50 μm.

Reversion annealing is a heat treatment step within a more comprehensive thermo-mechanically controlled processing (TMCP) [23–30] which is the most common way for metastable austenitic steels to produce an ultrafine-grained (UFG) microstructure. The TMCP always includes a cold deformation step to induce a high amount of α'-martensite in the microstructure.

At first, the present material UFG 17-7-6 was forged at 1200 °C reducing the diameter from an initial 50 mm to 27 mm (Fig. 13.1). Afterwards, the metastable austenite was deformed at RT by rotary swaging further reducing the diameter to 8.3 mm in 11 passes and , thereby, inducing a high α'-martensite fraction of about

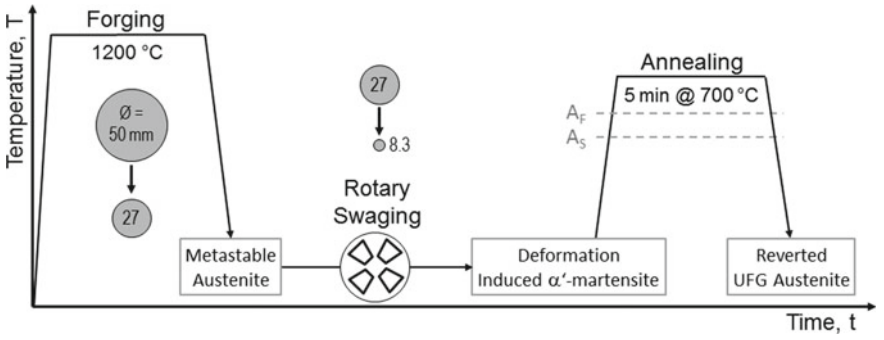

Fig. 13.1 Schematic representation of the thermo-mechanically controlled processing to achieve an UFG microstructure. After [16]

75 vol.%. The final step was an annealing treatment at 700 °C for 5 min to provoke the reversion of this α'-martensite back to austenite, called reversion annealing in literature. As reported by Weidner et al. [31] for a steel of similar chemical composition, the reversion path is based on a shear process without diffusion which is typical for interstitial free steels [32–35]. Thus, this TMCP route led to an UFG microstructure with an average grain size of 0.7 μm (cf. Sect. 13.4.1).

Quenching and partitioning (Q&P) is a thermal processing technology aiming for mechanical properties meeting the demands for the third generation of advanced high-strength steels (AHSS) [36–40], i.e. a very high strength comparable to martensitic steels but at a higher ductility. The key factor for these properties is the microstructure after Q&P consisting of tempered α'-martensite and interstitially-enriched austenite. However, usual Q&P processing includes austenization followed by quenching to a temperature well above RT due to the relatively high martensite start (M_s) temperature of the steels. In addition, a subsequent partitioning treatment is necessary before cooling down to RT. In contrast, the present steel Cr14NC11.15 exhibits a M_s temperature slightly below RT simplifying this temperature-time control. This novel Q&P process designed by Wendler et al. [21] requires a subzero cooling in a second step (Fig. 13.2) to induce athermal α'-martensite whose target fraction can be adjusted by variation of the cooling temperature T_c. Finally, a partitioning treatment has to be performed to provoke a diffusion of interstitials *C* and *N* from the supersaturated α'-martensite to the retained austenite. For the present steel two different cooling temperatures of −120 °C and −20 °C have been used in combination with a partitioning at 450 °C for 3 min (Fig. 13.2).

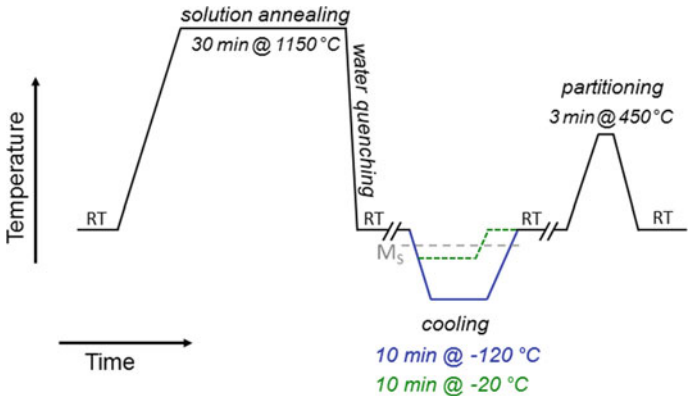

Fig. 13.2 Schematic representation of the Q&P process to achieve an ultra-high strength austenitic-martensitic microstructure. After [22]

13.2.3 Fatigue Testing

All fatigue tests presented in this work are total strain controlled tests performed either on a Landmark 250 or a Landmark 100, both servo-hydraulic testing systems by MTS (Eden Prairie, USA). Constant strain amplitude tests under symmetrical push-pull conditions (strain ratio $R_\varepsilon = -1$) were conducted in the range of $0.25\% \leq \Delta\varepsilon_t/2 \leq 2\%$ following a triangular strain function with a constant strain rate of 4×10^{-3} s^{-1}.

Furthermore, a Feritscope® (Fischerscope® MMS® PC, Sindelfingen, Germany) has been attached to the specimens to record the evolution of α'-martensite in situ during cyclic deformation. As this device is calibrated for measuring the δ-ferrite phase fraction denoted in Fe-%, its readings have to be multiplied by a correction factor of 1.7 to obtain the actual α'-martensite fraction [41]. However, this linear correlation is only valid up to 55 Fe-%, which is exceeded in some of the presented tests. Hence, all α'-martensite evolutions presented in this chapter are the pure Feritscope® readings in Fe-% without any correction factor.

The fatigue specimens exhibited a gauge length of 14 mm at a diameter of 5 mm (UFG 17-7-6) and 6 mm (all other materials), respectively. They were ground and polished mechanically before testing.

13.2.4 Analytical Methods

Scanning electron microscopy (SEM) was used to characterize the microstructure of the different materials before and after cyclic deformation. Therefore, imaging methods like backscattered electron (BSE) imaging, electron channeling contrast imaging (ECCI) and SEM in transmission mode (t-SEM) as well as the analytical method electron backscattered diffraction (EBSD) are employed. The EBSD (EDAX,

New Jersey, USA) scans are used for calculation of the average grain size $\bar{d}$ according to the following relationship

$$\bar{d} = \frac{\sum_{i=1}^{N} A_i \cdot d_i}{\sum_{i=1}^{N} A_i} \tag{13.1}$$

where A_i and d_i are the area and diameter of the i^{th} grain, respectively. All SEM investigations were performed on a field emission gun Mira 3 FE-SEM by Tescan (Brno, Czech Republic) operated at an acceleration voltage between 20 and 30 kV.

Transmission electron microscopy (TEM) was applied for the UFG 17-7-6 material which was thinned by electrolytic etching. The investigations were carried out on a field emission gun JEOL JEM-2200FS operated at 200 kV.

X-ray micro-computed tomography (μ-CT) was used for defect characterization in the additive manufactured EBM 16-6-6 material and the HP 16-6-6 for reference purposes. The analyzed volumes were 45.6 mm^3 (EBM) and 48.2 mm^3 (HP), respectively. The Nikon system was operated at 160 kV with a micro-focus of 3 μm using a tungsten filament for X-ray emission (further details of setup are given in [42]). The data was analyzed by the software VGSTUDIO MAX 3.1 using the algorithm "VGEasyPore".

13.3 Influence of Chemical Composition on the Fatigue Behavior

This chapter investigates the influence of different concentrations of Ni on the fatigue behavior and deformation mechanisms of three hot pressed high alloy austenitic steels[1] (HP 16-6-4, HP 16-6-6, HP 16-6-9, cf. Table 13.1). Ni is an austenite stabilizer and increases the stacking fault energy (SFE) of a material and, thereby, strongly influences the characteristics of plastic deformation.

13.3.1 Cyclic Deformation Behavior

The cyclic deformation curves of Fig. 13.3 indicate a distinct difference between the variants with low and medium Ni content compared to the HP 16-6-9 with 9 wt.% Ni. The latter exhibits a pronounced primary hardening whose intensity decreases with decreasing strain amplitude and finally merges to continuous cyclic softening at $\Delta\varepsilon_t/2 = 0.2\%$. This behavior is typical for high alloy austenitic steels and related to an increase in dislocation density and interactions between the dislocations [43, 44]. For the highest strain amplitude $\Delta\varepsilon_t/2 = 2\%$ cyclic hardening goes on until failure whereas it is replaced by cyclic softening for the other strain amplitudes

[1] The present discussion is based on investigations by Glage and summarizes results of his doctoral thesis [13].

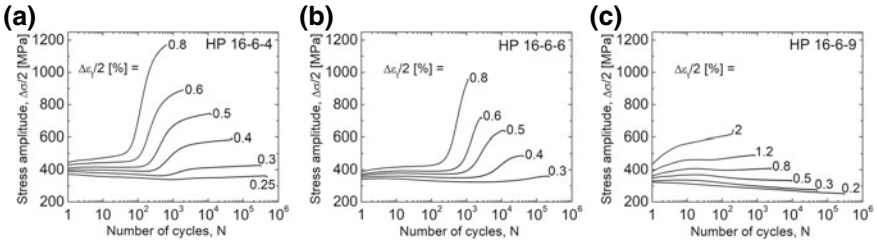

Fig. 13.3 Cyclic deformation curves for different strain amplitudes of the materials HP 16-6-4 (**a**), HP 16-6-6 (**b**) and HP 16-6-9 (**c**). After [13, 18, 19]

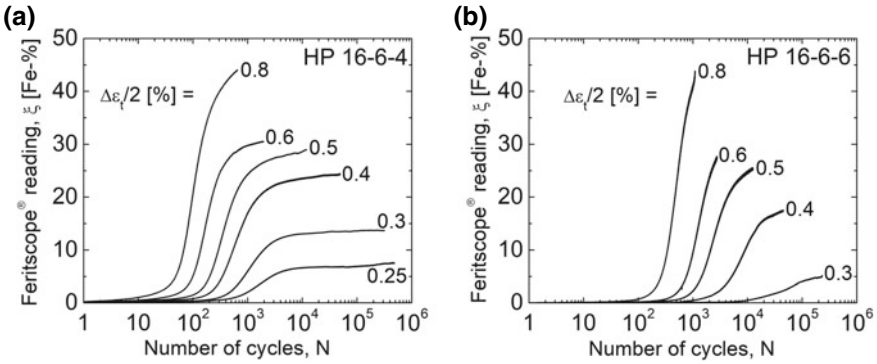

Fig. 13.4 α'-martensite evolution during cyclic deformation at different strain amplitudes for the materials HP 16-6-4 (**a**) and HP 16-6-6 (**b**). After [13, 19]

probably caused by rearrangement of dislocations. However, in case of the high strain amplitudes $\Delta\varepsilon_t/2 \geq 0.8\%$ secondary hardening, mainly attributed to the formation of fatigue-induced twinning (Sect. 13.3.2), sets in after a certain number of cycles. The twin boundaries lead to a reduction of the mean free path of dislocations [45] often called dynamic Hall-Petch effect in literature, e.g. [46], leading to an increase of the stress amplitudes.

In the beginning of cyclic deformation the qualitative courses of the cyclic deformation curves of the other two HP steels (Fig. 13.3a, b) are similar to the described behavior, although the primary hardening slightly decreases with decreasing Ni content. A substantial difference occurs once the secondary hardening sets in. Its magnitude significantly increases with decreasing Ni content and, in addition, the secondary hardening is triggered at a lower number of cycles. Besides the chemical composition, the intensity and onset is of course affected by the applied strain amplitude, i.e. a shorter incubation period and increasing magnitude with increasing strain amplitude. Especially in case of the HP 16-6-4 the cyclic hardening merges to a saturation-like stage at low and medium strain amplitudes continuing until fracture. However, including the α'-martensite evolution (Fig. 13.4) in the investigation

of cyclic deformation behavior shows obviously, that the secondary hardening correlates quite well with the cyclic deformation behavior. In fact, the α'-martensite formation causes the cyclic hardening as it is well-known for metastable austenitic steels, e.g. [9, 44, 47–49]. In the present alloys, this hardening effect is not solely due to the higher hardness of the martensitic phase, but a strong impact is attributed to (i) the lower grain size of the α'-martensite compared to the austenite and (ii) a reduced mean free path for dislocations as the α'-martensite nuclei preferentially form within deformation bands [4, 50].

Based on the finding that the cyclic hardening is due to the martensitic phase transformation, the reasons for the differences between the materials as well as for the different onset times and intensities can be discussed. Figure 13.5 shows the threshold value of the cumulated plastic strain $\lambda_{p,\mathrm{th}}$ which has to be exceeded to trigger the α'-martensite formation [9, 48, 49] plotted against the applied total strain amplitudes. This threshold value stems from the premiss that the deformation-induced α'-martensite formation is triggered by a double shear mechanism of at least two intersecting stacking faults on different slip planes [1, 51]. Thus, the threshold value decreases with increasing strain amplitude (Fig. 13.5) as a consequence of an increase in lattice defects and a higher density of deformation bands, i.e. more sites for α'-martensite nucleation [43, 49, 52]. Consequently, decreasing strain amplitudes lead to increasing incubation periods for the martensitic phase transformation (Fig. 13.4) and the accompanied secondary hardening (Fig. 13.3a, b). Furthermore, the lower threshold values of the HP 16-6-4 steel compared to HP 16-6-6 are due to its lower austenite stability.

The cyclic hardening causes a decrease in the plastic strain amplitude $\Delta\varepsilon_{\mathrm{pl}}/2$, i.e. the plasticity within a cycle decreases. As a consequence of this, the driving force for further α'-martensite formation decreases as well which leads to the described stage of saturation-like behavior, especially in case of medium and small amplitudes. An additional contribution to this behavior is attributed to internal stresses due to the formation of α'-martensite inhibiting a further phase transformation.

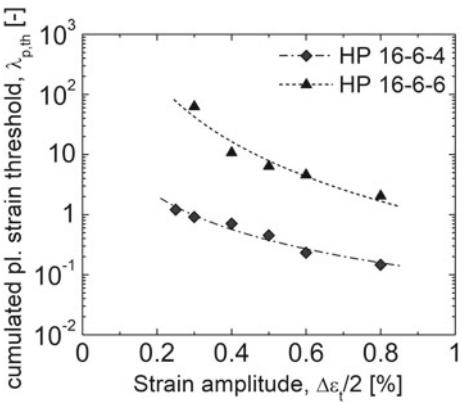

Fig. 13.5 Threshold values of the cumulated plastic strain $\lambda_{p,\mathrm{th}}$ plotted against the applied strain amplitudes. After [13]

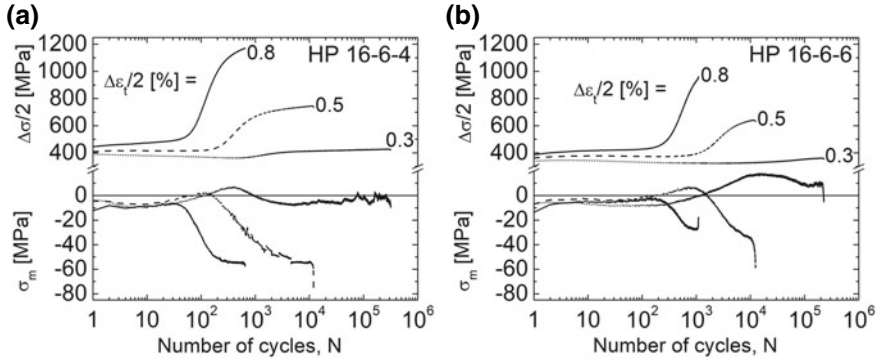

Fig. 13.6 Stress amplitudes and mean stresses of selected strain amplitudes versus number of cycles for the HP 16-6-4 (**a**) and HP 16-6-6 (**b**). After [13]

Figure 13.6 illustrates the connection between stress amplitude and mean stress arising during cyclic deformation. As discussed above, the martensitic phase transformation provokes an increase of the stress amplitude which, in addition, goes along with a decreasing mean stress whose magnitude as well increases with increasing strain amplitude. This behavior was also observed by other authors [47, 53, 54] and is attributed to the volume expansion accompanying the α'-martensite formation. Prior to the described behavior, a stage of increasing mean stress is observed which is more pronounced with decreasing strain amplitude, i.e. with a less pronounced α'-martensite formation. This increase of the mean stress is probably due to highly faulted areas, i.e. regions with a high density of stacking faults called ε-martensite in literature. This ε-martensite causes a volume contraction and, thereby, an increasing mean stress in total strain controlled fatigue tests. However, this effect is overcompensated once the α'-martensite formation and its volume expansion sets in resulting in the described decreasing mean stresses.

13.3.2 Microstructure After Cyclic Deformation

The formation of stacking faults, ε-martensite and α'-martensite is verified by SEM investigations and exemplarily shown in Fig. 13.7 for the HP 16-6-4 steel cyclically deformed at $\Delta\varepsilon_t/2 = 0.25\%$. A high amount of deformation bands is formed inside the grains (Fig. 13.7a, b) and their stacking fault density increases with ongoing plastic deformation. However, after cyclic deformation these bands are often indexed as ε-martensite by EBSD (Fig. 13.7d, yellow coloured) due to the high density of stacking faults changing the stacking sequence of the {1 1 1} planes from ABCABC of the fcc crystal lattice to the hexagonal ABAB [7]. In accordance with other authors, e.g. [55], these highly faulted deformation bands are a preferred nucleation site for

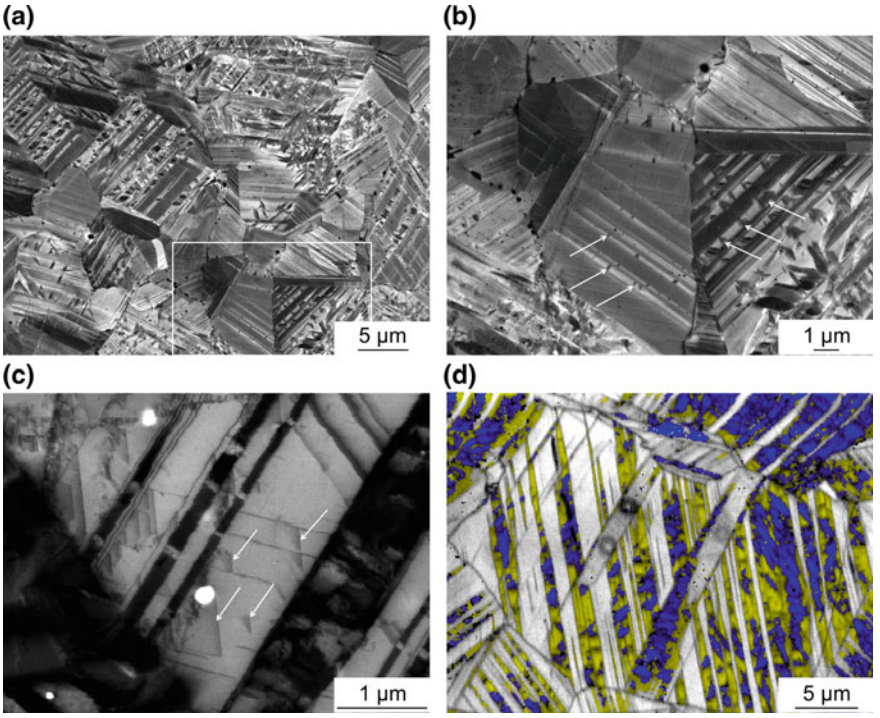

Fig. 13.7 Microstructure of the steel HP 16-6-4 after cyclic deformation at $\Delta\varepsilon_t/2 = 0.25\%$. BSE (**a**, **b**) and ECCI (**c**) images as well as EBSD phase map (**d**, blue—α'-martensite, yellow—ε-martensite, grey—band contrast). After [13, 19]

α'-martensite as revealed by Fig. 13.7b (white arrows) and d indicating a martensitic phase transformation in the order $\gamma \rightarrow \varepsilon \rightarrow \alpha'$.

Some individual stacking faults are also present in between the deformation bands as shown in Fig. 13.7c (white arrows). Furthermore, this micrograph reveals the quite planar glide character of the material due to its low SFE.

The increased SFE of the HP 16-6-9 on the other hand causes a change in the deformation mechanisms, which in addition are depending on the applied strain amplitude. At small strain amplitudes only few grains contain deformation bands which are usually oriented approximately 45° in relation to the loading axis (Fig. 13.8a, b). As already known for the steel HP 16-6-4 the deformation bands consist of stacking faults. In the vicinity of the crack tip a higher deformation band density (Fig. 13.8c) is observed due to the higher local plasticity. Figure 13.8d even reveals $\Sigma 3$-twin boundaries which are marked in yellow indicating deformation bands of sufficient thickness with respect to the resolution of the EBSD scan thus being fatigue-induced twins.

At a higher strain amplitude of $\Delta\varepsilon_t/2 = 0.8\%$ the density of deformation bands increases. In between the bands dislocation cells are formed (Fig. 13.8e) indicating

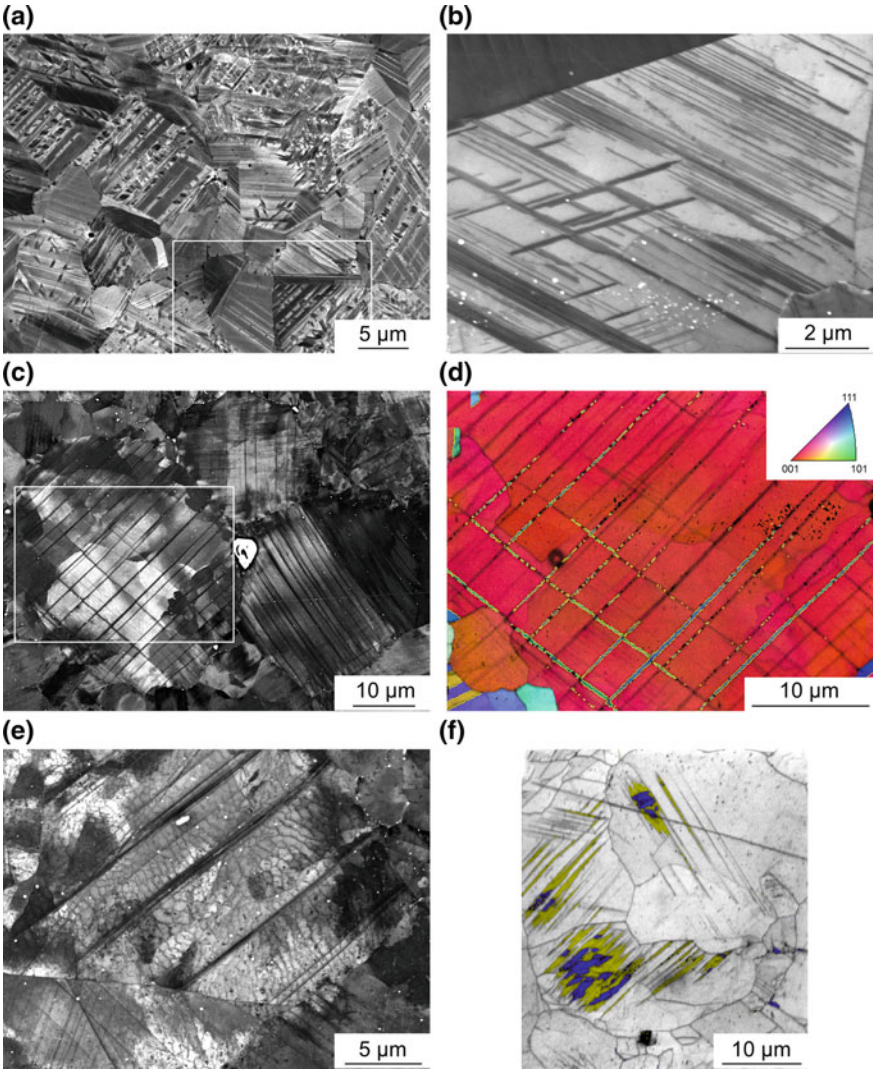

Fig. 13.8 BSE (**a**) and ECCI (**b**, **c**, **e**) images and EBSD orientation (**d**) and phase (**f**) maps of the steel HP 16-6-9 cyclically deformed at $\Delta\varepsilon_t/2 = 0.4\%$ (**a**–**d**) and $\Delta\varepsilon_t/2 = 0.8\%$ (**e**, **f**), respectively. Loading axis is horizontally. After [13, 18, 19]

the beginning transition to a wavy glide character [56]. Nevertheless, a rare formation of α'-martensite via the intermediate ε-martensite is observed as well (Fig. 13.8f) at this high strain amplitude. However, the secondary hardening in the cyclic deformation curve (Fig. 13.3c) is rather due to fatigue-induced twinning as the α'-martensite fraction remains low and the twins are strong obstacles for dislocation movement reducing the mean free path for dislocations on a second slip system [18, 46, 57].

13.3.3 Fatigue Life

The fatigue life estimation for the HP materials according to Basquin-Manson-Coffin is shown in Fig. 13.9a. Obviously, the most metastable steel HP 16-6-4 exhibits a superior lifetime at small strain amplitudes compared to HP 16-6-9 and vice versa. Accordingly, the α'-martensite formation seems to be detrimental at high strain amplitudes due to the decreased ductility of the material which is a determining factor in this lifetime regime [58]. On the other hand, at small strain amplitudes the α'-martensite formation leads to a significant decrease in the plastic strain amplitude and, thereby, to an increase in the fatigue life. This strain amplitude-dependent impact of the martensitic phase transformation on the fatigue life causes a crossover of the lifetime curves for the different austenite stabilities at a total strain amplitude of approximately $\Delta\varepsilon_t/2 = 0.5\%$ (Fig. 13.9a).

For the lifetime description of all HP variants with just one power law, Glage [13] proposed the plastic stress-strain product SSP_{pl}:

$$SSP_{pl} = \sqrt{\frac{\Delta\sigma}{2}\frac{\Delta\varepsilon_{pl}}{2}E} \tag{13.2}$$

As already discussed, the α'-martensite formation provokes an increase of the stress amplitude $\Delta\sigma/2$ which is accompanied by a decrease in the plastic strain amplitude $\Delta\varepsilon_{pl}/2$. The SSP_{pl} considers both parameters resulting in much smaller differences between the material variants (Fig. 13.9b). Despite the fact that variant specific lifetime curves would still exhibit slightly different slopes, it is possible to provide a surprisingly good lifetime description for all materials with just one power law (Fig. 13.9b). In fact, almost all test data is located within a scatter band of factor 3.

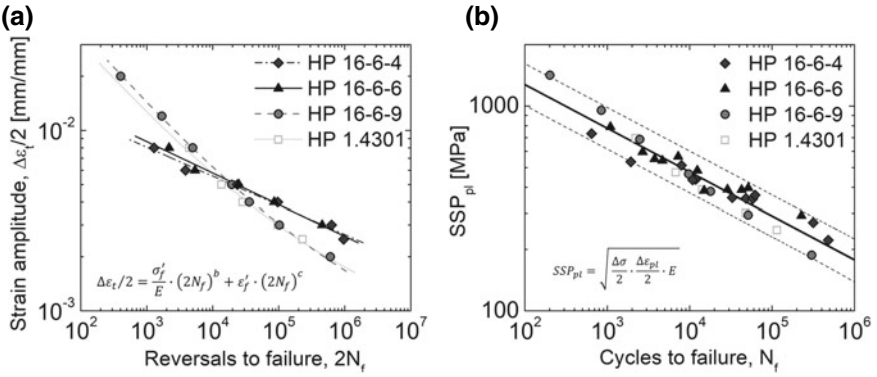

Fig. 13.9 Total strain based fatigue life curves (**a**), and SSP_{pl} parameter for lifetime estimation with one power law and corresponding scatter band of factor 3 (**b**). After [13, 19]

13.4 Influence of the Manufacturing Method on the Fatigue Behavior

This section compares the fatigue properties of the same steel grade (base composition 16-6-6, cf. Table 13.1) manufactured via different processing routes: (i) Casting, (ii) additive manufacturing by EBM and (iii) reversion annealing to achieve an UFG microstructure.[2] In addition, the results will be compared to the HP counterpart which was introduced in Sect. 13.3. The manufacturing methods are described in more detail in Sect. 13.2.2.

13.4.1 Microstructure of the Undeformed State

The microstructures of the different material states before cyclic deformation are shown in Fig. 13.10. The biggest difference is observed regarding the average grain size. The cast material by far exhibits the biggest grain size of 774 μm whereas the smallest one is observed for the UFG state with 0.7 μm. In between these two materials, the EBM and HP states fit in with average grain sizes of 38 μm and 10 μm, respectively. However, for an additive manufactured material the microstructure of the EBM 16-6-6 (Fig. 13.10b) is relatively isotropic which is attributed to multiple phase transformations caused by the process-inherent cyclic heat treatment [14, 15]. Nevertheless, the grains are characterized by a slightly elongated shape oriented along the build direction as indicated by an average aspect ratio of 0.34 and a grain shape orientation of 91°, cf. Fig. 13.10b.

Besides anisotropy, another issue regarding additive manufactured materials are process-induced defects like lack of fusion which have a detrimental effect on the mechanical properties, in particular the fatigue lifetime. The present EBM 16-6-6 exhibited a relative density of 99.4% compared to over 99.99% for the HP 16-6-6 according to μCT-scans. As depicted in Fig. 13.11, the EBM material contains a high number of small pores with a sphericity of more than 0.5, i.e. with a relatively round and spherical shape. The pore density decreases significantly for higher equivalent pore diameters d_P. Accordingly, less than 20 pores with a $d_P > 200$ μm were detected. However, the sphericity decreases with increasing d_P and the two biggest pores with a d_P of almost 1600 μm exhibit a sphericity below 0.2. In contrast, the few defects in the HP state all exhibit a $d_P < 100$ μm and sphericities above 0.5.

[2]For a discussion in detail of the individual material states the reader is referred to [12] (cast), [14] (EBM) and [16] (UFG) which the present discussion is based on.

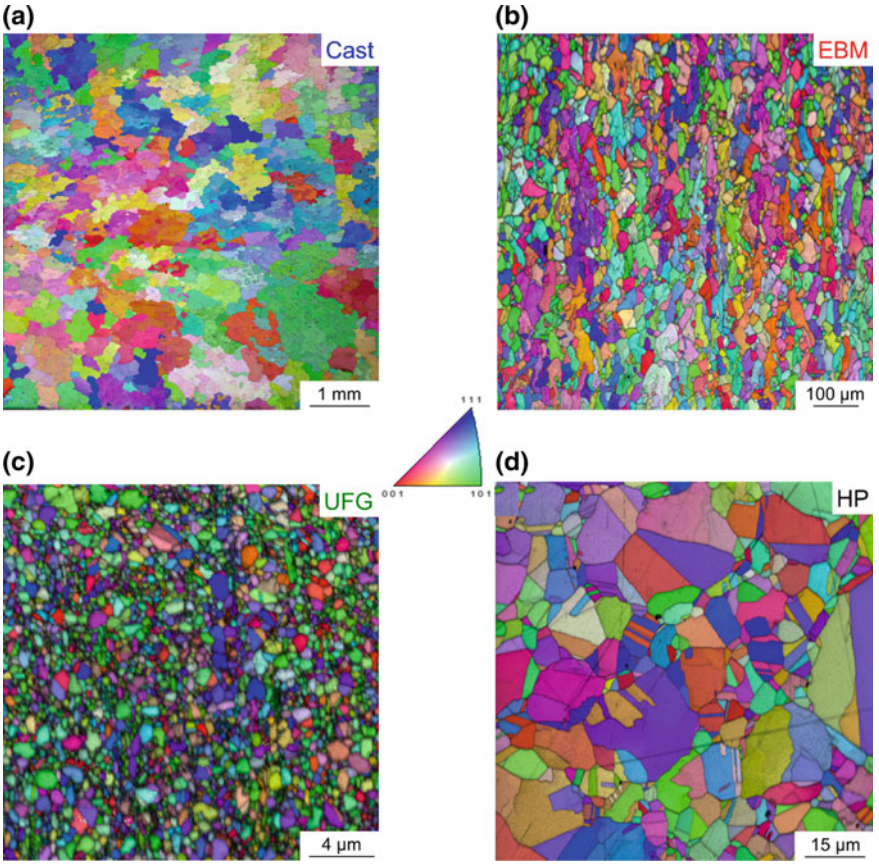

Fig. 13.10 EBSD orientation maps of the microstructures before cyclic deformation of the cast (**a**), EBM (**b**, build direction vertical), UFG (**c**) and HP (**d**) state, respectively. (**d**) After [14]

13.4.2 Cyclic Deformation Behavior and α′-Martensite Formation

The stress amplitudes at the beginning of cyclic deformation strongly depend on the material state and, in particular, on the grain size (Fig. 13.12). The cast 15-6-6 with the biggest grain size exhibits the lowest initial stress amplitudes of 200–300 MPa. With decreasing grain size the stress amplitudes of the first cycles increase to about 290–400 MPa for the EBM state and are once again slightly higher in case of the HP reference material (Fig. 13.3b). By far the highest initial stress amplitudes are observed for the UFG state with about 600–1000 MPa. These differences are supposed to stem from a reduced mean free path for dislocation movement as the number of obstacles in terms of grain boundaries increases with decreasing

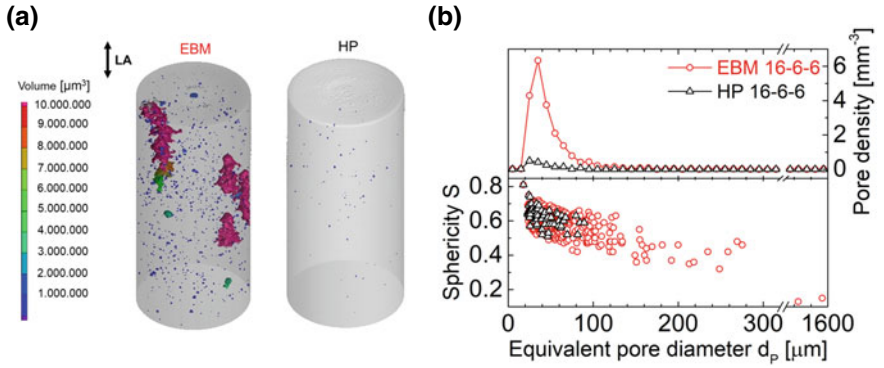

Fig. 13.11 µCT results of the EBM and HP 16-606 materials. **a** 3D-volume defect distribution (LA: loading axis) and **b** pore density and sphericity plotted against the equivalent pore diameter. The diameter of the scanned gauge length was 3 mm. After [14]

grain size of the austenite. In this context it has to be noted, that the materials discussed here all exhibit a mostly planar glide character. Wavy glide materials on the other hand exhibit other dislocation arrangements like bundles or cells whose size is significantly smaller compared to conventional grain sizes, i.e. the grain boundaries have a minor influence on the dislocation movement. Accordingly, in wavy glide a grain size dependence regarding the cyclic stress is only observed for UFG and NC materials [59].

A further difference is observed for the cyclic hardening behavior of the material states. Whereas the cast and the EBM materials exhibit similar behavior compared to the HP state discussed in Sect. 13.3.1, i.e. a strong cyclic hardening especially at high strain amplitudes caused by α'-martensite formation (Fig. 13.13), the cyclic hardening is less pronounced for the UFG material (Fig. 13.12c). Although the α'-martensite fraction after cyclic deformation at high strain amplitudes is the highest for the UFG state, the induced cyclic hardening is the least pronounced. This is attributed to the origins of α'-martensite induced hardening, namely (i) the higher strength of α'-martensite compared to austenite, (ii) the smaller grain size of α'-martensite and

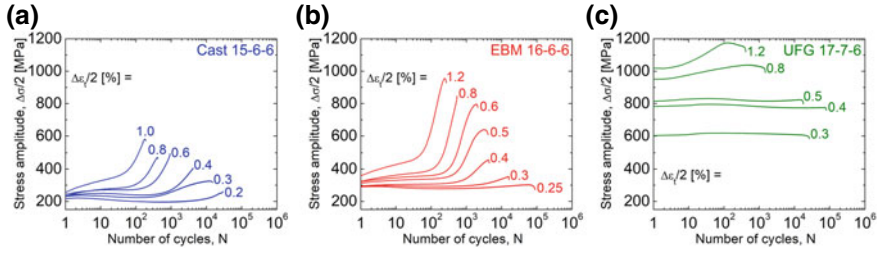

Fig. 13.12 Cyclic deformation curves of the cast (**a**), EBM (**b**) and UFG (**c**) states. After [12] (**a**), [14] (**b**) and [16] (**c**)

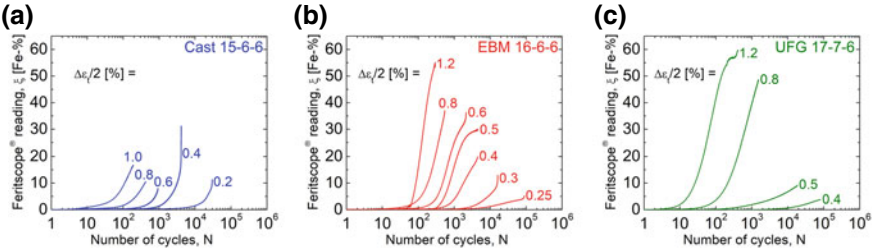

Fig. 13.13 α'-martensite evolution during cyclic deformation at different strain amplitudes for the material states cast (**a**), EBM (**b**) and UFG (**c**). After [12] (**a**), [14] (**b**) and [16] (**c**)

(iii) the reduced mean free path for dislocation movement in the austenite due to the formation of α'-martensite nuclei in the deformation bands [4, 50]. As the average austenitic grain size of 0.7 µm in the UFG material is already quite small, the α'-martensite formation does not lead to a distinct grain refinement. Furthermore, no deformation bands are formed and the influence of the α'-martensite formation on the mean free path is negligible as will be seen in Sect. 13.4.3. However, as only the first out of three hardening mechanisms is relevant in the UFG state, the least pronounced increase of the cyclic stress compared to the other material states where all three mechanisms are active is consistent.

Moreover, a difference in the incubation period for the onset of α'-martensite formation is observed. Figure 13.14 shows the cumulated plastic strain threshold $\lambda_{p,\mathrm{th}}$ which has to be exceeded to trigger the phase transformation plotted against the applied strain amplitude. As expected, the threshold value decreases with increasing strain amplitude (cf. Sect. 13.3.1 for more detailed discussion on this). The only exception is the EBM state cyclically deformed at $\Delta\varepsilon_t/2 = 1.2\%$. As obvious in Fig. 13.13b, the signal of the Feritscope® is quite unusual for the respective specimen probably due to a misalignment or other experimental issues during the test. However,

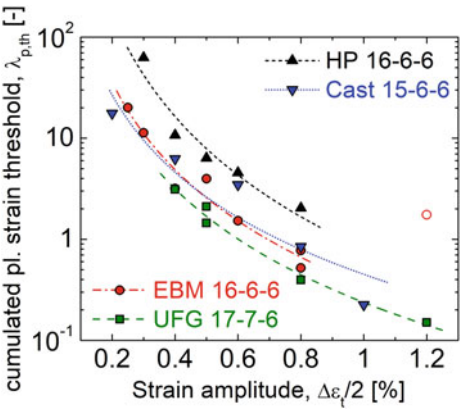

Fig. 13.14 Cumulated plastic strain threshold $\lambda_{p,\mathrm{th}}$ which has to be exceeded to trigger the fatigue-induced α'-martensite formation plotted against the applied total strain amplitude for the different material states

due to this irregularity, this specimen is excluded from the following discussion on the incubation period.

The EBM and cast states exhibit similar threshold values $\lambda_{p,\mathrm{th}}$ (Fig. 13.14) which are reduced in comparison to the already known HP material. This difference most probably stems from differences in the chemical composition. The values given in Table 13.1 are valid for the powders of the EBM and HP states, respectively. However, the bulk EBM material contains 0.5 wt.% less Mn than the HP state due to evaporation during EBM processing [15, 60]. The cast material as well exhibits a lower Mn content and a slightly lower Ni content than the HP state. This reduced content of austenite stabilizers leads to a decrease in austenite stability [61, 62] and a shift of the cumulated plastic strain threshold $\lambda_{p,\mathrm{th}}$ to lower values.

The UFG state on the other hand exhibits a slightly higher Mn and Ni content than the HP material but an even lower threshold $\lambda_{p,\mathrm{th}}$ than the EBM and cast states. Hence, in this case another factor has to be more dominant than the higher austenite stability due to the chemical composition. This is supposed to be the significantly higher stress amplitude at the onset of α'-martensite formation. These high cyclic stresses lead to the formation of small α'-martensite nuclei at an earlier stage of deformation compared to the other material states.

13.4.3 Microstructure After Cyclic Deformation

The microstructural features developing during cyclic deformation are similar in case of the cast, EBM processed and HP states. Figures 13.15a, b exemplarily show a grain of the EBM state cyclically deformed at $\Delta\varepsilon_t/2 = 0.3\%$. Deformation bands containing a high density of stacking faults have developed inside the grain. The stacking fault density increases with ongoing plastic deformation and as already discussed in Sect. 13.3.2 at a high density the deformation bands get indexed as ε-martensite by EBSD indicating a highly faulted microstructure (Fig. 13.15b). Furthermore, α'-martensite nuclei form inside the deformation bands acting as dislocation barriers for the stacking faults. Thus, the martensitic phase transformation occurs via the intermediate ε-martensite, i.e. $\gamma \rightarrow \varepsilon \rightarrow \alpha'$. At higher strain amplitudes several glide systems are activated and intersecting deformation bands provide a preferred nucleation site for α'-martensite [1, 2, 63]. In general, the α'-martensite formation is triggered by a double shear mechanism of at least two intersecting stacking faults on different slip planes.

However, this characteristic deformation band structure is not observed in the UFG material. Instead, individual stacking faults often reach through the entire grain (Fig. 13.15c, d). At this grain size, the stacking faults are supposed not to nucleate within the grains but at the grain boundaries, i.e. single partial dislocations are emitted from grain boundaries and propagate into the grain interior until they reach the grain boundary on the opposite side or some other obstacle. However, the stacking fault density in the grains is supposed to increase in this manner until ε-martensite is indexed by EBSD as well, cf. [16]. Due to the high stresses quite small α'-martensite

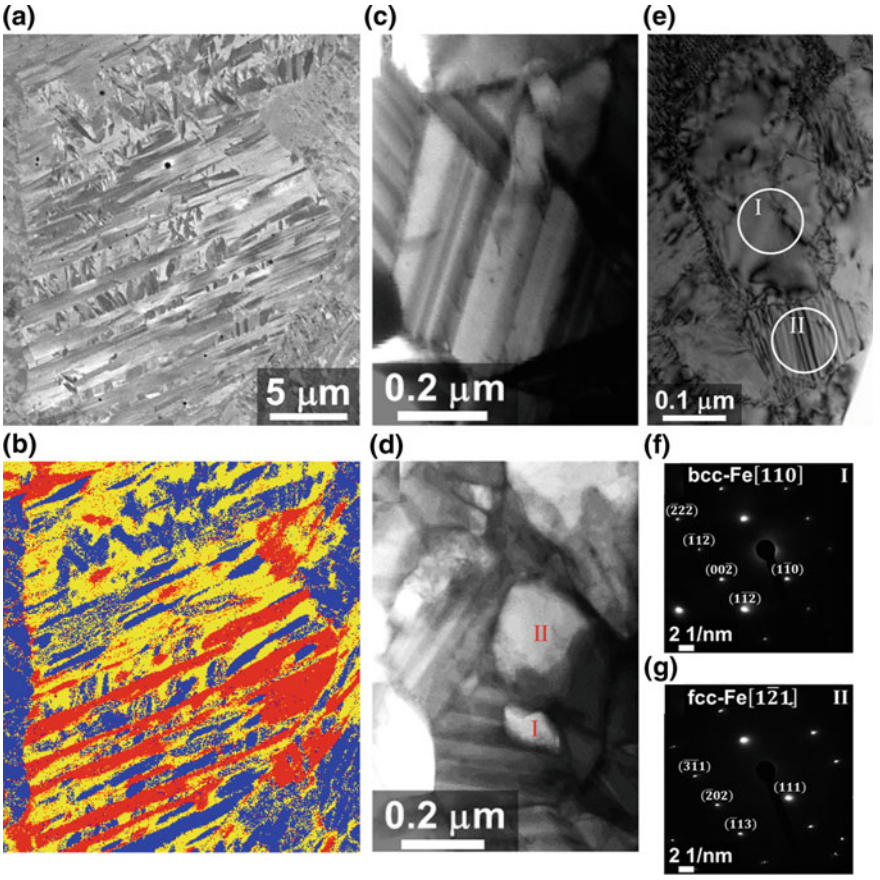

Fig. 13.15 **a**, **b** BSE image and corresponding EBSD phase map of the EBM state cyclically deformed at $\Delta\varepsilon_t/2 = 0.3\%$ (loading axis is vertical; red—austenite, yellow—ε-martensite, blue—α'-martensite). **c**, **d** t-SEM micrographs and **e** TEM bright field image of the UFG state cyclically deformed at $\Delta\varepsilon_t/2 = 0.8\%$. **f**, **g** SAED patterns of the areas marked by I and II in (**e**). After [14] (**a**, **b**) and [16] (**c**–**g**)

nuclei form inside these highly faulted grains (Fig. 13.15d, marked by I and II) and grow until the whole grain is martensitic. SAED patterns verify this assumption. The area marked by I in Fig. 13.15e is already transformed to α'-martensite as indicated by its bcc SAED pattern (Fig. 13.15f). It exhibits a Nishiyama-Wassermann orientation in relation to the adjacent fcc area marked by II (Fig. 13.15e, g). Hence, the α'martensite nucleated inside this grain, i.e. even at this small size the grains do not transform entirely at once.

13.4.4 Fatigue Life

Figure 13.16 shows the fatigue life curves of the discussed material states. In addition, a curve labeled EBM 16-6-6 ann. is plotted which represents a solution annealed (1050 °C, 30 min) state of the EBM material (see [14] for further details). However, the shortest fatigue life with the highest scatter is observed for the cast material. The quite big grain size with just a few grains per cross section may contributes to this inferior behavior. Further factors are supposed to be the inhomogeneous microstructure in terms of segregations and the porosity originating from the casting process.

In contrast, the highest fatigue life is observed for the UFG material. In the high cycle fatigue (HCF) regime where the strength is an important lifetime determining factor this is a quite usual behavior and often reported in literature, e.g. [59, 64, 65]. In the low cycle fatigue (LCF) regime on the other hand, the increased strength does not lead to a significant reduction of the plastic strain amplitude and the ductility of the material becomes an essential factor for fatigue life. Hence, coarse grained (CG) materials usually exhibit an enhanced lifetime in the LCF regime due to their higher ductility [59, 64, 65]. In contrast, the present UFG state exhibits the highest lifetime even in the LCF regime. This behavior is supposed to be related to the different phases, more precisely a more homogenous strain partitioning between the austenitic and martensitic phase in comparison to the other material states. As already discussed above, the grain size of the austenite and α'-martensite is similar in the UFG state (<1 μm). Thus, the difference in strength is due to the different hardness values of the individual phases. As Weidner et al. [50] revealed by nano indentation experiments on the present steel alloy this difference is just about 25% in favor of a higher hardness of the α'-martensite. In the CG materials the smaller grain size of the α'-martensite increases the resistance against plastic deformation significantly due to the Hall-Petch effect. Thus, in CG materials the austenite has to carry a disproportionally high share of the strain in relation to its phase fraction. With increasing α'-martensite fraction, i.e. with increasing strain amplitude, this mismatch increases as well. In the UFG state with similar grain size and, thus, similar

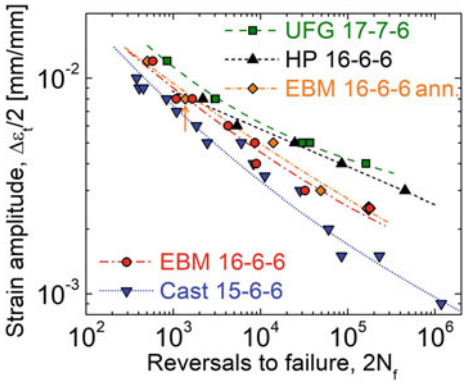

Fig. 13.16 Total strain based fatigue life curves of the different material states. Data from [12] (cast), [14] (EBM), [16] (UFG) and [13] (HP)

resistance against plastic deformation, the α'-martensite has to bear its fair share of the applied strain. Hence, the more homogenous strain distribution overcompensates the decreased ductility in comparison to the CG materials and leads to a higher fatigue life in the LCF regime [16].

The fatigue life of the EBM as-built and annealed states lies in between the cast and HP material. In this context, the relatively high porosity of the material after EBM processing (cf. Sect. 13.4.1) has to be taken into account. Figure 13.17 shows the fracture surface of an annealed EBM specimen ($\Delta\varepsilon_t/2 = 0.8\%$) with severe lack of fusion defects. Some of these defects reach dimensions of up to 500 µm and are located directly underneath the surface. Despite this quite detrimental condition, the cyclic deformation curve does not seem to be affected by these defects. Even the fatigue life almost matches the calculated fatigue life curve (Fig. 13.16, marked

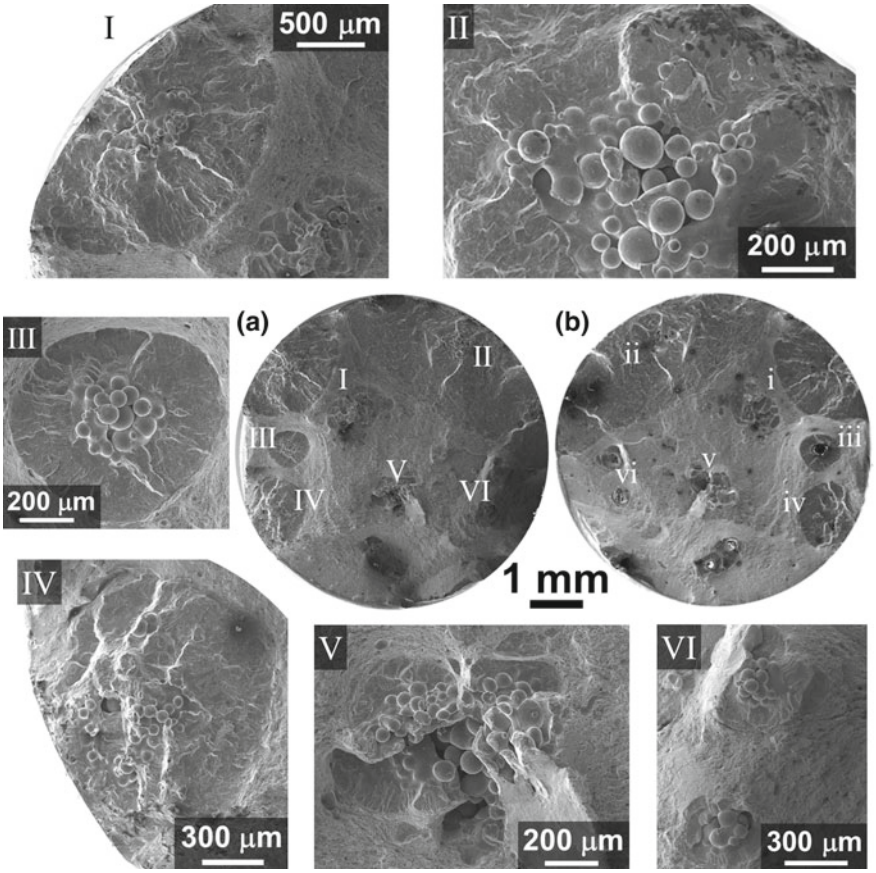

Fig. 13.17 Both sides of the fracture surface (**a**, **b**) of the EBM 16-6-6 ann. specimen cyclically deformed at $\Delta\varepsilon_t/2 = 0.8\%$. (I-VI) Magnified views of selected defects marked by I-VI in (**a**). After [14]

by an arrow). Moreover, the scatter of the EBM states is surprisingly low and the fatigue performance quite good when keeping in mind the severe defects. Of course the detrimental effect of the defects regarding the lifetime increases with decreasing strain amplitude because the crack initiation phase becomes more dominant [58]. Hence, the fatigue life decreases in comparison to the HP state but it is still quite reasonable. This damage tolerant behavior is supposed to stem from the high ductility of the material combined with its outstanding hardening capability. The process-inherent defects act as notches and the highest stresses occur at the roots of the notches. Thus, the deformation in the vicinity of the defects is quite pronounced at the beginning of cyclic deformation. Consequently, these areas exhibit the highest cyclic hardening and, thus, transfer the deformation to other areas of the material. Of course, this "shielding effect" gets the more effective the higher the hardening capability of the material is, which in the present alloy is quite high as revealed by the cyclic deformation curves (Fig. 13.12b). Another beneficial factor is of course the high ductility of the material which reduces the stress concentrations at the defects as also observed for an additive manufactured 316 L austenitic steel by other authors [66].

13.5 Influence of Particle Reinforcement

This section presents the influence of a particle reinforcement on the fatigue properties and cyclic deformation behavior of metastable austenitic steels.[3] Therefore, composites based on the HP 16-6-6 and HP 16-6-9 (cf. Sect. 13.3.1) with 5 and 10 vol.% zirconia, respectively, were processed via HP (cf. Sect. 13.2.2). The zirconia was partially stabilized by MgO (Mg-PSZ) enabling a tetragonal phase fraction of about 32% (cf. Table 13.2).

13.5.1 Cyclic Deformation Behavior of Particle Reinforced Steel-Matrix-Composites

The cyclic deformation curves in Fig. 13.18 reveal the reinforcing effect of the Mg-PSZ particles. Especially at medium and high strain amplitudes the initial stress amplitudes increase with increasing Mg-PSZ fraction. The qualitative courses of the composites based on the HP 16-6-6 steel (Fig. 13.18a–c) are similar to the cyclic deformation curves of the particle-free steel exhibiting an initial cyclic hardening followed by cyclic softening at medium and low strain amplitudes. The subsequent cyclic hardening due to the fatigue-induced α'-martensite formation is observed as

[3]The present discussion is based on investigations by Glage and summarizes results of his doctoral thesis [13] and the publications [18, 19].

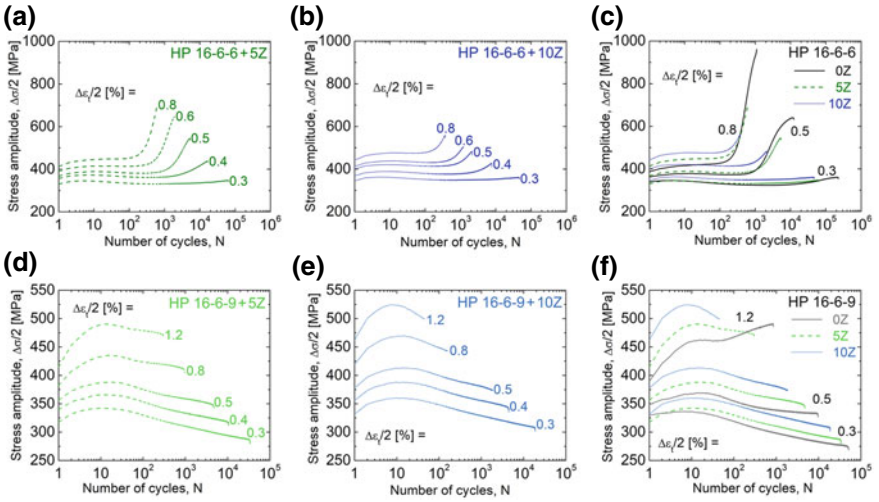

Fig. 13.18 Cyclic deformation curves of the composites reinforced with 5% Mg-PSZ (**a**, **d**) and 10% Mg-PSZ (**b**, **e**) based on the HP 16-6-6 (**a**, **b**) and HP 16-6-9 steels (**d**, **e**), respectively. (**c**, **f**) Comparison of the composite materials with the unreinforced HP 16-6-6 (**c**) and HP 16-6-9 (**f**). After [13] (**c**) and [18, 19] (**d**–**f**)

well but is considerably less pronounced and decreases significantly with increasing Mg-PSZ fraction. This diverging cyclic hardening gets even more obvious with increasing strain amplitudes.

For the variants based on the HP 16-6-9 steel (Fig. 13.18d–f) the secondary hardening due to deformation-induced twinning (cf. Sect. 13.3.1) is even suppressed entirely in case of the composites. A primary hardening similar to the particle-free steel but at higher stress levels is observed followed by cyclic softening until failure. Even the highest strain amplitude of $\Delta\varepsilon_t/2 = 1.2\%$ does not exhibit a secondary hardening regime.

The inhibition of the cyclic hardening due to fatigue-induced α'-martensite formation and twinning, respectively, is attributed to the occurring damage inside the composite materials in terms of rupture and debonding of particles as well as coalescence of cracks. These particle-related damage mechanisms seem to be more dominant than the still active hardening mechanisms in the steel matrices and lead to the observed macroscopic cyclic softening [13, 18, 19]. Thus, the damage evolution will be discussed in more detail in the next section.

13.5.2 Damage Evolution

The damage evolution is investigated by means of the damage parameters D_T (under tension) and D_C (under compression) which are based on the changes of

the specimens' stiffness and are calculated according to Hartmann et al. [67] as follows

$$D_T(N) = \frac{E_{T,0} - E_T(N)}{E_0} \tag{13.3}$$

$$D_C(N) = \frac{E_{C,0} - E_C(N)}{E_0} \tag{13.4}$$

where $E_{T,0}$ and $E_{C,0}$ are the stress dependent stiffnesses of the undamaged material and E_0 is the stiffness at zero stress. A fatigue test accompanied by a Long Distance Microscope (Institute of Physics of Materials, Brno, Czech Republic) revealed the validity of D_T as an indicator for damage by comparing the latter with the evolution of the surface crack length [13]. However, among the present materials the HP 16-6-9 steel and its composites have the best ability for investigations on the damage parameter evolution as the calculations are not influenced by a phase transformation [13].

Both damage parameters generally increase with increasing number of cycles as shown in Fig. 13.19. For small strain amplitudes $\Delta\varepsilon_t/2 \leq 0.3\%$ the evolution is similar for tension (D_T) and compression (D_C) in both material states. Of course, at the end of lifetime, D_T strongly increases due to the formation of a macrocrack which significantly decreases the specimen stiffness under tensile stress. However, up to that point no considerable damage seems to take place at small strain amplitudes and the increase of the damage parameters is mainly attributed to a stiffness reduction in consequence of the plastic deformation. For higher strain amplitudes the magnitude of D_T and D_C start to differ and further diverge with increasing strain amplitude. In case of the particle-free steel, crack initiation and subsequent crack growth lead to a decrease in specimen stiffness. In the composite with 10 vol.% Mg-PSZ particle rupture, particle debonding and crack coalescence additionally contribute to the

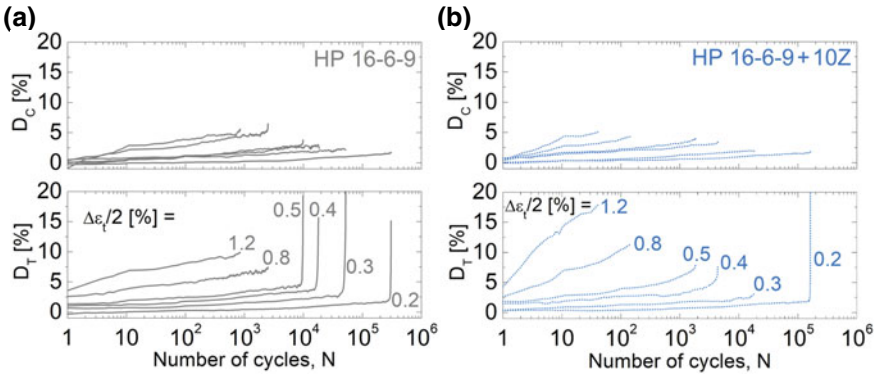

Fig. 13.19 Evolution of the damage parameters D_C and D_T for the particle-free HP 16-6-9 steel (**a**) and its counterpart reinforced with 10 vol.% Mg-PSZ (**b**). After [13]

stiffness reduction under tension causing a stronger increase of D_T (Fig. 13.19b). These particle-related damage mechanisms seem to be rare and negligible at small strain amplitudes but the impact on D_T increases markedly with higher loads. The reduction of the load-bearing cross section is of course less obvious in compression as the cracks and debonded interfaces are mostly closed and, thus, are contributing to the load transfer which explains the diverging evolution of D_T and D_C [13, 67].

13.5.3 Cyclically Deformed Microstructure

This section presents the microstructure of the composite HP 16-6-9+10Z with focus to the Mg-PSZ particles. For description of the deformation mechanisms of the steel matrix the reader is referred to Sect. 13.3.2. The BSE image in Fig. 13.20a gives an overview on the typical damage mechanisms related to the particle reinforcement, i.e. particle rupture, debonding and crack coalescence. Which of the former two mechanisms occurs depends on the particle shape and in particular its size. Particle rupture is mainly observed for large particles which often break perpendicular to the loading axis. Debonding is found for all particle sizes and is the dominant mechanism for small particles which break rarely. Similar size effects have been observed for particle reinforced aluminum matrix composites [68].

Figure 13.20b shows a BSE image of a Mg-PSZ particle embedded in the austenitic matrix after cyclic deformation at a high strain amplitude. Deformation is clearly visible inside the particle and the corresponding EBSD image (Fig. 13.20c) reveals the monoclinic phase for the band-like structures. The remaining particle is most probably in the tetragonal condition of ZrO_2. Hence, it is assumed that a stress-assisted phase transformation from the tetragonal to the monoclinic condition has occurred during cyclic deformation. In contrast, the monoclinic fringe at the interface to the austenitic matrix most probably stems from a depletion of stabilizing elements

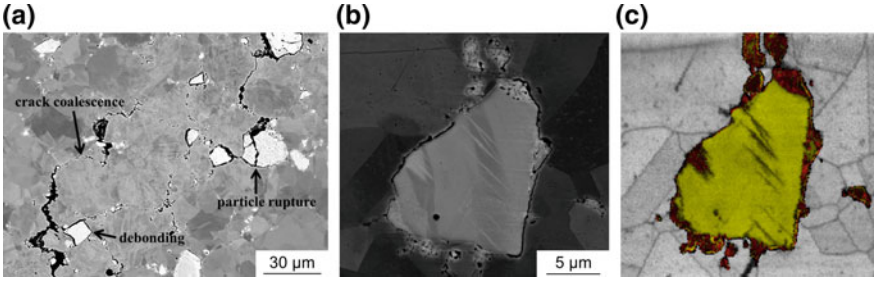

Fig. 13.20 **a** BSE image of HP 16-6-9+10Z showing the particle-related damage mechanisms after cyclic deformation at $\Delta\varepsilon_t/2 = 0.3\%$. **b**, **c** BSE image and EBSD phase map of the same Mg-PSZ particle in a HP 16-6-9+10Z specimen cyclically deformed at $\Delta\varepsilon_t/2 = 0.8\%$ (red—m-ZrO_2, yellow—c/t-ZrO_2; grey—band contrast). Loading axis was horizontal. After [18]

(mainly Mg) due to diffusion to interface phases and/or into the austenite during HP [69].

13.5.4 Fatigue Life

The influence of the particle reinforcement on the fatigue life is shown in Fig. 13.21 for the HP 16-6-6 and HP 16-6-9. The fatigue life decreases with increasing volume fraction of Mg-PSZ particles for both variants. Nevertheless, there are differences in the lifetime in dependence of the applied strain amplitude. For the HP 16-6-9 (Fig. 13.21b) the lifetime reduction due to the particles decreases with decreasing strain amplitude and the lifetime curves converge at high fatigue lifetimes. This is in accordance with the damage behavior discussed in the previous section. As the particle-related damage decreases with decreasing strain amplitude its detrimental influence on the lifetime decreases as well leading to the convergence.

One would expect similar results for the HP 16-6-6 as the particle-related damage should influence the fatigue life in a similar manner. However, a convergence of the fatigue life curves is not observed (Fig. 13.21a). The lifetime reduction due to the particle reinforcement stays constant or even tends to increase with decreasing strain amplitude. This is not attributed to a change in the particle-related damage but to a less pronounced α'-martensite formation in the composites compared to the unreinforced steel, cf. [13, 17, 19]. As discussed in Sect. 13.3.3, the α'-martensite formation is beneficial for the fatigue life in the HCF regime. Thus, the decreased particle-related damage at small strain amplitudes is more or less compensated by a detrimental reduction of the α'-martensite formation. Overall, the fatigue life decreases with increasing particle volume fraction for all strain amplitudes applied.

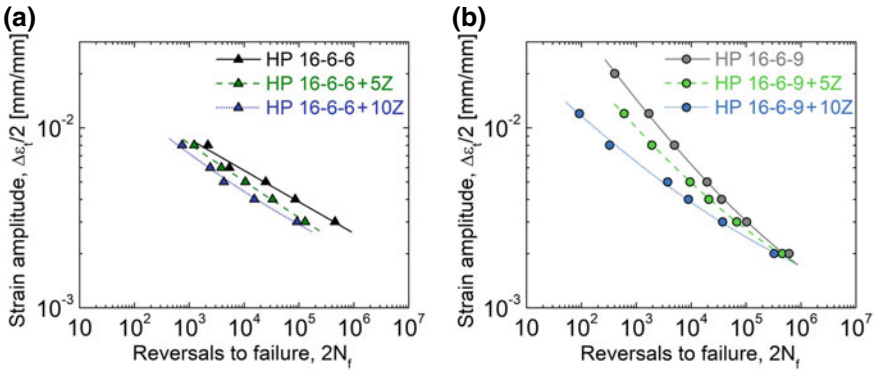

Fig. 13.21 Total strain based fatigue life curves of the composites materials based on the HP 16-6-6 (**a**) and the HP 16-6-9 (**b**) in comparison to its unreinforced counterparts. After [13] (**a**) and [18, 19] (**b**)

13.6 Fatigue Properties of a Q&P Ultra-High Strength Steel

This section presents the fatigue properties of an ultra-high strength austenitic steel alloy which was designed to exceed the strength of the steels discussed in the previous sections at simultaneously reasonable ductility [21]. As this steel is fully austenitic at room temperature, the usual quenching and partitioning (Q&P) process has been modified (cf. Sect. 13.2.2), provoking the formation of α'-martensite during a cooling step. Two material states which differ in the α'-martensite fraction due to different cooling temperatures ($T_{c,1} = -120$ °C, $T_{c,2} = -20$ °C) have been cyclically deformed. Moreover, Q&P and, thus, the fatigue tests were performed in the cast condition of this stainless steel.[4]

13.6.1 Microstructure After Q&P

Magnetic measurements reveal different α'-martensite fractions after Q&P of 45 vol.% for the material state cooled down to $T_c = -120$ °C and of 22 vol.% for $T_c = -20$ °C, respectively. The different phase fractions are also evident in the light optical micrography images of etched specimens in Fig. 13.22. The α'-martensite appears darker and especially for $T_c = -20$ °C (Fig. 13.22b) the dendritic structure of the cast material is still apparent. The dendrite cores solidify first and contain less alloying elements compared to the interdendritic regions. Thus, the martensite start temperature M_s of the former is higher triggering a preferred formation of α'-martensite during the cooling stage.

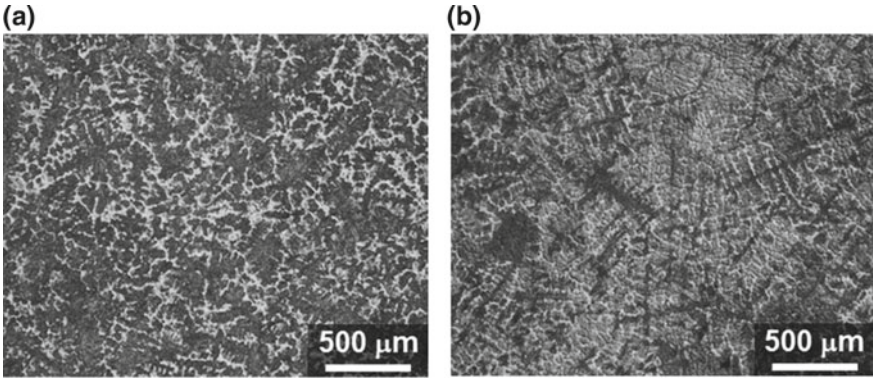

Fig. 13.22 Micrographs taken by light optical micrography of the etched microstructures of the −120 °C (**a**) and −20 °C (**b**) state after Q&P. After [22]

[4]For a discussion in more detail the reader is referred to [22] for the fatigue properties of this steel and to [21] for the modified Q&P processing.

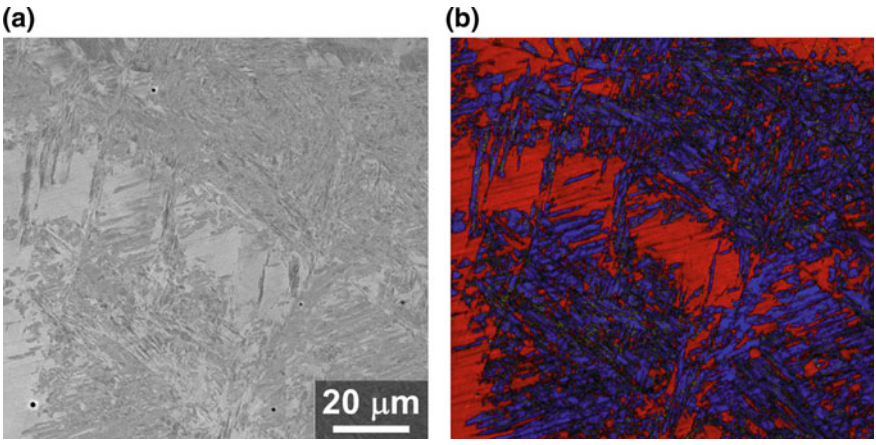

Fig. 13.23 BSE image (**a**) and corresponding EBSD phase map with superimposed band contrast (**b**, red—austenite, yellow—ε-martensite, blue—α'-martensite) of the −120 °C state after Q&P. After [22]

A micrograph at higher magnification is shown in Fig. 13.23a in terms of a BSE image. The corresponding EBSD phase map (Fig. 13.23b) reveals large blocky austenitic areas of about 20 µm in size which are most probably interdentritic regions with higher austenite stability. In addition, fine so-called interlath austenite is observed in areas which are mostly martensitic. Besides mechanical properties, this is important in context with the partitioning treatment and the provoked diffusion of *C* and *N* from the supersaturated α'-martensite into austenite. Due to a limited diffusion length of the interstitial elements *C* and *N* the stabilizing effect will most likely be more pronounced in the interlath austenite [21]. Furthermore, the α'-martensite fraction after the cooling stage is supposed to have an influence on the extent of diffusion and, thus, stabilization, i.e. with increasing α'-martensite fraction the austenite stabilization should increase as well.

13.6.2 Cyclic Deformation Behavior

The cyclic deformation curves of the −120 °C state (partitioned condition) are given in Fig. 13.24a. The stress amplitudes are quite high and even exceed 1400 MPa for $\Delta\varepsilon_t/2 = 1.2\%$. Moreover, the cyclic stress markedly increases with increasing strain amplitude indicating a high amount of obstacles for dislocation glide most probably due to the high amount of α'-martensite. In addition, carbides inside the α'-martensite formed during partitioning may contribute to the high cyclic stress. However, at high strain amplitudes the material exhibits a continuous cyclic hardening until failure.

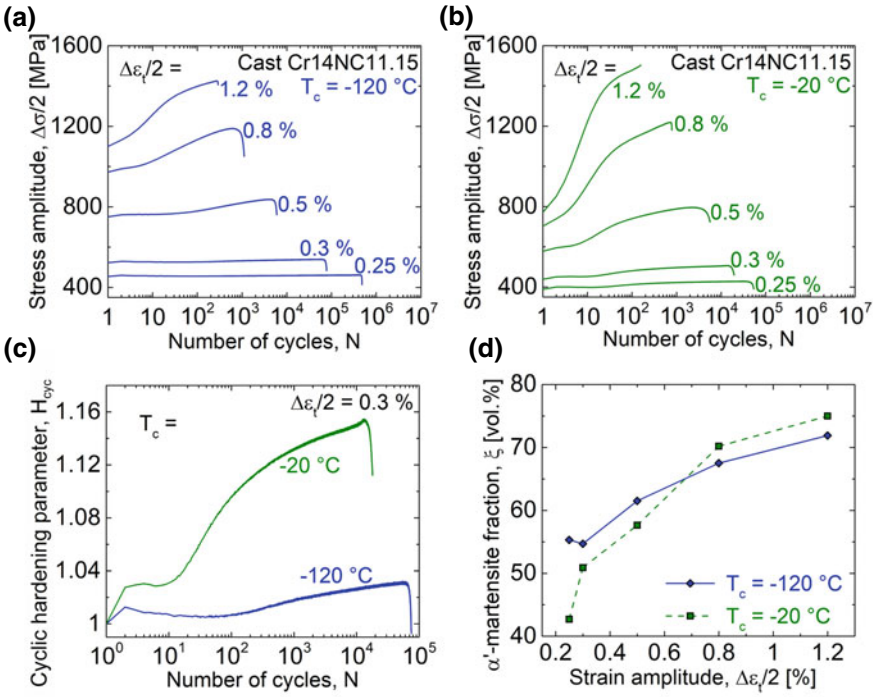

Fig. 13.24 Cyclic deformation curves of the −120 °C (**a**) and −20 °C (**b**) states, cyclic hardening parameter H_{cyc} for a strain amplitude of $\Delta\varepsilon_t/2 = 0.3\%$ (c) and α'-martensite fraction after cyclic deformation (**d**), respectively, of the Q&P ultra-high strength steel. After [22]

After several cycles the hardening gets more pronounced which is attributed to a fatigue-induced formation of α'-martensite, cf. Sect. 13.3.1. In contrast, the course of the cyclic deformation curves for the small strain amplitudes $\Delta\varepsilon_t/2 \leq 0.3\%$ seem to be relatively constant, i.e. without any cyclic softening or hardening. However, this is just a scaling issue due to the wide range of the ordinate. For this reason, a cyclic hardening parameter H_{cyc} is introduced calculated according to

$$H_{cyc} = \frac{(\Delta\sigma/2)_{N_i}}{(\Delta\sigma/2)_{N=1}} \tag{13.5}$$

where $\Delta\sigma/2_{Ni}$ and $\Delta\sigma/2_{N=1}$ are the stress amplitudes of the current and first cycle, respectively. Figure 13.24c shows the course of H_{cyc} for the strain amplitude of $\Delta\varepsilon_t/2 = 0.3\%$. A similar behavior to the high alloy austenitic steels discussed in the previous sections is observed. At beginning of cyclic deformation a short stage of cyclic hardening is observed followed by cyclic softening. After an incubation period secondary hardening sets in and continues until failure, cf. Sect. 13.3.1. Thus, similar mechanisms in terms of dislocation interaction and martensitic phase transformation are supposed to be active in the Q&P steel as well.

Qualitatively, the −20 °C material state exhibits similar cyclic deformation curves (Fig. 13.24b) but the stress amplitudes at the beginning of cyclic deformation are considerably lower and the cyclic hardening is more pronounced. The reduced initial stress amplitudes are due to the lower initial α'-martensite fraction. In contrast, due to a lower austenite stability the fatigue-induced α'-martensite formation is more pronounced compared to the −120 °C state and this difference significantly increases with increasing strain amplitude. Whereas at medium and small strain amplitudes the overall α'-martensite fraction after failure (Fig. 13.24d) remains lower in case of the −20 °C state, at $\Delta\varepsilon_t/2 \geq 0.8\%$ its phase transformation during cyclic deformation even overcompensates the lower initial fraction leading to higher overall values. This is reflected in the cyclic deformation curves as well. Just in the case of the high strain amplitudes the −20 °C state exceeds its counterpart in terms of the maximum stress amplitude. Hence, the cyclic stresses correlate quite well with the α'-martensite fraction and seem to be relatively independent on the type of α'-martensite, i.e. thermally-induced or fatigue-induced. However, for the strain amplitude $\Delta\varepsilon_t/2 = 1.2\%$ the crossover of stress amplitudes already occurs in an early stage of cyclic deformation (13 cycles) as the fatigue-induced phase transformation is quite strong.

13.6.3 Fatigue Life

As discussed in Sect. 13.3.3 different austenite stabilities cause a crossover of the fatigue life curves in case of high alloy austenitic steels (Fig. 13.9a). As the austenite stability of the present Q&P steels differs as well, a similar behavior could be expected. In contrast, the −120 °C state exhibits a superior fatigue life at all applied strain amplitudes (Fig. 13.25). The lifetime advantage even increases with decreasing strain amplitude. Well known for the high alloy steels, α'-martensite is assumed to have a beneficial effect on the fatigue life in the HCF regime due to the higher strength

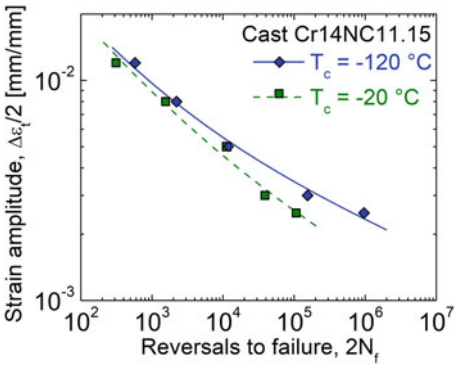

Fig. 13.25 Total strain based fatigue life curves of the −120 °C (blue) and −20 °C (green) states of the Q&P ultra-high strength steel. After [22]

of the material, but a detrimental effect in the LCF regime due to the decrease in ductility. Thus, at high strain amplitudes the pronounced fatigue-induced phase transformation in the −20 °C state which overcompensates its lower initial α'-martensite fraction (cf. Sect. 13.6.2) leads to the inferior fatigue life. At small strain amplitudes on the other hand, the fatigue-induced phase transformation is less pronounced and the overall α'-martensite fraction as well as the cyclic stresses of the −20 °C state never reach the level of its counterpart. In this fatigue regime a higher strength markedly reduces the plastic strain amplitude and, thus, reduces the damage and enhances the lifetime. Accordingly, once again the −120 °C state exhibits a higher fatigue life.

13.6.4 Microstructure After Cyclic Deformation

The BSE, ECCI and EBSD images of Fig. 13.26 give an impression of the microstructure of the Q&P steel after cyclic deformation. As already observed for the qualitative course of the cyclic deformation curves, the micrographs reveal distinct similarities with the other high alloy austenitic steels. Figure 13.26a shows an austenitic area surrounded by α'-martensite. A lot of deformation bands on different slip systems have formed inside the austenite. Within these deformation bands α'-martensite nuclei are found (marked by white arrows in Fig. 13.26a, b) which in part are quite small. According to the EBSD phase maps in Fig. 13.26g, i the deformation bands are often indexed as ε-martensite, i.e. the density of stacking faults is quite high in these areas. Thus, analogue to the other high alloy austenitic steels presented in this work, the α'-martensite is supposed to form in the sequence $\gamma \rightarrow \varepsilon \rightarrow \alpha'$.

However, the plasticity is not limited to the deformation bands but also stacking faults form in between the deformation bands on different slip systems as revealed by ECCI images in Fig. 13.26c, d. Moreover, all micrographs reveal a quite planar glide character as no dislocation arrangements due to wavy glide like dislocation cells have been observed.

Even though the triggered microstructural mechanisms are similar in both Q&P states, there are some indications for their different austenite stabilities as well. The α'-martensite fraction inside the deformation bands appears higher for the −20 °C state (Fig. 13.26e, f) when comparing specimens cyclically deformed at the same strain amplitude. Hence, the martensitic phase transformation occurs more rapidly in the −20 °C state due to its lower austenite stability. These observations support the statements regarding the cyclic hardening behavior discussed in Sect. 13.6.2.

13.7 Conclusions

Several aspects of the cyclic deformation and fatigue behavior of metastable austenitic steels were discussed in the present work including the influence of a

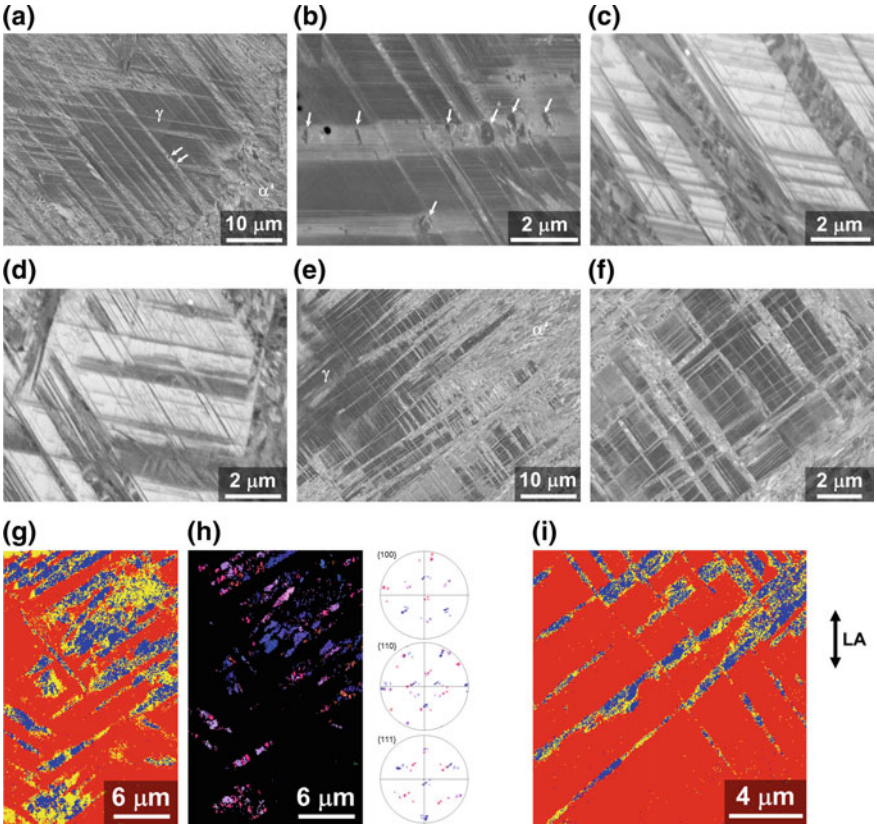

Fig. 13.26 Microstructures of the −120 °C (**a**–**d**, **g**, **h**) and −20 °C (**e**, **f**, **i**) state cyclically deformed at $\Delta\varepsilon_t/2 = 0.3\%$ (**a**, **c**–**f**, **i**), $\Delta\varepsilon_t/2 = 0.5\%$ (**b**) and $\Delta\varepsilon_t/2 = 0.8\%$ (**g**, **h**), respectively. **a**, **b**, **e**, **f** BSE images. **c**, **d** ECCI images. **g**, **i** EBSD phase maps (red—austenite, yellow—ε-martensite, blue—α'-martensite). **h** EBSD orientation map of the α'-martensite phase of (**g**) and corresponding bcc pole figures. Loading axis is vertical for all micrographs. After [22]

particle reinforcement and the chemical composition. Furthermore, different manufacturing methods in terms of casting, additive manufacturing, hot pressing and reversion annealing and their effect on the fatigue properties were investigated. Finally, a newly designed ultra-high strength steel produced via a modified Q&P route was presented. The main conclusions are summarized in the following.

- The SFE of an austenitic steel controls its dislocation glide character (planar or wavy) and the activation of other deformation mechanisms in terms of deformation-induced α'-martensite formation and twinning. With decreasing SFE besides dislocation movement, a fluent transition from twinning to ε-martensite and α'-martensite formation is observed.

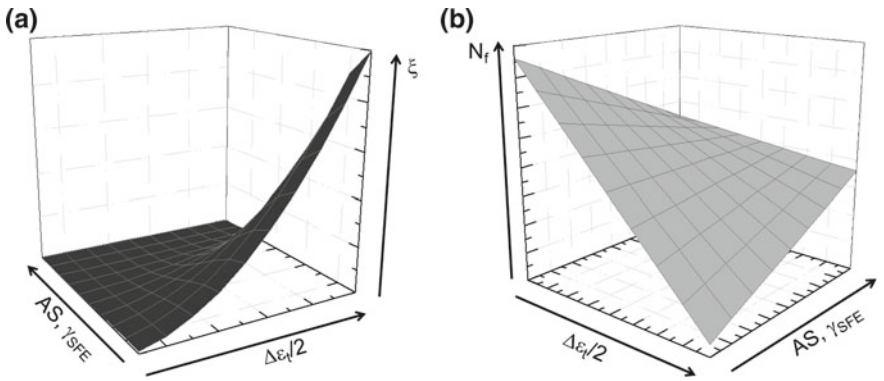

Fig. 13.27 α'-martensite fraction ξ (**a**) and fatigue life N_f (**b**) of high alloy austenitic steels as a function of strain amplitude $\Delta\varepsilon_t/2$, austenite stability (AS) and stacking fault energy γ_{SFE}, respectively. After [13]

- The SFE has a major influence on the mechanical properties and the cyclic deformation behavior as the fatigue-induced twinning and even more the fatigue-induced α'-martensite formation lead to a significant cyclic hardening.
- Besides a decreasing SFE, of course increasing strain amplitudes promote the formation of α'-martensite (Fig. 13.27a).
- The fatigue life is affected by the α'-martensite formation as well. The latter is beneficial in the HCF regime due to its strengthening effect but detrimental in the LCF regime due to the lower ductility. This opposing character leads to different slopes of the fatigue life curves and, thus, to their crossover. More precisely, the slope decreases with decreasing SFE (Fig. 13.9a), i.e. the fatigue life difference between high and small strain amplitudes increases (Fig. 13.27b), and vice versa.
- The martensitic phase transformation of all investigated steels occurs via the sequence $\gamma \rightarrow \varepsilon \rightarrow \alpha'$. The intermediate ε-martensite is assumed to stem from highly faulted areas, i.e. a high stacking fault density.
- The grain size of the steel affects the cyclic deformation behavior and the martensitic phase transformation. In particular ultra-fine grained (UFG) materials with grain sizes below 1 μm exhibit significantly higher initial stress amplitudes but a less pronounced cyclic hardening due to α'-martensite formation. Furthermore, the UFG grains are not characterized by a deformation band structure but their interior is subjected to an increase in stacking fault density as a whole.
- The remarkable hardening capability in combination with the high ductility of the high alloy steels yield an outstanding damage tolerance. A shielding effect due to the high hardening at defects and a transition of the deformation to adjacent areas is assumed to occur. Especially with regard to additive manufactured materials which suffer upon process-inherent defects like lack of fusion this damage tolerance brings advantages in terms of a less affected cyclic deformation behavior and a more than reasonable fatigue life.

- A reinforcement with Mg-PSZ particles causes a strengthening effect in terms of increasing stress amplitudes with increasing Mg-PSZ particle fraction. On the other hand, the detrimental particle-related damage in terms of debonding, particle rupture and crack coalescence increases with increasing strain amplitude. Hence, the fatigue life of the composites is reduced in the total-strain controlled experiments, especially in the LCF regime.
- The cast austenitic steel subjected to a modified Q&P processing exhibited extraordinary high stress amplitudes. Of the two material states which differ in the α'-martensite fraction after Q&P especially the state with the higher fraction achieved quite high cyclic stresses right from the beginning of cyclic deformation.

Acknowledgements The authors gratefully acknowledge the work and research of Dr. -Ing. Alexander Glage providing a major contribution to the present chapter. Furthermore, special thanks go to the Deutsche Forschungsgemeinschaft (DFG, German Research Foundation) for funding the Collaborative Research Centre "TRIP-Matrix-Composite" (project number 54473466—SFB 799, subproject B3). For preparation of SEM and TEM specimens the authors wish to thank R. Prang, K. Zuber, K. Becker and A. Leuteritz (all TU Bergakademie Freiberg).

References

1. G.B. Olson, M. Cohen, J. Less-Common Met. **28**, 107 (1972)
2. G.B. Olson, M. Cohen, Metall. Trans. A **6**, 791 (1975)
3. A. Weidner, H. Biermann, JOM **67**, 1729 (2015)
4. S. Martin, S. Wolf, S. Decker, L. Krüger, U. Martin, Steel Res. Int. *86*, 1187 (2015)
5. S. Martin, S. Wolf, U. Martin, L. Krüger, Solid State Phenom. **172–174**, 172 (2011)
6. H. Mughrabi, Procedia Eng. **2**, 3 (2010)
7. S. Martin, C. Ullrich, D. Šimek, U. Martin, D. Rafaja, J. Appl. Crystallogr. **44**, 779 (2011)
8. A. Weidner, A. Glage, S. Martin, J. Man, V. Klemm, U. Martin, J. Polák, D. Rafaja, H. Biermann, Int. J. Mater. Res. **102**, 1374 (2011)
9. H. Biermann, A. Glage, M. Droste, Metall. Mater. Trans. A **47**, 84 (2016)
10. L. Rémy, A. Pineau, Mater. Sci. Eng. **36**, 47 (1978)
11. A. Jahn, A. Kovalev, A. Weiß, S. Wolf, L. Krüger, P.R. Scheller, Steel Res. Int. *82*, 39 (2011)
12. A. Glage, A. Weidner, H. Biermann, Steel Res. Int. **82**, 1040 (2011)
13. A. Glage, Ph.D. thesis, Technische Universität Bergakademie Freiberg, 2014
14. M. Droste, J. Günther, D. Kotzem, F. Walther, T. Niendorf, H. Biermann, Int. J. Fatigue **114**, 262 (2018)
15. J. Günther, F. Brenne, M. Droste, M. Wendler, O. Volkova, H. Biermann, T. Niendorf, Sci. Reports **8**, 1298 (2018)
16. M. Droste, C. Ullrich, M. Motylenko, M. Fleischer, A. Weidner, J. Freudenberger, D. Rafaja, H. Biermann, Int. J. Fatigue **106**, 143 (2018)
17. S. Martin, S. Richter, S. Decker, U. Martin, L. Krüger, D. Rafaja, Steel Res. Int. **82**, 1133 (2011)
18. A. Glage, C. Weigelt, J. Räthel, H. Biermann, Int. J. Fatigue **65**, 9 (2014)
19. A. Glage, C. Weigelt, J. Räthel, H. Biermann, Adv. Eng. Mater. **15**, 7 (2013)
20. J. Speer, D.K. Matlock, B.C. de Cooman, J.G. Schroth, Acta Mater. **51**, 2611 (2003)
21. M. Wendler, C. Ullrich, M. Hauser, L. Krüger, O. Volkova, A. Weiß, J. Mola, Acta Mater. **133**, 346 (2017)

22. M. Droste, M. Wendler, O. Volkova, H. Biermann, Adv. Eng. Mater. 51 (2018)
23. A. Weidner, A. Müller, A. Weiß, H. Biermann, Mater. Sci. Eng., A **571**, 68 (2013)
24. M. Moallemi, A. Najafizadeh, A. Kermanpur, A. Rezaee, Mater. Sci. Eng., A **530**, 378 (2011)
25. A. Rezaee, A. Kermanpur, A. Najafizadeh, M. Moallemi, Mater. Sci. Eng., A **528**, 5025 (2011)
26. F. Forouzan, A. Najafizadeh, A. Kermanpur, A. Hedayati, R. Surkialiabad, Mater. Sci. Eng., A **527**, 7334 (2010)
27. M. Karimi, A. Najafizadeh, A. Kermanpur, M. Eskandari, Mater. Charact. **60**, 1220 (2009)
28. M. Eskandari, A. Najafizadeh, A. Kermanpur, Mater. Sci. Eng., A **519**, 46 (2009)
29. D.L. Johannsen, A. Kyröläinen, P.J. Ferreira, Metall. Mater. Trans. A **37**, 2325 (2006)
30. R. Song, D. Ponge, D. Raabe, J.G. Speer, D.K. Matlock, Mater. Sci. Eng., A **441**, 1 (2006)
31. A. Weidner et al., in *IOP Conference Series: Materials Science and Engineering, 17th International Conference on Textures of Materials*, vol. 82 (IOP Publishing 2015), article no. 012069
32. R.D.K. Misra, Z. Zhang, P.K.C. Venkatasurya, M.C. Somani, L.P. Karjalainen, Mater. Sci. Eng., A **528**, 1889 (2011)
33. R.D.K. Misra, S. Nayak, S.A. Mali, J.S. Shah, M.C. Somani, L.P. Karjalainen, Metall. Mater. Trans. A **41**, 3 (2010)
34. R.D.K. Misra, S. Nayak, P.K.C. Venkatasurya, V. Ramuni, M.C. Somani, L.P. Karjalainen, Metall. Mater. Trans. A **41**, 2162 (2010)
35. R.D.K. Misra, Z. Zhang, P.K.C. Venkatasurya, M.C. Somani, L.P. Karjalainen, Mater. Sci. Eng., A **527**, 7779 (2010)
36. J. Kähkönen, D.T. Pierce, J.G. Speer, E. de Moor, G.A. Thomas, D. Coughlin, K. Clarke, A. Clarke, JOM **68**, 210 (2016)
37. S. Yan, X. Liu, W.J. Liu, H. Lan, H. Wu, Mater. Sci. Eng., A **620**, 58 (2015)
38. E.J. Seo, L. Cho, B.C. de Cooman, Metall. Mater. Trans. A **46**, 27 (2015)
39. M. de Sanctis, G. Lovicu, R. Valentini, A. Dimatteo, R. Ishak, U. Migliaccio, R. Montanari, E. Pietrangeli, Metall. Mater. Trans. A **46**, 1878 (2015)
40. D.V. Edmonds, J.G. Speer, Mater. Sci. Technol. **26**, 386 (2010)
41. J. Talonen, P. Aspegren, H. Hänninen, Mater. Sci. Technol. **20**, 1506 (2004)
42. S. Siddique, M. Imran, M. Rauer, M. Kaloudis, E. Wycisk, C. Emmelmann, F. Walther, Mater. Des. **83**, 661 (2015)
43. S. Ganesh Sundara Raman, K.A. Padmanabhan, Int. J. Fatigue **17**, 271 (1995)
44. F. Hahnenberger, M. Smaga, D. Eifler, Int. J. Fatigue **69**, 36 (2014)
45. L. Rémy, Acta Metall. **26**, 443 (1978)
46. O. Bouaziz, S. Allain, C. Scott, Scr. Mater. **58**, 484 (2008)
47. M. Bayerlein, H. Mughrabi, M. Kesten, B. Meier, Mater. Sci. Eng., A **159**, 35 (1992)
48. M. Bayerlein, H.-J. Christ, H. Mughrabi, Mater. Sci. Eng., A **114**, L11 (1989)
49. G. Baudry, A. Pineau, Mater. Sci. Eng., A **28**, 229 (1977)
50. A. Weidner, U.D. Hangen, H. Biermann, Philos. Mag. Lett. **94**, 522 (2014)
51. H. Schumann, Krist. Techn. **12**, 363 (1977)
52. S.-G. Hong, S.-B. Lee, T.-S. Byun, Mater. Sci. Eng., A **457**, 139 (2007)
53. G. Franke, C. Altstetter, Metall. Trans. A **7**, 1719 (1976)
54. D. Hennessy, G. Steckel, C. Altstetter, Metall. Trans. A **7**, 415 (1976)
55. D. Borisova, V. Klemm, S. Martin, S. Wolf, D. Rafaja, Adv. Eng. Mater. **15**, 571 (2013)
56. Y. Li, C. Laird, Mater. Sci. Eng., A **186**, 87 (1994)
57. H.-G. Lambers, C.J. Rüsing, T. Niendorf, D. Geissler, J. Freudenberger, H.J. Maier, Int. J. Fatigue **40**, 51 (2012)
58. H. Mughrabi, Philos. Trans. A **373**, 20140132 (2015)
59. H. Mughrabi, H.W. Höppel, Int. J. Fatigue **32**, 1413 (2010)
60. A. Šalak, M. Selecká, *Manganese in Powder Metallurgy Steels* (Cambridge International Science Publishing Ltd, Springer, 2012)
61. M. Wendler, A. Weiß, L. Krüger, J. Mola, A. Franke, A. Kovalev, S. Wolf, Adv. Eng. Mater. **15**, 558 (2013)
62. M. Wendler, J. Mola, L. Krüger, A. Weiß, Steel Res. Int. **85**, 803 (2014)

63. J.A. Venables, Philos. Mag. **7**, 35 (1962)
64. H. Mughrabi, H.W. Höppel, M. Kautz, Scr. Mater. **51**, 807 (2004)
65. H.W. Höppel, M. Kautz, C. Xu, M. Murashkin, T.G. Langdon, R.Z. Valiev, H. Mughrabi, Int. J. Fatigue **28**, 1001 (2006)
66. S. Leuders, T. Lieneke, S. Lammers, T. Tröster, T. Niendorf, J. Mater. Res. **29**, 1911 (2014)
67. O. Hartmann, K. Herrmann, H. Biermann, Adv. Eng. Mater. **6**, 477 (2004)
68. W. Li, Z.H. Chen, D. Chen, J. Teng, L. Changhao, J. Mater. Sci. **46**, 1153 (2011)
69. A. Glage, S. Martin, S. Decker, C. Weigelt, M. Junghanns, C.G. Aneziris, U. Martin, L. Krüger, H. Biermann, Steel Res. Int. **83**, 554 (2012)

Chapter 14
Behaviour of Metastable and Stable Austenitic Stainless Steels Under Planar-Biaxial Load

Carl H. Wolf, Sebastian Henkel and Horst Biermann

Abstract The aim of the present study was to investigate the behaviour of a powder metallurgically produced high alloy X5CrMnNi16-7-6 metastable austenitic stainless steel under planar-biaxial loading. For this purpose, cruciform specimens made of this material were subjected both to quasi-static loading and to cyclic loading for low cycle fatigue and crack growth investigations. In addition to quasi-static shear loading with load axes force ratio $\lambda = -1$ and quasi-static equibiaxial loading with $\lambda = 1$, further specimens were subjected to a load ratio of $\lambda = 0.5$ to determine the yield surface. Quasi-static sequence tests with permanently changing λ were carried out to determine load sequence effects. The characterization of the low cycle fatigue behavior was carried out under equibiaxial tensile loading with load axes strain ratio $\Phi = 1$ and shear loading with $\Phi = -1$. Furthermore, investigations were carried out at different strain ratios. The description of the low cycle fatigue lives was performed using the Basquin-Manson-Coffin relationship. For both quasi-static and LCF experiments, the martensite content was measured in situ, so that the influence of the phase transformation on the material behaviour could be described. The fatigue crack growth investigations were performed on cruciform specimens under uniaxial, equibiaxial and initially equibiaxial and subsequently phase-shifted loading on a stable austenitic steel variant. In order to describe the fatigue crack growth, a finite element (FE) analysis of the specimen geometry was carried out first, so that a correlation between force and resulting stress in the uncracked specimen could be established. A geometry function for straight growing cracks was established by correlation between force and resulting stress in the specimen and K-solution

C. H. Wolf (✉) · S. Henkel · H. Biermann
Institute of Materials Engineering, Technische Universität Bergakademie Freiberg, Gustav-Zeuner-Str. 5, 09599 Freiberg, Germany
e-mail: Carl.Wolf@ww.tu-freiberg.de

S. Henkel
e-mail: henkel@ww.tu-freiberg.de

H. Biermann
e-mail: biermann@ww.tu-freiberg.de

H. Biermann and C. G. Aneziris (eds.), *Austenitic TRIP/TWIP Steels and Steel-Zirconia Composites*, Springer Series in Materials Science 298,
https://doi.org/10.1007/978-3-030-42603-3_14

at different crack lengths. A comparison of the crack growth between uniaxial or equibiaxial and phase-shifted loading with kinking crack paths was made by means of Paris law.

14.1 Introduction

On real components, multiaxial stress states often occur. These are caused, for example, by stress gradients in the area around notches, but also by several simultaneously acting loads in different directions. Even in material testing, an exclusively uniaxial material test is rarely carried out, since necking in the tensile test of plastically deformable materials already represents a multiaxial loading condition [1].

In the present work, a newly developed, high-alloy, metastable austenitic stainless steel is studied under multiaxial quasi-static as well as multiaxial low-cyclic fatigue (LCF) loading. Moreover, multiaxial fatigue crack growth (FCG) was investigated. This steel exhibits the TRIP effect [2, 3] (**TR**ansformation **I**nduced **P**lasticity) caused by a transformation of γ-austenite to α'-martensite via a hexagonal structure called ε-martensite [4–8]. The phase transformations take place with volume effects, i.e. during the phase transformation from γ-austenite to ε-martensite a volume contraction and during the subsequent phase transformation from ε-martensite to α'-martensite a volume expansion occur.

Knowledge of the influence of the TRIP effect on the deformation and strain hardening behavior under multiaxial loading is relevant for the application of this material. With this expertise, forming processes can be simulated and safety reserves of e.g. pipes and pressure vessels can be calculated. Moreover, in the automotive industry, increasingly complex forming processes require knowledge of yield surface and strain hardening behavior [9, 10]. Often only uniaxial material data is available for calculations and component design, so that multiaxial stress cases are usually converted into uniaxial equivalent stress cases [1]. Various transmission hypotheses are usually used for this purpose. For ductile materials, the distortion energy hypothesis according to von Mises, Huber and Hencky is usually utilized, which was initially established as a yield condition. For brittle materials, the maximum normal stress theory according to Rankine is applied. These hypotheses can be utilized to describe most technical applications for isotropic materials under static loading. The better the material behavior is phenomenologically known, the better are the results of e.g. the finite element method calculations. This also includes the knowledge of the yield surface and the elastic-plastic deformation behaviour [11]. For the purpose of generating defined multiaxial stress states under quasi-static loading, planar-biaxial experiments on cruciform specimens are suitable [9, 12, 13].

In addition to the interest in quasi-static multiaxial stress states, there has been an interest in the influence of various multiaxial strain states on crack initiation and crack propagation behavior for more than 40 years [14, 15]. Unfortunately, there are only few data in the literature with different phase shifts φ between the principal strains ε_1 and ε_2 in the range of $0° \leq \varphi \leq 180°$ [16–18]. Some authors determined the

longest fatigue life under shear loading, i.e. with $\lambda = -1$, compared to other loading cases like uniaxial or biaxial tension [16, 19–22]. Pascoe and de Villiers [20] found, that the fatigue life for specimens loaded equibiaxially, i.e. with $\lambda = 1$, had the shortest fatigue life. Ogata and Takahashi [16] stated, that fatigue life for uniaxially loaded specimens is even shorter than for equibiaxially loaded specimens. Many authors [16, 17, 19–23] correlated fatigue life N_f with the von Mises equivalent strain amplitude $\Delta\varepsilon_{\mathrm{vM}}/2$ as a scalar parameter. Furthermore, numerous theories have been established for the calculation of fatigue life under multiaxial loadings in the LCF regime, see e.g. [14, 16, 20, 24–29]. Uniaxial cyclic investigations on metastable high-alloy austenitic steels like AISI 301 and 304 L showed, that the formation of α'-martensite led to an increasing stress amplitude, i.e. the strength increased significantly during cyclic deformation. Consequently, this leads to higher fatigue life in high-cycle fatigue and to a reduction of the fatigue life in the LCF regime in comparison to a stable steel [7, 30–33].

The calculation of fatigue life for fatigue crack growth is also often based on uniaxial data [34–37]. However, components are often multiaxially loaded due to their geometry or loadings in different directions [38, 39], e.g. thin walled structural components as pressure vessels [40] or the outer skin of an aircraft [41, 42] as well as blade integrated disks in aircraft engines [43, 44]. During the service life of the components, both in-phase and out-of-phase loadings can occur. The change from in-phase to out-of-phase loading can lead to crack branching [45–49] as well as kinking of the crack path [49, 50]. To test the influence of such loading conditions on FCG, cruciform specimens serve as a link between uniaxial laboratory tests and complex component tests [40], since they can be used to investigate the material behaviour under well-defined biaxial stress conditions [9, 43].

Up to now, there is no standardized specimen design for cruciform specimens, but there are five commonly used specimen designs. These specimen designs differ in the specimen thickness, i.e. uniform specimen thickness or thinned out measuring area, the radius between the load arms and the design of the load arms. Thin specimens of uniform thickness and with (i) large radii between the load arms were examined e.g. by [51–53], (ii) small radii between the loading arms were examined e.g. by [47, 50, 54–61] and (iii) small radii between the loading arms as well as relief slits within the load introduction arms were examined e.g. by [41, 42, 53, 60, 62]. Specimens with (iv) a thickness-reduced measuring area and small radii between the loading arms were examined e.g. by [16, 43, 44, 53, 63–67]. The specimen design (v), used by many researchers [40, 45, 46, 48, 49, 56, 59, 60, 63, 68–80], was realized by inserting relief slits in the load introduction arms of specimen design (iv). These slits realize a good decoupling of the forces, as it was shown in [81].

A disadvantage of these many specimen geometries is that there is no simple formula or rather solution to calculate the stress intensity factor K or rather its range ΔK, i.e. for both straight and curved crack paths, thus, the K-solution must be determined material-dependently. This calculation can be time-consuming so that it is not always carried out. The consequence is that for planar-biaxial crack growth experiments, the crack growth is described in different dependencies: (i) exclusive consideration of the fatigue crack growth in a–N plots, as done e.g. by [44, 50], (ii) consideration

of the fatigue crack growth in da/dN–N plots, as done by Neerukatti et al. [49], (iii) consideration of the fatigue crack growth in da/dN–a plots, as done by Wang et al. [79], (iv) consideration of the fatigue crack growth in da/dN–ΔG plots, see [47, 55], and (v) consideration of the fatigue crack growth in a–N plots as well as crack growth rate plots (da/dN–ΔK plots), as done by many authors, cf. e.g. [40, 41, 45, 46, 48, 51, 52, 54–56, 58, 61, 66–70, 74–78, 80]. In this article, both a–N plots and da/dN–ΔK plots are used for the study of the fatigue crack growth. Furthermore, a comparison with the Paris law is made.

14.2 Materials and Methods

14.2.1 Material

A newly developed metastable austenitic stainless steel X5CrMnNi16-7-6 called »16-7-6« in the following was studied. A significant characteristic of this material is the **TR**ansformation **I**nduced **P**lasticity, called TRIP effect [2, 3]. It is achieved by a transformation of γ-austenite to α'-martensite via a hexagonal structure called ε-martensite [4–8]. The main alloying elements are chromium (≈16 wt.%), manganese (≈7 wt.%) and nickel (≈6 wt.%). The chemical compositions of the individual batches for the various investigations varied slightly and are given in Table 14.1. However, these variations result in a pronounced martensitic transformation, as with »16-7-6 (Batch 1)« and »16-7-6 (Batch 2)«, or the material is rather stable, as in »16-7-6 (Batch 3)«. The »16-7-6 (Batch 1)« was used for the quasi-static investigations, the »16-7-6 (Batch 2)« was used for the LCF investigations and the »16-7-6 (Batch 3)« was used for the fatigue crack growth investigations. All materials were produced by powder metallurgy (PM).

The powder for the specimens was manufactured by inert gas atomisation (TLS, Bitterfeld, Germany). It was subsequently hot pressed under vacuum at a temperature of 1050 °C at a pressure of 30 MPa to a circular blank (Fraunhofer IKTS, Dresden, Germany). The heating and cooling rate was 10 K/min. The blanks had a thickness of (i) ≈11 mm and a diameter of ≈140 mm for the quasi-static specimens, (ii) a thickness of ≈16 mm and a diameter of ≈140 mm for the LCF specimens and

Table 14.1 Chemical compositions of the investigated steel in wt.%. The composition of the elements marked with * was determined by spark emission. The composition of the elements marked with ** and with *** was determined by combustion method and by melt extraction, respectively

	Fe*	Cr*	Mn*	Ni*	C**	N***	Si*
16-7-6 (Batch 1)	Bal.	15.9	6.2	6.2	0.05	0.04	0.9
16-7-6 (Batch 2)	Bal.	16.1	6.0	6.0	0.04	0.04	0.9
16-7-6 (Batch 3)	Bal.	16.2	7.2	6.7	0.049	0.056	0.94

(iii) a thickness of ≈15 mm and a diameter of ≈150 mm for the fatigue crack growth specimens. However, the cross-shaped biaxial-planar specimens have dimensions of (i), (iii) 332 mm × 332 mm, or (ii) 197 mm × 197 mm, respectively, so that the discs were welded into a commercial AISI304 base material. For this purpose, the following production steps were carried out:

1. A hole with a diameter of (i) and (iii) 140 mm, or (ii) 130 mm was cut by water jet cutting into the square plates made of AISI304 (PRO VA Blechbearbeitung GmbH, Olbernhau, Germany) with a thickness of (i) and (ii) 10 mm or (iii) 15 mm and an edge length of (i) and (iii) 340 mm, or (ii) 200 mm.
2. The hole in the square plate was enlarged to a diameter of (i) and (iii) 144.8 mm, or (ii) 134.8 mm by milling.
3. The circular blanks were milled to a diameter of (i) and (iii) 145 mm, or (ii) 135 mm and a height of (i) and (ii) 10 mm, or (iii) 15 mm.
4. Afterwards the circular blanks were cooled with liquid nitrogen for 30 min and subsequently placed into the squared plates, so that a specimen base plate is formed from one circular blank and one squared plate, which are held together by means of an interference fit.
5. The circular blank and the squared plate of the specimen base plate were welded together using an electron beam.
6. Afterwards, the specimen base plates were solution annealed at 1050 °C for 30 min and then quenched with nitrogen at 9 bar (G+M Vacutherm Härterei-und Oberflächentechnik GmbH, Brand-Erbisdorf, Germany).
7. Then, the specimens base plates were milled into their cruciform specimen shape, cf. Fig. 14.1.
8. The specimens for quasi-static investigations and for fatigue crack growth investigations were further mechanically processed after milling:
   - Quasi-static specimens:
     The slits of the »Triple-slit« and the »Double-slit« specimens were subsequently inserted by water jet cutting, cf. Fig. 14.1a, b.
   - Fatigue crack growth specimens:
     A hole with diameter of $d = 4$ mm was drilled in the middle of the specimens. Afterwards, two notches with a length of $l = 3$ mm each were inserted by electro-discharge machining, cf. Fig 14.1d.
9. Finally, the surfaces were polished mechanically.

14.2.2 Quasi-static Loading

The cruciform specimens for quasi-static tests were designed according to [82–84]. This geometry was developed using FE simulations with the aim of a homogeneous stress and strain distribution in the measuring area. In this work, two different specimen geometries were used, which are based on those proposed by [83, 84]. The

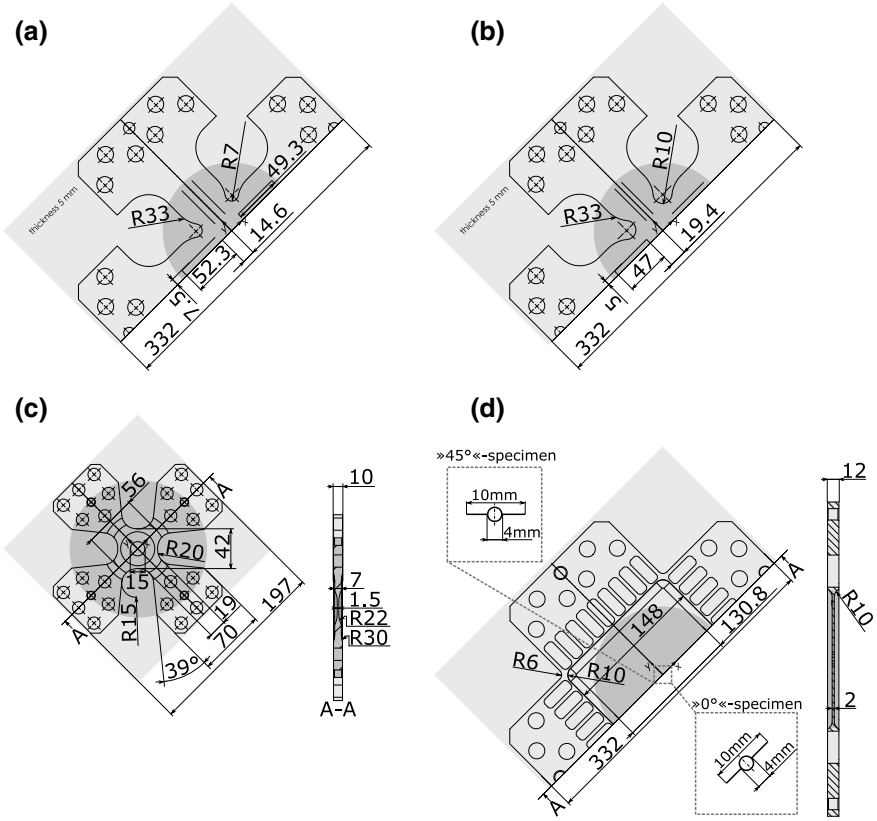

Fig. 14.1 Cruciform specimen geometries for biaxial-planar **a**, **b** quasi-static, **c** low cycle fatigue as well as **d** fatigue crack growth investigations with the essential dimensions in mm and the material illustration: light grey represents AISI304 and dark grey represents PM. Quasi-static specimen with **a** 3 slits (»Triple-slit« specimen) and **b** 2 slits (»Double-slit« specimen). **d** Fatigue crack growth specimen with notches aligned parallel to one loading axis (»0°«-specimen, rectangle bottom right) and at an angle of 45° to both load axes (»45°«-specimen, rectangle top left)

thickness of the specimens was 5 mm. The two specimen shapes used differ on the one hand in the number of slits within the loading arms and on the other hand in the transmission radius. The specimens with three slits called »Triple-slit« specimen had a transmission radius of 7 mm, cf. Fig. 14.1a. The specimens with two slits called »Double-slit« specimen had a transmission radius of 10 mm, cf. Fig. 14.1b. The length of the slits was different for both specimens. On the »Triple-slit« specimen, the middle slit was longer than the slits to the left and right. The two slits of the »Double-slit« specimen had the same length and were shorter than the slits of the »Triple-slit« specimen. Furthermore, the »Triple-slit« specimen had a homogeneous stress and strain distribution in the area of the yield strength at equibiaxial loading with $\lambda = 1$, where λ is the load ratio of the forces of both loading axes according to

(14.1). The »Double-slit« specimen also showed a homogeneous stress and strain distribution without stress and strain concentration areas. In particular, higher strains up to failure were possible in this case. Details of the two specimen designs are given in [85].

$$\lambda = \frac{F_x}{F_y} \tag{14.1}$$

with F_x and F_y the forces in axes x and y, respectively.

In addition to tests with a constant load ratio, i.e. shear loading with $\lambda = -1$, equibiaxial loading with $\lambda = 1$, and tests with $\lambda = 0.5$, sequence tests with alternating λ were also carried out to determine a part of the subsequent yield surface and characterize the hardening behavior as proposed by [86, 87]. The stresses were calculated using the partial unloading method [87]. Hooke's law was then used to calculate the principal stresses for the plane stress state [87].

The load ratios of the sequence tests were given in [85]. In addition to the biaxial tests, uniaxial tests were performed on both flat and cylindrical specimens. The flat specimens were tested on a MTS Landmark 250 (MTS Systems Corporation, Eden Prairie, USA).

14.2.3 Low Cycle Fatigue

The LCF experiments were performed on specimens with a planar thinned measuring area with a diameter of 15 mm and a thickness of 1.5 mm. In the highly loaded measuring area in the middle of the specimens there was a homogeneous stress distribution. The specimen geometry is shown in Fig. 14.1c. The design was similar to that reported repeatedly in the literature, cf. e.g. [16–20, 23, 88].

The LCF tests were performed under total strain-control, whereby the strains ε_x and ε_y were measured by a biaxial extensometer (Sandner Messtechnik GmbH, Biebesheim, Germany). Different strain states Φ, where Φ is the strain ratio of the strains of both axes, cf. (14.2), were investigated with a strain rate of $\dot{\varepsilon} = 0.004/\mathrm{s}$.

$$\Phi = \frac{\varepsilon_x}{\varepsilon_y} \tag{14.2}$$

In addition to equibiaxial tensile strain tests with $\Phi = 1$ and shear tests with $\Phi = -1$, strain ratios of $\Phi = 0.5$, $\Phi = -0.1$ and $\Phi = -0.5$ have also been tested. The schematic course of the triangular strain-time function for $\Phi = 1$ is shown in Fig. 14.2a, for $\Phi = -1$ in Fig. 14.2b and for $\Phi = -0.5$ in Fig. 14.2c. For shear and for equibiaxial strain, the frequencies and amplitudes of the strains had the same values, Fig. 14.2a, b, while the amplitudes differed for $\Phi = -0.5$, cf. Fig. 14.2c.

The von Mises equivalent strain amplitude $\Delta\varepsilon_{\mathrm{vM}}/2$ was calculated according to [89]. The tested von Mises equivalent strain amplitudes $\Delta\varepsilon_{\mathrm{vM}}/2$ were in the range

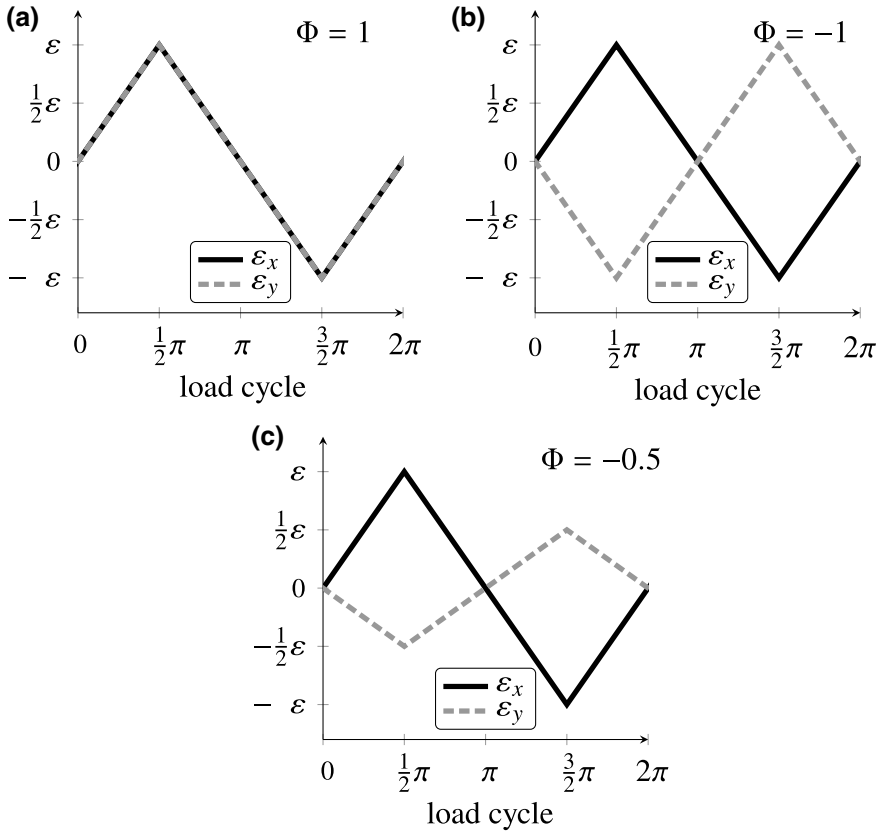

Fig. 14.2 Schematic course of the strains ε_x and ε_y for different strain ratios Φ for in-phase loading

of $0.3 \cdot 10^{-2} \leq \Delta\varepsilon_{vM}/2 \leq 0.6 \cdot 10^{-2}$. In addition, uniaxial reference tests were performed on a MTS Landmark 250 (Eden Prairie, USA).

The characterization of the cyclic deformation behaviour is based on the von Mises force amplitude $\Delta F_{vM}/2$ due to the fact that the cross section could not be determined and numerical calculations as performed by Itoh et al. [19] were not available. The calculation of $\Delta F_{vM}/2$ was carried out according to [18] using the forces F_x and F_y at maximum principal strains in axis x, cf. (14.3). It is assumed that hardening and yielding took place in a defined cross-section and the maximum stresses and strains occur in the thinned measuring area of the specimen with a homogeneous distribution.

$$F_{vM} = \sqrt{(F_x)^2 + \left(F_y\right)^2 - F_x \cdot F_y} \tag{14.3}$$

14.2.4 Fatigue Crack Growth

The fatigue crack growth experiments were performed on cruciform specimens with a thinned measuring area and slitted arms as proposed by Brown and Miller [69] on the base of [81]. The design is widely used [40, 45, 46, 48, 49, 56, 59, 60, 63, 68–80]. It shall simulate the internal crack in a plate of infinite size and small thickness according to [90]. The slitted arms shall ensure a good decoupling of the forces [40, 81, 91]. Furthermore, the stresses in the cross section of the gauge area shall be higher compared to the stresses in the loading arms. The thickness of the measuring area was approximately 2 mm. The exact specimen thickness may vary slightly due to polishing, so that the exact specimen thickness was measured after the tests.

Depending on the investigation, two different configurations of the start notch have been used [40, 76, 77, 91]. On the one hand, uniaxial investigations have been performed at the cruciform specimens with the notches aligned parallel to one loading axis, i.e. at an angle of 0° to one loading axis. This kind of specimen is called »0°«-specimen and shown in Fig. 14.1d. On the other hand, the equibiaxial as well as biaxial investigations with a phase shift have been performed on specimens with notches aligned at an angle of 45° to both loading axes. This kind of specimen is called »45°«-specimen and is also shown in Fig. 14.1d. The hole in the middle of both specimens had a diameter of $d = 4\,\text{mm}$. The total length of both notches was $2 \cdot a = 10\,\text{mm}$, i.e. the notches represented two cracks with a length of $a = 5\,\text{mm}$ each at the beginning of the investigation.

The length of the two cracks was calculated from the center of the cruciform specimen. As long as the crack grew straight, i.e. in the direction of the start notches, the crack length a was measured as the Euclidean distance between starting notch tip and the respective crack tip. Subsequently, the radius of the hole, i.e. $d/2 = 2\,\text{mm}$, and the length of the notch, $l = 3\,\text{mm}$, were added to that Euclidean distance. As soon as the crack path kinked, the Euclidean distance between the currently observed measuring point and the previously observed measuring point was calculated. This distance was added to the crack length of the previously considered measuring point. This means that the crack length is ultimately the sum of the crack length of the straight crack and the individual crack lengths of the kinked crack path. Unfortunately, the measurement errors were added. To minimize measurement errors, the scatter band reduction proposed in [92] in accordance with ASTM E647 [93] was performed. In other words, the given crack length is the arc length of the crack.

The investigations were conducted force controlled with a frequency of 20 Hz and a force ratio of $R = 0.1$. If a force ratio different to $R = 0.1$ was used, it is indicated. The exact forces are given in a recent work [77]. In the case of uniaxial loading, the forces were applied just in y-direction. In the case of biaxial loading, the forces were applied in x- and y-direction. The course of the forces for equibiaxial loading is shown in Fig. 14.3a. Figure 14.3b shows the course for phase-shifted loading with a phase shift of $\varphi = 90°$. The phase shift φ is the time dependent shift of the two forces relative to each other. In the case of in-phase loading, the load ratio λ, cf. (14.1),

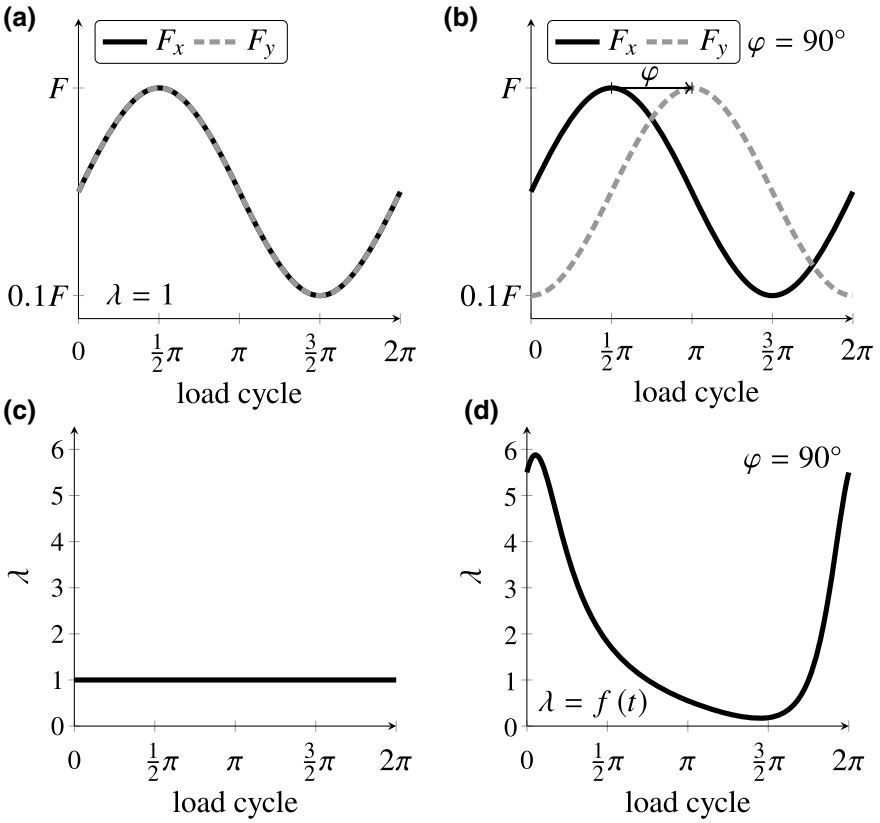

Fig. 14.3 Schematic course of **a**, **b** the applied forces in x- and y-direction and **c**, **d** the resultant biaxial force ratio λ during one load cycle for **a**, **c** in-phase loading as well as **b**, **d** ouf-of-phase loading with a phase shift of $\varphi = 90°$

was $\lambda = 1$ during the entire load cycle, cf. Fig. 14.3c. In the case of out-of-phase loading, the load ratio λ changed permanently during the load cycle, cf. Fig. 14.3d for the example of $\varphi = 90°$.

Four different load cases were investigated: (i) uniaxial loading, (ii) equibiaxial loading, (iii) first equibiaxial loading to start the fatigue crack growth and afterward phase-shifted loading, and (iv) first equibiaxial loading to start the fatigue crack growth and afterward phase-shifted loading with an increase of the phase shift after a change in the crack length a of more than $\Delta a = 1.5$ mm.

For the calculation of the stress intensity factor K and range ΔK, the occurring stresses have to be known. They were calculated using commercial software ABAQUS for 2D finite element analyses with a linear elastic material model and unit forces of $f_x = 1$ kN or $f_y = 1$ kN [91]. The investigations showed, that a material-independent solution for the transmission of force into stress can be given. An applied force of $F_y = 1$ kN in y-direction resulted in a stress of $\sigma_y = 2.94$ MPa in y-direction

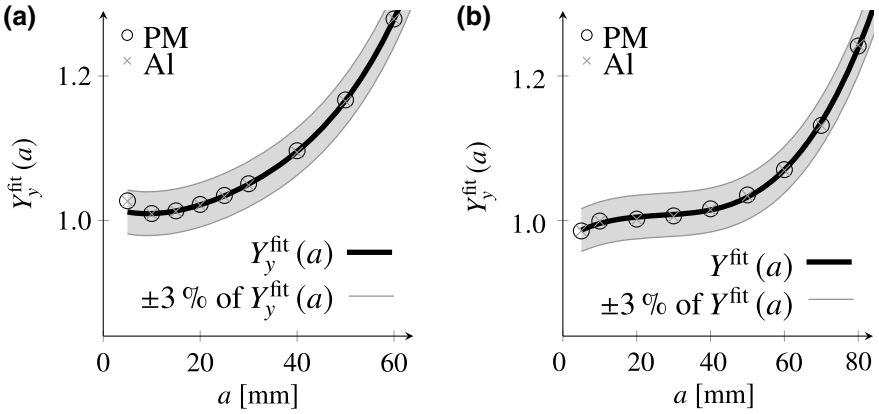

Fig. 14.4 Plot of the geometry functions $Y(a)$ versus the crack length a for the **a** »0°«-specimen and **b** »45°«-specimen. Comparison of the exact solutions for PM and Al with the determined fit function and the ±3% deviation [91]

in the center of the specimen. An applied force of $F_x = 1\,\text{kN}$ in x-direction resulted in a stress of $\sigma_y = -0.05\,\text{MPa}$ in y-direction in the center of the specimen. Due to the principal of superposition and the possibility of scaling, cf. [40, 76, 77, 91], the effective stress can thus be determined at each time of the load cycle. Furthermore, in dependence of the alignment of the start notches, i.e. for the »0°«-specimen as well as for the »45°«-specimen, material-independent and crack length dependent geometry functions $Y(a)$ were determined, cf. [91]. Figure 14.4a, b show the geometry functions $Y_y(a)$ for the »0°«-specimen and $Y(a)$ for the »45°«-specimen, respectively. Both plots in Fig. 14.4 show the exact solution of the geometry factor $Y(a)$ at different crack lengths for the investigated steel, called PM, as well as for an aluminium alloy, called Al. The calculations are based on the material parameters Young's modulus $E = 192\,\text{GPa}$ and Poisson's ratio $\nu = 0.24$ for PM and $E = 72\,\text{GPa}$ and $\nu = 0.34$ for the Al alloy, respectively. It becomes clear, that the geometry functions approximate the calculated geometry factors well for both materials, in each case for the corresponding notch configuration for straight crack paths. Influences on the fatigue crack growth due to differences in the thickness of the measuring area can be corrected using a thickness correction [76]. As soon as the crack paths begin to kink, the calculation of the K-solution has to be done using FE-calculations, cf. [76, 77].

14.2.5 Experimental Details

The planar-biaxial investigations were performed on a servo-hydraulic tension-compression system (Instron 8800, Instron, Norwood, USA), cf. Fig. 14.5. The test rig had four actuators in two perpendicular loading axes. In addition, depending on

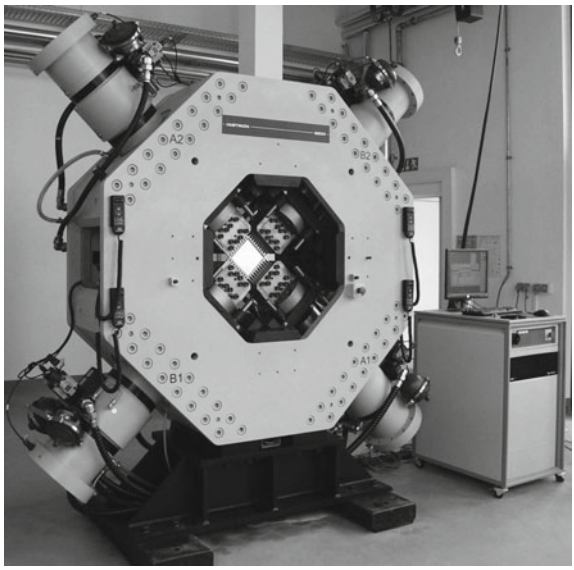

Fig. 14.5 Servo-hydraulic planar-biaxial tension-compression test system [1]

the test, i.e. quasi-static, LCF or FCG tests, various other measuring instruments were attached, cf. Fig. 14.6.

A biaxial orthogonal extensometer (Sandner Messtechnik GmbH, Biebesheim, Germany) was applied for the quasi-static investigations as well as for the LCF investigations, cf. #1 in Fig. 14.6a, c, d. The extensometer had four ceramic arms with a gauge length of 13 mm for strain measurement in the two orthogonal axes. It was mounted in the middle of the measuring area at one side of the specimen, cf. #1 in Fig. 14.6a for quasi-static investigations [85, 87] and #1 in Fig. 14.6c, d for LCF investigations [18, 94]. The measured strains corresponded to principal strains.

The ferrite measuring device Fischerscope MMS PC (Helmut Fischer GmbH, Sindelfingen, Germany), cf. #2 in Fig. 14.6a, c, d, was applied at the quasi-static investigations as well as for the LCF investigations to measure the martensite content opposite to the extensometer. The martensite content was calculated according to [95] by multiplying the measured ferrite content calibrated for δ-ferrite by a factor of 1.7.

Support plates were mounted on the specimen during quasi-static tests with compressive loading, cf. #3 in Fig. 14.6b to prevent buckling.

Fatigue crack growth tests were carried out by applying crack gages (Krak Gage B20, Russenberger Prüfmaschinen AG, Neuhausen, Switzerland) to the front of specimen, cf. #4 in Fig. 14.6e. The crack length for cracks that extend the two start notches was measured using the indirect potential method using Fractomat (Russenberger Prüfmaschinen AG, Neuhausen, Switzerland).

Furthermore, a high speed camera (mvBlueCOUGAR-XD 104 bG, Matrix Vision GmbH, Oppenweiler, Germany), cf. #5 in Fig. 14.6f, with optics was located at the back of the specimen to document the crack opening. For this purpose a speckle pattern was sprayed onto the specimen surface to evaluate the movement of the

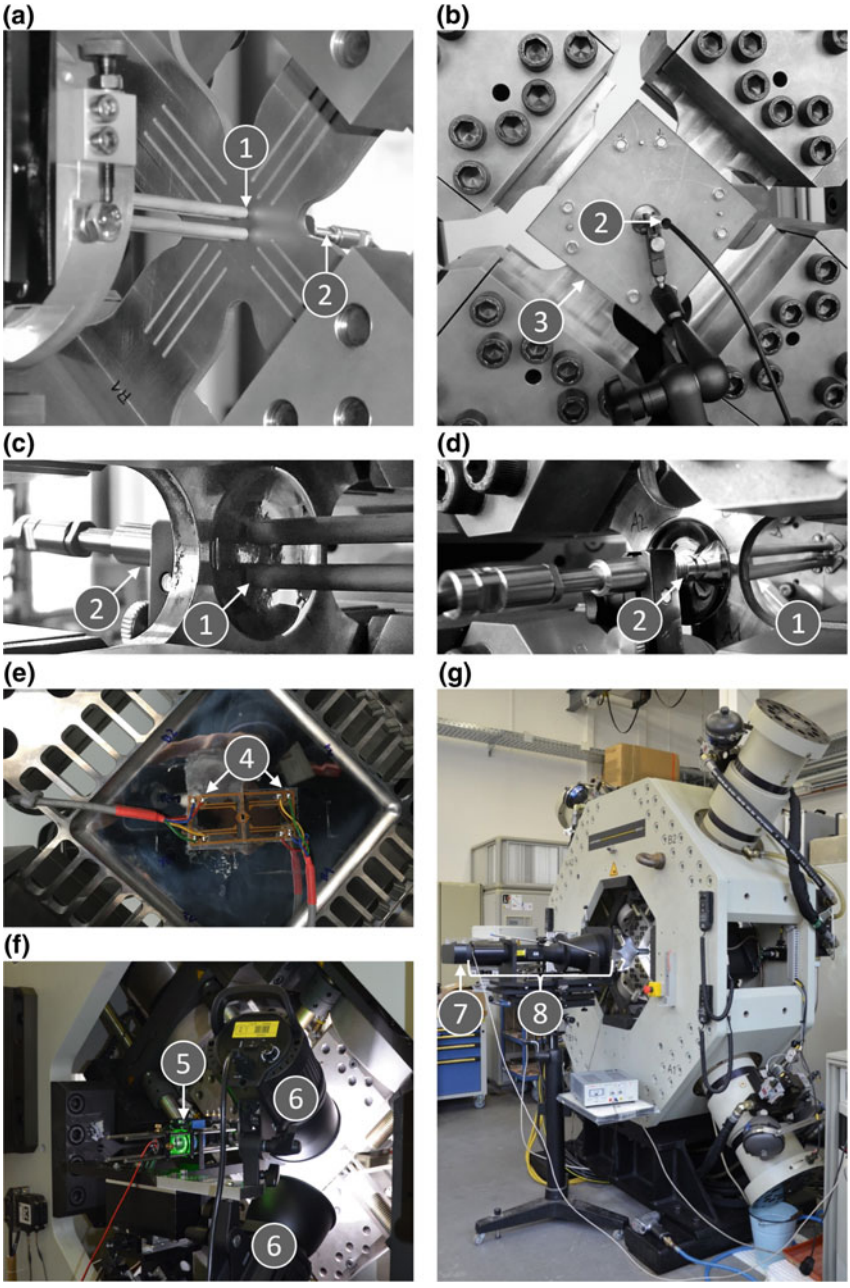

Fig. 14.6 Test setup for experiments with **a**, **b** quasi-static loading as well as **c**, **d** low cycle fatigue and **e**–**g** fatigue crack growth experiments and illustration of the measuring instruments used: #1 biaxial orthogonal extensometer, #2 ferrite sensor, #3 support plates, #4 crack gage, #5 high speed camera, #6 lighting, #7 high resolution scanner camera with #8 telecentric optics [23, 87]

crack edges using digital image correlation software (ARAMIS v6.3.1, GOM GmbH, Braunschweig, Germany). For this, it was important that the measuring spot is uniformly illuminated. This was achieved with two LED spotlights (Mettle EL-600, Mettle Photographic Equipment Corporation, Changzhou, China), cf. #6 in Fig. 14.6f.

The documentation of the crack tip coordinates and the measurement of the crack lengths for kinking crack paths was carried out with a line scanner camera (Pentacon SCAN 6000, Pentacon GmbH, Dresden, Germany) with telecentric optics, which was installed in front of the test rig, cf. #7 and #8 in Fig. 14.6g, cf. [71] for further details.

14.3 Quasi-static Loading

The evaluation of the uniaxial and the biaxial tests with constant load ratio λ are shown in Fig. 14.7a. The yield point used was the 0.2% yield point $R_{p0.2}$ applied for materials without a pronounced yield point. The yield strength of the uniaxial tests was 288 ± 21 MPa in tension and 288 ± 28 MPa in compression. Furthermore the symmetry points for the uniaxial loading are indicated. This material can be described with the von Mises equivalent stress hypothesis. A comparison of the results between the »Triple-slit« specimens and the »Double-slit« specimens shows a higher equivalent yield strength of the »Double-slit« specimens in comparison to the »Triple-slit« specimens. These differences are visible in quadrant I of the von Mises yield surface, cf. Fig. 14.7a. In quadrants II and IV, differences in yield strength between the two specimen geometries of up to 90 MPa are visible.

The comparison of the stress-strain curve of the uniaxial experiments with the stress-strain curve of the »Double-slit« specimens illustrates, that the »16-7-6 (Batch 1)« can be described with the von Mises equivalent stress hypothesis. For shear loading, i.e. $\lambda = -1$, strains of up to 20 % are possible. In the uniaxial experiments a significant scatter was found. The results of the biaxial tests are within this scatter band. From this it can be concluded that the partial unloading method is suitable for determining the stress-strain curve for those biaxial experiments.

By means of sequence tests on a »Triple-slit« specimen and a »Double-slit« specimen the subsequent yield surfaces were studied. Load sequence effects occurred. In this paper, only the results of the »Triple-slit« specimen are presented. The results of the »Double-slit« specimen are given elsewhere [85].

Figure 14.7b shows the load path and Fig. 14.7c shows the stress path in the principal stress plane $\sigma_1 - \sigma_2$ of the »Triple-slit« specimen. The corresponding stress-strain curve as well as the martensite evolution is given in Fig. 14.7d.

In the load sequence test of the »Triple-slit« specimen, the load was first increased at a load ratio of $\lambda = 0.3$ until (1) an equivalent plastic strain $\varepsilon_{\text{eq-pl}}$ of $\varepsilon_{\text{eq-pl}} = 2\%$ was reached, cf. Fig. 14.7c. At this equivalent plastic strain, the equivalent stress σ_{eq} was $\sigma_{\text{eq}} = 350$ MPa. Therefore, the yield surface for $\sigma_{\text{eq}} = 350$ MPa is shown in Fig. 14.7c (solid line) under the assumption of isotropic hardening. At this load, 0.3% of α'-martensite had already formed. Subsequently, the loading was gradually

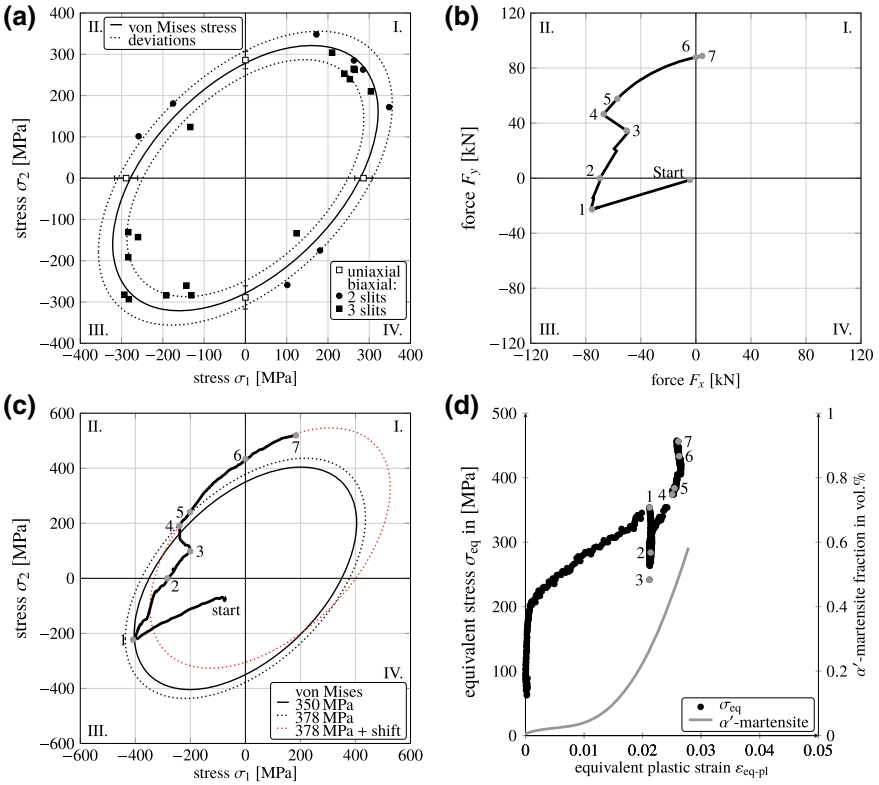

Fig. 14.7 Results of the quasi-static biaxial-planar experiments. **a** Experimentally determined von Mises yield surface of the »16-7-6 (Batch 1)« by uniaxial and planar-biaxial tests using the »Triple-slit« and the »Double-slit« specimens. **b** Load path and **c** stress paths of sequential tests within the principal stress plane with an initial load ratio of $\lambda = 0.3$ at the »Triple-slit« specimen with **d** the corresponding stress-strain curve and martensite evolution [85]

changed, starting (1) with the initial load ratio of $\lambda = 0.3$, through (2) a load ratio of $\lambda = 0$ and ending (3) with a load ratio of $\lambda = -0.7$. The load path passed through the elastic area. When the load ratio of $\lambda = -0.7$ was reached, the force was again increased up to (4) an equivalent plastic deformation of $\varepsilon_{\text{eq-pl}} = 2.5\%$. Further α'-martensite was formed. At the equivalent plastic strain of $\varepsilon_{\text{eq-pl}} = 2.5\%$, an equivalent stress of $\sigma_{\text{eq}} = 378\,\text{MPa}$ was reached. In the subsequent gradual loading change, starting (4) with the load ratio of $\lambda = -0.7$ and ending (5) with a load ratio of $\lambda = -1$, the equivalent stress followed the yield surface for $\sigma_{\text{eq}} = 378\,\text{MPa}$. The further stepwise change of the load ratio from (5) $\lambda = -1$ through (6) a load ratio of $\lambda = \infty$ to (7) $\lambda = 20$ was accompanied by further hardening and a further α'-martensite formation without further plastic deformation, i.e. elastic material behaviour was observed. This effect can be explained by kinematic hardening, so that a shifted yield surface for $\sigma_{\text{eq}} = 378\,\text{MPa}$ was drawn, cf. Fig. 14.7c, red dotted ellipse. The shift was

$\sigma_1 = 90\,\text{MPa}$ and $\sigma_2 = 110\,\text{MPa}$. This ellipse corresponds to the observed loading path. This confirms the hypothesis of kinematic hardening which is accompanied by the formation of further α'-martensite. The stresses were determined by means of partial unloading method. The results showed that the partial unloading method is also suitable for the measurement of kinematic hardening effects under multiaxial loading.

In the presented sequence test as well as in the sequence test of [85], no yield surface matching the load path could be determined. The reason for this is the formation of α'-martensite. This results in the assumption that the α'-martensite formation of the microstructure depends on the stress state. Changes in the stress state led to an activation of other glide systems. An intersection of these with the martensite led to strain hardening. Detailed explanation on this are made in the following paragraphs on microstructure. It is also assumed that anisotropic yield surface is present since strain hardening is correlated with a combination of isotropic and kinematic hardening. As long as no α'-martensite formation took place, isotropic material behaviour was present. A similar material behaviour with initial isotropic flow curve and kinematic hardening during subsequent deformation can also be found in the literature [87, 96–98].

The investigations of the microstructure were performed ex situ at »Triple-slit« specimen for shear loading with $\lambda = -1$ and equibiaxial tension with $\lambda = 1$ up to equivalent strains of $\varepsilon_{\text{eq-pl}} = 8.6\%$ and $\varepsilon_{\text{eq-pl}} = 8\%$, respectively. The scanning electron microscope (SEM) images in back scattered electron (BSE) contrast clearly showed the formation of deformation bands in the austenitic matrix [85]. α'-martensite nuclei were formed in these deformation bands in accordance with uniaxial reference tests, see e.g. [99, 100]. Uniaxial monotonic tests by the authors of [100] showed that the deformation bands were areas of strain localizations. These form large stacking faults due to the movement of partial dislocations. The stacking fault density, the local strain and the thickness of the deformation bands increased with increasing plastic strain. The α'-martensite nuclei were preferentially formed on the intersection points of deformation bands or at intersection points of individual stacking faults with deformation bands. This in turn corresponds to the increase in strain as a function of the crystallographic orientation of the α'-martensite nuclei in relation to the load axis. Shear loading resulted in austenitic grains being covered with deformation bands containing α'-martensite islands. In contrast, tensile loading resulted in a lower density of the deformation bands. The individual deformation bands of the austenitic matrix can be distinguished. Furthermore, the α'-martensite island density was significantly lower for uniaxial loading.

The electron backscatter diffraction (EBSD) investigations of the microstructure of the »Triple-slit« specimen for shear loading with $\lambda = -1$ and equibiaxial tension with $\lambda = 1$ show significant differences, cf. Fig. 14.8. The number of austenite grains containing deformation bands is significantly higher for shear loading, cf. Fig. 14.8a, than for equibiaxial loading, cf. Fig. 14.8b. Furthermore, much more α'-martensite nuclei were formed under shear loading, i.e. the density of α'-martensite nuclei is much higher for shear loading in comparison to the equibiaxial tension loading. In the EBSD images it becomes clear that the formation of deformation bands was inten-

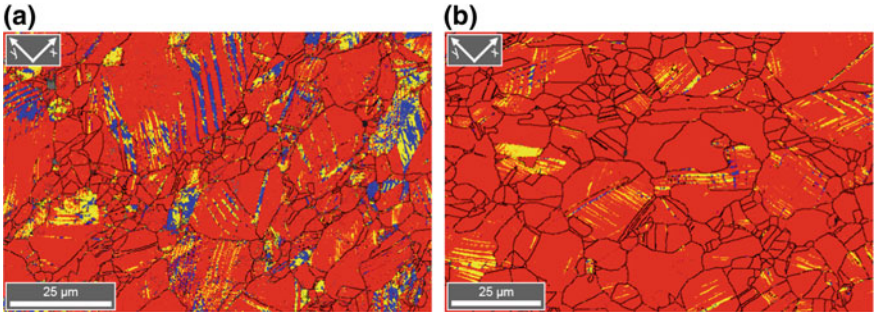

Fig. 14.8 EBSD phase maps of »Triple-slit« specimens after **a** shear loading up to $\varepsilon_{\text{eq-pl}} = 8.6\%$ and **b** equibiaxial tensile loading up to $\varepsilon_{\text{eq-pl}} = 8\%$ with austenite (red), ε-martensite (yellow) and α'-martensite (blue) [85]

sified due to the high stacking fault density, which had a hexagonal structure, when subjected to shear loading. This is particularly evident from the fact that in the specimen subjected to shear loading, individual austenite grains were completely covered with a hexagonal structure, cf. Fig. 14.8a, and their thickness or rather their density were much more pronounced than for equibiaxial loading. Furthermore, the volume fraction of the deformation-induced α'-martensite is considerably higher for shear loading than for equibiaxial tensile loading. This corresponds to the measurements of the ferromagnetic phase fraction by means of a ferrite sensor [85].

14.4 Low Cycle Fatigue

The cyclic deformation behaviour and the martensitic transformation were investigated for »16-7-6 (Batch 2)«. The characterization is based on the von Mises force amplitude $\Delta F_{\text{vM}}/2$. The LCF behaviour of the material can be divided into three stages, cf. Fig. 14.9 [94]. Due to the cyclic loading, primary hardening took place at the beginning. Subsequently softening took place, which was finally followed by secondary hardening. Such material behaviour is already well-known from uniaxial studies, see e.g. [7, 31, 32]. The course of the cyclic deformation curves for the investigated equibiaxial tensile loading, i.e. the strain ratios of $\Phi = 1$ and $\Phi = 0.5$, was almost identical, cf. [94]. However, with negative strain ratios Φ, the von Mises force amplitude $\Delta F_{\text{vM}}/2$ decreased with decreasing strain ratio Φ, cf. Fig. 14.9a.

With negative strain ratios, the onset of secondary hardening was earlier and the magnitude was increased, i.e. the more negative the strain ratio was, the stronger and earlier the secondary hardening was, cf. Fig. 14.9a. Furthermore, at negative strain ratios, it was found that the maximum fatigue life was measured for the strain ratio of $\Phi = -1$ and the shortest fatigue life for the strain ratio of $\Phi = -0.1$, i.e. the larger the strain ratio at negative strain ratio was, the longer the fatigue life was. This leads to the assumption that shear loading with $\Phi = -1$ supports yielding, secondary

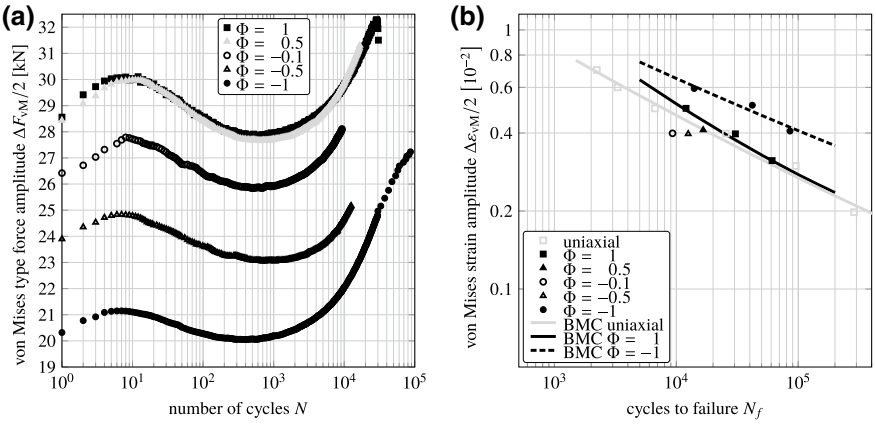

Fig. 14.9 **a** Cyclic deformation curves and **b** estimation of fatigue life of »16-7-6 (Batch 2)« [94] under uniaxial and biaxial cyclic loading with different strain ratios Φ showing the von Mises equivalent strain amplitude of $\Delta\varepsilon_{vM}/2$ versus N_f [94]

hardening and reduces axial forces. This was also reported in [18]. Due to the shear loading the secondary hardening was most pronounced due to an early start of cyclic hardening. Therefore the fatigue life for shear stress was also the highest.

In contrast to negative strain ratios, von Mises force amplitudes $\Delta F_{vM}/2$ were almost identical for positive strain ratios, cf. Fig. 14.9a. However, in these experiments the cross-sectional area was not identical, as was assumed for the von Mises force amplitude $\Delta F_{vM}/2$. Further experiments with an increase in von Mises strain amplitude $\Delta\varepsilon_{vM}/2$ in the range between $0.3 \cdot 10^{-2} \leq \varepsilon_{vM}/2 \leq 0.6 \cdot 10^{-2}$ showed an earlier onset of the secondary hardening due to a higher plastic deformation, as the martensitic phase transformation took place during the cyclic deformation.

For the investigated von Mises strain amplitude of $\Delta\varepsilon_{vM}/2 = 0.4 \cdot 10^{-2}$ for the strain ratios of $\Phi = -1$, $\Phi = -0.5$, $\Phi = -0.1$, $\Phi = 0.5$ and $\Phi = 1$ as well as for uniaxial experiments, a significant increase in the α'-martensite content was observed after an incubation period and correlated with the onset of secondary hardening, see [18]. The course of the martensite formation curves for the strain ratios of $\Phi = -1$, $\Phi = -0.5$, $\Phi = -0.1$ and the uniaxial investigations were almost identical up to the point of failure. However, for the strain ratios of $\Phi = 0.5$ and $\Phi = 1$, the martensitic transformation started later. The α'-martensite amount at fatigue failure ranged from an α'-martensite amount of 5 vol% at a strain ratio of $\Phi = 0.5$ up to an α'-martensite amount of 45 vol% at a strain ratio of $\Phi = -1$. In conclusion, it can be stated that the α'-martensite formation depends on the platic strain amplitude $\varepsilon_{vM}/2$, which is responsible for secondary hardening. This is in accordance to [7, 31, 32]. Furthermore, the formation of α'-martensite is promoted by uniaxial or shear loading, since the martensite content was significantly lower for all other types of loading, i.e. $\Phi = -0.5$, $\Phi = -0.1$, $\Phi = 0.5$ and $\Phi = 1$.

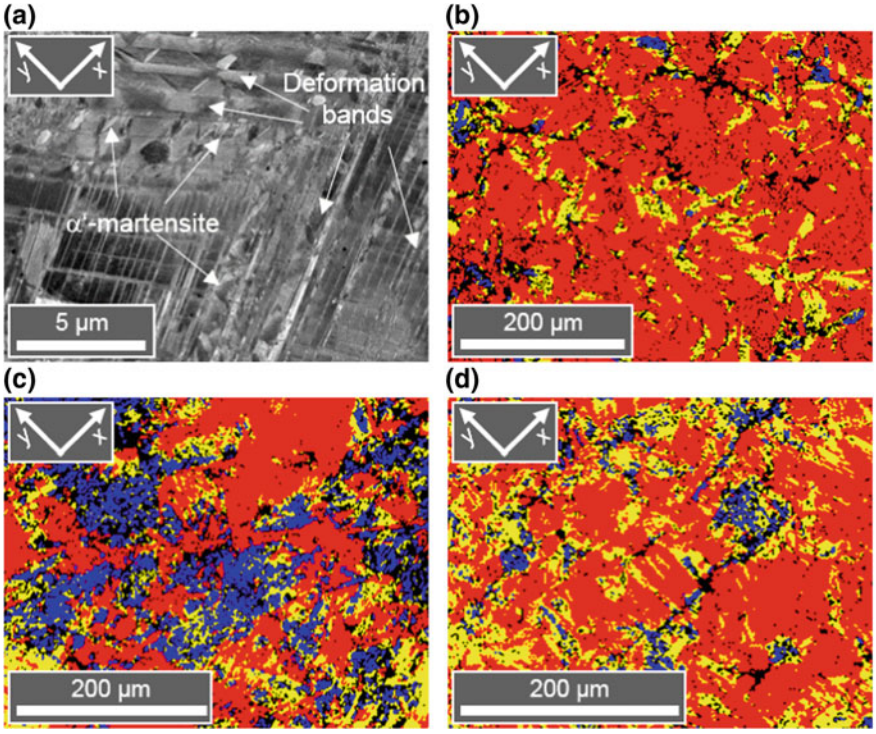

Fig. 14.10 SEM micrographs of the »16-7-6 (Batch 2)« after cyclic loading at $\Delta\varepsilon_{vM}/2 = 0.4 \cdot 10^{-2}$. **a** Deformation bands and α'-martensite shown in the BSE contrast after cylclic shear loading with $\Phi = -1$. **b–d** EBSD phase maps after cyclic **b** equibiaxial loading with $\Phi = 1$, **c** shear loading with $\Phi = -1$ and **d** loading with $\Phi = 0.5$ with austenite (red), ε-martensite (yellow) and α'-martensite (blue) [94]

The SEM images in BSE contrast, cf. Fig. 14.10a, show lens-shaped α'-martensite in the deformation bands. These are often located at the intersection points of deformation bands [101]. This is a typical microstructure for cyclic deformation and in accordance with the observations of e.g. [5]. The thin deformation bands do not contain α'-martensite nuclei. This is also consistent with findings by the authors of [5]. A high stacking fault density resulting in a hexagonal structure called ε-martensite was found by EBSD and electron channeling contrast imaging (ECCI) in the deformation bands, cf. [5].

EBSD measurements were made in the SEM on vibration-polished surfaces, Fig. 14.10b–d. The phase maps show fcc austenite (red), hexagonal ε-martensite (yellow) and bcc α'-martensite (blue) at different von Mises strain ratios Φ at a von Mises strain amplitude of $\Delta\varepsilon_{vM}/2 = 0.4 \cdot 10^{-2}$. Figure 14.10b–d show the phase maps after cyclic deformation with equibiaxial loading of $\Phi = 1$, shear loading of $\Phi = -1$, and deformation with $\Phi = -0.5$. It becomes clear that the α'-martensite always lies within the hexagonal phase (yellow). This in turn confirms the

assumption that the transformation from fcc austenite to α'-martensite took place via ε-martensite. The comparison of Fig. 14.10b–d shows that the largest fraction of α'-martensite and ε-martensite were formed under shear loading with a fraction of $\approx$15% each, cf. Fig. 14.10c. The lowest fraction of α'-martensite and ε-martensite was measured under equibiaxial loading, cf. Fig. 14.10b. The most intensive formation of ε-martensite was found after a loading with a strain ratio of $\Phi = 0.5$, although the regions with α'-martensite were very small, cf. Fig. 14.10d. A martensitic phase transformation was also measured in the plastic zone of the formed cracks. However, this is not shown here.

The fatigue life was compared by applying the von Mises strain amplitude $\Delta\varepsilon_{vM}/2$ versus the number of load cycles to failure, cf. Fig. 14.9b. The comparison of the fatigue life of the »16-7-6 (Batch 2)« at different strain ratios shows clearly, that fatigue lives were the shortest for $\Phi = 0.5$, $\Phi = -0.1$ and $\Phi = -0.5$ in comparison to the uniaxial as well as biaxial shear loading and the equibiaxial loading. To be more precise, these fatigue lives for uniaxial or equibiaxial loading are within the scatter band of 2. It can therefore be concluded that the Basquin-Manson-Coffin relationship (BMC) for uniaxial loading is conservative for equibiaxial loading for the investigated material. In contrast, the authors of [19] observed at AISI304 steel that the fatigue lives for $\Phi = -0.5$, $\Phi = 0$ and $\Phi = 0.5$ are between those of equibiaxial loading with $\Phi = 1$ and shear loading with $\Phi = -1$. Fatigue life of the »16-7-6 (Batch 2)« under shear loading $\Phi = -1$ is about 7–8 times higher than under equibiaxial $\Phi = 1$ or uniaxial loading, respectively. The differences in fatigue life decrease with increasing von Mises equivalent strain amplitude $\varepsilon_{vM}/2$ due to plastic deformation. This is in accordance with the findings of [18] for the cast material. Furthermore, the results show that the highest fatigue lives occurred at shear loading compared to uniaxial loading in agreement with the literature for planar biaxial investigations [16, 17, 19, 20, 23] and tension-torsion tests [21, 22, 102]. For austenitic steels with a low stacking fault energy, the differences in fatigue lives are larger than for austenitic steels with a high stacking fault energy [22].

The discussion of the resulting equivalent force amplitudes and fatigue lives is based on the assumption of von Mises. However, the deviations of equivalent force amplitudes and fatigue lives can also be interpreted that the von Mises hypothesis cannot be applied in the present case. The von Mises criterion was used, as the criterion is valid for plastically deformable materials. Under equibiaxial loading in the tension-compression regime there is a scatter of about 2–3, with a shorter fatigue life compared to uniaxial loading. Under shear loading the fatigue life is about 7–8.5 times higher than under uniaxial loading for the same von Mises strain amplitude, i.e. the damage caused by shear loading is overestimated. In order to be able to describe the service life reserve or the reduced damage caused by shear loading, alternative models should be used which take the effect of the hydrostatic part of the stress tensor on damage into account.

14.5 Fatigue Crack Growth

14.5.1 Crack Paths

The fatigue crack growth investigations on the »16-7-6 (Batch 3)« were carried out on five different specimens. One specimen was loaded unaixially (specimen »uni«), one specimen was loaded equibiaxially (specimen »equi«), two specimens were first equibiaxially and subsequently phase-shifted loaded (specimens »0°/22.5°« and »0°/180°«) and one specimen was first equibiaxially and then phase-shifted loaded with phase shift increases of 15° after given crack growth intervals (specimen »stepw. 0°–90°«). The courses of the two cracks of the respective specimens were identical or symmetrical, respectively. This is also valid for the crack paths of all four cracks of specimen »0°/180°«. As expected, the uniaxial loading of specimen »uni« led to a straight crack path, which runs perpendicular to the loading axis y, cf. Fig. 14.11a. Furthermore, the equibaixial loading during the entire test of specimen »equi« resulted in a crack path that runs at an angle of 45° to both loading axes in the direction of the starting notches, cf. Fig. 14.11b. This was due to the fact that the start notches were also aligned at an angle of 45° to both loading axes and that the equibiaxial loading led to a pure Mode I crack opening. SEM investigation of the crack path revealed that there was a micro crack branching at the end of the investigation, cf. Fig. 14.12a. The reason for this seems to be an edge influence as well as force coupling.

A change of the phase shift from in-phase loading to out-of-phase loading led to a change of the crack propagation direction in most investigations. The change from the initial equibiaxial loading to a subsequent phase-shifted loading of $\varphi = 22.5°$ for specimen »0°/22.5°« resulted in a gradual change of the crack propagation direction without branching, cf. Fig. 14.11c. Branching as a result of a phase-shifted loading occured after phase change to 180° in specimen »0°/180°«, cf. Fig. 14.11d. At the triple point of cracks 1, 1-1 and 1-2, i.e. at the point where the change from in-phase to out-of-phase loading and therefore branching occured, no further micro cracks were observed in SEM investigations, cf. Fig. 14.12b. The obtained crack paths are in accordance with those predicted in [103]. However, it was expected that both branched cracks would grow initially, but one crack would not grow further after some load cycles [75]. Due to the change to a $\varphi = 180°$ phase-shifted loading, there were two principal stress directions which occured in succession. They were shifted by exactly half of the load cycle, i.e. $N/2$. The cracks 1-1 and 1-2 or 2-1 and 2-2, respectively, grew on initially curved paths, but then finally perpendicular to the principal stress directions. This is in accordance with [104, p. 131]. The cracks strived for this crack path according to the maximum circumferential stress criterion according to [105]. This criterion is commonly used for crack growth direction predictions [106–108].

The change from an initial in-phase loading to a subsequent 15° phase-shifted loading of specimen »stepw. 0°–90°« resulted in a kinking at a very small angle, Figs. 14.11e, f and 14.13a. This relatively small angle of crack path kinking was

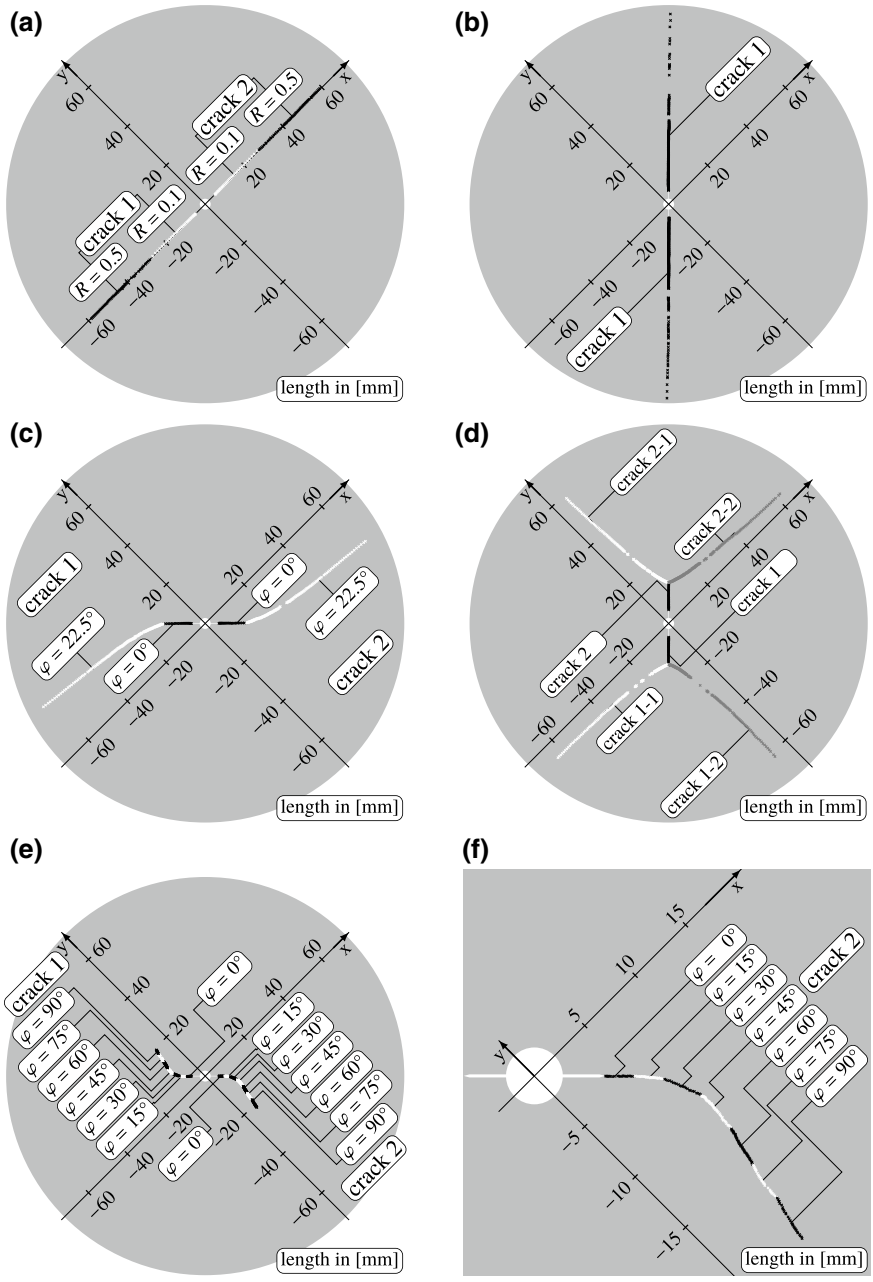

Fig. 14.11 Crack paths of the **a** uniaxially loaded specimen »uni«, **b** equibiaxially loaded specimen »equi«, **c** first equibiaxially and afterwards phase-shifted loaded specimen »0°/22.5°« with $\varphi = 22.5°$ and **d** »0°/180°« with $\varphi = 180°$. **e** First equibiaxially and afterwards phase-shifted loaded specimen »stepw. 0°–90°« with a stepwise increase of the phase shift in steps of 15° with $0° \leq \varphi \leq 90°$. **f** Enlarged view of (**e**), crack 2 [77]

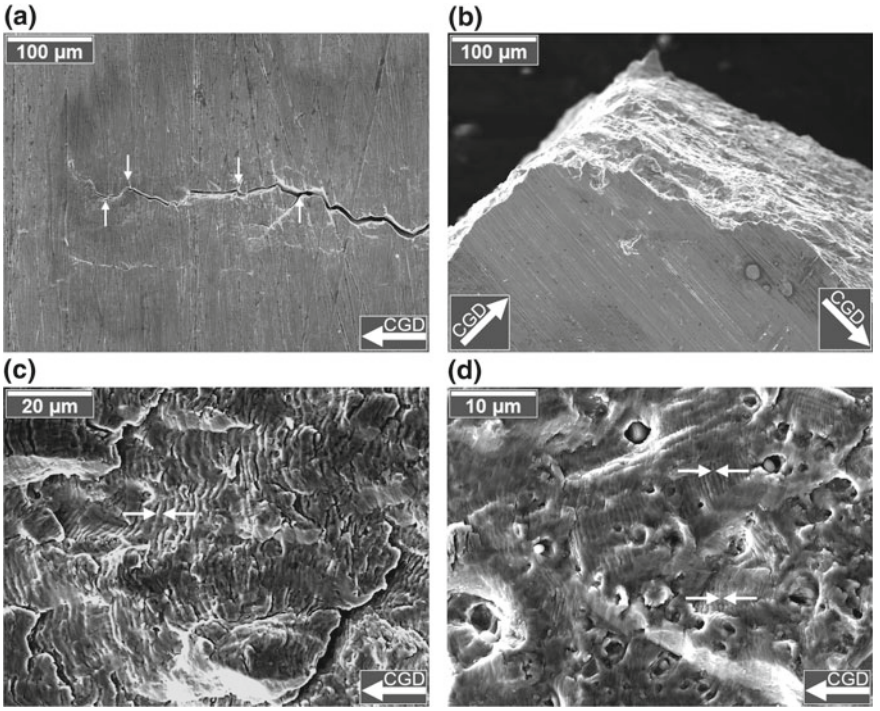

Fig. 14.12 SEM micrographs with crack growth direction (CGD) of the **a** crack paths and the **b–d** fractured surfaces of the specimens **a**, **c** »equi« as well as **b**, **d** »0°/180°«. **a** Crack path of crack 1 of the specimen »equi« at the end of the investigation. **b** Triple point of crack 1 branching into cracks 1-1 and 1-2 of the steel specimen »0°/180°«. **c** Fractured surface of crack 1 of specimen »equi« at a crack length of $a \approx 70\,\mathrm{mm}$ $\left(\Delta K_{\mathrm{eq}} \approx 70\,\mathrm{MPa}\sqrt{\mathrm{m}}\right)$. **d** Fractured surface of crack 1-2 of specimen »0°/180°« at a crack length of $a \approx 60\,\mathrm{mm}$ $\left(\Delta K_{\mathrm{eq}} \approx 80\,\mathrm{MPa}\sqrt{\mathrm{m}}\right)$ [77]

due to a small Mode II component, cf. [76], due to the slight phase shift φ. In the two changes of the phase shift φ, i.e. from $\varphi = 15°$ to $\varphi = 30°$ and from $\varphi = 30°$ to $\varphi = 45°$, a significant kinking of the crack path occured. In addition to kinking at a large angle, microbranching was observed at both changes of phase shift, Fig. 14.13b, c. The further increases of the phase shift by 15° had no further pronounced impact on the crack path.

14.5.2 Crack Growth Rates

The consideration of crack growth is carried out with both a–N plots, Fig. 14.14a, b, and $\mathrm{d}a/\mathrm{d}N$–ΔK plots, Fig. 14.14c, d. In addition to the symmetrical crack paths, the courses of the a–N curves of both cracks or even all four cracks were also identical.

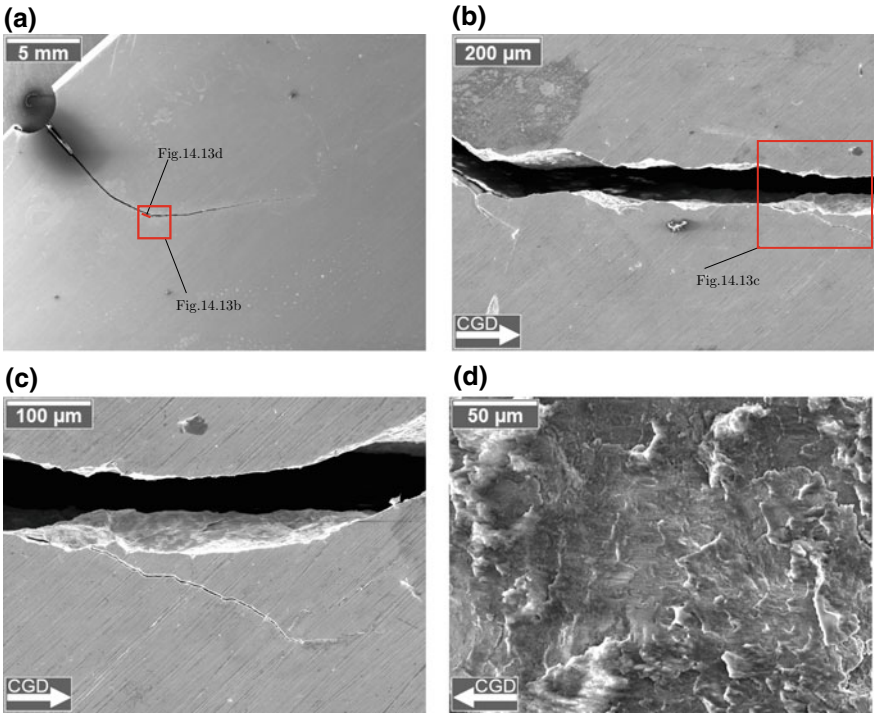

Fig. 14.13 SEM micrographs with crack growth direction (CGD) of the **a–c** crack paths and **d** the fractured surface of specimen »stepw. 0°–90°«. **a** Location of the enlarged view of image (**b**). **b** Location of the enlarged view of image (**c**). **c** Branching and subbranching as well as **d** face friction at the transition from straight to curved crack path, cf. Fig 14.13a [76]

Therefore only one complete crack with all of its branched cracks is plotted in the a–N and $\mathrm{d}a/\mathrm{d}N$–ΔK plots.

The a–N plot initially shows two main a–N curves, cf. Fig. 14.14a. The uniaxially loaded specimen »uni« appears to grow faster than the equibiaxially loaded specimen »equi«. However, the $\mathrm{d}a/\mathrm{d}N$–ΔK plot clearly shows that crack growth occured at almost the same rate $\mathrm{d}a/\mathrm{d}N$ at the same cyclic stress intensity ΔK_{eq}. The differences in the course of the a–N curve can be found in the specimen thickness and the various load situations, i.e. the equivalent stress intensity ranges were different for the same crack lengths, cf. [76]. The crack growth rate of the specimen »equi« was checked by measuring the fatigue striations in the captured SEM image, cf. Fig. 14.12c. The mean value of 10 load cycles was an increase of the crack length of $\Delta a \approx 1.5\,\mu\mathrm{m}$ per load cycle. This is consistent with the measurement and calculation of the crack growth rate $\mathrm{d}a/\mathrm{d}N$ using crack gage and the Fractomat, cf. Fig. 14.14c grey dots at $\Delta K_{\mathrm{eq}} \approx 70\,\mathrm{MPa}\sqrt{\mathrm{m}}$ with $\mathrm{d}a/\mathrm{d}N = 1.5 \times 10^{-3}$ mm per load cycle. By means of the $\mathrm{d}a/\mathrm{d}N$–ΔK course of the uniaxially and equibiaxially loaded specimens »uni« and »equi«, the Paris law was set up, cf. Fig. 14.14c, black dotted line. Thus a comparison

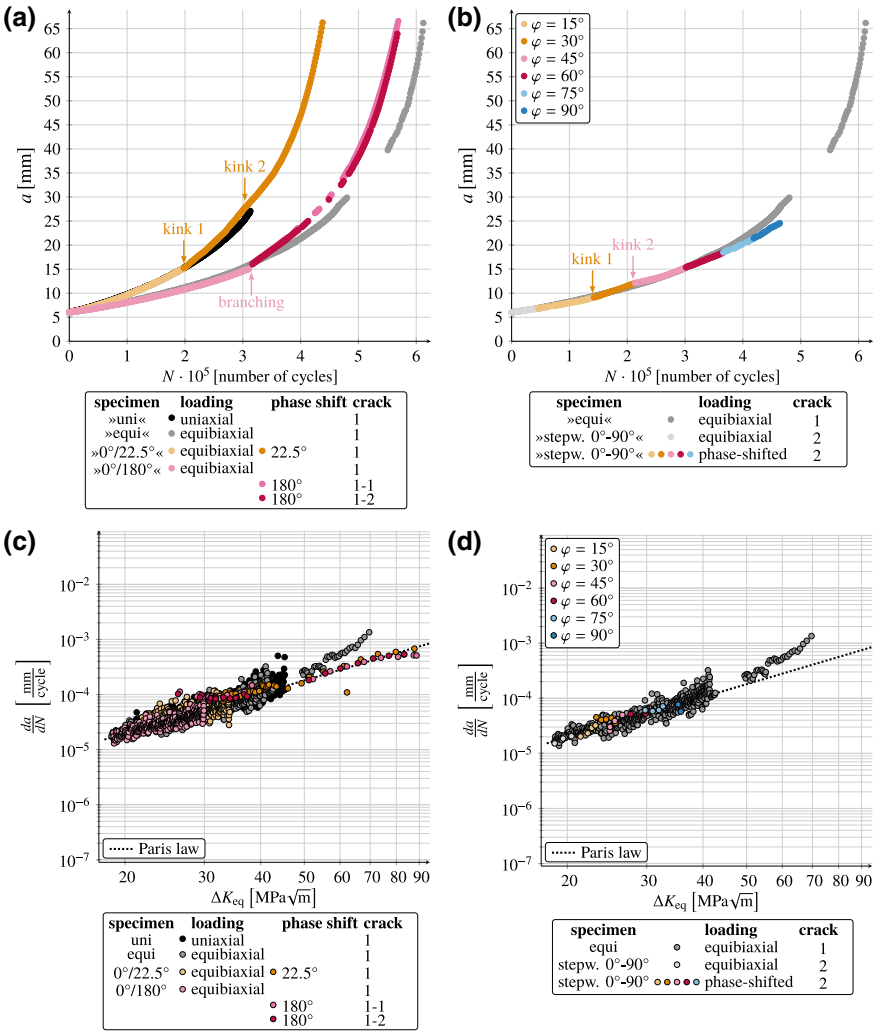

Fig. 14.14 Results of the fatigue crack growth experiments [76, 77]. a–N plots of specimens **a** »uni«, »equi«, »0°/22.5°« and »0°/180°« and **b** »stepw. 0°–90°« with representation of the phase shift φ compared to the equibiaxially loaded specimen »equi«. $\mathrm{d}a/\mathrm{d}N - \Delta K$ plots of specimens **c** »uni«, »equi«, »0°/22.5°« and »0°/180°« and **d** »stepw. 0°–90°« with representation of the phase shift φ compared to the equibiaxially loaded specimen »equi« [76, 77]

of the crack growth rates da/dN under phase-shifted loading is possible with uniaxial or rather equibiaxial loading.

Specimen »0°/22.5°« was first equibiaxially loaded and afterwards loaded with a phase shift of $\varphi = 22.5°$. The equibiaxially loaded crack of the specimen »0°/22.5°« followed the course of the uniaxially loaded specimen »uni« in the a–N plot, cf. Fig. 14.14a. The comparison of the crack growth rate da/dN versus the cyclic stress intensity factor ΔK reveals, that the crack growth rate was similar to the crack growth rate of the equibiaxially loaded specimen »equi«, cf. Fig. 14.14c. It has to be noted, that a thickness correction had to be carried out for calculation of ΔK, cf. [76]. Natural scattering in crack growth, as reported in [109], which is e.g. caused by inhomogeneities [110] can be excluded in the PM material.

The course of the a–N plot of the specimen »0°/22.5°« shows two kinks, cf. Fig. 14.14a, orange dots. The first kink occured after changing from in-phase to out-of-phase loading. This change led to a change in the crack opening Mode. As long as the crack was loaded equibiaxially, it was pure Mode I crack opening. As soon as the crack was loaded with phase shift, a Mixed Mode crack opening occurred. The kink in the a–N plot correlates with the start of the kinking of the crack path, cf. Fig. 14.11c. The second kink in the a–N plot occurred at the end of the kinking of the crack path, i.e. when no further curvature occured. The first kink in the a–N plot provided a faster fatigue crack growth rate and the second kink provided a slower fatigue crack growth rate. The reason for the faster crack growth was the Mode II portion of crack opening or rather the cyclic stress intensity factor ΔK_{eq}. This is in accordance to the findings of [48], that Mode II loaded cracks grow faster than Mode I loaded cracks.

Specimen »0°/180°« was first equibiaxially loaded and afterwards loaded with a phase shift of $\varphi = 180°$. As long as the crack was equibiaxially loaded, the course of the a–N plot of the specimen »0°/180°« is identical to the a–N course of the equibiaxially loaded specimen »equi«, cf. Fig. 14.14a, because both specimens had an almost identical thickness and were subjected to the same loading. Thus, the crack growth rates were almost equal for equibiaxial loading, cf. Fig. 14.14c. The subsequent change from in-phase loading to out-of-phase loading of specimen »0°/180°« with a phase shift of $\varphi = 180°$ led to a branching of the crack into two cracks. The two branched cracks seem to grew faster if one compares the a–N curves of both cracks with the a–N curves of the equibiaxially loaded specimen »equi«, cf. Fig. 14.14a. A comparison of the crack growth rates of the branched cracks with Paris' law line shows that first an accelerated fatigue crack growth took place in the two branched cracks, cf. Fig. 14.14c, red dots. After a certain crack growth, the crack growth rate followed Paris' law. The initially accelerated crack growth was due to the Mixed Mode loading. The decrease of the Mode II portion with increasing crack length at the two branched cracks led to the fact that the crack growth finally took place again under Mode I crack opening and the crack growth rate followed Paris' law. This is consistent with the findings by Wang et al. [48] who have found that Mode II loaded cracks grow faster than Mode I loaded cracks. The reduction of the Mode II fraction in the crack growth can be verified by FE calculations and SEM images. The crack growth rate measured with a scanner camera and then calculated could

also be validated with SEM images. At a crack length of about 60 mm, an average increase of the crack length of $\Delta a \approx 0.7\,\mu m$ per load cycle was measured as an average of 10 fatigue striations, cf. Fig. 14.12d. This is in accordance with the calculated crack growth rates, cf. Fig. 14.14c red dots at $\Delta K_{eq} \approx 80\,MPa\sqrt{m}$ with $da/dN = 0.7 \cdot 10^{-3}$ mm per load cycle.

Specimen »stepw. 0°–90°« was first equibiaxially loaded and afterwards phase-shifted loaded with a subsequent increase of the phase shift. As long as the crack was equibiaxially loaded, the course of the a–N plot of the specimen »stepw. 0°–90°« equals the a–N course of the equibiaxially loaded specimen »equi«, cf. Fig. 14.14b, because both specimens had an almost identical thickness and were subjected to the same loading. Furthermore, the crack growth rates were almost equal for equibiaxial loading, cf. Fig. 14.14d. In addition to the kinks in the crack path caused by the change in the phase shift φ, cf. Fig. 14.11e, f, kinks in the a–N curve can also be observed, cf. Fig. 14.14b. Analogous to the crack path, a kink in the a–N curve occured at the change from a phase-shifted loading of $\varphi = 15°$ to a phase-shifted loading of $\varphi = 30°$, cf. Fig. 14.14b. As with specimen »0°/22.5°«, the accelerated crack growth can be explained by Mode II contribution. The Mode II portion on the fatigue crack growth can also be seen on the fractured surface, where face friction is clearly visible, cf. Fig. 14.13d. In addition to the increased crack growth rate, the change of the phase shift φ reduced the cyclic equivalent crack intensity factor ΔK_{eq}, cf. Fig. 14.14d. The second kink occured when the phase shift was changed from $\varphi = 30°$ to $\varphi = 45°$. Initially, a slightly slower fatigue crack growth for the $\varphi = 45°$ loaded crack was observed, cf. Fig. 14.14d. Subsequently, the fatigue crack growth followed Paris' law.

14.6 Conclusions

The material behavior of a powder metallurgically produced high alloy X5CrMnNi16-7-6 austenitic stainless steel was investigated under both quasi-static and cyclic loading for low cycle fatigue and fatigue crack growth. The following results were achieved in quasi-static tests:

- The yield surface can be described by von Mises criterion.
- Sequence tests with permanently changing λ showed load sequence effects, i.e. a kinematic hardening with α'-martensite formation was observed.
- The highest martensite volume fraction was measured for shear loading.

The following results were achieved in low cycle fatigue tests:

- The fatigue life of low cycle fatigue tests can be divided into three stages: (i) primary hardening, (ii) softening and (iii) secondary hardening as observed for uniaxial tests by [7, 31, 32].

- The lowest fatigue lives were determined for loads with strain ratio of $\Phi = -0.5$, -0.1 and 0.5, the highest fatigue lives were determined for shear loading $\Phi = -1$.
- During secondary hardening, the von Mises force amplitude $F_{vM}/2$ increased.
- The larger the von Mises strain amplitude increased, the more α'-martensite was formed.
- The highest amount of α'-martensite was induced and the highest numbers of cycles to failure occurred for shear loading.
- Deviations of equivalent force amplitudes and fatigue lives can also be interpreted that the von Mises hypothesis cannot be applied in the case of multiaxial elastic-plastic cyclic loading.

The following results were achieved in fatigue crack growth investigations:

- The crack paths of the two single cracks of each specimen or in the further course the four branched cracks of specimen »0°/180°« revealed a symmetrical course.
- Differences in the a–N curves were due to differences in the specimens thickness and different load cases, respectively.
- The calculation of the cyclic stress intensity factor was based on the proposed geometry functions. This made a simple comparison with kinked or branched cracks under phase-shifted loading possible.
- It became clear that phase shift loaded cracks initially grew at an accelerated crack growth rate under Mode II crack opening. By kinking or branching, the Mode II proportion of the crack tip loading decreased in the further course and the crack growth rate followed the Paris' law.

Acknowledgements The authors thank and acknowledge gratefully funding of subproject B4 within Collaborative Research Center TRIP-Matrix-Composites (Project number 54473466—CRC 799) by the German Research Foundation or Deutsche Forschungsgemeinschaft (DFG). Further thanks go to Dipl.-Ing. Kai Nagel, Dr.-Ing. Dirk Kulawinski and Dipl.-Ing. Stephanie Ackermann, who were involved in the experiments. In particular, the authors want to thank the colleagues of the Collaborative Research Center for their support and cooperation.

References

1. S. Henkel, D. Kulawinski, S. Ackermann, H. Biermann, in *Moderne Methoden der Werkstoffprüfung* (Wiley-VCH, 2015), pp. 121–157. https://doi.org/10.1002/9783527670673.ch4
2. L. Krüger, S. Wolf, U. Martin, S. Martin, P.R. Scheller, A. Jahn, A. Weiß, J. Phys. Conf. Ser. **240**, 012098 (2010). https://doi.org/10.1088/1742-6596/240/1/012098
3. A. Jahn, A. Kovalev, A. Weiß, S. Wolf, L. Krüger, P.R. Scheller, Steel Res. Int. **82**(1), 39 (2010). https://doi.org/10.1002/srin.201000228
4. S. Martin, C. Ullrich, D. Šimek, U. Martin, D. Rafaja, J. Appl. Crystallogr. **44**(4), 779 (2011). https://doi.org/10.1107/s0021889811019558
5. A. Weidner, A. Glage, H. Biermann, Procedia Eng. **2**(1), 1961 (2010). https://doi.org/10.1016/j.proeng.2010.03.211
6. A. Weidner, S. Martin, V. Klemm, U. Martin, H. Biermann, Scr. Mater. **64**(6), 513 (2011). https://doi.org/10.1016/j.scriptamat.2010.11.028

7. M. Bayerlein, H.J. Christ, H. Mughrabi, Mater. Sci. Eng. A **114**, L11 (1989). https://doi.org/10.1016/0921-5093(89)90871-x
8. D. Hennessy, G. Steckel, C. Altstetter, Metall. Trans. A **7**(3), 415 (1976). https://doi.org/10.1007/bf02642838
9. A. Hannon, P. Tiernan, J. Mater. Process. Technol. **198**(1–3), 1 (2008). https://doi.org/10.1016/j.jmatprotec.2007.10.015
10. J.P. Boehler, S. Demmerle, S. Koss, Exp. Mech. **34**(1), 1 (1994). https://doi.org/10.1007/bf02328435
11. C.H. Busche, *Bestimmung und Beschreibung des Elastizitätsmoduls von Blechwerkstoffen nach dem Umformen* (Shaker Verlag, 2007)
12. S. Demmerle, J. Boehler, J. Mech. Phys. Solids **41**(1), 143 (1993). https://doi.org/10.1016/0022-5096(93)90067-p
13. V. Bonnand, J. Chaboche, P. Gomez, P. Kanouté, D. Pacou, Int. J. Fatigue **33**(8), 1006 (2011). https://doi.org/10.1016/j.ijfatigue.2010.12.018
14. M.W. Brown, K.J. Miller, Proc. Inst. Mech. Eng. **187**(1), 745 (1973). https://doi.org/10.1243/pime_proc_1973_187_161_02
15. M. Parsons, K. Pascoe, Mater. Sci. Eng. **22**, 31 (1976). https://doi.org/10.1016/0025-5416(76)90133-6
16. T. Ogata, Y. Takahashi, in *Multiaxial Fatigue and Fracture* (Elsevier, 1999), pp. 101–114. https://doi.org/10.1016/s1566-1369(99)80010-7
17. S. Henkel, J. Fischer, L. Balogh, T. Ungar, H. Biermann, J. Phys. Conf. Ser. **240**, 012042 (2010). https://doi.org/10.1088/1742-6596/240/1/012042
18. S. Ackermann, D. Kulawinski, S. Henkel, H. Biermann, Int. J. Fatigue **67**, 123 (2014). https://doi.org/10.1016/j.ijfatigue.2014.02.007
19. T. Itoh, M. Sakane, M. Ohnami, J. Eng. Mater. Technol. **116**(1), 90 (1994). https://doi.org/10.1115/1.2904261
20. K.J. Pascoe, J.W.R. de Villiers, J. Strain Anal. **2**(2), 117 (1967). https://doi.org/10.1243/03093247v022117
21. T. Yokobori, H. Yamanouchi, S. Yamamoto, Int. J. Fract. Mech. **1**(1), 3 (1965). https://doi.org/10.1007/bf00184149
22. V. Doquet, Fatigue Fract. Eng. Mater. Struct. **20**(2), 227 (1997). https://doi.org/10.1111/j.1460-2695.1997.tb00280.x
23. D. Kulawinski, S. Ackermann, A. Glage, S. Henkel, H. Biermann, Steel Res. Int. **82**(9), 1141 (2011). https://doi.org/10.1002/srin.201100111
24. B.R. You, S.B. Lee, Int. J. Fatigue **18**(4), 235 (1996). https://doi.org/10.1016/0142-1123(96)00002-3
25. E. Macha, C.M. Sonsino, Fatigue Fract. Eng. Mater. Struct. **22**(12), 1053 (1999). https://doi.org/10.1046/j.1460-2695.1999.00220.x
26. M.W. Brown, K.J. Miller, Fatigue Fract. Eng. Mater. Struct. **1**(2), 231 (1979). https://doi.org/10.1111/j.1460-2695.1979.tb00380.x
27. R. Lohr, E.G. Ellison, Fatigue Fract. Eng. Mater. Struct. **3**(1), 1 (1980). https://doi.org/10.1111/j.1460-2695.1980.tb01101.x
28. T. Itoh, M. Sakane, M. Ohnami, D.F. Socie, J. Eng. Mater. Technol. **117**(3), 285 (1995). https://doi.org/10.1115/1.2804541
29. A. Fatemi, D.F. Socie, Fatigue Fract. Eng. Mater. Struct. **11**(3), 149 (1988). https://doi.org/10.1111/j.1460-2695.1988.tb01169.x
30. A. Glage, A. Weidner, H. Biermann, Proc. Eng. **2**(1), 2085 (2010). https://doi.org/10.1016/j.proeng.2010.03.224
31. A. Glage, A. Weidner, H. Biermann, Steel Res. Int. **82**(9), 1040 (2011). https://doi.org/10.1002/srin.201100080
32. U. Krupp, C. West, H.J. Christ, Mater. Sci. Eng. A **481–482**, 713 (2008). https://doi.org/10.1016/j.msea.2006.12.211
33. M. Smaga, F. Walther, D. Eifler, Mater. Sci. Eng. A **483–484**, 394 (2008). https://doi.org/10.1016/j.msea.2006.09.140

34. A. Burgold, S. Henkel, S. Roth, M. Kuna, H. Biermann, Mater. Test. **60**(4), 341 (2018). https://doi.org/10.3139/120.111156
35. D.F. Martelo, A.M. Mateo, M.D. Chapetti, Int. J. Fatigue **80**, 406 (2015). https://doi.org/10.1016/j.ijfatigue.2015.06.029
36. H.J. Lim, Y.J. Lee, H. Sohn, Mech. Syst. Sig. Process. **120**, 356 (2019). https://doi.org/10.1016/j.ymssp.2018.10.018
37. O. Scott-Emuakpor, T. George, C. Cross, M.H.H. Shen, AIAA J. **48**(1), 63 (2010). https://doi.org/10.2514/1.39296
38. P.R.G. Anderson, G.G. Garrett, Int. J. Fract. **16**(3), R111 (1980). https://doi.org/10.1007/bf00013388
39. C.D. Hopper, K.J. Miller, J. Strain Anal. Eng. Des. **12**(1), 23 (1977). https://doi.org/10.1243/03093247v121023
40. S. Henkel, C.H. Wolf, A. Burgold, M. Kuna, H. Biermann, Fract. Struct. Int. **13**, 135 (2019). https://doi.org/10.3221/igf-esis.48.16
41. E. Breitbarth, M. Besel, S. Reh, Int. J. Fatigue **108**, 116 (2018). https://doi.org/10.1016/j.ijfatigue.2017.12.005
42. E. Breitbarth, M. Besel, Int. J. Fatigue **113**, 345 (2018). https://doi.org/10.1016/j.ijfatigue.2018.04.021
43. G. Dhondt, C. Kontermann, *Proceedings of 6th International Conference Crack Paths (CP 2018). Conference USB flash drive* (Verona (I), 2018)
44. V. Giannella, G. Dhondt, C. Kontermann, R. Citarella, Int. J. Fatigue **123**, 296 (2019). https://doi.org/10.1016/j.ijfatigue.2019.02.029
45. C.F. Qian, M.O. Wang, B.J. Wu, S.H. Dai, J.C.M. Li, J. Eng. Mater. Technol. **118**(3), 349 (1996). https://doi.org/10.1115/1.2806817
46. C.F. Qian, M.O. Wang, B.J. Wu, S.H. Dai, J.C.M. Li, J. Eng. Mater. Technol. **118**(3), 356 (1996). https://doi.org/10.1115/1.2806818
47. S. Mall, V. Perel, Int. J. Fatigue **74**, 166 (2015). https://doi.org/10.1016/j.ijfatigue.2015.01.005
48. M.O. Wang, R.H. Hu, C.F. Qian, J.C.M. Li, Fatigue Fract. Eng. Mater. Struct. **18**(12), 1443 (1995). https://doi.org/10.1111/j.1460-2695.1995.tb00867.x
49. R.K. Neerukatti, S. Datta, A. Chattopadhyay, N. Iyyer, N. Phan, Fatigue Fract. Eng. Mater. Struct. **41**(2), 387 (2017). https://doi.org/10.1111/ffe.12690
50. E.U. Lee, R.E. Taylor, Eng. Fract. Mech. **78**(8), 1555 (2011). https://doi.org/10.1016/j.engfracmech.2010.11.005
51. R. Yuuki, K. Akita, N. Kishi, Fatigue Fract. Eng. Mater. Struct. **12**(2), 93 (1989). https://doi.org/10.1111/j.1460-2695.1989.tb00516.x
52. H. Kitagawa, R. Yuuki, K. Tohgo, Fatigue Fract. Eng. Mater. Struct. **2**(2), 195 (1979). https://doi.org/10.1111/j.1460-2695.1979.tb01355.x
53. Z. Zhu, Z. Lu, P. Zhang, W. Fu, C. Zhou, X. He, Met. **9**(8), 823 (2019). https://doi.org/10.3390/met9080823
54. V. Shlyannikov, A. Zakharov, Eng. Fract. Mech. **123**, 86 (2014). https://doi.org/10.1016/j.engfracmech.2014.02.013
55. H.E. Misak, V.Y. Perel, V. Sabelkin, S. Mall, Int. J. Fatigue **55**, 158 (2013). https://doi.org/10.1016/j.ijfatigue.2013.06.003
56. V. Shlyannikov, A. Tumanov, A. Zakharov, Theor. Appl. Fract. Mech. **73**, 68 (2014). https://doi.org/10.1016/j.tafmec.2014.06.016
57. M. Lepore, F. Berto, D. Kujawski, Theor. Appl. Fract. Mech. **100**, 14 (2019). https://doi.org/10.1016/j.tafmec.2018.12.008
58. A. Shanyavskiy, Eng. Fract. Mech. **78**(8), 1516 (2011). https://doi.org/10.1016/j.engfracmech.2011.01.019
59. V. Shlyannikov, A. Zakharov, Theor. Appl. Fract. Mech. **91**, 52 (2017). https://doi.org/10.1016/j.tafmec.2017.03.014
60. C. Dalle Donne, K.H. Trautmann, H. Amstutz, in *Multiaxial Fatigue and Deformation: Testing and Prediction* (ASTM International, 2000), pp. 405–422. https://doi.org/10.1520/stp13517s

61. R. Sunder, B. Ilchenko, Int. J. Fatigue **33**(8), 1101 (2011). https://doi.org/10.1016/j.ijfatigue.2010.11.018
62. C.D. Donne, *Übertragbarkeit von Risswiderstandskurven von Standardproben auf biaxial belastete, bauteilähnliche Kreuzproben* (VDI Verlag, 1997)
63. A. Makinde, L. Thibodeau, K.W. Neale, Exp. Mech. **32**(2), 138 (1992). https://doi.org/10.1007/bf02324725
64. I.H. Wilson, D.J. White, J. Strain Anal. **6**(1), 27 (1971). https://doi.org/10.1243/03093247v061027
65. S. Taira, K. Tanaka, M. Kan, A. Yamada, Proc. 22nd Japan Cong. Mat. Res. pp. 130–137 (1979)
66. T. Hoshide, K. Tanaka, A. Yamada, Fatigue Fract. Eng. Mater. Struct. **4**(4), 355 (1981). https://doi.org/10.1111/j.1460-2695.1981.tb01132.x
67. K. Tanaka, T. Hoshide, A. Yamada, S. Taira, Fatigue Fract. Eng. Mater. Struct. **2**(2), 181 (1979). https://doi.org/10.1111/j.1460-2695.1979.tb01354.x
68. P. Bold, M. Brown, R. Allen, Wear **144**(1–2), 307 (1991). https://doi.org/10.1016/0043-1648(91)90022-m
69. M.W. Brown, K.J. Miller, in *Multiaxial Fatigue* (ASTM International, 1985), pp. 135–153. https://doi.org/10.1520/stp36221s
70. S. Datta, A. Chattopadhyay, N. Iyyer, N. Phan, Int. J. Fatigue **109**, 103 (2018). https://doi.org/10.1016/j.ijfatigue.2017.12.018
71. S. Henkel, D. Holländer, M. Wünsche, H. Theilig, P. Hübner, H. Biermann, S. Mehringer, Eng. Fract. Mech. **77**(11), 2077 (2010). https://doi.org/10.1016/j.engfracmech.2010.04.013
72. V.N. Shlyannikov, Eng. Fract. Mech. **108**, 3 (2013). https://doi.org/10.1016/j.engfracmech.2013.03.011
73. H. Theilig, D. Hartmann, M. Wünsche, S. Henkel, P. Hübner, Key Eng. Mater. **348–349**, 857 (2007). https://doi.org/10.4028/www.scientific.net/kem.348-349.857
74. A.C. Pickard, J. Strain Anal. Eng. Des. **50**(1), 25 (2014). https://doi.org/10.1177/0309324714551082
75. S. Henkel, E. Liebelt, H. Biermann, S. Ackermann, Fract. Struct. Int. **9**(34), 466 (2015). https://doi.org/10.3221/IGF-ESIS.34.52
76. C.H. Wolf, S. Henkel, A. Burgold, Y. Qiu, M. Kuna, H. Biermann, Adv. Eng. Mater. **21**(5), 1800861 (2018). https://doi.org/10.1002/adem.201800861
77. C.H. Wolf, S. Henkel, A. Burgold, Y. Qiu, M. Kuna, H. Biermann, Int. J. Fatigue **124**, 595 (2019). https://doi.org/10.1016/j.ijfatigue.2019.03.011
78. S. Xiao, M. Brown, in *Mechanical Behaviour of Materials V* (Elsevier, 1988), pp. 659–664. https://doi.org/10.1016/b978-0-08-034912-1.50089-8
79. M.. Wang, R.H. Hu, C.J. Zhang, S.H. Dai, in *Proceedings of the 7th International Conference on Pressure Vessel Technology*, vol. 2 (VdTÜV, 1992), pp. 1413–1427
80. J.J. Kibler, R. Roberts, J. Eng. Ind. **92**(4), 727 (1970). https://doi.org/10.1115/1.3427838
81. E. önch, D. Galster, Br. J. Appl. Phys. **14**(11), 810 (1963). https://doi.org/10.1088/0508-3443/14/11/319
82. J. Granlund, Structural steel plasticity: experimental study and theoretical modelling. Ph.D. thesis, Lulea University of Technology, 1997
83. J. Gozzi, Plastic behaviour of steel: Experimental investigation and modelling. Ph.D. thesis, Lulea University of Technology, 2004
84. J. Gozzi, A. Olsson, O. Lagerqvist, Exp. Mech. **45**(6), 533 (2005). https://doi.org/10.1007/bf02427907
85. D. Kulawinski, S. Ackermann, A. Seupel, T. Lippmann, S. Henkel, M. Kuna, A. Weidner, H. Biermann, Mater. Sci. Eng. A **642**, 317 (2015). https://doi.org/10.1016/j.msea.2015.06.083
86. M. Kuroda, V. Tvergaard, Acta Mater. **47**(14), 3879 (1999). https://doi.org/10.1016/s1359-6454(99)00213-x
87. D. Kulawinski, K. Nagel, S. Henkel, P. Hübner, H. Fischer, M. Kuna, H. Biermann, Eng. Fract. Mech. **78**(8), 1684 (2011). https://doi.org/10.1016/j.engfracmech.2011.02.021

88. A. Samir, A. Simon, A. Scholz, C. Berger, Int. J. Fatigue **28**(5–6), 643 (2006). https://doi.org/10.1016/j.ijfatigue.2005.08.010
89. C.M. Sonsino, V. Grubisic, Materialwiss. Werkstofftech. **15**(11), 378 (1984). https://doi.org/10.1002/mawe.19840151104
90. A.A. Griffith, *Proceedings of the 1st International Congress for Applied Mechanics* (Delft, 1924), pp. 55–63
91. C.H. Wolf, A. Burgold, S. Henkel, M. Kuna, H. Biermann, *Proceedings of 12th International Conference on Multiaxial Fatigue and Fracture* (2019) (In press)
92. A. Savitzky, M.J.E. Golay, Anal. Chem. **36**(8), 1627 (1964). https://doi.org/10.1021/ac60214a047
93. ASTM E647-15e1, Standard test method for measurement of fatigue crack growth rates. Technical Report (ASTM International, West Conshohocken, PA, 2015)
94. S. Ackermann, T. Lippmann, D. Kulawinski, S. Henkel, H. Biermann, Fract. Struct. Int. (34), 580 (2015). https://doi.org/10.3221/IGF-ESIS.34.64
95. J. Talonen, P. Aspegren, H. Hänninen, Mater. Sci. Technol. **20**(12), 1506 (2004). https://doi.org/10.1179/026708304x4367
96. D. Mohr, M. Oswald, Exp. Mech. **48**(1), 65 (2007). https://doi.org/10.1007/s11340-007-9053-9
97. D. Mohr, J. Jacquemi, J. Mech. Phys. Solids **56**(10), 2935 (2008). https://doi.org/10.1016/j.jmps.2008.07.003
98. A. Olsson, Stainless steel plasticity: material modelling and structural applications. Ph.D. thesis, Lulea University of Technology, 2001
99. S. Martin, S. Wolf, U. Martin, L. Krüger, Solid State Phenom. **172–174**, 172 (2011). https://doi.org/10.4028/www.scientific.net/ssp.172-174.172
100. A. Weidner, C. Segel, H. Biermann, Mater. Lett. **143**, 155 (2015). https://doi.org/10.1016/j.matlet.2014.12.098
101. G.B. Olson, M. Cohen, Metall. Trans. A **6**(4), 791 (1975). https://doi.org/10.1007/bf02672301
102. A. Nitta, T. Ogata, K. Kuwabara, Fatigue Fract. Eng. Mater. Struct. **12**(2), 77 (1989). https://doi.org/10.1111/j.1460-2695.1989.tb00515.x
103. D. Infante-Garcia, G. Qian, H. Miguélez, E. Giner, Int. J. Fatigue **123**, 87 (2019). https://doi.org/10.1016/j.ijfatigue.2019.01.019
104. M. Kuna, *Finite Elements in Fracture Mechanics* (Springer, Netherlands, 2013). https://doi.org/10.1007/978-94-007-6680-8
105. F. Erdogan, G.C. Sih, J. Basic Eng. **85**(4), 519 (1963). https://doi.org/10.1115/1.3656897
106. L. Pook, Eng. Fract. Mech. **167**, 2 (2016). https://doi.org/10.1016/j.engfracmech.2016.02.055
107. H. Richard, A. Eberlein, G. Kullmer, Eng. Fract. Mech. **174**, 10 (2017). https://doi.org/10.1016/j.engfracmech.2016.12.005
108. R. Brighenti, A. Carpinteri, A. Spagnoli, Acta Mech. **225**(11), 3123 (2014). https://doi.org/10.1007/s00707-014-1111-7
109. C. Lapetra, J. Mayo, J. Dominguez, Fatigue Fract. Eng. Mater. Struct. **19**(5), 589 (1996)
110. D.A. Virkler, B.M. Hillberry, P.K. Goel, J. Eng. Mater. Technol. **101**(2), 148 (1979). https://doi.org/10.1115/1.3443666

Chapter 15
Scanning Electron Microscopy and Complementary In Situ Characterization Techniques for Characterization of Deformation and Damage Processes

Anja Weidner, Robert Lehnert and Horst Biermann

Abstract This chapter presents results on in situ deformation experiments performed either inside the scanning electron microscope or in combination with other complementary in situ characterization techniques such as digital image correlation, acoustic emission or infrared thermography. The range of materials investigated extends from austenitic CrMnNi steels enabling TRIP (TRansformation Induced Plasticity) and/or TWIP (TWinning Induced Plasticity) effect and austenitic-martensitic-carbidic CrMnNi steels after quenching and partitioning to MgO-partially stabilized zirconia and TRIP matrix composites. The performed mechanical tests include both tensile and compressive loading as well as cyclic loading in a temperature range from room temperature up to 200 °C. The great potential of the applied in situ characterization techniques is their complementarity, which is shown, in particular, by the seven case studies presented. The combination of different techniques—such as the in situ deformation within the SEM combined with the digital image correlation—has a high potential to gain a deeper understanding on strain localizations by different microstructural features such as deformation bands, twin bundles or martensitic nuclei. In addition, these complementary in situ techniques can contribute to the modelling of the deformation behavior of TRIP/TWIP steels, in particular, or for any other kind of materials with complex deformation processes. Here, the acoustic emission measurements offer, in particular, a great potential, since this is the only real time in situ characterization technique delivering bulk information with a time-resolution in the range of microseconds.

A. Weidner (✉) · R. Lehnert · H. Biermann
Institute of Materials Engineering, Technische Universität Bergakademie Freiberg, Gustav-Zeuner-Str. 5, 09599 Freiberg, Germany
e-mail: weidner@ww.tu-freiberg.de

H. Biermann and C. G. Aneziris (eds.), *Austenitic TRIP/TWIP Steels and Steel-Zirconia Composites*, Springer Series in Materials Science 298,
https://doi.org/10.1007/978-3-030-42603-3_15

15.1 Introduction

Advanced High-Strength Steels (AHSS) have been the focus of automotive industry due to their improved formability and crash behavior. The TRIP (TRansformation Induced Plasticity)-assisted steels based on retained austenite belonging to the group of AHSS of the first generation exhibit high strength, but quite low ductility. In contrast, the group of high-alloy austenitic steels with displacive transformations—TRIP and TWIP (TWinning Induced Plasticity) steels—belonging to the AHSS of the second generation exhibits high tensile strengths between 500 to 900 MPa at concurrently excellent levels of ductility (between 40 and 70% of total elongation) [1].

High-alloy austenitic TRIP steels exhibit a phase transformation following the austenite (fcc)—ε-martensite (hcp)—α'-martensite (bcc) path. Olson and Cohen [2] described this two-step shear mechanism for the first time in 1972. The phase transformation occurs via the interaction of Shockley partial dislocations on two different slip systems. During the deformation of high-alloy austenitic TRIP steels, deformation bands are formed consisting of a high density of stacking faults arranged in average on each second {111} lattice plane of the austenite. Therefore, these deformation bands appear with a hexagonal lattice structure—referred in the literature as ε-martensite [3–5]. In contrast to TRIP steels, the high-alloy TWIP steels exhibit a pronounced twinning leading to even superior ductility. Twinning occurs via the accumulation of stacking faults on subsequent {111} lattice planes [5].

The chemical concept of the present high-alloy CrMnNi TRIP/TWIP steels is based on a low content of interstitial elements carbon and nitrogen, a high amount of chromium, manganese and nickel [6]. In particular, the variation of the nickel content allows to control both the austenite stability as well as the stacking fault energy. Therefore, the metastable austenitic steels can exhibit either a TRIP or TWIP effect or a combination of both, depending on the nickel content or the deformation temperature [7, 8].

During the last decade, numerous investigations have been performed on high-alloy CrMnNi cast steels regarding to both their mechanical behavior under different loading conditions as well as the corresponding microstructures and the related strain hardening mechanisms. Thus, CrMnNi steels were tested under (i) static [7], (ii) cyclic [9], (iii) biaxial [10], (iv) dynamic [11], and (v) hydrostatic high-pressure conditions [12]. Detailed microstructural investigations using different techniques such as (i) X-ray diffraction [13], (ii) scanning electron microscopy [14], and (iii) conventional as well as high-resolution transmission electron microscopy (HR-TEM) [5, 15] gained a deeper understanding and knowledge of the ongoing microstructural processes and their influence on the mechanical properties. In addition, these results were complemented by investigations on wrought steels [16] and powder-metallurgically produced steels [17] within the same alloying concept.

Since high-alloy CrMnNi cast TRIP steels are usually characterized by a low yield strength due to their coarse-grained microstructure, two approaches were considered to improve the yield strength: (i) manufacture of ultrafine grained (ufg) CrMnNi

TRIP steels [18], and (ii) application of quenching and partitioning (Q&P) process to slightly modified chemical design of the CrMnNi TRIP steels [19]. For the first approach, a thermo-mechanical-controlled process consisting of cold working and subsequent reversion annealing treatment was applied leading to grain sizes of less than 1 μm resulting in significant increase in yield strength at still reasonable ductility [18]. Furthermore, the fatigue life has been also improved for ufg TRIP steels at low strain amplitudes [20]. The aim of the Q&P treatment was a two-phase microstructure consisting of austenite and tempered martensite in order to achieve an increase in strength with only a slight reduction in ductility [19].

In addition, the studied CrMnNi steels were used for metal matrix composites (MMC) together with metastable zirconium dioxide as particle reinforcement. Partially MgO-stabilized zirconium dioxide exhibits a stress-assisted phase transformation from tetragonal into monoclinic phase. The combination of phase transformations in steel matrix and zirconia particles results in an increase in the capacity of absorption of mechanical energy [21].

The microstructure associated with TRIP and TWIP effects in the high-alloy CrMnNi cast steels is rather complex, and depends, in addition, on various parameters such as temperature, strain rate, grain size and grain orientation [22]. In order to understand the resulting strengthening behavior of TRIP/TWIP steels caused by this complex microstructure, it is necessary to gain a deeper knowledge of both: (i) local contribution of individual microstructural constituents to global deformation and strengthening behavior as well as (ii) evolution of underlying microstructural processes such as (i) dislocation glide, (ii) formation of stacking faults, (iii) twinning, and (iv) martensitic phase transformation operating often simultaneously during straining of material.

Therefore, in situ deformation experiments in combination with further characterization techniques are an excellent and powerful method for investigation of these aspects. The field of in situ experiments offers a broad spectrum of different methods such as (i) optical microscopy, (ii) SEM analysis, (iii) full-field measurements using digital image correlation (DIC) and infrared thermography (IR-TG), (iv) acoustic emission measurements (AE), and, finally, (v) fully-coupled, full-field measurements. Besides the fact that all these methods possess their respective advantages and disadvantages, their complementary application in combination with other post-mortem investigations provides great potential for the investigation of complex correlations.

This chapter cannot address all the above-mentioned techniques and results in detail. Therefore, it is focused on (i) in situ deformation in the scanning electron microscope in combination with digital image correlation, (ii) in situ acoustic emission measurements, (iii) thermographic measurements, and (iv) nanoindentation experiments inside SEM. In the first part of the chapter an overview on the used in situ characterization techniques is given combined with some selected state-of-the-art results. The second part describes in more detail the investigated materials: (i) high-alloy CrMnNi TRIP/TWIP steels, (ii) austenitic-martensitic-carbidic (AMC) steels after Q&P treatment, (iii) partially MgO-stabilized zirconia, and (iv) metal-matrix composite (MMC). Finally, the third part provides results on some case studies

on the above-mentioned materials using different types of in situ techniques such as (i) in situ SEM-DIC, (ii) acoustic emission, (iii) thermography, and (iv) nanoindentation.

15.2 In Situ Characterization Techniques

15.2.1 In Situ Deformation in Scanning Electron Microscope

In situ deformation in the scanning electron microscope (SEM) offers the possibility to observe deformation and damage mechanisms occurring under different loading conditions with high local resolution. In addition to direct imaging methods using secondary electrons (SE) or backscattered electrons (BSE), analytical methods such as energy dispersive X-ray spectroscopy (EDS), wavelength dispersive X-ray spectroscopy (WDS) or electron backscatter diffraction (EBSD) can be used to obtain a detailed knowledge on the deformation and damage behavior. Already in the 1970s, deformation experiments were transferred to the SEM to investigate deformation processes in more detail. Thus, the first in situ tensile tests in SEM were performed by Roberts et al. [23] in 1976 investigating the damage behavior around manganese-sulfide inclusions in steels. With the development of special loading stages suitable for operation in SEM, the possible load scenarios became more complex. Uniaxial tension and compression tests were joined by bending [24] and also fatigue tests [25]. In order to get a better understanding of the mechanisms involved, the experiments were combined with analytical methods such as electron backscattered diffraction [26]. Through the combination with other complementary methods such as DIC or AE, the in situ deformation in SEM has developed into a highly local, but at the same time volume-integral characterization method.

15.2.2 Full-Field Measurement Methods

Both the digital image correlation and the infrared-thermography are known as contactless and visual full-field measurement techniques. Both provide spatial distribution of physical quantities such as displacement, strain, or temperature on surface or even in bulk of specimens under external load. This is a great advantage compared to the application of strain gauges, extensometers or thermocouples, which provide integral information of regions only where they were applied (gauge length, contact point of thermocouple) [27].

Full-field measurements experienced a large improvement due to enormous development in camera as well as microcomputer technology enabling automated image processing within reasonable time [28] making these techniques very attractive for investigation of localized deformation processes and plastic instabilities occurring during plastic deformation of various kinds of materials. Even more information

can be gained by the combination of both methods known as fully-coupled full-field measurements using simultaneous recording of displacement/strain fields and thermal fields enabling investigations of phenomena of thermomechanical coupling during plastic deformation at microscopic scale [28].

15.2.2.1 Digital Image Correlation

With the possibility to perform in situ deformation tests in the SEM it was just a short step to combine these deformation experiments with digital image correlation. The advantage of deformation experiments within the SEM is the determination of deformation fields with a high lateral resolution and the combination with analytical characterization methods such as EBSD. In order to achieve the highest possible resolution of DIC, it is necessary to generate high-resolution micrographs. Therefore, it is essential to set optimal beam conditions to minimize image distortion, drift, charging and other artifacts [29]. Probably one of the most challenging tasks for the application of DIC on SEM micrographs is a good contrast pattern at the specimen surface without influencing the image conditions. Moreover, the size of the individual features of the pattern should have dimensions well below the features, which will be studied by DIC. In multiphase microstructures such as dual phase steels, the inherent microstructure can already provide a suitable contrast [30]. The only prerequisite in this case would be small size and a fine distribution of the phase components. Short-term etching and the different etching attack on the individual phases generate a topography on the surface which leads to a sufficient contrast for SEM micrographs using secondary electrons. The resolution of this method is determined by the grain size of the phase components. Single phase materials can also be contrasted by etching of the surface where the resulting etch pits are used for the correlation [31]. Another method to contrast surface structures are particle deposition methods using e.g. SiO_2 particles (colloidal silica). The advantage of this method lies in the large-area contrast of the surface, but particle agglomerations can be challenging. In order to achieve a high resolution of the DIC it is necessary to use as small particles as possible for the contrast. The smaller the particles are the higher the resolution of the DIC can be. Yan et al. [26] investigated the damage behavior of a dual phase (DP) steel under tensile load and used for describing the quality/resolution of DIC measurement the product of subset size in nm and subset size in px. In their work they achieved a subset size of 100 nm and 17 px, respectively, by deposition of colloidal silica. Gioacchino and Fonseca [32] investigated the deformation behavior of the steel AISI 304L under uniaxial load. The contrast patterns were achieved by the deposition of gold nanoparticles which result in a subset size of 216×216 nm^2 and 6×6 px, respectively. Due to the small subset size, occurring deformation bands with sub-μm resolution were recorded. Wang et al. [33] combined EBSD and DIC to investigate the deformation and damage behavior of a low-alloy Q&P steel showing initiation of micro-cracks in regions of tempered martensite where strain was accommodated. Similar observations were made by Ghadbeigi et al. [34] on a commercial

dual phase steel (DP 600) observing a heterogeneous strain distribution and localization within large ferritic grains. Na et al. [35] studied the behavior of a low carbon martensitic steel under tensile load. Using complementary EBSD measurements it was shown that the shear distribution in martensite correlates with the sub-cell formation and contributes, thus, to grain refinement. Weidner et al. [31] studied the deformation behavior of a high-alloy CrMnNi cast TRIP steel under tensile load. A short time etching was used for contrasting the surface which also resulted in a sub-μm resolution.

15.2.2.2 Thermography

Infrared thermography is an optical contactless temperature measurement method. Each body with a temperature above absolute zero emits electromagnetic radiation with a wavelength distribution in the range of 0.8 μm up to 14 μm depending on the temperature, which is described by Planck's radiation law [36]. The surface temperature of the body can be determined, therefore, by the detection of this infrared radiation. All plastic deformation processes are associated with the emission of energy and lead, thus, directly to an increase in temperature [37–39]. Therefore, IR thermography is suitable as a real-time in situ method to characterize temperature increase occurring during plastic deformation, strain localization and/or phase transformations [40].

Saeed-Akbari et al. [41] investigated the deformation behavior of high manganese TWIP steels showing a strong Portevin Le Chatelier (PLC) effect during deformation at varying strain rates using infrared thermography. It was shown that the increase in stacking fault energy due to the adiabatic heating caused by the formation of the PLC band is dependent on the chemical composition. Bodelot et al. [42] performed so-called fully-coupled full-field measurements by a combination of thermography and digital image correlation on an austenitic stainless steel under tensile loading. Due to the high resolution obtained, a correlation between dissipated energy in form of increased temperature and local plastic deformation on the grain scale was achieved. Chen et al. [43] also combined DIC and IR thermography during hole expansion test of an austenitic TWIP and an interstitial free (IF) steel.

15.2.3 Acoustic Emission

Acoustic emission is—according to ASTM—related to the sudden release of energy within a solid under certain stimulus (e.g. mechanical load, temperature, chemical attack etc.), which results in elastic waves in the ultrasonic frequency domain propagating through material [44]. These elastic waves can be detected by transducers (e.g. piezo, capacitive or optical sensors) attached to the surface. Among them, piezo transducers exhibit the highest sensitivity regarding surface displacements in the range of 10^{-14} m [44]. The AE method is a powerful tool for in situ application

during mechanical loading allowing studies on kinetics of both deformation and damage processes occurring in various kinds of materials. Due to the high sampling rate, acoustic emission has been established as a real in situ testing method, which supplies a fully integral volume information.

Basically, the acoustic signals can be divided into two types: (i) transient or so-called burst-type signals, and (ii) so-called continuous signals. Transient signals are caused by a spontaneous released energy due to fast processes like crack formation [44] or martensitic phase transformation [45]. They are characterized by a short rise time, a high amplitude and a certain dwell time. Continuous acoustic signals are, in particular, laboratory noise or noise generated by environmental influences like thermal, electric or mechanical noise [46]. These continuous signals are characterized by a high fluctuation with a lower amplitude and a longer duration, which can be described by a root mean square value of the voltage measured at the transducer. Well-known source of continuous signals is the movement of dislocations during plastic deformation [47]. In most cases, an overlap of both transient and continuous AE signals is observed, in particular, when different sources are activated during loading of the material. In contrast to the threshold-based AE data acquisition [48], continuous AE data acquisition provides the full volume integral information considering both the elastic waves generated by different AE sources (transient signals, continuous signals) as well as the wave propagation through the material and the transfer function of the transducer [47]. The recorded AE data can be evaluated in the time domain by various parameters such as (i) number of counts, (ii) rise time of the signal, and (iii) peak amplitude. Furthermore, recorded AE data can be analyzed in the frequency domain gaining additional information [49]. For this purpose, the complete AE data stream is treated by a Fast Fourier Transformation (FFT) of the AE signals measured by the transducer into the so-called source function (AE signals related to specific sources) and the transfer function (wave propagation, properties of the transducer etc.). Thus, the data stream is divided into windows with a size of 2^n readings with a defined overlap of these windows in order not to lose signals at the boundaries of these windows and a subtraction of the noise level of AE data is performed. The results of the FFT of the AE data stream are individual power spectral density (PSD) functions which can be characterized by numerous parameters [45]. The most important parameters are (i) the energy of the PSD function E, which corresponds to the area beneath the curve, and (ii) the median frequency f_m corresponding to the frequency at which the areas below a two-part PSD are equal in size [50]. Subsequently, AE signals of the same origin and, consequently, identical PSD have to be found, which is done by a cluster algorithm. Pomponi and Vinogradov [46] developed a special cluster algorithm (adaptive sequential k-means (ASK) clustering) which allows to differentiate AE signals of various origins. The advantage of this ASK-algorithm is the non-iterative way of working and the low required resources which allow a real time processing. Another advantage is that the number of clusters does not have to be set a priori, thus, it is a non-supervised, data driven process. Through continuous signal analysis, the AE has developed into a methodology that can be used to analyze and characterize microstructural deformation and damage processes. In particular, processes that are fast and involve large

volumes are suitable for detection by AE because the effected volume correlates directly with the energy of the acoustic signal.

Van Bohemen [51] investigated the martensitic transformation behavior of low alloy carbon steel and combined dilatometry with acoustic emission measurements. The investigations revealed a correlation between the energy of the acoustic signals, the formed martensite and the plastically deformed austenite. In addition, correlations between dislocation densities and acoustic signals were observed. Vinogradov et al. [45] investigated the deformation behavior of three different high-alloy austenitic TRIP/TWIP steels with different austenite stability under tensile load. Characteristic PSD functions could be assigned to different deformation mechanisms: (i) dislocation motion, (ii) martensitic phase transformation, (iii) formation of twins, and (iv) formation of stacking faults. Linderov et al. [52] showed the influence of temperature on the change of kinetics of deformation processes in high-alloy TRIP/TWIP steel under tensile load. Mandel et al. [53] investigated the corrosion behavior of a high-alloy TRIP steel. The acoustic signals showed a good correlation between hydrogen bubble formation and cathodic polarization and also a strong time dependency, since the material was polarized in the passive state.

15.2.4 Nanoindentation

Nanoindentation is a powerful method for the characterization of micromechanical properties of microstructural features of materials in the micrometer range. Thus, indentation hardness and/or indentation modulus can be measured for individual phases of a multiphase material or thin coatings. During nanoindentation, the complete indentation process of an indenter with a well-defined geometry is continuously recorded as a load-displacement curve. In contrast to conventional hardness tests such as Vickers or Knoop, the indentation hardness is evaluated from the load-displacement curve according to the well-known Oliver-Pharr method [54] and not from the size of the indent. However, due to the low penetration depth, additional effects have to be considered for the calculation of the indentation hardness such as (i) the true contact area between the indenter and the specimen surface, (ii) the stiffness of the testing device, and (iii) thermal drift during indentation [55].

In addition, the material behavior during the indentation process affects the true contact area between indenter and surface which is known as so-called pile-up or sink-in effect [56]. During pile-up, the material around the intender is bulged up, increasing the actual contact area in comparison to the calculated contact area leading to an overestimation of the hardness of the material. For the sink-in effect, the actual contact area is overestimated and the hardness of the material will be underestimated. A further effect, which can occur during nanoindentation experiments is the so-called pop-in effect reflecting a discontinuity in the load-displacement curve during the loading. This pop-in effect can be caused by an avalanche-like dislocation movement [57] or by phase transformations [58].

In the last years, nanoindentation has become a widely used method, in particular, in scanning electron microscopes which allows the combination of the determination of micromechanical properties with the high-lateral resolution of the SEM. Weidner et al. [59] investigated the hardness of individual structural components in a deformed high-alloy TRIP steel with reduced carbon content. Through the combination with EBSD, the indents could be assigned to the individual phases. The α'-martensite formed during prior deformation showed only a slight increase in hardness compared to the deformed austenite of only approx. 25% which was attributed to the low carbon content of the steel. Ahn et al. [58] observed the γ-austenite to α'-martensite transformation in a low-alloy TRIP steel as a cause for pop-in events. For high-alloy TRIP steels, the indentation-induced transformation of ε-martensite to α'-martensite can also be responsible for pop-in events [60].

15.3 Materials

A general overview is given on materials used for the in situ investigations: (i) high-alloy austenitic cast steels including CrMnNi TRIP/TWIP steels with different austenite stabilities and austenitic-martensitic-carbidic steel after Q&P treatment, (ii) a MgO partially stabilized zirconia (Mg-PSZ) ceramic, and (iii) a metal matrix composite material consisting of austenitic TRIP steel and Mg-PSZ produced by powder metallurgy.

15.3.1 High-Alloy Austenitic Steels

The chemical alloying concept of the studied high-alloy TRIP/TWIP steels is based on a low carbon and nitrogen content (< 0.05 wt%) with 16 wt% of Cr, 7 wt% Mn and Ni [61]. By a variation of the nickel content (3, 6 and 9 wt%), the austenite stability and, consequently, the tendency to form α'-martensite during mechanical loading can be adjusted. Thus, the steel with 9 wt% Ni exhibits the highest austenite stability and undergoes a mechanical twinning during loading (TWIP effect). In contrast, the steel with 3 wt% Ni has the lowest austenite stability resulting in most pronounced TRIP effect. The steel with 6 wt% Ni with a medium austenite stability exhibits depending on the deformation temperature and loading conditions either a TRIP and/or TWIP effect during deformation. The high-alloy CrMnNi TRIP steels undergo a two-step phase transformation from γ-austenite via the intermediate ε-martensite into α'-martensite. The formation of ε-martensite occurs via movement of Shockley partial dislocations $\vec{b} = \frac{a}{6}\langle 112\rangle$ forming extended stacking faults due to the low stacking fault energy [22]. If the stacking faults are arranged on in average each second closed packed lattice plane of the austenite, the austenitic ABCABC stacking sequence is transferred to the hexagonal stacking sequence ABAB and, thus, ε-martensite is identified with a hexagonal lattice structure by EBSD [3, 5]. If the stacking faults

Table 15.1 Chemical composition of the CrMnNi cast TRIP/TWIP steels in wt% (Fe bal.). Content of carbon was determined by combustion infrared detection technique and the content of nitrogen by inert gas fusion infrared and thermal conductivity detection. M_s—Martensite start temperature. SFE—Stacking fault energy determined according to Dai et al. [62]

Steel	C	Cr	Mn	Ni	Si	N	M_S (K)	SFE (mJ/m^2)
X5CrMnNi16-6-3	0.05	16.0	6.4	3.2	0.8	0.06	313	4–10
X5CrMnNi16-6-6	0.05	16.0	6.0	6.1	1.0	0.05	245	9–15
X5CrMnNi16-6-9	0.05	15.3	5.8	8.6	0.9	0.05	230	15–21

are arranged on each closed packed plane of the austenite the ABCAB stacking sequence is transferred into ABCBA resulting in twin orientation. Therefore, both the stacking fault energy and, related to it, the temperature have a significant influence on the deformation behavior. At high SFEs, the deformation behavior is dominated by movement of regular dislocations $\vec{b} = \frac{a}{2}\langle 110\rangle$, whereas with a decrease in SFE the movement of partial dislocations is more favorable resulting in formation of twins and ε-martensite. In parallel, the formation of α'-martensite is increasing with a decrease in SFE.

The chemical composition of investigated cast steels is provided in Table 15.1. The variation of the nickel content has a significant influence on the austenite stability characterized by the martensite start temperature M_s and the stacking fault energy SFE triggering the deformation mechanisms. Thus, the initial microstructure of the steel with 9 wt% nickel is fully austenitic, the steel with 6 wt% nickel contains about 1–2 vol% of δ-ferrite, whereas the steel with 3 wt% nickel consists of about 15 vol% of δ-ferrite and 15 vol% of cooling martensite. The as-cast steel variants were solution annealed at 1323 K for 0.5 h to dissolve precipitates. The grain sizes of the steel variants vary between 100 μm up to the range of several millimeters.

Austenitic-martensitic-carbidic TRIP steel. High-alloy austenitic TRIP steels have good formability and high strength, but due to the fully austenitic microstructure they are characterized by a low yield strength [63]. In order to increase the yield strength, a quenching and partitioning (Q&P) treatment was developed by Wendler et al. [19] to achieve a two-phase microstructure consisting of austenite and tempered α'-martensite. Compared to the previous low-carbon CrMnNi steels, Q&P steels are characterized by an increased carbon and nitrogen content. During Q&P treatment, the fully austenitic steels are quenched to the temperature range $M_s < T < M_f$ (M_f—martensite finish temperature) to achieve an austenitic-martensitic microstructure. If the M_s temperature is already below room temperature, a cryogenic cooling up to liquid nitrogen temperature may be necessary. Due to the increased amount of interstitial alloying elements carbon and nitrogen, α'-martensite is supersaturated and, thus, tetragonally distorted after quenching. In this state, the yield strength and the ultimate tensile strength are significantly increased, but the ductility is limited. The quenching is followed by a so-called partitioning process. During partitioning (723 K for 5 min) carbon and nitrogen partly precipitate as carbides and/or nitrides, and diffuse from the supersaturated martensite into the retained austenite resulting in a stabilization of the austenite [64, 65]. Due to the increased austenite stability and

the increased ductility of the tempered martensite due to partitioning, a considerable increase in ductility with small reduction of ultimate tensile strength can be achieved [17].

Based on the chemical design of the high-alloy CrMnNi cast TRIP/TWIP steels a class of austenitic-martensitic-carbidic steels was developed by Wendler et al. [19], where the manufacturing process is based on a Q&P treatment. The steel was produced in a vacuum induction furnace and cast into a copper mold, which led to rapid solidification of the melt. The chemical composition after casting is shown in Table 15.2. The SFE for the given chemical composition has been calculated according to Dai et al. [62] to 17–23 mJ/m^2. Subsequently, miniature flat tensile specimens were separated from the cast block. These were solution annealed at 1423 K for 0.5 h. Afterwards, the specimens were quenched in water to room temperature followed by subzero cooling down to 213 K in an ethanol bath using liquid nitrogen.

After subzero cooling, the specimens were annealed at 723 K for 5 min to induce diffusion of carbon and nitrogen from the supersaturated α'-martensite into the retained austenite as well as precipitation of carbides and/or nitrides. The microstructure after partitioning is shown in Fig. 15.1. It can be seen that the retained austenite is not homogeneously distributed in the microstructure. There are areas with austenitic grains several μm in size—the so-called interdendritic austenite and also austenitic areas between the tempered martensite laths which have a thickness of less than 1 μm—the so-called interlath austenite. Due to the ferritic solidification of the remaining melt, δ-ferrite can also be found in the interdendritic austenite.

Table 15.2 Chemical composition of the as-cast AMC steel in wt%, (Fe bal.). Content of carbon was evaluated by combustion infrared detection technique and content of nitrogen by inert gas fusion infrared and thermal conductivity detection

	C	N	Cr	Mn	Ni	Si
X16CrNiMnSiN 15-3-3	0.16	0.11	14.5	3.0	3.3	0.4

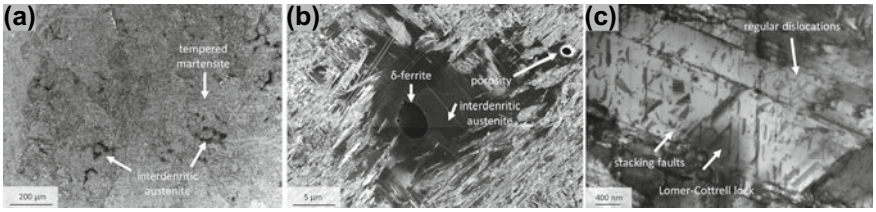

Fig. 15.1 Initial microstructure of austenitic-martensitic-carbidic steel. **a** SEM micrograph overview in backscattered electron contrast showing interdendritic austenite and tempered martensite. **b** Magnification of interlath austenite with marked δ-ferrite and porosity. **c** Interlath austenite with marked stacking faults, Lomer-Cottrell locks and regular dislocations observed in transmission SEM [66]

15.3.2 MgO Partially-Stabilized Zirconia

Zirconia can be present in three different modifications depending on temperature: (i) the cubic high-temperature phase (c)-ZrO_2 ($T > 2650$ K), (ii) the tetragonal phase (t)-ZrO_2 (1478 K $\leq T \leq$ 2650 K), and (iii) the monoclinic phase (m)-ZrO_2 which prevails at room temperature [67]. By addition of phase stabilizers like MgO, CaO, CeO or Y_2O_3 the cubic modification can be stabilized down to room temperature. During heat treatment, coherent tetragonal precipitates (lenses) are formed within the cubic lattice structure which can transform via a stress-assisted martensitic phase transformation into the monoclinic lattice structure. This martensitic phase transformation is accompanied by a shear of about 0.16 and a volume expansion of about 4.9% [68]. This volume expansion of ZrO_2 is related to the formation of compressive stresses, which can impede crack propagation. Thus, partially-stabilized ZrO_2 can yield good fracture toughness properties [69].

Porter et al. [70] modeled the transformation toughening in PSZ ceramics using Eshelby's analysis of transformed inclusions and observed a reasonable consistency with experimental results regarding the magnitude of the toughness. Porter and Heuer [71] investigated the evolution of microstructure during aging of MgO-partial stabilized ZrO_2 (Mg-PSZ) after solution annealing. The observations showed that the aging parameters have a strong influence on the microstructure and, thus, also on the mechanical properties. If the aging time is too short, too small (t)-ZrO_2 lenses are formed, which leads also to a reduction in fracture toughness. If the aging time is too long, the tetragonal precipitates continue to grow. If the size of the precipitates exceeds about 0.2 μm, the coherency is lost resulting in a transformation of the tetragonal lenses into monoclinic lattice structure during cooling to room temperature. Hannik [72] examined the growth of tetragonal precipitates in CaO, MgO and Y_2O_3 partially-stabilized ZrO_2 and observed similar behavior. The Mg-PSZ also showed a loss of tetragonal structure when the dimensions of the longest axis of the precipitates exceed 0.6 μm.

15.3.3 TRIP Matrix Composite

Metal matrix composites (MMC) combine properties of metals (high ductility and toughness) with those of ceramics (high strength and Young's modulus) to generate new material properties [73]. TRIP matrix composites merge the strain-induced martensitic phase transformation of a TRIP steel matrix and the stress-assisted martensitic phase transformation of Mg-PSZ resulting in a high capacity for absorption of mechanical energy [74]. TRIP matrix composites can be manufactured by a powder-metallurgical route followed either by conventional sintering process [75], hot pressing [76] or field-assisted sintering [77]. Hot pressing and field-assisted sintering result in shorter process times due to the superimposed mechanical load [77, 78] leading to lower porosity, smaller grain sizes and less pronounced diffusion

processes compared to conventional sintering regimes. Reduced diffusion processes are of high importance regarding the MgO stabilizer. Thus, the MgO stabilizer can diffuse out of the ZrO_2 particles during conventional sintering due to higher sintering times and temperatures leading to a destabilization of Mg-PSZ particles and a monoclinic phase transformation already during the manufacturing process.

Martin et al. [79] investigated the transformation behavior of a TRIP steel reinforced with Mg-PSZ under compressive stress. The MMC was manufactured using spark plasma sintering to keep the process time as short as possible. Compared to the unreinforced reference material, the MMC showed a higher stress level with the same compressive strain. Glage et al. [80] investigated a TRIP steel/Mg-PSZ composite in the regime of low-cycle fatigue and observed a strengthening effect under cyclic loading and a comparable fatigue life time for lower strain amplitudes.

For optimal mechanical properties the bonding of the ceramic particles to the metallic matrix is important. A weak bonding leads to rapid decohesion of the ceramic from the matrix and premature failure. Prüger et al. [81] investigated the correlation between interface strength and transformation behavior of the PSZ in a TRIP steel MMC under compressive load using micromechanical simulations. They could show that with increasing interface strength the phase transformation of the PSZ is favored and, thus, the work hardening behavior of the MMC increases.

15.4 Case Studies

15.4.1 Austenitic Cast Steels

15.4.1.1 Strain Localizations Studied by Digital Image Correlation

High-alloy CrMnNi cast TRIP/TWIP steels. Miniature flat tensile specimens were manufactured out of the solution annealed cast plates. The gauge length was 10 mm with a rectangular cross section of 2×4 mm^2. The specimens were carefully grinded and polished to obtain a deformation-free surface. Subsequently, the specimens were etched with a V2A agent (200 ml distilled water, 200 ml 32 pct hydrochloric acid, 20 ml 65 pct azotic acid, 0.6 ml Vogel's special reagent) for 1 min at 60 °C providing an excellent surface contrast pattern required for DIC calculations. Tensile tests were performed both at room temperature (RT) and elevated temperatures (373 K, 473 K) using a miniature push-pull loading stage (Kammrath & Weiss, Dortmund, Germany) placed in the chamber of a high-resolution scanning electron microscope. The higher temperatures were realized by a heating plate mounted on the back side of the specimens. Temperature was controlled by a thermocouple and kept constant over the entire deformation test using PID control. The quasi in situ tensile deformation was performed step wise and after each deformation step of $\Delta l = 50$ µm micrographs of predefined areas of interest (AOIs) were captured. The

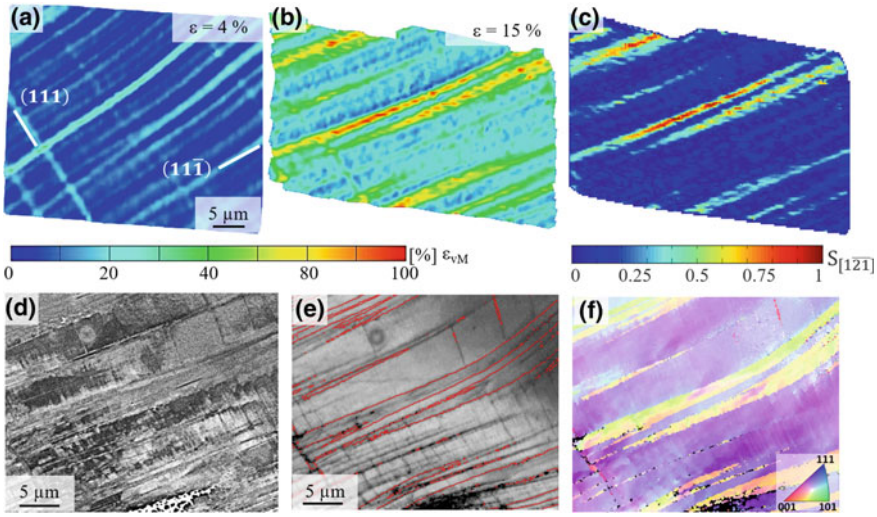

Fig. 15.2 Results of digital image correlation and EBSD measurements obtained on steel X5CrMnNi16-6-9 during tensile loading at RT and 4% (**a**) and 15% (**b**-**f**) of applied global strain. **a**, **b** Local strain field according to von Mises equivalent strain ε_{vM}. **c** Calculated magnitude of shear on the $(11\bar{1})$ plane in the direction of $\vec{b} = \frac{a}{6}[1\bar{2}\bar{1}]$. **d** SEM micrograph of formed deformation bands in backscattered electron contrast. **e** Band contrast map with highlighted Σ3 boundaries. **f** Crystallographic orientation in inverse pole figure coloring according to loading axis (horizontal)

deformation continued until a global strain of 15% was reached. After tensile deformation, specimens were vibration polished using colloidal silica for 24 h (or multiples of) to remove etching pits on the surface. Subsequently, AOIs were measured again using electron backscatter diffraction. Recorded high-resolution SEM micrographs were evaluated using software package ARAMIS [82] to calculate strain distribution. For more experimental details see [31].

*Steel with highest austenite stability (*9 wt*% nickel).* Figure 15.2 shows the deformation of the X5CrMnNi16-6-9 steel at room temperature where a pronounced twin formation is expected according to the higher SFE (compare Table 15.1). Figure 15.2a shows the strain distribution according to the von Mises equivalent strain (ε_{vM}) at the beginning of deformation (4% global strain). The formation of deformation bands related to the activation of two different slip systems oriented parallel to (111) and $(11\bar{1})$ plane, respectively, was observed. The strain is well localized and homogeneously distributed within these bands (about $\varepsilon_{vM} = 25\%$). With ongoing deformation, both the number of deformation bands as well as their thickness increase, in particular for the system belonging to $(11\bar{1})$ plane, which corresponds to the secondary slip system ($\mu = 0.36$). Moreover, the strain localization within these bands increases continuously (see Fig. 15.2b). Figure 15.2c shows the calculated magnitude of shear for the secondary slip system in the direction of the Burgers vector of the Shockley partial dislocations with the highest Schmid factor ($\vec{b} = \frac{a}{6}[1\bar{2}\bar{1}]$, $\mu = 0.34$). It turned out that not all deformation bands belonging to secondary slip

system exhibit similar magnitude of shear. Only few of these bands show a relatively high value of about 0.75. These bands with the highest magnitude of shear were identified by EBSD measurements as regions with a twin orientation to the matrix (see Fig. 15.2e, f) indicated by red lines according to the misorientation relationship of $60°\langle 111\rangle$ for $\Sigma 3$ (twin) boundaries. Figure 15.2d shows the deformation bands forming on the primary and secondary slip system in backscattered electron contrast. Slip bands or even twins were visible also for the primary slip system, but are quite narrow compared to the large and wide twins belonging to the secondary system. Furthermore, the pronounced distortion of the area of interest due to the favored deformation on the secondary system becomes apparent.

Figure 15.3 shows the deformation of X5CrMnNi16-6-9 steel at 473 K. The calculated von Mises equivalent strain at a global strain of 2% is shown in Fig. 15.3a. Here, the band-like distribution of the strain is recognizable as well. The deformation bands form on the primary slip system parallel to (111) and show von Mises equivalent strains of about $\varepsilon_{vM} = 10\%$. With increasing global strain, the deformation band structure is still visible, but the areas between the bands also show increased strain values, as can be seen in Fig. 15.3b. When considering the AOI using backscattered electrons (Fig. 15.3c), the formation of band-like structures can be seen as

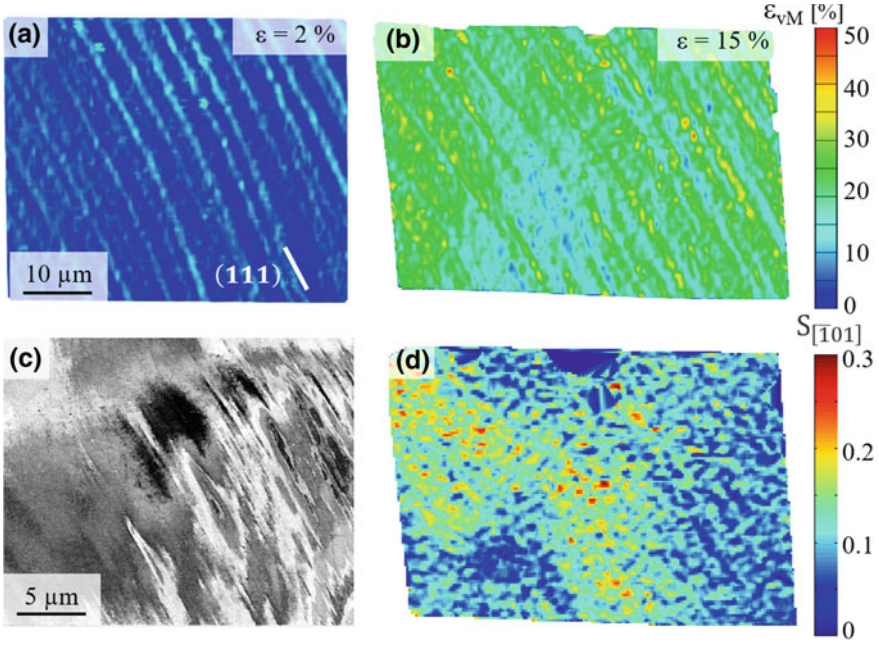

Fig. 15.3 Results of digital image correlation and EBSD measurements obtained on steel X5CrMnNi16-6-9 during tensile loading at 473 K. **a** Von Mises equivalent strain distribution (ε_{vM}) at 2% of applied global strain with marked primary slip system. **b** Von Mises equivalent strain distribution (ε_{vM}) at 15% of global strain. **c** SEM micrograph of area of interest in backscattered electron contrast. **d** Calculated magnitude of shear at 15% of global strain. Loading axis is horizontal

well. Twin formation was not observed using EBSD. In general, the strain is more homogeneously distributed over the AOI. This is due to the increased slip of regular dislocations due to the increased stacking fault energy compared to room temperature. This also becomes visible when considering the magnitude of shear, which is shown in Fig. 15.3d. In contrast to deformation at room temperature, where the magnitude of shear was highest in bands related to twins, a more or less homogeneous magnitude of shear between 0 and 0.2 is observed at 473 K.

Steel with medium austenite stability (6 wt*% nickel).* Figure 15.4 shows the evolution of strain during tensile deformation of X5CrMnNi16-6-6 cast steel at room temperature. Figure 15.4a shows localized strain within deformation bands at the beginning of the tensile deformation at 3.6% global strain. Noteworthy is the high lateral resolution of the SEM-DIC. The width of the deformation bands which are recognizable by digital image correlation is less than 1 μm.

The strain is very homogeneously distributed within the deformations bands, except the area marked with a white arrow which shows strain localization up to $\varepsilon_{vM} = 40\%$. With increase in macroscopic strain, the number of deformation bands increases, the deformation bands grow in their width and areas of local strain concentrations within these bands increase as well (see Fig. 15.4b). Figure 15.4d, e show the AOI in terms of backscattered electron (BSE) contrast and EBSD phase

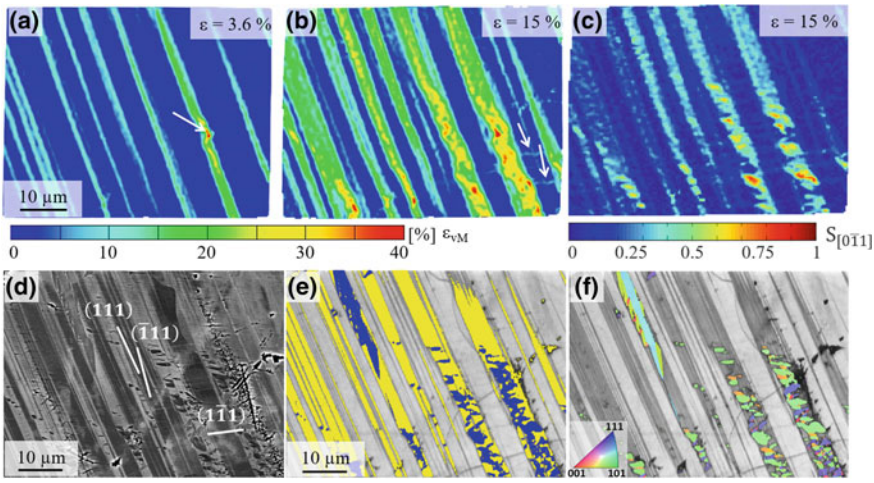

Fig. 15.4 Results of digital image correlation and EBSD measurements obtained on steel X5CrMnNi16-6-6 during tensile loading at RT. **a** Von Mises equivalent strain distribution (ε_{vM}) at 3.6% of applied global strain with marked area of enhanced strain. **b** Von Mises equivalent strain distribution (ε_{vM}) at 15% of applied global strain with indicated slip systems. **c** Calculated magnitude of shear on planes $(111)/(\bar{1}11)$ in the direction of $[0\bar{1}1]$. **d** SEM micrograph of area of interest in backscattered electron contrast. **e** Band contrast map with highlighted ε-martensite (yellow) and α'-martensite (blue). **f** Band contrast map with highlighted α'-martensite in inverse pole figure color code according to load axis (horizontal). Partly reproduced from [31]

map, respectively. Both figures reveal the formation of α'-martensite inside deformation bands. In Fig. 15.4e, grey areas correspond to austenite, yellow to ε-martensite and blue to α'-martensite. In comparison with Fig. 15.4b it can be seen that the formation of the deformation bands correlates with the formation of ε-martensite and the strain-increased regions within the bands correlate with the formation of α'-martensite. Figure 15.4f shows that only a certain number of different orientations of α'-martensite grains have been formed within the deformation bands, which is an indication for a variant selection. A comparison with Fig. 15.4c shows that the magnitude of shear calculated in the $[0\bar{1}1]$ direction correlates with the orientation of the α'-martensite grains. Only one martensite variant (green color) exhibits the highest magnitude of shear of about 0.7, while the other variants (orange and violet color) show significantly smaller values of shear [31]. In comparison, regions corresponding to ε-martensite show nearly homogeneously distributed shear of about 0.3, which is due to the fact that only one single ε-martensite variant has been formed [31].

Figure 15.5 shows the evolution of strain during tensile deformation of X5CrMnNi16-6-6 cast steel during tensile deformation at 373 K. Due to the increased temperature and, consequently, the increased SFE as well as reduced driving force

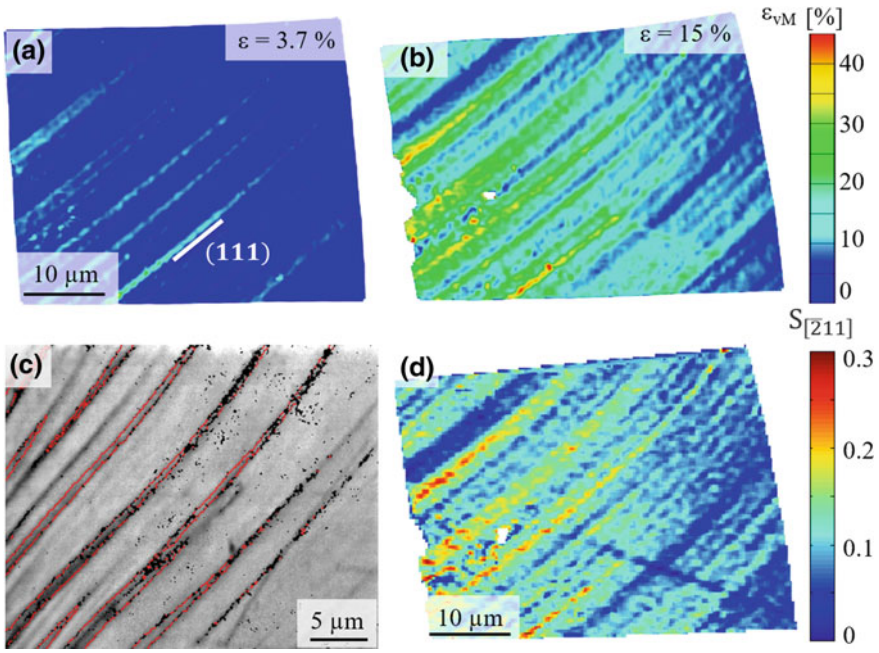

Fig. 15.5 Results of digital image correlation and EBSD measurements obtained on steel X5CrMnNi16-6-6 during tensile loading at 373 K. **a** Von Mises strain distribution (ε_{vM}) at ε = 3.7% with marked primary/secondary slip system. **b** Von Mises strain distribution (ε_{vM}) at ε = 15%. **c** Band contrast map with marked Σ3 boundaries. **d** Calculated magnitude of shear within the area of interest

of ΔG (Gibb's free energy), no formation of α'-martensite is observed. In Fig. 15.5a at 3.7% global strain, the localization of strain in bands was detected. The size of the bands which can be detected by DIC is below 1 μm and the strain distribution within these bands is quite homogeneous (Fig. 15.5b). With increase in macroscopic strain, the number of deformation bands further increases.

The von Mises strain localization within some bands is about 40% at $\varepsilon = 15\%$, but it is in other bands significantly lower. The comparison with results from EBSD measurements (Fig. 15.5c) reveals that regions with highest strain localizations correspond to areas where twins have been formed. The magnitude of shear (Fig. 15.5d) was calculated on (111) plane in $\left[\bar{2}11\right]$ direction. The regions with highest shear correspond well with the regions of twins. However, the magnitude of shear is about 0.25 and is, therefore, significantly lower than that Schumann predicted theoretically to be of about 0.7 for twinning [83]. One reason for lower magnitudes of shear could be that the thickness of twin bundles within the broader shear bands is below resolution of the DIC measurements [15]. On the other hand, it is more likely that twins formed in this steel variant are the results of movement and accumulation of partial dislocations. The theoretically calculated magnitude of shear for partial dislocations is of 0.3, which would be in good agreement with the experimentally determined values of about 0.25. Here obviously the areas with high von Mises strain correlate with areas with high shear, in comparison to the deformation at room temperature, where different α'-martensite variants led to a partially inhomogeneous shear distribution depending on which martensite orientation has formed. Such behavior was not observed at 373 K because twins with a uniform orientation have been formed during deformation. As a result, the twins also have a homogeneous shear distribution. Finally, the X5CrMnNi16-6-6 cast steel with medium austenite stability behaves at 373 K like the steel X5CrMnNi16-6-9 with higher austenite stability at room temperature.

Austenitic-martensitic-carbidic steel. Miniature flat tensile specimens were manufactured out of the Q&P treated steel X16CrNiMnSiN with same dimensions as described for the CrMnNi TRIP/TWIP steels. The surfaces of the specimens were grinded and vibration polished. Afterwards, AOIs were defined containing interdendritic austenitic grains, which were pre-characterized by EBSD. Subsequently the miniature specimens were etched for 2 min at 40 °C in V2A etching agent to achieve a structured surface. The quasi in situ deformation in the SEM was performed according to similar procedure as described above for CrMnNi TRIP/TWIP steels. After each deformation step several micrographs at two different magnifications were captured until uniform elongation of the specimen ($\varepsilon = 19\%$). The sequence of SEM images was stabilized using the VirtualDub software package [84] and local strain fields were evaluated using the VEDDAC software [85]. After tensile deformation, the gauge length of specimens were cut-off and vibration polished for four hours. Subsequently, EBSD measurements of the AOIs were carried out to evaluate the development of the microstructure after tensile deformation. In addition, XRD measurements were performed on both undeformed and deformed specimens. The phase analysis was carried out by a Rietveld–like refinement of the whole diffraction pattern using the MAUD software package [86]. According to the microstructure,

Table 15.3 Lattice parameters, volume fractions and related phases calculated according to Rietveld-like refinement using software package MAUD of steel X16CrNiMnSiN15-3-3 in Q&P condition, before and after deformation. According to [66]

	Lattice parameter (nm)	Volume fraction (%)	Phase
Non-deformed state	0.2875	69	Tempered martensite
	0.3597	25	Interdendritic austenite
	0.3609	6	Interlath austenite
Deformed state	0.2879	68	Tempered martensite
	0.2881	29	Fresh martensite
	0.3605	3	Interlath austenite

face-centered cubic and body-centered cubic iron were considered. The results are summarized in Table 15.3.

The XRD measurements on the initial state revealed 69 vol% of tempered martensite and 25 vol% of interdendritic austenite. In addition, 6 vol% of interlath austenite were identified based on a slightly increased lattice parameter of $a = 0.3609$ nm compared to the interdendritic austenite with $a = 0.3597$ nm. This difference of lattice constants for both austenitic phases is caused by different content of nitrogen and carbon due to various diffusion behavior. Diffusion occurs during partitioning from supersaturated, quenched martensite into austenite. The interdendritic austenite is characterized by grain sizes of >5 μm, whereas the grain size of interlath austenite is significantly smaller (<1 μm). Diffusion length of carbon was estimated by Ågren [87] to be less than 1 μm for partitioning at 723 K for 5 min. Due to the small size of the interlath austenite, it will have a higher carbon and nitrogen concentration than the interdendritic austenite. Thus, for interdendritic austenite the estimated diffusion length is too small to result in a significant increase in content of interstitial elements. The different lattice parameters are, therefore, explained by content of interstitial elements.

In the deformed state, no interdendritic austenite was identified by XRD and only 3 vol% of interlath austenite were remaining after tensile deformation up to $\varepsilon = 19\%$ with a lattice parameter of a = 0.3605 nm which is comparable to the undeformed state. This means, interlath austenite is much more stable during deformation. This is caused by the higher chemical stabilization due to the higher carbon and nitrogen content, but also due to the surrounding martensite which puts the austenite into a hydrostatic compression state, the so-called shielding effect [88]. In contrast, nearly all interdendritic austenite transformed during deformation. The amount of tempered martensite remains with 68 vol% nearly constant. After deformation, 29 vol% of fresh martensite were formed mostly from interdendritic austenite. The fresh martensite shows a small tetragonal distortion of about 0.6% in comparison to tempered martensite which is caused by higher carbon and nitrogen content, although interdendritic austenite does not gain significantly carbon and nitrogen during partitioning, as already mentioned above. However, the martensite existing before deformation has been tempered during partitioning, reducing the tetragonal distortion.

The influence of the grain orientation on the local deformation behavior of the interdendritic austenite was investigated by DIC in combination with EBSD measurements. Here, two different grain orientations were selected: (i) ⟨101⟩ and (ii) ⟨001⟩ lattice directions, respectively, parallel to the loading axis. The first one was oriented for slip of partial dislocations and the latter one was oriented for preferential slip of regular dislocations. The microstructural evolution during tensile deformation of ⟨101⟩ oriented interdendritic austenite grain is shown in Fig. 15.6a, b. At the beginning of deformation, a two-phase microstructure consisting of austenite and tempered martensite is present. With beginning of deformation, bands are evolving parallel to the primary slip system. Close to uniform elongation ($\varepsilon = 19\%$) a massive martensitic phase transformation occurs starting from the interface of interdendritic austenite/tempered martensite. Figure 15.6b shows that both ε-martensite (hcp) and fresh α'-martensite (bcc) can be found within deformation bands. In contrast,

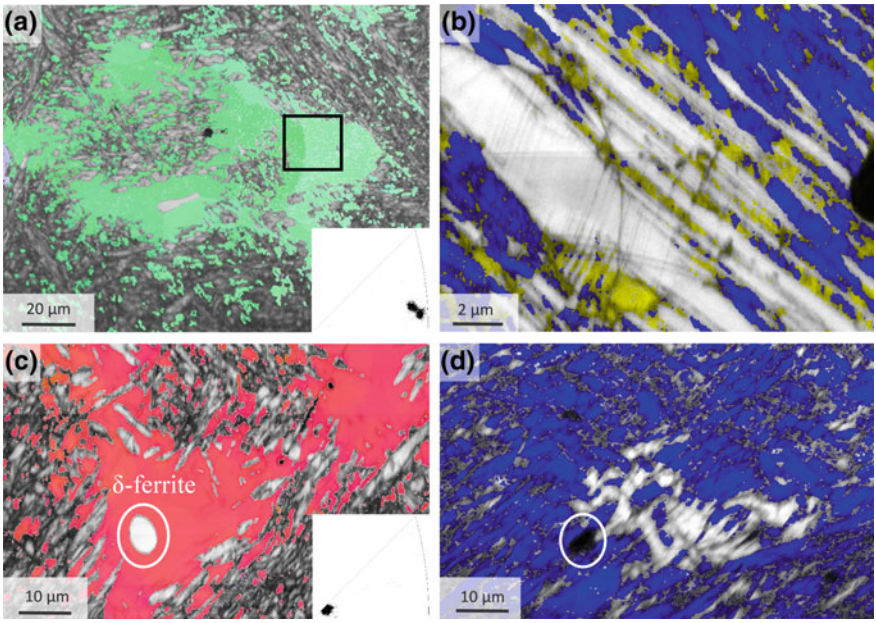

Fig. 15.6 Results of EBSD measurements of AOIs before and after tensile deformation of Q&P treated steel X16CrNiMnSiN15-3-3 at RT. **a** ⟨101⟩ grain orientation. Band contrast map of tempered martensite with austenite colored according to inverse pole figure color code of loading axis. **b** Band contrast map of marked area of (**a**) after deformation up to $\varepsilon = 19\%$ with γ-austenite (grey), ε-martensite (yellow) and fresh α'-martensite (blue). This AOI is studied in more detail in Fig. 15.7. **c** ⟨001⟩ grain orientation. Band contrast map of tempered martensite and marked δ-ferrite with austenite colored in inverse pole figure color code of loading axis. **d** Band contrast map after deformation up to $\varepsilon = 19\%$ with γ-austenite (grey) and tempered and fresh α'-martensite (blue) of the AOI with a marked place of the δ-ferrite shown in **c**. Loading axis is horizontal. Partly reproduced from [66]

Fig. 15.6c, d show the results for the deformation of the ⟨001⟩ oriented interdendritic austenitic grain. Here, no formation of deformation bands was observed. The EBSD measurements reveal only fresh-formed α'-martensite and no ε-martensite was detected. This is what was expected for these two different grain orientations and can be understood by the different behavior of dislocations. Whereas dislocations in grain ⟨101⟩ dissociate into Shockley partials leading to stacking faults, grain ⟨001⟩ is oriented for preferred movement of regular dislocations. Figure 15.6d shows the ⟨001⟩ oriented grain after 19% global strain. Within the austenite pronounced formation of fresh α'-martensite has occurred via the $\gamma \rightarrow \alpha'$ transformation. Thus, both grain orientations exhibit as expected different behavior in terms of the formation of fresh martensite during tensile deformation at RT.

Figure 15.7 shows the marked area of Fig. 15.6a (black rectangle) in more detail. Figure 15.7a shows the interdendritic austenitic grain with tempered martensite before deformation in secondary electron contrast after etching. Etching was optimized for a good contrast of the austenite. Therefore, both tempered martensite and

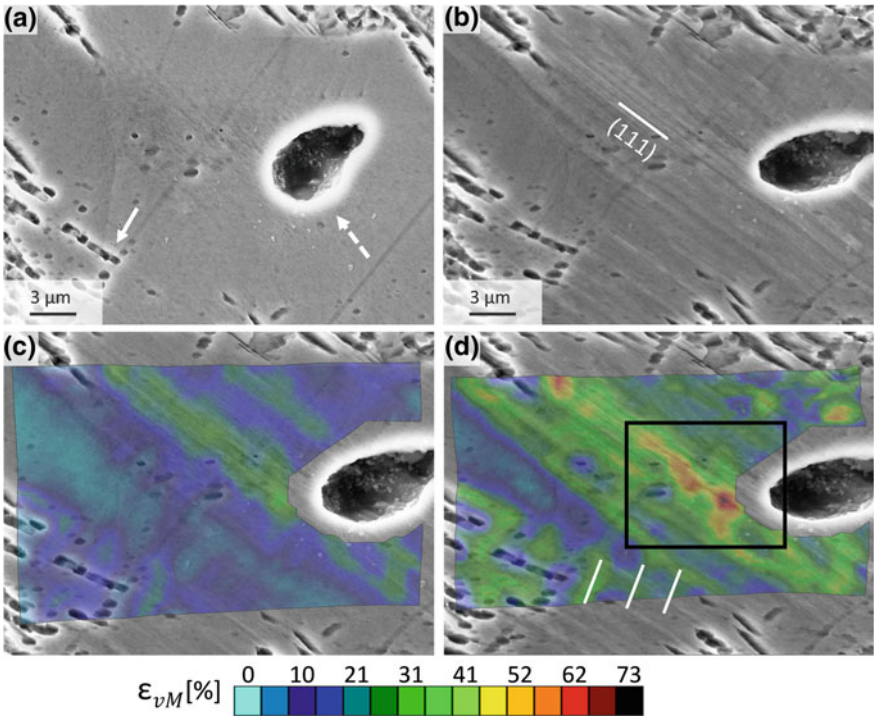

Fig. 15.7 ⟨101⟩ oriented austenitic grain during tensile deformation. **a** Area of interest at zero strain, etched, in secondary electron contrast with over etched δ-ferrite and α'-martensite marked by dashed and bold arrows. **b** Area of interest at 19% of global strain with marked trace of primary slip system. **c**, **d** Calculated von Mises equivalent strain (ε_{vM}) at 11% (**c**) and 19% (**d**) of global strain, respectively. Areas with increased strain levels are marked by black rectangle in (**d**). Partly reproduced from [66]

δ-ferrite were slightly over etched (marked by bold and dashed arrows in Fig. 15.7a, respectively). Figure 15.7b shows the same AOI at $\varepsilon = 19\%$. The formation of deformation bands within the interdendritic austenite is well observed. Furthermore, additional contrast changes within the deformation bands are recognizable. Figure 15.7c, d show the calculated von Mises equivalent strain at 11% and 19% of global strain, respectively. At $\varepsilon = 11\%$, the local accumulation of strain within deformation bands is clearly visible. Furthermore, the strain is homogeneously distributed within these bands. During tensile deformation, ε-martensite is formed which is associated with a homogenous shear operation leading to homogenous von Mises equivalent strain values of about $\varepsilon_{\mathrm{vM}} = 0.3$. With further tensile deformation, these bands grow in width and the activation of a secondary slip system is observed (see white lines in Fig. 15.7d). Furthermore, within the primary deformation bands, areas with enhanced strain localization are formed with values of $\varepsilon_{\mathrm{vM}}$ up to 0.7. Looking to the microstructure of the AOI at $\varepsilon = 19\%$ in Fig. 15.7b it can be seen that the areas of increased strain correlate well with the formation fresh α'-martensite.

Figure 15.6b showed also that α'-martensite formed during tensile deformation, in particular, at the previous interface of tempered martensite and interdendritic austenite. The formation of fresh martensite in this region could not be resolved by DIC. The very pronounced formation of α'-martensite resulted in a high local strain from one deformation step to the other resulting in a loss of the correlation between individual subsets in these areas. The preferred formation of fresh martensite at the austenite/tempered martensite interface can be assigned to the constraining effect [89]. Due to the high defect density at the interfaces caused by the formation of tempered martensite, the formation of fresh martensite is preferred.

Figure 15.8 shows the area of high strain values marked in Fig. 15.7d in more detail. It is visible that the areas of high strain values (see Fig. 15.8a) correlate well with the fresh-formed α'-martensite grains shown in Fig. 15.8b. Thus, two different α'-martensite variants have been formed exhibiting a twin orientation relationship ($\Sigma 3$ boundaries marked by green line).

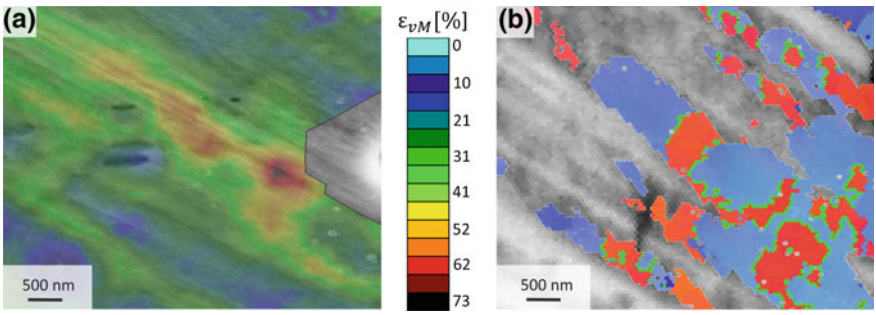

Fig. 15.8 AOI marked by black rectangle in Fig. 15.7d. **a** Calculated von Mises equivalent strain ($\varepsilon_{\mathrm{vM}}$) within deformation band after tensile deformation up to $\varepsilon = 19\%$. **b** Band contrast map with freshly formed α'-martensite shown in inverse pole figure color code according to loading axis. $\Sigma 3$ twin boundaries are indicated by green lines. Partly reproduced from [66]

15.4.1.2 Temporal Evolution of Deformation Mechanisms Studied by Acoustic Emission

Measurements of acoustic emission were performed in situ during tensile deformation of high-alloy X5CrMnNi16-6-x ($x = 3$, 6 or 9 wt%) cast steels in order to study the temporal evolution of ongoing deformation processes. Therefore, threshold-less, continuous AE signal acquisition method using a single AE sensor was applied. Different individual deformation mechanisms were identified as sources of acoustic emission and their evolution over the entire deformation process was evaluated. In addition, the influence of temperature on operating deformation mechanisms was evaluated. Details on experimental setup were published elsewhere [45, 90]. As demonstrated in [45], the detailed analysis of AE data obtained during tensile tests both in the time as well as frequency domain allowed for the separation of the following deformation mechanisms: (i) dislocation glide (movement of regular dislocations), (ii) formation of stacking faults (partial dislocation movement), (iii) twin nucleation, (iv) formation of α'-martensite, and (v) formation of Portevin Le Chatelier bands. Each of these mechanisms can be characterized by a specific set of AE parameters such as median frequency f_m and energy E of AE signals forming individual clusters of signals. The evolution of these individual clusters was followed over the entire deformation process. Thus, it was possible to evaluate which deformation mechanism becomes dominant at what stress or strain level during the tensile deformation. An example out of the variety of results is shown for the steel with the highest austenite stability (9 wt% nickel) in Fig. 15.9. For this steel it is known from microstructural investigations that mechanical twinning is the dominant deformation mechanism (Fig. 15.2), whereas at temperature $T > 80$ °C the movement of regular dislocations becomes dominant. Figure 15.9a, c show the results obtained at RT and Fig. 15.9b, d the results from tests at 373 K. The results are plotted either in terms of the cumulated AE energy E_Σ (Fig. 15.9a, b) or the cumulated number of AE cluster elements (Fig. 15.9c, d) always combined with the stress versus time response. These results illustrate well both the differences between the two AE sources (i) dislocation glide (low energy signals) and (ii) twin nucleation (high energy signals) as well as the influence of temperature on these mechanisms. Thus, both mechanisms are active at RT and 373 K. However, the mechanical twinning is dominant at RT whereas its activity is reduced at 373 K. In contrast, the dislocation glide becomes more important at 373 K compared to RT.

Furthermore, it was shown that the evolution of the identified clusters related to individual AE sources correlates well with other microstructural parameters or properties. Thus, it was shown in [45] that the evolution of the identified cluster for the α'-martensite formation correlates well with the evolution of the ferromagnetic phase fraction in case of steels X5CrMnNi16-6-6 and X5CrMnNi16-6-3 with medium and low austenite stability, respectively. Figure 15.10 summarizes the results from AE data analysis (magenta lines), the volume fraction of α'-martensite obtained from ferromagnetic phase fraction measurements using a feritescope (symbols) and the calculation of the volume fraction of α'-martensite according to the Olson-Cohen model [91] (dashed lines).

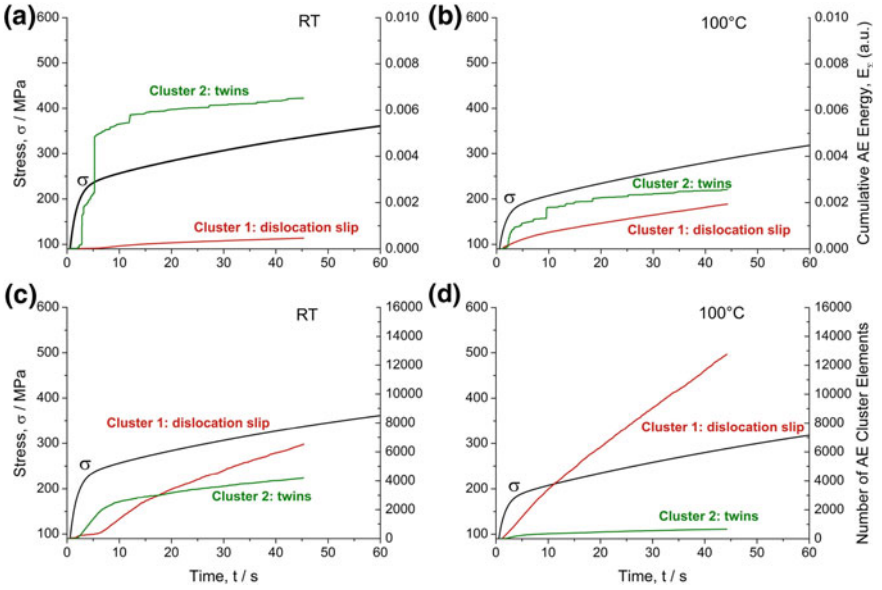

Fig. 15.9 Results of the AE measurements for steel X5CrMnNi16-6-9 tested in tension at RT (**a**, **c**) and 373 K (**b**, **d**). Temporal evolution of the identified mechanisms (i) dislocation glide and (ii) twin nucleation over the entire deformation process in terms of cumulative AE energy (**a**, **b**) and of number of AE cluster elements (**c**, **d**). Reproduced from [90]

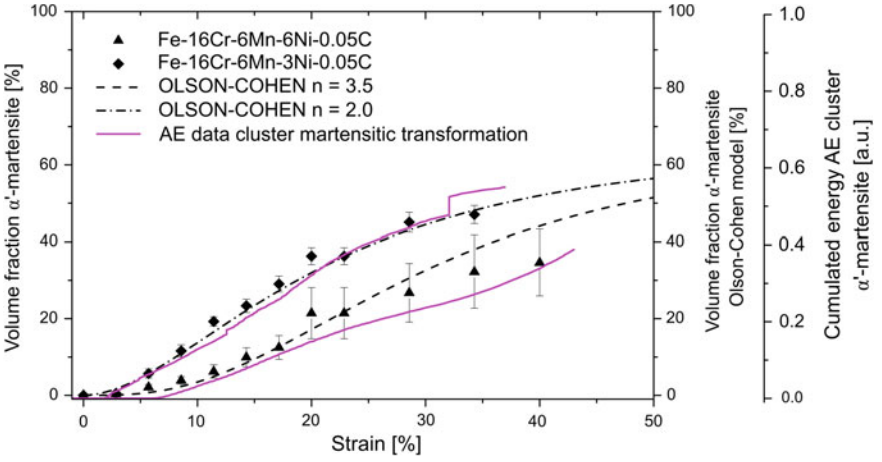

Fig. 15.10 Comparison of cumulated AE energy and volume fraction of strain-induced α'-martensite determined from feritescope measurements obtained during tensile tests at RT at a strain rate of 10^{-3} s^{-1} with model description of Olson and Cohen [91] for steel variants X5CrMnNi16-6-6 and X5CrMnNi16-6-3. Reproduced from [92]

Figure 15.10 demonstrates an excellent qualitative agreement between experimentally determined volume fraction of strain-induced α'-martensite with the evolution of the cumulated AE energy of the cluster related to α'-martensite formation. Both the onset of martensite formation as well as the different kinetics of α'-martensite formation are very well described by the evolution of the cumulated AE energy of signals related to the cluster corresponding to α'-martensite formation. In addition, both experimental data—AE and feritscope measurements—fit well with the Olson-Cohen model description of the kinetics of α'-martensite formation.

15.4.1.3 Portevin Le Chatelier Behavior Studied by Full-Field Measurements

The high-alloy X5CrMnNi17-7-4 cast steel exhibits an excellent strengthening behavior and high ductility yielding, as a consequence, a delay of the macroscopic strain localizations resulting in retarded necking and, finally, failure of the material at higher strain values. However, TRIP steel with the lowest nickel content (3 wt%) exhibits, in addition, serrated plastic flow known as the Portevin Le Chatelier (PLC) effect [93].

The PLC effect was studied on the high-alloy CrMnNi steel X5CrMnNi17-7-4 with 0.05% C, 17% Cr, 7% Mn, 3.7% Ni in the as cast condition after solution heat treatment (0.5 h at 1323 K followed by N_2 gas quenching). Due to the low austenite stability ($M_s = 333$ K), the initial microstructure consists beside the metastable austenite of about 15 vol% of martensite formed during cooling and 10 vol% of δ-ferrite due to ferritic solidification. The tensile tests were performed at room temperature using an electro-mechanical testing system (Zwick, Germany) using flat tensile specimens having a rectangular cross section of 8×4 mm^2 and a gauge length of 35 mm at a total length of 205 mm. The tests were carried out under crosshead displacement control with different nominal initial strain rates (10^{-4} s^{-1}, 10^{-3} s^{-1}, 10^{-2} s^{-1} and 10^{-1} s^{-1}, respectively). The mechanical tests were complemented by full-field measurements using in situ thermography measurements with the infrared thermography system VarioCamhr (InfraTec, Dresden, Germany) and digital image correlation using digital camera (Canon EOS 420D). One side of the gauge parts of the specimens was prepared for thermographic measurements by mechanical grinding and, subsequently, covered with a black thermo lacquer enabling a constant thermal emission of 0.96. The back side was prepared for digital image correlation using etching procedure as described above for SEM-DIC. Ferromagnetic measurements using feritescope were performed before and after the tensile tests in order to evaluate the volume fraction of strain-induced α'-martensite. Finally, the tensile tests were corroborated, in addition, by in situ acoustic emission measurements. For more experimental details see [93].

The mechanical tests revealed that for strain rates in the range of $10^{-4} \leq \dot{\varepsilon} \leq 10^{-2}$ s^{-1} pronounced inhomogeneous macroscopic flow was observed characterized by numerous serrations occurring in stress-strain curves. Moreover, a shift of the onset of serrated plastic flow within the stress-strain curve was recorded with an increase

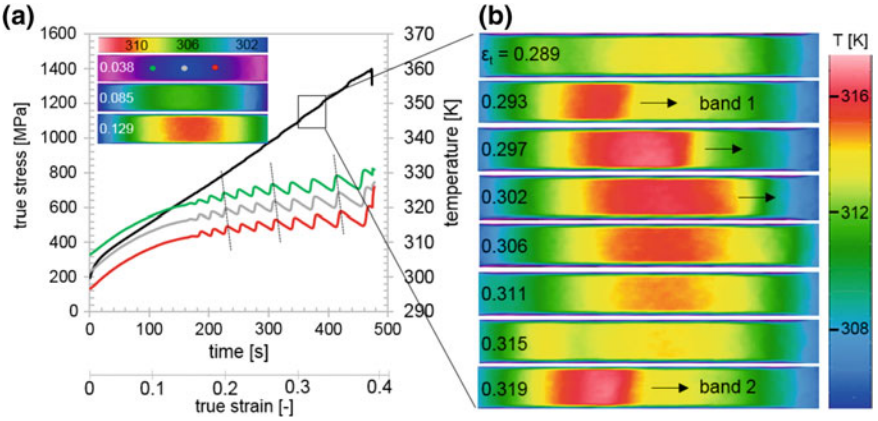

Fig. 15.11 Results of in situ infrared thermographic measurements during tensile tests of steel X5CrMnNi17-7-4 at room temperature and a nominal strain rate of 10^{-3} s^{-1}. **a** True stress versus true strain curve in combination with temperature-time curves measured at three points along the gauge length (green, grey, red points in the insert) and a sequence of infrared thermograms of the whole gauge length at three different strain levels for lower strain levels $\varepsilon < 0.15$. **b** Sequence of infrared thermograms of the whole gauge length for higher strain levels ($\varepsilon > 0.15$) showing the formation and propagation of two individual macroscopic bands of localized plastic strain. Reproduced from [92]

in strain rate. The tensile deformation was accompanied by both an increase in global temperature as well as volume fraction of strain-induced martensite. No serrated plastic flow was observed at the highest strain rate ($\dot{\varepsilon} = 10^{-1}$ s^{-1}), c.f. [93]. The serrations can be related, according to the common understanding in the literature [94], to the localization of plastic strain in macroscopic bands of several micrometer thickness propagating along the gauge length—known as PLC bands. The formation of these macroscopic bands of strain localizations is accompanied by temperature increase which can be recorded using infrared thermography [93]. Figure 15.11 shows exemplarily the results of in situ thermographic measurements during tensile test at room temperature and a nominal strain rate of 10^{-3} s^{-1}. Figure 15.11a shows the true stress versus true strain curve (black) in combination with temperature evolution profiles evaluated at three different points along the gauge length (green, grey, red). For better visibility, the temperature-time curves are shifted by $\Delta T = 5$ K. A continuous temperature increase was recorded in the first part of the stress-strain curve ($\varepsilon < 0.15$) which can be correlated directly with both the onset of plastic deformation as well as the martensitic phase transformation. It is well known from previous investigations [95] that the martensitic phase transformation in this CrMnNi steel variant with 3 wt% Ni starts immediately after passing the yield point. The course of temperature-time curves at higher strain levels ($\varepsilon > 0.15$) reveals clearly an oscillating behavior related to the formation and movement of PLC bands along the gauge length. The PLC bands form on the left side of the gauge length (green curve) and move along the gauge length (grey and red curve). The temperature maxima for the three different points

can be followed indicating that one band is followed by another one. In addition, Fig. 15.11b shows a sequence of thermograms taken at different subsequent strain levels (given as ε_t) illustrating the development and propagation of two individual bands along the gauge length. The macroscopic localization of strain inside these bands is related to an increase of temperature of few Kelvin. Moreover, the frequency of emerging PLC bands is quite high. Thus, the specimen gauge length cannot cool down completely before the next band appears resulting in a continuous increase of temperature over the whole test. The analysis of the recorded thermograms allowed for the evaluation of the number of PLC bands, the maximum temperature increase within individual bands as well as their velocity propagating along the gauge length in dependence on the nominal strain rate. It was revealed that with increasing strain rate the number of emerging bands is decreasing whereas the temperature itself is increasing [96].

Furthermore, the evolution of local strain fields related to PLC bands was evaluated by digital image correlation. For this purpose, optical micrographs were taken using a digital camera during the tensile tests at RT and different nominal strain rates. The strain fields were recorded on the opposite side of specimens used for IR-TG measurements. The initiation and propagation of bands along the gauge length is accompanied not only by an increase in temperature, as described already above, but also by an increase in strain. This is exemplarily shown in Fig. 15.12a–c. Figure 15.12a shows not the entire deformation process. Instead, only a short sequence between 0.22 and 0.32 of true strain is plotted. The thermograms and the calculated strain fields are related to numbers 1 to 6 indicated in the stress-strain curve showing the sequence of two consecutive PLC bands. In the present case, the PLC bands initiated always at the lower part of the gauge length and propagated in bottom-up direction on both sides of the specimen as seen from the thermograms and DIC images in Fig. 15.12b–c. The local strain fields are provided in terms of von Mises equivalent strain ε_{vM}. It turned out from the fully-coupled measurements that the PLC bands are characterized by both temperature and strain localization. Thus, the localized strain within an individual band is about 3%. In addition, the nominal strain rate has a significant influence on the formation of PLC bands. In general, it can be summarized

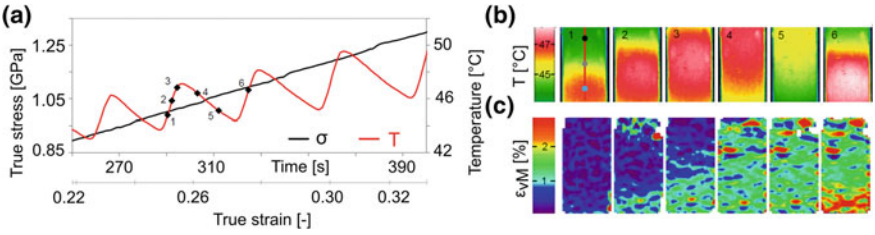

Fig. 15.12 Results of the full-field measurements on two opposite sides of the gauge length of the specimen of X5CrMnNi17-7-4 steel tested in tension at room temperature and a nominal strain rate of 10^{-3} s^{-1}. **a** Section of the true stress-true strain curve and the temperature-time curve. **b** Infrared thermograms taken at points 1 to 6 indicated in (**a**). **c** Corresponding local strain fields calculated for the opposite side of the gauge length. Partly reproduced from [93]

that as lower the strain rate is as more frequently PLC bands occurs. In contrast, both the increase in temperature as well as the velocity of PLC bands are smaller than at higher strain rates. Moreover, different band propagation directions were observed. Thus, at lower strain rates, bands nucleate at different places and run either top-down or bottom-up. At higher strain rates, bands nucleate either at the upper or lower part of the gauge length and propagate then in one direction only [96].

15.4.1.4 Local Hardness of Individual Microstructure Constituents Studied by Nanoindentation

In addition to microstructure evolution and kinetics of deformation processes, the local mechanical behavior of CrMnNi TRIP steel with medium austenite stability X5CrMnNi16-6-6 was investigated by nanoindentation. The focus was set on the local hardness of individual microstructural components (γ-austenite, ε-martensite and α'-martensite). To investigate the strain-hardening behavior, initial hardness of the austenite was determined on an undeformed reference specimen and compared to the local hardness of tensile pre-deformed specimen ($\varepsilon = 15\%$). For this purpose, different grain orientations were chosen both with respect to the loading axis during tensile pre-deformation as well as with respect to the indentation axis. Details on the experimental setup can be found in [60].

In the initial state, the measured indentation hardness is between 4.1 and 4.9 GPa and only slightly dependent on grain orientation. In accordance with literature [97], grain orientations with indentation axis near ⟨111⟩ show the highest indentation hardness. In some of the indentation experiments, pronounced pop-in events occurred during the indentation of undeformed austenite as shown exemplarily by a load-displacement curve in Fig. 15.13a. At about 550 μN a pronounced deviation from

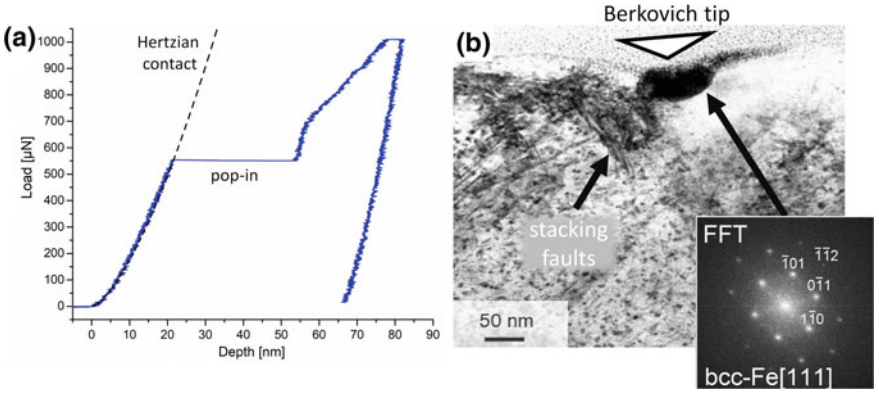

Fig. 15.13 Nanoindentation on undeformed austenite. **a** Load-displacement curve with occurring pop-in event and Hertzian elastic contact solution fitted to the elastic part of the curve. **b** α'-martensite nucleus formed during nanoindentation experiment with stacking faults located close to the indent

the Hertzian elastic contact solution (dashed line) is observed—the so-called pop-in event. The displacement of this single pop-in event is quite large of about 30 nm. In order to clarify whether the pop-in is the result of an avalanche-like movement of dislocations or of an indentation-induced martensitic phase transformation, a lamella was extracted across the indentation area using focused ion beam (FIB) technique. The lamella was investigated in TEM and the results are shown in Fig. 15.13b.

Figure 15.13b shows that directly below the indent an α'-martensite grain has been formed which was proofed by the diffraction pattern obtained from the Fast-Fourier Transformation of high-resolution TEM image (see insert). In the direct vicinity to the α'-martensite nucleus, stacking faults were found which are assumed to be caused by the indentation of the austenite. In order to examine whether α'-martensite formation can be regarded as the reason for the pop-in event, the theoretical displacement caused by α'-martensite transformation was calculated. The maximum shape strain of the martensitic transformation is assumed to be of 0.24 [98] for the case that the indentation axis is parallel to the direction of maximum shape change. The thickness of the α'-martensite nucleus was measured to be 50 nm which corresponds to a pop-in displacement of about 12 nm. Consequently, α'-martensite formation cannot be the only reason for the pop-in event which corresponds to a displacement of more than 30 nm. More likely, the combination of the formation of stacking faults and α'-martensite together caused this huge displacement. Ahn et al. [99] observed similar pop-in behavior in a high nitrogen steel and excluded also the α'-martensite formation as the only reason for the pop-in event.

In order to determine the indentation hardness of the microstructural constituents in the tensile pre-deformed state, indentation maps were placed within austenitic grains of different orientations covering all three microstructural constituents in a pre-deformed state of $\varepsilon = 15\%$: (i) austenite, (ii) deformation bands with ε-martensite, and (iii) α'-martensite grains. The indentation was performed with a load of 1 mN and the indents were placed with a minimum distance of 1.5 µm. An example for a grain with ⟨125⟩ as indentation axis is shown in Fig. 15.14 (see [60]).

Here, Fig. 15.14a, b show results of EBSD measurements for the area with indentation map and Fig. 15.14c of a single indent placed within the area of a deformation band yielding a pop-in event in the load-displacement curve. The area of FIB lamella for TEM investigations is indicated by white rectangle. Figure 15.14d–f show the corresponding t-SEM and TEM results. In the EBSD maps the austenitic phase is shown in grey, the ε-martensite bands in yellow and the α'-martensite in blue color. Details on all load-displacement curves and indentation hardness and modulus are summarized in [60]. In general, it can be summarized that the overall indentation hardness values of the tensile pre-deformed state are increased in average of about 19% compared to the non-deformed state as it was expected. In addition, an orientation dependency was found for indentation hardness values in the pre-deformed specimen. Thus, austenitic grains with ⟨101⟩ or ⟨111⟩ orientation of the loading axis during the tensile pre-deformation showed higher indentation hardness values compared to other grain orientations such as ⟨001⟩. These grain orientations are favored for the formation of largely extended stacking faults resulting in a significant reduction of mean free path of dislocations yielding pronounced strain hardening. In contrast,

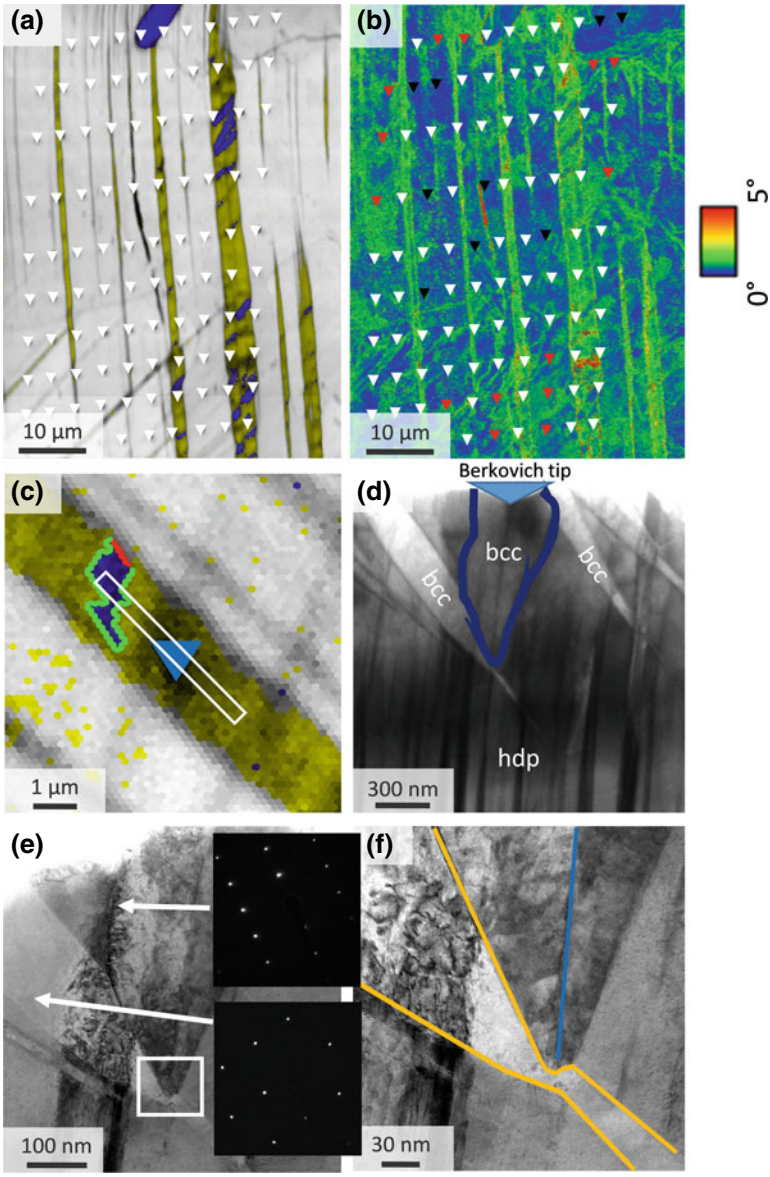

Fig. 15.14 Results of microstructural investigation complementing nanoindentation measurements on steel X5CrMnNi16-6-6. **a** EBSD phase map of austenitic grain with ⟨125⟩ orientation of the indentation axis. Grey—austenite, yellow—ε-martensite, blue—α'-martensite, indents marked by white triangles. **b** Overlay of Kernal average misorientation map (max. misorientation angle of 5°) with 10 × 10 indentation map. Indents corresponding to maximum or minimum indentation hardness are indicated by red and black triangles, respectively. **c** Detail of deformation band with ε-martensite and α'-martensite and an indent yielding pronounced pop-in event. Area for taking FIB lamella is indicated by white rectangle. **d** Transmission-SEM (t-SEM) micrograph of the FIB lamella. **e**, **f** Results of TEM investigations. Partly reproduced from [60]

grain orientations close to ⟨001⟩ are favored for slip of regular dislocations resulting in a lower density of deformation bands and α'-martensite nuclei causing lower strain hardening effect. Such an example is shown in Fig. 15.14a for orientation ⟨125⟩ of loading axis.

In addition, austenite orientations which showed increased slip of regular dislocations can experience clear differences in the strain hardening. Figure 15.14b shows a kernal average misorientation (KAM) map with marked indents within austenite. Red triangles correspond to indents within an austenite with high KAM and black triangles correspond to indents within austenite with low KAM. Thus, areas with increased KAM show an average indentation hardness increase of about 12% compared to indents within lower KAM. This is due to the higher defect density; the higher KAM is a result of a higher number of geometrically necessary dislocations and thus correlates with a higher dislocation density [100].

The indentation hardness of ε-martensite was always higher than the hardness of the deformed austenite and was between 5.7 and 8.5 GPa. A dependency of the hardness on the orientation of the ε-martensite was recognizable. (0001) perpendicular to the direction of indentation showed the highest indentation hardness. In addition, some ε-martensite orientations showed also a distinct pop-in behavior. Figure 15.14c shows a band contrast map with a deformation band consisting of ε-martensite and an α'-martensite nucleus which has formed by the pre-deformation. The green and red lines mark the Kurdjumov-Sachs orientation relationship [101] between α'/ε and α'/γ. The blue triangle marks the position of an indent with occurring pop-in event within ε-martensite. In order to investigate the reason for the pop-in event a FIB lamella was extracted (marked by white box). Figure 15.14d, e show the cross section of the extracted FIB lamella observed in SEM in transmission mode (t-SEM) and in TEM, respectively.

The lamella shows numerous bcc nuclei with a plate-like structure which are inclined at an angle of approximately 45°. By selected area diffraction (SAED) it was shown that all of that plate-like α'-martensite nuclei had the same orientation. Due to the similar orientation and morphology, it can be concluded that these α'-martensite nuclei are the result of the pre-deformation. Directly beneath the indent an additional bcc grain has formed. In contrast to all other martensite nuclei, this one has a different morphology and also a different orientation, which implies that this α'-martensite is the result of indentation. In addition, the 45° tilted α'-martensite grain shows a small misalignment which is marked by the white box in Fig. 15.14e and is shown in detail in Fig. 15.14f. This misalignment (marked by orange lines) is caused by the indentation-induced martensite. The expanding α'-martensite grain ran up to or even into the already existing deformation-induced α' martensite and caused a small shearing effect. Furthermore, the indentation-induced martensite contains a grain boundary (marked by blue line). SAED observations and the fact that just one pop-in event was noticeable in the load displacement curve indicate that the formed indentation-induced α'-martensite grains are twins [60].

The hardness of the α'-martensite introduced by the pre-deformation was determined to 6.3 GPa up to 10.5 GPa. However, the hardness of α'-martensite depends on several aspects. On the one hand, hardness is determined by the orientation of the

crystal. For example, α'-martensite grains with an orientation close to $\langle 111 \rangle$ showed the highest indentation hardness. Furthermore, the grain size does affect the determined indentation hardness since additional interfacial effects between dislocations and grain boundaries have to be considered. In addition, also the defect density of the studied α'-martensite additionally influences the determined indentation hardness [60].

15.4.2 Phase Transformation Behavior of Mg-PSZ Studied by Acoustic Emission

The phase transformation and damage behavior of MgO partially-stabilized zirconia (Mg-PSZ) provided by FRIATEC (Germany) was studied by acoustic emission corroborated by SEM investigations. The microstructure of the initial state before deformation in Fig. 15.15a shows polycrystalline grain structure with cubic-tetragonal crystal lattice, pores and spinels [102]. In particular, tetragonal lenses are embedded into a cubic matrix. Spinels are formed typically at the grain boundaries, but also inside grains. Moreover, in the vicinity of spinels a further microstructural feature becomes apparent—monoclinic lenses. This transformation of the cubic/tetragonal phase into the monoclinic phase in these regions is the consequence of a separation of the MgO as the stabilizer of the tetragonal phase occurring during the sinter process.

Figure 15.15b, c show the microstructure of Mg-PSZ after compression test up to 2 GPa. Both the martensitic phase transformation as well as the damage of Mg-PSZ can be revealed. Thus, band-like structures exhibiting monoclinic crystal lattice evolve under various angles with respect to the loading axis (horizontal) within some grains. This tetragonal/monoclinic phase transformation is associated with a volume expansion of about 4.9% [103] enabling enhanced damage tolerance of the ceramic due to crack-closure effects. However, pronounced damage is observed in addition to the phase transformation. Thus, numerous short cracks where observed within

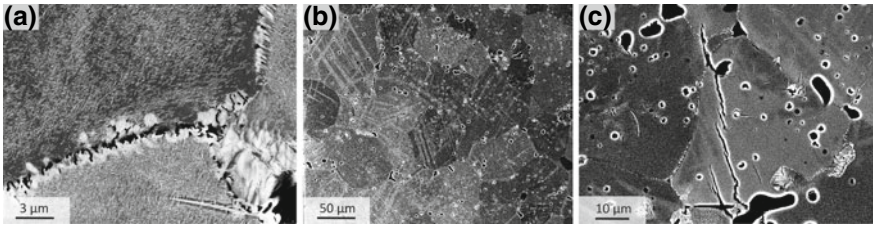

Fig. 15.15 Microstructure of Mg-PSZ. **a** Initial state showing tetragonal lenses in individual grains of Mg-PSZ. Secondary phases like spinel and silicates are formed at the grain boundaries leading to local transformation into monoclinic zirconia phase. **b** Microstructure of a Mg-PSZ after compression test up to 2 GPa showing both phase transformation and damage behavior. **c** Cracks running along monoclinic deformation bands

grains initiating either on pores or spinel precipitates. Cracks were also observed running along deformation bands with monoclinic structure (see Fig. 15.15c). The formation of cracks as well as the martensitic phase transformation release elastic waves within the Mg-PSZ which can be recorded as acoustic signals by a transducer placed at the specimen surface. For the in situ acoustic emission measurements a rectangular specimen of $2 \times 2 \times 4$ mm^3 was stepwise deformed under compression with stress intervals of 200 MPa in the stress range of 1.2–2 GPa applying partial unloading at each stress interval.

For the mechanical test, the push-pull loading stage described above for in situ tensile tests was modified using two compression platens made from tungsten-carbide. One side of the compression parts was manufactured as a ball-shaped scraper for self-centering of the whole setup including ceramic specimen. For each loading step the AE data stream was continuously recorded. Figure 15.16 shows the results of the compression tests and the acoustic emission measurements. Thus, Fig. 15.16a shows the stress versus compressive strain curves for five loading steps. In Fig. 15.16b, the complete AE data stream (grey) is shown together with the stress versus time curve for the last loading sequence between 1 and 2 GPa (grey curve in Fig. 15.16a). The results of the analysis of the AE data are summarized in Fig. 15.16c, d showing two

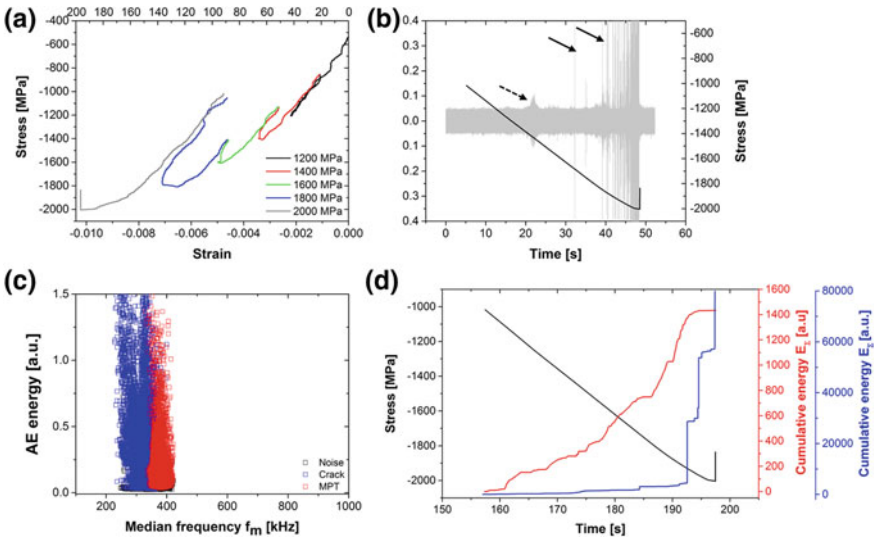

Fig. 15.16 Results of acoustic emission measurements during compression tests up to 2 GPa including partial unloading. **a** Stress-compressive strain curves. **b** Overlay of stress versus time curve and recorded acoustic emission stream measurement for the last loading cycle from 1 GPa up to 2 GPa. **c** Results of the AE cluster analysis showing two identified clusters with different properties (AE energy E and median frequency f_m) in frequency domain revealing two different source mechanisms: (i) phase transformation—red, (ii) crack formation—blue. **d** Temporal evolution of the two clusters during compression. Note the two different scales for the cumulative AE for both clusters

identified sources of acoustic emission (Fig. 15.16c) and their temporal evolution (Fig. 15.16d).

It becomes obvious that during the first loading sequence between 400 MPa and 1.2 GPa no pronounced changes occur in the specimen. Thus, the loading and unloading curves follow the same path without any change in the slope showing a fully elastic behavior. The same is observed from the acoustic emission. No special features beside the laboratory noise were detected. However, the situation is changing with increase in stress level applied to the specimen already starting with the second loading cycle between 800 MPa and 1.4 GPa. Here, a deviation of the stress-strain response for the loading and unloading path is observed above 1.2 GPa, which may be explained by damage occurring within the specimen or by the begin of phase transformation from tetragonal to monoclinic phase. This deviation between loading and unloading path becomes more pronounced with increase in applied stress levels. Thus, most pronounced difference is observed for the last loading sequence between 1.0 and 2.0 GPa, which finally led to the brittle failure of the specimen at 2.0 GPa. Moreover, a pronounced and increasing deviation from the elastic behavior is observed during the loading paths up to 1.6, 1.8 and 2.0 GPa giving rise to the assumption that a martensitic phase transformation occurred at these load levels. This assumption is well supported by the results of the AE data analysis. For these three stress levels, two different types of transient AE signals can be revealed from the complete data stream.

Whereas the first type is of high amplitude transient signals characterized by a very short rise time (close to the end of the data stream, bold arrows Fig. 15.16b), the second type is of low amplitude, but still transient signals with increased rise time (dashed arrow Fig. 15.16b). The results of the AE cluster analysis revealed two different clusters of signals (beside the laboratory noise), which can be related due to their different parameters in the frequency domain clearly to two different sources. Thus, cluster 1 contains all signals characterized by high AE energy and narrow band of median frequency around 300 kHz (blue symbols). Signals of this cluster are caused by initiation and propagation of brittle cracks. This is supported by the signals with the highest AE energies corresponding to the cracks leading to final failure (marked by bold arrows in Fig. 15.16b). Cluster 2 is composed by signals with lower AE energy compared to members of Cluster 1 and also a narrow band of median frequency at around 400 kHz (red symbols). Signals of this cluster are caused by the martensitic phase transformation from tetragonal to monoclinic phase (marked by dashed arrow in Fig. 15.16b). These findings are supported by the temporal evolution of these clusters over the entire compression path shown in Fig. 15.16d. Here, the evolution of the cumulated AE energy is shown for both clusters in combination with the stress versus time curve. Beside the different scale of cumulative AE energy, both clusters reveal also different temporal evolution. Whereas for Cluster 1 a moderate increase of E_{Σ} is observed until a significant rise right before the final failure, Cluster 2 shows a continuous increase until the end of the test. The results of the AE data analysis can be supported by additional XRD measurements for interrupted tests at different stress levels (1.2, 1.6, 1.8 GPa). At 2.0 GPa no XRD measurements were performed since the specimens failed and only

small pieces were retained. The phase analysis done by XRD revealed clearly an increase in the volume fraction of monoclinic phase from 18% in the undeformed state up to 36% obtained after compression test up to 1.8 GPa. Both the AE results and the results of XRD measurements are supported by literature data claiming on a transformation stress in compression of above 800 MPa for the tetragonal/monoclinic phase transformation [104].

15.4.3 Damage Behavior of TRIP Matrix Composite Studied by Digital Image Correlation

TRIP matrix composites made of TRIP steel X5CrMnNi16-6-6 and 10 vol% of Mg-PSZ were studied using in situ deformation in SEM both under uniaxial tensile or cyclic loading at room temperature. The TRIP matrix composites were manufactured by a powder metallurgical route and consolidated by uniaxial pressing at 1523 K. Typical microstructure is shown in Fig. 15.17. Here, different types of Mg-PSZ particles are visible. First of all, along grain boundaries or at the steel/ceramic interface additional phases enriched with silicon and aluminum were detected corresponding to spinel or silicate. In addition, different microstructures of Mg-PSZ

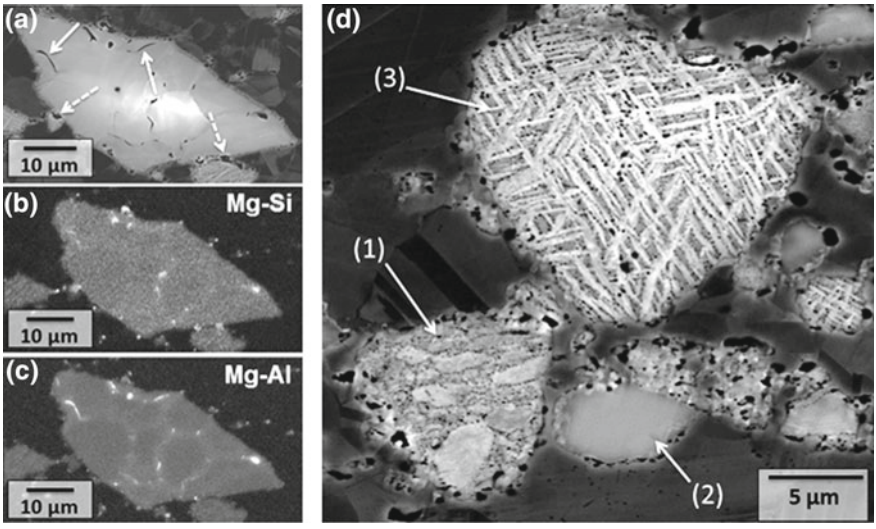

Fig. 15.17 Microstructure of Mg-PSZ particles embedded in steel matrix of X5CrMnNi16-6-6 after uniaxial pressing. **a**, **d** SEM micrographs in backscattered electron contrast. Spinel marked by bold white arrows. Silicate marked by dashed white arrows. **b**, **c** EDX element maps of Mg–Si (**b**) and Mg–Al (**c**). (**d**) Three different types of microstructures of Mg-PSZ particles. (1) Agglomerate of small monoclinic Mg-PSZ particles. (2) Cubic/tetragonal Mg-PSZ particle with monoclinic rime. (3) Mg-PSZ particle with monoclinic needles embedded in cubic/tetragonal matrix [105]

were observed such as (1) agglomerates of small monoclinic Mg-PSZ particles, (2) cubic/tetragonal Mg-PSZ particles with a rime of monoclinic structure in the vicinity of the steel/ceramic interface, and (3) large Mg-PSZ particles with monoclinic needles embedded in a cubic/tetragonal matrix. In the cubic/tetragonal areas of Mg-PSZ grains no tetragonal lenses as described above for the pure Mg-PSZ ceramic were observed. The formation of spinel or silicate particles at grain boundaries or interfaces of the ceramic is the consequence of diffusion processes of MgO as the stabilizer for the cubic/tetragonal phase. As a further consequence, the Mg-PSZ particles are destabilized and transform into the monoclinic phase already during the manufacturing process.

Figure 15.18 shows exemplarily the development of damage of a ceramic particle during cyclic loading with a total strain amplitude of $\varepsilon_{a,t} = 4 \times 10^{-3}$ as a function of number of cycles. Figure 15.18a shows the initial microstructure around individual Mg-PSZ particle demonstrating good bonding between steel matrix and ceramic particle. Nevertheless, spinel and silicate precipitates were found. Already after few cycles, the crack formation can be seen on a silicate at the interface between particle and steel matrix (see arrow Fig. 15.18b). The crack grows in the further course of cyclic loading (Fig. 15.18c) along the interface and leads, thus, to the decohesion of the particle from the steel matrix. At $N = 1750$, additional decohesion is clearly visible on the opposite side (see arrow Fig. 15.18c). Preferably the debonding of the particles occurs at boundaries perpendicular to the load direction starting at silicate precipitates. The second damage mechanism observed is the fracture of the ZrO_2 particles. Similar to the decohesion, the fracture occurs perpendicular to the load direction (horizontal). Furthermore, both the formation of deformation bands as well as the formation of α'-martensite within these bands was observed in austenitic grains of the steel matrix. However, within the ceramic particles no martensitic phase transformation was detected neither in the middle of the particle nor in the vicinity of cracks.

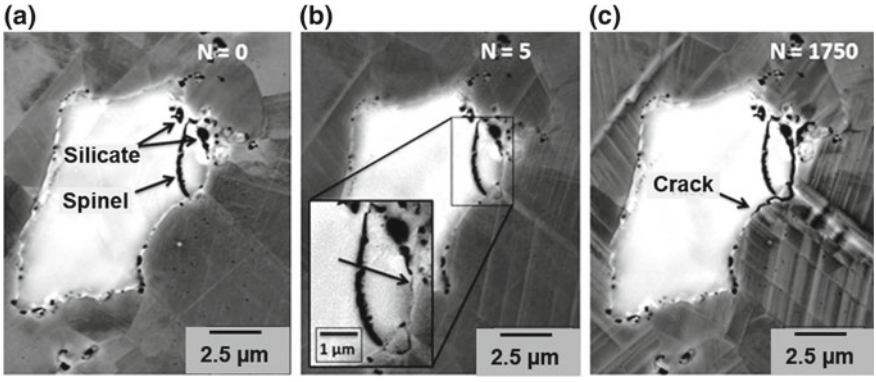

Fig. 15.18 Damage evolution on a Mg-PSZ particle in X5CrMnNi16-6-6 TRIP steel during cyclic deformation with a total strain amplitude of $\varepsilon_{a,t} = 4 \times 10^{-3}$. **a** Initial microstructure. **b** After 5 cycles. **c** After 1750 cycles. Load direction is horizontal [105]

Investigations on the damage behavior of TRIP-matrix composites were performed also under tensile loading at room temperature and were complemented by DIC calculations. Both the damage behavior as well as the strain localization within the austenitic matrix were studied. In comparison to DIC measurements on pure steel specimens, the application of DIC on composite materials is somehow more challenging. Thus, the etching procedure used for the steel specimens was not applicable since, in particular, the interface boundaries were attacked by the etching agent. To obtain a small-sized point pattern at the specimen surface a plasma process was used for the deposition of fine precipitates. Using this contrast, it was possible to perform DIC calculations for composite material under tensile load using SEM micrographs in secondary electron contrast. Figure 15.19 shows two SEM micrographs (Fig. 15.19a, b) taken at different macroscopic strain levels ($\varepsilon = 1.09\%$ and $\varepsilon = 3.47\%$) and the corresponding results of the DIC calculations in terms of von Mises equivalent strain (Fig. 15.19c, d). Both the SEM images as well as the local strain fields reveal that damage at the steel/ceramic interface occurs quite early in the deformation process already at 1% of elongation (marked by black arrows). In addition, the formation of deformation bands as well as α'-martensite were detected by DIC at strain levels of about $\varepsilon = 3.47\%$ (marked by white arrows). At $\varepsilon = 3.47\%$,

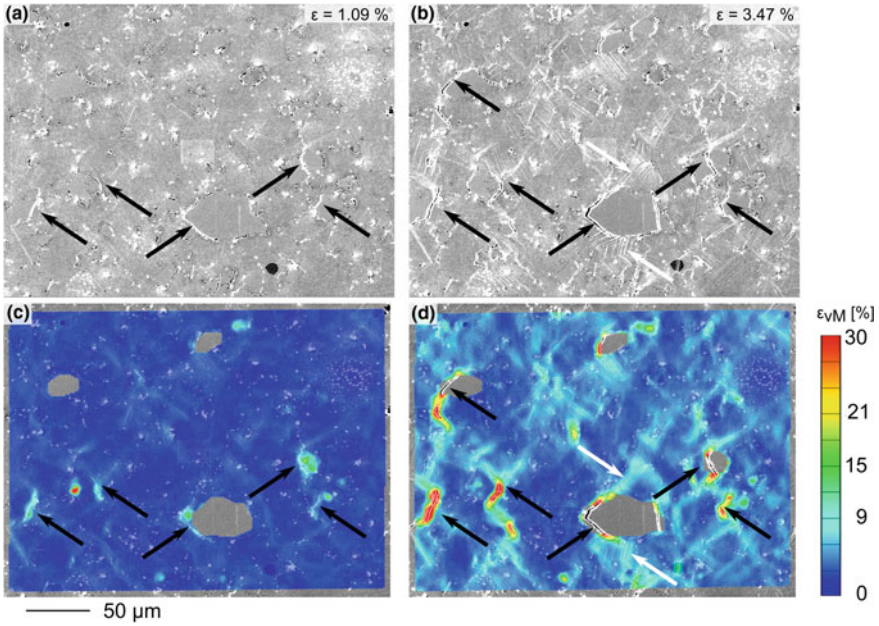

Fig. 15.19 Results of digital image correlation applied on SEM micrographs obtained during in situ tensile deformation at RT up to 4% global strain on TRIP matrix composite made of X5CrMnNi-16-6-6 with 10 vol% Mg-PSZ. (**a**, **b**) SEM micrographs in secondary electron contrast at $\varepsilon = 1.09\%$ (**a**) and $\varepsilon = 3.47\%$ (**b**), respectively. (**c**, **d**) Local strain fields obtained from DIC calculations at $\varepsilon = 1.09\%$ (**a**) and $\varepsilon = 3.47\%$ (**b**), respectively. Loading axis horizontal [92]

certain amount of steel/ceramic interface boundaries has been damaged and individual short cracks are grown together leading to final failure of the specimen (outside AOI). Furthermore, fracture of individual Mg-PSZ particles was also observed.

15.5 Conclusions

The local deformation behavior of high-alloy CrMnNi TRIP/TWIP steels, Q&P steels, MgO-partially stabilized zirconia and TRIP matrix composite have been studied using various in situ techniques such as (i) in situ deformation in scanning electron microscope in combination with digital image correlation, (ii) nanoindentation, (iii) acoustic emission measurements, and (iv) full-field measurements using infrared thermography and digital image correlation. The following general conclusions regarding the application of complementary in situ techniques can be drawn:

- The applied SEM-DIC technique for studies on strain localizations both in TRIP/TWIP as well as Q&P steels allowed a sub-micrometer resolution both at room temperature as well as at elevated temperatures enabling the calculation of the magnitude of shear for stacking fault mediated deformation bands, twin bundles and α'-martensite grains. Even in small regions (<5 μm) of interdendritic austenite in Q&P steel, the strain localization was measured for the fresh-formed martensite.
- The AE measurements during tensile deformation of CrMnNi TRIP/TWIP steels both at room temperature and at 373 K allowed the separation of the individual deformation mechanisms such as (i) dislocation glide, (ii) movement of partial-dislocations, (iii) twinning, and (iv) the martensitic phase transformation. The application of the ASK-cluster algorithm allowed to study the kinetics of these different deformation mechanisms. Furthermore, an excellent agreement of the temporal evolution of AE data related to martensitic phase transformation with the evolution of the martensitic volume fraction both experimentally obtained by ferromagnetic measurements as well as from the Olson-Cohen model was obtained.
- The application of infrared thermography and digital image correlation based on optical microscopy allowed the investigation of propagating macroscopic strain localizations in terms of Portevin Le Chatelier effect in the steel with the lowest austenite stability. Macroscopic strain is localized in PLC bands causing also a temperature increase. The propagating bands were well characterized and analyzed by both full-field measurement techniques. A good correlation of temperature fields and local strain fields was obtained, which allowed the determination of characteristic parameters for the evolution and propagation of these bands.
- Nanoindentation experiments performed on non-deformed and pre-deformed CrMnNi TRIP steel specimens revealed both pop-in effects caused by either martensitic phase transformation and/or formation of stacking faults as well as an

orientation dependence of the indentation hardness. Furthermore, different indentation hardness values were obtained with increasing values in the following order: (i) pre-deformed austenite, (ii) deformation bands consisting of stacking faults, and (iii) α'-martensite.

- For MgO-partially stabilized zirconia, the application of AE measurements during compressive loading up to 2 GPa revealed that the onset of phase transformation from tetragonal to monoclinic phase occurs above 1200 MPa. As a second AE source the formation of cracks leading to final failure of the specimens was identified.
- The deformation and damage behavior of TRIP matrix composite studied by in situ tensile and cyclic loading experiments in SEM revealed that the steel/ceramic interface undergoes a decohesion quite early during the deformation process, mainly caused by the presence of silicate precipitates at the interface. Beside this fact, the application of the DIC techniques bears also some difficulties. Thus, the contrast patterning at the surface for getting high-resolution DIC results is challenging. Nevertheless, first results showed that both strain localization inside deformation bands in the steel matrix as well as crack initiation and propagation at the steel/ceramic interface can be detected by DIC.

Acknowledgements This work was funded by the German Research Foundation (Deutsche Forschungsgemeinschaft, DFG) in subproject B5, and was created as part of the Collaborative Research Center TRIP-Matrix-Composites (Project number 54473466—CRC 799). The experimental work and research of Dipl.-Ing. Christian Segel is gratefully acknowledged providing substantial contribution on in situ testing in SEM and DIC. In addition, the authors thank Dipl.-Ing. Alexandra Illgen for performing the investigations on Portevin Le Chatelier effect using thermography and digital image correlation. Dr. Mikhail Motylenko is gratefully acknowledged for TEM investigations and Dr. Christian Schimpf for XRD analysis on the Q&P steel. Special thanks go to Prof. Alexei Vinogradov and Ph.D. Mikhail Linderov for their support regarding the AE data acquisition and analysis. In addition, many thanks go to K. Zuber, A. Leuteritz and R. Prang for preparation of specimens for SEM and TEM investigations and to G. Schade for support during mechanical tests.

References

1. D. Raabe, D. Ponge, O. Dmitrieva, B. Sander, Scr. Mater. **60**, 1141 (2009). https://doi.org/10.1016/j.scriptamat.2009.02.062
2. G.B. Olson, M. Cohen, J. Less-Common Metals **28**, 107 (1972)
3. A. Weidner, S. Martin, V. Klemm, U. Martin, H. Biermann, Scripta Mater. **64**, 513 (2011). https://doi.org/10.1016/j.scriptamat.2010.11.028
4. S. Martin, C. Ullrich, D. Šimek, U. Martin, D. Rafaja, J. Appl. Crystallogr. **44**, 779 (2011). https://doi.org/10.1107/S0021889811019558
5. S. Martin, C. Ullrich, D. Rafaja, Mater. Today: Proc. **2**, S643 (2015). https://doi.org/10.1016/j.matpr.2015.07.366
6. A. Jahn, A. Kovalev, A. Weiß, S. Wolf, L. Krüger, P.R. Scheller, Steel Res. Int. **82**, 39 (2011). https://doi.org/10.1002/srin.201000228

7. A. Jahn, A. Kovalev, A. Weiβ, P.R. Scheller, S. Wolf, L. Krüger, S. Martin, U. Martin, in *Composite Structures* (2009)
8. S. Martin, S. Wolf, U. Martin, L. Krüger, D. Rafaja, Metall. Mater. Trans. A **47**, 49 (2016). https://doi.org/10.1007/s11661-014-2684-4
9. H. Biermann, A. Glage, M. Droste, Metall. Mater. Trans. A **47**, 84 (2016). https://doi.org/10.1007/s11661-014-2723-1
10. D. Kulawinski, S. Ackermann, A. Seupel, T. Lippmann, S. Henkel, M. Kuna, A. Weidner, H. Biermann, Mater. Sci. Eng., A **642**, 317 (2015). https://doi.org/10.1016/j.msea.2015.06.083
11. R. Eckner, L. Krüger, M. Motylenko, A.S. Savinykh, S.V. Razorenov, G.V. Garkushin, EPJ Web Conf. **183**, 03007 (2018). https://doi.org/10.1051/epjconf/201818303007
12. S. Ackermann, S. Martin, M.R. Schwarz, C. Schimpf, D. Kulawinski, C. Lathe, S. Henkel, D. Rafaja, H. Biermann, A. Weidner, Metall. Mater. Trans. A **47**, 95 (2016). https://doi.org/10.1007/s11661-015-3082-2
13. D. Rafaja, C. Krbetschek, D. Borisova, G. Schreiber, V. Klemm, Thin Solid Films **530**, 105 (2013). https://doi.org/10.1016/j.tsf.2012.07.067
14. A. Weidner, A. Glage, H. Biermann, Proced. Eng. **2**, 1961 (2010). https://doi.org/10.1016/j.proeng.2010.03.211
15. D. Borisova, V. Klemm, S. Martin, S. Wolf, D. Rafaja, Adv. Eng. Mater. **15**, 571 (2013). https://doi.org/10.1002/adem.201200327
16. A. Jahn, A. Kovalev, A. Weiß, P.R. Scheller, Steel Res. Int. **82**, 1108 (2011). https://doi.org/10.1002/srin.201100063
17. C. Weigelt, G. Schmidt, C.G. Aneziris, R. Eckner, D. Ehinger, L. Krüger, C. Ullrich, D. Rafaja, J. Alloys Compd. **695**, 9 (2017). https://doi.org/10.1016/j.jallcom.2016.10.176
18. A. Weidner, A. Müller, A. Weiss, H. Biermann, Mater. Sci. Eng., A **571**, 68 (2013). https://doi.org/10.1016/j.msea.2013.02.008
19. M. Wendler, C. Ullrich, M. Hauser, L. Krüger, O. Volkova, A. Weiß, J. Mola, Acta Mater. **133**, 346 (2017). https://doi.org/10.1016/j.actamat.2017.05.049
20. M. Droste, C. Ullrich, M. Motylenko, M. Fleischer, A. Weidner, J. Freudenberger, D. Rafaja, H. Biermann, Int. J. Fatigue **106**, 143 (2018). https://doi.org/10.1016/j.ijfatigue.2017.10.001
21. D. Ehinger, L. Krüger, U. Martin, C. Weigelt, C.G. Aneziris, Steel Res. Int. **83**, 565 (2012). https://doi.org/10.1002/srin.201100302
22. S. Martin, S. Wolf, U. Martin, L. Krüger, SSP **172–174**, 172 (2011). https://doi.org/10.4028/www.scientific.net/SSP.172-174.172
23. W. Roberts, B. Lehtinen, K.E. Easterling, Acta Metall. **24**, 745 (1976). https://doi.org/10.1016/0001-6160(76)90109-7
24. H. Zhou, L. Mishnaevsky, P. Brøndsted, J. Tan, L. Gui, Chin. Sci. Bull. **55**, 1199 (2010). https://doi.org/10.1007/s11434-009-0560-1
25. J. Geathers, C.J. Torbet, J.W. Jones, S. Daly, Int. J. Fatigue **70**, 154 (2015). https://doi.org/10.1016/j.ijfatigue.2014.09.007
26. D. Yan, C.C. Tasan, D. Raabe, Acta Mater. **96**, 399 (2015). https://doi.org/10.1016/j.actamat.2015.05.038
27. M. Grediac, F. Hild, *Full-Field Measurements and Identification in Solid Mechanics* (Wiley, New York, NY, 2012)
28. M. Grédiac, Compos. A **35**, 751 (2004). https://doi.org/10.1016/j.compositesa.2004.01.019
29. H. Schreier, J.-J. Orteu, M.A. Sutton, *Image Correlation for Shape, Motion and Deformation Measurements* (Springer, US, Boston, MA, 2009)
30. C.C. Tasan, J.P.M. Hoefnagels, M.G.D. Geers, Scr. Mater. **62**, 835 (2010). https://doi.org/10.1016/j.scriptamat.2010.02.014
31. A. Weidner, C. Segel, H. Biermann, Mater. Lett. **143**, 155 (2015). https://doi.org/10.1016/j.matlet.2014.12.098
32. F. Di Gioacchino, J. Quinta da Fonseca, Exp. Mech. **53**, 743 (2013). https://doi.org/10.1007/s11340-012-9685-2
33. M.-M. Wang, J.-C. Hell, C.C. Tasan, Scr. Mater. **138**, 1 (2017). https://doi.org/10.1016/j.scriptamat.2017.05.021

34. H. Ghadbeigi, C. Pinna, S. Celotto, Mater. Sci. Eng., A **588**, 420 (2013). https://doi.org/10.1016/j.msea.2013.09.048
35. H. Na, S. Nambu, M. Ojima, J. Inoue, T. Koseki, Scr. Mater. **69**, 793 (2013). https://doi.org/10.1016/j.scriptamat.2013.08.030
36. N.A. Fouad, T. Richter, *Leitfaden Thermografie im Bauwesen: Theorie, Anwendungsgebiete, praktische Umsetzung*, 4., überarb. und erw. Aufl (Fraunhofer IRB-Verl, Stuttgart, 2012)
37. S. Bagavathiappan, B.B. Lahiri, T. Saravanan, J. Philip, T. Jayakumar, Infrared Phys. Technol. **60**, 35 (2013). https://doi.org/10.1016/j.infrared.2013.03.006
38. W. Boas, M.E. Hargreaves, Proc. R. Soc. A **193**, 89 (1948)
39. W.S. Farren, G.I. Taylor, Proc. Royal Soc. A: Math. Phys. Eng. Sci. **107**, 422 (1925). https://doi.org/10.1098/rspa.1925.0034
40. E.A. Pieczyska, S.P. Gadaj, W.K. Nowacki, H. Tobushi, Exp. Mech. **46**, 531 (2006). https://doi.org/10.1007/s11340-006-8351-y
41. A. Saeed-Akbari, A.K. Mishra, J. Mayer, W. Bleck, Metall. Mater. Trans. A **43**, 1705 (2012). https://doi.org/10.1007/s11661-011-1070-8
42. L. Bodelot, E. Charkaluk, L. Sabatier, P. Dufrénoy, Mech. Mater. **43**, 654 (2011). https://doi.org/10.1016/j.mechmat.2011.08.006
43. L. Chen, J.-K. Kim, S.-K. Kim, G.-S. Kim, K.-G. Chin, B.C. De Cooman, Steel Res. Int. **81**, 552 (2010). https://doi.org/10.1002/srin.201000044
44. C.U. Große, M. Ohtsu (eds.), *Acoustic Emission Testing: Basics for Research—Applications in Civil Engineering* (Springer, Berlin, 2008)
45. A. Vinogradov, A. Lazarev, M. Linderov, A. Weidner, H. Biermann, Acta Mater. **61**, 2434 (2013). https://doi.org/10.1016/j.actamat.2013.01.016
46. E. Pomponi, A. Vinogradov, MSSP **40**, 791 (2013). https://doi.org/10.1016/j.ymssp.2013.03.017
47. C.B. Scruby, J. Phys. E: Sci. Instrum. 946 (1987)
48. A. Weidner, H. Biermann, JOM **67**, 1729 (2015). https://doi.org/10.1007/s11837-015-1456-y
49. A. Vinogradov, M. Nadtochiy, S. Hashimoto, S. Miura, Mater. Trans., JIM **36**, 496 (1995) https://doi.org/10.2320/matertrans1989.36.496
50. A. Vinogradov, A. Lazarev, Scr. Mater. **66**, 745 (2012). https://doi.org/10.1016/j.scriptamat.2012.01.053
51. S.M.C. van Bohemen, Phil. Mag. **95**, 210 (2015). https://doi.org/10.1080/14786435.2014.994574
52. M.L. Linderov, C. Segel, A. Weidner, H. Biermann, A.Y. Vinogradov, Phys. Met. Metall. **119**, 388 (2018). https://doi.org/10.1134/S0031918X18040130
53. M. Mandel, W. Kietov, L. Krueger, Defect Diffus. Forum **367**, 42 (2016). https://doi.org/10.4028/www.scientific.net/DDF.367.42
54. W.C. Oliver, G.M. Pharr, J. Mater. Res. **7**, 1564 (1992). https://doi.org/10.1557/JMR.1992.1564
55. K.L. Johnson, *Contact Mechanics* (Cambridge University Press, Cambridge, 1985)
56. Y. Wang, D. Raabe, C. Klüber, F. Roters, Acta Mater. **52**, 2229 (2004). https://doi.org/10.1016/j.actamat.2004.01.016
57. C. Begau, A. Hartmaier, E.P. George, G.M. Pharr, Acta Mater. **59**, 934 (2011). https://doi.org/10.1016/j.actamat.2010.10.016
58. T.-H. Ahn, C.-S. Oh, D.H. Kim, K.H. Oh, H. Bei, E.P. George, H.N. Han, Scr. Mater. **63**, 540 (2010). https://doi.org/10.1016/j.scriptamat.2010.05.024
59. A. Weidner, U.D. Hangen, H. Biermann, Philos. Mag. Lett. **94**, 522 (2014). https://doi.org/10.1080/09500839.2014.941027
60. R. Lehnert, A. Weidner, M. Motylenko, H. Biermann, Adv. Eng. Mater. (2019). https://doi.org/10.1002/adem.201800801
61. A. Weiss, H. Gutte, M. Radtke, P.R. Scheller, WO 2008/009722 A1 (24 Jan 2008)
62. D. Qi-Xun, W. A.-D. Xiao-Nong Cheng, L. Xin-Min, Chin. Phys. **11**, 596 (2002) https://doi.org/10.1088/1009-1963/11/6/315

63. A. Glage, A. Weidner, H. Biermann, Steel Res. Int. **82**, 1040 (2011). https://doi.org/10.1002/srin.201100080
64. J. Mola, B.C. De Cooman, Metall. Mat. Trans. A **44**, 946 (2013). https://doi.org/10.1007/s11661-012-1420-1
65. M. Wendler, M. Hauser, O. Fabrichnaya, L. Krüger, A. Weiß, J. Mola, Mater. Sci. Eng., A **645**, 28 (2015). https://doi.org/10.1016/j.msea.2015.07.084
66. R. Lehnert, A. Weidner, C. Schimpf, M. Wendler, H. Biermann, Materialia 100498 (2019) https://doi.org/10.1016/j.mtla.2019.100498
67. S. Martin, H. Berek, C.G. Aneziris, U. Martin, D. Rafaja, J. Appl. Crystall. **45**, 1136 (2012). https://doi.org/10.1107/S0021889812038733
68. R.H.J. Hannink, P.M. Kelly, B.C. Muddle, J. Am. Ceram. Soc. **83**, 461 (2004). https://doi.org/10.1111/j.1151-2916.2000.tb01221.x
69. A.G. Evans, A.H. Heuer, J. Am. Ceram. Soc. **63**, 241 (1980). https://doi.org/10.1111/j.1151-2916.1980.tb10712.x
70. D.L. Porter, A.G. Evans, A.H. Heuer, Acta Metall. **27**, 1649 (1979). https://doi.org/10.1016/0001-6160(79)90046-4
71. D.L. Porter, A.H. Heuer, J. Am. Ceram. Soc. **62**, 298 (1979). https://doi.org/10.1111/j.1151-2916.1979.tb09484.x
72. R.H.J. Hannink, J. Mater. Sci. **13**, 2487 (1978). https://doi.org/10.1007/BF00808066
73. C.G. Aneziris, W. Schärfl, H. Biermann, U. Martin, Int. J. Appl. Ceram. Technol. **6**, 727 (2009). https://doi.org/10.1111/j.1744-7402.2008.02321.x
74. S. Martin, S. Richter, A. Poklad, H. Berek, S. Decker, U. Martin, L. Krüger, D. Rafaja, J. Alloys Compd. **577**, S578 (2013). https://doi.org/10.1016/j.jallcom.2012.02.014
75. H. Berek, A. Yanina, C. Weigelt, C.G. Aneziris, Steel Res. Int. **82**, 1094 (2011). https://doi.org/10.1002/srin.201100064
76. A. Glage, C. Weigelt, J. Räthel, H. Biermann, Adv. Eng. Mater. **15**, 550 (2013). https://doi.org/10.1002/adem.201200334
77. S. Martin, S. Richter, S. Decker, U. Martin, L. Krüger, D. Rafaja, Steel Res. Int. **82**, 1133 (2011). https://doi.org/10.1002/srin.201100099
78. R. Eckner, M. Krampf, C. Segel, L. Krüger, Mech. Compos. Mater. **51**, 707 (2016). https://doi.org/10.1007/s11029-016-9541-z
79. S. Martin, S. Decker, L. Krüger, U. Martin, D. Rafaja, Adv. Eng. Mater. **15**, 600 (2013). https://doi.org/10.1002/adem.201200330
80. A. Glage, S. Martin, S. Decker, C. Weigelt, M. Junghanns, C.G. Aneziris, U. Martin, L. Krüger, H. Biermann, Steel Res. Int. **83**, 554 (2012). https://doi.org/10.1002/srin.201100288
81. S. Prüger, L. Mehlhorn, U. Mühlich, M. Kuna, Adv. Eng. Mater. **15**, 542 (2013). https://doi.org/10.1002/adem.201200323
82. GOM GmbH, *ARAMIS GOM Optical Measuring Techniques* (2008)
83. H. Schumann, Krist. Tech. **9**, 1141 (1974)
84. *VirtualDub* (n.d.)
85. Chemnitzer Werkstoffmechanik GmbH, *VEDDAC* (Chemnitz, 2017)
86. L. Lutterotti, S. Matthies, H. Wenk, CPD Newslett. **21**, 14 (1999)
87. J. Ågren, Scr. Metall. 1507 (1986)
88. P.J. Jacques, F. Delannay, J. Ladrière, Metall. Mater. Trans. A **32**, 2759 (2001). https://doi.org/10.1007/s11661-001-1027-4
89. D. De Knijf, R. Petrov, C. Föjer, L.A.I. Kestens, Mater. Sci. Eng., A **615**, 107 (2014). https://doi.org/10.1016/j.msea.2014.07.054
90. M. Linderov, C. Segel, A. Weidner, H. Biermann, A. Vinogradov, Mater. Sci. Eng., A **597**, 183 (2014). https://doi.org/10.1016/j.msea.2013.12.094
91. G.B. Olson, M. Cohen, Metall. Mater. Trans. A **6**, 791 (1975)
92. A. Weidner, *Deformation mechanisms of TRIP/TWIP steels—in situ characterization techniques* (Springer Nature, Berlin, 2020)
93. A. Müller, C. Segel, M. Linderov, A. Vinogradov, A. Weidner, H. Biermann, Metall. Mater. Trans. A **47**, 59 (2016). https://doi.org/10.1007/s11661-015-2953-x

94. A. Portevin, F. Le Chatelier, Acad. Sci. **176**, 507 (1923)
95. H. Biermann, J. Solarek, A. Weidner, Steel Res. Int. **83**, 512 (2012). https://doi.org/10.1002/srin.201100293
96. A. Weidner, A. Müller, H. Biermann, Mater. Today: Proc. **2**, S623 (2015). https://doi.org/10.1016/j.matpr.2015.07.361
97. J.J. Roa, G. Fargas, A. Mateo, E. Jiménez-Piqué, Mater. Sci. Eng., A **645**, 188 (2015). https://doi.org/10.1016/j.msea.2015.07.096
98. S. Morito, H. Tanaka, R. Konishi, T. Furuhara, T. Maki, Acta Mater. **51**, 1789 (2003). https://doi.org/10.1016/S1359-6454(02)00577-3
99. T.-H. Ahn, S.B. Lee, K.-T. Park, K.H. Oh, H.N. Han, Mater. Sci. Eng., A **598**, 56 (2014). https://doi.org/10.1016/j.msea.2014.01.030
100. M. Calcagnotto, D. Ponge, E. Demir, D. Raabe, Mater. Sci. Eng., A **527**, 2738 (2010). https://doi.org/10.1016/j.msea.2010.01.004
101. G. Kurdjumow, G. Sachs, Zeitschrift Für Physik **64**, 325 (1930). https://doi.org/10.1007/BF01397346
102. D. Pavlyuchkov, S. Martin, B. Reichel, C. Weigelt, O. Fabrichnaya, Adv. Eng. Mater. **17**, 1323 (2015). https://doi.org/10.1002/adem.201400521
103. Y. Ma, E.H. Kisi, J.K. Shane, A.J. Studer, J. Am. Ceram. Soc. **87**, 465 (2004)
104. L.S. Pan, S. Horibe, J. Mater. Sci. **31**, 6523 (1996). https://doi.org/10.1007/BF00356258
105. C. Segel, A. Weidner, H. Biermann, in (Verbundwerkstoffe Tagungsband Chemnitz, 2013)

Chapter 16
X-Ray Computer Tomography for Three-Dimensional Characterization of Deformation and Damage Processes

Harry Berek, Marie Oppelt and Christos G. Aneziris

Abstract The investigation of phase transformations in metastable ceramic systems such as zirconia often requires local phase analysis within the areas of interest. Electron backscatter diffraction is a suitable method. The effect of the combination with focused ion beam sample preparation was determined in this work. In addition metal matrix compositemetal matrix composite honeycombs and foams as well as beads were investigated. The foams and honeycombs were composed of austenitic steel exhibiting TRansformation Induced Plasticity (TRIP) and magnesia partially stabilized zirconia. Both components exhibit martensitic phase transformation during deformation, thus generating the potential for improved mechanical properties such as strength, ductility, and energy absorption capability. The aim of these investigations was to show that stress-assisted phase transformations within the ceramic reinforcement correspond to strong local deformation, and to determine whether they can trigger martensitic phase transformations in the steel matrix. To this end, in situ interrupted compression experiments were performed in an X-ray Computed Tomography Device (XCT). By using a recently developed reconstruction algorithm, local deformation was calculated and regions of interest were defined. Corresponding cross sections were prepared and used to analyze the local phase composition by electron backscatter diffraction. The results show a strong correlation between local deformation and phase transformation.

16.1 Introduction

Metal matrix composites (MMCs) have been in the focus of research and development for many years. The growing demand on light-weight materials with acceptable mechanical properties is one reason. In general, the metal matrix consists of low-density materials like aluminum or magnesium. A new generation of MMCs, the

H. Berek · M. Oppelt (✉) · C. G. Aneziris
Institute of Ceramic, Glass and Construction Materials, Technische Universität Bergakademie Freiberg, Agricolastr. 17, 09599 Freiberg, Germany
e-mail: marie.oppelt@ikgb.tu-freiberg.de

H. Biermann and C. G. Aneziris (eds.), *Austenitic TRIP/TWIP Steels and Steel-Zirconia Composites*, Springer Series in Materials Science 298,
https://doi.org/10.1007/978-3-030-42603-3_16

so-called TRIP-matrix composites, has been developed within the last decade [1, 2]. Its constituents are TRIP steel and Mg-PSZ ceramic particles. The steel matrix of these MMCs exhibits a TRIP effect (TRansformation Induced Plasticity), thus possessing excellent mechanical properties with concurrent high strength and high ductility [3]. The TRIP effect is caused by a deformation induced martensitic phase transformation from austenite (fcc) to α'-martensite (bcc) via an intermediate state of highly faulted austenite or ε-martensite (hcp).

There are three different Zirconia modifications; namely cubic ($2650\ \mathrm{K} < T < T_\mathrm{m}$), tetragonal ($1478\ \mathrm{K} < T < 2650\ \mathrm{K}$), and monoclinic ($T < 1478\ \mathrm{K}$) [4]. The phase transformation from the tetragonal phase to the monoclinic phase is accompanied by a volume expansion of 3–5%, which leads to deformations in the areas surrounding the zirconia particles and high shear. The tetragonal high-temperature phase can be stabilized down to room temperature by the addition of certain stabilizers as Y_2O_3, CaO, or MgO. Partially stabilized zirconia exhibits a stress-assisted martensitic phase transformation [5]. In the TRIP matrix composites, MgO partially stabilized zirconia (Mg-PSZ) is used. The combination of the deformation-induced phase transformation of the steel matrix with the stress-assisted martensitic phase transformation of the Mg-PSZ produces composite materials with high damage tolerance [6]. This opens up a wide field of application for high-strength materials that possess the capability of absorbing mechanical energy during, for example, crash loading.

Suitable designs for this purpose are in particular honeycomb structures, foams and hollow spheres. They offer a combination of low density and high energy absorption capability. Therefore, in situ deformation experiments of such specimens were performed by X-ray computed tomography XCT. The aim was, in addition to the three-dimensional mapping of deformation and damage, to investigate the relationship between local deformation and local phase composition. This should also allow statements on the trigger stress. Wide space occupied the development of the required investigation methods. For the in situ compression deformation in the XCT a special apparatus was developed and built. This allows forces up to 100 kN. Furthermore, it was necessary to carry out local phase analysis with a resolution of less than 1 µm. A suitable method for this is electron backscatter diffraction (EBSD) [7]. This is a surface-sensitive method. The information depth is a maximum of 100 nm. In this near-surface area, no disturbances of the original deformation-related microstructure due to sample processing must be present. Therefore, methods of target preparation had to be developed. It was ascertained that the local chemical composition of the examined MMC has a decisive influence on the local phase composition. In particular, the ZrO_2 particles can be destabilized in the sintering process. This reduces the fraction of metastable (transformable) phases. The result is the formation of silicates and spinels from reactions of impurities in the powder constituents used and an associated diffusion of the stabilizers to the steel/ceramic interfaces. The consequence is a wide dispersion of the local phase composition. The corresponding distribution functions must be determined in order to be able to describe the influence of a deformation on the phase composition [8, 9].

Within this work the target preparation for a optimal EBSD and XCT analysis of composites was investigated [10]. One method for determining the mechanical

properties of small samples at relatively small forces is the small punch test. First researches has been conducted. Furthermore MMC foams [11] and honeycombs [12] were examined. The aim of these investigations was to show that stress-assisted phase transformations within the ceramic reinforcement correspond to strong local deformation, and to determine whether they can trigger martensitic phase transformations in the steel matrix. Besides, in situ interrupted compression experiments were performed in an X-ray computed tomography device. Furthermore composite beads with graded layer structures (prepared with the alginate gelation technology) were examined and valued with X-ray computed tomography [13].

16.2 Experimental Details

Figure 16.1 shows the used XCT CT-Alpha from ProCon X-Ray Garbsen. It displays the punctiform X-ray source, the rotation table and the flat detector. Alternatively, two different X-ray sources can be used. Three different detectors were used. The technical data are:

- Directional ray tube 225 kV, Feinfocus Garbsen, Germany, 2008
- Transmission tube 160 kV, Feinfocus Garbsen, Germany, 2008
- Detector Hamamatsu C7942SK-05, Hamamatsu Photonics K.K. Hamamatsu City, Japan, 2008, 2400 × 2400 pixel, 50 μm × 50 μm pixel size
- Detector Dexela 1512, 1944 × 1536 pixel, 75 μm × 75 μm pixel size
- Detector PerkinElmer XRD 1620 AN CS, Perkin Elmer Optoelectronics, Fremont, Kanada, 2008, 2448 × 2448 pixel, 200 μm × 200 μm pixel size.

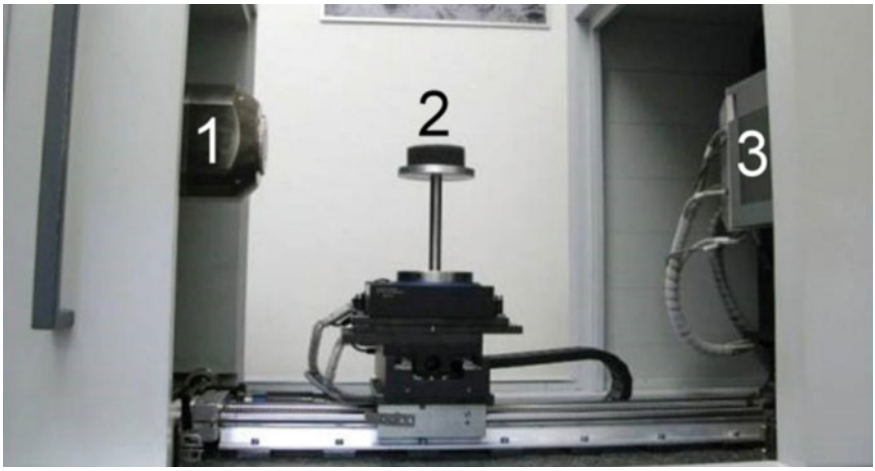

Fig. 16.1 Laboratory XCT with the main components 1 X-ray tube (left). 2 Turning device with sample plate (center). 3 Flat detector (right)

The device for in situ compressive deformation was manufactured by the company Hegewald & Peschke (Nossen, Germany) after co-development. Figure 16.2 illustrates the basic structure. It displays a transmission system that transmits the torque of an electric motor to a spindle. This spindle moves a pressure plate. The sample is located between this lower and an upper pressure plate. The load cell is firmly connected to the gearbox housing via flanges and a CFC tube. During movement of the spindle the sample and the CFC tube are simultaneously under compression and tension respectively. A CT scan is possible, because the entire system can be mounted on the turntable of XCT. The absorption of X-radiation by the CFC tube is negligible. The CFC tube used for the experiments was supplied by the Institute for Construction and Composite Construction e.V. (TU Chemnitz, Germany).

One method for determining the mechanical properties of small samples at relatively small forces is the small punch test [15]. Cylindrical discs are deformed with the aid of spherical pressure stamp in the middle. The entire load within the specimen is rotationally symmetric with defined areas of compressive and tensile loading. Figure 16.3 shows the basic arrangement. Because of the rotational symmetry, the method is very well suited for in situ investigations in XCT at low forces. In order to

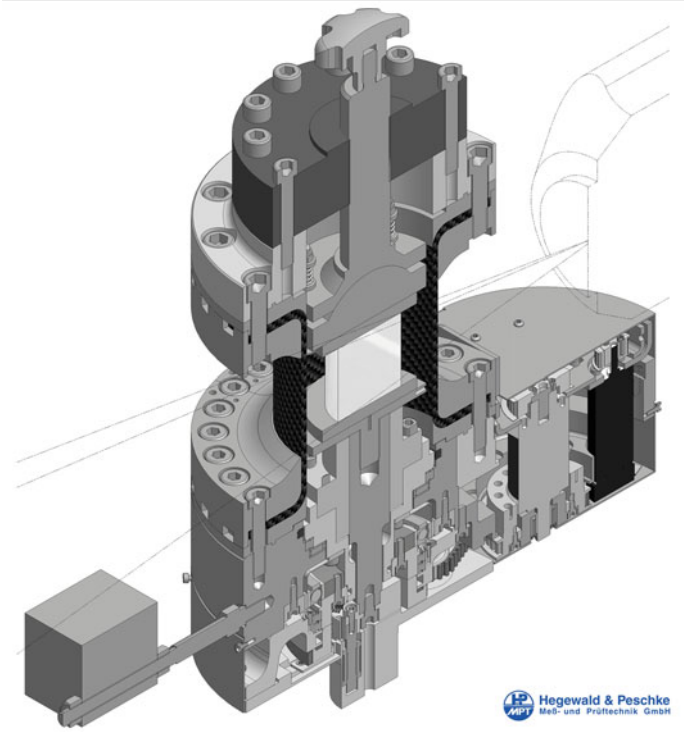

Fig. 16.2 Schematic representation of the structure of the in situ device for pressure deformation [14]

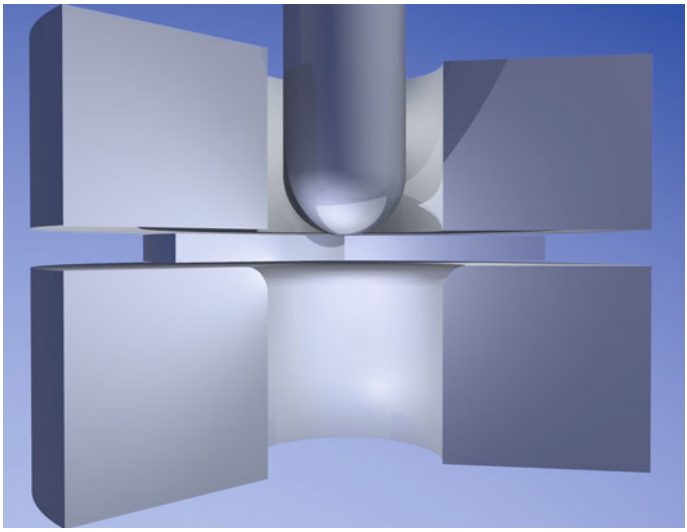

Fig. 16.3 Basic arrangement of the small punch test [15]

avoid a superposition of the absorbance contrasts of sample holder and sample, the entire sample holder shown in Fig. 16.3 consists of Si_3N_4. This material is characterized by extremely low X-ray absorption and high fracture toughness at the same time. In the present study, an in situ deformation device Deben CT5000 was used (Deben UK Ltd, Bury St. Edmunds Suffolk, UK). This is designed for forces up to 5000 N and a higher resolution in the XCT is possible, due to the small dimensions. It was installed for this purpose in a XCT ZEISS Xradia510 type. In this combination a volume resolution (voxel size) of 0.7 µm was possible at a sample diameter of 4 mm. Figure 16.4 illustrates the arrangement with installed deformation device. Part of the microstructure analysis was investigated in a SEM XL30 from Philips equipped with a EDX/EBSD-System from Edax. FIB preparation and characterization of the microstructure were performed in a FEI Versa3D dual beam system. This microscope is equipped with a 30 kV Ga+ ion source. An EDX- and EBSD analytical system Team from EDAX was used. Phase analysis was carried out for single points or for defined scans. The topographic information was obtained using the forward scatter detector (FSD), which was positioned below the EBSD screen. The preparation in the Versa3D microscope was performed by milling of cross sections at sharp edges of the samples. Thus, areas in the range of 50 μm^2 could be investigated. In addition, embedded and polished samples were used in order to get defined initial surface conditions for the FIB preparation. The final preparation step for the embedded samples was vibration polishing in a Buehler VibroMet2. The polished samples were coated with PtPd20 layers in the range between 0.1 and 0.5 nm using a Cressington 208 HR Sputter Coater. Lattice parameters for the phase identification by EBSD were taken from an ICDD database [16]. These data were also the starting point for the XRD-whole-pattern fitting process.

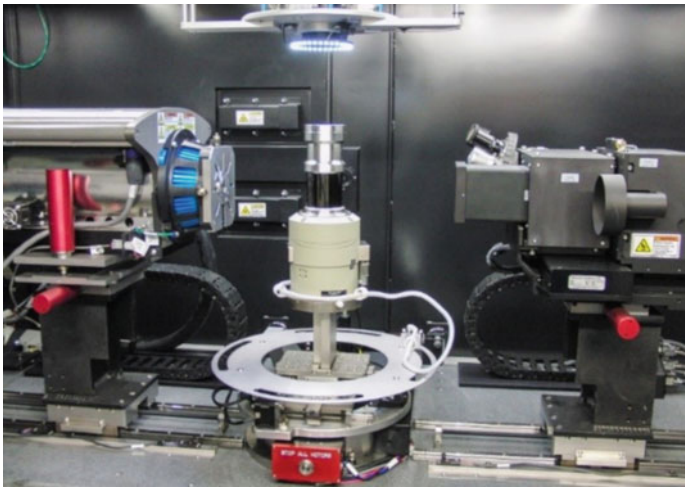

Fig. 16.4 Deformation instrument Deben CT5000 in XCT Zeiss XRadia510, left: X-ray tube, middle: deformation device on the turntable, right: X-ray microscope

To characterize the graded beads, the X-ray computed tomography (X-ray CT) was conducted using a Zeiss Xradia 510 Versa X-ray microscope (XRM). This XRM is equipped with a 160 kV tungsten target X-ray source and scintillator detectors filmed from the back by a CCD camera (2048 $\times$ 2048 pixel) through a microscopy system. Therefore the total magnification results from the geometric magnification of the cone beam multiplied by the optical magnification of the microscope. The volume reconstruction was done using the Zeiss XRM reconstructor software. This software works with a filtered back projection algorithm and an additional beam hardening correction method. Detailed parameters used for tomography studies as well as for volume reconstruction are given by Oppelt et al. [13].

16.3 Results and Discussion

16.3.1 Target Preparation and Effect of Focused Ion Beam Sample Preparation

If specimen areas of interest can be optically detected with an accuracy of approximately 0.5 mm, a metallographic ground preparation is possible. For this purpose, the samples are cut with a diamond saw, embedded in epoxy resin, ground and polished to a particle size of 1 μm. The last step is followed by vibration polishing with a SiO_2 suspension MasterMet2 from Buehler. This was done by a polishing machine VibroMet2 from Buehler. To ensure sufficient electrical conductivity of the samples,

all polished surfaces were coated with about 0.2 nm Pt/Pd (Cressington 208 HR Sputter Coater). All corresponding parameters are the result of an optimization prozess [9].

Another method of target preparation is Focused Ion Beam (FIB). Here, the areas of interest can be selected directly in the SEM. After determining a suitable cut surface, this is exposed by means of FIB and polished. It has been found that ceramic materials not only show the radiation damage known from metals and semiconductors, but also phase transformations are possible [10].

In case of metastable Y-PSZ and Mg-PSZ, phase transformations or damage were observed independence of the parameters ion energy, ion current and incidence angle. Damage was the dominating effect for angles of 72° while phase transformations occurred during FIB-preparation with 30 kV, 30 nA and 5° incidence angle. The expected local temperature increase due to the ion bombardment (30 kV, 30 nA) is about 700 K for ZrO_2. Thus, the observed phase transformations could be explained on the basis of the increased temperature (700 °C) in the corresponding Y-PSZ phase diagram. In case of Mg-PSZ, the transition temperature is 1083 °C. The local temperature rise was obviously lower. The excitation energy for the observed phase transformation was smaller than expected from the phase diagrams of the thermodynamic equilibrium. Using 5 kV, 4.8 nA and 5° incidence angle no phase transformations and no damage were observed. Thus, these conditions are suited for the FIB preparation of metastable zirconia. The investigation of phase transformations in zirconia requires a separation between zirconia and the other phases of the structure. Otherwise cubic structures of the steel matrix, zirconia and precipitations cannot be distinguished. This discrimination was realized using the combination of EDX- and EBSD-mapping. One has to keep in mind, that the interaction volumes of EDX and EBSD are different. However the given zirconia particle sizes enable the definition of phase boundaries by EDX with a sufficient resolution. A complete analysis of a scanned sample contains the following steps [8, 9]:

(1) Scanning of at minimum 10 typical areas for each sample:
For each point of a scanned sample area the EDX spectrum and the EBSP are analyzed simultaneously. The typical map size was 20 μm × 20 μm with a step size of 0.2 μm.
(2) Analysis of the EDX maps and determination of the threshold values at phase boundaries.
(3) Filtering of the EBSD maps:
This is carried out on the base of the EDX threshold values and separation into different phase areas.
(4) Calculation of the phase distributions within the different phase areas:
The decision for one of the possible phases for each EBSP is based on the number of detected diffraction bands on the one hand and the difference between the measured angles between the diffraction bands and the corresponding angles between expected lattice planes on the other hand (fit). The phase with the highest number of corresponding diffraction bands and the lowest fit is taken.

The aim of the analysis of the target preparation was to study the influence of a FIB preparation on the phase composition of Mg-PSZ and Y-PSZ. Figure 16.5 illustrates a typical FIB cross section preparation.

As a first step, a platinum layer is deposited on the sample surface in order to get a defined cross section with little curtaining and without further damage of the sample. A metal-organic compound is used as a precursor for Pt. Typically this is dissociated with the aid of the ion beam and the metal is deposited. During the first seconds of this process, interactions between the ion beam and the sample surface have to be considered. Modifications may be necessary in case of fine sensitive surface structures. The stopping range of ions is in the same order of magnitude as the depth of possible damage. Therefore electrons may be used for the formation of a first layer of Pt. After deposition of the first layer of Pt atoms the damage stops. The second step is milling at an angle perpendicular to the sample surface followed by low energy polishing as a third step. As a result the sample surface is characterized by a damage depth Y smaller than the EBSD information depth [10].

Figure 16.6 shows a typical fractured surface of Y-PSZ. As it can be clearly observed, the structure was bimodal with grains in the range of 10 μm and below

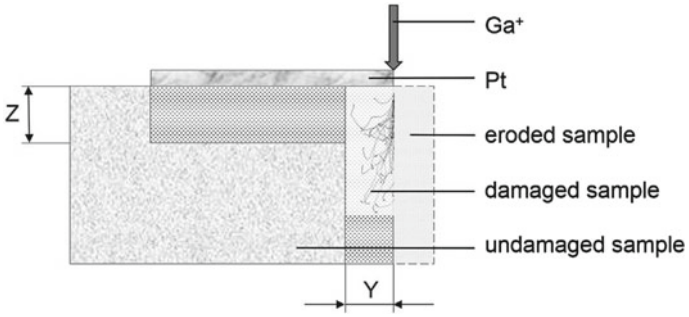

Fig. 16.5 Scheme of the sample damage during FIB cross sectioning [10]

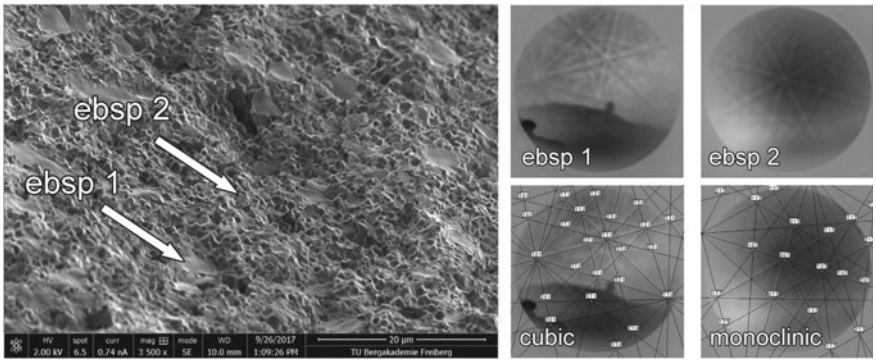

Fig. 16.6 EBSD phase analysis on a fractured surface of Y-PSZ [10]

1 μm. Electron backscatter diffraction patterns (EBSP) could be obtained without further preparation. The only problem was to find a matching geometry. As expected, the peaks were indexed as monoclinic or cubic/tetragonal. Examples are given in Fig. 16.6. Note that the cubic and tetragonal crystal structures of stabilized zirconia cannot be distinguished by EBSD. The crystal parameters may change continuously with the concentration of the stabilizer as mentioned above. Each state between cubic and tetragonal is possible. Thus, the resolution of EBSD is not sufficient as opposed to XRD [10].

Typical results of the EBSD phase analysis on polished cross sections are given in Fig. 16.7. The bimodal microstructure can be clearly recognized in the SEI image. It also appears in the phase map. The bigger particles were indexed as cubic/tetragonal zirconia (green), while the smaller particles consisted of monoclinic zirconia (red). The inverse pole figure (IPF) exhibits a random distribution of crystallographic orientation. The band contrast map also shows the bimodal structure. It represents the contrast at the observed diffraction bands in a greyscale. Thus, it illustrates the distribution of the local crystal perfection. The monoclinic grains exhibit a higher number of lattice defects than cubic/tetragonal grains. As stated in the introduction, the concentration of the stabilizer Y is not homogeneous. In particular, it is higher in the cubic/tetragonal grains than in the monoclinic ones. Hence the system is partially destabilized. As a result, the monoclinic fraction within the sample shows a variability in the local Y concentration [10].

After a FIB preparation of cross sections, a complete different phase composition was found. Corresponding results are presented in Fig. 16.8. As it can be seen in the SEI image, a tip was coated with platinum and then cut with 30 kV Ga+ ions at an angle of 90° relative to the Pt-coated surface. The beam current during the final polishing with an incident angle of 1° to the cut surface was 3 nA. Curtaining occurred due to inhomogeneity of the initial sample surface as well as of the Pt coating. This effect let to the dark lines in the band contrast map and also in the phase map. Surprisingly, the EBSD phase analysis showed a dense structure and clear diffraction patterns without much damage. The microstructure was completely cubic/tetragonal, in contradiction to the XRD and initial EBSD phase analysis on polished samples. The Yttrium distribution was comparable to the initial state, indicating that no further destabilization occurred. In order to explain this behavior, FIB milling and polishing were conducted on mechanically polished surfaces with different incident angle and energy of the ion beam [10] Detailed phase maps and results are given by Berek et al. [10]. Identical areas of mechanically polished samples were scanned before and after additional FIB preparation with different ion energy and angle. A summary of the results is given in Table 16.1. The fraction of indexed points represents the ratio between the number of indexed points and the total number of points within the scan. The band contrast is a measure of the sharpness of the diffraction bands and also for the crystal perfection. The values of the band contrast can be compared if all diffraction patterns are taken under equal experimental conditions.

Differences in the initial states (from vibration polish) are attributed to local inhomogeneities. Note that after FIB with 30 kV, 30 nA and 5° incidence angle the fraction of indexed points rose while the fit and the band contrast were stable. The fit

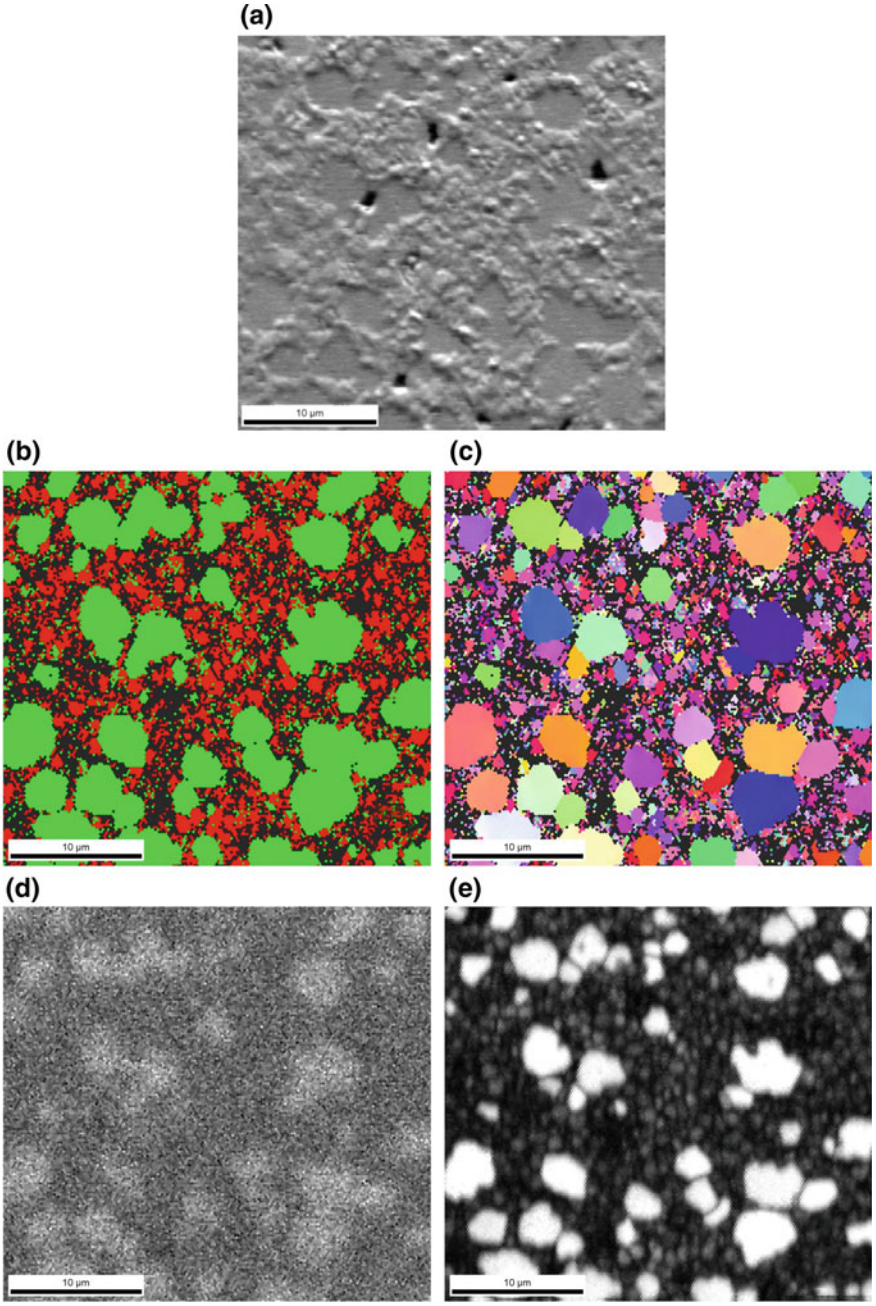

Fig. 16.7 EBSD phase analysis on a polished surface of Y-PSZ. **a** SEI image of the analyzed area. **b** Phase map (green: cubic/tetragonal, red: monoclinic). **c** Inverse pole figure image. **d** EDX elemental distribution for Y. **e** Band contrast [10]

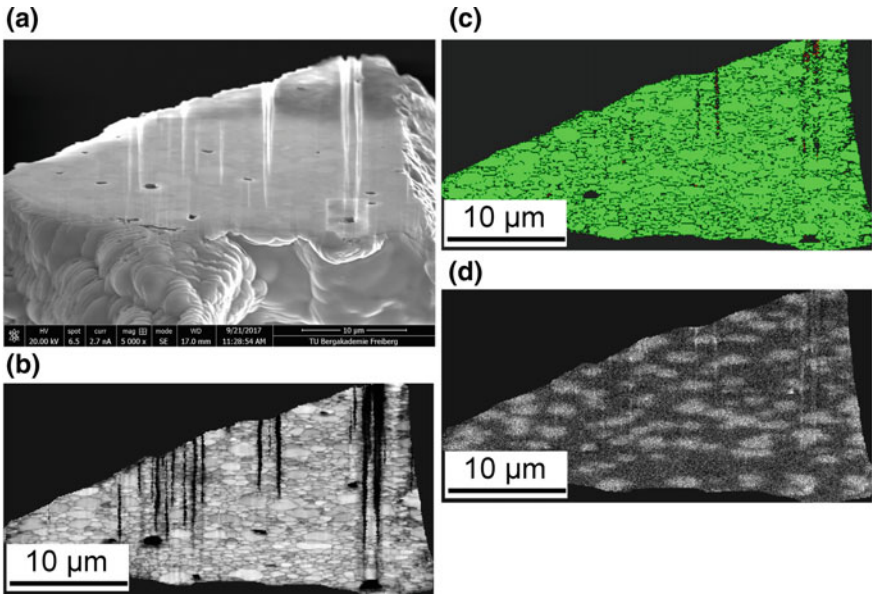

Fig. 16.8 EBSD phase analysis on a FIB cross section of Y-PSZ with the FIB parameters 30 kV and 3 nA. **a** SEI image. **b** Band contrast. **c** Phase map (green: cubic/tetragonal). **d** EDX elemental distribution for Y [10]

Table 16.1 Influence of FIB preparation on EBSD phase analysis of Y-PSZ [10]

	Monoclinic fraction	Fit	Fraction of indexed points	Band contrast (defined above in text)
	(Mol-%)	(°)	(%)	(–)
Vibration polished	21.1	1.05	38.4	3977
FIB (30 kV, 30 nA, 72°)	5.2	1.35	26.8	1772
Vibration polished	23.4	1.06	40.1	3962
FIB (5 kV, 4.8 nA, 72°)	2.0	1.21	34.0	3834
Vibration polished	35.8	1.03	43.1	4747
FIB (30 kV, 30 nA, 5°)	1.1	1.06	64.1	4501
Vibration polished	37.4	1.07	48.9	4380
FIB (5 kV, 4.8 nA, 5°)	34.0	1.06	49.7	3954

is defined as the medium difference of angles between all identified diffraction bands and the corresponding lattice planes of the crystal structure of interest. Obviously the structural transformation was followed by a crystal growth. FIB with 5 kV, 4.8 nA and 5° incidence angle led to nearly unchanged values. Thus, one can conclude that the influence of crystal damage at 5 kV is negligible. No amorphous layer could be

identified. Phase transformations in zirconia are connected with volume changes. However, no cracks were observed in the transformed regions.

16.3.2 MMC Foams

Open cell foam structures were produced with the aid of 30 pore per inch (ppi) polyurethane foam (pore size distribution in the range of 0.5 up to 3 mm) of size $50 \times 50 \times 20$ mm^3 as templates [16–18].

One typical MMC foam is shown in Fig. 16.9. Three mixtures based on 100 vol% steel powder (0Z), 95 vol% steel/5 vol% Mg-PSZ-powder (5Z) and 90 vol% steel/vol% Mg-PSZ-powder (10Z) were mixed with organic additives. The manufacturing technology and the composition of the organic additives is described in [16–18]. The used process is one of the most promising manufacturing routes to produce open cell composite foams and is based on the patent of Schwartzwalder et al. [19]. It is a replication method using polyurethane sponge as a template.

In the given case the steel powder (Bitterfeld, Germany) had a mean particle size of 45 μm and the ceramic powder (Saint Gobain, USA) had a mean particle size of 3.1 μm respectively. Tables 16.2 and 16.3 give the corresponding chemical compositions.

The sintering conditions of the samples were 2 h at 1350 °C in Ar atmosphere. The in situ experiments were performed in a CT-ALPHA (ProCon X-Ray Garbsen, Germany), using a 160 kV transmission X-ray tube (Feinfocus Garbsen, Germany). High resolution X-ray absorption images were taken with a flat detector C7942SK-05

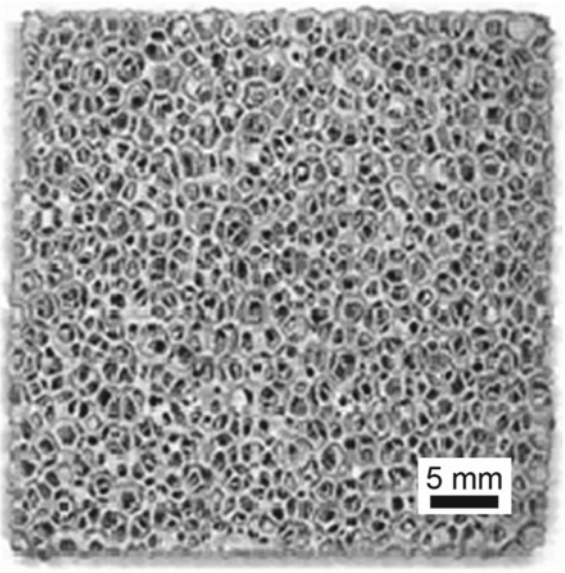

Fig. 16.9 Typical MMC foam [21]

Table 16.2 Chemical composition of the steel matrix in wt% [11]

C	Cr	Mn	Ni	Si	P	S	N	Fe
0.027	18.1	1.3	7.8	0.4	0.04	0.02	0.06	Bal.

Table 16.3 Oxide content of Mg-PSZ in wt% [11]

ZrO_2	MgO	TiO_2	Al_2O_3	HfO_2	SiO_2	CaO
Bal.	2.84	0.19	0.5	1.85	0.07	0.2

(Hamamatsu, Japan). This detector has 2400 × 2400 pixels with a size of 50 µm × 50 µm each on an area of 120 mm × 120 mm. The typical resulting spatial resolution (voxel size) within the sample was 15 µm. The maximum possible sample size was always determined by the X-ray attenuation coefficients.

Loading plates of different geometries were used in order to enable full transmission of the samples without shadowing. The displacement was measured below the sample in the actuator. The deformation of the mechanical setup was found to be negligible. In the given case foam samples with a size of 10 mm × 10 mm × 20 mm were investigated. The deformation speed was about 10^{-3} s^{-1}. The CT data were analysed with the software package VGSTUDIO MAX 2.1 (Volume Graphics GmbH Heidelberg, Germany). This program provides the possibility to calculate the exact position of the sample surface with a sub voxel resolution thus correcting the so called partial volume effect. The partial volume effect normally leads to undefined three dimensional surfaces because voxels on the sample surface belong partly to the sample and partly to the surrounding.

A typical result of this kind of sample surface calculation is given in Fig. 16.10. Note that there are pores inside the foam material. This is a result of the manufacturing technology. We assume that these pores are acting as week areas during deformation. Therefore they are included in the calculation of the total sample surface. Based on the defined surface of the foam including the surfaces of pores, cell wall thicknesses can be calculated. This is realized by the determination of shortest distances between nearest surface areas within a search angle of 30°. Triple points of the foam cells always have a higher thickness than single cell walls due to surface tension effects of the slurry used. As a result of the manufacturing process pores are located mainly in the triple points. This is connected with weak points. Therefore the cell wall thickness at pores is included in the analysis.

Figure 16.11 shows typical stress-strain curves for a steel—5 vol% zirconia composite. Three areas are clearly visible. Following DIN 50134 [22] there are different ranges for the compressive stress (elastic deformation, cracking, densification) they can be separated using different ranges for the compressive stress R where R_{100} is the stress in the plateau:

(R_x: $x = x\%$ of plateau stress $R_{\text{pland the foam respectively. Ourt}}$; R_{plt} = average value of stresses between $e_d = 20\%$ and $e_d = 40\%$; e_d = strain [22]).

1. Elastic deformation between R_{20} and R_{70}

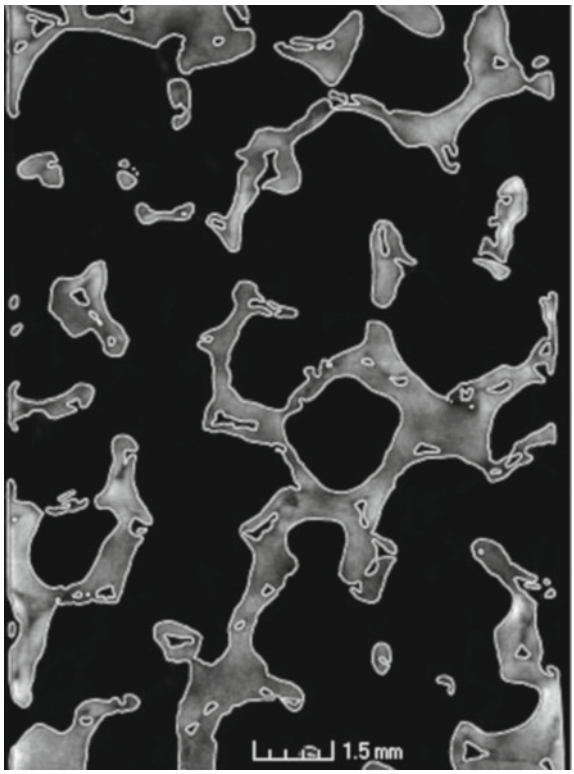

Fig. 16.10 Reconstructed cross section [11]

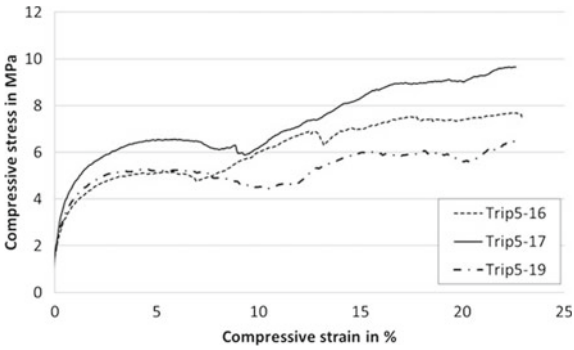

Fig. 16.11 Stress strain curves of three foams [11]

2. Cracking leading to a plateau between R_{70} and R_{130}
3. Densification leading to a significant increase above R_{130}.

Note, that there is a large scatter in the data. The cell wall thickness is inhomogeneous within the sample depending on the inhomogeneity of the starting materials and the manufacturing technology.

Results of a stopped in situ experiment are shown in Fig. 16.12.

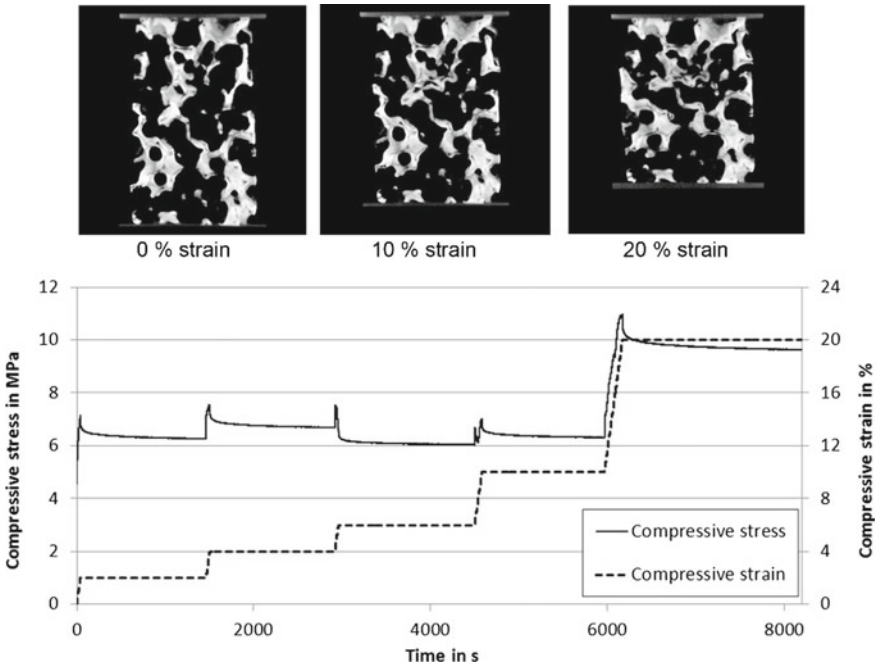

Fig. 16.12 Scheme of a stopped in situ deformation experiment and calculated sections for 0, 10 and 20% strain [11]

The compression was stopped after 2, 4, 6, 10 and 20% compressive strain respectively. After stopping the deformation process stress relaxation occured. This is connected with a significant dropdown of the compressive stress within a few minutes while the compressive strain was held constant. After this period an equilibrium state is reached. The maxima in the curves of the compressive stress correspond to the curves in Fig. 16.11. XCT scans were taken in the equilibrium state under constant stress. In order to show deformation processes with a sufficient spatial resolution, defined regions of interest were considered. In the case of Fig. 16.12 calculated 3D pictures of thin layers taken at the same position of the sample after 0, 10 and 20% compressive strain are shown. First cracks appear at the weakest cells. These are cells of a rather big size, a small cell wall thickness and an extension perpendicular to the deformation axis. A localized damage is clearly visible. Starting point in deed are smaller cell walls. As can be seen in Fig. 16.13, there is a typical deformation band starting from the area of first cracks.

For the deformation of MMC foams under compressive stress in agreement with the literature three regimes were found: elastic deformation, plastic collapse and densification. The normalized deformation maps given by Ashby [23] show the principal behaviour of the stress strain curves in dependence on the densities of the bulk material of the foam and the foam respectively. Our results confirm this view. The data are shifted slightly to smaller compressive stress values. As Elliott [24] found

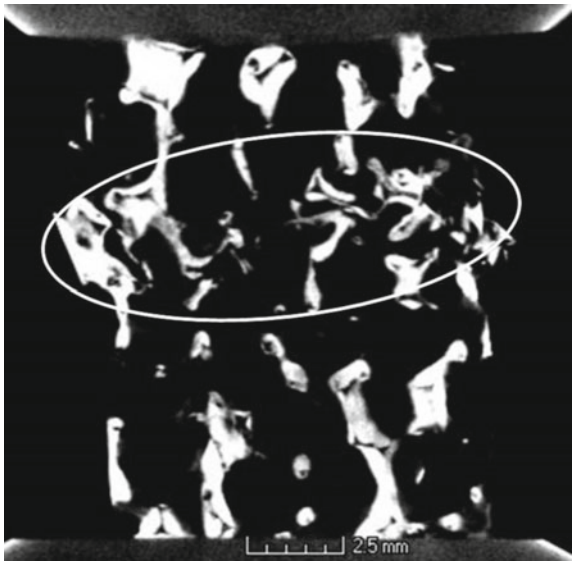

Fig. 16.13 Reconstructed cross section after 20% compression [11]

for polyurethane foams the compression of MMC foams also lead to the cooperative collapse of connected cells. Note that the foams of the given study were manufactured by the replica technique on the base of polyurethane foam (as shown in Chap. 1 of this volume). We observed deformation bands arising in regions of smaller cell wall thicknesses. Singh [25] found this kind of anisotropy in open celled Ti foams. The deformation was dependent on size, shape and orientation of the cells under consideration. Obviously deformation bands start at bigger cells with a small cell wall thickness and some extension perpendicular to the deformation direction. The rising of this kind of deformation bands can be explained by the dramatic change of the stress distribution in the neighbouring cells after the first brake of a cell wall. The correlation between local deformation and local phase composition was investigated by Berek et al. [21].

Figure 16.14 shows the result of a digital volume correlation calculation. The gradient magnitude is a measure of the local deformation. Thus, region 3 shows maximum deformation. Figure 16.15 exhibits a typical cross section of this region as the result of a local preparation process with its correspondence to the reconstructed XCT image. Local phase analyses of a number of particles like the one in Fig. 16.16 lead to the results in Fig. 16.17.

Note, that the transformation from the cubic structure to the tetragonal one is a continuous deformation process in dependence on the local concentration of stabilizers as was shown in [26]. Thus, the distinction between cubic and tetragonal zirconia is not possible by EBSD. However, it becomes clear, that the regions of high deformation (c.f. Fig. 16.14) correspond to regions of pronounced phase transformation (Fig. 16.17).

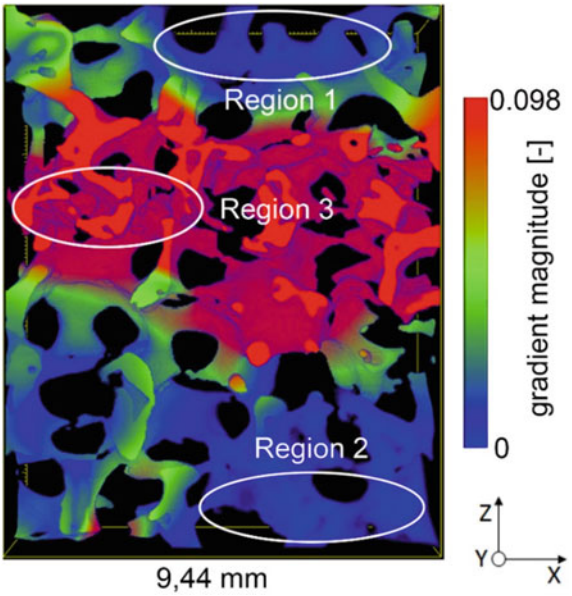

Fig. 16.14 Overlay of the slice of a reconstructed 3D image (background) and the gradient magnitude of the deformation field (highlighting) with defined regions of interest after 20% compressive deformation in the Z direction [21]

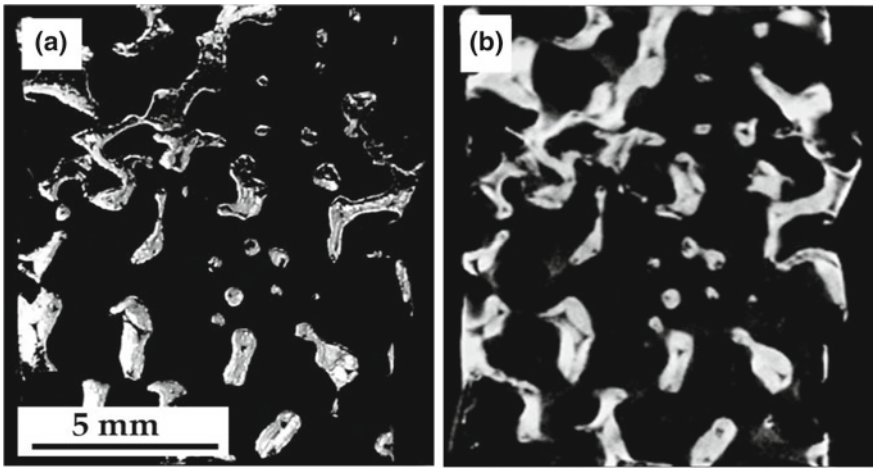

Fig. 16.15 Correlation between a reconstructed 2D image and the corresponding cross section after 20% compression in the Z direction. **a** Photograph of the cross section. **b** 2D slice from the reconstructed 3D image [21]

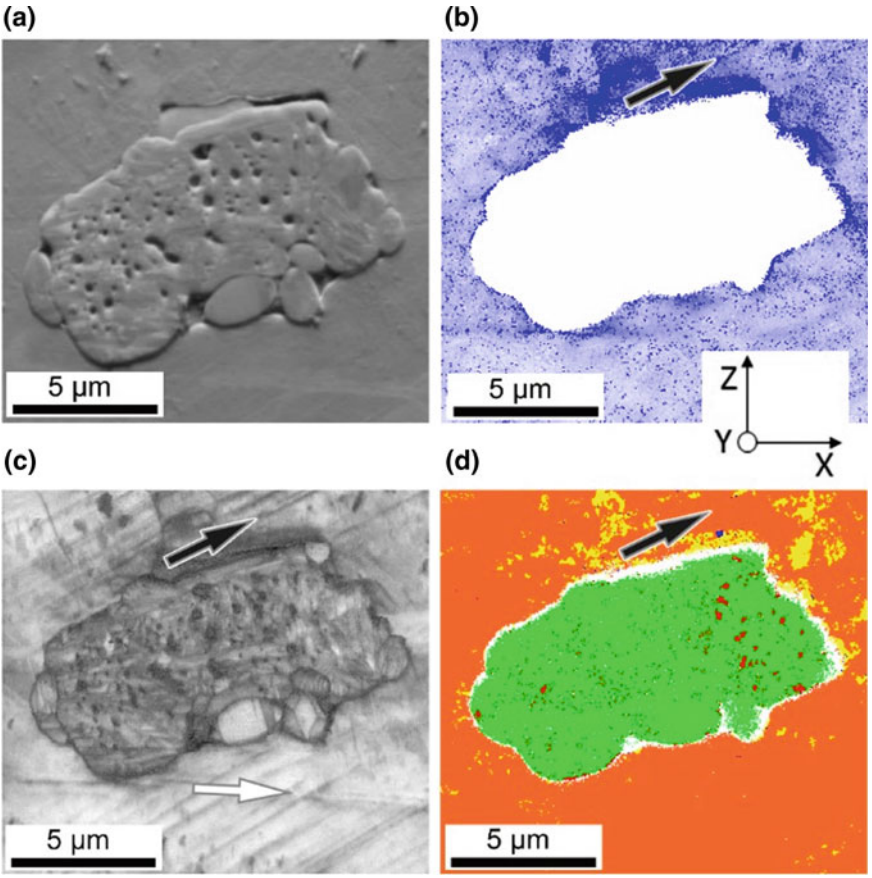

Fig. 16.16 EBSD analysis of a zirconia agglomerate after 20% compression in the Z direction. **a** EDS image. **b** Kernel average misorientation map for the steel matrix. **c** Band contrast map. **d** Phase map (green: monoclinic zirconia; red: cubic/tetragonal zirconia; orange: austenite; blue: α'-martensite; yellow: ε-martensite; white: points not indexed) [21]

16.3.3 MMC-Honeycomb Structures

The manufacturing technology of honeycomb square cell composites is based on the well-established extrusion technique [27, 28] and is described in Chap. 5 of this volume. Before extrusion the inorganic powder materials were mixed within 30 min in a tumble drum with yttria stabilized zirconia balls. In a second step the plasticizers and binders were added and the material was further mixed in a conventional mixer (Toni Technik, Germany) for 5 min. Finally, water was added and the recipes were kneaded until a homogeneous and plastic paste was achieved. Due to a combined de-airing single screw extruder with vacuum chamber and sigma kneader type LK III 2A (LINDEN, Germany) honeycomb structures were extruded with a square

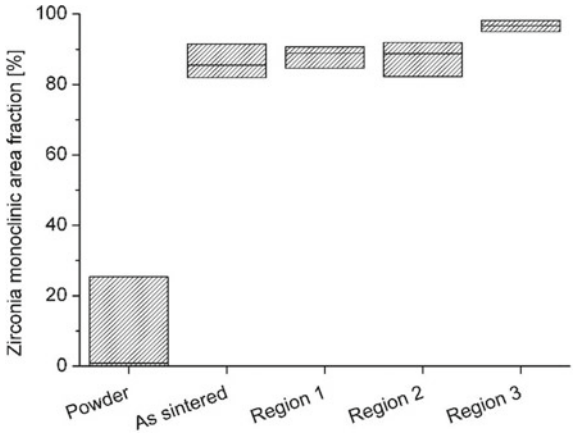

Fig. 16.17 Box plots of the distributions of monoclinic zirconia fractions at different states and in different regions showing the 25th percentiles at the lower edges and the 75th percentiles at the upper edges of the boxes [21]

Table 16.4 Chemical composition of the steel matrix in wt%

C	Cr	Mn	Ni	Si	Mo	N	Fe
0.031	16.2	7.1	5.9	1.12	0.06	0.011	Bal.

Table 16.5 Chemical composition of Mg-PSZ zirconia powder in wt%

ZrO_2	MgO	SiO_2	HfO_2	Al_2O_3	TiO_2
Bal.	3.4	2.4	1.7	0.6	0.1

shape of 25 × 25 mm^2 and a honeycomb structure of 14 × 14 channels (200 cpsi—channels per square inch). After extrusion the specimens were dried stepwise at 40–80–110 °C in an air-circulated dryer within 12 h at each temperature and decreasing humidity from 80 to 20%. Afterward cubic samples of 25 mm length were cut and placed on alumina tiling. The debinding step took place at 350 °C for 90 min in air atmosphere with a heating rate of 1 K/min. To prevent oxidation effects during further heat treatment the honeycombs were placed with stock in graphite crucibles after debinding. Finally the samples were sintered pressure less in a 99.999% argon atmosphere using an electrical furnace type HT 1600 GT Vac (LINN, Germany) with oxidic furnace lining and $MoSi_2$ heating elements. After heating with 5 K/min the temperature of 1350 °C was kept constant for 120 min followed by cooling with 10 K/min to room temperature. Open porosity and bulk density were determined based on Archimedes principle and DIN EN 1389 with toluol as immersion fluid [27]. In the given case 10 vol% of Mg-PSZ powder was mixed with TRIP-steel powder. The chemical compositions are given in Tables 16.4 and 16.5.

In order to perform in situ compression experiments in an XCT, samples with 2 × 2 channels were used. Figure 16.18a, b show corresponding photographs.

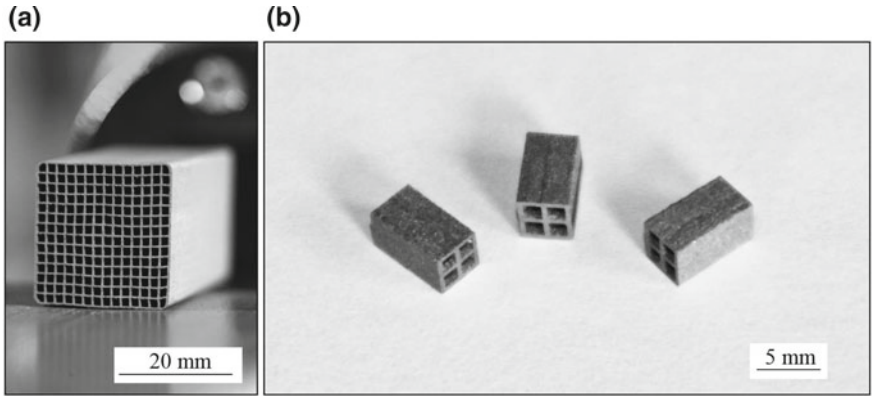

Fig. 16.18 Extruded MMC honeycomb structure (**a**) and samples for in situ experiments under compressive load in an XCT (**b**)

The experiments were performed in a CT-ALPHA in the same procedure as shown for the foams. The typical resulting spatial resolution (voxel size) within the honeycomb sample was 10 μm. A specially constructed load frame from Hegewald & Peschke Measuring Technology Nossen, Germany, was used. Two loading plates are positioned in a carbon fibre reinforced polymer tube between the top load cell and the bottom mechanical actuator. The deformation speed was about 10^{-3} s^{-1}.

The CT data were analysed in the same way as mentioned before with the software package VGSTUDIO MAX 2.1 from Volume Graphics GmbH Heidelberg, Germany. Within previous work ex situ compressive out of plane deformation experiments on honeycomb structures based on Austenitic stainless steel AISI 304L were performed [1, 2, 27, 29]. As a result of EBSD phase analysis it was concluded that stress induced martensitic phase transformations of metastable tetragonal zirconia to the stable monoclinic structure occured below 10% of compressive strain [27, 29]. A rather high amount of the monoclinic phase (>80%) was observed in the as sintered state. The reason for this behaviour was found to be destabilisation due to diffusion of magnesium and the formation of grain boundary precipitations at sintering temperature and during subsequent cooling.

The most important differences to the present work are the composition of the steel alloy used and the performance of quasi in situ deformation in the XCT. The steel alloy 16-7-6 has a significantly higher amount of manganese while the nickel content was slightly reduced. Figure 16.19 shows typical deformation curves of MMC samples (see Fig. 16.18b). Force and deformation were measured directly. The real sample cross section area was determined using wall thicknesses, which were calculated on the base of the XCT-scans.

The geometrical dimensions of the samples were 3.5 × 3.5 × 6 mm^3 with cell wall thicknesses of about 0.37 mm. After linear elastic deformation there was a broad range of plastic deformation with typical strain hardening. This strain hardening is a superposition of both martensitic transformation processes of steel and zirconia. The

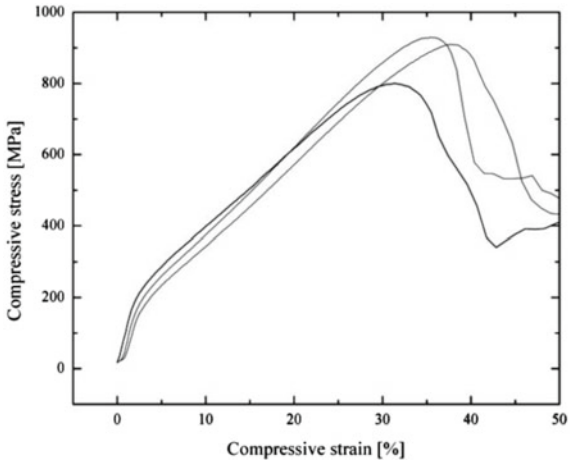

Fig. 16.19 Deformation curves of MMC honeycombs under compressive load in out of plane direction [12]

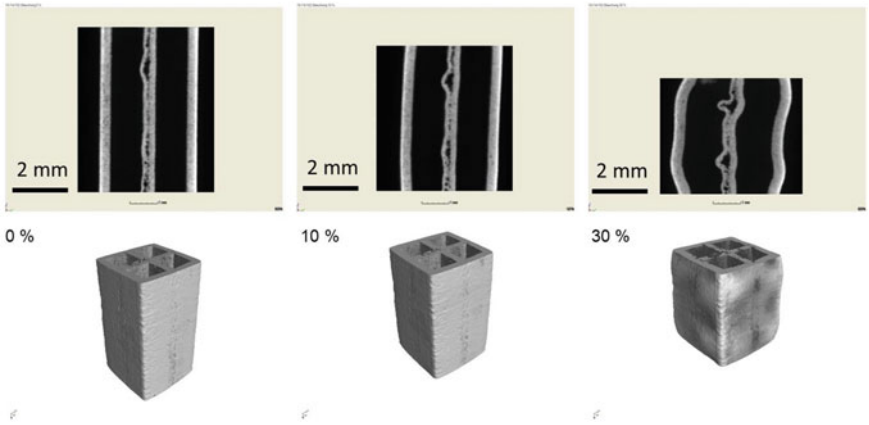

Fig. 16.20 XCT images of MMC honeycombs at different levels of compressive strain [12]

expected deformation behaviour of such kind of square celled honeycombs is torsion-flexural buckling of the cell walls [30] followed by a progressive folding process [6, 31, 32]. For stresses higher than the so called bifurcation stress the structure becomes instable and a softening is observed [30, 33]. In the given case this bifurcation stress is close to the maximum compressive stress. During the deformation process the X-ray absorption picture can be observed directly. In every case the first cracks occurred immediately after passing the maximum. Figure 16.20 gives typical XCT results. Sections were calculated at the same sample position but different levels of deformation thus allowing the study of the deformation behaviour directly.

The deformation is still in the plastic range without breaking of the walls. The sections show a porous region in the middle. Buckling is observed after 30% compression. These results are in correspondence with [14]. The investigation of the deformation behaviour of cruciform honeycomb MMC-samples (as seen in Fig. 16.20 but without the outside wall) within the XCT showed that cruciform MMC-specimens underwent a plastic deformation with irreversible torsion and warping actions. Even small imperfections, particularly piercing defects in the cell walls, had an effect on their critical bifurcation. After finishing the XCT scans, samples we prepared for the EBSD phase analysis. After embedding in epoxy, they were carefully polished. As a result, one can directly compare the calculated XCT sections with the polished sample areas. A minimum of 10 sample areas was scanned by EBSD thus enabling the study of the distribution of the phase composition. The agglomerates of zirconia typically contain a cubic/tetragonal core in a monoclinic body. Note that the lattice parameters of cubic and tetragonal zirconia differ only about 2%. Thus the resolution of EBSD is not sufficient to distinguish these structures. Furthermore there are intermediate metastable states. The lattice parameters can be directly related to the magnesia concentration [26]. Nevertheless the monoclinic structure can be clearly distinguished from the cubic/tetragonal structure by EBSD and the martensitic tetragonal-monoclinic transformation is responsible for transformation toughening. Hence, the determination of the monoclinic phase content is essential. Figure 16.21 gives the corresponding results.

These box plots exhibit minima, maxima and the 25, 50 and 75% percentiles of the corresponding distributions of the measured monoclinic phase fractions. Obviously similar to earlier investigations there is a considerable phase transformation during sintering and subsequent cooling. However the change is much smaller in this study in comparison to earlier studies with low manganese alloyed steels [8, 29]. In the as sintered state the value for the 25 percentile is about 60% of monoclinic zirconia. That

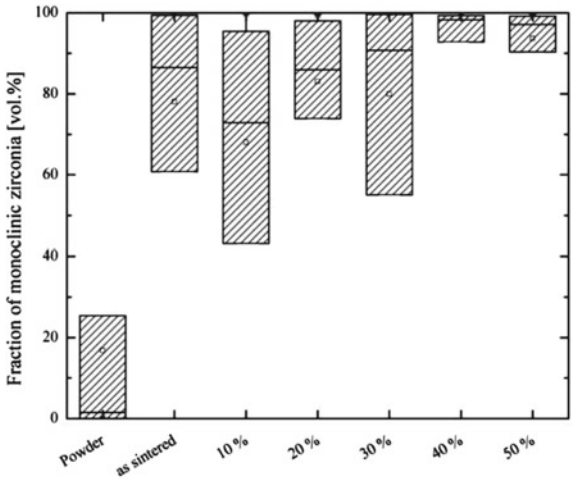

Fig. 16.21 Box plots of the distributions of monoclinic zirconia fractions at different states and in different regions showing the 25th percentiles at the lower edges and the 75th percentiles at the upper edges of the boxes [12]

means a remarkable amount of metastable zirconia for phase transformation is left. The range between 0 and 10% of compressive strain was investigated in more detail because earlier investigations show, that most of the phase transformation occurred in this region. However, in the present case the phase distribution stays stable up to 30% of deformation. This effect can be related to the higher manganese content of the steel alloy used. Mn^{2+} stabilizes metastable zirconia in a similar way as Mg^{2+} [34, 35]. On the other hand manganese forms precipitates with silicon and aluminum like magnesium thus acting as a competitor. In the end there is less diffusion of magnesium out of the zirconia and some diffusion of manganese into the zirconia thus stabilizing the metastable phases. Most of the stress-assisted phase transformation takes place between 30 and 40% of compressive deformation. Obviously, the stress limit for the phase transformation in Mn stabilised zirconia is much higher than in Mg stabilised zirconia. It is in the range of the stress maximum of the stress-strain-curve.

16.3.4 Composite Beads with Graded Layer Structures

The manufacturing technology of the composite beads is based on an alginate gelation and described detailed in Chap. 1 of this volume. Beads with graded layer compositions were prepared using a gel-casting process by alginate gelation. The used method is based on the gelation of sodium alginate in direct contact with calcium ions in an aqueous solution as solidifying agent. The used sodium alginate serves as gelation agent. During the forming process, alginate and bivalent ions react by attracting each other's molecular chains and the transition of water-soluble Na- to water-insoluble Ca-alginate takes place. Suspensions for the fabrication of composite beads with graded layer structures were prepared from austenitic stainless steel powder (TLS Technik, Germany) and magnesia (3.25 wt%) partially stabilized zirconia (Saint Gobain) [13].

The core of the beads consists of a mixture of 90% steel-powder and 10% zirconia powder and are coated with a slurry of 95% steel-powder and 5% zirconia powder. The outmost layer consisted of 100% steel. To get an overview about the complete bead, an investigation in XRM (Versa X-ray microscope) with a voxel size of 1.1 µm was conducted. The bead was fixed on a block of Si_3N_4. No additional preparation of the bead was necessary. Figure 16.22a shows a section through the reconstructed volume. Three essential components which are the steel matrix, ZrO_2-particles/agglomerates with precipitations and pores can be distinguished in the particle section. The study with the XRM proves the result of SEM that there are no gradation zone and no cracks between the different layers. The histogram during measurement shows an asymmetric peak of absorption. It comprises a wide impulse edge to higher absorption coefficients. This impulse edge can be traced back to ZrO_2. Therefore, the different areas were coloured based on the histogram. As a result, the position of ZrO_2 within the (less absorbing) steel matrix can be distinguished. It is particularly clear that the surface layer does not contain ZrO_2. Further tests were performed to show if a higher image resolution can be reached using the

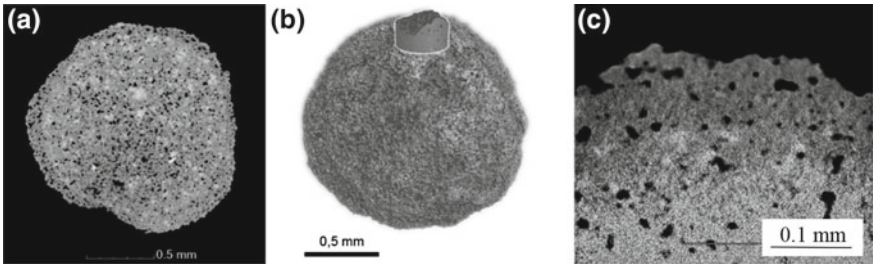

Fig. 16.22 Reconstructed cross section based on a XRM-scan of MMC bead sample; grey: austenite; light grey: ZrO_2 and precipitations; black: pores resp. ambient; **a** XRM-scan of a volume part of MMC sphere using a Zeiss Xradia 510 Versa, **b** position of part c in the volume, **c** reconstructed cross section (grey: austenite, light grey: ZrO_2 and precipitations, black: pores resp. not indicated) [13]

Zeiss Xradia 510 Versa. Therefore a high resolution scan with a 20 ×-objective for large optical magnification was performed. A pixel size of 0.41 µm using a camera binning of 2 (2 × 2 pixels are averaged and combined to one) was reached. Figure 16.22a–c illustrates the reconstructed cross section of a part of the volume. The Zeiss Xradia 510 Versa enables different types of drift corrections. Besides the default thermal drift correction of the X-ray spot on the tungsten target, a mechanical sample drift correction can be applied which takes into account the unwanted movement of the sample. With respect to the appearance of different drift phenomena, the reconstruction required the use of an additional binning 2. Thus, the voxel size of the reconstructed volume results in about 0.8 µm. Nevertheless, a surface zone free of ZrO_2 can be observed [13].

Additional to the XRM-scans of the beads after sintering, XRM-scans of deformed beads were performed. The goal was to show potential differences in crack initiation and crack morphology after deformation by uniaxial compressive loading. Layered beads (Bead a), particle reinforced beads with 90 vol% steel and 10 vol% zirconia (Bead b) as well as pure steel beads (Bead c) were tested. Figure 16.23a–c shows reconstructed cross sections of these three different beads after deformation up to 20%. The voxel size of the reconstructed volumes is 2.2 µm. As it was found for the XRM-scan of the MMC bead sample, the histogram comprises an asymmetrical peak of absorption. There is a wide impulse edge to higher absorption coefficients which is related to ZrO_2. Therefore, the different areas were coloured in the histogram, plotted in yellow. As a result, the position of ZrO_2 within the (less absorbing) steel matrix can be illustrated. Figure 16.23a shows a boundary zone free of zirconia, whereby Fig. 16.23b illustrates a regular distribution of zirconia particles. The crack initiation into the specimens was of major interest. Therefore, cross sections in the area of maximal crack width were chosen. The sample surface is marked in white. It can be seen in the cross sections that the crack in sample a (graded layer bead) does not reach the bead's centre. Bead b (90 vol% steel + 10 vol% zirconia) shows a greater crack propagation. The crack in sample c (pure steel bead) nearly reaches through the complete sample. As expected, the crack initiation starts at the surface

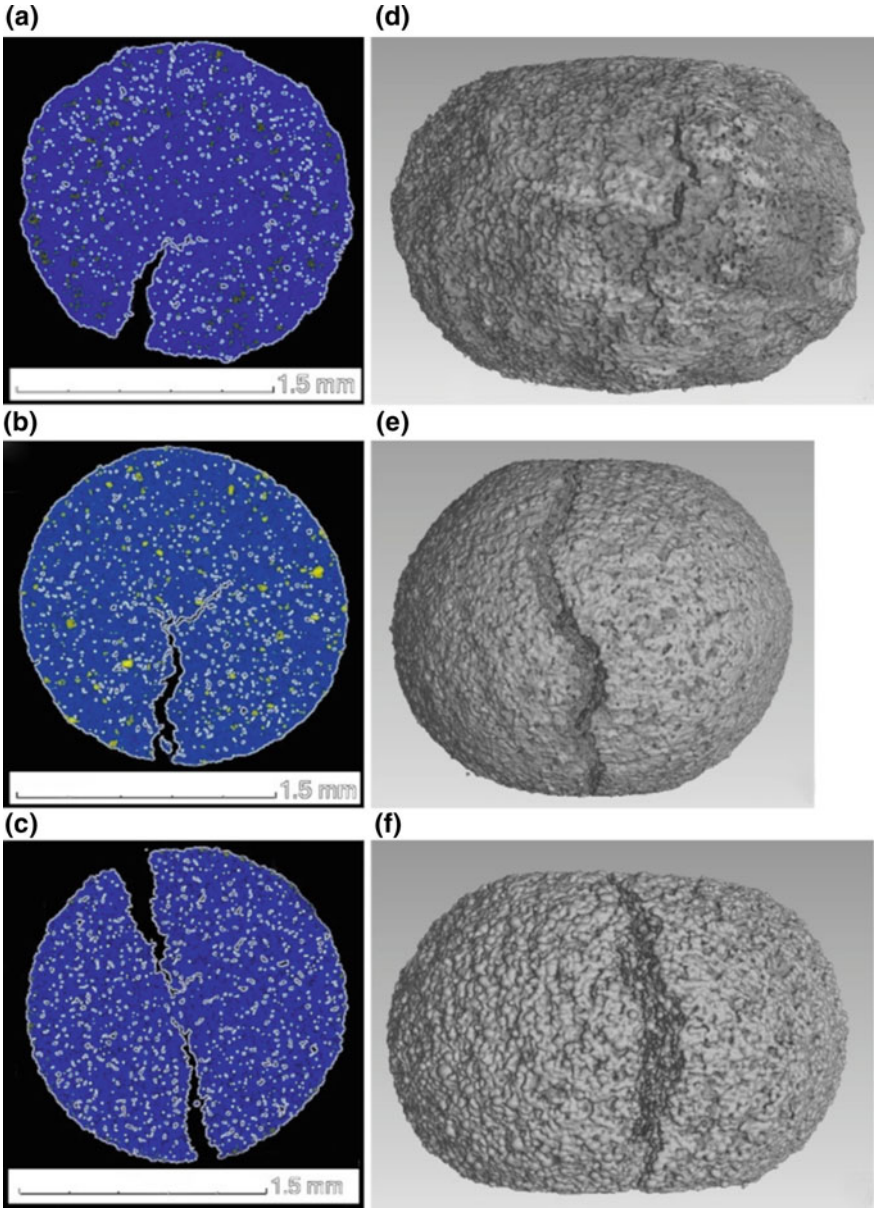

Fig. 16.23 **a–c**: Reconstructed cross sections in x-y-plane with maximal crack length. **a** graded layer bead; **b** 90 vol% steel and 10 vol% zirconia; **c** pure steel bead; blue: steel matrix; yellow: zirconia particles; white: surface marks; **d–f**: Reconstructed volumes with crack in y-plane; **d** graded layer bead; **e** 90 vol% steel and 10 vol% zirconia; **f** pure steel bead [13]

in the range of maximal tension. Figure 16.23d–f illustrates these areas in side view. Sample a (graded layer bead) shows an incipient crack while the other beads present continuous cracks. All pictures of XRM illustrate a very good gradation between the different layers and no detachment of the coating. Further studies with in situ-CT load cells are planned to verify the findings and show the mechanism of failure [13].

16.4 Conclusions

Within this work the target preparation for an optimal EBSD and XCT analysis of composites was investigated and furthermore MMC foams and honeycombs were examined. Focused ion beam preparation is a very helpful tool for producing polished cross sections of defined regions in inhomogeneous samples with complicated shape. The different aspects of the interaction between the ion beam and the sample should be considered. In case of metastable Y-PSZ and Mg-PSZ, phase transformations were observed after FIB preparation with 30 kV, 30 nA and 5° incidence angle. Damage was the dominating effect for angles of 72°. The expected local temperature increase due to the ion bombardment (30 kV, 30 nA) is about 700 K for ZrO_2. Thus, the observed phase transformations could be explained on the basis of the increased temperature (700 K) in the corresponding Y-PSZ phase diagram. In case of Mg-PSZ, the transition temperature is 1083 °C. The local temperature rise was obviously lower. The excitation energy for the observed phase transformation was smaller than expected from the phase diagrams of the thermodynamic equilibrium. Using 5 kV, 4.8 nA and 5° incidence angle no phase transformations and no damage were observed. Thus, these conditions are suited for the FIB preparation of metastable zirconia [10].

An experimental setup for in situ investigations under compressive stress in a laboratory XCT was developed and successfully tested. Complete deformation curves can be taken. The size of the samples is limited due to the transferability. Nevertheless the results for MMC foams based on TRIP-steel and Mg-PSZ correspond to results on rather bulk samples investigated by a conventional testing machine. XCT scans can be taken in the frame of stopped in situ experiments. In this way the deformation behavior of defined sample regions can be investigated. Thus interrupted in situ experiments as described by Berek et al. [11] are well suited to investigate the deformation behavior of foams and other samples which are transferable for the X-rays used. For the deformation of MMC foams under compressive stress three regimes were found in agreement with the literature: elastic deformation, plastic collapse, and densification. The deformation was dependent on size, shape and orientation of the cells under consideration. Obviously deformation bands start at bigger cells with a small cell wall thickness and some extension perpendicular to the deformation direction. The occurence of this kind of deformation bands can be explained by the dramatic change of the stress distribution in the neighbor cells after the first brake of a cell wall [11].

Furthermore the experimental setup for interrupted in situ investigations under compressive load in a laboratory XCT up to 100 kN load was developed and successfully tested to demonstrate that the crush resistance and equally the energy absorption capability of cruciform TRIP-steel structures (honeycombs) are improved by the addition of 10 vol% of Mg-PSZ. The strain hardening of the composite material can be explained by the combined effects of particle reinforcement and martensitic phase transformations in the TRIP-steel and the Mg-PSZ reinforcement at the same time. The XCT investigations showed that the cruciform specimens underwent a plastic deformation with irreversible torsion and warping effects. The composite specimens exhibit a higher initial compressive peak stress followed by structure softening and the formation of an expanded plateau region. Even small imperfections, particularly piercing defects, in the honeycomb's cell walls had an appreciable effect on their critical bifurcation load. An accelerated inhomogeneous buckling in the flange edge regions was observed in case of cruciform samples. On the basis of these experimental studies, the characterization of the deformation and failure behavior of the honeycomb structures or comparable cellular materials by analytical modeling can be promoted [14].

With the aid of XRM and X-ray CT it was possible to examine and evaluate layered composite beads. To show potential differences in crack initiation and crack morphology after deformation by uniaxial compressive loading XRM scans of deformed beads were performed. All pictures show the perfect layer formation and the crack initiation starts at the surface in the range of maximal tension.

Acknowledgements The authors gratefully acknowledge the financial support of the Deutsche Forschungsgemeinschaft (DFG, German Research Foundation) for funding this research project B5 within the frame of the Collaborative Research Center (CRC) 799—TRIP-Matrix-Composites—project number 54473466. The authors would like to thank all colleagues and student assistants for their help in measurements and for their work in sample preparation within the runtime of CRC 799.

References

1. C. Aneziris, W. Schärfl, H. Biermann, U. Martin, Int. J. Appl. Ceram. **6**, 727–737 (2009)
2. H. Biermann, U. Martin, C. Aneziris, A. Kolbe, A. Müller, W. Schärfl, Adv. Eng. Mater **11**, 1000–1006 (2009)
3. S. Martin, S. Wolf, U. Martin, L. Krüger, D. Rafaja, Metall. Mater. Trans. A **47A**, 49–58 (2016)
4. E. Kisi, C. Howard, Key Eng. Mater. 153–154, 1–36 (1998)
5. D. Green, R. Hannink, M. Swain, *Transformation Toughening Of Ceramics* (CRC Press, Boca Raton, Florida) (1998)
6. D. Ehinger, L. Krüger, U. Martin, C. Weigelt, C. Aneziris, Steel Res. Int. **82**, 1048–1056 (2011)
7. Schwartz, M. Kumar, B. Adams, *Electron Backscatter Diffraction in Materials Science* (Kluwer Academic, Plenum New York (2000)
8. H. Berek, A. Yanina, C. Weigelt and C. Aneziris, Steel Res. Int. **82**(9) (2011)
9. H. Berek, *In-situ-Druckverformung zellularer Werkstoffe in einem Röntgen-Tomographen* (TU Bergakademie Freiberg, Habilitation) (2013)
10. H. Berek, C. Aneziris, Ceram. Int. **44**, 17643–17654 (2018)

11. H. Berek, U. Ballaschk,C. Aneziris, Adv. Eng. Mater. **13**, 1101–1107 (2011)
12. H. Berek, U. Ballaschk, C. Aneziris, S. Hahn, in *Proceedings: International Conference on Cellular Materials CELLMAT2012*, Dresden (2012)
13. M. Oppelt, T. Leißner, H. Berek, C. Baumgart, L. Krüger, Adv. Eng. Mater. 1800615, (2018)
14. U. Ballaschk, H. Berek, D. Ehinger, C. Aneziris, L. Krüger, Adv. Eng. Mater. **15**, 590–599 (2013)
15. M. Abendroth, Private communication, TU Bergakademie Freiberg (2018)
16. ICDD, ICDD PDF-2 database release 2008 [online]. https://www.icdd.com
17. C. Aneziris, H. Berek, M. Hasterok, H. Biermann, S. Wolf, L. Krüger, Adv. Eng. Mater. **12**(3) (2010)
18. H. Berek, C. Aneziris, M. Hasterok, H. Biermann, S. Wolf, L. Krüger, in *PTM2010 Solid-Solid Phase Transformations in Inorganic Materials*, Avignon, France (2010)
19. H. Berek, C. Aneziris, M. Hasterok, H. Biermann, S. Wolf, L. Krüger, Solid State Phenom. 172–174, 709–714 (2011)
20. K. Schwartzwalder, A. V. Somers, U.S. Patent 3,090,094, 1963
21. H. Berek, U. Ballaschk, C. Aneziris, K. Losch, K. Schladitz, Mater. Charact. **107**, 139–148 (2015)
22. Testing of metallic materials-Compression test of metallic cellular materials, in *DIN 50134*, ed. (2008)
23. M. Ashby, Met. Trans. A **14** A, 1755–1769 (1983)
24. J. Elliott, A. Windle, J. Hobdell, G. Eeckhaut, R. Oldman, W. Ludwig, Am. J. Mater. Sci. **37**, 1547–1555 (2002)
25. R. Singh, P. Lee, T. Lindley, C. Kohlhauser, C. Hellmich, M. Bram, Acta Biomater. **6**, 2342–2351 (2010)
26. S. Martin, H. Berek, C. Aneziris, U. Martin, D. Rafaja, J. Appl. Cryst. **45**, 1136–1144 (2012)
27. C. Weigelt, C. Aneziris, H. Berek, D. Ehinger, U. Martin, Adv. Eng. Mater. 1–2 (2012)
28. C. Weigelt, C. G. Aneziris, A. Yanina, S. Guk, Steel Res. Int. **82**(9), 1080–1086 (2011)
29. H. Berek, C. Aneziris, M. Hasterok, C. Weigelt, in Werkstoffe und werkstofftechnische Anwendungen, 13. Werkstofftechnisches Kolloquium; TU Chemnitz, Chemnitz (2010)
30. F. Coté, V. Deshpande, N. Fleck, A. Evans, Mat. Sci. Eng. A. **83**, 272–280 (2004)
31. R. K. Mc Farland, AIAA J. **1**(6), 1380–1385 (1963)
32. T. Wierzbicki, Int. J. Impact Eng. **1**(2), 157–174 (1983)
33. M. Yang, P. Quiao, J. Sandw. Struct. Mater **10**, 133–160 (2008)
34. V. Dravid, V. Ravikumar, J. Am. Ceram. Soc. **77**, 2758–2762 (1994)
35. M. Lajavardi, D. Kenney, S. Lin, J. Chin. Chem. Soc. **47**, 1055–1063 (2000)

Chapter 17
The Corrosion Behavior of High-Alloy CrMnNi Steels—A Research Work on Electrochemical Degradation in Salt- and Acid-Containing Environments

Marcel Mandel, Volodymyr Kietov and Lutz Krüger

Abstract The electrochemical corrosion behavior of high-alloy cast steels as well as of steel/ceramic composites was analyzed by conventional polarization, electrochemical impedance and long term-outdoor exposure tests in sulfuric acid and chloride containing solutions. Additionally, for the determination of corrosion initiation processes and its subsequent implications, potentiodynamic polarization and electrochemical noise were combined with the acoustic emission technique. The results of these studies show that several corrosion mechanisms occur simultaneously when the surface is potentiodynamically stressed, and that pitting corrosion starts with a specific time-shift to its initiation at the surface.

17.1 Introduction

A wide range of techniques and analysis tools have been developed for studying the electrochemical corrosion behavior of high-alloy steels, with such techniques providing detailed information about the specific characteristics of steels in defined environments. The subsequent chapter explains how the electrochemical corrosion of high-alloy TRIP/TWIP steels with zirconium dioxide particle reinforcement was analyzed by a number of methods, such as conventional cyclic polarization, electrochemical impedance, indoor and outdoor exposure tests and special analytical tools, such as the combination of linear polarization and electrochemical noise measurement, as well as the acoustic emission method. For the presented results, the corrosion behavior of the analyzed steel and composite materials in salt- and/or acid-containing media was dictated primarily by the main alloying elements chromium, manganese and nickel as well as by the zirconia particle reinforcement. Due to the pronounced

M. Mandel (✉) · V. Kietov · L. Krüger
Institute of Materials Engineering, Technische Universität Bergakademie Freiberg, Gustav-Zeuner Str. 5, 09599 Freiberg, Germany
e-mail: mandel@iwt.tu-freiberg.de

H. Biermann and C. G. Aneziris (eds.), *Austenitic TRIP/TWIP Steels and Steel-Zirconia Composites*, Springer Series in Materials Science 298,
https://doi.org/10.1007/978-3-030-42603-3_17

passivity, pitting and uniform corrosion were observed, which are the predominant corrosion mechanisms and the focus for the subsequent interpretation of data in the relevant media.

17.2 The Effect of Transformation-Induced Plasticity (the TRIP Effect) on the Electrochemical Degradation of a High-Alloy CrMnNi Steel

Due to the large number of their excellent mechanical properties, their high corrosion resistance and acceptable cost-benefit ratios, high-alloy stainless steels are commonly used in a wide range of applications. As a certain type of this material class, high-alloy TRIP steels offer further enhancement of the mechanical characteristics due to the transformation induced plasticity effect, which arises from a microstructural phase transformation of the metastable austenite phase into a martensite phase during an energy-absorbing process [1–3]. This characteristic combined with good corrosion durability facilitates their integration in the technical configuration for safety-relevant components by reducing costs for subsequent corrosion-protection measures.

With the focus on the material's corrosion behavior, a particular advantage of high-alloy steels is their good corrosion resistance and durability in most aggressive environments. This corrosion resistance is predominantly due to the formation of a chromium-enriched passive oxide layer that restrains the metal-dissolution process during corrosion attack to a technically acceptable level. A further improvement is achieved by the addition of nickel and manganese. Nickel tends to agglomerate as an interlayer at the metal/oxide interface in its metallic state and can also affect the dissolution rate of the entire steel component, whereas manganese increases the solubility of nitrogen and molybdenum, elements that significantly enhance the pitting-corrosion durability of steels [4].

The effect of plastic deformation on the pitting corrosion sensitivity of high-alloy CastX6CrMnNi16-7-3—with the composition given in Table 17.1—was analyzed in a sodium chloride solution [5].

For the evaluation, two degrees of deformation—with $\varepsilon = 9\%$ and $\varepsilon = 18\%$—were defined and the influence of plastic deformation was investigated by cyclic voltammetry before comparison with the initial state. Figure 17.1 presents the scanning electron microscopy (SEM) micrographs for the initial state and after plastic deformation of the TRIP steel, with those components identified that acted in an anodic/cathodic manner during the corrosion attack.

Table 17.1 Chemical composition of high-alloy CastX6CrMnNi16-7-3 TRIP steel in wt%

C	N	Cr	Mn	Ni	Mo	Al	Ti	Si	Fe
0.06	0.13	16.3	6.71	3.06	0.037	0.061	0.0023	0.91	Bal.

In addition to the δ-ferrite, which was the dominant anodic component in the initial state (Fig. 17.1a), a number of deformation bands formed inside the austenitic phase during the deformation process (Fig. 17.1b) and also served as anodic components, whereas beside the δ-ferrite for $\varepsilon = 18\%$, elongated α'-martensite needles dictated the anodic dissolution process of the cast steel (Fig. 17.1c). The results of the polarization tests and the electron micrographs after the corrosion process are shown in Figs. 17.2 and 17.3.

The anodic polarization behavior clearly exhibited a strong dependency on the state of deformation. The initial state revealed the expected passivation and the initiation of metastable pitting corrosion when the anodic potential increased. For $\varepsilon = 9\%$, the corrosion potential $E_{\mathrm{Corr},1}$ increased significantly, but the range of passivity was reduced. It was assumed that this effect could be attributed to the homogeneously formed and distributed micro-anodes inside the large austenite grains (Fig. 17.1b). For the highest analyzed degree of deformation of $\varepsilon = 18\%$, the corrosion potential dropped again to the level of the initial state, and no significant passivation or pitting behavior was detected. In comparison to the initial state and $\varepsilon = 9\%$, the

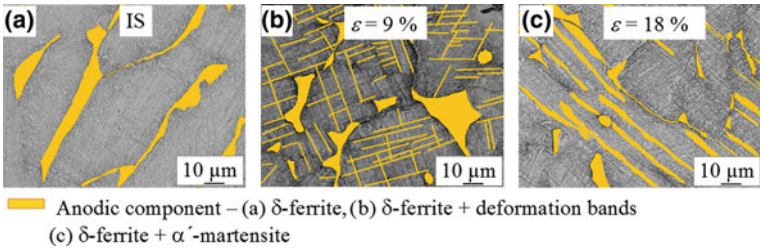

Fig. 17.1 SEM micrographs of **a** the initial state, **b** $\varepsilon = 9\%$ and **c** $\varepsilon = 18\%$, and the anodically active components during a corrosion attack [5]

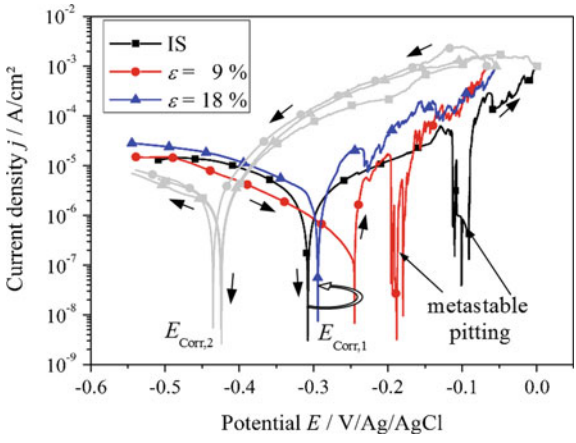

Fig. 17.2 Cyclic polarization curves of the high-alloy CrMnNi steel at different degrees of deformation in 5 wt% sodium chloride solution. $E_{\mathrm{Corr},1}$—corrosion potential before polarization, $E_{\mathrm{Corr},2}$—corrosion potential after polarization. IS—initial state [5]

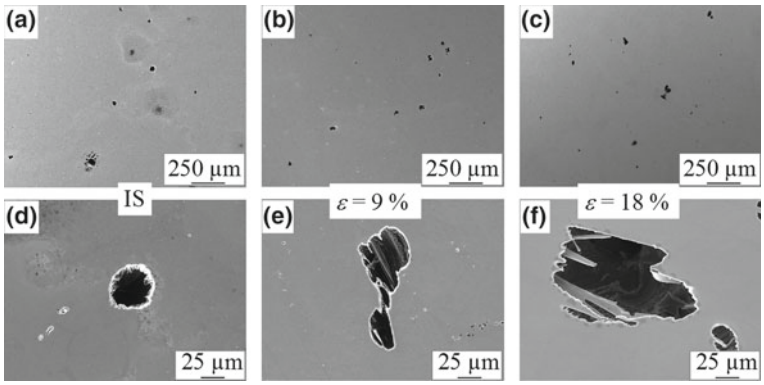

Fig. 17.3 SEM micrographs after polarization in 5 wt% sodium chloride solution. **a** Initial state. **b** $\varepsilon = 9\%$. **c** $\varepsilon = 18\%$. **d**, **e** and **f** detailed views [5]

highest degree of deformation also resulted in the highest degree of corrosion sensitivity during anodic polarization. In comparison, the reverse scan did not indicate any clear difference in polarization behavior, with all deformation states exhibiting similar curve trends and secondary corrosion potentials $E_{\mathrm{Corr},2}$. This characteristic clearly shows that after its initiation, the pitting corrosion attack—which was found for each state after the cyclic polarization (Fig. 17.3)—dictates the ongoing corrosion behavior of the whole steel sample and is independent of the degree of deformation.

17.3 Influence of Particle Reinforcement on the Corrosion Behavior of a High-Alloy Steel in Sodium Chloride Solution

The corrosion behavior of the spark plasma sintered zirconia particle-reinforced high-alloy X5CrMnNi14-6-6 steel was investigated by potentiodynamic polarization in a sodium chloride solution [6]. The chemical compositions of the steel and zirconia powder used are given in Tables 17.2 and 17.3.

Table 17.2 Chemical composition of the high-alloy X5CrMnNi14-6-6 steel in wt%

C	Cr	Mn	Ni	Al	S	Si	Fe
0.04	14.02	6.14	6.11	0.11	0.02	0.91	Bal.

Table 17.3 Chemical composition of the Mg-PSZ powder in wt%

ZrO_2	MgO	HfO_2	SiO_2	Al_2O_3	TiO_2
Bal.	3.37	1.73	2.43	0.63	0.14

Figure 17.4 presents the micrographs of the sintered materials without Mg-PSZ (i.e., 0 vol%) and with contents of 5 and 10 vol%. In comparison to the reinforced composites, the material without particle reinforcement exhibited an increased degree of porosity (Fig. 17.4a). For the composite materials (Fig. 17.4b, c), it was obvious that when the particle content increased, the matrix/particle interfaces also increased significantly, which drastically affected the corrosion behavior of the materials.

In Fig. 17.5 the potentiodynamic polarization curves in a 5 wt% sodium chloride solution are shown, while Fig. 17.6 presents the corresponding electron micrographs after corrosion of the sintered materials.

The polarization curves of the material without (0 vol%) and with 5 vol% particle content showed slight passivation, which was more pronounced for the unreinforced material than for the composite. In comparison, the composite material with 10 vol% Mg-PSZ exhibited the lowest corrosion potential and no significant passivation behavior, which indicated a higher degree of corrosion sensitivity.

The micrographs observed after corrosion attack clearly showed the formation of corrosion pits for the materials with 0 and 5 vol% Mg-PSZ (Fig. 17.6a, b), which was

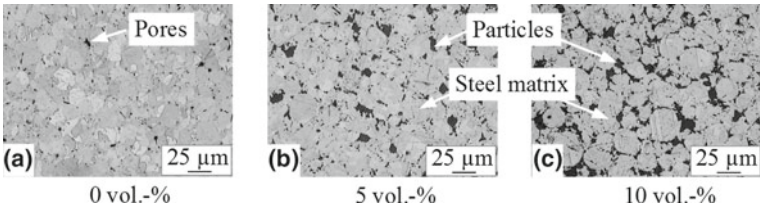

Fig. 17.4 Optical micrographs of the spark plasma sintered and Mg-PSZ particle-reinforced high-alloy steel. **a** without (0 vol%), **b** with 5 vol% and **c** with 10 vol% particle contents [6]

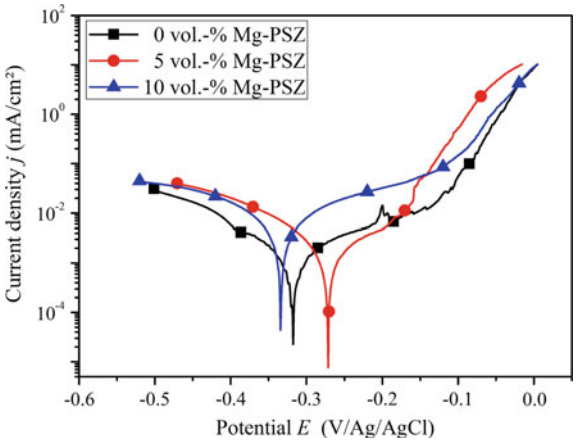

Fig. 17.5 Potentiodynamic polarization curves of the spark plasma sintered high-alloy steel with different Mg-PSZ particle contents in 5 wt% sodium chloride solution [6]

in full agreement with the anodic polarization behavior identified. It was assumed that pitting was initiated at the pores for the unreinforced material, because such pores represented critical weak points in and on the surface that interrupted the formation of a dense and continuous passive oxide layer. For the composite with 5 vol% Mg-PSZ, the micrograph clearly indicated that pitting had its origin at the matrix/particle interface. For the composite with 10 vol% Mg-PSZ, the corrosion attack was more homogeneous and no pitting was observed, with the entire surface indicating a uniform corrosion attack (Fig. 17.6c). As a primary result, the polarization curves and the micrographs clearly indicated that by increasing the Mg-PSZ particle content, the corrosion mechanism changed from pitting to general corrosion. Due to the increase in the particle content up to 10 vol%, the formation of a dense and compact passive oxide layer was suppressed and the composite became more susceptible to corrosion. To evaluate the passive oxide destabilization, the contents of iron and the main alloying elements found in the electrolyte was analyzed by ICP-MS (Inductively Coupled Plasma Mass Spectrometry) after the polarization. The results are presented in Fig. 17.7.

The comparison clearly shows that significant increases in the contents of iron, chromium, nickel and manganese are detectable in the solution when the Mg-PSZ

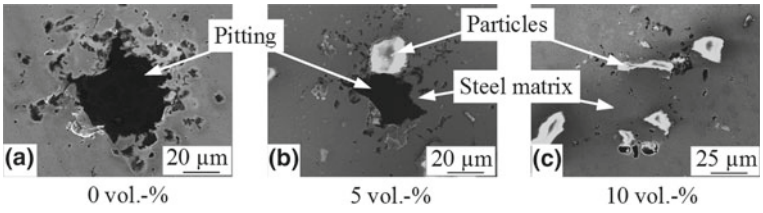

Fig. 17.6 SEM micrographs of the spark plasma sintered Mg-PSZ particle-reinforced steel after polarization in 5 wt% sodium chloride solution [6]

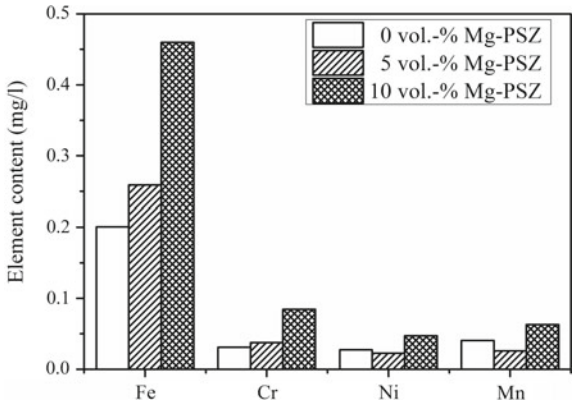

Fig. 17.7 Content of iron and main alloying elements in the electrolyte after potentiodynamic polarization in 5 wt% sodium chloride solution [6]

content is increased up to 10 vol%. The electrolyte analysis confirms that the passivation behavior of the steel matrix is drastically reduced when the particle content increases and the entire composite is more susceptible to an aggressive medium.

In a further study, the corrosion behavior of the unreinforced material (0 vol%) and the composite with 10 vol% Mg-PSZ particle content was investigated by a one-year outdoor exposure test and compared to the results obtained after potentiodynamic polarization in a 5 wt% sodium chloride solution [7]. For the outdoor exposure test, the specimens were stored in an outdoor exposure test rig in Dresden, Germany and sprayed weekly with a 3 wt% sodium chloride solution.

Figure 17.8 presents the micrographs after the polarization test in the 5 wt% sodium chloride solution and after the one-year outdoor exposure test.

After polarization, the material without particle reinforcement was attacked by pitting corrosion (I in Fig. 17.8a), whereas the particle-reinforced composite exhibited a uniform corrosion attack and an attack at the particle/matrix interface (II in Fig. 17.8b), which was accompanied by intensified particle detachment (III in Fig. 17.8b). Similar behavior was observed after one year of outdoor exposure testing. Pits were identified on the surface of the unreinforced material (Fig. 17.8c), while a large number of small cavities were found on the composite material that had resulted from the detachment of Mg-PSZ particles (Fig. 17.8d). In addition to these localized corrosion attacks, the intensified formation of red rust was observed. This behavior was more pronounced for the composite material and also confirmed the higher corrosion sensitivity and lower passivation ability that was identified

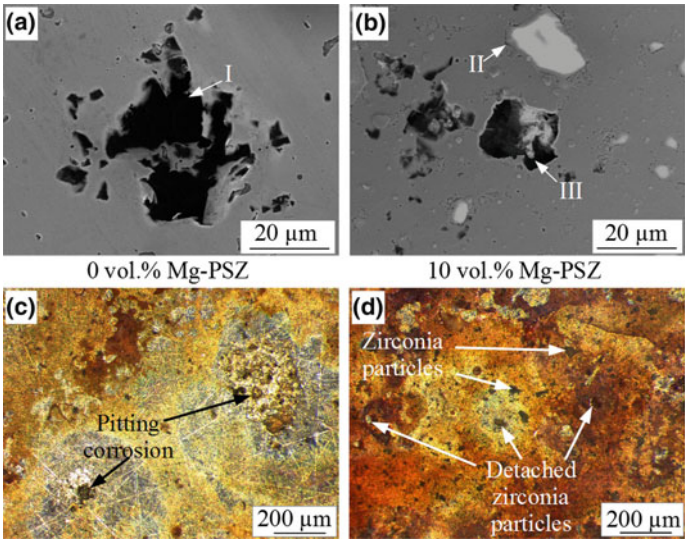

Fig. 17.8 Micrographs of the spark plasma sintered high-alloy steel after potentiodynamic polarization in 5 wt% sodium chloride solution and after one year of outdoor exposure. **a** and **c** without particle reinforcement. **b** and **c** with 10 vol% Mg-PSZ. For I, II and III, see text [7]

during the polarization test. The results of the study show that under similar conditions, the results of the short-time polarization test can be used to approximate the corrosion behavior associated with long-term outdoor exposure tests.

17.4 Electrochemical Corrosion of the Particle-Reinforced High-Alloy Steel at Different Temperatures

The electrochemical corrosion behavior of the composite material with 10 vol% Mg-PSZ was investigated in a 5 wt% sodium chloride solution by cyclic polarization and electrochemical impedance at temperatures of 25, 35, 45 and 55 °C. In a separate test, the critical temperature for intensified particle detachment was determined [8]. Figure 17.9 presents the optical micrographs of the composite material in its initial state.

Figure 17.10 shows the impedance spectra at different temperatures before the cyclic polarization, which clearly indicate a strong temperature dependency. In the Nyquist plot (Fig. 17.10a) for each temperature, a simple semi-circle is described by the data points, which indicate the reduction of the charge-transfer resistance when the temperature increases. From the Bode illustrations (Fig. 17.10b, c), one time constant was extracted for each temperature. Figure 17.11 shows the electrode configuration and the equivalent circuit that was used for modeling and curve fitting. The results are summarized in Table 17.4. The parameters Q and α did not depend on the temperature to a significant degree, whereas $R_{t,bp}$ declined when the temperature increased, indicating an increase in the charge transfer processes when the temperature increased. Similar behavior was noted for the electrolyte resistance R_e, signifying an increase in the conductivity of the test solution. Figure 17.12 presents the cyclic polarization curves for the selected temperatures, which clearly illustrate the significant enhancement of the corrosion kinetics when the temperature rises. The corrosion potentials before (1 in Fig. 17.12) and after (2 in Fig. 17.12) the polarization process did not exhibit any significant dependency on the temperature, whereas the anodic parts of the curves revealed that there was no passivation and that the slopes

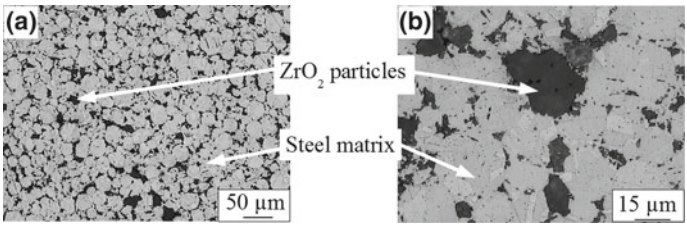

Fig. 17.9 Micrographs of the spark plasma sintered particle-reinforced high-alloy steel with 10 vol% Mg-PSZ. **a** Overview of particle distribution in the steel matrix. **b** Detailed view of particle agglomeration [8]

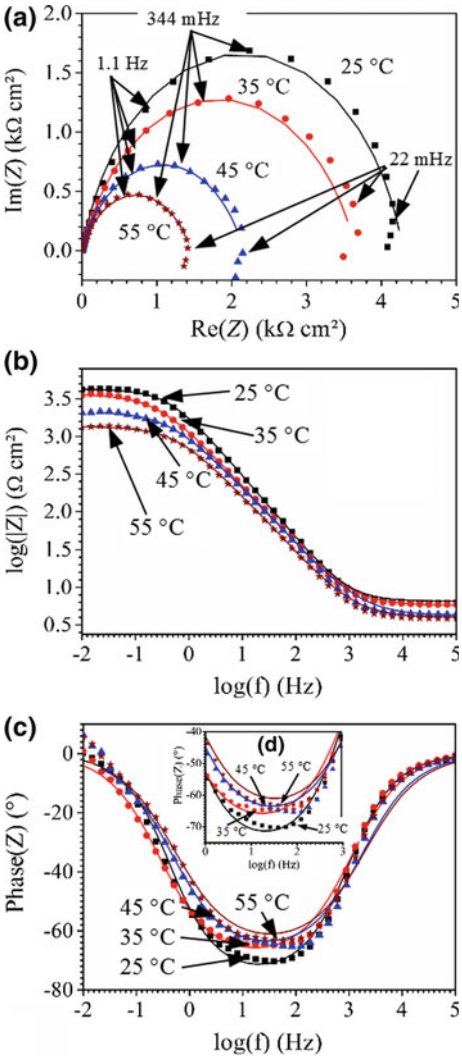

Fig. 17.10 Electrochemical impedance spectra of the spark plasma sintered high-alloy steel before cyclic polarization at different temperatures [8]

increased in line with the temperature. The more negative values for the corrosion potential 2 in Fig. 17.12 clearly indicated a more corrosion-sensitive electrode state at each temperature after the polarization. From the progression of the curve, it was deduced that the temperature influenced the corrosion potentials minimally, though it affected the polarization behavior significantly. Figure 17.13 shows the electron micrographs of the composite material after cyclic polarization. For 25 and 35 °C, the surfaces showed evidence of a predominantly homogenous corrosion attack with weak localized corrosion attacks (arrows in Fig. 17.13a, b), which were related to the increased porosity due to Mg-PSZ particle detachment.

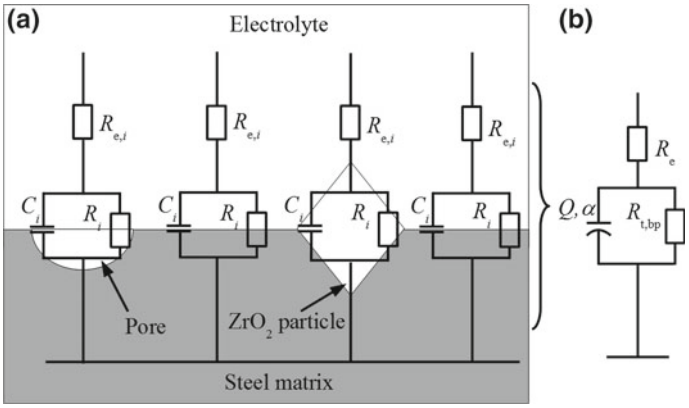

Fig. 17.11 **a** Schematic illustration of the electrode configuration before cyclic polarization, and **b** equivalent circuit used for curve fitting. R_i, C_i and $R_{e,i}$ stand for the local and R_e, Q, α, and $R_{t,bp}$ the global impedance parameters before polarization

Table 17.4 Impedance curve fitting results before polarisation in 5 wt% NaCl solution on 10 vol% Mg-PSZ particle-reinforced steel

T (°C)	R_e (Ω cm^2)	Q ($\mu\Omega^{-1}$ cm^{-2} s$^{\alpha}$)	α	$R_{t,bp}$ (kΩ cm^2)
25	6.2	176	0.82	4.0
35	5.3	302	0.74	2.1
45	5.0	180	0.80	1.6
55	4.5	322	0.74	1.5

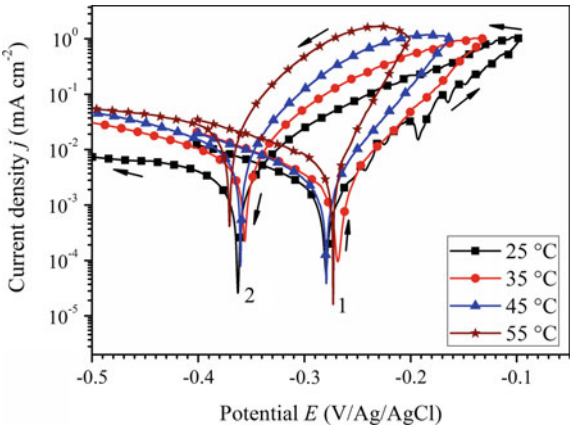

Fig. 17.12 Cyclic polarization curves of the spark plasma sintered particle-reinforced high-alloy steel at different temperatures. 1—E_{Cor} before polarization. 2—E_{Cor} after polarization [8]

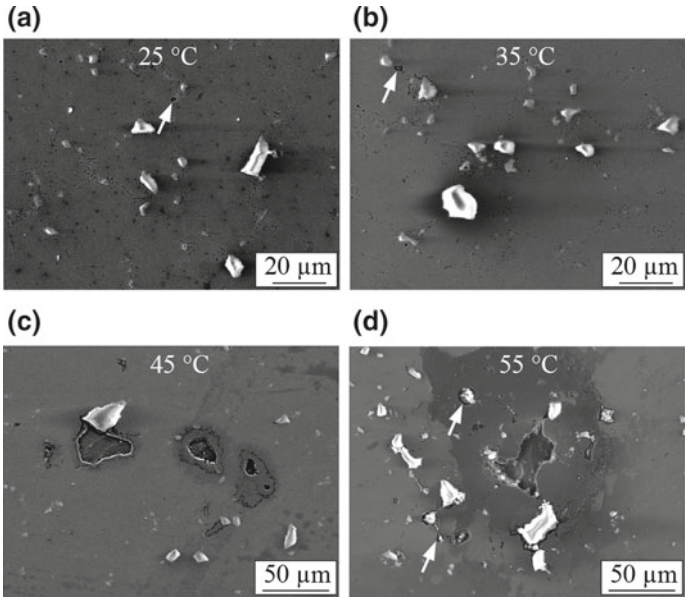

Fig. 17.13 SEM micrographs of the particle-reinforced composite after cyclic polarization in 5 wt% NaCl solution at different temperatures [8]

The micrographs observed for 45 and 55 °C clearly show an attack by localized corrosion that had its origin at the particle/matrix interface (arrows in Fig. 17.13d). It was obvious that when the temperature increased above 35 °C, particle detachment occurred in a more intensified fashion as a result of the enhanced corrosion kinetics at the interface. From the results of the electron microscope observations, it was certain that a critical temperature for intensified particle detachment had to exist in the range of 35 to 45 °C. Figure 17.14 presents the electrochemical impedance spectra measured after the polarization test. Similarly to the initial state shown in Fig. 17.10, the Nyquist illustration revealed a semi-circle for each temperature with a significant decrease of the charge transfer resistance for $T = 45$ °C and $T = 55$ °C (Fig. 17.14a). From the Bode plots (Fig. 17.14b, c), two time constants were identified for all temperatures, which were related to charge transfer processes at the interface between the composite and the layer generated by film formation and redox reactions inside the film formed. The surface structure and the equivalent circuit used for curve fitting are presented in Fig. 17.15.

After polarization, the global impedance parameters of the composite/film interface were expressed by Q_1, α_1 and $R_{t,ap}$ and for the film by Q_2, α_2 and R_f. The results obtained by curve fitting are summarized in Table 17.5.

For 25 and 35 °C, the parameters Q_1, α_1 and $R_{t,ap}$ were dictated by the pores and Mg-PSZ particles. At temperatures of $T = 45$ °C and $T = 55$ °C, the impedance values included the increased porosity, the attacked interface at the particles and the pits that were formed. For the determination of the critical pitting temperature, the

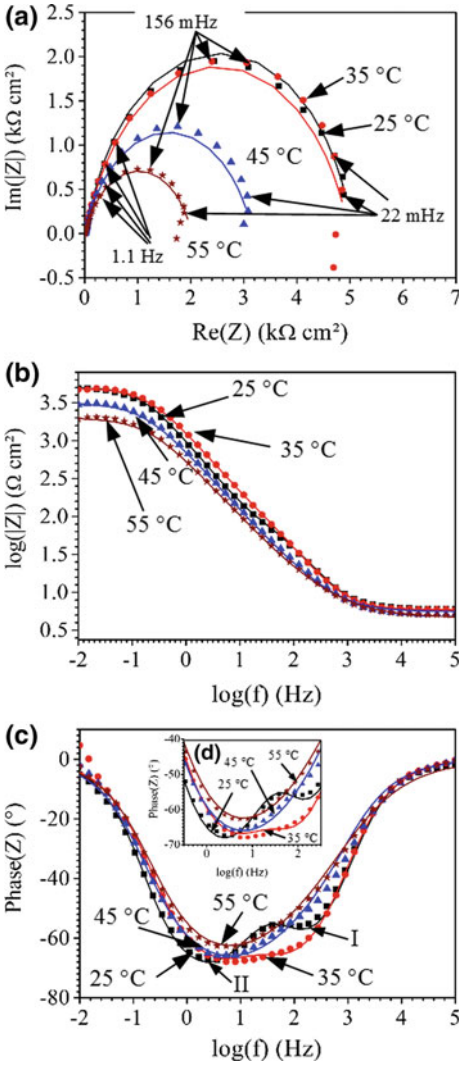

Fig. 17.14 Electrochemical impedance spectra of the particle-reinforced composite determined after cyclic polarization in 5 wt% sodium chloride solution for different temperatures [8]

current-time relationship for continuously increasing temperature was recorded, and is shown in Fig. 17.16.

The correlation revealed a slight increase in current density up to a temperature of 34 °C, including a peak between 32 and 33 °C. This characteristic was related to particle detachment. When the temperature increased further, the current density increased significantly and exhibited fluctuations up to a temperature of 38 °C—which was related to the intensified particle detachment that was evident. For higher temperatures, the current density increased drastically and indicated pitting corrosion

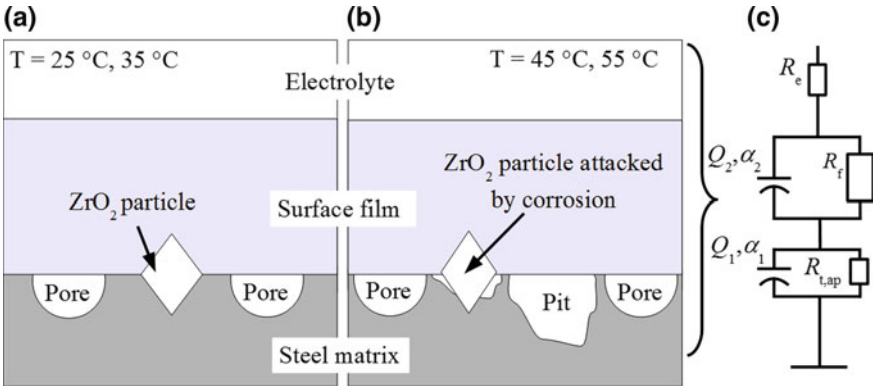

Fig. 17.15 **a**, **b** Schematic illustration of the composite interface after polarization in 5 wt% sodium chloride solution at different temperatures. **c** Equivalent circuit used for curve fitting of the impedance spectra [8]

Table 17.5 Impedance curve fitting results after polarisation in 5 wt% NaCl solution on 10 vol% Mg-PSZ particle-reinforced steel. T in °C, R_e, $R_{t,ap}$ in Ω cm^2 and R_f in kΩ cm^2, Q_1, Q_2 in μΩ^{-1} cm^{-2} s$^{\alpha}$

T	R_e	Q_1	α_1	$R_{t,ap}$	Q_2	α_2	R_f
25	6.3	390	0.92	17	215	0.83	5.4
35	5.5	496	0.91	29	64.3	0.79	4.3
45	5.2	229	0.77	13	54.5	0.83	3.2
55	4.8	1260	0.58	11	104	0.78	1.8

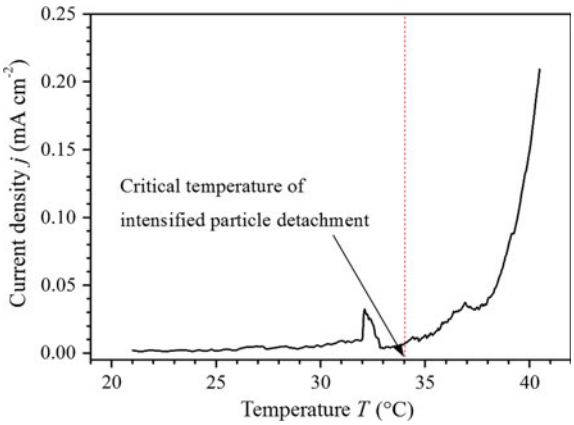

Fig. 17.16 Current density—temperature relationship for determination of the critical temperature of the composite [8]

attack. Consequently, the critical temperature for intensified particle detachment and subsequent pitting corrosion attack on the composite was approximately 34 °C.

17.5 Potentiodynamic Polarization of CastX5CrMnNi16-7-9 in Sulfuric Acid Solution Combined with Acoustic Emission Analysis

The acoustic emission (AE) technique for the investigation of corrosion phenomena is an excellent method for analyzing the different processes taking place in parallel at the electrode surface [9, 10]. As shown by Boinet et al. [9], acoustic emission analysis facilitates the separation of surface degradation processes and gas bubble evolution by determination of the frequency of AE signals. To evaluate the corrosion activity of the high-alloy cast steel CastX5CrMnNi16-7-9 in sulfuric acid solution, the AE method was applied during potentiodynamic polarization. The chemical composition and characteristic microstructure of the initial state are given in Table 17.6 and Fig. 17.17.

In contrast to the widely used two-cell configuration, which is discussed in detail elsewhere [11], the modified test set-up shown in Fig. 17.18 was used, which also facilitated the observation of the gas bubble stream leaving the electrode surface [12].

The polarization characteristic and corresponding AE activity is presented in Fig. 17.19. To illustrate the correlation between polarization and acoustic emission as well as the involvement of the 30-minute OCP measurement (OCP—open circuit

Table 17.6 Chemical composition of the high-alloy cast steel CastX5CrMnNi16-7-9 in wt%

C	N	Cr	Mn	Ni	Mo	Al	Cu	W	Si	Fe
0.048	0.076	15.7	6.29	9.23	0.082	0.047	0.011	0.02	0.853	Bal.

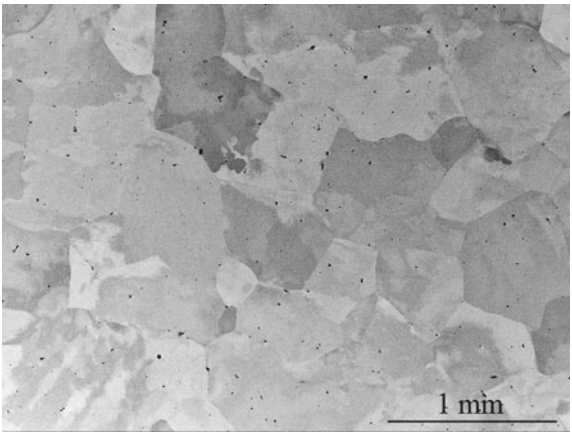

Fig. 17.17 Electron micrograph of CastX5CrMnNi16-7-9 [12]

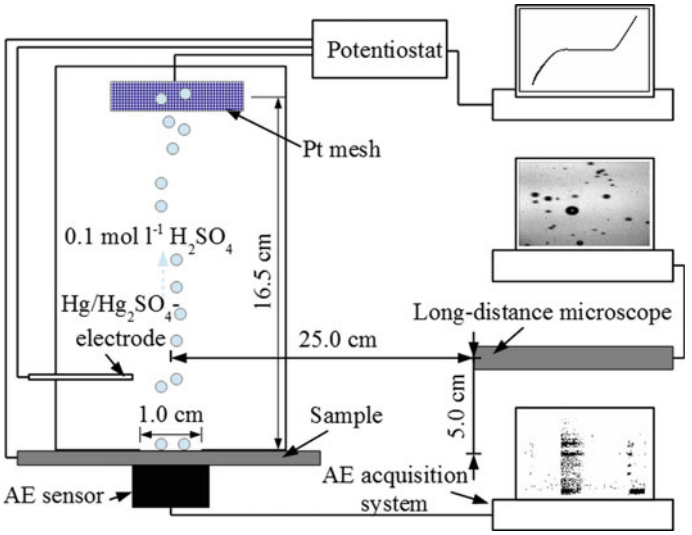

Fig. 17.18 Schematic illustration of the test set-up used for investigation of the acoustic activity and gas bubble evolution process for a steel electrode during potentiodynamic polarization in a 0.1 M H_2SO_4 solution [12]

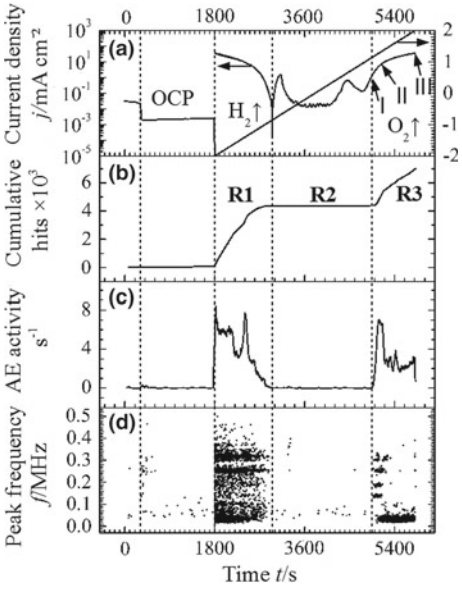

Fig. 17.19 Correlation between the potentiodynamic polarization and measured acoustic emissions. **a** Open circuit measurement (OCP) and polarization behavior. **b** Cumulative AE hit number. **c** AE activity. **d** Peak frequency of AE signals. I, II and III indicate current densities upon oxygen evolution analysis [12]

potential), the time t was chosen as the common x-axis. In general, 3 regions of acoustic activity (R1, R2 and R3) where recognized during the polarization. Region R1 was indicated by a high level of acoustic activity (Fig. 17.19b, c) and corresponded fully to the cathodic branch of the polarization curve when intensified H_2 gas bubble evolution was initiated. Region 2 (R2) was characterized by low AE activity, whereas region 3 (R3) indicated a further increase in acoustic emissions, which was attributed to the evolution of oxygen at the electrode.

Before polarization, the OCP measurement revealed a conspicuous AE event number in the frequency range of $f = 150$–460 kHz after approximately $t \sim 400$ s (Fig. 17.19d) that corresponded to a significant decline in potential of $\Delta E = 570$ mV (Fig. 17.19a). The literature indicates that this frequency range is typical for the evolution of a hydrogen bubble at the electrode surface. Consequently, it was concluded that the decline in potential observed indicated the transition of the electrode into the steady state, which was accompanied by the release of hydrogen gas bubbles from the steel surface. The analysis of region 1 (R1) showed the existence of two characteristic processes which occurred almost simultaneously at the steel electrode. One of these was the intensified hydrogen bubble evolution observed during cathodic polarization (see Fig. 17.20a), and generated AE signals in the frequency range of $f =$ 100–430 kHz. The hydrogen gas bubbles had a diameter in the range of 200–640 μm. The second type of AE was observed in the lower frequency range of $f = 20$–100 kHz and was attributed to the hydrogen-assisted exfoliation process (Fig. 17.20b). The AE data analysis of region R1 revealed two classes of AE signals by determination of its spectral AE energy and signal duration. The results are presented in Fig. 17.20c and clearly show two specific clusters (C1 and C2).

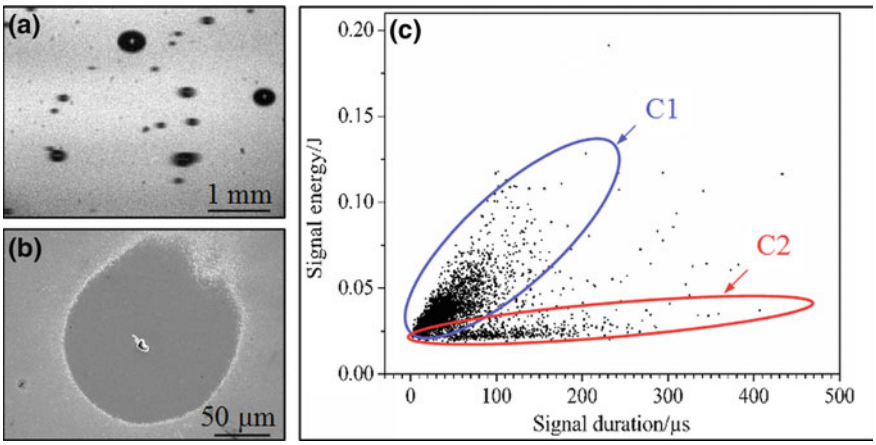

Fig. 17.20 Hydrogen evolution **a** and hydrogen-assisted exfoliation of the passive oxide **b** are the characteristic AE sources during cathodic polarization. The AE data analysis **c** indicated a high energy and low duration for the hydrogen bubble evolution process (cluster C1), and low energy with high signal duration for the exfoliation process (cluster C2) [12]

Cluster C1 was characterized by a high spectral energy and low signal duration and corresponded to hydrogen bubble evolution. In cluster C2, the signals were typified by lower spectral energies and higher durations, and correlated to the hydrogen-assisted exfoliation process.

At the transition into anodic polarization, the AE hit number and activity (Fig. 17.19 b, c) decreased drastically. Just a low number of AE signals were identified in region R2, with most of them in the frequency range below 100 kHz, which was attributed to electrochemical degradation processes on the steel surface. The surface analysis by SEM identified a corrosion attack at the pore edges (Fig. 17.21) that remained constant when the potential increased within region R2.

Figure 17.22 presents a detailed view of the AE peak frequency characteristics of region R3 (Fig. 17.22a) and the corresponding cluster analysis (Fig. 17.22b). Similar to region R1, the subsequent AE data analysis exhibited a high signal energy and low duration for the AE hits with $f > 100$ kHz and low energy and high duration for the AE signals with $f < 100$ kHz.

After passing the potential of $E_1 = 1.15$ V versus Hg/Hg_2SO_4, a second increase in AE activity occurred that correlated with the onset of oxygen gas bubble formation.

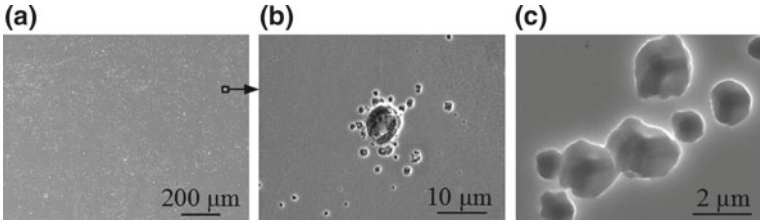

Fig. 17.21 Characteristic damage evolution on the steel surface during anodic polarization in region R2. **a** Overview. **b** Detailed view showing corrosion attack at the pore edges. **c** Detailed view showing corrosion attack at the passive oxide [12]

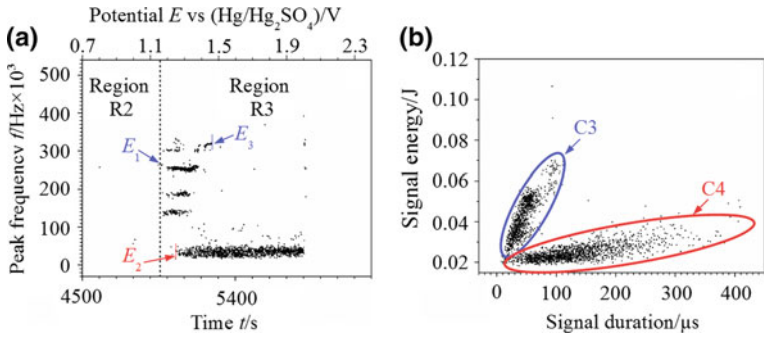

Fig. 17.22 **a** Observed peak frequency-time relations as a function of the applied potential. **b** The corresponding AE cluster analysis. E_1, E_2 and E_3 denote the specific potentials of the clusters C3 and C4 [12]

The analysis of the gas stream revealed a bubble diameter in the range of 240–430 μm and the AE data exhibited a corresponding peak frequency of $f > 100$ kHz, which was similar to the hydrogen bubble diameter and peak frequency range observed in region R1. Additionally, when the potential was increased further up to $E_2 = 1.25$ V versus Hg/Hg_2SO_4, gas bubbles of significantly lower diameters of approximately 50 μm were identified in the gas stream (Fig. 17.23b). Simultaneously, an increase in the number of AE events within the peak frequency of $f = 20$–60 kHz was observed (Fig. 17.22a), which was in a similar frequency range to the signals attributed to the hydrogen-assisted exfoliation in region R1 (Fig. 17.19 d). The oxygen gas bubbles with diameters of 240–430 μm were designated as oxygen bubbles of Type 1, while the bubbles with a diameter of approx. 50 μm were designated as oxygen bubbles of Type 2.

Moreover, when the potential was increased further up to $E \sim 1.45$ V versus Hg/Hg_2SO_4, the AE signals with a peak frequency of $f > 100$ kHz ended abruptly, which corresponded well with the disappearance of Type 1 oxygen bubbles in the gas stream. Up to the end of the polarization process, only Type 2 oxygen gas bubbles were identified in the gas stream (Fig. 17.23c).

The damage evolution of the steel surface observed by scanning electron microscopy showed a clearly inhomogeneous corrosion attack (Fig. 17.24a) when the steel was polarized up to point II (II in Fig. 17.19a). In accordance with the observations made after cathodic polarization, pores were the preferred locations for the genesis of Type 1 oxygen gas bubbles (Fig. 17.24b). In addition, the rest of the surface was marked by regions of localized corrosion attacks (F-I in Fig. 17.24c) and areas of full depassivation (F-II in Fig. 17.24c). The drastic increase in damage evolution was attributed to an oxygen-assisted exfoliation process, which identified the steel surface as the location for the formation of Type 2 oxygen gas bubbles. Up to the end of the polarization process (III in Fig. 17.19a), the scanning electron micrographs showed a fully depassivated steel surface and corrosion attack at the grain boundaries due to intergranular corrosion (Fig. 17.24d). As a side effect of the exfoliation process (Fig. 17.24f), a dissolution of the pores was observed that eliminated the basis of Type 1 oxygen bubble evolution (Fig. 17.24e).

Consequently, the rate at which oxygen bubbles was released at the pores had to decrease when the passive oxide dissolution increased. This behavior was in full

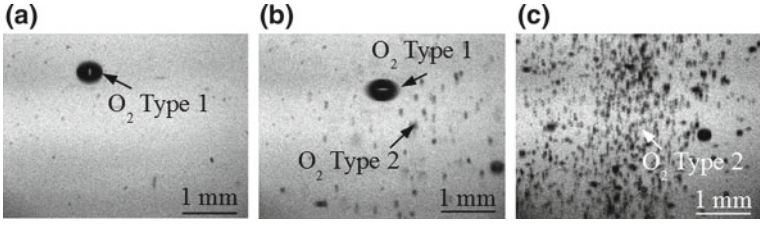

Fig. 17.23 Photographs of the oxygen gas bubble stream at anodic applied potential **a** at I in Fig. 17.19a, **b** at II in Fig. 17.18a, **c** at the end of the polarization test (III in Fig. 17.19a) [12]

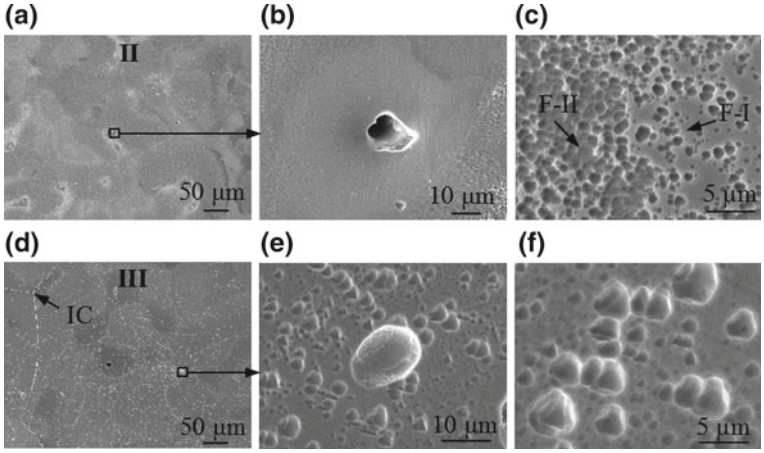

Fig. 17.24 SEM micrographs of the steel surface after polarization up to point II (**a–c**) and up to the end of the polarization test (**d–f**). IC—Intergranular corrosion. For F-I and F-II, see text [12]

accordance with the observed decline in the release of Type 1 oxygen bubbles and the identified potential limitation of AE events with frequencies of $f > 100$ kHz (Fig. 17.19d).

17.6 Analysis of Pit Initiation on CastX3CrMnNi16-7-9 by the Combination of Electrochemical Noise and Acoustic Emission Measurement

The electrochemical noise (EN) and acoustic emission (AE) methods are highly suitable monitoring and analysis tools for the investigation of corrosion initiation processes under steady state conditions [9–17]. The EN technique is based on the measurement of potential and/or current fluctuations, which facilitates the determination of the activity of a corrosion system. The AE technique—based on the measurement of elastic waves—is useful in identifying different corrosion mechanisms occurring at the same time on a surface [12]. One outstanding characteristic is that both methods are non-destructive and highly sensitive, which facilitates the identification of corrosion initiation processes.

Due to these advantageous properties, the EN and AE techniques were combined in the identification of pit initiation at the surface of the high-alloy cast steel CastX5CrMnNi16-7-9—with the chemical composition and microstructure given in Table 17.6 and Fig. 17.17—in a 5 wt% sodium chloride solution [18]. The investigation was carried out with the test set-up shown in Fig. 17.25. Details of the experimental specifications of the electrochemical noise and acoustic emission measurements are given in [18].

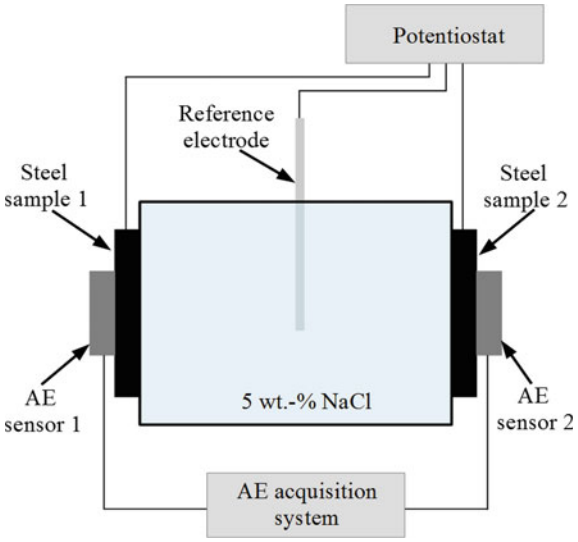

Fig. 17.25 Test set-up used for characterization of the pit initiation behavior of Cast X5CrMnNi16-7-9 by means of combined electrochemical noise and acoustic emission measurement [18]

Figure 17.26 presents the results of the 70-hour test, which exhibited two characteristic types of AE events and four specific regions of noise behavior. For a more sensitive analysis of the EN behavior, the standard deviations of the potential and current noise—σ_E and σ_i—were determined and evaluated. The results are shown in Fig. 17.27.

From the point of view of the EN behavior (Fig. 17.27), region EN-I was characterized by strong fluctuations, indicating the high electrochemical activity of the steel surface before transitioning into a nearly steady state after approximately 3 h, which is given by region EN-II. In region EN-II, the signal fluctuations were significantly lower, indicating that the steel surface had transitioned into a passive state. In addition to this predominantly inactive electrochemical state, a spontaneous short-time event was observed after approximately 16 h of exposure. This event was attributed to localized passive oxide deterioration caused by the chloride ions in the solution, indicating metastable pitting corrosion. Region EN-II ended abruptly after approximately 20 h of exposure, which was indicated by a drastic increase in potential and current fluctuations that characterized region EN-III. The high degree of fluctuations in region EN-III indicated a highly active surface state. This behavior was related to the onset of an active pitting corrosion attack. Region EN-III had a duration of 15 h and ended after approximately 35 h of exposure. The transition into region EN-IV was characterized by a continuous decline in the fluctuations to the point of low electrochemical activity, indicating the repassivation of active pits. Nevertheless, EN-IV also exhibited time intervals of increased activity, which were attributed to a spontaneous and irregular reactivation of previously formed pits and active pit growth. When considering the results of the acoustic emission test, no acoustic activity could

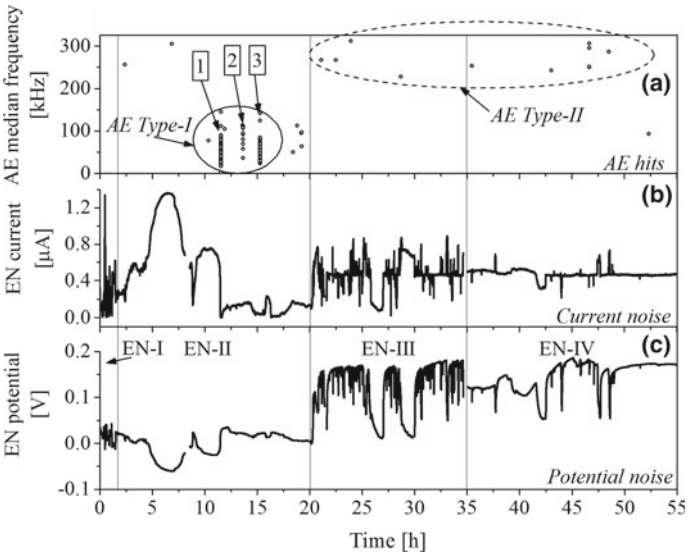

Fig. 17.26 Electrochemical noise behavior and corresponding AE characteristics of CastX5CrMnNi16-7-9 during a 70 h exposure test in 5 wt% NaCl solution. **a** Median frequency of the AE signals. **b** and **c** Current and potential noise signals [18]

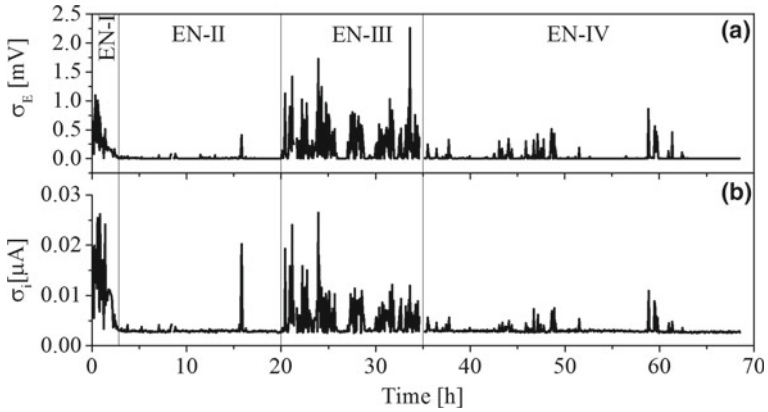

Fig. 17.27 Standard deviation of the potential **a** and current **b** noise extracted from the signals given in Fig. 17.26b, c [18]

be observed after 10 h of exposure (see Fig. 17.26a). Indications of AE activity were identified after $t = 11.6$ h, $t = 13.7$ h and $t = 15.3$ h, which were marked by the numbers 1, 2 and 3 in Fig. 17.26a and which lay entirely within region EN-II. The events arose in three clusters with a median peak frequency of $f < 100$ kHz, indicating three corrosion attacks at the steel surface. For higher exposure times—especially in the regions EN-III and EN-IV—a second class of events with a median peak frequency

of $f > 100$ kHz were observed. The AE signal analysis and the characteristic shape of the waveform (Fig. 17.28) clearly described two different types of AE signals.

The signals with a peak frequency of $f < 100$ kHz were designated as AE Type I signals and the events with $f > 100$ kHz were characterized as AE Type II signals (see Fig. 17.26a). With respect to the findings described in the literature [9, 12], it can be stated that AE Type I signals are characteristic for spontaneous and localized passive oxide breakdown, whereas the irregularly distributed events that give rise to AE Type II signals may be attributed to subsequent hydrogen bubble evolution inside previously formed pits [19, 20]. SEM observations after test completion confirmed localized deterioration in the form of three pits that developed on the steel surface under corrosive attack (Fig. 17.29). Consequently, the electrochemical noise and corresponding acoustic emission development made it possible to identify and follow the point of pit initiation ($t = 11.6$ h) and the subsequent pit evolution process.

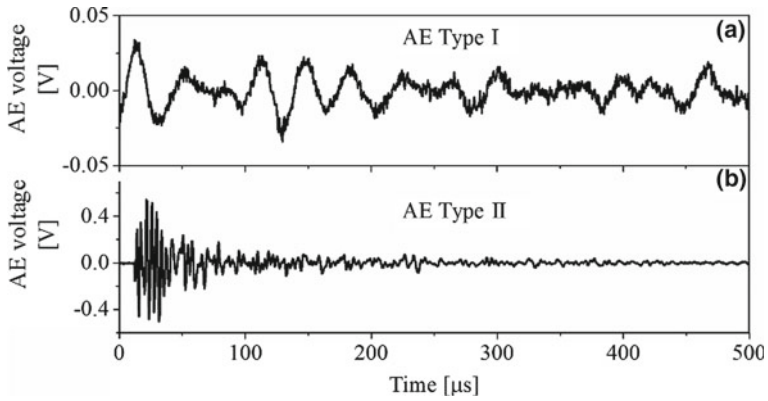

Fig. 17.28 Wave forms of the **a** AE Type I and **b** AE Type II signals [18]

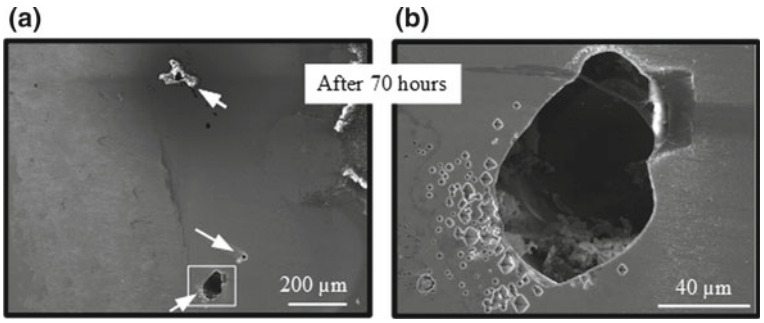

Fig. 17.29 SEM micrograph of the CastX5CrMnNi16-7-9 steel after the 70 h electrochemical noise and acoustic emission measurement test. **a** Overview. Arrows indicate the locations of pitting corrosion. **b** Detailed view of the pit marked with a rectangle in **(a)** [18]

17.7 Analysis of Electrochemical Noise by Continuous Wavelet Transform

As shown in [18], the electrochemical noise technique is a highly sensitive and, therefore, highly appropriate analysis method for online corrosion monitoring and the identification of different stages in pit evolution. Several techniques in noise data analysis were developed to ensure the precise acquisition of information about the corrosion process. Widely used techniques such as certain statistical methods, the Fourier transformation and wavelet analysis are practiced [14, 21, 22], though highly specified analytical procedures have also been developed to identify and isolate localized and uniform corrosion attacks [23, 24]. In principle, the above-mentioned mathematical techniques analyze the changes in the fluctuations of the noise signal and provide information about the onset, duration and kinetics of a corrosion system [25–27]. A corrosion system that is highly active electrochemically is identified by transients of high frequencies and high amplitudes, whereas a noise signal of lower intensity indicates a more passive corrosion state [14, 28]. Aballe et al. use the discrete wavelet transform (DWT) for subsequent noise data analysis [29, 30], which provides specific information about short-time and long-term corrosion processes. The DWT method was applied for the noise transient analysis of CastX5CrMnNi16-7-9 (with the chemical composition and microstructure presented in Table 17.6 and Fig. 17.17) in sulfuric acid and sodium chloride solutions. In the acid medium, the hydrogen bubble evolution was identified as the process that generated characteristic short-time corrosion events, whereas long-term transients in the salt-containing solution are characteristic for pit initiation and subsequent evolution processes [17]. As a further method for noise analysis, the continuous wavelet transform (CWT) is used for identification of the dynamic behavior of a system [31]. In consideration of the findings in the literature [21, 29–31], the CWT was applied for the investigation of the noise behavior of the high-alloy cast steel CastX15CrNiMnN19-3-4 (with the chemical composition given in Table 17.7) in sulfuric acid and in sodium chloride solutions, as well as in a combination of both media.

The noise behavior was measured for 2 h and the corresponding CWT analysis was carried out for a time interval of 20 min for each system. Figure 17.30 presents the results in a 0.1 M H_2SO_4 solution.

The normalized and detrended noise signal exhibited many short-time current transients of high amplitude, indicating a high proportion of corrosion events of short duration. The subsequent CWT analysis exhibited maxima of the CWT coefficients in the upper and middle frequency region between $f = 0.063$–16 Hz, but with the highest value for the transient after approximately 40 min (Fig. 17.30a) with $f = 4$–10 Hz (marked by the ellipse in Fig. 17.30b). In contrast, the current noise signal for the

Table 17.7 Chemical composition of the CastX15CrMnNiN19-3-4 in wt%

C	N	Cr	Ni	Mn	Si	Fe
0.148	0.165	19.1	4.12	2.85	0.5	Bal.

cast steel in sodium chloride solution exhibited significantly less transients of lower amplitude, indicating a system that was less active electrochemically (Fig. 17.31a). The signal analysis exhibited a clear maximum in the lower frequency region with $f =$ 0.063–0.25 Hz (Fig. 17.31b), which corresponded to the highest transient identified after approximately 6 min of exposure. Figure 17.32a) presents the results of the noise measurement in the mixed electrolyte, which contained identical volume fractions of sulfuric acid and sodium chloride solutions.

The comparison to the results using the unmixed solutions (Figs. 17.31 and 17.32) clearly indicates a drastic increase in the number of transients. The subsequent signal analysis identified maxima in the lower frequency region (with $f = 0.016$–1 Hz) of significantly higher duration, indicating long-lasting corrosion processes in the range of 1 s to 1 min. The scanning electron micrographs observed after the noise measurements revealed an enhanced intergranular corrosion attack in the unmixed acid solution (Fig. 17.33a) and in the combined electrolyte (Fig. 17.33c). In the sodium chloride solution, the corrosion attack was significantly less. Localized corrosion and the formation of corrosion products arranged in a circle around the pit were observed (Fig. 17.33b), which was a quite different mode of behavior in comparison to that observed in the acid solution.

From the micrographs, it was obvious that the corrosion attack in the unmixed acid and the combined electrolyte was nearly identical. This behavior clearly indicated that the acid dominated the corrosion attack in the combined solution, and that the sodium chloride seemed to have little or no effect on the corrosion attack. When considering the CWT noise analysis, however, the influence of the salt became clear. The

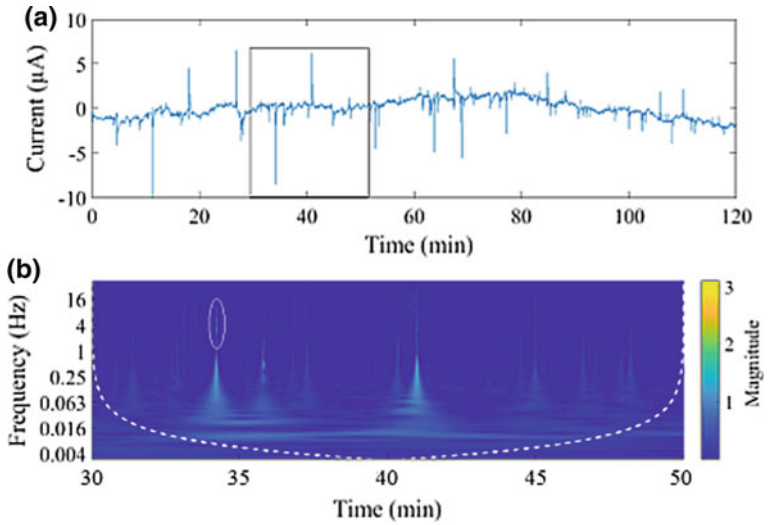

Fig. 17.30 **a** Current noise-time relation of CastX15CrMnNiN19-3-4 in 0.1 M sulfuric acid solution and **b** corresponding CWT analysis of the noise signal for the time interval marked by the rectangle in (**a**). The ellipse marks the magnitude maximum. Dashed line—the cone of influence

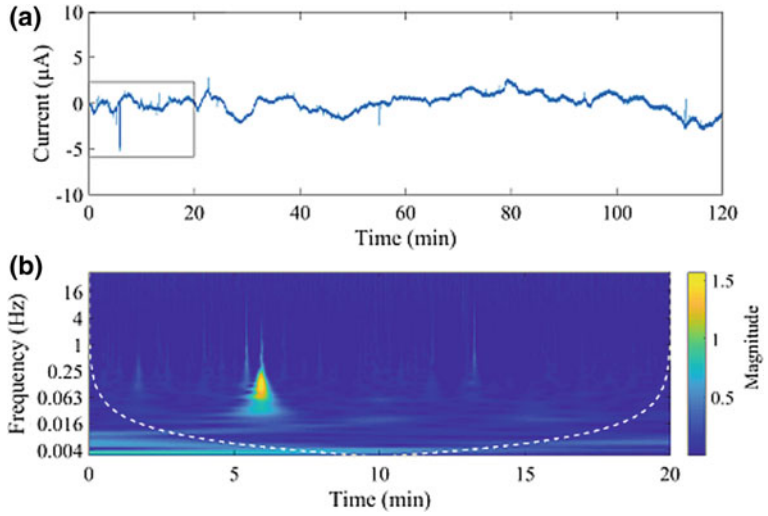

Fig. 17.31 **a** Current noise-time signal of CastX15CrMnNiN19-3-4 in 5 wt% sodium chloride solution. **b** CWT analysis for the time interval marked by the rectangle in (**a**). Dashed line—the cone of influence

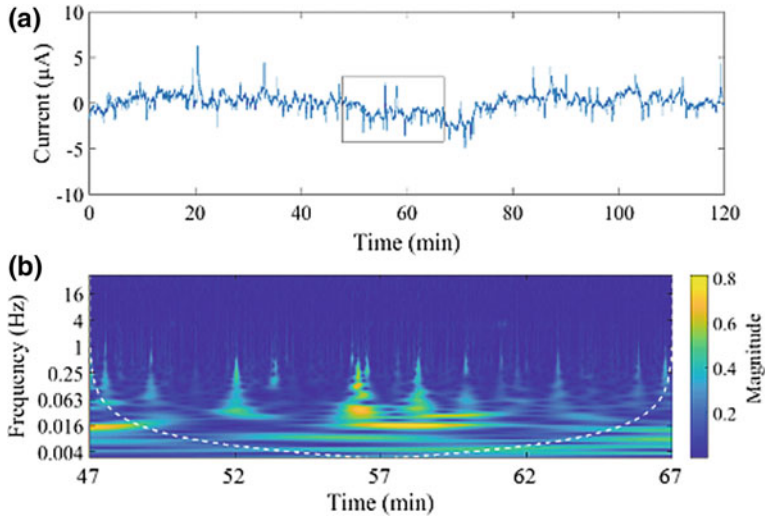

Fig. 17.32 **a** Noise-time signal of CastX15CrMnNiN19-4-3 in a combined 0.1 M H_2SO_4 + 5 wt% sodium chloride solution. **b** Continuous wavelet transform for the time interval marked by the rectangle in (**a**). Dashed line—the cone of influence

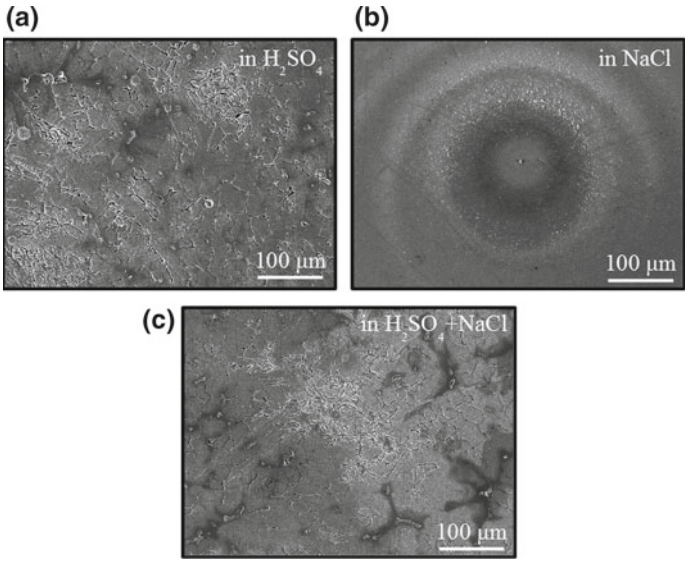

Fig. 17.33 SEM micrographs of the CastX15CrMnNiN19-3-4 after noise measurement in **a** 0.1 M H_2SO_4, **b** in 5 wt% NaCl, and **c** in 0.1 M H_2SO_4 + 5 wt% NaCl at a ratio of 1:1 vol%

maxima in the low-frequency range (Fig. 17.32b)—indicating long-term corrosion processes—indicated a longer-lasting intergranular corrosion attack. Consequently, it was assumed that in the unmixed acid solution, the corrosion attack was characterized by spontaneous active dissolution of the grain boundaries, accompanied by spontaneous repassivation. In the combined electrolyte, the attack also occurred spontaneously, but the repassivation process was drastically hindered, which was predominantly attributed to the Cl^- ions.

The study shows the advantage of utilizing electrochemical noise analysis, which facilitated the identification and isolation of short-time and long-term corrosion events simultaneously. In comparison, the effect was not identifiable by SEM observation after a two-hour exposure test.

17.8 Conclusion

In this chapter, several studies of the electrochemical corrosion behavior of high-alloy cast steels and steel/ceramic composite materials in sulfuric acid and chloride containing aqueous solutions are presented and discussed. For the analysis numerous polarization techniques, outdoor exposure tests and combined methods were carried out. The analyzed characteristics in dependence of applied potential, frequency and temperature give specific information about the influence of the TRIP effect to the corrosion characteristics, were used to design and describe the composite/electrolyte interphase and let extract specific parameters for the evaluation of the pitting

corrosion sensitivity. Finally, the combination of polarization, electrochemical noise and acoustic emission was used to estimate and separate simultaneous occurring corrosion mechanisms, and more precisely, to identify the time-dependence of specific initiation phenomena and corresponding corrosions damage evolution processes.

Acknowledgements The authors greatly acknowledge the financial support of this works by the Deutsche Forschungsgemeinschaft (DFG, German Research Foundation) as part of the Collaboration Research Centre 799 "TRIP-Matrix Composites" project—Projektnummer 54473466—SFB 799, subproject B6.

References

1. S. Wolf, S. Martin, L. Krüger, U. Martin, U. Lorenz, Steel Res. Int. **83**, 529 (2012)
2. L. Krüger, S. Wolf, S. Martin, U. Martin, A. Jahn, A. Weiß, P.R. Scheller, Steel Res. Int. **82**, 1087 (2011)
3. S. Martin, S. Wolf, U. Martin, L. Krüger, D. Rafaja, Metall. Mater. Trans. A **47**, 49 (2016)
4. C.-O.A. Olsson, D. Landolt, Electrochim. Acta **48**, 1093 (2003)
5. M. Mandel, F. Böhme, M. Hauser, M. Wendler, F. Tuchscheerer, L. Krüger, Steel Res. Int. **87**, 1105 (2016)
6. M. Mandel, L. Krüger, S. Decker, Mater. Corros. **66**, 1456 (2015)
7. M. Mandel, L. Krüger, S. Decker, Materialwiss. Werktofftech. **46**, 1039 (2015)
8. M. Mandel, L. Krüger, S. Decker, Corros. Sci. **90**, 323 (2015)
9. M. Boinet, J. Bernard, M. Chatenet, F. Dalard, S. Maximovitch, Electrochim. Acta **55**, 3454 (2010)
10. H. Inoue, R. Tsuzuki, S. Nohara, C. Iwakura, Electrochem. Solid-State Lett. **9**, A504 (2006)
11. J. Xu, X. Wu, E.-H. Han, Corros. Sci. **53**, 448 (2011)
12. M. Mandel, V. Kietov, T. Dubberstein, L. Krüger, Electrochim. Acta **240**, 350 (2017)
13. W. Liu, D. Wang, X. Chen, C. Wang, H. Liu, Corros. Sci. **124**, 93 (2017)
14. Y. Hou, C. Aldrich, K. Leokova, L.L. Machuca, B. Kinsella, Corros. Sci. **112**, 63 (2016)
15. L. Calabrese, L. Bonaccorsi, M. Galeano, E. Proverbio, D. Di Pietro, F. Cappuccini, Corros. Sci. **98**, 573 (2015)
16. M. Mandel, W. Kietov, L. Krüger, Defect and Diffusion Forum **367**, 42 (2016)
17. M. Mandel, V. Kietov, L. Krüger, Diffusion Foundations **22**, 48 (2019)
18. V. Kietov, M. Mandel, L. Krüger, Combination of electrochemical noise and acoustic emission for analysis of the pitting corrosion behavior of an austenitic stainless cast steel. Adv. Eng. Mater. (2018). https://doi.org/10.1002/adem.201800682
19. K. Wu, W.-S. Jung, J.-W. Byeon, Corros. Sci. **105**, 8 (2016)
20. C. Jirarungsatian, A. Prateepasen, Corros. Sci. **52**, 187 (2010)
21. A. Aballe, M. Bethencourt, F.J. Botana, M. Marcos, J.M. Sánchez-Amaya, Electrochim. Acta **46**, 2353 (2001)
22. F.H. Cao, Z. Zhang, J.X. Su, Y.Y. Shi, J.Q. Zhang, Electrochim. Acta. **51**, 1359 (2006)
23. A.M. Homborg, E.P.M. van Westing, T. Tinga, X. Zhang, P.J. Oonincx, G.M. Ferrari, J.H.W. de Wit, J.M.C. Mol, Corros. Sci. **66**, 97 (2013)
24. A.M. Homborg, R.A. Cottis, J.M.C. Mol, Electrochim. Acta **222**, 627 (2016)
25. M.G. Pujar, U. Kamachi Mudali, S. Sekhar Singh, Corros. Sci. **53**, 4178 (2011)
26. Y.-J. Tan, N.N. Aung, T. Liu, Corros. Sci. **48**, 23 (2006)
27. K. Hladky, J.L. Dawson, Corros. Sci. **21**, 317 (1981)
28. B.P. Markhali, R. Naderi, M. Mahdavian, M. Sayebani, S.Y. Arman, Corros. Sci. **75**, 269 (2013)
29. A. Aballe, M. Bethencourt, F.J. Botana, M. Marcos, Electrochim. Acta **44**, 4805 (1999)
30. A. Aballe, M. Bethencourt, F.J. Botana, M. Marcos, Electrochem. Commun. **1**, 266 (1999)
31. P. Montes-García, F. Castellanos, J.A. Vásquez-Feijoo, Corros. Sci. **52**, 555 (2010)

Chapter 18
CFD Analysis of the Particle and Melt Flow Behavior During Fabrication and Processing of TRIP-Matrix-Composites

Sebastian Borrmann, Sebastian Neumann and Rüdiger Schwarze

Abstract Computational fluid dynamics simulations are conducted to supplement experimental investigations in order to gain a deeper understanding of physical effects during fluid flow and heat transfer in steel making and processing. This offers the possibility to examine physical effects of the liquid steel in greater detail and isolated of entire processes. Liquid steel is present in the fabrication processes of TRIP-Matrix-Composites, namely gas atomization of the steel melt to produce powder, and liquid steel infiltration into ceramic structures. It also occurs during further processing, e.g. in welding or coating. Numerical simulations of these processes are performed with the finite volume method using the free open-source software package OpenFOAM. The libraries are extended where needed. This includes formulations for phase change, heat sources, latent heat, additional forces, calculations for material properties in multiphase flows, and particle tracking. The models are used to simulate electron beam welding, infiltration, gas atomization, and flame spraying and to reveal significant effects for each particular process.

18.1 Introduction

Producing TRIP-steels and TRIP-Matrix-Composites through casting and powder metallurgy involves many physical effects both in the solid and molten state. This also applies for further processing like welding or flame spraying. A detailed understanding of these physical effects is crucial to achieve desired properties of the final product. Besides various experimental investigations, which are thoroughly described in this book, numerical simulations can be carried out to enhance this understanding.

The infiltration of ceramic structures like foams or bulk material is one route of producing TRIP-Matrix-Composites. In a second route, powder metallurgical processes, like e.g. atomization (Chap. 3), sintering (Chaps. 6 and 9) and powder

S. Borrmann (✉) · S. Neumann · R. Schwarze
Institute of Mechanics and Fluid Dynamics, Technische Universität Bergakademie Freiberg, Lampadiusstr. 4, 09599 Freiberg, Germany
e-mail: sebastian.borrmann@imfd.tu-freiberg.de

H. Biermann and C. G. Aneziris (eds.), *Austenitic TRIP/TWIP Steels and Steel-Zirconia Composites*, Springer Series in Materials Science 298,
https://doi.org/10.1007/978-3-030-42603-3_18

forging (Chap. 8), are used. In order to produce the steel powder, gas atomization of the steel melt is performed. In both routes, the behavior of the molten steel is one main cause for the final material character. During further processing of the material, steel melts particularly occur during coating and joining processes. For the former, flame spraying can be used for metal matrix composites (MMC). For the latter, electron beam (EB) welding was found to show excellent weldability for TRIP-steels [1] and was therefore used.

For the numerical simulation of infiltration, atomization, flame spraying, and EB welding, computational fluid dynamics (CFD) simulations are used. The aim of these simulations is to create numerical models of the actual processes in order to reduce the amounts of costly experiments and to gain additional insights into the melt flow behavior and further related physical effects. In order to represent processes as effectively as possible, the right choice of fundamental equations to be solved and correct numerical model setups are crucial.

All CFD simulations of the described processes are based on the numerical solution of the conservation equations of mass, momentum and energy. The mass conservation equation for incompressible fluids with constant density has the form:

$$\nabla \cdot \boldsymbol{u} = 0, \tag{18.1}$$

with the velocity vector $\boldsymbol{u}$. The momentum conservation equation for incompressible fluids has the form

$$\frac{\partial \boldsymbol{u}}{\partial t} + \nabla \cdot (\boldsymbol{u}\boldsymbol{u}) = -\frac{1}{\varrho}\nabla p + \nabla \cdot (\nu \nabla \boldsymbol{u}), \tag{18.2}$$

where t is the time, ϱ is the density, p is the pressure and ν is the kinematic viscosity. Since melt flow problems are accompanied by large temperatures and temperature gradients, the energy conservation equation is also solved to take the influence of temperature into account:

$$c_p \frac{\partial T}{\partial t} + c_p \nabla \cdot (\boldsymbol{u}T) = \frac{1}{\varrho}\nabla \cdot (k \nabla T), \tag{18.3}$$

with the temperature T, the heat capacity c_p, and the thermal conductivity k.

Equations (18.1)–(18.3) form a system of partial differential equations, which is solved by means of the finite volume method (FVM) [2, 3] within the free, open source CFD software OpenFOAM [4].

If in addition to the steel melt, other fluid phases like gases are involved, the phases need to be distinguished. This is accomplished by using the volume of fluid (VOF) method and solving the transport equation for the phase fraction α:

$$\frac{\partial \alpha}{\partial t} + \mathbf{u} \cdot \nabla \alpha = 0. \tag{18.4}$$

A very detailed description of the VOF method employed in OpenFOAM is given by Klostermann et al. [5].

For the particular processes, (18.1)–(18.3) were extended by source terms and other refinements. These extensions and their applications will be shown in the following sections for infiltration, gas atomization and EB welding.

18.2 Infiltration

Besides powder metallurgical processes, combination of steel and ceramic structures on the macro-scale is another possibility for the creation of TRIP-Matrix-Composites. In this production route, two different main approaches are investigated. One is the casting of liquid steel into molds that are filled with ceramic structures or particles. The other is the infiltration of ceramic foam structures with liquid steel (Chap. 4) [6]. The latter was investigated by means of CFD intensively by Klostermann et al. [7, 8] and Schwarze et al. [9, 10]. In order to perform beneficial CFD simulations, different steps need to be considered. These are efficient meshing strategies [8], steel flow and heat transfer inside the foam structure [7], and melt surface dynamics for the 2-phase-flow system [9, 10].

18.2.1 Meshing Strategies

Sophisticated meshing strategies are the first step to efficient CFD simulations. The mesh is used to generate grid points in order to discretize the fundamental equations (18.1)–(18.3). The mesh offers a significant impact on the quality and time-consumption of the simulation. In order to evaluate a meaningful meshing strategy for the discussed infiltration simulations, two different approaches were examined. A mesh, produced by a semi-automatic generation algorithm for hexahedral meshes, developed by Klostermann et al. [8], is compared with a mesh generated by a full-automatic tetrahedral meshing technique. The comparison is performed for the flow in a Kelvin structure.

The main advantage of full-automatic techniques with tetrahedral or mixed tetrahedral/hexahedral grid cells is its independence of the geometry. Any forms can be meshed and automatically refined at critical areas. As an example, Fig. 18.1 shows a CT scan of realistic ceramic foam (Fig. 18.1a) and the respective mesh (Fig. 18.1b). The automatic meshing also leads to quickly accessible meshing results. However, when the investigation of specific physical phenomena is desired, abstracted and well defined geometries are often examined. In these cases, structured meshes might lead to faster simulations and possibly more accurate results. To keep the meshing effort small, it is useful to employ automation for the geometry and mesh generation as much as possible. Since the Kelvin structure is a popular approach to approximate foam structures, Klostermann et al. [8] developed a strategy that does both geometry

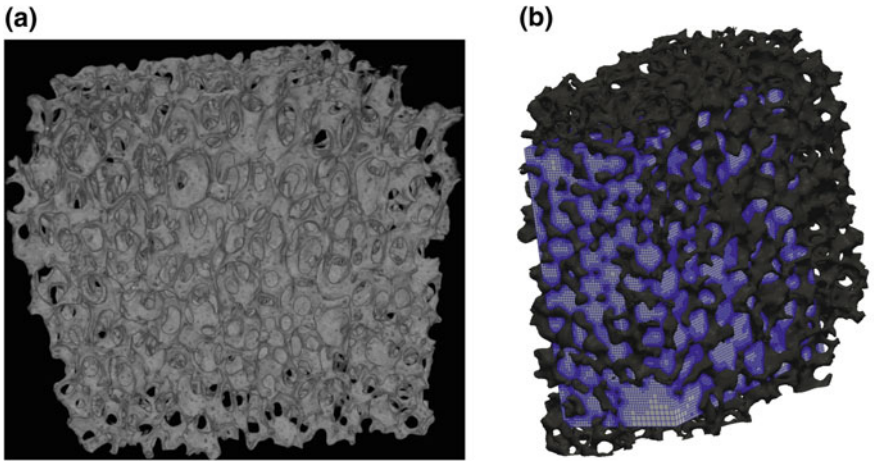

Fig. 18.1 **a** CT scan of a real ceramic foam [8] and **b** the automatically generated unstructured mesh with mesh refinement near foam boundaries [9]

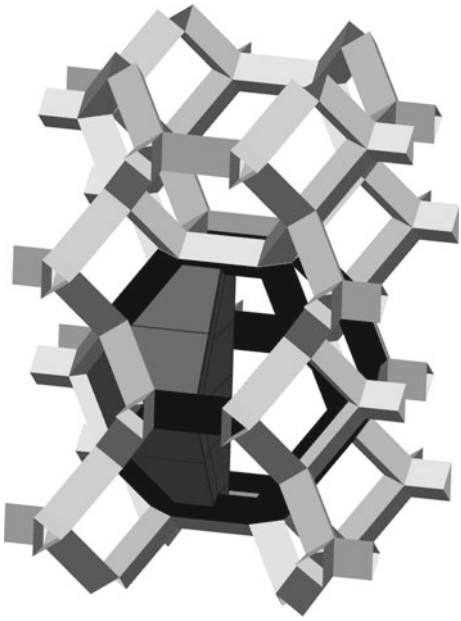

Fig. 18.2 A section of the generated Kelvin cell structure with triangular struts of one Kelvin cell (black) and one quarter of a Kelvin cell volume (dark grey) [8]

and block-structured mesh generation for composed macroscopic forms that consist of single Kelvin structures. Figure 18.2 shows an excerpt of the geometry. For a detailed explanation of the meshing strategy, the reader is referred to Klostermann et al. [8].

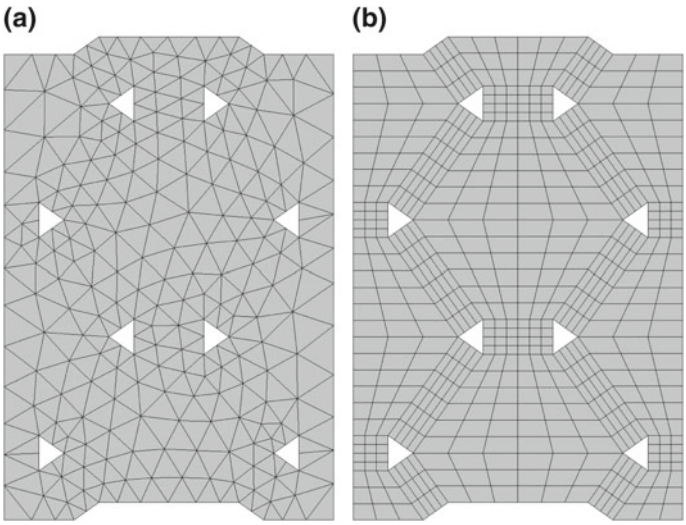

Fig. 18.3 Comparison of two different meshing approaches: **a** automatic unstructured mesh and **b** semi-automatic block-structured mesh [8]

In order to directly compare the two meshing approaches, the same geometry was meshed. Figure 18.3 shows sections of the two approaches. Both meshes were created with a similar number of grid cells. Steady, incompressible flow simulations through the Kelvin structure were performed to compare the mesh qualities, simulation errors and calculation time. Firstly, the block-structured hexahedral mesh mostly showed lower errors for different error estimates and two different Reynolds-number flows. Only in some cases, the errors of the unstructured tetrahedral mesh were slightly smaller. Secondly, the necessary number of iterations that was needed for convergence, was a lot smaller for the structured hexahedral mesh in all cases. Thirdly, the calculation time per iteration was lower with the hexahedral mesh. All in all, the performance of the hexahedral mesh was up to 94% better than of the tetrahedral mesh. In order to minimize computational costs the block-structured technique was consequently used for further studies of flow infiltration into Kelvin structures.

18.2.2 Mesoscale Flow in Kelvin Structure

Meshing the pores of the ceramic foam, as shown in Sect. 18.2.1 is very useful if only the melt flow is simulated. In order to represent the process of infiltration more physically, heat transfer between the liquid steel melt and the solid ceramic foam struts needs to be accounted for as well. To track the heating of the foam itself, the solid structure is meshed.

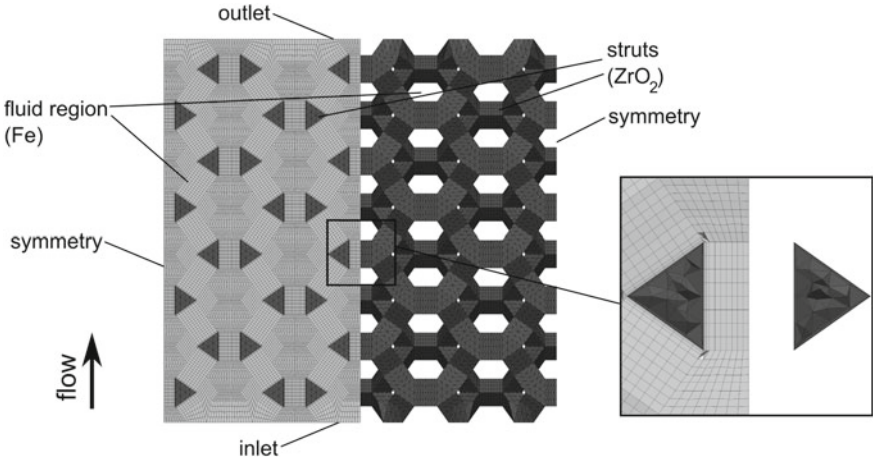

Fig. 18.4 Simulation domain with boundaries, regions and mesh for the fluid zone (light grey), primary meshed with hexahedric cells, and the solid structure (dark grey), primary meshed with tetrahedric cells [7]

Therefore, the mesh was extended to the ZrO_2 struts in order to simulate complete heat transfer between the infiltrating liquid steel melt and the solid ceramic foam [7]. Figure 18.4 shows both parts of the composed mesh in the calculation domain. The left part of Fig. 18.4 shows the grid for the fluid region, while the right part demonstrates the mesh in the solid region in more detail.

The aim of the performed CFD simulations was to investigate the flow and the heat transfer on the pore-scale (mesoscale). The single-phase flow focused on thermal effects with constant material properties and neglected the free surface flow and solidification. The equations for mass (18.1), momentum (18.2) and energy (18.3) were solved. The energy equation (18.3) is reassembled with the thermal diffusivity $a = \frac{\lambda}{\varrho c_p}$ to:

$$\frac{\partial T_{\mathrm{Fe}}}{\partial t} + \mathbf{u} \cdot \nabla T_{\mathrm{Fe}} = a_{\mathrm{Fe}} \nabla \cdot \nabla T_{\mathrm{Fe}}. \tag{18.5}$$

Additionally, a heat transfer equation for the solid region was solved:

$$\frac{\partial T_{\mathrm{ZrO_2}}}{\partial t} = a_{\mathrm{ZrO_2}} \nabla \cdot \nabla T_{\mathrm{ZrO_2}}. \tag{18.6}$$

The following explicit boundary conditions were used at the interface between the melt and the struts:

$$T_{\mathrm{Fe}} = T_{\mathrm{ZrO_2}} \tag{18.7}$$

$$k_{\mathrm{Fe}} \nabla T_{\mathrm{Fe}} = k_{\mathrm{ZrO_2}} \nabla T_{\mathrm{ZrO_2}}. \tag{18.8}$$

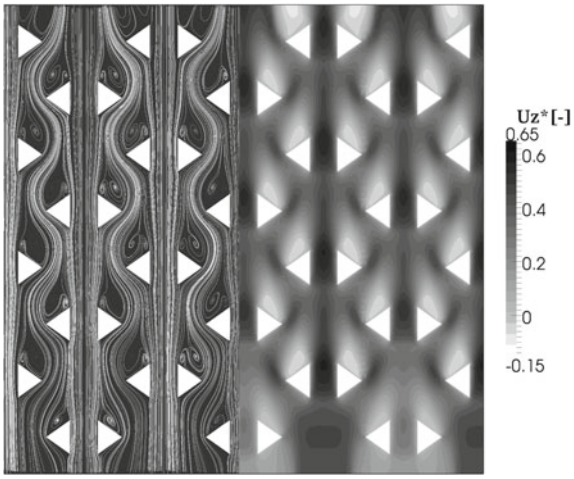

Fig. 18.5 Flow visualization via stream lines (left) and normalized flow velocity in mean flow (z-)direction (right) [7]

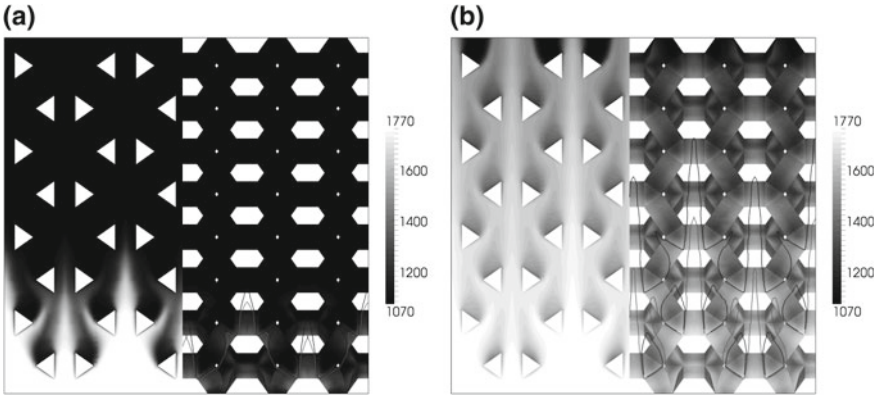

Fig. 18.6 Temperature fields in the liquid zone (left) and the solid struts (right) after **a** $t^* = 0.49$ and **b** $t^* = 6.14$ melt through time [7]

For details about the numerical model setup and the thermophysical properties, the reader is referred to Klostermann et al. [7].

The flow field is represented in Fig. 18.5. On the left hand side, the flow is visualized by streamlines, which illustrates the channeling of the flow in two alternating patterns, straight and meandering. Recirculation is visible through swirls behind the struts. On the right hand side, these recirculation areas are quantified, where the normalized velocity U_z^* in z-direction is negative, and therefore white. In realistic infiltration processes with a free melt surface, these recirculation areas could result in cavities as gas entrapment would possibly occur.

Figure 18.6 shows the temperature field of (a) the flow field and (b) the struts for the melt through times $t^* = 0.49$ (Fig. 18.6a) and $t^* = 6.14$ (Fig. 18.6b). The

ceramic was preheated to 1080 K. While the temperature field followed the fluid flow, the heating of the solid struts was delayed. Both behaviors were as expected. The temperature field of the liquid steel also revealed areas of lower temperatures in the recirculation areas behind the struts. We expect the melt to solidify in this area first, where gas entrapment is very likely as well.

18.2.3 Melt Surface Dynamics

In the previous considerations, the free melt surface and the gas phase have been neglected. An additional investigation of the multiphase system is, however, essential to cover further effects like cavity development. In order to investigate the behavior of the free surface of the steel melt in the porous ceramic foam during infiltration and to distinguish between the fluid phases, the model was extended by the VOF method [see (18.4)]. The material properties density ϱ and dynamic viscosity η were averaged between the steel melt phase (index m) and the gas phase (index g) depending on α in each grid cell [9]:

$$\varrho = \alpha\varrho_{\mathrm{m}} + (1-\alpha)\varrho_{\mathrm{g}} \tag{18.9}$$

$$\eta = \alpha\eta_{\mathrm{m}} + (1-\alpha)\eta_{\mathrm{g}}. \tag{18.10}$$

Figure 18.7 shows a simulation of the infiltration of liquid steel into the ceramic matrix with a highly resolved surface tracking [9]. The gas is noticeable as dark entrapped bubbles in between the lighter steel melt. The bubbles form as a consequence of the rapid infiltration behind the struts.

The detailed simulations came with tremendous computational effort because very small time steps Δt were necessary. The required time step for free surface flow is calculated by the following condition [11]:

$$\Delta t = C_\eta \frac{\eta \Delta x}{\sigma}, \tag{18.11}$$

where C_η is a constant and Δx is the cell length. As described by Schwarze and Klostermann [10], this time step condition is much more dominant than the usual Courant-Friedrichs-Lewy-condition, which reads:

$$\Delta t = \mathrm{Co}\frac{u\Delta t}{\Delta x}. \tag{18.12}$$

Here Co is the Courant number, which is in most cases $\mathrm{Co} \leq 1$ to ensure stability, and u is the velocity magnitude. In (18.11) C_η most widely depends on numerical treatment of the model equations and therefore the time step is very sensitive to adequate implementations. Schwarze and Klostermann [10] have found that the material parameter averaging between the phases have a particular impact. Thus, an

improved strategy was found for the viscosity interpolation and the harmonic mean was adopted:

$$\eta = \frac{\eta_g \eta_m}{(1-\alpha)\eta_m + \eta_g \alpha} \tag{18.13}$$

Testing different time steps with the different viscosity averaging equations reveals their impact on the stability of the simulation. In Fig. 18.8, the standard (18.10) and the improved (18.13) viscosity averaging algorithms are compared. For the low time-step Δt_1 both implementations worked stable. By increasing the time step to Δt_2, the standard implementation destabilized. However, with the improved viscosity

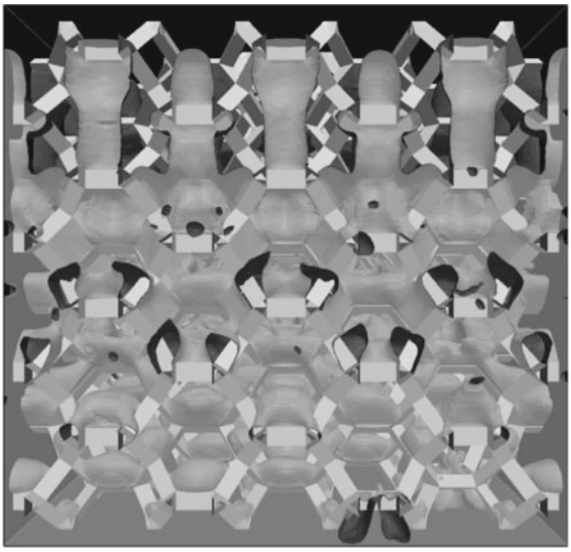

Fig. 18.7 Contour of the infiltrating steel melt (bright) with gas and entrapped bubbles (dark) [9]

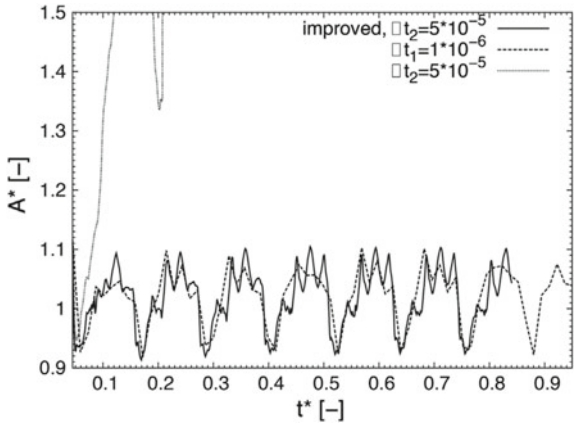

Fig. 18.8 Melt surface area as a function of time. Comparison of the low time step $t_1 = 1 \cdot 10^{-6}$ (dashed line) with a higher time step $t_2 = 5 \cdot 10^{-5}$ for non-improved (dotted line) and improved (solid line) viscosity algorithms [10]

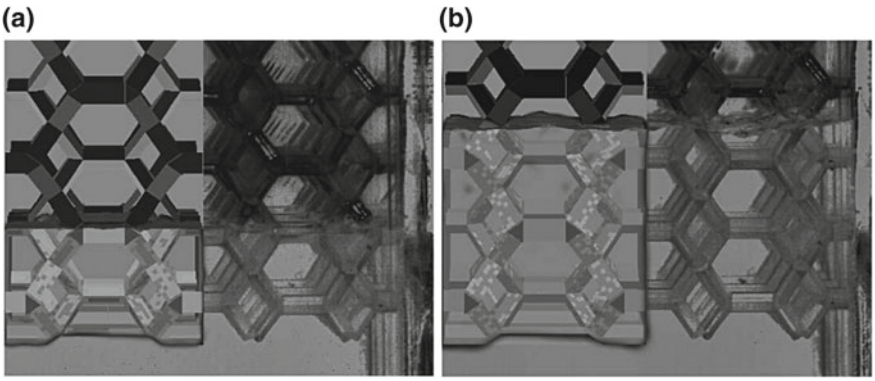

Fig. 18.9 Comparison of the free surface between simulation (left) and model experiment (right) for two different through times **a** $t^* = 0.199$ and **b** $t^* = 0.364$ [10]

averaging, the results were comparable to the smaller time step and the simulations remained stable. Figure 18.9 shows a qualitative comparison of the infiltration process between simulation and experiment, It reveals a very good agreement.

18.3 Atomization

Alongside infiltration of macroscopic structures, powder metallurgy is the main route for the fabrication of TRIP-Matrix-Composites. The controlled production of steel powder with desired properties and particle size distributions is one of the major challenges. In the light of this, CFD models were developed and simulations were performed to gain an understanding of parameters that influence the development of steel droplets during the primary breakup of molten steel [12]. In order to apply additional models like secondary breakup or applications like flame spraying, particle size distributions need to be tracked. By converting the continuous Euler phase of the VOF simulations to disperse Lagrangian particles, this can be accomplished. For that purpose, a particle tracking and conversion model has been developed and implemented [13]. The application of tracked particle size distributions for powder flame spraying is shown accordingly.

18.3.1 Influence of Process Parameters on Primary Breackup

The production of MMC using a sintering process needs analog particle sizes for the ceramic and steel powders to obtain a high green strength [14]. Atomization, the predominant production process for steel powder, subdivides into two main tech-

niques, the free fall design and the close coupled (confined) design [15]. The main difference of the designs is the positioning of the nozzles, which deliver the inert gas for the atomization of the steel melt jet. Therefore, different atomization states are feasible. In case of the closed coupled design, a prefilming process of the metal melt jet develops due to the flow structure of the inert gas, which finally atomizes the melt into droplets. On contrary, a compact metal melt jet develops for the free fall design, which is atomized by an inert gas stream at a defined distance. Due to the inert gas atomization, steel powder particles with diameters in range of 0.04–2000 µm are generated [16]. A method to enforce the atomization process is the direct manipulation of the free falling melt jet. Therefore, a primary breakup process is forced by defined disturbances for the inflow of the melt in the nozzle. This leads to a pre-disintegration of the metal melt jet into ligaments and larger droplets [12]. In general, an experimental investigation of the steel melt atomization is very complex. Mainly, the high melt temperature limits the measurements [17]. The management and control of the process of metal melt gas atomization is a kind of 'black art' due to the demanding process conditions and requirements [18]. Furthermore, experimental setups require a certain durability and stability as well as optical accessibility for a detailed analysis of the process. Consequently, numerical simulations are a meaningful alternative to research metal melt atomization processes to shed light on specific influencing attributes.

Critical factors for primary breakup of the metal melt jet using a free fall design are constructive parameters (e.g. the nozzle design, nozzle obstruction via the stopper rod) and operation conditions (e.g. rotation of the melt flow, nozzle inlet flow disturbances). Basically, a numerical investigation determines their influence to the metal melt jet behavior downstream of the nozzle. Figure 18.10 shows sketches of a tube nozzle (Fig. 18.10a) and a divergent-convergent industrial nozzle (Fig. 18.10b). The presented numerical simulation depends on different assumptions such as:

- three-dimensional and transient flow behavior,
- fully developed laminar melt inflow,
- the flow regime is in transition range between laminar and turbulent flow,
- isothermal and incompressible conditions with constant material properties.

Therefore, the governing equations for continuity (18.1) and momentum (18.2) are solved. The turbulence is not modeled with an explicit subgrid model. Instead, implicit large eddy simulations (ILES) were performed, which generate the dissipation of the small structures by a specific spatial numerical discretization scheme of the convection terms in the momentum equation. By the means of the VOF, introduced in Sect. 18.2.3 [see (18.4), (18.9), (18.10)] the dynamics of the phase interface between the melt and gas is tracked during the simulation.

Figure 18.11 shows the a simulation result of a temporal metal melt jet behavior downstream the industrial nozzle. The nozzle outlet diameter is consistent $D = 4\,\mathrm{mm}$ for both geometries (see Fig. 18.10). The axial nozzle inlet velocity is constant $U_{\mathrm{ax}} = 1.55\,\mathrm{ms}^{-1}$ based on the fluid column of the melt inside the tundish. Additionally, a circumferential velocity of $u_{\mathrm{rot}} = 1.83\,\mathrm{ms}^{-1}$ is defined, which mimics the rotation of the melt inside the tundish caused by the magnetic heating process. For

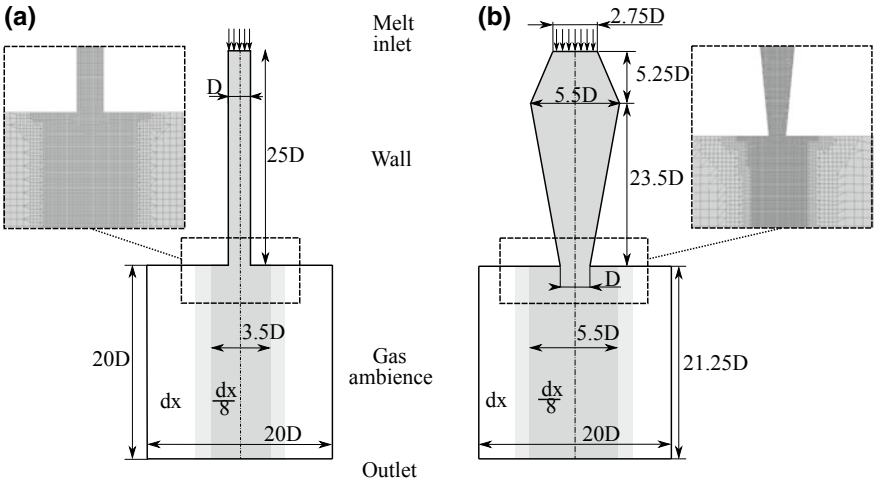

Fig. 18.10 Sketch of the simulation domains for **a** constant tube nozzle and **b** divergent-convergent industrial nozzle with boundary conditions, dimensions ($D = 4$ mm) and mesh refinement area (gray background and details in frame) [12]

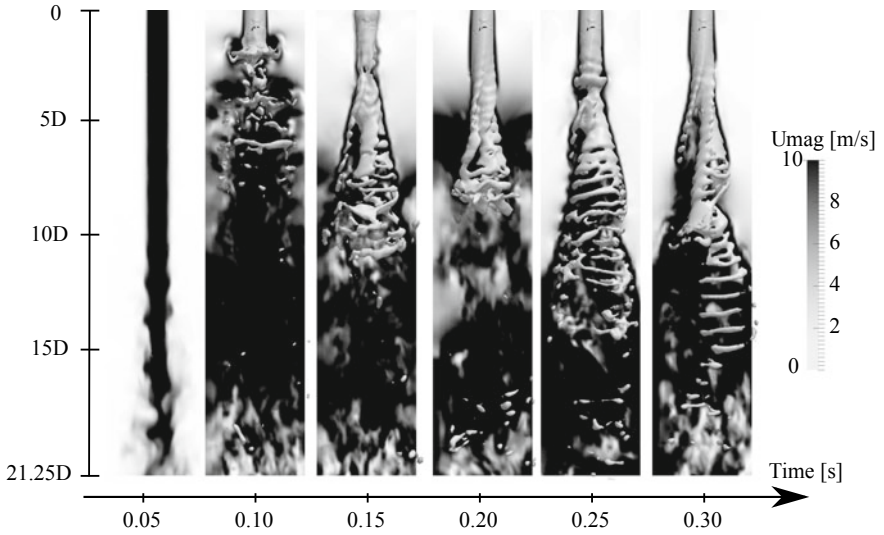

Fig. 18.11 Temporal jet behavior regarding the industrial nozzle for a circumferential velocity of $u_{\mathrm{rot}} = 1.83\,\mathrm{ms}^{-1}$ at the nozzle inlet. The contour plot of the jet ($\alpha = 0.5$) and the gas velocity field (background) are shown

detailed information of the specifications, the reader is kindly referred to the work of Neumann et al. [12]. In Fig. 18.11, the contour plot of the jet is depicted by the phase fraction $\alpha = 0.5$ for the industrial nozzle. It should be noted that the interface between the melt and gas phase smears over 4–5 cells [8]. However, respecting this criterion a high computational grid resolution is defined. Additionally, the gas velocity field is shown in the background. In general, the temporal behavior of the melt jet shows the primary breakup of ligaments and larger droplets. A helical structure superposed by a hollow-cone jet shape develops, whereas close to the nozzle a compact almost cylindrical jet occurs with less surface waves. Here, the disintegration is directly driven by the circumferential velocity of the steel melt, which shows a high potential to improve the secondary atomization process due to the high excitation of the melt jet. Therefore, Fig. 18.12 displays a detailed analysis of the different nozzle designs considering different circumferential velocities. Depending on the nozzle design different stages of the jet behavior can be observed. The tube nozzle (Fig. 18.12a) shows for:

- $u_{\mathrm{rot}} = 0$ less disturbances of the melt jet, which lead to surface waves and diameter changes,
- $u_{\mathrm{rot}} < u_{\mathrm{ax}}$ a stabilization of the jet leading to a smoothing of the secondary structures,
- $u_{\mathrm{rot}} \approx u_{\mathrm{ax}}$ a helix shaped metal melt jet with less excitations onto the jet surface,
- $u_{\mathrm{rot}} > u_{\mathrm{ax}}$ an irregular jet behavior, which splits into two parts.

On contrary, the results for the industrial nozzle design (Fig. 18.12b) show a higher excitation level of the melt surface. However, there are also different jet behavior stages considering the circumferential velocity contribution. In case of $u_{\mathrm{rot}} < 0.5u_{\mathrm{ax}}$, the general jet behavior is preserved compared to the undisturbed variant. Surface waves, diameter changes and partial disintegration occurs. A helical jet shape develops by increasing the circumferential velocity to $u_{\mathrm{rot}} > 0.5u_{\mathrm{ax}}$. Furthermore, the jet tip moves with time and ligaments and larger droplets disintegrate. However, the surfaces waves are persistent. For $u_{\mathrm{rot}} > u_{\mathrm{ax}}$, the helical jet is superposed by a hollow-cone shape and the jet oscillates frequently. Higher velocity increases the spreading and separation of the jet. The ligaments and particles are in magnitude of the secondary structures. In summary, the nozzle design mainly influences the jet excitation due to surface waves. However, the decay of the melt jet is primarily forced by specific operation conditions. Deeper insights in this research can be found in the work of Neumann et al. [12].

18.3.2 Particle Tracking and Conversion

Originally, the VOF method is capable of resolving arbitrarily formed interfaces (e.g. water surface). However, a direct tracking of specific parameter (e.g. particle size) is not immediately available for VOF simulations. This is comparable to experimental research, where a specific evaluation process is required to identify the desired

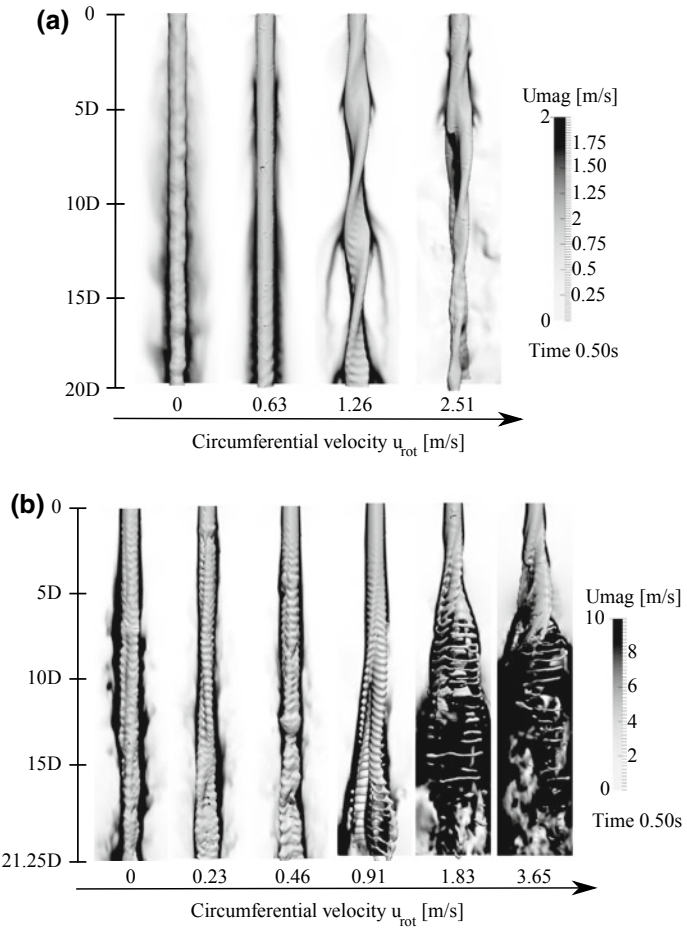

Fig. 18.12 The jet behavior for different nozzle designs **a** tube nozzle and **b** industrial diverging-converging nozzle and different circumferential velocities of the melt at the nozzle inlet for the time of 0.5 s. The contour plot of the jet ($\alpha = 0.5$) and the gas velocity field (background) are shown

variable [19]. The same applies for VOF simulations, where a specific tracking routine manages this task. In case of steel melt atomization, droplet or particle related characteristics are of particular interest (e.g. particle size distribution). However, a VOF simulation of a steel melt atomization needs a sufficient mesh resolution to resolve the droplets, which are in the magnitude of 0.1–1000 μm [16]. This in combination with a multiplicity of droplets in the dense spray region would cause excessive computational costs [20, 21]. Here, VOF simulations are limited to the complete primary breakup process, where the droplet sizes are reasonable for VOF. Secondary breakup processes are mostly described by an Eulerian-Lagrangian approach, where the com-

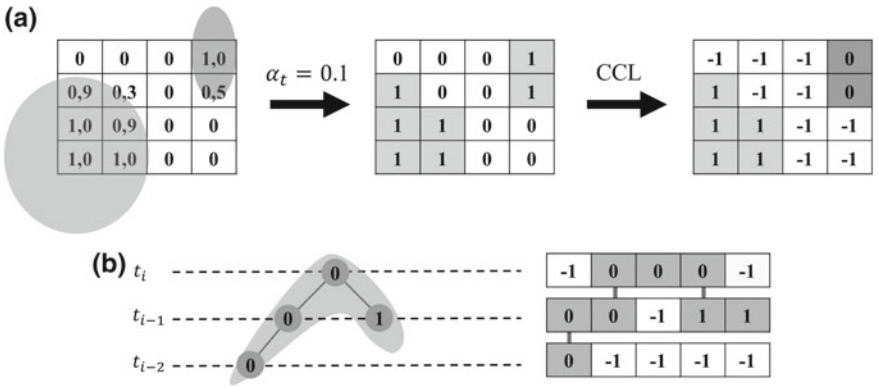

Fig. 18.13 **a** Spatial CCL: Particles (grey) represented by the phase fraction field (left), particle face identification via phase fraction threshold (middle), grouping of cells by CCL to particle slices (right) and **b** temporal CCL: Particle movement through layer evaluation over time

putational costs are much lower [22, 23]. Therefore, the VOF droplet information (e.g. particle size, position and velocity) have to be transferred from the Eulerian to the Lagrangian simulation. Here, a capable tracking algorithm is indispensable.

In general, there are two fundamental methods, namely three- or two-dimensional tracking [24–30]. 3D-tracking detects particles in the entire domain, while 2D-tracking defines a fixed positioned evaluation layer for the detection of the Eulerian particles. Both methods employ the connected component labeling (CCL) approach, which is based on the graph theory. However, whereas the 3D-tracking demands exclusively spatial CCL, 2D-tracking needs spatial and additionally temporal CCL for the Eulerian particle detection. In Fig. 18.13, the variants are outlined exemplarily. The basis for the tracking algorithm is the phase fraction α field given by the VOF simulation. Regarding the spatial detection (Fig. 18.13a), particles have to be identified first. Therefore, an interrogation sequence of the phase fraction threshold has to be satisfied in order to be considered for the actual CCL step for the condition $\alpha > \alpha_t$. Afterwards, neighborhood relationships between the detected cells have to be analyzed. Finally, individual particles are classified. The 3D spatial CCL directly detects an entire particle, whereas the 2D spatial CCL identifies slices of the particles due to the 2D evaluation layer (arbitrarily placeable). Therefore, an additional temporal CCL is important to connect multiple slices to one particle.

The simulations considering VOF metal melt atomization are performed in OpenFOAM v1812 [31]. Therefore, the officially implemented tracking algorithm, called the extract Eulerian Particles function object, is advanced to incorporate sophisticated source code for the temporal tracking. Figure 18.13b shows the correct temporal connection of the individual slices over ensuring correct neighborhood relationships within different particles.

To study the performance of the enhanced tracking algorithm, an extensive numerical validation of a well-known test case is intended where almost all circumstances

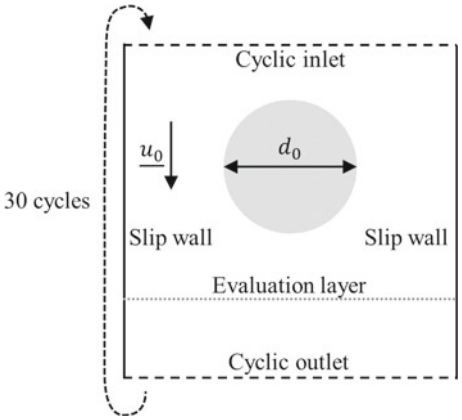

Fig. 18.14 Numerical case setup for a recirculating water droplet in air with the related boundary conditions [13]

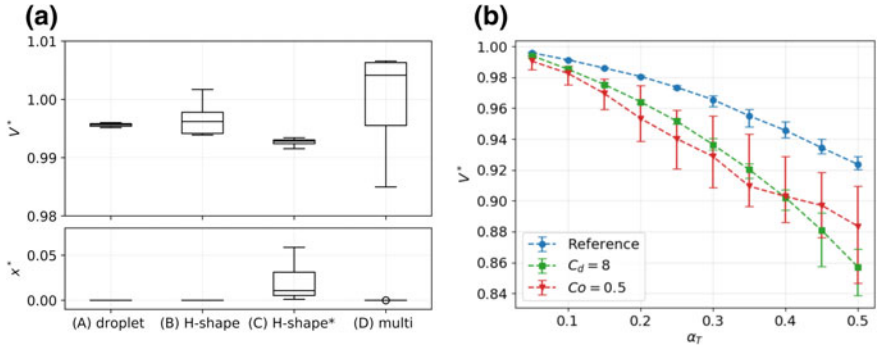

Fig. 18.15 **a** Particle tracking results with enhanced algorithm for (A) spherical particle, (B) and (C) H-shaped particle and (D) 12 particles of various shapes and sizes [13]. **b** Sensitivity analysis of the phase fraction threshold α_t (Reference $\alpha_t = 0.05$, $C_d = 16$ and $Co = 0.1$)

of the simulation are controllable. Therefore, the test case of a moving water droplet in air is chosen using different setups, see Fig. 18.14. Different particle shapes (spherical, H-shaped) and number of particles (single, multiple particles) are analyzed defining different diameters d_0 and velocities $\underline{u}_0$. Furthermore, the influence of the mass and momentum equations are analyzed. Using the frozenFlow option of OpenFOAM enables simulations with constant domain velocity and negligence of the surface tension of the droplet. The simulation domain is defined by cyclic boundary conditions at the inlet and outlet, such that the particle can directly reenter the domain after leaving. This allows an iterative analysis of the tracking algorithm for constant particle conditions. In total, 30 cycles for each setup are performed. The mesh resolution is 32 cells per diameter.

Figure 18.15a shows the simulation results of the VOF simulation with the enhanced 2D-tracking algorithm, with the normalized droplet volume V^* and normalized displacement x^*, which are described by:

$$V^* = V_p / V_0, \tag{18.14}$$

$$x^* = \sqrt{(x_{x,p} - x_{x,0})^2 + (x_{y,p} - x_{y,0})^2} \frac{1}{d_0}, \tag{18.15}$$

within the box plot diagram. The diagram reveals a very good accuracy of the considered particle attributes. The discrepancy of all regarded setups is less than 3% for the normalized volume. Noticeable aberrations are existent for H-shaped droplet B) and the setup with multiple droplets of different shapes and sizes D). The normalized position of the particle is generally almost zero. However, if surface tension is considered (marked with *), the shape of the particle cannot be preserved and partially the droplet breaks up and shift in position. This leads to the higher discrepancies in case C) of Fig. 18.15a. Altogether, the enhanced tracking algorithm shows satisfying results for all tested parameters.

Since the reliability of the enhanced tacking algorithm is proven, a sensitivity analysis of the most influencing parameter should declare its limitations. Therefore, the influence of the phase fraction threshold α_t, the droplet resolution $C_d = \frac{d_0}{\Delta x}$ and the Courant number [Co, see (18.12)] to the normalized volume V^* are investigated and illustrated in Fig. 18.15b. The reference configuration (blue) is defined by $\alpha_t = 0.05$, $C_d = 16$ and $\mathrm{Co} = 0.1$. Alternative 1 (green) has a reduced droplet resolution of $C_d = 8$ and alternative 2 (red) has a increased Courant number of $\mathrm{Co} = 0.5$ compared to the reference. The remaining variables are equal to the reference. Figure 18.15b shows comparable trends for the different configurations. With rising phase fraction threshold increases the deviation of the tracked particle volume to the initialized. Regarding the reference configuration, the normalized volume differs ≈8% for the maximal tested phase fraction threshold. However, compared to the alternatives it shows less aberration and a low standard deviation. Less stringent adjustments for the droplet resolution and Co (green and red line) highly impair the particle volume detection. With rising phase fraction threshold, the difference to the reference results increases. Furthermore, the standard deviation is significantly influenced. In summary, the phase fraction threshold is the most critical parameter, which can highly influence the tracking results in VOF simulations. For further details, the reader is referred to the work of Spitzenberger et al. [13].

18.3.3 Flame Spraying

Flame Spraying is a coating technique, where steel and ceramic powders or sintered rods are molten to droplets and sprayed on a substrate. During flame spraying, the hot gas mixture is combusted in order to melt the coating material, which is either feeded

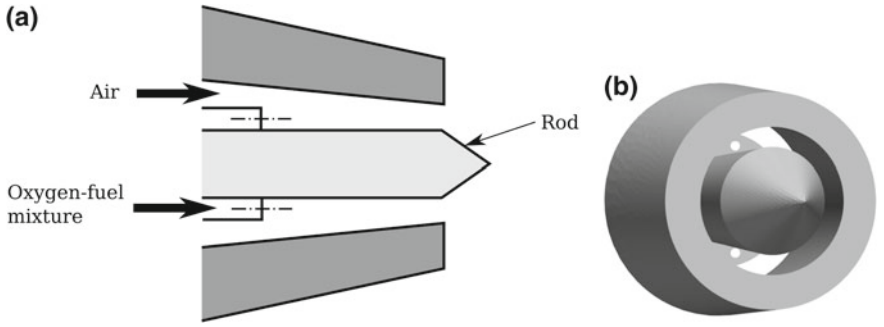

Fig. 18.16 **a** Sketch of the nozzle with an annular air inlet and orifices for the oxygen-fuel mixture inlet and **b** front view of the 3D nozzle geometry

as powder or a sintered rod. The air stream then atomizes the molten material and carries the droplets towards the substrate. For the basic principle of thermal spraying techniques, the reader is referred to the literature [32]. This technique is shown as an example for the need of Lagrangian particle tracking.

In the CFD model, the process is subdivided into two decoupled calculations for gas and droplet injection. At first, an oxygen-fuel mixture and air are injected through different inlets in the nozzle. An annular orifice is used for the air while the oxygen-fuel mixture enters through twelve circular orifices. Figure 18.16a shows a sketch of the nozzle geometry, and Fig. 18.16b a 3D view of the nozzle used in the simulation. In the CFD model, combustion and melting are not taken into account. The hot oxygen-fuel mixture and cold air are injected in the nozzle and subsequently form a free jet. The hot mixture streams towards the substrate, whereas the temperature and velocity fields are calculated in a steady state simulation. An example of the resulting velocity field is shown in Fig. 18.17.

Since combustion, melting and atomization are not calculated in this model, Lagrangian particles are injected into the domain at the rod tip in the second part of the simulation. Therefore, the particle size distribution of the introduced melt droplets needs to be predefined. It can be estimated through upstream calculations of the gas atomization (Sect. 18.3.1) and tracking of the particle sizes (Sect. 18.3.2). This approach is most accurate for powder flame spraying processes, where the powder is used directly instead of the intermediate sintering into rigid rods. Therefore, in the case of rod flame spraying, Gaussian distribution with an estimated mean diameter can be used alternatively.

After introducing the droplets into the domain, they are carried by the pre-calculated gas jet toward the substrate and impact and stick to its surface. Figure 18.18 visualizes this process. The impact of the Lagrangian particles is only sufficient to estimate the location of the coating. In order to calculate the actual coating buildup, the Lagrangian point particles need to be transformed into particles with finite sizes that are able to deform and solidify after the surface impact. This procedure is part

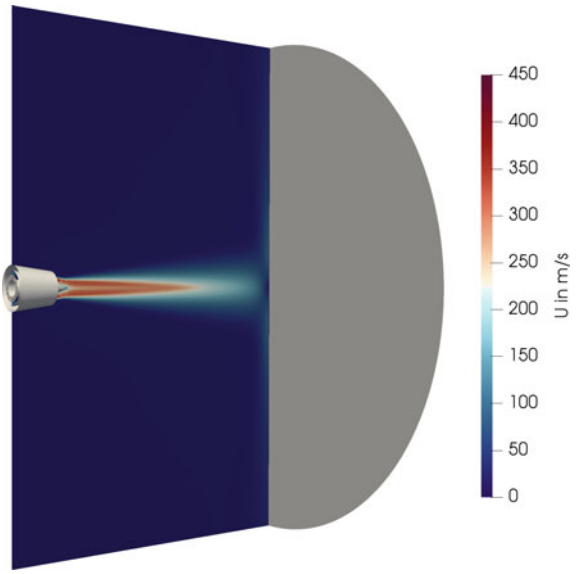

Fig. 18.17 Velocity field of the free gas jet behind the flame spraying nozzle

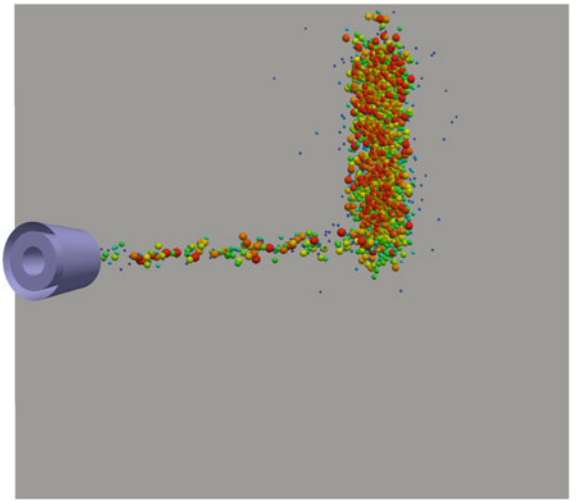

Fig. 18.18 Flight of the Lagrangian droplets behind the flame spraying nozzle and impact on the substrate. Droplets are colored by their size and are oversized for visualization

of ongoing studies. Furthermore, more accurate particle size distributions could be achieved by directly measuring the particles after flame spraying.

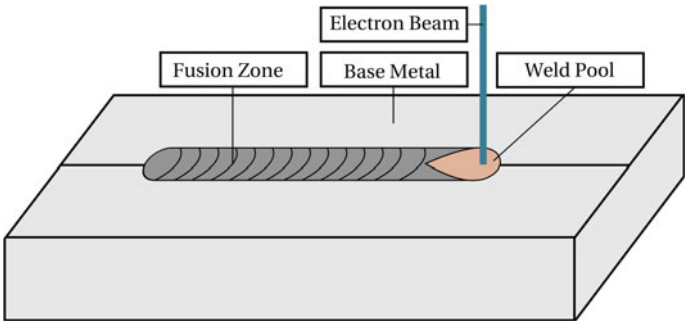

Fig. 18.19 Sketch of the physical domain during EB welding with essential regions for consideration within the numerical model

18.4 Electron Beam Welding

Experimental investigations of EB welding of TRIP-steels and TRIP-Matrix-Composites are thoroughly described by Halbauer and Buchwalder (Chap. 10). While Buchwalder et al. has already proven the excellent weldability of CrMnNi cast-steels [1], Halbauer et al. intensified the investigations for cold-rolled steels [33] and dissimilar joints [34, 35]. The numerical models described here are based on their experimental work.

The basis for numerical investigations of EB welding are, on the one hand, underlying physical effects, and on the other hand, the experimental conditions. The former are described by fundamental mathematical equations and their translation into numerical equations via discretization on finite grids that reproduce the experimental domain. The latter are described by the structure and components of the domain and boundary and initial conditions. Recently, a comprehensive CFD study of the melt flow and keyhole dynamics was carried out by Huang et al. [36] with constant thermophysical properties. Furthermore, Borrmann et al. investigated the temperature sensitivity of the thermophysical properties of X3CrMnNi 16-7-6 TRIP-steel during EB welding [37] and the coupling between steel melt and ceramic particles in EB welding of TRIP-Matrix-Composites [38] in their CFD simulations.

The basic domain for EB welding simulations can be seen in Fig. 18.19. It sketches the essential parts of the welding process that need to be taken into account.

The welding seam is produced by heating the base material up to the melting point. As a result, a tear-drop-shaped weld pool forms. When the melt cools down at the trailing edge of the weld pool, it solidifies and forms the fusion zone. The in-depth weld pool and fusion zone shapes are illustrated in Fig. 18.20. It is evident that the geometry is highly anisotropic and therefore its three-dimensional character needs to be considered.

In the experiments, the weld pool is formed in consequence of the EB energy input, which has a highly transient behavior. In order to reduce computational costs to an acceptable level, the EB is not resolved as such. Instead, a heat source is

Fig. 18.20 3D-view of fusion zone (dark grey) and molten weld pool (red)

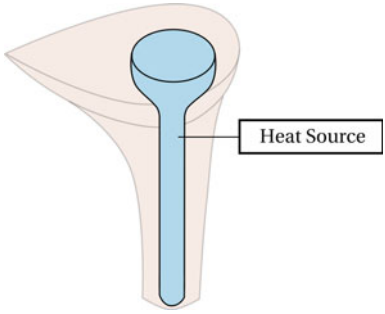

Fig. 18.21 Sketch of the heat source (light blue) inside the weld pool (red). It is used for modeling the heat input, rather than calculating the electron beam itself

operated, which mimics the EB heat input into the material. Figure 18.21 sketches its basic idea. The value and form of the heat source is constant throughout the whole simulation. However, the form of the weld pool is varying over time.

Detailed explanations of the physical effects and their numerical implementations are described in the following sections.

18.4.1 Phase Change and Heat Source Model

The increased complexity of the physical problem that arises as a consequence of heating and phase change requires additional source terms. For this reason, the fundamental equations (18.2) and (18.3) were extended, based on the elaborations of Voller and Prakash [39], Rösler and Brüggemann [40], and Miehe [41]. The momentum equation (18.2) is extended by the source term S_m, which accounts for the solid fraction and damps flow in solid and partially solid regions:

$$S_\mathrm{m} = -\frac{\nu}{d^2}\frac{f_\mathrm{s}^2}{(1-f_\mathrm{s})^3 + c_2}, \tag{18.16}$$

and the source term S_b, which accounts for the Boussinesq approximation, with which the density dependents linearly on the temperature in the gravity term:

$$S_\mathrm{b} = \boldsymbol{g}[1 - \beta(T - T_\mathrm{liq})]. \tag{18.17}$$

In the preceding source terms, d is a characteristic length scale of the solid material like e.g. a grain size, f_s represents the solid fraction, which lies in between 0 and 1,

c_2 is a numerical constant to prevent division by zero for $f_s = 1$, $\boldsymbol{g}$ is the gravitational acceleration, β is the thermal expansion coefficient and T and T_{liq} are the temperature of the fluid element and the liquidus temperature, respectively. Extending (18.2) with (18.16) and (18.17) leads to the final momentum equation that is solved in the EB welding model:

$$\frac{\partial \boldsymbol{u}}{\partial t} + \nabla \cdot (\boldsymbol{u}\boldsymbol{u}) = -\frac{1}{\varrho_0}\nabla p + \nabla \cdot (\nu \nabla \boldsymbol{u}) + S_m + S_b. \tag{18.18}$$

To account for the latent heat of fusion H_ℓ during melting and solidification, (18.3) is extended by the source term S_ℓ, which is denoted as:

$$S_\ell = H_\ell \left(\frac{\partial f_s}{\partial t} + \nabla \cdot (\boldsymbol{u} f_s) \right), \tag{18.19}$$

Additionally, the heat source term S_q, which is sketched in Fig. 18.21 is added to the energy conservation equation:

$$S_q = \frac{1}{\varrho} q(x, y, z). \tag{18.20}$$

Combining (18.3), (18.19) and (18.20) leads to the form:

$$c_p \frac{\partial T}{\partial t} + c_p \nabla \cdot (\boldsymbol{u} T) = \frac{1}{\varrho} \nabla \cdot (k \nabla T) + S_\ell + S_q, \tag{18.21}$$

which is solved in the numerical model for EB welding.

The heat source model is responsible for forming the weld pool during melting and subsequently the fusion zone after solidification. Because of the complex shape of the welding seam, which the heat source needs to mimic, it consists of a double ellipsoidal part for the weld nail head and a conical part for the middle and lower region, as proposed by Lundbäck and Runnemalm [42]. The double ellipsoidal part q_e, recommended by Goldak et al. [43], was used:

$$q_e(x, y, z) = \frac{6\sqrt{3} Q_{in}}{a_e b_e c_e \pi^{3/2}} \exp\left(\frac{-3x^2}{a_e^2}\right) \exp\left(\frac{-3y^2}{b_e^2}\right) \exp\left(\frac{-3z^2}{c_e^2}\right). \tag{18.22}$$

The conical part q_c is:

$$q_c(x, y, z) = \frac{6 Q_{in}}{a_c b_c c_c \pi (1 + d_c)} \exp\left(\frac{-3x^2}{a_c^2}\right) \left[1 - \frac{(1 - d_c)|y|}{b_c}\right] \exp\left(\frac{-3z^2}{c_c^2}\right). \tag{18.23}$$

Here, Q_{in} is the heat, which is produced by the electron beam, $a_{c/e}$, $b_{c/e}$, and $c_{c/e}$ are the width, height and length of the heat source parts conical c and double ellipsoidal e, respectively. x, y and z are the Cartesian coordinates and d_c is the narrowing of

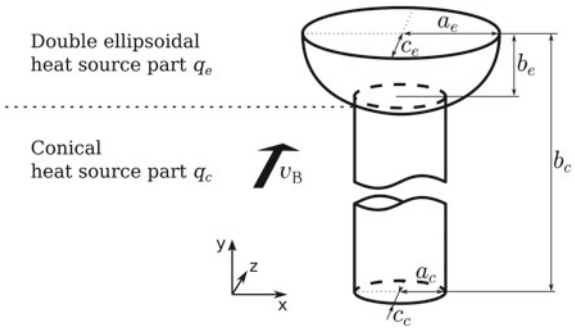

Fig. 18.22 Heat source geometry with the geometrical heat source parameters that define the size of the individual heat source parts [37]

Table 18.1 Material composition of the X3CrMnNi 16-7-6 TRIP-steel

	C	Cr	Mn	Ni	Si	Fe
Mass fraction w_t (%)	0.044	16.2	7.07	6.52	0.88	Bal.

the conical part, if its diameter is decreasing with depth. Figure 18.22 illustrates the heat source geometry and the related parameters.

Combining (18.22) and (18.23) leads to

$$q(x, y, z) = \gamma q_e(x, y, z) + (1 - \gamma) q_c(x, y, z), \tag{18.24}$$

with the weighting factor γ. Then, (18.24) is inserted into (18.20).

The fundamental equations (18.18) and (18.21) were discretized with FVM with second order accuracy schemes. For thorough details about the numerical model, and the values of all thermophysical properties, the reader is referred to Borrmann et al. [37].

The introduced model was used to calculate the formation of the weld pool and subsequently the fusion zone of a welding seam that has been produced experimentally beforehand. The chemical composition of the welded base metal is shown in Table 18.1. Based on this composition, temperature dependent thermophysical properties were derived and transferred to the numerical model. Details about these properties and their importance are described by Borrmann et al. [37].

In order to determine target values for the outcome of the numerical model, welding seams have been produced within a vacuum chamber. The related parameters, which are deduced from the evaluation of the welds, are listed in Table 18.2. A cross section of the welding seam that is used here is shown in Fig. 18.23. The typical fusion zone geometry with upper nail head and long and narrow middle and bottom part is clearly recognizable. The weld reinforcement and root are also apparent in the experimental cross section. However, in the numerical simulation those are not considered.

Due to melt convection and heat conduction, the weld pool enlarges over time and therefore, the related heat source needs to be significantly smaller than the weld pool.

Table 18.2 Welding conditions and geometrical dimensions of the weld cross section

Weld geometry	Unit	Value
Beam voltage U_B	kV	80
Beam current I_B	mA	40
Efficiency η	–	0.9
Heat input Q_{in}	W	2880
Nail head width w_{NH}	mm	2.35
Nail head height h_{NH}	mm	1.40
Weld width w_{WS}	mm	0.70
Weld height h_{WS}	mm	10.0

Table 18.3 Heat source geometry parameters

γ (%)	a_e (mm)	b_e (mm)	c_e (mm)	a_c (mm)	b_c (mm)	c_c (mm)	d_c (%)
0.38	1.18	1.40	1.18	0.12	10	0.12	1

Appropriate parameters are shown in Table 18.3. Figure 18.24 illustrates the coherence between heat source and weld pool. Due to the choice of heat source parameters, the upper double-ellipsoidal part of the heat source appears as a hemisphere, which is significantly smaller than the nail head of the weld pool. This applies for length, width and depth, likewise. The conical part of the heat source is noticeably smaller as well.

During the transient simulation, the weld pool and fusion zone are created gradually. Figure 18.25 shows process snapshots for four consecutive points in time. At the beginning of the simulation, the base material is heated exactly at the location of the heat source. The melting follows this behavior and therefore, the weld pool is shaped according to the heat source geometry in Fig. 18.25a. In the process of time, the weld pool widens and prolongs due to heat transfer through convection in the weld pool, heat conduction and further melting of the base material. This can be seen in Fig. 18.25b, c. Furthermore, the weld pool clearly solidifies and builds the fusion zone, which is indicated as a new area in blue. At later time steps, the geometry of the weld pool and fusion zone sustains, as seen in Fig. 18.25d. The cross section of the welding seam can be obtained once the weld pool is solidified and the fusion zone is formed. Comparing it to the experimental weld geometry, see Fig. 18.26, reveals the accordance between experiment and numerical model. Further examples for weld geometries can be found in Borrmann et al. [37].

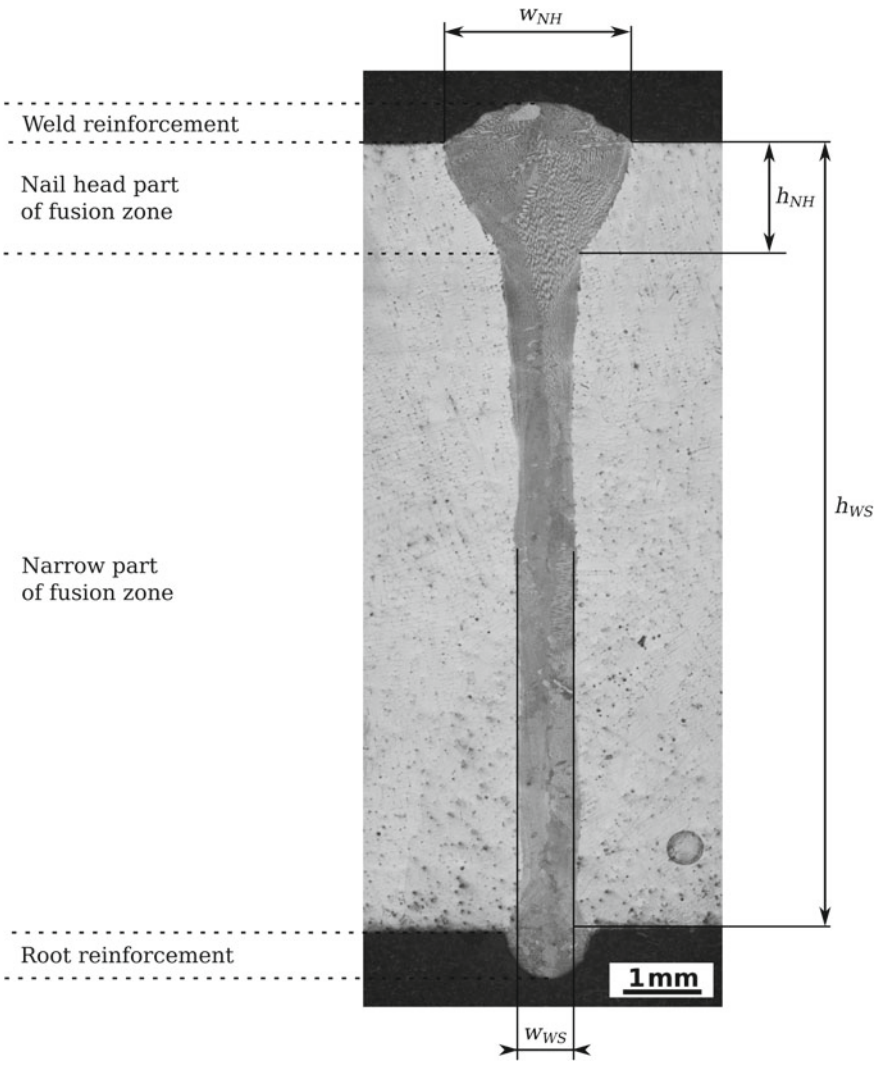

Fig. 18.23 Cross section of the experimentally obtained EB welding seam with definitions of fusion zone areas and dimensions [37]

18.4.2 Influence of Keyhole on Fluid Flow

In EB welding, the formation of a vapor column, the so called keyhole, plays an important roll for the formation of deep welds. The necessity to perform EB welding under very low ambient pressure, like in our experiments $p_A = 2\,\text{Pa}$, leads to a physical particularity during vaporization. The saturated vapor pressure $p_{s,0}$, which is the balanced pressure that determines the related vaporization temperature $T_{s,0}$, is

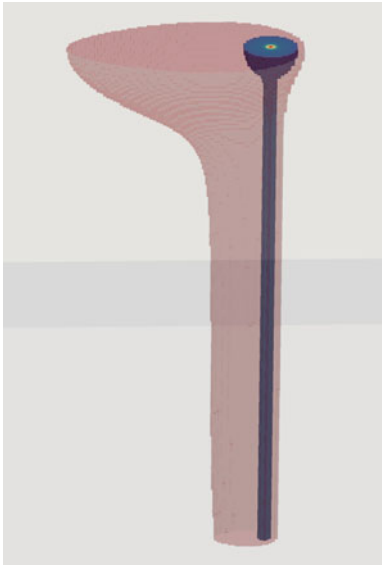

Fig. 18.24 Heat source (dark blue) and weld pool (red) that forms due to heat conduction and convection during the simulation

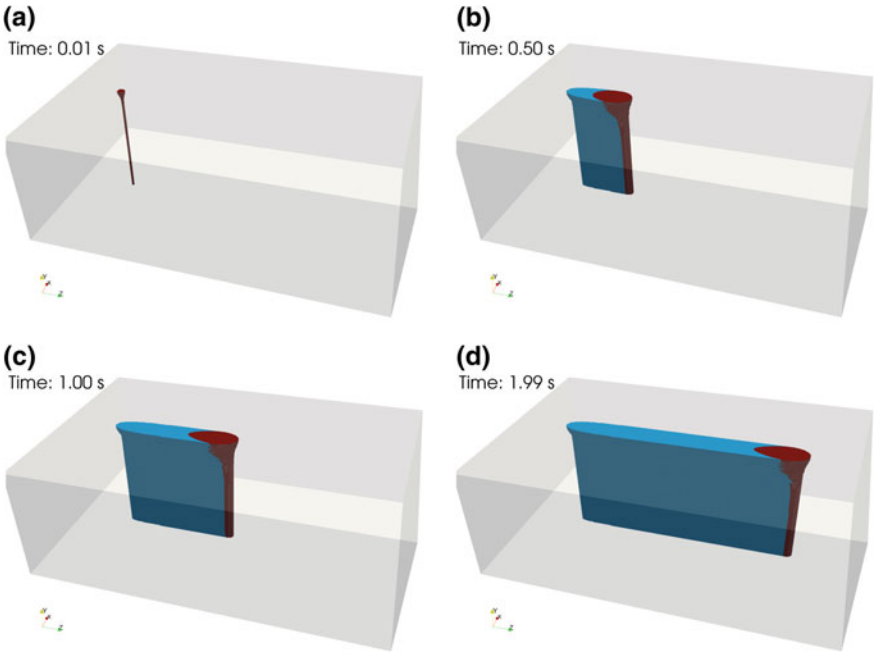

Fig. 18.25 States of the material at four different time steps (**a** $t = 0.01$ s, **b** $t = 0.50$ s, **c** $t = 1.00$ s, **d** $t = 1.99$ s) during the simulation: weld pool (red), welding seam (blue) and base material (light grey)

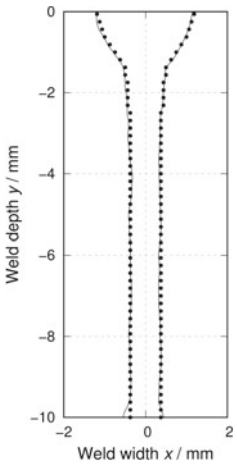

Fig. 18.26 Comparison of the welding seam cross sections of experiment (solid line) and simulation (dotted line) [37]

significantly lower than the pressure p_0 with vaporization temperature T_0 under standard conditions. $p_{s,0}$ is composed of the ambient pressure, the hydrostatic pressure of the steel column, and the dynamic pressure, which is affected by the melt flow velocity. Depending on the locally balanced $p_{s,0}$, $T_{s,0}$ can be calculated by using the simplified Clausius-Clapeyron equation [44]:

$$\ln \frac{p_{s,0}}{p_0} = \frac{\Delta H_{m,v}}{R} \left(\frac{1}{T_{vap}} - \frac{1}{T_{s,0}} \right). \tag{18.25}$$

Solving (18.25) for $T_{s,0}$ leads to:

$$T_{s,0} = \frac{1}{\frac{1}{T_0} - \frac{R}{\Delta H_{m,v}} \ln \left(\frac{p_{s,0}}{p_0} \right)}. \tag{18.26}$$

Since $T_{s,0}$ is considerably lower than T_0, vaporization occurs a lot earlier and closer to the melting temperature.

Due to the low ambient pressure, the hydrostatic pressure of the steel melt column gains in importance. Therefore, the vaporization temperature increases noticeably with increasing depth, due to a rising steel melt column. Additionally, the melting occurs very rapidly during EB welding with very high beam intensities. This leads to an overheating of the steel regarding its vaporization temperature $T_{s,0}$ to an increased vaporization temperature T_s. As a consequence of the overheating, the vapor pressure after vaporization increases noticeably. The now occurring pressure difference results in the so-called recoil pressure p_r. It might as well be solved with the Clausius-Clapeyron equation:

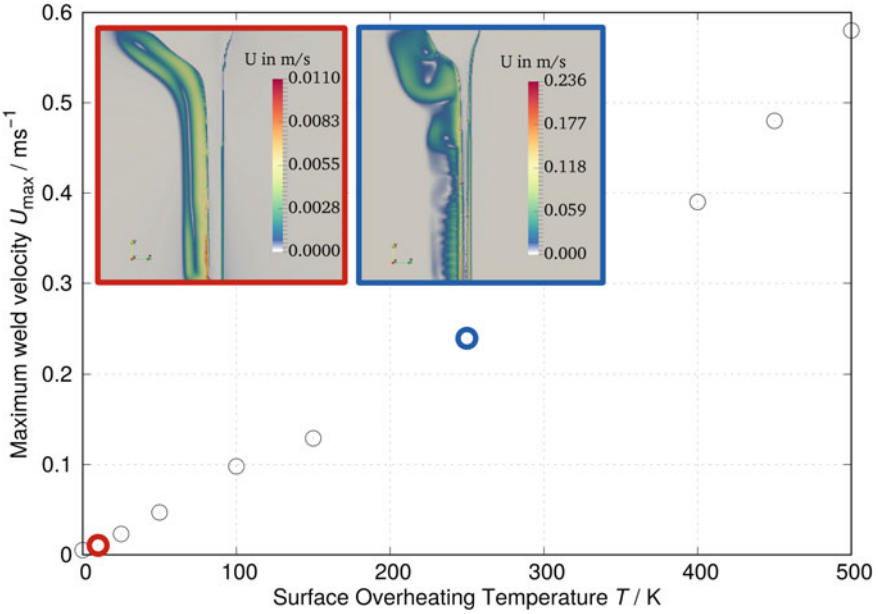

Fig. 18.27 Maximum weld velocity $u_{\max}$ as a function of surface overheating temperature ΔT. Examples are given for $\Delta T = 10\,\mathrm{K}$ (red) and $\Delta T = 250\,\mathrm{K}$ (blue)

$$p_\mathrm{r} = p_{\mathrm{s},0} \left\{ \exp\left[\frac{\Delta H_{\mathrm{m,v}}}{R} \left(\frac{1}{T_{\mathrm{s},0}} - \frac{1}{T_\mathrm{s}} \right) \right] - 1 \right\} \tag{18.27}$$

In dependence of the overheating temperature, the recoil pressure has a significant impact on the surface velocity of the melt around the keyhole. Figure 18.27 clarifies this dependence by showing the maximum keyhole surface velocity, depending on the overheating temperature ΔT. A nearly linear correlation arises. Two example velocity profiles are given for $\Delta T = 10\,\mathrm{K}$ (red circle) and $\Delta T = 250\,\mathrm{K}$ (blue circle). The keyhole is indicated as the grey area within the weld pool. While the maximum weld velocity occurs at the keyhole surface in both cases, it is more than 20 times greater for the higher overheating temperature. Two additional effects are noticeable. Firstly, with increasing surface overheating, the keyhole tends to be tighter, because vaporization occurs at higher temperatures, whereby the keyhole has less time to develop. Secondly, the melt flow shows increased vorticity due to higher velocities and, as a consequence thereof, a higher Reynolds number. Since the simulations were performed without turbulence modeling, only vortexes that are resolvable through the mesh resolution are calculated.

The consideration of vaporization and the keyhole emergence, lead to an altered geometry of the weld cross-section in the simulation due to a widening of the weld pool. To correct this deviation, the heat source model parameters can be adjusted. In order to further refine the model, the front and rear length of the heat source,

Table 18.4 Heat source parameters for the adjusted geometry

γ (%)	a_e (mm)	b_e (mm)	$c_{e,r}$ (mm)	$c_{e,f}$ (mm)	a_c (mm)	b_c (mm)	$c_{c,r}$ (mm)	$c_{c,f}$ (mm)	d_c (%)
0.52	1.18	1.40	4.6	1.18	0.085	10	0.34	0.085	1

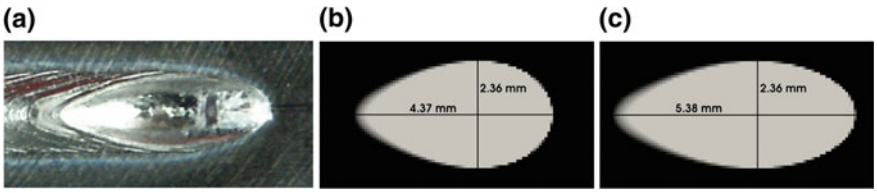

Fig. 18.28 Comparison of the solidified weld pool length in **a** the experiment with the top view of the simulated weld pool, **b** without keyhole and **c** with keyhole [37]

indicated by f and r, respectively, were adjusted according to recommendations by Goldak et al. [43]. While the front part stays half the size of the weld width, the rear part parameter is increased to the double weld width. Nevertheless, the melt pool doesn't follow the heat source specifications precisely, because of further heat conduction, convection in the melt pool, and the recoil pressure. The refined heat source parameters are shown in Table 18.4. In order to restrict the infinite expansion of the Gaussian distribution, values with less than 5% of the integral size were truncated. The clipped amount was added to the integral distribution size accordingly.

The weld pool length is indicated in Fig. 18.28. Figure 18.28a shows the experimental size, after solidification. The visible length of the solidified weld pool is 6.5 mm. Figure 18.28b, c present the weld pool sizes without and with the keyhole, respectively. While the welding seam cross section matches in both cases, the weld pool length agrees better to the experiment with using the keyhole and further heat source refinements. The relative error in case (b) is $\delta = 32.8\%$ and in case (c) $\delta = 17.2\%$. The remaining error indicates that further improvements like free surface representation together with surface tension and corresponding effects need to be considered for more precise studies.

18.4.3 Dissimilar Welding of MMC-Steel

The weldabilty of TRIP-steel has been shown to work very well [1]. The situation is different, however, for the TRIP-Matrix-Composite. Steel and ZrO_2 powder is combined to form the MMC. The presence of ZrO_2 particles in the melt leads to effects that impair the weld result, like melt ejection and cavities. We assume that direct interaction between the particles and the electron beam and the interaction with the overheated melt pool and keyhole can lead to large energy input and potentially

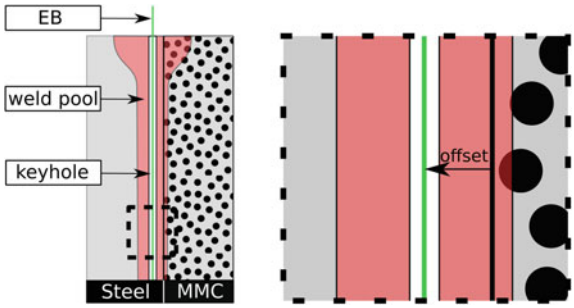

Fig. 18.29 Sketch of the dissimilar welding strategy with beam offset [38]

even rapid vaporization of the ceramic particles. In order to find solutions to ensure the weldabilty of the MMC, experimental studies were performed [34, 35]. Very good weldability was achieved, when the MMC plate was welded together with a particle-free TRIP-steel plate. By using a beam offset towards the latter, the electron beam as well as the melt pool are shifted. In that way, the disturbance of the ceramic particles is avoided. The main principle of this beam offset welding strategy is shown in Fig. 18.29. The weld pool cross-section is illustrated by the typical geometry in red. By shifting the beam as far as indicated, neither the beam, nor the emerging keyhole are interacting with the ceramic particles, illustrated as black spheres. However, they might still be present in the weld pool. In that way, they are separated from the steel matrix in the MMC and might float up or through the weld pool toward the particle-free steel. In order to investigate this behavior, the numerical model was further extended with the coupling between melt flow and ceramic particles. The necessary extensions are presented, together with parameter studies and results. For the complete numerical model and investigations, the interested reader is referred to Borrmann et al. [38].

The particle movement was driven by forces that are exerted to the particles by the melt flow. This was considered by solving their equation of motion, which reads

$$m_\mathrm{p}\frac{\mathrm{d}\mathbf{u}_\mathrm{p}}{\mathrm{d}t} = \mathbf{F}_\mathrm{B} + \mathbf{F}_\mathrm{G} + \mathbf{F}_\mathrm{D}. \tag{18.28}$$

Here, m_p is the particle mass and u_p is the particle velocity. The gravity force $\mathbf{F}_\mathrm{G}$ and buoyancy force $\mathbf{F}_\mathrm{B}$ are calculated with

$$\mathbf{F}_\mathrm{G} + \mathbf{F}_\mathrm{B} = m_\mathrm{p}\mathbf{g}\left(1 - \frac{\varrho_0}{\varrho_\mathrm{p}}\right) \tag{18.29}$$

with the particle density ϱ_p. The drag force $\mathbf{F}_\mathrm{D}$ is calculated by

$$\mathbf{F}_\mathrm{D} = \frac{1}{2}\rho_0 C_\mathrm{D} A|\mathbf{u} - \mathbf{u}_\mathrm{p}|\left(\mathbf{u} - \mathbf{u}_\mathrm{p}\right), \tag{18.30}$$

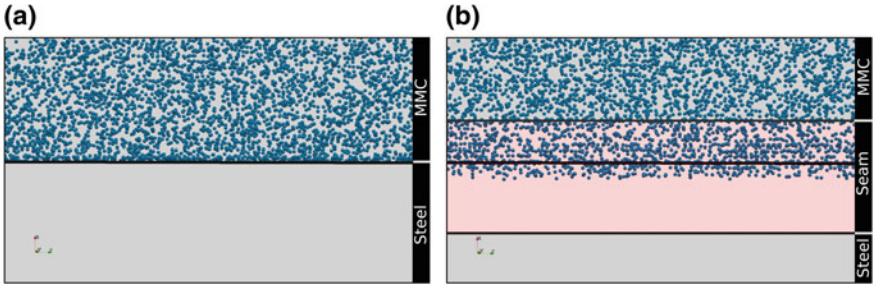

Fig. 18.30 Top view of the calculation domain **a** before and **b** after welding simulation with base material (grey) and welding seam (red). One welding partner is filled with particles (blue), the other is particle-free [37]

where C_D is the drag coefficient, and A is the representative particle area. The particles were moved in each time step subsequently to the melt flow calculation. C_D is defined with:

$$C_D = \begin{cases} 24\left(1 + \frac{1}{6}\mathrm{Re}^{\frac{2}{3}}\right) & \mathrm{Re} \leq 1000 \\ 0.424\,\mathrm{Re} & \mathrm{Re} > 1000. \end{cases} \tag{18.31}$$

Re is the particle Reynolds number, which is:

$$\mathrm{Re} = \frac{\varrho|\mathbf{u} - \mathbf{u}_p|d_p}{\eta}. \tag{18.32}$$

After the field calculations for the melt are finished, particle forces are calculated. The particles are displaced at the beginning of each time step. Figure 18.30 shows the particle displacement.

Figure 18.30a shows the top view of an initial particle distribution. The particles are generated at one half of the continuous domain on an equidistant mesh before the simulation starts. During the formation of the welding seam, particles were moved and displaced. Figure 18.30b shows the particle distribution after the end of the simulation. The welding seam, which connects the particle-free steel and the MMC, is now present. An offset of the seam reveals the offset of the heat source toward the particle-free steel. It is evident that ceramic particles were moved to a region inside the seam, where no particles were present previously.

Depending on the offset-ratio, it can be estimated if the particles would move toward the keyhole and interact with the steel vapor and the electron beam, which would still cause bad weldabilty. Therefore, different offset ratios were investigated. In Fig. 18.31, the total number of particles $n_{p,d}$ that were displaced and enriched in the previously particle-free steel is shown. Depending on the beam offset, the particle count differs significantly. The beam offset values are referring to the half of the nail head width such that for 100% offset, the welding seam is located completely on the particle-free welding partner. Between no beam offset (0%) and a small beam offset

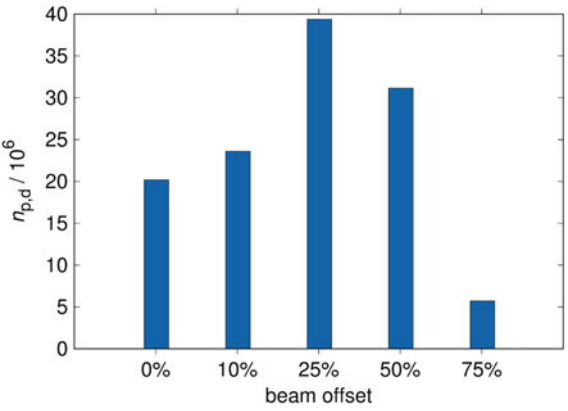

Fig. 18.31 Total number of particles that are enriched in the particle-free steel after welding in dependence of the relative beam offset [38]

(25%), the total number of enriched particles doubles. Even though less particles are extracted from the MMC in the second case, the separation is higher than in the first case, because the particles were transported towards a greater region in the particle-free steel. For higher offsets, the trend reverses and the particle enrichment decreases as the count of separated particles is much smaller than for low beam offsets. One reason for this is the fact that for high beam offsets, the total weld pool area decreases disproportionately, because the offset has a higher impact on the displacement of the narrow area of the weld pool. For the highest beam offset (75%), the narrow welding seam part is completely located at the particle-free steel welding partner, which leads to a kind of braze welding. Therefore, the total number of displaced particles decreases largely.

The number of particles in the core area of the weld pool is of special interest. The core area is defined as a cylinder with half the diameter of the narrow part of the welding seam. A comparison between the state before and after welding is shown in Fig. 18.32. It is evident that the particle-count in the core area nearly remains the same for 0 and 10% beam offset. Increasing the offset leads to a shift toward a region, where no particles were present in the initial state. However, for 25 and 50% beam offset, particles were enriched in this area, after welding. While this is possible in the simulation, for real EB welding applications, particle would interact with the electron beam and disturb the process. Because of the particle enrichment, this would even be the case for the higher beam offsets. Only for the highest investigated beam offset of 75% no particles occurred in the core of the weld pool. This means that optimal welding conditions occur for high beam offsets, where the majority of the weld pool lies on the particle-free steel side. Because of the braze welding effect, the bond of the welding partners is still given [34].

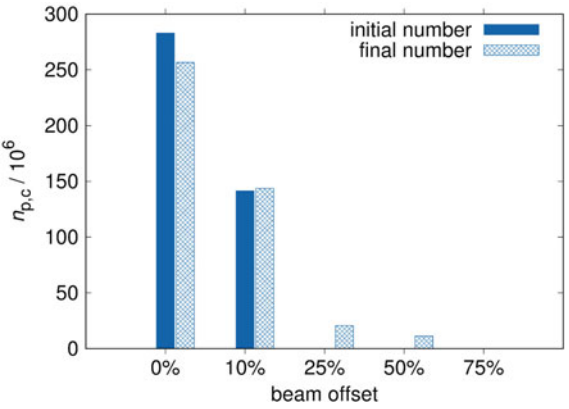

Fig. 18.32 Number of particles in the weld pool core before (solid) and after (meshed) welding [38]

18.5 Conclusion

The relevant processes for the production and further processing of TRIP-steel and TRIP-Matrix-Composites were investigated using CFD simulations. Various numerical models were implemented and existing solvers were extended.

Implementations into OpenFOAM have been made to improve stability, reduce computational costs in VOF calculations, to transform between different approaches, namely Eulerian and Lagrangian, and to calculate and couple particular physical effects. All implementations have been applied for chosen examples. The ability to calculate the infiltration of steel melt into macroscopic foam structures and free surface tracking to predict the possibility of infiltration and cavities has been achieved. The atomization model is able to predict primary breakup and reinforcing process parameters and track droplet sizes, position and velocity after primary breakup. Lagrangian particle distributions can be used to investigate sizes of coatings in flame spraying and the impacting positions and speed of droplets. The EB welding model is able to calculate weld pool shapes and melt velocities. Furthermore, the movement, depletion and accumulation of ceramic particles in the welded components can be evaluated. Through the calculation of the keyhole and therefore the penetration depth, the welding model is also able to estimate the weldability for varying EB parameters like beam intensity and feed rate.

Further extensions of the numerical models are possible. This includes the secondary breakup of the Lagrangian phase particles during gas atomization to get final particle size distributions. Furthermore, the coating buildup during flame spraying can be achieved with a reverse particle tracking algorithm which creates VOF droplets from Lagrangian particles. Models for solidification and surface tracking can be combined to include further effects like surface tension and Marangoni convection into the welding model and to evaluate their influence on particle-melt-interaction.

Acknowledgements Gefördert durch die Deutsche Forschungsgemeinschaft (DFG)—Projektnummer 54473466—SFB 799 (Funded by the Deutsche Forschungsgemeinschaft (DFG,

German Research Foundation)—Projektnummer 54473466—SFB 799). The authors thank Jens Klostermann under co-supervision of Prof. Christoph Brücker for his fundamental work in SFB 799, subproject C1 and for setting the course for the further developments in the present research. The following subprojects that particularly supported our work are highly acknowledged: A1, A2, A7, C2, C5, and T4. The authors want to explicitly thank all the contributors to the models and results that have been presented in this chapter: Richard Acker, Amjad Asad, Horst Biermann, Kinnor Chattopadhyay, Tobias Dubberstein, Patrick Gehre, Lars Halbauer, Martin Heinrich, Christoph Kratzsch, Markus Radajewski, Paul Rähmer, Ivan Saenko, Andy Spitzenberger, Marco Weider, Anja Weidner, and Christian Weigelt. The computations were performed on a Bull Cluster at the Center for Information Services and High Performance Computing (ZIH) at TU Dresden and the High Performance Compute Cluster at University Computer Centre (URZ) at TU Bergakademie Freiberg.

References

1. A. Buchwalder, K. Rüthrich, R. Zenker, H. Biermann, Adv. Eng. Mater. **15**, 566 (2013)
2. J.H. Ferziger, M. Perić, *Computational Methods for Fluid Dynamics* (Springer, Berlin, 1996)
3. H.K. Versteeg, W. Malalasekera, *An introduction to Computational Fluid Dynamics: The Finite*, vol. method, 2nd edn. (Pearson, Harlow, 2007)
4. H.G. Weller, G. Tabor, H. Jasak, C. Fureby, Comput. Phys. **12**, 620 (1998)
5. J. Klostermann, K. Schaake, R. Schwarze, Int. J. Numer. Meth. Fluids **71**, 960 (2013)
6. M. Weider, K. Eigenfeld, Steel Res. Int. **82**, 1064 (2011)
7. J. Klostermann, R. Schwarze, M. Weider, C. Brücker, Steel Res. Int. **82**, 1113 (2011)
8. J. Klostermann, R. Schwarze, C. Brücker, Eng. Comput. **29**, 95 (2013)
9. R. Schwarze, J. Klostermann, C. Brücker, Steel Res. Int. **82**, 56 (2011)
10. R. Schwarze, J. Klostermann, Steel Res. Int. **87**, 465 (2016)
11. J. Brackbill, D. Kothe, C. Zemach, J. Comput. Phys. **100**, 335 (1992)
12. S. Neumann, T. Dubberstein, H. Chaves, C. Kirmse, R. Schwarze, Steel Res. Int. **87**, 1002 (2016)
13. A. Spitzenberger, S. Neumann, M. Heinrich, R. Schwarze, SoftwareX **11**, 100382 (2020)
14. A. Glage, S. Martin, S. Decker, C. Weigelt, M. Junghanns, C.G. Aneziris, U. Martin, L. Krüger, H. Biermann, Steel Res. Int. **83**, 554 (2012)
15. N. Ashgriz (ed.), *Handbook of Atomization and Sprays: Theory and Applications* (Springer, Boston, 2011)
16. T. Dubberstein, H.P. Heller, Steel Res. Int. **84**, 845 (2013)
17. S. Markus, U. Fritsching, K. Bauckhage, Mater. Sci. Eng. A Struct. **326**, 122 (2002)
18. J. Thompson, O. Hassan, S. Rolland, J. Sienz, Powder Technol. **291**, 75 (2016)
19. C. Kirmse, H. Chaves, Steel Res. Int. **87**, 1295 (2016)
20. M. Gorokhovski, M. Herrmann, Annu. Rev. Fluid Mech. **40**, 343 (2008)
21. K. Warncke, S. Gepperth, B. Sauer, A. Sadiki, J. Janicka, R. Koch, H.J. Bauer, Int. J. Multiphase Flow **91**, 208 (2017)
22. P.J. O'Rourke, A.A. Amsden, SAE Technical Paper, 872089 (1987)
23. F.X. Tanner, SAE Technical Paper, 970050 (1997)
24. W. Edelbauer, F. Birkhold, T. Rankel, Z. Pavlovi, P. Kolar, Comput. Fluids **157**, 294 (2017)
25. H. Grosshans, R.Z. Szász, L. Fuchs, Int. J. Numer. Methods Fluids **74**, 898 (2014)
26. M. Herrmann, J. Comput. Phys. **229**, 745 (2010)
27. Y. Ling, S. Zaleski, R. Scardovelli, Int. J. Multiphase Flow **76**, 122 (2015)
28. H. Ström, S. Sasic, O. Holm-Christensen, L.J. Shah, Int. J. Heat Fluid Flow **62**, 104 (2016)
29. A. Vallier, Ph.D. thesis, Lund University, 2013
30. D. Zuzio, J.L. Estivalézes, B. DiPierro, Comput. Fluids **176**, 285 (2018)

31. OpenFOAM® v1812, https://www.openfoam.com/releases/openfoam-v1812/. Accessed 20 Dec 2018
32. P.L. Fauchais, J.V.R. Heberlein, M.I. Boulos, *Thermal Spray Fundamentals: From Powder to Part* (Springer, Boston, 2014)
33. L. Halbauer, R. Zenker, A. Weidner, A. Buchwalder, H. Biermann, Steel Res. Int. **86**, 436 (2015)
34. L. Halbauer, A. Buchwalder, R. Zenker, H. Biermann, Weld World **60**, 645 (2016)
35. L. Halbauer, R. Laubstein, M. Radajewski, A. Buchwalder, L. Krüger, H. Biermann, Adv. Eng. Mater. **21** (2018)
36. B. Huang, X. Chen, S. Pang, R. Hu, Int. J. Heat Mass Transf. **115**, 159 (2017)
37. S. Borrmann, C. Kratzsch, L. Halbauer, A. Buchwalder, H. Biermann, I. Saenko, K. Chattopadhyay, R. Schwarze, Int. J. Heat Mass Transf. **139**, 442 (2019)
38. S. Borrmann, A. Asad, L. Halbauer, A. Buchwalder, H. Biermann, R. Schwarze, Adv. Eng. Mater. **21**, 1800741 (2019)
39. V.R. Voller, C. Prakash, Int. J. Heat Mass Transf. **30**, 1709 (1987)
40. F. Rösler, D. Brüggemann, Heat Mass Transf. **47**, 1027 (2011)
41. A. Miehe, Ph.D. thesis, TU Bergakademie Freiberg, 2014
42. A. Lundbäck, H. Runnemalm, Sci. Technol. Weld. Join. **10**, 717 (2005)
43. J. Goldak, A. Chakravarti, M. Bibby, Metall. Trans. B **15**, 299 (1984)
44. A.N. Volkov, L. Zhigilei, Int. J. Heat Mass Transf. **112**, 300 (2017)

Chapter 19
Thermodynamic Modelling in the Frames of the TRIP-Matrix-Composite Development

Ivan Saenko and Olga Fabrichnaya

Abstract The present chapter is focused on thermodynamic modelling as a part of a complex development of metal-ceramic composite materials. Within this chapter the main examples of successful application of thermodynamic calculation for a solving of technological problems are highlighted, basic theory and methods of thermodynamic investigations and modelling are described in details and the most important results are briefly given. The purpose of this chapter is to give a deep understanding of thermodynamic modelling from basic experiments to modern methods of simulation. There is a set of recommendations for performing thermodynamic assessment and creation of multicomponent thermodynamic databases.

19.1 Introduction

Knowledge of phase equilibria and the underlying thermodynamics play a crucial role in the understanding of development and application of materials. Thereby, phase diagrams represent a kind of roadmaps for materials development and provide important information for understanding of technological aspects of design and usage of materials. However, the most of the modern materials consist of more than two or three components, what makes the graphical representation of these systems challenging and complex. Moreover, there is only limited information for many multicomponent systems. Method of computational thermodynamics is very powerful tool for prediction and extrapolation helping to fill these gaps of the areas without experimental information [1].

In the frame of a development of an innovative composite material, thermodynamic simulation using the CALPHAD method (Calculation of Phase Diagrams) can be used in order to support an optimization of chemical composition of the alloy and to develop a production process.

I. Saenko · O. Fabrichnaya (✉)
Institute of Materials Science, Technische Universität Bergakademie Freiberg, Gustav-Zeuner-Str. 5, 09599 Freiberg, Germany
e-mail: fabrich@ww.tu-freiberg.de

H. Biermann and C. G. Aneziris (eds.), *Austenitic TRIP/TWIP Steels and Steel-Zirconia Composites*, Springer Series in Materials Science 298,
https://doi.org/10.1007/978-3-030-42603-3_19

The TRIP-Matrix-Composite is an example of innovative material, which is based on high-alloyed austenitic TRIP-steel and reinforcing ceramic particles of zirconia partially stabilized by MgO (Mg-PSZ). Thereby, thermodynamic calculations can provide information about the stable and metastable phase formation in the material as well as the accompanying energetic effects and basic information of the physico-chemical parameters of the manufacturing processes.

Metal Matrix Composites containing highly alloyed TRIP-steel as metallic component and MgO partially stabilized ZrO_2 as ceramic component are considered as promising new construction materials with high energy absorption. Under deformation metastable austenite transforms into martensite, which results in an increasing strength. It should be mentioned that MgO stabilized ZrO_2 also shows stress-induced martensitic transformation from tetragonal into monoclinic phase [2]. The increased toughness of this ceramic phase is attributed to a stress-induced transformation. For a good performance of the composite material a strong adhesion between the metallic and the ceramic components is required in order to transmit stresses between the different phases. The infiltration and powder metallurgy/sintering processes selected in the Collaborative Research Center 799 (CRC799) to produce Fe–ZrO_2 based TRIP matrix composites may cause heterogeneous reactions in the matrix materials, in the ceramic particles and at the interfaces that can significantly influence on the mechanical properties of final composite materials. This information can be used to derive the structure development in the constituent materials and their compatibility and long-term stability. Therefore, the CALPHAD method was applied in the CRC 799 for many years as a valuable tool for materials design as knowledge of the phases that are present in a material and their compositions is essential for modelling the behavior and properties. It was widely applied for optimization of chemical composition of steel matrix with following annealing improving of its microstructure [3], for prediction and understanding of the local deformation mechanisms [4], for modelling of interfacial reaction between steel matrix and ceramic particles [5], as well as for understanding of phase transformations of the metastable austenite into martensite in the Fe–CrMnNi–N–C model alloy [6]. Additionally, the CALPHAD method provided a basement for further modelling method concerning the development of the TRIP-Matrix-Composite i.e. thermo-mechanical modelling [7], simulation of electron beam welding [8] and phase field modelling.

This Chapter will consider a basement of computational thermodynamics, reveal experimental side of thermodynamic modelling and present the latest results concerning the TRIP-Matrix-Composite development.

19.2 Experimental Techniques

Since the CALPHAD approach is a phenomenological method, its parametric functions must be assessed using experimental data before any prediction and/or extrapolation can be made. In order to get a maximum of information, all types of experimental measurements that are related to thermodynamic properties must be considered

and assessed. Collected experimental data are applied for adjusting of optimized parameters of the Gibbs energy functions.

Thereby, the reliability and accuracy of the experimental data have to be critically evaluated taking into account, which one of the various experimental techniques was used. Measured experimental data can be roughly classified into a few principal types: "thermodynamic data" and "phase-diagram data" [9]. The most of thermodynamic data can be directly applied to describe Gibbs energy functions of individual phases, while experimental data on the phase relations can be used for optimization of those functions for reproducing of phase diagrams of the system and thermodynamic data within their uncertainty. Since the phase diagram is representing equilibrium states of the system corresponding to minimum of its Gibbs energy being the sum of the properties of the individual phases multiplied to their mole amount respectively [10] at various conditions the phase relations are dependent on thermodynamic properties of the individual phases. Optimization of the Gibbs energy functions is a complex procedure, which will be described further (Sect. 19.3.2).

19.2.1 Sample Preparation

Development of the TRIP-Matrix-Composite requires a multicomponent thermodynamic description, which would include all alloying elements of the matrix, as well as components of ceramics such as ZrO_2 and MgO as well as oxides appearing due to steel oxidation and impurities. Consequently, both type of materials had to be investigated, not only steel matrix but also components of ceramics. Therefore, two different techniques of specimen preparation were applied for investigations of steel and ceramic systems.

In the case of steel systems, two or three components alloys were prepared by arc-melting method in Ar-atmosphere. Chemically pure metals were used as raw materials. Precursors have been weighed in accordance to the nominal compositions using laboratory scale ABJ 120-4M (KERN & Sohn GmbH). In order to achieve good homogeneity of the chemical composition in the bulks, the samples were turned-over and re-melted three times during acr-melting. The melting chamber was evacuated to ~10^{-5} atm and refilled with argon three times. An ingot of Ti (ca. 3 g) was placed in one of the molds and was melted before the melting of the samples in order to adsorb rests of oxygen and prevent possible oxidation. The weight losses due to vaporization should be generally less than 1 mass%. Next, samples obtained by arc melting were encapsulated in quartz tubes with reduced Ar atmosphere. The pressure of Ar was chosen in order to reach 1 atm. at the homogenization temperature. The encapsulated samples were heat treated for a long time afterwards they were quenched into ice-cold water.

For ceramic systems, the co–precipitation method was used for sample preparation. Chemically pure salts of desired metals have been used as the initial materials. In the first step, the salts were diluted and dissolved by distilled water in order to obtain

more suitable consistence for the co-precipitation process (solutions around of 0.4–1.2 mol/l in dependence on precursors). The concentration of obtained initial solutions was determined by Inductively Coupled Plasma-Optical Emission Spectrometry (ICP-OES) spectrometry. Calculated volumes of initial solutions were mixed together in order to get ~2 g of oxide powder of desired molar ratio. The obtained solution was dropped from a burette at a low speed (around 1 ml per minute) into a beaker containing about 500 ml of the aqueous solution of NH_4OH with pH value above 9.0. In order to increase particles in the obtained suspension, it was heated up and held at 333 K for 1–2 h before filtration. In order to control the chemical composition, co-precipitated suspension and filtrates were analyzed by ICP-OES. Since the composition of the samples obtained by ICP deviated significantly from nominal composition, an evaporation process was applied instead of filtration. Then, the substance obtained after filtration/evaporation was dried at 353 K for 2–3 days. Finally, pyrolysis of the dried precipitate powder was performed at 1073–1273 K for 3 h in air. The obtained oxide powder was pressed into cylindrical pellets at 250 MPa and sintered in air atmosphere in Pt-crucibles using NABERTHERM furnace in order to reach equilibrium state. Annealing duration was chosen depending on sintering temperature and on development of microstructures.

19.2.2 Phase-Diagram Data

The quantities measured in phase diagrams are either temperatures of phase boundaries at fixed composition and invariant equilibria determined by thermal analysis or phase compositions at fixed temperatures determined by sample equilibration. There are several experimental methods for measuring the phase-diagram data. They are described in details by Lukas et al. [9]. In the frames of current investigation, X–ray powder diffraction (XRD), scanning electron microscopy combined with an energy dispersive X–ray spectrometry (SEM/EDX) and differential thermal analysis (DTA) were applied in order to get essential information about phase relations, required for thermodynamic assessment of two and three component system. Experimental data for multicomponent systems are usually not used directly in an assessment, but, if the extrapolation from the lower-order systems gives wrong results, one may use these data for modification of parameters describing the lower-order systems or by introducing high-order parameters and new phases. Additionally, if phases are not stable in a binary system the parameters of metastable phases can be assessed from a higher order system.

19.2.2.1 Structural Investigation

After long time annealing, the important step is to determine the phase assemblage of heat-treated samples. The most powerful analytical techniques for identifying the phases is X-ray or neutron diffraction. Moreover, these techniques are also important

for the determination of crystal structures. Lattice parameters and site occupancies as functions of composition and temperature can be obtained to provide detailed information about the internal lattice of crystalline substances, including cite occupancies, unit cell dimensions, bond–lengths and bond–angles. This information is necessary to find right models for thermodynamic description.

In the frames of current investigation, X-ray powder diffraction (XRD) was applied using URD63 diffractometer (Seifert, FPM, Freiberg, Germany) equipped with graphite monochromator and CuKα radiation ($\lambda = 1.5418$ Å). The goniometer of the diffractometer has the Bragg-Brentano geometry. Powder samples were measured placed on monocrystalline silicon substrate with (510) orientation. In this case, the orientation of the substrate does not show any peak on the XRD patter in the range of 15°–110° of 2θ. The Rietveld refinement was applied for the characterization of all measured diffraction patterns in order to obtain the volume fractions of present phases as well as lattice parameters. This method allows determining the site-occupancy parameters by analyzing the polycrystalline samples. Each solid phase has its own characteristic diffraction pattern, as a function of intensity in dependence on the diffraction angle 2θ. The program Maud [11] was used for Rietveld refinement.

19.2.2.2 Microstructural Investigation

A very useful tool in phase-diagram determination is micrography at higher magnification using a scanning electron microscope (SEM), or a transmission electron microscope (TEM). Equipped with an energy dispersive spectrometer (EDS), these devices allow measuring the chemical composition of the microstructural features. For example, boundaries in phase diagrams, which are often deduced from results of characterization of sample series with different compositions after equilibration at fixed temperatures, can be plotted as composition versus a temperature. Afterword, these results can be applied for modelling of homogeneity ranges of solid phases etc.

The microstructures of the samples were analyzed using Scanning Electron Microscopy (SEM). The investigations were carried out on the LEO 1530 Gemini (Zeiss, Germany). The microscope was equipped with a field emission cathode, used at the acceleration voltage of 20 kV with working distance of 8–10.5 mm. In addition, energy–dispersive X–ray spectroscopy (EDX) was used in order to verify chemical compositions of samples, to determine phase compositions which are also used for identification of phases, as well as to estimate composition of liquid in eutectic reactions. An uncertainty range for EDX measurement is around 2–4 at.%.

For imaging in the SEM, samples must be electrically conductive, at least at their surface, and electrically grounded in order to prevent the accumulation of electrostatic charge at the surface at the interaction with the electron beam. Therefore, samples composed of oxides were grinded and polished and then coated with an ultrathin graphite layer.

19.2.2.3 Thermal Analysis

Differential thermal analysis (DTA) was applied in order to detect temperatures of phase transitions and reactions occurring in the sample as well as melting temperatures. The technique of thermal analysis is based on the measuring of the temperature difference between the sample versus a reference as a function of time and temperature during programmed heating and cooling cycles. Any exothermic or endothermic changes occurring in the sample is registered by comparison with the reference as the temperature difference of the thermocouple signals in μV (thermal voltage). The inert material, which does not react with crucible and does not have phase transformations in the investigated temperature range can be used as a reference. However, it should be noted that empty crucibles are mostly used as reference at present.

In the frame of this work, DTA was performed using SETARAM SETSYS EVOLUTION 1750 (SE 1750) and SETARAM SETSYS EVOLUTION 2400 (SE 2400). The SE 1750 device equipped with a type B thermocouple (Pt/Rh 70%/30%—Pt/Rh 94%/6%, by weight) works in an inert atmosphere of argon or helium in the interval of temperatures up to 2023 K. The SE 2400 device equipped with a type C thermocouple (W/Re 95%/5%—W/Re 74%/26%, by weight) works in an inert atmosphere of helium up to 2673 K. As the crucible's materials Pt/Rh10% was used for SE 1750 and pure W was used for SE 2400 in the case of ceramic materials. For metallic samples, ceramic crucibles should be used. Thereby, corundum is the most common ceramic material.

Both if these devices have an opportunity for thermogravimetric analysis (TGA), which is very useful tool for measuring the mass change of a material as a function of temperature and time during heating and cooling program.

Calibration procedure of the apparatuses was systematically carried out by using pure reference elements with known melting temperatures. Measured temperatures were recounted according to a correction function acquired at the last correction procedure. Temperature calibration of SE 1750 was performed using melting points of Al, Ag, Au, Cu and Ni. The correction procedure for SE 2400 was carried out using melting points of Al, Al_2O_3 from literature and temperature of solid phase transformation in $LaYO_3$ measured in SE 1750. These materials were chosen because of their passivity concerning to crucible's materials. Correction polynomials were obtained by fitting derived points using the least–squares method. The temperatures of transformations were determined as on–set point i.e. intersection of the tangent line constructed in the point of highest slope and baseline. Since correction procedures were carried out using on–set point, temperatures of transformations should be also determined by on–set points.

19.2.3 Thermodynamic Data

There are many different techniques for determining thermodynamic properties of individual phases directly. They are described in the book of Lukas et al. [9]. In

this chapter, only two types of measurements will be discussed further, namely drop solution and differential scanning calorimetry that were used in the frames of current work.

19.2.3.1 Differential Scanning Calorimetry

In the present work, differential scanning calorimetry (DSC) measurements were carried out in order to obtain the heat capacity of single phases in the investigated systems. This information is important for the thermodynamic assessments and modelling of multicomponent systems. The heat capacity measurements in the temperature range from 235 to 675 K were carried out using the device DSC 8000 (Perkin Elmer, Pt/Rh crucible, Ar or He flow, heating rate 10 K/min). The measurements in the temperature range from 235 to 675 K were divided into small intervals of 100–150 K. The DSC measurements in the temperature range from 623 to 1220 K were performed in one temperature range using the device DSC Pegasus 404C (NETZSCH, Pt/Rh crucible, Ar flow, heating rate 10 K/min).

The classical three-step continuous method [12] with a constant heating rate was used to measure specific heat capacity:

- The determination of the heat flow rate of the zero–line (with empty sample and reference sides). This step takes into account the heat capacity of inner parts of the device.
- The calibration step—a sample of the material, whose heat capacity is precisely defined (synthetic sapphire), is measured in the sample crucible.
- Calorimetrical measurement of an unknown sample.

Calibration was performed using a certified sapphire standard in the case of ceramic materials. For metallic systems, calibration was performed using certified standard materials depending on the reliable temperature range of their heat capacity: copper standard was used in the temperature range from 100 to 320 K; molybdenum from 300 to 673 K and platinum from 573 to 1473 K. The mass and radius of sample pellets were kept the same as for standard materials. The measurements of two different samples were repeated two times with maximal uncertainty 3%. It should be mentioned that the C_P measurements at high temperatures using DSC equipment are becoming less reliable due to increase of heat radiation which decreased registered signal. This effect was considered during fitting of the experimental data. Fitting of the obtained results was performed using the Maier-Kelley equation. In order to exclude any phase transformation during the heat capacity measurement, XRD analyses of the obtained samples were performed before the heat capacity measurements and afterward.

19.2.3.2 Drop Solution Calorimetry

The principle of this method is that two (or more) different well-defined samples are combined in the calorimeter and react to give a single sample, which again must be well defined. Well defined means that all the variables upon which the enthalpy depends must be known: each sample must be in internal equilibrium; its temperature and composition must be known. Drop solution calorimetry method was applied in order to determine the enthalpy of formation of oxide compounds. These measurements were performed using an Alexis 800 heat-flux micro calorimeter (SETARAM, France). The samples pressed into pellets (Ø 1 mm, mass 3–9 mg) were dropped directly from room temperature into the calorimeter with a solvent at $T =$ 973 K and the enthalpy increments of dropping and solution of a set of 9 pellets were measured. The sodium molybdate $3Na_2O \cdot 4MoO_3$ was used as the solvent. The calorimeter was calibrated by using the molar enthalpy increment of dropping standard sapphire spheres. Error of the measurement was stated to be twice the standard deviation of the mean value.

19.3 CALPHAD Method

Computational thermodynamics is powerful tool for solution of various problems in materials science, particularly used in the construction of phase diagrams [10]. At the beginning of the previous century, a thermodynamic modelling a phase diagrams of a metal-based system was firstly performed by Johannes van Laar using regular solutions models, what has evolved in more recent years to the CALPHAD (Calculation of Phase Diagrams) [13]. The CALPHAD method has been pioneered by American metallurgist Larry Kaufman since the 1970s [9, 14, 15]. Calculation of phase equilibrium is based on minimization of the Gibbs energy of the system which is the sum of the Gibbs energies of individual phases multiplied respectively to their mole amount or from equality of chemical potential for components in the equilibrated phases. The Gibbs energy of individual phase is described by thermodynamic model representing its dependence on temperature, pressure and composition [14]. Therefore, phase diagrams are related to the thermodynamic properties of individual phases which can be also determined experimentally using calorimetry, vapor pressure measurements and electrochemical data. These different kinds of data are used for optimization of thermodynamic parameters simultaneously to reproduce both phase diagrams and experimental thermodynamic data. The obtained set of thermodynamic descriptions of individual phases can be used to calculate different kinds of phase diagrams.

It should be noted that thermodynamic data of some components are very well determined and they are not optimized, the other parameters such as mixing parameters of solution phases and metastable end-members of solid solutions should be optimized. The thermodynamic properties of intermediate phases usually also need to be optimized. The aim of the CALPHAD method is to obtain a consistent description of all phases in the system reproducing the thermodynamic properties

and phase diagrams within uncertainty of measurements. The self-consistent thermodynamic database allows predicting of the phase relations and thermodynamic properties in regions where experimental information is not available as well as calculation of metastable phase diagrams, calculation of diffusion-less transformation and simulations of non-equilibrium processes assuming local equilibration.

Methodology of the CALPHAD method and main principles of thermodynamic databases development are described in many fundamental books [9, 14–16] and basics research [1, 17]. In this chapter, the main information about CALPHAD will be described very shortly.

19.3.1 Methodology

The Gibbs energy is described as a function of temperature, pressure and composition. The thermodynamic descriptions of this function of the pure phases of end members of solid solutions at a certain P and T referred to the enthalpy of its phase at room temperature 298 K are in the following form:

$$G(P,T) = \Delta_f H^0_{298} + \int_{298}^{T} C_P \mathrm{d}T - T\left(S^0_{298} + \int_{298}^{T} (C_P/T)\mathrm{d}T\right) + \int_{1}^{P} V\,\mathrm{d}P \quad (19.1)$$

where S^0_{298} is the standard entropy, $\Delta_f H^0_{298}$ is the enthalpy of formation and C_P is the heat capacity given by

$$C_P = a + bT + cT^{-2} + dT^2 + eT^{-3} + \cdots \quad (19.2)$$

The magnetic contribution $\mathrm{G_{mag}}$ can be taken into account according to Inden–Hillert–Jarl [18] formalism (19.3).

$$\mathrm{G_{mag}} = T R \ln(\beta_0 + 1) g(\tau) \quad (19.3)$$

where $\tau = T/T^*$, T^* is the critical temperature (the Curie temperature T_C for ferromagnetic materials or the Neel temperature T_N for antiferromagnetic materials), β_0 the average magnetic moment per atom and $g(\tau)$ is a function depending on τ [19].

The molar volume in (19.1) is calculated as a function of pressure and temperature using the Murnaghan equation,

$$V(P,T) = V(1,T)\left(1 + \frac{K'_P \cdot P}{K_T}\right)^{-1/K'_P} \quad (19.4)$$

where K_T is isothermal bulk modulus, which can be expressed as

$$K_T = 1/\left(\beta_0 + \beta_1 T + \beta_2 T^2 + \beta_3 T^3\right) \tag{19.5}$$

and K'_P is the pressure derivative of bulk modulus which in some cases has a temperature dependency:

$$K'_P = K'_{P298} + K'_{PT}(T - 298)\ln\left(\frac{T}{298}\right) \tag{19.6}$$

K'_{P298} is the pressure derivative of bulk modulus at 298 K, K'_{PT} is its temperature derivative.

The molar volume at 1 bar is expressed as a function of temperature

$$V(1, T) = V^0_{1,298} \exp\left(\int_{298}^{T} \alpha(T)\mathrm{d}T\right) \tag{19.7}$$

where $V^0_{1,298}$ is the molar volume at 1 bar and 289 K. $\alpha(T)$ is the temperature dependent thermal expansion

$$\alpha(T) = \alpha_0 + \alpha_1 T + \alpha_2 T^{-1} + \alpha_3 T^{-2} \tag{19.8}$$

The Gibbs energy $G_{A_aB_b}(T)$ of a stoichiometric phase A_aB_b in case of absence of heat capacity data was modeled using Neumann-Kopp rule as:

$$G_{A_aB_b} = a\mathrm{GHSER}_A + b\mathrm{GHSER}_B + \alpha + \beta T \tag{19.9}$$

where GHSER_i is the Gibbs energy of the pure element i referred to the enthalpy of pure element i at 298 K in its standard element reference (SER) state, α and β are parameters to be optimized.

Solution phases and stoichiometric phases with homogeneity ranges can be described by compound energy formalism [16].

The simplest non-ideal solution model is the substitutional model with the Gibbs energy of expressed as follows:

$$G = \sum_i^n x_i G_i + RT \sum_i^n x_i \ln x_i + \Delta G^{\mathrm{Ex}} \tag{19.10}$$

where x_i are the mole fractions, G_i is the Gibbs energy of an end-member i, $\sum_i^n x_i G_i$ is the surface of reference terms, $RT \sum_i^n x_i \ln x_i$ is the contribution to the Gibbs energy resulting from the configurational entropy of mixing for disordered solution, and ΔG^{Ex} is the excess Gibbs energy of mixing.

The excess Gibbs energy of mixing was modelled using Redlich–Kister polynomials [20], expressed as:

$$\Delta G^{\mathrm{Ex}} = \sum_{i \neq j, i<j} x_i x_j \sum_{v=0}^{n} L_{i,j}^{v} \left(x_i - x_j\right)^{v} \tag{19.11}$$

where $L_{i,j}^{v}$ is the mixing parameter between end-members i and j, while v is integer number.

The sublattice model in the form of compound energy formalism is used for solid phases having several crystallographic sites. The Gibbs energy of solution described by the sublattice model with three sublattices is given by

$$\Delta G^{\mathrm{mix}} = \sum_{i} \sum_{j} \sum_{k} Y_i^s Y_j^t Y_k^u G_{ijk} + RT \sum_{s} \alpha_s \sum_{i} Y_i^s \ln(Y_i^s) + \Delta G^{\mathrm{Ex}} \tag{19.12}$$

where Y_i^s is the mole fraction of constituent i on sublattice s, α_s is the number of sites on sublattice s per mole of formula unit of phase and ΔG^{Ex} is the excess Gibbs energy of mixing expressed as

$$\Delta G^{E} = \sum_{t} y_j^t \sum_{u} y_k^u \sum_{s} y_i^s y_l^s L_{i,l}^s + \sum_{s} y_i^s \sum_{t} y_j^t \sum_{u} y_k^u y_m^u L_{k,m}^u + \sum_{s} y_i^s \sum_{u} y_k^u \sum_{t} y_j^t y_n^t L_{j,n}^t \tag{19.13}$$

$$L_{i,l}^s = \sum_{n} \left(Y_i^s - Y_l^s\right)^n L_{i,l} \tag{19.14}$$

where $L_{i,l}^s$ are binary interaction parameters between species i and l on sublattice s. Higher-order interaction parameters could also be included giving more complicated excess Gibbs energy terms.

19.3.2 Optimization

The optimization process is the most important step of a creation of a thermodynamic database, which gives the best fit of experimental data taking into account the error of every data point. Each individual phase is described by thermodynamic model presenting an analytical function of the Gibbs energy dependence on temperature and composition (pressure is usually fixed at 1 bar) with adjustable parameters. These parameters are optimized using the least-squares method to obtain a description which reproduces experimental data with minimal deviation. However, the least-squares method can work well only if the scatter of experimental data is completely random. Non-randomly distributed deviations of some data may completely destroy the utility of the least-squares method. They must be classified as systematic errors and excluded from the optimization. Therefore subjective judgments are required and decisions have to be taken on the selection of data during the optimization. From

that point of view, the technique can also be called an assessment [9]. Unfortunately, including all available data in optimization does not necessarily lead to satisfactory results. Some experimental data could be in conflict to each other or can show large systematic errors. Thereby, setting different weights for these data points can help to recognize the influence of different experiments on the result of optimization. This procedure helps to identify which data are contradictory. However, it is usually impossible to optimize all parameters simultaneously. There are too many parameters and they have different influence on phase diagrams [17].

The optimization methodology of CALPHAD method can be subdivided into following stages:

1. Collection of diverse experimental information available in literature (crystallographic data for phases, phase equilibria, calorimetry, electrochemical data, vapor pressure measurements).
2. The selection of thermodynamic models based on crystallographic information for phases in the system under investigation. This implies selection of sublattices and their occupancies by constituents in agreement with crystal structure.
3. The consideration of temperature dependence of end-member parameters and introducing of mixing parameters for the Gibbs energy description of phase.
4. The optimization of the thermodynamic parameters using all available experimental as well as theoretical data.
5. The storage of the optimized parameters in computer–readable thermodynamic datasets.
6. The calculation of phase diagrams and various phase equilibria using the thermodynamic datasets.

The principle of the CALPHAD approach is schematically presented in Fig. 19.1.

19.4 The Latest Results Concerning the TRIP-Matrix-Composite Development

In the beginning of the development of the new composite, an extensive thermodynamic database for steel-based materials (Fe, Mn, Cr, Ni, Ti, Mo, W, V, Si, C and N) was created in the frames of CALPHAD method. Therefore the main research point was focused on an optimization of the alloy for the matrix. Afterwards, focus of thermodynamic modelling was shifted to the development of a database for the ceramic materials (ZrO_2, MgO, Al_2O_3, FeO, Fe_2O_3, MnO, Mn_2O_3).

In the beginning of the project, there were currently several thermodynamic databases for Fe-based multicomponent systems that were developed for the modelling of specific processes in the respective steels. They were based on critical assessments of binary and ternary systems available in the literature. For example, the TCFE7 commercial database included 25 elements and many binary and ternary systems (http://www.thermocalc.com/Products/Database). Moreover, this database contains descriptions of some solid oxide phases such as spinel, wustite and corundum in order to predict the tendency of different steels to oxidize. Additionally, there was the

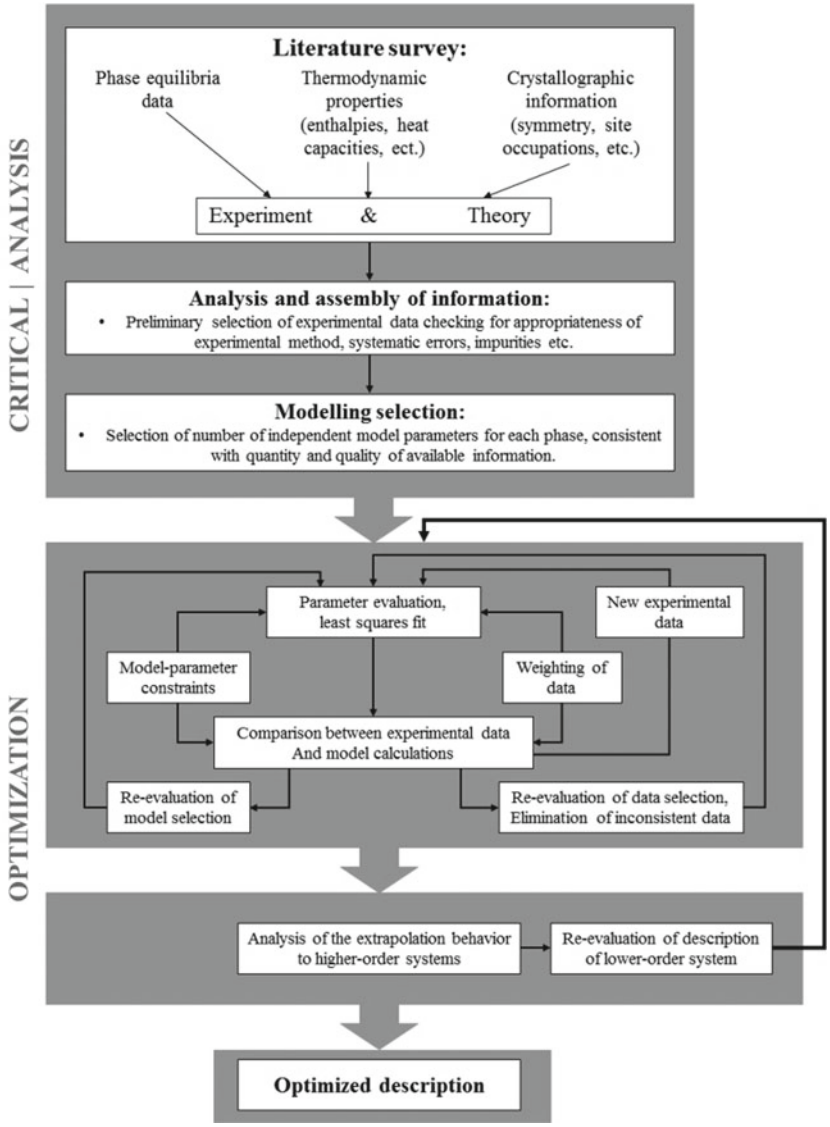

Fig. 19.1 A schematic diagram of the CALPHAD assessment

commercially available database TCOX, which contained 12 elements and descriptions of many oxide phases as well as the ionic melt, which describes both metallic and oxide melting behavior (http://www.thermocalc.com/Products/Database). However, all commercial databases have reproduced most of important binary system such as Fe–Mn, Fe–Ni, Zr–Mn, Zr–Fe very poorly, what could not be accepted for deep process of materials design.

A non-commercial steel database, which was under development in group of B. Hallstedt, contained 8 elements Fe, Al, Mn, Nb, Si, V, C and N and was aimed for modelling phase equilibria in Mn-rich steels [21]. However, this database did not include Cr and Ni, which were very important for highly alloyed TRIP-steels. Therefore, the CRC 799 project required to develop a unique multicomponent steel database, which would fit all specific needs of design process in the fames of the TRIP-Matrix-Composite development.

A new thermodynamic database for steels containing eleven elements (Fe, Mn, Mo, Cr, Ni, Ti, Si, V, W, N, C), has been developed by P. Franke within the first period of the CRC project [22]. Thermodynamic description of one of the most important systems Fe–Cr–Ni was developed based on advanced thermodynamic modelling. Obtained thermodynamic description considered magnetic contribution and chemical ordering in the Fe–Cr–Ni system [22]. This thermodynamic dataset for the ternary system Cr–Fe–Ni which has been reported in the literature for the range from medium to high temperatures has been supplemented with datasets from the binary subsystems at lower temperatures. The magnetic and the chemical ordering transitions which are known from the binary Fe–Ni system were extrapolated into the ternary system Cr–Fe–Ni. The phase diagram of Cr–Fe–Ni alloys at temperatures below 773 K was predicted (Fig. 19.2). The magnetic contribution to the Gibbs energy of Ni-rich alloys induces a miscibility gap which appears in the binary phase diagram of Fe–Ni as a small triangle-like field ending in a tricritical point. In the ternary system, Cr–Fe–Ni the miscibility gap is present as a broad two-phase field in the vicinity of the composition $FeNi_3$. At lower temperatures, this miscibility gap participates in a sequence of changing equilibria when it interferes with the chemically ordered $L1_2$ phase.

Several ternary systems in the Fe–Mn–Cr–Ni–Ti–Si–C–N system were accepted from literature data, checked for the consistency and published in LB series [23].

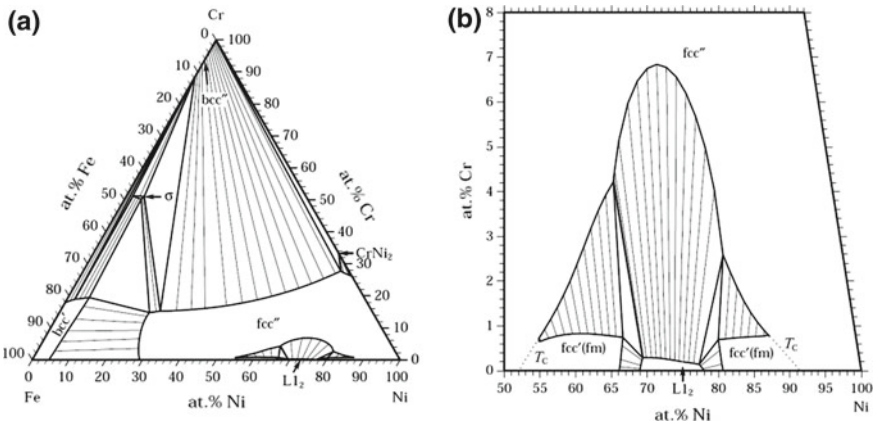

Fig. 19.2 **a** Calculated isothermal section of the Fe–Cr–Ni system at 773 K; **b** Enlarged part of calculated isothermal section at 773 K [22]

With this element selection calculations of the phase equilibria and modelling of the crystallization process using Scheil simulation for austenitic TRIP-steels became possible and reliable. Among the systems published in LB were Fe–Cr–Mn, Fe–Cr–Ni, Fe–Cr–C, Fe–Mn–C, Fe–Ni–C and others. The developed database covers a wide range of evaluated systems in comparison with other available databases. Thus, it also covers non-iron systems.

The second milestone was the interfacial interaction between Mg-PSZ and steel, which was experimentally studied by Franke et al. [5]. Experimental details (SPS pre-sintering, annealing in Ar etc.) were reported in [5]. SEM/EDX investigations demonstrated the formation of Mg_2SiO_4 at the interface between the ceramic component and steel. It was determined that Mg-PSZ contained SiO_2 impurities around of 2.4 mass%. It was stated, that another possible source for the SiO_2 could be the Si content within the TRIP-steel (~0.5 mass%). Thermodynamic calculations were performed to explain destabilization of Mg-PSZ and formation of Mg_2SiO_4 forsterite. The activity of MgO at the investigated temperature and the composition was calculated using the ZrO_2–MgO thermodynamic database available in literature [24]. The SiO_2 activity necessary for formations of silicates Mg_2SiO_4 and $MgSiO_3$ was calculated using the thermodynamic data from literature [25]. Experimental studies of an interaction between steel and pure ZrO_2 and between steel and CaO stabilized ZrO_2 showed that silicates did not form at the investigated conditions [5]. Thermodynamic calculations were also performed for the ZrO_2–SiO_2 and ZrO_2–CaO systems and ranges of the SiO_2 activity were determined at which silicates should form. The oxygen partial pressure was calculated at which the SiO_2 starts to form from Si dissolved in the steel. The corresponding limiting activity of Si in the TRIP-steel and the concentration of Si in the steel were calculated.

The ceramic material used in the present project is ZrO_2 stabilized by 3.4 mass% of MgO. A comprehensive thermodynamic assessment of the ZrO_2–MgO system was available in literature. However, all of the data were based on a substitutional model for the solid and liquid phases. Consequently, re-assessment based on the more advanced modelling using the compound energy formalism had to be performed. Additionally, it was experimentally found that an addition of Titanium can improve bonding between ZrO_2 ceramic particles and austenitic steel containing Mn, Cr and Ni [26]. Therefore, ceramic systems containing TiO_2 became one of the important tasks as well. Moreover, during the investigation of the interfacial interaction between Mg-PSZ and steel [5] it was found that the C–ZrO_2 (fluorite) was destabilized due to reaction between MgO and impurities in ceramic material such as Al_2O_3 and SiO_2. Therefore, systems with Al_2O_3 and SiO_2 became one of the main points.

Thermodynamic descriptions of the systems MgO–Al_2O_3 and MnO–Al_2O_3 based on the compound energy formalism for solid phases and partially ionic liquid model were available in literature [27, 28]. However, the model of the spinel phase in the MnO–Al_2O_3 system had to be extended by introducing an interstitial sublattice to be compatible with the model used for the MgO–Al_2O_3 system.

Many thermodynamic assessments for the systems containing TiO_2, Ti_2O_3, MgO, FeO, MnO and other oxides were performed in the group of A. D. Pelton (http://www.sgte.org/fact/documentation/FToxide). Solid phases were modelled by the compound

energy formalism, while the liquid phase was described by a modified quasi-chemical model [29]. The database for ZrO_2-based systems was set up with the help of very limited experimental literature data. However, the ZrO_2 containing phases do not contain the chemical element Ti, which makes it impossible to calculate the interaction with titanium oxides, which are very important for the planned work. Commercial steel and oxide databases have been developed by the FactSage group (http://www.sgte.org/factsage/fact/factsage/FactSage). Although these databases contain descriptions for the TiO_2–Ti_2O_3–MO systems (M = Mg, Fe, Mn), only very limited data are available for ZrO_2-based systems. Model for liquid is not compatible with models used in the present study.

Therefore, the thermodynamic database of the ZrO_2–MgO–MnO–Al_2O_3 system had to be developed for modelling of the interactions between Al_2O_3 impurities, Mg-PSZ and Fe–CrMnNi-TRIP-steels. In a similar way the SiO_2 containing binary descriptions of the MgO–SiO_2, MnO–SiO_2, ZrO_2–SiO_2 systems had to be combined with databases of the ZrO_2–MgO, ZrO_2–MnO systems and the thermodynamic database of the ZrO_2–MgO–MnO–SiO_2 system had to be developed to model phase relations between SiO_2 impurities, Mg-PSZ and the steel phases.

The thermodynamic description for the quasibinary system ZrO_2–MgO (Fig. 19.3) was based on own experimental investigations with XRD, SEM/EDX and DTA as well as existing literature data [30]. The industrial Mg-PSZ ceramic was also tested in the initial state and after heat treatments at 1523 K with DTA. Differences between

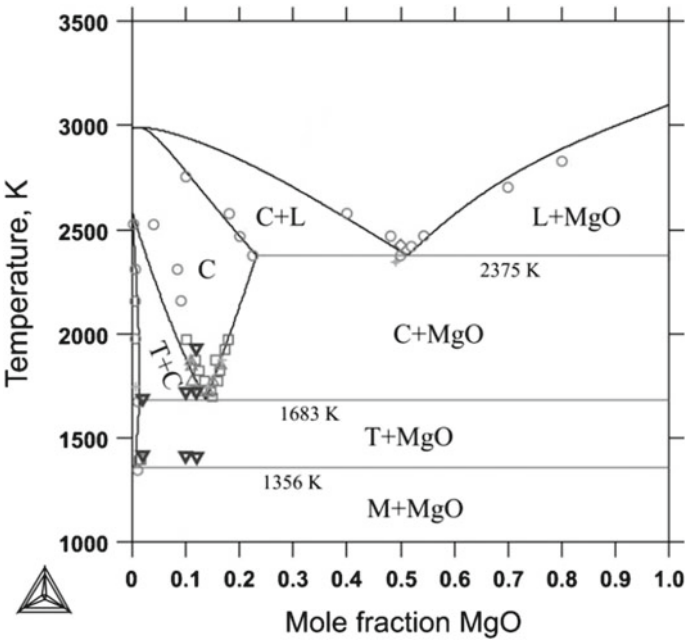

Fig. 19.3 The calculated ZrO_2–MgO phase diagram together with experimental data [30]

the calculations in the ZrO_2–MgO and the experimental data could be attributed to the presence of Al_2O_3 additives in the industrially produced samples. The additives cause the formation of the $MgAl_2O_4$ phase with spinel structure.

As the ZrO_2–MgO–Al_2O_3 quasi-ternary system had only a very limited amount of experimental data available in literature, the phase equilibria were investigated in more detail in the work of Pavlyuchkov et al. [31]. Throughout the composition range, the solid phase equilibria in the ZrO_2–MgO–Al_2O_3 system were investigated using DTA, XRD, and SEM/EDX. Thereby, the isothermal sections at 1523, 1873 and 2023 K have been constructed. Furthermore, the stability of ternary X-phase at 2073 K found by Tassot et al. [32] was confirmed. The temperature limits of the X-phase stability limits were determined in the range between 1894 and 2094 K. In addition, two ternary eutectic reactions and one eutectic maximum could be determined experimentally. The experimental data thus obtained were used to develop a thermodynamic description for this system. Thus, the liquidus and solidus surface projections and the isopleth section ZrO_2–$MgAl_2O_4$ were calculated [31]. The calculations showed that much more complicated phase relations exist in this system in comparison to the literature data [33, 34]. The calculated liquidus and solidus surface's projections of the ZrO_2–MgO–Al_2O_3 phase diagram are presented in Fig. 19.4.

As part of a separate work of Fabrichnaya and Pavlyuchkov [35], a thermodynamic description for the ternary Zr–Fe–O system using the CalPhaD approach was developed based on experimental data from literature. Thermodynamic parameters of ZrO_2–FeO and ZrO_2–Fe_3O_4 systems were assessed using literature data [36–38]. The solubility of FeO and Fe_2O_3 in the ZrO_2 and of ZrO_2 in the Fe_2O_3 and Fe_3O_4 phases were taken into account and described with the compound-energy formalism. The two sublattice model of partially ionic liquid was used for the description of the melt phase. The descriptions obtained for the ZrO_2–FeO and ZrO_2–Fe_3O_4 systems were combined into the description of the ZrO_2–FeO–Fe_2O_3 system. The isothermal section at 1473 K and the liquidus surface projection have been calculated for

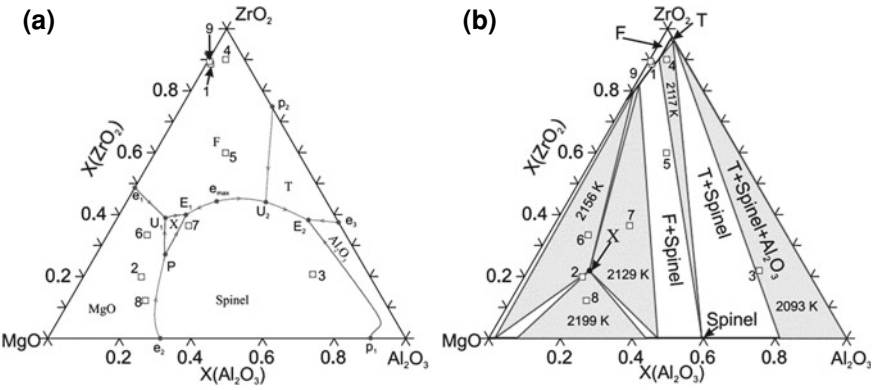

Fig. 19.4 Liquidus **a** and solidus **b** surface's projections of the ZrO_2–MgO–Al_2O_3 phase diagram [31]

the system using the complex data set. The calculated isopleth sections ZrO_2–FeO and ZrO_2–Fe_3O_4 are shown in Fig. 19.5a, b together with the experimental data. Figure 19.6 shows the liquidus surface projection of the ZrO_2–FeO–Fe_2O_3 system. The equilibria between the metallic melt and the solid ZrO_2 phase were calculated and compared with the literature values [39, 40]. Similar to other calculations [41], significant differences between the calculated oxygen solubilities in the Fe–Zr melt and the experimental results were found. New experimental study should be performed to resolve this contradiction.

The phase equilibria in the systems ZrO_2–MnO and ZrO_2–MnO–Mn_2O_3 were investigated experimentally with DTA in Ar atmosphere and by heat treatment in air in the temperature range between 1523 and 1873 K [42]. The reaction temperatures were determined with DTA-TG, the phase compositions in the samples with XRD and

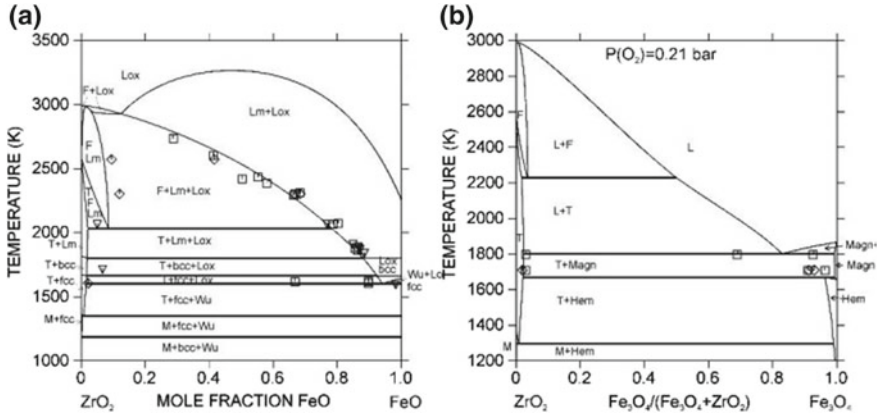

Fig. 19.5 **a** Calculated isopleth section of ZrO_2–FeO; **b** calculated isopleth section of ZrO_2–Fe_3O_4 [35]

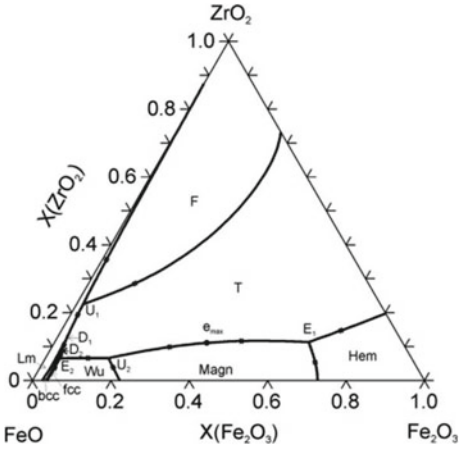

Fig. 19.6 Liquidus surface of the ZrO_2–FeO–Fe_2O_3 system calculated using advanced thermodynamic description of the Zr–Fe–O system [35]

the chemical compositions of the phases with SEM/EDX. Based on the experimental data, the thermodynamic parameters were optimized and phase diagrams at oxygen partial pressures of 10^{-4} bar and in air were calculated. The phase diagrams are shown in Fig. 19.7a, b along with the experimental data.

Phase equilibria in the ZrO_2–MgO–MnO–Mn_2O_3 system were investigated experimentally in air and in Ar atmosphere in the work of Pavlyuchkov et al. [43]. The samples were characterized with XRD and SEM/EDX. The reactions occurring in these systems were determined by DTA-TG experiments under He atmosphere. Isothermal sections constructed at low partial pressure of O_2 are presented in Fig. 19.8.

At the last stage of the TRIP-Matrix-Composite development, the main objective was the further development of the thermodynamic database for ZrO_2-based

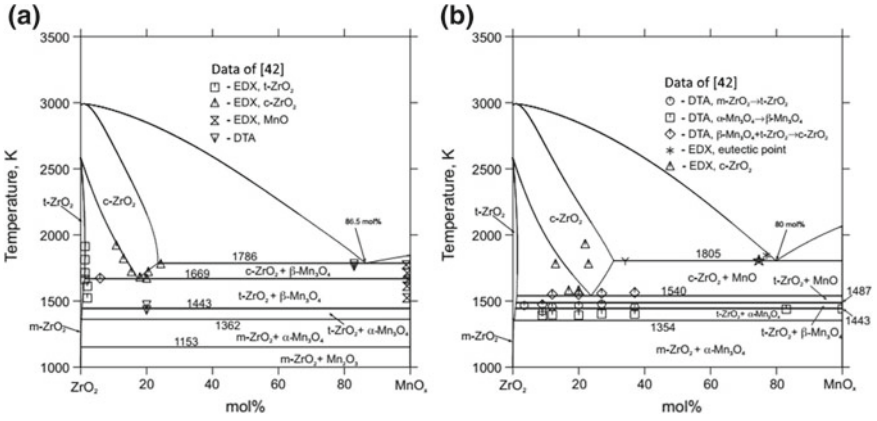

Fig. 19.7 Calculated phase diagrams of the ZrO_2–MnO_x systems at **a** $pO_2 = 0.21$ bar and **b** $pO_2 = 1 \times 10^{-4}$ bar, along with the experimental data [42]

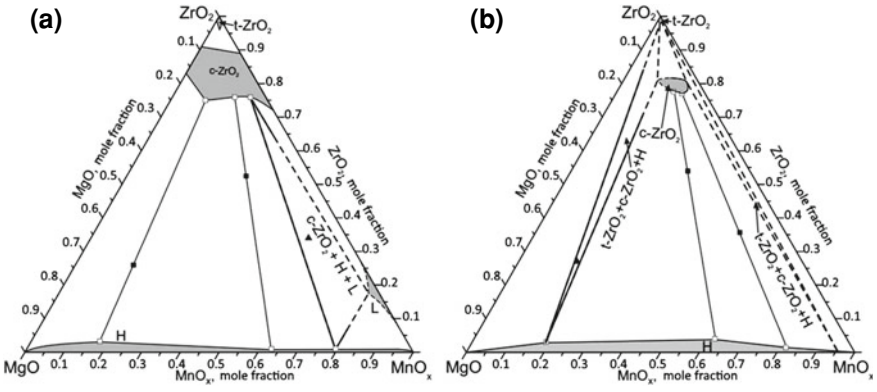

Fig. 19.8 Isothermal section of ZrO_2–MgO–MnO_x under helium atmosphere ($PO_2 = 10^{-4}$ bar) **a** at 1913 K and **b** at 1523 K [43]

ceramic materials and their implementation in the existing steel database. The combined database will make complete simulation of interfacial reactions between steel and ceramics in the TRIP metal matrix composite material possible. Therefore, the following partial goals result:

1. Further development of the thermodynamic database for the ZrO_2–MgO–FeO–MnO–Fe_2O_3–Mn_2O_3–TiO_2–Al_2O_3 system is to be promoted.
2. The next task is to assemble the thermodynamic databases for ceramic materials with the steel database. The main goal of this work is the creation of a thermodynamic database, which allows the calculation of the chemical reactions taking place at the interface between steel and ceramic. This task requires the integration of binary and ternary descriptions from the literature into the newly generated database as well as the adaptation of the thermodynamic parameters. The incorporation of oxygen into the data set requires the implementation of system descriptions such as Fe–O, Mn–O, Cr–O, Ni–O and the associated ternary systems Fe–Ni–O, Fe–Mn–O, Fe–Cr–O, Ni–Cr–O, etc. The integration of Zr requires the thermodynamic modelling of Zr–Fe, Zr–Mn, Zr–Ni systems as well as other Zr-containing systems. Therefore, the expansion of the steel database with Zr was planned. The binary descriptions Zr–O and Ti–O are implemented in the complex steel ceramics database.

First, high-temperature phase transformations in strongly metastable austenitic-martensitic Fe–CrMnNi–N–C cast steels were studied using SEM/EXD and DTA based on preliminary CALPHAD calculations. Our studies of the Fe–15Cr–3Mn–3Ni–0.1N cast stainless steels with five different carbon contents, in particular the SEM imaging and EDX elemental mapping of the segregation of Cr and Ni, have shown that the solidification mode changes from primary ferritic to primary austenitic with increasing carbon content. This is in contradiction to thermodynamic calculations (Fig. 19.9) of a primary ferritic solidification of all alloys, but can be explained by the experimental conditions, e.g. by the solidification rate, which creates a nonequilibrium state and facilitates therefore the austenitic solidification. Melting temperatures determined by DTA measurements showed no clear trend with respect to the carbon content in the investigated steel compositions, probably due to the influence of local chemical inhomogeneities. The experimental temperature range for melting is narrow and lies above the calculated melting range, probably due to an overheating effect. The transformation temperature for the solid-solid phase transformation fcc(γ) $\rightarrow$ fcc(γ) + bcc(δ) was also measured by DTA. In agreement with the calculations, it increases with increasing carbon content for steels NC05 to NC15, but above 0.155 wt% C it remains approximately constant regardless of the further increasing carbon content. Again, several effects can explain the deviation from the calculation in alloys with a higher carbon content: local fluctuations of the chemical composition, but also a reduced overheating due to an increased transformation rate at higher temperatures. The transformation fcc(γ) $\rightarrow$ fcc(γ) + bcc(δ) was found to be fully reversible, that means it occurs during heating and cooling at almost the same temperature, thus the undercooling is very small.

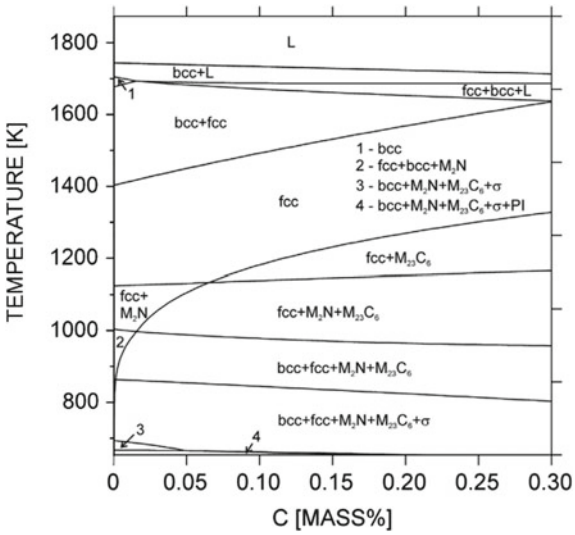

Fig. 19.9 Vertical section of the phase diagram of the steel Fe–15Cr–3Mn–3Ni–0.1N–xC in dependence on the carbon content [6]

Furthermore, the reversion transformation of a thermal martensite $\alpha' \rightarrow \gamma$ was shown for the steels NC05 and NC10, which contain a significant fraction of martensite formed during quenching. For the other alloys, the effect was below the detection limit of DTA because of the low volume fractions (<5 vol%) of martensite present. The onset temperature of the transformation decreased with the carbon content.

Concerning further thermodynamic modelling of the ceramic systems, thermodynamics of the Mg–Mn–O system has been modeled based on new heat capacity measurements of the $MgMn_2O_4$ and Mg_6MnO_8 phases [44]. Phase diagram data, structural information, and thermochemical data were used in the assessment. All solid solution phases were modeled using the compound energy formalism. Mg-solubility in the cubic spinel has been modeled according to the findings in a previous study of Pavlyuchkov et al. [43], which suggests that Mg solubility reported by earlier studies was too low. Thus, the older reports on the Mg solubility in the cubic spinel were not considered. In general experimental data found in the literature was well reproduced. The results presented were significant for further thermodynamic modelling of the Mg–Mn–Zr–O system.

Phase relations in the ZrO_2–TiO_2 system were investigated in the temperature range from 1303 to 1903 K using XRD and SEM/EDX. Melting reactions in this system were studied using DTA followed by microstructure investigation [45]. The Liq = β-$(Zr_xTi_{1-x})_2O_4$ + TiO_2 eutectic and the Liq + T-ZrO_2 = β-$(Zr_xTi_{1-x})_2O_4$ peritectic reactions were determined at 2029 K and 2117 K respectively. Composition of eutectic was determined by SEM/EDX to be 83.2 ± 1.0 mol%. First, the drop solution calorimetry method was applied using AlexSys 800 (SETARAM Instrumentation) in order to measure enthalpy of formation of the β-$ZrTiO_4$ compound from oxides (-18.3 ± 5.3 kJ mol^{-1}). Molar heat capacities of the β-$(Zr_xTi_{1-x})_2O_4$ compound was measured in the range 233–1223 K. Experimental thermodynamic values

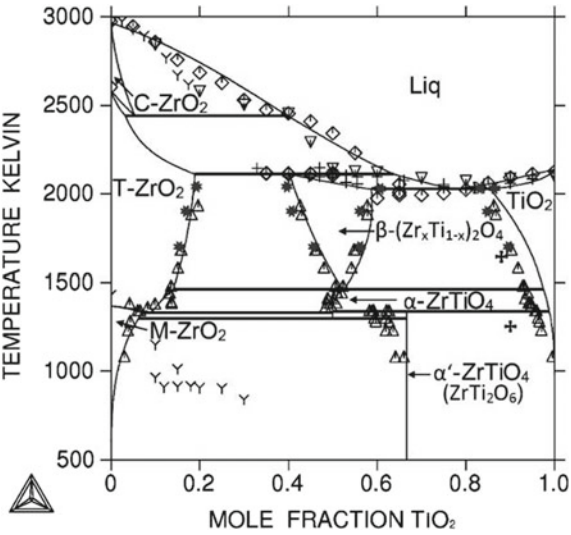

Fig. 19.10 Calculated phase diagram of the ZrO_2–TiO_2 system along with experimental data [45]

(i.e. heat capacity and enthalpy of formation of β-$ZrTiO_4$ compound) determined in [45] were used in order to optimize the description of heat capacity of α-$ZrTiO_4$ and β-$(Zr_xTi_{1-x})_2O_4$, as well as the contribution of the formation enthalpy of the β-$Zr_xTi_{1-x}O_4$ phase, respectively. Using the obtained experimental results together with literature data, the thermodynamic parameters in the ZrO_2–TiO_2 system were derived. Calculated phase diagram is presented in the Fig. 19.10.

Later on, based on the newly obtained results for the ZrO_2–TiO_2 system, the ZrO_2–TiO_2–MgO ternary system was experimentally investigated in the temperature range from 1533 K up to melting temperatures using XRD, SEM/EDX and DTA [46]. Isothermal sections of the system were constructed based on experimental data at 1533, 1683 and 1883 K. It has been determined that TiO_2 doping did not stabilized T-ZrO_2 phase in this system which transformed to monoclinic structure on cooling. Ternary compound described by formula $Zr_4TiMg_2O_{12}$ has been discovered. Homogeneity range of the compound was not established. However, based on experimental results, it was stated that the homogeneity range was insignificant and this compound was practically stoichiometric. The ternary compound has a trigonal structure of the Pr_7O_{12}-structure type. Nevertheless, further crystallographic investigations are necessary to establish the cations occupancies in the crystal structure of the phase. High temperature limit of the phase stability of the ternary compound has been determined to be 1664 K. Using results obtained by DTA and SEM/EDX, liquidus projection for the ZrO_2–TiO_2–MgO system has been constructed. The eutectic reactions Liq = C-ZrO_2 + β-$(Zr_xTi_{1-x})_2O_4$ + $MgTi_2O_5$, Liq = TiO_2 + β-$(Zr_xTi_{1-x})_2O_4$ + $MgTi_2O_5$ and Liq = $MgTi_2O_5$ + C-ZrO_2 + $MgTiO_3$ have been determined at 1800 K, 1851 K and 1872 K respectively. Based on the obtained experimental results, thermodynamic

description of the ZrO_2–TiO_2–MgO system was developed. Comparison of calculated and experimental results shows a good mutual agreement. Experimental and calculated liquidus projection of the system is shown in the Fig. 19.11.

As it was said above, the integration of Zr into steel database was required for combining of thermodynamic databases for ceramic materials with the steel database. Therefore, experimental differential scanning calorimetry measurements and ab initio simulations were carried out to define the heat capacities of Zr_3Fe and C15–$ZrFe_2$ compounds from 0 K up to their maximum stability temperatures [47]. Experimental measurements of heat capacity of each compound were performed for the first

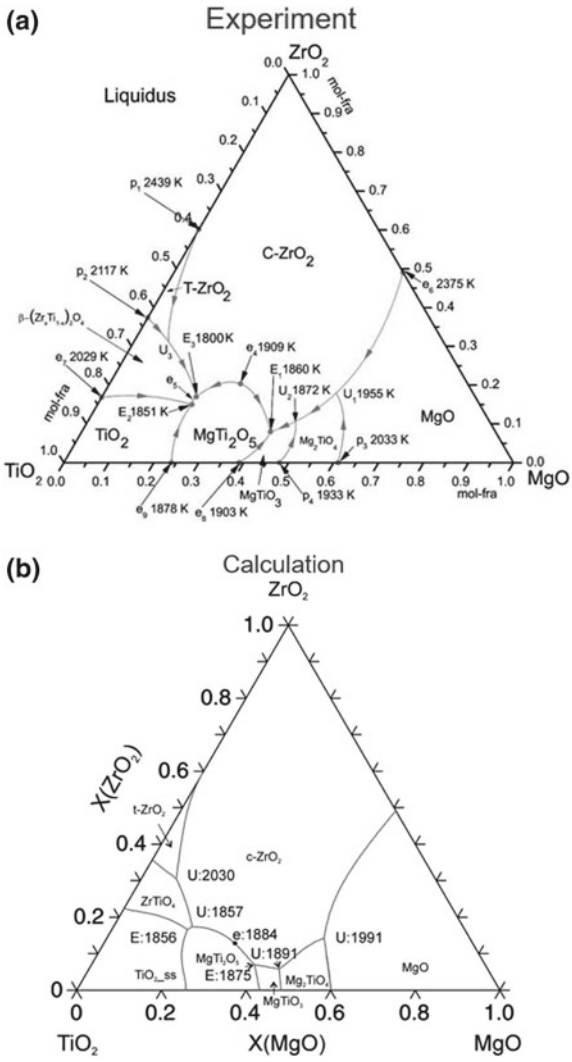

Fig. 19.11 **a** Constructed liquidus projection of the ZrO_2–TiO_2–MgO system [46] and **b** current results of CALPHAD calculation

time in wide range of temperatures. Density functional theory and quasi-harmonic approximation (QHA) were employed to calculate the Gibbs energy of the studied systems as a function of volume and temperature. Using the combination of DFT + QHA approach and experimental DSC analysis the main thermodynamic functions $C_P(T)$ and parameters S^{298} and ΔH^0 for Zr_3Fe and $ZrFe_2$ intermetallic phases were obtained form 0 K up to temperatures of their stability. In addition, experimental measurements of thermal expansion coefficient were performed for verification of DFT calculations. Analysis of theoretical and experimental data on α_V and C_P shows that QHA remarkably underestimates the anharmonic and magnetic effects starting from temperatures ~200 to 300 K. However, for low-temperature regions we observed very good agreement between theory and experiment.

Experimental measurements of heat capacity of Zr_2Fe were performed using DSC in the temperature range from 220 to 450 K for the first time [48]. Obtained results were compared with theoretical calculations of $C_P(T)$ presented by Ali et al. [49]. Using the combination of calculated [49] and experimental results, temperature dependence of heat capacity $C_P(T)$ for Zr_2Fe was described in the temperature range of 0–450 K as well. The standard entropy S^{298} of Zr_2Fe was evaluated using obtained heat capacity data. Taking into account recent experimental data on heat capacity and ab initio calculations of enthalpy of formation for intermetallic compounds and most reliable data for phase diagram [50, 51] thermodynamic re-assessment of the Fe–Zr system has been performed [48]. Liquid and solid solution phases such as bcc, fcc, and hcp have been described using substitutional model. Compound energy formalism has been used in order to describe homogeneity ranges of the C15- and C36–$ZrFe_2$ Laves phases. In the results, it has been demonstrated that the set of obtained thermodynamic parameters describes experimental data better than thermodynamic descriptions published earlier. Calculated phase diagram of the Fe–Zr system is presented in Fig. 19.12 along with experimental data.

Afterwards, the Zr–Mn system was studied using XRD, SEM/EDX, DSC and DTA by Flandorfer et al. [53] and in the present study. The heat capacity of the C14–$ZrMn_2$ phase was measured in the temperature range of 770 to 1320 K. Based on the obtained results, thermodynamic description was developed. The calculated phase diagram is presented in Fig. 19.13.

Newly obtained thermodynamic parameters of the Zr–Mn and Fe–Zr systems were combined together with Fe–Mn parameters [53] into description of Fe–Zr–Mn system based on binary extrapolation. This database was created for calculations of the ternary diagram which was further used for selection of sample compositions. Experimental investigation of Zr–Fe–Mn system included study of quasi-binary C14–$ZrMn_2$–C15–$ZrFe_2$ system and ternary phase equilibria. Quasi-binary section of the ternary system was studied by diffusion couple (DC) method. DC was prepared from single phase C14–$ZrMn_2$ and C15–$ZrFe_2$ samples by spark plasma sintering (SPS) plating. Obtained samples were heat-treated at 1173 and 1373 K in order to examine phase relation at different temperatures. Microstructure of the DCs was then studied using SEM/EDX with engaging of line-scan for analysis of composition gradient. Samples for ternary phase relations investigation, corresponding to three phase regions, were prepared by arc melting. Samples were heat-treated at

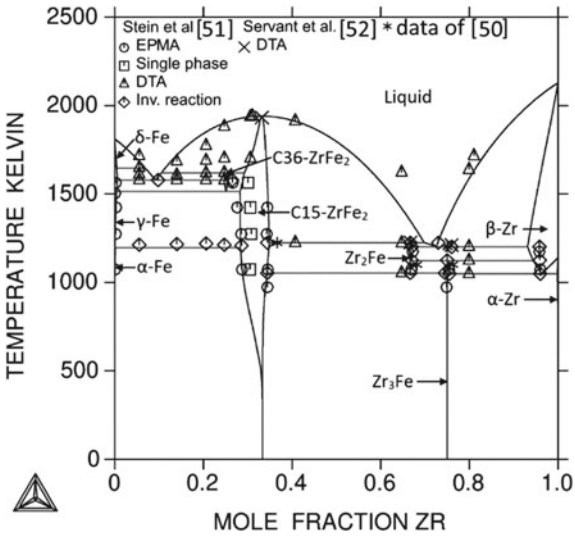

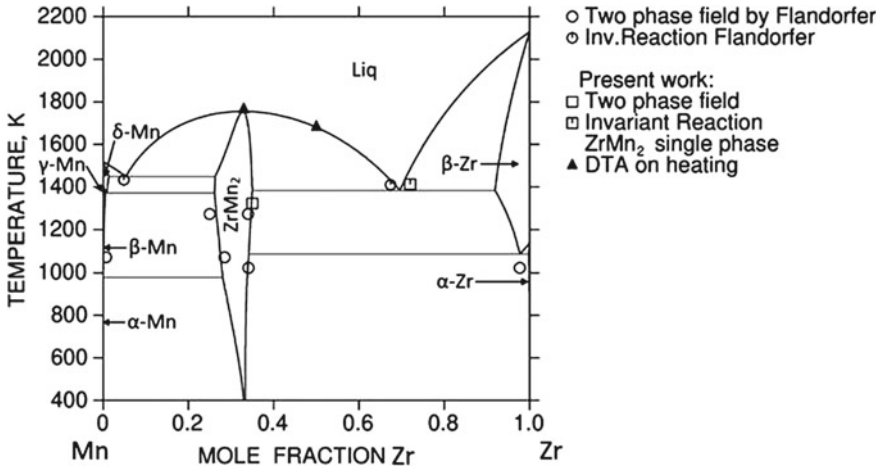

Fig. 19.12 Calculated Fe–Zr phase diagram [50] along with experimental data from the works of Stein et al. [51] and Servant et al. [52]

Fig. 19.13 Calculated Zr–Mn phase diagrams along with experimental data of Flandorfer et al. [53]

1073 K and quenched into water. They were then studied using XRD and SEM/EDX for phase identification and phase relation and chemical composition analysis.

There was contradiction in literature data for this system connected with the area on the phase diagram corresponding to the two-phase region C15–C14. In the work [54] a two-phase region was reported, while in the work [55] an anomaly change of magnetic moment was observed and XRD results indicated formation of C36 Laves phase structure in the composition range between C15 and C14 Laves phases. In

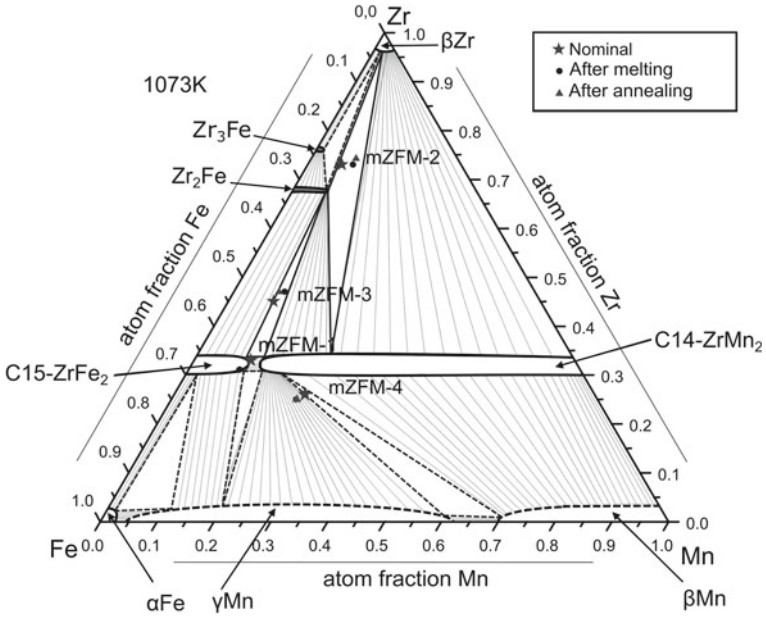

Fig. 19.14 Constructed isothermal section of the Fe–Zr–Mn system at 1073 K

the present work results from SEM/EDX investigation indicated absence of a phase with an intermediate composition. Therefore, it was concluded that two solid solution phases C15 and C14 were present in the system coexisting with each other in the range between 60 and 80 mol% $ZrFe_2$. Measured solubility ranges of the boundaries of the phases are in good agreement with the literature data [54].

It should be mentioned, that ternary Fe–Zr–Mn system was studied the first time. It was partially constructed based on the results obtained on ternary system and thermodynamic assessments of the composing binary systems. Obtained results are presented in the Fig. 19.14.

19.5 Conclusions

Within the present work, substantial amount of results were obtained for thermodynamic modelling of the system related to the TRIP-Matrix-Composite development. Advanced methods of thermodynamic simulations were applied for optimization of chemical composition of steel matrix and ceramic particles, for prediction and understanding of mechanisms occurring in the material, for finding new solutions of technological issues. Additionally, the methods of thermodynamic modelling provided a basement for further development of the TRIP-Matrix-Composite.

Thermodynamic database was developed for 11 elements Fe, Mn, Cr, Ni, Ti, Si, N, C, Mo, W, V. Obtained thermodynamic description reproduces most of the available experimental results. Thereby, it gives more reliable extrapolations in comparison to other commercial or noncommercial thermodynamic descriptions. Concerning development of thermodynamic oxide description, 3 binary, 7 ternary and a quaternary systems were investigated and modeled in cooperation with other projects.

However, the main uncompleted task is the integration of Zr, what requires the thermodynamic modelling of binary systems such as Zr–Ni, Zr–Cr and ternary system of iron, zirconium and main alloying elements of steel matrix. Moreover, the incorporation of oxygen into the data set of the steel database requires the implementation of system descriptions such as Fe–O, Mn–O, Cr–O, Ni–O and the associated ternary systems Fe–Ni–O, Fe–Mn–O, Fe–Cr–O, Ni–Cr–O, etc.

Acknowledgements Current work was funded by the Deutsche Forschungsgemeinschaft (DFG, German Research Foundation)—Projektnummer 54473466–SFB 799. The authors thank Prof. Seifert, Dr. Franke and Dr. Pavlychkov for scientific support and co-working in the sub-project C2 in the frame of SFB 799.

References

1. U.R. Kattner, Tecnol. Metal Mater. Min. **13**(1), 3–15 (2016). https://doi.org/10.4322/2176-1523.1059
2. S. Martin, S. Richter, S. Decker, U. Martin, L. Krüger, D. Rafaja, Steel Res. Int. **82**(9), 1133–1140 (2011). https://doi.org/10.1002/srin.201100099
3. M. Wendler, B. Reichel, R. Eckner, O. Fabrichnaya, L. Krüger, A. Weiß, J. Mola, Metall. Mater. Trans. A **47**(1), 139–151 (2016). https://doi.org/10.1007/s11661-014-2716-0
4. S. Martin, O. Fabrichnaya, D. Rafaja, Mater. Lett. **159**, 484–488 (2015). https://doi.org/10.1016/j.matlet.2015.06.087
5. P. Franke, M. Ksyta, H.J. Seifert, Steel Res. Int. **82**(9), 1149–1157 (2011). https://doi.org/10.1002/srin.201100132
6. O. Fabrichnaya, C. Ullrich, M. Wendler, G. Savinykh, D. Rafaja, J. Alloys Compd. **686**, 511–521 (2016). https://doi.org/10.1016/j.jallcom.2016.06.026
7. M. Hauser, M. Wendler, O. Fabrichnaya, O. Volkova, J. Mola, Mater. Sci. Eng., A **675**, 415–420 (2016). https://doi.org/10.1016/j.msea.2016.08.080
8. L. Halbauer, R. Eckner, M. Wendler, O. Fabrichnaya, A. Buchwalder, L. Krüger, R. Zenker, H. Biermann, Steel Res. Int. **87**(12), 1627–1637 (2016). https://doi.org/10.1002/srin.201600028
9. H.L. Lukas, S.G. Fries, B. Sundman, *Computational Thermodynamics* (Cambridge University Press, Cambridge, 2007)
10. Z.-K. Liu, Y. Wang, *Computational Thermodynamics of Materials* (Cambridge University Press, Cambridge, 2016)
11. L. Lutterotti, Nucl. Instrum. Methods Phys. Res. B **268**(3–4), 334–340 (2010). https://doi.org/10.1016/j.nimb.2009.09.053
12. G. Della Gatta, M.J. Richardson, S.M. Sarge, S. Stølen, Pure Appl. Chem. **78**(7), 1455–1476 (2006). https://doi.org/10.1351/pac200678071455
13. O.B. Fabrichnaya, S.K. Saxena, P. Richet, E.F. Westrum, *Thermodynamic Data, Models, and Phase Diagrams in Multicomponent Oxide Systems* (Springer, Berlin, Heidelberg, 2004)
14. L. Kaufman, H. Bernstein, *Computer Calculation of Phase Diagrams with Special Reference to Refractory Metals* (Academic Press Inc, New York, 1970)

15. N. Saunders, A.P. Miodownik, *Calphad* (Pergamon, Oxford, 1998)
16. M. Hillert, J. Alloys Compd. **320**(2), 161–176 (2001). https://doi.org/10.1016/S0925-8388(00)01481-X
17. R. Schmid-Fetzer, D. Andersson, P.Y. Chevalier, L. Eleno, O. Fabrichnaya, U.R. Kattner, B. Sundman, C. Wang, A. Watson, L. Zabdyr, M. Zinkevich, Calphad **31**(1), 38–52 (2007). https://doi.org/10.1016/j.calphad.2006.02.007
18. M. Hillert, M. Jarl, Calphad **2**(3), 227–238 (1978). https://doi.org/10.1016/0364-5916(78)90011-1
19. A.T. Dinsdale, Calphad **15**(4), 317–425 (1991). https://doi.org/10.1016/0364-5916(91)90030-N
20. O. Redlich, A.T. Kister, Ind. Eng. Chem. **40**(2), 345–348 (1948). https://doi.org/10.1021/ie50458a036
21. D. Djurovic, B. Hallstedt, J. von Appen, R. Dronskowski, Calphad **35**(4), 479–491 (2011). https://doi.org/10.1016/j.calphad.2011.08.002
22. P. Franke, H.J. Seifert, Calphad **35**(1), 148–154 (2011). https://doi.org/10.1016/j.calphad.2010.10.006
23. Scientific Group Thermodata Europe (SGTE), *Thermodynamic Properties of Inorganic Materials* (Springer, Berlin, London, 2000)
24. S. Serena, M.A. Sainz, S. de Aza, A. Caballero, J. Eur. Ceram. Soc. **25**(5), 681–693 (2005). https://doi.org/10.1016/j.jeurceramsoc.2004.02.011
25. B. Hallstedt, Calphad **16**(1), 53–61 (1992). https://doi.org/10.1016/0364-5916(92)90038-Y
26. D. Wittig, A. Glauche, C.G. Aneziris, T. Minghetti, C. Schelle, T. Graule, J. Kuebler, Mater. Sci. Eng., A **488**(1–2), 580–585 (2008). https://doi.org/10.1016/j.msea.2007.11.065
27. B. Hallstedt, J. Am. Ceram. Soc. **75**(6), 1497–1507 (1992). https://doi.org/10.1111/j.1151-2916.1992.tb04216.x
28. A.B. Farina, F.B. Neto, Calphad **33**(4), 711–718 (2009). https://doi.org/10.1016/j.calphad.2009.09.003
29. A.D. Pelton, G. Eriksson, D. Krajewski, M. Göbbels, E. Woermann, Z Phys. Chem. **207**(Part_1_2), 163–180 (1998). https://doi.org/10.1524/zpch.1998.207.part_1_2.163
30. D. Pavlyuchkov, G. Savinykh, O. Fabrichnaya, Adv. Eng. Mater. **15**(7), 618–626 (2013). https://doi.org/10.1002/adem.201200316
31. D. Pavlyuchkov, G. Savinykh, O. Fabrichnaya, J. Euro. Ceram. Soc. **34**(5), 1397–1408 (2014). https://doi.org/10.1016/j.jeurceramsoc.2013.11.038
32. P. Tassot, G. Knig, F. Seifert, F. Liebau, J. Mater. Sci. **21**(10), 3479–3482 (1986). https://doi.org/10.1007/BF00553788
33. A.S. Berezhnoj, R.A. Kordyuk, DAN URSR (4), 506–508 (1964)
34. A.V. Shevchenko, G.I. Gerasimyuk, L.M. Lopato, S.G. Yusupova, Inorg. Mater. **29**, 117–118 (1993)
35. O. Fabrichnaya, D. Pavlyuchkov, Metall. Mater. Trans. A **47**(1), 152–159 (2015). https://doi.org/10.1007/s11661-015-2805-8
36. S.V. Bechta, E.V. Krushinov, V.I. Almjashev, S.A. Vitol, L.P. Mezentseva, Y.B. Petrov, D.B. Lopukh, V.B. Khabensky, M. Barrachin, S. Hellmann, K. Froment, M. Fischer, W. Tromm, D. Bottomley, F. Defoort, V.V. Gusarov, J. Nucl. Mater. **348**(1–2), 114–121 (2006). https://doi.org/10.1016/j.jnucmat.2005.09.009
37. T.S. Jones, S. Kimura, A. Muan, J. Am. Ceram. Soc. **50**(3), 137–142 (1967). https://doi.org/10.1111/j.1151-2916.1967.tb15063.x
38. R.H.G.A. Kiminami, Ceramica (Sao Paulo) (33), 207–209 (1987)
39. R.J. Fruehan, MT **5**(2), 345–347 (1974). https://doi.org/10.1007/bf02644100
40. D. Janke, W.A. Fischer, Archiv für das Eisenhüttenwesen **47**(4), 195–198 (1976). https://doi.org/10.1002/srin.197603805
41. W. Huang, Calphad **28**(2), 153–157 (2004). https://doi.org/10.1016/j.calphad.2004.07.007
42. D. Pavlyuchkov, G. Savinykh, O. Fabrichnaya, J. Euro. Ceram. Soc. **35**(13), 3623–3632 (2015). https://doi.org/10.1016/j.jeurceramsoc.2015.06.005

43. D. Pavlyuchkov, D. Dilner, G. Savinykh, O. Fabrichnaya, J. Am. Ceram. Soc. **99**(9), 3136–3145 (2016). https://doi.org/10.1111/jace.14327
44. D. Dilner, D. Pavlyuchkov, T. Zienert, L. Kjellqvist, O. Fabrichnaya, J. Am. Ceram. Soc. **100**(4), 1661–1672 (2017). https://doi.org/10.1111/jace.14686
45. I. Saenko, M. Ilatovskaia, G. Savinykh, O. Fabrichnaya, J. Am. Ceram. Soc. **101**(1), 386–399 (2017). https://doi.org/10.1111/jace.15176
46. I. Saenko, V. Tsukrenko, M. Ilatovskaia, D. Pavlyuchkov, G. Savinykh, O. Fabrichnaya, Adv. Eng. Mater. **21**(5), 1800655 (2018). https://doi.org/10.1002/adem.201800655
47. B.O. Mukhamedov, I. Saenko, A.V. Ponomareva, M.J. Kriegel, A. Chugreev, A. Udovsky, O. Fabrichnaya, I.A. Abrikosov, Intermetallics **109**, 189–196 (2019). https://doi.org/10.1016/j.intermet.2019.01.018
48. R. Lück, H. Wang, J. Alloys Compd. **191**(2), L11–L12 (1993). https://doi.org/10.1016/0925-8388(93)90055-R
49. K. Ali, P.S. Ghosh, A. Arya, J. Alloys Compd. **723**, 611–619 (2017). https://doi.org/10.1016/j.jallcom.2017.06.154
50. I. Saenko, A. Kuprava, A. Udovsky, O. Fabrichnaya, Calphad **66**, 101625 (2019). https://doi.org/10.1016/j.calphad.2019.05.002
51. F. Stein, G. Sauthoff, M. Palm, J. Phase Equilibria Diffus. **23**(6), 480 (2002). https://doi.org/10.1361/105497102770331172
52. C. Servant, C. Gueneau, I. Ansara, J. Alloys Compd. **220**(1–2), 19–26 (1995). https://doi.org/10.1016/0925-8388(94)06036-3
53. H. Flandorfer, J. Gröbner, A. Stamou, N. Hassiotis, A. Saccone, P. Rogl, R. Wouters, H. Seifert, D. Macciò, R. Ferro, G. Haidemenopoulos, L. Delaey, G. Effenberg, Mater. Res. Adv. Tech. (88), 529–538 (1997)
54. V.V. Petkov, Russ. Metall. **5**, 113–115 (1972)
55. K. Kanematsu, J. Phys. Soc. Jpn. **31**(5), 1355–1360 (1971). https://doi.org/10.1143/JPSJ.31.1355

Chapter 20
Thermodynamic-Mechanical Modeling of Metastable High Alloy Austenitic CrMnNi Steels

Michael Hauser, Marco Wendler, Javad Mola, Olga Fabrichnaya, Olena Volkova and Andreas Weiß

Abstract The deformation-induced formation of α'-martensite was investigated by tensile testing of a X5CrNi18-10 wrought austenitic steel and X3CrMnNi16-7-3/6/9 (Ni contents of 3, 6, and 9 mass%) as well as X15CrNiMnN19-4-3 cast austenitic steels at temperatures between −80 and 400 °C. The results were presented in the form of Stress-Temperature-Transformation (STT) and Deformation-Temperature-Transformation (DTT) diagrams. The diagrams laid foundations for the development of a method for the quantitative determination of strength and elongation contributions by means of induced and often overlapping deformation processes in the austenite. The summation of such contributions yielded the tensile strength and the uniform elongation of the steel. In order to determine the critical Gibbs free energy for the formation of martensite at temperatures between M_s and M_d, the chemical and mechanical contributions to deformation-induced martensite formation were determined by CALPHAD method using Thermo-Calc software. The mechanical contribution was estimated by determining the triggering stress for the formation of martensite using an in situ magnetic measurement device. This was done using the model proposed by Patel and Cohen. The magnitudes of shear strain (γ_0) and dilatational strain (ε_0), required for the calculations, were obtained based on the martensite crystallography theory of Wechsler-Lieberman-Read. The sum of the chemical and mechanical contributions yielded the critical driving force for the martensitic transformation.

M. Hauser (✉) · M. Wendler · O. Volkova · A. Weiß
Institute of Iron and Steel Technology, Technische Universität Bergakademie Freiberg, Leipziger Str. 34, 09599 Freiberg, Germany
e-mail: michael.hauser@iest.tu-freiberg.de

J. Mola
Material Design and Structural Integrity Lab, Osnabrück University of Applied Sciences, 49076 Osnabrück, Germany

O. Fabrichnaya
Institute of Materials Science, Technische Universität Bergakademie Freiberg, Gustav-Zeuner-Str. 5, Freiberg, Germany

H. Biermann and C. G. Aneziris (eds.), *Austenitic TRIP/TWIP Steels and Steel-Zirconia Composites*, Springer Series in Materials Science 298,
https://doi.org/10.1007/978-3-030-42603-3_20

20.1 Introduction

Depending on the chemical composition and deformation temperature, deformation mechanisms such as dislocations cell formation, mechanical twinning, and martensitic transformation may occur in the austenite phase of austenitic high-alloy steels [1–12]. The martensite commonly forms at intersections of glide bands in the austenite. At low temperatures where martensite formation is enabled, glide bands may consist of stacking fault bundles, ε martensite, and mechanical twins [13, 14].

In austenitic steels exhibiting the transformation-induced plasticity (TRIP) effect, the knowledge of the minimum driving force necessary for the martensite formation is of primary importance. The concept of defining a critical driving force for the martensite nucleation was first put forward by Cohen and coworkers [15, 16] and has been extended by Ghosh and Olson to include the effect of alloying elements [17]. This concept enables the thermodynamic modeling of metastable austenitic steels and can be used as a powerful tool to design new engineering materials [18–23]. The accuracy of such calculations will then depend on the reliability of the thermodynamic data. The thermodynamic database is particularly trustworthy in the chemical composition range where it has been calibrated by experimental data [24, 25].

The focus of the present work is the thermodynamic-mechanical modeling of metastable high alloy austenitic CrMnNi steels. To collect the experimental results needed for modeling, several steels were investigated. With the aid of thermodynamic data and flow curve analysis, it is possible to describe the dependence of mechanical properties on deformation mechanisms and phase transformation.

20.2 Experimental Methods

The chemical composition of the investigated steels are shown in Table 20.1. The steel X5CrNi18-10 was produced from BGH Edelstahl Freital GmbH, Germany. The steel X3CrMnNi16-7-6 was molten in an induction furnace and cast into a sand mould by ACTech GmbH, Freiberg, Germany. The steels X3CrMnNi16-7-3/9 were melted in a vacuum induction furnace and cast into a water-cooled copper mould. The steel X15CrNiMnN19-4-3 was melted in the vacuum induction furnace under a

Table 20.1 Chemical composition of the investigated cast steels in mass%

Alloy	C	N	Cr	Mn	Ni	Si	Fe
X5CrNi18-10	0.045	0.018	17.2	1.82	8.8	0.5	bal.
X3CrMnNi16-7-3	0.028	0.009	16.4	7.0	3.1	1.0	bal.
X3CrMnNi16-7-6	0.034	0.033	15.5	6.1	6.1	1.0	bal.
X3CrMnNi16-7-9	0.031	0.013	16.4	6.9	9.0	1.1	bal.
X15CrNiMnN19-4-3	0.154	0.167	18.7	2.9	4.2	0.5	bal.

nitrogen partial pressure of 450 mbar followed by casting into a water-cooled copper mould with a dimension of 230 × 35 × 95 mm^3. To avoid pore formation in the ingot, the nitrogen partial pressure was raised to 1500 mbar during casting.

To ensure the absence of machining-induced martensite near the surface of tensile specimens, solution heat treatments were performed after machining of tensile specimens. The solution heat treatment aimed at the dissolution of carbides and nitrides likely existing in the as-cast microstructure The solution heat treatment consisted of holding the X5CrNi18-10 steel at 1050 °C for 60 min, the X3CrMnNi16-7-3/6/9 steels at 1050 °C for 30 min and the X15CrNiMnN19-4-3 steel at 1150 °C for 30 min under an argon atmosphere.

Using a Zwick 1476-type universal testing machine, tensile specimens were tested at a constant crosshead displacement speed with an initial strain rate of 4×10^{-4} s^{-1}. With the aid of a thermal chamber which surrounded the tensile specimen and the specimen fixtures, different temperatures in the range of −40 and 200 °C were adjusted. The tensile tests below −40 °C were performed with the aid of an Instron S5982 universal testing machine.

An in situ magnetic measurement system was devised to determine the α'-martensite content formed during tensile tests [21]. The experimental setup is shown in Fig. 20.1. The magnetic measurement system consisted of two coils. The

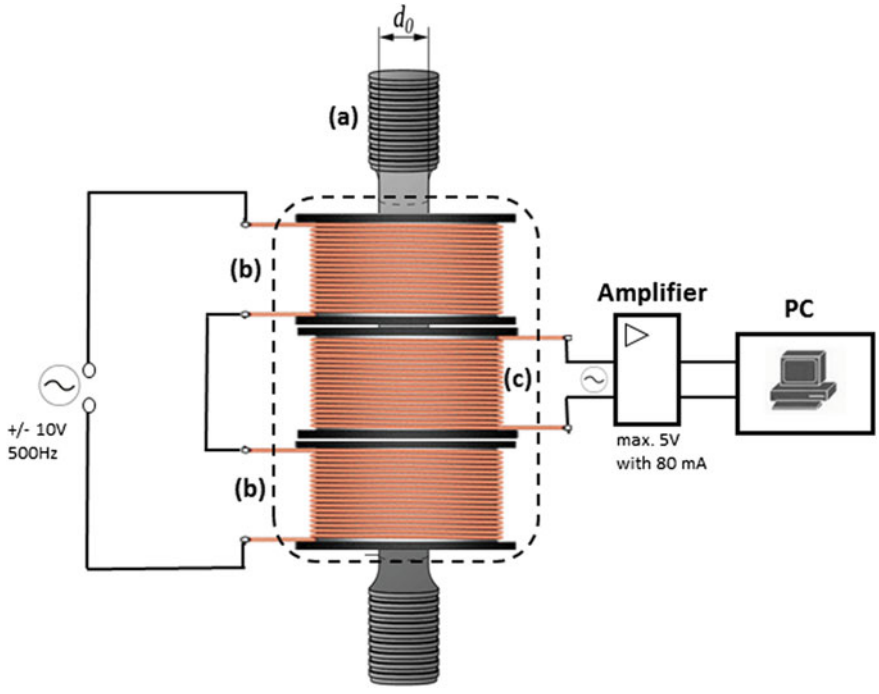

Fig. 20.1 Experimental setup showing tensile specimen and in situ magnetic measurement system with **a** tensile specimen, **b** first coil and **c** second coil

first coil served to generate an electromagnetic field which magnetized the martensite phase as it formed during tensile loading. The magnetization of martensite phase in tensile specimens induced an electrical potential difference (voltage) in the second coil which was recorded. To avoid interactions between the magnetic field and the surrounding components in the thermal chamber, a relatively small current (0.35 A) was used. This led to a magnetic field strength of 15 kA/m in the gauge section of tensile specimens. To avoid thermal degradation of the polymer components of the magnetic coil, in situ magnetic measurements were only conducted in the temperature range −80 to 40 °C.

The conversion of the voltage induced in the second coil to martensite fraction was done by a correlation procedure. The correlation procedure consisted of performing interrupted tensile tests followed by magnetic saturation measurements with an ex situ unit in order to quantify the α'-martensite fractions at the point of interruption. The procedure is described in more detail by Hauser et al. [21].

For the ex situ quantification of the ferromagnetic phase fraction in tensile specimens, a Metis MSAT-type magnetic saturation device equipped with a Lakeshore 480 fluxmeter was used. This equipment enabled the measurement of magnetic flux density after saturation magnetization of specimens cut from tensile specimens. The ferromagnetic phase fraction was calculated after an internal correction for the chemical composition. The correction took the influence of alloying elements on the magnetic moment of pure iron into account. The measurement accuracy with this method is within ±1%. Magnetic saturation measurements prior to tensile tests enabled the quantification of delta ferrite fractions retained after solution annealing. The delta ferrite fraction in solution annealed tensile specimens was also determined by quantitative metallography. These measurements closely reproduced the delta ferrite fraction based on ex situ magnetic saturation measurements. The microstructure was studied by means of electron channeling contrast imaging (ECCI) and electron backscatter diffraction (EBSD) techniques in a Zeiss LEO-1530 GEMINI-type field emission scanning electron microscope (FESEM). To calculate Gibbs free energies for the austenite (fcc) and ferrite (bcc) phases, the thermodynamic database developed by Franke et al. with the Thermo-Calc Software was used [26].

20.3 Theoretical Background

In metastable austenitic steels, martensite formation can occur spontaneously at temperatures below the martensite start (M_s) temperature and completes at the martensite finish (M_f) temperature. Martensite formation can also be triggered by deformation at temperatures up to M_d temperature, which leads to the so-called Transformation-Induced Plasticity (TRIP)-effect. The austenite stability can be described as the sum of energy contributions which are beneficial to the martensitic phase transformation and those which hinder it. Whereas the mechanical energy (W_{mech}), and at sufficiently low temperatures, the chemical driving force ($\Delta G_{chem}^{\gamma \rightarrow \alpha'}$) have a positive effect on the

phase transformation, the non-chemical contribution ($\Delta G_{\mathrm{nc}}^{\gamma\rightarrow\alpha'}$) as defined in the following and the adiabatic heating (Q_{ad}) of the sample delay the phase transformation. When the total Gibbs free energy change ($\Delta G_{\mathrm{total}}$) is negative, thermodynamic driving force is available for the austenite to martensite transformation. Different energy contributions are included in (20.1) [18, 25, 27].

$$\Delta G_{\mathrm{total}} = \Delta G_{\mathrm{chem}}^{\gamma\rightarrow\alpha'} + \Delta G_{\mathrm{nc}}^{\gamma\rightarrow\alpha'} + W_{\mathrm{mech}} + Q_{\mathrm{ad}} \tag{20.1}$$

While the adiabatic heating of the sample can be avoided by applying a low strain rate, the non-chemical energy contributions still need to be taken into account. The non-chemical energy contributions include the energy due to the lattice shear (ΔG_{sh}), surface and interface energies (ΔG_{sur}) and elastic strain energy (E^{str}), see in (20.2). All these energy contributions can be summed up to the critical driving force for the martensite formation ($\Delta G_{\mathrm{crit}}^{\gamma\rightarrow\alpha'}$) [17, 22, 23, 28].

$$\Delta G_{\mathrm{nc}} = \Delta G_{\mathrm{sur}} + \Delta G_{\mathrm{sh}} + E^{\mathrm{str}} \triangleq \Delta G_{\mathrm{crit}}^{\gamma\rightarrow\alpha'} \tag{20.2}$$

In Fig. 20.2, the Gibbs free energy for martensite formation is shown as a function of temperature. The martensitic phase transformation can only occur at temperatures

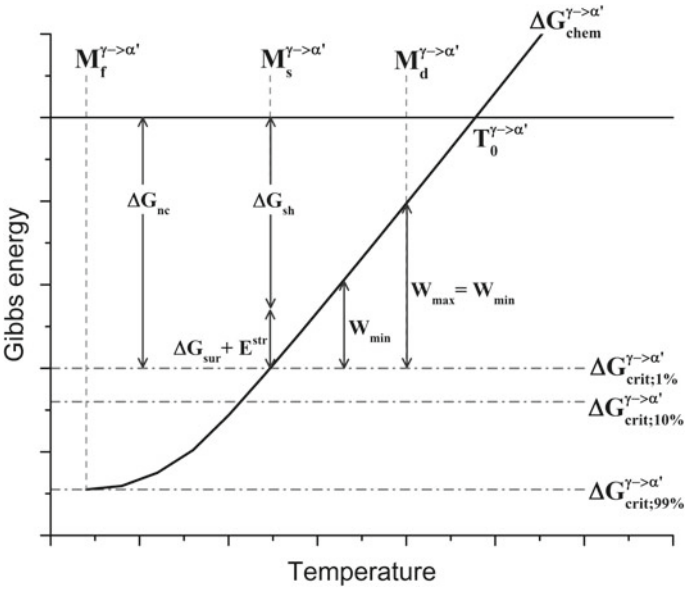

Fig. 20.2 Schematic representation of the temperature dependence of the chemical driving force for α'-martensite formation ($\Delta G_{\mathrm{chem}}^{\gamma\rightarrow\alpha'}$), minimum external mechanical work required to trigger the transformation (W_{min}), maximum applicable mechanical work (W_{max}), and critical driving forces for the formation of various martensite fractions ($\Delta G_{\mathrm{crit}}^{\gamma\rightarrow\alpha'}$), and non-chemical contributions ΔG_{nc}

below $T_0^{\gamma\rightarrow\alpha'}$, where the Gibbs free energies for austenite and ferrite of the same chemical composition are equal. Nevertheless, an additional energy contribution is needed to reach the critical driving force. At the M_s temperature and below, the chemical energy alone is high enough to trigger the martensitic phase transformation spontaneously. In the temperature range between M_s and M_d temperatures, on the other hand, the critical driving force can be reached by an additional energy contribution supplied by mechanical deformation. Therefore, the M_d temperature is the highest temperature where deformation-induced martensite formation can occur and thus the upper temperature limit to achieve the TRIP-effect with the maximum mechanical energy applicable to the material (W_{max}). During uniaxial tensile test, W_{max} denotes the maximum mechanical work applicable to austenite until the onset of localized deformation (necking). The applicable work determines the capacity of material to absorb external energy, thereby the amount of martensite that can be induced by deformation. Below the M_d temperature, one can define a minimal mechanical energy (W_{min}) which is needed to trigger the martensitic phase transformation. W_{min} reaches zero at M_s temperature. The larger the applied mechanical work with respect to W_{min}, the larger the induced martensite fraction [18, 22, 23].

Looking at the spontaneous martensitic transformation from a thermodynamic point of view, three possible cases can arise at low temperatures (Fig. 20.3). Case

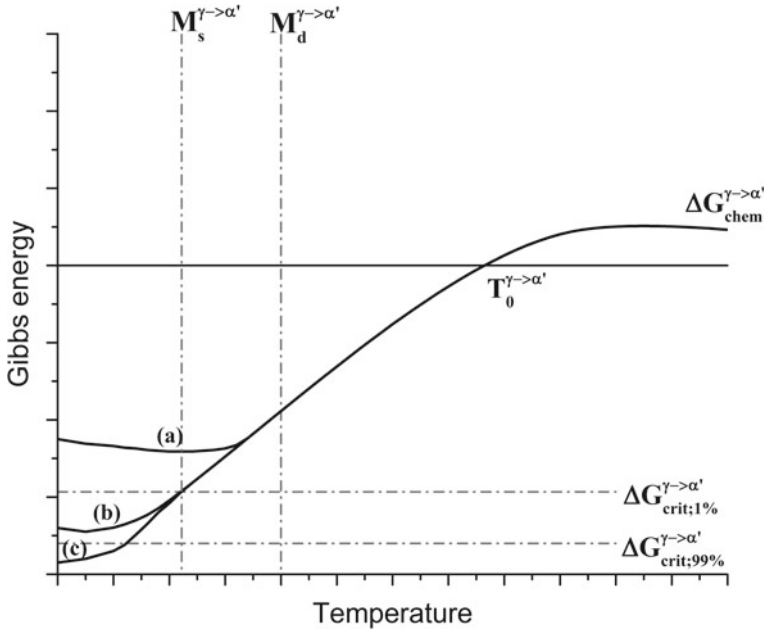

Fig. 20.3 Schematic representation of the temperature dependence of the chemical driving force for α'-martensite formation ($\Delta G_{chem}^{\gamma\rightarrow\alpha'}$), showing cases associated with the absence of spontaneous martensite (**a**), partial formation of spontaneous martensite (**b**), and full transformation to spontaneous martensite (**c**)

(a) describes a metastable austenite without phase transformation. This case arises when the chemical driving force does not reach the critical driving force. Nevertheless, an additional mechanical energy might still enable the deformation-induced martensite formation. In case (b), as-quenched martensite formation occurs. Due to the increasing austenite stability at lower temperatures, caused by magnetic transition of austenite from paramagnetic to antiferromagnetic, the martensite formation might come to a standstill below the Néel temperature. In case (c), the martensitic phase transformation proceeds until completion because the chemical driving force is large enough to supply the critical driving force for the full transformation, namely $\Delta G^{\gamma\rightarrow\alpha'}_{\text{crit;99\%}}$ [11, 22, 28].

The procedure proposed by Patel and Cohen for the calculation of the minimum and maximum mechanical work needed to induce martensite is discussed in detail in the following [29]. When loading metastable austenite, the applied stress leads to unequal resolved shear stresses on glide systems in the austenite, thereby favoring the selective formation of martensite variants [11]. For transformations associated with pure shear, the habit plane for the transformation will make an angle of 45° with respect to the external loading direction. However, due to the dilatational component associated with martensitic transformation [29, 30], the habit plane for the deformation-induced martensite formation does not necessarily make an angle of 45° with the tensile loading direction [23].

The mechanical work W_{mech} which can trigger the martensite formation during the tensile test depends on the molar volume (V_{m}) of the deformed tensile test specimen, the orientation of the habit plane, and the magnitude of the external stress (σ_a). According to (20.3), the mechanical work consists of two terms: the first term is the shear stress (τ_r) responsible for the shear strain (γ_0) parallel to the habit plane and the second term is the normal stress (σ_{N}) responsible for the volume expansion normal to the habit plane (ε_0) [23]. Experimental values of the investigated steels are shown in (Table 20.2).

$$W_{\text{mech}} = V_{\text{m}}\left[\tau_r * \gamma_0 + \sigma_{\text{N}} * \epsilon_0\right] \tag{20.3}$$

Assuming that the tensile load is applied at an angle (θ) to a potential habit plane normal, the normal and shear components of stress can be deduced from the Mohr's circle construction for tension as shown in Fig. 20.4.

Equation (20.4) can be derived by inserting the stress components from Fig. 20.4 in (20.3).

$$W_{\text{mech}} = V_{\text{m}}\left[\sigma_{a/2} * \gamma_0 \sin(2\theta) + \sigma_{a/2} * \epsilon_0(1 + \cos(2\theta))\right] \tag{20.4}$$

The term W_{min} in Fig. 20.2 can be estimated by inserting the triggering stress for martensite formation at temperatures between M_{s} and M_{d} in (20.4). The summation of this term with the chemical driving force for α'-martensite formation ($\Delta G^{\gamma\rightarrow\alpha'}_{\text{chem}}$) gives an estimate of the critical driving force for martensite formation. The maximum applicable mechanical work contributing to the formation of martensite (W_{max}), on

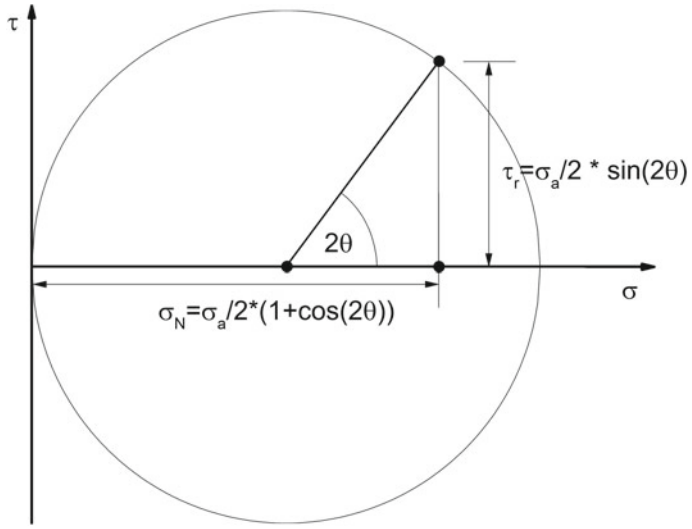

Fig. 20.4 Mohr's circle for tension showing shear (τ_r) and normal (σ_N) components of stress as functions of the applied stress (σ_a) and the angle between the potential habit plane normal and loading direction (θ) [23]

Table 20.2 Lattice parameters of austenite and martensite and the corresponding shear strain (γ_0), volume expansion (ε_0), and the angle θ_{max}

Alloy	a_γ (Å)	$a_{\alpha'}$ (Å)	$c_{\alpha'}$ (Å)	γ_0 (–)	ε_0 (–)	θ_{max} (°)
X5CrNi18-10	3.589	2.873	2.873	0.2260	0.0253	41.81
X3CrMnNi16-7-3	3.596	2.878	2.878	0.2263	0.0230	42.10
X3CrMnNi16-7-6	3.594	2.875	2.875	0.2266	0.0225	42.16
X3CrMnNi16-7-9	3.593	2.873	2.873	0.2318	0.0267	41.72
X15CrNiMnN19-4-3	3.591	2.884	2.858	0.2258	0.0259	41.73

the other hand, can be calculated by inserting the true stress at the onset of necking in (20.4). To calculate the angle θ associated with the maximum value of W_{mech}, the differential of (20.4) with respect to θ must be set to zero. This condition is represented in (20.5) [23].

$$\frac{dW_{mech}}{d\theta} = 0 \Rightarrow \tan 2\theta_{max} = \frac{\gamma_0}{\varepsilon_0} \tag{20.5}$$

The ε_0, γ_0, and θ_{max} values are influenced by the lattice parameters of austenite and martensite, which in turn depend on the chemical composition. To determine these quantities for the investigated steel, the martensite crystallography theory due to Wechsler-Lieberman-Read was used [31–33]. The following equations enable to calculate the shear and dilatational components of the invariant-plane strain based

on the lattice parameters of austenite (a_γ) and martensite (a_α) [31]:

$$\gamma_0 = \left[\left(\frac{2 * a_\alpha^2}{a_\gamma^2} - 1 \right) * \left(1 - \frac{2 * a_\alpha^4}{a_\gamma^4} \right) \right]^{\frac{1}{2}} \tag{20.6}$$

$$\epsilon_0 = \frac{V_\alpha}{V_\gamma} - 1 = \frac{2 * a_\alpha^3}{a_\gamma^3} - 1. \tag{20.7}$$

20.4 Model Development Based on an Austenitic X5CrNi18-10 Steel

Figure 20.5 shows the flow curves (dashed lines) of the X5CrNi18-10 steel (AISI 304) at various temperatures. With decreasing temperature, the flow curves shift to higher stresses. The uniform tensile elongation values, in contrast, pass through a maximum at intermediate tensile testing temperatures. In the temperature range of 140–23 °C, the elongation increases as the temperature decreases. The highest elongation was reached at room temperature and decreased again at lower deformation temperatures. Three solid lines are superimposed on the flow curves in Fig. 20.5. Two of these lines indicate the inflection points on the flow curves, namely where the sign of

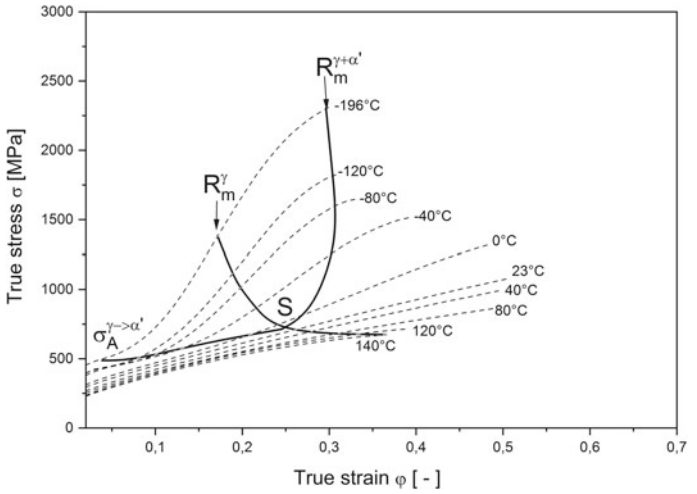

Fig. 20.5 Temperature dependent flow curves for the X5CrNi18-10 steel. Superimposed on the flow curves are the trigger stress $\sigma_A^{\gamma \to \alpha'}$, the tensile strength of the austenite R_m^γ and tensile strength of the steel $R_m^{\gamma+\alpha'}$ with neglected strengthening contributions other than the deformation-induced martensite formation [18]

the second derivative of the flow curves reverses. The inflection points only occur for the stress-strain curves obtained at temperatures below 23 °C. The first inflection point, marked $\sigma_A^{\gamma\to\alpha'}$ in Fig. 20.5, represents the triggering stress for the deformation-induced martensite formation. According to Weiß et al., the second inflection point, marked R_m^{γ}, corresponds to the tensile strength of the austenite [18, 28]. The first and second inflection points are associated with a minimum and a maximum in the strain-hardening rate, respectively. The third line, marked $R_m^{\gamma+\alpha'}$ in Fig. 20.5, indicates the tensile strength level expected if the strengthening contributions other than the deformation-induced martensite formation are neglected [18, 28].

The point marked with "*S*" in Fig. 20.5 almost lies on the 23 °C curve and may be identified with the approximate stress and strain coordinates of 705 MPa and 0.28, respectively. The point *S* denotes where the first ($\sigma_A^{\gamma\to\alpha'}$) and second ($R_m^{\gamma}$) inflection points of the flow curve coincide. This means that the triggering stress $\sigma_A^{\gamma\to\alpha'}$ and the tensile strength R_m^{γ} of the austenite are equal, which defines the $M_{\mathrm{d}}^{\gamma\to\alpha'}$ temperature. The formation of martensite primarily occurs via $\gamma \to \varepsilon \to \alpha'$ formation. However, the martensitic phase transformation via $\gamma \to \alpha'$ martensite formation is possible too [18, 28].

Figure 20.6 shows the measured fractions of ε- and α'-martensite in tensile specimens tested at various temperatures until the onset of necking. As the testing temperature decreased from 140 to 40 °C, the ε-martensite fraction increased continuously to a maximum level of approximately 17%. At temperatures between 40 and 23 °C, the fraction of ε-martensite decreased, reaching zero at room temperature. In the

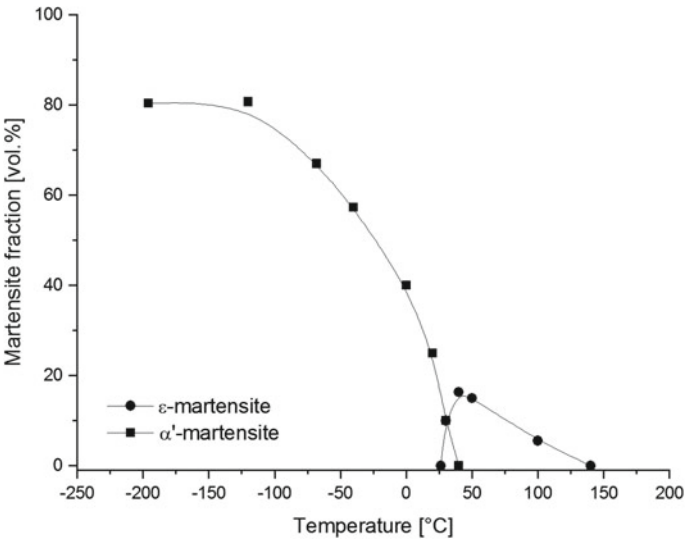

Fig. 20.6 Temperature dependence of ε- and α'-martensite contents in tensile specimens strained in uniaxial tension until the onset of necking [18]

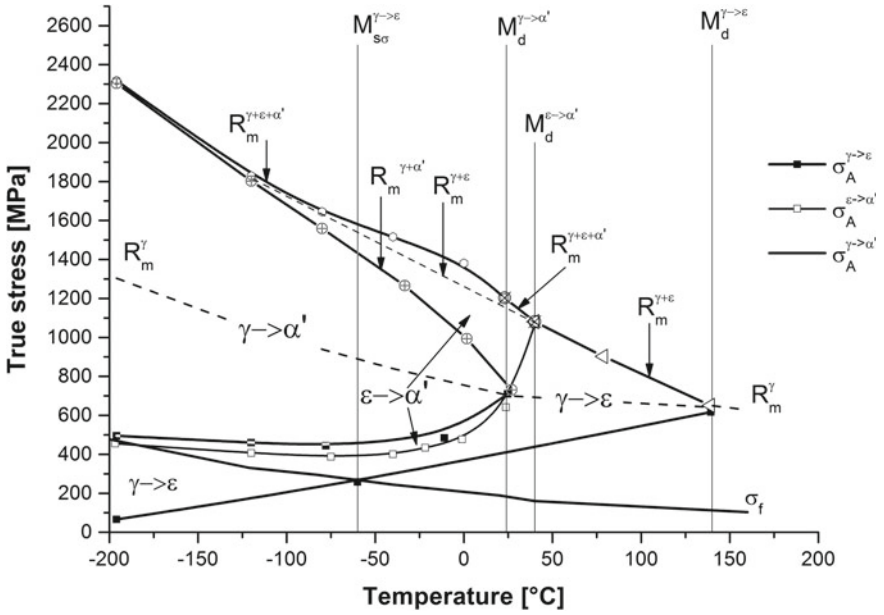

Fig. 20.7 Stress-temperature-transformation diagram (STT) for the X5CrNi18 10 steel [18]

temperature range between 40 °C and room temperature, the decrease in the fraction of ε-martensite was almost equal to the increase in the α'-martensite fraction [18, 28].

Figure 20.7 shows the Stress-Temperature-Transformation (STT) diagram for the X5CrNi18-10 steel. The yield stress σ_f, the triggering stresses $\sigma_A^{\gamma\to\varepsilon}$, $\sigma_A^{\varepsilon\to\alpha'}$ and $\sigma_A^{\gamma\to\alpha'}$ and on the other hand the corresponding tensile strengths $R_m^{\gamma+\varepsilon}$, $R_m^{\gamma+\varepsilon+\alpha'}$ and $R_m^{\gamma+\alpha'}$ are shown in the diagram. The triggering stress $\sigma_A^{\gamma\to\alpha'}$ was estimated from the first inflection point of the flow curve. The triggering stresses for the $\gamma \to \epsilon$ and $\varepsilon \to \alpha'$ martensitic transformations were obtained experimentally through microstructural analyses of interrupted tensile test specimens. The tensile strength of austenite R_m^{γ} was estimated by the extrapolation of the tensile strength values above $M_{\mathrm{d}}^{\gamma\to\varepsilon}$ to lower temperatures. The tensile strength $R_m^{\gamma+\varepsilon}$ below $M_{\mathrm{d}}^{\varepsilon\to\alpha'}$ temperature is a linear extrapolation of the course between $M_{\mathrm{d}}^{\varepsilon\to\alpha'}$ and $M_{\mathrm{d}}^{\gamma\to\varepsilon}$ temperature. The intersection of triggering stress with specific tensile strengths $\left(R_m^{\gamma+\varepsilon};\, R_m^{\gamma+\varepsilon+\alpha'};\, R_m^{\gamma+\alpha'}\right)$ for a given strain-induced transformation defines the $\mathrm{M_d}$ temperature corresponding to that transformation, shown in Fig. 20.7. The $M_{\mathrm{d}}^{\gamma\to\varepsilon}$, $M_{\mathrm{d}}^{\varepsilon\to\alpha'}$ and $M_{\mathrm{d}}^{\gamma\to\alpha'}$ temperatures are approximately 413 K (140 °C), 313 K (40 °C), and 296 K (23 °C), respectively. The $M_{s\sigma}^{\gamma\to\varepsilon}$ temperature is located at the intersection point of yield stress σ_f and the triggering stress $\sigma_A^{\gamma\to\varepsilon}$ near 213 K (−60 °C). The stress region, bounded by the triggering stress and the corresponding tensile strength for each martensitic transformation, marks the stress interval in which the relevant transformation occurs ($\gamma \to \varepsilon/\varepsilon \to \alpha'/\gamma \to \alpha'$). The wider the transformation interval, the

higher are the formed fractions of ε und α' martensite and, hence, the tensile strength of the steel. Below $M_{\mathrm{d}}^{\gamma\rightarrow\alpha'}$ temperature, the ε-martensite only formed before the α'-martensite formation was triggered. As soon as the triggering stress $\sigma_A^{\gamma\rightarrow\alpha'}$ was reached, ε-martensite was replaced by the α'-martensite [18, 28].

The strength contributions due to the induced deformation mechanisms in the austenite could be derived from the STT diagram in the following form. The summation of all strength contributions yields the true stress corresponding to the tensile strength R_m^{steel} of the steel. At temperatures above the $M_{\mathrm{d}}^{\gamma\rightarrow\varepsilon}$ temperature, the strain hardening of austenite occurred only via dislocation glide and increase of dislocation density. Under these circumstances, the tensile strength R_m^{steel} is equal to the tensile strength R_m^{γ} of austenite, as shown in (20.8) [18, 28].

$$R_m^{\mathrm{steel}} = R_m^{\gamma} \tag{20.8}$$

In the temperature range between the $M_{\mathrm{d}}^{\gamma\rightarrow\varepsilon}$ and $M_{\mathrm{d}}^{\varepsilon\rightarrow\alpha'}$ temperatures, two deformation processes are superimposed in the austenite. These were the strain-induced ε-martensite formation and dislocation glide. As (20.9) indicates, the tensile strength of the steel in this temperature range is the sum of the tensile strength of austenite and the strengthening due to the $\gamma \rightarrow \varepsilon$ transformation $\Delta\sigma^{\gamma\rightarrow\varepsilon}$ [18, 28].

$$R_m^{\mathrm{steel}} = R_m^{\gamma+\varepsilon} = R_m^{\gamma} + \Delta\sigma^{\gamma\rightarrow\varepsilon} \tag{20.9}$$

In the temperature range between the $M_{\mathrm{d}}^{\varepsilon\rightarrow\alpha'}$ and $M_{\mathrm{d}}^{\gamma\rightarrow\alpha'}$ temperatures, the dislocation glide, the strain-induced ε martensite formation, and the strain-induced $\varepsilon \rightarrow \alpha'$ martensite formation processes are superimposed. The tensile strength R_m^{steel} can be calculated in this temperature range by using (20.10) [18, 28].

$$R_m^{\mathrm{steel}} = R_m^{\gamma+\varepsilon+\alpha'} = R_m^{\gamma} + \Delta\sigma^{\gamma\rightarrow\varepsilon} + \Delta\sigma^{\varepsilon\rightarrow\alpha'} \tag{20.10}$$

Below $M_{\mathrm{d}}^{\gamma\rightarrow\alpha'}$ temperature, the strain-induced $\gamma \rightarrow \alpha'$ martensite is increasing the tensile strength R_m^{steel} of the steel by an amount equal to $\Delta\sigma^{\gamma\rightarrow\alpha'}$, shown in (20.11) [18, 28].

$$R_m^{\mathrm{steel}} = R_m^{\gamma+\varepsilon+\alpha'} = R_m^{\gamma} + \Delta\sigma^{\gamma\rightarrow\varepsilon} + \Delta\sigma^{\varepsilon\rightarrow\alpha'} + \Delta\sigma^{\gamma\rightarrow\alpha'} \tag{20.11}$$

The behavior described in Fig. 20.7 and (20.8)–(20.11) arises from the interplay between the strain-induced ε or α' martensite formation and the dislocation glide in the austenite. Referring to the STT diagram, the stress increments achieved by various deformation-induced mechanisms can be obtained according to Weiß et al. [18, 28] by a procedure involving mirroring of the triggering stress values with respect to the tensile strength of the austenite (R_m^{γ}).

The strain contributions due to deformation-induced mechanisms can be summarized using the so-called deformation-temperature-transformation (DTT) diagrams.

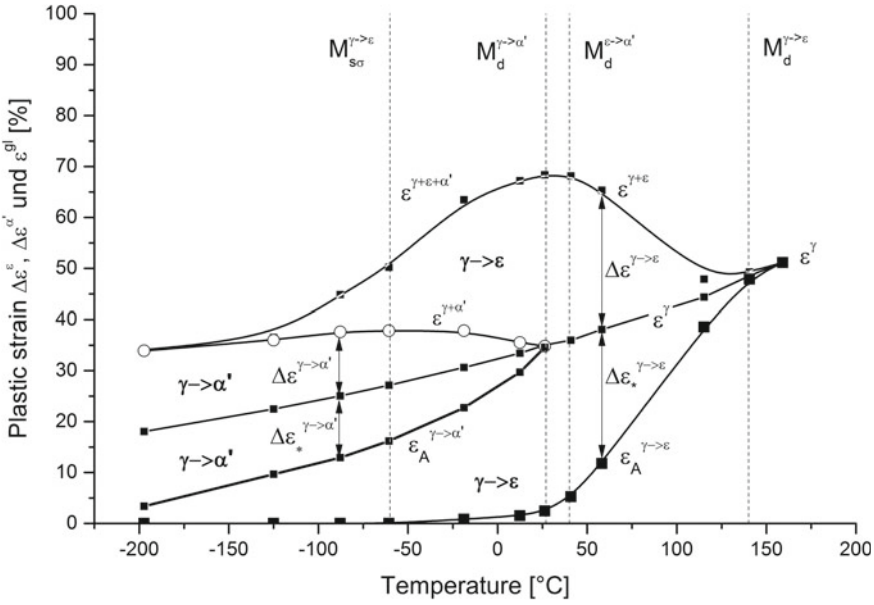

Fig. 20.8 Deformation-temperature-transformation diagram (DTT) of the X5CrNi18-10 steel [18]

Figure 20.8 shows the DTT diagram for the X5CrNi18-10 steel where the plastic elongations associated with the strain-induced $\gamma \rightarrow \varepsilon \rightarrow \alpha'$ and $\gamma \rightarrow \alpha'$ deformation processes are indicated [18, 28].

The uniform elongation of the steel (uppermost curve in Fig. 20.8), uniform elongation of the austenite ε^{γ}, and the elongations $\varepsilon_A^{\gamma\rightarrow\varepsilon}$ and $\varepsilon_A^{\gamma\rightarrow\alpha'}$ corresponding to the tensile trigger stress values $\sigma_A^{\gamma\rightarrow\varepsilon}$ and $\sigma_A^{\gamma\rightarrow\alpha'}$, respectively, are shown in Fig. 20.8. In addition, the plastic elongations $\Delta\varepsilon^{\gamma\rightarrow\varepsilon}$ and $\Delta\varepsilon^{\gamma\rightarrow\alpha'}$ contributed by the strain-induced ε-martensite and α'-martensite formation, respectively, as well as the values $\Delta\varepsilon_*^{\gamma\rightarrow\varepsilon}$ and $\Delta\varepsilon_*^{\gamma\rightarrow\alpha'}$ contributed by the glide in the austenite, are shown in Fig. 20.8. It is also shown that the elongation values $\Delta\varepsilon^{\gamma\rightarrow\varepsilon}$ and $\varepsilon_*^{\gamma\rightarrow\varepsilon}$ as well as $\Delta\varepsilon^{\gamma\rightarrow\alpha'}$ and $\Delta\varepsilon_*^{\gamma\rightarrow\alpha'}$ are equal [28]. The measured plastic elongations are a consequence of deformation-induced martensite formation as well as the plastic elongation pertaining to the induced glide processes in the austenite in the transformation range. Equations (20.12)–(20.14) describe the plastic elongation behavior of the X5CrNi18 10 steel in various temperature intervals with different deformation mechanisms. Equation (20.12) applies above the $M_{\mathrm{d}}^{\gamma\rightarrow\varepsilon}$ temperature, in which the uniform elongation of the steel ($\varepsilon^{\mathrm{steel}}$) is equal to the uniform elongation of the austenite (ε^{γ}) [18, 28].

$$\varepsilon^{\mathrm{steel}} = \varepsilon^{\gamma} \tag{20.12}$$

Between $M_{\mathrm{d}}^{\gamma\rightarrow\varepsilon}$ and $M_{\mathrm{d}}^{\gamma\rightarrow\alpha'}$ temperatures (20.13) applies.

$$\varepsilon^{\text{steel}} = \varepsilon^{\gamma+\varepsilon} = \varepsilon^{\gamma} + \Delta\varepsilon^{\gamma\rightarrow\varepsilon} \tag{20.13}$$

Below the $M_{\text{d}}^{\gamma\rightarrow\alpha'}$ temperature (20.14) applies.

$$\varepsilon^{\text{steel}} = \varepsilon^{\gamma+\varepsilon+\alpha'} = \varepsilon^{\gamma} + \Delta\varepsilon^{\gamma\rightarrow\varepsilon} + \Delta\varepsilon^{\gamma\rightarrow\alpha'} \tag{20.14}$$

At the $M_{\text{d}}^{\gamma\rightarrow\varepsilon}$ temperature, the plastic elongation value $\varepsilon_A^{\gamma\rightarrow\varepsilon}$ coincides with the uniform elongation of the austenite (ε^{γ}). Below that temperature, the anomalous temperature dependence of the uniform elongation ($\varepsilon^{\text{steel}}$), associated with noticeable ductility enhancement at lower temperatures, begins. At the $M_{\text{d}}^{\gamma\rightarrow\alpha'}$ temperature, the uniform elongation of the steel reaches a maximum. Below the $M_{s\sigma}^{\gamma\rightarrow\varepsilon}$ temperature, the stress-induced ε martensite formation begins, which does not lead to a plastic elongation. In the $\gamma \rightarrow \varepsilon \rightarrow \alpha'$ transformation range, the plastic elongation $\Delta\varepsilon^{\gamma\rightarrow\varepsilon}$ contributed by the strain-induced ε-martensite formation equaled the plastic elongation value $\Delta\varepsilon_*^{\gamma\rightarrow\varepsilon}$ contributed by the glide in the austenite. The X5CrNi18-10 steel serves as an example for a method to describe the shear and glide processes occurring in the austenite. It is assumed that no glide processes were activated in the strain-induced ε and α' martensite phases. Strength and ductility contributions by the induced glide processes in the martensitic phases must be taken into account when spontaneous ε- or α'-martensite, which raise the yield strength of the steel, are present in the starting microstructure [18, 28].

20.5 Effect of Nickel on the Deformation Mechanisms of Metastable CrMnNi Cast Steels

To describe the influence of chemical composition on the deformation mechanisms, the X3CrMnNi16-7-3, X3CrMnNi16-7-6 and X3CrMnNi16-7-9 cast steels with primarily austenitic microstructures have been developed [5, 34]. The true-stress versus true-strain curves of the investigated steels are shown in Fig. 20.9. These flow curves, obtained at various temperatures, are the basis for the development of STT and DTT diagrams [19]. The yield strength, tensile strength, and uniform elongation can be determined directly from the flow curves. To determine the triggering stress ($\sigma_A^{\gamma\rightarrow\alpha'}$) for the deformation-induced α'-martensite formation, the first derivatives of the flow curves, namely the work hardening rate, has to be calculated. A typical steel with deformation-induced α'-martensite formation shows two inflection points. The first inflection point corresponds to the triggering stress for the austenite to martensite formation. The second inflection point, on the other hand, can be correlated with the maximum of deformation-induced α'-martensite formation rate [21]. In the case of deformation-induced twinning or ε-martensite formation, no inflection point is observed. Therefore, the triggering stress for twinning or ε-martensite formation has to be determined by microstructural investigations after interrupted tensile tests [19].

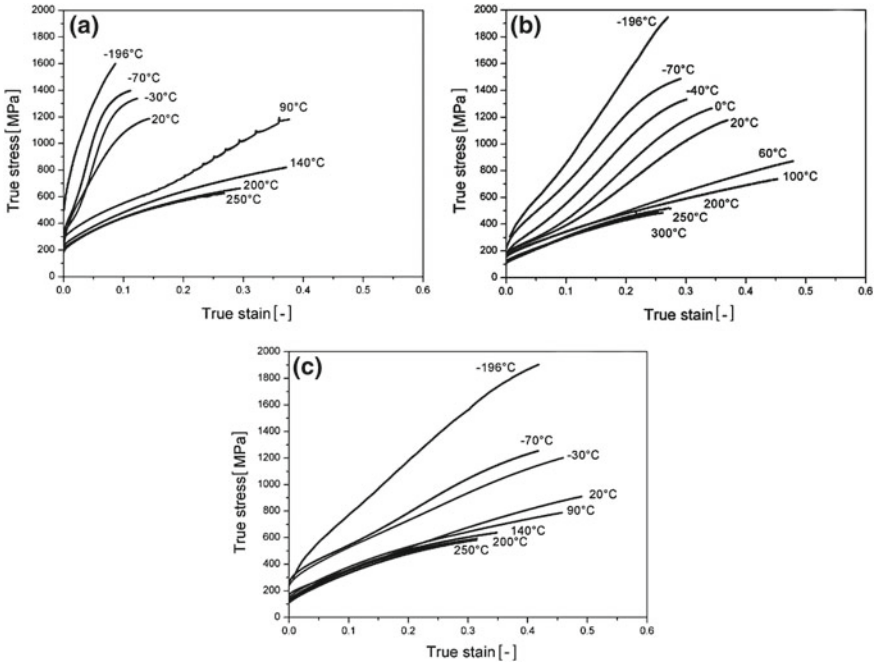

Fig. 20.9 True stress-strain curves for tensile specimens of **a** X3CrMnNi16-7-3, **b** X3CrMnNi16-7-6 and **c** X3CrMnNi16-7-9 steel in the temperature range of −196 to 250 °C [19, 34]

The STT and DTT diagrams for the steel X3CrMnNi16-7-3 are shown in Fig. 20.10. The triggering stresses and the tensile strength of the phases determine the stress-temperature fields for the deformation-induced processes (martensite formation, twinning, dislocations glide, etc.). The location of these fields depends on the chemical composition of the investigated steel [20]. All solid lines in the diagrams are experimentally determined. The dashed lines are predicted or approximated. In contrast to the X3CrMnNi16-7-6 and X3CrMnNi16-7-9 steels, the microstructure of the X3CrMnNi16-7-3 steel prior to tensile tests was not fully austenitic and the low austenite stability, the critical temperatures for deformation-induced twinning $T_{\mathrm{d}}^{\gamma\rightarrow\mathrm{Tw}}$ (300 °C) and deformation-induced α'-martensite formation $M_{\mathrm{d}}^{\gamma+\varepsilon,(\mathrm{Tw})\rightarrow\alpha'}$ (140 °C) were higher compared to the other two steels [5, 20, 34]. According to microstructural investigations, it is assumed that the ε martensite formation occurs in the approximate temperature range 40–300 °C. With increasing temperature and thus increasing stacking fault energy, deformation twinning replaces the ε martensite formation [4]. Due to the low triggering stresses for the strain-induced α'-martensitic transformation at low temperatures, the ε-martensite formation is practically suppressed below room temperature. The maximum true strain of about 0.4 is reached at a temperature of approximately 120 °C. The temperature anomaly of elongation (broad maximum in Fig. 20.11) in the steel X3CrMnNi16-7-3 is mainly caused by the strain-induced ε-TRIP [20]. The elongation contribution caused by the α'-martensite formation is

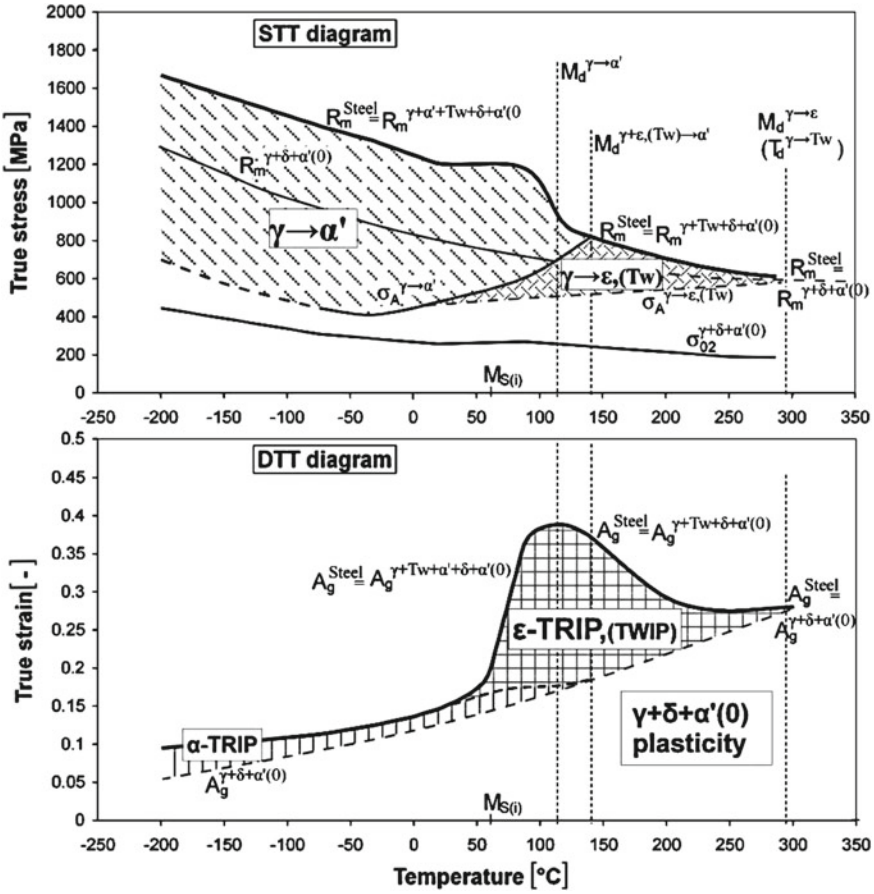

Fig. 20.10 STT and DTT diagrams for the X3CrMnNi16-7-3 steel [19]

negligible, because the α'-martensite after tensile tests is either deformation-induced or formed spontaneously.

Figure 20.11 shows the STT and DTT diagrams for the steel X3CrMnNi16-7-6. Compared to the X3CrMnNi16-7-3 steel, the critical transformation temperatures and the transformation fields are shifted to lower temperatures [35]. The $T_{\mathrm{d}}^{\gamma\rightarrow\mathrm{Tw}}$ temperature and the $M_{\mathrm{d}}^{\gamma+\varepsilon,(\mathrm{Tw})\rightarrow\alpha'}$ temperature are 250 °C and 100 °C, respectively. In the temperature range between 0 and 50 °C, the triggering stress for α'-martensite formation is very low. Therefore, the austenite transforms into martensite practically without twinning or ε-martensite formation. At a deformation temperature of 60 °C, ε-martensite was found in the microstructure [19, 36]. Additionally, the kinetics of the α'-martensite formation is shown in the STT diagram. Therefore, compared to the STT diagram of the X3CrMnNi16-7-3 steel, the STT diagram for the X3CrMnNi16-7-6 steel additionally includes the isolines for α'-martensite fraction as marked in

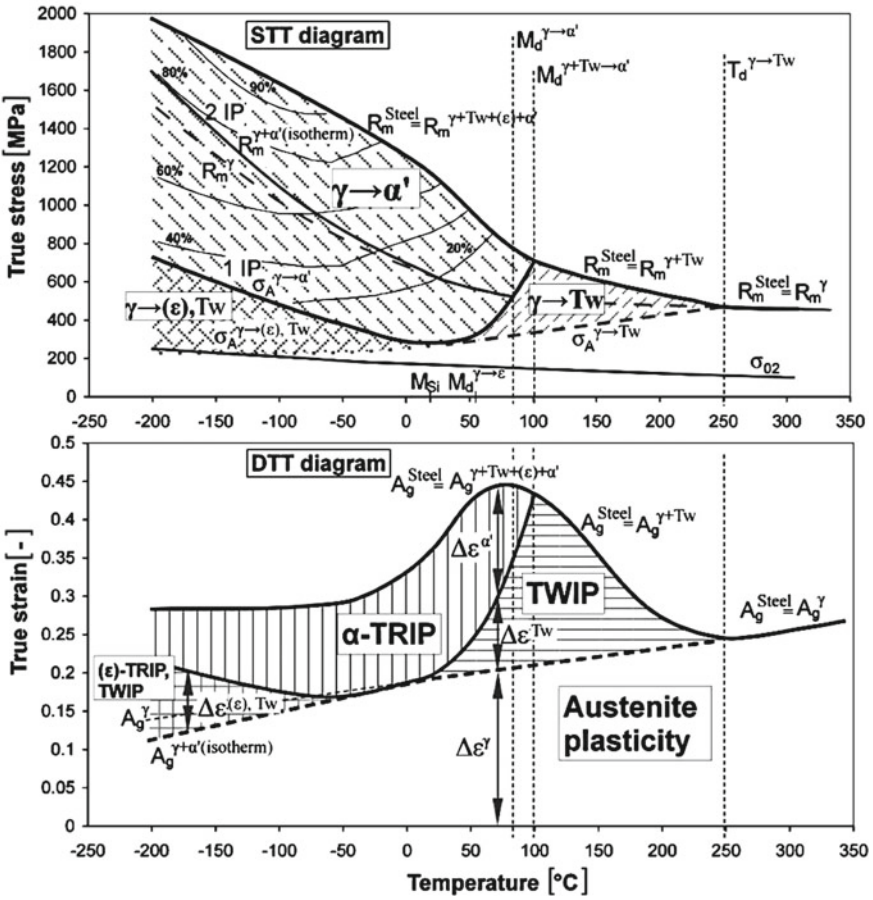

Fig. 20.11 STT and DTT diagrams for the X3CrMnNi16-7-6 steel [19]

the $\gamma \rightarrow \alpha'$ transformation field. Moreover, the X3CrMnNi16-7-6 steel is capable of forming isothermal martensite, which is not taken into account in the STT diagram [20]. Accordingly, the stress values measured at the second inflection point are higher than the R_m^{γ}. This measurable stress $R_m^{\gamma+\alpha'(\text{isotherm})}$ enables an approximation of R_m^{γ}.

The uniform elongation A_g^{Steel} of the X3CrMnNi16-7-6 steel, the uniform elongation of the austenite A_g^{γ} and corresponding deformation mechanisms are shown in the DTT diagram in Fig. 20.11. Additionally, the elongation contributions due to the dislocations glide in the austenite $\Delta\varepsilon^{\gamma}$, deformation twinning $\Delta\varepsilon^{\text{Tw}}$, and strain-induced martensite transformation $\Delta\varepsilon^{\alpha'}$ are included in the DTT diagram. The temperature anomaly starting at 250 °C is a result of the stacking fault formation and twinning, which leads to an enhanced elongation with decreasing temperature [19, 20]. Below the $M_{\text{d}}^{\gamma+\text{Tw}\rightarrow\alpha'}$ temperature (80 °C), the gradual replacement of stacking fault formation and twinning by α'-martensite formation leads a decrease in elongation.

The STT and DTT diagrams for the steel X3CrMnNi16-7-9 are shown in Fig. 20.12. Compared to the steels X3CrMnNi16-7-3 and X3CrMnNi16-7-6, the stability of austenite is increased due to the higher Ni content. Accordingly, the critical temperatures are shifted to lower temperatures. The $T_d^{\gamma \rightarrow Tw}$ temperature is around 200 °C. Austenite, which is deformed by twinning, transforms below $M_d^{\gamma+Tw \rightarrow \alpha'}$ (50 °C) into martensite. In the temperature range between −50 and −70 °C, the triggering stress for α'-martensite formation is very low, and austenite transforms directly into martensite almost without twinning. The maximum true strain of about 0.5 is reached at a temperature of 30 °C. A superposition of three deformation mechanisms—glide deformation of the austenite, TWIP effect, and TRIP effect—takes place at this temperature and causes the highest elongation.

The various austenite stabilities of the dendritic cast structure caused by the segregation of the alloying elements Cr, Mn, Ni during solidification of the austenitic

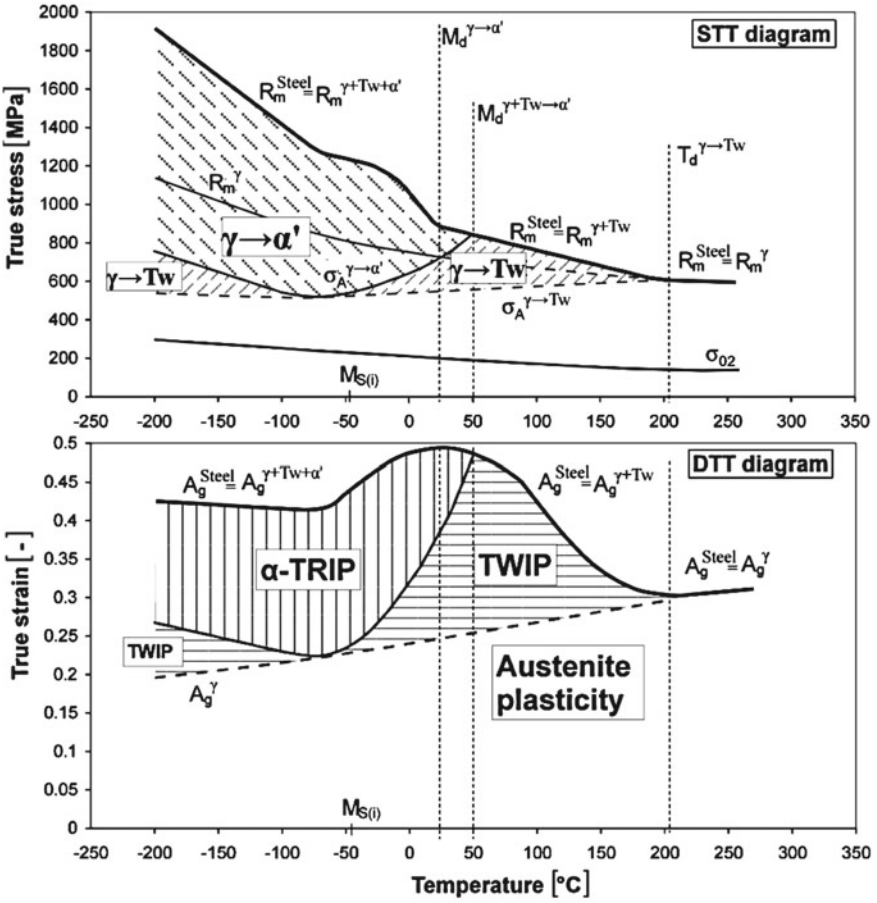

Fig. 20.12 STT and DTT diagrams for the X3CrMnNi 16-7-9 steel [19]

steels X3CrMnNi 16-7-3/6/9 leads to a shift of critical temperatures. Accordingly, the center of dendrites are more metastable than interdendritic regions of austenite.

For further information the reader is revered to read the publication of Martin et al. [37] and Mola et al. [10].

20.6 Thermodynamic-Mechanical Modeling Based on Austenitic CrMnNi–C–N Cast Steel

Figure 20.13 shows the true stress-strain curves for the interstitially-alloyed X15CrNiMnN19-4-3 cast steel deformed until fracture at temperatures between −80 and 400 °C. Carbon and nitrogen were alloyed to the steel to increase the strength by solid solution solidification. The highest elongation of 53% was reached at 60 °C, which is almost equal to the M_d-temperature (70 °C). The formation of α'-martensite at lower temperatures resulted in a pronounced strengthening and a steady decrease in elongation. Reduction of tensile elongation at temperatures below the M_d temperature is a common observation in austenitic stainless steels, including the steels discussed above [22]. The noticeable work hardening at −80 °C resulted in the highest (engineering) tensile strength of 1500 MPa, which correlates to a true tensile strength of 2000 MPa.

The phase fractions of martensite and austenite after tensile deformation until fracture at different temperatures is shown in Fig. 20.14. The steel does not form as-quenched martensite at temperatures as low as −196 °C. Therefore, the martensite contents in Fig. 20.14 represent the deformation-induced martensite only. The highest martensite content of about 81 vol% was formed during deformation at −80 °C.

To determine the deformation mechanisms activated during tensile tests, SEM investigations were carried out on tensile specimens deformed until fracture at −80, 70 and 200 °C (Fig. 20.15). The tensile direction is horizontal aligned to the plane of view. ECCI image of Fig. 20.15a shows the presence of various operating

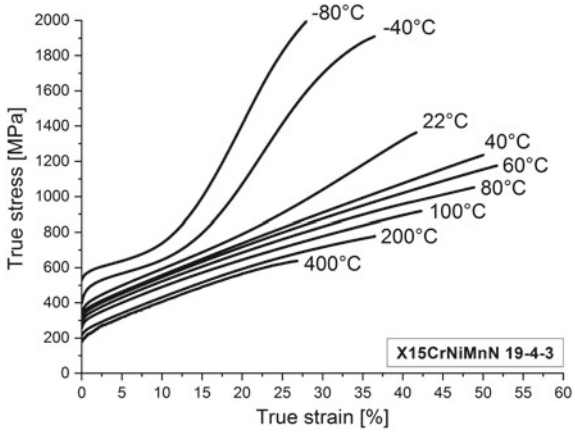

Fig. 20.13 True stress-strain curves of tensile specimens of the X15CrNiMnN19-4-3 cast steel in the temperature range of −80 to 400 °C

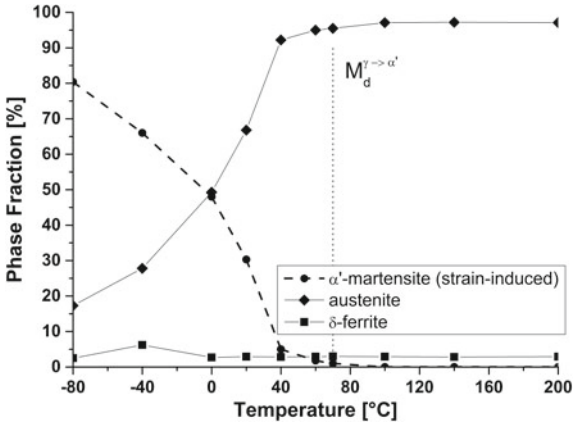

Fig. 20.14 Phase fractions in the microstructure of tensile specimens of the X15CrNiMnN19-4-3 steel tested at various temperatures

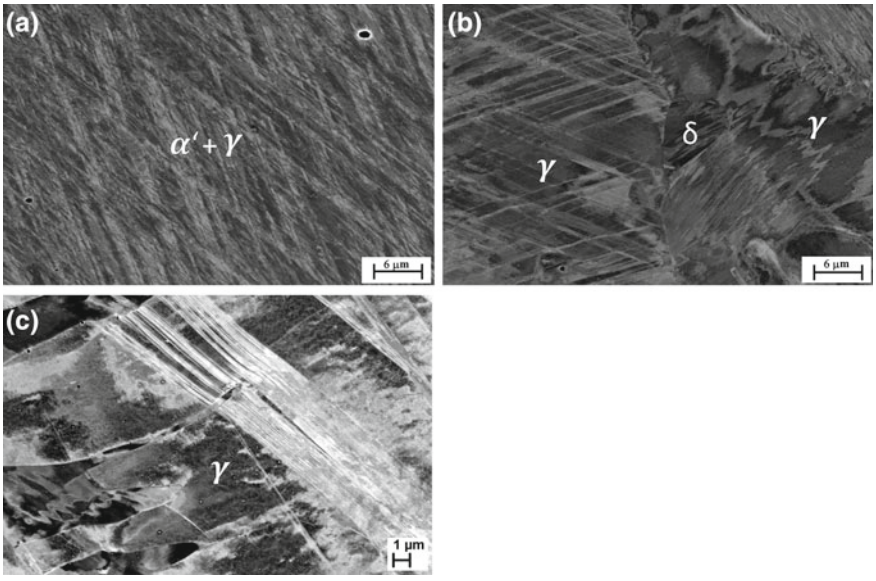

Fig. 20.15 Microstructures obtained after tensile deformation at different temperatures: ECCI micrographs of specimens deformed at −80 °C (**a**), 70 °C (**b**) and 200 °C (**c**) of the X15CrNiMnN19-4-3 steel

straight deformation bands with α'-martensite in the microstructure of the specimen deformed at −80 °C. This indicates the dominance of planar glide due to the high activity of Shockley partial dislocations at −80 °C [9]. According to the MSAT measurement results (Fig. 20.15) a large volume fraction of austenite transformed to

α'-martensite. The ECCI image of the specimen tensile tested at 70 °C (Fig. 20.15b) shows two austenite grains with different microstructural characteristics. Whereas the microstructure of the austenite grain on the left resembles the microstructure shown in Fig. 20.15a, diffuse contrast changes in the austenite grain to the right imply the dominance of wavy glide [8, 38]. Abrupt transition in the glide mode across a grain boundary is more consistent with the differences in the crystallographic orientation of the neighboring grains than with the possible segregation of alloying elements in the cast steel. After all, the forces exerted on the leading and trailing partial dislocations of the primary slip system depend on the crystal orientation [9, 39]. The ECCI image of the specimen deformed at 200 °C in Fig. 20.15c on the other hand shows only a diffuse contrast changes in the austenite grain what a dominance of wavy glide means. This sequence has been similarly observed in the X3CrMnNi16-7-6 steel [4, 5, 40, 41].

To describe the occurring deformation mechanisms during tensile loading, interrupted tensile tests with subsequent microstructure investigations have been performed. ECCI image and EBSD phase map of a tensile sample deformed at 0 °C to 800 MPa are shown in Fig. 20.16. It is well established that the type of deformation-induced processes in austenitic steels depends on the stacking fault energy; as the stacking fault energy decreases, the deformation mechanism changes from perfect dislocation glide to deformation twinning, ε-martensite formation, and α'-martensite formation in that sequence [42]. Due to the coexistence of a small ε-martensite fraction in the deformation bands, the martensitic transformation according to the sequence $\gamma \rightarrow \varepsilon \rightarrow \alpha'$ (Fig. 20.16b) is very likely. The mechanism of formation of deformation-induced twins and ε-martensite is very similar and only differs in the stacking sequence of $\{111\}\gamma$ close-packed planes; thus stacking faults on successive $\{111\}\gamma$ planes generate deformation twins, whereas their overlap on every second $\{111\}\gamma$ plane results in the formation of ε-martensite [4]. Accordingly, these two byproducts of stacking faults have been observed to coexist in the microstructure of deformed austenitic steels [43].

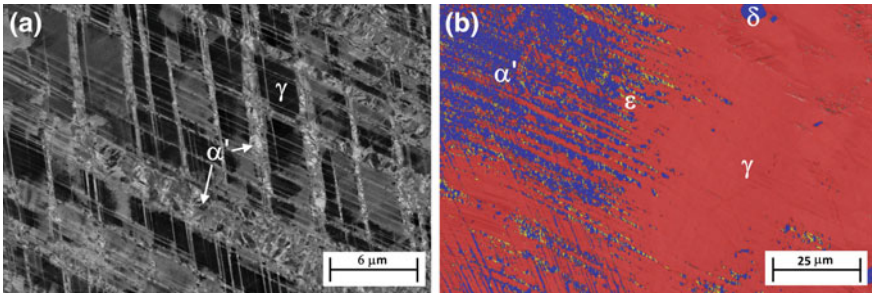

Fig. 20.16 Microstructures obtained after tensile testing at different temperatures: ECCI image and EBSD phase map of a specimen deformed at 0 °C to 800 MPa. In the EBSD phase map, red, yellow, and blue denote phases with fcc, hcp, and bcc crystal structures, respectively

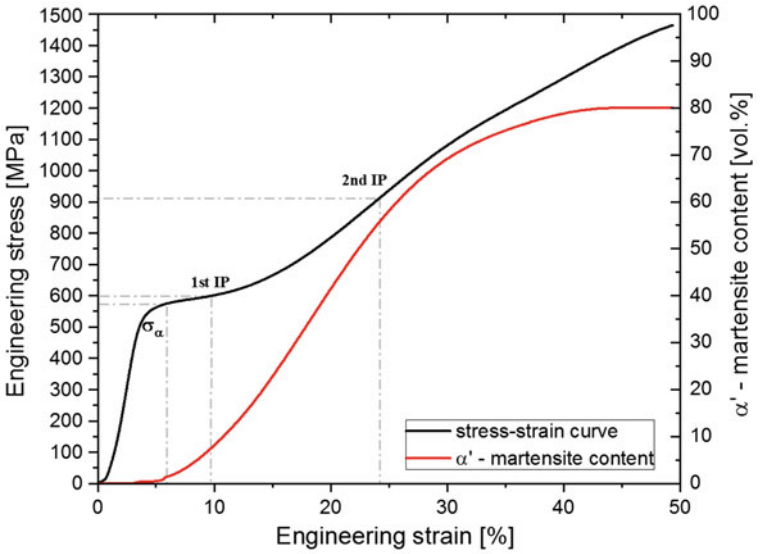

Fig. 20.17 Evolution of deformation-induced α'-martensite fraction during tensile deformation at −80 °C of the X15CrNiMnN19-4-3 steel superimposed on the stress-strain curve

In order to correlate the stress-strain curve with the deformation-induced α'-martensite fraction, the evolution of martensite fraction during tensile test at −80 °C, obtained from in situ magnetic measurements, is superimposed on the stress-strain curve (Fig. 20.17). The evolution of α'-martensite fraction with strain resembles the available literature data on the kinetics of deformation-induced martensite formation in metastable austenitic alloys. The increase in the work hardening rate caused by the deformation-induced formation of α'-martensite is known to cause a first inflection point in the stress-strain curve of metastable austenitic steels [36]. Taking the stress at which almost 1 vol% α'-martensite has formed by deformation as the triggering stress for the deformation-induced α'-martensite formation (σ_A), it does not match the first inflection point (IP) of the stress-strain curve. As marked in Fig. 20.17, the first inflection point during tensile deformation at −40 °C occurs after the formation of almost 3–5 vol% martensite in the microstructure. In other words, the first inflection point gives a slightly overestimated approximation of the triggering stress. Between the first and second inflection points, the martensite formation rate remains almost constant [21].

The STT and DTT diagrams of the X15CrNiMnN19-4-3 are shown in Fig. 20.18. The area between the triggering stress and the tensile strength, marked $\gamma \rightarrow \alpha'$ in Fig. 20.18, denotes the stress-temperature field favorable for the deformation-induced martensitic transformation. In different temperature ranges, different deformation mechanisms are activated. The dominant mechanisms are deformation-induced martensite formation below M_d, deformation twinning between M_d and T_d, and glide of perfect dislocations above T_d temperature. The temperature range where

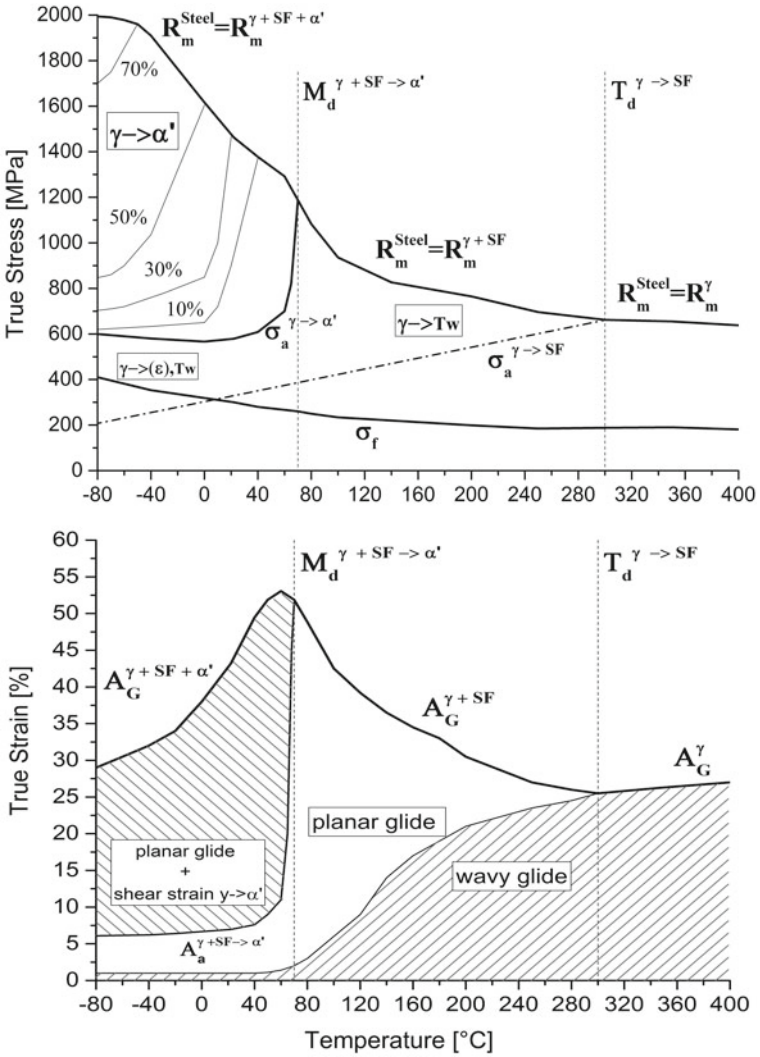

Fig. 20.18 STT and DTT diagrams for the X15CrNiMnN19-4-3 steel

these processes occur depends on the chemical composition. Deformation-induced martensite formation is absent at temperatures above approximately 70 °C, leading to a weak temperature dependence of tensile strength. Upon deformation-induced martensite formation at lower temperatures, the tensile strength increases at a much faster rate. The martensite tends to form within the slip bands in the austenite, thereby restricting dislocations glide within the existing bands. As a result, additional slip bands must be activated to sustain plastic deformation. This explains the high rate

of strain hardening. In the temperature range between 70 and −80 °C, the triggering stress for deformation-induced martensite was determined by in situ magnetic measurements to be in the range 600–1180 MPa.

The DTT diagram enables the separation of strain contributions owing to the glide of dislocations in the austenite as well as those due to the deformation-induced twinning and martensitic transformation. The summation of these strain contributions yields the experimental elongation (A_G^{Steel}) of the steel, which reaches a maximum at 53% in the studied temperature range of −80 to 400 °C. Since the strain contributions of twinning, ε-martensite formation and dislocation glide are difficult to separate, the DTT diagram in Fig. 20.18 shows only the summation of these contributions.

Due to the high amount of interstitial elements, the X15CrNiMnN19-4-3 has a higher yield strength than the X3CrMnNi16-7-3/6/9 steels at equal deformation temperatures. Although the martensite content of the X15CrNiMnN19-4-3 at room temperature is significantly lower (30.3 vol%) than the martensite content of the X3CrMnNi16-7-3 (82 vol%), is the yield strength (342–298 MPa) and the ultimate tensile strength (1663–1198 MPa) is higher. The M_d temperature of the X15CrNiMnN19-4-3 steel (70 °C) is located between the X3CrMnNi16-7-6 (100 °C) and X3CrMnNi16-7-9 (50 °C).

In Fig. 20.19, the Gibbs energy changes for the martensite formation based on the thermodynamic database are compared with the values calculated using the procedure explained in the following and discussed in more detail by Hauser et al. [22]. Whereas the dash-dotted line predicts a continuous increase in the chemical driving force at lower temperatures (down to −196 °C), the chemical driving force

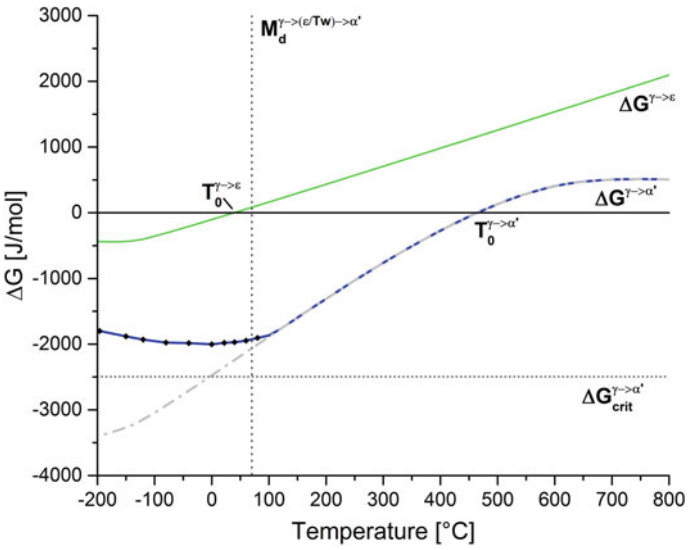

Fig. 20.19 Gibbs energy changes for $\gamma \rightarrow \varepsilon$ and $\gamma \rightarrow \alpha'$ phase transformations calculated by Thermo-Calc and corrected Gibbs energy $\gamma \rightarrow \alpha'$ with the aid of tensile tests with in situ magnetic measurements for the X15CrNiMnN19-4-3 steel [22]

based on the revised values remains almost constant below −80 °C. The observed deviation is most likely caused by changes in the mechanical and physical properties of austenite near the Néel temperature. The critical Gibbs free energies for the formation of martensite at different temperatures were determined by the addition of the chemical and mechanical contributions. The chemical term was obtained from thermodynamic calculations. The mechanical term, on the other hand, was obtained by calculating the mechanical energy supplied to tensile specimens up to the onset of martensitic transformation. The critical driving force for the formation of α' (−2496 J/mol) was obtained by determining the mechanical energy necessary to trigger the deformation-induced α'-martensite formation at 0 °C. Driving forces for the formation of α'-martensite at other tensile test temperatures were then obtained by subtracting the mechanical energies applied to trigger the martensitic transformation from the critical driving force. Additionally, the calculated Gibbs free energy for ε-martensite formation is shown in Fig. 20.19. Due to the low critical driving force of ε-martensite, the ε-martensite formation starts immediately below the $T_0^{\gamma\rightarrow\varepsilon}$. Since the α'-martensite is more stable, the $\varepsilon \rightarrow \alpha'$ phase transformation starts at the moment where the critical driving force for α' martensite is reached.

20.7 Conclusions

The focus of the subproject C3 was the thermodynamic-mechanical modeling of metastable high alloy austenitic CrMnNi steels. To achieve this, several steels were investigated in cooperation with different subprojects of the Collaborative Research Center 799. With the aid of thermodynamic data and flow curve analysis, it is possible to describe the mechanical properties based on the deformation mechanisms and phase transformations. The investigated metastable austenitic steels exhibited the transformation induced plasticity (TRIP) and twinning induced plasticity (TWIP) effects.

First, a new method was developed for the quantitative determination of strength and plastic elongation contributions due to deformation-induced processes during uniaxial tensile loading of austenitic steels. The method was demonstrated using a commercial X5CrNi18-10 steel. For this purpose, the dependence of the overlapping deformation processes in the austenite on the temperature and applied tensile stress was studied in the temperature range of −196 to 40 °C. It was shown that every deformation process leads to a strength and plasticity contribution commensurate with its dominance. The sum of all contributions yielded the tensile strength and the uniform elongation of the steels. Stress-temperature-transformation (STT) and deformation-temperature-transformation (DTT) diagrams were constructed with the aid of flow curve analysis and microstructural examinations. Plastic deformation of martensite was excluded in the developed method. Therefore, the method is only valid for metastable austenitic steels whose initial microstructure is free of as-quenched ε- or α'-martensite.

The influence of the chemical composition on the deformation mechanisms of metastable CrMnNi cast steels was investigated using three high alloy steels, namely X3CrMnNi16-7-3, X3CrMnNi16-7-6 and X3CrMnNi16-7-9. The influence of martensite formation on the mechanical properties of the three steels was studied by tensile tests between −196 and 300 °C. With increasing nickel content, the critical temperatures shifted to lower temperatures. For instance, the M_d-temperature decreased from 140 °C at 3% Ni to 50 °C at 9% Ni. Furthermore, the increase in the Ni content was associated with a change in the deformation mechanism at room temperature from a pronounced TRIP effect to a mixture of TRIP and TWIP effects.

A mathematical model was applied to describe the mechanical work due to uniaxial tensile loading. This enabled to determine the critical driving force for the martensitic phase transformation. The deformation-induced formation of α'-martensite was investigated by tensile testing of X15CrNiMnN19-4-3 cast austenitic steel between −80 and 400 °C. The steel did not exhibit spontaneous α'-martensite formation at temperatures as low as −196 °C. The triggering mechanical energies for the deformation-induced α'-martensite formation were calculated after determining the onset of α'-martensite formation by in situ magnetic measurements during tensile tests. The results enabled to calculate modified driving forces for the occurrence of the $\gamma \rightarrow \alpha'$ phase transformation.

Acknowledgements The authors would like to thank Dr. Alexander Kovalev for the research on the 1st generation steels. Sincere thanks are due to the colleagues at the Institute of Iron and Steel Technology (IEST), Institute of Materials Engineering and the Institute of Materials Science (IWW) for their support and assistance on the experiments: Ms. C. Ullrich and Mr. B. Reichel for the SEM, ECCI and XRD measurements; Dr. T. Kreschel und Mr. G. Franke for the heat treatments; Mrs. G. Schubert for the dilatometry experiments and hardness tests; Mr. P. Neuhold for producing the steels; Dr. R. Eckner and Mr. G. Schade for the tensile tests; Mrs. I. Grahl and Mrs. J. Kreschel for the metallographic sample preparation and light optical microscope observations; Mr. M. Block for the machining of specimens; and all the student assistants for the magnetic measurements. The financial support of the Deutsche Forschungsgemeinschaft (DFG, German Research Foundation) in the framework of Collaborative Research Center 799 (Project number 54473466) subproject C3 was gratefully acknowledged. The authors would also like to thank Prof. P. R. Scheller, the previous director of IEST, for his support on preparing the C3 subproject proposal. Special thanks are extended to all the colleagues from SFB 799 for the valuable and fruitful scientific discussions.

References

1. R.G. Stringfellow, D.M. Parks, G.B. Olson, Acta Metall. Mater. **40**, 1703 (1992)
2. F.D. Fischer, G. Reisner, E. Werner, K. Tanaka, G. Cailletaud, T. Antretter, Int. J. Plast **16**, 723 (2000)
3. F. Lecroisey, A. Pineau, Metall. Trans. **3**, 391 (1972)
4. S. Martin, S. Wolf, U. Martin, L. Krüger, D. Rafaja, Metall. Mat. Trans. A **47**, 49 (2014)
5. S. Wolf, S. Martin, L. Krüger, U. Martin, U. Lorenz, Steel Res. Int. **83**, 529 (2012)
6. M. Wendler, B. Reichel, R. Eckner, O. Fabrichnaya, L. Krüger, A. Weiß, J. Mola, Metall. Mater. Trans. A **47**, 139 (2016)
7. J.F. Breedis, Acta Metall. **13**, 239 (1965)

8. M. Pozuelo, J.E. Wittig, J.A. Jiménez, G. Frommeyer, Metall. Mater. Trans. A **40**, 1826 (2009)
9. R. Rahimi, C. Ullrich, V. Klemm, D. Rafaja, B.C. De Cooman, H. Biermann, J. Mola, Mater. Sci. Eng., A **649**, 301 (2016)
10. J. Mola, M. Wendler, A. Weiß, B. Reichel, G. Wolf, B.C. De Cooman, Metall. Mater. Trans. A **46**, 1450 (2015)
11. M. Wendler, C. Ullrich, M. Hauser, L. Krüger, O. Volkova, A. Weiß, J. Mola, Acta Mater. **133**, 346 (2017)
12. F. Abrassart, Metall. Trans. **4**, 2205 (1973)
13. K. Spencer, K.T. Conlon, Y. Bréchet, J.D. Embury, Mater. Sci. Technol. **25**, 18 (2009)
14. S. Martin, S. Wolf, U. Martin, L. Krüger, Solid State Phenom. **172–174**, 172 (2011)
15. M. Cohen, E.S. Machlin, V.G. Paranjpe, Am. Soc. Metals **242** (1950)
16. L. Kaufman, M. Cohen, Prog. Metal Phys. **7**, 165 (1958)
17. G. Ghosh, G.B. Olson, Acta Metall. Mater. **42**, 3361 (1994)
18. A. Weiß, H. Gutte, J. Mola, Metall. Mater. Trans. A **47**, 112 (2016)
19. A. Kovalev, A. Jahn, A. Weiß, S. Wolf, P.R. Scheller, Steel Res. Int. **83**, 576 (2012)
20. A. Kovalev, M. Wendler, A. Jahn, A. Weiß, H. Biermann, Adv. Eng. Mater. **15**, 609 (2013)
21. M. Hauser, M. Wendler, S. Ghosh Chowdhury, A. Weiß, J. Mola, Mater. Sci. Technol. **31**, 1473 (2015)
22. M. Hauser, M. Wendler, O. Fabrichnaya, O. Volkova, J. Mola, Mater. Sci. Eng., A **675**, 415 (2016)
23. M. Hauser, M. Wendler, A. Weiß, O. Volkova, J. Mola, Adv. Eng. Mater. **21**, 1800676 (2019)
24. M. Palumbo, Calphad **32**, 693 (2008)
25. G. Ghosh, G.B. Olson, J. Phase Equilibria **22**, 199 (2001)
26. S.G.T.E. (SGTE), in *Ternary Steel Systems: Phase Diagrams and Phase Transition Data*, ed. by P. Franke, H.J. Seifert (Springer, Berlin, Heidelberg, 2012), pp. 64–64
27. G.B. Olson, M. Cohen, Metall. Trans. A **7**, 1915 (1976)
28. H. Gutte, A. Weiß, *Spannungs- und verformungsinduzierte Martensitbildungen in metastabilen austenitischen CrNi-Stählen, Habilitation* (TU Bergakademie, Freiberg, 2011)
29. J.R. Patel, M. Cohen, Acta Metall. **1**, 531 (1953)
30. H.K.D.H. Bhadeshia, ISIJ Int. **42**, 1059 (2002)
31. H. Schumann, *Kristallgeometrie - Einfürhung in die Theorie der Gittertransformationen metallischer Werkstoffe*, 1st edn. (Deutscher Verlag für Grundstoffindustrie, Leipzig, 1979)
32. H. Ledbetter, M.L. Dunn, Mater. Sci. Eng., A **285**, 180 (2000)
33. H. Arslan, H. Arslan, T. Dogan, Phys. Metals Metall. **114** (2013)
34. A. Jahn, A. Kovalev, A. Weiß, S. Wolf, L. Krüger, P.R. Scheller, Steel Res. Int. **82**, 39 (2011)
35. A. Kovalev, Thermodynamisch-mechanische Modellierung der verformungsinduzierten α'-Martensitbildung in austenitischen Cr-Mn-Ni-Stählen, Dissertation (TU Bergakademie Freiberg, 2016)
36. A. Kovalev, A. Jahn, A. Weiß, S. Wolf, P.R. Scheller, Steel Res. Int. **82**, 1101 (2011)
37. S. Martin, O. Fabrichnaya, D. Rafaja, Mater. Lett. **159**, 484 (2015)
38. R. Rahimi, C. Ullrich, D. Rafaja, H. Biermann, J. Mola, Metall. Mater. Trans. A **47**, 2705 (2016)
39. H.-J. Kestenbach, Phil. Mag. **36**, 1509 (1977)
40. S. Martin, S. Wolf, S. Decker, L. Krüger, U. Martin, Steel Res. Int. **86**, 1187 (2015)
41. S. Martin, C. Ullrich, D. Šimek, U. Martin, D. Rafaja, J. Appl. Cryst. **44**, 779 (2011)
42. S. Allain, J.-P. Chateau, O. Bouaziz, S. Migot, N. Guelton, Mater. Sci. Eng., A **387–389**, 158 (2004)
43. L. Remy, A. Pineau, Metall. Trans. **5**, 963 (1974)

Chapter 21
Multi-scale Modeling of Partially Stabilized Zirconia with Applications to TRIP-Matrix Composites

Mohan Kumar Rajendran, Michael Budnitzki and Meinhard Kuna

Abstract The understanding of how the microstructure influences the mechanical response is an essential pre-requisite for materials tailored to match specific requirements. The aim of this chapter is to further this understanding in the context of Mg-PSZ-TRIP-steel composites on three different scales using a set of methods ranging from phase-field simulations over micromechanics to continuum constitutive modeling. On the microscale, using a Ginzburg-Landau type phase-field model the effects of cooling- and stress-induced martensitic phase transformation in MgO-PSZ is clearly distinguished. Additionally with this method the role of energy barrier in variant selection and the effect of residual stress contributing to the stability of the tetragonal phase are also investigated. On the mesomechanical scale, an analytical 2D model for the martensitic phase transformation and self-accommodation of inclusions within linear elastic materials has been successfully developed. The influences of particle size and geometry, chemical driving force, temperature and surface energy on the $t \rightarrow m$ transformation are investigated in a thermostatic approach. On the continuum scale, a continuum material model for transformation plasticity in partially stabilized zirconia ceramics has been developed. Nonlinear hardening behavior, hysteresis and monoclinic phase fraction during a temperature cycle are analyzed. Finally, The mechanical properties of a TRIP steel matrix reinforced by ZrO_2 particles are analyzed on representative volume elements. Here the mechanical properties of the composite as function of volume fraction of both constituents and the strength of the interface are studied.

M. K. Rajendran (✉) · M. Budnitzki · M. Kuna
Institute of Mechanics and Fluid Dynamics,
Technische Universität Bergakademie Freiberg,
Lampadiusstrasse 4, 09599 Freiberg, Germany
e-mail: mohan-kumar.rajendran@imfd.tu-freiberg.de

H. Biermann and C. G. Aneziris (eds.), *Austenitic TRIP/TWIP Steels and Steel-Zirconia Composites*, Springer Series in Materials Science 298,
https://doi.org/10.1007/978-3-030-42603-3_21

21.1 Introduction

21.1.1 Aims and Scopes of the Present Work

One central aim of the Collaborative Research Center SFB799 "TRIP-matrix composites" was the development of a particle reinforced composite, composed of a TRIP-steel metallic matrix and ceramic particles of partially stabilized zirconia PSZ. The underlying idea was to exploit the phase transformation capability of both constituents in order to enhance and to optimize the mechanical properties by making such a composite.

In particular, the combination of the strain-induced phase transformation in the TRIP steel and the stress-induced transformation in PSZ offers the opportunity to compensate local stress concentrations at considerably high plastic deformations. This reinforcing effect has been verified by several experiments with these metal-matrix-composites MMC under monotonous [1] loading.

In complementation to the fabrication and characterization of these MMC, a thorough theoretical-numerical modeling of the composite material was necessary to understand and to simulate the phase transformation and the deformation behavior of both constituents.

This work was devoted to the simulation of the phase transformation processes in the PSZ ceramics and the MMC, whereas in another work the behavior of the TRIP-steel was investigated. The aim was to provide proper constitutive equations for stress and temperature controlled tetragonal-to-monoclinic phase transformation of PSZ ceramics, based on physical assumptions accounting for the responsible micromechanical mechanisms. The problem has been approached at various length scales, see Fig. 21.1:

- At the **microscale** level it was needed to simulate the actual kinetics of the transformation process inside of single tetragonal phase particles in PSZ. This task could be best accomplished by using the phase-field method.
- To study the transformation conditions of an ensemble of tetragonal lentils in polycrystalline PSZ ceramics, a semi-analytical thermostatic approach was applied at the **mesoscale**.
- In order to enable quantitative strength analysis of structures made of PSZ and MMC, a phenomenological constitutive law at the **macroscale** was further developed and implemented in a FEM-environment.
- To support the development of tailored particle MMC TRIP-matrix composites, representative volume elements on the **composite level** were simulated, which allow to predict the mechanical properties of the composite as function of volume fraction of both constituents and the strength of the interface.

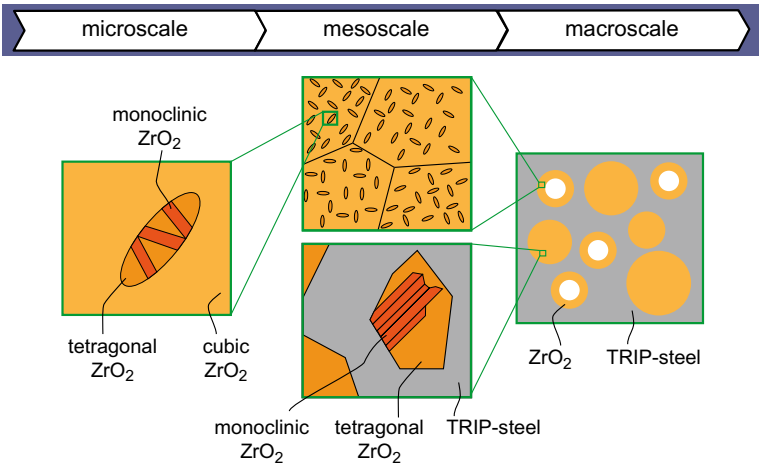

Fig. 21.1 Different scales of modeling partially stabilized zirconia

21.1.2 Introduction to Partially Stabilized Zirconia

Partially stabilized zirconia (PSZ) is widely used because of its enhanced fracture toughness and nonlinear stress-strain behavior. These favorable mechanical properties of PSZ result from a solid state phase transformation at regions of high stress concentration (e.g. crack tips). This effect, known as transformation toughening, was first reported by Garvie et al. [2] and was extensively investigated by [3–5]. Generally, some conditions have to be fulfilled for transformation toughening. The existence of a metastable phase in the material is required, which can be achieved either by microstructural parameters such as grain size or by changing the chemical composition. The martensitic (instantaneous) transformation from the metastable parent phase to the stable resultant phase has to be stress-induced.

The PSZ ceramic material under consideration is stabilized by MgO, resulting in finely dispersed lenticular precipitates of tetragonal (t-phase) embedded coherently in the grains of a polycrystalline cubic matrix material (see Fig. 21.2). These precipitates can transform into the monoclinic (m-phase) [7] triggered either by temperature or stress, resulting in the formation of multiple, partially self-accommodating variants. The $t \rightarrow m$ phase transformation, if unconstrained, is accompanied by a volume dilatation of about 4% and a shear strain of about 8%. The increase in volume induces (residual) compressive stresses in the cubic (c-phase) matrix leading to a shielding effect at stress concentrations, which contributes to the toughness of the material.

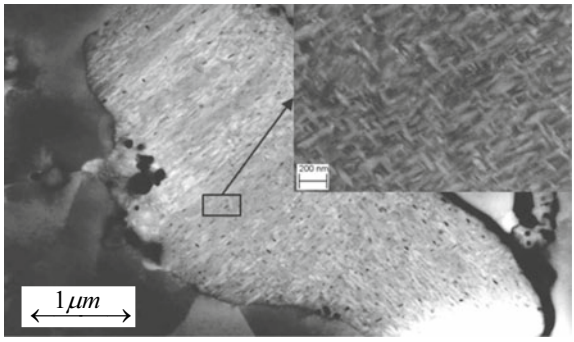

Fig. 21.2 Typical microstructure of a TRIP-PSZ composite produced in the CRC 799 by spark plasma sintering. The image shows a PSZ particle surrounded by TRIP steel together with a zoom into the particle showing the typical PSZ microstructure (reprinted from [6])

21.2 Micromechanical Phase-Field Approach

Phase-field is considered to be a powerful mathematical computational tool in simulations involving interface kinetics. In the past decades PF approach has been successfully established in various fields for materials science understanding such as: solidification, solid-state phase transformation, precipitate evolution and coarsening kinetics, grain growth, martensitic phase transformation (MPT) and also in damage and crack growth phenomena.

For past few decades there has been active research towards the direction of modelling partially stabilized zirconia (PSZ) materials. Wang et al. [8] was one of the early study on PSZ for $c \rightarrow t$ phase transformation involving Ginzburg-Landau (GL) phenomenological theory based PF model. Later in [9] the authors simulated alternating band structure formed by self-organized orientation variants of t-phase particles. In [10] the first three-dimensional model for generic $c \rightarrow t$ MPT was presented. Mamivand et al. [11] reported the first work on anisotropic and inhomogeneous PF modeling for $t \rightarrow m$ phase transformation in zirconia ceramics. The work discussed the simulation results based on different initial and boundary conditions in comparison to experimental observations. Further the authors [12] incorporated the effect of stress and temperature to capture the forward $t \rightarrow m$ and reverse $m \rightarrow t$ transformation to model pseudo-elastic behavior in polycrystalline zirconia.

A comprehensive work on non-conserved type GL-based phase-field models for generic martensitic phase transformation was developed in a series of three papers from Levitas et al. [13–15]. Levitas et al. used a $2-3-4$ or higher order polynomial for approximating the Gibbs energy and effective strain transition from austenite to any martensitic variant. This work principally relies on the phenomenological GL phase-field model developed by Levitas et al. with $2-4-6$ type Landau potential.

21.2.1 Phase-Field Method

The temporal and spatial evolution of non-conserved phase-field variables is described by the phenomenological Ginzburg-Landau kinetic equation

$$\frac{\partial \phi}{\partial t} = -L\left(-\beta \nabla^2 \phi + \frac{\partial \psi_{\mathrm{gl}}}{\partial \phi}\right). \tag{21.1}$$

Here L is the positive kinetic coefficient, and β is a positive gradient energy coefficient. The interface energy contribution provided by Levitas and Preston [13] was used.

Here the total enthalpy ψ_{gl} is described by additive contributions from an elastic ψ_{el} and a stress-independent chemical part of free enthalpy ψ_{ch}. The individual contributions are based on the work of Levitas and Preston [13, 14].

$$\psi_{\mathrm{gl}} = \psi_{\mathrm{el}}(\boldsymbol{\epsilon}, \boldsymbol{\epsilon}_{\mathrm{tr}}, \phi) + \psi_{\mathrm{ch}}(\theta, \phi). \tag{21.2}$$

The order parameter considered here ranges from $-1 \leqslant \phi \leqslant 1$, where $\phi = \pm 1$ are the two possible product variants of m-phase and $\phi = 0$ represents the parent t-phase in two dimensions, see Fig. 21.3b. The values ± 1 correspond to the variants having opposite shear (self accommodating variants) in order to form twins during $t \rightarrow m$ transformation. So, a single order parameter ϕ represents a group of phases consisting of variant m_+, its counter self accommodating variant m_- and the parent phase t in $t \rightarrow m$ transformation. As discussed in the work of Levitas et al. [15] the most opted $2-4-6$ polynomial for such a crystal set is used further to describe

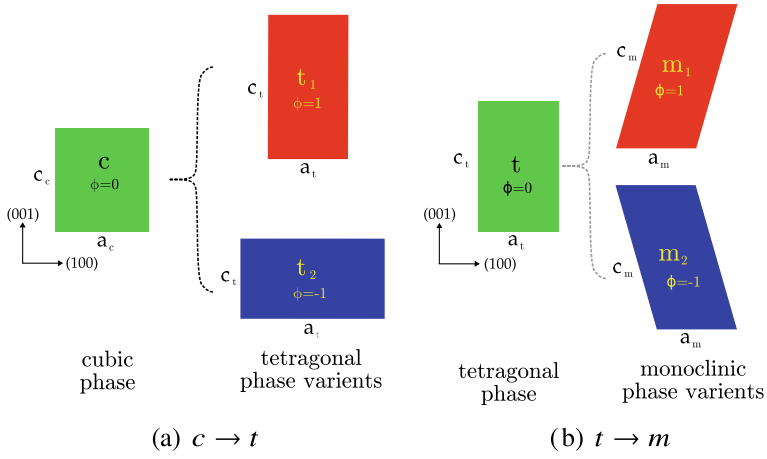

Fig. 21.3 Order parameter and lattice transformation representation of parent and product phases during martensitic phase transformation in zirconia ceramics. **a** $c \rightarrow t$ lattice transformation, **b** $t \rightarrow m$ lattice transformation schematic in two dimensions

the potential in this work and to model the phase transformation. A similar method is considered in representing parent c-phase and product variants of t-phase during $c \rightarrow t$ transformation.

In mechanics total strain tensor is decomposed into an elastic and an inelastic/transformation term, such as,

$$\boldsymbol{\epsilon} = \boldsymbol{\epsilon}_{\mathrm{el}} + \boldsymbol{\epsilon}_{\mathrm{tr}}(\tilde{\phi}). \tag{21.3}$$

Here $\boldsymbol{\epsilon}_{\mathrm{tr}}(\tilde{\phi})$ provides resultant transformation strain weighted with fraction of product phase $\varphi(\tilde{\phi})$. The modified order parameter $\tilde{\phi}$ is used instead of ϕ to avoid any unbounded solution which may lead to unphysical mechanical properties. This implies $\epsilon_{\mathrm{tr}}(0) = 0$ and $\epsilon_{\mathrm{tr}}(\pm 1) = \boldsymbol{\epsilon}_{\mathrm{tr}}^{m\pm}$ respectively. In same way fourth-rank effective elastic constants $\boldsymbol{E}_{\mathrm{eff}}$ can be written as fraction weighted with respect to product phase. The transformation/Bain strains and elastic constants are listed in Tables 21.1 and 21.2. For more detailed explanation on the PF method applied especially to simulation of zirconia material we refer to our previous work [16].

The Ginzburg-Landau equations are coupled to the basic equations of continuum mechanics by applying the week form of equilibrium of momentum in a FEM framework.

$$\boldsymbol{\nabla} \cdot \boldsymbol{\sigma} = 0. \tag{21.4}$$

The resulting second order partial differential equations for phase-field variable ϕ and displacement vector u_i are solved concurrently using the finite element method framework implemented in COMSOL multiphysics.

21.2.2 Model Setup

Since both the transformations $c \rightarrow t$ and $t \rightarrow m$ are martensitic, the aforementioned PF approach is used to describe both phase transformation scenarios in zirconia ceramics. It is known that, t-phase and m-phase crystal during $t \rightarrow m$ transformation share same crystal lattice points in a symmetrical manner leading to 12 possible orientation relations of parent lattice to product lattice in three dimensions (3 correspondences based on choice of lattice axis direction, two variants for each correspondence and two orientations for each variant). This is also similar to the case of c-phase and t-phase crystal during $c \rightarrow t$ transformation. In two dimensions the problem reduces to a simple set of two product crystal variants (see Fig. 21.3). The other cases of crystal transformation belong on the third dimension, so for simplification, they could be neglected from modeling. In $t \rightarrow m$ transformation this simple crystal lattice transformation set (see Fig. 21.3b) is enough to describe twin formation during transformation in two dimensions and thus could reproduce the effect of self accommodation in order to reduce the total strain energy of the system.

Since the specific domain setup differs in some cases of our simulations provided in the following subsections, they are discussed in detail in the corresponding

Table 21.1 Variant transformation strains involved in $c \rightarrow t$ and $t \rightarrow m$ transformation [8, 17, 18]

Lattice transformation	Transformation strain ϵ_{ij}
$c \rightarrow t_1$	$\epsilon_{\text{tr}}^{t1} = \begin{bmatrix} -0.0007 & 0 \\ 0 & 0.0197 \end{bmatrix}$
$c \rightarrow t_2$	$\epsilon_{\text{tr}}^{t2} = \begin{bmatrix} 0.0197 & 0 \\ 0 & -0.0007 \end{bmatrix}$
$t \rightarrow m_+$	$\epsilon_{\text{tr}}^{m+} = \begin{bmatrix} 0.012479 & 0.079614 \\ 0.079614 & 0.019139 \end{bmatrix}$
$t \rightarrow m_-$	$\epsilon_{\text{tr}}^{m-} = \begin{bmatrix} 0.012479 & -0.079614 \\ -0.079614 & 0.019139 \end{bmatrix}$

Table 21.2 Elastic stiffness (in GPa) of c-phase , t-phase and m-phase [19]

Phases	$\mathbf{E}_{11}$	$\mathbf{E}_{22}$	$\mathbf{E}_{33}$	$\mathbf{E}_{44}$	$\mathbf{E}_{55}$	$\mathbf{E}_{66}$	$\mathbf{E}_{12}$	$\mathbf{E}_{13}$	$\mathbf{E}_{16}$	$\mathbf{E}_{23}$	$\mathbf{E}_{26}$	$\mathbf{E}_{36}$	$\mathbf{E}_{45}$
c-phase	390	390	390	60	60	60	162	162	0	162	0	0	0
t-phase	327	327	264	59	59	59	100	62	0	62	0	0	0
m-phase	361	408	258	100	81	126	142	55	−21	196	31	−18	−23

subsections of selected results. Overall in common, we assume anisotropic elastic behaviour in both elastic and phase transformation domain in our simulations. The effective transformation strain and elastic constants at a material point inside the phase transformation domain are evaluated as a function of ϕ [16]. The description of anisotropy is necessary to capture variant orientation relationship and the effects of various external loading directions on MPT. The material parameters used in the model are listed in Tables 21.1 and 21.2.

21.2.3 Selected Results and Discussion

21.2.3.1 Phase Stability and Energy Barriers

Using CALPHAD [20] method an unambiguous representation of the temperature dependent Gibbs free energy values of individual phases from the thermodynamical aspect could be evaluated [21]. But the form of energy landscape for intermediate phase transition from parent to product phase is still ambiguous and is a missing piece of puzzle. Most of the phase-field methods rely on these energy landscape to reproduce a more relevant and accurate material behavior. There are two major methods used by phase-field to approximate the transformation path a common tangent

method [20] which expresses a linear behavior between parent and product phase minima. On other hand potential function methods [13, 22] utilize an non-linear analytical representation of path between parent and product phase minima. Both of these methods confide in phenomenological modeling of free energy based on the phase stability conditions. In this work a generic model for martensitic phase transformation developed by Levitas and Preston [14] is used and adapted for simulating zirconia ceramics material. We use $2-4-6$ potential function [16] method which is utilized to represent a non-linear behavior and exhibit a transition barrier based on thermo-mechanical conditions.

On the thermodynamic perspective of zirconia at ambient temperature, it is clear that the global minimum is at m-phase and the global maximum is at t-phase . So theoretically the metastable t-phase always tends to transform to stable m-phase . But in almost all commercial PSZ ceramics (refer MgO-ZrO_2micrographs from the book of Hannink et al. [18]) the t-phase is observed to be stable at ambient temperature. Multiple factors may cause such a stabilization, which include: stabilizer doping such as MgO, presence of residual stresses from prior $c \rightarrow t$ transformation, but also defects like dislocations and grain boundaries. Later in this work, the effect of residual stress is investigated. Here in this section we compare the potential functions from Mamivand et al. [11] and Levitas and Preston [14] commonly used in literature for modelling $t \rightarrow m$ transformations. We investigate the capabilities of these functions for such a stabilization.

The $2-4-6$ potential used by Mamivand et al. [11] for approximating the Gibbs energy contribution defines energy barrier just by the analytical function. The barrier is then levered by the enthalpy difference between the parent and product phase irrespective of temperature, see Fig. 21.4a. Even at ambient temperature the approximated Gibbs energy landscape provides an energy barrier considering only thermodynamic contribution by pure zirconia, which is in contradiction to true physical behaviour. In the case of Levitas and Preston [14] based formulation for temperatures below M_s the function doesn't exhibit any barrier for transformation.

At high temperature just above M_s (see Fig. 21.4d) the energy landscape calculated based on Mamivand's potential formulation shows local minima at the parent and product phase. For the same, a global maximum or energy barrier is visible at order parameter $\phi \approx 0.1$ (see $T < M_s$). But as the temperature increases this decreases the barrier, and after crossing the T_0 there remains an intermediate local minimum which is neither parent nor product phase, the local minimum is close to order parameter $\phi \approx 0.1$, see Fig. 21.4b, c. In contrast, Levitas type potential used in this work has no intermediate minimum rather provides a barrier between the parent and product phase for temperatures above M_s.

Based on Levitas et al. formulation, utilized in this work for zirconia ceramics at any temperature, a global/local minima is retained at the product phase. And for $T > M_s$ a local minimum is also retained in parent phase, see Fig. 21.4b, d. Thus the potential function used in this work results in a proper representation of zirconia ceramics material behaviour from a pure thermodynamic stand point.

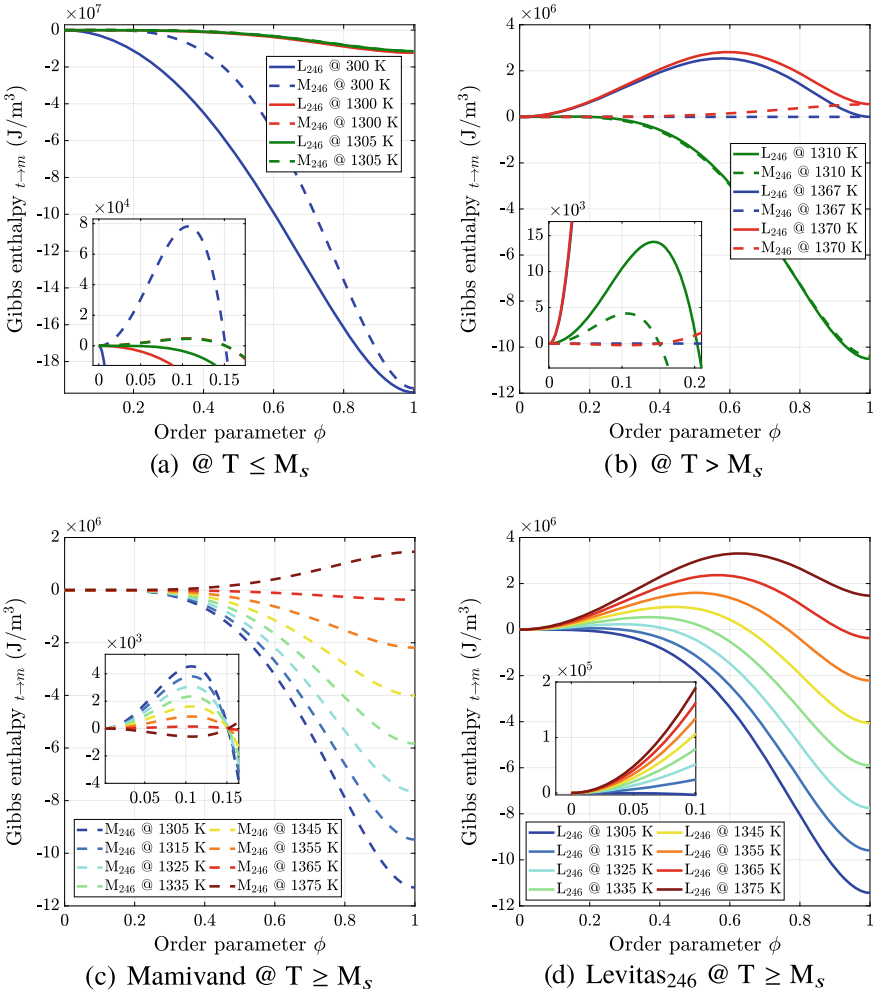

(a) @ T ≤ M$_s$ (b) @ T > M$_s$

(c) Mamivand @ T ≥ M$_s$ (d) Levitas$_{246}$ @ T ≥ M$_s$

Fig. 21.4 Comparison of estimated $2-4-6$ potential based thermodynamic Gibbs enthalpy $\psi_{\text{ch}}(\theta, \phi)$ as a function of order parameter during $t \to m$ transformation at various temperatures for Levitas and Preston [14] based model used for zirconia ceramics [16] to Mamivand et al. [11] model

21.2.3.2 Variant Selection by Energy Barriers

In this section we would like present distinctive differences in microstructure and evolution path between cooling induced and stress induced $t \to m$ transformations. We show that the different behaviour can be explained by the presence of an energy barrier in the Gibbs free enthalpy. In the latter case, sequential growth of monoclinic lamellae is observed because of possible variant selection based on energy barriers,

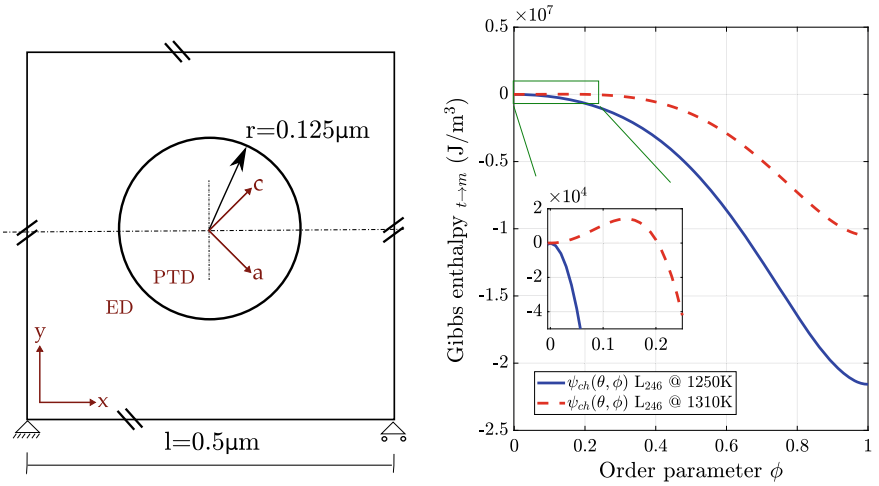

(a) Simulation domain setup (b) $\psi_{\text{ch}}(\theta, \phi)$ @ 1250 K and 1310 K

Fig. 21.5 **a** Representation of simulation domain with boundary conditions. Material coordinate system (abc) and geometrical coordinate system (xyz). Axis c and z are outward normal to the paper. **b** Comparison of stress-independent chemical free enthalpy

whereas cooling induced microstructure evolution is characterized by an almost homogeneous nucleation of the monoclinic phase.

For simulating different microstructure evolution, such a domain setup is chosen, where the t-phase lentils are stabilized in the cubic matrix after annealing. A single crystal setup with a square c-phase elastic domain (ED) of 0.5 μm × 0.5 μm with an embedded circular phase transformation domain (PTD) of radius 0.125 μm (see Fig. 21.5a) is created. As initial condition in PTD the tetragonal phase is superimposed with random noise on order parameter ϕ within a given range. The elastic domain here represents a cubic matrix surrounding a single t-phase particle. A circular form of embedded phase transformation domain is chosen in order to avoid any geometrical influence on the microstructure formation. The initial displacement is set zero in the whole domain. Additionally, a displacement periodic boundary condition is imposed at the boundaries. In order to mimic a rotated crystal around the b-axis (normal to the paper) (see Fig. 21.5a) the material parameters, transformation strain and elastic constants are transformed accordingly. Other common simulation and material parameters used are already discussed above and listed in Table 21.3.

For simulating stress induced transformation, we choose homogeneous isothermal conditions at 1310 K, above $M_s = 1305$ K. On the other hand, for cooling induced transformation we choose homogeneous isothermal condition at 1250 K below M_s. The Gibbs enthalpy landscapes based on pure thermodynamic contribution for both temperatures are compared in Fig. 21.5b.

Figure 21.6a–c show a cooling induced martensitic transformation in a single crystal, rotated by 45° around 'b'-axis (see Fig. 21.5a) with isothermal condition

Table 21.3 Input parameters used in $t \rightarrow m$ simulation

Description	Symbol	Value	Unit
m-phase start temperature	$M_s^{t\rightarrow m}$	1305	K
m-phase equilibrium temperature	$T_0^{t\rightarrow m}$	1367	K
Gradient energy coefficient	β	5×10^{-11}	J/m
Kinetic coefficient	L	2	m^3/Js
Material parameter	a	6	–

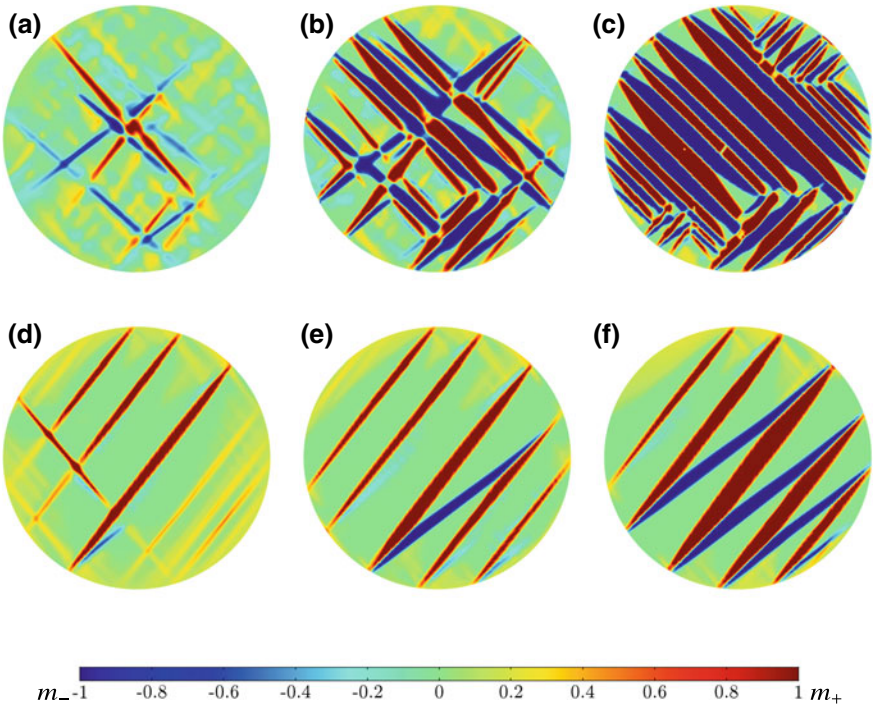

Fig. 21.6 A comparison between cooling induced case (top row (**a**–**c**)) and stress induced case (bottom row (**d**–**f**)). The color legend represents the order parameter ϕ. A sequential growth of lamella, observed during stress induced case due to variant selection based on external loading. Microstructure evolution snapshots at various stages of pseudo-time

below M_s at 1250 K. A surface plot inside the PTD shows the evolution of order parameter ϕ where the color legend represents, red being m^+, blue as m^- and green as t.

In cooling induced case there is no intermediate energy barrier between parent and product phase for transformation (see Fig. 21.5b) since the temperature is below M_s and here product m-phase is stable. So after initialization an almost homogeneous nucleation process takes place where all possible nucleation sites

of all possible variants are preferred to grow because of the adequate thermodynamic driving force (see Fig. 21.6a–d). In the numerical simulation, such condition will lead to different microstructure arrangements for different initialization. The evolved microstructures would be of mixed patterns where junction planes are parallel or orthogonal to 'c'-axis, which could be observed within a single grain (both orientation scenarios specified by Hannink et al. [18]). In Fig. 21.6c a large quantity of junction plane between two m-phase variants are orthogonal to 'c'-axis direction and there are small amount of junction planes (upper right, lower left and lower right) oriented parallel to 'c'-axis. Figures of both such lamella directions of twin formation have already been presented in the work of Hannink et al. [18] within a single t-phase lentil.

Simulation parameters here remain the same as cooling induced microstructure formation case, except the operating temperature being 1310 K above M_s and with $\sigma_{\text{app}} = 1$ GPa compression along 'b'-axis (see Fig. 21.5a). An initial superimposed noise with a range confined within the barrier of the Gibbs enthalpy landscape (see Fig. 21.5b) is applied.

Since the pure thermodynamic driving force is not adequate to trigger the transformation, there would not be martensitic evolution at all. As the compressive stress is superimposed additionally to the thermodynamic contribution, depending on the orientation of crystal relative to the applied stress some variants are preferred to grow by decreasing the energy barrier and some are obstructed by increasing the barrier. In other words, the energy landscape is skewed such that some variants have energy barrier and others don't, see Fig. 21.9a. This becomes clear by comparison between solid blue curve where no external stress is applied, and dashed red curve after application of external stress. Here in dashed red curve one variant experiences a barrier and the other doesn't. In this example (Fig. 21.6d–f) the m^+—red nucleation sites are preferred. At the initial stage, m^+ red variant nucleates and grows and meanwhile m^- blue variant vanishes because of the energy barrier. Additionally, by superimposing normal stress σ_{app} the driving force exceeds the minimum driving force required for transformation above M_s and triggers the transformation. Initially only m^+ variant lamellae grow such that they increase the strain energy. As the lamellae reach the grain boundary or imperfections, this piles up stress and triggers the m^- blue self accommodating variant thus reducing a part of the strain energy gained.

According to the investigation on MgO-$ZrO_2$by Kelly and Ball [17] the potential twinning plane/junction plane for twin related variants is either $[100]_m$/'a'-axis or $[001]_m$/'c'-axis, based on our model base axis orientation in Fig. 21.3. The resulting junction plane $[001]_m$/'c'-axis (see Fig. 21.6) is consistent with the experimental observations of [17, 18, 23, 24]. It is clear that among the two possible orientation scenarios specified by Hannink et al. [18] between m-phase and t-phase , junction plane parallel to 'c'-axis, twin-related variants retain some untransformed t-phase , which is also consistent with our observations. But the reason for possible conditions under which such oriented structure could be reproduced has not been discussed yet before.

21.2.3.3 Origin and Effect of Residual Stresses

The probable initial existence of residual stresses [25, 26] in the t-phase matrix as a result of the $c \rightarrow t$ transformation and their effect on $t \rightarrow m$ transformation is also not well understood yet. Such a residual stress is not yet considered in modeling for $t \rightarrow m$. In almost all commercial ceramics t-phase is stable at ambient temperature. Multiple factors may cause such a stabilization, here we look into the possibility and the effects of residual stress present prior to $t \rightarrow m$ transformation. In order to evaluate the peak residual stress which could be expected during $c \rightarrow t$ transformation, we simulate $c \rightarrow t$ transformation inside a c-phase matrix. The evolution of average pressure inside the t-phase lentil during transformation is tracked. This pressure is later used as an initial condition to mimic presence of residual stress during $t \rightarrow m$ transformation.

A simple model for single lentil setup within a square phase transformation domain is chosen with a size such that an average size of tetragonal lentil could be accommodated. This phase transformation domain is placed within an large elastic domain with c-phase . The transformation domain is initialized with c-phase and a circular seed of t-phase is placed at the centre of the phase transformation domain. The initialization and boundary conditions are set similar to those of model for $t \rightarrow m$. The domain is allowed to transform from cubic to tetragonal ($c \rightarrow t$) by undercooling at 1300 K without any external mechanical loading. The thermodynamic functions for evaluating Gibbs enthalpy values are taken from [11, 21]. We assume anisotropic elastic behavior for the whole domain. The elastic constants of respective phases are provided in Table 21.2. Based on the lattice constants from [8] one can evaluate the transformation strain (see Table 21.1), the critical temperature $M_s^{c\rightarrow t} = 1423$ K and equilibrium temperature $T_0^{c\rightarrow t} = 584$ K acquired from [27]. All other parameters are similar to those of previously explained model setup and listed in Tables 21.2 and 21.3.

Figure 21.7 shows single and multi-variant t-phase lentils evolving inside a c-phase matrix. As the initial tetragonal inclusion grows to lentil shape, its interior is under compression. On left half, the mean in-plane pressure $\sigma_{\bar{p}} = -(\sigma_{xx} + \sigma_{yy})/2$ is plotted. The legend red represents material under compression and blue represents material under tension. On the right half, the surface plot of order parameter ϕ is presented. Therein, green color represents c-phase and red color represents t-phase . In commercial ceramics, stable tetragonal lentils are observed at ambient temperature. So the peak mean in-plane pressure experienced by these t-phase lentils during their formation is considered to be the initial condition for $t \rightarrow m$ transformation. Figure 21.8 shows an evolution of the mean in-plane pressure versus the area fraction of a single t-phase lentil in an infinite domain. The numerical fluctuations during the initial stages are of no interest, but a strong saturation trend in the later stages is considerd resulting in a 0.21GPa mean in-plane pressure inside a lentil. Although a single lentil is considered here, in reality the cubic matrix is populated with multiple lentils so a superimposed stress state of multiple lentils will lead to higher value than the one estimated here.

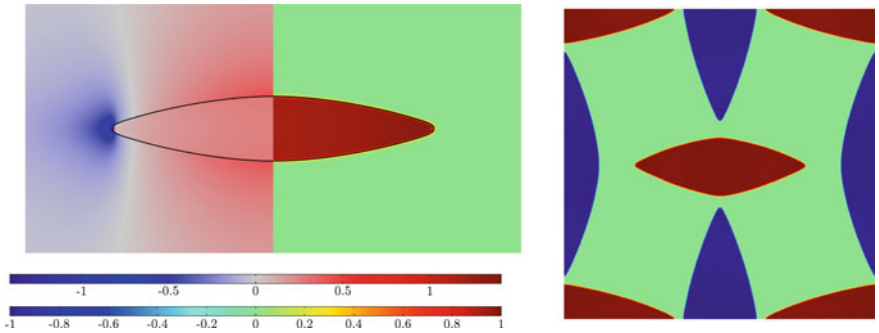

(a) Single lentil simulation (b) Multi lentil simulation

Fig. 21.7 Evolution of single-variant and multi-variant lentils during $c \rightarrow t$ transformation

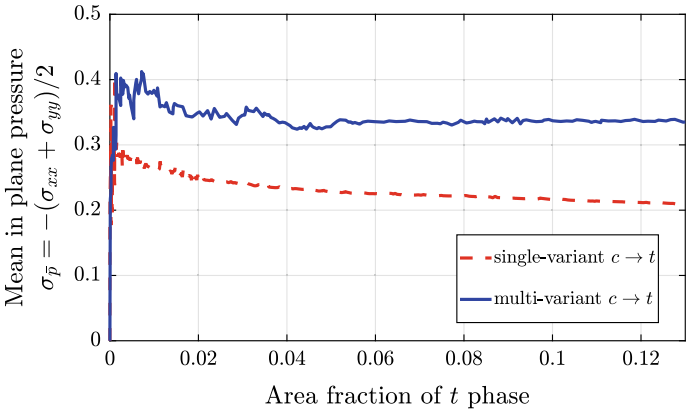

Fig. 21.8 Evolution of mean inplane pressure $\sigma_{\bar{p}}$ inside t-phase lentil versus fraction of t-phase

In order to evaluate the mean in-plane pressure on a multi lentil setup, a similar setup like a single lentil setup is choose. This setup represents a periodically placed RVE. The placement of the initial seeds are arranged such that they represent a proper microstructure. The seed at the center is replaced with a noise where an equal possibility is given to both variants to nucleate and grow. Because of the stress state of the neighboring t-phase lentils a selective nucleation of red variant takes place which is more favorable. The peak average pressure experienced by these t-phase lentils are tracked and plotted in Fig. 21.8. In this multi lentil setup the resulting mean in-plane pressure inside the lentils is 0.35 GPa which is larger than that of the single lentil simulation case. This gives a clear evidence of residual stress from prior $c \rightarrow t$ transformation.

As consequence of result from single and multi lentil simulations we choose $\approx$0.3 GPa as the initial pressure inside the lentil which is also consistent with the FEM based investigation on tetragonal inclusion in a cubic matrix by [26].

By applying a hydrostatic residual stress to the system an energy barrier is introduced thus allowing t-phase stability below M_s. This is visible in Fig. 21.9a on the solid blue line showing a local maximum near to the t-phase . The dotted green line shows the pure stress free chemical contribution of Gibbs enthalpy where the m-phase is stable and there is no energy barrier for $t \rightarrow m$ transformation. By superimposing an externally applied compressive stress one could skew the energy landscape, thus favouring a single variant so that stress induced transformation is possible below M_s temperature. A similar simulation setup for $t \rightarrow m$ transformation as described in the previous section is used. Additionally, for introducing a residual stress an equibiaxial type loading of $\sigma_{\bar{p}} = -0.3$ GPa is applied. The temperature is $T = 1250\,\text{K} < M_s$. Figure 21.9b shows the microstructure formed by stress induced transformation at 1250 K. It is clear that the residual stress from the $c \rightarrow t$ transformation contributed to the stability of t-phase . As the operating temperature decreases the residual stress required to introduce a barrier for transformation increases (see Fig. 21.10). By this it becomes clear that residual stress is not the only contribution involved in the t-phase stability.

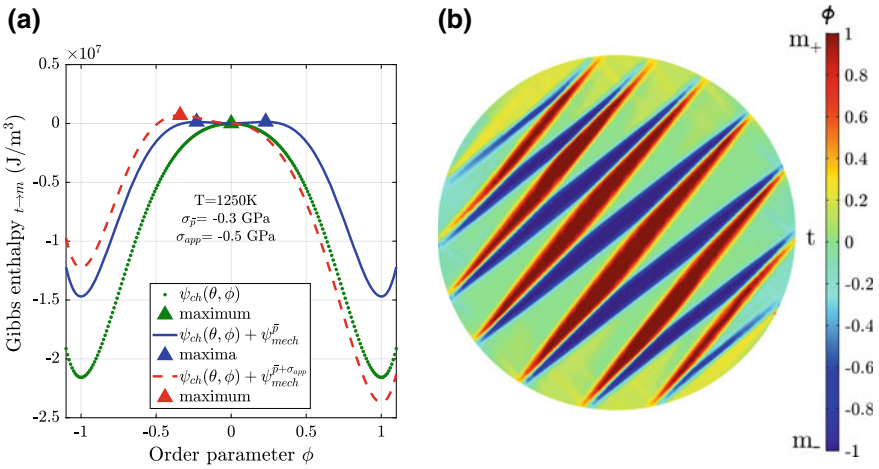

Fig. 21.9 Possibility of t-phase stability and stress induced transformation below M_s temperature at 1250 K, influence of residual stress and asymmetry in energy barrier by superimposing externally applied compression. On left, effect of residual stress and applied uniaxial compression on Gibbs enthalpy landscape below M_s at 1250 K. On right, surface plot of order parameter ϕ inside PTD. **a** Enthalpy landscape with various energy contributions, **b** surface plot of ϕ

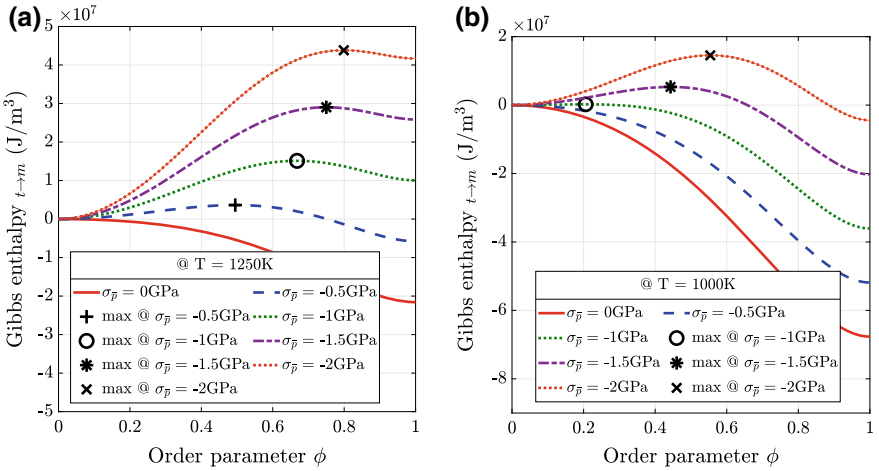

Fig. 21.10 Impact of residual stress on energy barrier at various temperatures. The intermediate local maxima showing presence of a energy barrier are represented with unique marker. A trend of increasing energy barrier with increasing residual stress is visible. **a** $T = 1250$ K, **b** $T = 100$ K

21.3 Mesomechanical Model

The understanding of how the microstructure influences the mechanical response is an essential pre-requisite for materials tailored to match specific requirements. The aim of the present work is to develop a transformation criterion for lenticular inclusions embedded into an elastic matrix based on the work of Hensl et al. [6] that accounts for the experimentally observed tension-compression asymmetry. This criterion is then used in order to investigate the influence of the microstructural features, such as size and shape of the inclusions, on the mechanical response. A homogenization approach, schematically depicted in Fig. 21.11, provides first insights into the response of a grain.

21.3.1 Transformation Criterion for a Single Precipitate Embedded in an Infinite Matrix

In this section we extend the transformation criterion developed in [6] in order to account for the pressure sensitivity of the material. This is done in a plane-strain setting based on a number of assumptions.

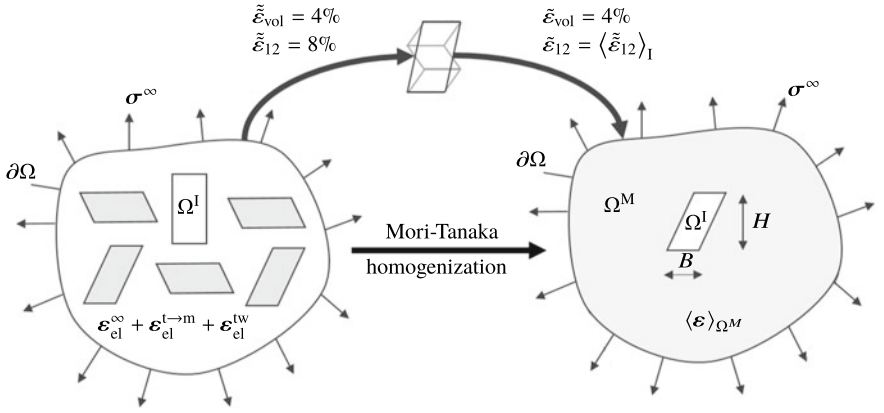

Fig. 21.11 Illustration of homogenization techniques used to model the effective material behavior of a polycrystal, influenced by the microstructure of each grain

21.3.1.1 Working Hypotheses

1. The elastic tensors of the cubic matrix and tetragonal precipitate (inclusion) are assumed to be isotropic and identical.
2. The inclusion is modeled as having a rectangular cross-section with width B, height H and aspect ratio $\alpha = H/B$ in its untransformed state.
3. The pseudo-twin structure after $t \to m$ transformation is modeled as a stack of equal-thickness lamellae, each of which carries a strain of $\tilde{\tilde{\varepsilon}}_{11} = \tilde{\tilde{\varepsilon}}_{22} = 2\%$ resulting in a relative volume change of $\tilde{\tilde{\varepsilon}}_{\mathrm{vol}} = 4\%$ and shear transformation strain $\tilde{\tilde{\varepsilon}}_{12} = \pm 8\%$ (specified in the crystallographic coordinate system[1]). Note that, while all lamellae are assumed to have the same thickness, the actual value of this thickness as well as the number of lamellae $2k$ are part of the solution and the corresponding effective shear strain of the inclusion is denoted by $\tilde{\boldsymbol{\varepsilon}}^{(k)} := \left\langle \tilde{\tilde{\varepsilon}} \right\rangle_{\mathrm{I}}$, where $\langle \cdot \rangle_{\mathrm{I}}$ is the averaging operator over the domain of the inclusion. Specifically, $\tilde{\varepsilon}_{11}^{(k)} = \tilde{\tilde{\varepsilon}}_{11}$, $\tilde{\varepsilon}_{22}^{(k)} = \tilde{\tilde{\varepsilon}}_{22}$ resulting in $\tilde{\varepsilon}_{\mathrm{vol}}^{(k)} = \tilde{\tilde{\varepsilon}}_{\mathrm{vol}} =: \tilde{\varepsilon}_{\mathrm{vol}}$ and $\tilde{\varepsilon}_{12}^{(k)} = \left\langle \tilde{\tilde{\varepsilon}}_{12} \right\rangle_{\mathrm{I}}$.
4. As the specific lamellae arrangement is not part of the solution, we estimate the elastic energy contribution resulting from the "zig-zag" at the inclusion boundary by assuming strictly alternating configuration (see Fig. 21.12).
5. We assume that phase transformation occurs when the Gibbs-enthalpy is equal in the transformed (G^{m}) and untransformed $\left(G^{\mathrm{t}}\right)$ states, i.e.,

$$\Delta G = G^{\mathrm{m}} - G^{\mathrm{t}} = \Delta E_{\mathrm{el}} + \Delta E_{\mathrm{ch}} + \Delta E_{\mathrm{sur}} \stackrel{!}{=} 0, \tag{21.5}$$

[1] If nothing else is specified, all tensor components in this work are referred to a coordinate system with orthonormal basis $(O, \{\boldsymbol{e}_1, \boldsymbol{e}_2\})$, where $\boldsymbol{e}_1$ is aligned along the tetragonal c-axis.

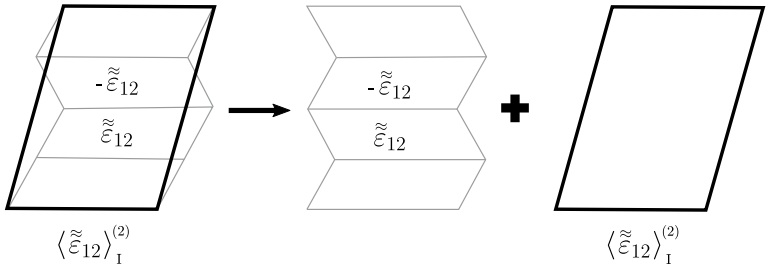

Fig. 21.12 Schematic illustration of the superposition scheme used to estimate the elastic energy of a "twinned" inclusion

where ΔE_{el} is the difference in the elastic strain energy, ΔE_{ch} is the difference in the chemical part of the bulk enthalpy and ΔE_{sur} is the difference in surface energy.

21.3.1.2 Energetic Contributions

The difference in surface energies is readily obtained as

$$\Delta E_{\mathrm{sur}} = 2(B + H)\Delta\beta_{\mathrm{I/M}} + (2k - 1)B\,\beta_{\mathrm{I/I}}, \tag{21.6}$$

where the first term is the contribution of the interface between inclusion and matrix and the second term corresponds to the newly formed interfaces between different monoclinic variants. Here $\beta_{\mathrm{I/M}}$ is the difference in surface energies between a tetragonal-cubic and a monoclinic-cubic interface and $\beta_{\mathrm{I/I}}$ is the surface energy for an interface between two different monoclinic variants. The difference in the chemical bulk enthalpy is given by

$$\Delta E_{\mathrm{ch}} = -BH\Delta H^{t\to m}\frac{T_0 - T}{T_0}, \tag{21.7}$$

where $\Delta H^{t\to m}$ is the specific transformation heat and T_0 is the equilibrium temperature between the tetragonal and monoclinic phases.

In general, the elastic strain energy is given by

$$E_{\mathrm{el}} = \frac{1}{2}\int_{\Omega} \boldsymbol{\sigma} : \boldsymbol{\varepsilon}_{\mathrm{el}}\,\mathrm{d}A. \tag{21.8}$$

In the untransformed case only the homogeneous far-field stress $\boldsymbol{\sigma}^{\infty}$ and the corresponding elastic strain $\boldsymbol{\varepsilon}_{\mathrm{el}}^{\infty} = \mathbb{C}^{-1} : \boldsymbol{\sigma}^{\infty}$ with elastic stiffness tensor $\mathbb{C}$ are present, i.e.,

$$E_{\mathrm{el}}^{\mathrm{t}} = \frac{1}{2}\int_{\Omega} \boldsymbol{\sigma}^{\infty} : \boldsymbol{\varepsilon}_{\mathrm{el}}^{\infty}\,\mathrm{d}A = \frac{1}{2}\boldsymbol{\sigma}^{\infty} : \boldsymbol{\varepsilon}_{\mathrm{el}}^{\infty}\int_{\Omega} \mathrm{d}A. \tag{21.9}$$

This energy is unbounded if the domain Ω is infinite. After $t \to m$ transformation and self-accommodation, additional elastic strains due to transformation $\boldsymbol{\varepsilon}_{\mathrm{el}}^{t\to m}$ and the formation of the lamellar structure $\boldsymbol{\varepsilon}_{\mathrm{el}}^{\mathrm{tw}}$ are introduced, i.e.,

$$\boldsymbol{\varepsilon}_{\mathrm{el}} = \boldsymbol{\varepsilon}_{\mathrm{el}}^{\infty} + \boldsymbol{\varepsilon}_{\mathrm{el}}^{t\to m} + \boldsymbol{\varepsilon}_{\mathrm{el}}^{\mathrm{tw}}. \tag{21.10}$$

The corresponding stress is

$$\boldsymbol{\sigma} = \boldsymbol{\sigma}^{\infty} + \boldsymbol{\sigma}^{t\to m} + \boldsymbol{\sigma}^{\mathrm{tw}} \tag{21.11}$$

and the energy difference between the transformed and untransformed states is immediately found to be

$$\Delta E_{\mathrm{el}} = E_{\mathrm{el}}^{\mathrm{m}} - E_{\mathrm{el}}^{\mathrm{t}} = \frac{1}{2}\int_{\Omega} \left[\left(\boldsymbol{\sigma}^{\infty} + \boldsymbol{\sigma}^{t\to m} + \boldsymbol{\sigma}^{\mathrm{tw}}\right) : \left(\boldsymbol{\varepsilon}_{\mathrm{el}}^{\infty} + \boldsymbol{\varepsilon}_{\mathrm{el}}^{t\to m} + \boldsymbol{\varepsilon}_{\mathrm{el}}^{\mathrm{tw}}\right) - \boldsymbol{\sigma}^{\infty} : \boldsymbol{\varepsilon}_{\mathrm{el}}^{\infty}\right] \mathrm{d}A. \tag{21.12}$$

Note that this difference is bounded, since the contribution of the homogeneous far-field stress cancels out and we find

$$\Delta E_{\mathrm{el}} = \underbrace{\boldsymbol{\sigma}^{\infty} : \int_{\Omega} \boldsymbol{\varepsilon}_{\mathrm{el}}^{t\to m}\,\mathrm{d}A}_{\Delta E_{\mathrm{el}}^{\mathrm{t}\to\mathrm{m},1}} + \underbrace{\boldsymbol{\sigma}^{\infty} : \int_{\Omega} \boldsymbol{\varepsilon}_{\mathrm{el}}^{\mathrm{tw}}\,\mathrm{d}A}_{\Delta E_{\mathrm{el}}^{\mathrm{tw},1}} + \underbrace{\frac{1}{2}\int_{\Omega} \boldsymbol{\sigma}^{t\to m} : \boldsymbol{\varepsilon}_{\mathrm{el}}^{t\to m}\,\mathrm{d}A}_{\Delta E_{\mathrm{el}}^{\mathrm{t}\to\mathrm{m},2}} + \underbrace{\int_{\Omega} \boldsymbol{\sigma}^{t\to m} : \boldsymbol{\varepsilon}_{\mathrm{el}}^{\mathrm{tw}}\,\mathrm{d}A}_{\Delta E_{\mathrm{el}}^{\mathrm{t}\to\mathrm{tw}}} + \underbrace{\frac{1}{2}\int_{\Omega} \boldsymbol{\sigma}^{\mathrm{tw}} : \boldsymbol{\varepsilon}_{\mathrm{el}}^{\mathrm{tw}}\,\mathrm{d}A}_{\Delta E_{\mathrm{el}}^{\mathrm{tw},2}}. \tag{21.13}$$

The evalution of the individual integrals is closely related to the procedure presented in [6], which in turn is based on the closed form solution for rectangular inclusions with eigenstrains [28].

It can be shown [6] that as a particular result of assuming equal-size monoclinic lamellae, $\Delta E_{\mathrm{el}}^{\mathrm{tw},1} = \Delta E_{\mathrm{el}}^{\mathrm{t}\to\mathrm{tw}} = 0$, while $\Delta E_{\mathrm{el}}^{\mathrm{tw},2}$ can be obtained in the form

$$\Delta E_{\mathrm{el}}^{\mathrm{tw},2} = -B^2 \frac{E\tilde{\tilde{\varepsilon}}_{12}^2}{4\pi k^2(1-\nu^2)} \underbrace{\sum_{\zeta=1}^{k}\sum_{\eta=1}^{k}\sum_{i=1}^{11} g_i\,(\zeta,\eta,\alpha,k)}_{F(\alpha,k)}, \tag{21.14}$$

where the $g_i\,(\zeta,\eta)$ are functions of the geometry of the inclusion and number of lamellae, which are listed in the appendix of [6]. In order to evaluate $\Delta E_{\mathrm{el}}^{\mathrm{t}\to\mathrm{m},1}$ we make use of the fact that in the domain of the inclusion Ω^{I} the elastic strain due to phase transformation can be computed as

$$\boldsymbol{\varepsilon}_{\mathrm{el}}^{t\to m} = \boldsymbol{\varepsilon}^{t\to m} - \tilde{\boldsymbol{\varepsilon}}^{(k)} \tag{21.15}$$

and can write

$$\Delta E_{\mathrm{el}}^{t\to m,1} = \boldsymbol{\sigma}^{\infty} : \int_{\Omega} \boldsymbol{\varepsilon}^{t\to m}\,\mathrm{d}A - \boldsymbol{\sigma}^{\infty} : \tilde{\boldsymbol{\varepsilon}}^{(k)} \int_{\Omega^{\mathrm{I}}} \mathrm{d}A \tag{21.16}$$

$$= \boldsymbol{\sigma}^{\infty} : \int_{\Omega} \boldsymbol{\varepsilon}^{t\to m}\,\mathrm{d}A - \boldsymbol{\sigma}^{\infty} : \tilde{\boldsymbol{\varepsilon}}^{(k)}\, BH. \tag{21.17}$$

Introducing the usual split into volumetric and deviatoric parts

$$\boldsymbol{\sigma}^{\infty} = \boldsymbol{s}^{\infty} - p^{\infty}\boldsymbol{I}, \quad \boldsymbol{\varepsilon}^{t\to m} = \boldsymbol{e}^{t\to m} + \frac{1}{3}\varepsilon_{\mathrm{vol}}^{t\to m}\boldsymbol{I}, \quad \tilde{\boldsymbol{\varepsilon}}^{(k)} = \tilde{\boldsymbol{e}}^{(k)} + \frac{1}{3}\tilde{\varepsilon}_{\mathrm{vol}}^{(k)}\boldsymbol{I}, \tag{21.18}$$

where $\boldsymbol{I}$ is the unit-tensor, and making use of working Assumption 3 we find

$$\Delta E_{\mathrm{el}}^{t\to m,1} = \boldsymbol{s}^{\infty} : \int_{\Omega} \boldsymbol{e}^{t\to m}\,\mathrm{d}A - p^{\infty} : \int_{\Omega} \varepsilon_{\mathrm{vol}}^{t\to m}\,\mathrm{d}A + \left(p^{\infty}\,\tilde{\varepsilon}_{\mathrm{vol}}^{(k)} - \boldsymbol{s}^{\infty} : \tilde{\boldsymbol{e}}^{(k)}\right) BH \tag{21.19}$$

$$= \boldsymbol{s}^{\infty} : \int_{\Omega} \boldsymbol{e}^{t\to m}\,\mathrm{d}A - p^{\infty} : \int_{\Omega} \varepsilon_{\mathrm{vol}}^{t\to m}\,\mathrm{d}A + \left(p^{\infty}\,\tilde{\varepsilon}_{\mathrm{vol}}^{(k)} - 2\sigma_{12}^{\infty}\,\tilde{\varepsilon}_{12}^{(k)}\right) BH. \tag{21.20}$$

The evaluation of the above integrals is more involved than may appear at the first glance, since the integrands are singular at every kink at the boundary of the inclusion, therefore integration is carried out using the same procedure that was applied in [6] by a transformation into equivalent line integrals

$$\Delta E_{\mathrm{el}}^{t\to m,1} = \sigma_{12}^{\infty} \lim_{r\to\infty} \int_0^{2\pi} [u_1 r\sin(\varphi) + u_2 r\cos(\varphi)]\,\mathrm{d}\varphi$$

$$- p^{\infty} \lim_{r\to\infty} \int_0^{2\pi} [u_1 r\cos(\varphi) + u_2 r\sin(\varphi)]\,\mathrm{d}\varphi + \left(p^{\infty}\,\tilde{\varepsilon}_{\mathrm{vol}}^{(k)} - 2\sigma_{12}^{\infty}\,\tilde{\varepsilon}_{12}^{(k)}\right) BH, \tag{21.21}$$

resulting in the relatively simple expression

$$\Delta E_{\mathrm{el}}^{t\to m,1} = \frac{BH}{2\,(1-\nu)}\left[(1-2\nu)\,p^{\infty}\tilde{\varepsilon}_{\mathrm{vol}}^{(k)} - \sigma_{12}^{\infty}\,\tilde{\varepsilon}_{12}^{(k)}\right], \tag{21.22}$$

where ν is POISSON's ratio. For further details on the integration procedure, cf. [6]. The remaining energy difference $\Delta E_{\mathrm{el}}^{t\to m,2}$ is calculated using a very similar procedure, resulting in

$$\Delta E_{\mathrm{el}}^{t\to m,2} = \frac{\mu}{1-\nu}BH\left[P_1\left(\tilde{\varepsilon}_{12}^{(k)}\right)^2 + \frac{2}{9}\frac{1-\nu+P_2}{1-2\nu}\left(\tilde{\varepsilon}_{\mathrm{vol}}^{(k)}\right)^2\right], \tag{21.23}$$

with

$$P_1 = \frac{1}{\pi}\left[\frac{1}{\alpha}\ln\left(1+\alpha^2\right) + \alpha\ln\left(1+\frac{1}{\alpha^2}\right)\right], \tag{21.24a}$$

$$P_2 = \frac{1}{\pi}\left[\arctan\left(\frac{1}{\alpha}\right) - \arctan(\alpha)\right]. \tag{21.24b}$$

Using a basis-free representation of the stress tensor we finally find

$$\begin{aligned}\Delta E_{\mathrm{el}} = {} & \frac{BH}{2\,(1-\nu)}\left[(1-2\nu)\,p^{\infty}\tilde{\varepsilon}_{\mathrm{vol}}^{(k)} - \left(\boldsymbol{e}_1\cdot\boldsymbol{\sigma}^{\infty}\cdot\boldsymbol{e}_2\right)\,\tilde{\varepsilon}_{12}^{(k)}\right] + \\ & + \frac{\mu}{1-\nu}BH\left[P_1\left(\tilde{\varepsilon}_{12}^{(k)}\right)^2 + \frac{2}{9}\frac{1-\nu+P_2}{1-2\nu}\left(\tilde{\varepsilon}_{\mathrm{vol}}^{(k)}\right)^2\right].\end{aligned} \tag{21.25}$$

21.3.1.3 The Transformation Criterion

Substituting the energy differences computed in the previous section into the transformation criterion (21.5) we find

$$\begin{aligned}\frac{1-\nu}{\alpha B^2\mu}\Delta G\left(\boldsymbol{\sigma}^{\infty}, T, k\right) = {} & \frac{1}{2\mu}\left[(1-2\nu)\,p^{\infty}\tilde{\varepsilon}_{\mathrm{vol}} - \left(\boldsymbol{e}_1\cdot\boldsymbol{\sigma}^{\infty}\cdot\boldsymbol{e}_2\right)\,\tilde{\varepsilon}_{12}^{(k)}\right] + \\ & + P_1\left(\tilde{\varepsilon}_{12}^{(k)}\right)^2 + \frac{2}{9}\frac{1-\nu+P_2}{1-2\nu}\tilde{\varepsilon}_{\mathrm{vol}}^2 - \frac{1}{2\pi k^2\alpha}\tilde{\varepsilon}_{12}^2 F(\alpha,k) \\ & - \Delta H^{\mathrm{t}\to\mathrm{m}}\frac{T_0-T}{T_0} \\ & + \frac{1-\nu}{\mu\alpha}\left[\frac{2}{B}\,(\alpha+1)\,\Delta\beta_{\mathrm{I/M}} + \frac{1}{B}\,(2k-1)\,\beta_{\mathrm{I/I}}\right] \stackrel{!}{=} 0,\end{aligned} \tag{21.26}$$

Note that (21.26) is not an equation that can be solved directly for the stress (at fixed temperature) or temperature (at fixed stress level) required to initiate the phase

transformation, since nearly all terms depend on the number of lamellae $2k$. This ambiguity is resolved by choosing the number of lamellae such that it minimizes the Gibbs free enthalpy in the transformed state, i.e.,

$$\hat{k} = \arg\min_{k \in \mathbb{N}^+} \Delta G\left(\boldsymbol{\sigma}^\infty, T, k\right). \tag{21.27}$$

Having thus determined a value for k, (21.26) can be rewritten e.g. as a criterion for the applied far-field stress at fixed temperature,

$$\left|\boldsymbol{e}_1 \cdot \boldsymbol{\sigma}^\infty \cdot \boldsymbol{e}_2\right| - (1-2\nu)\frac{\tilde{\varepsilon}_{\mathrm{vol}}}{\left|\tilde{\varepsilon}_{12}^{\left(\hat{k}\right)}\right|} p^\infty \stackrel{!}{=} C_1, \tag{21.28}$$

with

$$\begin{aligned} C_1 := \frac{1}{\left|\tilde{\varepsilon}_{12}^{\left(\hat{k}\right)}\right|}\Bigg(&2\mu P_1 \left(\tilde{\varepsilon}_{12}^{(k)}\right)^2 + \frac{4\mu}{9}\frac{1-\nu+P_2}{1-2\nu}\tilde{\varepsilon}_{\mathrm{vol}}^2 - \frac{\mu}{\pi k^2 \alpha}\tilde{\varepsilon}_{12}^2 F(\alpha, k) \\ &-2\mu\Delta H^{t\to m}\frac{T_0 - T}{T_0} + \frac{2(1-\nu)}{\alpha B}\left[2(\alpha+1)\Delta\beta_{\mathrm{I/M}} + (2k-1)\beta_{\mathrm{I/I}}\right]\Bigg). \end{aligned} \tag{21.29}$$

For future reference we note that in the present scenario the far-field stress is at the same time the average stress over the whole domain $\langle\boldsymbol{\sigma}\rangle$ and the average matrix stress $\langle\boldsymbol{\sigma}\rangle_{\Omega^{\mathrm{M}}}$. Since in a general setting the inclusion will transform depending on the stress in the surrounding matrix, we can reinterpret the criterion (21.28) and write

$$\left|\boldsymbol{e}_1 \cdot \langle\boldsymbol{\sigma}\rangle_{\Omega^{\mathrm{M}}} \cdot \boldsymbol{e}_2\right| - (1-2\nu)\frac{\tilde{\varepsilon}_{\mathrm{vol}}}{\left|\tilde{\varepsilon}_{12}^{\left(\hat{k}\right)}\right|} \langle p\rangle_{\Omega^{\mathrm{M}}} \stackrel{!}{=} C_1. \tag{21.30}$$

21.3.2 Uniaxial Loading

In this section we apply the transformation criterion to uniaxial loading conditions in order to investigate the tension-compression asymmetry predicted by the model as well as geometric effects.

21.3.2.1 Orientation Dependence of the Transformation Stress

In the case of uniaxial loading, i.e., $\boldsymbol{\sigma}^{\infty} = \bar{\sigma}_{11}^{\infty}\, \bar{\boldsymbol{e}}_1 \otimes \bar{\boldsymbol{e}}_1$, we find

$$\boldsymbol{e}_1 \cdot \boldsymbol{\sigma}^{\infty} \cdot \boldsymbol{e}_2 = \bar{\sigma}_{11}^{\infty}\, (\boldsymbol{e}_1 \cdot \bar{\boldsymbol{e}}_1)(\bar{\boldsymbol{e}}_1 \cdot \boldsymbol{e}_2) = \frac{1}{2}\bar{\sigma}_{11} \sin(2\varphi) \quad \text{and} \quad p^{\infty} = -\frac{1}{3}\bar{\sigma}_{11}, \tag{21.31}$$

where φ is the angle enclosed between the crystallographic a-axis and the direction of loading. The transformation criterion (21.28) reduces to

$$\left|\bar{\sigma}_{11}^{\infty}\right| = \frac{C_1}{\underbrace{\frac{1}{2}\sin(2\varphi) \pm \frac{1}{3}(1-2\nu)\dfrac{\tilde{\varepsilon}_{\mathrm{vol}}}{\left|\tilde{\varepsilon}_{12}^{(\hat{k})}\right|}}_{=:C_2}} =: \sigma_{\mathrm{tr}}, \tag{21.32}$$

where the positive sign holds for tensile and the negative for compressive loading. Es expected, the stress required to initiate phase transformation strongly depends on the orientation of the inclusion relative to the applied load and is minimal if the tetragonal c-axis is aligned along the direction of maximum shear (see Fig. 21.13). Due to the increase in volume during the phase transition an asymmetry between tensile and compressive loading is observed. Further, it is clear from Fig. 21.13 that, while under sufficiently large tensile loading all inclusions will transform, this is not true in compression. In that case no transformation will occur if the misalignment between the tetragonal a-axis and the loading direction is less than $\varphi_{\mathrm{lim}} \approx 8°$. As a consequence, the maximal achievable transformation strain in a texture-free polycrystal is larger under tensile loading.

21.3.2.2 Sensitivity with Respect to the Inclusion Size, Aspect Ratio and Interfacial Energy

Is is clear that the critical stress to initiate phase transformation depends not only on the orientation of the inclusion relative to the applied load as discussed above, but among other parameters also on its geometry and assumptions concerning the interface energy between monoclinic lamellae. The effect of these parameters is investigated here under unaxial compression for a fixed orientation $\varphi = 45°$ by varying the values given in Table 21.4 in the range of $\pm 10\%$. The results are shown in Figs. 21.14, 21.15 and 21.16 and concur to the expectations: The transformation stress decreases with increasing size B and aspect ratio α of the inclusions and increases with increasing surface energy $\beta_{\mathrm{I/I}}$.

The sensitivity to the inclusion size and shape is particularly pronounced; for $\alpha = 5$ a change in B from 29 to 24 nm results in a change in transformation stress

of 250% in relative terms (see Fig. 21.14). A similar effect is achieved by changing the aspect ratio from 6 to 4 (see Fig. 21.15). Further, it should be noted that the transformation stress abruptly changes at certain values of B. This effect is due to

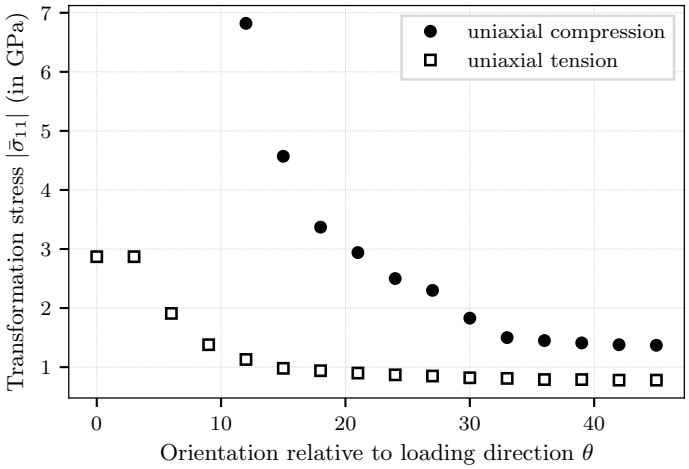

Fig. 21.13 Absolute value of the uniaxial stress necessary to induce phase transformation in dependence on the grain orientation φ with respect to the direction of external loading

Table 21.4 Baseline for the material parameters

B	α	E	ν	$\beta_{\mathrm{I/I}}$	$\Delta\beta_{\mathrm{I/M}}$	$\Delta H^{t\to m}$	T_0	T
36 nm	5.0	181 GPa	0.3	0.39 J/m^2 [25]	0.79 J/m^2 [25]	282 J/m^3 [29]	1150 K [30, 31]	22 K

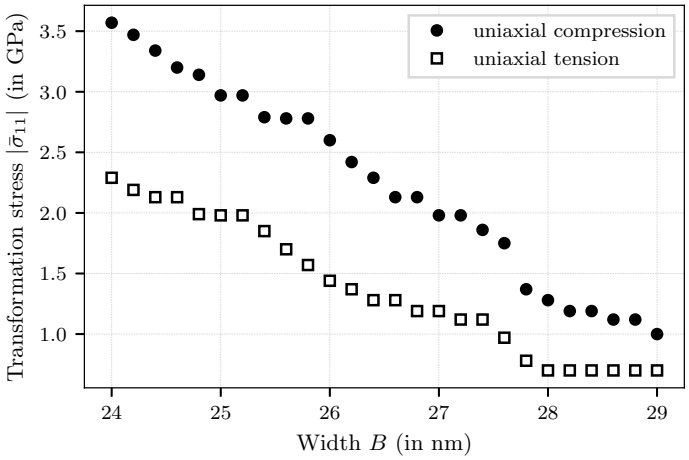

Fig. 21.14 Influence of the inclusion size B on the transformation stress under uniaxial compression for inclusions oriented under $\theta = 45°$ with respect to the direction of external loading

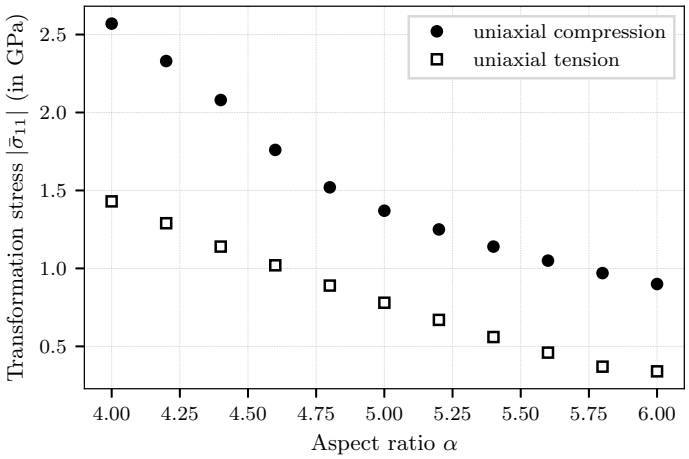

Fig. 21.15 Influence of the inclusion aspect ratio α on the transformation stress under uniaxial tension and compression for inclusions oriented under $\theta = 45°$ with respect to the direction of external loading

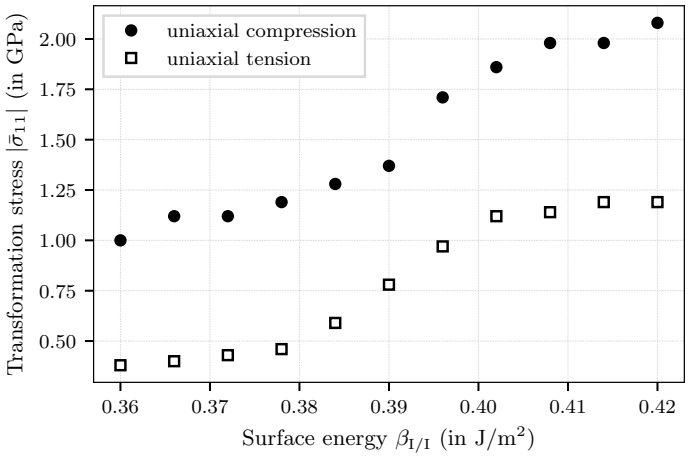

Fig. 21.16 Influence of the surface energy $\beta_{\mathrm{I/I}}$ between different monoclinic variants on the transformation stress under uniaxial tension and compression for inclusions oriented under $\theta = 45°$ with respect to the direction of external loading

the discrete nature of the optimization problem (21.27) and a direct consequence of our assumptions concerning the post-transformation microstructure; every jump of the transformation stress corresponds to a change in number of lamellae k and therefore to a change in microstructure.

21.4 Homogenization Within an Infinite Grain

The transformation criterion developed in the previous section can be used to describe the effective mechanical response of a PSZ grain with a volume fraction f_t of tetragonal inclusions, i.e. to relate the average stress $\langle\boldsymbol{\sigma}\rangle = \boldsymbol{\sigma}^\infty$ and the average strain $\langle\boldsymbol{\varepsilon}\rangle$ via an effective elastic stiffness tensor $\langle\mathbb{C}\rangle\left(\langle\boldsymbol{\sigma}\rangle_{\mathcal{B}_M}, T\right)$ in the form

$$\langle\dot{\boldsymbol{\sigma}}\rangle = \langle\mathbb{C}\rangle\left(\langle\boldsymbol{\sigma}\rangle_{\mathcal{B}_M}, T\right) : \langle\dot{\boldsymbol{\varepsilon}}\rangle, \tag{21.33}$$

where $\langle\boldsymbol{\sigma}\rangle_{\mathcal{B}_M}$ is the average matrix stress, which accounts for the interaction between the inclusions in accordance with Mori-Tanaka's method. In the case of monodispersed inclusions of size $\hat{B}$ the average matrix stress is given directly by [32]

$$\langle\boldsymbol{\sigma}\rangle_{\mathcal{B}_M} = \boldsymbol{\sigma}^\infty - f_\mathrm{m}\left(\langle\boldsymbol{\sigma}\rangle_{\mathcal{B}_M}, T\right)\mathbb{C}^\mathrm{M} : (\mathbb{S} - \mathbb{I}) : \tilde{\boldsymbol{\varepsilon}}^{(k)}\left(\langle\boldsymbol{\sigma}\rangle_{\mathcal{B}_M}, T, \hat{B}\right), \tag{21.34}$$

with monoclinic volume fraction $f_\mathrm{m}\left(\langle\boldsymbol{\sigma}\rangle_{\mathcal{B}_M}, T\right)$, elastic stiffness of the matrix $\mathbb{C}^\mathrm{M} = \mathbb{C}$ and ESHELBY tensor $\mathbb{S}$. Together with the transformation criterion (21.30) this equation can be used to determine the transformation strain in the inclusions, the average matrix stress and the monoclinic phase content. As the volume expansion during $t \to m$ transformation increases the tensile stresses in the matrix, which in turn facilitate the transformation, $f_\mathrm{m}\left(\langle\boldsymbol{\sigma}\rangle_{\mathcal{B}_M}, T\right) = f_\mathrm{t}$ immediately after the onset of the transformation and the process is autocatalytic. The corresponding effective elastic stiffness tensor is [33]

$$\begin{aligned}\langle\mathbb{C}\rangle\left(\langle\boldsymbol{\sigma}\rangle_{\mathcal{B}_M}, T, \hat{B}\right) = \mathbb{C}^\mathrm{M} + f_\mathrm{m}\left(\langle\boldsymbol{\sigma}\rangle_{\mathcal{B}_M}, T\right)\left[\mathbb{C}^\mathrm{I}\left(\tilde{\boldsymbol{\varepsilon}}^{(k)}\left(\langle\boldsymbol{\sigma}\rangle_{\mathcal{B}_M}, T, \hat{B}\right)\right) - \mathbb{C}^\mathrm{M}\right] : \\ : \{\mathbb{T}\} : \left[\left(1 - f_\mathrm{m}\left(\langle\boldsymbol{\sigma}\rangle_{\mathcal{B}_M}, T\right)\right)\mathbb{I} + f_\mathrm{m}\left(\langle\boldsymbol{\sigma}\rangle_{\mathcal{B}_M}, T\right)\{\mathbb{T}\}\right]^{-1},\end{aligned} \tag{21.35}$$

where $\mathbb{I}$ is the 4th-order identity, $\mathbb{C}^\mathrm{I}\left(\tilde{\boldsymbol{\varepsilon}}^{(k)}\left(\langle\boldsymbol{\sigma}\rangle_{\mathcal{B}_M}, T, \hat{B}\right)\right)$ the elastic (tangent) stiffness of the inclusions,

$$\begin{aligned}\mathbb{T}\left(\tilde{\boldsymbol{\varepsilon}}^{(k)}\left(\langle\boldsymbol{\sigma}\rangle_{\mathcal{B}_M}, T, B\right)\right) := \Big[\mathbb{I} + \mathbb{S} : \left(\mathbb{C}^\mathrm{M}\right)^{-1} \\ : \left[\mathbb{C}^\mathrm{I}\left(\tilde{\boldsymbol{\varepsilon}}^{(k)}\left(\langle\boldsymbol{\sigma}\rangle_{\mathcal{B}_M}, T, B\right)\right) - \mathbb{C}^\mathrm{M}\right]\Big]^{-1}\end{aligned} \tag{21.36}$$

and $\{\cdot\}$ denotes the orientation average. It is well known [18] that there exists an orientation relationship between the tetragonal inclusions and the cubic parent lattice such that the principal directions of the unit cells coincide, i.e., in a two dimensional scenario two families of inclusions (denoted by subscripts $\rightarrow$ and $\uparrow$) with mutually orthogonal c-axes exist in each grain. As a consequence, we find

$$\{\mathbb{T}\} = \frac{1}{2}\left(\mathbb{T}^{\rightarrow} + \mathbb{T}^{\uparrow}\right). \tag{21.37}$$

Choosing an orthonormal basis such that $\boldsymbol{e}_1$ is aligned along the c-axis of inclusion family $\rightarrow$, we find the following non-vanishing components of the ESHELBY tensors $\mathbb{S}^{\rightarrow}$ and $\mathbb{S}^{\uparrow}$

$$S^{\rightarrow}_{1111} = \frac{1}{2}\left[P_1 - (2P_2 + P_3)\right], \qquad S^{\rightarrow}_{1122} = -\frac{1}{2}\left[P_1 + (2P_2 + P_3)\right], \tag{21.38a}$$

$$S^{\rightarrow}_{2211} = -\frac{1}{2}\left[P_1 - (2P_2 + P_3)\right], \quad S^{\rightarrow}_{2222} = \frac{1}{2}\left[P_1 + (2P_2 + P_3)\right], \tag{21.38b}$$

$$S^{\rightarrow}_{1212} = \frac{1}{2}P_1, \qquad S^{\uparrow}_{1111} = \frac{1}{2}\left[P_1 + (2P_2 + P_3)\right], \tag{21.38c}$$

$$S^{\uparrow}_{1122} = -\frac{1}{2}\left[P_1 - (2P_2 + P_3)\right], \quad S^{\uparrow}_{2211} = -\frac{1}{2}\left[P_1 + (2P_2 + P_3)\right], \tag{21.38d}$$

$$S^{\uparrow}_{2222} = \frac{1}{2}\left[P_1 - (2P_2 + P_3)\right], \quad S^{\uparrow}_{1212} = \frac{1}{2}P_1, \tag{21.38e}$$

with P_1, P_2 defined in (21.24) and

$$P_3 = \frac{1}{\pi}\left[\frac{1}{\alpha}\ln\left(1+\alpha^2\right) - \alpha\ln\left(1+\frac{1}{\alpha^2}\right)\right]. \tag{21.39}$$

Prior to the $t \rightarrow m$ transformation $\mathbb{C}^{\mathrm{I}} = \mathbb{C}$ with bulk modulus K and shear modulus μ. To complete the formulation, assumptions concerning post-transformation behavior of $\mathbb{C}^{\mathrm{I}}$ are required, specifically

1. the elastic properties of the monoclinic and tetragonal phase are identical,
2. as long as $\left|\tilde{\varepsilon}^{(k)}_{12}\right| < \tilde{\tilde{\varepsilon}}_{12}$, the inclusions have no resistance to shear parallel to the c-axis, i.e. in the $\boldsymbol{e}_1 \otimes \boldsymbol{e}_2$-direction.

As a consequence we can write the (tangent) elastic stiffness of the inclusion in Voigt notation referring to the usual crystallographic coordinate system as

$$\mathbb{C}^{\mathrm{I}} = \begin{bmatrix} C^{\mathrm{I}}_{1111} & C^{\mathrm{I}}_{1122} & 0 \\ C^{\mathrm{I}}_{1122} & C^{\mathrm{I}}_{1111} & 0 \\ 0 & 0 & C^{\mathrm{I}}_{1212}\left(\tilde{\boldsymbol{\varepsilon}}^{(k)}\left(\langle\boldsymbol{\sigma}\rangle_{\mathcal{B}_M}, T, B\right)\right) \end{bmatrix}_{\boldsymbol{e}_i\otimes\boldsymbol{e}_j\otimes\boldsymbol{e}_k\otimes\boldsymbol{e}_l} \tag{21.40}$$

with

$$C^{\mathrm{I}}_{1111} = K + \frac{4}{3}\mu, \qquad C^{\mathrm{I}}_{1122} = K - \frac{2}{3}\mu,$$

and

$$C^{\mathrm{I}}_{1212}\left(\tilde{\boldsymbol{\varepsilon}}^{(k)}\left(\langle\boldsymbol{\sigma}\rangle_{\mathcal{B}_M}, T, B\right)\right) = \begin{cases}\mu & \left|\tilde{\varepsilon}^{(k)}_{12}\left(\langle\boldsymbol{\sigma}\rangle_{\mathcal{B}_M}, T, B\right)\right| = \tilde{\tilde{\varepsilon}}_{12},\\ 0 & \text{else.}\end{cases} \tag{21.41}$$

Under these assumptions we obtain from (21.35)

1. before the onset of transformation ($f_{\mathrm{m}}\left(\langle\boldsymbol{\sigma}\rangle_{\mathcal{B}_M}, T\right) = 0$)

$$\langle\mathbb{C}\rangle\left(\langle\boldsymbol{\sigma}\rangle_{\mathcal{B}_M}, T, \hat{B}\right) = \mathbb{C}, \tag{21.42}$$

2. after the onset of transformation ($f_{\mathrm{m}}\left(\langle\boldsymbol{\sigma}\rangle_{\mathcal{B}_M}, T\right) = f_{\mathrm{t}}$)

$$\langle\mathbb{C}\rangle\left(\langle\boldsymbol{\sigma}\rangle_{\mathcal{B}_M}, T, \hat{B}\right) = \begin{bmatrix} K + \left[\frac{4}{3} - Z_1(\varphi, f_{\mathrm{t}})\right]\mu & K - \left[\frac{2}{3} - Z_1(\varphi, f_{\mathrm{t}})\right]\mu & 0 \\ K - \left[\frac{2}{3} - Z_1(\varphi, f_{\mathrm{t}})\right]\mu & K + \left[\frac{4}{3} - Z_1(\varphi, f_{\mathrm{t}})\right]\mu & 0 \\ 0 & 0 & \left[1 - Z_2(\varphi, f_{\mathrm{t}})\right]\mu \end{bmatrix}, \tag{21.43}$$

where

$$Z_1(\varphi, f_{\mathrm{t}}) := Z(f_{\mathrm{t}})\sin^2(2\varphi), \qquad Z(f_{\mathrm{t}})\cos^2(2\varphi), \tag{21.44}$$

$$Z_2(\varphi, f_{\mathrm{t}}) := Z(f_{\mathrm{t}}) = \frac{f_{\mathrm{t}}}{1 - [1 - f_{\mathrm{t}}]P_{\mathrm{l}}}, \qquad \cos\varphi = \boldsymbol{e}_1 \cdot \bar{\boldsymbol{e}}_1 \tag{21.45}$$

3. after the transformation shear reaches its maximum value $\tilde{\tilde{\varepsilon}}_{12}$,

$$\langle\mathbb{C}\rangle\left(\langle\boldsymbol{\sigma}\rangle_{\mathcal{B}_M}, T, \hat{B}\right) = \mathbb{C}. \tag{21.46}$$

21.5 Continuum Mechanics Approach

A pragmatic engineering approach to phase transition is a phenomenological modeling based on non-linear constitutive laws in the framework of continuum mechanics. The fundamentals are outlined e.g. in [34]. In particular for partially stabilized zirconia (PSZ), such a model was developed by Sun et al. [29]. Based on the concept of representative volume element (RVE) and the Hill-Rice internal variable theory [35], this model provides a set of constitutive equations for the inelastic deformations caused by tetragonal-monoclinic $t \rightarrow m$ phase transformation as function of monoclinic volume fraction. The model is restricted to a material point only. The authors of [29] did not realize an implementation of their model into a numerical tool to solve a boundary value problem for applications to real structures of PSZ. Therefore, in the present work, the Sun model was implemented into the finite ele-

ment code ABAQUS [36] to allow simulations of the TRIP-matrix composite as will be reported in Chap. 22.

Due to missing quantitative data for the model parameters Sun et al. [29] introduced instead of this an additional hardening term in the transformation condition, which is limited to the special case of proportional mechanical loading under isothermal conditions. Another weakness of this model is the assumption and averaging of homogeneously distributed microscopic quantities over the RVE. Therefore, in Mehlhorn et al. [37] the basic concept of the Sun model has been extended to capture not only the mechanical but as well the thermally induced phase transformation and thermal expansion to simulate thermomechanical processes. Moreover, the influence of the size of transformable tetragonal particles in the cubic matrix has been incorporated. The basic assumptions and the specific formulation of the model within a thermodynamic framework will be presented in the following.

21.5.1 Constitutive Model for Phase Transformation in PSZ

21.5.1.1 Homogenization of PSZ Material

To find the effective material behavior, a RVE is considered with two spatially discrete components, see Fig. 21.17. The first component, called *matrix*, contains two crystallographic phases: the untransformable cubic zirconia and transformable, tetragonal particles embedded in the cubic phase. The second component, denoted as *inclusions*, contains monoclinic zirconia particles, which are generated by phase transformation from their metastable tetragonal parents when the RVE is sufficiently high loaded.

The micro-scale field quantities inside the RVE are denoted with lower case letters, such as the stress $\boldsymbol{\sigma}$ and the strain $\boldsymbol{\epsilon}$. By calculating the volume average of these microscopic quantities (denoted by the operator $\langle \cdot \rangle$), the respective macroscopic quantities are found, which are referred to with upper case letters $\boldsymbol{\Sigma}$ and $\boldsymbol{E}$. The

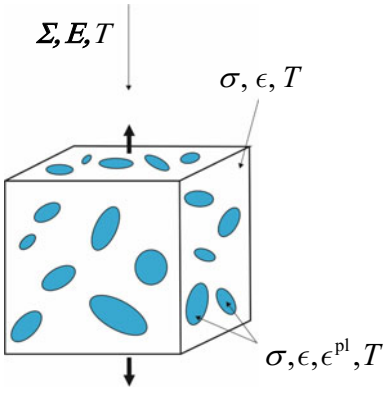

Fig. 21.17 Representative volume element of PSZ: matrix of cubic and tetragonal phase, inclusions of monoclinic particles

temperature T is assumed to be homogeneously distributed in the RVE. We denote the RVE domain with $\mathcal{B}_R$, the matrix and inclusion subdomains with $\mathcal{B}_M$ and $\mathcal{B}_I$, and their volumes with V_R, V_M and V_I, respectively. Thus, the relative volume fraction of transformed material is the basic internal variable calculated by

$$f_{\mathrm{m}} = V_I / V_R. \tag{21.47}$$

The macroscopic stress tensor is obtained by volume averaging as

$$\boldsymbol{\Sigma} = \langle \boldsymbol{\sigma} \rangle_{\mathcal{B}_R} = \frac{1}{V_R} \int_{\mathcal{B}_R} \boldsymbol{\sigma} \, \mathrm{d}V = f_{\mathrm{m}} \, \langle \boldsymbol{\sigma} \rangle_{\mathcal{B}_I} + (1 - f_{\mathrm{m}}) \, \langle \boldsymbol{\sigma} \rangle_{\mathcal{B}_M} . \tag{21.48}$$

The strain tensors can be decomposed into an elastic and plastic part $\boldsymbol{E} = \boldsymbol{E}^{\mathrm{el}} + \boldsymbol{E}^{\mathrm{pl}}$ and $\boldsymbol{\epsilon} = \boldsymbol{\epsilon}^{\mathrm{el}} + \boldsymbol{\epsilon}^{\mathrm{pl}}$, respectively. Using Hooke's law, the stress-strain relation for the RVE is determined by the elastic stiffness tensor $\mathbb{C}$

$$\boldsymbol{E}^{\mathrm{el}} = \mathbb{C}^{-1} : \boldsymbol{\Sigma} = \mathbb{C}^{-1} : \langle \boldsymbol{\sigma} \rangle_{\mathcal{B}_R} = \left\langle \mathbb{C}^{-1} : \boldsymbol{\sigma} \right\rangle_{\mathcal{B}_R} = \langle \boldsymbol{\epsilon} \rangle_{\mathcal{B}_R} . \tag{21.49}$$

The transformation strains exist only in the monoclinic inclusions and consist of a volumetric (dilatational) and a shear (deviatoric) component. This results in a macroscopic strain tensor

$$\boldsymbol{E}^{\mathrm{pl}} = \boldsymbol{E}^{\mathrm{pd}} + \boldsymbol{E}^{\mathrm{ps}} = f_{\mathrm{m}} \left\langle \boldsymbol{\epsilon}^{\mathrm{pd}} \right\rangle_{\mathcal{B}_I} + f_{\mathrm{m}} \left\langle \boldsymbol{\epsilon}^{\mathrm{ps}} \right\rangle_{\mathcal{B}_I} . \tag{21.50}$$

The microscopic volume dilatation $\boldsymbol{\epsilon}^{\mathrm{pd}}$ is assumed to be stress independent and constant ($\boldsymbol{I}$ denotes the rank-two unit tensor).

$$\boldsymbol{\epsilon}^{\mathrm{pd}} = \left\langle \boldsymbol{\epsilon}^{\mathrm{pd}} \right\rangle_{\mathcal{B}_I} = \frac{1}{3} \mathrm{tr}(\boldsymbol{\epsilon}^{\mathrm{pl}}) \boldsymbol{I}, \tag{21.51}$$

The shear component of the transformation strain $\boldsymbol{\epsilon}^{\mathrm{ps}}$, when averaged over a monoclinic volume element $d\mathcal{B}_I$, is proportionally related to the deviatoric stress $\boldsymbol{s}^M$ acting in the matrix material as follows

$$\boldsymbol{\epsilon}^{\mathrm{ps}} = \left\langle \boldsymbol{\epsilon}^{\mathrm{ps}} \right\rangle_{d\mathcal{B}_I} = A \frac{\boldsymbol{s}^M}{\sigma^M_{\mathrm{eq}}} \tag{21.52}$$

with the equivalent v.-Mises matrix stress σ^M_{eq}. The constant material parameter A describes the strength of the constraint imposed on the transformed monoclinic inclusions by the surrounding elastic matrix. The matrix stress $\boldsymbol{\sigma}^M$ is related to the macroscopic stress $\boldsymbol{\Sigma}$ acting on the RVE, via the elastic stiffness $\mathbb{C}$ and the amount f_{m} of transformed phase, and can be calculated by an Eshelby approach (see e.g. [38]) and the Mori-Tanaka homogenization scheme.

In addition, we consider a thermal expansion strain $\boldsymbol{E}^{\mathrm{th}}$ of the RVE, whereby $\Delta T = T - T_0$ denotes the difference between the temperature T at a specific process time and the initial or reference temperature T_0. The thermal expansion tensor $\boldsymbol{\alpha}$ is taken as constant.

$$\boldsymbol{E}^{\mathrm{th}} = \boldsymbol{\alpha}\Delta T. \tag{21.53}$$

21.5.1.2 Thermodynamic State Potentials

According to the thermodynamical framework of material modeling (see e.g. [39]), the constitutive equations of an elastic-plastic material can be derived from energy potential functions. The thermodynamical state of the RVE can be defined by the specific Helmholtz free energy φ_R, which is a function of the strain $\boldsymbol{E}$, the temperature T and the actual state of inelastic deformation represented by the monoclinic volume fraction f_{m} and the transformation strain $\langle \boldsymbol{\epsilon}^{\mathrm{ps}} \rangle_{\mathcal{B}_I}$.

$$\varphi_R = \varphi_R \left(\boldsymbol{E},\, T,\, f_{\mathrm{m}},\, \left\langle \boldsymbol{\epsilon}^{\mathrm{ps}} \right\rangle_{\mathcal{B}_I} \right). \tag{21.54}$$

The Helmholtz free energy φ_R of PSZ consists of three components: the stored elastic energy φ_R^{el}, the change in chemical free energy $\Delta\varphi_R^{\mathrm{ch}}$ and the surface free energy $\Delta\varphi_R^{\mathrm{sur}}$

$$\varphi_R = \varphi_R^{\mathrm{el}} + \Delta\varphi_R^{\mathrm{ch}} + \Delta\varphi_R^{\mathrm{sur}}. \tag{21.55}$$

The stored elastic energy φ_R^{el} is composed of two contributions: (i) the energy stored due to the elastic deformation, which is the total strain minus transformation and thermal strain terms $\boldsymbol{E}^{\mathrm{el}} = \boldsymbol{E} - \boldsymbol{E}^{\mathrm{pl}} - \boldsymbol{E}^{\mathrm{th}}$, and (ii) the elastic energy stored due to the internal stresses which are induced by the transformational eigenstrains $\boldsymbol{\epsilon}^{pl}$. Substituting the according expressions from (21.50) and (21.53), we get

$$\begin{aligned} \varphi_R^{\mathrm{el}} \left(\boldsymbol{E},\, T,\, f_{\mathrm{m}},\, \left\langle \boldsymbol{\epsilon}^{\mathrm{pl}} \right\rangle_{\mathcal{B}_I} \right) = \frac{1}{2} \left(\boldsymbol{E} - f_{\mathrm{m}} \left\langle \boldsymbol{\epsilon}^{\mathrm{pl}} \right\rangle_{\mathcal{B}_I} - \boldsymbol{\alpha}\Delta T \right) : \mathbb{C} : \left(\boldsymbol{E} - f_{\mathrm{m}} \left\langle \boldsymbol{\epsilon}^{\mathrm{pl}} \right\rangle_{\mathcal{B}_I} - \boldsymbol{\alpha}\Delta T \right) \\ - \frac{f_{\mathrm{m}}}{2V_R} \int_{\mathcal{B}_R} \boldsymbol{\sigma} : \boldsymbol{\epsilon}^{pl}\, \mathrm{d}V. \end{aligned} \tag{21.56}$$

A detailed derivation of the last term in the above equation is given in [40].

Given the difference of volume specific chemical free energy $\Delta\varphi^{\mathrm{ch}(t\to m)}$ between tetragonal and monoclinic phases of zirconia, the chemical free energy of the RVE $\Delta\varphi_R^{\mathrm{ch}}$ is changed during phase transformation by

$$\Delta\varphi_R^{\mathrm{ch}}\,(T,\, f_{\mathrm{m}}) = f_{\mathrm{m}}\, \Delta\varphi^{\mathrm{ch}}\,(T) = f_{\mathrm{m}}\, q \left(\frac{T}{T^*} - 1 \right). \tag{21.57}$$

In the present extension of the Sun model a temperature dependence of the phase transformation is incorporated by specifying $\Delta\varphi^{\mathrm{ch}}(T)$ as a function of the temperature, where q is the volume specific heat of transformation of zirconia and T^* is the tetragonal-monoclinic equilibrium temperature of zirconia.

Due to phase transformation the interface between particles and matrix exhibits a surface free energy $\Delta\varphi_R^{\mathrm{sur}}$. This energy term per volume of the RVE is calculated from the change of specific surface free energy $\Delta\varphi^{\mathrm{sur}(t\to m)}$ of zirconia and the monoclinic volume fraction f_{m} as follows

$$\Delta\varphi_R^{\mathrm{sur}}\left(f_{\mathrm{m}}\right) = \frac{3\,f_{\mathrm{m}}}{r(f_{\mathrm{m}})}\Delta\varphi^{\mathrm{sur}(t\to m)}. \tag{21.58}$$

In the original work [29] all transformable inclusions are assumed as spheres of equal size of radius $r(f_{\mathrm{m}}) = \text{const}$. However, the phase stability of a particle depends on its size as shown by Garvie [25], i.e. that smaller crystallites require a higher thermodynamical driving force to transform than larger particles. Therefore, Mehlhorn et al. [37] introduced a more realistic approach by assuming a continuous size distribution of transformable particles in the model. As a first approximation, this distribution function $h(r)$ may be chosen as constant in the

$$h(r) = \begin{cases} \frac{1}{r_{\max}-r_{\min}} & \text{for} \quad r_{\min} \le r \le r_{\max} \\ 0 & \text{for} \quad r < r_{\min} \text{ or } r > r_{\max}. \end{cases} \tag{21.59}$$

During loading, the phase transformation starts at largest particles with radius $r_{\max}$. A further increase in loading will trigger smaller particles to transform until all particles down to the radius $r_{\min}$ have become monoclinic. In the intermediate stage, the volume of all transformed particles, whose size is in the interval $[r, r_{\max}]$, is

$$V(r) = \frac{4}{3}\pi \int_r^{r_{\max}} h(\bar{r})\bar{r}^3\,\mathrm{d}\bar{r}, \quad f_{\mathrm{m}}(r) = \frac{V(r)}{V_R}. \tag{21.60}$$

constituting a corresponding volume fraction $f_{\mathrm{m}}(r)$ in the RVE. The maximum volume fraction is attained when all particles are monoclinic $f_{\mathrm{m}}^{\max} = f_{\mathrm{m}}(r_{\min})$. Inserting (21.59) in (21.60) leads to

$$f_{\mathrm{m}}(r) = \frac{1-(r/r_{\max})^4}{1-(r_{\min}/r_{\max})^4} f_{\mathrm{m}}^{\max}. \tag{21.61}$$

The inverse $f_{\mathrm{m}}^{-1}(r) = r(f_{\mathrm{m}})$ can be calculated analytically as follows

$$r\left(f_{\mathrm{m}}\right) = r_{\max}\left[1-\left(1-(r_{\min}/r_{\max})^4\right)\frac{f_{\mathrm{m}}}{f_{\mathrm{m}}^{\max}}\right]^{\frac{1}{4}}, \tag{21.62}$$

which marks the particle size dependent change in surface energy in (21.58).

By introducing a second thermodynamic dissipation function, an energetic transformation criterion was derived [29], which represents a combination of an isotropic expanding and kinematic shifting limit surface in the macroscopic stress space

$$F\left(\boldsymbol{\Sigma}, f_{\mathrm{m}}, \left\langle \boldsymbol{\epsilon}^{\mathrm{pl}} \right\rangle_{\mathcal{B}_I}\right) = \left(\boldsymbol{\Sigma} - f_{\mathrm{m}}\, \mathbb{C} : (\boldsymbol{\Lambda} - \mathbb{I}) : \left\langle \boldsymbol{\epsilon}^{\mathrm{pl}} \right\rangle_{\mathcal{B}_I}\right) : \left\langle \boldsymbol{\epsilon}^{\mathrm{pl}} \right\rangle_{d\mathcal{B}_I} - C(f_{\mathrm{m}}) = 0. \tag{21.63}$$

Hereby, the average matrix eigenstress $-f_{\mathrm{m}}\, \mathbb{C} : (\boldsymbol{\Lambda} - \mathbb{I}) : \left\langle \boldsymbol{\epsilon}^{\mathrm{pl}} \right\rangle_{\mathcal{B}_I}$ acts as backstress. ($\boldsymbol{\Lambda}$ is the so-called Eshelby tensor and $\mathbb{I}$ denotes the rank-four unity tensor.) The term $C(f_{\mathrm{m}})$ represents the energetic barrier, which must be overcome for phase transformation. It contains energy constants as well as a phenomenological hardening function depending linearly on f_{m}. Finally, the macroscopic constitutive law is obtained as relationship between the rates of strain and stress

$$\dot{\boldsymbol{E}} = \mathbb{C}^{-1} : \dot{\boldsymbol{\Sigma}} + \dot{f}_{\mathrm{m}} \left(\epsilon^{\mathrm{pd}} \boldsymbol{I} + A \frac{\boldsymbol{s}^M}{\sigma^M_{eq}} \right), \tag{21.64}$$

wherein the first term represents the elastic behavior and the second the inelastic deformation due to phase transformation. The general form resembles to a rate-independent associated flow. The rate of phase change $\dot{f}_{\mathrm{m}}$ is obtained from the consistency condition $\dot{F} = 0$.

This constitutive relationship is conformal with the second law of thermodynamics, demanding that the dissipation rate $\mathcal{D}$ is always positive. Obviously, the dissipation rate is proportional to the change in volume fraction of the monoclinic phase

$$\mathcal{D} = \begin{cases} D_0 \dot{f}_{\mathrm{m}} & \dot{f}_{\mathrm{m}} > 0 \text{ (tetragonal-to-monoclinic)} \\ -D_0 \dot{f}_{\mathrm{m}} & \dot{f}_{\mathrm{m}} < 0 \text{ (monoclinic-to-tetragonal)} \end{cases} \tag{21.65}$$

The proportionality factor D_0 is a phenomenological model parameter. The model accounts for both forward and reverse phase transformation by distinguishing between positive and negative rates of change. Also, the expression of C differs depending on whether forward or reverse transformation occurs.

21.5.2 Numerical Results

21.5.2.1 Particle Size Dependent Surface Energy Change

In order to understand, how the radius r of the currently active transforming particles varies with the monoclinic volume fraction f_{m} during the process of phase transformation, (21.62) is studied for three different size distribution functions $h_i(r_{\min}, i, r_{\max})$ with $i = 1, 2, 3$. For the upper limit of the particle size range a typical PSZ particle

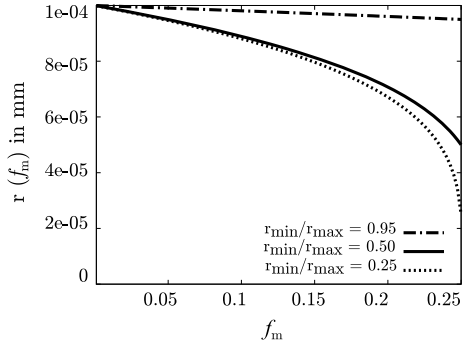

Fig. 21.18 Graphical representation of the function $r(f_\mathrm{m})$ in (21.62) for different particle size ratios and $f_\mathrm{m}^\mathrm{max} = 0.25$ [37]

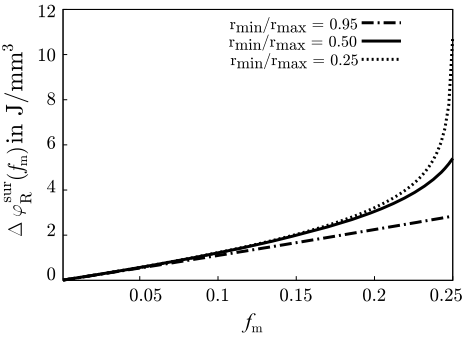

Fig. 21.19 Graphical representation of surface energy $\Delta\varphi_R^\mathrm{sur}$ in (21.58) for different particle size ratios [37]

radius of $r_\mathrm{max} = 1 \cdot 10^{-7}$ m is chosen. The values of r_min are taken as following fractions: $r_{\mathrm{min},1}/r_\mathrm{max} = 0.95$, $r_{\mathrm{min},2}/r_\mathrm{max} = 0.5$, and $r_{\mathrm{min},3}/r_\mathrm{max} = 0.25$. Figure 21.18 gives a graphical representation of (21.62), using these values. It is obvious that a narrow size distribution (as $r_\mathrm{min}/r_\mathrm{max} = 0.95$) is very close to a constant particle size of the original Sun model, resulting in a slight dependence of the radius r on the transformed volume fraction f_m. The wider the distribution function $h(f_\mathrm{m})$ is (i.e. with smaller particle size ratios $r_\mathrm{min}/r_\mathrm{max}$), the stronger is the nonlinear dependence of r on f_m.

The influence of $r(f)$ on the volume specific surface energy change $\Delta\varphi_R^\mathrm{sur}$ (21.58) is illustrated in Fig. 21.19. For a narrow particle size distribution with ratio $r_\mathrm{min}/r_\mathrm{max} = 0.95$, the surface energy change $\Delta\varphi_R^\mathrm{sur}$ grows almost linear with f_m similar as in the original Sun model. For smaller ratios $r_\mathrm{min}/r_\mathrm{max}$, the extended material model shows a strong nonlinear increase of $\Delta\varphi_R^\mathrm{sur}$, especially if $f_\mathrm{m} \to f_\mathrm{m}^\mathrm{max}$, as it can be seen for $r_\mathrm{min}/r_\mathrm{max} = 0.25$ in Fig. 21.19. This means, $\Delta\varphi_R^\mathrm{sur}$ acts as a transformation barrier, preventing very small particles from transforming even under high thermal or mechanical loading.

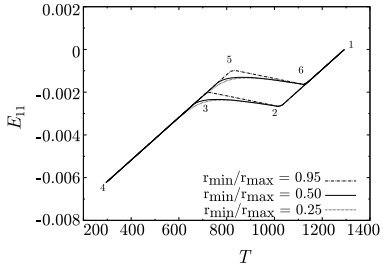

(a) Strain-temperature curves ($D_0 = 10$ MPa, $f_m^{max} = 0.25$)

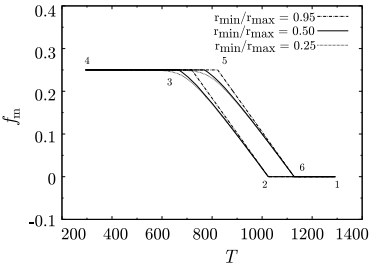

(b) Phase fraction-temperature curves ($D_0 = 10$ MPa, $f_m^{max} = 0.25$)

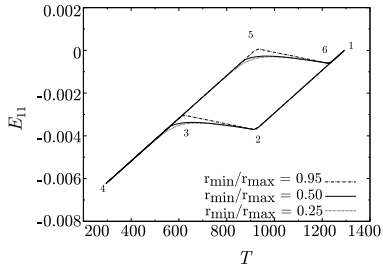

(c) Strain-temperature curves ($D_0 = 30$ MPa, $f_m^{max} = 0.25$)

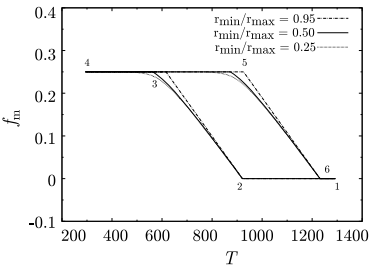

(d) Phase fraction-temperature curves ($D_0 = 30$ MPa, $f_m^{max} = 0.25$)

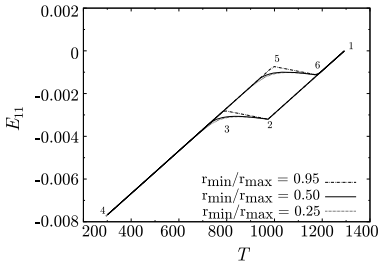

(e) Strain-temperature curves ($D_0 = 20$ MPa, $f_m^{max} = 0.15$)

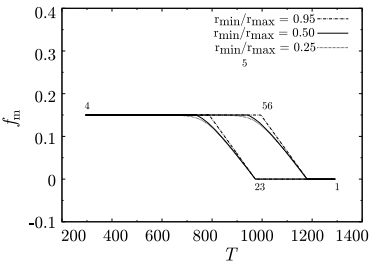

(f) Phase fraction-temperature curves ($D_0 = 20$ MPa, $f_m^{max} = 0.15$)

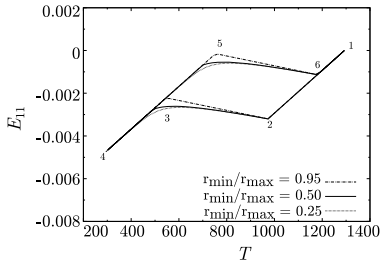

(g) Strain-temperature curves ($D_0 = 20$ MPa, $f_m^{max} = 0.35$)

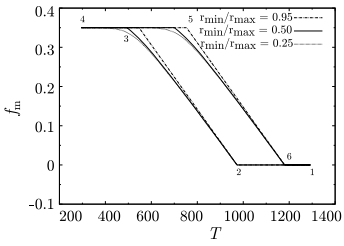

(h) Phase fraction-temperature curves ($D_0 = 20$ MPa, $f_m^{max} = 0.35$)

Fig. 21.20 Calculated strain-temperature curves and corresponding phase development for different particle size ratios. The sequence of the cooling-heating cycle is visualized by the numbers 1, …, 6 [37]

21.5.2.2 Temperature-Induced Phase Transformation

In order to demonstrate the ability of the extended material model to reproduce the hysteresis strain-temperature behavior of PSZ ceramics, a cooling-heating cycle 1373 K – 293 K – 1373 K is numerically simulated. The required model parameters associated with the changes in chemical energy (q and T^*, see (21.57)), are taken from literature: heat of transformation $q = 2.82\,\mathrm{J/m^3}$ and the phase equilibrium temperature $T^* = 1447\,\mathrm{K}$. The difference in specific surface energies between the tetragonal and monoclinic phase was set to $\Delta\varphi^{\mathrm{sur}(t\to m)} = 0.36\,\mathrm{J/m^2}$, see [37]. Since no values for the dissipation parameter D_0 and the amount of transformable tetragonal material $f_{\mathrm{m}}^{\max}$ were available, they were estimated in order to obtain physically meaningful results. Moreover, a variation of these parameters is performed to study their influence on the material model behavior. D_0 was specified to the values 10, 20, and 30 MPa. $f_{\mathrm{m}}^{\max}$ was set to 0.15, 0.25 and 0.35, respectively. For all remaining model parameters the values published by Sun et al. [29] are used.

Figure 21.20 shows the numerically obtained strain-temperature curves $E_{11} - T$ and the corresponding phase evolution f_{m}–T during the cooling-heating cycle for different sets of model parameters. As it can be seen, the typical strain hysteresis loops of PSZ ceramics are predicted by the material model, caused by a tetragonal-to-monoclinic transformation on cooling and a reverse transformation on heating. In each diagram, the influence of particle size distribution is included by varying the ratio ($r_{\mathrm{min,i}}$, $r_{\max}$). It can be seen in all diagrams, that smaller size ratios lead to a considerably nonlinear strain-temperature behavior and rounded transition curves. The influence of D_0 on the strain-temperature curves can be observed in Fig. 21.20a–d. D_0 governs the size of the strain hysteresis between cooling and heating. In contrast, $f_{\mathrm{m}}^{\max}$ influences the total transformation strain and hence the length of the temperature interval in which transformation occurs, see Fig. 21.20e–h.

These results demonstrate the feasibility of the extended material model, which forms a solid basis for simulations of structures and composites made of PSZ. Unfortunately, it was not possible to identify the required parameters for the type of MgO-stabilized ZrO_2 manufactured in the CRC799.

21.6 Simulations of ZrO_2-Particle Reinforced TRIP-Steel Composite

In order to assist the development of particle reinforced composites manufactured by a powder metallurgical process route from TRIP-steel and partially stabilized ZrO_2 ceramics particles, accompanying numerical simulations have been carried out. The mechanical properties of such a composite material are quite complex as they arise from the properties of its individual components, their volume content, and the properties of the interface between them. As explained in the previous sections, PSZ can undergo a stress-triggered phase transformation. This can lead to an additional

toughening effect compared to non-transformable ceramics as observed in [41]. The TRIP-steel exhibits a deformation induced phase transformation from the austenitic parent phase to martensite. By combining the two materials using TRIP steel as matrix and PSZ as strengthening particles, an elasto-viscoplastic particle-reinforced composite is created with the capability of phase transformation in each component.

21.6.1 Unit Cell Model of the Composite

A well established method to investigate the mechanical response of composites is a parameter study using a suitable mechanical cell model of the composite, which is simulated by means of the finite element method, see for example Mishnaevsky [42].

In this work, this approach has been applied to study the effective stress-strain behavior of this particulate TRIP steel-ZrO_2 composite. Details can be found in the publications of Mehlhorn, Prüger et al. [43–45]. The influence of the volume content of ZrO_2 particles and the interface properties on the overall response of the composite is investigated. Three different interface types are considered: (i) perfectly bonded, (ii) not bonded, and (iii) cohesive law, respectively, The calculations of the material responses are performed using a finite element analysis of unit cells of the composites under tensile, compressive and biaxial loading. Here, selected results will be reported.

Numerical simulations of composites require proper constitutive equations for both constituents. Here, the Sun model [29] as explained above is employed for the PSZ ceramics. For modeling the viscoplastic deformation and martensitic phase transformation of the TRIP steel, the constitutive law developed by Prüger [46] is applied. It describes the strain-induced transformation from a fully austenitic microstructure (γ) to martensite (α') under thermal and/or mechanical loading. Both material models were available as Fortran routines implemented via UMAT interface into the finite element software ABAQUS [47]. More information about the used material parameters for the PSZ and the specific TRIP-steel can be found in [43–45], and in Chap. 22.

In case of the particular composite, sintered together from steel and ceramic particles, one can assume a representative unit cell consisting of a large number of approximately equally sized and uniformly distributed ceramic particles in a TRIP steel matrix. For simplicity, the embedded ceramic particles are assumed to be spheres. This leads to the unit cell model shown in Fig. 21.21, which is a cube of edge length $2a$ with a single spherical ZrO_2 particle placed in its center.

The mechanical model exhibits a triple symmetry with respect to geometry and loading. Therefore the use of one-eighth of the RVE is admissible, and a corresponding FEM discretization is elaborated. Although the unit cell was numerically simulated under various stress triaxialities, only the results for uniaxial loading are reported here. Regarding the interface between the components, two limiting cases are discussed here: the perfectly bonded connection and the non-bonded, frictionless movable contact. An optimal composite possesses a high energy absorption capacity

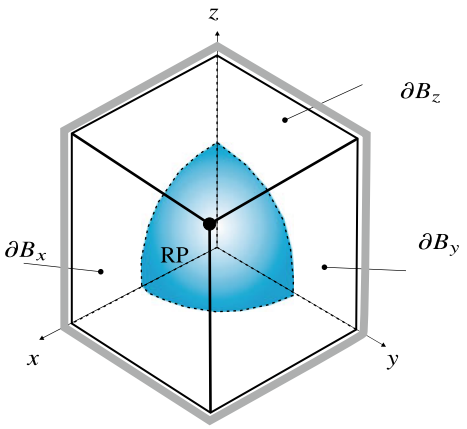

Fig. 21.21 Sketch of unit cell (one-eighth volume) for the TRIP-ZrO_2 composite. Symmetry boundary conditions are set on the coordinate planes $x = 0$, $y = 0$ and $z = 0$. Appropriate displacement and stress boundary conditions are prescribed on opposite planes ∂B_x, ∂B_y and ∂B_z for the different load cases.
The radius r of the particle is adjusted to the volume fraction f of zirconia content by $f(r) = \frac{V_{\text{sphere}}}{V_{\text{cube}}} = \frac{\pi r^3}{6a^3}$

and exhibits pronounced phase transformation in the ZrO_2 ceramic and the TRIP steel. The macroscopic true stress and true strain tensors Σ and $\mathbf{E}$ are used in order to evaluate the mechanical work according to $W = \int_0^{\bar{\mathbf{E}}} \Sigma : \mathrm{d}\mathbf{E}$, where $\bar{\mathbf{E}}$ denotes the considered deformation stage. Because the elastic strains are small, W equals approximately the energy absorption for sufficiently large total strains. In order to quantify the relative change in energy absorption capacity, this energy is related to those values W_{hom} obtained for a unit cell made only of TRIP steel.

During deformation an inhomogeneous distribution of the volume fractions of the monoclinic zirconia and the martensite develop in the ceramic and the TRIP steel, respectively. Therefore the averages of $f_{\alpha'}$ and f_{m} over the corresponding volumes are used. The simulation is stopped, when the maximum principle stress in the PSZ reaches its ultimate tensile strength $\sigma_{\text{cr}}^{\text{t}} = 1600\,\text{MPa}$.

21.6.2 Results and Discussion

The macroscopic true stress and true strain curves are calculated for different variants. The following diagrams show the second invariants Σ^{eq} and E^{eq} of both variables (to allow comparison with different stress states). The macroscopic strain invariant acts as a loading parameter, whereas the stress and the phase transformation in both components of the composite represent the material response. Table 21.5 summarizes the relative change in energy absorption capability for uniaxial tension.

Table 21.5 Energy absorption capacity for the composite with perfectly bonded and non-cohesive interface in uniaxial loading

f	0.05	0.05	0.10	0.10	0.20	0.20
Interface	Bonded	Non-cohesive	Bonded	Non-cohesive	Bonded	Non-cohesive
W/W_{hom}	1.06	0.92	1.16	0.85	1.37	0.72

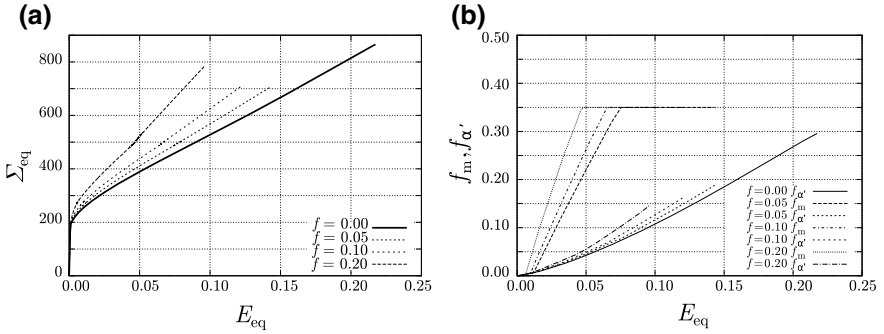

Fig. 21.22 Numerical results for the RVE with perfectly bonded interface in uniaxial loading: **a** stress-strain diagram and **b** phase development curves [43]

In case of the **perfectly bonded interface**, the stress-strain curves show a distinct dependence on the volume fraction of ZrO_2 ceramic f, as depicted in Fig. 21.22a. It can be observed that an increasing f leads to higher yield stresses and strain hardening rates compared to the unreinforced TRIP steel ($f = 0$). As consequence, a pronounced increase in the energy absorption W of the composite is obtained. Comparing the values given in Table 21.5, the ratio W/W^{hom} increases up to more than 35% (for same macroscopic equivalent strain). Due to the strong interface, load is transferred from the matrix to the reinforcement during deformation of the composite. Therefore high stresses occur in the ceramic, which reduces the maximal attainable strain with increasing zirconia content f. Regarding the phase transformation behavior, a higher volume fraction of zirconia f enhances the tendency to phase transformation in zirconia as well as in TRIP steel (Fig. 21.22b). The phase transformation capacity in the PSZ component is saturated to the maximum of 35% in a smaller strain interval. The tendency to phase transformation in the TRIP steel f'_α increases at higher zirconia content, but is limited due to failure of the ceramic.

In case of a **non-cohesive interface**, both the initial yield stress and the strain hardening rate tend to decrease with higher zirconia content f, see Fig. 21.23a. Figure 21.23b shows that the development of martensite is considerably higher than in the case of the perfectly bonded interface. At the end of deformation nearly 30% of martensite has evolved. Because of the non-cohesive interface, no tensile stresses are transferred from the TRIP steel matrix to the zirconia inclusion. Thus, no phase transformation is seen in zirconia. Moreover, the area of the load bearing cross-section consists of TRIP steel only and is the smaller the higher the zirconia content

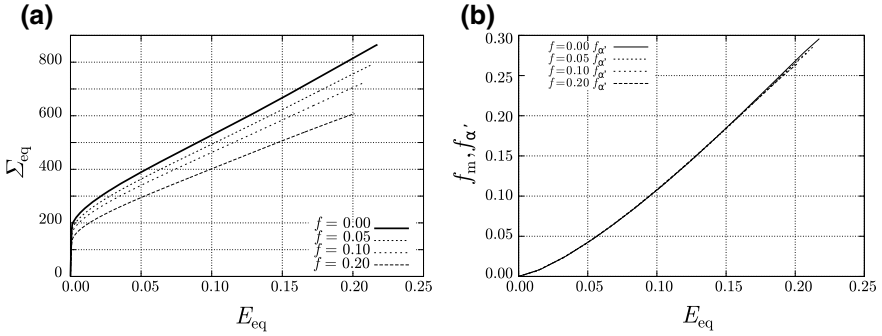

Fig. 21.23 Numerical results for the RVE with non-cohesive interface in uniaxial loading: **a** stress-strain diagram and **b** phase development curves [43]

becomes, which reduces macroscopic yield stress. After debonding, the particle acts partially like a void. However, no softening is observed in the macroscopic stress-strain response because of the hardening behavior of the TRIP steel and the locking effect caused by the particle.

One can conclude that the behavior of the real composite material lies between the two extreme cases considered here, since the interface between ceramic and steel has a finite strength. Moreover, the impact of particle reinforcement is stronger under compressive loading [45].

21.7 Conclusions

Based on the work of Levitas and Preston [13] for generic martensitic transformation, a phase-field model for MgO-ZrO_2 material was implemented [16]. The potential function used in this work results in a proper representation of transformation behavior of zirconia ceramics from a pure thermodynamic stand point. In the simulations different patterns of microstructures were found for cooling induced and stress induced transformation. These patterns are consistent with experimental observations by Hannink et al. [18]. It is evident that the presence of an energy barrier plays a key role in variant selection and the transformation path taken. By which, in stress induced case a sequential growth of lamellae was visible. In contrast, the cooling induced case is categorized with an almost homogeneous nucleation where all variants are preferred to evolve. Additionally on a single crystal level the simulations showed that, in the stress induced case, microstructure with junction planes parallel to the 'c'-axis is formed because of variant selection. It was shown that residual stresses inside t-phase lentils from $c \rightarrow t$ transformation have a magnitude of $\approx$0.3 GPa and contribute to the stability of the t-phase. Also the magnitude of stress required for introducing energy barrier increases with decreasing temperature below M_s.

A mesomechanical, two-dimensional model for Mg-PSZ with an energetic transformation criterion based on the analytical solution for a rectangular inclusion in an infinite matrix has been successfully developed. Using this model the influence of individual parameters such as size, geometry and surface energies on the transformation initiation and resulting microstructure can be efficiently studied. It predicts that the stability of the tetragonal inclusions deteriorates as the inclusions grow in size and aspect-ratio. Further, the tension-compression asymmetry of the transformation behavior known from experiments is captured correctly. A homogenization approach based on the Mori-Tanaka method predicts the transformation to be auto-catalytic within a grain.

A continuum material model for transformation plasticity in partially stabilized zirconia ceramics has been further developed to account for (i) particle size dependent phase transformation behavior, (ii) temperature dependent phase transformation, and (iii) thermoelastic deformation. These more physically based features lead to a nonlinear hardening behavior and smoothly rounded hysteresis curves for the strain and the generated monoclinic phase fraction during a temperature cycle. The influence of the tetragonal particle size distribution on phase transformation could be predicted qualitatively quite well.

Finally, the mechanical properties of a TRIP steel matrix reinforced by ZrO_2 particles are analyzed, taking the phase transformation in both constituents into account. The influence of the volume content and the interface properties of ZrO_2 particles on the overall response of the composite is investigated. Material variants with three different zirconia contents and two different interface types, perfectly bonded and non-cohesive, respectively, are considered. The calculations of the material responses are performed using a finite element analysis of representative volume elements of the composites under tensile, compressive and biaxial loading. The results indicate that the enrichment of the TRIP steel with zirconia particles leads to a significant strengthening effect provided the interface has cohesive properties.

Acknowledgements The authors gratefully acknowledge the the German Research Foundation or Deutsche Forschungsgemeinschaft (DFG) for supporting this work in subproject C4, and was created as part of the Collaborative Research Center TRIP-Matrix-Composites (Project number 54473466—CRC 799). We appreciate the contributions of former colleagues Dr.-Ing. Uwe Mühlich, Dr.-Ing. Stefan Prüger, and Lars Mehlhorn to the achievements.

References

1. S. Decker, L. Krüger, S. Richter, S. Martin, U. Martin, Steel Res. Int. **83**(6), 521 (2012)
2. R.C. Garvie, R.H.J. Hannink, R.T. Pascoe, Nature **258**(5537), 703 (1975)
3. A.G. Evans, A.H. Heuer, J. Am. Ceram. Soc. **63**(5–6), 241 (1980)
4. A.G. Evans, N. Burlingame, M. Drory, W.M. Kriven, Acta Metall. **29**(2), 447 (1981)
5. F.F. Lange, J. Mater. Sci. **17**(1), 240 (1982)
6. T. Hensl, U. Mühlich, M. Budnitzki, M. Kuna, Acta Mater. **86**, 361 (2014)
7. R.C. Garvie, J. Phys. Chem. **69**(4), 1238 (1965)
8. Y. Wang, H. Wang, L.Q.Q. Chen, A.G. Khachaturyan, J. Am. Ceram. Soc. **76**(12), 3029 (1993)

9. Y. Wang, H.Y.Y. Wang, L.Q.Q. Chen, A.G. Khachaturyan, J. Am. Ceram. Soc. **78**(3), 657 (1995)
10. Y. Wang, A.G. Khachaturyan, Acta Mater. **45**(2), 759 (1997)
11. M. Mamivand, M.A. Zaeem, H.E. Kadiri, L.Q. Chen, Acta Mater. **61**(14), 5223 (2013)
12. M. Mamivand, M. Asle Zaeem, H. El Kadiri, Int. J. Plast. **60**, 71 (2014)
13. V. Levitas, D. Preston, Three-dimensional Landau theory for multivariant stress-induced martensitic phase transformations I Austenite <–> martensite. Phys. Rev. B **66**(13), 1–9 (2002). https://doi.org/10.1103/PhysRevB.66.134206
14. V. Levitas, D. Preston, Three-dimensional Landau theory for multivariant stress-induced martensitic phase transformations. II. Multivariant phase transformations and stress space analysis. Phy. Rev. B **66**(13), 1–15. https://doi.org/10.1103/PhysRevB.66.134207
15. V. Levitas, D.L. Preston, D.W. Lee, Phys. Rev. B **68**(13), 1 (2003)
16. M.K. Rajendran, M. Kuna, M. Budnitzki, Undercooling versus stress induced martensitic phase transformation: the case of MgO—partially stabilized zirconia. Comput. Mater. Sci. **174**, 109460 (2019). https://doi.org/10.1016/j.commatsci.2019.109460
17. P.M. Kelly, C.J. Ball, J. Am. Ceram. Soc. **69**(3), 259 (1986)
18. R.H.J. Hannink, P.M. Kelly, B.C. Muddle, J. Am. Ceram. Soc. **83**(3), 461 (2000)
19. X.S. Zhao, S.L. Shang, Z.K. Liu, J.Y. Shen, J. Nucl. Mater. **415**(1), 13 (2011)
20. H. Lukas, S. Fries, B. Sundman, *Computational Thermodynamics—The CALPHAD Method* (Cambridge University Press, 2007)
21. D. Pavlyuchkov, G. Savinykh, O. Fabrichnaya, J. Eur. Ceram. Soc. **34**(5), 1397 (2014)
22. L.Q. Chen, W. Yang, Phys. Rev. B **50**(21), 15752 (1994)
23. G.K. Bansal, A.H. Heuer, Acta Metall. **20**(11), 1281 (1972)
24. G.K. Bansal, A.H. Heuer, Acta Metall. **22**(4), 409 (1974)
25. R.C. Garvie, J. Phys. Chem. **82**(2), 218 (1978)
26. C.R. Chen, S.X. Li, Q. Zhang, Mater. Sci. Eng. A **272**(2), 398 (1999)
27. W.E. Lee, M. Rainforth, *Ceramic Microstructures Property Control by Processing* (Chapman & Hall, 1994)
28. R. Garvie, M. Swain, J. Mater. Sci. **20**, 1193 (1985)
29. Q.P. Sun, K.C. Hwang, S.W. Yu, J. Mech. Phys. Solids **39**(4), 507 (1991)
30. C. Wang, M. Zinkevich, F. Aldinger, J. Am. Ceram. Soc. **89**(12), 3751 (2006)
31. I.W. Chen, Y.H. Chiao, Acta Metall. **31**(10), 1627 (1983)
32. T. Mori, K. Tanaka, Acta Metall. **21**(5), 571 (1973)
33. Y. Benvensite, Mech. Mater. **6**(2), 147 (1987)
34. F.D. Fischer, Q.P. Sun, K. Tanaka, Appl. Mech. Rev. **49**(6), 317 (1996)
35. J.R. Rice, J. Mech. Phys. Solids **19**(6), 433 (1971)
36. Abaqus, *Abaqus, Online documentation*, 6th edn. (Dassault Systems, 2014)
37. L. Mehlhorn, U. Mühlich, M. Kuna, Adv. Eng. Mater. **15**(7), 638 (2013)
38. D. Gross, T. Seelig, *Bruchmechanik—Mit einer Einführung in die Mikromechanik*, 4th edn. (Springer, Berlin Heidelberg, 2007)
39. A. Puzrin, G. Houlsby, Int. J. Plast. **16**(9), 1017 (2000)
40. T. Mura, Mechanics of elastic and inelastic solids, in *Micromechanics of Defects in Solids* (Springer, 1991)
41. D.B. Marshall, J. Am. Ceram. Soc. **69**(3), 173 (1986)
42. L.L. Mishnaevsky, Acta Mater. **52**(14), 4177 (2004)
43. L. Mehlhorn, S. Prüger, S. Soltysiak, U. Mühlich, M. Kuna, Steel Res. Int. **82**(9), 1022 (2011)
44. S. Prüger, L. Mehlhorn, S. Soltysiak, M. Kuna, Comput. Mater. Sci. **64**, 273 (2012)
45. S. Prüger, L. Mehlhorn, U. Mühlich, M. Kuna, Adv. Eng. Mater. **15**(7), 542 (2013)
46. S. Prüger, Thermomechanische Modellierung der dehnungsinduzierten Phasenumwandlung und der asymmetrischen Verfestigung in einem TRIP-Stahlguss. Ph.D. thesis, TU Bergakademie Freiberg, 2016
47. Hibbitt, Karlsson, Sorenson, *ABAQUS: Version 6.7 Documentation* (HKS, 2009)

Chapter 22
Modeling of the Thermomechanical Behavior, Damage, and Fracture of High Alloy TRIP-Steel

Andreas Seupel, Andreas Burgold, Stefan Prüger, Michael Budnitzki and Meinhard Kuna

Abstract The aim of this chapter is to give insight into the continuum mechanics based modeling of high alloy TRIP-steels. A powerful thermomechanical framework is presented, which incorporates finite viscoplasticity, the TRIP-effect, complete thermomechanical coupling, and non-local damage. Based on this, different variants of material models are developed. Thereby, selected topics concerning the material behavior of TRIP-steels are examined: Firstly, the mechanical behavior at different temperatures and strain rates is modeled including tension-compression-asymmetry and curve crossing effects. Secondly, the influence of phase transformation on fracture is investigated. Because of the TRIP-effect, higher stresses occur during crack tip blunting. Furthermore, a transformation induced shielding effect is revealed by the evaluation of material forces. Thirdly, damage evolution and crack extension are simulated with a cohesive zone model and with the non-local damage model, respectively. The damage related parameters of these models are determined using available experimental data. The developed numerical models enable quantitative assessments of failure in components made of TRIP-steels.

22.1 Introduction

In order to optimize design and functionality of components and structures made of TRIP-steels, appropriate macroscopic models for simulation purposes are required. Furthermore, micromechanically informed models can be used in numerical studies to improve the material design itself, e.g., the constitution of composite materials like the particle-reinforced TRIP-matrix composites considered in CRC 799 [1–5].

The particular challenges of modeling the deformation behavior of high alloy TRIP-steels are manifold: Firstly, a considerable variation of mechanical response with changing temperature is observed due to the high influence of temperature on the underlying deformation mechanisms (TRIP-effect: transformation induced plas-

A. Seupel (✉) · A. Burgold · S. Prüger · M. Budnitzki · M. Kuna
Institute of Mechanics and Fluid Dynamics, Lampadiusstraße 4, 09596 Freiberg, Germany
e-mail: Andreas.Seupel@imfd.tu-freiberg.de

H. Biermann and C. G. Aneziris (eds.), *Austenitic TRIP/TWIP Steels and Steel-Zirconia Composites*, Springer Series in Materials Science 298,
https://doi.org/10.1007/978-3-030-42603-3_22

ticity, TWIP-effect: twinning induced plasticity, dislocation glide, [6–8]). A thermomechanical coupling has to be taken into account in order to explain and model loading rate effects basically caused by the temperature dependency, e.g., the curve crossing effect [9, 10]. Another modeling aspect is given by the observed loading state dependent strain hardening of TWIP and TRIP-steels often recognized as tension-compression asymmetry or strength differential effect [11–14]. Moreover, the question arises, how the TRIP-effect influences the damage and fracture behavior of austenitic steels. This becomes of interest in safety applications, metal forming, and lightweight design. Taking damage and material degradation into account, conceptional problems arise: So-called local damage models imply an ill-posed boundary value problem in the classical continuum mechanics framework. A regularization method is necessary to circumvent pathological effects during numerical treatment, e.g., the mesh dependency well known from numerical analyses utilizing the Finite-Element-Method (FEM).

In this paper, two types of material models for high alloy TRIP-steels are presented – each developed to meet different requirements according to the CRC's state-of-the-art: Firstly, a micromechanically motivated model is considered and enhanced which is based on an advanced homogenization scheme [15]. Thereby, information on the state and micromechanical features of both phases, austenite and martensite, can be included. In addition, the model exhibits a higher predictive character than purely phenomenological approaches. For example, the model is successfully applied in micromechanical simulations conducted to assess and to improve the properties of particle reinforced TRIP-matrix-composites [16–18]. Furthermore, the model is used in fundamental investigations on fracture mechanics aspects of high alloy TRIP-steel, which reveal the role of martensitic phase transformation on ductility and fracture resistance [19–21]. Moreover, essential enhancements of the micromechanical model are proposed elsewhere, especially to incorporate thermomechanical coupling and stress state dependent hardening behavior of high alloy TRIP-steels [9, 22].

However, due to the high complexity and sophisticated numerical treatment of the micromechanical model, a robust phenomenological alternative is developed as basis for advanced damage modeling. The main aim is to set up a regularized damage model, which does not suffer from pathological localization effects. Simultaneously, a thermomechanically coupled variant of the model is proposed, which includes asymmetric strain hardening.

The paper is organized as follows: In the next section, a thermomechanical-micromorphic framework for finite deformations is briefly introduced, which is especially used as basis for the regularized damage model and to discuss thermodynamical aspects.

In the third section, the distinct material models are presented. As common starting point, a multiplicative viscoplasticity and martensite kinetics models for the strain induced regime are used.

In the fourth section, modeling results on thermomechanical material response, damage, and fracture are presented. The thermomechanically enhanced phenomenological model is calibrated to experimental results of a cast X3CrMnNi 16-6-6 TRIP-steel developed within the CRC 799. Afterwards, the model is assessed by

comparing the model predictions of thermomechanical loading and inhomogeneous deformation scenarios to available experiments. Using the micromechanical material model, numerical investigations on influence of the TRIP-effect on crack tip fields and fracture mechanics properties are discussed. Fracture of high alloy TRIP-steels is modeled by a cohesive zone approach, and finally by the micromorphic model of ductile damage.

22.2 Thermomechanical Framework

The thermomechanically coupled modeling as well as the regularized damage formulation are set up within the micromorphic framework proposed by Forest [23]. The thermomechanical DOF are the displacement vector $\vec{u}$ and the absolute temperature ϑ. The degrees of freedom (DOF) are enriched by a scalar valued micromorphic variable $\varepsilon_{\mathrm{nl}}$:

$$\mathrm{DOF} = \{\vec{u}, \vartheta, \varepsilon_{\mathrm{nl}}\}\,. \tag{22.1}$$

The micromorphic variable has a local counterpart, which should be enhanced by gradient effects.

The local material behavior depends on the evolution of state variables (SV). Inelastic, loading history dependent processes are treated by the thermodynamics of internal variables principle. The chosen state variables read

$$\mathrm{SV} = \left\{\boldsymbol{\varepsilon}^{\mathrm{el}}_{\log}, \vartheta, \kappa_\alpha, \varepsilon_{\mathrm{nl}}, \mathrm{grad}_{\mathrm{x}}\varepsilon_{\mathrm{nl}}\right\}, \tag{22.2}$$

where $\boldsymbol{\varepsilon}^{\mathrm{el}}_{\log}$ and κ_α denote the elastic logarithmic strain and an arbitrary set of scalar internal variables, respectively. Additionally, the material's state is influenced by the micromorphic variable $\varepsilon_{\mathrm{nl}}$ and its spatial gradient.

22.2.1 Balance Equations

The necessary mechanical and micromorphic balance equations can be deduced with help of the *principle of virtual power* [23, 24]. The continuity equation (conservation of mass, mass density ρ) is assumed:

$$\dot{\rho} + \rho\,\mathrm{div}_{\mathrm{x}}\vec{v} = 0, \tag{22.3}$$

where $\vec{v}$ denotes the substantial velocity. In what follows, virtual quantities are highlighted by an asterisk $()^*$. The internal virtual power P_{i}^* yields

$$P_{\mathrm{i}}^{*} = -\int_{\mathfrak{B}} p_{\mathrm{i}} \,\mathrm{d}v, \quad p_{\mathrm{i}}^{*} = \boldsymbol{\sigma} : \boldsymbol{D}^{*} + m_{\mathrm{nl}} \dot{\varepsilon}_{\mathrm{nl}}^{*} + \vec{M}_{\mathrm{nl}} \cdot \mathrm{grad}_{\mathrm{x}} \dot{\varepsilon}_{\mathrm{nl}}^{*}, \tag{22.4}$$

with the prescribed virtual power density p_{i}^{*}. The spatial domain currently occupied by the material body is given by $\mathfrak{B}$. The boundary of the material body and the infinitesimal volume element are denoted as $\partial\mathfrak{B}$ and dv, respectively. The symmetric CAUCHY-stress tensor and the rate of deformation tensor are denoted as $\boldsymbol{\sigma}$ and $\boldsymbol{D}$, respectively. The virtual power is enriched by the micromorphic variable and its gradient as well as by their conjugated generalized stresses m_{nl} and $\vec{M}_{\mathrm{nl}}$.

The external virtual power is formulated by volume specific and contact terms

$$P_{\mathrm{e}}^{*} = \int_{\mathfrak{B}} \rho \vec{f} \cdot \vec{v}^{*} \,\mathrm{d}v + \int_{\partial\mathfrak{B}_{\mathrm{t}}} \vec{t} \cdot \vec{v}^{*} \,\mathrm{d}a + \int_{\partial\mathfrak{B}_{\mathrm{m}}} m_{\mathrm{c}} \dot{\varepsilon}_{\mathrm{nl}}^{*} \,\mathrm{d}a, \tag{22.5}$$

where $\vec{f}$ is a mass specific force and $\vec{t}$ as well as m_{c} denote tractions acting on the infinitesimal surface element $\mathrm{d}a$.

Furthermore, a classical D'ALEMBERT inertia term is considered

$$P_{\mathrm{a}}^{*} = -\int_{\mathfrak{B}} \rho \dot{\vec{v}} \cdot \vec{v}^{*} \,\mathrm{d}v. \tag{22.6}$$

Evaluating the principle of virtual power,

$$P_{\mathrm{i}}^{*} + P_{\mathrm{e}}^{*} + P_{\mathrm{a}}^{*} = 0, \tag{22.7}$$

yields the following balance equations: Firstly, the balance of linear momentum is obtained, which is complemented by boundary and initial conditions:

$$\mathrm{div}_{\mathrm{x}} \boldsymbol{\sigma} + \rho \vec{f} = \rho \dot{\vec{v}} \qquad \forall \vec{x} \in \mathfrak{B}, \tag{22.8}$$

$$\vec{t} = \boldsymbol{\sigma} \cdot \vec{n} \qquad \forall \vec{x} \in \partial\mathfrak{B}_{\mathrm{t}} \tag{22.9}$$

$$\vec{u} = \bar{\vec{u}} \qquad \forall \vec{x} \in \partial\mathfrak{B}_{\mathrm{u}}, \tag{22.10}$$

$$\vec{v}\,(\vec{x}, t_0) = \vec{v}_0 \qquad \forall \vec{x} \in \mathfrak{B}. \tag{22.11}$$

The outward unit normal is introduced as $\vec{n}$.

Secondly, the micromorphic balance and related boundary conditions are obtained

$$\mathrm{div}_{\mathrm{x}} \vec{M}_{\mathrm{nl}} = m_{\mathrm{nl}} \qquad \forall \vec{x} \in \mathfrak{B}, \tag{22.12}$$

$$m_{\mathrm{c}} = \vec{M}_{\mathrm{nl}} \cdot \vec{n} \qquad \forall \vec{x} \in \partial\mathfrak{B}_{\mathrm{m}}, \tag{22.13}$$

$$\varepsilon_{\mathrm{nl}} = \bar{\varepsilon}_{\mathrm{nl}} \qquad \forall \vec{x} \in \partial\mathfrak{B}_{\mathrm{e}}. \tag{22.14}$$

Furthermore, the local forms of the thermodynamical principles read

$$\rho\dot{\psi} + \vartheta\dot{s} + s\dot{\vartheta} = p_{\mathrm{i}} - \mathrm{div}_{\mathrm{x}}\vec{q}_{\mathrm{th}} + \rho\, p_{\mathrm{th}} \qquad \text{(energy balance)}. \tag{22.15}$$

and

$$-\rho s\dot{\vartheta} - \rho\dot{\psi} + p_{\mathrm{i}} - \frac{1}{\vartheta}\vec{q}_{\mathrm{th}} \cdot \mathrm{grad}_{\mathrm{x}}\vartheta \geq 0. \qquad \text{(dissipation inequality)}. \tag{22.16}$$

Herein, the HELMHOLTZ free energy ψ is chosen as state potential. The specific entropy, the heat flux, and the mass specific heat source are denoted as s, $\vec{q}_{\mathrm{th}}$, and p_{th}, respectively. The term p_{i} denotes the physical counterpart of the virtual power given in (22.4).

22.2.2 Constitutive Assumptions and Equations

The high formability and ductile damage mechanisms of TRIP-steels imply a finite deformation framework as basis of constitutive modeling. As constitutive assumption, an additive split of the rate of deformation tensor $\boldsymbol{D}$ into an elastic, viscoplastic, and transformation induced part is considered:

$$\boldsymbol{D} = \boldsymbol{D}_{\mathrm{el}} + \boldsymbol{D}_{\mathrm{vpl}} + \boldsymbol{D}_{\mathrm{trip}}. \tag{22.17}$$

A state potential based on the logarithmic strain is proposed:

$$\psi = \psi\left(\boldsymbol{\varepsilon}^{\mathrm{el}}_{\mathrm{log}}, \vartheta, \kappa_\alpha, \varepsilon_{\mathrm{nl}}, \mathrm{grad}_{\mathrm{x}}\varepsilon_{\mathrm{nl}}\right). \tag{22.18}$$

The constitutive-dependent quantities $\left\{\boldsymbol{\sigma}, s, K_\alpha, m_{\mathrm{nl}}, \vec{M}_{\mathrm{nl}}\right\}$ have the same dependencies as ψ (principle of equi-presence). Utilizing the COLEMAN-NOLL-procedure [25], constitutive relations can be deduced from the dissipation inequality (22.16) plugging in the state potential (22.18):

$$\boldsymbol{\sigma} = \rho\frac{\partial\psi}{\partial\boldsymbol{\varepsilon}^{\mathrm{el}}_{\mathrm{log}}},\; s = -\frac{\partial\psi}{\partial\vartheta},\; \vec{M}_{\mathrm{nl}} = \rho\frac{\partial\psi}{\partial\mathrm{grad}_{\mathrm{x}}\varepsilon_{\mathrm{nl}}},\; m_{\mathrm{nl}} = \rho\frac{\partial\psi}{\partial\varepsilon_{\mathrm{nl}}}. \tag{22.19}$$

The conjugated thermodynamic forces to the internal variables are defined as

$$K_\alpha = \rho\frac{\partial\psi}{\partial\kappa_\alpha}. \tag{22.20}$$

Furthermore, expressions for the thermal and mechanical dissipation remain, which have to be fulfilled independently:

$$\gamma_{\mathrm{th}} = -\frac{1}{\vartheta}\vec{q}_{\mathrm{th}} \cdot \mathrm{grad}_{\mathrm{x}}\vartheta \geq 0, \tag{22.21}$$

$$\gamma_{\mathrm{m}} = \boldsymbol{\sigma} : \left(\boldsymbol{D}_{\mathrm{vpl}} + \boldsymbol{D}_{\mathrm{trip}}\right) - K_{\alpha}\dot{\kappa}_{\alpha} \geq 0. \tag{22.22}$$

The thermal and mechanical dissipation inequalities set restrictions on the definitions of the heat flux vector $\vec{q}_{\mathrm{th}}$, the evolution equations of the inelastic deformation rates $\left\{\boldsymbol{D}_{\mathrm{vpl}}, \boldsymbol{D}_{\mathrm{trip}}\right\}$, and the internal variables κ_{α} to be proposed.

22.2.2.1 State Potential

To specify the state potential (22.18), the set of state variables is complimented by the choice of scalar internal variables $\kappa_{\alpha} = \{r, f_{\mathrm{sb}}, z, D\}$:

- r: strain hardening variable (isotropic)
- f_{sb}: volume fraction of shear bands
- z: volume fraction of α'-martensite
- D: damage variable (isotropic)

Subsequently, a multiplicative viscoplasticity approach is introduced, as classified by Lemaître and Chaboche [26, Sect. 6.4.2]. Therefore, the state potential must not contain the hardening variable r to ensure non negative mechanical dissipation, see [26, Sect. 6.4.2]. Moreover, the stored energy in shear bands is neglected. Thus, the HELMHOLTZ free energy is given as $\psi\left(\boldsymbol{\varepsilon}^{\mathrm{el}}_{\mathrm{log}}, \vartheta, z, D, \varepsilon_{\mathrm{nl}}, \mathrm{grad}_{\mathrm{x}}\varepsilon_{\mathrm{nl}}\right)$:

$$\rho\psi = \rho\psi_{\mathrm{el}}\left(\boldsymbol{\varepsilon}^{\mathrm{el}}_{\mathrm{log}}, \vartheta, D\right) + \rho\psi_{\mathrm{chem}}\left(\vartheta, z\right) + \rho\psi_{\vartheta}\left(\vartheta\right) + \rho\psi_{\mathrm{nl}}\left(\varepsilon_{\mathrm{nl}}, \mathrm{grad}_{\mathrm{x}}\varepsilon_{\mathrm{nl}}\right). \tag{22.23}$$

The thermoelastic part reads

$$\psi_{\mathrm{el}} = (1 - D)\,\frac{1}{\rho}\frac{1}{2}\left(\boldsymbol{\varepsilon}^{\mathrm{el}}_{\mathrm{log}} - \alpha_{\mathrm{th}}\left(\vartheta - \vartheta_0\right)\boldsymbol{\delta}\right) : \boldsymbol{\mathcal{C}} : \left(\boldsymbol{\varepsilon}^{\mathrm{el}}_{\mathrm{log}} - \alpha_{\mathrm{th}}\left(\vartheta - \vartheta_0\right)\boldsymbol{\delta}\right). \tag{22.24}$$

Isotropic thermoelastic properties are assumed for the cast TRIP-steel, defined by the fourth order tensor of elastic stiffness $\boldsymbol{\mathcal{C}}$ and the thermal expansion coefficient α_{th}. Moreover, the elastic and thermal expansion properties are assumed to be similar for the austenitic and martensitic phase [27]. Damage D degrades the elastic energy leading to material softening.

The chemical part describes the difference in GIBBS-energy of the two phases given by a rule of mixture:

$$\psi_{\mathrm{chem}} = (1 - z)\,\psi_{\mathrm{a}}\left(\vartheta\right) + z\psi_{\mathrm{m}}\left(\vartheta\right). \tag{22.25}$$

The purely temperature dependent term

$$\psi_\vartheta = c_\epsilon^0 \left(\vartheta - \vartheta \ln \left(\frac{\vartheta}{\vartheta_*} \right) \right), \tag{22.26}$$

defines a constant part c_ϵ^0 of the specific heat similar for both phases with a reference temperature ϑ_*.

The last term in (22.23) comprises the micromorphic contributions. A conventional quadratic structure is prescribed, see [23]:

$$\begin{aligned} \rho \psi_{\mathrm{nl}} = & \frac{1}{2} H_{\mathrm{nl}} \left(\int_{t_0}^{t} \dot{\varepsilon}_{\mathrm{l}} \left(\boldsymbol{D}_{\mathrm{vpl}} \right) \, \mathrm{d}\tau - \varepsilon_{\mathrm{nl}} \right)^2 \\ & + \frac{1}{2} A_{\mathrm{nl}} \, \mathrm{grad}_{\mathrm{x}} \varepsilon_{\mathrm{nl}} \cdot \mathrm{grad}_{\mathrm{x}} \varepsilon_{\mathrm{nl}}. \end{aligned} \tag{22.27}$$

The first part penalizes the difference of the local strain like value, defined by the integral, and the micromorphic variable $\varepsilon_{\mathrm{nl}}$. The penalty stiffness is prescribed by the parameter H_{nl}. The integral defines a scalar value, which is extracted from the viscoplastic deformation rate $\boldsymbol{D}_{\mathrm{vpl}}$ serving as driving force for damage. The second term states the micromorphic gradient contribution weighted by the parameter A_{nl}.

22.2.2.2 Consistent Rate Formulation

The CAUCHY-stress defined in (22.19) can be evaluated using (22.23) and (22.24):

$$\boldsymbol{\sigma} = \rho \frac{\partial \psi}{\partial \boldsymbol{\varepsilon}_{\log}^{\mathrm{el}}} = (1 - D) \, \boldsymbol{\mathcal{C}} : \left(\boldsymbol{\varepsilon}_{\log}^{\mathrm{el}} - \alpha_{\mathrm{th}} \left(\vartheta - \vartheta_0 \right) \boldsymbol{\delta} \right). \tag{22.28}$$

Applying the effective stress concept [28], the constitutive equation reads

$$\hat{\boldsymbol{\sigma}} = \frac{\boldsymbol{\sigma}}{1 - D} = \boldsymbol{\mathcal{C}} : \left(\boldsymbol{\varepsilon}_{\log}^{\mathrm{el}} - \alpha_{\mathrm{th}} \left(\vartheta - \vartheta_0 \right) \boldsymbol{\delta} \right), \tag{22.29}$$

where $\hat{\boldsymbol{\sigma}}$ designates the effective stress acting on an undamaged cross section of the material; $\boldsymbol{\sigma}$ is then interpreted as the net stress. In what follows, a hat $\hat{(\cdot)}$ highlights quantities which are computed from the effective stress tensor $\hat{\boldsymbol{\sigma}}$.

The stress-strain relation has to be given in an objective rate form in order to implement the model into the user subroutine UMAT of the FEM-software ABAQUS. As objective time derivative, the logarithmic rate $\overset{\diamond}{(\cdot)}$ introduced by Xiao et al. [29, 30] is applied to both sides of (22.29). Hence, the rate formulation

$$\overset{\diamond}{\hat{\boldsymbol{\sigma}}} = \boldsymbol{\mathcal{C}} : \left(\boldsymbol{D}_{\mathrm{el}} - \alpha_{\mathrm{inst}} \boldsymbol{\delta} \dot{\vartheta} \right), \tag{22.30}$$

is consistent with the notion of elasticity [31], where α_{inst} denotes the instantaneous coefficient of thermal expansion. The logarithmic rate of the logarithmic strain tensor $\boldsymbol{\varepsilon}^{\mathrm{el}}_{\log}$ yields the rate of deformation tensor $\boldsymbol{D}_{\mathrm{el}}$ as shown in [30]. The logarithmic rate of the effective CAUCHY-stress reads

$$\overset{\diamond}{\hat{\boldsymbol{\sigma}}} = \frac{\mathrm{d}\hat{\boldsymbol{\sigma}}}{\mathrm{d}t} - \boldsymbol{\Omega}_{\log} \cdot \hat{\boldsymbol{\sigma}} - \hat{\boldsymbol{\sigma}} \cdot \boldsymbol{\Omega}^{\mathrm{T}}_{\log}. \tag{22.31}$$

The skew logarithmic spin $\boldsymbol{\Omega}_{\log}$ can be found in [29].

22.2.2.3 Generalized Stresses

The COLEMAN-relations for generalized stresses in (22.19) are specified as

$$\vec{M}_{\mathrm{nl}} = A_{\mathrm{nl}} \operatorname{grad}_{\mathrm{x}} \varepsilon_{\mathrm{nl}}, \tag{22.32}$$

$$m_{\mathrm{nl}} = H_{\mathrm{nl}} \left(\varepsilon_{\mathrm{nl}} - \int_{t_0}^{t} \dot{\varepsilon}_{\mathrm{l}} \left(\boldsymbol{D}_{\mathrm{vpl}} \right) \, \mathrm{d}\tau \right) = H_{\mathrm{nl}} \left(\varepsilon_{\mathrm{nl}} - \varepsilon_{\mathrm{l}} \right), \tag{22.33}$$

where the integral is substituted for reasons of clarity by ε_{l}. With (22.32) and (22.33) at hand, the micromorphic balance (22.12) can be rewritten in the established manner [23, 32]

$$L^2_{\mathrm{nl}} \Delta_{\mathrm{x}} \varepsilon_{\mathrm{nl}} = \varepsilon_{\mathrm{nl}} - \varepsilon_{\mathrm{l}} \qquad \forall \vec{x} \in \mathfrak{B}, \tag{22.34}$$

where the internal length L_{nl} is defined as

$$L^2_{\mathrm{nl}} = \frac{A_{\mathrm{nl}}}{H_{\mathrm{nl}}} \geq 0. \tag{22.35}$$

The spatial Laplacian is denoted as Δ_{x}. Thereby, the micromorphic balance (22.34) is identical to the partial differential equation of implicit gradient enhancement proposed by Peerlings et al. [33], which has been used in own preliminary studies [34, 35]. Following the suggestion in [33], trivial natural boundary conditions are prescribed on all free boundaries

$$\operatorname{grad}_{\mathrm{x}} \varepsilon_{\mathrm{nl}} \cdot \vec{n} = 0 \qquad \forall \vec{x} \in \partial \mathfrak{B}_{\mathrm{m}} = \partial \mathfrak{B}. \tag{22.36}$$

As result of this choice, the overall mean values of the micromorphic variable and its local counterpart are equal [34].

22.2.2.4 Thermodynamic Forces

The conjugated thermodynamic forces $K_\alpha = \{R, F_{\text{sb}}, Z, Y\}$ associated with the set of internal variables are specified by (22.20) as

$$R = \rho \frac{\partial \psi}{\partial r} = 0, \tag{22.37}$$

$$F_{\text{sb}} = \rho \frac{\partial \psi}{\partial f_{\text{sb}}} = 0, \tag{22.38}$$

$$Z = \rho \frac{\partial \psi}{\partial z} = \rho \psi_{\text{m}}(\vartheta) - \rho \psi_{\text{a}}(\vartheta) = \triangle g_{\text{chem}}^{\text{a}\to\text{m}}(\vartheta), \tag{22.39}$$

$$Y = \rho \frac{\partial \psi}{\partial D} = -\frac{1}{2}\left(\boldsymbol{\varepsilon}_{\log}^{\text{el}} - \alpha_{\text{th}}(\vartheta - \vartheta_0)\boldsymbol{\delta}\right) : \boldsymbol{\mathcal{C}} : \left(\boldsymbol{\varepsilon}_{\log}^{\text{el}} - \alpha_{\text{th}}(\vartheta - \vartheta_0)\boldsymbol{\delta}\right). \tag{22.40}$$

The driving force for martensitic phase transition Z consists of the energy difference $\triangle g_{\text{chem}}^{\text{a}\to\text{m}}(\vartheta)$, which is negative once the temperature is below the thermodynamic equilibrium temperature [36], i.e., in the region of interest. The energy release rate Y is always negative or zero, $Y \leq 0$.

22.2.3 Dissipation and Heat Equation

The mechanical dissipation (22.22) can be intermediately specified as

$$\gamma_{\text{m}} = \boldsymbol{\sigma} : \left(\boldsymbol{D}_{\text{vpl}} + \boldsymbol{D}_{\text{trip}}\right) - Z\dot{z} - Y\dot{D}. \tag{22.41}$$

The requirement $\gamma_{\text{m}} \geq 0$ is discussed in detail after introducing the evolution laws for the martensite volume fraction $\dot{z}$ and the damage variable $\dot{D}$ for the different modeling approaches.

The heat equation can be obtained from the energy balance (22.15), see [9]. Neglecting coupling terms and assuming FOURIERs law, a rudimentary format can be obtained typically used for computation purposes [9]:

$$\rho c_\epsilon^0 \dot{\vartheta} = \lambda_{\text{th}} \Delta_{\text{x}} \vartheta + \tilde{p} \qquad \forall \vec{x} \in \mathfrak{B} \tag{22.42}$$

with the heat source

$$\tilde{p} = \gamma_{\text{m}} + \rho\, p_{\text{th}}. \tag{22.43}$$

The specific heat c_ϵ^0 and the conductivity λ_{th} are assumed as constants.

22.3 Material Models

22.3.1 Preliminaries for both Models

Both considered material models are based on the previously introduced thermomechanical framework and a multiplicative viscoplasticity formulation discussed within the next subsection. In order to describe the α'-martensite formation, two modifications of the OLSON-COHEN model [37] (OC-model) for strain induced martensite evolution are developed for thermomechanical loading conditions: A micromechanically extended approach and a simplified empirical model allowing for a fast parameter calibration. The macroscopic TRIP-kinematics are introduced to conclude the section.

22.3.1.1 Multiplicative Viscoplasticity

In order to take characteristic strain rate effects of high alloy TRIP-steels into account, a multiplicative viscoplasticity framework is utilized. A dissipation potential of NORTON-type is proposed:

$$\phi\left(\boldsymbol{\sigma}\right) = \frac{\left(1-D\right)\dot{\varepsilon}_0\sigma_\mathrm{y}}{m+1}\left(\frac{\hat{\sigma}_\mathrm{eq}}{\sigma_\mathrm{y}}\right)^{(m+1)}. \tag{22.44}$$

The model parameters m and $\dot{\varepsilon}_0$ control the strain rate sensitivity. Isotropic strain hardening can be taken into account by the yield stress $\sigma_\mathrm{y}\left(r,z\right)$. Within the next sections, the potential (22.44) is extended by contributions of all invariants of the effective stress tensor:

$$\hat{I}_1 = \mathrm{tr}\left(\hat{\boldsymbol{\sigma}}\right), \qquad \hat{J}_2 = \frac{1}{2}\hat{\boldsymbol{S}}:\hat{\boldsymbol{S}}, \qquad \hat{J}_3 = \frac{1}{3}\mathrm{tr}\left(\hat{\boldsymbol{S}}\cdot\hat{\boldsymbol{S}}\cdot\hat{\boldsymbol{S}}\right), \tag{22.45}$$

where the stress deviator is introduced as

$$\hat{\boldsymbol{S}} = \hat{\boldsymbol{\sigma}} - \frac{1}{3}\hat{I}_1\boldsymbol{\delta}. \tag{22.46}$$

The unit tensor of second order is denoted as $\boldsymbol{\delta}$. The original NORTON-potential (22.44) is only influenced by the VON MISES equivalent stress

$$\hat{\sigma}_\mathrm{eq} = \sqrt{3\hat{J}_2}. \tag{22.47}$$

22.3.1.2 Strain Induced Martensite

The well established OC-model [37] is based on the observation that nuclei of α'-martensite are predominantly formed at intersections of shear bands. The evolution of shear band volume fraction f_{sb} is modeled as

$$\dot{f}_{\mathrm{sb}} = \alpha_{\mathrm{oc}} \left(1 - f_{\mathrm{sb}}\right) \dot{\varepsilon}_{\mathrm{eq}}, \tag{22.48}$$

where the parameter α_{oc} is a function of temperature and stress state [38–40]. As scalar measure of plastic deformation, the rate of equivalent (visco-)plastic deformation $\dot{\varepsilon}_{\mathrm{eq}}$ is utilized. The original evolution equation of α'-martensite volume fraction z proposed by Olson and Cohen [37] reads

$$\dot{z} = (1 - z)\, \beta_{\mathrm{oc}}\, n_{\mathrm{oc}}\, f_{\mathrm{sb}}^{(n_{\mathrm{oc}}-1)}\, \dot{f}_{\mathrm{sb}}. \tag{22.49}$$

The probability to form a martensite embryo at a shear band intersection is cast into the parameter β_{oc}. The specific geometric setting of the shear bands is taken into account by the parameter n_{oc}. Modifications of (22.48) and (22.49) are discussed in the separate section of the different material models.

22.3.1.3 TRIP Kinematics

During martensitic phase transformation, inelastic strains occur which become visible on the macroscopic scale of polycrystalline material [41, 42]. These so-called TRIP-strains comprise a volumetric part and a deviatoric part. Two effects lead to these inelastic strains: A formation of favorable oriented martensite variants according to the applied stress state (MAGEE-effect) and additional plastic deformation of the austentite during accommodation of newly formed martensite (GREENWOOD-JOHNSON-effect), see [43] and [44, p. 69ff]. An empirical evolution law of the TRIP-deformation rate reads

$$\boldsymbol{D}_{\mathrm{trip}} = \left(k_{\mathrm{gj}}\, \hat{\sigma}_{\mathrm{eq}} \frac{\mathrm{d}\varphi\,(z)}{\mathrm{d}z} + k_{\mathrm{s}} \right) \boldsymbol{N} \dot{z} + \frac{1}{3} \triangle_{\mathrm{v}} \boldsymbol{\delta} \dot{z} \tag{22.50}$$

with the flow normal

$$\boldsymbol{N} = \frac{3}{2\hat{\sigma}_{\mathrm{eq}}} \hat{\boldsymbol{S}}. \tag{22.51}$$

From (22.50), many modifications proposed in literature can be deduced [9, 12, 38, 39, 41, 45–50]. The first part shows that the magnitude of the TRIP-strain depends on the applied stress level as measured by Nagayama et al. [42]; the parameter k_{gj} is called GREENWOOD- JOHNSON-constant. The additional constant contribution k_{s} is used by Stringfellow et al. [38].

The volumetric strain is prescribed by the parameter $\triangle_{\mathrm{v}}$, which typically ranges from 2 to 4% depending on the carbon content of the considered alloy.

Nagayama et al. [42] and Ahrens [41] conducted experiments on temperature induced martensitic transformation and simultaneously applied external stresses. From these experiments, a magnitude for the stress dependent, deviatoric uni-axial TRIP-strain of about 1.5–2.0 % can be found. This is in accordance to the statement of Martin [51, Sect. 2.1.6] that the TRIP-contribution to the whole inelastic deformation is comparatively small. The high ductility of high alloy TRIP-steels is attributed to the excellent strain hardening, which postpones localization effects.

22.3.2 Micromechanically Motivated Model

Starting with the assumption that formed α'-martensite nuclei and domains act as inclusions, homogenization schemes can be developed to predict the effective macroscopic material response. Thereby, the modeling gains a microstructural well-founded character. The utilized analytic homogenization approach is well documented in literature. Therefore, only a brief summary is given, which is needed to understand the results on crack tip loading in Sect. 22.4.3. For details, the reader is referred to the numerous available publications devoted to the model development within CRC 799 [9, 22, 47, 52, 53]. Damage effects are neglected for this approach, i.e., $D = 0$ and $\hat{\boldsymbol{\sigma}} = \boldsymbol{\sigma}$.

22.3.2.1 Homogenization Method

It is assumed that the viscoplastic properties of austenite and martensite differ widely. Therefore, independent dissipation potentials according to (22.44) are introduced for each phase. The rate of viscoplastic equivalent strain follows for each phase l as

$$\dot{\varepsilon}_{\mathrm{eq}}^{(l)} = \frac{\partial \phi^{(l)}\left(\sigma_{\mathrm{eq}}^{(l)}\right)}{\partial \sigma_{\mathrm{eq}}^{(l)}} = \dot{\varepsilon}_0 \left(\frac{\sigma_{\mathrm{eq}}^{(l)}}{\sigma_{\mathrm{y}}^{(l)}}\right), \tag{22.52}$$

where $l = \mathrm{a}$ and $l = \mathrm{m}$ denote austenite and martensite, respectively. The macroscopically effective properties are determined as described in [15, 22]. A variational principle is utilized, which is established by Ponte Castañeda and Suquet [54]. The necessary condition for an optimally chosen linear comparison composite is deduced in the case of statistically isotropic and uniformly distributed phases with isotropic behavior as

$$\sigma_{\mathrm{eq}}^{(l)} = \sigma_{\mathrm{eq}} \sqrt{\frac{1}{\nu^{(l)}} \frac{\partial \Theta^{\mathrm{hom}}}{\partial \Theta^{(l)}}}, \tag{22.53}$$

where the effective compliance Θ^{hom} is computed using a lower Hashin-Shtrikman bound

$$\Theta^{\mathrm{hom}} = \frac{v^{\mathrm{m}}\left(\frac{2}{\Theta^{\mathrm{a}}}+\frac{3}{\Theta}\right)+v^{\mathrm{a}}\left(\frac{2}{\Theta^{\mathrm{m}}}+\frac{3}{\Theta}\right)}{\frac{v^{\mathrm{m}}}{\Theta^{\mathrm{m}}}\left(\frac{2}{\Theta^{\mathrm{a}}}+\frac{3}{\Theta}\right)+\frac{v^{\mathrm{a}}}{\Theta^{\mathrm{a}}}\left(\frac{2}{\Theta^{\mathrm{m}}}+\frac{3}{\Theta}\right)}. \tag{22.54}$$

Therein, $v^{(l)}$ denotes the volume fraction of phase l, i.e., $v^{\mathrm{m}} = z$ and $v^{\mathrm{a}} = 1 - z$. The value of Θ is chosen as $\Theta = \max\left(\Theta^{\mathrm{a}}, \Theta^{\mathrm{m}}\right)$, where the compliance of a single phase is defined as

$$\Theta^{(l)} = \frac{3}{\sigma_{\mathrm{eq}}^{(l)}}\dot{\varepsilon}_{\mathrm{eq}}^{(l)}. \tag{22.55}$$

The strain hardening functions of each phase $\sigma_{\mathrm{y}}^{(l)}$ are chosen as power laws.

A stress state dependent yielding and strain hardening can be introduced by taking the third invariant of stress deviator J_3 into account. This leads to major modifications of the homogenization scheme. The reader is referred to the work of Prüger [22] dealing with this topic.

22.3.2.2 Martensite Kinetics and TRIP-kinematics: Stringfellow-Model

An established modification of the OC-model has been proposed by Stringfellow et al. [38]. Further enhancements have been incorporated, e.g., in [9, 39, 40]. Due to the homogenizations approach, plastic deformations of the single phases are accessible. Thus, the dependencies of the martensite kinetics on equivalent plastic strain are substituted as functions of the viscoplastic strain in austenite $\dot{\varepsilon}_{\mathrm{eq}}^{\mathrm{a}}$. The modified OC-kinetics of strain induced martensite, following [9], read as

$$\dot{z} = (1-z)\left(A\dot{f}_{\mathrm{sb}} + B\left(\dot{g} - \dot{\bar{g}}\right)\right) \tag{22.56}$$

with prefactors

$$A = \beta_{\mathrm{oc}}\, n_{\mathrm{oc}}\, f_{\mathrm{sb}}^{(n_{\mathrm{oc}}-1)}\, P, \tag{22.57}$$

$$B = \beta_{\mathrm{oc}}\, f_{\mathrm{sb}}^{n_{\mathrm{oc}}} \frac{\mathrm{d}P}{\mathrm{d}g} H\left(\dot{P}\right), \tag{22.58}$$

and the normal distribution

$$P = \frac{1}{\sqrt{2\pi}\, s_{\mathrm{g}}} \int_{-\infty}^{g} \exp\left[-\frac{1}{2}\left(\frac{g^* - \bar{g}}{s_{\mathrm{g}}}\right)^2\right] \mathrm{d}g^*. \tag{22.59}$$

Therein, g denotes the driving force for martensite formation and $\bar{g}$ a barrier function [55]:

$$\bar{g} = \bar{g}_0 + \bar{g}_1 \varepsilon_{\mathrm{eq}}^{\mathrm{a}}. \tag{22.60}$$

The driving force g is formulated as the sum of the chemical contribution $Z(\vartheta)$ and a mechanical part motivated from the energy term $\boldsymbol{\sigma} : \boldsymbol{D}_{\mathrm{trip}}$ [22, Sect. 5.4]:

$$g = -Z + \left(\left(k_{\mathrm{gj}} \, \sigma_{\mathrm{eq}} \frac{\mathrm{d}\varphi(z)}{\mathrm{d}z} + k_{\mathrm{s}} \right) \sigma_{\mathrm{eq}} + \triangle_{\mathrm{v}} \sigma_{\mathrm{h}} \right). \tag{22.61}$$

The chemical driving force Z is typically determined by thermodynamical calculations, see [47]. Moreover, s_{g} is a fitting parameter of the model.

As mentioned above, the parameter of shear band formation α_{oc} is a function of temperature and stress state. Prüger [22] proposes the approach

$$\alpha_{\mathrm{oc}}(h, \vartheta) = \left\langle \alpha_1 + \alpha_2 \vartheta + \alpha_3 \vartheta^2 - \alpha_4 \arctan(h) \right\rangle, \tag{22.62}$$

where the stress triaxiality is introduced as

$$h = \frac{\sigma_{\mathrm{h}}}{\sigma_{\mathrm{eq}}} \tag{22.63}$$

with the hydrostatic stress

$$\sigma_{\mathrm{h}} = \frac{1}{3} I_1. \tag{22.64}$$

The MACAULY-brackets

$$\langle x \rangle = \begin{cases} 0 & x < 0 \\ x & x \geq 0 \end{cases} \tag{22.65}$$

in (22.62) ensure a monotonically increasing shear band volume fraction.

For the micromechanical approach, the generally introduced TRIP-deformation rate $\boldsymbol{D}_{\mathrm{trip}}$ defined in (22.50) is utilized.

22.3.3 Phenomenological Model

The phenomenological modeling strategy is developed as a robust engineering tool comprising characteristic aspects of the thermomechanical, stress state dependent and damage behavior of high alloy TRIP-steel. Finally, two variants of the model are implemented into a FE-code: The first variant contains all thermomechanical

features, the second includes ductile damage within the micromorphic framework at isothermal conditions. A combination of both is subject of current work.

22.3.3.1 Viscoplastic Flow Rules

As already introduced in the state potential (22.24), damage degrades the elastic properties and thus the bearable stress, see (22.28). Ductile damage is microscopically caused by the nucleation, growth, and coalescence of microvoids. At high stress triaxialities, growth of voids is the dominant damage mechanism, which influences the plastic yielding and flow behavior [56, 57]. In this regime, the impact of hydrostatic stresses on plastic flow needs to be taken into account. A heuristic modification of the NORTON-potential (22.44) through a contribution of the hydrostatic stress is proposed

$$\phi\left(\boldsymbol{\sigma}\right) = \frac{\left(1-D\right)\dot{\varepsilon}_0\sigma_\mathrm{y}}{m+1}\left(\frac{\hat{\sigma}_\mathrm{eq}^2 + q_1 D\left\langle\hat{\sigma}_\mathrm{h}\right\rangle^2}{\sigma_\mathrm{y}^2}\right)^{\left(\frac{m+1}{2}\right)}. \tag{22.66}$$

A similar elliptic yield function in the rate independent framework is utilized in the gradient-enhanced damage model of Seupel and Kuna [35]. Dissipation potentials of similar structure are likewise proposed in creep damage mechanics [58].

An associated viscoplastic flow is assumed

$$\boldsymbol{D}_\mathrm{vpl} = \frac{\partial\phi}{\partial\boldsymbol{\sigma}} = \dot{\varepsilon}_\mathrm{eq}\boldsymbol{N} + \dot{\varepsilon}_\mathrm{h}\boldsymbol{\delta}, \tag{22.67}$$

which leads to deviatoric and volumetric viscoplastic strains. The prefactors in (22.67) are identified as equivalent and volumetric viscoplastic strain rates

$$\dot{\varepsilon}_\mathrm{eq} = \dot{\varepsilon}_0\frac{\hat{\sigma}_\mathrm{eq}}{\sigma_\mathrm{y}}\left(\frac{\hat{\sigma}_\mathrm{eq}^2 + q_1 D\left\langle\hat{\sigma}_\mathrm{h}\right\rangle^2}{\sigma_\mathrm{y}^2}\right)^{\left(\frac{m-1}{2}\right)}, \tag{22.68}$$

$$\dot{\varepsilon}_\mathrm{h} = \dot{\varepsilon}_0\frac{\left\langle\hat{\sigma}_\mathrm{h}\right\rangle q_1 D}{3\sigma_\mathrm{y}}\left(\frac{\hat{\sigma}_\mathrm{eq}^2 + q_1 D\left\langle\hat{\sigma}_\mathrm{h}\right\rangle^2}{\sigma_\mathrm{y}^2}\right)^{\left(\frac{m-1}{2}\right)}, \tag{22.69}$$

respectively. The model parameter q_1 controls the hydrostatic stress dependency. As long as q_1 is set to zero or no damage occurs $D = 0$, the original volume preserving NORTON-type flow is obtained. A relation between (22.68) and (22.69) can be found [59]:

$$\dot{\varepsilon}_\mathrm{h} = \frac{q_1 D\left\langle h\right\rangle}{3}\dot{\varepsilon}_\mathrm{eq}. \tag{22.70}$$

In presence of damage, the hydrostatic plastic flow linearly depends on stress triaxiality h. This is in accordance to micromechanical findings within creep damage mechanics [60], but contrary to the known exponential influence deduced in [56, 57], cf. [61]. In contrast to the GURSON-model, the volumetric plastic strain of the present model can just increase, because a volumetric flow occurs only for positive hydrostatic stresses.

An additional influence of the third stress invariant $\hat{J}_3$ on plastic flow is neglected, which is in accordance with investigations on initial yielding of the considered TRIP-steel conducted by Kulawinski et al. [62]. The asymmetric strain hardening is fully captured by the definition of the evolution equation for the hardening variable r.

22.3.3.2 Isotropic Strain Hardening

An empirical mixture rule is adopted in order to take the influence of formed α'-martensite on strain hardening into account, which has been successfully applied in other studies [12, 27, 50]. Thus, the yield stress reads

$$\sigma_{\mathrm{y}}\left(r, z, \vartheta\right) = \sigma_0\left(\vartheta\right) + Z_1 m_{\mathrm{z}}\left(z\right) + H\left(r\right). \tag{22.71}$$

Furthermore, only the initial yield stress σ_0 is considered as function of temperature as employed for an AISI 304 steel elsewhere [27]. The additional hardening contribution of martensite is captured by the second term, where $m_{\mathrm{z}}\left(z\right)$ is introduced to modify the shape of the flow curve during martensite evolution. The choice of the hardening function ensures that no strain softening can occur during martensite formation for $\vartheta = \text{const}$. Material degradation arises only due to the evolution of the damage variable D.

Because of the direct influence of the stress state dependent martensitic phase transition, asymmetric strain hardening in uni-axial tension and compression is naturally predicted by the model. Hence, a higher strain hardening would be predicted in tension than in compression due to the enhanced phase transformation in tension, whereas the inverse trend is experimentally observed [12], [63, Sect. 5.3.2]. To take the realistic asymmetric strain hardening into account, Seupel and Kuna [12] propose an evolution of the hardening variable r depending on the orientation in stress space, which is described by the LODE-angle

$$\cos 3\phi = \frac{3\sqrt{3}}{2} \frac{\hat{J}_3}{\hat{J}_2^{\frac{3}{2}}}. \tag{22.72}$$

The evolution of the hardening variable reads

$$\dot{r} = \left(1 + \frac{b}{2}\left(1 - \cos 3\phi\right)\right) \dot{\varepsilon}_{\mathrm{eq}} \geq 0, \tag{22.73}$$

where the parameter $b > -1$ controls the influence of stress state. For $b = 0$, the hardening variable coincides with the equivalent viscoplastic strain. For $b > 0$, the hardening rate is increased in case of uni-axial compression ($\cos 3\phi = -1$) compared to uni-axial tension ($\cos 3\phi = 1$), which is in accordance with the experimentally revealed behavior.

The same tendencies in strain hardening are observed, if the TWIP-mechanism is active [11, 63]. The tension-compression asymmetry vanishes, if planar dislocation glide is the dominant deformation mechanism, see [63, Sect. 5.3.2]. For the considered steel, the transition of deformation mechanisms is explained as function of temperature [6, 51]. Accordingly, the hardening asymmetry should depend on deformation mechanism and/or temperature, respectively. Therefore, the parameter b is assumed as function of martensite volume fraction and temperature in the following manner:

$$b\left(z,\vartheta\right) = \begin{cases} b_0 \exp\left(-\left(\frac{\vartheta - T_0}{T_1}\right)^2\right) \exp\left(-\left(\frac{z - z_0}{z_1}\right)^2\right) & \vartheta \geq T_0 \\ b_0 \exp\left(-\left(\frac{z - z_0}{z_1}\right)^2\right) & \vartheta < T_0 \end{cases} \tag{22.74}$$

Thereby, the asymmetric hardening asymptotically vanishes for temperatures above T_0. When martensite transformation is active, the asymmetry can additionally vary during loading at constant temperature due to the second exponential function, which contains the fitting parameters z_0 and z_1.

22.3.3.3 Martensite Kinetics and TRIP-Kinematics: Empirical Model

Motivated by the sound investigations on stress state dependency of strain induced martensite formation and the suggested empirical kinetics approach of Beese and Mohr [64], a less sophisticated, empirical extension of the OC-kinetics can be proposed. The original evolution equation introduced by Olson and Cohen [37] is considered, see (22.49). In β_{oc}, the probability that a shear band intersection becomes a martensite embryo is included. As shown in [37], the parameters α_{oc} and β_{oc} are functions of temperature. Similar to the proposal in (22.62) for the parameter of shear band formation, Seupel and Kuna [12] use

$$\alpha_{\mathrm{oc}}\left(h,\vartheta\right) = \alpha_{\mathrm{t}}\left(\vartheta\right)\left[\alpha_0 + \alpha_1\left(\frac{2}{\pi}\arctan\left(\alpha_2 h\right) + 1\right)\right]. \tag{22.75}$$

As discussed in [9], the non-linear function of stress triaxiality should saturate to a certain level. As long as $\alpha_1 \geq 0$, no negative shear band rate can be caused by the stress state. Regarding $\alpha_1 < 0$, a non-negative rate of shear bands is obtained, if the parameters fulfill $\alpha_0 \geq 0$ and $\alpha_1 \geq -\frac{\alpha_0}{2}$. As temperature influence, probability functions are chosen [37]:

$$\alpha_{\mathrm{t}}\left(\vartheta\right) = \begin{cases} \exp\left(-\left(\frac{\vartheta-\alpha_3}{\alpha_4}\right)^2\right) & \vartheta \geq \alpha_3 \\ 1 & \vartheta < \alpha_3. \end{cases} \tag{22.76}$$

For β_{oc}, a similar structure given by (22.75) and (22.76) is assumed with parameters $\beta_0 - \beta_4$. Despite the empirical character of the extended kinetics law, less parameters are needed compared to the enhanced STRINGFELLOW-approach (Sect. 22.3.2.2).

The generally introduced TRIP-deformation rate (22.50) is utilized with the following parameters:

$$k_{\mathrm{gj}} = 8.1 \times 10^{-5}\,\mathrm{MPa}^{-1}, \quad \varphi\left(z\right) = \left(2 - z\right) z, \quad k_{\mathrm{s}} = 0, \quad \triangle_{\mathrm{v}} = 0.02. \tag{22.77}$$

This set of parameters leads to a comparatively small contribution of transformation induced plasticity to the whole deformation.

22.3.3.4 Ductile Damage

Damage models devoted to high alloy TRIP-steels have been mainly developed for applications at cryogenic temperatures employing concepts of continuum damage mechanics [65–67]. A ductile damage mechanism is assumed as common feature of the mentioned approaches. Regularized damage models for TRIP-steels are less investigated, except first studies [12].

The evolution of ductile damage is known to be dependent on plastic deformation and stress state. Seupel and Kuna [35] propose an empirical, regularized model for ductile damage, which is able to predict failure due to void based mechanisms at high stress triaxialities and shear dominated failure. The mentioned model is a gradient-enhanced version of local engineering approaches, e.g., [68]. In the present section, the approach of Seupel and Kuna [35] is adopted for the micromorphic-viscoplastic framework.

The empirical approach to ductile failure is based on the hypothesis, that damage can be neglected in a certain deformation range, but evolves rather fast after initiation [68]. The initiation of damage is captured by a loading history dependent indicator function $\omega\left(\varepsilon_{\mathrm{eq}}, \boldsymbol{\sigma}\right)$, which is not directly coupled to the constitutive equations similar to well known failure criteria. Exceeding a critical value $\omega \geq \omega_{\mathrm{c}}$ determines the initiation of damage, i.e., the onset of evolution of the local damage driving force $\dot{\varepsilon}_{\mathrm{l}}\left(\boldsymbol{D}_{\mathrm{vpl}}\right)$. Its evolution is proposed as

$$\dot{\varepsilon}_{\mathrm{l}} = \begin{cases} 0, & \omega\left(\boldsymbol{\sigma}, \varepsilon_{\mathrm{eq}}, z\right) < \omega_{\mathrm{c}} \\ q_2 \dot{\varepsilon}_{\mathrm{eq}} + q_3 \dot{\varepsilon}_{\mathrm{h}} \overset{(22.70)}{=} \left(q_2 + \frac{q_1 q_3 D\langle h\rangle}{3}\right) \dot{\varepsilon}_{\mathrm{eq}}, & \omega\left(\boldsymbol{\sigma}, \varepsilon_{\mathrm{eq}}, z\right) \geq \omega_{\mathrm{c}}. \end{cases} \tag{22.78}$$

The model parameters q_2 and q_3 can be adjusted to weight between shear ($\dot{\varepsilon}_{\mathrm{eq}}$) and void growth dominated damage ($\dot{\varepsilon}_{\mathrm{h}}$), respectively. It should be mentioned, that the local damage driving strain ε_{l} is associated to the dissipation potential and viscoplas-

tic flow. Mediavilla et al. [69] propose a non-local damage model using a comparable driving strain, but therein the plastic yielding stays purely deviatoric.

The micromorphic counterpart $\varepsilon_{\mathrm{nl}}$ of the damage driving strain is given by solving the micromorphic balance (22.34). To reach at a regularized damage model, the damage evolution is formulated with help of the micromorphic (non-local) variable $\varepsilon_{\mathrm{nl}}$. Following [69], an auxiliary variable κ is defined to avoid pathological healing effects, cf. [34, 35],

$$\dot{\kappa} \geq 0, \qquad \dot{\kappa}\,(\varepsilon_{\mathrm{nl}} - \kappa) = 0, \qquad \varepsilon_{\mathrm{nl}} - \kappa \leq 0. \tag{22.79}$$

An exponential dependency of damage evolution on κ is assumed:

$$\dot{D} = \begin{cases} 3\,(1-D)\,\frac{\dot{\kappa}}{\varepsilon_{\mathrm{c}}} & D < D_{\mathrm{c}} \\ D_{\max} a^{*} \exp\left(-a^{*}\,(\kappa - \kappa^{*})\right)\dot{\kappa} & D \geq D_{\mathrm{c}} \end{cases} \tag{22.80}$$

or in integrated form

$$D = \begin{cases} 1 - (1-D_0)\exp\left(-3\frac{\kappa}{\varepsilon_{\mathrm{c}}}\right) & D < D_{\mathrm{c}} \\ D_{\max}\left(1 - \exp\left(-a^{*}\,(\kappa - \kappa^{*})\right)\right) & D \geq D_{\mathrm{c}} \end{cases} \tag{22.81}$$

with

$$a^{*} = \frac{3}{\varepsilon_{\mathrm{c}}}\frac{(1-D_{\mathrm{c}})}{(D_{\max} - D_{\mathrm{c}})}, \tag{22.82}$$

$$\kappa^{*} = -\frac{\varepsilon_{\mathrm{c}}}{3}\ln\left(\frac{1-D_{\mathrm{c}}}{1-D_0}\right) + \frac{1}{a^{*}}\ln\left(1 - \frac{D_{\mathrm{c}}}{D_{\max}}\right). \tag{22.83}$$

Because κ is a monotonically increasing variable without upper limit, a totally damaged state ($D \approx 1$) can be reached asymptotically. In order to ensure the robustness of the model near to total failure, the numerical value of damage is limited by a prescribed saturation of D towards $D_{\max} < 1$ as proposed by Seupel and Kuna [35] (second case in (22.80) and (22.81), respectively).

The exponential damage law is motivated by the evolution of porosity assuming a nearly volume preserving matrix material, c.f. [57]. The purely void growth based damage mechanism is included in the current formulation by imposing $\varepsilon_{\mathrm{c}} = 1, q_2 = 0$ and $q_3 = 1$ with $D_0 > 0$. The additional parameter ε_{c} can be used to adjust the slope of the damage law. The saturation value of damage is prescribed as $D_{\max} = 0.999 \approx 1$ and the transition value is set to $D_{\mathrm{c}} = 0.995$, i.e., near the state of total material failure.

To avoid a spurious widening of the total damaged zone, Seupel and Kuna [35] suggest to fix the local contribution $\dot{\varepsilon}_{\mathrm{l}} = 0$ in case the totally damaged state $D \geq D_{\mathrm{c}}$ is reached. This patch solution damps the widening of the totally damaged domain, but other sophisticated methods, cf. [70], should be taken into account in ongoing

works. The zone of totally damaged integration points or finite elements mimics the actually discontinuous crack.

22.3.3.5 Thermodynamic Consistency

The mechanical dissipation introduced in (22.41) can be specified for the phenomenological model as

$$\gamma_{\mathrm{m}} = \sigma_{\mathrm{eq}} \left(\dot{\varepsilon}_{\mathrm{eq}} + \hat{\sigma}_{\mathrm{eq}} k_{\mathrm{gj}} \frac{\mathrm{d}\varphi\,(z)}{\mathrm{d}z} \dot{z} \right) + \sigma_{\mathrm{h}}\ (\dot{\varepsilon}_{\mathrm{h}} + \triangle_{\mathrm{v}} \dot{z}) - \triangle g_{\mathrm{chem}}^{\mathrm{a} \rightarrow \mathrm{m}} \dot{z} - Y \dot{D}. \quad (22.84)$$

The rates of the introduced internal variables are constructed to yield $\dot{\kappa}_{\alpha} \geq 0$. The first part of γ_{m} (σ_{eq} (...)) is always larger or equal to zero. The damage contribution is likewise non-negative, because $Y \leq 0$. The chemical contribution is positive as long as the temperature is below the thermodynamic equilibrium temperature. For temperatures above, this restriction is not fulfilled automatically and this part has to be controlled. For experimentally calibrated models, $\dot{z}$ should vanish in this temperature region, i.e., the chemical part is typically thermodynamically consistent. The dissipation contribution of volumetric plastic strain is always non-negative, see (22.69), whereas the volumetric TRIP-strains can cause a negative dissipation in compression states [9], i.e., if $\sigma_{\mathrm{h}} < 0$. To ensure positive dissipation, the hydrostatic TRIP-part is neglected in the mechanical dissipation as proposed by Mahnken and Schneidt [46]. Nonetheless, it should be mentioned that the damage model without martensite evolution is thermodynamically consistent in a strict sense.

22.3.4 Numerical Implementation

In order to analyze complex boundary value problems numerically, the material models are implemented into the FE-code ABAQUS via the user-defined subroutine UMAT. Implementation aspects of the micromechanically motivated and phenomenological model within the thermomechanical framework are discussed in literature [22, 34, 35]. One particular aspect should be emphasized: The implementation of the micromorphic damage model is simplified due to the similarity of the HELMHOLTZ-type equation (22.34) and the steady state case of the heat equation (22.42) as pointed out in [34]. A simple renaming of variables ($\varepsilon_{\mathrm{nl}} \leftrightarrow \vartheta$), a modification of the heat source ($\tilde{p} \leftrightarrow -\varepsilon_{\mathrm{nl}} + \varepsilon_{\mathrm{l}}$), and the interpretation of the conductivity $\lambda_{\mathrm{th}} \leftrightarrow L_{\mathrm{nl}}^2$ allow a fast implementation into the commercial FE-code. A major advantage is the usage of the available thermomechanical finite element library and post-processing tools, which becomes interesting for engineering applications.

22.4 Results

In this section the introduced models are applied. A detailed study on the phenomenological modeling approach from Sect. 22.3.3 is conducted to demonstrate its ability to comprise the influence of stress state and temperature on martensite kinetics as well as strain hardening behavior. Furthermore, the micromechanically motivated model from Sect. 22.3.2 is used in order to study the stress field in front of a crack. Additionally, the crack driving force is formulated in consideration of plastic deformation and phase transformation. Finally, a cohesive zone approach and the micromorphic damage model (Sect. 22.3.3) are utilized to simulate ductile fracture in a particular TRIP-steel.

22.4.1 Material

Consistent experimental investigations on a cast TRIP-steel X3CrMnNi 16-6-6 (see [53, 63]) are used as reference for calibration and validation purposes. The exact chemical composition is given in Table 22.1. A detailed characterization of the material can be found in [63]. The material used to manufacture the CT-specimen for fracture mechanics test exhibits a slightly deviating composition, see Table 22.1.

22.4.2 Deformation and Phase Transition Behavior

For the phenomenological model from Sect. 22.3.3, a step-by-step calibration strategy is pursued: Firstly, the model parameters of the martensite kinetics law are estimated with help of experimental data. Afterwards, the temperature and stress state dependent isotropic strain hardening law is fitted to a characteristic subset of tests. Following Prüger et al. [9], a simultaneous calibration to uni-axial tests at quasi-static loading, but different temperatures can be used as starting point. Damage effects are neglected at this stage of modeling. The validity of the model is assessed by predictions of the material behavior at other temperature conditions, strain rates, and inhomogeneous loading states. A comparable assessment for the micromechanically motivated model discussed in Sect. 22.3.2 can be found in recent literature [9, 22].

Table 22.1 Chemical composition of considered cast TRIP-steels in mass %

Alloy	Fe	C	N	Cr	Mn	Ni	Si
X2CrMnNi 15-5-7	Bal.	0.03	0.03	15.5	6.1	6.1	0.9
X2CrNiMn 15-7-5	Bal.	0.023	0.086	14.5	5.36	6.85	0.88

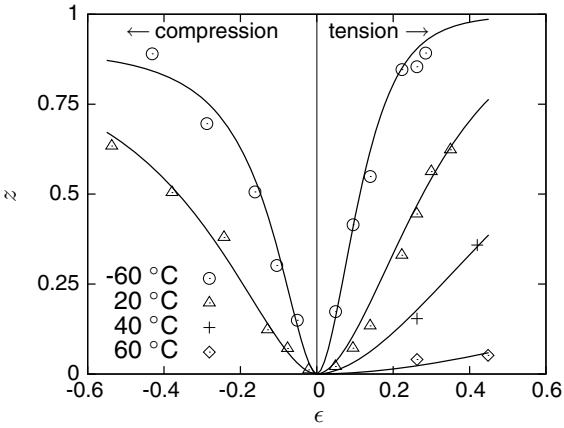

Fig. 22.1 Martensite volume fraction z versus true strain ϵ curves for uni-axial tension-compression loadings at different temperatures and constant strain rate $\dot{\epsilon}_t = 4 \times 10^{-4}\ \mathrm{s}^{-1}$: symbols correspond to experimental data of cast X3CrMnNi 16-6-6, solid lines correspond to the fitted empirical model (Sect. 22.3.3.3)

22.4.2.1 Martensite Kinetics

The empirical model of strain induced martensite kinetics (Sect. 22.3.3.3) is calibrated using experimental data from uni-axial, quasi-static tensile and compression tests at different temperatures ranging from −60 to 60 °C [6, 10, 63, 71]. The calibration result is shown in Fig. 22.1 in terms of evolving martensite volume fraction during straining. A good match of the martensite evolutions is obtained with the *a priori* estimation of the model parameters given in Table 22.2 and the exponent $n_{oc} = 1.868$. For calibration purposes, the approximate coincidence of true strain ϵ and the equivalent plastic strain ε_{eq} is assumed. Due to the occurrence of additional TRIP-strains depending on stress, a small deviation is to be expected finally.

22.4.2.2 Asymmetric Strain Hardening

The isotropic strain hardening contributions in (22.71) are chosen as functions of the hardening variable r, the temperature ϑ, and the martensite volume fraction z in the following manner [34]:

Table 22.2 Model parameters of empirical martensite kinetics (22.76)

α_0	α_1	α_2	α_3	α_4	β_0	β_1	β_2	β_3	β_4
–	–	–	K	K	–	–	–	K	K
2.77	1.14	−100	233.15	63.26	2.27	2.88	100	313.15	27.36

Table 22.3 Model parameters of isotropic strain hardening (22.85)–(22.87)

σ_0	H_0	q	H_{inf}	r_c	Z_1	Z_2	c_1	c_2
MPa	MPa	–	MPa	–	MPa	–	–	K
174.2	1305.6	0.927	269.0	0.277	510.1	1.193	-0.0014	373.15

Table 22.4 Model parameters of asymmetric strain hardening (22.74)

b_0	T_0	T_1	z_0	z_1
–	K	K	–	–
2.259	228.431	90.441	0.276	0.314

$$H(r) = \begin{cases} H_0 r^q & r \le r_c \\ H_0 r_c^q + H_{\text{inf}} \left(1 - \exp\left(-\frac{H_0 q r_c^{q-1}}{H_{\text{inf}}} (r - r_c)\right)\right) & \text{else} \end{cases}, \tag{22.85}$$

$$\sigma_0(\vartheta) = \exp\left(c_1 (\vartheta - c_2)\right) \sigma_0, \tag{22.86}$$

$$m_z(z) = 1 - \exp(-Z_2 z). \tag{22.87}$$

Thermoelastic properties for the considered steel are taken from literature [9]. Appropriate values for the parameters of strain rate sensitivity m and $\dot{\varepsilon}_0$ are also proposed in literature [9, 48]: $m = 40$ and $\dot{\varepsilon}_0 = 4 \times 10^{-4}\ \text{s}^{-1}$. Nine model parameters for isotropic strain hardening are to be identified and calibrated (22.85)–(22.87). Additionally, five parameters for stress state dependent evolution of the hardening variable have to be estimated, see (22.74). The final sets of estimated parameters are summarized in Tables 22.3 and 22.4.

As reference test data, force versus elongation curves of uni-axial, quasi-static tension and compression tests at −60, 20 and 100 °C [6, 10, 63, 71] are chosen. At these temperatures, different amounts of martensite are reached, from nearly 100% down to 0%, see Fig. 22.1. The reasonable calibration results are illustrated in Fig. 22.2.

The stress state dependent strain hardening becomes clearly visible in terms of the true stress versus strain curves, see Fig. 22.3. In addition to the calibrated temperatures, predictions are made for 60 and 200 °C. The corresponding experimental data is published in [6, 10, 63, 71]. From −60 to 60 °C, substantial higher stress levels are attained in uni-axial compression compared to tension. The asymmetry vanishes at about 200 °C, because neither martensite nor shear bands are formed, which is predicted by the model. Moreover, the qualitative change in strain hardening with temperature is reflected. The prediction at 60 °C in the compression regime deviates slightly. This indicates that other effects, especially the TWIP-effect, and their influence on strain hardening have to be considered in ongoing works.

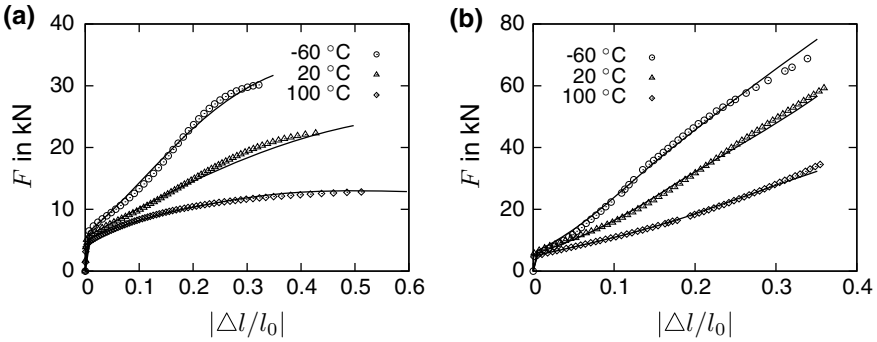

Fig. 22.2 Force F versus elongation $\Delta l/l_0$ curves at different temperatures and constant engineering strain rate $\dot{\epsilon}_t = 4 \times 10^{-4}\ s^{-1}$, symbols correspond to experimental data of cast X3CrMnNi 16-6-6, solid lines correspond to the fitted phenomenological model, **a** Uni-axial tension, **b** Uni-axial compression

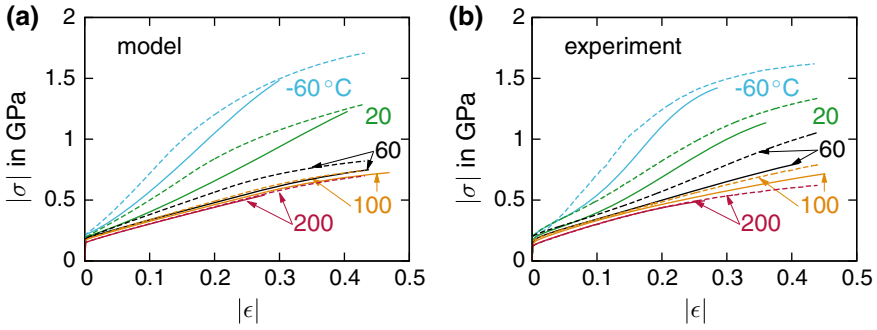

Fig. 22.3 True stress σ versus true strain ϵ curves for different temperatures and stress states at $\dot{\epsilon}_t = 4 \times 10^{-4}\ s^{-1}$, solid lines correspond to tensile and dashed lines to compressive loadings, respectively; **a** Model predictions, **b** Experimental data of cast X3CrMnNi 16-6-6

22.4.2.3 Strain Rate Dependency

A characteristic strain rate effect of high alloy TRIP-steels is the so-called curve crossing observed in tensile tests [9]: The temperature increase during plastic deformation inhibits the formation of α'-martensite and thereby restricts the strain hardening capability. The temperature increases with increasing strain rates, because adiabatic conditions are asymptotically reached. The typical experimental observation based on data from [10, 63, 71, 72] is shown in Fig. 22.4: After a higher stress level at low strains, the curves of higher strain rates drop below the quasi-static reference curve. In order to reproduce this behavior, a thermomechanical coupling is mandatory [9].

For the numerical simulations via FEM, a FE-implementation of the whole experimental setup becomes necessary in order to consider the heat transfer from the specimen to clamps and environment. A detailed description of the utilized

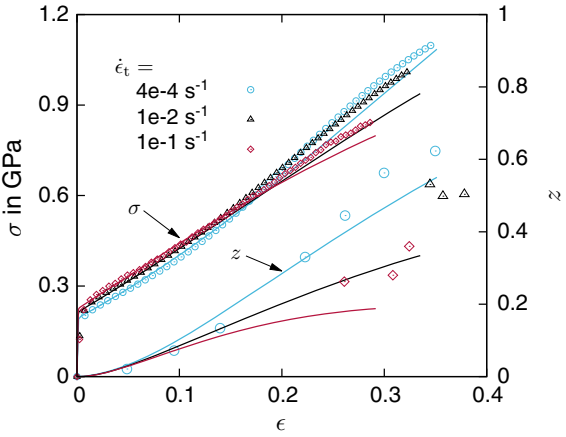

Fig. 22.4 Stress σ and martensite volume fraction z versus true strain ϵ curves at different technical strain rates $\dot{\epsilon}_t$ during uni-axial tension test: symbols correspond to experimental data of cast X3CrMnNi 16-6-6, solid lines denote the model prediction

FE-model is given in [9]. For the micromechanically motivated model introduced in Sect. 22.3.2, the ability to cover the curve crossing effect is shown in [9]. The same analysis is conducted for the phenomenological model with the results summarized in Fig. 22.4: Qualitatively, the curve crossing in strain hardening and the lower α'-martensite content at higher strain rates can be reproduced. A good match of the experimental stress versus strain curves is visible for strains $\epsilon < 0.18$ for all considered strain rates. The predictions cannot fit for higher strain rates exactly, because there is an initial deviation of the quasi-static case at strains larger than 0.18. Additionally, due to the full dissipative formulation of the model, a temperature increase ($\Delta\vartheta \approx 70$ K) is predicted which is considerably higher than measured in experiments ($\Delta\vartheta \approx 45$ K, [63]). As result, the strain hardening and martensite formation are weakened too much. This can be adjusted by introducing an empirical TAYLOR-QUINNEY-coefficient controlling the amount of dissipated power, see [73]. Despite the discussed need of improvements, the predictions of the models are physically reasonable.

22.4.2.4 Inhomogeneous Loading States

In addition to the uni-axial tests from [63], a series of round notched tensile tests has been conducted [53]. As test conditions, room temperature (20 °C) and quasi-static loading has been applied. A detailed description of the test setup and the evaluation procedure are given in [53]. The predictions of the calibrated material model are assessed by a comparison with the experimental results in Fig. 22.5. Good predictions of the force response are nearly made up to the onset of failure indicated by a rather sudden load drop for all differently notched specimens. Due to neglected damage, clear overestimations in the post-failure regime are visible. The indicated softening within the simulated curves is purely due to necking. Material softening caused by damage is taken into account in Sect. 22.4.4.2.

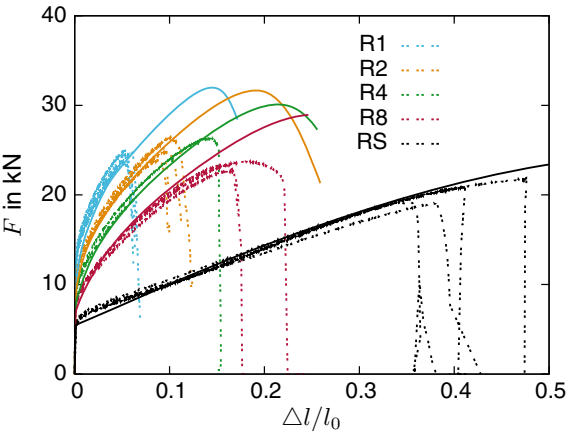

Fig. 22.5 Force F versus elongation $\Delta l/l_0$ curves for differently notched tensile tests, numbers highlight the notch radius in mm (RS—smooth test); solid lines correspond to the model prediction, dashed lines denote experiments of cast X3CrMnNi 16-6-6

22.4.3 Stress Analysis and Material Forces for Cracks in TRIP-steels

In this section, the micromechanically motivated material model from Sect. 22.3.2 is applied for fracture mechanics investigations. The material parameters are based on experimental data of cast steel X3CrMnNi 16-6-6, see Table 22.1 and references [20, 21, 53].

22.4.3.1 Crack Tip Fields in Front of a Blunting Crack Tip

In ductile materials, cracks tend to blunt during opening. Thereby, finite strains occur in front of the tip leading to characteristic shapes of the stress and strain fields. The phase transformation influences these crack tip fields and leads to some new characteristics, which are shown within this section.

From linear elastic fracture mechanics it is known, that the stresses become singular at the crack tip. The same holds for elastic-plastic fracture mechanics at small strains, compare the well established HRR-field [74, 75]. If plasticity and finite strains are considered, the situation is different. In this case crack tip blunting is incorporated, which means that an initially sharp crack deforms to a notch like shape. The stress fields are not singular any more. The stress component perpendicular to the surface of the blunted notch vanishes (σ_{11} in the ligament), because of the free surface. The crack opening stress (σ_{22}) reaches a maximum value at a distance in front of the crack and a finite value at the surface of the notch, see McMeeking [76]. If the considered material has a very high work hardening capacity, it is possible that the distinctive σ_{22} maximum does not occur. Instead the stress monotonically increases towards the crack tip and reaches high values there. This is reported by Yuan et al. [77] for an austenitic steel with pronounced strain hardening.

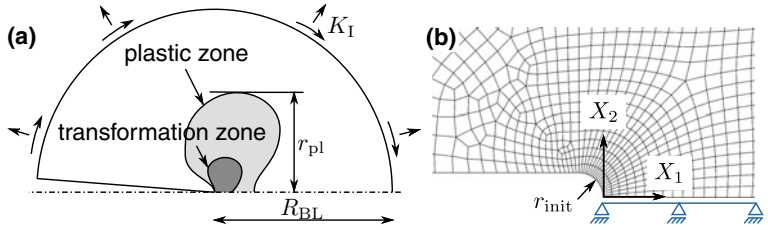

Fig. 22.6 **a** Sketch of the boundary-layer approach, **b** Detailed view of the initial crack tip and the finite element mesh together with the utilized coordinate system, reprinted from [20], with permission from Elsevier

In order to study the fields at a blunting crack without influence of a specific specimen geometry, small scale yielding under plain strain conditions is assumed. This is realized by a boundary-layer model, which is a circular region surrounding the crack tip, compare Fig. 22.6. Displacements known from the linear elastic K-field are prescribed on the boundary. In order to ensure small scale yielding, zones of inelastic deformation have to be small compared to the radius R_{BL}. In the case of strain induced phase transformation the transformation zone is always embedded inside the plastic zone, and thus $r_{pl} \ll R_{BL}$ is sufficient.

The boundary value problem is solved numerically employing finite elements. The boundary-layer model is discretized by quadrilateral elements with quadratic shape functions and reduced integration (ABAQUS: CPE8R). A zoomed view of the mesh near the crack is given in Fig. 22.6. It is typical to use a small initial radius at the crack tip in blunting studies, which is also shown in the figure. If the radius blunts to several times of its initial size, the resulting stress fields will be the same as for an initially sharp crack. The advantage of this initial radius is that distorted elements will show up later compared to the sharp crack tip. Further information can be found in [20].

The simulations yield steady state solutions for the mechanical fields. Thus, for example the distributions of stresses at different load levels K_I are self similar. They coincide in a single curve, if the distance to the initial crack tip in the reference configuration X_1 (Fig. 22.6) is normalized by J/σ_0, which is proportional to the crack tip opening displacement. Hereby, J is the J-integral and σ_0 is the initial yield stress of the material. Under small scale yielding and plane strain J is related to the prescribed K-factor and the elastic constants via

$$J = \frac{K_I^2(1-\nu^2)}{E}. \tag{22.88}$$

In order to point out the effect of the transformation hardening and the transformation strains, different model materials are considered, see Table 22.5. Figure 22.7 shows the corresponding true stress-strain curves and the evolution of martensite volume fraction. The variants are realized by an appropriate choice of the material

Table 22.5 Investigated model materials—Overview

Variant	Description, *influence*
TRIP	TRIP-steel
$\Uparrow$	*Volumetric transformation strain*
$\triangle_{\mathrm{v}} = 0$	TRIP-steel without volumetric transformation strain
$\Uparrow$	*Deviatoric transformation strain*
$\boldsymbol{\epsilon}_{\mathrm{trip}} = \mathbf{0}$	TRIP-steel without any transformation strain,
$\Uparrow$	*Transformation induced hardening*
Aust.	Austenite (without phase transformation)

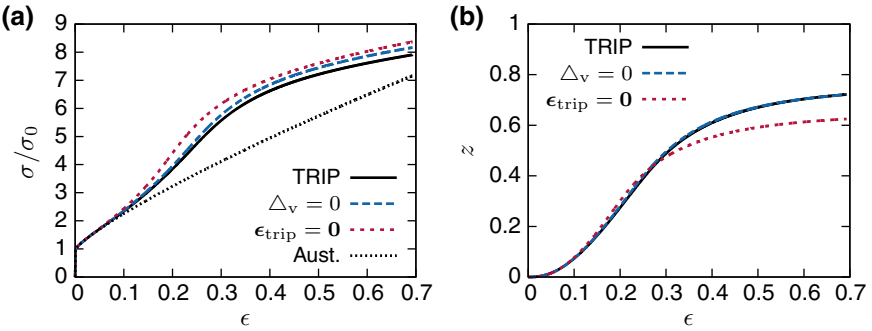

Fig. 22.7 Uniaxial behavior of the different model materials, **a** True stress-strain curves (σ vs. ϵ), **b** Evolution of martensite volume fraction z versus true strain ϵ

parameters, compare [20]. On the one hand, there is the TRIP-steel showing the full phase transformation with corresponding hardening and straining. On the other hand, there is a non-transforming austenite as reference. In between, there are two variants of TRIP-steel to study the role of deviatoric and volumetric transformation strain: one without volumetric transformation strain ($\triangle_{\mathrm{v}} = 0$), and the other one without any transformation strain ($\boldsymbol{\epsilon}_{\mathrm{trip}} = \mathbf{0}$).

At first, results for the TRIP-steel are discussed. The course of the stress components in the ligament is depicted in Fig. 22.8. Towards the crack tip (from right to left) an increase of the stress components is visible. The component σ_{11} reaches a maximum at $X_1 = 0.23J/\sigma_0$ and goes down to zero with smaller distance X_1. The stress component σ_{22} increases continuously towards the tip and does not show a maximum at some distance in front of the tip. This is consistent with [77] for material exhibiting high strain hardening. Furthermore, the crack opening stress σ_{22} shows a characteristic curvature, which is highlighted by the inflection points in Fig. 22.8. These characteristics are triggered by phase transformation. They occur in or near to the region with considerable martensite volume fraction, see Fig. 22.9. The stress triaxiality h, which is also depicted in Fig. 22.9, has a maximum in front of the tip and goes down to a finite non-zero value towards the crack.

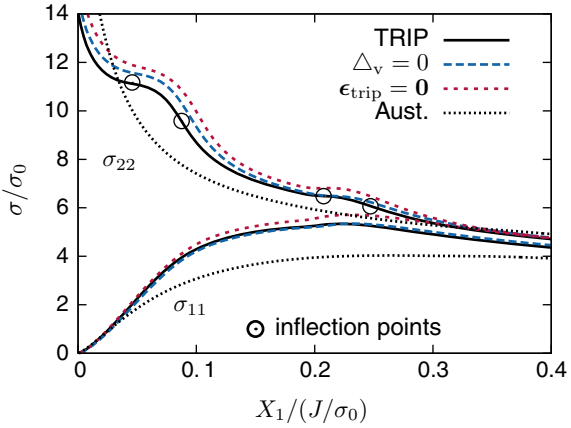

Fig. 22.8 Distribution of the stress components σ_{11} and σ_{22} in front of the blunting crack in the ligament for the different model materials, $X_1/(J/\sigma_0)$ is the normalized distance to the crack tip in the undeformed configuration

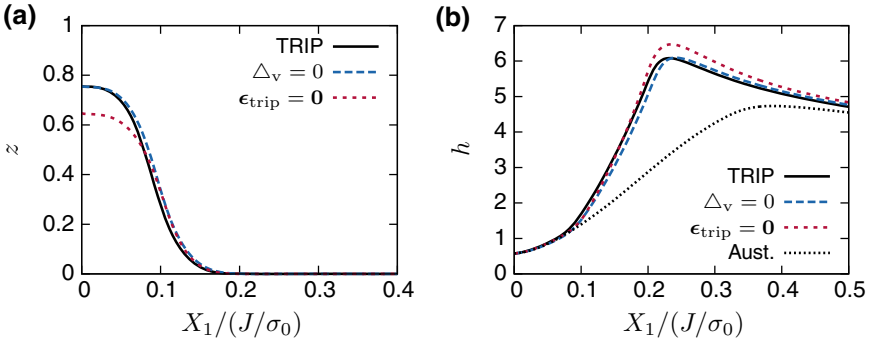

Fig. 22.9 Distribution of the martensite volume fraction z (**a**) and stress triaxiality h (**b**) in the ligament for the model materials, $X_1/(J/\sigma_0)$ is the normalized distance to the crack tip

In the next step the different model materials are taken into account. Comparing austenite to TRIP-steel, it becomes clear that phase transformation leads to higher stresses and stress triaxiality in the region near to the transformation zone. This is consistent with findings of Stringfellow [78]: By comparing TRIP-steel to non-transforming austenite, an increase of equivalent stress due to phase transformation was found. Considering the other two TRIP-variants one can conclude that the main effect comes from transformation induced hardening. The TRIP-steel without transformation strain already shows all the characteristic features (inflection points, increased stresses). The transformation strains reduce the stress components because of strain softening and affect the stress fields considerably near the tip, where the highest martensite volume fraction is present.

Interestingly, there is a region very near to the crack tip, where the stresses are highest in the austenite. This is explained with the different hardening behavior of the model materials. It can already be seen in Fig. 22.7, that the TRIP-steel variants reach higher stresses, but the austenite has the higher hardening modulus at strains larger than 0.3. Asymptotically, the stress-strain curve of pure austenite leads to the highest stresses, which is observed in the crack tip fields.

The implications of these observations on fracture in TRIP-steels were discussed in detail by Burgold et al. [20]. In the case of cleavage, phase transformation could have a negative effect, because of the higher principal stresses. But there is an open question, how martensite affects the critical fracture strength. In the case of ductile fracture, the transformation has a positive impact on toughness, because the transformation induced hardening hinders the growth of micro voids. This is supported by the work of Hütter et al. [79], who studied the effect of hardening on the ductile fracture mechanism by micromechanical simulations. In both cases (ductile fracture and cleavage) a shielding effect due to phase transformation can occur, because martensite evolution dissipates mechanical work, which is not available for crack growth anymore.

22.4.3.2 Material Forces in Consideration of Phase Transformation

In this section the influence of phase transformation on the crack driving force in TRIP-steels and a possible shielding effect are investigated. Therefore, the theory of material forces (also called configurational forces) is applied, which are generalized thermodynamic forces acting on defects, see e.g. [80–82]. A great advantage of the approach is that it distinguishes between the material force acting on the crack tip and those occuring in zones of inelastic deformation, see e.g. [83–86]. Generally, a material force $\vec{G}_\mathrm{D}$ acting on defects in a domain surrounded by the contour Γ reads

$$\vec{G}_\mathrm{D} = \int_\Gamma \boldsymbol{Q} \cdot \vec{n} \; \mathrm{d}S \tag{22.89}$$

with the unit normal vector $\vec{n}$ and the energy-momentum tensor of elasto-statics $\boldsymbol{Q}$ according to Eshelby, see [81]. The tensor $\boldsymbol{Q}$ is calculated by

$$\boldsymbol{Q} = \psi \boldsymbol{\delta} - (\operatorname{grad} \vec{u})^\mathrm{T} \cdot \boldsymbol{\sigma} \tag{22.90}$$

with the unit tensor of second order $\boldsymbol{\delta}$.

In this section we assume small strains, isothermal and static conditions, and the absence of body forces. The small strain tensor can be additively decomposed into elastic and inelastic strains.

$$\boldsymbol{\varepsilon} = \boldsymbol{\varepsilon}_\mathrm{el} + \boldsymbol{\varepsilon}_\mathrm{trip} + \boldsymbol{\varepsilon}_\mathrm{vpl} \tag{22.91}$$

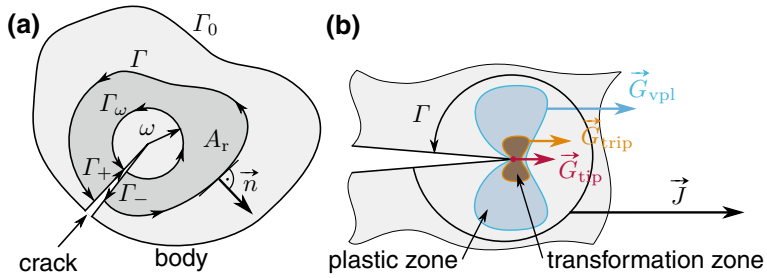

Fig. 22.10 **a** Cracked body with different contours and regular subpart A_r, **b** Different material forces near a crack tip in TRIP-steel acting on different defects

The application of material forces to TRIP-steel has been discussed in detail by Kuna et al. [21]. Thereafter, a local balance of material forces is established by taking the divergence of $\boldsymbol{Q}$, which after some rearrangements leads to

$$\operatorname{div} \boldsymbol{Q} + \boldsymbol{\sigma} : \operatorname{grad} \boldsymbol{\varepsilon}_{\mathrm{vpl}} + \boldsymbol{\sigma} : \operatorname{grad} \boldsymbol{\varepsilon}_{\mathrm{trip}} + \left| \triangle g_{\mathrm{chem}}^{\mathrm{a}\to\mathrm{m}} \right| \operatorname{grad} z = \vec{0}. \tag{22.92}$$

The term $\triangle g_{\mathrm{chem}}^{\mathrm{a}\to\mathrm{m}}$ describes the difference in the chemical energy of austenite and martensite and is known from Sect. 22.2.2.4. Following (22.92) the divergence of $\boldsymbol{Q}$ is balanced by material body forces resulting from gradients of the internal variables $\boldsymbol{\varepsilon}_{\mathrm{trip}}$, $\boldsymbol{\varepsilon}_{\mathrm{vpl}}$ and z. The gradient terms enter the derivation, because the gradient of the HELMHOLTZ potential ψ is evaluated, see [21].

Furthermore, the global balance of material forces is achieved by integrating the local balance (22.92) over a regular subpart A_r of the body. Figure 22.10 depicts the case of a cracked body with its regular subpart (domain A_r) and an enclosing contour $C = \Gamma + \Gamma_+ + \Gamma_- - \Gamma_\omega$. Applying the divergence theorem to the integrated local balance and some rearrangements enable the formulation of the material force acting on the crack tip:

$$\vec{G}_{\mathrm{tip}} = \lim_{\omega\to 0} \int_{\Gamma_\omega} \boldsymbol{Q} \cdot \vec{n} \, \mathrm{d}S = \vec{J} - \vec{G}_{\mathrm{trip}} - \vec{G}_{\mathrm{vpl}} \tag{22.93}$$

$$\vec{J} = \int_{\Gamma} \boldsymbol{Q} \cdot \vec{n} \, \mathrm{d}S \tag{22.94}$$

$$\vec{G}_{\mathrm{trip}} = \lim_{\omega\to 0} \int_{A_r} -\left(\boldsymbol{\sigma} : \operatorname{grad} \boldsymbol{\varepsilon}_{\mathrm{trip}} + \left| \triangle g_{\mathrm{chem}}^{\mathrm{a}\to\mathrm{m}} \right| \operatorname{grad} z \right) \, \mathrm{d}A \tag{22.95}$$

$$\vec{G}_{\mathrm{vpl}} = \lim_{\omega\to 0} \int_{A_r} -\boldsymbol{\sigma} : \operatorname{grad} \boldsymbol{\varepsilon}_{\mathrm{vpl}} \, \mathrm{d}A \tag{22.96}$$

The crack driving force $\vec{G}_{\text{tip}}$ is a J-integral evaluated over a vanishingly small contour Γ_ω surrounding the crack tip. It is computed by subtracting material forces $\vec{G}_{\text{trip}}$ and $\vec{G}_{\text{vpl}}$, which result from inelastic processes in the domain A_{r}, from the usual J-integral vector $\vec{J}$. $\vec{G}_{\text{tip}}$ turns out to be a modified J-integral, which is path independent in the case of plastic deformations and phase transformations.

The different material forces relevant for the considered TRIP-steel are illustrated in Fig. 22.10. There is the usual J-integral describing the sum of material forces for all defects inside the contour Γ. The crack driving force $\vec{G}_{\text{tip}}$ acts directly on the tip. The material forces due to inelastic processes $\vec{G}_{\text{trip}}$ and $\vec{G}_{\text{vpl}}$ act on the transformation zone and the plastic zone, respectively. In the case, that Γ only includes a part of these zones, the terms $\vec{G}_{\text{trip}}$ and $\vec{G}_{\text{vpl}}$ are material forces acting on this part of the zones. As long as the inelastic material forces are positive, they decrease the available crack driving force, see (22.93), which indicates a shielding effect.

The material forces are computed numerically by finite elements within the software package ABAQUS. Therefore, postprocessing of the FE results is performed. With the help of the equivalent domain integral method, nodal material forces are formulated, compare [19, 21, 83]. The global material forces (22.93)–(22.96) are then achieved by a weighted summation of the nodal material forces.

In the following, material forces are evaluated for the example of small scale yielding under plain strain conditions. Again the boundary-layer model, Fig. 22.6, is used, this time without an initial radius at the tip. Material parameters and additional information concerning the numerical model can be found in [21].

A cohesive zone (ABAQUS built-in) is placed at the ligament in order to incorporate crack initiation and propagation. One reason is that the path independence of the crack driving force can be elaborated under non-proportional loading. The other reason is that the cohesive zone model (CZM) contains a parameter G_0 called work of separation, which is exactly the dissipated work per area of crack extension. It is therefore the critical value of the crack driving force during crack extension, which has to be calculated correctly by the proposed material force method.

A bilinear traction separation relation is applied, which includes reversible opening of the cohesive zone until the cohesive strength t_0 is reached. The corresponding value of the separation is s_0. Loading beyond this point is connected to damage evolution and a descending load carrying capacity of the cohesive zone. At the separation s_{t} the cohesive zone is totally damaged and cannot carry tractions anymore. During the complete separation process until s_{t}, the work of separation G_0 is consumed.

The mesh consists of fully integrated quadrilateral elements with quadratic shape functions (ABAQUS: CPE8). The mesh design in the region of crack extension can be seen in the following figures.

A detailed view of different nodal material forces (notation: node (K)) is shown in Fig. 22.11. The upper crack face is depicted with the initial crack tip approximately in the center. A close scrutiny of these figures reveals, that there are substantial material forces at the nodes connected to the cohesive zone (nodes on the crack face right to the initial tip). Since the CZM incorporates the fracture process, these are nodal material forces acting on the smeared crack tip. Furthermore, there are

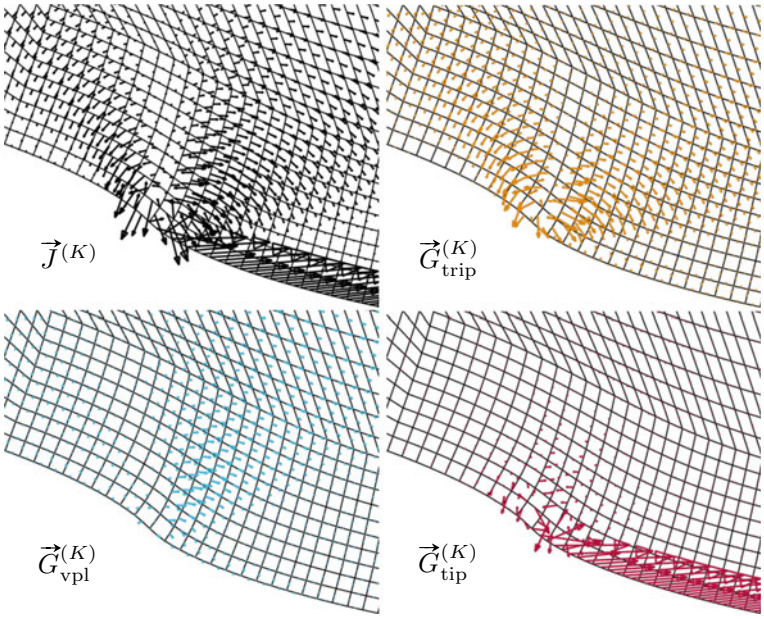

Fig. 22.11 Distribution of the different nodal material forces (node (K)), which are nodal contributions to the material forces of (22.93)–(22.96), the region near the initial crack tip (center of the crack flank) is shown during fracture initiation, cohesive elements are not shown here, reprinted from [21], with permission from Springer Nature

considerable nodal material forces in the bulk resulting from viscoplastic deformation and phase transformation. In contrast to the nodal contributions to the usual J-integral $\vec{J}^{(K)}$, the nodal contributions to the material force acting on the tip $\vec{G}^{(K)}_{\mathrm{tip}}$ nearly vanish in the volume, because of the subtraction of the inelastic nodal material forces $\vec{G}^{(K)}_{\mathrm{trip}}$ and $\vec{G}^{(K)}_{\mathrm{vpl}}$. Small remaining vectors can be explained with numerical errors in the computation of the gradients of the internal variables. They have actually no influence on the material forces after summation of the nodal contributions, see the next paragraph.

The nodal material forces are summed up to get material forces acting on the crack, the plastic zone and the transformation zone. In the case of crack propagation under mode I only the x_1-components are non-zero. These components of the different material forces are plotted in Fig. 22.12. Firstly, plausibility is checked: The regular J-integral J_1 equals the J-integral J_1^{SSY}, which is prescribed at the boundary layer, see again (22.88). Furthermore, once the cohesive zone is fully initiated, the crack driving force G_1^{tip} equals the work of separation G_0 of the CZM. The symbols in the diagram mark start and end of the fracture initiation process. At $s^{\mathrm{tip}} = s_0$, the first cohesive element reaches the cohesive strength and starts to damage. At $s^{\mathrm{tip}} = s_{\mathrm{t}}$, the first cohesive element reaches total damage and for the first time $G_1^{\mathrm{tip}} = G_0$ is

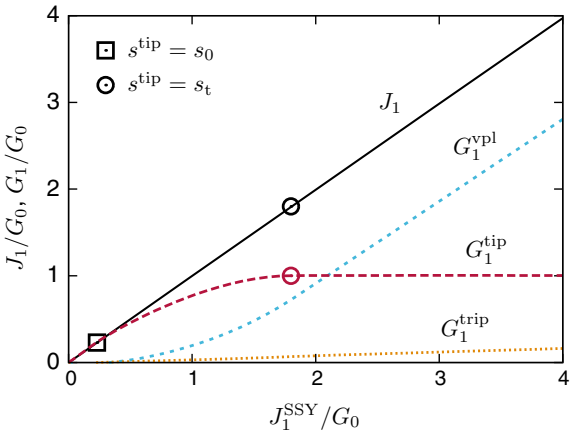

Fig. 22.12 Evolution of the nonzero component of the material forces for the boundary-layer model, J_1^{SSY} is the prescribed J-integral (external loading), G_0 is the work of separation of the CZM, start and end of fracture initiation is marked by symbols, reprinted from [21], with permission from Springer Nature

fulfilled. Thus, the proposed material force method is verified to give reasonable results.

Secondly, the contributions of the inelastic processes can be viewed in detail, Fig. 22.12. In contrast to the local distribution of the nodal material forces, the plasticity induced material force G_1^{vpl} is dominant compared to the transformation induced G_1^{trip}. This is because the plastic zone is much larger than the transformation zone in the example. Both contributions are positive, which underlines the shielding effect of viscoplasticity and martensitic phase transformation.

In Fig. 22.13, the path independence of the formulated crack driving force is demonstrated by evaluating G_1^{tip} for different domains and comparing it to the usual J-integral J_1. Until the start of fracture initiation in the CZM, both values are equal. For the case of monotonically and proportionally loaded cracks, the classical J-integral is known to be approximately path independent even if inelastic material behavior is present. This changes during crack initiation: J_1 becomes path dependent whereas the material force acting directly on the crack tip G_1^{tip} remains path independent.

22.4.4 Damage and Fracture of High Alloy TRIP-steel

Now, the simulation of damage and crack extension in high alloy TRIP-steel is elaborated in more detail. On the one hand, a cohesive zone model (CZM) is applied and appropriate cohesive parameters are estimated. On the other hand, damage evolution and crack growth is modeled by the phenomenological model, Sect. 22.3.3, including the developed non-local ductile damage formulation.

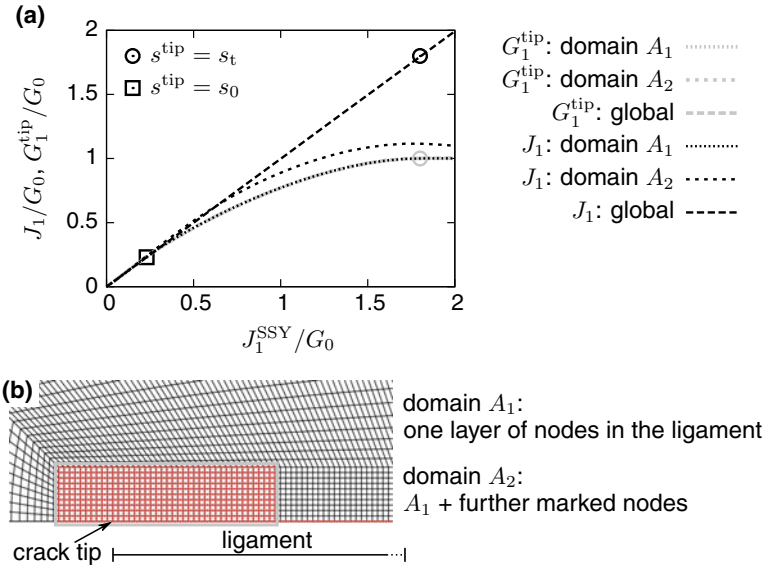

Fig. 22.13 Demonstration of the path independence of the crack driving force G_1^{tip}, **a** Evaluation of the J-integral J_1 and G_1^{tip} for different domains, J_1^{SSY} is the prescribed J-integral, G_0 is the work of separation of the CZM, **b** Definition of the different domains used in the diagram, adapted from [21], with permission from Springer Nature

22.4.4.1 Simulation of Crack Growth Using a Cohesive Zone Model

In the last section, the versatility of the cohesive zone model for the simulation of crack extension was shown. In particular, the material parameter G_0 (work of separation) is the critical value of the material force acting on the crack tip. To apply this fracture criterion, it is important to identify G_0 for the given material.

In this section, the cohesive zone parameters are identified for the cast TRIP-steel X2CrNiMn 15-7-5. The chemical composition of the investigated steel is given in Table 22.1. The corresponding experiments are carried out on CT-specimens with chevron notch, see Fig. 22.14 and the paper by Burgold et al. [87] for further details. Fracture mechanical experiments on austenitic steels are a difficult task, because of the high work hardening capability and ductility. Excessive large scale yielding, which is shown in Fig. 22.14, impose challenges to the experiments and standard methods for measuring the crack length since compliance method or potential drop method do not work [87]. Therefore, special optical techniques (see Henkel et al. [88]) are used in order to measure crack extension Δa and crack tip opening displacement CTOD δ at the surface of the specimen. From the experiments, force-displacement curves and crack growth resistance curves in terms of CTOD versus crack extension are obtained.

Because of large necking and thickness reduction during the tests three dimensional finite element calculations at finite strains are carried out, see [87, 89],

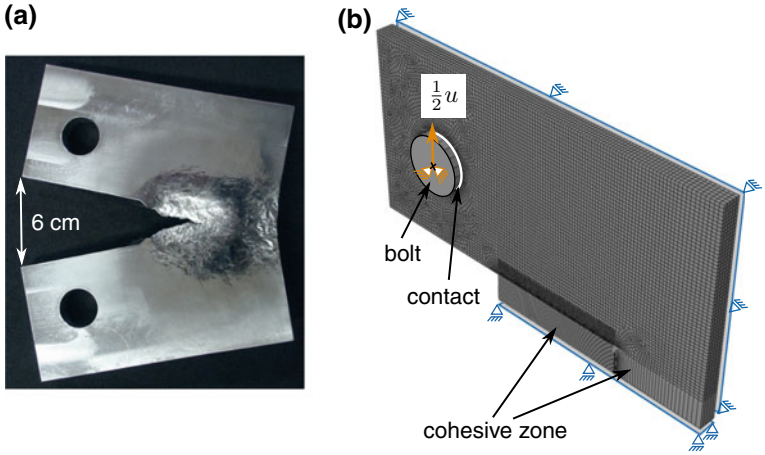

Fig. 22.14 **a** Deformed CT-specimen made of austenitic cast steel, **b** Finite element model with boundary conditions, displacement u is prescribed on the bolt, reprinted from [87], with permission from Carl Hanser Verlag GmbH & Co. KG, München

employing the commercial FE software ABAQUS. A quarter of the CT-specimen is modeled, compare Fig. 22.14. A vertical displacement u is prescribed on the bolt, that is connected to the deformable body by a contact algorithm.

The utilized CZM was developed by Roth et al. [90, 91]. Hereby, a smooth exponential traction separation relation is applied, which has an adjustable shape due to two shape parameters $\hat{\varepsilon}$ and $\hat{\omega}$. One finding of the study is, that the choice $\hat{\varepsilon} = \hat{\omega} = 1$ facilitates a good fit of the experimental data. Therewith, the well known traction separation relation from Xu and Needleman [92] is obtained.

The body is discretized by fully integrated continuum elements with linear shape functions (ABAQUS: C3D8). One layer of cohesive elements, which are user defined elements (UEL) [90, 91], is placed in the ligament. In contrast to ABAQUS built-in cohesive elements, the user elements work correctly on symmetry planes under large deformations.

It turned out to be sufficient to model the material behavior of the applied steel by a simplified constitutive law, in which transformation strains are not considered. The yield function of the rate independent model for isothermal conditions is given by

$$y_{\mathrm{pl}}(\boldsymbol{\sigma}, \sigma_{\mathrm{y}}) = \sigma_{\mathrm{eq}}(\boldsymbol{\sigma}) - \sigma_{\mathrm{y}} \leq 0 \tag{22.97}$$

with the VON MISES equivalent stress σ_{eq} and the yield stress σ_{y}. An associated flow rule is considered and the evolution equation for the plastic rate of deformation takes the form

$$\boldsymbol{D}_{\mathrm{pl}} = \dot{\Lambda}_{\mathrm{pl}} \frac{\partial y_{\mathrm{pl}}}{\partial \boldsymbol{\sigma}} = \dot{\varepsilon}_{\mathrm{eq}} \boldsymbol{N}. \tag{22.98}$$

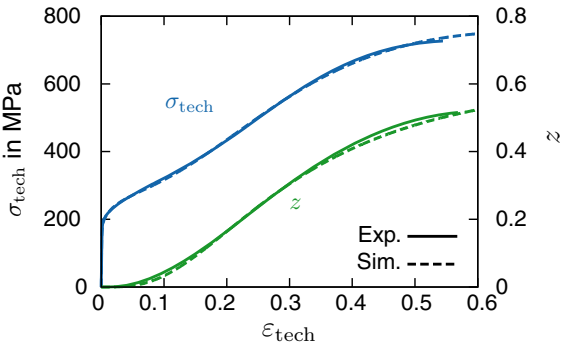

Fig. 22.15 Engineering stress-strain curves and evolution of martensite volume fraction z under uniaxial tension, comparison between experimental data and simulation with the material model

Hereby, the plastic multiplier $\dot{\Lambda}_{\text{pl}}$ is equal to the rate of equivalent plastic strain $\dot{\varepsilon}_{\text{eq}}$. The tensor $\boldsymbol{N}$ is the flow normal known from (22.51).

The evolution of the yield stress σ_{y} is defined by the hardening law (22.71). This relation is simplified because the isothermal case is considered and LODE-angle dependence is not taken into account ($r = \varepsilon_{\text{eq}}$ because $b = 0$ in (22.73))

$$\sigma_{\text{y}}\left(\varepsilon_{\text{eq}}, z\right) = \sigma_0 + Z_1 m_z\left(z\right) + H\left(\varepsilon_{\text{eq}}\right). \tag{22.99}$$

Thus, in addition to Z_1 the initial yield stress σ_0 becomes a material parameter. The work hardening term $H\left(\varepsilon_{\text{eq}}\right)$, see (22.85), is modified by $r_{\text{c}} \to \infty$ and reads

$$H\left(\varepsilon_{\text{eq}}\right) = H_0\, \varepsilon_{\text{eq}}^{q} \tag{22.100}$$

with the parameters H_0 and q. The martensite influence term $m_z\left(z\right)$ is given by (22.87) with the parameter Z_2.

The martensite kinetics is based on the empirical approach of Sect. 22.3.3.3. Therefore, the volume fraction of shear bands evolves as described by (22.48), in which α_{oc} is directly taken as material parameter. The rate of martensite volume fraction is computed by (22.49) with β_{oc} and n_{oc} as additional material parameters.

The parameters of the material model are adequately calibrated to data from tensile tests of the cast TRIP-steel X2CrNiMn 15-7-5, see Fig. 22.15. In addition to the mechanical data, the martensite volume fraction z is measured in situ by a novel magnetic device developed by Hauser et al. [93] and is applied in the calibration procedure. The identified parameters are given in Table 22.6.

Table 22.6 Parameters of the rate independent TRIP-steel model

σ_0	H_0	q	Z_1	Z_2	α_{oc}	β_{oc}	n_{oc}
MPa	MPa	–	MPa	–	–	–	–
153.8	434.2	0.401	370.9	2.06	5.66	0.988	3.805

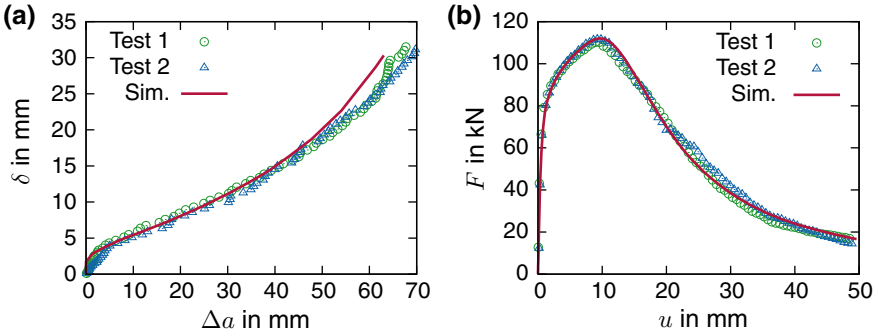

Fig. 22.16 Comparison of experiments and simulation, **a** Crack growth resistance curves in terms of CTOD δ and crack extension Δa, **b** Force-displacement curves (F vs. u)

Table 22.7 Identified set of cohesive zone parameters

t_0	G_0	$\hat{\varepsilon}$	$\hat{\omega}$
MPa	kJ/m^2	–	–
700	425	1	1

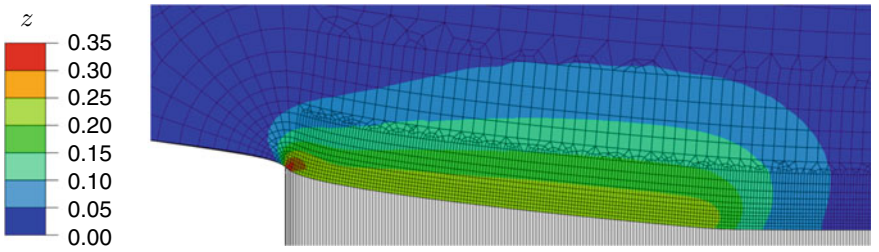

Fig. 22.17 Plot of the distribution of martensite volume fraction z during crack extension, note the cohesive elements (white) in the ligament

Ultimately, the remaining independent cohesive parameters G_0 and t_0 have been chosen in a way, that the simulated force-displacement curve and crack growth resistance curve fit the experimental ones. The results are depicted in Fig. 22.16. Data from two realizations of the experiment are compared to the simulation with the final parameter set, which is given in Table 22.7. The two tests show only small differences and the simulation fits both tests very well. This supports the identified set of parameters and the whole modeling approach. Thus, the fracture process in the investigated CT-specimens is characterized by the given cohesive parameters. This concept was also successfully applied to a non-transforming austenitic steel in [87].

Finally, the martensite distribution around the crack is illustrated in Fig. 22.17. The highest amount (0.3–0.35) of martensite is formed during crack tip blunting near the

initial crack tip. During crack extension a zone of martensite volume fraction between 0.2 and 0.25 is moved through the ligament.

22.4.4.2 Simulations Using the Micromorphic Model of Ductile Damage

Here, the micromorphic damage extensions of the phenomenological model from Sect. 22.3.3 will be used for simulation of ductile crack growth at isothermal conditions. Test results of the cast TRIP-steel X3CrMnNi 16-6-6 are utilized for calibration and validation. As described in [35], the calibration strategy for the considered class of damage models consists of three steps:

1. Choosing and fitting an isotropic strain hardening law to data of smooth and slightly notched tensile tests
2. Estimating an appropriate damage indicator function using FE-analysis and experimental results, e.g., of notched tensile tests
3. Fitting the damage parameters (q_1–q_3, ε_c and L_{nl}) to match results of a fracture mechanics test

For the first calibration step, the parameters of the strain hardening model for cast X3CrMnNi 16-6-6 (Sect. 22.4.2) are slightly modified. This is done in order to improve the fit to the notched tensile tests discussed in Sect. 22.4.2.4.

For the second calibration step, undamaged FE-simulations of the notched tensile tests are performed to extract the loading history which leads to initiation of damage in critical regions, see [35]. As critical region, the center of the specimen at the symmetry plane is defined, since here the highest stress triaxiality occurs. The history until the rather sudden deviation of simulated and experimental force versus elongation curves is taken into account. The equivalent strain to damage initiation is plotted versus the stress triaxiality in Fig. 22.18. For all considered notch radii, a drop of triaxiality during deformation is observed, which is in contrast to recent results of a pressure vessel steel [35]. This behavior can be attributed to the strain hardening of the TRIP-steel: The high hardening capability delays a localization of deformation and the blunting of the notch decreases the triaxiality of the loading state. As indicator of damage initiation, the integral formulation

$$\omega\left(h, \varepsilon_{eq}\right) = \int_0^{\varepsilon_{eq}(t)} \Omega\left(h\right)\, \mathrm{d}\varepsilon_{eq}, \tag{22.101}$$

$$\Omega\left(h\right) = \Omega_1 + \Omega_2 \exp\left(\Omega_3 h\right) \tag{22.102}$$

is used, which constitutes a modified Rice-Tracey-approach, see illustration in Fig. 22.18. The identified parameters read $\Omega_1 = 0.094$, $\Omega_2 = 0.666$, and $\Omega_3 = 2.721$.

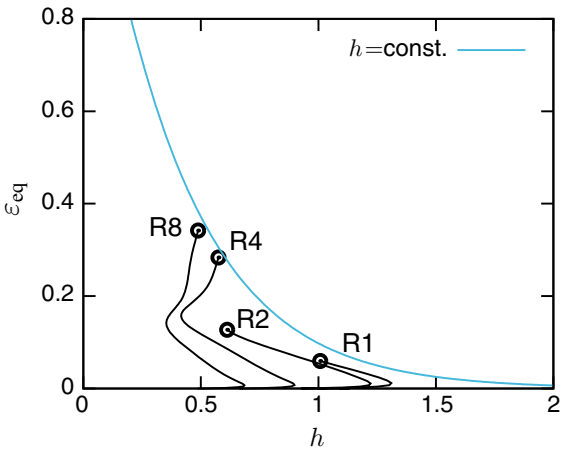

Fig. 22.18 Damage initiation locus (equivalent plastic strain ε_{eq} vs. stress triaxiality h): Loading history at the critical locations for the differently notched tensile tests, circles mark damage initiation; the damage initiation locus for constant triaxiality during loading is added as solid blue line

In addition to the notched tensile tests, fracture mechanics experiments are necessary in order to perform the third step of the proposed parameter calibration. Due to missing experimental results on fracture parameters of cast X3CrMnNi 16-6-6, a numerical prediction serves as fracture mechanics reference. Appropriate parameters of a cohesive zone model are available for a similar steel in Sect. 22.4.4.1. These results are utilized to make a realistic guess for the fracture behavior of X3CrMnNi 16-6-6. A simulation of the 3D-CT-specimen is performed using the calibrated cohesive zone model from Sect. 22.4.4.1 and the calibrated material model for X3CrMnNi 16-6-6. Because fracture is completely described by the cohesive zone, damage of the bulk material is neglected. The obtained reference force versus displacement curve and the crack growth resistance curve in terms of CTOD versus crack length are shown in Figs. 22.19 and 22.21. The crack extension Δa is evaluated using the maximum stress criterion with respect to the undeformed configuration at the surface of the specimen as explained in [94]. This criterion can be similarly evaluated for the cohesive zone model and the ductile damage approach.

The CT-specimen, see Fig. 22.14 and reference [87], is implemented as FE-model in ABAQUS. To avoid highly distorted elements, a small radius $r_t = 0.05$ mm is applied at the crack tip as suggested in literature (see Fig. 22.20, [35, 76, 94]), which is permissible for the expected blunting prior to crack propagation. A 3D-finite element formulation employing reduced integration with quadratic shape functions for the displacement and linear shape functions for the micromorphic DOF are used (ABAQUS: C3D20RT). Along the ligament, a mesh size of $b_e/L_{nl} = 0.25$ is prescribed, where b_e is the edge length of the element, see Fig. 22.20. This recommendation can be found in literature to obtain converged results [34, 35, 95]. The axi-symmetric models of notched tensile tests are also meshed with the mentioned restrictions in regions of interest (ABAQUS elements: CAX8RT).

During the calibration process, the parameters q_1 and q_3 are fixed to the value 3. Only the internal length L_{nl}, the influence of equivalent strain q_2 (void nucle-

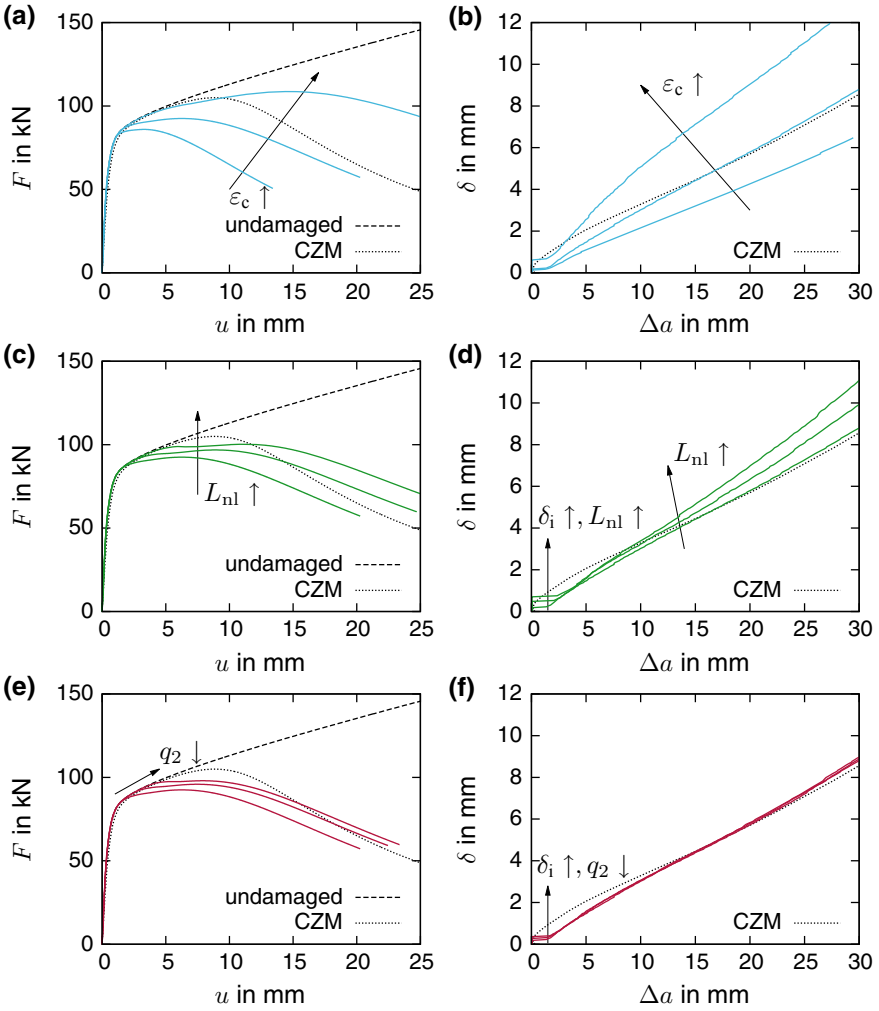

Fig. 22.19 Influence of different parameters of the damage evolution law on structural response of the CT-specimen (force F vs. displacement u curves, crack growth resistance CTOD δ vs. Δa), Top row (**a**, **b**): $\varepsilon_c = \{0.2, 0.3, 0.5\}$, Middle row (**c**, **d**): $L_{nl} = \{0.5, 0.75, 1\}$ mm, Bottom row (**e**, **f**): $q_2 = \{0.01, 0.025, 0.1\}$

ation), and the acceleration parameter ε_c are varied. Considerable small values are prescribed for q_2, because void growth is assumed as the main damage mechanism in the considered domain of moderate to high stress triaxialities.

In order to assess the influence of the free parameters, a sensitivity study is performed. The reference set of parameters is prescribed as: $\varepsilon_c = 0.3$, $L_{nl} = 0.5$ mm, and $q_2 = 0.1$. The results are summarized in Fig. 22.19 and compared to the reference cohesive zone simulation as well as the pure blunting solution: With varying ε_c,

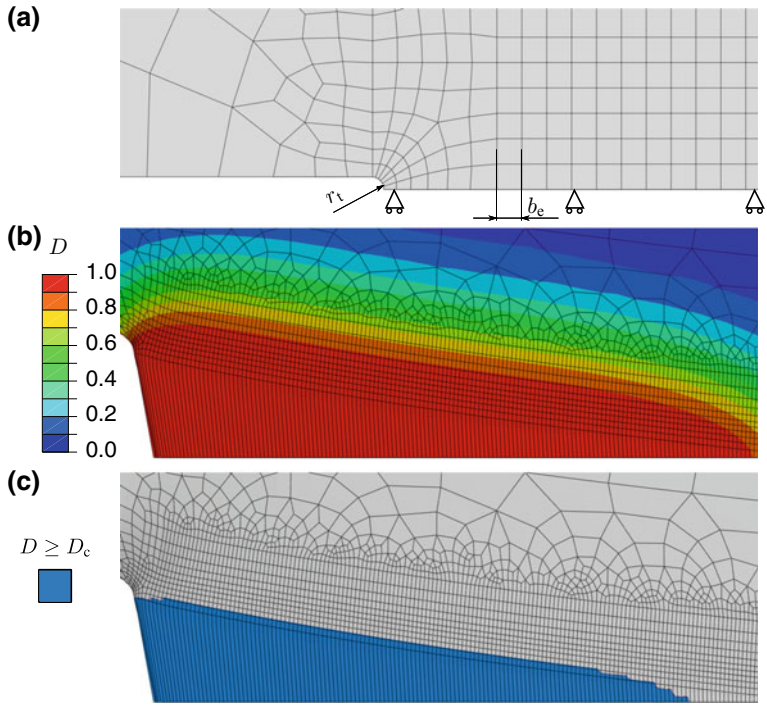

Fig. 22.20 Simulation of the CT-specimen, **a** Initial FE-mesh with crack tip rounding, **b** Deformed structure with damage distribution D at a crack extension of $\approx$15 mm, **c** Highlighted elements undergoing total damage

the slope of the crack growth resistance curve and the decreasing branch can be controlled. Simultaneously, the force level is changed. The internal length L_{nl} can be used to calibrate the maximum force and the crack initiation value, here the critical crack tip opening δ_{i}. Changing q_2 determines the deviation of the force response from the undamaged solution.

Motivated by the sensitivity study, a rough accordance is obtained with the manual calibration of the damage parameters: $\varepsilon_{\mathrm{c}} = 0.2$, $L_{\mathrm{nl}} = 1.0$ mm, and $q_2 = 0.01$. The response of the calibrated model is illustrated in Fig. 22.21. The location and amount of the maximum force need further improvement and the crack tip opening is underestimated. But the softening branch of the force versus displacement curve and the slope of the crack growth resistance curve are in acceptable accordance. It should be mentioned that a considerably large crack propagation can be modeled in a robust manner ($\Delta a = 30$ mm); the simulations are interrupted externally after reaching the prescribed crack length. The contour plots in Fig. 22.20 show that damage is distributed over some layers of elements indicating the regularized character of the proposed damage model. The crack is represented by a layer of total

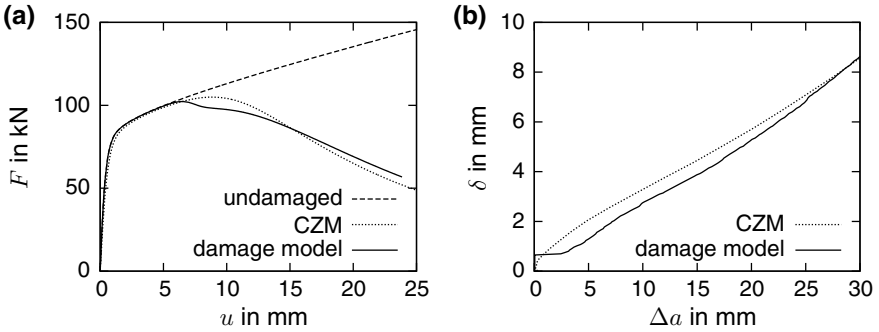

Fig. 22.21 Calibration results of micromorphic damage model with cohesive zone simulation (CZM) as reference, simulation without damage is added, **a** Force F versus displacement u, **b** CTOD δ versus crack extension Δa

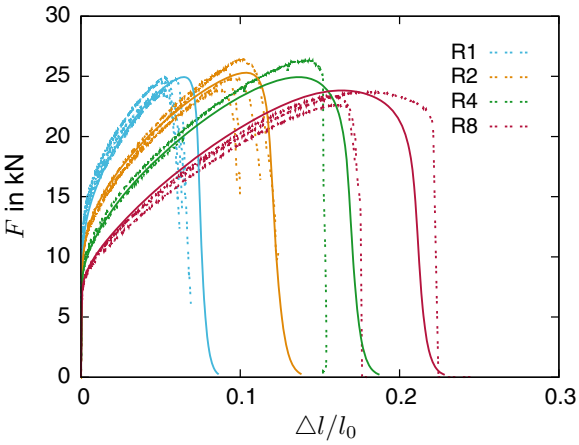

Fig. 22.22 Force F versus elongation $\Delta l/l_0$ curves for notched tensile tests; solid lines correspond to the damage model prediction, dashed lines denote experiments

damaged, highly distorted elements. Hence, the applied patch solution for damping pathological widening of the damage zone works well in this special case.

With the estimated damage initiation and evolution parameters at hand, the notched tensile tests are simulated until failure. A comparison of predicted and experimental force versus elongation response reveals a reasonable agreement, see Fig. 22.22. The elongation at failure is slightly overestimated by the simulation for the small notch radii, but the load carrying capability is fully captured.

In conclusion, the proposed and calibrated micromorphic approach of ductile damage for high alloy TRIP-steel is able to reproduce the deformation, damage, and failure behavior including stable crack propagation.

22.5 Conclusions

Based on a profound thermomechanical framework, a micromechanically based material model and a phenomenological approach are developed, which account for typical phenomena attributed to high alloy TRIP-steel: stress state dependent strain hardening, loading rate sensitivity and temperature dependency. In addition, a regularized ductile damage model, which is formulated with help of the micromorphic approach, is included.

For the phenomenological modeling approach, the applicability is demonstrated by calibration and validation with experiments of a cast X3CrMnNi 16-6-6 steel exhibiting strain induced α'-martensite formation. After calibrating the model to a subset of experiments (quasi-static loaded, uni-axial tension and compression tests at different temperatures), some predictive simulations are conducted. Firstly, predictions of stress-strain response at temperatures, which are not considered during calibration, are of reasonable quality. Especially, the disappearance of the tensions-compression asymmetry of strain hardening with increasing temperature is correctly reflected. Secondly, acceptable results are obtained for tensile tests at increased strain rates, where the thermomechanical coupling becomes important: The characteristic curve crossing of strain hardening curves is clearly captured by the model. Finally, simulations of notched tensile tests yield good agreement to available experiments. Hence, the model is also validated for inhomogeneous deformation.

With the help of the micromechanically motivated model, the effect of martensitic phase transformation on the loading situation at crack tips is investigated. The course of the stresses in front of a blunting crack shows characteristic curvature attributed to phase transformation. The most important influence is an increase in the stress components due to transformation induced hardening. Additional hardening affects ductile fracture in a positive manner, because the growth of microvoids is postponed. Another study examined the crack driving force for TRIP-steels under consideration of plastic deformation and phase transformation. By applying the theory of material forces a modified J-integral was formulated, which is path independent under these circumstances. Resulting from this, a shielding effect due to both inelastic strains was observed for small scale yielding.

Taking fracture process into account, a pragmatic cohesive zone model is successfully calibrated to reproduce crack propagation during loading of a CT-specimen. In combination with the cohesive zone, a simplified material model for isothermal and quasi-static conditions turned out to be sufficient to enable a good fit of the CT-tests. Finally, the micromorphic ductile damage model is applied to predict damage, crack propagation and failure of different structures made of a cast X3CrMnNi 16-6-6 steel (CT-specimen, notched tensile tests). A reasonable agreement to experimental and numerical reference data is obtained after performing a developed calibration strategy.

Hence, versatile modeling tools for TRIP-steels are available, which are ready to be applied in simulations of future engineering applications.

Acknowledgements The authors gratefully acknowledge the Deutsche Forschungsgemeinschaft (DFG, German Research Foundation) for funding the research in the framework of the Collaborative Research Center "TRIP-Matrix-Composite", (project number 54473466—SFB 799, subproject C5). In addition the authors thank the involved staff from SFB 799 and from the Institute of Mechanics and Fluid Dynamics (TU Freiberg) as well as Dr. Uwe Mühlich for their collaboration and numerous fruitful discussions.

References

1. H. Biermann, U. Martin, C.G. Aneziris, A. Kolbe, A. Müller, W. Schärfl, M. Hermann, Adv. Eng. Mater. **11**, 1000 (2009)
2. D. Ehinger, L. Krüger, U. Martin, C. Weigelt, C.G. Aneziris, Steel Res. Int. **82**, 1048 (2011)
3. D. Ehinger, L. Krüger, U. Martin, C. Weigelt, C.G. Aneziris, Int. J. Solids Struct. **66**, 207 (2015)
4. C. Weigelt, C.G. Aneziris, H. Berek, D. Ehinger, U. Martin, Adv. Eng. Mater. **14**(1–2), 53 (2012)
5. A. Jahn, A. Kovalev, A. Weiß, S. Wolf, L. Krüger, P.R. Scheller, Steel Res. Int. **82**, 39 (2011)
6. S. Martin, S. Wolf, U. Martin, L. Krüger, Solid State Phenomen. **172–174**, 172 (2011)
7. M. Linderov, C. Segel, A. Weidner, H. Biermann, A. Vinogradov, Mat. Sci. Eng. A **597**, 183 (2014)
8. C. Ullrich, S. Martin, C. Schimpf, A. Stark, N. Schell, D. Rafaja, Adv. Eng. Mater. **21**(5), 1801101 (2019)
9. S. Prüger, A. Seupel, M. Kuna, Int. J. Plast. **55**, 182 (2014)
10. S. Wolf, S. Martin, L. Krüger, U. Martin, Mat. Sci. Eng. A **594**, 72 (2014)
11. A. Seupel, R. Eckner, A. Burgold, M. Kuna, L. Krüger, Mat. Sci. Eng. A **662**, 342 (2016)
12. A. Seupel, M. Kuna, in *Proceedings of the 14th International Conference on Computational Plasticity - Fundamentals and Applications, COMPLAS 2017* (2017), pp. 576–587
13. M.P. Miller, D.L. McDowell, Int. J. Plast. **12**(9), 875 (1996)
14. J. Serri, M. Martiny, G. Ferron, Int. J. Mech. Sci. **47**(6), 884 (2005)
15. I. Papatriantafillou, M. Agoras, M. Aravas, G. Haidemenopoulos, Comput. Method. Appl. M. **195**, 5094 (2006)
16. L. Mehlhorn, S. Prüger, S. Soltysiak, U. Mühlich, M. Kuna, Steel Res. Int. **82**(9), 1022 (2011)
17. S. Prüger, L. Mehlhorn, S. Soltysiak, M. Kuna, Comp. Mater. Sci. **64**, 273 (2012)
18. S. Prüger, L. Mehlhorn, U. Mühlich, M. Kuna, Adv. Eng. Mater. **15**(7), 542 (2013)
19. A. Burgold, M. Kuna, S. Prüger, Procedia Mater. Sci. **3**(0), 461 (2014). 20th European Conference on Fracture
20. A. Burgold, M. Kuna, S. Prüger, Eng. Fract. Mech. **138**, 169 (2015)
21. M. Kuna, A. Burgold, S. Prüger, Int. J. Fract. **193**, 171 (2015)
22. S. Prüger, Thermomechanische Modellierung der dehnungsinduzierten Phasenumwandlung und der asymmetrischen Verfestigung in einem TRIP-Stahlguss. Ph.D. thesis, TU Bergakademie Freiberg (2016). (in German)
23. S. Forest, J. Eng. Mech. **135**(3), 117 (2009)
24. P. Germain, SIAM J. Appl. Mech. **25**(3), 556 (1973)
25. B.D. Coleman, W. Noll, Arch. Ration. Mech. An. **13**(1), 167 (1963)
26. J. Lemaitre, J.L. Chaboche, *Mechanics of solid materials* (Cambridge University Press, 1998)
27. H. Hallberg, P. Håkansson, M. Ristinmaa, Int. J. Plasticity **23**, 1213 (2007)
28. J. Lemaitre, Nucl. Eng. Des. **80**, 233 (1984)
29. H. Xiao, O.T. Bruhns, A. Meyers, Acta Mech. **124**, 89 (1997)
30. H. Xiao, O.T. Bruhns, A. Meyers, Acta Mech. **138**, 31 (1999)
31. A. Eshraghi, K.D. Papoulia, H. Jahed, J. Appl. Mech. **80**(2), 021027 1 (2013)
32. E. Diamantopoulou, W. Liu, C. Labergere, H. Badreddine, K. Saanouni, P. Hu, Int. J. Damage Mech. **26**(2), 314 (2017)

33. R.H.J. Peerlings, R. de Borst, W.A.M. Brekelmans, J.H.P. de Vree, Int. J. Numer. Meth. Eng. **39**, 3391 (1996)
34. A. Seupel, G. Hütter, M. Kuna, Eng. Fract. Mech. **199**, 41 (2018)
35. A. Seupel, M. Kuna, Int. J. Damage Mech. **28**(8), 1261 (2019)
36. I. Tamura, Met. Sci. **16**, 245 (1982)
37. G.B. Olson, M. Cohen, Metall. Trans. A **6A**, 791 (1975)
38. R.G. Stringfellow, D.M. Parks, G.B. Olson, Acta Metall. Mater. **40**(7), 1703 (1992)
39. Y. Tomita, T. Iwamoto, Int. J. Mech. Sci. **37**(12), 1295 (1995)
40. T. Iwamoto, T. Tsuta, Y. Tomita, Int. J. Mech. Sci. **40**, 173 (1998)
41. U. Ahrens, Beanspruchungsabhängiges Umwandlungsverhalten und Umwandlungsplastizität niedrig legierter Stähle mit unterschiedlich hohen Kohlenstoffgehalten. Ph.D. thesis, TU Paderborn (2003). (in German)
42. K. Nagayama, T. Terasaki, K. Tanaka, F.D. Fischer, T. Antretter, G. Cailletaud, F. Azzouz, Mat. Sci. Eng. A **308**, 25 (2001)
43. F.D. Fischer, G. Reisner, E. Werner, K. Tanaka, G. Cailletaud, T. Antretter, Int. J. Plast. **16**, 723 (2000)
44. M. Berveiller, F.D. Fischer (eds.), *Mechanics of Solids with Phase Changes* (Springer, 1997)
45. R. Mahnken, A. Schneidt, T. Antretter, Int. J. Plast. **25**, 183 (2009)
46. R. Mahnken, A. Schneidt, Arch. Appl. Mech. **80**, 229 (2010)
47. S. Prüger, M. Kuna, S. Wolf, L. Krüger, Steel Res. Int. **82**(9), 1070 (2011)
48. R. Zaera, J.A. Rodríguez-Martínez, A. Casado, J. Fernández-Sáez, A. Rusinek, R. Pesci, Int. J. Plast. **29**, 77 (2012)
49. H. Hallberg, P. Håkansson, M. Ristinmaa, Int. J. Solids Struct. **47**(11–12), 1580 (2010)
50. A. Seupel, M. Kuna, Appl. Mech. Mater. **784**, 484 (2015)
51. S. Martin, Deformationsmechanismen bei verschiedenen Verformungstemperaturen in austenitischem TRIP/TWIP-Stahl. Ph.D. thesis, TU Bergakademie Freiberg (2013). (in German)
52. S. Prüger, M. Kuna, Proc. Appl. Math. Mech. **11**, 425 (2011)
53. S. Prüger, M. Kuna, K. Nagel, H. Biermann, Computational Plasticity XI Fundamentals and Applications 869–881 (2011)
54. P.P. Castañeda, P. Suquet, Adv. Appl. Mech. **34**, 172 (1997)
55. F. Lani, Q. Furnémont, T.V. Rompaey, F. Delanney, P.J. Jaques, T. Pardoen, Acta Mater. **55**, 3695–3705 (2007)
56. J.R. Rice, D.M. Tracey, J. Mech. Phys. Solids **17**, 201 (1969)
57. A.L. Gurson, J. Eng. Mater. Technol. **44**, 2 (1977)
58. M. Kuna, S. Wippler, Eng. Fract. Mech. **77**, 3635 (2010)
59. N. Aravas, Int. J. Numer. Meth. Eng. **24**, 1395 (1987)
60. A.C.F. Cocks, J. Mech. Phys. Solids **37**(6), 693 (1989)
61. J. Besson, Int. J. Damage Mech. **19**, 3 (2010)
62. D. Kulawinski, S. Ackermann, A. Seupel, T. Lippmann, S. Henkel, M. Kuna, A. Weidner, H. Biermann, Mat. Sci. Eng. A **642**, 317 (2015)
63. S. Wolf, Temperatur- und dehnratenabhängiges Werkstoffverhalten einer hochlegierten CrMnNi-TRIP/TWIP-Stahlgusslegierung unter einsinniger Zug- und Druckbeanspruchung. Ph.D. thesis, TU Bergakademie Freiberg (2012). (in German)
64. A.M. Beese, D. Mohr, Acta Mater. **59**, 2589 (2011)
65. C. Garion, B. Skoczen, Int. J. Damage Mech. **12**, 313 (2003)
66. S.W. Yoo, C.S. Lee, W.S. Park, M.H. Kim, J.M. Lee, Comp. Mater. Sci. **50**, 2014 (2011)
67. C.S. Lee, B.M. Yoo, M.H. Kim, J.M. Lee, Int. J. Damage Mech. **22**(1), 95 (2012)
68. J. Lian, M. Sharaf, F. Archie, S. Münstermann, Int. J. Damage Mech. **22**(2), 188 (2013)
69. J. Mediavilla, R.H.J. Peerlings, M.G.D. Geers, Comput. Method. Appl. M. **195**, 4617 (2006)
70. B. Vandoren, A. Simone, Comput. Method. Appl. M. **332**, 644 (2018)
71. L. Krüger, S. Wolf, U. Martin, P. Scheller, A. Jahn, A. Weiß, DYMAT 1069–1074 (2009)
72. L. Krüger, S. Wolf, S. Martin, U. Martin, A. Jahn, A. Weiß, P.R. Scheller, Steel Res. Int. **32**(8), 1087 (2011)
73. R. Zaera, J.A. Rodríguez-Martínez, D. Rittel, Int. J. Plast. **40**, 185 (2013)

74. J. Hutchinson, J. Mech. Phys. Solids **16**(1), 13 (1968)
75. J.R. Rice, G.F. Rosengren, J. Mech. Phys. Solids **16**, 1 (1968)
76. R. McMeeking, J. Mech. Phys. Solids **25**(5), 357 (1977)
77. H. Yuan, G. Lin, A. Cornec, Int. J. Fract. **71**(3), 273 (1995)
78. R.G. Stringfellow, Mechanics of Strain-Induced Transformation Toughening in Metastable Austenitic Steels. Ph.D. thesis, Massachusetts Institute of Technology (1990)
79. G. Hütter, L. Zybell, U. Mühlich, M. Kuna, Comp. Mater. Sci. **80**, 61 (2013)
80. M.E. Gurtin, *Configurational Forces as Basic Concepts of Continuum Physics* (Springer, New York, 2000)
81. R. Kienzler, G. Herrmann, *Mechanics in Material Space* (Springer, Berlin Heidelberg, 2000)
82. G.A. Maugin, *Configurational forces: thermomechanics, physics, mathematics, and numerics* (CRC Press, 2011)
83. T. Nguyen, S. Govindjee, P. Klein, H. Gao, J. Mech. Phys. Solids **53**(1), 91 (2005)
84. B. Näser, M. Kaliske, R. Müller, Comput. Mech. **40**(6), 1005 (2007)
85. N. Simha, F. Fischer, G. Shan, C. Chen, O. Kolednik, J. Mech. Phys. Solids **56**(9), 2876 (2008)
86. O. Kolednik, R. Schöngrundner, F. Fischer, Int. J. Fract. **187**(1), 77 (2014)
87. A. Burgold, S. Henkel, S. Roth, M. Kuna, H. Biermann, Mater. Test. **60**(4), 341 (2018)
88. S. Henkel, D. Holländer, M. Wünsche, H. Theilig, P. Hübner, H. Biermann, S. Mehringer, Eng. Fract. Mech. **77**(11), 2077 (2010)
89. A. Burgold, S. Roth, M. Kuna, Advances in Fracture and Damage Mechanics XVII 167–172 (2018)
90. S. Roth, G. Hütter, M. Kuna, Int. J. Fract. **188**(1), 23 (2014)
91. S. Roth, Entwicklung und Implementierung zyklischer Kohäsivzonenmodelle zur Simulation von Werkstoffermüdung. Ph.D. thesis, TU Bergakademie Freiberg (2015). URL http://nbn-resolving.de/urn:nbn:de:bsz:105-qucosa-209735. (in German)
92. X.P. Xu, A. Needleman, Modell. Simul. Mater. Sci. Eng. **1**(2), 111 (1993)
93. M. Hauser, M. Wendler, S.G. Chowdhury, A. Weiß, J. Mola, Mater. Sci. Tech. **31**(12), 1473 (2015)
94. G. Hütter, T. Linse., U. Mühlich, M. Kuna, Int. J. Solids Struct. **50**, 662 (2013)
95. T. Linse, G. Hütter, M. Kuna, Eng. Fract. Mech. **95**, 13 (2012)

Chapter 23
Properties of Phase Microstructures and Their Interaction with Dislocations in the Context of TRIP Steel Systems

Rachel Strobl, Michael Budnitzki and Stefan Sandfeld

Abstract Transformation Induced Plasticity (TRIP) steels undergo a diffusionless phase transformation from austenite to martensite, resulting in a material exhibiting desireable material properties such as exceptional balance of strength and ductility as well as good fatigue behavior. Computational modeling at the mesoscale is potentially a suitable tool for studying how plastic deformation interacts with phase transformations and ultimately affects the bulk properties of these steels. We introduce models that represent the phase microstructure in a continuum approach and couple a time-dependent Ginzburg-Landau equation with discrete dislocation via their elastic strain energy densities. With this, the influence of several dislocation configurations are examined, namely a single dislocation, a "penny-shaped crack", and a "dislocation cascade". It is shown that the strain due to the presence of dislocations has a significant influence on the resultant martensitic microstructure. Furthermore, the importance of using a non-local elasticity approach for the dislocation stress fields is demonstrated.

23.1 Introduction

The solid-solid phase transformation in transformation induced plasticity (TRIP) steels leads to desirable properties for engineering applications. In the case of a Cr-Mn-Ni steel matrix, a high fault austinite phase is converted to α-martensite, and a high number of dislocations are active during the process of phase transformation, as also seen via in situ experiments, e.g., as in [1].

R. Strobl · M. Budnitzki · S. Sandfeld (✉)
Institute of Mechanics and Fluid Dynamics, Lampadiusstraße 4, Freiberg, Germany
e-mail: stefan.sandfeld@imfd.tu-freiberg.de

R. Strobl
e-mail: rachel.strobl@imfd.tu-freiberg.de

M. Budnitzki
e-mail: michael.budnitzki@imfd.tu-freiberg.de

H. Biermann and C. G. Aneziris (eds.), *Austenitic TRIP/TWIP Steels and Steel-Zirconia Composites*, Springer Series in Materials Science 298,
https://doi.org/10.1007/978-3-030-42603-3_23

Computer simulations and numerical modeling of TRIP-steels can be very beneficial for understanding the interaction of different microstructural phenomena, such as planar defects (e.g., phase transformations) and linear defects (dislocations), all of which may have significant influence on the mechanical properties of the bulk material. Dislocations are responsible for plastic deformation of metals; they may interact among themselves and can also be nucleated, e.g., during martensitic phase transformations. The combination of martensitic phase transformations and dislocation activity results in lattice distortions and may ultimately lead to increased work hardening.

Predictive modeling requires to spatially resolve the relevant physical phenomena and to describe their evolution in time. E.g., molecular dynamics (MD) simulations are inherently able to model both phase transformations and dislocations [2–4]. However, the computational cost for solving Newton's equation of motion together with the interaction of *all* atoms for volumes and strain rates that are comparable to experimentally used ones is very high. As a consequence, typical MD simulations operate with strain rates that are several orders of magnitudes higher than the experimentally used strain rates and, at the same time, are also restricted to relatively small systems with typical sizes ranging from several nanometers to a few hundreds of nanometers.

Phenomenological continuum models of plasticity can reach relevant timescales and length scales, however, details regarding phase transformations or dislocations can only be incorporated indirectly and are generally not directly based on the underlying mechanisms. A macroscopic continuum model also cannot resolve the interface of two phases properly due to a highly coarsened resolution. Phase field models (PFMs) are based on the minimization of total energy and are "mesoscopic" methods in which individual atoms or their interactions are not explicitly represented, but in which microscopic effects are still able to be considered. However, this requires either input from lower scale methods or parameterization with experimental data.

The general phase field approach is based on a set of order parameters, $\phi_1, \ldots, \phi_n$, continuous functions in space, which represent the different phases in the system. The time evolution of the order parameters is governed by the minimization of total energy. Based on this, the relevant physical properties are described as functions of the order parameters. The governing PFM equation is the time dependent Ginsburg-Landau (TDGL) evolution equation [5], first implemented for martensitic phase transformations by Khachaturyan [6].

In the following we will introduce a coupled phase field—dislocation framework that shows how dislocations or idealized cracks interact with phase boundaries between a martensitic and an austenitic phase. A second focus is then on a general approach in the context of non-local elasticity for representing the stress field of discrete dislocations.

The following nomenclature is employed throughout this chapter: We denote vectors by bold lower case latin $\mathbf{a}$ and greek $\boldsymbol{\alpha}$ letters, and the dot operator "$\cdot$" denotes the scalar product $\mathbf{a} \cdot \mathbf{b} \in \mathcal{R}$. We will, however, abuse this notation and use the dot "$\cdot$" as well for inner products, whenever appropriate.

Second order tensors are denoted by bold uppercase latin letters $\mathbf{A}$. We introduce a scalar product between second order tensors denoted by ":" as $\mathbf{A} : \mathbf{B} := \mathrm{tr}\mathbf{A} \cdot \mathbf{B}^{\top}$,

where $\mathbf{B}^\top$ is the transpose of $\mathbf{B}$ and $\mathrm{tr}(\cdot)$ denotes the trace operator. In an inner product space this product implies the norm $\|\mathbf{A}\| := \sqrt{\mathbf{A} : \mathbf{A}}$. Given an orthogonal tensor $\mathbf{R}$ and an arbitrary order tensor $\mathbf{\Phi}$, $\mathbf{R} * \mathbf{\Phi}$ denotes the RAYLEIGH product of $\mathbf{R}$ and $\mathbf{\Phi}$; for a second order tensor $\mathbf{A}$, we have $\mathbf{R} * \mathbf{A} = \mathbf{R} \cdot \mathbf{A} \cdot \mathbf{R}^\top$.

Third order tensors are denoted by bold calligraphic letters $\mathcal{A}$ and "$\vdots$" is the corresponding full contraction operator. Fourth order tensors are denoted by black board upper case letters $\mathbb{A}$.

23.2 Interaction Between Martensitic Phase Transformations and Dislocations

23.2.1 Phase Field Equations

The high strain induced via a phase transformation between face centered cubic (FCC) austenite and body centered cubic (BCC) martensite may trigger the nucleation of a large number of dislocations inside the material. Both dislocations and martensitic phase transformations affect the bulk properties of steels, and therefore, representing the interaction between dislocations and interfaces, and how this affects the phase transformation are essential for micromechanical modeling.

Thus, our computational model consists of two parts: the evolution of the phase microstructure is governed by the TDGL equation which minimizes the total energy in the system. The second part of the model considers discrete edge dislocations in a two-dimensional domain, for which an analytical solution of stress is available [7]. Such methods of coupling PFM and dislocations have been successfully applied for materials such as nickel-based superalloys [8, 9]. The modeling of the phase transformation will not consider any intermediate phases, and therefore only one order parameter, ϕ, is needed. It will also be assumed in the model that inside the martensitic phase, the dislocation mobility will approach zero, resulting in no movement of the dislocations inside the martensite phase. The TDGL requires the gradient energy at the phase boundary, the elastic strain energy, and a transformation potential. Here, contributions to the free energy arise from the elastic energy, W, the separation potential, f, and gradient energy. The time-dependent evolution of the order parameter is then given by

$$\frac{\partial \phi}{\partial t} = -M\left(\frac{\partial W}{\partial \phi} + G\left(\frac{\kappa_s}{L_{\mathrm{char}}}\frac{\partial f}{\partial \phi} + \kappa_g L_{\mathrm{char}} \Delta\phi\right)\right), \tag{23.1}$$

where ϕ is the order parameter describing the current phase at each point in space. The material specific parameters are mobility, M, interfacial energy density, G, characteristic length scale, L_{char}, and the calibration constants, κ_s and κ_g, which control the width of the interface between the two phases [10].

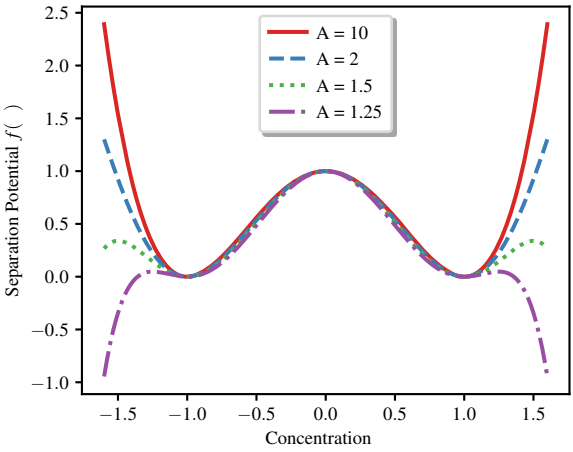

Fig. 23.1 Potential of phase transition. The two wells signify martensite variants 1 and 2. The local maximum signifies a metastable austenite phase

W is the elastic strain energy density which takes the form

$$W(\varepsilon, \phi) = \mathbf{E}_{\text{el}} : \mathbf{S} \tag{23.2}$$

where $\mathbf{E}_{\text{el}}$ is the elastic strain tensor and $\mathbf{S}$ is the stress tensor.

The second term describes the potential of phase transformation. In our model, we use a so-called "2-4-6 potential" (see Fig. 23.1), given as

$$f(\phi) = \frac{(3A^2 - 1 - 2\phi^2)(1 - \phi^2)^2}{(3A^2 - 1)}, \tag{23.3}$$

where A is a fit parameter which can be obtained from lower scale simulation methods. The final term accounts for the gradient of the interface between the two phases [11].

23.2.2 Dislocations and Mechanical Equilibrium Conditions

The stress field around a dislocation follows—outside the core region—linear elasticity. Any solid body in static equilibrium obeys the mechanical equilibrium equation, i.e., the divergence of the stress tensor, $\mathbf{S}$, must be zero,

$$\nabla \cdot \mathbf{S} = 0\,. \tag{23.4}$$

While this follows from the conservation of linear momentum, the conservation of angular momentum is responsible for the symmetry of the stress tensor, $\mathbf{S} = \mathbf{S}^{\mathrm{T}} \Leftrightarrow \mathrm{S}_{ij} = \mathrm{S}_{ji}$. Assuming linear elastic material, the stresses and strains are related by the

stiffness tensor, $\mathbb{C}$, as

$$\mathbf{S} = \mathbb{C} : \mathbf{E}_{\mathrm{e}}\left(\mathbf{E},\ \phi\right), \tag{23.5}$$

where, in a phase field ansatz, the elastic strain tensor, $\mathbf{E}_{\mathrm{e}}\left(\mathbf{E},\ \phi\right)$, is a function of the order parameter as well as of the total strain, $\mathbf{E}$. We assume a small strain context in our model, and therefore strains may be additively decomposed into their elastic and inelastic parts:

$$\mathbf{E}_{\mathrm{e}}\left(\mathbf{E},\ \phi\right) = \mathbf{E} - \mathbf{E}_{\mathrm{inel}}\,. \tag{23.6}$$

The tensor of inelastic strains, $\mathbf{E}_{\mathrm{inel}}$, consists of the transformation strain $\mathbf{E}_{\mathrm{tr}}$ and the dislocation eigenstrain $\mathbf{E}_{\mathrm{dis}}$. In the following we will only consider a horizontal slip system in a plane strain model. The plane components of the stress tensor for a single dislocation in an infinite, linear elastic medium then follow the following analytical solution [7]:

$$\mathrm{S}_{11} = \frac{-\mu\, b}{2\pi\,(1-\nu)}\,\frac{y\,(3x^2+y^2)}{(x^2+y^2)^2}, \tag{23.7}$$

$$\mathrm{S}_{22} = \frac{-\mu\, b}{2\pi\,(1-\nu)}\,\frac{y\,(x^2-y^2)}{(x^2+y^2)^2}, \tag{23.8}$$

$$\mathrm{S}_{12} = \frac{\mu\, b}{2\pi\,(1-\nu)}\,\frac{x\,(x^2-y^2)}{(x^2+y^2)^2}, \tag{23.9}$$

where b is the absolute value of the Burgers vector, μ is the shear modulus, and ν is Poisson's ratio. In order to avoid the unphysical diverging behavior close to the dislocation core, a numerical regularization approach as proposed in [12] is used; a physically more rigorous approach is presented in the subsequent section. The resulting stress components are shown in Fig. 23.2. The strain tensor, which governs the dislocation eigenstrain, can then be straightforwardly obtained from $\mathbf{E}_{\mathrm{dis}} = \mathbb{C}^{-1} : \mathbf{S}$. Equation (23.2) couples the phase field model and the dislocation model through the eigenstrain of dislocations and the eigenstrain contribution due to the phase transformation. While in this work we only consider stationary dislocation configurations, in general, the equation of motion for the dislocations would be a second equation where the two models are coupled.

23.2.3 Simulation Setup and Boundary Conditions

In order to observe the interaction between the dislocation and the phase field interface, a martensitic phase transformation needs to be triggered first. In our first simulation setup this is done via a martensitic "seed", which is an artificial inclusion of the martensite phase. The first simulation setup consists of a circular martensitic seed surrounded by an austenite matrix, as shown in Fig. 23.3a, with one dislocation placed inside the austenite phase. The entire domain measures 200 nm by 200 nm.

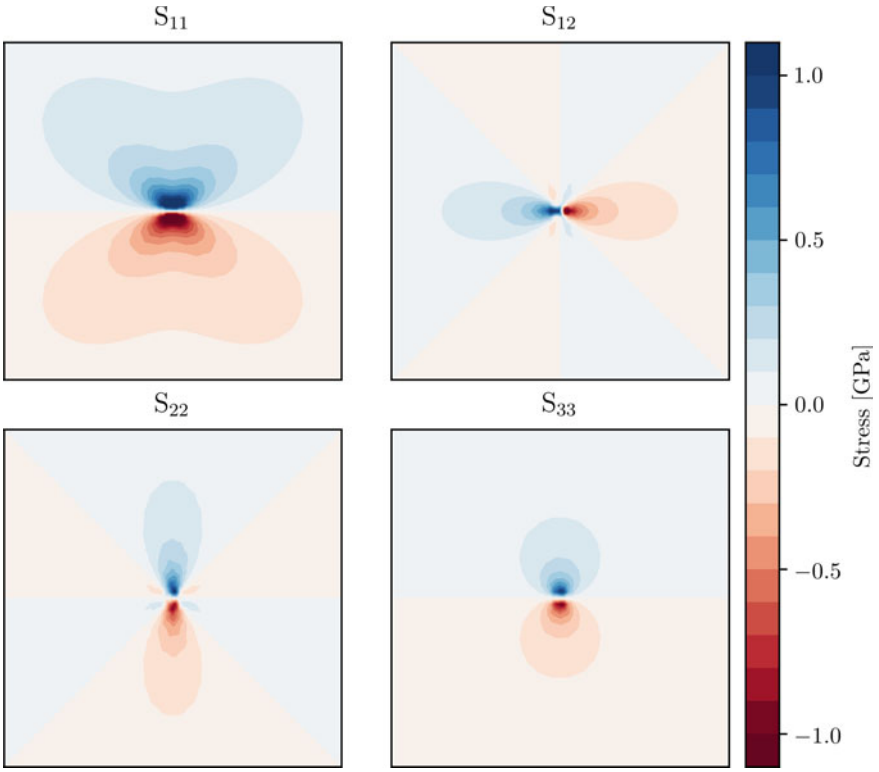

Fig. 23.2 Individual components to the stress tensor for a single dislocation, according to (23.7)–(23.9)

In our second simulation setup we use a penny-shaped crack, as shown in Fig. 23.3b, to initiate a phase transformation. The introduction of several stationary positive and negative dislocations on either ends of a crack mode II crack tip effectively mimics a small crack inside of a material. The equivalent dislocation distribution function of the crack is given by Weertman [13].

In both setups, free boundaries were considered. To avoid a rigid body motion, the domains were fixed in one corner, and in an adjacent corner, a zero displacement was prescribed in vertical direction only to avoid over-constraining the system. The two martensite variants are considered by one order parameter which is $\phi = 1$ for variant 1 and $\phi = -1$ for variant 2. The simulations progress by time integrating the TDGL, and we let them evolve until a quasi-static configuration is reached. The numerical implementation was done using the finite element method. We used quadratic shape functions and a rectangular mesh with 100 elements into each direction.

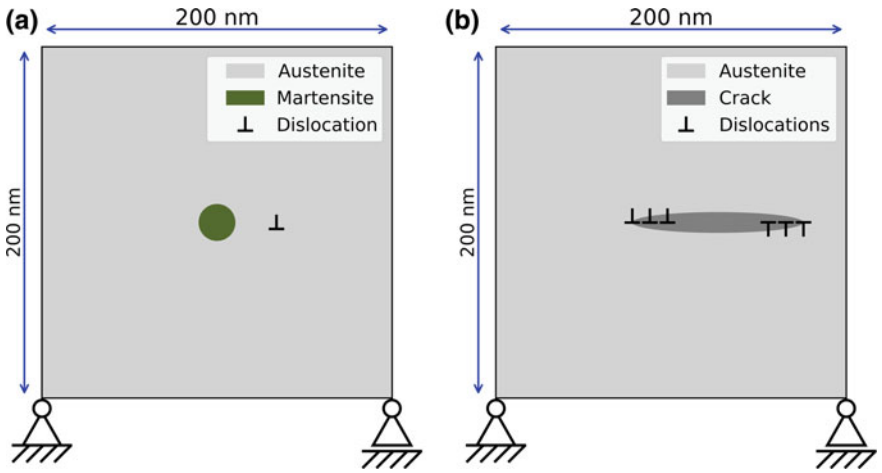

Fig. 23.3 Schematic of initial setups of the simulations showing **a** a martensitic seed surrounded by an austenite matrix, and **b** a penny-shaped crack in an austenite matrix

23.2.4 Simulation Results

23.2.4.1 Martensitic Seed and Edge Dislocation

Our first simulation set up considers the geometry and initial values shown in Fig. 23.3a. Figure 23.4 shows the order parameter, the S_{12} component of the stress tensor, and the elastic energy density at three distinct points in time. The initial configuration with the circular seed is an artificial and energetically highly unfavorable microstructural state. This is why immediately at the beginning of the simulation the horizontal and vertical martensitic bands originating from the location of the seed were created, as shown in the first snapshot. However, due to the spatially heterogeneous structure with changing transformation strains across the interfaces stresses and elastic strain energy are still high (Fig. 23.4 bottom and middle row) which show that equilibrium has not yet reached.

The TDGL minimizes total energy in the system, so as time progresses, the system will attempt to transform into a state where energy decreases. If there was no dislocation present, the system would be perfectly symmetric in the vertical and horizontal direction, and there would be no physical reason for one band to be preferred. The preferred band direction would only be decided based on numerical errors or other artifacts. However, the introduction of the dislocation breaks the symmetry (compare the right red region of the stress in Fig. 23.4 at $t = t_s$) and thereby determines the growth direction of the band. At the intermediate time step t_m, the horizontal band has already shrinked to nearly 50% of its original thickness, and the energy as well as the stress level have strongly decreased.

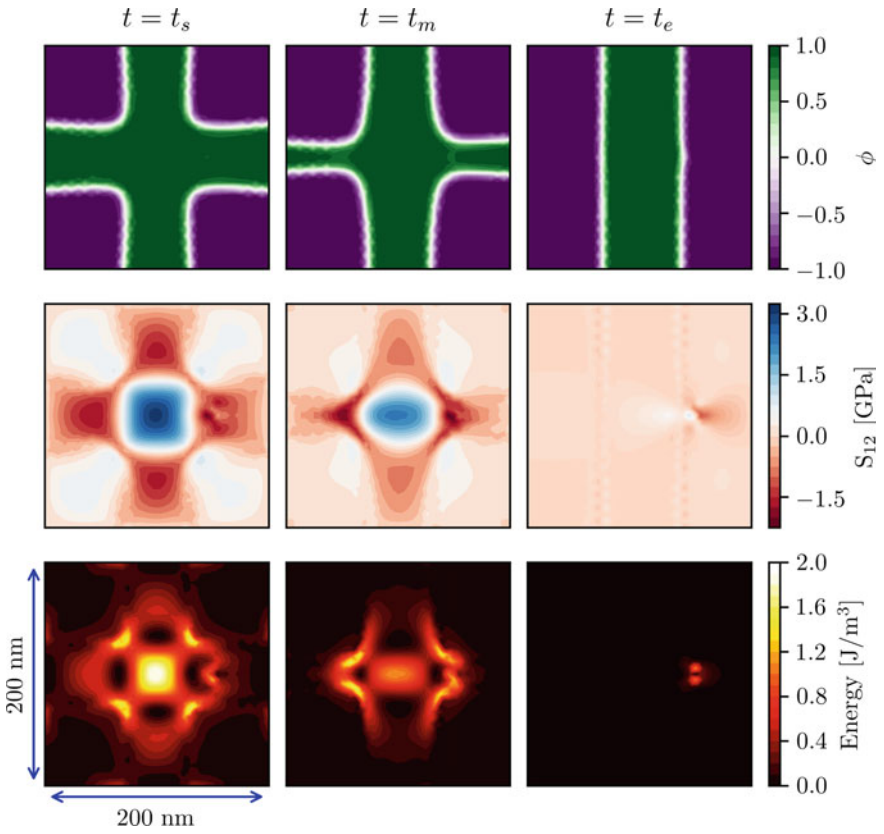

Fig. 23.4 Temporal evolution of order parameter, elastic energy density, and S_{12} with one dislocation. t_s is an early point in time, t_m is an intermediate time, and at t_e the quasi-static state is reached

At the quasi-stationary time, a fully formed, vertical martensitic band structure is observed, and a minimized energy and stress is reached. The band structure is at equilibrium because of the total strain is exactly the eigenstrain (except for the dislocation contribution), resulting in a deformed but stress-free state. However, the stress around the dislocation will not change because the dislocation is fixed in place. The "try" to relax this further causes a slight distortion from the original straight interface, as seen in Fig. 23.4. The shear stress at t_e still shows very slight remnants of the vertical phase microstructure; the reason is that the interface of the martensite band is not perfectly straight but has small fluctuations due to the used finite element approximation. Reducing the element size would remedy this effect.

23.2.4.2 Penny Shaped Crack in Austenitic Matrix

The introduction of a penny shaped crack induces enough eigenstrain in the system to trigger a phase transformation and is therefore an interesting way to get rid of the artificial initial seed. Similar as in the previous example, at the first snapshot in time, two perpendicular martensite bands can be observed (Fig. 23.5, left). Here, the stress field of the crack is responsible for the symmetry breaking. Again, the heterogenous microstructure causes a high stress and high strain energy density, which also decreases during the time integration of the TDGL equation. At the intermediate time step, one can additionally observe that the interfaces of the vertical band are pinned into place by the stress field of the crack, compare the slightly wavy structure of the band in Fig. 23.5. This "bump" is then progressing towards the top and the bottom such that at the stationary state the band stretches into vertical direction and has a thickness that is dictated by the crack length as shown in the right column in Fig. 23.5. At this point on time, a relaxed state with a minimum energy and a minimized stress is reached.

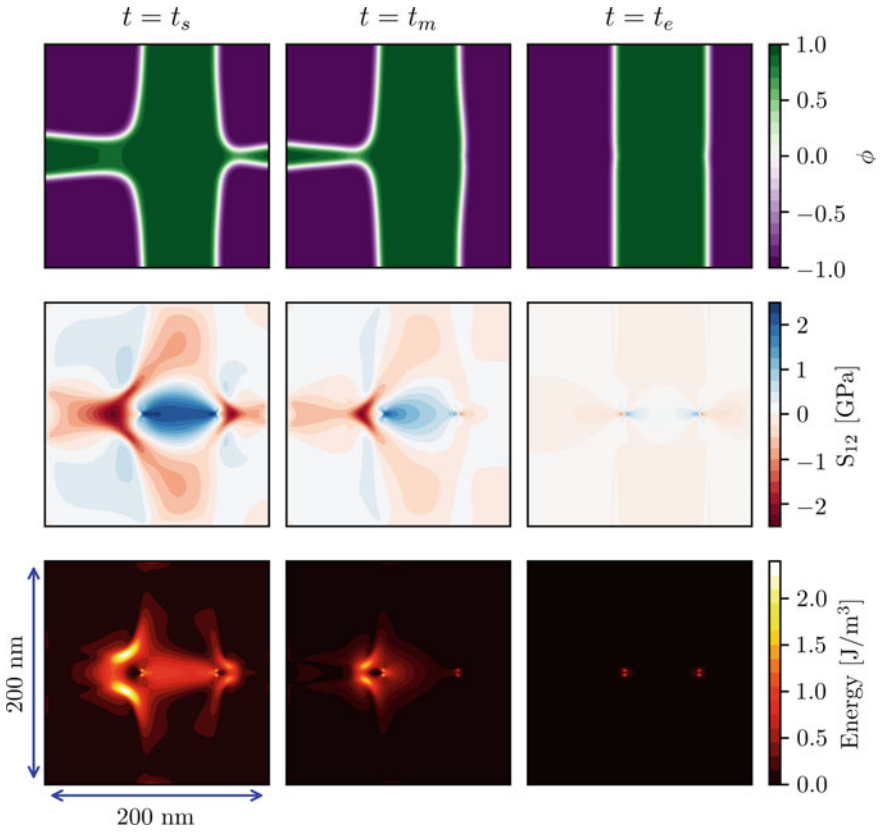

Fig. 23.5 Evolution in time of order parameter, elastic energy density, and S_{12} with a penny-shaped crack

23.3 On the Interaction of Planar Defects with Dislocations Within the Phase-Field Approach

23.3.1 Introduction

Phase field approaches have proven to be a very powerful tool for the investigation of the formation and evolution of microstructures due to solid-solid phase transformations and twinning. This appears to be the natural framework for the investigation of the interaction of planar crystal defects such as phase- or twin-boundaries with line defects (dislocations, disclinations). A typical phase field model for diffusionless (martensitic) transformations comprises of an evolution equations of ALLEN-CAHN-type for the order parameters ϕ_β

$$M_\beta \dot{\phi}_\beta = \alpha \Delta \phi_\beta - \rho \partial_{\phi_\beta} \psi, \tag{23.10}$$

where M_β and α are constants, ρ denotes the mass density, and ψ is a bulk free energy density. Assuming a small perturbation setting, the linear strain tensor $\mathbf{E}$ can be additively decomposed into elastic $\mathbf{E}_\mathrm{e}$ and inelastic (i.e., eigenstrain) $\mathbf{E}_\mathrm{tr}$ contributions, such that $\mathbf{E}_\mathrm{e}\big(\mathbf{E},\ \phi_\beta\big) = \mathbf{E} - \mathbf{E}_\mathrm{tr}\big(\phi_\beta\big)$. Assuming linear elasticity, the stress $\mathbf{S}$ is given by $\mathbf{S} = \mathbb{C} : \mathbf{E}_\mathrm{e}\big(\mathbf{E},\ \phi_\beta\big)$, and the free energy density takes the form

$$\psi\big(\mathbf{E},\ \phi_\beta,\ \theta\big) = \frac{1}{2}\mathbf{E}_\mathrm{e}\left(\mathbf{E},\ \phi\right) : \mathbb{C} : \mathbf{E}_\mathrm{e}\left(\mathbf{E},\ \phi\right) + \psi_\mathrm{b}\big(\phi_\beta,\ \theta\big)\,. \tag{23.11}$$

As a consequence, the evolution equation (23.10) can be rewritten as

$$M_\beta \dot{\phi}_\beta = \alpha \Delta \phi_\beta + \mathbf{S} : \partial_{\phi_\beta} \mathbf{E}_\mathrm{tr} - \rho \partial_{\phi_\beta} \psi_\mathrm{b}\,. \tag{23.12}$$

In classical elasticity theory the stresses diverge as the defect line is approached. In particular for dislocations the singularity is of $1/r$-type. As per (23.12), this results in singular driving forces for the evolution of the order parameters, effectively negating the concepts such as a nucleation barrier or a pile-up stress. Different approaches to regularize the stress in the core region exist in literature based either on the concept of a distributed BURGER's vector [12, 14–16] or generalized continuum theories [17–20]. However, the first strain gradient approach advocated by Po et al. [20] has the advantage that the obtained regularization is independent of the type of defect in question and therefore does not require any defect-specific information for the determination of model parameters. In principle, these parameters can directly be obtained from atomistic interaction potentials [21].

The purpose of this work is to follow a micromorphic approach and to derive a framework which consistently couples first strain gradient elasticity to ALLEN-CAHN-type microstructure evolution ensuring non-singular driving forces on the order parameters in the presence of line defects.

23.3.2 Balance Equations and Boundary Conditions

The principle of virtual power (PVP) provides a systematic way of deriving field equations and boundary conditions for arbitrary mechanical and coupled problems (cf. [22–24]). In the present work it is used in the following form: The virtual power of the inertia forces $\mathscr{P}^*_{\mathrm{a}}$ balances the virtual power $\mathscr{P}^*_{\mathrm{int}}$ of the internal and $\mathscr{P}^*_{\mathrm{ext}}$ of the external forces acting on any sub-domain $\mathscr{S}$ of the material body $\mathscr{B}$ for any admissible virtual velocity field $\mathbf{v}^*$ and virtual rate of order parameter field $\dot{\phi}^*$, i.e.,

$$\mathscr{P}^*_{\mathrm{a}} = \mathscr{P}^*_{\mathrm{int}} + \mathscr{P}^*_{\mathrm{ext}} \,. \tag{23.13}$$

For the sake of simplicity we disregard any higher order inertia terms [25] as well as inertial forces acting on the order parameter, resulting in

$$\mathscr{P}^*_{\mathrm{a}} = \int_{\mathscr{S}} \rho \dot{\mathbf{v}} \cdot \mathbf{v}^* \, \mathrm{d}V \,. \tag{23.14}$$

The power of internal forces is given by

$$\mathscr{P}^*_{\mathrm{int}} = -\int_{\mathscr{S}} \left(\mathbf{S}^\top : \mathbf{L}^* + \mathcal{T} \vdots \operatorname{grad} \mathbf{L}^* - \pi \, \dot{\phi}^* + \boldsymbol{\xi} \cdot \operatorname{grad} \dot{\phi}^* \right) \mathrm{d}V, \tag{23.15}$$

with $\mathbf{L}^* := \operatorname{grad} \mathbf{v}^*$. Here $\mathbf{S}$ and $\mathcal{T}$ are the CAUCHY and higher order stresses, respectively, while π and $\boldsymbol{\xi}$ are thermodynamic forces that directly correspond to the internal microforce and microstress introduced by Gurtin [26]. We note that the invariance requirement of $\mathscr{P}^*_{\mathrm{int}}$ with respect to superimposed rigid body motions results in $\mathbf{S} = \mathbf{S}^\top$. For the power of external forces we consider the very simple case of no body or contact forces acting on $\mathbf{L}^*$ and $\operatorname{grad} \dot{\phi}^*$, and only a contact (micro)force ζ acting $\dot{\phi}^*$

$$\mathscr{P}^*_{\mathrm{ext}} = \int_{\mathscr{S}} \mathbf{f} \cdot \mathbf{v}^* \rho \, \mathrm{d}V + \int_{\partial \mathscr{S}} \left(\mathbf{t} \cdot \mathbf{v}^* + \zeta \, \dot{\phi}^* \right) \mathrm{d}a \,. \tag{23.16}$$

In order to obtain the consequences of the PVP, the integrals in (23.15) are transformed using the following identities

$$\operatorname{div}(\mathbf{S} \cdot \mathbf{v}^*) = (\operatorname{div} \mathbf{S}) \cdot \mathbf{v}^* + \mathbf{S} : \mathbf{L}^*, \tag{23.17}$$

$$\operatorname{div}(\mathcal{T} : \mathbf{L}^*) = (\operatorname{div} \mathcal{T}) : \mathbf{L}^* + \mathcal{T} \vdots \operatorname{grad} \mathbf{L}^*, \tag{23.18}$$

$$\operatorname{div}\big((\operatorname{div} \mathcal{T}) \cdot \mathbf{v}^*\big) = (\operatorname{div} \operatorname{div} \mathcal{T}) \cdot \mathbf{v}^* + (\operatorname{div} \mathcal{T}) : \mathbf{L}^*, \tag{23.19}$$

$$\operatorname{div}(\boldsymbol{\xi} \, \dot{\phi}^*) = (\operatorname{div} \boldsymbol{\xi}) \, \dot{\phi}^* + \boldsymbol{\xi} \cdot \operatorname{grad} \dot{\phi}^*, \tag{23.20}$$

and the divergence theorem, resulting in

$$\mathscr{P}^*_{\text{int}} = \int_{\mathscr{S}} \big(\operatorname{div}\mathbf{S} - \operatorname{div}\operatorname{div}\mathcal{T}\big)\cdot\mathbf{v}^*\,\mathrm{d}V - \int_{\partial\mathscr{S}} \mathbf{n}\cdot\big(\mathbf{S}^\top - \operatorname{div}\mathcal{T}\big)\cdot\mathbf{v}^*\,\mathrm{d}a$$
$$- \int_{\partial\mathscr{S}} \mathbf{n}\cdot\mathcal{T} : \mathbf{L}^*\,\mathrm{d}a + \int_{\mathscr{S}} \big(\pi + \operatorname{div}\boldsymbol{\xi}\big)\,\dot{\phi}^*\,\mathrm{d}V - \int_{\partial\mathscr{S}} \mathbf{n}\cdot\boldsymbol{\xi}\,\dot{\phi}^*\,\mathrm{d}a\,. \tag{23.21}$$

Introducing the surface gradient operator

$$\operatorname{grad}_S(\cdot) = \operatorname{grad}(\cdot) - \partial_{\mathbf{n}}(\cdot)\otimes\mathbf{n}, \tag{23.22}$$

where $\partial_{\mathbf{n}}$ is the directional derivative in the direction of the outward normal $\mathbf{n}$, the third integral in expression (23.21) can be rewritten as

$$\int_{\partial\mathscr{S}} \mathbf{n}\cdot\mathcal{T} : \mathbf{L}^*\,\mathrm{d}a = \int_{\partial\mathscr{S}} \mathbf{n}\cdot\mathcal{T} : \operatorname{grad}_S\mathbf{v}^*\,\mathrm{d}a + \int_{\partial\mathscr{S}} \mathbf{n}\cdot\mathcal{T} : \partial_{\mathbf{n}}\mathbf{v}^*\otimes\mathbf{n}\,\mathrm{d}a \tag{23.23}$$
$$= \int_{\partial\mathscr{S}} \operatorname{div}_S\big(\mathbf{n}\cdot\mathcal{T}\cdot\mathbf{v}^*\big)\,\mathrm{d}a - \int_{\partial\mathscr{S}} \operatorname{div}_S\big(\mathbf{n}\cdot\mathcal{T}\big)\cdot\mathbf{v}\,\mathrm{d}a +$$
$$+ \int_{\partial\mathscr{S}} \mathbf{n}\cdot\mathcal{T} : \partial_{\mathbf{n}}\mathbf{v}^*\otimes\mathbf{n}\,\mathrm{d}a. \tag{23.24}$$

Finally, applying the surface divergence theorem and, for the sake of simplicity, neglecting any wedge line and corner contributions, we find

$$\int_{\partial\mathscr{S}} \operatorname{div}_S\big(\mathbf{n}\cdot\mathcal{T}\cdot\mathbf{v}^*\big)\,\mathrm{d}a = \int_{\partial\mathscr{S}} \big(\operatorname{div}_S\mathbf{n}\big)\mathbf{n}\otimes\mathbf{n} : \mathcal{T}\cdot\mathbf{v}^*\,\mathrm{d}a. \tag{23.25}$$

Enforcing (23.13) we arrive after a number of straightforward algebraic manipulations at the following field equations on $\mathscr{B}$

$$\rho\dot{\mathbf{v}} = \operatorname{div}(\mathbf{S} - \operatorname{div}\mathcal{T}) + \rho\mathbf{f}, \tag{23.26a}$$
$$0 = \operatorname{div}\boldsymbol{\xi} + \pi, \tag{23.26b}$$

and boundary conditions on $\partial\mathscr{B}$

$$\mathbf{t} = (\mathbf{S} - \operatorname{div}\mathcal{T})\cdot\mathbf{n} - \operatorname{div}_S(\mathbf{n}\cdot\mathcal{T}), \tag{23.26c}$$
$$\zeta = \boldsymbol{\xi}\cdot\mathbf{n}\,. \tag{23.26d}$$

We note that, introducing the total stress

$$\mathbf{S}_{\text{t}} := \mathbf{S} - \operatorname{div}\mathcal{T}, \tag{23.27}$$

the balance of linear momentum (23.26a) regains its standard form for simple materials

$$\rho\dot{\mathbf{v}} = \operatorname{div}\mathbf{S}_{\mathrm{t}} + \rho\mathbf{f}, \tag{23.28}$$

which is convenient for the numerical implementation.

23.3.3 Constitutive Equations

The following equations are formulated assuming the small perturbation hypothesis, i.e., both the displacement $\mathbf{u}$ as well as the displacement gradient can be considered small, $\mathbf{u} \ll L$ and $||\operatorname{grad}\mathbf{u}|| \ll 1$. In this case the deformation is characterized by the linear strain tensor $\mathbf{E} = \frac{1}{2}\left(\operatorname{grad}\mathbf{u} + (\operatorname{grad}\mathbf{u})^{\top}\right)$. Its gradient will be denoted $\mathcal{Y} := \operatorname{grad}\mathbf{E}$.

23.3.3.1 Laws of State

We choose the following ansatz for the free energy density and thermodynamic forces

$$\begin{aligned}
&\psi = \psi\left(\mathbf{E},\, \mathcal{Y},\, \phi,\, \operatorname{grad}\phi,\, \theta\right), && \boldsymbol{\xi} = \boldsymbol{\xi}\left(\mathbf{E},\, \mathcal{Y},\, \phi,\, \operatorname{grad}\phi,\, \theta\right),\\
&\mathbf{S} = \mathbf{S}\left(\mathbf{E},\, \mathcal{Y},\, \phi,\, \operatorname{grad}\phi,\, \theta\right), && \pi = \pi\left(\mathbf{E},\, \mathcal{Y},\, \phi,\, \operatorname{grad}\phi,\, \theta,\, \dot{\phi}\right).\\
&\mathcal{T} = \mathcal{T}\left(\mathbf{E},\, \mathcal{Y},\, \phi,\, \operatorname{grad}\phi,\, \theta\right),
\end{aligned}$$

The second law of thermodynamics in the form of the CLAUSIUS-DUHEM inequality is given for the isothermal case by

$$\begin{aligned}
\left(\mathbf{S} - \rho\partial_{\mathbf{E}}\psi\right) : \dot{\mathbf{E}} + \left(\mathcal{T} - \rho\partial_{\mathcal{Y}}\psi\right) \vdots \dot{\mathcal{Y}} - \left(\pi\ + \rho\partial_{\phi}\psi\right)\dot{\phi} +\\
+ \left(\boldsymbol{\xi} - \rho\partial_{\operatorname{grad}\phi}\psi\right)\cdot\operatorname{grad}\dot{\phi} \geqslant 0
\end{aligned} \tag{23.29}$$

an can be exploited using the classical COLEMAN-NOLL procedure to arrive at the laws of state

$$\mathbf{S} = \rho\partial_{\mathbf{E}}\psi, \qquad \mathcal{T} = \rho\partial_{\mathcal{Y}}\psi, \qquad \boldsymbol{\xi} = \rho\partial_{\operatorname{grad}\phi}\psi \tag{23.30}$$

and the residual dissipation inequality

$$-\pi_{\mathrm{d}}\,\dot{\phi} \geqslant 0, \quad \text{with} \quad \pi_{\mathrm{d}} := \pi + \rho\partial_{\phi}\psi\,. \tag{23.31}$$

23.3.3.2 Free Energy and Dissipation Potential

As customary in phase field models for solid-solid transformations, the free energy density can be split into an elastic-, a bulk chemical- and an interface-contribution

$$\psi = \psi_{\mathrm{e}}\left(\mathbf{E},\, \mathcal{Y},\, \phi,\, \theta\right) + \psi_{\mathrm{b}}\left(\phi,\, \theta\right) + \psi_{\mathrm{i}}\left(\phi,\, \operatorname{grad}\phi,\, \theta\right)\,. \tag{23.32}$$

In our formulation, the elastic free energy is of HELMHOLTZ-type, i.e.,

$$\begin{aligned}\rho\psi_{\mathrm{e}}\left(\mathbf{E},\, \mathcal{Y},\, \phi,\, \theta\right) = \frac{1}{2}\mathbf{E}_{\mathrm{e}}\left(\mathbf{E},\, \phi\right) : \mathbb{C}(\phi) : \mathbf{E}_{\mathrm{e}}\left(\mathbf{E},\, \phi\right) \\ + \frac{1}{2}\big(\mathbb{C}(\phi) : \mathcal{Y}\cdot\boldsymbol{\Lambda}(\phi)\big)\vdots\mathcal{Y},\end{aligned} \tag{23.33}$$

where $\mathbf{E}_{\mathrm{tr}}(\phi)$ is the inelastic strain, $\mathbf{E}_{\mathrm{e}}\left(\mathbf{E},\, \phi\right) := \mathbf{E} - \mathbf{E}_{\mathrm{tr}}(\phi)$ is the elastic strain, $\mathbb{C}$ the stiffness tensor and $\boldsymbol{\Lambda}(\phi)$ a gradient length scale tensor (cf. [20]). The specific choice of functional dependence of $\mathbf{E}_{\mathrm{tr}}(\phi)$, $\psi_{\mathrm{b}}\left(\phi,\, \theta\right)$ and $\psi_{\mathrm{i}}\left(\phi,\, \operatorname{grad}\phi,\, \theta\right)$ on the order parameter ϕ is of no relevance at this point, we will assume that the interface energy is of the form

$$\rho\psi_{\mathrm{i}}\left(\phi,\, \operatorname{grad}\phi,\, \theta\right) := \frac{\alpha}{2}\,||\operatorname{grad}\phi||^2 + g(\phi,\, \theta)\,. \tag{23.34}$$

Using the laws of state (23.30) we immediately find

$$\mathbf{S} = \mathbb{C}(\phi) : \mathbf{E}_{\mathrm{e}}\left(\mathbf{E},\, \phi\right) = \mathbb{C}(\phi) : \big(\mathbf{E} - \mathbf{E}_{\mathrm{tr}}(\phi)\big), \tag{23.35a}$$

$$\mathcal{T} = \mathbb{C}(\phi) : \mathcal{Y}\cdot\boldsymbol{\Lambda}(\phi), \tag{23.35b}$$

$$\boldsymbol{\xi} = \alpha\,\operatorname{grad}\phi, \tag{23.35c}$$

and combining the first two equations

$$\mathcal{T} = \mathbb{C}(\phi) : \operatorname{grad}\left(\mathbb{C}^{-1}(\phi) : \mathbf{S}\right)\cdot\boldsymbol{\Lambda}(\phi) + \mathbb{C}(\phi) : \operatorname{grad}\mathbf{E}_{\mathrm{tr}}(\phi)\cdot\boldsymbol{\Lambda}(\phi)\,. \tag{23.36}$$

Equation (23.27) can now be used in two ways: In conjunction with the laws of state (23.35a) and (23.35b) it is a constitutive equation for the total stress $\mathbf{S}_{\mathrm{t}}$, which enters the balance of linear momentum (23.28)

$$\mathbf{S}_{\mathrm{t}}\big(\mathbf{E},\, \mathcal{Y},\, \phi\big) = \mathbb{C}(\phi) : \mathbf{E}_{\mathrm{e}}\left(\mathbf{E},\, \phi\right) - \operatorname{div}\big[\mathbb{C}(\phi) : \mathcal{Y}\cdot\boldsymbol{\Lambda}(\phi)\big]\,. \tag{23.37}$$

When combined with (23.36), (23.27) can be used to determine the true stress $\mathbf{S}$ from the total stress $\mathbf{S}_{\mathrm{t}}$

$$\begin{aligned}\mathbf{S} - \operatorname{div}\big[\mathbb{C}(\phi) : \operatorname{grad}\big(\mathbb{C}^{-1}(\phi) : \mathbf{S}\big) \cdot \boldsymbol{\Lambda}(\phi)\big] \\ = \mathbf{S}_{\mathrm{t}} + \operatorname{div}\big(\mathbb{C}(\phi) : \operatorname{grad}\mathbf{E}_{\mathrm{tr}}(\phi) \cdot \boldsymbol{\Lambda}(\phi)\big)\,.\end{aligned} \tag{23.38}$$

In order to complete the phase field formulation we require a constitutive equation for π_{d}, which is obtained in the spirit of classical irreversible thermodynamics as

$$\dot{\phi} = -\partial_{\pi_{\mathrm{d}}}\Omega\,(\pi_{\mathrm{d}}) \tag{23.39}$$

from a dissipation potential $\Omega\,(\pi_{\mathrm{d}})$ that is homogeneous of degree two

$$\Omega\,(\pi_{\mathrm{d}}) := \frac{1}{2}M^{-1}\pi_{\mathrm{d}}^2, \tag{23.40}$$

where M is the so called mobility constant. Combining (23.26b), (23.31), (23.35c), (23.39) and (23.40) we find the classical ALLEN-CAHN equation

$$M\dot{\phi} = \alpha\,\Delta\phi - \rho\,\partial_{\phi}\psi, \tag{23.41}$$

or, specifically,

$$\begin{aligned}M\dot{\phi} = \alpha\,\Delta\phi + \mathbf{S} : \partial_{\phi}\mathbf{E}_{\mathrm{tr}} - \frac{1}{2}\mathbf{E}_{\mathrm{e}}\,(\mathbf{E},\,\phi) : \partial_{\phi}\mathbb{C}(\phi) : \mathbf{E}_{\mathrm{e}}\,(\mathbf{E},\,\phi) \\ - \frac{1}{2}\big(\mathbb{C}(\phi) : \mathcal{Y} \cdot \partial_{\phi}\boldsymbol{\Lambda}(\phi)\big) - \frac{1}{2}\big(\partial_{\phi}\mathbb{C}(\phi) : \mathcal{Y} \cdot \boldsymbol{\Lambda}(\phi)\big) \vdots \mathcal{Y} \\ - \rho\,\partial_{\phi}\psi_{\mathrm{b}}(\phi,\,\theta) - \partial_{\phi}g(\phi,\,\theta)\,.\end{aligned} \tag{23.42}$$

Note that all terms that appear in the driving force, and as per [17] the CAUCHY stress $\mathbf{S}$ in particular, are non-singular even in the presence of dislocations.

23.3.4 Special Cases

For phase transformations the crystal lattice on both sides of the interface will, in general, be different leading to different elastic properties and a different dislocation core structure. In this case the (23.28), (23.37), (23.38) and (23.42) retain their full complexity. In the following, we consider a number of scenarios for which this is not the case.

23.3.4.1 Homogeneous Bulk Material

In the bulk phase the order parameter does not vary in space, i.e., $\operatorname{grad}\phi = \mathbf{0}$, $\mathbb{C}(\phi) = \mathbb{C}$, $\boldsymbol{\Lambda}(\phi) = \boldsymbol{\Lambda}$, $\mathbf{E}_{\mathrm{tr}}(\phi) = \mathbf{0}$. The ALLEN-CAHN equation is fulfilled automatically and

(23.38), (23.37) recover the form derived by Po et al. [20]

$$\begin{aligned}&\mathbf{S} - \operatorname{div}\big((\operatorname{grad}\mathbf{S})\cdot\boldsymbol{\Lambda}\big) = \mathbf{S}_\mathrm{t}, \text{ with}\\ &\mathbf{S}_\mathrm{t}\big(\mathbf{E},\,\mathcal{Y}\big) = \mathbb{C} : \big[\mathbf{E} - \operatorname{div}\big(\mathcal{Y}\cdot\boldsymbol{\Lambda}\big)\big]\,.\end{aligned} \tag{23.43a}$$

For materials with cubic symmetry the gradient length scale tensor $\boldsymbol{\Lambda}$ is isotropic, i.e., $\boldsymbol{\Lambda} = \ell^2\mathbf{I}$, and the above expressions can be further simplified to the form derived by Lazar et al. [17]

$$\begin{aligned}&\mathbf{S} - \ell^2\Delta\mathbf{S} = \mathbf{S}_\mathrm{t}, \text{ with}\\ &\mathbf{S}_\mathrm{t}\big(\mathbf{E},\,\mathcal{Y}\big) = \mathbb{C} : \big(\mathbf{E} - \ell^2\operatorname{div}\mathcal{Y}\big) = \mathbb{C} : \big(\mathbf{E} - \ell^2\Delta\mathbf{E}\big)\,.\end{aligned} \tag{23.43b}$$

23.3.4.2 Grain Boundaries as Planar Defects

The crystal lattices on both sides of a grain boundary differ only by a rotation $\mathbf{Q}(\phi)$. Hence, we assume that the chemical bulk energy is independent of the order parameter, i.e., $\psi_\mathrm{b}(\phi,\,\theta) = \psi_\mathrm{b}(\theta)$. Then the elastic stiffness $\mathbb{C}(\phi)$ and the gradient length scale tensor $\boldsymbol{\Lambda}(\phi)$ can be expressed as $\mathbb{C}(\phi) = \mathbf{Q}(\phi) * \mathbb{C}$ and $\boldsymbol{\Lambda}(\phi) = \mathbf{Q}(\phi) * \boldsymbol{\Lambda}$, respectively. Furthermore, without loss of generality, $\mathbf{E}_\mathrm{tr}(\phi) = \mathbf{0}$. For this case (23.38), (23.37) and (23.42) take the form

$$\mathbf{S} - \operatorname{div}\Big[\big(\mathbf{Q}(\phi) * \mathbb{C}\big) : \operatorname{grad}\Big(\big(\mathbf{Q}(\phi) * \mathbb{C}^{-1}\big) : \mathbf{S}\Big)\cdot\big(\mathbf{Q}(\phi) * \boldsymbol{\Lambda}\big)\Big] = \mathbf{S}_\mathrm{t}, \tag{23.44a}$$

with

$$\mathbf{S}_\mathrm{t}\big(\mathbf{E},\,\mathcal{Y},\,\phi\big) = \mathbb{C}(\phi) : \mathbf{E} - \operatorname{div}\big[\big(\mathbf{Q}(\phi) * \mathbb{C}\big) : \mathcal{Y}\cdot\big(\mathbf{Q}(\phi) * \boldsymbol{\Lambda}\big)\big], \tag{23.44b}$$

and

$$\begin{aligned}M\dot{\phi} = \alpha\Delta\phi - \frac{1}{2}\mathbf{E} : \big(\partial_\phi\mathbf{Q}(\phi) * \mathbb{C}\big) : \mathbf{E} - \frac{1}{2}\big(\big(\mathbf{Q}(\phi) * \mathbb{C}\big) : \mathcal{Y}\cdot\big(\partial_\phi\mathbf{Q} * \boldsymbol{\Lambda}\big)\big) -\\ - \frac{1}{2}\big(\big(\partial_\phi\mathbf{Q}(\phi) * \mathbb{C}\big) : \mathcal{Y}\cdot\big(\mathbf{Q}(\phi) * \boldsymbol{\Lambda}\big)\big) \vdots \mathcal{Y} - \partial_\phi g(\phi,\,\theta)\,.\end{aligned} \tag{23.44c}$$

The isotropy of the gradient length scale tensor $\boldsymbol{\Lambda}$ for cubic crystals implies that $\mathbf{Q}(\phi) * \boldsymbol{\Lambda} = \boldsymbol{\Lambda} = \ell^2\mathbf{I}$, which simplifies (23.44) to the following form

$$\mathbf{S} - \ell^2\operatorname{div}\Big[\big(\mathbf{Q}(\phi) * \mathbb{C}\big) : \operatorname{grad}\Big(\big(\mathbf{Q}(\phi) * \mathbb{C}^{-1}\big) : \mathbf{S}\Big)\Big] = \mathbf{S}_\mathrm{t}, \tag{23.45a}$$

with

$$\mathbf{S}_\mathrm{t}\big(\mathbf{E},\,\mathcal{Y},\,\phi\big) = \mathbb{C}(\phi) : \mathbf{E} - \ell^2\operatorname{div}\big[\big(\mathbf{Q}(\phi) * \mathbb{C}\big) : \mathcal{Y}\big], \tag{23.45b}$$

and

$$M\dot{\phi} = \alpha\Delta\phi - \frac{1}{2}\mathbf{E} : \big(\partial_\phi \mathbf{Q}(\phi) * \mathbb{C}\big) : \mathbf{E} - \frac{1}{2}\ell^2 \big(\big(\partial_\phi \mathbf{Q}(\phi) * \mathbb{C}\big) : \mathcal{Y}\big) \vdots \mathcal{Y} - \partial_\phi g(\phi,\, \theta)\,. \tag{23.45c}$$

23.3.4.3 Twin Boundaries as Planar Defects

Since the twin variants on both sides of the boundary are related by mirror and/or rotational symmetry transformations between the unit cells, we can—as in the case of grain boundaries—assume that the bulk chemical energy remains unchanged, i.e., $\psi_\mathrm{b}(\phi,\, \theta) = \psi_\mathrm{b}(\theta)$, and the elastic stiffness $\mathbb{C}(\phi)$ and the gradient length scale tensor $\mathbf{\Lambda}(\phi)$ can be expressed using an orthogonal tensor $\mathbf{Q}(\phi)$ as $\mathbb{C}(\phi) = \mathbf{Q}(\phi) * \mathbb{C}$ and $\mathbf{\Lambda}(\phi) = \mathbf{Q}(\phi) * \mathbf{\Lambda}$, respectively. Under these assumptions we find

$$\begin{aligned}\mathbf{S} - \mathrm{div}\Big[\big(\mathbf{Q}(\phi) * \mathbb{C}\big) : \mathrm{grad}\,\Big(\big(\mathbf{Q}(\phi) * \mathbb{C}^{-1}\big) : \mathbf{S}\Big) \cdot \big(\mathbf{Q}(\phi) * \mathbf{\Lambda}\big)\Big] \\ = \mathbf{S}_\mathrm{t} + \mathrm{div}\big[\mathbb{C}(\phi) : \mathrm{grad}\,\big(\mathbf{E}_\mathrm{tr}(\phi)\big) \cdot \mathbf{\Lambda}(\phi)\big],\end{aligned} \tag{23.46a}$$

with

$$\mathbf{S}_\mathrm{t}\big(\mathbf{E},\, \mathcal{Y},\, \phi\big) = \mathbb{C}(\phi) : \mathbf{E}_\mathrm{e}(\mathbf{E}) - \mathrm{div}\big[\big(\mathbf{Q}(\phi) * \mathbb{C}\big) : \mathcal{Y} \cdot \big(\mathbf{Q}(\phi) * \mathbf{\Lambda}\big)\big], \tag{23.46b}$$

and

$$\begin{aligned}M\dot{\phi} = \alpha\Delta\phi + \mathbf{S} : \partial_\phi \mathbf{E}_\mathrm{tr} - \frac{1}{2}\mathbf{E}_\mathrm{e}(\mathbf{E},\, \phi) : \big(\partial_\phi \mathbf{Q}(\phi) * \mathbb{C}\big) : \mathbf{E}_\mathrm{e}(\mathbf{E},\, \phi) \\ - \frac{1}{2}\big(\big(\mathbf{Q}(\phi) * \mathbb{C}\big) : \mathcal{Y} \cdot \big(\partial_\phi \mathbf{Q} * \mathbf{\Lambda}\big)\big) \\ - \frac{1}{2}\big(\big(\partial_\phi \mathbf{Q}(\phi) * \mathbb{C}\big) : \mathcal{Y} \cdot \big(\mathbf{Q}(\phi) * \mathbf{\Lambda}\big)\big) \vdots \mathcal{Y} - \partial_\phi g(\phi,\, \theta)\,.\end{aligned} \tag{23.46c}$$

For cubic lattices these expressions simplify to

$$\mathbf{S} - \ell^2 \mathrm{div}\Big[\big(\mathbf{Q}(\phi) * \mathbb{C}\big) : \mathrm{grad}\,\Big(\big(\mathbf{Q}(\phi) * \mathbb{C}^{-1}\big) : \mathbf{S}\Big)\Big] \tag{23.47a}$$

$$= \mathbf{S}_\mathrm{t} + \ell^2 \mathrm{div}\big[\mathbb{C}(\phi) : \mathrm{grad}\,\mathbf{E}_\mathrm{tr}(\phi)\big], \tag{23.47b}$$

with

$$\mathbf{S}_\mathrm{t}\big(\mathbf{E},\, \mathcal{Y},\, \phi\big) = \mathbb{C}(\phi) : \mathbf{E}_\mathrm{e}(\mathbf{E},\, \phi) - \ell^2 \mathrm{div}\big[\big(\mathbf{Q}(\phi) * \mathbb{C}\big) : \mathcal{Y}\big], \tag{23.47c}$$

and

$$\begin{aligned}M\dot{\phi} = \alpha\Delta\phi + \mathbf{S} : \partial_\phi \mathbf{E}_\mathrm{tr} - \frac{1}{2}\mathbf{E}_\mathrm{e}(\mathbf{E},\, \phi) : \big(\partial_\phi \mathbf{Q}(\phi) * \mathbb{C}\big) : \mathbf{E}_\mathrm{e}(\mathbf{E},\, \phi) - \\ - \frac{1}{2}\ell^2 \big(\big(\partial_\phi \mathbf{Q}(\phi) * \mathbb{C}\big) : \mathcal{Y}\big) \vdots \mathcal{Y} - \partial_\phi g(\phi,\, \theta)\,.\end{aligned} \tag{23.47d}$$

23.3.4.4 Phase Boundaries Between Cubic Phases

In the case of phase boundaries between different cubic phases the gradient length scale tensor $\boldsymbol{\Lambda}$ is isotropic on both sides of the interface, even though not necessarily constant across the interface, i.e., $\boldsymbol{\Lambda} = \ell(\phi)^2\mathbf{I}$. This allows us to reduce (23.38), (23.37) and (23.42) to the following form

$$\begin{aligned}\mathbf{S} - \operatorname{div}\left[\ell(\phi)^2\,\mathbb{C}(\phi) : \operatorname{grad}\left(\mathbb{C}^{-1}(\phi) : \mathbf{S}\right)\right] \\ = \mathbf{S}_{\mathrm{t}} + \operatorname{div}\left(\ell(\phi)^2\,\mathbb{C}(\phi) : \operatorname{grad}\mathbf{E}_{\mathrm{tr}}(\phi)\right),\end{aligned} \tag{23.48a}$$

with

$$\mathbf{S}_{\mathrm{t}}\left(\mathbf{E},\ \mathcal{Y},\ \phi\right) = \mathbb{C}(\phi) : \mathbf{E}_{\mathrm{e}}\left(\mathbf{E},\ \phi\right) - \operatorname{div}\left(\ell(\phi)^2\,\mathbb{C}(\phi) : \mathcal{Y}\right), \tag{23.48b}$$

and

$$\begin{aligned}M\dot{\phi} = \alpha\Delta\phi + \mathbf{S} : \partial_\phi\mathbf{E}_{\mathrm{tr}} + \frac{1}{2}\mathbf{E}_{\mathrm{e}}\left(\mathbf{E},\ \phi\right) : \partial_\phi\mathbb{C}(\phi) : \mathbf{E}_{\mathrm{e}}\left(\mathbf{E},\ \phi\right) \\ - \ell(\phi)\partial_\phi\ell(\phi)\left(\mathbb{C}(\phi) : \mathcal{Y}\right) \vdots \mathcal{Y} - \frac{\ell(\phi)^2}{2}\left(\partial_\phi\mathbb{C}(\phi) : \mathcal{Y}\right) \vdots \mathcal{Y} \\ - \rho\partial_\phi\psi_{\mathrm{b}}(\phi,\ \theta) - \partial_\phi g(\phi,\ \theta)\,.\end{aligned} \tag{23.48c}$$

23.3.5 Examples

This section contains a number of examples that demonstrate basic properties of the proposed model.

23.3.5.1 Regularization in the Dislocation Core

As shown in Sect. 23.3.4.1, the present model reduces to the set of equations proposed by Po et al. [20] in the homogeneous bulk phase. Figure 23.6 shows the shear stress component S_{12} in the glide plane of a single edge dislocation with and without regularization ($\ell = 2$ nm). In the classical case, the stress in the dislocation core is singular, whereas it is well defined for the regularized solution.

23.3.5.2 Effect of the Regularization on the Interaction of Dislocations with a Phase Boundary

The following scenario considers a two-phase material with an initially flat interface between the austenite (A) and martensite (M) phases (see Fig. 23.7, left figure) and an immobile dislocation structure within the austenite. The material is cooled below the martensite start temperature, i.e., the interface will move to the right, interacting with the dislocation structure. This interaction significantly varies depending on the

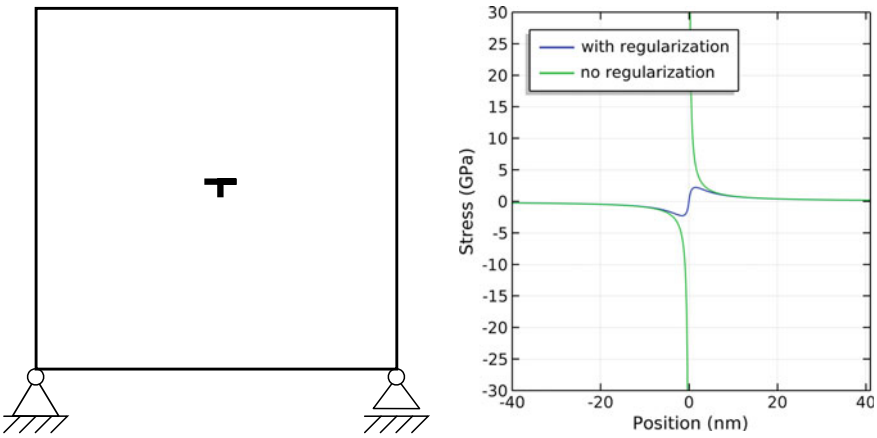

Fig. 23.6 Shear stress component S_{12} in the glide plane of a single edge dislocation

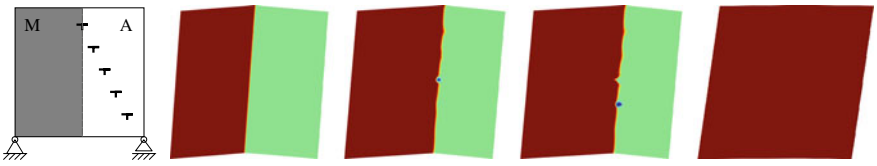

Fig. 23.7 Phase evolution for $\ell = 2$ nm

choice of the regularization. For a large regularization length ($\ell = 2$ nm) the stress in the dislocation core is relatively low, which enables the chemical driving force to pull the interface across the dislocation structure, resulting in a fully martensitic material (Fig. 23.7). With decreasing regularization length ($\ell = 1$ nm) the stress in the dislocation core increases, which leads to a stronger interaction with the interface, which, as a consequence, is arrested at the rightmost dislocation (Fig. 23.8). After the interface is immobile, the second martensitic variant is formed, which consumes the austenite. For an even smaller regularization length ($\ell = 0.5$ nm) the interface is arrested earlier in its progress (Fig. 23.9).

If, however, no regularization is present, this trend does not continue. The stress singularity in the dislocation core triggers the formation of martensite well ahead of the initial interface, enabling it to "overrun" the immobile dislocation structure

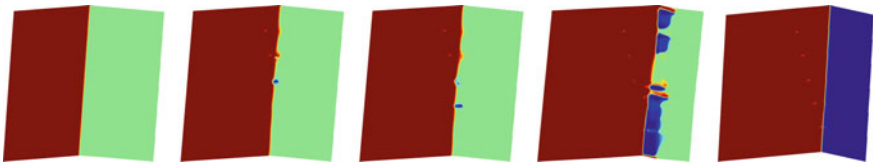

Fig. 23.8 Phase evolution for $\ell = 1$ nm

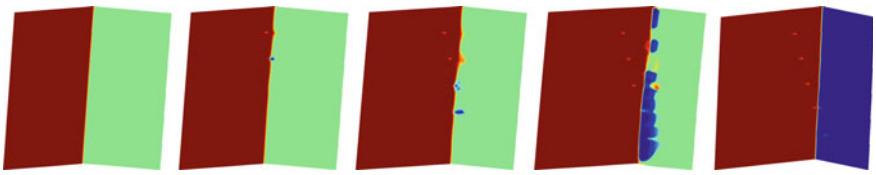

Fig. 23.9 Phase evolution for $\ell = 0.5$ nm

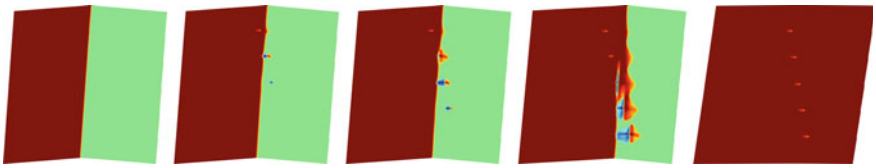

Fig. 23.10 Phase evolution without regularization

(Fig. 23.10). The result in this case is mesh sensitive, since the computed stress magnitude depends on the choice of discretization and therefore is unsuitable for quantitative investigations of the interaction of planar defects with dislocations.

23.4 Conclusions

In order to model the interaction of phase transformations and dislocations, we have coupled a time-dependent Ginzburg-Landau equation with the stress/strain fields of stationary configurations of discrete dislocations. This allowed us to study the effect that dislocations have on the resulting evolution of the microstructure. Coupling two simulation models for different deformation mechanisms is usually more involved than just the simulation of one phenomenon. However, the present work also showed that such a "multiphysical" approach might show a particular promise since, e.g., the artificial initial seed for the phase microstructure becomes superfluous, which makes our simulations more realistic.

However, only using stationary dislocation configurations is clearly not realistic: these dislocations would usually move and interact among themselves. Thus, future work will consider such behavior where the evolution of the phase microstructure is governed by the TDGL and the dislocation dynamics is governed by an equation of motion, both of which are coupled.

Acknowledgements The authors gratefully acknowledge the Deutsche Forschungsgemeinschaft (DFG) for supporting this work carried out within the framework of Collaborative Research Center SFB 799 (subproject C9).

References

1. A. Weidner, H. Biermann, J. Mech. **67**(8), 1729 (2015). https://doi.org/10.1007/s11837-015-1456-y
2. B. Li, X.M. Zhang, P.C. Clapp, J.A. Rifkin, J. Appl. Phys. **95**(4), 1698 (2004). https://doi.org/10.1063/1.1638609
3. J. Shim, Y. Cho, S. Kwon, W. Kim, B. Wirth, Appl. Phys. Lett. **90**(2), 021906 (2007). https://doi.org/10.1063/1.2429902
4. A. Ibarra, D. Caillard, J. San Juan, M.L. Nó, Appl. Phys. Lett. **90**(10), 101907 (2007). https://doi.org/10.1063/1.2710076
5. L.D. Landau, Zh. Eksp. Teor. Fiz. **7**, 19 (1937). [Ukr. J. Phys. 53, 25 (2008)]
6. A. Khachaturyan, *Theory of Structural Transformations in Solids* (Wiley, New York, 1983)
7. J.P. Hirth, J. Lothe, *Theory of Dislocations* (McGraw-Hill, New York, 1967)
8. R. Wu, S. Sandfeld, Scripta Mater. **123**, 42 (2016). https://doi.org/10.1016/j.scriptamat.2016.05.032
9. R. Wu, M. Zaiser, S. Sandfeld, Int. J. Plastic. **95**, 142 (2017). https://doi.org/10.1016/j.ijplas.2017.04.005
10. D. Schrade, B. Xu, R. Müller, D. Gross, *Proceedings of the ASME Conference on Smart Materials, Adaptive Structures and Intelligent Systems*, vol. 1 (2008), p. 299. https://doi.org/10.1115/SMASIS2008-411
11. R. Schmitt, C. Kuhn, R. Müller, K. Bhattacharya, Technische Mechanik **34**(1), 23 (2014). https://doi.org/10.24352/UM.OVGU-2017-051
12. W. Cai, A. Arsenlis, C.R. Weinberger, V.V. Bulatov, J. Mech. Phys. Solids **54**(3), 561 (2006). https://doi.org/10.1016/j.jmps.2005.09.005
13. J. Weertman, *Dislocation Based Fracture Mechanics* (World Scientific Pub Co Inc, 1996), pp. 2–5
14. R. Peierls, Proc. Phys. Soc. **52**(1), 34 (1940). https://doi.org/10.1088/0959-5309/52/1/305
15. F.R.N. Nabarro, Proc. Phys. Soc. **59**(2), 256 (1947). https://doi.org/10.1088/0959-5309/59/2/309
16. J. Lothe, *Elastic Strain Fields and Dislocation Mobility, Modern Problems in Condensed Matter Sciences*, vol. 31, ed. by V.L. Indenbom, J. Lothe (Elsevier, 1992), pp. 175–235. https://doi.org/10.1016/B978-0-444-88773-3.50008-X
17. M. Lazar, G.A. Maugin, E.C. Aifantis, Phys. Status Solidi B **242**(12), 2365 (2005). https://doi.org/10.1002/pssb.200540078
18. M. Lazar, G.A. Maugin, E.C. Aifantis, Int. J. Solids Struct. **43**(6), 1787 (2006). https://doi.org/10.1016/j.ijsolstr.2005.07.005
19. M. Lazar, G. Po, Phys. Lett. A **379**(24), 1538 (2015). https://doi.org/10.1016/j.physleta.2015.03.027
20. G. Po, M. Lazar, N.C. Admal, N. Ghoniem, Int. J. Plastic. **103**, 1 (2018). https://doi.org/10.1016/j.ijplas.2017.10.003
21. N.C. Admal, J. Marian, G. Po, J. Mech. Phys. Solids **99**, 93 (2017). https://doi.org/10.1016/j.jmps.2016.11.005
22. G. Maugin, Acta Mech. **35**(1–2), 1 (1980)
23. P. Germain, SIAM J. Appl. Math. **25**(3), 556 (1973). https://doi.org/10.1137/0125053
24. G. Del Piero, J. Mech. Mater. Struct. **4**(2), 281 (2009). https://doi.org/10.2140/jomms.2009.4.281
25. R. Mindlin, Arch. Ration. Mech. An. **16**(1), 51 (1964)
26. M. Gurtin, Physica D **92**(3–4), 178 (1996)

Chapter 24
Towards the Crystal Plasticity Based Modeling of TRIP-Steels—From Material Point to Structural Simulations

Stefan Prüger and Björn Kiefer

Abstract With the complex multi-scale behavior of high-alloyed TRIP steels in mind, this contribution aims to complement recently established continuum mechanical modeling approaches for such materials, by considering their anisotropic inelastic response at the single crystal level. This approach generally enables the consideration of initial textures and their deformation-induced evolutions. It also represents the key theoretical and algorithmic foundation for future extensions to include phase transformation and twinning effects. Several rate-independent and rate-dependent formulations are investigated. The former are naturally associated with Karush-Kuhn-Tucker type inequality constraints in the sense of a multi-surface plasticity problem, whereas in the latter, these constraints are handled by penalty-type approaches. More specifically, the primary octahedral slip systems of face-centered cubic crystal symmetry are explicitly taken into account in our model application of the general framework and hardening models of increasing complexity are incorporated. To test the efficiency and robustness of the different formulations, material point simulations are carried out under proportional and non-proportional deformation histories. A rate-independent augmented Lagrangian formulation is identified as most suitable in the considered context and its finite element implementation as a User-defined MATerial subroutine (UMAT) is consequently studied in depth. To this end, the loading orientation dependence of the deformation and localization behaviors are analyzed through simulation of a mildly notched tensile specimen as a representative inhomogeneous boundary value problem.

S. Prüger (✉) · B. Kiefer
Institute of Mechanics and Fluid Dynamics,
Technische Universität Bergakademie Freiberg, Lampadiusstrasse 4,
09596 Freiberg, Germany
e-mail: Stefan.Prueger@imfd.tu-freiberg.de

H. Biermann and C. G. Aneziris (eds.), *Austenitic TRIP/TWIP Steels and Steel-Zirconia Composites*, Springer Series in Materials Science 298,
https://doi.org/10.1007/978-3-030-42603-3_24

24.1 Introduction

During the past decades, new steel grades with improved mechanical properties, such as high strength and pronounced ductility, have been developed, mainly motivated by light-weight applications in the automotive industry, cf. [1–3]. The initially fully-austenitic steel, X3CrMnNi16-6-6, developed in the DFG Collaborative Research Center 799, clearly belongs to this group of advanced high-strength steels. Extensive mechanical and microstructural characterization, see [4–9] revealed that the mechanical properties can be attributed to the evolution of the microstructure during deformation, i.e. depending on temperature, stacking-fault energy and strain-rate, the face-centered cubic (fcc) austenite (γ) forms twins or stacking-faults with hexagonal close-packed structure (ε) or transforms to body-centered cubic (bcc) martensite (α'). In particular, the different deformation mechanisms can occur concurrently, as shown in Fig. 24.1, which renders the formulation of constitutive models at the macroscopic scale a challenging task, cf. [10–12]. Although such models are already quite complex, they rarely incorporate the effect of evolving anisotropy due to texture evolution, which is of great importance in forming simulations. Furthermore, the application of such models in structural simulations is naturally associated with a length scale, at which the characteristic sizes of the microstructure are small compared to other dimensions of the problem. Therefore, employing such models to predict the behavior of devices at the micrometer scale seems to be questionable. In contrast, crystal plasticity based modeling approaches can in principle account for these effects, however, an appropriate scale-transition law has to be incorporated to give reasonable predictions at macroscopic scale. Keeping in mind that the deformation behavior of the TRIP-steel under consideration is mainly influenced by interaction of the deformation mechanisms at multiple scales—ranging from interactions between grains to interactions of stacking-faults with martensitic inclusions within a single grain—a crystal plasticity based multi-scale modeling approach seems to be even more appropriate. Although the kinematic aspects of the different deformation mechanisms are reasonable well understood, their incorporation into conventional crystal plasticity models is a challenging subject of ongoing research, especially for TRIP-steels.

Aiming for a comprehensive description of the transformation behavior in low-alloyed TRIP-steels, a material model that incorporates the stress-assisted transformation from fcc austenite to body-centered tetragonal (bct) martensite under thermomechanical loading is proposed in [13], which also takes into account the twinned martensite microstructure. The influence of the initial crystal orientation on the mechanical and the transformation behavior under homogeneous deformation is studied in [14] for the two cases of a single austenitic grain and an austenitic grain embedded in a ferritic, elastic-plastic matrix, which is described by a phenomenological, isotropic J_2-plasticity model. In [15] the material model is extended to account for anisotropic plastic slip by means of a crystal plasticity model, which is employed both within the austenitic grains and in the ferritic matrix. A significant influence of the initial orientation of the austenitic grains—embedded in a single or oligocrystalline ferritic matrix—is found for macroscopically homogeneous deformation states.

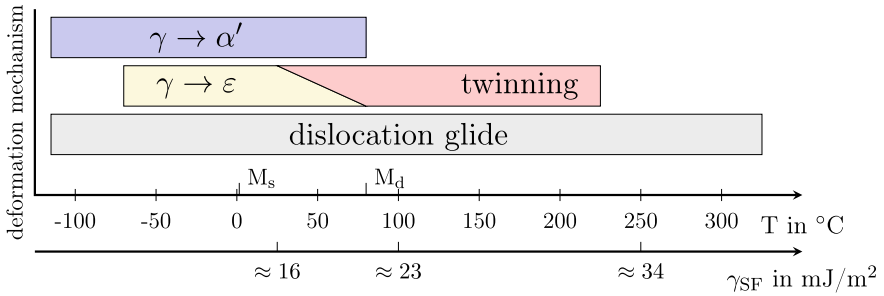

Fig. 24.1 Deformation mechanisms observed in the TRIP-steel X3CrMnNi16-6-6 as functions of temperature T or equivalently stacking-fault energy γ_{SF}. Data taken from [6]

Furthermore, in [16] this model is applied to the simulation of a representative volume element of a low-alloyed TRIP-steel with an idealized microstructure containing multiple austenite grains embedded in discretely resolved polycrystalline ferrite matrix under macroscopically homogeneous thermomechanical loading. Here the influence of the sequence of thermal and mechanical loading on the mechanical response and transformation behavior is investigated. The multi-scale character of the deformation and transformation behavior of low-alloyed TRIP-steels is accounted for in [17] by assuming an idealized lath martensite microstructure and combining the elastic-plastic material response of the two phases, austenite and martensite, with a criterion for the stress-assisted transformation and explicitly enforcing the compatibility and the stress equilibrium at their interfaces. In contrast to the models mentioned above, a single crystal material model for an initially fully-austenitic steel that shows a strain-induced transformation from fcc austenite to bcc martensite is considered in [18] and the transformation kinetics of Stringfellow [19] is applied at the single crystal scale and the evolution of deformation bands/bands of stacking-faults that act as nucleation sites for martensite is explicitly taken into account. Good agreement between numerical simulations and experimental results from uniaxial tensile tests for a wide range of strain rates is observed. A gradient extended crystal plasticity model that includes both stress-assisted and strain-induced austenite to martensite phase transformation is proposed in [20, 21] and is employed to study size effects in nanoindentation and in three-point bending tests and to investigate the influence of grain boundaries and twins in austenite grain on the transformation behavior. Consistent with thermodynamical considerations in [13, 14], a single crystal model that accounts for the stress-assisted austenite to martensite transformation is discussed in [22] and extended to include twinning [23]. Here again, the influence of the initial crystal orientation on the mechanical behavior under homogeneous deformations is considered. Increasing research activity in the field of high-manganese TWIP steels has led to the development of two single crystal material models [24, 25] that account for three different deformation mechanisms, namely slip, twinning and stacking-fault formation/ε-martensite formation. The latter model includes a dislocation density based hardening law, which is successfully calibrated based on quasi-static tensile

tests of a polycrystaline TWIP-steel together with the corresponding microstructure evolution in terms of ε-martensite and twin volume [26]. Rather recently, a single crystal plasticity model that incorporates the stress-assisted austenite to martensite transformation is applied to the prediction of polycrystalline response of two and three phase low-alloyed TRIP-steels and the corresponding forming limit diagrams [27]. Furthermore, the well-known transformation kinetics model of Olson-Cohen [28] is extended in [29] to account for the crystallographic nature of the formation of deformation bands/bands of stacking-faults. The kinetics law is then coupled to a crystal plasticity model to describe the strain-induced transformation from austenite to martensite. The comparison between numerical simulations and the results of polycrystalline experiments shows that the temperature and stress-state dependency of the mechanical response and the transformation behavior is well captured. For further information on the application of crystal plasticity models, the reader is referred to the comprehensive reviews [30–32].

Although the above literature review shows that numerous models have been proposed, which account for the coupling of two or three deformation mechanisms or the different nature of stress-assisted and strain-induced martensitic transformation, a material model that thoroughly captures all the deformation mechanisms mentioned in Fig. 24.1 and their transition over a wide range of temperatures still seems to be missing. In order to develop such a model—possessing a modular structure and being robust at the same time—a numerical framework has to be identified that allows for a robust and efficient implementation. While the above mentioned models are almost exclusively based on rate-dependent formulations, it is argued in [33] that such an approach may introduce an artificial rate-dependence into the model's response, if such a formulation is chosen only for numerical convenience and not due to experimental results. Hence, a systematic study regarding different numerical implementations has to be carried out to assess the efficiency and the robustness of the corresponding stress-update algorithms also considering different model complexity. The contribution at hand aims for such a study and will provide recommendations for appropriate algorithms both for rate-dependent and rate-independent formulations. Therefore, the choice of rate-dependence in the constitutive description of the different deformation mechanisms can solely be made based on experimental observations rather than numerics. The current study employs a single crystal plasticity model that is able to capture the deformation behavior of stable austenitic stainless steels as illustrated in [34]. Thus, an adequate description of the TRIP-steel X3CrMnNi16-6-6 at temperatures $T > 220$ °C is considered, where dislocation glide is the main deformation mechanism, see Fig. 24.1. This model will also form the basis for further model developments, eventually providing a modular constitutive description of the TRIP-steel under consideration. In order to enlighten the effect of rate-dependence on the constitutive response and the robustness of the corresponding stress update algorithms, the study comprises four different formulations and hardening laws of different complexity.

This contribution is structured as follows. The single crystal plasticity model is discussed in Sect. 24.2, while the comparison of the different formulations under homogeneous proportional and non-proportional loading histories is considered in

Sect. 24.3. In Sect. 24.4, a rate-independent formulation is employed to study the orientation dependence of the deformation and localization behavior of a mildly notched single crystal tensile specimen. Section 24.5 summarizes the main findings and outlines current and future research efforts on this topic.

24.2 Material Model

The constitutive behavior of face-centered cubic single crystals at finite deformations is described by a material model that builds on the approach proposed by Schmidt-Baldassari [35] in the rate-independent case and the formulation employed in [36–38] for the rate-dependent case. It is based on the multiplicative split of the deformation gradient into an elastic and a plastic part according to the proposal of Kröner [39] and Lee [40]

$$\mathbf{F} = \mathbf{F}^{\mathrm{e}} \cdot \mathbf{F}^{\mathrm{p}}. \tag{24.1}$$

In addition to this kinematic assumption, the intermediate configuration defined by such a split is taken as isoclinic as suggested in [41].

The elastic behavior, defined with respect to that intermediate configuration, is assumed to be governed by the isotropic, volumetric-isochorically decoupled free energy function of compressible Neo-Hooke type

$$\Psi^{\mathrm{e}} = \frac{1}{2}\kappa \left[\ln\left(J^{\mathrm{e}}\right)\right]^2 + \frac{1}{2}\mu \left[\overline{\mathbf{C}}^{\mathrm{e}} : \mathbf{I} - 3\right]. \tag{24.2}$$

Herein, J^{e} and $\overline{\mathbf{C}}^{\mathrm{e}}$ denote the determinant of the elastic part of the deformation gradient $\mathbf{F}^{\mathrm{e}}$ and the unimodular part of the elastic right Cauchy-Green tensor. The latter is obtained from the elastic Cauchy-Green tensor

$$\mathbf{C}^{\mathrm{e}} = \mathbf{F}^{\mathrm{eT}} \cdot \mathbf{F}^{\mathrm{e}} \tag{24.3}$$

via $\overline{\mathbf{C}}^{\mathrm{e}} = J^{\mathrm{e}-2/3}\mathbf{C}^{\mathrm{e}}$, while κ and μ are the bulk and shear moduli, respectively. The second Piola-Kirchhoff stress in the intermediate configuration $\widehat{\mathbf{S}}$ is defined as

$$\widehat{\mathbf{S}} = 2\,\frac{\partial \Psi^{\mathrm{e}}}{\partial \mathbf{C}^{\mathrm{e}}} \tag{24.4}$$

and specifically reads as

$$\widehat{\mathbf{S}} = J^{\mathrm{e}}\,\frac{\partial \Psi^{\mathrm{e}}_{\mathrm{vol}}}{\partial J^{\mathrm{e}}}\,\mathbf{C}^{\mathrm{e}-1} + 2\,\frac{\partial \Psi^{\mathrm{e}}_{\mathrm{iso}}}{\partial \mathbf{C}^{\mathrm{e}}} = \kappa \ln\left(J^{\mathrm{e}}\right)\mathbf{C}^{\mathrm{e}-1} + J^{\mathrm{e}-2/3}\mu\left[\mathbf{I} - \frac{1}{3}\,\mathrm{tr}\left(\mathbf{C}^{\mathrm{e}}\right)\mathbf{C}^{\mathrm{e}-1}\right] \tag{24.5}$$

for the elastic free energy density given in (24.2), cf. [42] for a detailed derivation. Furthermore, the Mandel stress tensor $\mathbf{M}$, which is also defined with respect to the

intermediate configuration, can be expressed as

$$\mathbf{M} = \mathbf{C}^{\mathrm{e}} \cdot \widehat{\mathbf{S}} = \left[\kappa \ln (J^{\mathrm{e}}) - \frac{1}{3} \mu \operatorname{tr} (\overline{\mathbf{C}}^{\mathrm{e}}) \right] \mathbf{I} + \mu \, \overline{\mathbf{C}}^{\mathrm{e}}. \tag{24.6}$$

The assumption of elastic isotropy is a reasonable approximation only for a few cubic metals, e.g. α-Tungsten, aluminum and vanadium [43], which are characterized by a Zener anisotropy index close to one [44]. This assumption is considered acceptable for the current contribution due to its simplicity. However, an extension of the material model to incorporate elastic anisotropy can be carried out by replacing the free energy density in (24.2) by the quadratic anisotropic free energy function discussed in [45], which is more suitable for moderately large elastic deformations. In contrast to the elastic behavior, the inelastic deformation of a single crystal is inherently anisotropic because it is governed by a finite number of distinct slip systems associated with the crystal lattice. For most face-centered cubic crystals it is reasonable to consider only the primary octahedral slip systems, consisting of $\{111\}$ slip planes and $\langle 110 \rangle$ slip directions, see Table 24.1. The inelastic slip on the different slip systems, γ_α, is linked to the plastic part of the deformation gradient and the plastic velocity gradient $\mathbf{L}^{\mathrm{p}}$ via the evolution equation

$$\mathbf{L}^{\mathrm{p}} = \dot{\mathbf{F}}^{\mathrm{p}} \cdot \mathbf{F}^{\mathrm{p}-1} = \sum_{\alpha=1}^{n} \dot{\gamma}_\alpha \, \mathbf{s}_\alpha \otimes \mathbf{n}_\alpha, \tag{24.7}$$

in which $\mathbf{s}_\alpha$ and $\mathbf{n}_\alpha$ denote the slip direction and the slip plane normal of the system α. In addition, these vectors are of unit length $|\mathbf{s}_\alpha| = |\mathbf{n}_\alpha| = 1$ and are mutually orthogonal $\mathbf{s}_\alpha \cdot \mathbf{n}_\alpha = 0$, where the latter property results in the inelastic part of the deformation gradient being isochoric. The onset of inelastic deformation on each slip system is described by limit surfaces of the form

$$\Phi_\alpha := \tau_\alpha - \left[\mathrm{Y}_0 + Y_\alpha(\varepsilon_\beta) \right]. \tag{24.8}$$

Herein, τ_α denotes the resolved shear stress on the slip system α and is computed as

$$\tau_\alpha = \mathbf{M} : [\, \mathbf{s}_\alpha \otimes \mathbf{n}_\alpha \,], \tag{24.9}$$

while Y_0 and Y_α respectively correspond to the initial yield stress and the driving force thermodynamically conjugate to the hardening variable ε_α. The driving force is consequently defined as

$$Y_\alpha := \frac{\partial \Psi^{\mathrm{p}}}{\partial \varepsilon_\alpha}, \tag{24.10}$$

where an additional split of the free energy due to elastic and inelastic effects has been assumed. In the current contribution, two different hardening functions are considered.

Table 24.1 Primary slip systems of a face-centered cubic single crystal

Miller indices	Schmid/Boas notation [46]	Slip plane normal	Slip direction
$(1,1,1)[1,\bar{1},0]$	B5	$\mathbf{n}_1 = \mathbf{n}_{13} = [1,1,1]/\sqrt{3}$	$\mathbf{s}_1 = -\mathbf{s}_{13} = [1,-1,0]/\sqrt{2}$
$(1,1,1)[1,0,\bar{1}]$	B4	$\mathbf{n}_2 = \mathbf{n}_{14} = [1,1,1]/\sqrt{3}$	$\mathbf{s}_2 = -\mathbf{s}_{14} = [1,0,-1]/\sqrt{2}$
$(1,1,1)[0,1,\bar{1}]$	B2	$\mathbf{n}_3 = \mathbf{n}_{15} = [1,1,1]/\sqrt{3}$	$\mathbf{s}_3 = -\mathbf{s}_{15} = [0,1,-1]/\sqrt{2}$
$(1,1,\bar{1})[1,\bar{1},0]$	C5	$\mathbf{n}_4 = \mathbf{n}_{16} = [1,1,-1]/\sqrt{3}$	$\mathbf{s}_4 = -\mathbf{s}_{16} = [1,-1,0]/\sqrt{2}$
$(1,1,\bar{1})[1,0,1]$	C3	$\mathbf{n}_5 = \mathbf{n}_{17} = [1,1,-1]/\sqrt{3}$	$\mathbf{s}_5 = -\mathbf{s}_{17} = [1,0,1]/\sqrt{2}$
$(1,1,\bar{1})[0,1,1]$	C1	$\mathbf{n}_6 = \mathbf{n}_{18} = [1,1,-1]/\sqrt{3}$	$\mathbf{s}_6 = -\mathbf{s}_{18} = [0,1,1]/\sqrt{2}$
$(1,\bar{1},1)[1,1,0]$	D6	$\mathbf{n}_7 = \mathbf{n}_{19} = [1,-1,1]/\sqrt{3}$	$\mathbf{s}_7 = -\mathbf{s}_{19} = [1,1,0]/\sqrt{2}$
$(1,\bar{1},1)[1,0,\bar{1}]$	D4	$\mathbf{n}_8 = \mathbf{n}_{20} = [1,-1,1]/\sqrt{3}$	$\mathbf{s}_8 = -\mathbf{s}_{20} = [1,0,-1]/\sqrt{2}$
$(1,\bar{1},1)[0,1,1]$	D1	$\mathbf{n}_9 = \mathbf{n}_{21} = [1,-1,1]/\sqrt{3}$	$\mathbf{s}_9 = -\mathbf{s}_{21} = [0,1,1]/\sqrt{2}$
$(\bar{1},1,1)[1,1,0]$	A6	$\mathbf{n}_{10} = \mathbf{n}_{22} = [-1,1,1]/\sqrt{3}$	$\mathbf{s}_{10} = -\mathbf{s}_{22} = [1,1,0]/\sqrt{2}$
$(\bar{1},1,1)[1,0,1]$	A3	$\mathbf{n}_{11} = \mathbf{n}_{23} = [-1,1,1]/\sqrt{3}$	$\mathbf{s}_{11} = -\mathbf{s}_{23} = [1,0,1]/\sqrt{2}$
$(\bar{1},1,1)[0,1,\bar{1}]$	A2	$\mathbf{n}_{12} = \mathbf{n}_{24} = [-1,1,1]/\sqrt{3}$	$\mathbf{s}_{12} = -\mathbf{s}_{24} = [0,1,-1]/\sqrt{2}$

Firstly, a purely phenomenological, Taylor-type hardening formulation of the form

$$Y_\alpha = \Delta \mathrm{Y}\left[1 - \exp\left(-\mathrm{h}A\right)\right] \tag{24.11}$$

is introduced, which incorporates the cumulative inelastic slip $A = \sum_\alpha \varepsilon_\alpha$ and is parameterized by the asymptotic increase in the yield stress ΔY as well as the dimensionless shape parameter h. It can be deduced from the inelastic part of the free energy function, i.e.

$$\Psi^{\mathrm{p,Taylor}} = \Delta \mathrm{Y}\left[A + \frac{1}{\mathrm{h}}\exp\left(-\mathrm{h}A\right)\right], \tag{24.12}$$

by means of (24.10). The application of the cumulative inelastic slip A in the hardening function (24.11) idealizes the interaction between different slip systems, but due to its simplicity, it has been extensively used to develop robust algorithmic frameworks for single crystal plasticity models [47–49].

Secondly, the alternative anisotropic hardening function

$$Y_\alpha = \Delta \mathrm{Y} \sum\nolimits_\beta \mathrm{h}^{\alpha\beta}\left[1 - \exp\left(-\mathrm{h}\varepsilon_\beta\right)\right], \tag{24.13}$$

proposed in [50], is considered, which introduces the symmetric interaction matrix $\mathrm{h}^{\alpha\beta}$ in a phenomenological manner. It allows for a more complex interaction of different slip systems and contains up to 6 material constants [46]. In the current contribution the structure of the interaction matrix is adopted from [51]. The energy corresponding to this type of hardening function is formulated as a quadratic form

$$\Psi^{\mathrm{p,GC}} = \frac{1}{2}\Delta \mathrm{Y}\mathrm{h} \sum\nolimits_\alpha s_\alpha \sum\nolimits_\beta \mathrm{h}^{\alpha\beta} s_\beta \tag{24.14}$$

in terms of the auxiliary variable s_α. The exponential type hardening is obtained from a non-associated evolution equation for s_α, which eventually leads to

$$s_\alpha = \frac{1}{\mathrm{h}} \left[1 - \exp\left(-\mathrm{h} \varepsilon_\alpha \right) \right]. \tag{24.15}$$

The driving force Y_α, introduced in (24.13), is obtained by taking the derivative of (24.14) with respect to s_α and the subsequent substitution of (24.15) to eliminate s_α from the resulting expression. Note that the hardening function (24.13) is exactly the one employed in the "GC model" in [36], which emanates from the small strain formulation presented in [50]. In order to close the system of equations evolution laws for the internal state variables have to be defined.

In the rate-independent formulation one obtains

$$\dot{\varepsilon}_\alpha = -\dot{\lambda}_\alpha \frac{\partial \Phi_\alpha}{\partial Y_\alpha} \tag{24.16}$$

for the hardening variables and for the inelastic velocity gradient

$$\mathbf{L}^{\mathrm{p}} = \sum_{\alpha=1}^{n} \dot{\lambda}_\alpha \frac{\partial \Phi_\alpha}{\partial \mathbf{M}} \tag{24.17}$$

from an associated formulation, which introduces the Lagrange multipliers $\dot{\lambda}_\alpha$, that are subject to the Karush-Kuhn-Tucker (KKT) conditions

$$\Phi_\alpha \leq 0 \quad \dot{\lambda}_\alpha \geq 0 \quad \dot{\lambda}_\alpha \Phi_\alpha = 0. \tag{24.18}$$

Considering the limit surface (24.8) and comparing the inelastic velocity gradient given in (24.17) with the evolution equation for the plastic part of the deformation gradient (24.7), one can readily identify

$$\dot{\gamma}_\alpha = \dot{\lambda}_\alpha \tag{24.19}$$

$$\dot{\varepsilon}_\alpha = \dot{\lambda}_\alpha \tag{24.20}$$

in the rate-independent case. In contrast to the commonly adopted, computational expensive active-set search algorithms to handle the inequalities in the KKT conditions, two different formulations of the rate-independent problem are considered here, which employ equality constraints only.

Firstly, the *augmented Lagrangian formulation*, initially proposed in connection with crystal plasticity in [35], is employed, which takes the principle of maximum plastic dissipation as starting point and reformulates the inequality constrained optimization problem into an equality constrained optimization problem by means of so-called slack variables [52, pp. 72, 158–164]. The Lagrange multipliers are then obtained from

$$\dot{\lambda}_\alpha = \max\left(0, \eta^* \Phi_\alpha\right), \tag{24.21}$$

in which the viscosity-like parameter η^* is introduced for purely numerical reasons, as it regularizes the problem, while the constraints are exactly enforced by means of the Lagrange multipliers.

Secondly, a formulation based on *nonlinear complementary functions* (NCP-functions) is considered. These functions have originally been proposed for constrained optimization problems, cf. [53]. A slightly more general form of NCP-functions is introduced by Kanzow and Kleinmichel in [54] and employed in the current contribution, which reads as

$$\sqrt{\left[\Phi_\alpha + \dot{\lambda}_\alpha\right]^2 - \Theta\, \Phi_\alpha \dot{\lambda}_\alpha} + \Phi_\alpha - \dot{\lambda}_\alpha = 0. \tag{24.22}$$

In particular, the parameter $\Theta = 0$ is chosen here and the Lagrange multipliers are obtained from (24.22) rather than from (24.18).

In the rate-dependent formulation, the KKT conditions in (24.18) are no longer applicable and the corresponding Lagrange multipliers are replaced by a potentially stress-dependent viscosity law v. This yields

$$\dot{\varepsilon}_\alpha = -v_\alpha(\tau_\alpha, Y_\alpha)\, \frac{\partial \Phi_\alpha}{\partial Y_\alpha} \tag{24.23}$$

and

$$\mathbf{L}^{\mathrm{vp}} = \sum_{\alpha=1}^{n} v_\alpha(\tau_\alpha, Y_\alpha)\, \frac{\partial \Phi_\alpha}{\partial \mathbf{M}}. \tag{24.24}$$

Assuming that an equation analogous to (24.7) holds for the viscoplastic part of the deformation gradient $\mathbf{F}^{\mathrm{vp}}$ in the context of a rate-dependent formulation, one may identify the general format for the evolution equations as

$$\dot{\gamma}_\alpha = v_\alpha(\tau_\alpha, Y_\alpha) \tag{24.25}$$

$$\dot{\varepsilon}_\alpha = v_\alpha(\tau_\alpha, Y_\alpha). \tag{24.26}$$

To study the influence of the type of viscosity law on the deformation behavior of single crystals — in particular in the rate-independent limit — this contribution considers two specific cases:

Firstly, the approach initially proposed by Perzyna [55] and extensively used in the groups of Cailletaud and Forest, cf. [36–38, 50, 51, 56–60], is considered, in which the viscosity law takes the form

$$v_\alpha^{\mathrm{PCF}} = \frac{1}{\eta} \left\langle \frac{\Phi_\alpha}{\mathrm{K}} \right\rangle^{\mathrm{n}}. \tag{24.27}$$

The positive material parameters K, n and η denote a stress-like scaling factor, the rate sensitivity exponent and a time-like parameter, respectively, where the inverse of the latter can be interpreted as a reference strain rate. The Macaulay brackets are defined as

$$\langle x \rangle = \begin{cases} x & \text{if } x > 0 \\ 0 & \text{else} \end{cases} \tag{24.28}$$

and are identical to the max-function, $m(x) = \max(0, x)$, and the ramp function, $r(x) = \frac{1}{2}(x + |x|)$.

Secondly, the viscosity law introduced by Cuitiño and Ortiz in [61] and employed for instance in Miehe's group, cf. [47–49], which specifically reads

$$v_\alpha^{\mathrm{OM}} = \frac{1}{\eta}\left[\left[\frac{\langle \Phi_\alpha \rangle}{\tau_\alpha^y(\varepsilon_\beta)} + 1\right]^{\mathrm{n}} - 1\right] \tag{24.29}$$

is also employed in the studies presented here. Note that the current slip resistance of the particular slip system α is denoted by τ_α^y and possesses the same functional dependency on the hardening variable ε_β as the quantity $\mathrm{Y}_0 + Y_\alpha(\varepsilon_\beta)$, but in (24.29) only Φ_α is explicitly dependent on both τ_α and Y_α. Therefore, the slip resistance τ_α^y is treated as history dependent normalization quantity, rather than an additional function of Y_α. This allows one to automatically guarantee thermodynamic consistency and enforce that the slip γ_α evolves identically to the hardening variables ε_α.

In order to carry out material point calculations and structural simulations, the different formulations of the rate-dependent and the rate-independent material models have been implemented into the scientific computing environment MATLAB and subsequently into the finite element program ABAQUS via the User-defined MATerial interface (UMAT). The evolution equations for the internal state variables are integrated by means of an implicit Euler backward scheme and a projection technique is employed to enforce the incompressibility constraint for the inelastic part of the deformation gradient. Details of the corresponding algorithms and the associated tangent operator can be found in [62].

24.3 Material Response Under Homogeneous Deformation

In this chapter, the material model described in Sect. 24.2 is employed in the simulation of a fully deformation-controlled simple shear test as well as a non-proportional tension/compression-shear cycle. The results obtained with the different formulations are illustrated in the subsequent sections.

24.3.1 Simple Shear Loading

Due to its simplicity, the fully deformation-controlled simple shear test is extensively used in the literature to assess the robustness of various stress-update algorithms for single crystal plastictiy, cf. [35, 47, 63–69]. For comparison, this test is also employed here, where the coefficients of the associated deformation gradient are prescribed as

$$[\mathbf{F}] = \begin{bmatrix} 1 & \gamma(t) & 0 \\ 0 & 1 & 0 \\ 0 & 0 & 1 \end{bmatrix}. \tag{24.30}$$

In particular, the simple shear motion, introduced in [63] is considered, in which the crystal lattice is misaligned with respect to the global coordinate axes and is characterized by the following orientation in terms of Euler angles $\{\varphi_1, \Phi, \varphi_2\} = \{0°, 18.4349°, 0°\}$ in Bunge notation [70], i.e. a sequential rotation about the z-, x- and z-axes is considered. The material parameters employed in the simulation correspond to an ideal plastic behavior at the scale of the slip system and are specified in Table 24.2. Therefore, any effective hardening or softening observed in the subsequently shown stress-strain diagrams is attributed to the reorientation of the crystal lattice, which approaches a stable orientation for large shear γ, asymptotically leading to a constant shear stress. Additionally, the rate-dependent material response is characterized by the rate exponent n = 20 for the OM-viscosity function (24.29), while for the PCF-viscosity function (24.27) parameters are set to n = 10 and K = 10^{-3} GPa, consistent with the experimentally observed range of rate-sensitivity exponents [71]. The influence of the chosen increment size $\Delta\gamma$ on the stress-strain curve is depicted in Fig. 24.2. In the rate-independent formulation, the augmented Lagrangian algorithm takes 15, 60 and 600 steps to reach the final shear amplitude $\gamma = 6$, while the Kanzow NCP-function respectively requires 100, 600, 1200 and 1800 steps. It can be seen that both formulations converge to the same material response for the smallest increment size. The augmented Lagrangian formulation reproduces the characteristic features of the stress-strain curve even for very large shear increments and the stress response converges monotonically as the shear increment is refined. In contrast, the formulation based on the Kanzow NCP-function requires significantly smaller shear increments to ensure the numerical convergence of the Newton-type algorithm. But even though the numerical convergence is achieved, the simulated stress-strain curve is very sensitive to the chosen increment size, in particular in the strain range $2 \leq \gamma \leq 6$. Herein, the constitutive response converges to the results of the augmented Lagrangian formulation with decreasing shear increment size in a non-monotonic manner. Although not shown in Fig. 24.2a, the same observations

Table 24.2 Material parameters for finite strain, simple shear loading

κ in GPa	μ in GPa	Y_0 in GPa	ΔY in GPa	h	η in s
49.98	21.1	0.06	0.0	0.0	50.0

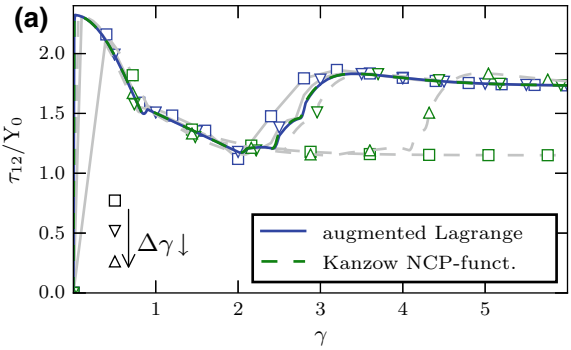

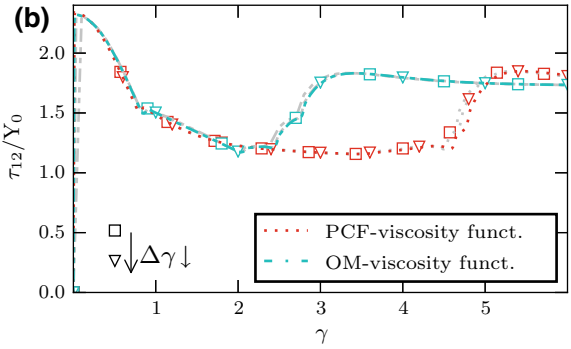

Fig. 24.2 Influence of the shear increment size $\Delta\gamma$ on simulated stress-strain curves for finite strain, simple shear loading, **a** rate-independent and **b** rate-dependent formulations. Gray lines with symbols indicate the stress response for different shear increment sizes, while colored lines correspond to the stress response obtained with the smallest shear increment size

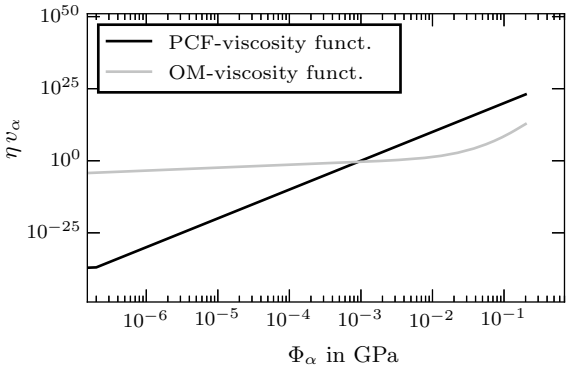

Fig. 24.3 Normalized viscosity functions for viscous parameters adopted in the simple shear test

have been made for the original Fischer-Burmeister NCP-function, which is recovered by the choice $\Theta = 2$ in (24.22).

In the rate-dependent formulation, the stress-strain curve under quasi-static loading condition, $\dot{\gamma} = 10^{-5}\mathrm{s}^{-1}$, is determined in 60, 180 and 600 steps for the OM-viscosity function and in 420, 600 and 1800 steps for the PCF-viscosity function. Figure 24.2b shows that apart from small deviations, which are due to the different viscosity functions and viscous parameters employed, the stress-strain curves feature the same behavior up to $\gamma \approx 2.3$. For larger shear strains however, a significant differ-

ence in the computed stress response is observed. While the OM-formulation leads to a stress-strain curve possessing the same characteristics as the rate-independent case, the PCF-formulation yields a stress response for which the transition to higher stress levels is significantly delayed. The working hypothesis explaining this observation is that small differences in the evolution of the plastic slip γ_α determined from the PCF- and OM-viscosity functions accumulate and that such an accumulation eventually leads to sudden deviation in the stress response at $\gamma \approx 2.3$. The presence of small differences between the different rate-dependent formulations is clearly visible from the comparison of the normalized viscosity functions (24.27) and (24.29), as illustrated in Fig. 24.3. In order to check the hypothesis, a sensitiv-

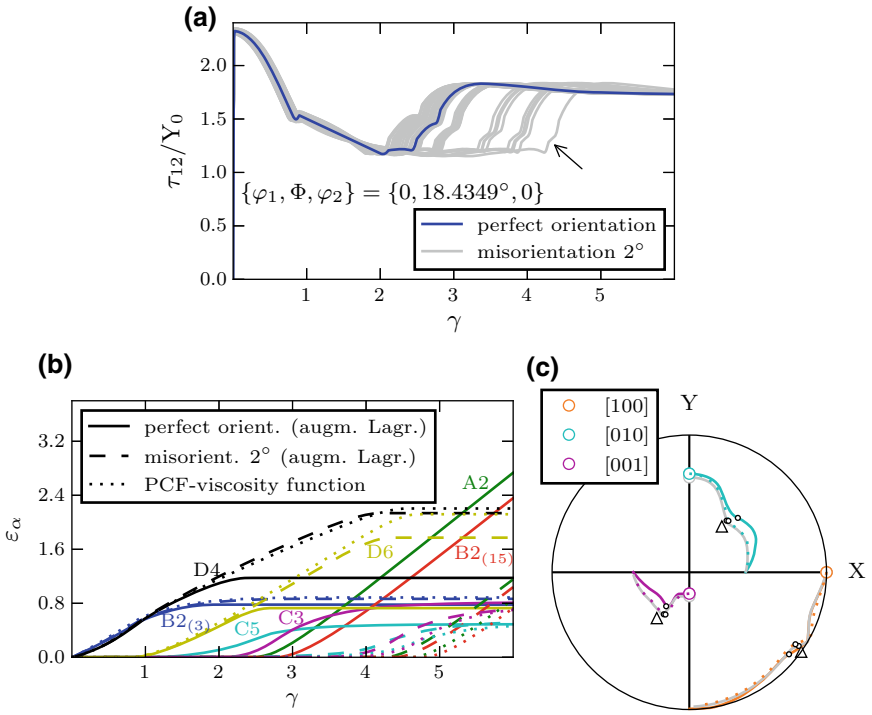

Fig. 24.4 Influence of an initial misorientation on: **a** the normalized stress-strain curve, **b** the evolution of the hardening variables and **c** the reorientation of the ⟨100⟩ directions in the pole figure employing a stereographic projection for finite strain, simple shear loading. The gray lines in **a** denote different realizations of perturbed initial orientations possessing a misorientation of 2°, while the arrow indicates the specific orientation for which the evolution of ε_α and the reorientation behavior are shown in (**b**) and (**c**), respectively.The labels of the different slip systems employed in **b** is consistent with Table 24.1. Note that, in **c** colored and gray solid lines represent the response of the augmented Lagrangian formulation for a perfectly oriented and a misaligned crystal, while the dotted lines correspond to the results of the rate-dependent PCF-formulation for a perfectly oriented crystal. Additionally, small black circles indicate the orientation at $\gamma = 2.0$, while the triangles denote a stable crystallographic orientation

ity analysis is performed, in which the influence of a small initial misorientation (2°) on the stress-strain curve is investigated. The simulations are carried out by means of the augmented Lagrangian formulation of the rate-independent material model and the shear component γ is incremented in 600 equidistant steps. The corresponding results are shown in Fig. 24.4a. It can be seen that the initial part of the stress-strain curve is rather nonsensitive to the perturbation of the initial orientation and that the initial misorientation strongly affects the stress-strain curve only in the range $2 \leq \gamma \leq 4.5$, which is consistent with the scatter observed in Fig. 24.2 for the different step sizes and formulations. Observing that small differences in the initial conditions lead to considerable deviations in the stress response indicates a stability problem, in particular a bifurcation. However, it is not caused by the Taylor ambiguity problem [72], where several combinations of plastic slip variables exist that lead to the same stress state. This is because, as shown in the literature, both the rate-independent augmented Lagrangian formulation as well as the rate-dependent formulations yield unique solutions for the slip system selection and the corresponding rates [67, 72] and thus the Taylor ambiguity problem is avoided. Conducting a systematic variation of the initial orientation according to $\phi_1 = \phi_2 = 0°$ and $\Phi \in [0°, 45°]$ reveals that the stability issue mentioned above is related to the discrete nature of the plastic flow of the single crystal. In fact choosing initial orientations in the range $\Phi \in [22.5°, 45°]$ asymptotically leads the reorientation of the crystal towards the stable orientation indicated by triangles in Fig. 24.4c. In the narrow range $\Phi \in [17°, 22°]$ the crystal approaches a different stable orientation, while for $\Phi \in [0°, 16°]$ a constant rotation of the crystal lattice is predicted by the material model. As the initial orientation $\{\varphi_1, \Phi, \varphi_2\} = \{0°, 18.4349°, 0°\}$ and the perturbed initial orientations considered are very close to the boundary of the two ranges of Φ, the sensitivity of the stress response to small perturbations is not surprising. It is therefore concluded that small initial misorientations or the accumulation of small differences in the evolution of the plastic slip variables in the rate-dependent case are responsible for selection of slip systems made by the corresponding algorithms. In addition to the stress-strain response, Fig. 24.4b illustrates the evolution of the hardening variables for three different cases. In particular, a rate-independent, perfectly oriented crystal as well as a rate-independent crystal with a specific misorientation of 2°, indicated by an arrow in Fig. 24.4a and a rate-dependent, perfectly oriented crystal based on the PCF-formulation is considered. Note that the slip systems, which are active only in the range $0 \leq \gamma \leq 1$ and overall show a low activity, i.e. $\varepsilon_\alpha < 0.35$, are not shown for the sake of clarity. Comparing the pattern of activation and deactivation of the slip systems of the perfectly oriented and the misaligned crystal, it is obvious that the initial misorientation delays the deactivation of the slip systems D4 and D6 as well as the activation of the systems C3, C5, A2 and $B2_{(15)}$, where the latter corresponds to slip system 15 in Table 24.1. This delay is responsible for the postponed transition to the orientation $\{\varphi_1, \Phi, \varphi_2\} = \{90°, 45°, 0°\}$, for which a constant yield stress and no rotation of the crystal is observed [63]. Furthermore, it is observed that the pattern of activation and deactivation of the slip systems computed for the perfectly oriented, rate-dependent crystal is similar to the pattern obtained for the misaligned, rate-independent crystal. This indicates that the slip γ_α deter-

mined via the rate-dependent formulation causes a small misalignment of the crystal compared to the results of the rate-independent response of the perfectly oriented crystal employing the augmented Lagrangian formulation, as shown in Fig. 24.4c. This leads to a different reorientation of the ⟨100⟩ directions and a delayed transition towards the orientation $\{\varphi_1, \Phi, \varphi_2\} = \{90°, 45°, 0°\}$. These observations therefore support the hypothesis introduced above and give an explanation for the differences in the stress response presented in Fig. 24.2.

Technically, the misorientation $\Delta\mathbf{R}$ is incorporated by means of the Euler-Rodrigues formula

$$\Delta\mathbf{R} = \mathbf{I} + [1 - \cos(\alpha)] + \sin(\alpha)\,\mathbf{A} \quad \text{with} \quad \mathbf{A} = -\boldsymbol{\epsilon} \cdot \mathbf{a}, \tag{24.31}$$

where $\boldsymbol{\epsilon}$ is the Levi-Civita tensor, while $\mathbf{a}$ denotes the rotation axis and α the corresponding angle. The misorientations employed in this section are generated by taking the rotation axis according to the 42 equally spaced points on the unit sphere [73] and the rotation angle $\alpha = 2°$. The initial orientation of the crystal with a predefined misorientation $\mathbf{R}^*$ is then obtained, according to [74, p. 68] from

$$\Delta\mathbf{R} = \mathbf{R}^* \cdot \mathbf{R}^{-1}, \tag{24.32}$$

in which $\mathbf{R}$ is the unperturbed initial orientation.

24.3.2 *Non-proportional Tension/compression-Shear Loading*

While the fully deformation-controlled simple shear test provided valuable insight into the robustness of the different formulations in the ideal plastic case, the capabilities of the different formulations in the hardening case are assessed now under complex loading conditions employing a non-proportional load cycle, similar to the one proposed in [38]. It corresponds to a uniaxial tension/compression loading combined with a simple shear loading and approximately mimics the deformation path observed in the dual actuator loading system described in [75] or a thin-walled tubular specimen in a tension-torsion testing device [76]. The temporal change of the coefficients of the deformation gradient tensor associated with this so-called *butterfly* test are prescribed according to

$$[\mathbf{F}] = \begin{bmatrix} * & F_{12}(t) & * \\ 0 & F_{22}(t) & * \\ * & * & * \end{bmatrix} \tag{24.33}$$

and are illustrated in Fig. 24.5a. The remaining coefficients, indicated by $*$, are determined by an iterative procedure, the *c*onstitutive driver, described in [77, 78] that enforces the associated components of the first Piola-Kirchhoff stress to vanish, see

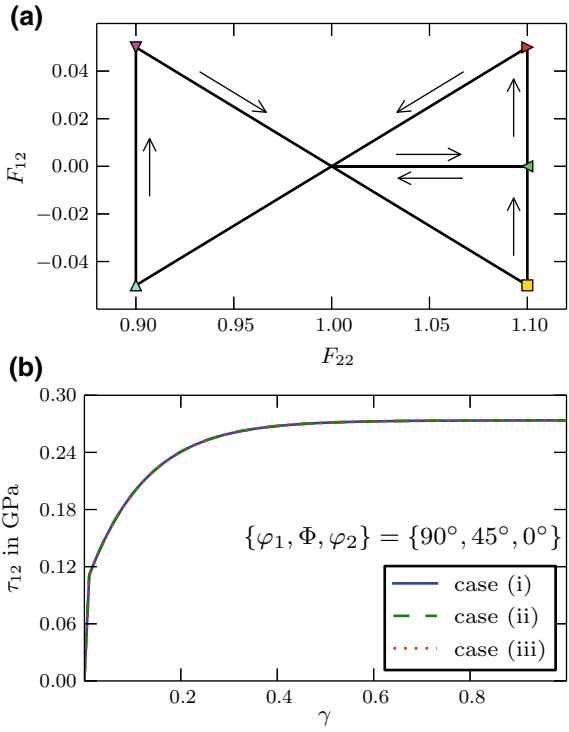

Fig. 24.5 **a** Biaxial, non-proportional deformation path in the butterfly test and **b** stress-strain curve for simple shear loading considering different interaction matrices, indicated by case (i),(ii) and (iii), see Table 24.3

also [79, p. 562f] for a spatial formulation. Furthermore, this procedure is enhanced by an adaptive time-stepping algorithm to allow for a step size adjustment of the prescribed components F_{12} and F_{22} based on the convergence behavior.

Recall that the degree of anisotropy in the hardening behavior of the single crystal material model depends on the choice of the interaction matrix in the hardening law, given in (24.13). Since its coefficients can be estimated from non-proportional tests involving strain path changes, cf. [80], it is interesting to study the influence of the interaction matrix on the performance of the different formulations in case of the butterfly test. Therefore, the initial orientation of the crystal is taken as $\{\varphi_1, \Phi, \varphi_2\} = \{0°, 0°, 0°\}$, i.e. the crystal axes are aligned with the axes of the global coordinate system and the hardening parameters are chosen according to Table 24.3, while the remaining parameters are taken from Table 24.2. The coefficients of the interaction matrix are adopted from the literature without modifications, while the hardening parameters ΔY are rescaled in the cases (ii) and (iii). This rescaling is necessary in order to solely study the effect of the deviation of the interaction matrix from the Taylor-type hardening case, because according to (24.13) keeping the parameter ΔY constant would result in considerably different hardening rates. Therefore, the hardening parameters ΔY are adjusted in such a manner that the stress-strain curves coincide under simple shear loading for the arbitrarily chosen orientation $\{\varphi_1, \Phi, \varphi_2\} = \{90°, 45°, 0°\}$, see Fig. 24.5b.

Table 24.3 Hardening parameters employed in the comparative study under finite deformation tension/compression-shear loading

case	Y_0 in GPa	ΔY in GPa	h	h_0	h_1	h_2	h_3	h_4	h_5	References
(i)	0.06	0.049	10	1.0	1.0	1.0	1.0	1.0	1.0	–
(ii)	0.06	0.04083	10	1.0	1.4	1.4	1.4	1.4	1.4	[58]
(iii)	0.06	0.01704	10	1.0	4.4	4.75	4.75	4.75	5.0	[37]

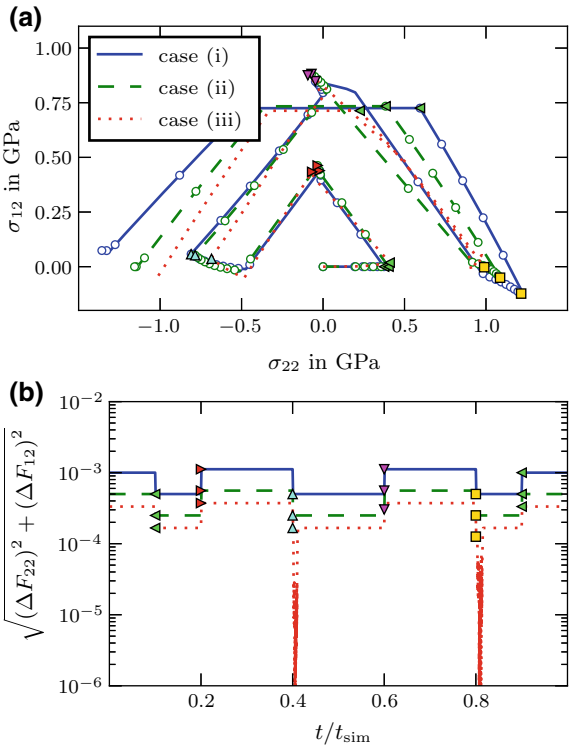

Fig. 24.6 Influence of the interaction matrix on: **a** the stress path in the butterfly test for different numbers of increments and **b** the norm of the prescribed deformation increment for the rate-independent, augmented Lagrangian formulation. The three different interaction matrices are indicated by case (i), (ii) and (iii), in agreement with Table 24.3. The filled symbols denote changes in the deformation path consistent with Fig. 24.5a

The calibrated material model is used to simulate the stress response to the non-proportional deformation path illustrated in Fig. 24.5a employing the rate-independent, augmented Lagrangian formulation and the rate-dependent formulation based on the OM-viscosity function, because both formulations proved robust and yielded consistent results in the fully deformation-controlled test conducted in Sect. 24.3.1. For the rate-independent formulation, the computed stress path is illustrated in Fig. 24.6a, in which the reference simulations, depicted with colored lines, required 1000, 2000 and 4500 increments for the different interaction matrices in cases (i), (ii) and (iii), respectively. Furthermore, white circles denote simulation results obtained with coarser increment sizes in the cases (i) and (ii), in which 50 and 1500 increments were employed, still yielding sufficiently accurate predictions of

the stress path. It is clearly visible from Fig. 24.6a that the interaction matrix significantly influences the stress response, especially at the latter stages of the deformation path, suggesting that the material parameters entering the interaction matrix could in principle be identified from such a non-proportional test.

Besides this observation, the choice of interaction matrix also significantly influences the performance of the augmented Lagrangian formulation in conjunction with the constitutive driver. In particular, while a rather coarse incrementation can be chosen in case (i), i.e. an interaction matrix corresponding to Taylor-type hardening is employed, the beneficial robustness of the formulation is diminished in case of the two-parameter interaction matrix (ii) and especially in case of the four-parameter interaction matrix (iii), at least if the same accuracy as in the reference simulation is sought. This aspect is also illustrated in Fig. 24.6b, which shows the evolution of the norm of prescribed deformation gradient components for the reference simulations. While no adaptive adjustment of the increment size is necessary in cases (i) and (ii), it is worth noting that at least one and a half times the number of increments are required in case (ii) compared to the reference simulation with Taylor-type hardening (i) to obtain a stress response independent of the chosen step size. In case (iii), an adaptive adjustment of the increment size is even necessary, particularly at the change in the deformation path from the combined tension/compression-shear loading to only shear loading in order to ensure convergence of the constitutive driver, yielding increment sizes below 10^{-6}. Thus, although the augmented Lagrangian formulation proved very robust in a fully deformation-controlled test in the absence of hardening, similar results cannot be obtained in situations where the hardening is anisotropic. This is due to the inclusion of interaction matrices other than the one corresponding to Taylor-type hardening and in particular in situations that involve iterative procedures to ensure stress-free conditions in certain directions. This is not surprising, because interaction matrices not associated with Taylor-type hardening allow for a change of the shape of the elastic domain and not only its size, which confronts the corresponding stress-update algorithm with a significantly more difficult task.

Furthermore, the rate-dependent formulation based on the OM-viscosity function is now employed in the simulation of the non-proportional tension/compression-shear cycle, where the deformation gradient coefficients are prescribed at $\dot{F}_{22} = 10^{-2}\,\mathrm{s}^{-1}$ and $\dot{F}_{12} = 5 \times 10^{-3}\,\mathrm{s}^{-1}$, respectively. The computed stress path is illustrated in Fig. 24.7a. Again, reference solutions are indicated by colored lines. Here, they were respectively obtained with 1000, 2000 and 3300 increments for the three different interaction matrices. In the cases (i) and (ii), additional simulations have been carried out with a coarser incrementation, employing 800 and 1000 increments. The corresponding results are again depicted with white circles. For these two cases, only minor differences are observed compared to the rate-independent results and the deviations can be attributed to the chosen viscosity parameters and the moderate loading rate. Note that the stress-update algorithm corresponding to the rate-dependent OM-formulation allows for a further reduction of the number of increments in case (i) and (ii), but this results in a significant loss of accuracy in the predicted stress path.

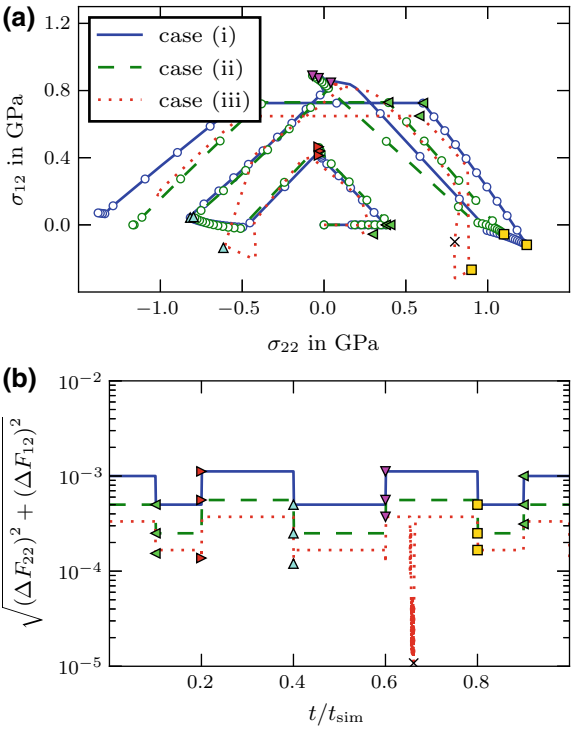

Fig. 24.7 Influence of the interaction matrix on: **a** the stress path in the butterfly test for different numbers of increments and **b** the norm of the prescribed deformation increment for the rate-dependent formulation based on the OM-viscosity function. The three different interaction matrices are indicated by case (i), (ii) and (iii), in agreement with Table 24.3. The filled symbols denote changes in the deformation path consistent with Fig. 24.5a

In case (iii), associated with the four-parameter interaction matrix, the stress path predicted by the rate-dependent formulation differs significantly from the results of the rate-independent formulation. A noticeable difference is already observed in the first part of the loading cycle, corresponding to a constrained uniaxial tensile loading, in which $F_{12} = F_{21} = 0$. Here, non-zero shear stresses σ_{12} of considerably different magnitude develop for both the rate-dependent and rate-independent formulation, as depicted in Fig. 24.8b. These stresses can be attributed to the above mentioned constraint in combination with the activation of the slip systems given in Table 24.4. While the four-parameter interaction matrix provokes the activation of five slip systems in the rate-independent formulation, eight slip systems are active in the rate-dependent formulation, as shown in Fig. 24.8a. Note that for the latter the eight hardening variables ε_α do not evolve identically. On the contrary, the simulations conducted with the interaction matrices (i) and (ii), identical slip along the same set of active systems is determined. Thus, the high-symmetry of the initial orientation is preserved during the first part of the loading cycle and the constraint is automatically fulfilled.

Comparing the complete stress paths obtained for the rate-dependent and the rate-independent formulations in case of the interaction matrix (iii) once again, it becomes apparent that the different slip activity during the initial stage of the non-proportional

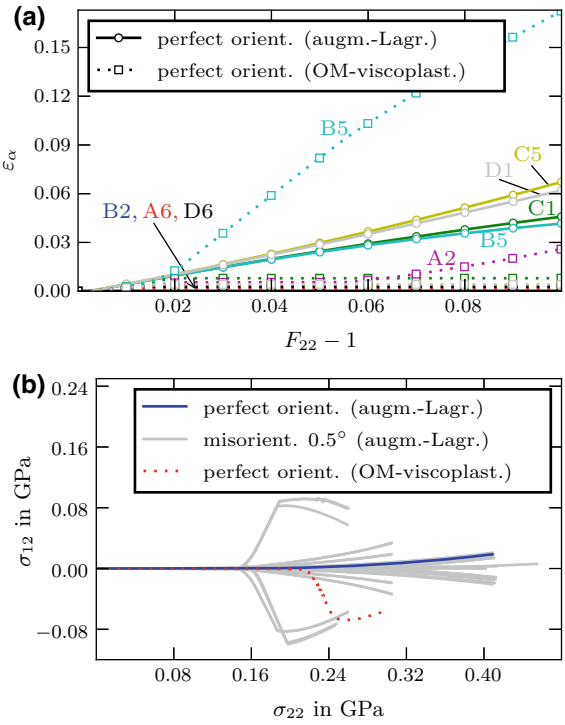

Fig. 24.8 **a** Evolution of the hardening variables under constrained uniaxial tension, **b** influence of initial misorientation on stress path under constrained uniaxial tension during the initial stage of the non-proportional deformation path

Table 24.4 Hardening variables ε_α at $F_{22} = 1.1$ in constrained uniaxial tension during the initial stage of the non-proportional loading

	B2	C1	A6	A2	B5	C5	D6	D1
augm.-Lagr.	–	0.04587	–	–	0.04160	0.06728	9.8×10^{-6}	0.06205
OM-viscoplast.	0.00155	0.00797	0.00154	0.02586	0.17239	0.00369	0.00285	0.00419

test results in a more complex stress path for the rate-dependent formulation. This observation is also reflected in a different history of the prescribed deformation increments shown in Fig. 24.7b, which is obtained by the adaptive procedure mentioned above. However, the sudden decrease in the increment size, indicated by a black cross in Fig. 24.7a, b, is not linked to any sharp change in the stress path. It is rather caused by rapidly changing shear components of the deformation gradient, determined from corresponding zero stress condition, to allow for a constant slip activity.

Similar to the approach employed in Sect. 24.3.1, a sensitivity analysis is conducted to investigate the deviation of the stress paths during the initial constrained uniaxial tensile loading. To this end, the initial orientation is perturbed employing (24.31) and (24.32) and choosing $\alpha = 0.5°$. A wide range of stress paths is obtained for selected perturbed initial orientations employing the rate-independent augmented Lagrangian formulation. The corresponding results are illustrated in

Fig. 24.8b together with the uniaxial stress path of the perfectly oriented single crystal simulated employing the rate-dependent OM-viscosity function. The striking similarity in the results of the two formulations is the sudden change of the shear stress σ_{12}, which is observed immediately at the initiation of plastic flow in the rate-independent formulation for some perturbed initial orientations. In the rate-dependent result however this sudden deviation from uniaxial tension is shifted to higher stresses.

Due to the fact, that the loading axis is aligned with a direction of high symmetry for the perfect cube orientation $\{\varphi_1, \Phi, \varphi_2\} = \{0°, 0°, 0°\}$—yielding up to eight potentially active slip systems—the stress response obtained either experimentally or from numerical simulations is rather sensitive to small misorientations [61, 68]. As mentioned above the interaction matrix in case (iii) initially provokes the activation of this set of eight slip systems associated with the high symmetry orientation in the rate-dependent formulation (see Fig. 24.8a and Table 24.4). However, at an uniaxial stretch $F_{22} \approx 1.02$, several slip systems are deactivated and concentrated slip on system B5 is observed, which accompanies the sudden change in the shear stress σ_{12} in the response of the rate-dependent model.

The strong sensitivity of the actual stress path to small initial misorientations, illustrated in Fig. 24.8b, indicates an unstable orientation, which is also supported by two results found in the literature. Firstly, the combinatorial search conducted in [67] for a single crystal—with an anisotropic hardening law (based on a six-parameter interaction matrix)—under incompressible, uniaxial tension loading in cube orientation revealed that there exist three different slip system solutions. One corresponds to the activation of eight systems, while the other two only activate four systems. This is consistent with the results presented in [72], where it was also found that the Taylor ambiguity problem occurs if anisotropic hardening is included in the model for fcc single crystals. Secondly, it has been reported in [72] that the value of the rate-sensitivity exponent influences the stability of a crystallographic orientation. In particular, crystallographic orientations which are stable in simulations carried out by rate-independent formulations can become unstable in the corresponding rate-dependent formulation, if the viscous parameters are not chosen such that they are able to recover the rate-independent limit. The choice of viscous parameters and the Taylor ambiguity problem are therefore regarded as the key factors for the significant deviations in the stress path and slip activity obtained by the rate-independent and rate-dependent formulations. The large difference in the plastic slip activity may also be amplified due to application of the iterative procedure to determine the non-zero shear components of deformation gradient, which eventually leads to an unsymmetric plastic slip. The initial variation in stress path clearly has an influence on the subsequent evolution of the stress along the remaining non-proportional deformation path. Thus, it cannot be expected that the stress path obtained by the rate-dependent formulation in Fig. 24.7 returns to the one of the augmented Lagrangian formulation in Fig. 24.6 for the interaction matrix employed in case (iii).

24.4 Constrained Tension Test

To further illustrate the robustness of the rate-independent, augmented Lagrangian formulation, it is tested within the finite element solution of a spatially inhomogeneous finite deformation boundary value problem. In particular, a constrained tension test is simulated employing a tensile specimen with a geometrical imperfection. The corresponding dimensions are given in Fig. 24.9, where the imperfection is introduced in terms of two symmetrical notches reducing the width of the specimen at its center to 90% of the original width. Along the lower edge of the specimen the displacement in 2-direction is fixed, while at the upper edge a proportionally increasing displacement is homogeneously prescribed. Additionally, the influence of two different types of boundary conditions is studied. Firstly, a clamped condition, in which the displacement in 1-direction $u_1 = 0$ is prescribed at both edges and secondly, a free lateral contraction condition, for which the displacement in 1-direction $u_1 = 0$ is only enforced at points A and B in Fig. 24.9, is considered. In either case, the displacement in 3-direction is also fixed for the entire specimen. The geometry of the specimen is discretized with 400 three-dimensional linear hexahedral elements, denoted as C3D8 according to ABAQUS conventions. The material model outlined in Sect. 24.2 with Taylor-type hardening, (24.11), is employed in the simulation. The corresponding material parameters are given in Table 24.5. With this model at hand, the influence of the initial orientation of the crystal on the force displacement curve is studied first. Therefore, four different initial orientations with respect to loading axis, namely $\{\varphi_1, \Phi, \varphi_2\} = \{30°, 45°, 0°\}$; $\{0°, 0°, 0°\}$; $\{0°, 45°, 30°\}$ and $\{289°, 163.6°, 42.5°\}$ are chosen, where the Schmid factor m of the most favor-

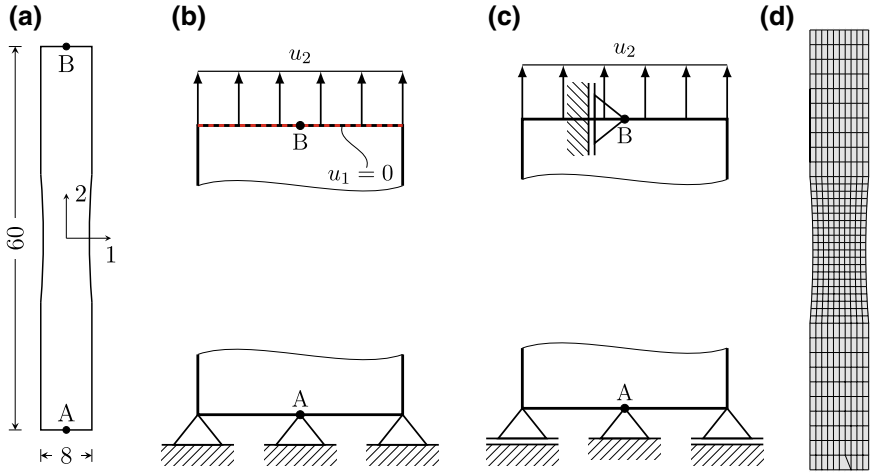

Fig. 24.9 **a** Geometry of a mildly notched tensile specimen of unit thickness with a notch radius of 125 mm and an initial reduction the of specimen width to 90%, **b** clamped and **c** free contraction boundary conditions, **d** finite element mesh

Table 24.5 Material parameters employed in the constrained tension test

κ in GPa	μ in GPa	Y_0 in GPa	ΔY in GPa	h
49.98	21.1	0.06	0.049	10

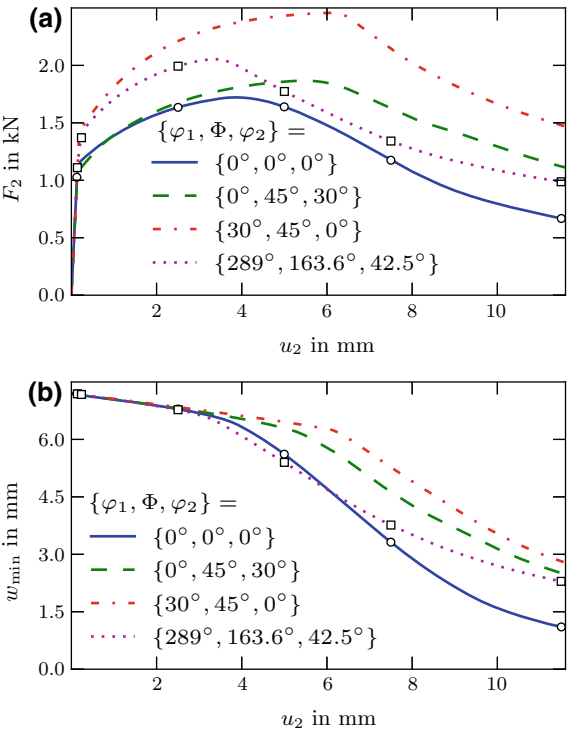

Fig. 24.10 Influence of the initial orientation on the overall force-displacement curve (**a**) and the minimal width $w_{\min}$ of the specimen measured in 1-direction (**b**). Symbols indicate the deformation at which field distributions of the logarithmic strain LE_{22} are shown in Fig. 24.12

ably orientated slip systems take the values of $m = 0.3291$; $m = 0.4082$; $m = 0.4183$; $m = 0.5$, respectively, if the crystal is deformed under homogeneous uniaxial tension. Consistent with the Schmid factors, the orientation $\{30°, 45°, 0°\}$ requires the highest force to activate the plastic flow, as shown in Fig. 24.10a. For the orientation $\{289°, 163.6°, 42.5°\}$, a considerably lower force is required at initial yield, but the plastic flow is accompanied by strong initial hardening, leading to almost the same force level as the former orientation (Fig. 24.10a).

Besides the influence of the initial orientation on the initial yield and the hardening behavior, the onset of necking and localization of the deformation is also strongly affected by the choice of initial orientation. While the force-displacement curves for the orientations $\{0°, 0°, 0°\}$ and $\{0°, 45°, 30°\}$ show a rather smooth transition to the geometrically-induced softening, more rapid drops in the applied force are observed for the other two orientations. A similar trend is observed for the respective minimal width of the specimen $w_{\min}$ measured in 1-direction, shown in Fig. 24.10b, where

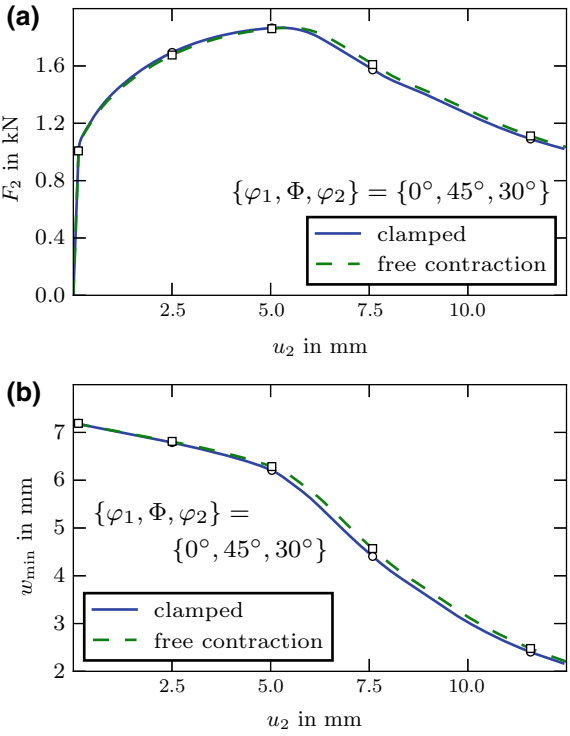

Fig. 24.11 Influence of the boundary conditions on the overall force-displacement curve (**a**) and the minimal width $w_{\min}$ of the specimen measured in 1-direction (**b**). Symbols indicate the deformation at which field distributions of the logarithmic strain LE_{22} are shown in Fig. 24.13

the former two orientations continuously deviate from the initially linear relation between $w_{\min}$ and u_2, while especially the orientation $\{30°, 45°, 0°\}$ is characterized by a sudden change in the specimen width. In each case, the deformation at which the deviation from this linear relation occurs, does not coincide with the maximum applied force, but happens, as expected, at considerably smaller deformations. The deformed specimen geometry and the spatial distribution of the logarithmic strain in longitudinal direction, i.e. (LE_{22}) are illustrated in Fig. 24.12, where the latter is computed from

$$\mathrm{LE} = \frac{1}{2} \ln \left(\mathbf{F} \cdot \mathbf{F}^{\mathrm{T}} \right). \tag{24.34}$$

The evolution of the strain fields further confirms the important influence of the initial orientation on the mode of localization (symmetric/unsymmetric). In case of the highly symmetric crystal orientation, $\{0°, 0°, 0°\}$, the strain field is symmetric even during necking. The location, at which the highest strain is observed, is shifted rapidly from the notch surface, for the elastic solution, shown on the left in the top row of Fig. 24.12, to the center of the specimen during elastic-plastic loading. In contrast, the strain field of the initial orientation $\{289°, 163.6°, 42.5°\}$ shows a smooth transition at the initiation of plastic deformation. While during the initial stages of elastic-plastic loading a rather large volume experiences pronounced deformation,

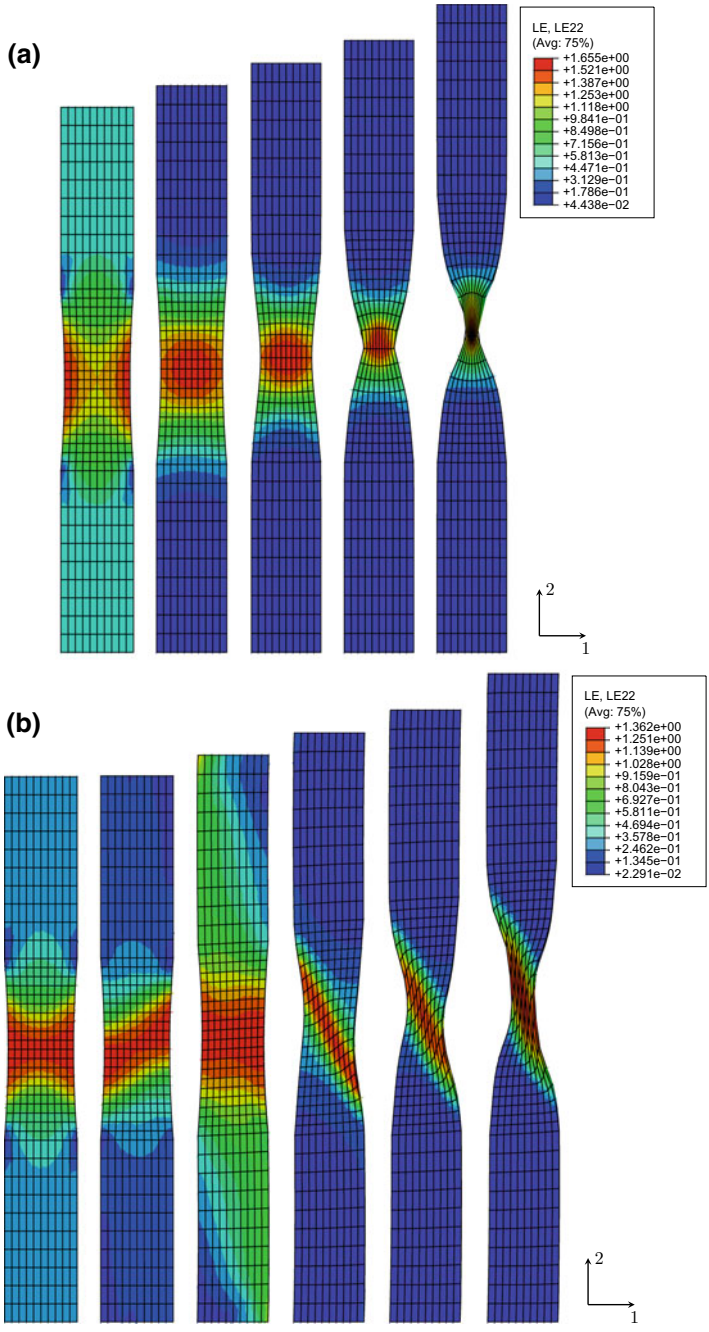

Fig. 24.12 Influence of the initial crystal orientation on the evolution of the logarithmic strain LE_{22}, **a** $\{\varphi_1, \Phi, \varphi_2\} = \{0°, 0°, 0°\}$ and **b** $\{\varphi_1, \Phi, \varphi_2\} = \{289°, 163.6°, 42.5°\}$

the deformation eventually localizes within a band. Interestingly, the inclination of the deformation band changes during the loading history due to the reorientation of the crystal.

Motivated by similar studies presented in [81], the influence of the boundary conditions indicated in Fig. 24.9 shall now be analyzed. Inspecting the respective force-displacement curves, depicted in Fig. 24.11a, only minor differences are observed for these two scenarios. In particular, the clamped condition leads to a slight increase of the required force at moderate elongations ($u_2 \leq 5$ mm) and to an earlier localization, compared to the free lateral contraction condition. Especially, the latter observation is also clearly visible in the evolution of the minimal specimen width, see Fig. 24.11b. Although the influence of the boundary condition is not as pronounced as reported in [81], the main characteristic, namely the earlier localization for the clamped condition is consistent with the results from the literature. The reason why the current simulation only shows a small sensitivity with respect to the boundary condition is that the reference case employed a double slip formulation, while the current model includes all primary slip systems of the fcc material. Moreover, inspecting the strain fields in Fig. 24.13 reveals that the clamped condition has significant influence only in the initial loading stages, where it leads to the development of a localization band immediately after plastic yielding—an effect that is absent in the free lateral contraction case. However, as the prescribed deformation is increased the strain fields become increasingly similar, although they differ in absolute values of LE_{22}.

Finally, it is worth emphasizing two aspects that pertain to all of the numerical tensile test studies. Firstly, although significant deformation increments can occur at the Gauss point level for elements within a developing deformation band, the material routine, in fact, did not require a reduction in the global time step. This again emphasizes the robustness of the augmented Lagrangian formulation, also in the context of inhomogeneous deformation states. Secondly, it is well-known that the formation of localization bands in the geometrically-induced softening regime leads to spurious mesh-dependencies of numerical results. The reason is that in *local* formulations—which lack the notion of an intrinsic length scale — localization zones degenerate to discontinuities surfaces, whose predicted widths solely depend on the spatial resolution of the finite element mesh. Generalized continuum formulations have been proposed in the literature that circumvent this problem and also naturally incorporate size effects, cf. [82–85] for gradient extended formulations and [86–89] for micromorphic formulations. However, the application of the proposed material model within the framework of a generalized continuum formulation is beyond the scope of the current contribution.

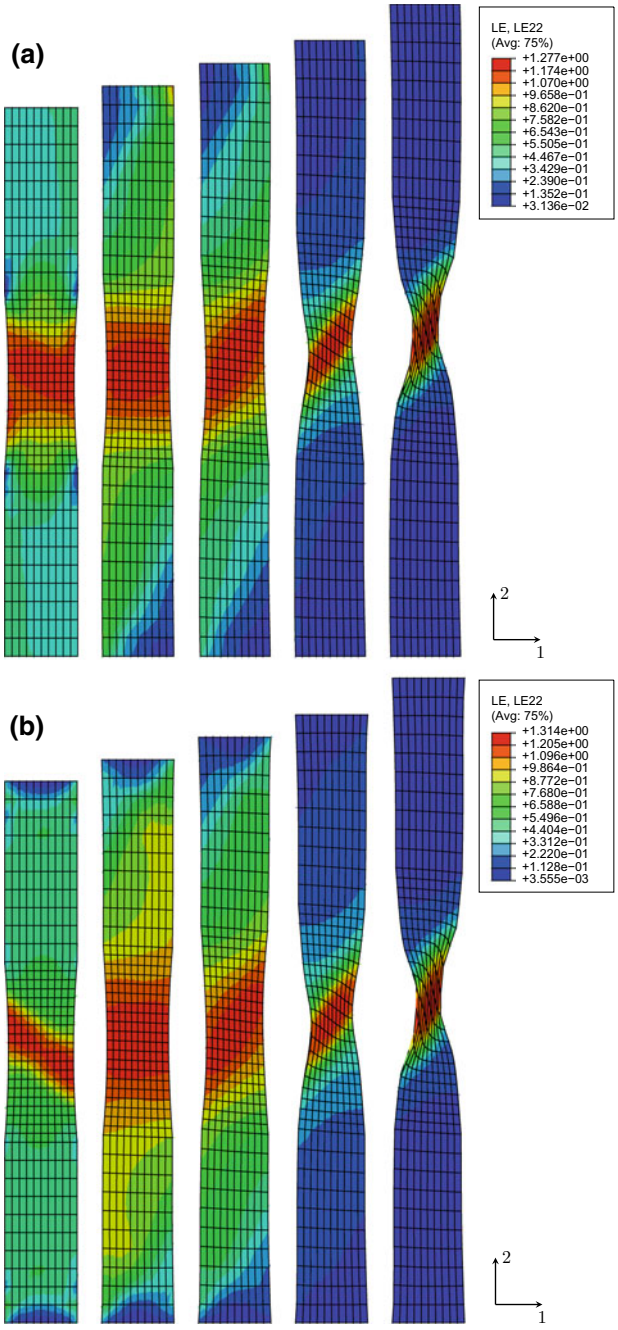

Fig. 24.13 Influence of the boundary conditions on the evolution of the logarithmic strain LE_{22} for an initial orientation $\{\varphi_1, \Phi, \varphi_2\} = \{0°, 45°, 30°\}$. **a** free lateral contraction and **b** clamped condition

24.5 Conclusions

In the current contribution, a material model for face-centered cubic single crystals, suitable for finite deformations, was discussed. Four different formulations were considered accounting for both rate-dependent and rate-independent flow behavior. Furthermore, a nonlinear anisotropic hardening law based on an interaction matrix has been incorporated, which accounts for the interaction of different slip systems in a phenomenological manner. The robustness of the corresponding stress update algorithms was assessed under homogeneous deformation states employing proportional and non-proportional loading histories. In the rate-independent case the augmented Lagrangian based formulation, originally proposed in [35], proved to be very robust, while the rate-dependent model adopted from [61] provided convincing results. However, increasing the complexity of the hardening law by choosing the parameters in the interaction matrix increasingly different from Taylor-type hardening, had a strong impact on the performance of the corresponding algorithms, resulting in a strong reduction of the prescribed deformation increment size. But this observation can readily be explained by the fact that such anisotropic interaction matrices induce an evolution of the shape of the elastic domain and not only its size, complicating the stress update considerably. Thus, the successful application of these two stress-update algorithms even in the case of anisotropic hardening emphasized their robustness.

In order to assess the performance of the rate-independent, augmented Lagrangian formulation under inhomogeneous deformations, an implementation of this model as a user-defined material subroutine (UMAT) into the finite element program ABAQUS has been employed in the simulation of a single crystalline, mildly notched tensile specimen. Herein, a strong influence of the initial orientation on the deformation and localization behavior was observed. Even during the formation of localization bands in the specimen—resulting in substantial deformation increments at the Gauss point level—an adjustment of the global time step was not necessary, confirming the robustness of the augmented Lagrangian formulation in connection with a Taylor-type hardening law also under inhomogeneous deformation states.

Having identified robust numerical frameworks for both the rate-dependent and the rate-independent case, current research efforts are focused on model extensions towards the inclusion of martensitic phase transformation and twinning by means of analytical homogenization approaches. Furthermore, a comparison with experimental results at the single crystal scale is sought, from which the constitutive parameters will be identified.

Acknowledgements The authors gratefully acknowledge the Deutsche Forschungsgemeinschaft (DFG, German Research Foundation) for funding the research in the framework of the Collaborative Research Center "TRIP-Matrix-Composite", (project number 54473466—SFB 799, subproject C10).

References

1. O. Bouaziz, H. Zurob, M. Huang, Steel Res. Int. **84**(10), 937 (2013)
2. T. Nanda, V. Singh, V. Singh, A. Chakraborty, S. Sharma, Proc. Inst. Mech. Eng. Part L J. Mater. Des, Appl. (2016)
3. C. Lesch, N. Kwiaton, F. Klose, Steel Res. Int. **88**(10), 1700210 (2017)
4. S. Martin, S. Wolf, U. Martin, L. Krüger, Solid State Phenomena **172–174**, 172 (2011)
5. S. Wolf, Temperatur- und dehnratenabhängiges Werkstoffverhalten einer hochlegierten CrMnNi-TRIP/TWIP-Stahlgusslegierung unter einsinniger Zug- und Druckbeanspruchung. Dissertation, Technische Universität Bergakademie Freiberg (2012) (in German)
6. S. Martin, Deformationsmechanismen bei verschiedenen Verformungstemperaturen in austenitischem TRIP/TWIP-Stahl. Dissertation, Technische Universität Bergakademie Freiberg (2013) (in German)
7. S. Wolf, S. Martin, L. Krüger, U. Martin, Mater. Sci. Eng.: A **594**, 72 (2014)
8. S. Martin, S. Wolf, S. Decker, L. Krüger, U. Martin, Steel Res. Int. **86**(10), 1187 (2015)
9. C. Ullrich, S. Martin, C. Schimpf, A. Stark, N. Schell, D. Rafaja, Adv. Eng. Mater. **21**(5), 1801101 (2019)
10. S. Prüger, A. Seupel, M. Kuna, Int. J. Plast. **55**, 182 (2014)
11. S. Prüger, Thermomechanische Modellierung der dehnungsinduzierten Phasenumwandlung und der asymmetrischen Verfestigung in einem TRIP-Stahlguss. Dissertation, TU Bergakademie Freiberg, Freiberg (2016) (in German)
12. A. Seupel, M. Kuna, in *XIV International Conference on Computational Plasticity. Fundamentals and Applications, COMPLAS 2017*, ed. by E. Oñate, D. Owen, D. Peric, M. Chiumenti (2017), pp. 576–587
13. S. Turteltaub, A. Suiker, Int. J. Solids Struct. **43**, 4509 (2006)
14. S. Turteltaub, A. Suiker, J. Mech. Phys. Solids **53**, 1747 (2005)
15. D. Tjahjanto, S. Turteltaub, A. Suiker, Continuum Mech. Thermodyn. **19**(7), 399 (2008)
16. D. Tjahjanto, S. Turteltaub, A. Suiker, S. van der Zwaag, Philos. Mag. **88**(28/29), 3369 (2008)
17. V. Kouznetsova, M. Geers, Mech. Mater. **40**(8), 641 (2008)
18. M. Lee, S. Kim, H. Han, Int. J. Plast. **26**(5), 688 (2010)
19. R. Stringfellow, D. Parks, G. Olson, Acta Metall. Mater. **40**(7), 1703 (1992)
20. S. Gupta, Micromechanical modeling of martensitic phase transformation in steels based on non-local crystal plasticity. Dissertation, Ruhr-Universität Bochum (2014)
21. S. Gupta, A. Ma, A. Hartmaier, Int. J. Solids Struct. **155**, 213 (2018)
22. R. Khan, F. Zahedi, A. Siddiqui, Proc. Manuf. **5**, 772 (2016)
23. R. Khan, T. Pervez, S. Qamar, Mech. Mater. **95**, 83 (2016)
24. C. Sun, N. Guo, M. Fu, S. Wang, Int. J. Plast. **72**, 186 (2016)
25. S. Wong, M. Madivala, U. Prahl, F. Roters, D. Raabe, Acta Mater. **118**, 140 (2016)
26. M. Madivala, A. Schwedt, S. Wong, F. Roters, U. Prahl, W. Bleck, Int. J. Plast. **104**, 80 (2018)
27. T. Park, L. Hector, X. Hu, F. Abu-Farha, M. Fellinger, H. Kim, R. Esmaeilpour, F. Pourboghrat, Int. J. Plast. (2019)
28. G. Olson, M. Cohen, Metall. Trans. A **6**(4), 791 (1975)
29. M. Zecevic, M. Upadhyay, E. Polatidis, T. Panzner, H. Van Swygenhoven, M. Knezevic, Acta Mater. **166**, 386 (2019)
30. F. Roters, P. Eisenlohr, L. Hantcherli, D. Tjahjanto, T. Bieler, D. Raabe, Acta Mater. **58**(4), 1152 (2010)
31. F. Roters, Advanced Material Models for the Crystal Plasticity Finite Element Method-Development of a general CPFEM framework. Habilitation (RWTH, Aachen, 2011)
32. F. Roters, M. Diehl, P. Shanthraj, P. Eisenlohr, C. Reuber, S. Wong, T. Maiti, A. Ebrahimi, T. Hochrainer, H.O. Fabritius, S. Nikolov, M. Friák, N. Fujita, N. Grilli, K. Janssens, N. Jia, P. Kok, D. Ma, F. Meier, E. Werner, M. Stricker, D. Weygand, D. Raabe, Comput. Mater. Sci. **158**, 420 (2019)
33. M. Knezevic, M. Zecevic, I. Beyerlein, R. Lebensohn, Comput. Meth. Appl. Mech. Eng. **308**, 468 (2016). https://doi.org/10.1016/j.cma.2016.05.025

34. A. Guery, F. Hild, F. Latourte, S. Roux, Mech. Mater. **100**, 55 (2016). https://doi.org/10.1016/j.mechmat.2016.06.007
35. M. Schmidt-Baldassari, Comput. Meth. Appl. Mech. Eng. **192**(11), 1261 (2003)
36. E. Busso, G. Cailletaud, Int. J. Plast. **21**(11), 2212 (2005)
37. O. Casals, S. Forest, Comput. Mater. Sci. **45**(3), 774 (2009)
38. S. Forest, M. Rubin, Eur. J. Mech. A. Solids **55**, 278 (2016)
39. E. Kröner, Arch. Ration. Mech. Anal. **4**(1), 273 (1959)
40. E. Lee, J. Appl. Mech. **36**(1), 1 (1969)
41. J. Mandel, Int. J. Solids Struct. **9**(6), 725 (1973)
42. C. Miehe, M. Lambrecht, Commun. Numer. Methods Eng. **17**(5), 337 (2001)
43. H. Ledbetter, S. Kim, in *Handbook of Elastic Properties of Solids, Liquids and Gases*, vol. 2, Chap. 8, ed. by M. Levy (Academic Press, Cambridge, 2001), pp. 107–122
44. S. Ranganathan, M. Ostoja-Starzewski, Phys. Rev. Lett. **101**, 055504 (2008)
45. R. Mahnken, Commun. Numer. Methods Eng. **21**(8), 405 (2005)
46. P. Franciosi, A. Zaoui, Acta Metall. **30**(8), 1627 (1982)
47. C. Miehe, Int. J. Solids Struct. **33**(20), 3103 (1996)
48. C. Miehe, J. Schröder, J. Schotte, Comput. Meth. Appl. Mech. Eng. **171**(3–4), 387 (1999)
49. C. Miehe, J. Schröder, Int. J. Numer. Methods Eng. **50**(2), 273 (2001)
50. L. Méric, G. Cailletaud, J. Eng. Mater. Technol. **113**(1), 171 (1991)
51. M. Khadyko, S. Dumoulin, G. Cailletaud, O. Hopperstad, Int. J. Plast. **76**, 51 (2016)
52. D. Bertsekas, *Constrained Optimization and Lagrange Multiplier Methods*. No. 4 in Optimization and Neural Computation (Athena Scientific, 1996)
53. A. Fischer, Optimization **24**(3–4), 269 (1992)
54. C. Kanzow, H. Kleinmichel, Comput. Optim. Appl. **11**(3), 227 (1998)
55. P. Perzyna, Revue de Physique Appliquée **23**(4), 445 (1988)
56. L. Méric, G. Cailletaud, M. Gaspérini, Acta Metall. Mater. **42**(3), 921 (1994)
57. C. Gérard, B. Bacroix, M. Bornert, G. Cailletaud, J. Crépin, S. Leclercq, Comput. Mater. Sci. **45**(3), 751 (2009)
58. F. Šiška, S. Forest, P. Gumbsch, D. Weygand, Modell. Simul. Mater. Sci. Eng. **15**(1), S217 (2007)
59. F. Šiška, D. Weygand, S. Forest, P. Gumbsch, Comput. Mater. Sci. **45**(3), 793 (2009)
60. C. Ling, B. Tanguy, J. Besson, S. Forest, F. Latourte, J. Nucl. Mater. **492**, 157 (2017)
61. A.M. Cuitiño, M. Ortiz, Modell. Simul. Mater. Sci. Eng. **1**(3), 225 (1993)
62. S. Prüger, B. Kiefer, A comparative study of integration algorithms for finite single crystal (visco-)plasticity (Submitted)
63. A. Bertram, M. Kraska, Arch. Mech. **47**(2), 203 (1995)
64. P. Steinmann, E. Stein, Comput. Meth. Appl. Mech. Eng. **129**(3), 235 (1996)
65. J. Schröder, C. Miehe, Comput. Mater. Sci. **9**(1), 168 (1997)
66. J. Raphanel, G. Ravichandran, Y. Leroy, Int. J. Solids Struct. **41**(22), 5995 (2004)
67. M. Ben Bettaieb, O. Débordes, A. Dogui, L. Duchêne, C. Keller, Int. J. Plast. **32-33**, 184 (2012)
68. H. Petryk, M. Kursa, Int. J. Numer. Methods Eng. **104**(3), 157 (2015)
69. H. Akpama, M. Ben Bettaieb, F. Abed-Meraim, Int. J. Numer. Methods Eng. **108**(5), 363 (2016)
70. H.J. Bunge, *Texture Analysis in Materials Science—Mathematical Methods* (Cuvillier Verlag, Göttingen, 1993)
71. J. Chaboche, Int. J. Plast. **24**(10), 1642 (2008)
72. T. Mánik, B. Holmedal, Int. J. Plast. **55**, 152 (2014)
73. Z. Bažant, B. Oh, ZAMM—J. Appl. Math. Mech. (Zeitschrift für Angewandte Mathematik und Mechanik) **66**(1), 37 (1986)
74. U. Kocks, C. Tome, H.R. Wenk, *Texture and Anisotropy*, 2nd edn. (Cambridge University Press, Cambridge, 2000)
75. D. Mohr, M. Oswald, Exp. Mech. **48**(1), 65 (2008)
76. R. McMeeking, Int. J. Solids Struct. **18**(3), 199 (1982)
77. A. Rieger, Zur Parameteridentifikation komplexer Materialmodelle auf der Basis realer und virtueller Testdaten. Dissertation, Universität Stuttgart (2005) (in German)

78. G. Scheday, Theorie und Numerik der Parameteridentifikation von Materialmodellen der finiten Elastizität und Inelastizität auf der Grundlage optischer Feldmeßverfahren. Dissertation, Universität Stuttgart, Stuttgart (2003) (in German)
79. I. Doghri, *Mechanics of Deformable Solids: Linear, Nonlinear, Analytical and Computational Aspects* (Springer, Berlin, Heidelberg, 2000)
80. C. Gérard, G. Cailletaud, B. Bacroix, Int. J. Plast. **42**, 194 (2013)
81. E. de Souza Neto, D. Peric, D. Owen, *Computational Methods of Plasticity* (Wiley, Hoboken, 2008)
82. S. Bargmann, B. Reddy, B. Klusemann, Int. J. Solids Struct. **51**(15–16), 2754 (2014)
83. M. Ekh, S. Bargmann, M. Grymer, Acta Mech. **218**(1–2), 103 (2011)
84. J. Mayeur, D. McDowell, Int. J. Plast. **57**, 29 (2014)
85. B. Kiefer, T. Waffenschmidt, L. Sprave, A. Menzel, Int. J. Damage Mech. **27**(2), 253 (2018)
86. S. Forest, in *Generalized Continua and Dislocation Theory: Theoretical Concepts, Computational Methods and Experimental Verification*, ed. by C. Sansour, S. Skatulla, CISM Courses and Lectures (Springer Vienna, Vienna, 2012), pp. 181–287
87. S. Forest, K. Ammar, B. Appolaire, N. Cordero, A. Gaubert, in *Plasticity and Beyond: Microstructures, Crystal-Plasticity and Phase Transitions*, ed. by J. Schröder, K. Hackl, C.I.S.M. International Centre, for Mechanical Sciences (Springer Vienna, Vienna, 2014), pp. 131–198
88. S. Wulfinghoff, E. Bayerschen, T. Böhlke, Int. J. Plast. **51**, 33 (2013)
89. G. Hütter, Int. J. Solids Struct. **110–111**, 15 (2017)

Index

H. Biermann and C. G. Aneziris (eds.), *Austenitic TRIP/TWIP Steels and Steel-Zirconia Composites*, Springer Series in Materials Science 298,
https://doi.org/10.1007/978-3-030-42603-3